ICF10

Honolulu (USA)

2001

Vol. C

ORAL/POSTER REFERENCE: ICF100862OR

FRACTURE TOUGHNESS AND FAILURE MECHANISM OF POLYMER–INTRODUCED POROUS HAP COMPOSITES

H. Suemasu[1], T. Wada[2], M. Aizawa[3], K. Gozu[1] and A. Nozue[1]

[1] Department of Mechanical Engineering, Sophia University,
Kioicho, Chiyodaku, Tokyo, Japan
[2] Graduate School, Sophia University.
[3] Department of Chemistry, Sophia University.

ABSTRACT

Polymer–introduced porous hydroxyapatite (HAp) is developed for a substituting material of human bones. Firstly, Methylmethacrylate monomer containing polymerization initiator is introduced into the open pores in the HAp ceramics under a reduced pressure. The monomer is polymerized inside the pore by heating it at 60°C for 48 hours. By using the above process, the polymethylmethacrylate, often used as a biocompatible polymer because of its stability in body fluids, well fills the pore of the porous HAp ceramics. ALP activity test and inplant test in rabbit bone show good biocompatibility of above HAp/PMMA composite. The effect of the molecular weight of PMMA polymer on the fracture toughness is studied by using compact tension (CT) test method. The toughness is improved by the introduction of the PMMA polymer into the pore compared to that of pure HAp ceramic. A large inelastic deformation is observed in the CT test before final failure. The toughness has not clear tendency about the molecular weight of the polymer. The toughening mechanism by introducing the compliant polymer is proposed. The estimated toughness agrees well with the toughness of the present composite.

Key Words

Biomaterial, HAp, PMMA, Toughness, Composite

Introduction

Hydroxyapatite (HAp) ceramic material attracts great attention as a bone substitute for its good biocompatibility, because it is same material as animal bone major ingredient. However, the properties of the HAp ceramic is not sufficient to use as bone substitute because of its high elastic modulus as well as low fracture toughness compared to the bone. If the high toughness and lower elastic modulus without loss of biocompatibility is attained, it will be a promising material for human artificial bone. Bonfield[1] developed

a polyethylene containing HAp particles and Kikuchi [2] proposed TCP/copoly-L-lactide composite.

By introducing biocompatible polymer into the porous HAp ceramic developed by Aizawa et al.[3], the tougher and more compliant composite was proposed[4]. In the present paper, the toughness measured is reported and the toughening mechanism is proposed.

Fabrication of HAp/PMMA composites

After formed to arbitrary shape by a pressure of 30~40MPa at a room temperature, the fibrous HAp particles was sintered to fabricate porous HAp ceramic at 1200°C for 5 hours. MMA monomer containing azobis (isobutyronitrile) (AIBN) was repeatedly introduced in the open pores of the HAp ceramic in Nitrogen gas condition. The introduced PMMA was polymerized inside the pores by heating at 60°C for 48 hours. The PMMA polymer filled well the pore as shown in Fig.1. The molecular weight of the PMMA was controlled by changing the amount of AIBN from 1/100 to 1/10000 to investigate the effect of the introduced polymer.

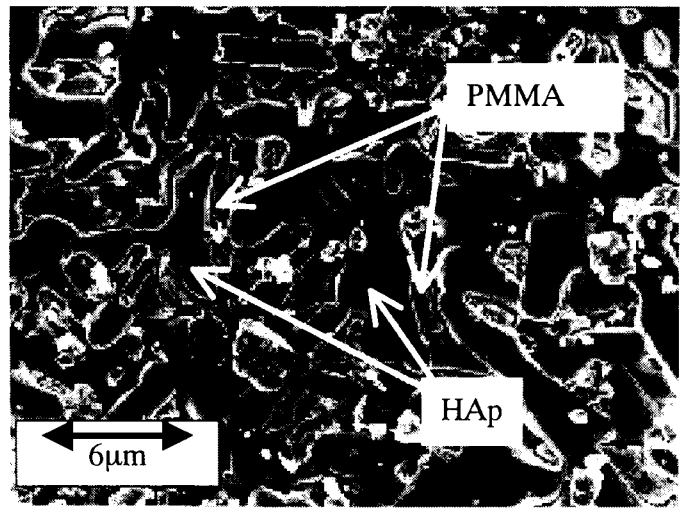

Fig.1 HAp/PMMA composite.

Experiment

The fracture toughness of the HAp/PMMA composite was measured following a standard test method (ASTM E399). A specimen for the fracture toughness test is shown in Fig.2. A relationship between the load and displacement is shown in Fig.3. There exists a quite large inelastic deformation before the final failure. The toughness was estimated by using maximum load and the original crack length following the equation given by the ASTM standard. It may underestimate real fracture toughness of the present material. The toughness obtained is plotted against the molecular weight of PMMA in Fig.4. The measured values are

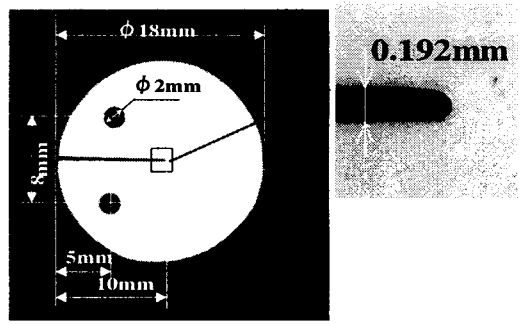

Fig.2 Test specimen (ASTM-E399)

about 1.5 $MPam^{1/2}$ throughout the molecular weight region tested. The results do not show evident dependence on the molecular weight.

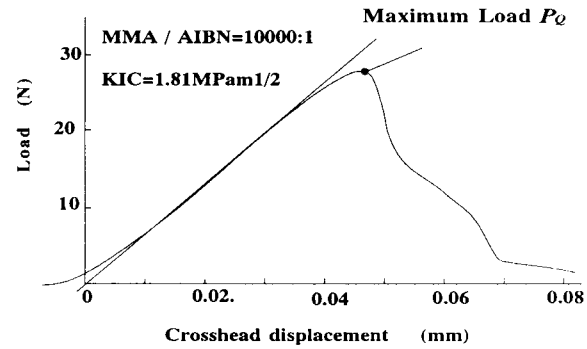

Fig.3 The relationship between the applied load and the displacement

Toughening mechanism and Toughness of HAp/PMMA composite

By introducing PMMA polymer in the open pores of the HAp ceramic, the composite becomes quite tough compared with the pure HAp ceramic. The material properties of HAp ceramic, PMMA polymer and present composite are shown in Table 1. The PMMA is very tough compared with the HAp ceramic with respect to the energy release rate. It is very important to clarify the toughening mechanism of the composite to improve the toughness.

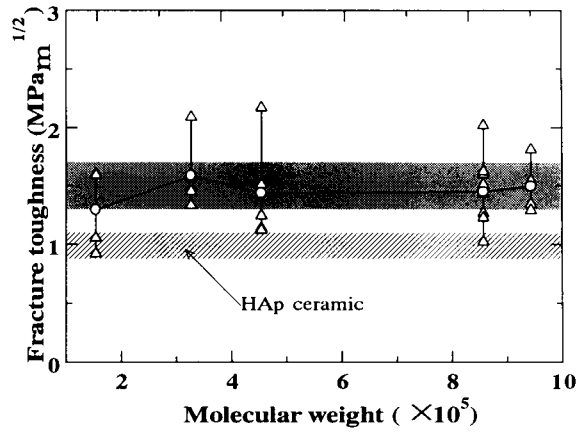

Fig.4 The toughness of HAp/PMMA composite and molecular weight of PMMA polymer.

Table 1

Material properties of HAp ceramics, PMMA polymer and HAp/PMMA composite

	HAp	PMMA	HAp/PMMA
Young's Modulus(GPa)	100	2.7～3.4	~50
G_C ($J\ m^{-2}$)	10	300～400	~45
K_C ($M\ Pa^{1/2}$)	1	0.9～1.4	~1.6
Strength (MPa)	-	500～750	-
Elongation (%)	-	2～10	-

First, we assume that the both materials absorb the mechanical energy at the fracture surface as they exist independently. This assumption corresponds to the case that the polymer size is sufficiently large compared to the inelastic region in the polymer just ahead of the crack tip as shown in Fig.5. In this case the absorbing energy may satisfy the rule of mixture and be expressed as

$$(G_C)_{\text{composite}} = (G_C)_{\text{HAp}} V_{\text{HAp}} + (G_C)_{\text{PMMA}} V_{\text{PMMA}} \tag{1}$$

where V_{HAp} and V_{PMMA} are volume fractions of HAp and PMMA, respectively. G_c is critical energy release rate. If the PMMA is perfectly introduced into the pore, $V_{\text{HAp}}+V_{\text{PMMA}}=1$. The Young's modulus is assumed to be expressed the following expression, which is based on the assumption that the cubic polymer is uniformly distributed in the HAp ceramic.

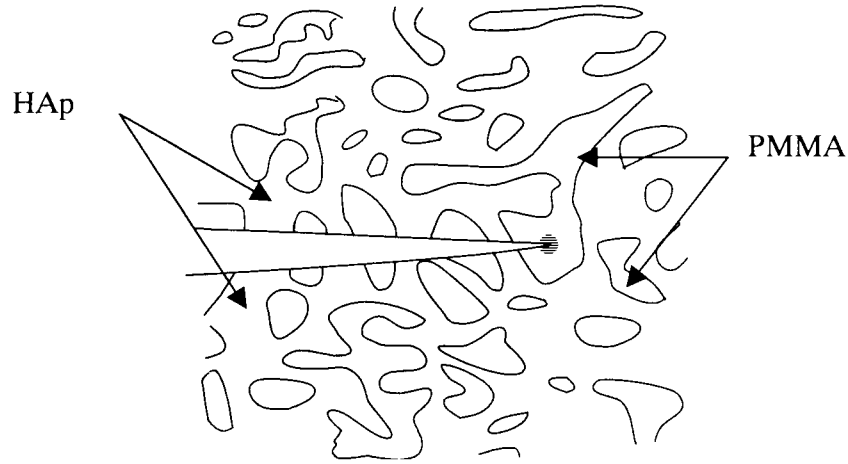

Fig.5 A failure model when the pour size is large compared with the inelastic region

$$E = \frac{1}{\dfrac{\sqrt[3]{V_p}}{E_p \sqrt[3]{V_p^{\,2}} + E_{HAp}\left(1-\sqrt[3]{V_p^{\,2}}\right)} + \dfrac{1-\sqrt[3]{V_p}}{E_{HAp}}} \tag{2}$$

The estimate of Young's modulus is more accurate than the simple rule of mixture. K_{Ic} can be obtained from the critical energy release rate G value and Young's modulus E.

$$K_{IC} = \sqrt{EG_C} \tag{3}$$

The estimated toughness and Young's modulus are plotted against the volume fraction of the HAp V_{HAp} in Fig.6. The estimated Young's modulus agrees well with the experimental results. However, the toughness is well below the estimated value, which might be thought to be a rough estimate of its lower bound because it is obtained without any consideration of complex coupling of the polymer and HAp ceramic in fracture process.

When the pore size is small and the polymer is ductile, the polymer bridges the crack surface as shown in Fig.7, because the strongly deformed region in front of the crack tip is larger than the pore size. The possible energy absorbed by a unit volume polymer is

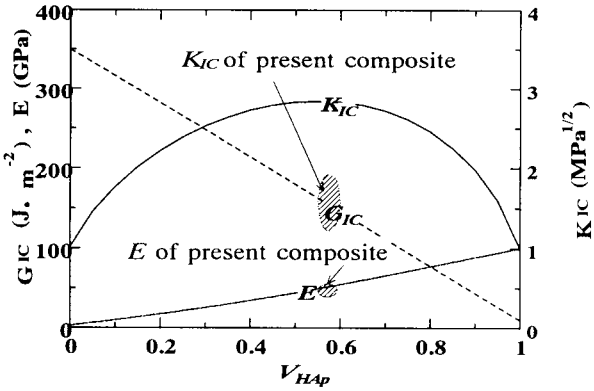

Fig.6 The estimated material properties with respect to volume fraction V_{HAp}.

$$U = \int_0^{\varepsilon_{max}} \sigma d\varepsilon \tag{4}$$

The average volume of a strongly deformed region of a bridging polymer may be written as

$$v = kd \times \pi d^2 / 4 = k\pi d^3 / 4 \tag{5}$$

where $\pi d^2/4$ and kd are the area and the length of the strongly deformed region of the polymer cut by the propagating crack as illustrated in Fig.7. The factor k may be a function of interface strength and size and shape of microstructure. The expected number of the bridging polymer may be given as

$$N = \frac{V_p}{\pi d^2 / 4} \tag{6}$$

The expected energy possible to be absorbed at the crack surface is given as

$$G_c = G_{HAp} V_{HAp} + NvU = G_{HAp} V_{HAp} + V_p kdU \tag{7}$$

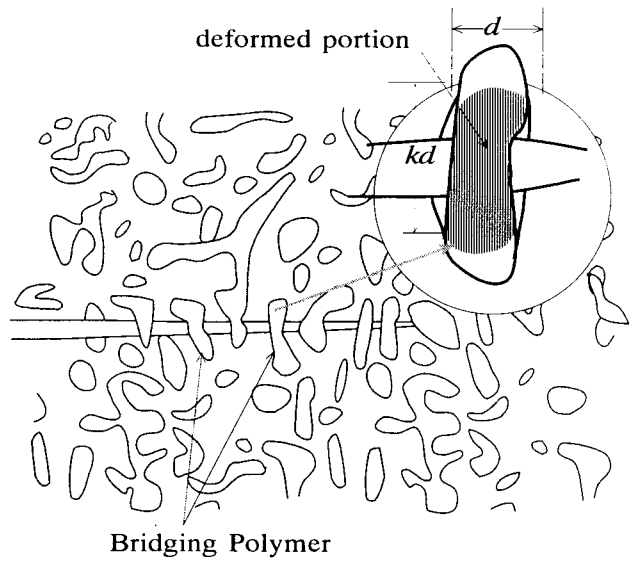

Fig.7 A Failure model with bridging polymers.

From the strength and elongation of the PMMA shown in Table 1, the energy absorbed by a unit volume U is estimated to be about 5×10^6. As the shape of the polymer filling the pore is not circle, size of the pore is difficult to say. Most of the polymer sizes in the SEM micrograph of Fig.1 are among 1~5μm. The estimated toughness by using the value $U=5\times10^6$ is plotted in Fig.8 against the polymer size d. Though the toughness of the present HAp composite 1.5~2 MPa/m$^{1/2}$ is a little higher than the estimated value, this theory well predicts the toughness of the HAp composite.

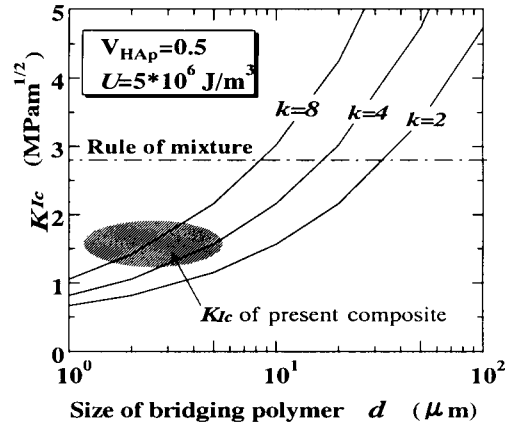

Fig.8 Effect of the size of the bridging polymer on the toughness

SUMMARY

A tough, low modulus and biocompatible composite material (1.5~2 MPam$^{1/2}$, about 50 GPa) is fabricated by introducing polymer into the open pores of porous hydroxyapatite. A toughening mechanism is proposed and the toughness estimated well agrees with the experimental results. The possibility of more toughening by increasing the pore size is suggested from the present theoretical .

ACKNOWLEDGEMENT

The present research is supported by the Japan Society for Promotion of Science.

REFERENCES

1. Bonfield W., An Introduction to Bioceramics(edited by L.L. Hench and J. Wilson), Vol.1, World Scientific, 1993.
2. Kikuchi M. et. al., J.Biomed. Mater. Res.(Appl. Biomater.) , 48, 1999, 108-110.
3. Aizawa M. et.al., J. Ceramic Society of Japan, 108, 2000, 249-253.
4. Aizawa M. et.al., Bioceramics, 12, 1999, 453-456.

ORAL REFERENCE: ICF100438OR

FRACTURE TOUGHNESS AND FRACTURE PROCESSES IN DUCTILE METALLIC FOAMS

C. Motz and R. Pippan

Erich Schmid Institute of Material Science,
Austrian Academy of Sciences, A-8700 Leoben, Austria

ABSTRACT

For structural applications of aluminium foams, besides tensile and compressive behaviour, fatigue and energy absorbing the fracture mechanic behaviour is important. Fracture mechanic tests were performed on compact tension (CT) specimens of sizes from W=50 mm to W=300 mm made of ALPORAS® foams with different densities. In addition to standard tests, in-situ fracture experiments in a scanning electron microscope were performed. Besides the load and the load line displacement also crack extension via a potential drop technique, crack tip opening displacement and local deformations were measured. The deformation is strongly localized on different length scales. In front of the notch root a fracture process zone with concentrated deformation develops. The crack propagates through the foam building many secondary cracks and crack bridges. The determination of fracture toughness values in terms of stress intensity factor K, J-integral and crack tip opening displacement is discussed. The comparison of the K vs. Δa (crack extension), J vs. Δa and COD vs. Δa with the actual fracture processes at the crack tip and load displacement response reveals that COD_5 gives the most reliable values to characterize the fracture toughness. The critical values for COD_5 range from 0.35 mm to 1.0 mm depending on the relative density of the foam.

KEYWORDS

metallic foams, cellular solids, fracture toughness, fracture processes, local deformation.

INTRODUCTION

In the last few years metallic foams, e.g. made of aluminium or magnesium alloys, have become commercially available due to improvements in the manufacturing processes. This new class of materials exhibits partly unusual mechanical properties compared to common metals. For successful design of load bearing structural elements, besides the well-investigated compression and energy absorbing behaviour [1-4], also the fracture behaviour and fracture toughness values are needed. Until now only a limited number of publications [5-7] addressing this topic are available. The aim of this investigation is to provide a closer look at fracture processes and the determination of fracture toughness values for these foams. Thus, standard fracture mechanic tests and additionally in-situ fracture tests in the scanning electron microscope were performed do determine fracture processes and fracture toughness values. For the tests, an ALPORAS® aluminium foam, which is commercially available, with different densities was used. Standard fracture mechanic parameters, like stress intensity factor K, J-integral and crack opening displacement COD, were

determined. All investigations were accompanied with local surface strain measurements, which show the development of the fracture process zone during crack initiation and crack propagation.

EXPERIMENTAL SETUP

Specimen preparation

All investigations were carried out on ALPORAS® aluminium foams with two densities, 0.25 g/cm^3 and 0.40 g/cm^3. Chemical composition, production route and material properties of these foams are described in [8]. Standard compact tension (CT) specimens with a size range of W=50 mm to W=300 mm and a thickness of B=30 mm were used. The specimens were machined with a diamond wire saw to avoid damage of the foam. All specimens had an open surface, whereby the average cell size of the foam was about 3.5 mm. For the pre-crack a diamond wire saw cut with a notch tip radius of about 150 µm was used, which gave undistinguishable experimental results compared to specimens pre-cracked in fatigue (see also [9]).

Standard fracture mechanic tests

Standard fracture mechanic tests were carried out on a displacement controlled universal mechanic testing machine at room temperature and at a cross-head speed of 0.2 mm/min for specimen sizes W≤100 mm and 0.5 mm/min for W>100 mm. The load and the load line displacement were measured with a standard load cell and a clip gauge, respectively. Additionally, the crack or notch opening displacement (COD) was determined with a videoextensiometer 5 mm behind the initial crack tip. The crack extension was monitored by a potential drop technique and was verified by optical observations. Images from the foam surface were taken at different load line displacements with a CCD-camera at a resolution of 1528x1146 pixels and were used for local surface deformation measurements and for documentation of the crack extension, subsequently. The procedure for local deformation measurements is described in detail in [10].

In-situ experiments

In order to investigate crack initiation, crack propagation and local deformations during crack growth, in-situ fracture tests in the scanning electron microscope (SEM) were performed. Due to the restricted space inside the SEM the specimen size is limited to W=50 mm and B=25 mm. A small in-situ loading device, with a displacement rate of 0.15 mm/min, was used to fracture the CT-specimens. In order to assign the different stages of the fracture process to the load versus load line displacement curve, the load and the displacement were measured too. Images from the foam surface, containing 1 to 6 cells, with a resolution up to 4000x3200 pixels were taken at different load line displacements. Subsequently, these images were analysed to measure crack extension, local deformations and to identify the fracture processes.

RESULTS AND DISCUSSION

Standard fracture mechanic tests

Due to the somewhat unusual mechanical behaviour of ductile metallic foams, e.g. a marked stress plateau in compression, a deformation dependence of the Young's modulus or strain localisation during deformation, also in the fracture mechanics tests some atypical effects can be expected. Fig. 1 shows a typical load F and crack extension Δa versus load line displacement v_{LLD} curve and a corresponding surface deformation map for a foam with a density of 0.40 g/cm^3. It is evident from the load curve that these foams reveal only a very small linear elastic stage, followed by an extended plastic regime. The plastic deformation is strongly localised in a fracture process zone (FPZ), which can bee seen in the surface strain maps and can result in micro cracking of some high strained cell walls. In the region of the peak load a main crack starts from the notch root and propagates in a relatively large FPZ through the specimen, whereby the load decreases. This is usually accompanied with a characteristic kink in the crack extension curve, followed by a regime of larger crack growth rate. Both, the load and the crack extension curve, show in the region of stable crack growth a certain waviness, which is related to the inhomogeneous structure of the foam and results in a variation in the local crack growth resistance.

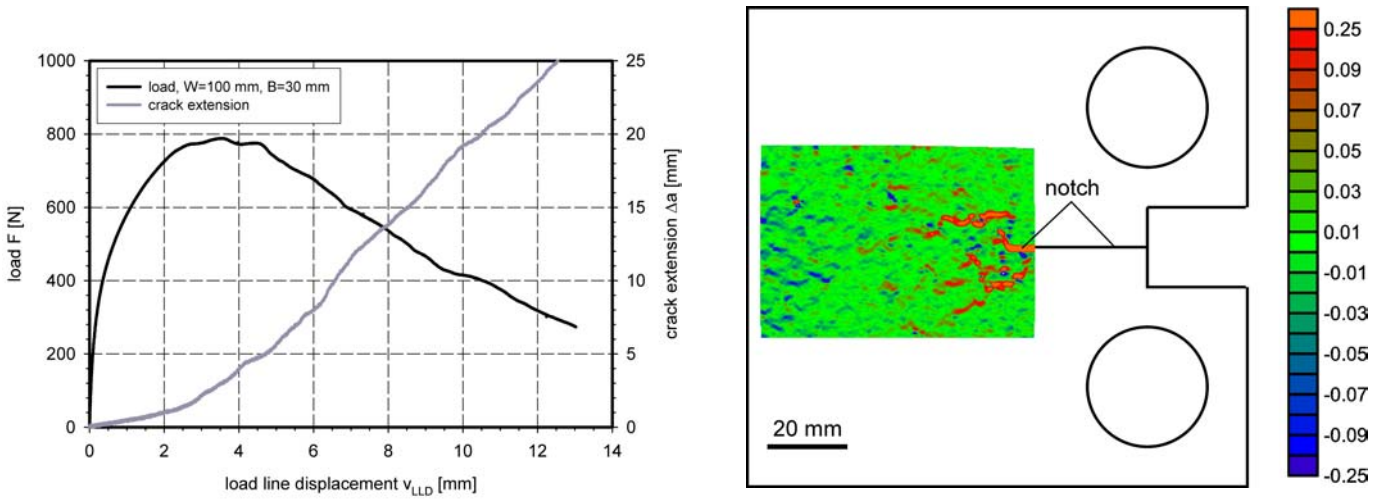

Figure 1 Load and crack extension versus load line displacement curve (left image) and corresponding surface strain map at a crack extension of 5 mm (right image, ε=x100%) for an ALPORAS® aluminium foam CT-specimen with a density of 0.40 g/cm^3, W=100 mm and B=30 mm.

Because of the wide plastic regime in the load versus load line displacement curve no valid fracture toughness values in terms of the critical stress intensity factor K_{IC} according to ASTM E399 could be obtained with the specimen sizes used in this investigation. The calculated K_Q values are relatively low and vary between 0.35 to 1.0 MPa·m$^{1/2}$ depending on the density of the foam. Fig. 2 shows K versus crack extension Δa curves for two foams with different densities. Both foams reveal an increase of the fracture toughness with crack propagation up to a crack extension of about 5 mm (it looks like a R-curve behaviour). This toughness enhancement with increasing Δa is caused by plasticity, but also toughening mechanisms like crack bridging [6] and the formation of a FPZ containing localised yielding and micro cracking may contribute. In the region of larger crack extensions a decrease of K can be observed, which is dramatically in the case of the lower density foam. The "softening mechanisms" that are causing this drop in K (and also in the plastic limit load ratio F/F_Y) are not clear until now.

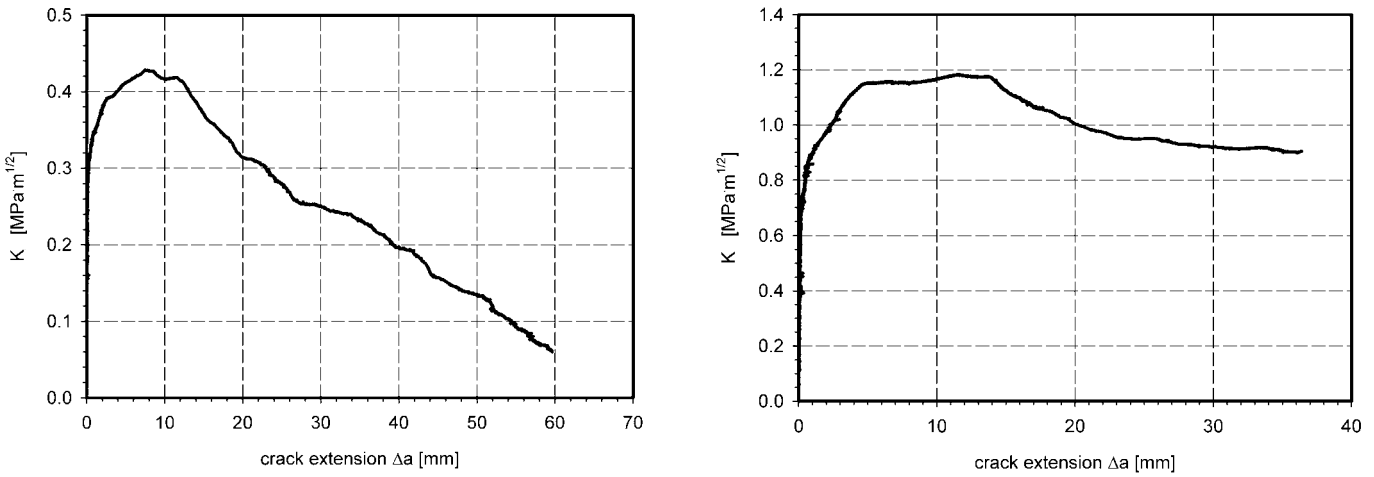

Figure 2 Stress intensity factor K versus crack extension Δa curve for two foams with a density of 0.25 g/cm^3 (left image) and 0.40 g/cm^3 (right image). CT-specimens with W=290 mm and B=30 mm were used.

Fig. 3 shows the load - plastic limit load ratio versus load line displacement plots for the same two foams as depicted in Fig. 2. Also in the load - plastic limit load ratio F/F_Y (load divided by the corresponding plastic limit load) curves a significant drop in the region of larger crack extensions (or larger load line displacements) can be observed. Especially the lower density foam (0.25 g/cm^3) reveals a dramatically drop in the plastic limit load ratio. It seems that both foams do not reach the stage of full plastification (F/F_Y=1). But due to the very small linear elastic regime of these foams it is difficult to measure the yield stress σ_y. So

the absolute values of the F/F_Y ratios depend on the chosen yield stress and may differ slightly, if $\sigma_{0.1}$, $\sigma_{0.2}$ or $\sigma_{0.5}$ are used for the yield strength.

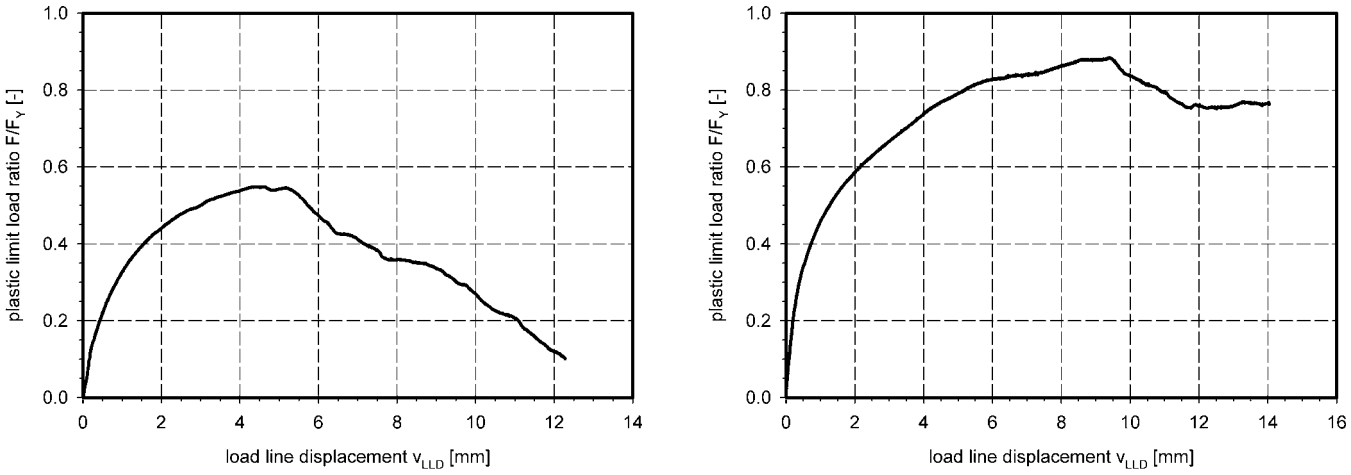

Figure 3 Plastic limit load ratio F/F_Y versus load line displacement curves for the two foams, which are depicted in Fig. 2. Left image shows the foam with the density of 0.25 g/cm^3 and the right image the foam with 0.40 g/cm^3.

Since valid fracture toughness values based on K_{IC} could not be obtained in these tests, single specimen J-integral determinations according to ASTM standard E813 and E1152 were performed. Fig. 4 shows J-integral versus crack extension plots for different specimen sizes and different foam densities. Although in all J-integral tests the specimen size criterion was fulfilled, a certain size dependence of the initial J-value $J_{0.2}$ and the J-curve can be observed. Furthermore, the initial part of the J-integral curves shows an atypical shape and a large scatter, which makes the determination of initial J-values, like J_i or $J_{0.2}$, according to the standards difficult or impossible. A typical plateau in the J-integral curves that is associated with a steady state J-value J_{SS}, as reported in [6], cannot be observed in all samples. For the foams with lower densities a decrease in the J-integral curve at large crack extensions is evident. This is in agreement with the previous observations in the K vs. Δa and F/F_Y vs. v_{LLD} curves. In general, the application of ASTM standards (E813, E1152), which are designed for solid metals, to metallic foams is problematic. Due to their special mechanical behaviour, metallic foams exhibit a different response in the fracture mechanic tests as assumed in common standards.

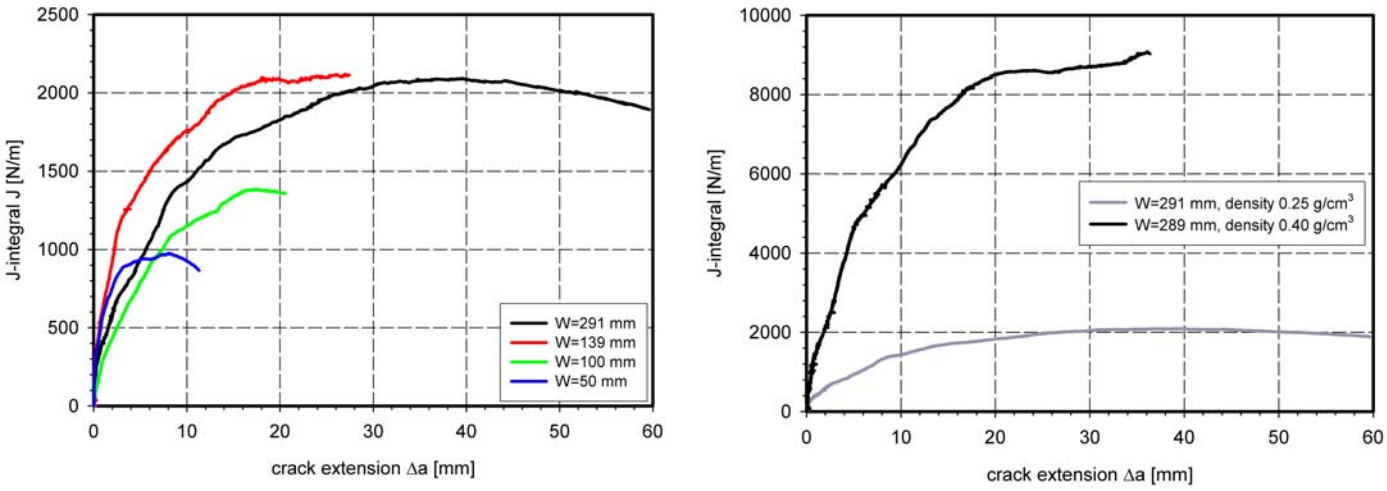

Figure 4 J-integral versus crack extension plots for different specimen sizes and at a constant density of 0.25 g/cm^3 (left image) and for different densities at constant specimen size (right image).

The described methods calculate from the global mechanical response the fracture toughness values (stress intensity factor K, J-integral). A more direct method is provided by the crack opening displacement (COD) concept. In this investigation the COD_5 value is used, which is measured 5 mm behind the initial crack tip or

notch root [11]. Fig. 5 shows COD_5 and CTOD (crack "tip" opening displacement, which is determined 5 mm behind the actual crack tip; in our case this corresponds to 1.5 times the mean cell diameter) versus crack extension curves for two foams with different densities. It was found that the COD_5 curves show a characteristic kink at low crack extensions (about ½ of the mean cell diameter), which can be associated with an "initial" fracture toughness value. The CTOD curves that deliver an actual fracture toughness value did not show a decrease at larger crack extensions, which is in contrast to the K vs. Δa and J vs. Δa curves. It seems that the possible softening mechanisms do not influence the resistance against crack propagation in terms of CTOD or crack tip opening angle, but have an impact on the general mechanical behaviour of the CT-specimens. Further detailed investigations are needed to identify the softening mechanisms and to find an approbate method for the determination of fracture toughness values in terms of J.

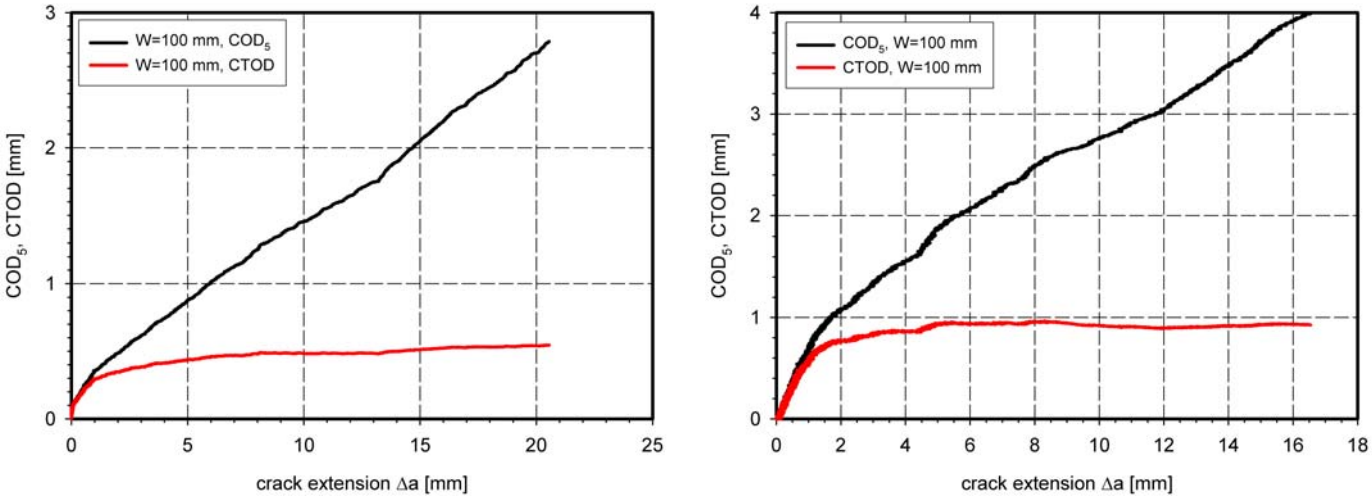

Figure 5 COD_5 and CTOD versus crack extension curves for two foams with different densities, 0.25 g/cm^3 (left image) and 0.40 g/cm^3 (right image).

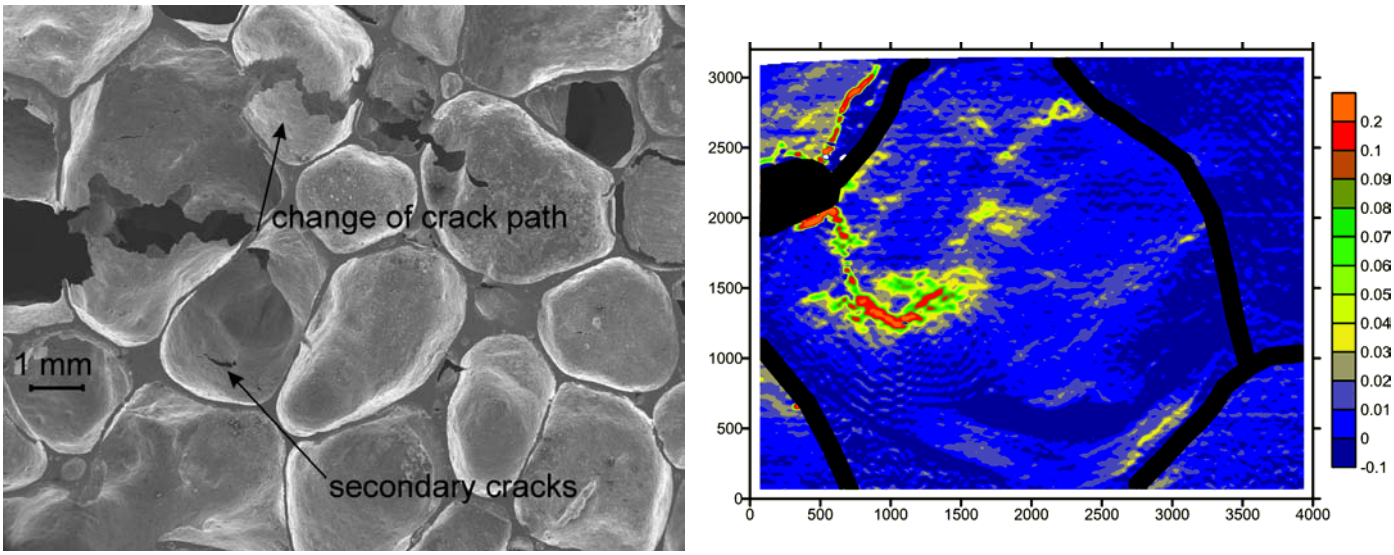

Figure 6 SEM micrograph from the region in front of the notch root of an in-situ cracked CT-specimen after a crack extension of about 6 mm (left image) and local in-cell-wall strain map from the first cell in front of the notch root at crack initiation, showing the plastic zone (right image, 4000 pixels are equivalent 3.3 mm). Strains are given in loading direction, ε=x100%, and the black lines mark the boundaries of the cells.

In-situ fracture tests

With a small loading device in-situ fracture tests in the scanning electron microscope (SEM) were performed to investigate the fracture processes. Loading of the specimen results in a very early, inhomogeneous plastic deformation of the foam. The strains are localised on different length scales. On the lower level, the cell walls, only some small regions in the walls are deformed, whereby the rest remains nearly undeformed. An

example is depicted in Fig. 6. On the higher length scale, the cell structure, only few weaker cells show larger deformations (see Fig. 1). With increasing load a fracture process zone develops in front of the notch root, which contains localised plastic yielding and micro cracking. At about 80% of the peak load a main crack starts from the notch root to propagate through the foam structure. This is accompanied by building of crack bridges up to 1 - 3 cell sizes behind the crack tip and by micro cracking of cell walls in the FPZ (see Fig. 6). The crack follows the path of lowest fracture resistance, which is in general the path with the thinnest cell walls.

CONCLUSION

Standard fracture mechanic tests based on the stress intensity factor, the J-integral and the COD concept were performed on ALPORAS® aluminium foams with different densities. Additionally, in-situ fracture tests in the SEM and local surface deformation measurements were carried out. The surface strain measurements reveal a very localised deformation of the foam on different length scales. During the crack growth a large fracture process zone develops, which contains localised plastic yielding and micro cracking of several cell walls. Due to the very small linear elastic part in the load versus load line displacement curve no valid K_{IC} values according to ASTM E399 could be obtained. Although all performed J-integral tests were valid, the standard determination of fracture toughness values in terms of an initial J-value is not useful. The ASTM standards are optimised for solid metals and their application to ductile metallic foams is usually not possible and they should be adapted to the special properties of the foams. It was found that measurements of crack opening displacement in terms of COD_5 gives a better approach to useful fracture toughness values.

ACKNOWLEDGEMENT

The financial support by the Austrian Fonds zur Förderung der wissenschaftlichen Forschung and of the Österreichischen Nationalbankfonds (Project P13231PHY/FWF535) is gratefully acknowledged.

REFERENCES

1. H. Bart-Smith, A.-F. Bastawros, D. R. Mumm, A. G. Evans, D. J. Sypeck, H. N. G. Wadley, (1998) Acta Mater. 46, 10, 3583-3592
2. H. Fusheng, Z. Zhengang, G. Junchang, (1998) Metall. and Mat. Trans. 29A, 2497-2502
3. R. Gradinger, F. G. Rammerstorfer, (1999) Acta Mater. 47, 1, 143-148
4. E. Andrews, W. Sanders, L.J. Gibson, (1999) Mat. Science and Eng. A270, 113-124
5. Y. Sugimura, J. Meyer, M.Y. He, H. Bart-Smith, J. Grenstedt, A.G. Evans, (1997) Acta Mater. 45, 12, 5245-5259
6. O.B. Olurin, N.A. Fleck, M.F. Ashby, (2000) Mat. Science and Eng. A291, 136-146
7. C. Motz, R. Pippan, Proc. ECF13, M. Fuentes, M. Elices, A. Martin-Meizoso & J.M. Martinez-Esnaola, Eds., Elsevier Sciences (2000), 160c1.pdf (CDROM), 1-8
8. T. Miyoshi, M. Itoh, S. Akiyama, A. Kitahara, (2000) Adv. Eng. Materials 2, No. 4, 179-183
9. K.Y.G. McCullough, N.A. Fleck, M.F. Ashby, (1999) Acta Mater. 47, 2331-2343
10. A. Tatschl (2000), Neue experimentelle Methoden zur Charakterisierung von Verformungs-vorgängen, Ph.D. thesis, University of Leoben, Austria
11. K.H. Schwalbe, A. Cornec, Fatigue of Eng. Mat. (1991), 14, 405-412

Fracture toughness characterization of hydrogen embrittled Cr-Mo steel

Yoru WADA and Yasuhiko TANAKA[1)]

1)Muroran Research laboratory, The Japan steel Works,ltd
4-Chatsu machi Muroran city, Hokkaido, 051-8505 JAPAN

ABSTRACT

Since pressure vessels for petroleum use are operated at high temperature high pressure hydrogen gas, it is a special concern whether a crack at a stressed region grow by internal hydrogen embrittement (I.H.E.) mechanism during shutdown low to temperature ambience. In this study, fracture mechanics tests were conducted to clarify how hydrogen assisted crack of 2.25Cr-1Mo steels grows under I.H.E. condition. Hydrogen was pre-charged inside of the steel by high pressure, high temperature hydrogen autoclave and tests were conducted at room temperature air ambience. As a result, for the majority of steels tested, the stress intensity factor at hydrogen crack growths by I.H.E. mechanism were very low at initiation (=K_{IH}~30MPa·$m^{1/2}$)) and grows faster if an active, rising load was applied. The old 60's made generation steel, which has higher temper embrittlment susceptibility, exhibited a higher crack velocity and resulted in fast fracture (K_{IC-H}) during rising loading. On the contrary, if a load was applied for a static, fixed crack mouth displacement manner (i.e. falling load condition), the crack velocity significantly decreased and finally stopped to give a higher threshold stress intensity factor (=K_{th}) except for higher strength steel. Higher strength steel (; Enhanced 2.25Cr-1Mo grade material) tended to continue to propagate despite under fixed displacement condition and falls on to a very low K_{th}.

KEYWORDS

I.H.E., Hydrogen charging, 2.25Cr-1Mo steel,K_{IH}, K_{IC-H}, K_{th}

INTRODUCTION

In the pressure vessel with overlay or attachment of stainless steel inside of the wall, a high stress may be arised at discontinuous and complex structure area due to thermal expansion mismatch between stainless steel

(SS) and base Cr-Mo steel. Furthermore, when pressure vessel cooled down to ambient temperature, hydrogen atoms absorbed inside of the Cr-Mo steel rather accumulates between interface of SS and Cr-Mo steel than degassing outside of the wall which may cause disbonding or initiation of hydrogen embrittled cracking. Figure 1 shows the calculation example of shutdown procedure. It is shown from the analysis that the crack at welded structure driving force arises at stainless structure welded area. Therefore, special attention should be paid whether the crack at the interface of stainless steel and Cr-Mo base initiates and penetrates through wall, which may cause final collapse of the entire vessel. In this study, fracture mechanics tests were conducted to investigate how hydrogen assisted cracking of 2.25Cr-1Mo steels grows by I.H.E. mechanisms examining loading method, materials toughness level and steel strength.

NOMENCLATURE

RL :Rising load

CD :Constant Displacement

K_{IH} :Stress intensity for onset of subcritical crack growth

K_{th} :the threshold intensity factor for hydrogen charging environment.

K_{IC-H}:material toughness measured in the hydrogen charging environment.

MATERIALS

Table 1 shows chemical composition of steels tested. Impurities Si, P and Sn were intentionally added to simulate the old temper embrittled steel controlling J-factor=(Si+Mn)x(P+Sn)x10^4 wt% level. After hot rolling, those heats were subjected to the quenched and tempered heat treatment + PWHT at 690°C for 8hrs. followed by step cooling. Table 2 shows mechanical properties. Low J steel is the new generation made steel with high fracture toughness at room temperature. Mid J and High J steels were temper embrittled by step cooling. The compact tension specimen were machined and Ni/Au were plated to prevent hydrogen degassing from inside of the steel. Hydrogen were charged in autoclave at 420°C, 12MPa for 48hrs followed by water quenching to room temperature and preserved in liquid nitrogen container until fracture mechanics test in air environment.

CRACK GROWTH BEHAVIOR

Effect of loading condition

Slow rising load (:RL) and constant displacement(:CD)loading method (Figure 2) were applied on hydrogen crack growth testing. Load was controlled by Crack Mouth Opening Displacement(CMOD) with a speed of 0.00003mm/sec. efficacious for hydrogen embrittlement [1)]. Crack was monitored by D.C. potential drop method. Figure 3 shows typical result of RL+CD test. Crack initiation was occurred after 3hrs of a rising load test. Continuous propagation was observed during rising load applied. After CMOD kept constant, the crack growth rate decreased and finally stopped after 12hrs.. Figure 4 shows the repetitional RL and CD test. Subsequent imposing of rising load obviously enhances crack growth, whereas crack growth was deactivated by keeping CMOD constant. Finally, a remarkable increase in crack growth observed in the later RL stage and resulted in fast fracture.

K and da/dt relation

Typical relationship between K and crack growth rate (da/dt) for 610MPa tensile strength steel is shown in Figure 5. Under RL condition, crack start to grow rapidly at low initiation point K_{IH}, and continue to propagate at relatively constant speed of 10^{-4}mm/sec order of magnitude for K_I level ranging from 30 to 80MPa·$m^{1/2}$. After CMOD kept constant, K_I and da/dt relationship can be drawn as steeper falling line, which finally reaches threshold slightly decreasing from holded K_I. Since repetitional RL+CD result indicate that crack stops at any holded K_I level ($<K_{IC-H}$), threshold K_{th} may exist in between K_{IH} and K_{IC-H} affected by the holded CMOD value.

Effect of temper embrittlement

K_{IH} were measured by RL condition for a temper embrittled old and newer high toughness heats and were plotted as a function of its material's FATT in Figure 6. Regardless of FATT of its heat, majority of steels exhibits low initiation sensitivity of cracking; K_{IH}=30MPa·$m^{1/2}$. K-curves for Low J and Mid J steels are compared in Figure7. Initiation occur at low K_I point in two heats, but cracking resistibility is higher for low J steel, whereas Mid J steel cracking propagates in low K_I and led to K_{IC-H}. Fracture appearances are compared in Figure 8. Intergranular cracking was dominant in Mid J steel whereas LowJ steel heat exhibits almost quasi-cleavage with some intergranular fracture surfaces. Although difference in fracture surfaces recognized, the role of hydrogen on the initiation kinetics should still to have to be studied.

Effect steel strength level

Crack growth measurement of RL+CD tests were conducted for enhanced and annealed heat and results are shown together in Figure 9. Three heats show entirely different cracking characteristics respectively where the enhanced heat exhibited a very aggressive propagation under long term CD condition, on the other hand, the only little cracking was observed in the annealed heat. These tendency indicates that the higher strength steel is susceptible to delayed type cracking under static CD condition falls on to lower K_{th} and lower strength steel as well as was already suggested by the previous studies.[2)]

SUMMARY

Crack growth characteristics for a variety of 2.25Cr-1Mo steels were clarified and summarized. Schematic illustration of K and da/dt relationship is shown in Figure 10.

1. Imposing of active rising load obviously enhances crack initiation and growth rate, whereas crack growth was deactivated by keeping CMOD constant.
2. Crack start to grow rapidly at low initiation point K_{IH}, and continue to propagate at relatively constant speed and as K_I level increases, fast fracture occurs at K_{IC-H}.
3. Initiation of cracking KIH did not make much difference in temper embrittled and new high toughness steel. But cracking resistibility is higher for low J steel, whereas Mid J steel propagates cracking in low K_I and reached K_{IC-H}.
4. The higher strength steel is susceptible to delayed type cracking under static CD condition falling on to lower K_{th} and lower strength steel as well as was already suggested by the previous studies.

REFERENCES

1) J.Watanabe, T.Ishiguro, T, Iwadate and K.Ohnishi(1987), *Hydrogen Embrittlement of 21/4Cr-1Mo and 3Cr- 1Mo- 0.25V-B Pressure Vessel Steels*",presented at API/MPC Task Group Meeting on Materials for Pressure Vessels May 1987

2) W.E.Erwin and J.G.Kerr(1982);WRC Bulletin 275,2

Table1 Chemical compositions(wt%) and mechanical properties of steels tested

Steel	C	Si	Mn	P	S	Cr	Mo	Sn	Sb	J-factor	FATT ℃	TS MPa
Low J	0.14	**0.08**	**0.55**	**0.005**	0.0007	2.42	1.08	**0.010**	0.0011	95	**-76**	613
Mid J	0.15	**0.25**	**0.55**	**0.015**	0.0013	2.39	1.03	**0.024**	0.0009	312	**6**	623
Annealed	0.15	0.24	0.53	0.013	0.0013	2.45	1.02	0.022	0.0006	270	7	**552**
Enhanced	0.16	0.28	0.40	0.009	0.0150	2.16	1.01	0.004	0.001	88	4	**668**

J-factor=(Si+Mn)X(P+Sn)x10^4

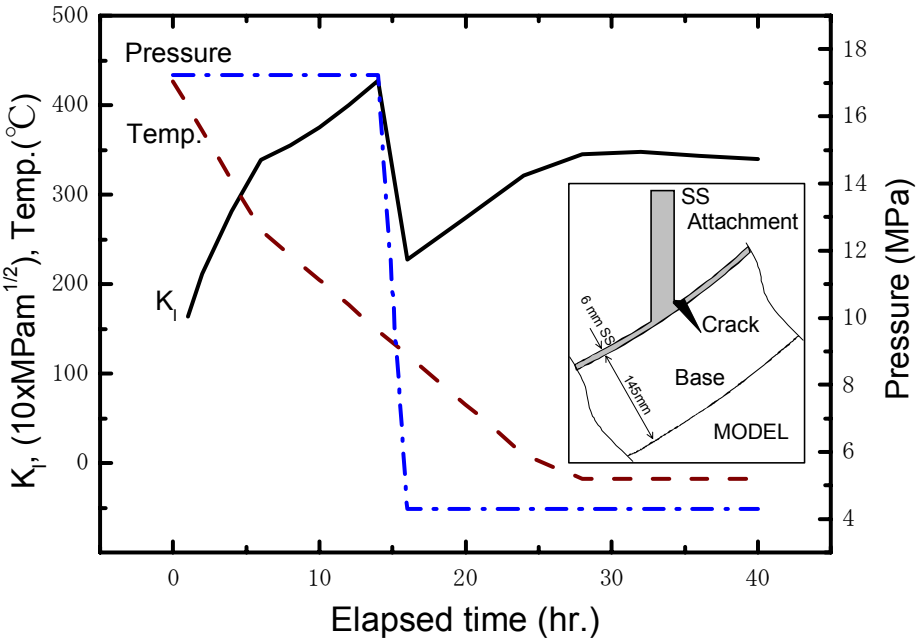

Figure 1 Example of shutdown temeperature, pressure and calculated result of crack loading at a bottom shell section with a stainless attachment

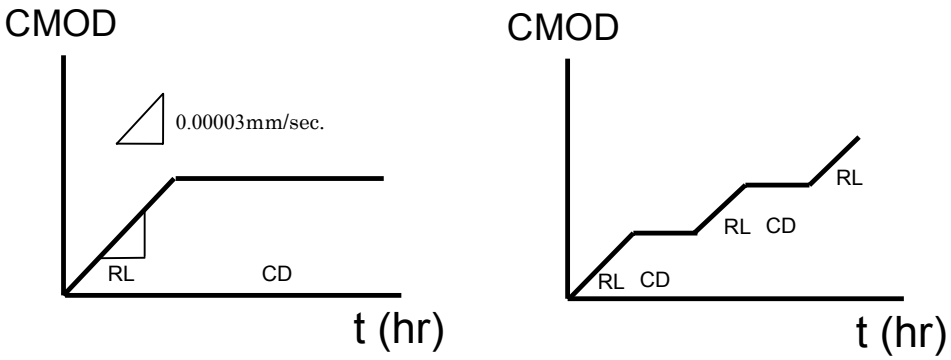

Figure 2 Loading pattern for hydrogen embrittlment fracture mechanics test

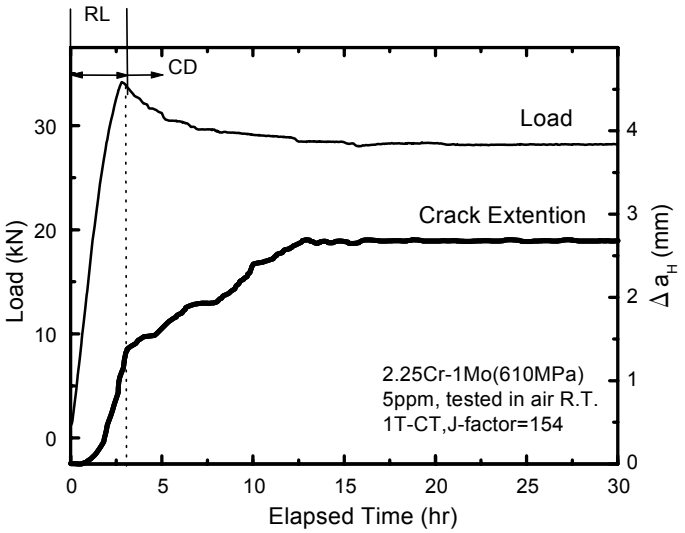

Figure3 Typical crack growth behavior of RL+CD test

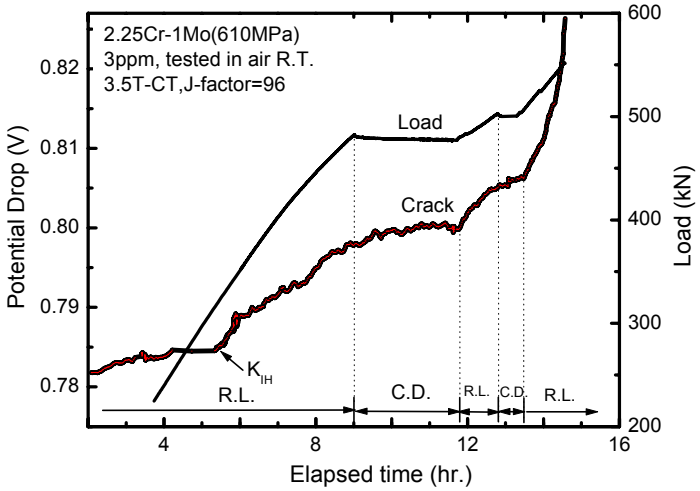

Figure 4 Crack growth behavior of repetitional RL and CD loading

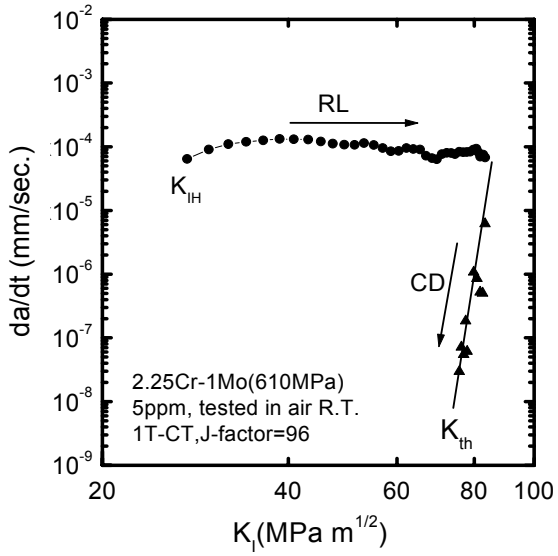

Figure 5 K and da/dt relationship of a RL+CD test

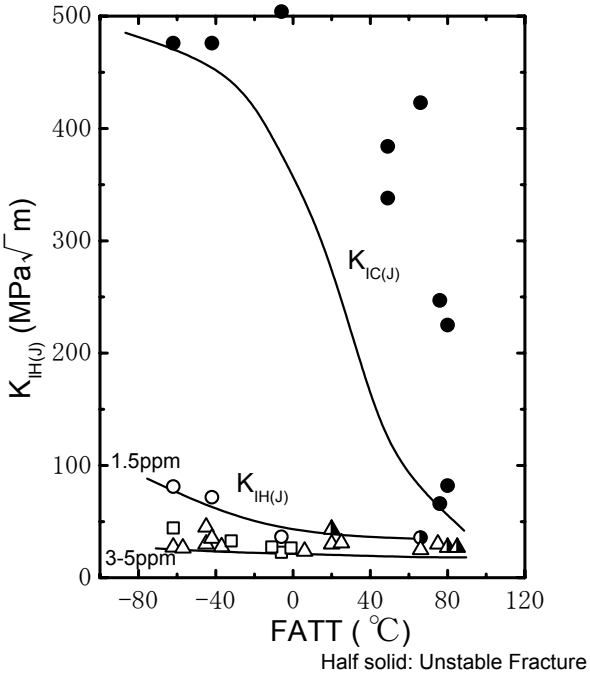

Figure6 K_{IH} and K_{IC} for a variety of temper embrittled steels

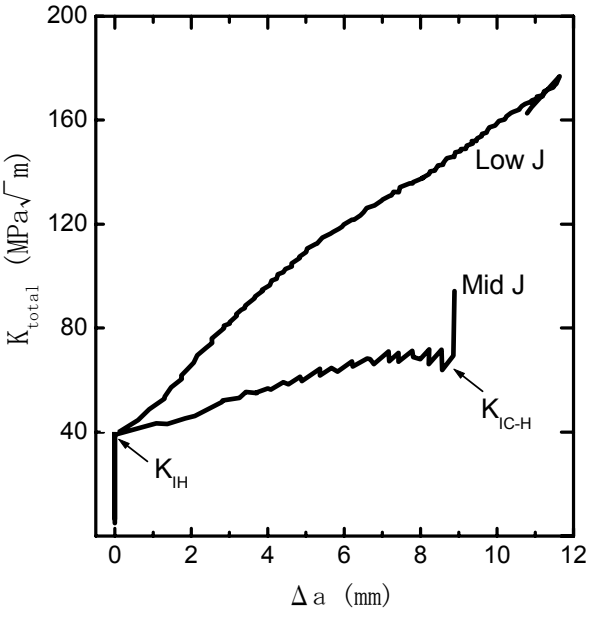

Figure 7 K-curves of Mid J and Low J heats

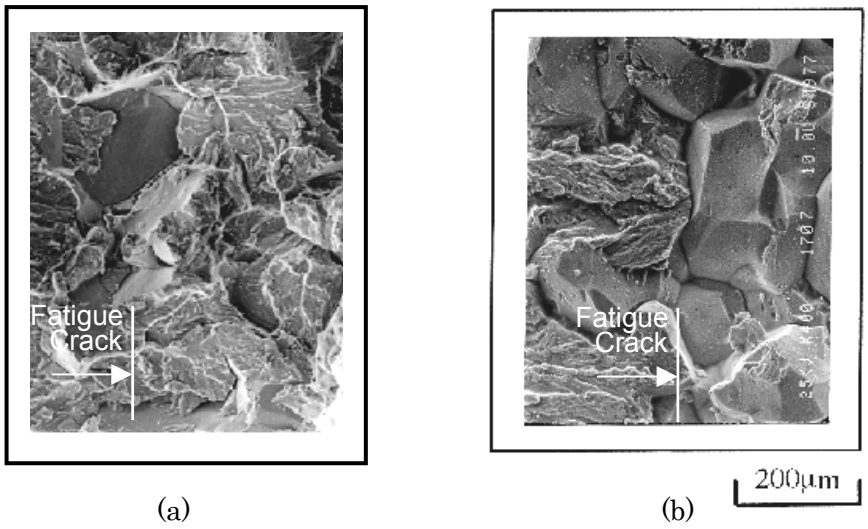

Figure 8 Fractography of Low J (a) and Mid J (b) heats

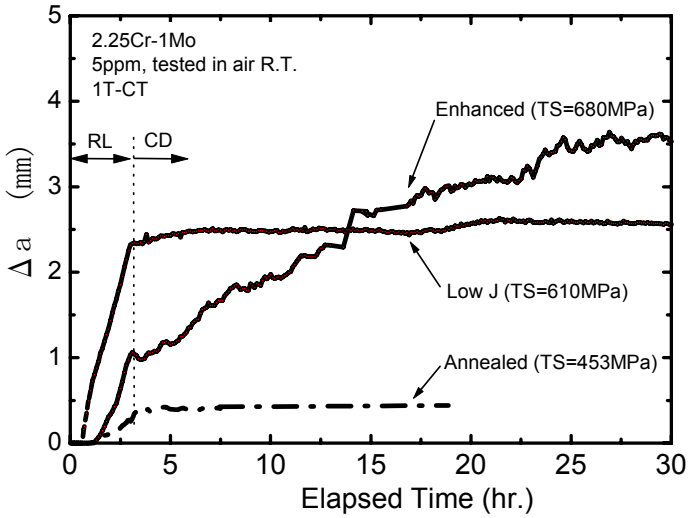

Figure 9 Crack growth measurement of RL+CD tests for various strength steel

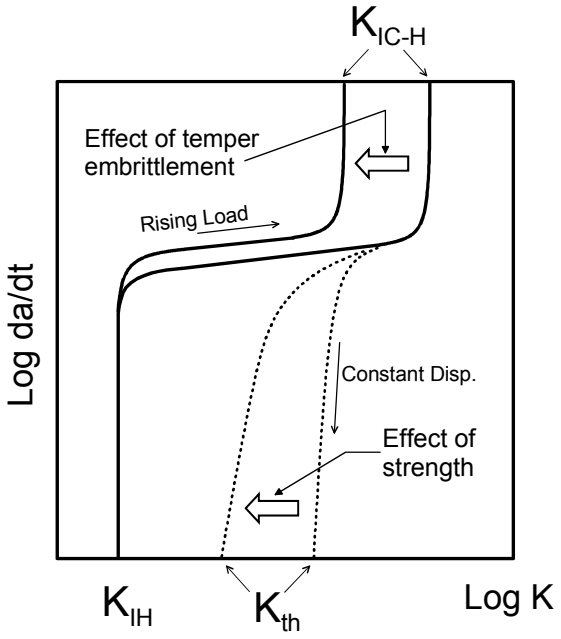

Figure 10 Schematical illustration of I.H.E. crack growth curve of 2.25Cr-1Mo steel

POSTER REFERENCE: 0711

FRACTURE TOUGHNESS ENVELOPE OF A LIMESTONE ROCK AT HIGH CONFINING PRESSURE AND TEMPERATURE

N. A. Al-Shayea[1] and K. Khan[2]

[1] Civil Engineering Department, KFUPM, Dhahran 31261, Saudi Arabia
[2] Research Institute, KFUPM, Dhahran 31261, Saudi Arabia

ABSTRACT

Fracture locus or envelope under a mixed-mode I-II loading can be obtained by plotting the normalized mode-II versus mode-I fracture toughness values. The envelope obtained can be used as a criterion for fracture failure for that material. However, testing conditions have a strong impact on that envelope. The objective of this paper is to present some results of an experimental program that was made to obtain fracture toughness envelope for a limestone rock from Saudi Arabia. Brazilian disks with an inclined central notch were tested under diametral compression, to get variety of mixed mode I-II fracture cases. Tests were conducted using disks with different sizes, and different notch type. Tests were made at different confining pressure from 0 to 28 MPa, and different temperature from 27 to 116^{o}C. Fracture toughness envelopes for the tested rock were obtained for both positive and negative regions (opening and closing of the crack) and at various environmental conditions. A quadratic equation, which fit the experimental results more satisfactory, were proposed as a failure criteria. One of the major contributions of this paper is the effect of high confining pressure and temperature on the fracture toughness envelopes of rocks.

KEY WORDS

Rock fracture, mixed Mode I-II, fracture envelope, high temperature and pressure.

INTRODUCTION

Studying the fracture toughness of rocks at elevated temperatures and confining pressures is valuable for a number of practical situations such as hydraulic fracturing used to enhance oil and gas recovery from a reservoir, and the disposal or safe storage of radioactive waste in underground cavities. Based on the loading type, there are three basic crack propagation modes in a fracture process, namely: Mode I (extension, opening), Mode II (shear, sliding), and Mode III (shear, tearing). Any combination of these modes can occur as a mixed-mode. Most, if not all, studies in the past have focused on fracture toughness determination under confining pressures only for Mode-I failure conditions. Nevertheless, due to randomly oriented cracks in rocks and/or in-situ stress conditions, cracks tend to propagate under the influence of a combined action of the basic

failure modes called mixed mode [1,2]. In the case of rocks, the combination of Mode-I and Mode-II (mixed Mode I-II) failure is more common. Therefore, consideration of mixed Mode I-II loading in addition to pure Mode-I becomes important in fracture toughness investigation.

Due to this mixed mode failure pattern, in addition to mode-I, fracture toughness under mode-II becomes important to be considered. When Brazilian disks with an inclined central notch are tested under diametral compression (Figure 1), a variety of mixed mode I-II fracture cases are obtained. For a particular material, a fracture locus or envelope can be obtained by plotting normalized mode-II versus mode-I fracture toughness. The envelope obtained could be used as a failure criterion in fracture toughness study for a particular material and testing condition in a way similar to the use of Mohr-Coulomb failure envelope for strength.

Usually, the fracture toughness of rock is determined at ambient conditions. However, under varying temperatures and confining pressures, the measured fracture toughness has been shown to vary. The fracture toughness behavior of a deep-seated rock formation requires the testing to be conducted in a manner that simulates the *in-situ* conditions such as temperature and confining pressure.

THEORETICAL BACKGROUND

Facture Toughness

When a notched rock specimen is subjected to an externally applied load, stress concentrates in the vicinity of the crack tip. When this concentrated stress reaches a critical value, failure occurs due to propagation of the preexisting crack. The fracture toughness is then calculated in terms of the stress intensity factor (SIF). In this paper, a circular Brazilian disk with a central notch under diametrical compression (Figure 1) was used to investigate fracture toughness. The following mathematical expressions, proposed by Atkinson *et al*. [3], were used for the fracture toughness calculation:

$$K_I = \frac{P\sqrt{a}}{\sqrt{\pi}RB} N_I \tag{1}$$

$$K_{II} = \frac{P\sqrt{a}}{\sqrt{\pi}RB} N_{II} \tag{2}$$

where, K_I is Mode-I stress intensity factor; K_{II} is Mode-II stress intensity factor; R is radius of the Brazilian disk; B is thickness of the disk; P is compressive load at failure; a is half crack length; and N_I *and* N_{II} are non-dimensional coefficients which depend on *a/R* and the orientation angle (β) of the notch with the direction of loading. For linear elastic fracture mechanics (LEFM), the small crack approximation proposed by Atkinson *et al.* [3] can be used to determine the values of N_I and N_{II} for half crack to radius ratio ($a/R \leq 0.3$), as follows:

$$N_I = 1 - 4\sin^2\beta + 4\sin^2\beta * (1 - 4\cos^2\beta)(a/R)^2 \tag{3}$$

$$N_{II} = \left[2 + (8\cos^2\beta - 5)(a/R)^2\right] \tag{4}$$

Fracture toughness for pure Mode-I ($\beta = 0$) is taken as K_{IC}; and that for pure Mode-II ($\beta \approx 29^o$) is taken as K_{IIC}.

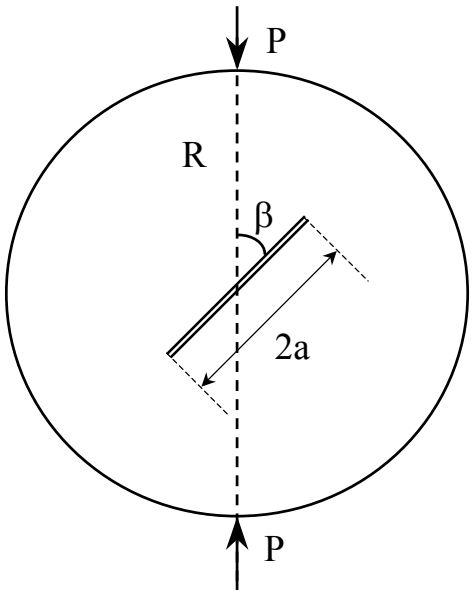

Figure 1: A schematic for Brazilian disk under diametrical compression

Failure Theories

There are numerous failure criteria for crack initiation and propagation under mixed mode I-II loading condition. The most popular ones are: (1) the maximum tangential stress (σ) criterion, (2) the maximum energy release rate (G) criterion, and (3) the minimum strain energy density (S) criterion. The available experimental data shows that no distinct theoretical failure criterion is applicable to all cases. Also, these criteria imply that K_{IC} is larger than K_{IIC}, while experimental data show the opposite. Moreover, due to the fact that the existing failure criteria were developed based on the tensile loading rather than the compressive, they hold good only in the positive region (crack opening) and cannot predict the fracture behavior in the negative zone (crack opening)

Many researchers have recommended using empirical relations for practical applications. Huang and Wang [4] and Sun [5] have used one of three empirical equations of straight line, ellipse, and homogenous quadratic to fit the experimental fracture toughness data in the (K_I/ K_{IC})-(K_{II}/ K_{IIC}) plane. Also, an exponential relationship was used [6,7].

EXPERIMENTAL PROGRAM

Sample Preparation

Rock blocks were collected from a limestone rock formation outcropping in the Central Province of Saudi Arabia. Cores were obtained from these blocks using 98 mm and 84 mm coring tube pits. Cores were sliced into circular disks using a high-speed circular saw. The thickness (B) of the sliced disks was in the range of 20-24 mm. A notch was machined in the center of the disks. Straight notch was made using a 0.25 mm diamond-impregnated wire saw, while chevron notch was made using a slow-speed circular saw. The notch making process is explained in more details elsewhere [8].

Rock properties

The investigated limestone rock was beige in color. Its physical properties included a dry density of 2.586 gm/cm^3, a specific gravity of 2.737, and porosity of 5.4%. The mechanical characteristics included a uniaxial unconfined compressive strength of 105 MPa, a tensile strength of 2.31 MPa, a modulus of elasticity of 54 GPa, and a Poisson's ratio of 0.276.

Testing

A strain-controlled loading frame having a capacity of 100 KN was used for the load application with a strain rate of 0.08 mm/min. Disk specimens were diametrically loaded with different values of the crack inclination angle (β) ranging from 0° to 75° with a 15° increment. The applied load and load-point displacement were acquired using a computerized data logger. Tests were made at ambient conditions, at high confining pressure σ_3) of 28 MPa, and at high temperature of 116°. The details of the experimental program can be found elsewhere [9].

RESULTS AND DISCUSSIONS

The values for mode I and mode II fracture toughness (K_I) and (K_{II}) were determined using equations 1 to 4. Table 1 summarizes the values of K_{IC} and K_{IIC} at different conditions for straight notch. For all conditions, K_{IC} is smaller than K_{IIC}, in contrary to the values provided by the famous failure theories. Figure 2-a shows the variation of K_I and K_{II} with β for D = 98 mm, at different conditions. It can be seen that the high confining pressure has a tremendous impact on the fracture toughness, while the effect of high temperature has a minor effect.

The normalized fracture toughness values of (K_I/K_{IC}) and (K_{II}/K_{IIC}) were determine for various cases. The plot of (K_{II}/K_{IIC}) vs. (K_I/K_{IC}) is named the fracture toughness envelope, which is the fracture locus for the general mixed-mode I-II loading. Crack initiates when a point ((K_I/K_{IC}), (K_{II}/K_{IIC})) falls on the envelope. Figure 2-b gives a comparison between fracture toughness envelopes at different conditions (ambient, σ_3 = 28 MPa, and T = 116 °C). Figure 3-a shows fracture toughness envelopes for D = 98 and 84 mm, at both positive region (crack opening) and negative region (crack closing). Also, Figure 3-b shows similar results for straight and Chevron notches. A second-degree polynomial was used to fit the experimental data at various conditions, and at both positive and negative region, Figures 2 to 3. The general form of the fitting is:

$$\left(K_{II}/K_{IIC}\right) = A + B\left(K_I/K_{IC}\right) + C\left(K_I/K_{IC}\right)^2 \tag{5}$$

where, *A*, *B*, and *C* are the coefficient for the second order polynomial used for the regression. The values of *A*, *B*, and *C* for various experimental conditions are tabulated in Table 2.

It can be seen from Figure 6 that the results for all three conditions fall into a relatively close bound in the positive zone; however, distinct regions of data exist in the negative side. Note that the results for the specimens tested at high temperature fall close to the data for ambient conditions in the negative zone revealing that the fracture toughness is not very much affected by the temperature used in this study. However, fracture toughness envelope at high confining pressure, in the negative region, is extremely lower than that at ambient condition.

TABLE 1

COMPARISON BETWEEN K_{IC}, K_{IIC}, AND THEIR RATIO AT VARIOUS CONDITIONS

Condition	Diameter (mm)	K_{IC} (Mpa $m^{1/2}$)	K_{IIC} (Mpa $m^{1/2}$)	K_{IIC}/K_{IC}
Ambient	98	0.42	0.92	2.19
	84	0.35	0.75	2.14
σ_3 = 28 MPa	84	1.19	1.49	1.25
	98	1.57	2.18	1.39
T = 116°C	98	0.52	1.00	1.92

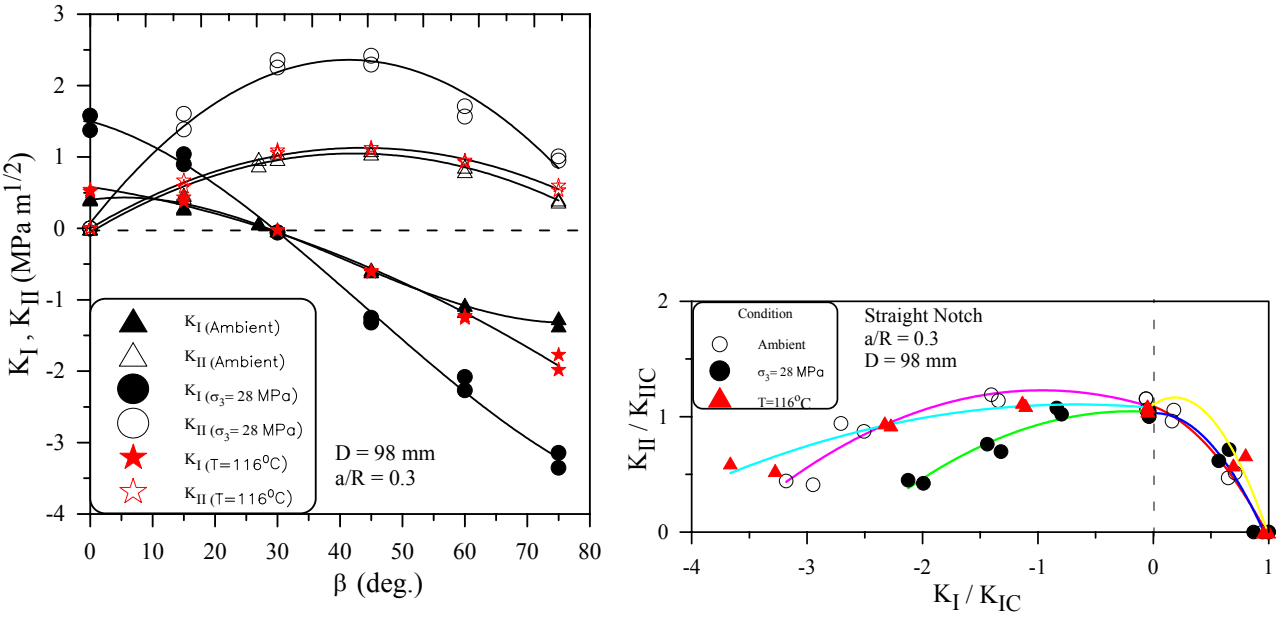

(a) **(b)**

Figure 2: Compar ison of (a) fracture toughness, (b) fracture envelopes

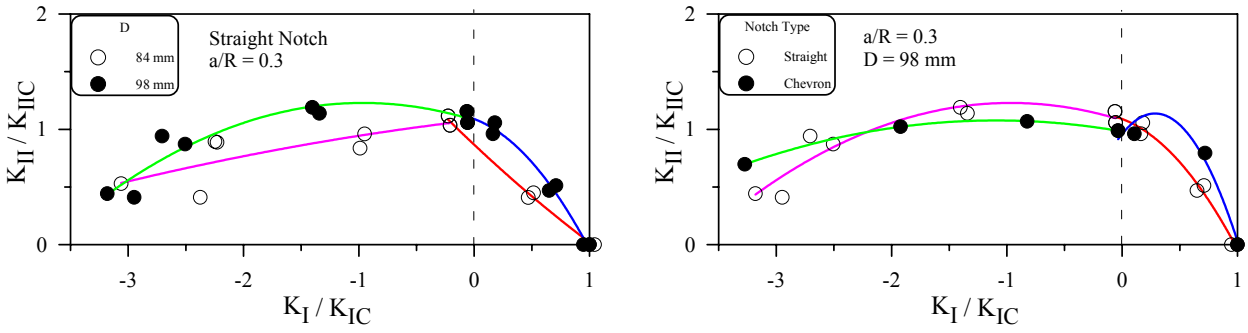

(a) **(b)**

Figure 3: Fracture envelopes for Brazilian disks with (a) different D, (b) different notches

TABLE 2
REGRESSION PARAMETERS FOR VARIOUS CONDITIONS

Condition	Notch Type	D (mm)	Positive Region			Negative Region		
			A	*B*	*C*	*A*	*B*	*C*
Ambient	Chevron	98	0.9589	1.2436	–2.1709	0.9811	–0.1746	–0.0799
	Straight	84	0.8664	–0.9402	0.0928	1.0797	0.1162	–0.0203
	Straight	98	1.0891	–0.3701	–0.7584	1.0779	–0.3120	–0.1616
σ_3 = 28 MPa	Straight	98	1.0290	0.0461	–1.1663	1.0399	–0.0670	–0.1779
T = 116°C	Straight	98	1.1046	0.6635	–1.7977	1.0759	–0.0882	–0.0661

CONCLUSIONS

For the investigated limestone rock, the effect of confining pressure on K_{IC} and K_{IIC} is much more significant than the effect of temperature. K_{IC} increased by 274% under σ_3 = 28 MPa, but the corresponding value at T = 116°C was 24%. K_{IIC} increased by 137% under σ_3 = 28 MPa, but the corresponding value at T = 116°C was only 9%. Also, the effect of confining pressure on K_{IC} is much more significant than its effect on K_{IIC}. The above observations lead to the conclusion that the Mode-II component may be the most critical mode controlling failure at high values of temperature and confining pressure.

ACKNOWLEDGEMENTS

The authors acknowledge the support of King Fahd University of Petroleum and Minerals for providing computing and laboratory facilities.

REFERENCES

1. Whittaker, B. N., Singh, R. N. and Sun, G. (1992), "*Rock Fracture Mechanics; Principles, Design and Applications*", Developments in Geotechnical Engineering, Elsevier Publishers, Netherlands.
2. Lim, I. L., Johnston, I. W. and Choi, S. K., Assessment of mixed mode fracture toughness Testing methods for rock., *Int. J. Rock Mech. Min. Sci. & Geomech. Abstr.,* Vol. 31, No. 3,. pp. 265-272 (1994).
3. Atkinson, C., Smelser, R. E. and Sanchez, J. (1982), "Combined Mode Fracture via the Cracked Brazilian Disk", *Intl. Journal of Fracture*, Vol. 18, pp. 279-291.
4. Huang, J. and Wang, S. (1985), "An Experimental Investigation Concerning the Comprehensive Fracture Toughness of Some Brittle Rocks", *Int. J. Rock Mech. Min. Sci. and Geomech. Abstr*., Vol. 22, No. 2, pp. 99-104.
5. Sun, G.X. (1990), *Application of Fracture Mechanics to Mine Design*, PhD Thesis, Dept. of Mining Engineering, University of Nottingham, England.
6. Awaji, H. and Sato, S. (1978), "Combined Mode Fracture Toughness Measurement by the Disk Test", *Journal of Engineering Materials and Technology,* Vol. 100, pp. 175-182.
7. Lim, I. L., Johnston, I. W., Choi, S. K. and Boland, J. N. (1994), "Fracture Testing of a Soft Rock with Semicircular Specimens Under Three Point Bending-Part 1", *Int. J.Rock Mech. Min. Sci & Geomech. Abstr.,* Vol. 31, No. 3, pp. 185-197.
8. Khan, K., and Al-Shayea, N. A., "*Effects of Specimen Geometry and Testing Method on Mixed-*Mode *I-II Fracture Toughness of a Limestone Rock from Saudi Arabia"*, Rock Mechanics and Rock Engineering, July-Sept. 2000, 33 (3), 179-206.
9. Al-Shayea, N. A., Khan, K. and Abduljauwad, S.N., *"Efffects of Confining Pressure and Temperature on Mixed-Mode (I-II) Fracture toughness of a Limestone Rock Formation",* International Journal of Rock Mechanics and Rock Sciences, June 2000, 37 (4), 629-643.

ORAL REFERENCE: ICF100562OR

FRACTURE TOUGHNESS MEASUREMENT OF SMALL CRACKS IN HIGH STRENGTH STEEL WIRE

B. Bromage and T. J. Marrow

Manchester Materials Science Centre, UMIST, Manchester, UK, M60 1QD
An EPSRC Project with Corus

ABSTRACT

High strength pearlitic steel wire, typically used as tyre bead, can fail during production due to the propagation of naturally occurring longitudinal and transverse flaws. These can lead to failure when the wire is deformed and straightened to produce the desired cast for ease of coiling. The wire has had significant processing costs added to it at this stage, and the prevention of this type of failure is of concern to the wire drawing industry. At the present time, there is no understanding of the influence of process variables, such as flaw size and the amount of deformation that is induced for straightening.

The fracture toughness of this grade of wire was unknown, and could not be determined by standard test techniques due to the small dimensions of the wire (1.83mm diameter). Small transverse flaws were produced by fatigue crack propagation from spark-eroded notches. Compliance measurements and the direct-current potential drop method were used to demonstrate stable crack propagation before unstable failure. The measured fracture toughness (J_{1c} =18kJm^{-2}) was consistent with the toughness of steels with coarser pearlite microstructures (an interlamellar spacing of 0.15μm, as opposed to 0.003μm), measured in conventional test specimens with long cracks [5]. The measured toughness has been used to predict the behaviour of longitudinal flaws during the wire straightening process. This paper reports part of a project which aims to produce a process control model.

KEYWORDS

Wire, Steel, High-Strength, Toughness, Fracture, J-Integral, and Potential Drop Technique

INTRODUCTION

The material being investigated was hard-drawn pearlitic steel wire, 1.83mm diameter, 0.8 wt.% carbon, with a tensile strength of 2.1GPa, and a yield strength of 1.8GPa. Analysis of the fracture performance of this wire requires a better understanding of the failure mechanism of the wire, and also the development of techniques to detect and monitor crack growth in small samples. A method to test wire containing transverse flaws (which are not usually the cause of failures) was simpler, so was investigated first. With the knowledge

gathered from these tests, failure originating from longitudinal flaws (which usually cause failures) will be investigated in future work. **Figure 1** identifies the crack planes, Y-Z is termed longitudinal, and X-Z is termed transverse.

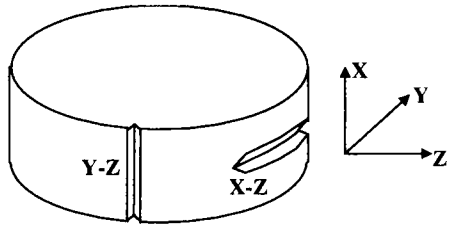

Figure 1. Crack plane identification

Cracked samples were produced by growing a fatigue crack from a spark eroded notch in the wire. To control the fatigue crack growth it was necessary to know the stress intensity (K) at the crack tip. Stress intensity factors for cracks (of length, a) in round bars (of diameter, D) were developed by James and Mills [1] and were suitable to use to calculate the required load (proportional to stress, σ) and subsequent stress intensity during sample preparation. Shorter cracks (less than 500μm) tended to have a semi-circular crack front for which the following equation was used;

$$\frac{K}{\sigma\sqrt{\pi a}} = 0.926 - 1.771\left(\frac{a}{D}\right) + 26.421\left(\frac{a}{D}\right)^2 78.481\left(\frac{a}{D}\right)^3 + 87.911\left(\frac{a}{D}\right)^4 \quad (1)$$

Longer cracks tend to have a straight crack front, producing higher stress intensities. Forman and Shivkumar [2] produced a closed form expression that fits well for cracks shorter than 1100μm, see Eqns. 2 and 3.

$$\frac{K}{\sigma\sqrt{\pi a}} = g\left[0.752 + 2.02\left(\frac{a}{D}\right) + 0.37\left(1 - \sin\frac{\pi a}{2D}\right)^3\right] \quad (2)$$

$$g = \frac{\frac{1.84}{\pi}\left[\tan\left(\frac{\pi a}{2D}\right) \Big/ \frac{\pi a}{2D}\right]^{1/2}}{\cos\frac{\pi a}{2D}} \quad (3)$$

Once the samples were produced, fracture tests were carried out on them. Analysis of the test data, using elastic-plastic fracture mechanics, was performed using the J-integral, following the original methods of Begley and Landes [3]. The J-integral can be viewed as the potential energy difference between two identically loaded specimens with different crack lengths. It measures the work available to drive crack growth and is analogous to strain energy release rate (G). Failure occurs when J reaches some critical value (J_{1c}), which is equivalent to G_{1c}.

METHODOLOGY

The philosophy behind the tests was to produce a set of samples containing a range of flaw sizes (150 – 1250μm). These were then pulled in tension and the load-deflection data was recorded. This data and the

fracture surfaces were then analysed using fracture mechanics relationships to determine a fracture toughness value.

The samples were prepared by spark eroding a notch to a depth of either 100μm or 200μm (the former being used to produce cracks shorter than 450μm) using thin copper foil (50μm) at a low voltage (100V). A fatigue crack was grown from this notch, its length was monitored using a calibrated potential drop technique. The cracks were grown in stages, and the load was reduced as the crack grew progressively longer, to minimise the effect of plastic zone on the toughness measurements. The initial load range was 1200N (R = 0.1), decreasing to 250N. The maximum stress intensity factor at the end of pre-cracking was approximately 10MPa$\sqrt{m}$.

Fracture tests were carried out by pulling the samples in tension at 1mm per minute. The British Standard for fracture testing [4] was followed as closely as possible. The load and deflection data were recorded using a load cell and an extensometer (gauge length 10mm), both of which were calibrated. Previous work on similar wire by Gasterich et al. [5] suggested that monitoring the change in compliance (associated with crack growth) as a way of determining the point of failure might give a large amount of scatter. If this was found to be the case an alternative method, the direct current potential drop technique, would be investigated hopefully to give a more accurate result.

The fracture surfaces were then cleaned in an ultrasonic bath using acetone and mounted on scanning electron microscope stubs. The fracture surfaces were investigated, and crack lengths recorded. The surfaces were expected to consist of 3 regions; spark eroded notch, fatigue pre-crack, and unstable crack growth. The interrupted fracture samples were expected to consist of 5 regions; spark eroded notch, fatigue pre-crack, ductile crack growth, post fracture-test fatigue crack, and unstable crack growth.

RESULTS

All the fracture surfaces were analysed using a field emission gun scanning electron microscope and the crack lengths recorded. Distortions of the images at low magnification were accounted for in the measurements. The surfaces showed the different regions of crack growth as expected. **Figure 2** is an image of a typical sample. Picture **(a)** shows the point at which the crack length was measured, images **(b)** and **(c)** show the different regions seen on the fracture surface.

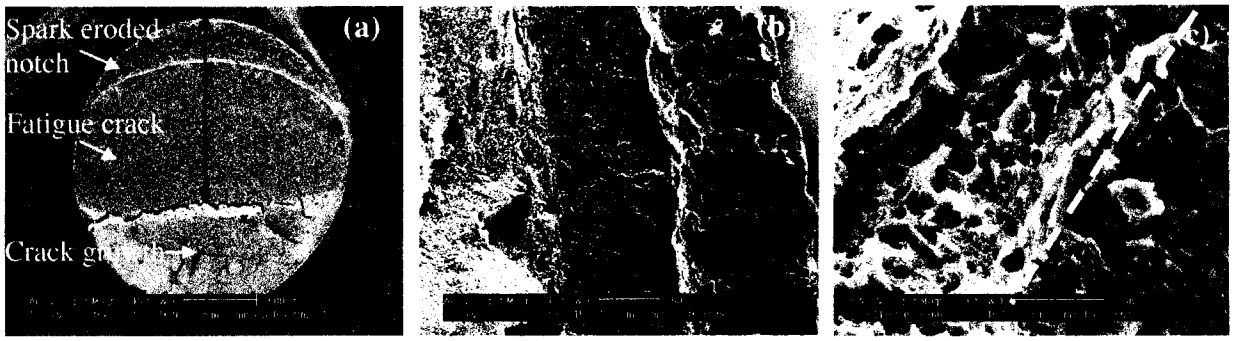

Figure 2. (a) Measurement of crack length, (b) Appearance of (right to left) spark eroded notch, fatigue crack and crack growth. (c) Close-up of fatigue/ductile failure interface.

Analysis of the test data using the compliance based method to determine the point of failure gave a large degree of scatter, and a higher than expected value of J_{1c}. Therefore the crack lengths were monitored using the calibrated direct-current potential drop technique used to monitor the fatigue pre-crack length. The point

at which the crack length grew was taken as the point of failure and the sample was then pulled to failure. Interrupted fracture tests were performed to verify that the direct-current potential drop technique was accurately detecting the onset of crack growth (and, therefore, measuring J_{1c}). These involved stopping the fracture test when crack growth was detected and then growing the crack to failure under fatigue conditions.

Fracture surface analysis

Crack growth was predicted to occur when the voltage driving the current through the wire changed from increasing linearly with strain (corresponding to the change in cross-sectional area as the wire was pulled), to non-linearly (**figure 3**).

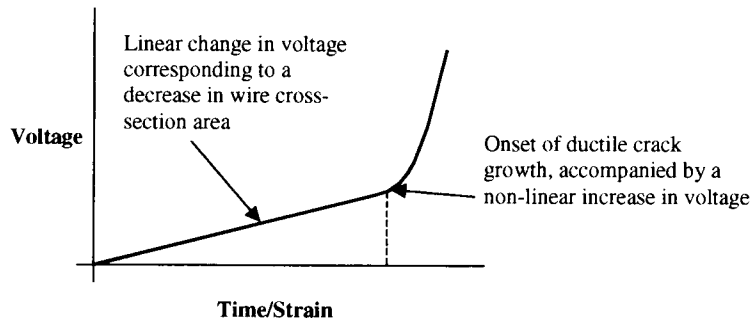

Figure 3. Generic Voltage versus Time/Strain plot produced using a direct current potential drop technique to monitor crack growth.

Analysis of the interrupted fracture samples using a scanning electron microscope show that this change in gradient of the voltage does correspond to crack growth (**figure 4**).

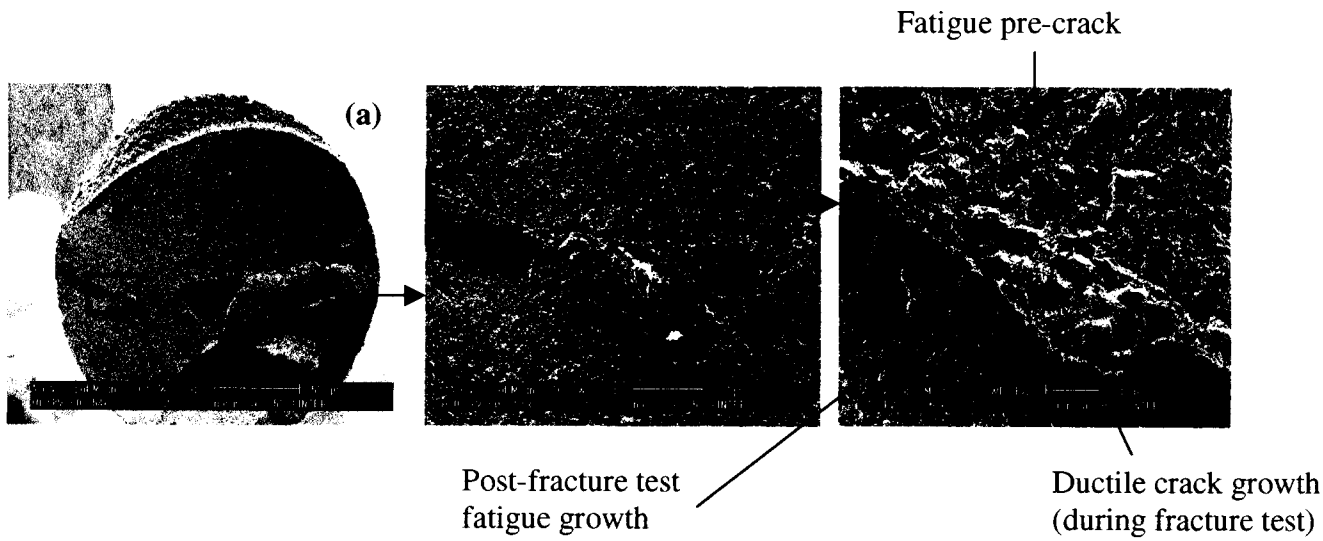

Figure 4. Interrupted fracture test sample. Image c shows the fatigue pre-crack, ductile crack, then post fracture test fatigue crack, that prove that the potential drop technique does detect the onset of crack growth.

The spark-eroded notch is a crescent, of approximate length 200μm. From this notch a fatigue pre-crack was grown, the striations of which could barely be resolved (approximately 1μm between each). Below this is a very fine band (approximately 40μm wide) of ductile crack growth, which occurred during the fracture test (ductile dimples can be seen in **figure 4 (c)**). At this point the increase in voltage became non-linear and the fracture test was stopped. Below this is a region of post fracture fatigue growth, showing the same characteristics as the pre-crack. Finally a region of fatigue crack growth can be seen which occurred when the critical crack length was reached (during post-fracture fatigue growth).

Determination of J_{1c}

Analysis of the load-deflection data using linear-elastic fracture mechanics showed that K_Q was not a material constant. This indicated that elastic-plastic conditions applied at the crack tip, and that plastic deformation was not insignificant. The J-integral analysis followed the original methods of Begley and Landes. **Figure 5** is a graph of J versus deflection which was used to then determine J_{1c}, J increases with increasing deflection.

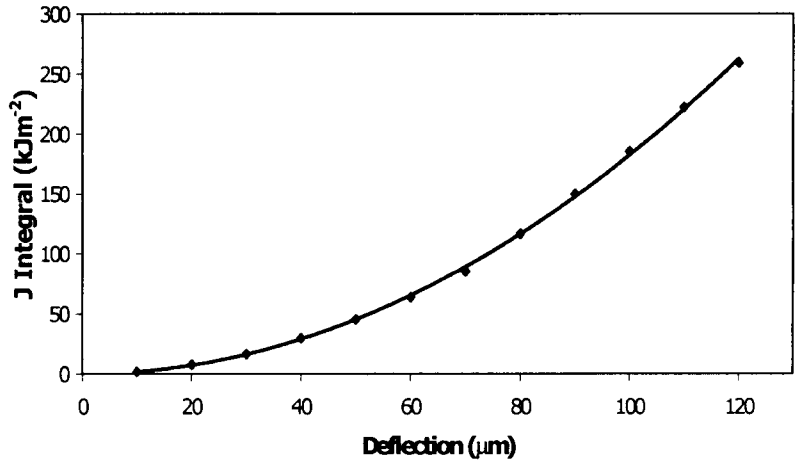

Figure 5. Graph of J versus Deflection calculated from fracture test data using Begley and Landes methodology [3]

Figure 6 is a graph of J_{1c} versus crack length for the compliance and potential drop techniques. A much lower average J_{1c} of 18kJm^{-2} was found for the latter, with a scatter of 7kJm^{-2} for longer cracks (greater than 500μm), and 11kJm^{-2} for shorter cracks. This scatter cannot be attributable to the effect of crack shape, or error in the measurement of crack length.

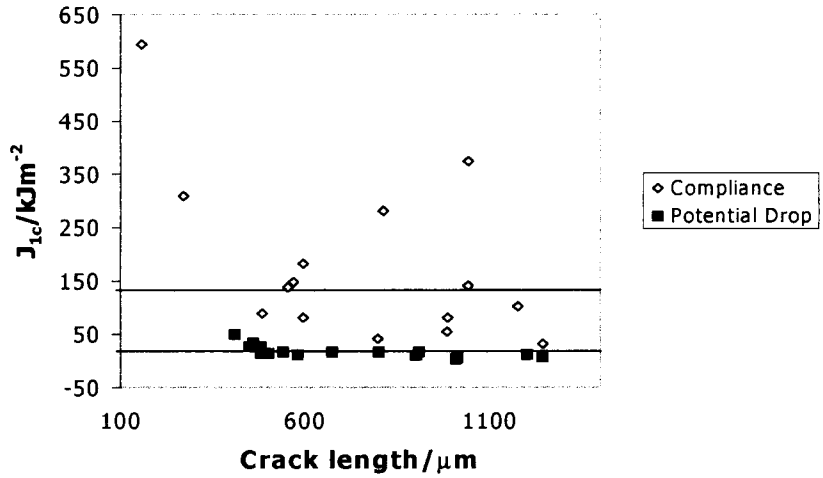

Figure 6. J_{1c} versus Crack length, average J_{1c} = 18kJm^{-2}, showing the improvement in consistency of results by using the DCPD technique to detect crack growth.

DISCUSSION

The large amount of scatter produced using this compliance based method corresponded well with the range of scatter seen in a similar material by Gasterich et al. [5], which covered the toughness values for initiation and propagation. This suggested that due to the compliance based nature of the tests, and the relatively small

change in stiffness accompanying- crack growth, the point of failure (i.e. onset of crack growth) was not being detected. The use of the direct current potential drop technique to monitor crack growth during the fracture tests gave a J_{1c} value which was nearer to that determined by Gasterich [5] and contained only a small degree of scatter.

Investigation of the fracture surfaces in the field emission gun scanning electron microscope showed that ductile crack growth did occur when the voltage increase became non-linear. Therefore, the toughness value recorded at that point will be the J_{1c} value for this wire containing flaws in the X-Z direction (**figure 1**).

There is an increase in toughness for shorter cracks. This is probably due to the crack tip becoming more constrained by the surrounding material moving from the central region of the wire (where plane strain conditions apply) towards the outer surface. In this region material is constrained from flowing and relieving the stresses acting on the crack tip. This leads to failure at a lower applied load than for plane stress conditions. When the crack tip exists nearer the surface of the wire the material surrounding it is less constrained and can flow and blunt the crack tip. This means that to cause failure, a larger applied load is required to reach the critical stress.

CONCLUSIONS/FURTHER WORK

- The direct current potential drop technique can be used to accurately detect crack growth in small diameter wire specimens.
- Shorter cracks have a higher toughness, attributable to the increase in constraint.
- The toughness value calculated is the J_{1c} for the wire.
- $J_{1c} = 18kJm^{-2}$, which can be used in a finite element model of the wire containing cracks lying in a different orientation (Y-Z, rather than X-Z). Artificial short longitudinal flaws will be assessed in test conditions that simulate the twisting and bending of wire production. This will determine whether failure criteria is mixed mode or predominantly mode I.

ACKNOWLEDGEMENTS

The authors would like to thank Corus, and Rom Wire, for the material and assistance in this project.

REFERENCES

[1] James, L. A. and Mills, W. J. (1988). *Review and Synthesis of Stress Intensity Factor Solutions Applicable to Cracks in Bolts; Eng. Fract. Mech.* 30, 641

[2] Forman, R. G. and Shivakumar, V. (1986). In: *Review and Synthesis of Stress Intensity Factor Solutions Applicable to Cracks in Bolts; Eng. Fract. Mech.* 30, 641

[3] Begley, J. A. and Landes, J. D. (1972). *The J Integral as a Fracture Criterion; Proceedings of the 1971 National Symposium on Fracture Mechanics,* Part II, 1

[4] British Standard, (1991). *Fracture Mechanics Toughness Test; BS 7448,* Part I.

[5] Gasterich, H-J Hagedorn, K. E. Radko, K. and Pawelski, O. (1993). *Influence of the Microstructure of Higher Carbon Steels on Fracture Mechanics Properties, Steel Research,* 64, No. 8/9, 414

FRACTURE TOUGHNESS OF NIOBIUM/SAPPHIRE INTERFACES: EFFECT OF INTERFACE DOPING AND ION ASSISTED DEPOSITION

G. S. Was[1] and H. Ji[2]

[1]Departments of Nuclear Engineering and Radiological Sciences, and Materials Science and Engineering, University of Michigan, Ann Arbor, MI 48109, USA
[2]Optoelectronics Division, Agere Systems, Reading, PA 19612, USA

ABSTRACT

In this work, the effect of chemical composition and crystal orientation relationship on the interface fracture toughness of niobium/sapphire system was studied. We used several techniques to assess the interface fracture toughness, including microscratch, microwedge scratch, and delamination of patterned lines. Results showed a general trend of the effect of silver at the interface where the interface fracture toughness decreased with the amount of silver. Ion bombardment during film deposition (IBAD) significantly increased the interface fracture toughness through a combination of interface mixing and a controlled orientation relationship.

KEYWORDS

Niobium, interface fracture toughness, delamination, ion bombardment, films, microwedge, microscratch

INTRODUCTION

The overall objective of this project was to control the fracture toughness of the interface between niobium films and sapphire substrates by controlling the interface properties. Scratch tests have shown [1] that the interface fracture toughness correlates with silver interlayer thickness for niobium films deposited by electron beam evaporation. It has also been shown [2] that ion bombardment during film deposition can be used to strengthen the interface by matching the crystal orientation across the interface and by interface mixing. Therefore, the approach used in this project involved both weakening the interface by doping it with silver [3,4] and strengthening it by controlling the orientation relationship and the degree of interface mixing.

Quantitative techniques for measuring interface fracture toughness in thin films are not well developed. In this paper, we have deduced values of interface fracture toughness using observations of failures that occurred during microscratching, microwedge scratching and from an analysis of bucking and curling of patterned niobium lines on sapphire. We were also able to assess the effectiveness of simultaneous ion bombardment during film deposition on the interface fracture toughness.

RESULTS AND DISCUSSION

Microscratch Experiments

Four sets of samples were made where a set constituted a series of depositions with varying interface silver level. All the films have a thickness of about 100 nm, as measured by the Dektak3 profilometer. The amount of silver at the niobium/sapphire interface varies from less than 0.8 monolayers to 6.4 monolayers as measured by RBS. Details of the experiment are given in ref. [5]. All samples with measurable silver level (>0.8 monolayer) at the interface failed during the scratch test with the niobium films delaminating from the sapphire substrates in a "brittle manner". The failure was characterized by multiple spallations as the film detached from the substrate (Fig. 1a). Buckling was also observed along the scratch track in areas prior to the first spall. The tangential load shows abrupt changes corresponding to the spalls and the breakthroughs of pile-up material in front of the indenter. Interfacial toughness can be obtained from the geometry of the first spallation and the tangential load at which it happened. On the other hand, there was no indication of interfacial failure during the scratch test for the sample with <0.8 monolayer of silver at the interface, as well as the sample without silver . The film underwent ploughing with no evidence of delamination (Fig. 1b). No value of interface fracture toughness was estimated for these two samples because of the absence of interfacial failure.

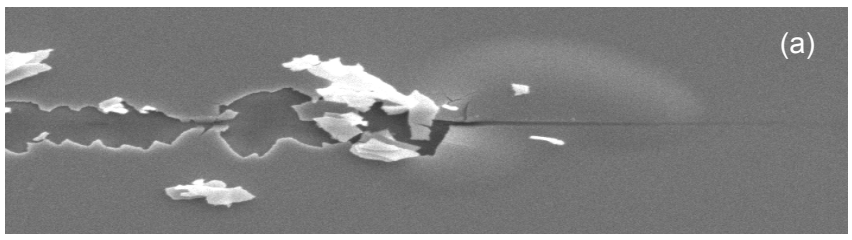

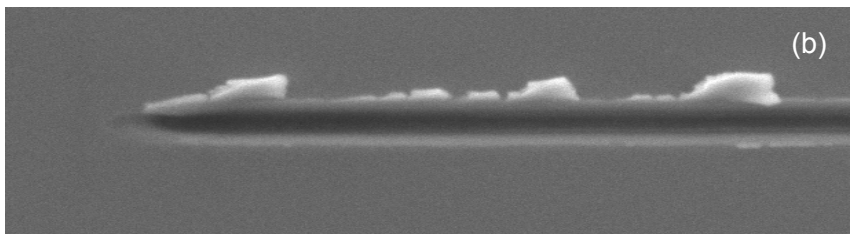

Figure 1: SEM micrographs of scratch tracks for (a) sample with interface delamination (PVD, 4.2 monolayers of silver), and (b) sample without interface delamination (PVD, < 0.8 monolayers of silver).

The results from microscratch test showed a strong correlation between the interface fracture toughness and the amount of silver at the interface, as plotted in Fig. 2a. This result is in good agreement with the general trend of the interface fracture toughness as a function of the work of adhesion. As been pointed out by Elssner *et al*. [2], the interface fracture toughness G_c, increases exponentially with the work of adhesion W_{ad}: $G_c \propto W_{Ad}^n$, where the exponent n is a function of the orientation of the metal constituent. They found that the value of n for the (100) interface plane of niobium is 1.9, and that for the (110) interface plane of niobium is 3.

The leveling off in interface fracture toughness at a silver level of 4.2 monolayers implies that the silver coverage reached 100% at a level of 4.2 monolayers. For the interface without silver, the work of adhesion (W_{ad}) is that of pure niobium/sapphire: 800 mJ/m^2 [6]. For interfaces that have 100% coverage of silver, it was found that the interface fracture occurred at the silver/sapphire interface [7], which has a work of adhesion of 150 mJ/m^2 [8]. Assuming a linear interpolation of the work of adhesion for intermediate value of silver coverage, Fig. 2a can be replotted as a function of the work of adhesion (Fig. 2b). A least square fit of this curve using a power law function gave a value of 3.0 for the exponent n in Eq. 3. This result is in very good agreement with the value of 3.0 obtained by Elssner *et al*. [2].

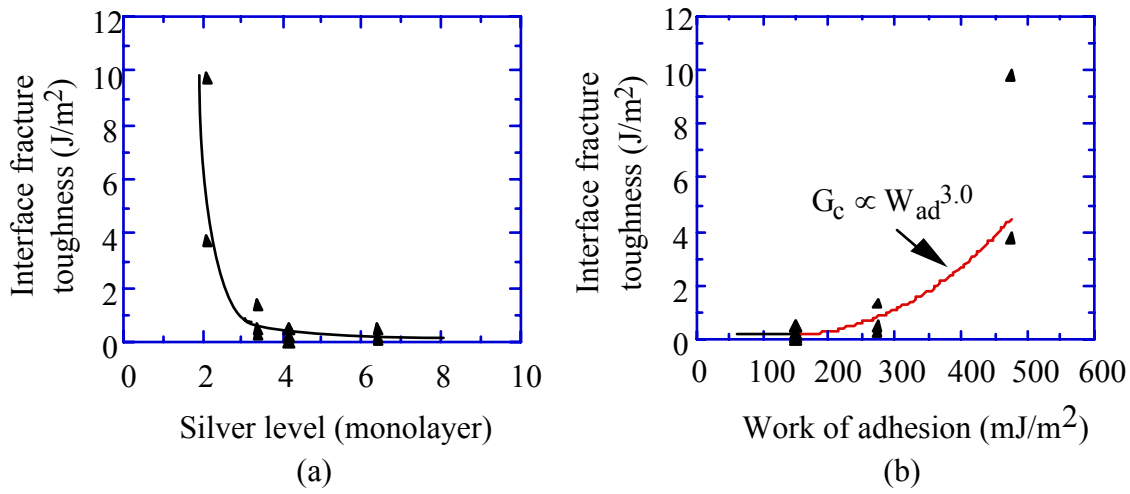

Figure 2: Interface fracture toughness of niobium/sapphire interface as a function of (a) silver level at the interface, and (b) work of adhesion of the interface, and a least squares power law fit yielding n = 3.0.

Microwedge scratch test

Samples with and without silver at the interface experienced interface delamination under the microwedge scratch test. As shown in Fig. 3a, a portion of the film with a constant width was spalled. The tangential load at which the interface delamination occurred was recorded, and the strain energy release rate is calculated by Gerberich et al. [9] A decrease in interface fracture toughness due to the presence of silver at the interface is observed. The average interface fracture toughness for the sample without silver at the interface is 12.44 J/m^2, while the average interface fracture toughness for the sample with silver at interface is 4.54 J/m^2. The estimated values of the interface fracture toughness are consistent in magnitude with that of other metal/ceramic system where for W/SiO_2 interface G_c was found to be 16 J/m^2 and 4 J/m^2 for 1.5 μm and 0.5 μm thick films, respectively [10]. This result is also consistent with the silver effect found by the microscratch test where the presence of silver weakened the interface of niobium/sapphire.

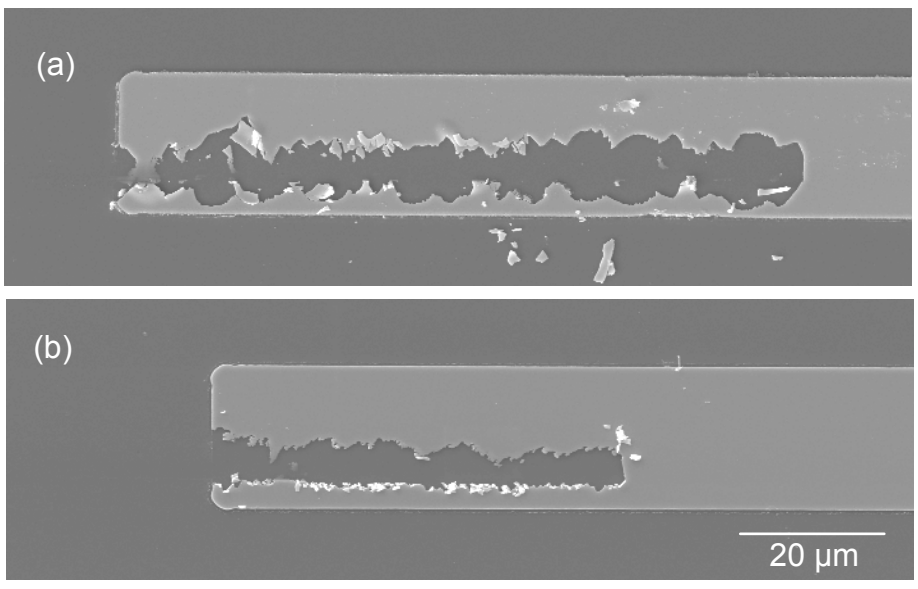

Figure 3: Micrographs of microwedge scratch tracks of (a) the PVD sample with 6.4 monolayer of silver at niobium/sapphire interface , and (b) a PVD sample with no silver at the interface.

Analysis of buckles and curls in patterned lines

Interface fracture toughness was also estimated from the delamination of patterned niobium lines on sapphire substrates. Both curls and buckles were found on some PVD samples. Buckling usually occurs when the film detaches from the substrate in the middle of the line, and curling occurs when the detachment is at one end of the line.

Interface fracture toughness from buckled lines

Buckling was observed for niobium films on sapphire substrate in the patterned line forms, with interfacial silver levels range from 2.5 monolayer to 7.6 monolayer. Figure 4a shows a representative micrograph of the buckles. The buckles indicate that the residual stress in the niobium film must be compressive. The buckle height and length for buckled lines were measured from the photo.

The stress in the niobium film can be determined using the analysis of buckle height given by Hutchinson and Suo [11]. The values of the film stress and the interface fracture toughness for lines that delaminated in the form of buckles ranges from 1.17 GPa to 5.57 GPa in compression, and the interface fracture toughness ranges between 0.62 J/m^2 and 13.6J/m^2. Given a 3% error in the measurement of the buckle height, the error in the film stress and interface fracture toughness is less than 5%.

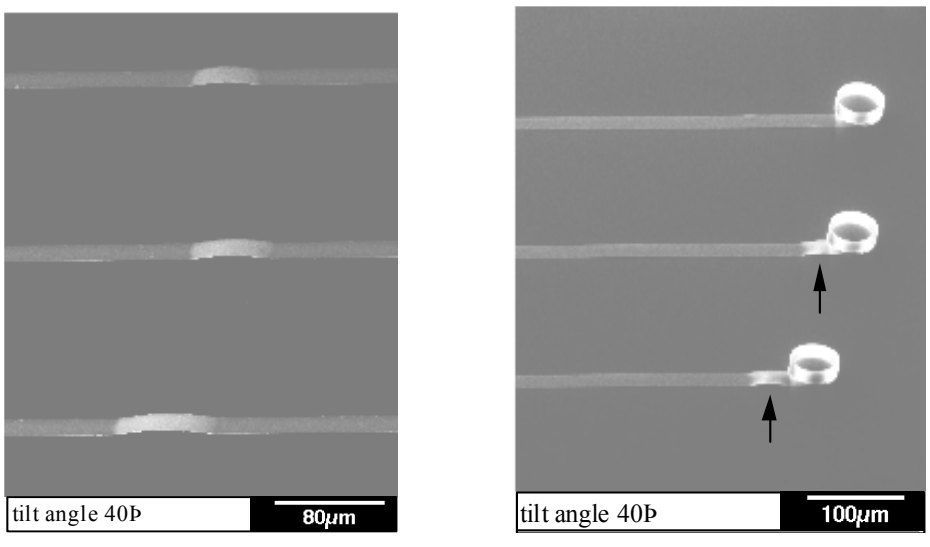

(a) (b)

Figure 4: SEM pictures of (a) buckled niobium lines on sapphire substrate (PVD, 3.0 monolayers of silver), and (b) curled photoresist/niobium bilayer lines on a sapphire substrate with lines detached from the substrate at the niobium/sapphire interface (PVD, 2.1 monolayers of silver). The arrows point to buckles.

While the magnitude of the stress is not unreasonable for niobium films given hardness measurement of 6 GPa [12], the reason that these films are in compression is unknown. A possible explanation for the formation of the buckles that does not require compressive residual stress in niobium is that the buckles formed at an earlier stage under external force induced by processing or an interface defect (e.g. gas bubble at the interface), causing the niobium to yield. However, optical inspection of the sample showed no observable defects before the photoresist was stripped off.

Interface fracture toughness from curled lines

Figure 4b is a SEM micrograph of the PVD sample with 2.1 monolayers of silver at the niobium/sapphire interface . The photo was taken after the dry etch step when lines were first observed to detach from the substrate. The final step of the photolithography process (stripping the photoresist) was omitted from this sample. Therefore the sample is a bilayer with a 1.35 µm thick photoresist layer on top of a 0.1 µm thick niobium film, deposited on a sapphire substrate which was pre-deposited with silver. As shown in Fig. 4b, the lines were detached from the substrate at one end. The detached portion of the bilayer (photoresist and niobium) curled up, indicating that there was a stress gradient in the bilayer system in which the stress in the photoresist is tensile relative to the niobium film. The observation of buckles next to the curled ends indicates that the stress in the niobium film must be compressive. Given the radius of the curvature, R, of the curls, and the niobium film stress of -1.32 GPa determined from the buckling analysis on a sample with similar deposition condition , the stress in the photoresist is estimated to be 38 MPa in tension.

The fracture toughness of the interface, determined using the analysis in ref. [11], is 0.95 J/m^2. As shown in Fig. 4b, both buckling and curling occurred on the same sample. This can be explained by the stress states in

the photoresist and the niobium film. Buckling occurs when the detached segment is bounded by an attached portion of the film, and at least part of the film thickness is in compression. Curling occurs when the detachment extends to the end of the line and there is a stress gradient in the film. In this way, buckling and curling on the same sample and even in the same line is not inconsistent. The photoresist/niobium bilayer buckled once an interface crack was formed, due to the compressive stress in the niobium film. When the buckle formed, the previously tensile photoresist was driven even more tensile. This is the case for the buckles observed next to the curls in these lines. However, once one end of the buckle was detached from the substrate and the constraint from the substrate was removed, the photoresist/niobium bilayer, subjected to the tensile stress in the photoresist and the compressive stress in the niobium, curled in the opposite direction.

No clear trend of the effect of silver on interface adhesion can be established based on the results from delamination of patterned lines. All the PVD samples that had interface delamination in the form of either buckles or curls have silver at the interface, ranging from 2.1 monolayers to 6.5 monolayers. The sample without silver at the interface did not show any interface failure, indicating a stronger interface. However, two other samples that have a relatively high interfacial silver level (4.2 and 7.6 monolayers) did not have any interface failure either.

Effect of IBAD on Interface Fracture Toughness

Ion beam assisted deposition (IBAD) was used to establish the interfacial orientation relationships of either (11$\bar{0}$) Nb || (0001) sapphire and [001] Nb || [1$\bar{1}$00] sapphire or (110) Nb || (0001) sapphire and [001] Nb || [11$\bar{2}$0] sapphire. Silver was introduced at the interface of these samples so that a comparative study could be conducted between the samples with only silver at the interface and samples with both silver and strong in-plane orientation relationship at the interface. The silver level ranged from 0.7 to 6.5 monolayer for the set with the nominal thickness of 100 nm, and 0 to 6 monolayers for the set that had nominal film thickness of 500 nm. This silver level range is similar to that in the study of the effect of silver on interface fracture toughness in PVD samples.

No interface fracture was observed in any of the IBAD samples using the microscratch test. The stress state in the IBAD films was more compressive than that in the PVD films [14], and compressive stress is expected to promote interface delamination in the microscratch test. Therefore, the absence of delamination in the IBAD films indicates a strong interface. All the scratch tracks were similar to that shown in Fig. 1b in which the indenter tip simply ploughed into the niobium layer and eventually broke through the interface to make contact with the sapphire substrate. Even samples with the highest silver level (6.5 monolayers) exhibited strong interfacial adhesion such that there was no observable delamination.

Results of the microwedge scratch test revealed a stronger interface for IBAD samples as compared to the PVD sample as well. Only the sample with the highest amount of silver at the interface (11.4 monolayers) showed delamination. The interface fracture toughness for this sample was 107.91 J/m^2, much higher than that of the PVD samples measured with the same technique (4.54 J/m^2 and 12.44 J/m^2). The IBAD sample without silver at the niobium/sapphire interface showed no interface delamination. The wedge tip ploughed into the niobium film, indicating a strong interface. Delamination of patterned lines on sapphire substrate also indicated a stronger interface for the IBAD samples. Six out of nine PVD samples showed line delamination in the forms of either buckles or curls, while only the one sample with the highest silver level at the interface (6 monolayers) of the four IBAD samples had line detachment from the substrate after the dry etch step. It was found that the delamination occurred at the niobium/sapphire interface. Failure occurred by curling at the end of the lines, similar to that shown in Fig. 4b. The average radius of curvature of the curls was 28 μm. Using the stress of -184.9 MPa obtained from substrate curvature measurement, the interface fracture toughness was found to be 3.22 J/m^2, almost 3.5 times higher than that for the PVD sample with less silver (2.1 monolayer) measured by the same technique (from curls).

Another cause of the strong interface for IBAD samples is ion mixing at the interface. Interface mixing is a common observation in IBAD samples due to ion bombardment during film deposition. Interface mixing is determined via Rutherford backscattering (RBS) analysis. RBS analysis of both PVD and IBAD samples showed that the interface of the IBAD sample was mixed, compared to that for the PVD sample. Mixing at

interface usually promotes the adhesion between the film and substrate [13], and is a likely cause of the increased interface fracture toughness exhibited by the IBAD samples.

SUMMARY

Although results of interface fracture toughness measured from different tests, and sometimes within the same test, are not always consistent, general trend of the effect of silver has be established where the interface fracture toughness decreases with the amount of silver at the niobium/sapphire interface. Furthermore, the microscratch test results showed that the interface fracture toughness was related to the work of adhesion through a power law relation with the exponent equals to 3, supporting the result of Elssner *et al*. [2]. The ability to produce interface delamination depends on the test technique, but the values of interface fracture toughness obtained from different techniques fall into the same range (tens of J/m^2 to tenth of J/m^2). Ion bombardment during film deposition (IBAD) significantly increased the interface fracture toughness. Both ion mixing and development of an orientation relationship at the interface enhance the adhesion. The high interface adhesion of the IBAD niobium-sapphire system can be attributed to either one of the two factors or a combination of the two. Ion mixing is believed to be the primary cause.

ACKNOWLEDGMENTS

The authors would like to thank Dr. W. W. Gerberich and Dr. J. Nelson for providing help on microwedge scratch test. Qiong Zhao helped on preparing the samples used in the microwedge scratch test. The authors acknowledge the Michigan Ion Beam Laboratory for Surface Modification and Analysis and the Electron Microbeam Analysis Laboratory at the University of Michigan for the use of their facilities. This work was supported under NSF grant #DMR-9411141.

REFERENCES

1. H. Ji, G. S. Was, J. W. Jones, and N. R. Moody, (1997) *Mat. Res. Soc. Symp. Proc*., Vol. 458, p 191.
2. G. Elssner, D. Korn, and M Rühle, (1994) *Scr. Metall. et Mater.* 31, no. 8, 1037.
3. M. P. Seah, (1980) *Acta Metall*., 28, 955.
4. J. R. Rice, Z. Suo, and J. S. Wang, (1989) In: *Metal-Ceramic Interfaces*, M. Rühle, M. F. Ashby, A. G. Evans, and J. P. Hirth, (Eds), Pergamon Press, Oxford.
5. H. Ji, G. S. Was, J. W. Jones and N.R. Moody, (1997), Proc. Mater. Res. Soc., Materials Research Society, Pittsburgh, vol 458, p. 191.
6. G. Elssner, T. Suga, and M. Turwitt, (1985) *J. Phys. (Orsay*), 46-C4, 597.
7. D. Korn, G. Elssner, H. F. Fischmeister, and M. Rühle, (1992) *Acta. Metall. Mater*. 40, suppl., S355.
8. M.G.Nicholas, (1989) In: *Surfaces and Interfaces of Ceramic Materials*', p. 393, L.-C.Dufour (Ed), Norwell, MA, Kluwer Academic.
9. M. P. dE Boer, M. Kriese, and W. W. Gerberich (1997), *J. Mater. Res*. 12, No. 10, 2673.
10. M. P. dE Boer, H. Huang, and W. W. Gerberich, (1995) *Mat. Res. Soc. Symp. Proc*., Vol. 356, p. 821.
11. J. W. Hutchinson and Z. Suo, (1992) *Advances in Applied Mechanics* 29, 63.
12. H. Ji, G. S. Was, J. W. Jones, and N. R. Moody, (1996) *Mat. Res. Soc. Symp. Proc*. Vol. 434, p. 153.
13. J. E. E. Baglin, (1986) In: *Ion beam modification of insulators*, p. 585, P. Mazzoldi and G. W. Arnold (Eds), Amsterdam, Elsevier.

ORAL REFERENCE: xxxxx

FRACTURE TOUGHNESS OF POLYMER INTERFACES: FROM THE MOLECULAR TO THE CONTINUUM SCALE

C. Creton[1], E.J. Kramer[2], H.R. Brown[3] and C.Y. Hui[4]

[1] Laboratoire PCSM, E.S.P.C.I. 10, Rue Vauquelin, 75231 Paris Cédex 05, FRANCE
[2] Department of Materials Engineering, University of California, Santa Barbara, CA 93106, USA
[3] BHP Steel Institute, University of Wollongong, Wollongong, NSW 2522, AUSTRALIA
[4] Department of Theoretical and Applied Mechanics, Cornell University, Ithaca, NY 14853, USA

ABSTRACT

In order to be mechanically strong, an interface must be able to transfer stress across it. For very narrow interfaces between polymers, this capability is weak and a significant reinforcement can be achieved by the use of suitably chosen connector molecules (block copolymers) or by a broadening of the interface (random copolymers). In both of these cases the stress is transferred by entanglements between polymer chains. We review the main molecular characteristics which are necessary for this reinforcement effect to take place. Furthermore, recent theoretical advances on the relationship between interfacial stress and fracture toughness are discussed and the essential role of plastic deformation in the immediate vicinity of the interface is specifically addressed.

KEYWORDS

Fracture, polymer interfaces, adhesion, crazing, block copolymer, random copolymer

INTRODUCTION

Controlling the level of adhesion between two polymers is essential for many applications such as multiphase polymeric alloys, multilayer structures or adhesives. In all of these cases adhesion is caused by molecular interactions at the interface, but the level of adhesion is typically measured with a destructive test. Ideally one would like to be able to relate the macroscopic measurement of fracture toughness, which typically gives a critical energy release rate G_c, with the underlying surface chemistry (chemical bonds, specific interactions or simply entanglements). Recent experimental advances on the micromechanics of cracking at interfaces combined with easier access to polymers with well-defined chemical structures and surface analysis techniques have made it possible, at least for glassy polymers, to bridge the gap between the molecular and the continuum scale[1].

Interfaces between polymers which are immiscible are typically very narrow, with an interpenetration distance which is significantly smaller than the average distance between entanglement points in the bulk polymers. This lack of entanglements is responsible for the very low level of adhesion (typically a few J/m^2) which is measured. One strategy to increase the level of adhesion of such interfaces is to replace the natural entanglement network at the interface with connecting molecules such as block copolymers which will be able to entangle with the bulk polymers on either side of the interface acting as molecular stitches. An

example of such molecules are given on figure 1. Alternatively random copolymers, also shown on figure 1, can reinforce the interface by effectively reducing the immiscibility and increasing the interfacial width.

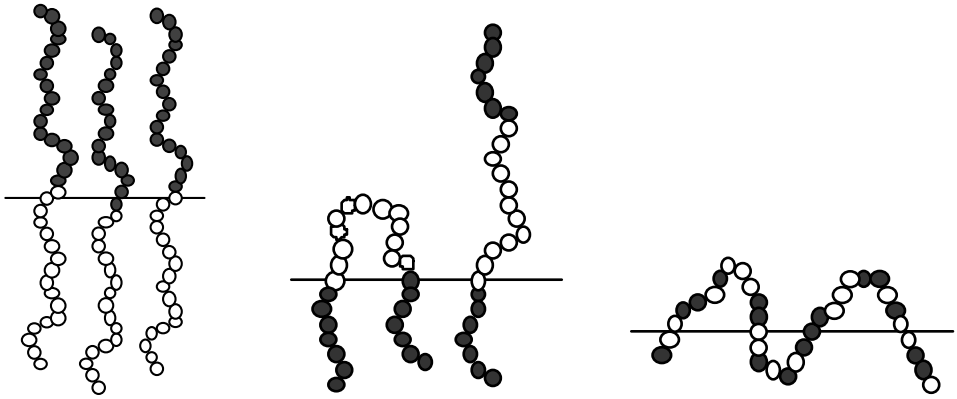

Figure 1: Schematic of connecting molecules at interfaces between A and B immiscible polymers. (Dark beads represent monomers of A and light beads represent B monomers). From left, diblock copolymers, triblock copolymers and random copolymers. The latter type of molecule acts by broadening the interface.

EXPERIMENTAL METHODS

In order to obtain the necessary information to bridge the gap between the molecular scale and the continuum scale, several techniques must be used. At the molecular level, one must be able to work with well-defined molecules, in particular for the block copolymers which are used as connecting chains. The molecular structure of the interface must be characterized before and after fracture if possible. For this purpose partial deuteration of the molecules present at the interface is invaluable and allows the use of ion beam techniques (to measure the amount of deuterium present on each surface after fracture) or neutron reflectivity (to measure interfacial width before fracture). If nitrogen is present, X-ray photoelectron spectroscopy (XPS) can also be quantitative to measure the amount of block copolymer at the interface.
At the macroscopic level, suitable fracture mechanics tests are needed to characterize the fracture toughness of the interface G_c. The double cantilever beam test combines ease of sample preparation and measurement with a great flexibility in controlling the degree of mode mixity at the interface during crack propagation[2]. This last point is important because the G_c of interfaces generally depends on the phase angle of loading in a non-trivial way. We found this to be particularly true of interfaces between glassy polymers where very small amounts of shear stresses could significantly modify the measured G_c by causing small crazes to grow in the bulk polymers[2,3].
Finally at the intermediate microscopic level, it is important to use observation tools such a electron or optical microscopy to investigate how is local plasticity near the interface is affected by a modification of the molecular structure at the interface or by a change in the plastic deformation properties of the bulk polymers.

CONNECTING CHAINS BETWEEN GLASSY POLYMERS

The simplest and most informative case is that of an interface between immiscible A/B glassy polymers reinforced with a variable amount of A-B diblock copolymer. In that case one can safely assume that all the stress transfer capability is due to the presence of the block copolymers. For long copolymer chains, which do not disentangle, the stress transfer capability of the interface σ_{int} is given by:

$$\sigma_{int} = f_b \, \Sigma \qquad (1)$$

where f_b is the force to break a covalent bond (approximately 2nN) and Σ is the areal density of connector chains present at the interface. As long as σ_{int} remains below the crazing stress of both A and B polymers, G_c is low and the interface fails by simple chain fracture. If $\sigma_{int} > \sigma_{craze}$, i.e. if $\Sigma > \Sigma^* = \sigma_{int}/f_b$, a craze precedes the propagating crack and G_c becomes much higher. If shorter copolymer chains are used, and the interface

fails by chain pullout rather than by chain scission this transition can be shifted to higher values of areal density $\Sigma^{\dagger}$ or suppressed altogether[4]. The degree of polymerization of the block where this starts to occur is of the order of the average degree of polymerization between entanglements N_e. Therefore a reasonably good picture of the fracture mechanisms is given by a plot of Σ/Σ^* as a function of N/N_e as shown on figure 2[1]. The limiting value for Σ, which we will define as Σ_{sat} is a decreasing function of N for steric reasons so that maximum values of G_c are typically obtained for values of N/N_e between 4 and 8.

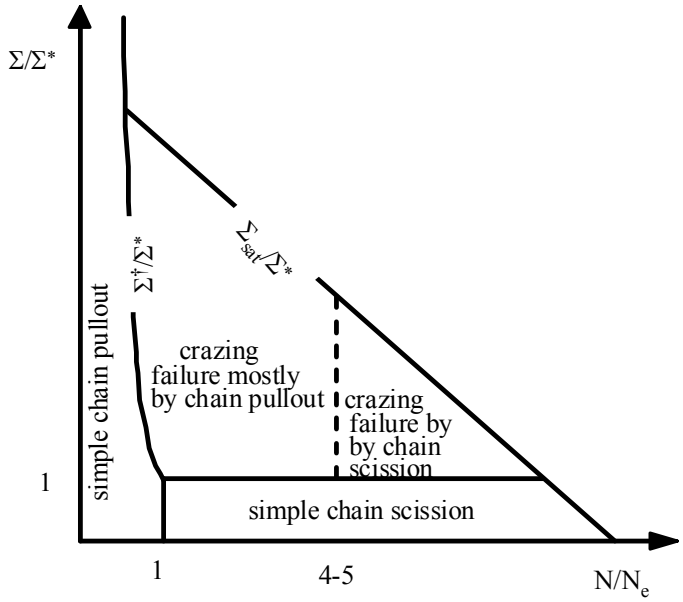

Figure 2: Fracture mechanisms map for interfaces between glassy polymers reinforced with connecting chains. Failure mechanisms are represented as a function of normalized degree of polymerization N/N_e and normalized areal density of connectors Σ/Σ^*.

CRAZE GROWTH AND STABILITY

In the regime where fracture of the interface is preceded by a craze, the fracture toughness can be related to the interfacial stress with the help of a model recently proposed by Brown for crack growth in a craze[5]. The key features of the model are the description of the craze zone as an elastic anisotropic strip with a local stress concentration at the crack tip. The larger the stress that the interface can sustain and the larger will be the amount of elastic energy needed in the strip for the crack to propagate. Since this amount of elastic energy is directly proportional to the width of the craze, we now have a direct connection between the maximum width of the craze h_f and the interfacial stress. Remembering that the macroscopic G_c is given for such a strip model by[6]:

$$G_c \sim \sigma_{craze} h_f$$

A direct connection can be made between G_c and the interfacial stress. The final result of the model which can be experimentally tested is[5,7,8]:

$$G_c = \frac{\delta^{\mp} \sigma_{craze}}{\ln\left\{\left[1-\left(1.2\sigma_{craze}/\sigma_{\text{int}}\right)^2\right]^{-1}\right\}} \tag{3}$$

which reduces to:

$$G_c = \frac{\delta^{\mp}}{1.44}\frac{\sigma_{\text{int}}^2}{\sigma_{craze}} \tag{4}$$

for strong interfaces where G_c > 50 J/m^2. $\delta^{\mp}$ has the physical meaning of an opening displacement and is characteristic of the elastic and geometric parameters of the craze itself. It does not vary much from one polymer to another.

It should be noted that σ_{craze} and h_f are directly analogous to the parameters $\hat{\sigma}$ and $\hat{\delta}$ used in cohesive zone models[9].

The dependence of G_c on σ_{int}^2 has been mainly tested for two experimental systems: diblock copolymers of polystyrene-poly2-vinylpyridine (PS-PVP) at the interface between PS and PVP[4] and for diblock copolymers of PS-polymethylmethacrylate (PS-PMMA) at the interface between poly(oxyphenylene) (PPO) and PMMA[10]. The agreement between the model is qualitatively and quantitatively very good.

REINFORCEMENT BY BROADENING OF THE INTERFACE

While in the case of connector molecules at the interface of very immiscible polymers, the value of σ_{int} is unambiguously given by equation 1, if the two polymers are less immiscible and the interfacial width becomes of the order of the average distance between entanglement points, a significant stress can be transferred by the entanglements formed at the interface. In this case experiments have shown that G_c is a unique function of the width of the interface a_i, provided that the molecular weight of the polymers is well above the average molecular weight between entanglements[11]. As shown on figure 3, however the increase in G_c with a_i shows clear transitions between different regimes: for thin interfaces one can argue that $\sigma_{int} < \sigma_{craze}$ and no plastic zone is formed at the interface; above a certain value of a_i, G_c increases dramatically implying that the crack is preceded by a craze. Finally at high values of a_i , G_c saturates and bulk toughness is retrieved. Although the exact value of a_i at the transition point varies somewhat from a system to another, it is always of the order of 10 nm. Therefore if a random copolymer is able to sufficiently reduce the immiscibility and broaden the interface to 10 nm, one expects to see a very large effect on the adhesive properties. This result has been confirmed experimentally for PS-r-PMMA random copolymers[12] and PS-r-PVP random copolymers at interfaces between their respective homopolymers[13,14].

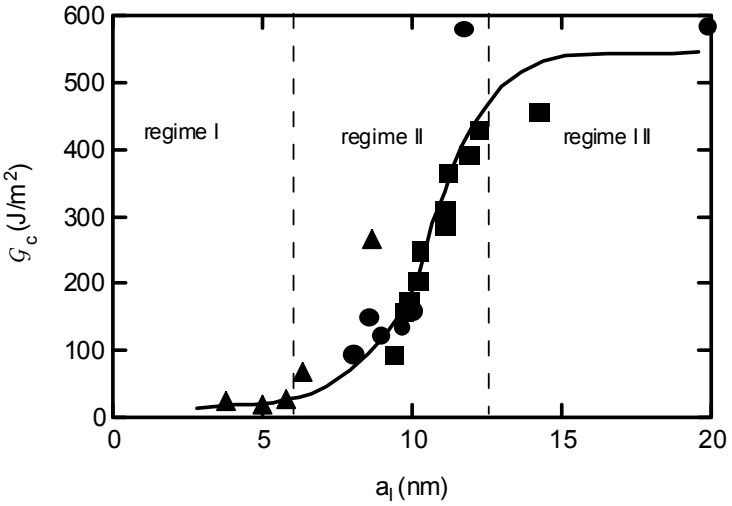

Figure 3: Fracture toughness G_c of interfaces between glassy homopolymers as a function of their width a_i. Data from [15].

GENERALIZATION OF THE MODEL

The craze growth model developed in the preceding sections is very attractive since it directly relates a macroscopic value G_c with molecular parameters and material parameters such as σ_{craze} which can be independently measured. While the original model was developed for glassy polymers which readily craze, subsequent studies have shown that the main features of the model (summarized in equations 3 and 4) may be much more robust. Fracture experiments of interfaces between semi-crystalline polymers, reinforced with

polymer chains chemically grafted at the interface followed well equation 4[16]. Furthermore, in the crazing regime, the measured value of $\mathcal{G}_c$ was found to directly increase with $1/\sigma_{craze}$ as predicted by equation 4. Figure 5 shows experiments performed on two systems where the molecular structure at the interface is identical (giving therefore the same value of σ_{int}) but the crazing stress (in this case rather the yield stress in hydrostatic tension) varies by a factor of 5. Accordingly the $\mathcal{G}_c$ values for the system with the lower yield stress are five times higher than for the harder system[17].

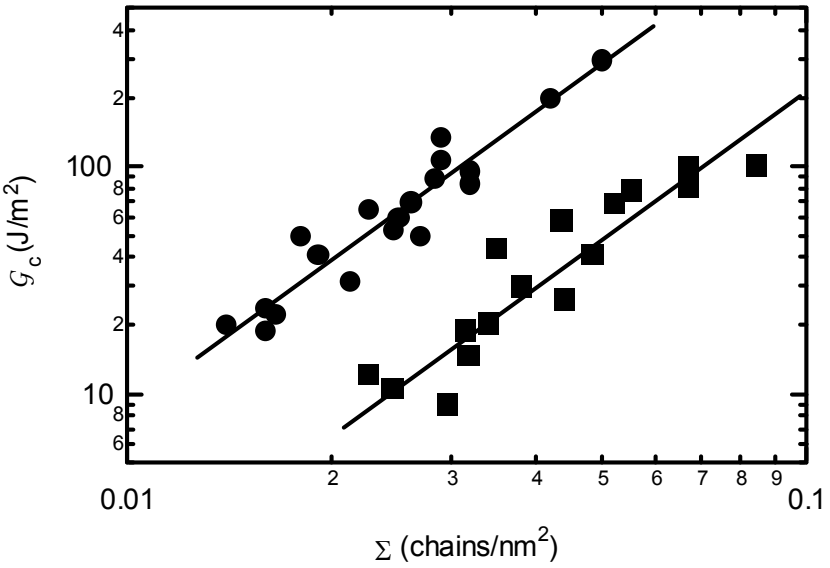

Figure 5: $\mathcal{G}_c$ vs. Σ for an interface between polypropylene (PP) (■) or a blend of PP with ethylene-propylene rubber (PP/EPDM)(●) and polyamide-6 (PA6), reinforced by end-grafted PP chains. The yield stresses of the PP and PP/EPDM blends are 21 and 4 MPa respectively. Data from [17].

Optical and electron microscopy observations of the plastically deformed zone ahead of the crack tip show that in both systems the dissipation is localized in a strip analogous to a Dugdale plastic zone near the interface.
This is not however a very general case. If the softer polymer for example, is able to nucleate diffuse plasticity in the hard matrix, far away from the crack tip, greatly increasing the dissipated energy associated with the propagation of the crack, the correlation between interfacial structure and $\mathcal{G}_c$ can be much more complicated and is no longer described by Brown's model[18].

CONCLUSIONS

We have shown that the fracture toughness of interfaces between polymers is dependent on the molecular structure at the interface as well as on the bulk properties of the polymers on either side of the interface. This relationship is now relatively well established for interfaces between glassy polymers and the main results have been summarized here. Two important points must be emphasized:

- In order to obtain a high value of fracture toughness, the interface must be able to transfer a stress which is at least as high as the crazing stress of one of the bulk polymers on either side of the interface.

- If this condition is met, $\mathcal{G}_c$ will depend on the interfacial stress σ_{int} and on the bulk crazing stress σ_{craze}. If all the plastic deformation is confined in a localized craze near the interface, G_c is well predicted by equations 3 and 4.

REFERENCES

1. Creton, C.,Kramer, E. J.,Brown, H. R.and Hui, C. Y. to appear in *Adv. Polym. Sci.*
2. Brown, H. R. (1990) *J.Mat.Sci.* 25, 2791.

3. Xiao, F.,Hui, C.-Y.,Washiyama, J.and Kramer, E. J. (1994) *Macromolecules* 27, 4382.
4. Creton, C.,Kramer, E. J.,Hui, C. Y.and Brown, H. R. (1992) *Macromolecules* 25, 3075.
5. Brown, H. R. (1991) *Macromolecules* 24, 2752.
6. Dugdale, D. S. (1960) *J. Mech. Phys. Solids* 8, 100.
7. Hui, C. Y.,Ruina, A.,Creton, C.and Kramer, E. J. (1992) *Macromolecules* 25, 3948.
8. Sha, Y.,Hui, C. Y.,Ruina, A.and Kramer, E. J. (1995) *Macromolecules* 28, 2450.
9. Zehnder, A. T.and Hui, C. Y. (2000) *Scripta mater.* 42, 1001.
10. Char, K.,Brown, H. R.and Deline, V. R. (1993) *Macromolecules* 26, 4164.
11. Schnell, R.,Stamm, M.and Creton, C. (1998) *Macromolecules* 31, 2284.
12. Brown, H. R. to appear in *Macromolecules.*
13. Dai, C. A.,Osuji, C. O.,Jandt, K. D.,Dair, B. J.,Ober, C. K.and Kramer, E. J. (1997) *Macromolecules* 30, 6727.
14. Xu, Z.,Kramer, E. J.,Edgecombe, B. D.and Fréchet, J. M. J. (1997) *Macromolecules* 30, 79.
15. Schnell, R.,Stamm, M.and Creton, C. (1999) *Macromolecules* 32, 3420.
16. Boucher, E.,Folkers, J. P.,Hervet, H.,Léger, L.and Creton, C. (1996) *Macromolecules* 29, 774.
17. Kalb, F.,Léger, L.,Creton, C.,Plummer, C. J. G.,Marcus, P.and Magalhaes, A. to appear in *Macromolecules*
18. Plummer, C. J. G.,Kausch, H. H.,Creton, C.,Kalb, F.and Léger, L. (1998) *Macromolecules* 31, 6164.

ORAL REFERENCE: ICF10 0193OR

FRACTURE TOUGHNESS TESTS FOR MICRO-SIZED SPECIMENS

K. Takashima[1], Y. Higo[1] and M. V. Swain[2]

[1] Precision and Intelligence Laboratory, Tokyo Institute of Technology,
4259 Nagatsuta, Midori-ku, Yokohama 226-8503, Japan.
[2] Faculty of Dentistry and Department of Mechanical & Mechatronic Engineering,
The University of Sydney, Australian Technology Park, Everleigh NSW 1430, Australia.

ABSTRACT

A fracture toughness testing method appropriate to micro-sized specimens has been designed and fracture tests have been performed on micro-sized specimens for MEMS applications. Cantilever beam type specimens with dimensions of 10 x 10 x 50 μm^3 were prepared from a Ni-P amorphous thin film and notches with different directions, which are perpendicular and parallel to the deposition growth direction, were introduced by focused ion beam machining. Fatigue pre-cracks were introduced ahead of the notches. Fracture tests were carried out using a newly developed mechanical testing machine for micro-sized specimens. Fracture behavior is different between the two types of specimens. K_{IC} values were not obtained as the criteria of plane strain requirements were not satisfied for this size of the specimen, so that the provisional fracture toughness K_Q values were obtained. The K_Q value of the specimen with crack propagation direction being parallel to the deposition growth direction was 4.2 $MPam^{1/2}$, while that with crack propagation direction being perpendicular to the deposition growth direction was 7.3 $MPam^{1/2}$. These results suggest that the electroless deposited amorphous alloy thin film has anisotropic mechanical properties. It is necessary to consider the anisotropic fracture behavior when designing actual MEMS devices using electroless deposited amorphous films.

KEYWORDS

Fracture toughness, Thin film, Micro-sized specimen, MEMS, Anisotropy

INTRODUCTION

Microelectromechanical systems (MEMS) or microsized machines are under intensive development for utilization in many technological fields such as information and biomedical technologies. These MEMS devices are usually fabricated from a thin film deposited on a substrate by suitable surface micromachining techniques, and the micro-sized elements prepared from a thin film layer are used as mechanical components. The evaluation of fracture toughness of thin films is then extremely important to ensure the reliability of MEMS devices. In addition, micro-elements on MEMS devices are considered to be subjected to load in both the direction of “in-plane” and “out-of-plane” of the thin film. The fracture toughness values for both in-plane and out-of-plane directions are thus required for actual design of MEMS devices, as the fracture toughness of thin films prepared by sputtering or other

deposition techniques has been considered to have anisotropy even for amorphous alloys [1].

In this investigation, micro-sized cantilever type specimens were prepared from an electroless deposited Ni-P amorphous alloy thin film and fracture tests for two types of specimens with different crack growth dierctions, which are “in-plane” and “out-of-plane” of the thin film, were performed. Fracture behavior of the specimens is then discussed.

EXPERIMENTAL PROCEDURE

The material used in this investigation was a Ni-11.5 mass%P amorphous alloy thin film electroless plated on an Al-4.5 mass%Mg alloy. The thickness of the amorphous layer was 12 μm and that of the Al-4.5 mass%Mg alloy substrate was 0.79 mm. A disk with a diameter of 3 mm was cut from the Ni-P/Al-Mg sheet by electro discharge machining. The amorphous layer was separated from the Al-Mg alloy substrate by dissolving the substrate with a NaOH aqueous solution.

Two types of micro-sized cantilever beam specimens with different notch orientations were prepared from the amorphous layer by focused ion beam machining, and are referred to as “in-plane type specimen” and “out-of-plane type specimen” as shown in Figs. 1 (a) and (b), respectively. Figures 2(a) and (b) show

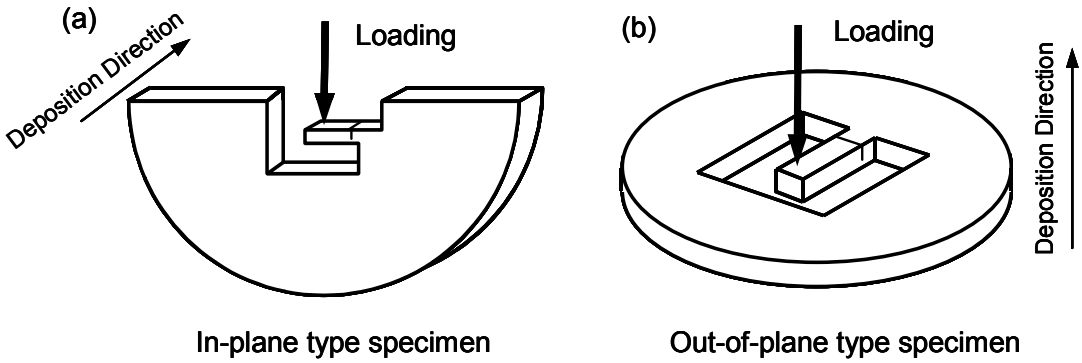

Figure 1: Two types of specimen orientations. The crack propagation direction is perpendicular to the deposition growth direction for in-plane type specimen (a), while the crack propagation direction is parallel to the deposition growth direction (b).

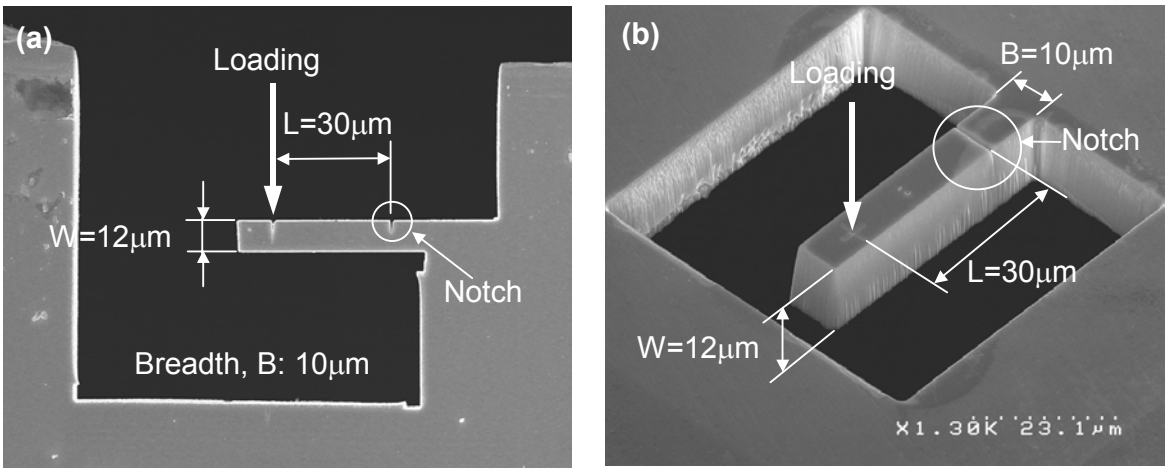

Figure 2: Scanning electron micrographs of micro-sized specimens prepared by focused ion beam (FIB) machining. (a) in-plane type specimen and (b) out-of-plane type specimen. Notches were also introduced by FIB.

scanning electron micrographs of the micro-sized specimens. The crack will propagate perpendicular to the deposition direction in the in-plane type specimen, while the crack will propagate parallel to the deposition direction in the out-of-plane type specimen. The breadth of the specimen, B, was 10μm, the distance from the loading point to the notch position, L, was 30μm, and the width of the specimen, W, was 10μm. Notches with a depth of 2.5 μm were introduced into the specimens as shown in Fig. 1 by focused ion beam machining. The width of the notch was 0.5 μm, and the notch radius was thus deduced to be 0.25 μm. The notch position was 10 μm from the fixed end of the specimen.

In our previous studies [2, 3], we have demonstrated that the introduction of a fatigue pre-crack is required to evaluate fracture toughness even for micro-sized specimens. A fatigue pre-crack was then introduced ahead of the notch in air at room temperature under constant load amplitude using a mechanical testing machine for micro-sized specimens, which was developed in our previous investigation [4, 5]. The length of the fatigue pre-crack was adjusted to be approximately 2.5 μm. The total crack length over specimen width (a/W) was then approximately 0.5 for all the specimens. Fracture tests were also carried out in air at room temperature using the same mechanical testing machine which was used for introducing fatigue pre-cracks.

RESULTS AND DISCUSSION

Fracture Behavior

Figure 3 shows load-displacement curves during fracture tests for the in-plane and the out-of-plane type specimens. The fracture behavior is different between these two types of specimens. The maximum load of the out-of-plane type specimen is higher than that of in-plane type specimen in spite of the size of specimen and the length of fatigue pre-crack being approximately the same. This suggests that the electroless plated Ni-P amorphous thin film exhibits anisotropic fracture behavior.

As crack opening displacement was not able to be measured for these specimen, the crack initiation load was not able to be determined. The maximum load was then assumed to be the crack initiation load and this load was used to calculate fracture toughness value. Stress intensity factor, K, is calculated from the equation for a single edge notched cantilever beam specimen [6]. The total pre-crack length was measured from scanning electron micrographs of the fracture surfaces. The calculated provisional fracture toughness values (K_Q) for the out-of-plane and in-plane specimens are 7.3 and 4.2 MPam$^{1/2}$,

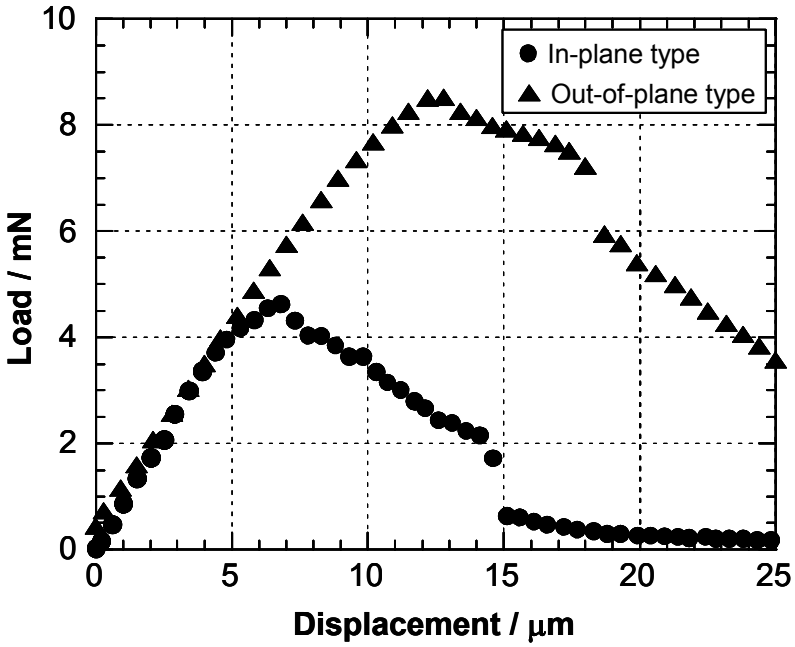

Figure 3: Load-displacement curves for in-plane and out-of-plane type micro-sized specimens.

respectively. However, these values are not valid plane strain fracture toughness values (K_{IC}), as the criteria of plane strain requirements were not satisfied for this specimen size. Actually, a plastic zone was observed clearly at the crack tip. As the plane strain requirements are determined by K and σ_y (yield stress), it is rather difficult for micro-sized specimens to satisfy these requirements. Consequently, another criterion such as J integral might be required to evaluate fracture toughness of such micro-sized specimens.

Fracture Surfaces

Figures 4 (a) and (b) show scanning electron micrographs of fracture surfaces for the specimens with different crack orientations. Fine equispaced markings aligned perpendicular to the crack propagation direction are observed ahead of the notch. This kind of markings were also observed on fatigue fracture surface of micro-sized Ni-P amorphous alloy specimens in our previous investigation [7], and are considered to be striations. Vein patterns which have been observed on static fractured surfaces on Ni-P amorphous alloy are visible ahead of the fatigue pre-cracked region. The fracture surface of the in-plane type specimen is relatively flat. In contrast, the fracture surface of the out-of-plane type specimen is rough, and the crack seems to propagate tortuously. The difference in K_Q values is considered to result from the difference in fracture surface morphologies.

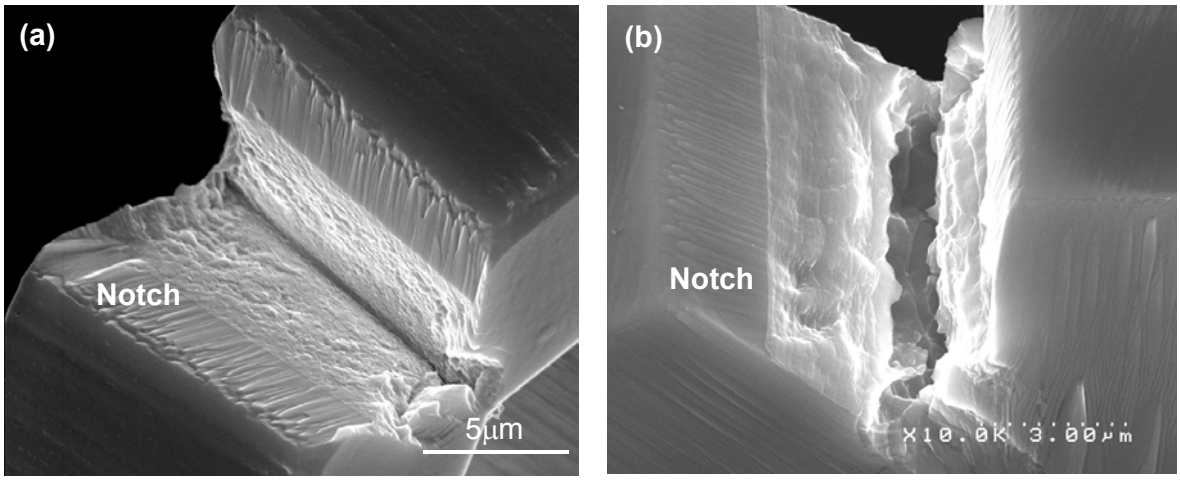

Figure 4: Scanning electron micrographs of fracture surfaces of (a) in-plane type specimen and (b) out-of-plane type specimen, respectively.

Another notable feature of the fracture surface is the existence of slant fractured regions near the side surfaces of the crack. The width of the slant fractured region is approximately 1 μm for in-plane type specimens and 3 μm for out-of-plane type specimens. If these are shear lips, these regions should be plane stress dominated regions. The expected width of the shear lip is then calculated based on fracture mechanics [8]. The calculated value of shear lip width at K_Q is 1.2 μm for in-plane type specimen and is 3.4 μm for out-of-plane type specimen (the value of σ_y = 2.0 GPa in this amorphous alloy thin film was quoted in this calculation [9]). These sizes are very close to those of the slant fractured regions in Figs. 3 (a) and (b). Therefore, these slant fractured zones are considered to be plane stress dominated regions and the flat region is considered to correspond to plane strain dominated one.

Origin of Anisotropic Fracture

The provisional fracture toughness, K_Q, of the out-of plane specimen was much higher than that of the in-plane specimen. Electron diffraction pattern of the Ni-P amorphous alloy thin film (the beam direction is parallel to the deposition growth direction) showed only a halo pattern which is characteristic of an amorphous phase. Therefore, there is no medium or long range ordering in the direction perpendicular to the deposition growth direction in this amorphous thin film. However, it has not been confirmed whether there is medium or long range ordering in the direction parallel to the deposition

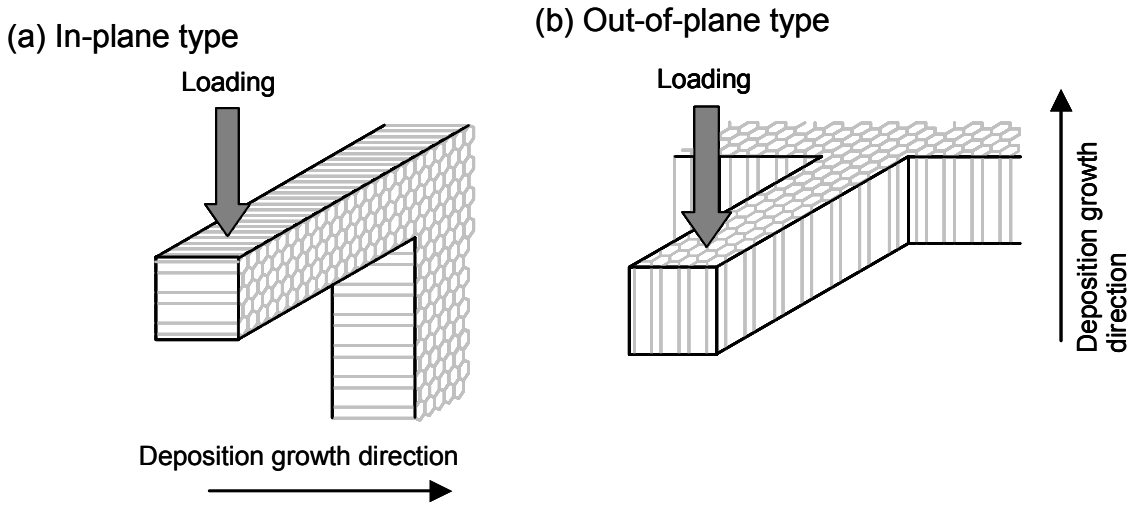

Figure 5: Schematic images of columnar structure aligned towards the growth direction in the elecroless deposited Ni-P amorphous alloy thin film.

growth direction. The difference in K_Q values and fracture surfaces between these two specimens suggests that there is some ordering towards the growth direction. Actually, anisotropic magnetic properties have been often observed for sputtered and deposited amorphous thin films [10]. Consequently, there may exist some columnar type domain structures oriented towards the deposition growth direction as schematically shown in Fig. 5. Actually, such a columnar structure was observed for electro-deposited amorphous Fe-P alloys [11]. If there is such a columnar structure aligned towards the growth direction, the cantilever specimens have an anisotropy. This may be one reason that the K_Q of the out-of-plane specimen is higher compared to that of the in-plane specimen.

CONCLUSIONS

Fracture tests have been performed on micro-sized cantilever beam specimens prepared from an electroless plated Ni-P amorphous alloy thin film. Two types of specimens with different crack growth directions, which are perpendicular and parallel to the deposition growth directions, were prepared to investigate anisotropic fracture behavior of the thin film.

Fracture behavior is different between the two types of specimens. As K_{IC} values were not obtained because the criteria of plane strain were not satisfied for this micro-sized specimen, the provisional fracture toughness K_Q values were measured. The K_Q value of the specimen with crack propagation direction being parallel to the deposition growth direction was 7.3 $MPam^{1/2}$, while that with crack propagation direction perpendicular to the deposition growth direction was 4.2 $MPam^{1/2}$. This result suggests that the electroless plated Ni-P amorphous alloy thin film has anisotropic fracture properties. It is important to consider the anisotropic fracture behavior when designing actual MEMS devices using electroless deposited amorphous films.

Acknowledgment **–** This work was partly supported by the Grant-in-Aid for Scientific Research (B) (2) No. 12555186 from the Ministry of Education, Science, Sports and Culture, Japan.

REFRENCES

1. Lewis D. B. and Marshall, G. W. (1996) *Surface and Coating Tech*., **78**, 150.
2. Ichikawa, Y., Maekawa, S., Takashima, K., Shimojo, M., Higo, Y. and Swain, M. V. (2000). In: *Materials Science of Microelectromechanical Systems (MEMS) Devices II,* pp. 273-278, deBoer, M. P., Heuer, A. H., Jacobs, S. J. and Peeters, E., (Eds). The Materials Research Society, Pennsylvania.

3. Takashima, K., Shimojo, M., Higo, Y. and Swain, M. V. (2000). In: *Proc. Microscale Systems: and Measurements Symposium*, pp.32-35, Soc. for Experimental Mechanics, Inc.
4. Takashima, K., Kimura, T., Shimojo, M., Higo, Y., Sugiura, S. and Swain, M. V. (1999). In: *Fatigue '99 (Proc. 7th Int. Fatigue Cong.)*, pp. 1871-1876, Wu, X-R. and Wang, Z-G., (Eds). Higher Education Press, Beijing.
5. Higo, Y., Takashima, K., Shimojo, M., Sugiura, S., Pfister, B. and Swain, M. V. (2000). In: *Materials Science of Microelectromechanical Systems (MEMS) Devices II*, pp. 241-246, deBoer, M. P., Heuer, A. H., Jacobs, S. J. and Peeters, E., (Eds). The Materials Research Society, Pennsylvania.
6. Okamura, H. (1976). *Introduction to Linear Fracture Mechanics*, Baifukan, Tokyo, (in Japanese).
7. Maekawa, S., Takashima, K., Shimojo, M., Higo, Y. and Swain, M. V. (2000). In: *Materials Science of Microelectromechanical Systems (MEMS) Devices II*, pp. 247-252, deBoer, M. P., Heuer, A. H., Jacobs, S. J. and Peeters, E., (Eds). The Materials Research Society, Pennsylvania.
8. Knott, J. F. (1976). *Fundamentals of Fracture Mechanics*, Butterworths, London.
9. Morita, A., Takashima, K. and Higo, Y., to be published.
10. Lanchava, B., Hoffmann, H., Bechert, A., Gegenfurtner, S., Amann, C. and Rohrmann, I. (1997) *J. Magnetism and Magnetic Materials*, **176**, 139.
11. Armyanov, S., Vitkowa, S. and Blajiev, O. (1997) *J. Appl. Electrochemistry*, **27**, 185.

REFERENCE: ICF100613OR

FREE EDGE AND INTERACTION EFFECTS ON THE STRENGTH OF FINITE-SIZED INTERFACE BONDS

Henrik Myhre Jensen

Department of Solid Mechanics, Building 404
Technical University of Denmark
DK-2800 Lyngby, DENMARK

ABSTRACT

A fracture mechanics based analysis of the strength of a bond between a thin plate and a substrate is presented. The bond edge is regarded as a crack front, which is loaded under combined mode I, II and III conditions. A numerical procedure is used to study crack initiation. Results for bond strength are presented for bonds close to the plate edges and for closely spaced bonds.

KEYWORDS

Bond fracture, interface fracture, three dimensional fracture, fracture criteria, crack shape.

INTRODUCTION

A framework based on linear elastic interface fracture mechanics for studying initiation and propagation of cracks in bonds of arbitrary shape was formulated in Jensen [1]. The work is an extension of previous fracture mechanics based models for predicting the strength of spot welds (*e.g.* Pook [2] and Zhang [3]).

Adhesive bond failure was studied in Reedy and Guess [4] where bond strengths were correlated to the stress intensity factor for the singular stress field at the interface corner as in conventional linear fracture mechanics. The trends in the bond strength dependence on the thickness of the adhesive layer were well captured with this model. Other alternative approaches for studying interface bond failure include methods based on cohesive zone modelling such as Lin *et al.* [5] where these models have been applied to study fracture in weld joints.

The problem analysed is sketched in Fig. 1. A thin plate is bonded to a substrate in a region or several regions of arbitrary shape. The plate is loaded in its plane by a constant normal traction. The bond edge is treated as an interface crack front, and the energy release rate, the decomposition into modes I, II and III and the mixed mode fracture criterion is based on the interfacial fracture mechanics concepts in Jensen *et al.* [6]. The radius of curvature of the crack front is taken to be considerably larger than the thickness, h, of the plate. Results are presented to illustrate the effects of the plate edges and closely spaced bonds on the bond strength predictions.

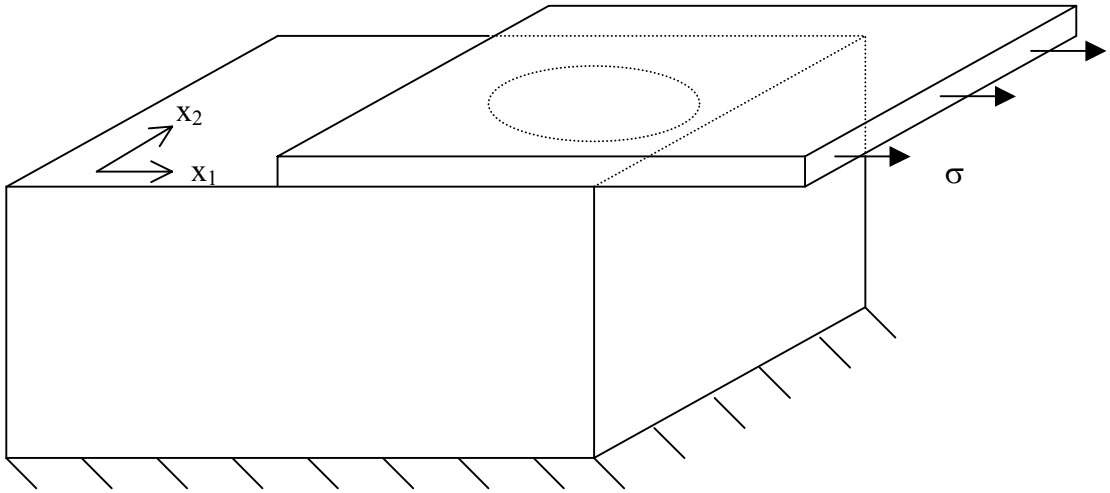

Figure 1: Schematic illustration of two overlapping plates bonded in a finite zone. The thin plate is loaded by a constant normal traction, $\sigma_{11} = \sigma$, as indicated.

FRACTURE MECHANICS

The edge of the bond zone is regarded as an interface crack front, which is subject to combined mode I, II and III loading. For the plate thickness, h, smaller than the extent of the bond zone, the energy release rate, G, and the mode I, II and III contributions to G can be calculated by the coupling of an inner, fracture mechanics based solution close to the crack tip with an outer solution for the stress state in the plate.

The relations between the combined mode I/II and the mode III energy release rates and the normal stress, σ_{nn}, and shear stress, σ_{nt}, in the plate along the crack front are given by [6]

$$G = G_{I/II} + G_{III} \quad , \quad G_{I/II} = \frac{1-\nu^2}{2E} h\sigma_{nn}^2 \quad , \quad G_{III} = \frac{1+\nu}{E} h\sigma_{nt}^2 \tag{1}$$

where E and ν are the Young's modulus and the Poisson's ratio for the plate, respectively.

A family of interface fracture criteria formulated in [6] for non-oscillating singular crack tip fields is applied here in the form

$$G_I + \lambda_2 G_{II} + \lambda_3 G_{III} = G_{1c} \tag{2}$$

where λ_2 and λ_3 denote parameters between 0 and 1 adjusting the relative contributions of mode II and III to the fracture criterion, and G_{1c} is the mode I fracture toughness of the bond. For $\lambda_2 = \lambda_3 = 1$ the fracture criterion is the Griffith criterion, while for $\lambda_2 = \lambda_3 = 0$ the fracture criterion is independent of mode II and III. The criterion (2) has been applied to thin film debonding problems in *e.g.* [6] and Jensen and Thouless [7]. It contains as a special case the fracture criterion applied for spot welds in Radaj [8] and [3]. The fracture criterion captures the mixed mode dependence of interface fracture toughness due to, for instance, plastic deformation at the crack tip or rough crack faces contacting under mode II and III dominant loading conditions.

For the present problem, which probably represents the simplest case possible since the stress state in the plate is planar so that the ratio between the mode I and mode II energy release rate along the crack front is constant, (1) and (2) reduces to

$$F \equiv \sigma_{nn}^2 + k\sigma_{nt}^2 = \sigma_c^2 \tag{3}$$

The ratio between the combined mode I/II energy release rate and the mode III energy release rate changes as the shear to normal stress ratio varies along the crack front. Denoting by ω the angle, which has been tabulated as a function of the elastic mismatch between the plate and the substrate in Suo and Hutchinson [9], then the parameters k and σ_c are given by

$$k = \frac{2\lambda_3}{(1-\nu)\left(1+(\lambda_2-1)\sin^2\omega\right)}$$
$$\sigma_c = \left(\frac{2EG_{1c}}{(1-\nu^2)h\left(1+(\lambda_2-1)\sin^2\omega\right)}\right)^{1/2} \tag{4}$$

In the following, it is assumed that $\nu = 1/3$ so that the usual mode independent Griffith fracture criterion corresponds to $k = 3$, while $k = 0$ corresponds to a fracture criterion independent of mode 3. In [6] a value close to $k = 1$ gave best agreement with experimental results for a polyamide/glass system, while the criterion applied in [8] and [3] for spot welded sheet metal corresponded to a value close to $k = 2$.

NUMERICAL RESULTS FOR BOND STRENGTH

In the calculations below, the bond shape (sketched in Fig. 1) is taken to be circular with diameter d, and its centre is located at the centre of a square plate of in-plane dimension αd with α specified below. The plate is loaded by a constant normal traction, σ, in the x_1-direction along a side parallel to the x_2-axis, and it is free along the other side parallel to the x_2-axis. The plate sides parallel to the x_1-axis are both free in the calculations below or symmetry conditions are specified on both sides so that the interaction between bonds in an infinite periodic array of identical bonds is modelled. Symmetry with respect to the x_1-axis is assumed and the results below are presented for the lower half of the crack front, only.

The stress state in the plate is solved numerically by the finite element method using typically 288 x 50 planar elements each consisting of two linear displacement triangles. The mesh is graduated with decreasing element sizes towards the interface crack for the best possible accuracy along the crack front.

In Fig. 2, the variation along the bond edge of F defined in (3) is shown in the case $k = 2$ with k defined in (4). The plate edges parallel to the x_1-axis are free in these calculations. By the fracture criterion (3), the most critical location along the bond edge, $\Theta = \Theta_c$, is at the peak value of F, which is denoted F_p so that $F(\Theta_c) = F_p$. The value of the applied traction, $\sigma = \sigma_0$, required to initiate crack propagation is

$$\sigma_0 = \frac{\sigma_c}{\sqrt{F_p}} \tag{5}$$

with σ_c given in (4). The angle Θ and the aspect ratio, α, defined as the ratio between the in-plane dimensions of the square plate and the bond diameter, are indicated in the inset in Fig. 2.

By Fig. 2 it is seen that F_p is significantly increased due to the presence of the free edge as in particular this increases the shear stress along the crack front close to the free edges. The applied traction is scaled by the aspect ratio, α, in Fig. 2 so that the resulting force acting on the bond is independent of the size of the plate. By (5) an increase in the peak value of F is equivalent to a decrease in the bond strength. Furthermore by (3) in the case $k = 2$ it is seen that the fracture criterion is more sensitive to shear stresses along the crack front than to normal stresses.

Calculations similar to those in Fig. 2 are presented in Fig. 3 but now with a value $k = 1$ so shear stresses contribute relatively less to the fracture criterion. It can be seen, as one would expect, that the strength of the bond in cases where the fracture criterion (3) applies with $k = 1$ is higher than bonds with

Figure 2: Variation along the bond edge of the function F defined in (3) for k = 2. The peak value, F_p, gives via (5) the bond strength and the location, Θ_c, along the bond edge for initial crack propagation.

Figure 3: Variation along the bond edge of the function F in the case k = 1.

k = 2. Furthermore, as the plate dimensions are decreased the most critical location along the crack front, Θ_c, decreases from 180^o to 148^o for $\alpha = 1.5$. For k = 2 the critical angle increases as the plate dimensions increase relative to the bond diameter from 115^o when $\alpha = 8$ to 135^o when $\alpha = 1.5$.

Figure 4: Variation along the bond edge of the function F in the case k = 1 and with periodic boundary conditions.

In Fig. 4 results are presented for k = 1 for cases where the boundary conditions along the plate edges parallel to the x_1-axis are changed from being free to being periodic in order to study the interaction effects resulting from closely spaced bonds. By comparison of Figs. 3 and 4 the interaction of bonds reduces the strength more than the effect of free edges. It is emphasised that the present procedure for calculating bond strength assumes that the radius of curvature of the crack front and the distance from the crack front to the plate edges must be large compared to the plate thickness. Also effects of large-scale plastic deformation and crack face contact have not been included in the analysis.

CONCLUSION

Significant effects of edges on the strength of finite bonds within plates have been demonstrated by numerical examples. The stresses along the crack front are enhanced due to the presence of the plate edge. There is a tendency for periodic boundary conditions to raise the stress levels more than free boundaries. Especially the shear stresses are increased due to periodic boundary conditions, and dependent on the factor k in the fracture criterion (3), this will affect the strength of the bonds significantly. Calculations carried out for k = 2 , not shown here, indicate a larger decrease in bond strength due to periodic boundary conditions than the results for k = 1 (compare Figs. 3 and 4).

Results for crack propagation following crack initiation under quasi-static conditions have been obtained in [1] based on a crack growth criterion. This issue has not been dealt with in the present work. It was shown in [1], however, that the ultimate strength of the bond might be significantly higher than initial strength where crack growth is initiated. Such effects could also be expected to play a role for the present problems.

ACKNOWLEDGEMENTS – Support from the the EFP-2001 research programme on scale effects in design with composites is gratefully acknowledged.

REFERENCES

[1] Jensen, H.M. (2001). Three dimensional numerical investigation of brittle bond fracture. *International Journal of Fracture* (in press).

[2] Pook, L.P. (1975). Fracture mechanics analysis of the fatigue behaviour of spot welds. *International Journal of Fracture* **11**, 173-176.

[3] Zhang, S. (1997). Stress intensities at spot welds. *International Journal of Fracture* **88**, 167-185.

[4] Reedy Jr., E.D. and Guess, T.R. (1997). Interface corner failure analysis of joint strength: Effect of adherend stiffness. *International Journal of Fracture* **88**, 305-314.

[5] Lin, G., Meng, X.-G., Cornec, A. and Schwalbe, K.-H. (1999). The effect of strength mis-match on mechanical performance of weld joints. *International Journal of Fracture* **96**, 37-54.

[6] Jensen, H.M., Hutchinson, J.W. and Kim, K.-S. (1990). Decohesion of a cut prestressed film on a substrate. *International Journal of Solids and Structures* **26**, 1099-1114.

[7] Jensen, H.M. and Thouless, M.D. (1993). Effects of residual stresses in the blister test. *International Journal of Solids and Structures* **30**, 779-795.

[8] Radaj, D. (1990). Local fatigue strength characteristic values for spot welded joints. *Engineering Fracture Mechanics* **37**, 245-250.

[9] Suo, Z. and Hutchinson, J.W. (1990). Interface crack between two elastic layers. *International Journal of Fracture* **43**, 1-18.

FUNCTIONALLY GRADED MATERIALS: EFFECT OF ELASTIC HETEROGENEITY ON THE TOUGHNESS

V. Cannillo[1] and W. C. Carter [2]

[1] University of Modena and Reggio Emilia, Modena, Italy
[2] Dept. of Materials Science and Engineering, Massachusetts Institute of Technology, USA

ABSTRACT

It has been demonstrated that gradients in the elastic modulus of a surface can affect the toughness of that surface [1,2]. Specifically, experimental results have correlated enhanced toughness with engineered gradients created by co-sintering a depth-dependent admixture of constituent particles with different elastic stiffnesses. While such engineered composites have average gradients that match the calculated optimal gradient, the composite microstructure will have variations in its lateral (in-surface-plane) properties and variations about the optimal gradient. The discrete nature of the particulate composites gives "stochastically graded" microstructures.

In this work, we numerically analyze the effect of stochasticity on the predicted optimal material properties and their variation. We achieve this analysis by generating a series of microstructures that have the same average surface gradient, but with variable placement of the second phase. An image-based computational tool, OOF [3] which maps material microstructures onto finite element meshes, is used to determine the local stress state. The microstructural stress is used in conjunction with a statistical representation of failure. The effect of damage accumulation on the microstructural stresses is calculated iteratively. We characterize the effect of stochastic placement of second phase particles on the toughness of these materials with a specified gradient in their surface elastic coefficients and we investigate the stability of a surface crack in such materials.

KEYWORDS

Microstructure, finite elements, functionally graded materials, Weibull statistics

INTRODUCTION

Functionally graded materials (FGM) are composites that display spatially varying properties in one thickness direction and may be characterized by spatial microstructure variations. The spatial microstructures variations are usually achieved through a non uniform distribution of the second phase and these variations can be tailored in order achieve favorable responses to prescribed thermo-mechanical loads. FGM have received recent interest due to their particular properties: functionally graded surfaces provide new microstructural designs for enhanced surface damage resistance performance in ceramic materials. In particular, Giannakopoulos et al. [1,2] demonstrated that gradients in the elastic modulus of a surface can affect the toughness of that surface. In their experimental work, enhanced toughness has

been correlated with engineered gradients created by co-sintering a depth-dependent admixture of constituent particles with different elastic moduli.

In recent years, a lot of work has been carried out to study the behavior of FGM. Specifically, the finite element method has gained increasing use to determine the overall mechanical response of the materials to given solicitations. Usually FEM approaches are applied on the scale of the entire structure, the macro scale, using commercial codes such as ABAQUS (see for example [2] and [4]). On the other hand, unit cell models based on the FE analysis have been considered. However, these models cannot account for spatial variability of the constituents, due to the assumption that a structure is composed of the same microstructural representative volume element (RVE) in every part. Thus, the standard micromechanics approaches based on the concept of RVE are not suitable in the analysis of FGM, since the RVE cannot be univocally defined because of continuously changing properties through thickness. In fact, such engineered composites have average gradients that match the calculated optimal gradient on the macro scale, but the composite microstructure will have variations in its lateral properties and variations about the optimal gradient. The discrete nature of particulate composites that have been examined experimentally results in "stochastic gradients" in both microstructural directions. Neither the effect of lateral variations or perturbations about a prescribed gradient have been studied analytically.

The aim of this work is to investigate the microstructural randomness and discreteness for fixed macroscopic material gradients. Thus, a discrete computational micromechanical model is adopted. An image based finite element code, OOF, is adopted. The peculiarity of this tool is that it is able to analyze arbitrary microstructures, by mapping digitized images of microstructures and their local properties to a two-dimensional finite element mesh. In this way microstructural features can be readily modeled. To the authors' knowledge, the influence of randomness of microstructure on the macroscopic global response of FGM has been studied in literature only for the problem of thermal residual stresses [6], using a physically based micromechanics model. Here we analyze the effect of microstructural discreteness on the fracture and damage behavior of FGM, coupling OOF that calculates the local stress state with a statistical approach for brittle fracture, as described in the following section.

METHOD AND MATERIAL

As cited in the previous section, the image-based computational tool OOF is used in conjunction with a statistical representation of failure. In order to study the crack propagation, a new finite element has been implemented [7], based on a probabilistic approach for brittle fracture: the two-parameters Weibull law [8]. The microstructural mesh generation is performed using OOF and the microstructural stresses are calculated for the given loading conditions. Depending on the local probabilities of failures, this element loses stiffness as it undergoes damage and microstructural stresses are redistributed among the next elements. Thus, the effect of damage accumulation due to failure of the material can be calculated iteratively and damage can be accumulated.

The FGM considered in this study is the one experimentally characterized by Jitcharoen et al. [2]. This material is a graded alumina-glass composite whose Young modulus increases with depth beneath the surface. The thermo-mechanical properties of the constituents are summarized in Table 1.

TABLE 1

	Young modulus (GPa)	CTE (10^{-6} °C^{-1})	Poisson's ratio
Alumina	386	8.8	0.22
Glass	72	8.8	0.22

The coefficients of thermal expansion (CTE) of the two phases are approximately the same, so that thermal residual stresses do not arise upon cooling from the processing temperature.

The variation in Young's modulus of as much as 50%, introduced over a distance of 2mm, follows the law [2]

$$E(z)= E_{surface} +E_0 z^k$$

where $E_{surface}$=254GPa, E_0=85.325GPa.mm^{-k} and k=0.497, 0mm< z <2mm. The authors demonstrated that this gradient in the elastic modulus led to optimal materials properties in the contact-damage behavior.

Since we want to numerically analyze the effect of stochasticity on the predicted optimal elastic gradient, a series of "random" microstructures that have the same average surface gradient, but with variable placement of the second phase, is generated. An example is given in Figure 1 (in white alumina, in black glass).

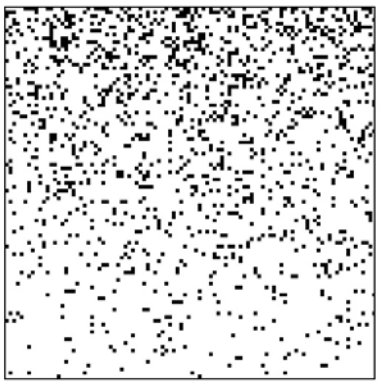

Figure 1: example of a random microstructure.

For each discrete depth z (corresponding to a layer), the Young modulus of the so represented composite can be calculated using the rule of mixtures relation

$$E_{graded}(z)= V_{glass}(z)E_{glass} + (1-V_{glass})E_{alumina}$$

where V_{glass} is the volume fraction of glass at each z. The profiles of elastic modulus were so calculated for 50 different random generated microstructures and reported in Figure 2. This picture reports the average values for each z and also average values +/- standard deviation (dashed lines). Thus a range of variability in the elastic modulus profile for real (i.e. discrete) microstructures is individuated.

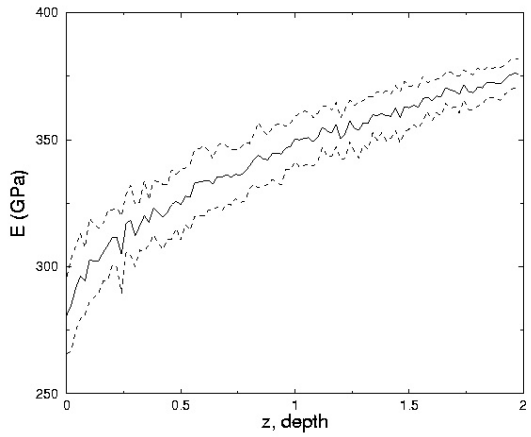

Figure 2:Young modulus vs depth z. Average values for 50 different microstructures

The average elastic modulus profile approximately coincides with that of a continuous (i.e. homogenized) material. The continuous material is achieved in this analysis generating a microstructure with several different layers, each one with a single value of elastic modulus. In the limit of an infinite number of

layers, the model is continuum. An example is illustrated in Figure 3, where for clarity the number of layers has been fixed to 20.

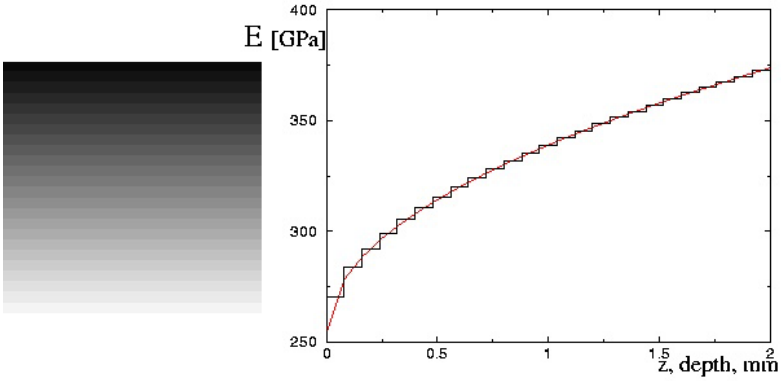

Figure 3 Continuously graded composite and corresponding Young modulus vs depth

RESULTS AND DISCUSSION

The 50 different microstructures generated as described in the previous section were meshed with OOF. Each mesh has about 20000 triangular elements. The thermo-elastic constants are known from Table 1, while the two Weibull parameters are assumed to be m=25 and σ_0=0.1GPa for both phases.
The effect of stochastic placement of the second phase on the toughness is characterized analyzing the microstructural damage evolution. We achieve this analysis placing a pre-existing surface vertical crack in each sample and incrementing the load up to the first failure. When the first element fails, local stresses are redistributed and the load can be incremented until the second failure occurs. In this manner, it is possible to track the damage evolution as the crack grows in the microstructure. Figure 4 displays the crack paths obtained for one microstructure. The elements that are damaged are colored in black.

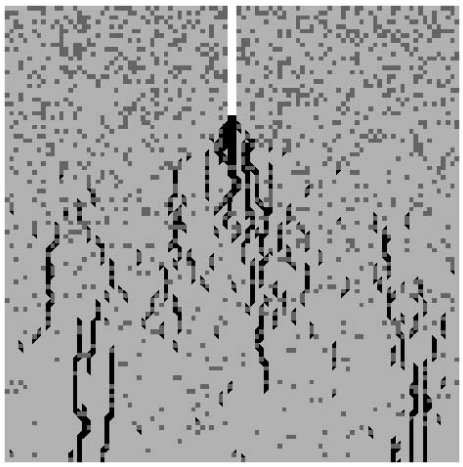

Figure 4: Damage evolution in a microstructure

In order to quantify the damage accumulation, a damage parameter has been defined as the area of the damaged elements divided by the total area. This parameter is plotted vs the strain applied in Figure 5 for one single graded microstructure and a sample of the same dimension of homogeneous material (with elastic modulus equal to the average elastic modulus through depth of the graded material). As can be noted from the picture, the sample of the graded material is less damaged, thus confirming the better performance of FGM over traditional materials.

Then, in order to quantitatively asses the effects of stochasticity of real microstructures on the fracture-damage behavior, the curves resulting from the 50 different computations have been averaged and standard deviations have been calculated. Figure 6 reports the average damage-vs-strain curve and the same curve +/- the standard deviation. The average curve (solid line) would coincide with the damage curve obtained with the continuously graded model. The two dashed curves (mean +/- standard deviation) plot how much the damage response can vary in real (and thus stochastic) microstructures. In other words, this micro-mechanic model is able to illustrate the influence of discreteness and randomness of the microstructure on the damage accumulation.

As observed also in previous studies [6], the need to consider microstructural features for modeling FGM is evident and therefore a complete micro-mechanical model should take into account the main microstructural details.

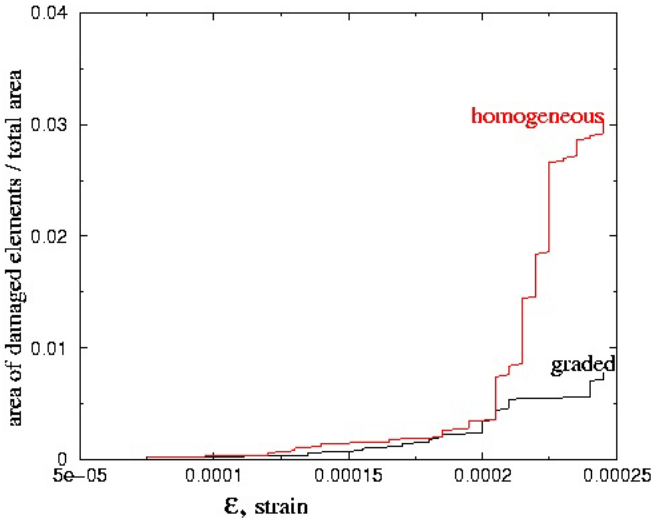

Figure 5: damage parameter for a graded microstructure and a homogeneous material

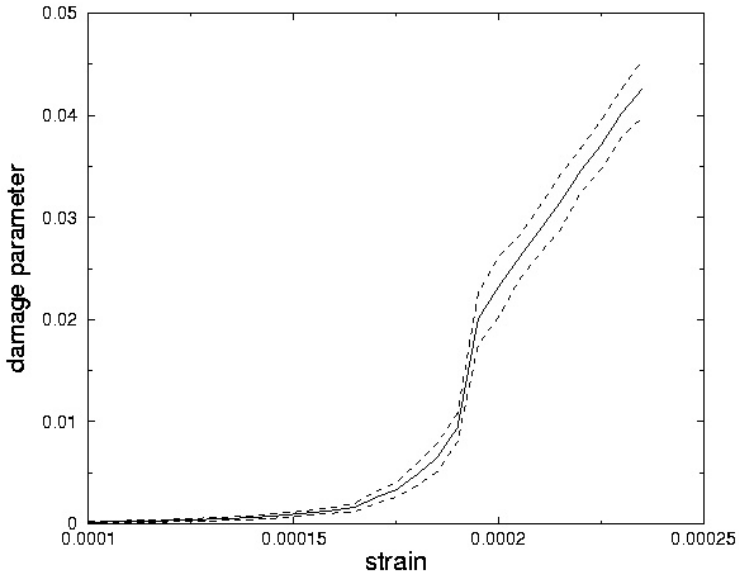

Figure 6: effects of stochasticity on the damage accumulation

Then, a new set of computations was performed on the same microstructures, but varying the Weibull moduli (m=25 for both phases, σ_0=0.34GPa and 0.06GPa for alumina and glass respectively). This choice of parameters corresponds to a realistic one for those materials, since the Weibull parameter σ_0 is a characteristic strength, related the mean fracture stress of the materials [9]. The fracture behavior in this case is different from the first set of experiments, resulting in less failures in the alumina phase where the

characteristic strength is higher compared to the previous case, i.e. the damage parameter remains lower. This results underlines how the choice of the Weibull parameters, usually determined experimentally, affects the global response.

CONCLUSIONS

The focus of the paper was to analyze the effect of randomness of microstructure of FGM on the fracture-damage behavior. To this aim, a micro-mechanics model able to consider the stochasticity of placement of second phase particles is adopted: OOF, a finite element code able to operate directly on microstructural images and to create finite element meshes that take into account microstructural features, is used in conjunction with a statistical approach for brittle fracture.

The numerical analyses for the stochastically graded microstructure can be compared with those obtained for a continuous (homogeneously graded) model which does not take into account the microstructural randomness and discreteness. The results demonstrate the need to consider microstructural details for accurately modeling FGM as regards their fracture and damage accumulation behavior. In fact, the heterogeneous microstructure can affect the initiation of cracks.

This work is currently in progress. In particular, the study aims to quantitatively assess the effect of the characteristic Weibull parameter on damage accumulation. Moreover the model could be extended to account for other factors not considered in this case, such as the adhesion (strong or weak) at the interface between the two phases.

REFERENCES

1. Giannakopoulos A.E. and Suresh S. (1997) *Int. J. Solids Struct.* 34, 2357.
2. Jitcharoen J., Padture N.P., Giannakopoulos A.E. and Suresh S. (1998) *J. Am. Ceram. Soc*. 81, 2301.
3. Carter W.C., Langer S.A. and Fuller E.R. The OOF manual: version 1.0, 1998. NIST Internal Report, NISTIR 6256, http://www.ctcms.nist.gov/oof/
4. Petterman H.E. (2000) *Mater. Sci. Engng. A* 276, 277.
5. Weissenbek E., Petterman H.E. and Suresh S. (1997) *Acta Mater*. 45, 3401.
6. Dao M., Gu P., Maewal A. and Asaro R.J. (1997) *Acta Mater*. 45, 3265.
7. Cannillo V., Carter W.C., to appear
8. Weibull W. (1951) *J. Appl. Mech.*, 18, 293.
9. Khalili A., Kromp K. *J.Mater Sci. Lett*. (1991) 26, 6741.

GRAIN BOUNDARY RESISTANCE TO CLEAVAGE FRACTURE IN Fe-3% SI ALLOY AND FE POLYCRYSTALS: EXPERIMENTS AND MODELING*

[1]A. S. Argon and Y. Qiao

[1]Department of Mechanical Engineering, Massachusetts Institute of Technology
Cambridge, MA 02139

ABSTRACT

Experiments on grain boundaries in bi-crystals of Fe-3%Si alloy have shown that cleavage cracks can break through high angle grain boundaries by entering from one grain into a neighboring one at a number of relatively evenly spaced places in a tiered form, depending primarily on the angle of twist misorientation, with the tilt misorientation being of relatively minor importance. At very low temperatures the specific resistance of grain boundaries to cleavage penetration in most cases can be assessed by a crack trapping model of penetration of the cleavage crack across the boundary and a well defined geometrical penalty of a crack deflection toughening effect as the tiered separate cleavage planes are bridged by additional cleavage cracking of the connecting ligaments in the adjoining grain. There is a definite transition between pure cleavage and mixed cleavage above –5C where the ligaments between the tiered cleavage cracks in the adjoining grain undergo sigmoidal plastic bending followed by ductile tearing, resulting in a definite increase of the overall specific fracture work by a factor of 2-3 above the level of pure cleavage.

In the propagation of a cleavage crack through a field of grains with random misorientations the above form of penetration of cleavage cracking across grain boundaries becomes considerably modified, first, through more irregularly shaped crack fronts probing grain boundaries no longer monolithically and, second, through large scale simple shear type separations of boundaries that are left behind as the cleavage cracking goes around the more difficult grains requiring some boundaries of such grains to be sheared off.

* Invited Lecture to be presented at the ICF-10 International Congress of Fracture on 3-7 December, 2001 in Hawaii

GRAIN-SIZE EFFECT ON FATIGUE CRACK INITIATION CONDITION OBSERVED BY USING ATOMIC-FORCE MICROSCOPY

Y. Nakai, T. Kusukawa, and Y. Maeda

Department of Mechanical Engineering, Kobe University,
1-1, Rokkodai, Nada, Kobe 657-8501, Japan

ABSTRACT

Slip-band formation and fatigue crack-initiation processes in α-brass were observed by means of atomic force microscopy (AFM), and the effects of the grain size, the stress amplitude, and the mean stress were discussed. In a fine grain material, fatigue cracks were initiated only from the slip-bands. In a coarse grain material, however, they were initiated either from the slip-bands or the grain boundaries. The depth of an intrusion drastically increased with its outgrowth to a crack, and with coalescence of cracks, the width of cracks increased rapidly. The depth of an intrusion increased with the number of loading cycles, and when the depth reaches a critical value, a transgranular crack was initiated from the intrusion. The critical value was given as a function of the slip-band angle relative to the stress axis. From the AFM observations, it was found that the critical value of the slip distance was independent of the slip-band angle relative to the stress axis, the stress amplitude, the mean stress, and the grain-size.

KEYWORDS

Fatigue, Micromechanics, Crack-initiation, Slip-band, α-brass, AFM

INTRODUCTION

It is well known that the fatigue process of metallic materials without macroscopic defects can be divided into initiation and growth processes of cracks and final unstable fracture. Among these processes, various studies have been conducted on the crack-growth behavior, and that can be quantitatively analyzed based on the fracture mechanics [1]. The initiation condition of fatigue micro-cracks, however, still has not clarified enough, because no method for successive, direct and quantitative observation of the process had been devised. The study on the fatigue crack initiation is especially important for the fatigue damage evaluation of micro-machine components because most of the fatigue life of these components is occupied by the crack initiation life [2].

For components without significant internal defects, free surface is normally the site for fatigue crack initiation, then microscopic observation is the most useful method to clarify the mechanisms of fatigue processes in materials, and the progress of metal fatigue study has strongly depended on the development of new microscopic

observation methods.

With conventional microscopes, such as optical microscopes (OM), transmission electron microscopes (TEM), and scanning electron microscopes (SEM), however, successive, quantitative three-dimensional observations of the crack nucleation portion in the specimen surface could not be conducted. In most of these studies, the crack-initiation mechanisms were discussed qualitatively. Since the surface morphology of materials can be observed with atomic-scale resolution, the scanning atomic force microscopy (AFM) is a powerful technique to study mechanisms of fatigue and fracture of solid materials. Nakai and his co-workers studied fatigue slip-bands, fatigue crack-initiation, and the growth behavior of micro-cracks in a structural steel [3], and α-brass [4, 5, 6].

In our previous study for α-brass, slip-band formation and fatigue crack-initiation processes were observed by means of AFM [4, 5]. Surface of a fatigued specimen was observed at the maximum stress, unloading state, and the minimum stress at the same number of cycles. In the initial stage of the fatigue process, slip-bands, which were formed only under tension stress or compression stress, were observed. These kinds of slip-bands, however, disappeared shortly. Under tension stress, cracks could be detected easily with the AFM image just after their initiation. Before crack-initiation, the height and the width of extrusions and the depth and the width of intrusions gradually increased with the number of cycles. When slip-bands developed cracks, one of these sizes was changed drastically, where sizes to be changed depended on the slip-band angle relative to the stress-axis and the shape of slip-bands. The shape of slip-bands tips was also observed, and they were compared with the results from the continuum distributed dislocation theory. The slip-bands had steep slope when they were blocked by grain boundaries, and the slip-bands descended by gradual slopes to plain surfaces when they terminated within grains [6].

In the present paper, slip-band formation and fatigue crack-initiation processes in α-brass were observed by means of AFM, and the conditions for the crack-initiation was discussed.

EXPERIMENTAL PROCEDURE

The material for the present study was 70-30 brass (α-brass). The chemical composition of the material (in mass %) was as follows: 69.92 Cu, 30.07 Zn, 0.0071 Fe, and 0.0026 Pb. After the specimens were made by the electric-discharge machining, they were heat treated at 320 °C for 180 s (Material A), or at 850 °C for 3600 s (Material B). The grain sizes of Material A and B were 20 μm and 1,100 μm, respectively. Before fatigue tests, surface of the specimens were electro-chemically polished. The specimen has a minimum cross-section of width 8 mm, and a thickness of 3 mm. It has a weak stress concentration with the elastic stress concentration factor of 1.03 under plane bending [4]. Since most of fatigue cracks were not initiated from the shallow notch root, the stress concentration factor was not considered in the calculation of the stress amplitude. The fatigue tests were carried out in a computer-controlled electro-dynamic vibrator operated at a frequency of 30 Hz under fully reversed cyclic plane bending moment ($R = -1$), or pulsating bending moment ($R = 0$).

To conduct a quantitative analysis of the development of fatigue slip-bands, the scanning atomic force microscopy (AFM) was employed for the present study. The scanning area for the observations was 30 μm 30 μm. Since it was very difficult to identify in advance where fatigue cracks would be initiated, replicas of the specimen surface were taken at the predetermined number of fatigue cycles. The replica films were coated by gold (Au) before observation. The replications were conducted at the maximum tensile stress. Although the height of the surface in the replica film was reversed from the specimen surface, the height of the replica film in the AFM images was reversed by an image processing technique.

EXPERIMENTAL RESULTS

Transgranular Cracking

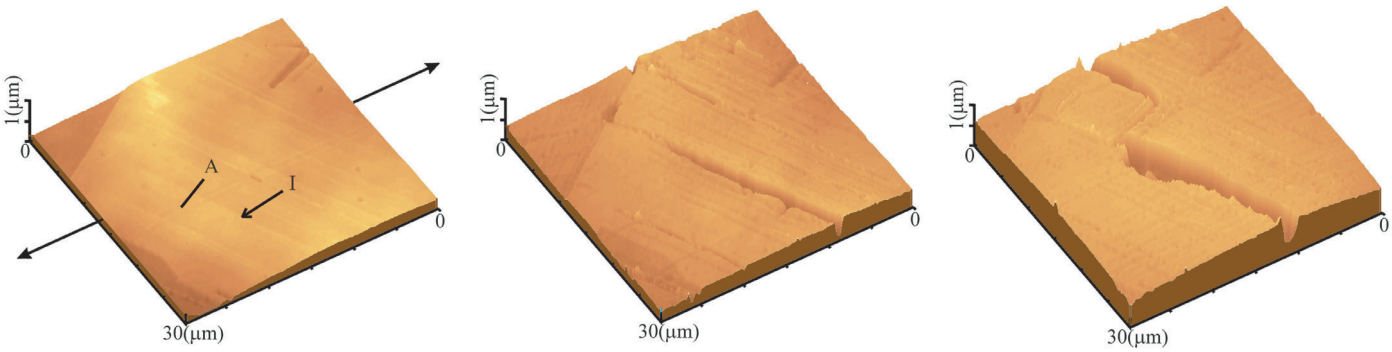

(a) $N = 5.9 \times 10^2$ cycles (b) $N = 9.1 \times 10^4$ cycles (c) $N = 4.5 \times 10^5$ cycles

Figure 1: AFM images of transgranular cracking ($\sigma_a = 173$ MPa, Material A).

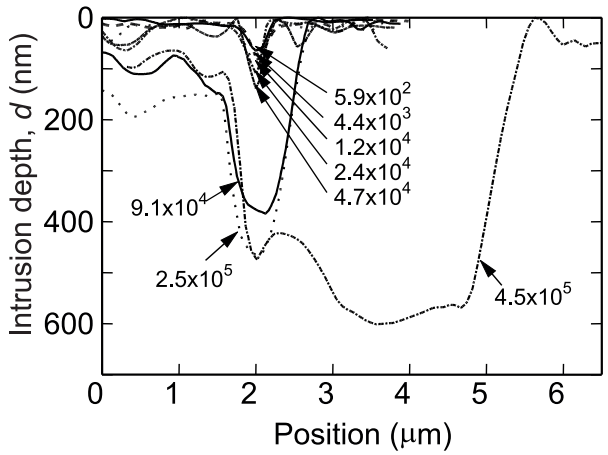

Figure 2: Change of intrusion geometry in fatigue ($\sigma_a = 173$ MPa, Material A).

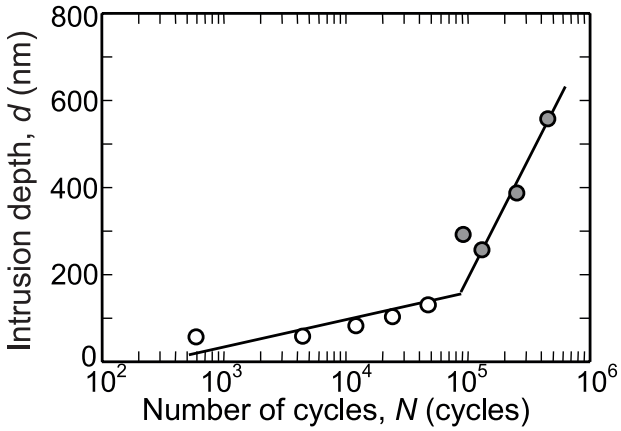

Figure 3: Change of intrusion depth in fatigue ($\sigma_a = 173$ MPa, Material A).

In this section, the conditions for the crack-initiation in α-brass will be discussed as a function of slip-band angle relative to the stress axis, stress amplitude, mean stress, and grain size. In α-brass, fatigue cracks were initiated either from slip bands or along grain boundaries.

Another example of transgranular cracking process is shown in Fig. 1. It is clear from these AFM images that two parallel fatigue cracks were initiated at $N = 9.1 \times 10^4$ cycles (Fig. 1 (b)), and they were coalesced at $N = 4.5 \times 10^5$ cycles (Fig. 1 (c)). The change of the geometry of Intrusion I at cross section A, which is indicated in Fig. 1 (a), is shown in Fig. 2. With crack-initiation at $N = 9.1 \times 10^4$ cycles, the depth of the intrusion increased rapidly, and with coalescence of cracks at $N = 4.5 \times 10^5$ cycles, the width of the cracks (intrusion) increased rapidly. Change of the depth of Intrusion I is shown in Fig. 3 as a function of the number of the fatigue cycles, N. Even though the measured value was not actual depth after crack initiation, the depth of the intrusion drastically increased with its outgrowth to a crack at $N = 9.1 \times 10^4$ cycles.

From surface observation, cracks much shorter than the grain-size were not found. Even just after the initiation, a crack prevailed whole grain, and Stage I crack growth was not observed. In the thickness direction, however, the depth of intrusion changed continuously before and after the crack initiation, *i.e.*, no jumping in the depth of intrusion was observed. It may indicates that Stage I crack growth, which is a fatigue crack growth along a slip-band, occurred in the thickness direction.

Intergranular Cracking

An example of the intergranular cracking is shown in Fig. 4. Slip-bands were formed in a grain on the right side of a grain-boundary, and they were parallel to the grain-boundary. Both intrusions and extrusions were observed in the grain. In the grain on the left size of the grain boundary, slip-bands are not observed. A fatigue crack was initiated from the grain-boundary at $N = 4.6 \times 10^4$. An intergranular crack was considered to have been initiated along grain-boundaries between grains with high Schmidt factor slip system and with low

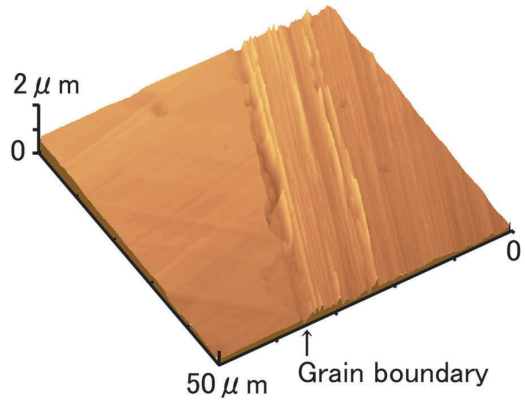

Figure 4**:** Intergranular fatigue crack initiation ($\sigma_a = 110$ MPa, $N = 7.9 \times 10^4$, Material B).

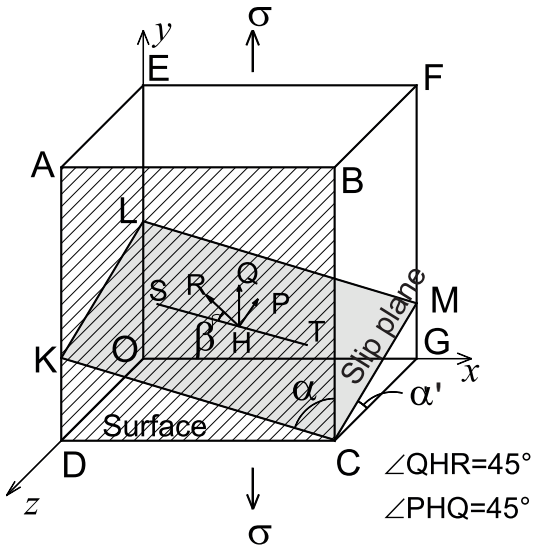

Figure 5**:** Slip-plane and directions relative to stress-axis and surface.

Schmidt factor slip system. The depth of the grain boundary, d, also increased with the number of cycles, N, and the crack-initiation could be easily identified from the change of the slope of the $\log N - d$ relationship.

DISCUSSION

Condition for the transgranular crack initiation is analyzed through a geometrical model proposed by Tanaka and Nakai [7, 8] shown in Fig. 5, which explains the relation between the surface-step and the slip-direction, where the Cube ABCDEFGO indicates a small region of a specimen that is located adjacent to the surface, and Point H is an arbitrary point on the slip-plane. In the figure, Plane ABCD represents the specimen surface, Plane CKLM represents the slip-plane, and y-axis and Arrow QH represents the loading-direction. Line CK is the slip-trace at the specimen surface and Line ST is a line on the slip-plane and that is parallel to Line KC. Arrow HR is the slip-direction on the slip-plane, and Arrow HP is the normal of the slip-plane. The surface-step induced by the slip is

$$d = s \cdot \sin\beta \cdot \cos\alpha', \tag{1}$$

where the value of s is the slip distance in the HR direction, the value of α' is the angle between the normal to the surface and the trace of the slip-band on the plane that is perpendicular to the surface and parallel to the loading-axis, and the value of β is the angle between the slip-direction and the slip-traces on the surface (see Fig. 5).

Cracks are considered to have been initiated from slip bands, which had slip system in the maximum resolved shear stress [7, 8]. These slip bands are what is called as ”persistent slip band (PSB)”. For ∠QHR = ∠PHQ = 45°, the resolved shear stress along the slip-direction takes the maximum value, and the following relationship should be satisfied.

$$\cos\beta = \sqrt{2}\cos\alpha. \tag{2}$$

For $\alpha = 90°$, the value of β should be $90°$, which gives the maximum slip-step on the surface for a given slip distance. For $\alpha = 45°$, the value of β should be $0°$ and no slip-step is formed on the specimen surface.

On slip-planes where the resolved shear stress takes the maximum value, the following equation should be satisfied.

$$\cot^2\alpha + \tan^2\alpha' = 1. \tag{3}$$

The relation between d and s can be derived as a function of α by substituting Eqs. (2) and (3) into Eq. (1).

Figure 6 shows the depth of intrusions for various numbers of cycles as a function of the intrusion angle relative to the stress-axis. In the figure, data from the same intrusion fall on the same angle. Open marks indicate data

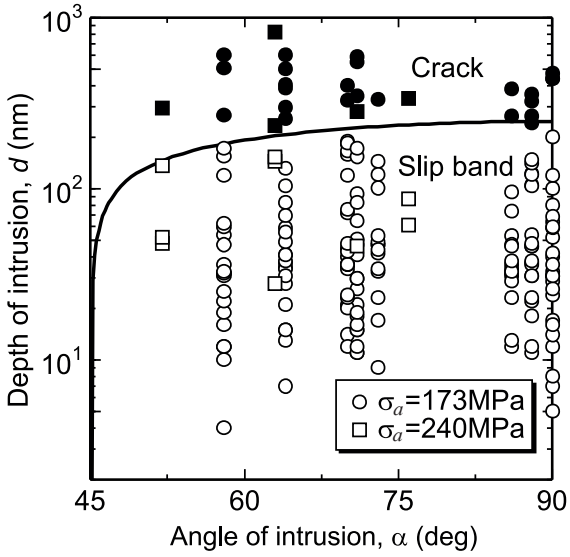

(a) Transgranular, Material A, $R = -1$

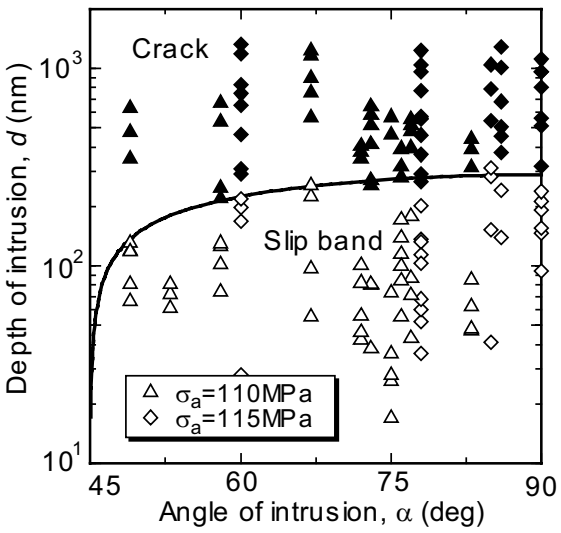

(b) Transgranular, Material B, $R = -1$

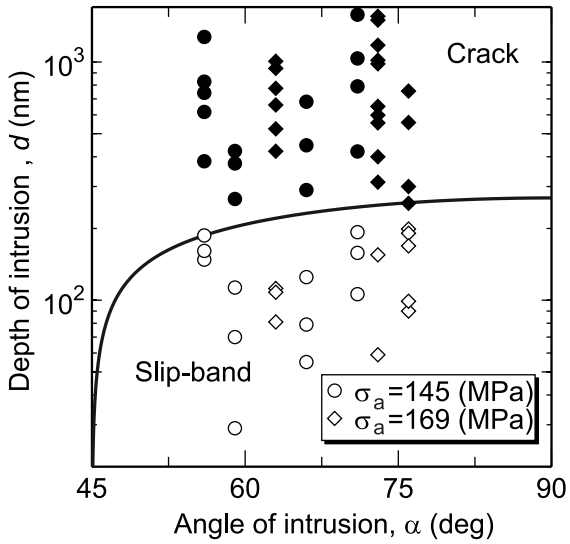

(c) Transgranular, Material A, $R = 0$

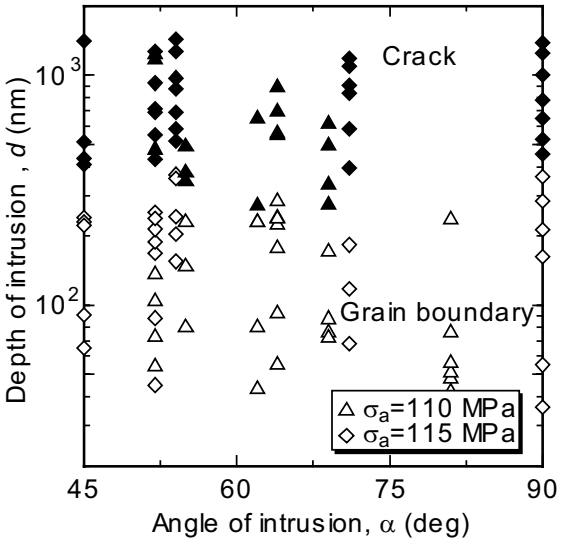

(d) Intergranular, Material B, $R = -1$

Figure 6**:** Fatigue crack initiation condition.

before the crack initiation, and solid marks show data after the crack initiation. The solid-lines in Fig. 6 show the relationship given from Eq. (1) for the value of $s = 380$ nm. For the transgranular crackings, which are shown in Fig. 6, data before the crack initiation fall below the solid lines, and data after the crack initiation locate above the solid lines. It indicates that there was a critical value of accumulated slip-distance, s. The critical value of s was 380 nm, independent of the stress amplitude, the mean stress, and the grain-size. When the accumulated slip distance of an intrusion in a slip-band grew up to the critical value, a cracks was initiated from the intrusion. These results indicate that the transgranular crack initiation is controlled by the damage accumulation due to the dislocation substructures rather than the stress concentration induced by the intrusion.

As shown in Fig. 6 (d), the grain boundary depth at the intergranular crack initiation was not a unique function of the grain boundary angle relative to the stress axis. Other mechanism for the intergranular crack initiation should be considered, which may include the incompatibilities of deformation between two adjacent grains.

Since the critical value of slip distance at crack initiationwas independent of mechanical and metallurgical conditions, the effects of these parameters on the fatigue crack initiation life should be attributed to their effect on the growth rate of slip distance. Therefore, the effects of the intrusion angle and the slip line length on the growth rate of the intrusion depth were examined. As shown in Figs 7 and 8, the rate was controlled not only by the intrusion angle and the slip-line length. It was affected by many factors, for example, constraint of deformation from adjacent grains. However, it is easy to predict when the depth reaches the critical value

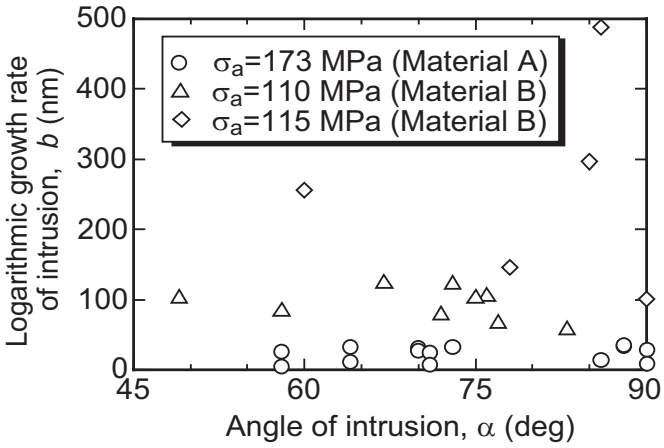

Figure 7**:** Growth rate of intrusion as a function of intrusion angle.

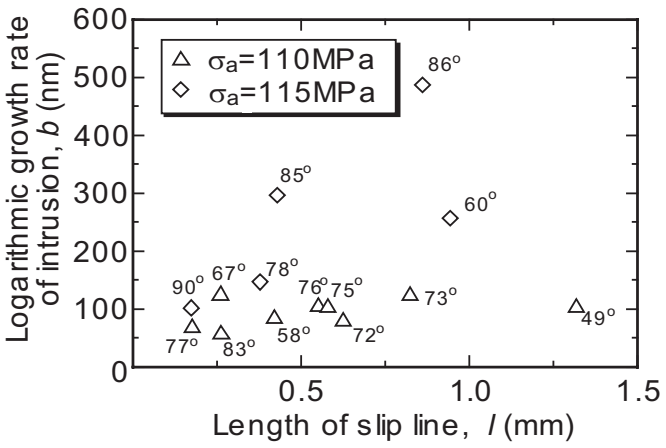

Figure 8**:** Growth rate of intrusion as a function of slip-band length.

because the intrusion depth increased linearly with the logarithm of the number of cycles like Fig. 3. Therefore, the location and remaining life of fatigue crack initiation can be predicted by measuring the intrusion depth few times before the crack initiation.

CONCLUSIONS

The fatigue slip-band formation and the fatigue crack-initiation process in 70-30 brass were observed by means of AFM, and the following results were obtained.

(1) The depth of an intrusion drastically increased with its outgrowth to a crack, and with coalescence of cracks, the width of cracks increased rapidly.

(2) For the transgranular crack initiation, the intrusion depth at the crack initiation depended on the slip-band angle relative to the stress axis. At crack initiation, the slip distance in the slip direction, however, was constant independent of the slip-band angle, the stress amplitude, the mean stress, and the grain size.

(3) Intergranular cracks were formed along grain-boundaries between highly deformed grains and grains without activating slip systems. For the intergranular crack initiation, the value of the intrusion depth (the grain boundary depth) at the crack initiation was not a unique function of the grain boundary angle relative to the stress axis.

REFERENCES

1. Tanaka, K. (1987). *JSME Int. J.*, 30, 1.
2. Nakai, Y., Hiwa, C., Imanishi, T., and Hashimoto, A. (1999). *Proc. Asian-Pacific Conf. on Fracture and Strength* '99, SM22 (CD-ROM).
3. Nakai, Y., Fukuhara, S., and Ohnishi, K. (1997). *Int. J. Fatigue*, S223.
4. Nakai,Y., Ohnishi, K., and Kusukawa, T. (1999). *Trans. Jpn Soc. Mech. Eng.*, 65A, 483.
5. Nakai, Y., Ohnishi, K., and Kusukawa, T. (1999). In: *Small Fatigue Cracks: Mechanics and Mechanisms*, pp. 343-352, Ravichandran, K. S., Ritchie, R. O., and Murakami, Y. (Eds). Elsevier, Oxford.
6. Nakai, Y., and Kusukawa, T. (2001). *Trans. Jpn Soc. Mech. Eng.*, 67A, 476.
7. Tanaka, K., Nakai, Y., and Maekawa, O. (1982). *J. Mat. Sci., Jpn*, 31, 376.
8. Tanaka, K., Hojo, M., and Nakai, Y. (1983). In: *Fatigue Mechanisms: Advances in Quantitative Measurement of Physical Damage*, pp.207-232, Lankford, J., Davidson, D. L., Morris, W. L., and Wei, R. P. (Eds). ASTM STP 811.

ORAL/POSTER REFERENCE: ICF100770OR

GROWTH OF CRACKS IN STEEL UNDER REPEATED THERMAL SHOCK IN A CHEMICALLY CONTROLLED ENVIRONMENT

B. Kerezsi, J.W.H. Price and R. Ibrahim

Department of Mechanical Engineering, Monash University, Caulfield Campus
East Caulfield, 3145, Victoria, Australia

ABSTRACT

Repeated thermal shock loading is common in many industrial situations including the operation of pressure equipment found in thermal power stations. Thermal shock can produce a very high stress level near the exposed surface that eventually may lead to crack nucleation. Further crack growth under the influence of repeated thermal shock is a very complex phenomenon due to both the transient nature of the highly non-linear thermal stresses and the strong influence of the environment. This paper describes an experimental analysis of crack growth in heated carbon steel specimens exposed to repeated thermal shocks using cold water. Analysis of the effect of steady state primary loads on the growth of the cracks is isolated using a unique test rig design. Environmental effects due to the aqueous nature of the testing environment are found to be a major contributor to the crack growth kinetics.

KEYWORDS

Crack growth, environmental effects, fatigue, pressure equipment, primary load, thermal shock.

INTRODUCTION

The growth and arrest of cracks due to repeated thermal shock loading is of interest in industrial applications where predictions can allow decisions to be made on the necessity of planned inspections and component replacements. Current methods for predicting repeated thermal shock (RTS) crack initiation lifetime and growth rates rely on standards and codes of practice such as the ASME Boiler and Pressure Vessel Code [1,2], and British Standard BS7910 [3], both of which use models based on isothermal fatigue tests and simplified stress profiles. The conservatism of these codes when analyzing RTS cracking is of concern, particularly when predicting crack growth rates after initiation has been observed. An over-estimation of this growth rate can lead to premature replacement of components that otherwise may have been left in service. A particular reference to the conservatism of the ASME code can be found in work by Czuck et al [4], where growth at the tip of a crack exposed to cyclic thermal shock loading was found to be an order of magnitude less than that predicted by using the code.

Cracking due to repeated thermal shock (RTS) is a particular problem in thermal power stations. Thermal shocks in boiler equipment are an inevitable side effect of normal operation with start-up and shut-down procedures thought to be especially damaging. Cyclic operation of traditionally base-loaded units only

increases the severity of the problem. In this work, tests that closely simulate the real life conditions of thermal shock encountered in thermal power station pressure components are completed. These tests are intended to develop data that will provide for realistic determination of lifetime to crack initiation and crack growth rates for service components as well as allow for an estimation of the conservatism of the current codes.

Many influential external factors that are present in thermal power plant equipment are ignored in existing codes. Foremost is the combined effect of external primary loads and the environment in which the crack is growing. The external loads can be a direct result of the pressure or mechanical loading of the components, the effect of which is to open any cracks, exposing them to the environment. The environment is dependent on the process in which the component is being used, which in the case of thermal power station equipment is often aqueous in nature (including chemical treatment to control pH and oxygen levels) and will modify conditions at the crack tip.

In this paper, selected results from crack growth tests using a unique test-rig arrangement are presented. Comparisons of the actual results with empirical prediction methods from current design codes are made.

EXPERIMENTAL TECHNIQUE

The testing completed in this investigation has been carried out on a thermal fatigue test rig that has been purpose built for the investigation of crack initiation and growth due to repeated thermal shock loading. Consisting of a convection furnace, static loading structure and quenching system it allows for the monitored growth of cracks for a wide variety of component geometries.

The key advantages of this rig over those used in previous studies are:

- The component is heated by convection, which means that there are no unwanted heat effects at the crack tip as may be the case for induction or resistance heating.
- The component is quenched by room temperature pH and O_2 controlled water.
- The specimen size is representative of typical industrial components.
- Large specimen size permits multiple simultaneous experiments.
- An unloaded “control” specimen can be used.
- Approximately one-dimensional conditions exist at any one crack because of the unique specimen design.

A thorough analysis of the development of the test rig and specimen design, including a review of previous trends in the experimental investigations of thermal shock cracking can be found in [5].

Tests conducted with this rig have concentrated on identifying the effects of environment and primary loads on crack initiation and growth during repeated thermal shock. This was completed by simultaneously testing sets of two low carbon steel flat plate specimens (grade AS 1548-1995 [6]) placed side by side. One specimen is subjected to a 90MPa (13ksi) uniform tensile stress and the other left unloaded. The specimens, with a combination of 0.25mm and 0.1mm radius notches machined into the quenched faces, were fitted vertically in the furnace. The upper specimen temperature was limited to 370°C to remove any creep effects. Dissolved oxygen levels (D.O.) were varied between tests, while the pH was held steady at around 8.0. The first set of tests used fully oxygenated tap water with a D.O. level of around 8ppm. This water was vigorously pre-boiled in the second set of tests, driving off excess oxygen and reducing the D.O. level to around 2ppm.

Each thermal cycle consisted of a slow heat to a central specimen temperature of 330°C followed by a 7s water quench. Cycle time was around 15 minutes. Due to the fact that the specimens were positioned vertically, the thermal gradient in the furnace prevented a uniform temperature from being achieved along the whole specimen length. Rather the temperature from top to bottom of the specimen varied linearly from 370°C to 290°C.

After each period of 500 thermal cycles, the specimens were removed from the furnace and investigated for cracking at a low magnification (10 to 60x). A rough estimate of crack initiation lifetime was defined as when a full-face hairline crack was visible at the base of the notch. Extrapolations of the long crack growth data were used to further refine when initiation was to have occurred. Any subsequent crack growth after initiation was measured on each side of the specimen. Through crack depth was taken as the average of these two measurements.

TEST RESULTS

Times to crack initiation in the notched specimens are shown graphically in figure 1. Unlike the authors' previous work [5], where elastic stress amplitude was used, times to crack initiation are plotted against the Neuber pseudostress amplitude (S'_a). The pseudostress is defined as the local strain amplitude at the notch (ε_a) multiplied by Young's Modulus (E).

$$S'_a = \varepsilon_a E \tag{1}$$

When the behaviour of the material remote from the notch is predominantly elastic, the pseudostress amplitude can be related to the nominal stress amplitude (S_n) and the local stress amplitude (σ_a). The final relationship, outlined in work by Prater and Coffin [7], is reproduced below:

$$S'_a = \frac{\left(k_f S_n\right)^2}{\sigma_a} \tag{2}$$

Here k_f is the notch fatigue factor, determined from a notch sensitivity analysis as used in [5]. A maximum value of 5.0 has been established for k_f in accordance with a "worst case notch" analysis. Use of equation (2) also requires knowledge of the cyclic stress strain relationship for the material. Prater and Coffin [7] provide data for carbon steel that has been adapted for use in this investigation.

Figure 1 also shows a curve based on ASME *fatigue* data. This curve is slightly different to the published *design* curve as shown in Section VIII of the ASME Code [2]. The design curve has a built-in conservatism of 2 times on stress and 20 times on lifetime on the fatigue data, whichever is the most conservative.

Crack growth results are shown on figure 2. Stress intensity factors have been plotted against the crack growth rate using the R-ratio to categorise the data. Both water and air environment crack growth curves for carbon steel, taken from the ASME Boiler and Pressure Vessel Code [3], are also plotted for comparison.

DISCUSSION

Crack Initiation

As shown in Fig. 1 and reported in [5], the application of a primary load displays little or no effect on crack initiation lifetime within the limitations of experimental variance. The same can be said for reducing the dissolved oxygen level from 8ppm to 2ppm.

In all of the test cases, the ASME *fatigue* curve seems to provide a good approximation of the relation between number of cycles to crack initiation and notch pseudostress amplitude. However, any attempt to use the ASME curves to predict crack initiation should be approached with care. This is because the ASME fatigue curves are based on uniaxial strain controlled testing of small cylindrical specimens. Failure in one of these specimens is defined as when complete fracture occurs. It is then assumed that the failure of these small specimens is equivalent to the initiation of a small crack in a larger structure.

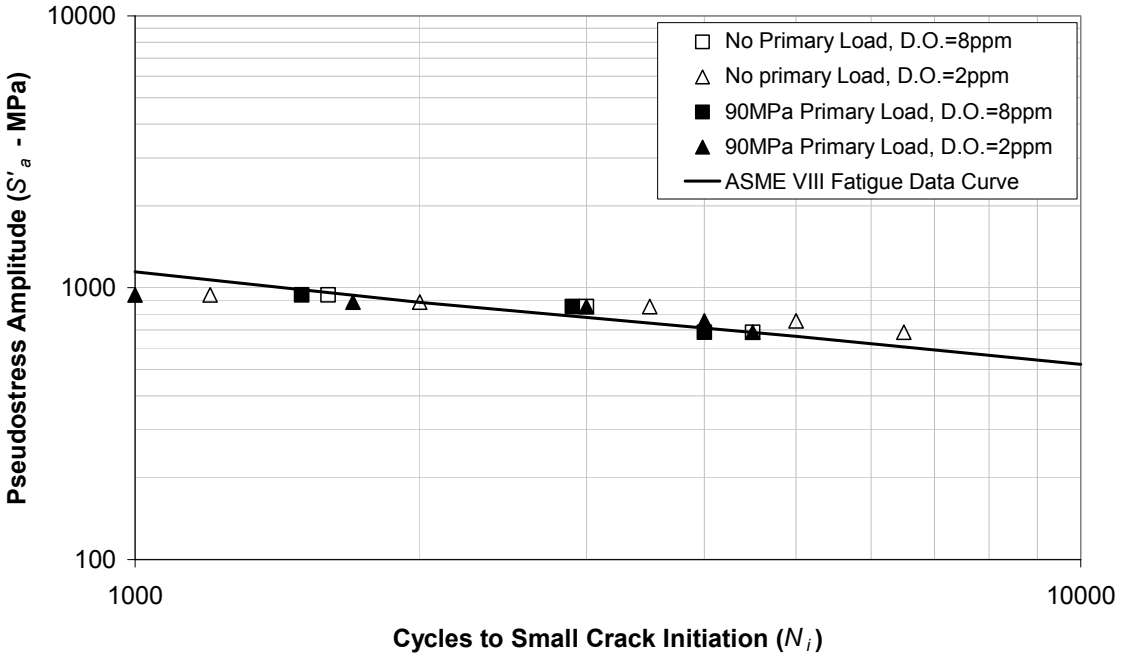

Figure 1: Effect of primary load and dissolved oxygen Level (D.O.) on small crack initiation lifetime.

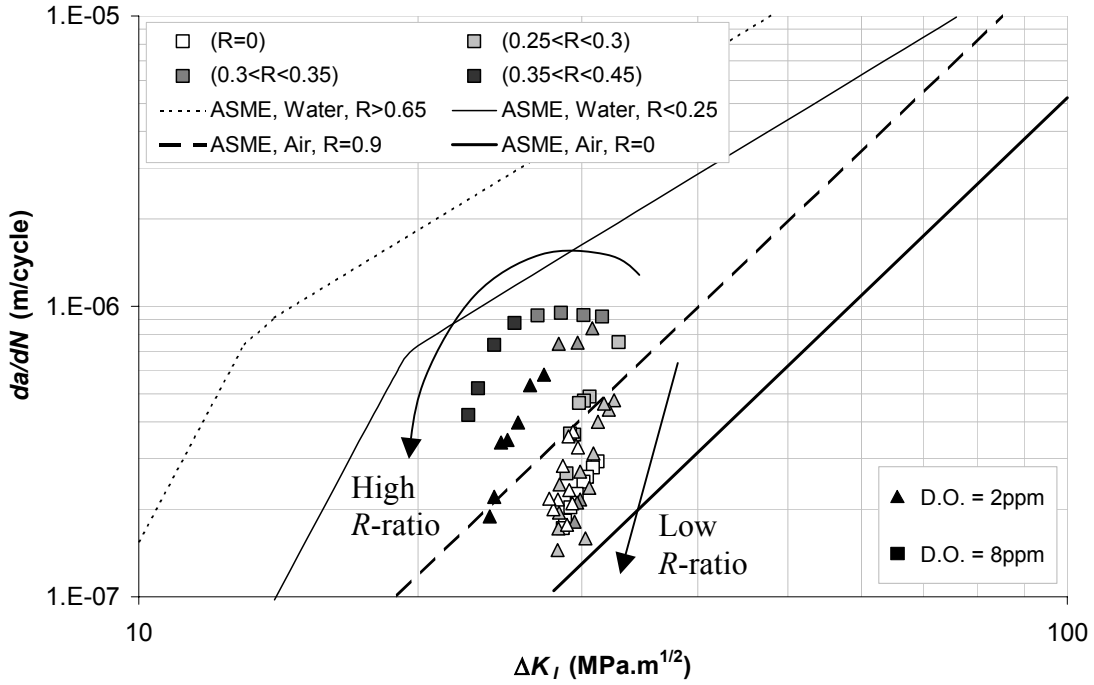

Figure 2: Crack growth rates as a function of stress intensity factor. Squares correspond to measurements made during testing with D.O.≈8ppm, triangles correspond to D.O.≈2ppm. The large arrows indicate only trends for individual crack growth – no curve fitting is implied.

Referring to ASTM E 8M – 96 [8], the standard small cylindrical specimen size for tensile tests is 12.5mm in diameter. Depending on the stress amplitude during fatigue testing and the presence of mean stresses, a small amount of crack growth will occur before specimen failure, probably in the order of a few millimetres. This means however that no exact "initiation" size can be known to allow comparison with experimental data from large specimens. Therefore, any correlation between the ASME code and the experimental work presented here must remain purely qualitative. Namely, the pseudostress developed at a notched carbon steel specimen exposed to RTS can be related to number of cycles to initiation in a linear manner similar to that shown by the ASME fatigue curve. Reciprocally this means the ASME fatigue curve can be used as a guideline for determining approximate times to develop small (<1mm) deep cracks in carbon steel exposed to RTS.

Crack Growth

A number of observations can be made from the crack growth data obtained by relating the change in stress intensity factor ΔK to the propagation rate da/dN.

- For all of the plotted points, the ASME water curves provide a conservative result (see Fig. 1). For some points this conservatism is more than an order of magnitude.
- From the trend of the data represented it seems that deceleration of all observed cracks is occurring.
- In specimens without steady state primary loaidng, crack growth rates begin decreasing immediately after crack initiation.
- In contrast, after initiation, cracks in the specimens with large steady state primary loading experience an increase in crack growth rate as the R-ratio increases. Then, after a period of rapid growth (at around 1 mm/1000 cycles), the rate decreases rapidly. It is possible that this high rate of crack growth, followed by the quick drop off may correspond to the start of an environmentally influenced diffusion controlled crack growth.

CONCLUSIONS

Results obtained from a test program developed to simulate repeated thermal shock conditions produced in operating thermal power station have shown:

1. The application of a primary stress had little or no affect on crack initiation lifetime during repeated thermal shock below the creep range. A reduction of dissolved oxygen levels in the quenching water from 8ppm to 2ppm also did not significantly affect initiation times. ASME Boiler and Pressure Vessel Code, Section VII, Division 2 [2] fatigue data may be used as a guideline for determining approximate times to develop small (<1mm) deep cracks in notched carbon steel specimens exposed to repeated thermal shock.

2. Environmental and primary load interaction is highly influential in the growth of thermal shock cracks. Cracks with a low R ratio (no primary stress) show signs of rapid deceleration and cracks with high R ratio show signs of deceleration after a period of environmentally enhanced growth. The ASME provided crack growth curves for a water environment are conservative in all cases.

ACKNOWLEDGMENTS

This work has been completed with the assistance of an Australian Research Council grant with contributions from HRL Technology Ltd, Optima Energy, Western Power, Pacific Power and the Electric Power Research Institute of USA

REFERENCES

1. ASME (1998). *ASME Boiler and Pressure Vessel Code, Section VIII, Division 2*, ASME, New York.
2. ASME (1998). *ASME Boiler and Pressure Vessel Code, Section XI*, ASME, New York.
3. BSI (1999). *BS 7910, Guide on methods for assessing the acceptability of flaws in fusion welded structures*, BSI, London.
4. Czuck, G., Mattheck C., Munz, D. and Stamm, H. *Nuclear Engineering and Design*, 84, pp. 189-199.
5. Kerezsi, B.B., Kotousov, A.G. and Price, J.W.H. (2000). *International Journal of Pressure Vessels and Piping*, 77, pp. 425-434.
6. Australian Standards (1995). *AS 1548-1995, Steel plates for pressure equipment*, Standards Australia, Homebush, NSW.
7. Prater T.A. and Coffin L.F. (1983). In: *Corrosion Fatigue: Mechanics, Metallurgy, Electrochemistry and Engineering, ASTM STP 801*, pp. 423-444.
8. ASTM (1996) *ASTM E 8M-96*, *Standard test method for tension testing of metallic materials [metric]*, ASTM, Philadelphia.

ORAL/POSTER REFERENCE: ICF100982OR

GROWTH OF FATIGUE CRACKS FROM COLD EXPANDED HOLES

M. J. Pavier, A. A. Garcia-Granada, V. D. Lacarac and D. J. Smith

Department of Mechanical Engineering, University of Bristol,
Queen's Building, University Walk, Bristol, BS8 1TR, UK

ABSTRACT

The cold expansion of fastener holes in aircraft components is a standard technique to improve fatigue life. However, there is uncertainty of the method for quantifying the improvement. In addition, there is concern that the beneficial residual stresses arising from cold expansion may relax due to creep, particularly in aircraft subjected to higher temperatures.

This paper begins with experimental measurements and finite element predictions of cold expansion residual stresses and their redistribution after creep. The results of fatigue crack growth experiments are then presented, demonstrating the benefits of the cold expansion process, even when creep relaxation occurs. Finally, a comparison of the fatigue crack growth rate is given with a prediction using base line data combined with the finite element calculation of residual stress.

KEYWORDS

Fatigue, residual stress, cold expansion, finite element analysis

INTRODUCTION

Cold expansion of holes in aluminium aircraft structures is commonly used to improve fatigue life [1]. When airframes are subjected to higher temperatures there is concern that the beneficial residual stresses resulting from cold expansion may relax due to creep. Predictions and measurements of residual stresses caused by the cold expansion process have been made [2, 3] and more recently the effects of creep relaxation have been investigated [4].

In this paper, experimental measurements and finite element predictions are presented of residual stresses in cold expanded holes, before and after creep relaxation. During creep relaxation, additional tensile load was superimposed to simulate the conditions in the aircraft. Experimental measurements of residual stress used a new method based on Sachs' boring to measure the average tangential residual stress. Axisymmetric and three dimensional finite element analyses were used to predict the stress distribution through the thickness of the component. The results of fatigue crack growth experiments for cracks growing from cold expanded holes are also presented. Comparisons of experimental crack growth with predicted growth using base line data and finite element residual stress predictions are made.

RESIDUAL STRESS MEASUREMENTS AND PREDICTIONS

Test Specimens

The material used in this research was a new aluminium alloy 2650 designed to provide creep resistance. Rectangular specimens with a thickness of 6 mm, a central hole of radius 3 mm, a width of 32 mm and a length of 140 mm were machined from the plate. The hole was cold expanded to a nominal expansion of 4 % using the FTI split sleeve method [5]. Specimens subject to creep relaxation were heated to 150°C inside an electric furnace and a load equivalent to a far field stress of 162 MPa was applied. The temperature and applied load were maintained for 1000 hours. To enable measurement of residual stress, discs of diameter 32 mm were cut from the specimens, centred on the hole.

Garcia-Sachs Method

Sachs' boring is a method of measuring the residual stresses around a hole by machining material from the hole edge and measuring the resulting strain change. Sachs boring can only measure an axisymmetric state of residual stress, but in this work non-axisymmetric residual stresses occur. The Garcia-Sachs method [6] has been developed, based on Sachs' boring, to measure such non-axisymmetric residual stress distributions. In this method the residual stresses are represented by a Fourier expansion. The strain change is measured at a number of angular positions and from these changes the magnitude of each component in the Fourier series or residual stress is inferred.

Material Properties

To predict the residual stresses arising from cold expansion it is important to measure accurately the reversed yielding behaviour of the material [2]. A series of cyclic tension and compression tests were therefore carried, both at room temperature and at 150°C. To evaluate the creep properties of the aluminium alloy 2650, several tests were carried out for different applied constant loads using static load creep test machines. For the range of temperatures and stresses considered in this work, the principal creep mechanism is power law creep.

Finite Element Predictions

The ABAQUS 5.7 finite element system was used to provide predictions of residual stress. An axisymmetric model was first used to simulate the cold expansion procedure [7] using a combined hardening model to approximate the cyclic stress-strain behaviour. Following the finite element prediction of the residual stress, a further step was used to model the creep relaxation [4]. A three dimensional model had to be used for this step, obtaining the initial residual stresses from the axisymmetric model. Additional load was applied and creep relaxation allowed to occur using a power law model with time hardening integration.

Results

Garcia-Sachs measurements of residual stress have been made for specimens after cold expansion and after creep relaxation under applied load. These experimental measurements have been compared with finite element predictions of residual stress using the combination of axisymmetric and three dimensional models described above. For conciseness, only results for the tangential residual stress are provided, in the direction normal to the loading direction.

Figure 1 presents a comparison of the residual stresses measured by the Garcia-Sachs method and the averaged through-the-thickness stress from finite element analysis. Error bars on the Garcia-Sachs results are based on the calculation of the standard deviation of stress assuming a standard deviation of strain measurement of $\pm 1\ \mu\varepsilon$ [4]. Agreement with the finite element prediction is excellent except very close to the hole edge where likely errors in the Garcia-Sachs method increase and differences between the experimental and finite element material behaviours are more important.

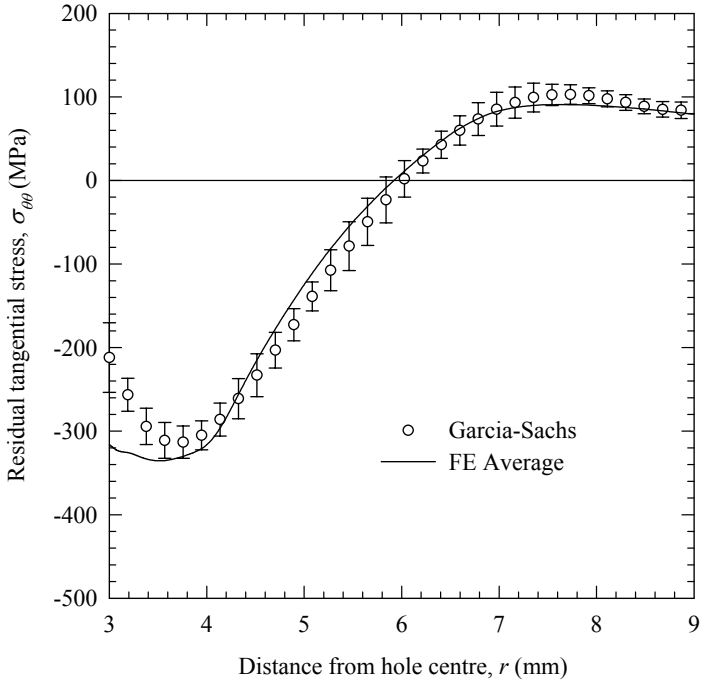

Figure 1: Measured residual tangential stresses after cold expansion compared with averaged finite element results.

Figure 2 shows Garcia-Sachs and finite element averaged stresses for the case where the residual stresses have been relaxed following creep relaxation with superimposed applied load. The agreement is reasonable although the measured residual stresses show more relaxation close to the hole edge than the finite element predictions.

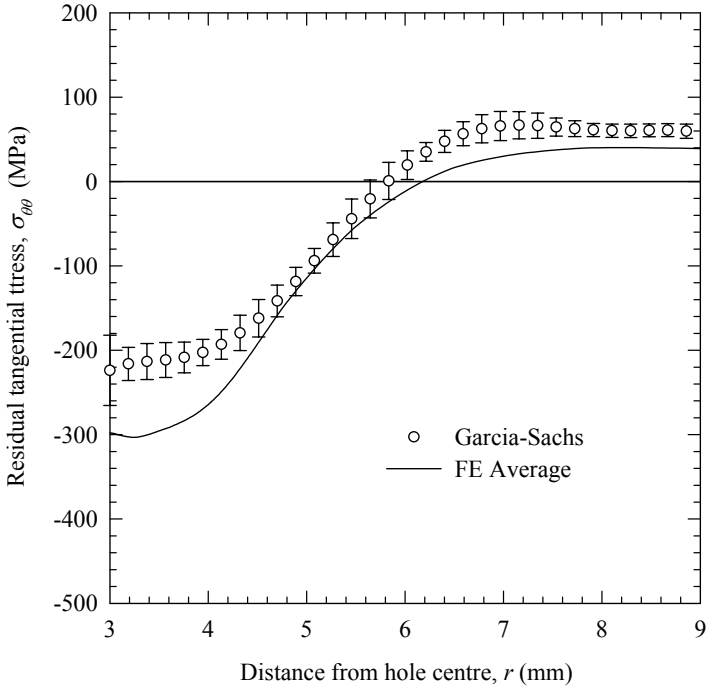

Figure 2: Measured residual tangential stresses after cold expansion followed by creep relaxation compared with averaged finite element results.

FATIGUE CRACK GROWTH MEASUREMENTS AND PREDICTIONS

Test Specimens

The test specimens for measurements of fatigue crack growth were of 6 mm thickness with a central hole of radius 3 mm, a width of 100 mm and a length of 245 mm. Two initial starter cracks were machined using an EDM technique on one face of the specimen and on both sides of the hole [8]. For specimens that had been subjected to cold expansion the starter cracks were located on the entrance face, defined by the FTI method.

Fatigue Loading

The specimens were fatigue loaded in a 250 kN servo hydraulic test machine at a rate of 10 cycles per second. The maximum load applied to the specimens was equivalent to a far field stress of 162 MPa. Various *R* ratios were used, but in the results described here an *R* ratio of 0.1 was used. Surface crack growth was measured on both surfaces of the specimen and on both sides of the hole using vernier microscopes as a function of the number of cycles of load. From these measurements, the rate of crack growth versus crack length was calculated.

Fatigue Properties

The crack growth rate was assumed to be a function of the effective range of stress intensity factor. This function was measured using a specimen of dimensions defined above with a non cold expanded hole. To ensure the measurements were not effected by closure, a high *R* ration of 0.7 was used.

Finite Element Predictions

Finite element predictions of fatigue crack growth rate were made using a two dimensional model of the test specimen. The model was run repeatedly using different crack lengths and the stress intensity factor calculated for each length. Predictions were also made of the load required to cause the crack to open enabling the effective range of stress intensity factor to be calculated for each crack length. The function of crack growth rate versus stress intensity range derived form high *R* ratio tests was then used to make predictions of crack growth rate.

Results

Measurements of crack length versus number of cycles are shown in Figure 3. The crack length in the figure is the average of the two lengths measured on the entrance face of the specimen. The measurements for three cases are presented: for a non cold expanded hole, a cold expanded hole and a cold expanded hole with creep relaxation while under applied load. Cold expansion can be seen to lower substantially the rate of fatigue crack growth. Creep relaxation removes some but not all of the benefit of cold expansion.

Figure 4 presents the experimental measurements of crack growth rate versus the crack length for the case of a specimen with a cold expanded hole. Measurements for both cracks on the entrance face of the specimen are provided: the crack to the left and to the right of the hole. Also shown are the finite element predictions of crack growth rate. The comparison shows the finite element model under-predicts the growth rate for small crack lengths and over-predicts the rate for large crack lengths. Because of the two dimensional nature of the finite element model, the crack is assumed to have a parallel through-the-thickness geometry whereas the actual crack has a complex three dimensional shape for small crack lengths. At large crack lengths the finite element predictions suggest the crack is always open during the entire load cycle whereas substantial closure is observed in the experiment. This closure is believed to be due to plasticity around the crack tip and would tend to reduce the effective stress intensity range and therefore the crack growth rate.

Finally, Figure 5 shows the experimental measurements and finite element predictions of crack growth rate for the case of a specimen with a cold expanded hole subject to creep relaxation. The crack growth rates for small holes are essentially the same as for cold expanded holes without creep. For cracks of intermediate length, from about 1 to 2 mm, the growth rates are higher. Again, the finite element model under-predicts the growth rate for small crack lengths and over-predicts the rate for large crack lengths.

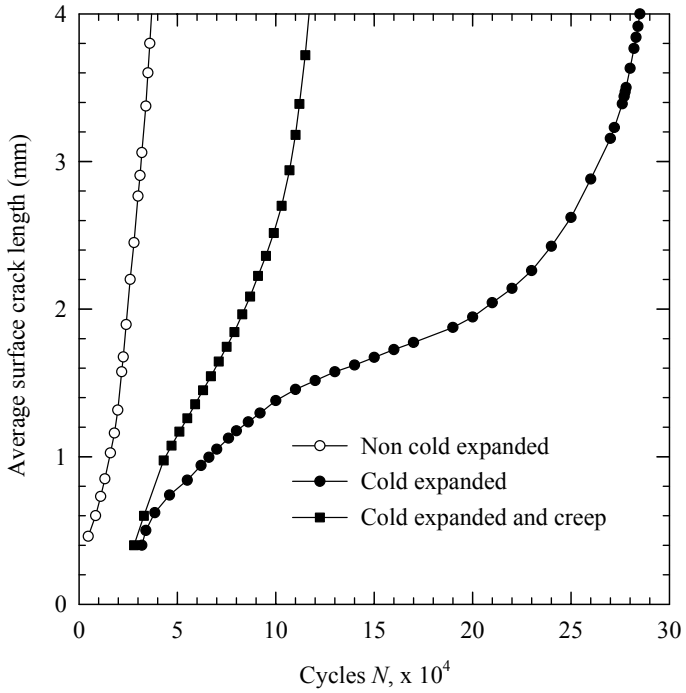

Figure 3: Average fatigue crack lengths versus number of cycles.

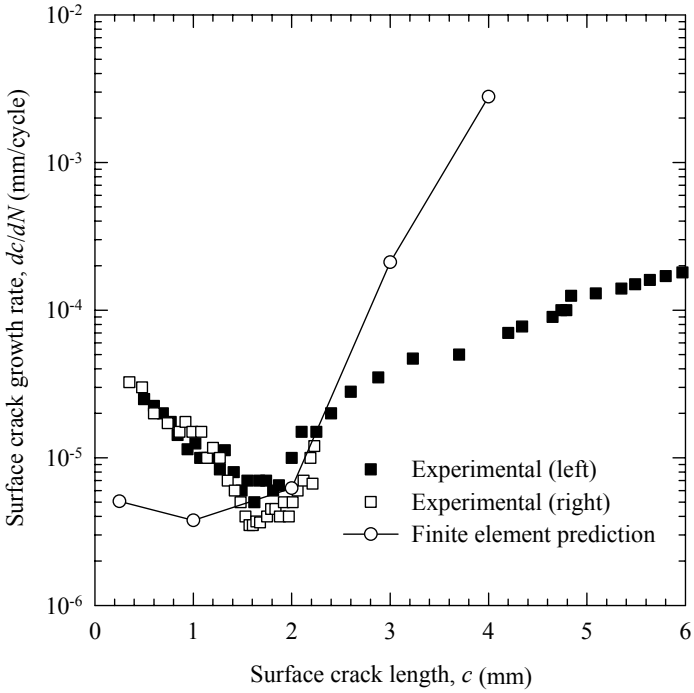

Figure 4: Measured fatigue crack growth rates for cold expanded specimens compared with averaged finite element results.

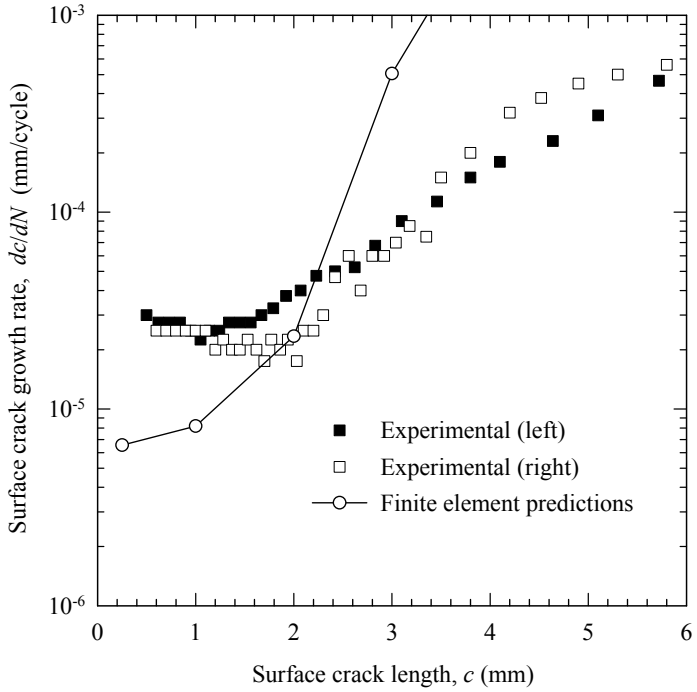

Figure 5: Measured fatigue crack growth rates for cold expanded specimens subjected to creep relaxation compared with averaged finite element results.

CONCLUSIONS

Residual stresses arising from cold expansion and after creep relaxation have been predicted using finite element simulations and measured using the Garcia-Sachs method. A generally good agreement was obtained between prediction and measurement except near the edge of the hole.

Fatigue crack growth rates have been measured for cracks growing from non cold expanded and cold expanded holes with and without creep relaxation. Creep relaxation reduces the resistance to fatigue, but there is still a benefit of cold expansion. Finite element predictions of growth rates have been made but only partial agreement with measurement has been obtained.

ACKNOWLEDGEMENTS

The work described here was sponsored by DTi and managed by DERA. Their financial support and assistance is gratefully acknowledged.

REFERENCES

1. Petrak, G.J. and Stewart, R.P. (1974) *Eng. Fract. Mech.*, 6, 275
2. Pavier, M.J., Poussard, C.G.C., and Smith, D.J. (1997) *J. Strain Analysis*, 32, 287
3. Smith, D.J., Poussard, C.G.C. and Pavier, M.J. (1998) *J. Strain Analysis*, 33, 263
4. Garcia-Granada, A.A., Lacarac, V.D., Holdway, P., Smith, D.J. and Pavier, M.J. (2001) to appear in *J. Eng. Mat. Tech.*
5. Fatigue Technology Inc., 150 Andover Park West, Seattle, Washington, USA.
6. Garcia-Granada, A.A., Smith, D.J. and Pavier, M.J. (2000) *Int. J. Mech. Sci.*, 42, 1027
7. Pavier, M.J., Poussard, C.G.C. and Smith, D.J. (1999) *Eng. Fract. Mech.*, 63, 751
8. Lacarac, V.D., Smith, D.J., Pavier, M.J. and Priest, M. (2000) *Int. J. Fatigue*, 22, 189

HIGH-RESOLUTION ANALYTICAL ELECTRON MICROSCOPY CHARACTERIZATION OF STRESS CORROSION CRACK TIPS

S. M. Bruemmer and L. E. Thomas

Pacific Northwest National Laboratory
P.O. Box 999, Richland, WA 99352

ABSTRACT

Recent results are presented demonstrating the application of cross-sectional analytical transmission electron microscopy (ATEM) to corrosion and cracking in high-temperature water environments. Microstructural, chemical and crystallographic characterizations of buried interfaces at near-atomic resolutions are shown to reveal evidence for unexpected local environments, corrosion reactions and material transformations. Information obtained by high-resolution imaging and analysis indicates the corrosion and deformation processes during crack advance and provides insights into the mechanisms controlling environmental degradation. Examples of intergranular attack and cracking in type 316 austenitic stainless steel and Ni-base alloy 600 are presented to illustrate the value of this approach. The presence of deeply attacked grain boundaries off the main cracks, revealed by TEM, is believed to indicate a major role of active corrosion in the stress-corrosion cracking (SCC) process. Corroded boundaries were filled with oxides to the leading edges of attack. Analyses of the oxide films and impurities in intergranular penetrations and crack tips with widths of 10 nm or less indicate influences of the grain boundary characteristics and the water chemistry. Boundary and precipitate corrosion structures can be used to identify the local electrochemistry promoting degradation in complex service environments. Solution impurities such as Pb are found in high concentrations at nm-width reaction zones in samples from steam-generator secondary-water environments indicating water access at leading edges of the attack and the influence of these impurities on the corrosion processes. Results for specific samples are used to demonstrate the ability of cross-sectional ATEM to reveal new details of buried corrosion structures that cannot be detected by other methods.

KEYWORDS

Crack tips, stress corrosion cracking, corrosion, intergranular fracture, grain boundary, segregation, corrosion products, passive films, solution impurities, deformation.

INTRODUCTION

The fundamental basis for mechanistic understanding and modeling of stress corrosion cracking (SCC) remains in question for many systems. Specific mechanisms controlling SCC can vary with changes in alloy characteristics, applied/residual stress or environmental conditions. The local crack electrochemistry, crack-tip mechanics and material metallurgy are the main factors controlling crack growth. These localized properties are difficult or impossible to measure in active cracks. Nevertheless, it is essential to quantitatively interrogate these crack-tip conditions if mechanistic understanding is to be obtained.

A major recent advance has been the ability to investigate SCC cracks and crack tips using analytical transmission electron microscopy (ATEM). ATEM enables the characterization of SCC cracks including trapped solution chemistries, corrosion product compositions and structures, composition gradients and defect microstructures along the crack walls and at the crack tip. A wide variety of methods for imaging and analyses at resolutions down to the atomic level can be used to examine the crack and corrosion film characteristics. Surface films and reaction layers have been examined by cross-sectional TEM techniques, but limited work had been conducted on environmentally induced cracks until recently [1-7]. A critical aspect of the recent work has been the development of sample preparation methods in which the crack corrosion products are protected during the ion-thinning process by embedding the cracks with a low-viscosity thermoplastic resin. This capability combined with modern ATEM techniques has enabled new insights into corrosion processes occurring at buried (limited communication with the bulk environment and surface electrochemical conditions) interfaces and is being used to identify mechanisms controlling SCC in service components.

The objective of this paper is to demonstrate capabilities of cross-sectional ATEM for the characterization of buried crack tips and corrosion interfaces at high resolution. New results are highlighted focusing on SCC in Fe- base and Ni-base stainless alloys. Examples are chosen to illustrate nanometer-scale structures that can only be examined effectively by ATEM methods.

CRACK-TIP SAMPLE PREPARATION AND CHARACTERIZATION APPROACH

The preparation of cross-section samples with suitable electron-transparent areas for high-resolution ATEM characterization was critical for the present work. The first step involves protecting the cracks by vacuum-impregnation with a low-viscosity thermosetting resin. Following impregnation, the section containing cracks is cut out and embedded in a stainless steel tube. The composite sample is then sliced with the main crack in cross section near the disk centers and mechanically polished. Dimple grinding is used to create a bowl-shaped depression at the area of interest. Thinning is then continued from both sides by low-angle ion micromilling with final milling performed at reduced beam energy and incident angle to remove most visible ion damage. Repeated cycles of ion thinning and TEM examination are applied to obtain suitably thin areas at crack tips or other locations of interest. Crack tips represent one of the most difficult regions to effectively protect, prepare and characterize. In nearly all the high-temperature water cases examined so far, cracks are heavily branched and are filled with corrosion products. It is possible that some of these products form during cooling from service temperatures, but most of the oxide phases are expected to form in high-temperature water and will probably restrict crack closure. A detailed description of cross-section sample preparation and possible artifacts has been published elsewhere [3,4].

ATEM characterizations were performed using a 200 kV field-emission-gun TEM with a thin-window, energy-dispersive x-ray spectrometer (EDS) and a parallel-detection electron-energy-loss spectrometer (PEELS) for microchemical analysis. High-resolution ATEM methods were used to analyze the narrow corrosion features near crack tips and along attacked grain boundaries. Besides conventional brightfield and precipitate darkfield imaging, these methods included crystal lattice imaging with Fourier-transform diffraction analysis, fine-probe (0.7-nm diameter) compositional analysis by EDS and PEELS, and fine-probe parallel-beam diffraction with electron probes as small as 5 nm in diameter. In addition, stereoscopic TEM photographs were used to observe finely porous structures along attacked grain boundaries. A Fresnel (off-focus) image contrast method was employed to reveal fine pores and other structures as small as 1 nm.

EXAMPLES OF CRACK-TIP CHARACTERIZATIONS

Results from 316SS and alloy 600 materials that experienced intergranular (IG) SCC in high-temperature (250-320°C), deoxygenated water environments are used to illustrate high-resolution characterizations of crack-tip, crack-wall and corrosion structures. Specific information on water environments and material conditions is given elsewhere [4-7].

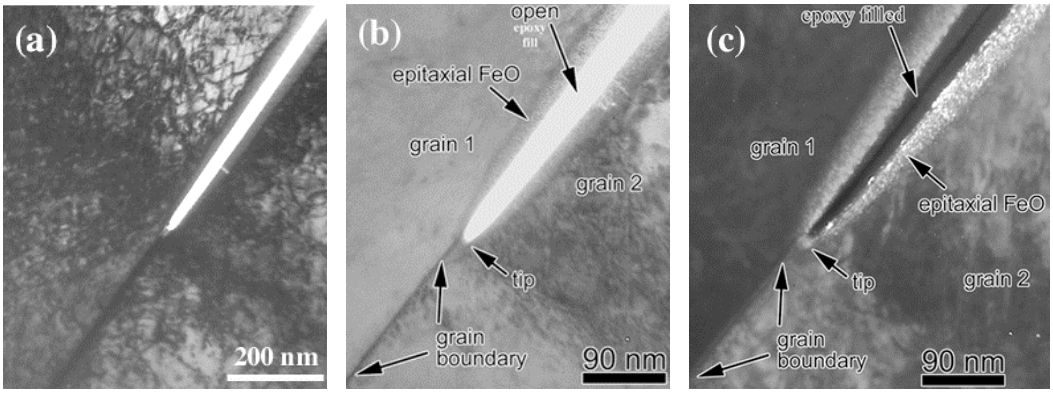

Figure 1: Example of a typical crack tip in the 316SS samples: (a) bright-field image with matrix dislocation structure in contrast, (b) bright-field image with matrix structure out of contrast to elucidate crack tip, and (c) FeO darkfield image highlighting epitaxial oxide on wall and at tip.

Crack-Tip Characterization in 316SS

The 316SS samples that will be discussed were removed from a service component after many years in a 250-290°C, deoxygenated water environment [6,7]. Cracked samples from several locations have been examined and many crack tips characterized. In nearly all cases, wide (>~0.5 μm) cracks were filled with a multi-layer corrosion product oxide, consisting of a Cr-rich FeO and spinel inner layer plus large-grained magnetite (Fe_3O_4) filling the center of the crack. This multi-layer film is similar to that reported at stainless steel surfaces [8,9] with the exception of the FeO-structure oxide. The focus here is on the crack tips as illustrated in Figure 1. A somewhat "classic" appearance of a SCC crack tip in a passive alloy is seen with a non-porous, epitaxial FeO-structure oxide film on the walls. The crack narrows to ~10 nm at the tip comparable to the oxide film thickness ahead of the tip and on the adjacent crack walls. Evidence of significant deformation (high dislocation density) is present in the metal surrounding the tip as illustrated in Figure 1(a), but localized slip bands have not been observed intersecting the crack. However, twins are seen at or near primary or secondary crack tips as demonstrated in Figure 2. Scanning electron microscopy indicates that most twins are present before the propagation of SCC cracks and that many cracks end at intersections of twins with grain boundaries [10]. The examples presented in Figure 2 show deformation twins immediately ahead of a crack tip in (a) and a crack that has propagated through several twins in (b). Oxide films at these crack tips were again found to be non-porous, but were predominately a nanocrystalline FeCr spinel versus the epitaxial FeO-structure oxide seen at other tips. Low levels of solution impurities (e.g., Na) were discovered in the oxides indicating that a caustic environment may have been in cracks.

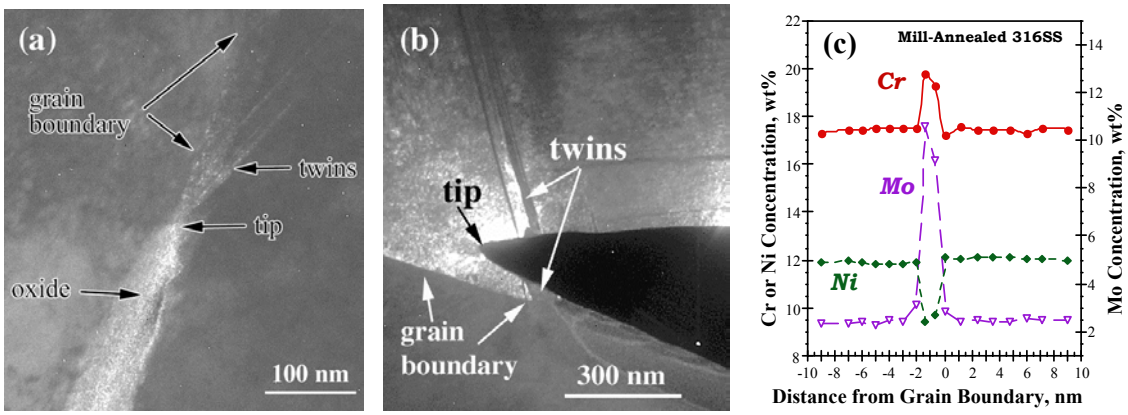

Figure 2: Crack-tip interactions with matrix twins in a 316SS sample with twin present immediately ahead of the crack tip in (a) and immediately behind the tip in (b) where the crack is clearly displaced off the grain boundary plane. The composition profile in (c) was taken across the grain boundary in a non-attacked base metal region well ahead of the crack tip.

A final important crack characteristic illustrated in Figures 1 and 2(b) is the crack-tip locations that are often adjacent to, and not centered on, the grain boundary. Crack propagation along a path several nm off the boundary was clearly evident at about one-third of the crack tips examined. The only measured material feature in these mill-annealed 316SS samples that may play a role is the grain boundary composition. Significant Mo and Cr enrichment is present at grain boundaries as shown in Figure 2(c). This non-equilibrium segregation has been seen in many mill-annealed stainless steel heats (often with B enrichment) and is most likely produced during initial processing before service [11]. The profile presented was obtained ahead of a crack tip that was centered off the boundary interface and it reveals the maximum segregation adjacent to the boundary. It is possible that the altered local composition influences dissolution and passivation, thereby SCC propagation.

Intergranular Attack and SCC in Alloy 600

Recent work [3-7] on cracked alloy 600, pressurized-water-reactor (PWR), steam-generator tubes has shown a remarkable tendency for IG attack along with SCC. TEM examinations of samples cracked in various high-temperature water environments has revealed narrow oxidized zones, 5-to 20-nm in width and up to tens of μm in length, along nearly every intersected grain boundary in the wakes of cracks. An example of these IG corrosion zones is shown in Figure 3 for mill-annealed alloy 600 after long-term exposure to PWR primary water at 330°C. TEM images show no visible cracks in the corrosion zones and no significant deformation of the surrounding metal matrix. Fresnel contrast imaging in Figure 3(a) shows that these structures are highly porous on a scale of 1-2 nm. Electron diffraction analyses revealed that the corrosion product consisted of nanocrystalline oxides (NiO, Cr_2O_3 and/or spinel depending on the particular environment). Lattice imaging identified individual crystallites with sizes down to a few nm as demonstrated in Figure 3(b). The fine porosity at the tip of a corrosion zone is illustrated in Figure 3(c). A complex network of nm-size voids and tunnels is present in the narrow oxide layer along an inclined grain boundary, as well as voids along the grain boundary plane ahead of the tip. The oxide at the attack tips was Cr_2O_3, even though the predominant oxide some distance (>100 nm) behind the tip was NiO (Cr and Fe levels similar to the matrix). Significant Cr enrichment at the oxidized tip was measured by high-resolution EELS, but the adjacent matrix was not depleted. The observation of pores in the metal ahead of the oxidation front suggests that vacancies may be injected during the corrosion process. Due to the narrow dimensions of the corroded IG zones in alloy 600, these structures have been undetectable by other examination methods including optical metallography, SEM or secondary-ion mass spectroscopy.

Exposure to secondary water or steam environments can produce similar IG attack and aggressive degradation of precipitates in alloy 600 samples [6,7]. An example of this behavior is shown in Figure 4 for once-through steam generator tubing removed from the high-superheat (steam) region. Alloy 600 tubing is put into service in the stress-relieved and sensitized condition with closely spaced

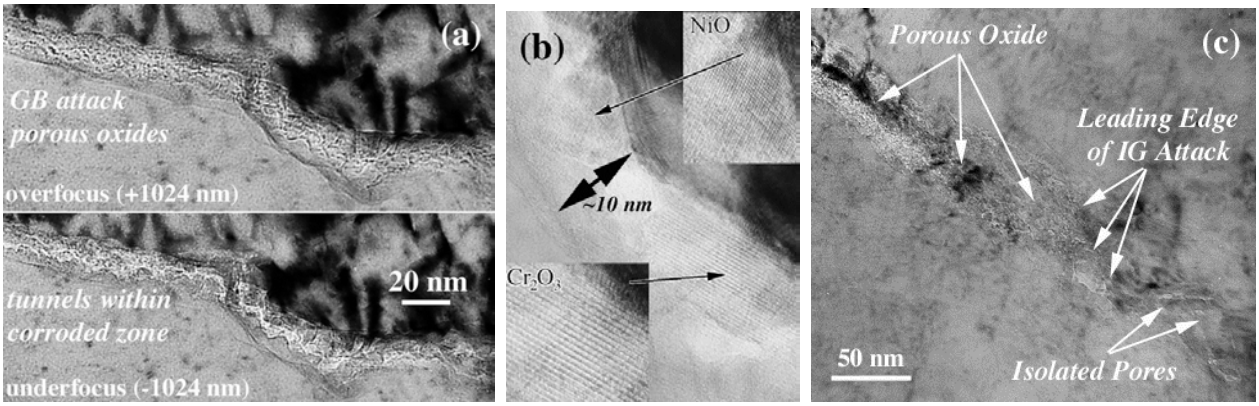

Figure 3: Intergranular attack of alloy 600 in high-temperature PWR primary water: (a) Fresnel contrast images showing narrow porous oxidized zone, (b) lattice images identifying crystallites of Cr_2O_3 and NiO in the corroded zone and (c) leading edge of attack with oxidized material ending within grain boundary plane and presence of isolated pores ahead of corroded region.

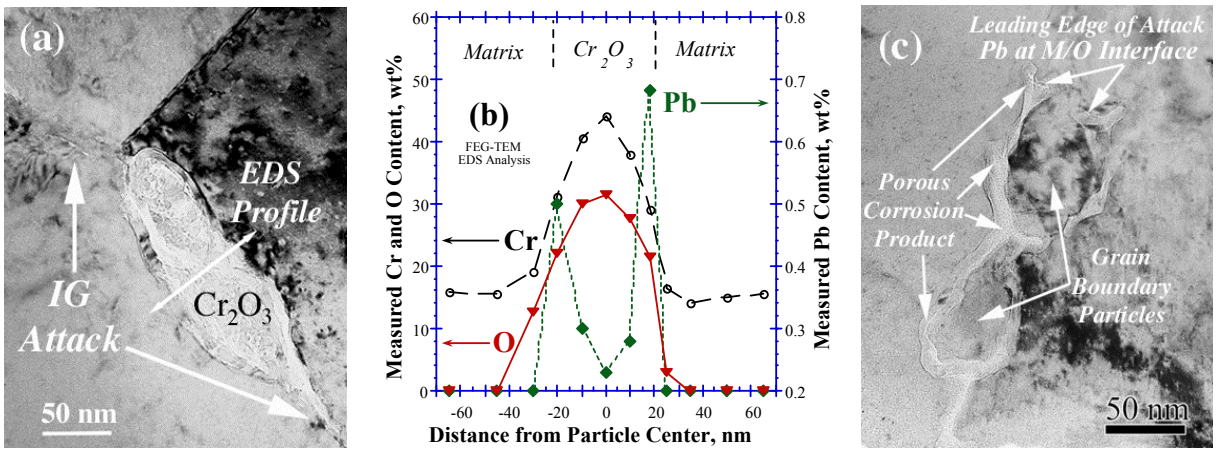

Figure 4: Intergranular attack of alloy 600 in high-temperature PWR secondary water: (a) former grain boundary Cr carbide converted to Cr oxide, (b) composition profile across attacked particle showing Pb enrichment at the metal-oxide (M/O) interface and (c) porous corrosion product oxides around grain boundary particles with Pb present at leading edge of attack.

Cr_7C_3 carbides and $Ni_{23}B_6$ borides. The porous oxide structure in the IG attack zones was similar to the primary-water samples, but the carbides were converted to fine-grained Cr_2O_3 oxides and borides were completely removed. Solution impurities appear to have a strong influence on the stability of these particles. EDS analyses of the oxidized particles (Figure 4a) revealed that environmental impurities, notably Pb, had penetrated the structures and concentrated in the reaction layers along the metal-oxide interfaces (Figure 4b). Further observations at the leading edges of attack showed tunnel-like corrosion zones formed around the IG particles as presented in Figure 4(c). A penetrative porous oxide is seen to envelop a partially converted Cr_7C_3 precipitate and end adjacent to a Ni-rich particle (former boride). The corrosion product in these tunnels consisted of nanocrystalline Cr-Ni spinel containing high concentrations of Pb at the leading edge of attack. This is consistent with Pb promoting dissolution and/or impairing passivity to enhance boundary and precipitate degradation.

DISCUSSION

The application of high-resolution ATEM methods to buried corrosion interfaces in stress-corrosion cracked materials has revealed important details of the degradation processes and mechanisms. This advance comes from two developments: (1) improvements in cross-sectional sample preparation on cracked materials, and (2) the availability of FEG TEMs that allow structural, compositional and crystallographic analyses at resolutions down to atomic dimensions. Significant findings of this continuing research include the recognition that active-path corrosion of grain boundaries plays a major role in SCC of alloy 600 in a wide variety of steam generator environments. This IG attack produces a remarkably thin (<20 nm in width) band of porous, non-protective oxide that extends for many μm. It is clear that water (or steam) penetrates throughout corroded structures. No evidence of plastic deformation was found associated with the IG attack and it appears that plasticity is not required for grain boundary degradation to occur. However, it is likely to accelerate growth rates via a stress-assisted corrosion process. Solution impurities such as Pb are shown to concentrate along the narrow (few nm) reaction layers at buried interfaces. High impurity enrichments at the leading edge of attack suggest that Pb promotes metal (and precipitate) dissolution and/or impairs oxide formation.

Secondary cracking was found in the austenitic stainless steel samples, but no evidence of significant IG attack. The formation of non-porous, protective oxides on crack walls and at the crack tip is more consistent with a classical SCC slip-oxidation mechanism. Crack-wall films are in general agreement with surface films reported on stainless steels after high-temperature water exposure. The presence of the FeO-structure inner film was unexpected and it appears to have a close structural relationship with the spinel phase that forms adjacent to this oxide. In general, non-porous protective films tend to form on exposed 316SS surfaces in these high-temperature water environments, while porous, non-

protective oxides are produced in the alloy 600 cracks and attacked boundaries. Cracks are generally quite tight (tip openings down to a few nm) in both alloys, but the 316SS samples reveal a high dislocation density at all crack tips suggesting that plasticity is an essential part of the SCC process.

This work has demonstrated the ability of ATEM to reveal new and important details of buried corrosion and SCC structures that cannot be detected by other methods. However, the current observations must be considered work in progress and additional work is needed to properly establish mechanisms controlling IGSCC. In particular, ATEM characterization of degradation structures must be performed on samples where mechanisms are better distinguished. Tests in high-temperature aqueous and gaseous environments should be performed under well-controlled solution chemistries and electrochemical conditions to establish a library of the corrosion signatures.

CONCLUSIONS

Cross-sectional ATEM has been used to effectively characterize corrosion and cracking in high-temperature water or steam environments. A wide variety of high-resolution imaging and analysis methods are employed to elucidate processes occurring during crack advance and provides insights into the mechanisms controlling environmental degradation. Fundamental differences are detected between corrosion structures in Fe-base and Ni-base stainless alloys. Deeply attacked grain boundaries off the main cracks are found in alloy 600 samples indicating a major role of IG corrosion in the SCC process. Corroded boundaries were filled with nanocrystalline oxides to the leading edges of attack. Precipitates in alloy 600 are also attacked and can be used to identify the local electrochemistry promoting degradation in complex service environments. Solution impurities such as Pb are found in high concentrations at nm-width reaction zones in samples from secondary-water environments documenting water access at leading edges of the attack and indicating how impurities influence the corrosion processes. Results presented demonstrate the ability of cross-sectional ATEM to reveal new details of buried corrosion structures that cannot be detected by other methods.

ACKNOWLEDGEMENTS

The technical assistance of C. E. Chamberlin and V. Y. Gertsman are recognized along with helpful discussions with P. M. Scott. Primary support comes from the Materials Sciences Branch, Office of Basic Energy Sciences, U.S. Department of Energy (DOE) under contract DE-AC06-76RLO 1830 with Battelle Memorial Institute. Additional support is acknowledged from EPRI, the B&W Owners Group Chemistry Committee and the DOE Office of Nuclear Energy, Science and Technology.

REFERENCES

1. Lewis, N., Perry, D.J. and Bunch, M.L. (1995) In: *Proc. Microscopy and Microanalysis* ed., Bailey, G.W. et al., Jones and Begnell Publishing, New York, 550.
2. Lewis, N., Attanasio, S., Morton, D.S. and Young, G.A. (2001) In: *Proc. Staehle Symposium on Chemistry and Electrochemistry of Corrosion and Stress Corrosion*, ed. Jones, R.H. TMS, p. 421.
3. Thomas, L.E., Charlot, L.A. and Bruemmer, S.M. (1996) In: *Proc. New Techniques for Characterizing Corrosion and Stress Corrosion*, Eds. Jones, R.H. and Baer, D.R. TMS, p. 175.
4. Thomas, L.E. and Bruemmer, S.M. (2000) *Corrosion J.*, 56, 572.
5. Thomas, L.E. and Bruemmer, S.M. (2000) In: *Proc. 9th Int. Conf. Environmental Degradation of Materials in Nuclear Power Systems-Water Reactors*, ed. Bruemmer, S., Ford, F.P., TMS, p. 41.
6. Bruemmer, S.M. and Thomas, L.E. (2001) In: *Proc. Staehle Symposium on Chemistry and Electrochemistry of Corrosion and Stress Corrosion*, ed. Jones, R.H. TMS, p. 123.
7. Bruemmer, S.M. and Thomas, L.E. (2001) *J. Surface and Interface Analysis*, in press.
8. Robertson, J. (1991) *Corrosion Sci.*, 32-4, 443.
9. Stellwag, B. (1998) *Corrosion Sci.*, 40-2/3 337.
10. Gertsman, V.Y. and Bruemmer, S.M. (2001) *Acta Metallurgica*, 49, 1589.
11. Karlsson, L. (1988) *Acta Metalurgica*, 36, 1.

ORAL/POSTER REFERENCE: ICF10788OR

HIGH-SPEED DEBONDING AND FRICTIONAL SLIDING IN COMPOSITE SYSTEMS: EXPERIMENTAL OBSERVATIONS AND NUMERICAL SIMULATIONS

J. Lambros, X. Bi and P. H. Geubelle

Department of Aeronautical & Astronautical Engineering,
University of Illinois, Urbana, IL 61801

ABSTRACT

This paper reports our recent progress on the experimental and numerical study of dynamic debonding and frictional push-out in model composite systems. A modified Split Hopkinson Pressure Bar system is adopted to perform the dynamic fiber push-out test. A Cohesive Volumetric Finite Element scheme is developed to capture the initiation and propagation of the crack along the fiber/matrix interface. Interface properties are extracted by comparison of experimental and numerical results. Details of the physical process are scrutinized by investigating numerically the propagation and evolution of axial stress along the entire system.

KEYWORDS

Dynamic, residual, debonding, frictional, push-out, SHPB, CVFE

INTRODUCTION

When a crack propagates in a composite material in a direction perpendicular to that of the reinforcing fibers, the failure process involves four basic mechanisms: matrix cracking, fiber/matrix debonding, fiber breakage and fiber pull-out. Under high-velocity impact conditions, a substantial part of the energy is dissipated in the frictional debonding and sliding of the bridging fibers located behind the advancing crack front. Because of the important effect they have on the fracture toughness of a composite, these two processes have been the subject of extensive experimental, numerical and analytical work. Most experimental investigations of fiber debonding and push-out process use model composites, in which a single embedded fiber is pulled or pushed out of the surrounding

matrix. The fiber diameter is typically chosen one to three orders of magnitude larger than that of the actual composite reinforcement to allow for a better control and visual analysis of the failure process. However, the vast majority of existing studies on these topics has been limited to the quasi-static loading case [1,2,3]. The few experimental investigations involving dynamic loading recently performed on various composite systems seem to indicate that the dynamic fiber sliding process presents some unusual and sometimes even contradictory characteristics [4,5]. Recently, existing models has been extended to high loading rates by taking into account the inertial effect of fiber and matrix [6].

The primary objective of this paper is to enhance, through a combined experimental and numerical investigation, the current understanding of *dynamic* debonding and frictional push-out in model fiber-reinforced composites.

EXPERIMENTAL ANALYSIS

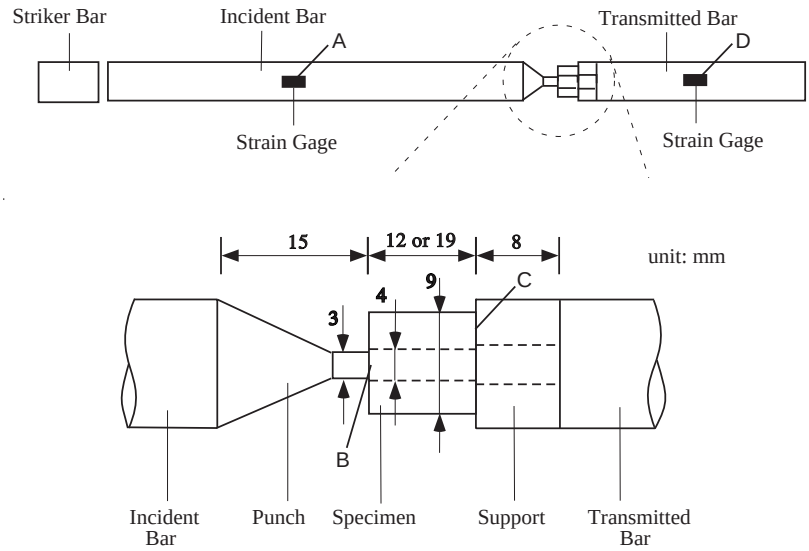

Figure 1: Schematic of the modified SHPB for dynamic fiber push-out test and its connection with a model composite specimen.

To investigate the fiber/matrix debonding and frictional push-out mechanism under high loading rates, a novel experimental setup has been developed and model mono-filament composites have been tested. The high-rate experiments are performed using a modified Split Hopkinson Pressure Bar (SHPB) system (Figure 1). A set of specially designed punch and support connect the model composite with the incident and transmitted bars of the SHPB, respectively. The tapered punch is used to apply compressive loading to a single fiber embedded in a surrounding matrix material. Once the interface debonds, the fiber slides into the hollow support. The contacting ends of the incident bar, punch, composite specimen, support and transmitted bar are connected with each other by grease to allow for free expansion in the radial direction. A schematic of the experimental setup is shown in Figure 1. In this experimental system, the incident bar, punch and support are all made of steel. As the transmitted signal is relatively small, aluminum is chosen for the transmitted bar. The model composite specimen is made in a specially designed mold and cured under room temperature. It consists of a metal fiber (steel or aluminum) embedded in an Epoxy (EPON 862) matrix. Specimen dimensions are also shown in Figure 1. For later use, the dynamic material properties of each individual constituent have been measured using standard high strain

rate SHPB dynamic compression tests. Following the traditional derivation of the SHPB equations, corresponding data reduction equations for the push-out test can be obtained.

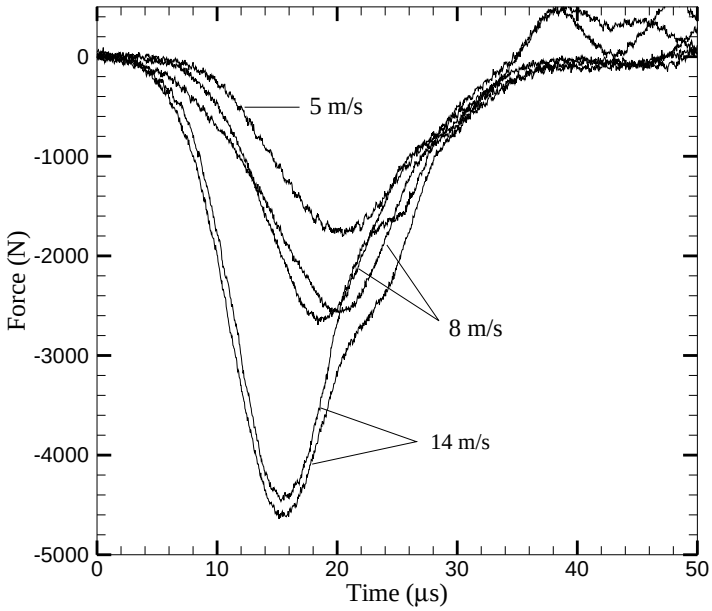

Figure 2: Experimental results: Effect of sliding speed on transmitted force in a model Steel/Epoxy composite (length = 36 mm, grit 36 roughness).

Figure 2 shows the effect of the sliding speed on the transmitted force. We can see from theses curves that both the peak force achieved and the rise time of the signal increase with increasing rate. The figure also illustrates the repeatability of these experiments. Using this technique we have studied the effect of impact speed, material mismatch, fiber length, surface roughness, and residual strain. For more results, please refer to [7].

NUMERICAL ANALYSIS

To process and support these experimental results, a special axisymmetric numerical analysis scheme has been developed and implemented. To extract adequately the complex failure process taking place in the dynamic fiber push-out event, the numerical scheme used in this analysis must account the presence of residual strains in the matrix, the spontaneous motion of the interface debonding front and the frictional contact between the fiber and matrix surfaces. The main component of the numerical method is the cohesive volumetric finite element scheme described hereafter. We then present a summary of the comparison between experimental and numerical results.

Cohesive Volumetric Finite Element Scheme

The spontaneous initiation and propagation of the debonding crack has been captured by a special method referred to as the Cohesive Volumetric Finite Element (CVFE) scheme [8,9]. In our fiber push-out CVFE model, a series of cohesive elements are introduced along the fiber/matrix interface within a conventional finite element mesh as shown in Figure 3. These cohesive elements basically act like nonlinear distributed springs linking standard volumetric elements at interfaces

where failure is possible. The nonlinear springs resist opening (or shearing in this case) in accordance to a prescribed traction-separation law as shown. Eventually, as the separation increases, the cohesive tractions go to zero, simulating the creation of a new free surface. In the general case, the traction-separation law relates the cohesive traction vector, defined by its normal and tangential components, to the displacement jump vector. Figure 3 also shows the relation between the cohesive traction and displacement jump for the pure shear failure. The maximum traction τ_{max} and fracture toughness G_{IIC} characterize the bonding strength of the interface. One goal of this work is to extract these properties by comparing experimental results with numerical analysis. Let us note that this CVFE model was successfully used in the simulation of quasi-static fiber push-out by Lin *et al.* [8].

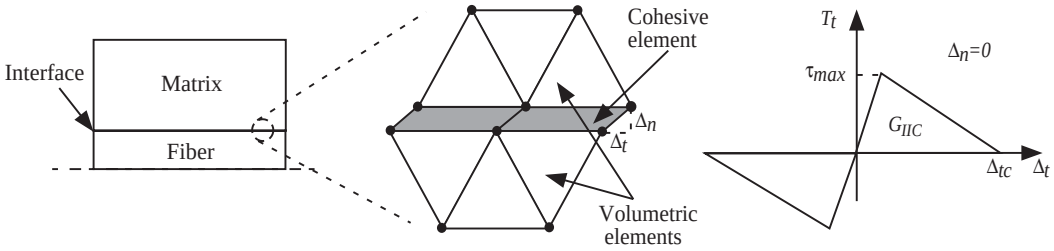

Figure 3: Schematic of interfacial cohesive elements. The two cohesive elements in the center figure are shown in their deformed configuration: in their undeformed configuration, these elements have no thickness and the adjacent nodes are superposed. The quasi-linear cohesive model is shown in the right figure for the pure shear mode.

Comparison between Numerical and Experimental Results

The numerical simulation described hereafter is carried out for an aluminum/EPON specimen, with the stress signal measured from the incident bar in experiments as the load boundary condition. The residual strain in the epoxy matrix is taken as -0.0022 [2]. The material properties of the constituents measured from traditional dynamic SHPB experiments are listed in Table 1.

Table 1: Material Properties of Constituents.

Material Properties	Steel	Aluminum	Epon
E (GPa)	207.0	69.0	5.65
ν	0.30	0.35	0.34
ρ (Kg/m^3)	8130.6	2650.0	1176.0

By fitting the numerical model with experimental results for the 6 m/s impacting speed case, it was found that the interface is characterized by a shear failure strength $\tau_{max} = 60$ MPa, a mode II fracture toughness $G_{IIC} = 150$ N/m, and a friction coefficient $\mu_f = 0.2$. As shown in Figure 4, these interface properties also capture the increase of the peak load with increasing impact speed. Also, the slope of the transmitted stress is well matched with experiments. As indicated by the increasing difference between experimental and numerical peak values of the transmitted stress with increasing sliding speed, these interface properties appear to have small rate sensitivity. For details of the numerical scheme and more simulation results, please refer to [10].

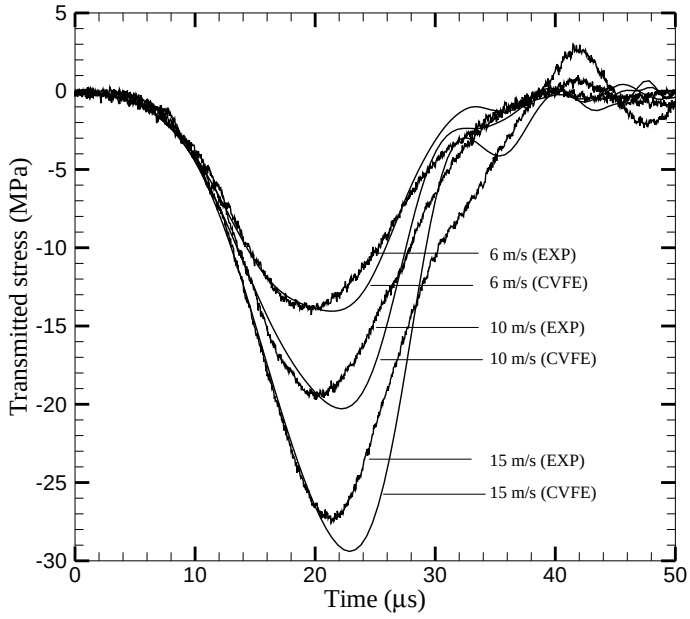

Figure 4: Comparison between numerical and experimental values of the transmitted stress for the model Aluminum/Epoxy composite. All CVFE curves have been computed with $\tau_{max} = 60\ MPa$, $G_{IIC} = 150\ N/m$ and $\mu_f = 0.2$.

Determination of Crack Initiation Point and Propagation Speed

Beyond the comparison with experimental measurement of the transmitted force, the numerical scheme also provides a unique tool to shed more light on the failure process, through a detailed study of the evolution of the axial stress at various locations in the SHPB system. Several observation points (indicated by A, B, C and D in Figure 1) have been tested. The evolution of the axial stress σ_{zz} at three of these points (A, C, D) and that of the crack tip location are presented in Figure 5 for Aluminum/Epoxy composite case (impact speed = 10 m/s) shown in Figure 4. Using the wave speed in the bar, the curve denoting the stress evolution in the middle of the incident bar (point A) is shifted backward in time to match that observed at the interface between the punch and the fiber (point B). To determine the crack initiation time, we performed another elastodynamic simulation in the absence of failure (i.e., by imposing a very high strength τ_{max} in the cohesive model). The corresponding axial stress evolution computed at point C is shown as a dotted curve in Figure 5. At time $t = 18\ \mu s$, we note a clear separation between the point C stress evolution curves with and without failure, indicating the onset of the interface failure process. This crack initiation time is confirmed by the crack tip evolution curve (solid curve in Figure 5). It should be noted that the appearance of the failure-induced kink in the stress curve at point C is unfortunately smoothed out by the time the signal reaches the mid point of the transmitted bar (point D), indicating the need to measure the stress wave closer to the composite specimen [10].
It is interesting to note that, in this particular case, the interfacial crack initiated from the support end of the composite specimen instead of the punch end, as it has been observed for quasi-static experiments involving composite constituents with a high modulus mismatch [2]. Let us note that this behavior also depends on the interface strength: for weak interface, the crack typically starts from the punch end. As indicated in Figure 5, the crack propagates rapidly toward the punch end at a speed of about 1650 m/s, slightly higher than the shear wave speed of epoxy ($C_{se} = 1340\ m/s$) but less than that of Aluminum ($C_{sa} = 3110\ m/s$), i.e., at a speed which is referred to as inter-sonic

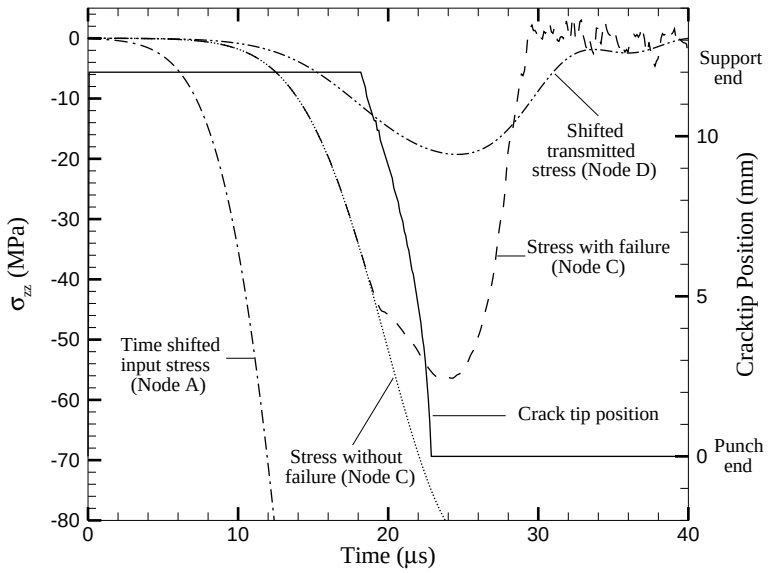

Figure 5: Numerical simulation of the force transfer process for model Aluminum/Epoxy composite with sliding speed of 10 m/s: time evolution of the axial stress at various locations of the push-out setup and of the crack tip location. Time $t = 0$ μs corresponds to the arrival of the initial loading wave at the punch location.

[11]. As the crack length reaches 75% of the fiber length, the crack propagation speed increases further to approximately 5500 m/s which represent 85% of dilatation wave speed in aluminum fiber ($C_d = 6460$ m/s).

ACKNOWLEDGEMENTS

The authors wish to thank the National Science Foundation for the support of this work through grant CMS-9712291.

REFERENCES

1. Tsai, K.-H. and Kim, K.-S. (1996). *J. Mech. Phys. Solids.* 44 (7), 1147.
2. Bechel, V. T. and Sottos, N. R. (1998) *J. Mech. Phys. Solids.* 46 (9), 1675.
3. Liang, C. and Hutchinson, J. W. (1993) *Mech. Mat.* 14, 207.
4. Khanna, S. K. and Shukla, A. (1994) *Exper. Mech.* 171.
5. Klopp, R. W. and Crocker, J. E. (1994) *J. Physique III.* 4, C8.47.
6. Cox, B.N., Sridhar, N. and Beyerlein, I. (2000) Submitted to *J. Mech. Phys. Solids.*
7. Li, Z., Bi, X., Lambros, J. and Geubelle, P. H. (2001) Submitted to *Exper. Mech.*
8. Lin, G., Geubelle, P. H. and Sottos, N. R. (1998) To appear in *Int. J. Solids Structures.*
9. Geubelle, P. H. and Baylor, J. (1998) *Composites (B).* 29B, 589.
10. Bi, X., Li, Z., Geubelle, P.H. and Lambros, J. (2001) Submitted to *Mech. Mat.*
11. Lambros, J. and Rosakis A.J., *J. Mech. Phys. Solids.* 43 (2), 169.

ORAL REFERENCE: ICF100377OR

HIGH STRAIN RATE BEHAVIOUR OF HIGH STRENGTH STEELS FOR AUTOMOTIVE APPLICATIONS

O. Moriau[1], P. Verleysen[2], J. Degrieck[2] and N. Akdut[1]

[1]OCAS N.V., Research Centre of the SIDMAR Group,
ARBED Group Flat Rolled Products Division,
J.F. Kennedylaan 3, B-9060 Zelzate, Belgium
[2]Department of Mechanical Construction and Production, University of Ghent,
Sint-Piertersnieuwstraat 41, B-9000 Gent, Belgium

ABSTRACT

The continuous requirement of the automotive industry for increased safety and weight savings related to the reduction of the fuel consumption, results in an increasing application of High Strength Steels (HSS). Currently also austenitic stainless steels are under investigation for structural and safety relevant parts due to their high potential in energy absorption and their high strength. In order to achieve a better performance and accuracy of crash test finite element simulations, the mechanical characteristics at high strain rates of these different steel grades are of great importance. Therefore, the strain rate sensitivity of steel grades like dual phase, micro-alloyed and 301LN stainless steel, produced in the ARBED group, is investigated in a range of strain rates between $10^{-2}s^{-1}$ and $1000s^{-1}$ using a hydraulic tensile machine and a recently developed impact test-bench based on the split Hopkinson bar method.
Special emphasis is addressed to the austenitic stainless steel, which shows a relative low ductility loss at high strain rates and is characterised by a change in strain hardening confirmed by the measurements of the martensite volume fraction. The interaction between strain rate, temperature and strain is discussed in terms of $\gamma \rightarrow \alpha$' transformation and strengthening behaviour.

KEYWORDS

Strain rate sensitivity, Hopkinson bar, high strength steels, austenitic stainless steels

INTRODUCTION

Since weight reduction has become more and more a hot topic in the automotive industry, industrial developments of new steel qualities with excellent deformability at high strength levels are a major concern in most steel industries. Although currently the automotive industry uses stainless steels only in small amounts for applications where corrosion resistance is an issue, austenitic stainless steel grades could challenge low-alloyed HSS grades for car body applications, due to their excellent mechanical properties. First assessments [1-4] have shown that the combination of high strength and good formability of austenitic stainless steels offers a high freedom in design. Due to their high impact energy absorption austenitic stainless steels are very well suited for e.g. safety relevant parts. However, it is essential to make the most efficient use of the available various steel grades in automotive applications to meet the competitive threat from alternative materials.

Currently, there are discussions going on concerning high strain rate testing methods and data needed to be optimised for the use of steel in Finite Elements Analysis (FEA) models. Crash models results show strain rates of up to $1000s^{-1}$ and therefore material data up to this strain rate level is needed. Not only the strain rate but also the temperature has an influence on the mechanical properties. Therefore, the combination of strain rate and temperature effects is of great interest. Indeed, it is well known that high temperature leads to a decrease of the mechanical characteristics, while high stain rate leads to an increase. A balance of the latter effects is important since the location of some crash relevant parts close to the engine leads to temperatures close to 80°C. With regard to the steel grades produced in the ARBED group and used for car body applications, in this study the strain rate sensitivity is investigated in the temperature range from –40°C to +80°C for different steel grades: Interstitial Free High Strength Steel IFHSS260, micro-alloyed steel ZStE420, galvanized Dual Phase steel DP500G and austenitic stainless steel 301LN.

MATERIALS AND TESTING PROCEDURE

Investigated materials

The mechanical properties were measured in rolling direction (RD) according to the standard EN10002 on a common tensile test-bench at room temperature with a strain rate of $5 \cdot 10^{-3} s^{-1}$ (see Table 1).

TABLE 1
MECHANICAL PROPERTIES OF THE INVESTIGATED STEEL GRADES IN ROLLING DIRECTION

Grade	Thickness mm	YS MPa	TS MPa	A80 %	n_0	r_0
IF HSS 260	1.20	260	394	36.6	0.201	1.37
ZStE 420	1.13	431	495	26.0	0.166	0.65
DP500G	1.15	368	558	25.0	0.151	0.84
301LN annealed condition	1.20	378	752	50.8	0.35-0.6	0.92

Dynamic tensile testing facilities

The dynamic tensile tests were performed in RD on a servo hydraulic high-speed tensile machine up to a strain rate of $10s^{-1}$ for 3 temperatures based on the automotive standards, i.e. -40°C, 20°C and 80°C. Flat tensile specimens with a 40mm gauge length were used at ram speeds up to 400mm/s. In order to complete the strain rate range up to $\dot{\varepsilon} = 1000s^{-1}$, tensile tests were performed on a split Hopkinson tensile bar set-up developed at the University of Ghent but only at room temperature. The experimental test facility consists of a 6m long input bar and a 3.15m long output bar, between which the test specimen is fixed, as schematically presented in Figure 1.

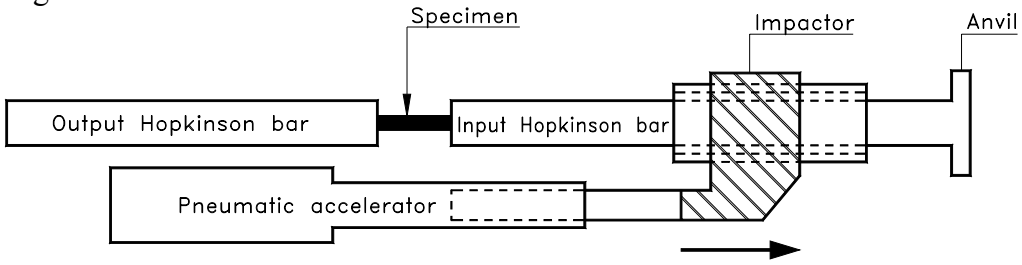

Figure 1: Schematic representation of a split Hopkinson tensile bar setup

Both the aluminium input bar and output bar have a diameter of 25 mm. The 5mm wide, flat steel sheet specimen has a gauge length of 10 mm. The anvil at the outer end of the input bar is hit by an impactor, which is pneumatically accelerated. The pneumatic accelerator has a capacity of 5kJ. A tensile wave with a duration of 1.2 msec is generated by the impact and propagates along the input bar towards the specimen.

Upon reaching the specimen the wave is partly reflected back into the input bar to form the reflected wave, and is partly transmitted to the output bar to form the transmitted wave.

The strain histories ε_i, ε_r and ε_t, respectively corresponding with the incident wave, the reflected wave and the transmitted wave, are measured by means of strain gauges. These strain gauges are located at well-known points on the input and the output bar, away from the specimen. The recorded signals are subsequently shifted, forward or backward, towards the interface planes with the specimen, in order to obtain forces and displacements at both ends of the specimen. The specimen dimensions given above were optimised using numerical simulations in order to have a uniaxial, homogeneous stress and deformation state in the specimen. With these assumptions the time histories of strain, strain rate and stress in the specimen can be obtained from the following expressions in Eqn. 1 [5]:

$$\varepsilon(t) = -\frac{2\ C_b}{L_s}\int_0^t \varepsilon_r(\tau)\,d\tau, \quad \dot{\varepsilon}(t) = -\frac{2\ C_b}{L_s}\varepsilon_r(t), \quad \sigma(t) = \frac{A_b\ E_b}{A_s}\varepsilon_t(t) \tag{1}$$

with E_b the elasticity modulus of the Hopkinson bars, A_s and A_b the cross section area of the specimen and of the Hopkinson bars respectively, C_b the velocity of propagation of longitudinal waves in the Hopkinson bars and L_s the specimen length. The main advantage of the Hopkinson test is that strain, strain rate and stress in the specimen are obtained without measurements on the specimen.

TEMPERATURE AND STRAIN RATE SENSITIVITY RESULTS

Strain rate sensitivity at room temperature

As expected, the IFHSS260 shows the highest ratio between dynamic ($\dot{\varepsilon} \approx 1000s^{-1}$) and quasi-static lower yield strength (YS_{dyn}/YS_{st}) close to 1.8 (Figure 2a) but also a reduction of 34% in uniform elongation (Figure 4). The micro-alloyed steel ZStE420 is characterised by a low YS_{dyn}/YS_{st} of 1.3 and also by a reduction of 46% in uniform elongation. The dual phase grade and the austenitic stainless steel have nearly the same ratio YS_{dyn}/YS_{st} close to 1.7 but do not show the same strain rate sensitivity of the yield point. Indeed, 301LN shows a continuous increase of the yield stress over the range of strain rates, while the yield strength of DP500G increases more slowly up to strain rates around $300s^{-1}$ and shows a higher strain rate sensitivity above $\dot{\varepsilon} = 300s^{-1}$. This latter observation is also valid for the other ferritic steels but in a less pronounced manner. Plotting the logarithm of the yield strength versus the logarithm of strain rate has validated the strain rate dependency of strain rate sensitivity on the yield strength for IFHSS260, ZStE420 and DP500G and the almost constant strain rate sensitivity of 301LN, as illustrated in Figure 2b.

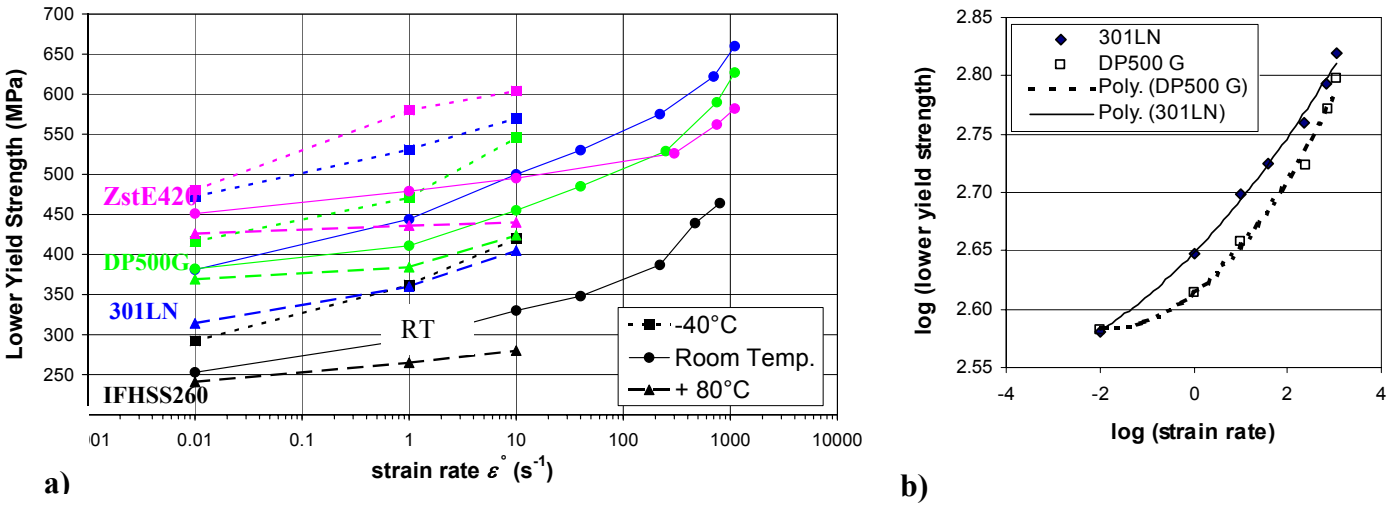

Figure 2: a) Influence of strain rate and temperature on the lower yield strength of the steel grades
b) Strain rate dependency of the strain rate sensitivity on lower yield strength at room temperature

Concerning tensile strength, strain rate sensitivity is quite similar for each steel grade with a ratio between dynamic ($\dot{\varepsilon}$ = 1100s^{-1}) and quasi-static tensile strength comprised between 1.10 and 1.24 (Figure 3). The strain rate dependency of the uniform elongation shown in Figure 4 underlines the high ductility of the austenitic stainless steel 301LN compared to the other steel grades. Even at $\dot{\varepsilon}$ = 1100s^{-1} the uniform elongation of 301LN is close to 50% and the tensile curve still presents a pronounced strain hardening.

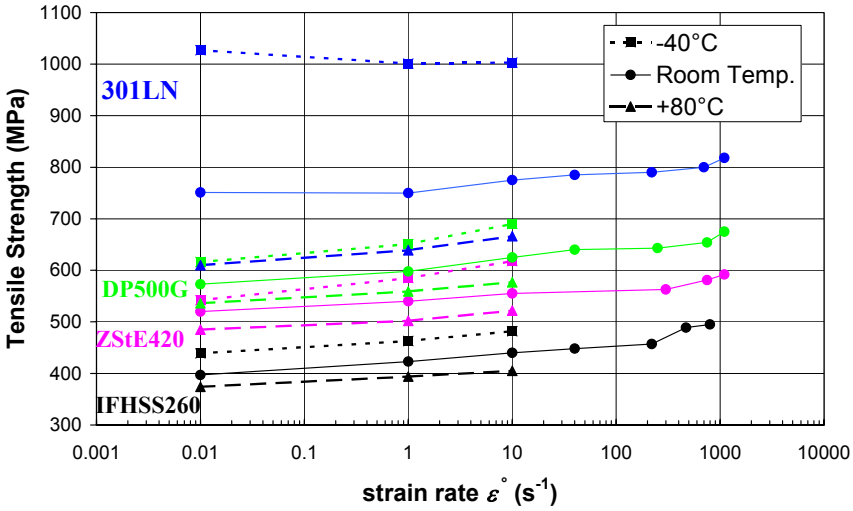

Figure 3: Influence of strain rate and temperature on the tensile strength of investigated steel grades

Influence of strain rate and temperature

The influence of strain rate and temperature in the range -40°C to +80°C defines stress domains in function of strain rate with an upper limit for -40°C describing a combined effect of strain rate and low temperature and a lower limit expressing the strain rate effect balanced by the higher temperature. Over the investigated range of strain rates the ferritic steels and DP500G are characterised by a maximum decrease of 50MPa for the lower yield strength or tensile strength at +80°C compared to room temperature. The increase of the lower yield strength noted at -40°C shows higher strain rate sensitivity due to a combined effect of temperature and strain rate (Figures 3, 4). The strain rate dependency of the uniform elongation, shown on Figure 4, is quite similar for ZStE420 and IFHSS260 with a higher reduction at -40°C compared to room temperature and a nearly constant value at 80°C. It must be noted that the dual phase steel DP500G did not show any increase or reduction in uniform elongation within the investigated temperature range, at least up to $\dot{\varepsilon}$ = 10s^{-1}. So, only the results at room temperature are presented in Figure 4.

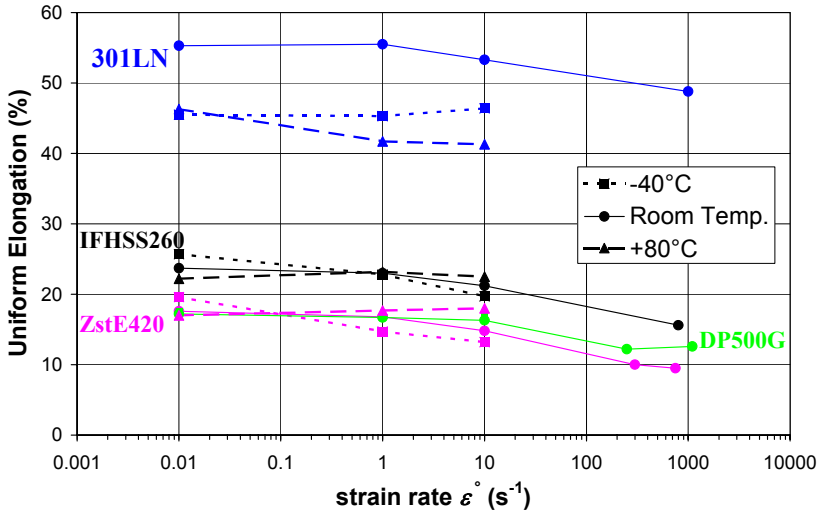

Figure 4: Influence of strain rate and temperature on the uniform elongation of investigated steel grades

The influence of strain rate and temperature on 301LN stainless steel is quite different due to the strain induced austenite to martensite ($\gamma \rightarrow \alpha'$) transformation. The austenitic steel is very sensitive to temperature

changes, which leads to a broader band for the yield strength and tensile strength curves than for the other steel grades. Compared to room temperature a decrease of 100 MPa in yield and tensile strength can generally be observed at 80°C for strain rates up to $10s^{-1}$. However, Figure 2 indicates that the high strain rate sensitivity is similar for each temperature, i.e. the curves related to the lower yield strength at different strength levels have the same slope. This high strain rate sensitivity allows 301LN to catch up with DP500G in yield strength at low strain rates after $\dot{\varepsilon} = 10s^{-1}$. At lower temperature the $\gamma \rightarrow \alpha$' transformation increases the strain hardening rate leading to a typical discontinuous tensile curve and very high values for the tensile strength accompanied by a decrease of the uniform elongation as shown on Figures 3 and 4. The influence of strain rate is related to adiabatic heating during the deformation, which restricts the $\gamma \rightarrow \alpha$' transformation. Hecker et al. have also observed the latter on austenitic stainless steel 304 [6]. Currently running volume fraction measurements, performed on the specimens tested at $\dot{\varepsilon} = 10^{-2}s^{-1}$ and $\dot{\varepsilon} = 10s^{-1}$ at increasing deformation levels, are confirming lower martensite volume fraction at high strain levels for high strain rate conditions. However, martensite is formed more readily at low strain levels during high strain rate testing than during quasi-static loading.

Energy absorption

The strain rate dependency at room temperature of the energy absorption of the different steels is indicated in Figure 5. The energy absorption is calculated at 10% true strain taking into account that in a crash situation automotive parts will hardly deform until fracture. On this figure the ratio of the dynamic over static absorbed energy is also plotted showing the higher ratio for the austenitic stainless steel and the ferritic steel IFHSS260 but naturally at lower energy levels. The evolution of energy absorption over the whole range of strain rate illustrates the need to characterise materials dynamically. Indeed ZStE420 and DP500G show the higher energy absorption under quasi-static testing conditions but the absorbed energy of 301LN increases stronger with the strain rate and finally, at $\dot{\varepsilon} = 1100s^{-1}$, reaches a value 6% higher than DP500G.

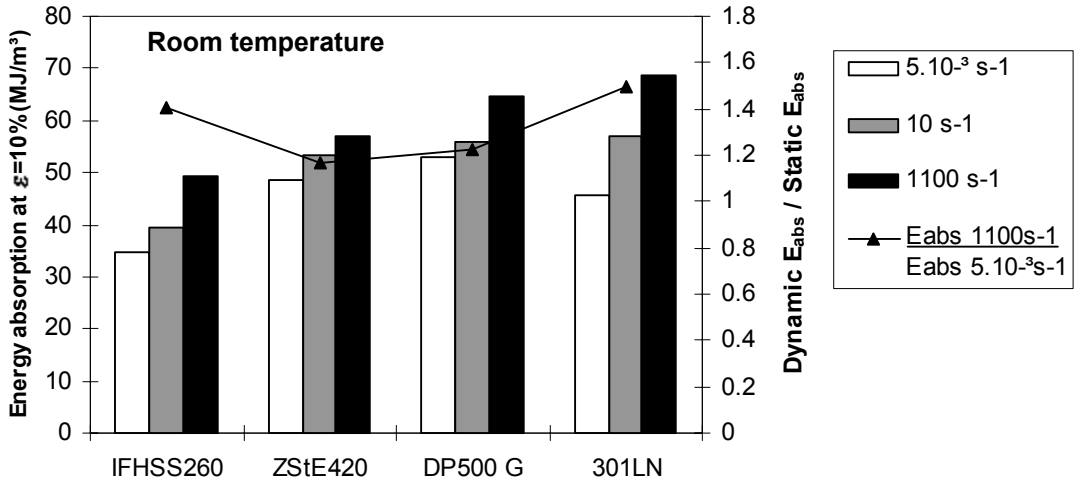

Figure 5: Energy absorption at 10% true strain (columns) and dynamic over static absorbed energy ratio (line) for the investigated steel grades at room temperature

The same behaviour is expected at 80°C with a more pronounced difference between dynamic and static conditions due to the lower yield strength of 301LN under quasi-static testing conditions. This great potential of dynamic energy absorption of 301LN is due to its higher strain hardening well described in Figure 6 showing the evolution of the dynamic strain hardening coefficient with strain at 80°C. Consequently, the difference in dynamic energy absorption between 301LN and the other steel grades like DP500G becomes larger when considering a higher true strain value than 10%.

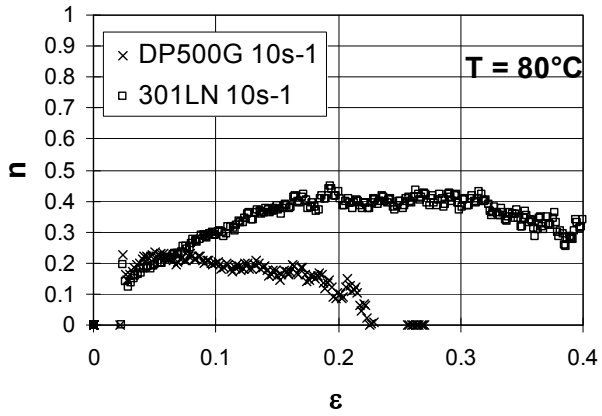

Figure 6: Dynamic strain hardening coefficient versus true strain for 301LN and DP500G at 80°C

CONCLUSION

The split Hopkinson bar testing facility developed at the University of Ghent has proven to be a very valuable technique for the determination of the dynamic mechanical properties of a wide range of steel grades. This technique is complementary to hydraulic test-benches by enabling reliable results at $\dot{\varepsilon} \geq 1000s^{-1}$. Even the austenitic stainless steel, which has a dynamic elongation higher than 50%, can be tested to rupture.

The analysis of the tensile tests performed at room temperature and up to $\dot{\varepsilon} = 1100s^{-1}$ shows that strain rate sensitivity of the lower yield strength is strain rate dependent only for IFHSS260, ZStE420 and DP500G. A low temperature of –40°C leads to higher strength values but also to higher strain rate sensitivity due to a combined effect of temperature and strain rate. In contrast, the austenitic stainless steel 301LN shows a constant strain rate sensitivity of the yield strength over the whole range of strain rates.

It has been shown that the study of combined temperature and strain rate effects is of great importance especially at 80°C where a decrease of the mechanical properties is observed. The austenitic steel is very sensitive to temperature changes and its mechanical properties are governed by the strain induced austenite to martensite transformation. The influence of strain rate is related to adiabatic heating during the deformation, which restricts the $\gamma \rightarrow \alpha'$ transformation. However, martensite forms more readily at low strain levels during high strain rate testing, which allows 301LN to absorb more energy in dynamic testing conditions. The need to characterise materials dynamically is well illustrated by the strain rate dependency of a crash relevant parameter like the energy absorption, which shows that austenitic stainless steel 301LN is more sensitive to strain rate than other steel grades, especially at 80°C despite a reduction of the transformed martensite volume fraction. The already high sensitivity to temperature of austenitic stainless steels could be even improved when considering it in a pre-hardened state. This will be an issue in the course of the European project "LIGHT&SAFE**"** coordinated by OCAS leading to broaden know-how on manufacturing techniques and durability of austenitic stainless steels for automotive applications.

REFERENCES

[1] Irving, B. (1998). *Welding Journal*. 11, 33.
[2] Emmons, J.B. and Douthett, J. (1996). Automotive frames of stainless steel, *Adv. Mat. & Proc*. 8, 23.
[3] Courbrough, G.J., Matlock, D.K. and Van Tyne C.J. (1993). *SAE Special Publications, Sheet Metal and Stamping Symposium International Congress and Exposition*, 279.
[4] Follansbee P.S. (1986). In: Metallurgical applications of shock-wave and high-strain-rate phenomena, 451, Murr L.E. et al. (Eds).
[5] Kolsky H.. (1949). *Proc. Phys. Soc.* Sec. B.62, pp. 676-700.
[6] Hecker S.S. et al. (1982). *Metallurgical Transactions A*. 13A, 619.

HIGH STRAIN RATE DEFORMATION BEHAVIOR OF AL-MG ALLOYS

T. Masuda[1], T. Kobayashi[2] and H. Toda[2]

[1]Graduate Student, Graduate School of Toyohashi University of Technology
[2]Department of Production Systems Engineering, Toyohashi University of Technology,
Toyohashi-city, AICHI, 441-8580, Japan

ABSTRACT

The aim of the present study is to characterize the strain rate dependency and the microstructural change behavior of Al-Mg series alloys over a wide range of strain rate. Impact tensile tests are carried out using a split-Hopkinson bar apparatus and servo hydraulic testing machine. SEM observation is made to analyze the microstructural changes of fracture surface. Al-Mg alloys show an increase in 0.2% proof stress, ultimate tensile strength, elongation, reduction of area and work hardening exponent with increasing strain rate. Although strain rate dependency of the stress and work hardening exponent are negligible up to the strain rate of approximately $10^2 s^{-1}$, the extent of rate sensitivity appears to increase from this strain rate. The elongation and reduction of area show linear increases with increasing strain rate. Although fracture surfaces mainly exhibit the shear type dimple pattern under the low strain rates, ordinary equiaxed dimple fracture is observed under the high strain rates.

KEYWORDS

Hopkinson bar, strain rate dependency, Al-Mg series alloys, impact tensile test, SEM, fracture surface, dimple, impact stress-strain curve

INTRODUCTION

The dynamic deformation behaviors of materials have become increasingly important in many applications related to the design especially in the field of transportation industry such as automobiles. Because Al-Mg series alloy has superior mechanical properties such as a high strength/weight ratio, good corrosion resistance and deformability, it is considered for many advanced applications where the structural components are subjected to dynamic loading. In order to optimize deformation and fracture performance of this alloy under the high strain rates, it is necessary to understand the dynamic deformation mechanisms [1].
It is recognized that materials often respond in different ways to high strain rate loading as compared to low strain rate loading. As strain rate is increased from static to dynamic, it results in an increase of the strength with increasing strain rate. Further, the flow stress of a material depends not only on the strain and strain rate but also on its microstructure especially at the dislocation level. In order to combine the micromechanisms of deformation and macroscopic constitutive relationships, there is a need to understand the microstructural changes which take place during deformation [2,3]. Therefore, it is the purpose of this work to study the

impact response of commercial Al-Mg series alloys deformed in the stain rate range of 10^{-4} to $10^{4}s^{-1}$ and, further, to investigate the microstructural changes.

MATERIALS AND EXPERIMENTS

Two kinds of work hardening aluminum alloys used in this investigation are 5052-H112 and 5083-H112 alloys. The chemical compositions are listed in Table1. Geometry and nominal dimensions of the tensile specimens are given in Fig.1 [4,5] and Fig. 2. All specimens used in static tensile, dynamic servo hydraulic tensile and dynamic split-Hopkinson bar tests have the same gage length and diameter.

TABLE 1

CHEMICAL COMPOSITIONS OF SAMPLES USED

(mass%)

	Si	Fe	Cu	Mn	Mg	Cr	Zn	Ti	Al
5052-H112	0.09	0.25	0.03	0.04	2.50	0.19	0.01	0.01	bal.
5083-H112	0.14	0.20	0.03	0.65	4.64	0.11	-	0.02	bal.

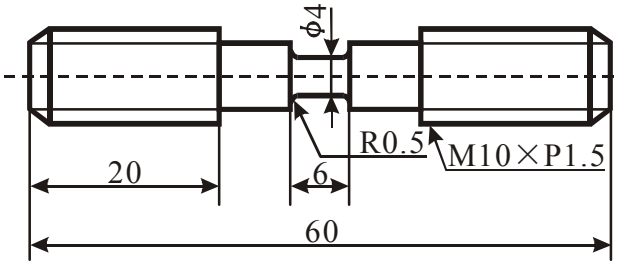

Figure 1: Geometry of a specimen in the static and dynamic tensile tests.

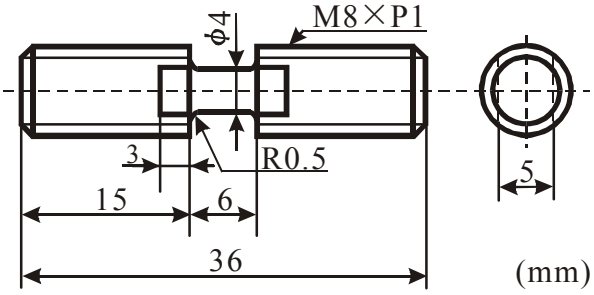

Figure 2: Geometry of a specimen in the split-Hopkinson bar test.

Static tensile experiments were carried out using the Instron testing machine. Intermediate rate tests were made on a servo-controlled hydraulic testing machine over a range of strain rates approximately from 10^{-1} up to $10^{3}s^{-1}$. The split-Hopkinson bar test was conducted for strain rate exceeding approximately $10^{3}s^{-1}$ [6,7]. All of tests were conducted at room temperature. Fracture surfaces of the tested specimens were observed with a scanning electron microscope.

RESULTS AND DISCUSSION

Stress-Strain Curves over a Wide Range of Strain Rates

Figures 3 and 4 show the typical stress-strain curves at four strain rates (4×10^{-4}, 10^{-1}, 1×10^{3} and $3\times10^{3}s^{-1}$) for the 5052-H112 and 5083-H112 alloys, respectively. In comparison with the result of the static loading condition, the 0.2% proof stress, ultimate tensile strength and elongation showed increases with increasing strain rate. Stress-strain curves showed a three-step process in which there were an initial elastic deformation region, uniform plastic deformation region until the maximum stress, then unstable deformation to the failure. In the static loading, the fracture occurred immediately when the stress reached the maximum stress. However, the flow stress decreased gradually at the high strain rate after the maximum stress. In the case of the dynamic tensile test using the split-Hopkinson bar apparatus, the stress-strain curves could be recorded exactly from the initial elastic deformation to the final fracture as compared to the other techniques.

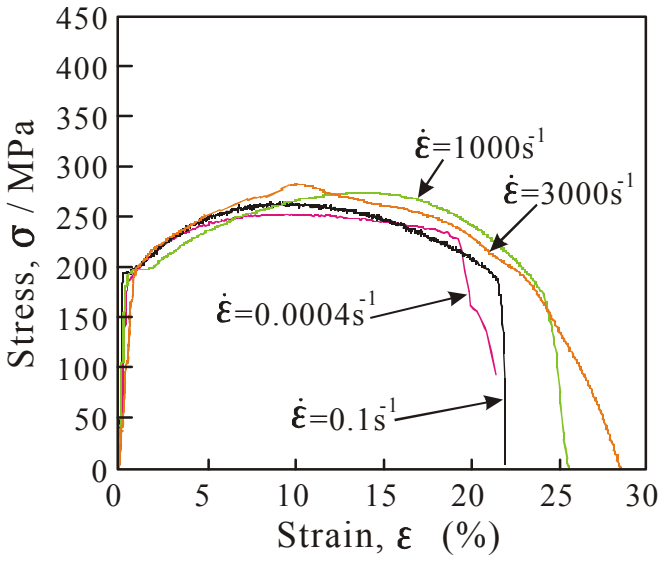

Figure 3: Typical stress-strain curves of the 5052-H112 alloy at various strain rates.

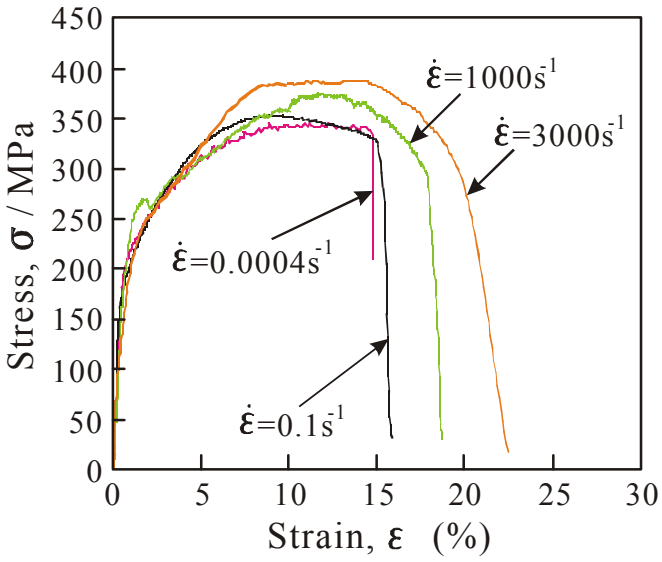

Figure 4: Typical stress-strain curves of the 5083-H112 alloy at various strain rates.

Strain Rate Dependency of Tensile Properties

Figures 5 and 6 show the 0.2% proof stress and ultimate tensile strength as a function of strain rate in the 5052-H112 and 5083-H112 alloys. Although strain rate sensitivity of the ultimate tensile strength is negligible up to the strain rate of approximately $10^2 s^{-1}$, the degree of rate sensitivity appears to increase for the higher strain rates. Tanimura, *et al.* [8] reported that the aluminum alloys containing magnesium solute atoms showed the negative strain rate dependency at intermediate strain rate. However, the negative strain rate dependency could be scarcely recognized in this study. The 5083-H112 alloy shows higher strength than the 5052-H112 alloy. Under the same strain rate range, the 5083-H112 alloy showed a larger strain rate dependency compared with the 5052-H112 alloy. While the 5052-H112 alloy showed an increase in the ultimate tensile strength of approximately 31MPa in the strain rate range of 4×10^{-4} to $3\times10^{3} s^{-1}$, that of the 5083-H112 alloy was approximately 43MPa.

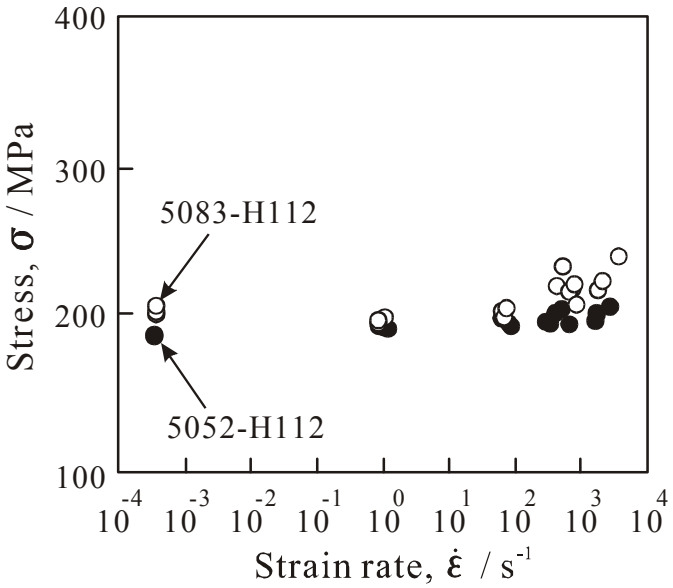

Figure 5: Variation of 0.2% proof stress with nominal strain rate.

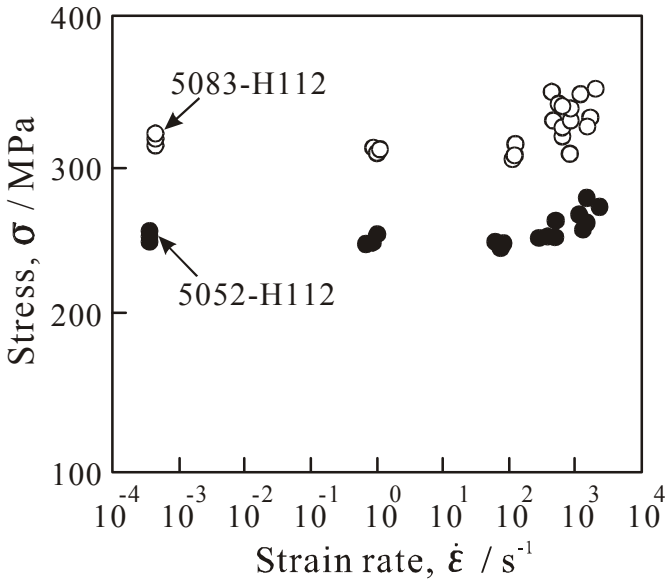

Figure 6: Variation of ultimate tensile strength with nominal strain rate.

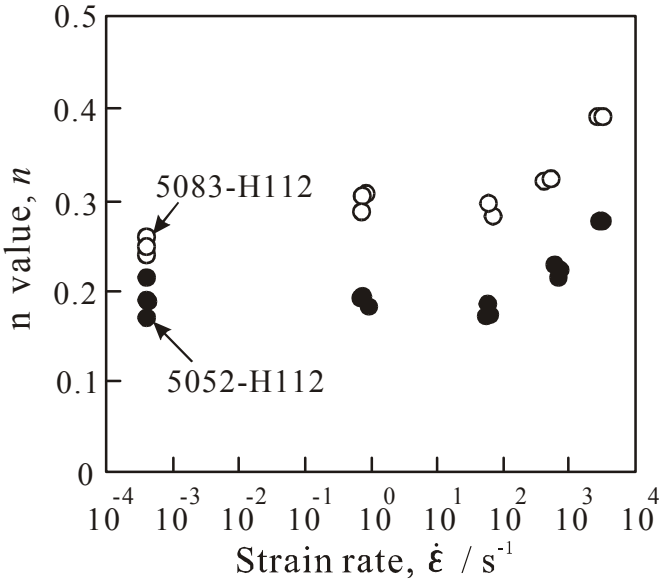

Figure 7: Variation of strain hardening exponent with nominal strain rate.

Figure 7 presents the variation of strain hardening exponent with the strain rate. The strain hardening exponent showed a similar strain rate dependency with the 0.2% proof stress and ultimate tensile strength. However, the increase in the strain hardening exponent was kept constant up to a strain rate of approximately $10^2 s^{-1}$. The 5083-H112 alloy contains approximately twice magnesium element as compared to the 5052-H112 alloy: however strain rate dependency was similar.

Figures 8 and 9 present the variation of elongation and reduction of area with strain rate. The elongation and reduction of area increase linearly with increasing strain rate. Although the strain rate dependency in elongation and reduction of area is negligible up to the strain rate of approximately $10^0 s^{-1}$, the degree of rate sensitivity appears to increase rapidly for the higher strain rates.

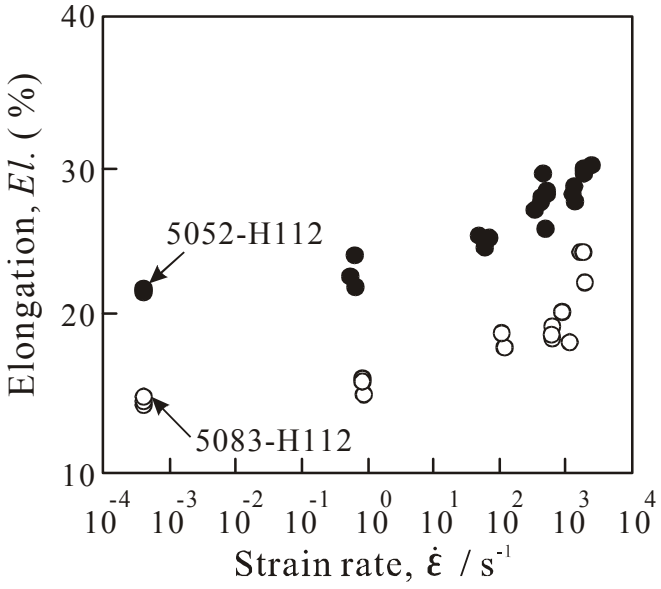

Figure 8: Variation of elongation with nominal strain rate.

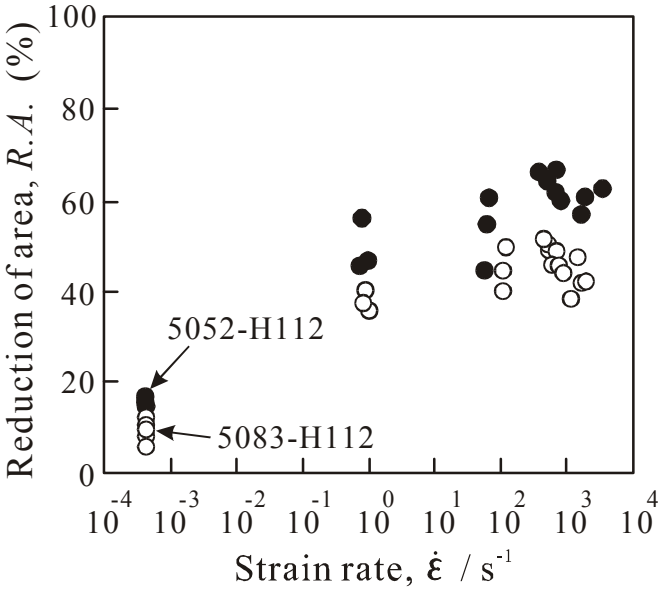

Figure 9: Variation of reduction of area with nominal strain rate.

Effect of the Strain Rate on Fracture Surface and Structure

Figure10 shows the SEM micrographs of the fracture surfaces of the 5052-H112 and 5083-H112 alloys at various strain rates. Both Al-Mg series alloys provide the flat surfaces at static load conditions. However, the fracture occurred by a combination of two different dimple sizes at higher strain rates, one of which is approximately 10 μm and the other is several micrometer in the case of 5083-H112 alloy having higher magnesium content. The fracture surface of low magnesium 5083-H112 alloy is mainly dominated by dimples of approximately 20 μm in diameter. Although the fracture surfaces mainly exhibited the shear type dimple pattern under low strain rates, ordinary equiaxed dimple fracture surfaces were observed under high strain rates. The specimen was largely necked at high strain rate. In both materials, the dimple size and depth increased with the strain rate.

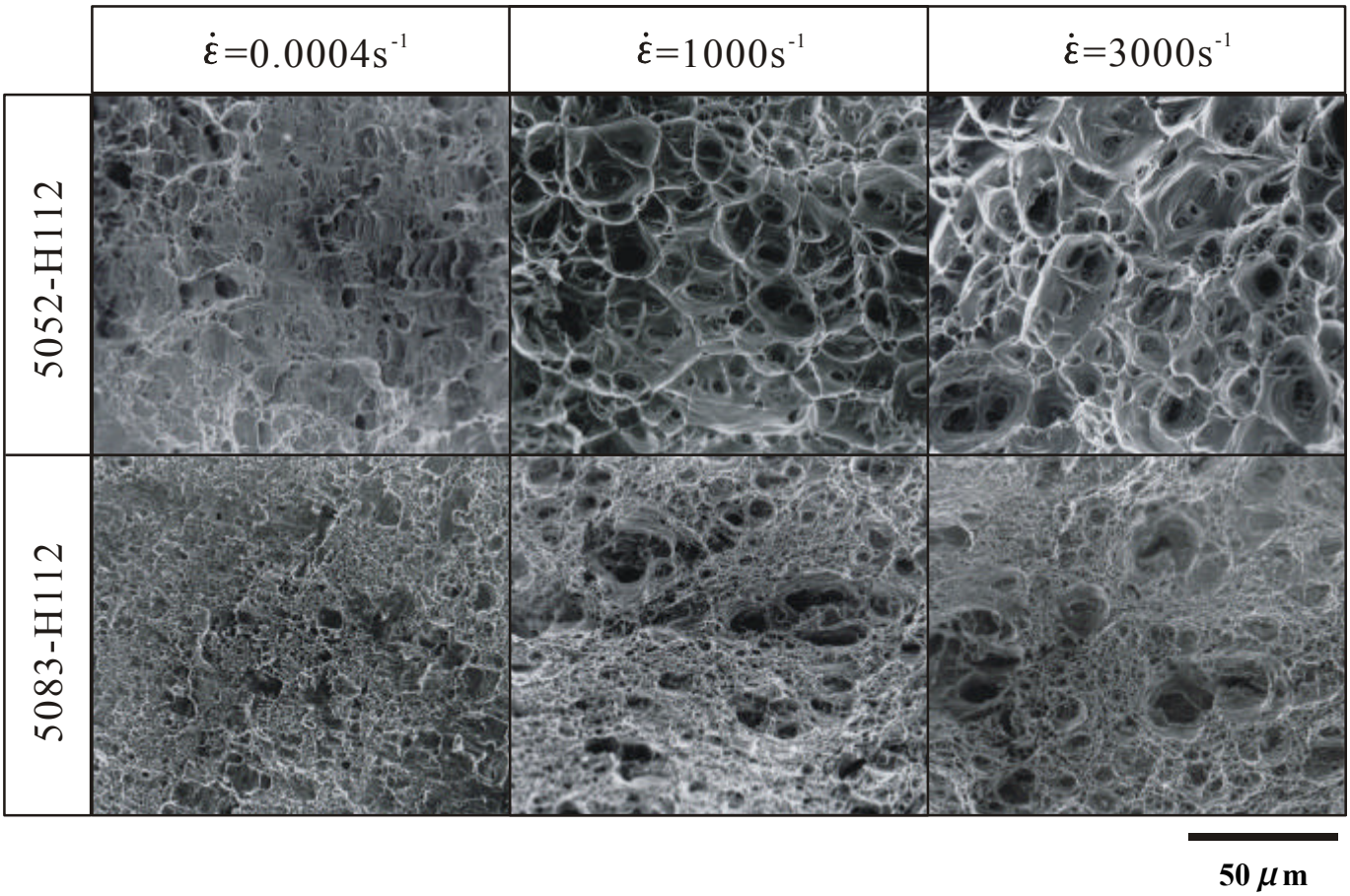

Figure 10: SEM micrographs of fracture surfaces at various strain rates.

CONCLUSIONS

The effect of strain rate on mechanical properties and microstructural changes in 5052-H112 and 5083-H112 aluminum alloys were examined over a wide range of strain rate. The following conclusions could be drawn.

1. The strain rate dependencies of two kinds of Al-Mg series alloys were very sensitive at high strain rate. As the strain rate increased, 0.2% proof stress and ultimate tensile strength increased. Under the same strain rate conditions, the 5083-H112 alloy showed more clear increase in strength than the 5052-H112 alloy.

2. The strain hardening exponent can be seen to increase with increasing strain rate. Strain hardening exponent showed similar degree of strain rate dependency with the 0.2% proof stress and ultimate tensile strength. However, the increasing rate of the strain hardening exponent was constant up to the strain rate of approximately 10^2s^{-1} for both materials.

3. The elongation and reduction of area increased markedly with increasing strain rate, and these dependencies were linear. Although strain rate dependencies in the elongation and reduction of area were negligible up to the strain rate of approximately $10^0 s^{-1}$, the degree of rate sensitivity appears to increase rapidly for the higher strain rates.

4. Although the fracture surfaces mainly exhibited the shear type dimple pattern under the low strain rates, ordinary equiaxed dimple fracture surfaces were observed under the high strain rates. The specimen was remarkably necked at the high strain rate. In both materials, the dimple size and depth increased as the strain rate increased.

REFERENCES

1. Nicholas, T. (1981) *Exp. Mech*., 21, 177.
2. Lindholm, U. S. (1964) *J. Mech, Phys. Solids*, 12, 317.
3. Perzyna, P. (1974). In: *Mechanical Properties at High Rates of Strain,* pp. 138-153, Harding, J.(Ed). Inst. Phys., Oxford.
4. Sugiura, N., Kobayashi, T., Yamamoto, I., Nishido, S. and Hayashi, K. (1995) *J. J. Inst. Light Met.,* 45, 633.
5. Sun, Z. M., Kobayashi, T., Fukunasu, H., Yamanoto, I. and Shibue, K. (1998) *Metall. Mater. Trans.* A, 29A, 263.
6. Masuda, T., Kobayashi, T. and Toda, H., Submitted to *J. J. Inst. Light Met.*.
7. Yokoyama, T. (1996) *J. Soc. Mat. Sci*., 7, 785.
8. Mukai, T., Higashi, K., Tuchida, S. and Tanimura, S. (1993) *J. Inst. Light Met.,* 43, 252.

ORAL REFERENCE: ICF100914OR

HIGH TEMPERATURE CREEP DAMAGE OF FABRICATED STRUCTURES

Frederick W. Brust

Engineering Mechanics Group, Battelle Memorial Institute, 505 King Ave,
Columbus, Ohio 43201

ABSTRACT

The need for structural systems to perform reliably at high temperatures continues to increase. Improvements in energy production, pollution control, chemical processes (especially, engine propulsion), efficient micro-process devices, among other applications, are possible with higher temperature operations. Higher temperature operation means that creep damage must be managed over the life of the component. One of the important mechanisms of creep damage development, matter diffusion, is investigated here. In particular, the effect of elastic accommodation on the grain boundary diffusion-controlled void growth is analyzed using an axisymmetric unit cell model. An incremental form of the virtual work principle was used to formulate the boundary value problem involving grain boundary diffusion. The model accounts for material elasticity and void interaction effects. Analyses are performed for initially spherical voids spaced periodically along the grain boundary. The results of the analyses on void growth rates agree well with the Hull-Rimmer [1] model after the initial transient time. During the elastic transient, void growth rates can be several orders of magnitude higher than the steady state growth rate. Though the elastic transient time may occupy a small portion of the total rupture time, in metallic components experiencing cyclic loading conditions with short hold times, elasticity effects may be important.

KEYWORDS

Creep, damage, diffusion, fracture, high temperature, steel.

INTRODUCTION

Failure in metals exposed to high temperature creep conditions predominantly occurs by nucleation and growth of cavities along grain boundaries, thus resulting in intergranular fracture. Nucleation of such cavities is mainly driven by diffusion of atomic flux from the lattice or interfaces into grain boundaries. Further growth of these cavities is aided by diffusion of atomic flux primarily from cavity surface into grain boundaries. The nucleation of these intergranular cavities in many instances occurs during the primary creep stage. In addition to diffusion mechanisms, the creep deformation of the material also contributes to cavity growth. The purpose of this paper is to quantitatively examine the effect of elastic transient on growth of spherical cavities. The growth of the cavities was controlled by grain boundary diffusion as well as material elasticity.

ANALYSIS

Consider a damaged material exposed to high temperature creep conditions in which voids were periodically arranged in parallel sheets. The initial shape of the voids was assumed to be spherical with a radius of 'a'. Interaction effects between voids lying within a sheet, with initial mean center-to-center spacing of 'b', were accounted for by approximating the voided medium as consisting of cylindrical unit cells, each with a void located at is center, as shown in Figure 1. Assuming axisymmteric conditions, only one quarter of the cylindrical unit cell needs to be modeled. The axisymmetric unit cell is shown as hatched region in Figure 1. The far-field stress state was assumed to be uniaxial. The grain material was assumed to be elastically linear and isotropic. Diffusion of matter takes place along the grain boundaries.

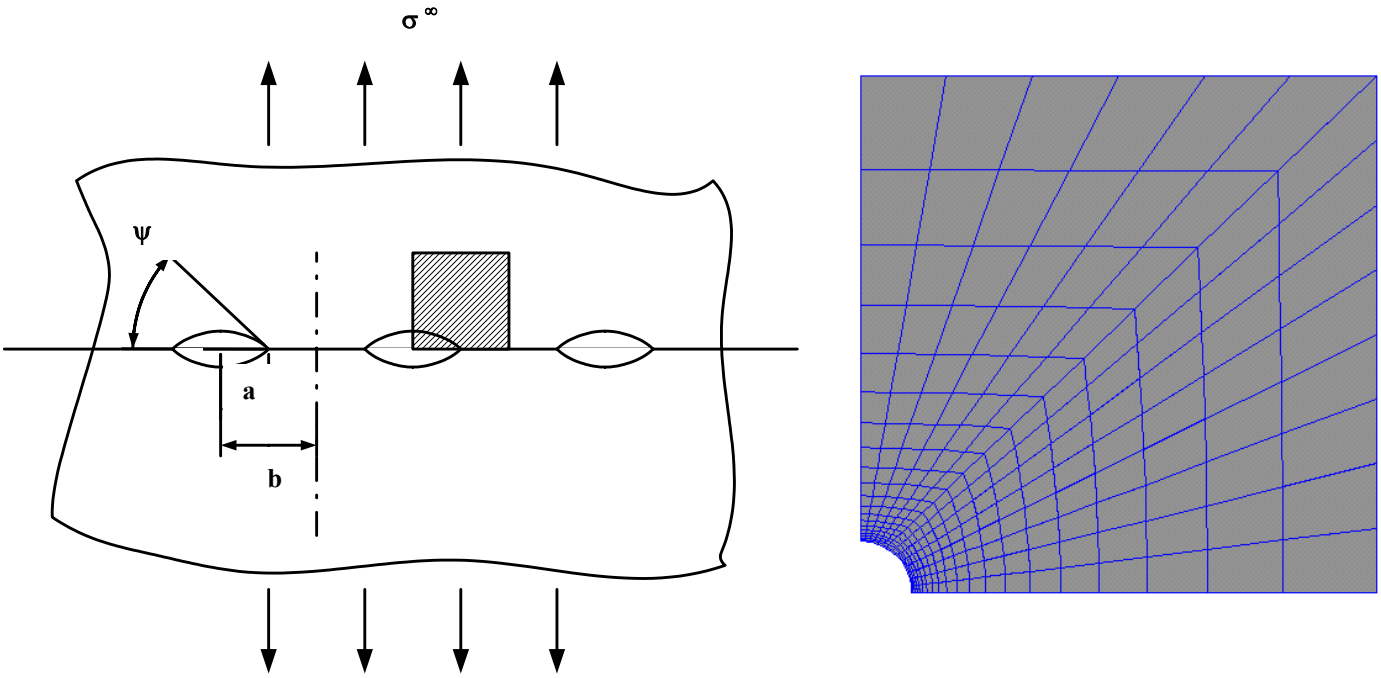

Figure 1. Dimensions and discretization for model.

We consider an incremental form of a functional, F, given by,

$$F = \int_V \sigma : \delta\Delta d \, dV - \int_S^T T \bullet \delta v + \int_A \frac{1}{2D} \Delta j \bullet \Delta j \, dA + \int_\Gamma \sigma_o \, m \bullet j \, d\Gamma \qquad (1)$$

for all kinematically associated fields, namely, the rate of deformation tensor, d, and the velocity, v, and the volumetric flux, j, crossing unit length in the grain boundary. In Equation (1), σ is the applied stress, T is the applied traction along the boundary S, A denotes the grain boundary area, and Γ denotes the collection of arcs where the grain boundaries meet the void surfaces. The normal stress, σ_o, on the grain boundary at the void tip, also known as the sintering stress, is given by,

$$\sigma_o = \gamma_s (\kappa 1 + \kappa 2) \qquad (2)$$

where γ_s is the surface energy, and κ_1 and κ_2 are the principal curvatures of the surface of the void. The diffusion parameter, D, used in Equation (1), is related to the grain boundary diffusion coefficient of the material by,

$$D = \frac{\delta_b D_b \exp(-Q_b / RT)\Omega}{kT} \qquad (3)$$

where D_b is the grain boundary diffusion coefficient at a given temperature, T, Ω is the atomic volume, δ_b is the thickness of the diffusion layer, Q_b is the activation energy, and R and k are the Gas and Boltzmann's constant. The functional [1] Starts from Needleman and Rice [2], with appropriate modifications to account for material elasticity, etc. It can be easily shown that F as given in equation (1) is not only stationary but also a global minimum for the true field. Exercising the variational principle on F, it can be shown that the full set of field equations for the considered problem will result.

Using the above formulation to develop the finite element equations (as elaborated in [3]), a special user element (UEL) was developed and used with the ABAQUS finite element software [4]. We have examined the transient effect for several metallic materials at a temperature, $T = 0.6\ T_m$ in this study. The properties of the materials are given in Table 1. We consider an average void spacing 10 μm (b = 5 μm). Using this value for b and a/ b = 0.1, we obtain a characteristic time, τ, also given in Table 1, for the materials considered in this study. The properties listed in Table 1 are obtained from Frost and Ashby [5]. In all the cases examined, the ratio of far-field stress to Young's modulus, σ^{∞}/E, was 10^{-3}. The characteristic time is defined as:

$$\tau = \frac{(b - a)^3}{ED} \qquad (4)$$

TABLE 1.
MATERIAL PROPERTIES OF THE METALLIC MATERIALS USED.

Material Property	**Aluminum**	**Copper**	**γ–Iron**
Young's Modulus, E (MPa)*	75.30	124.0	205
Poisson's Ratio, ν**	0.34	0.32	0.3
Atomic Volume, Ω (m^3) *	1.66×10^{-29}	1.18×10^{-29}	1.21×10^{-29}
Melting Point, T_m (K) *	933	1356	1810
Grain Boundary (GB) Diffusion Pre-exponential, $\delta_b D_b$ (m^3/s) *	5×10^{-14}	0.5×10^{-14}	7.5×10^{-14}
Activation Energy for GB Diffusion Q_b (kJ/mole) *	84	104	159
Characteristic Time, τ, secs	772	857	327
Grain Boundary Energy, γ_b (J/m^2) **	0.63	0.65	0.78
Surface Energy, γ_s (J/m^2) **	-	1.73	1.95

In Figure 2, the ratio of the void growth rate predicted by FEM and by the Hull-Rimmer model (the Hull-Rimmer classical solution neglect elastic accommodation, i.e., assumes rigid response [1]) is plotted against normalized time. The inset shows the transition from transient to steady state conditions. It can be seen that the transient time is larger for larger a/b values. The variation of the ratio of normal stress and applied stress along the grain boundary ahead of the cavity tip is shown in Figure 3 for a/b of 0.1. In the figure, X denotes the distance from the tip of the cavity along the grain boundary. While in the pure elastic case the peak stresses occur at the cavity tip, matter diffusing into the grain boundary from the cavity surfaces relaxes the stresses at the tip, even during the beginning stages of the transient. Consequently, the peak stress occurs away from the cavity during the transient stage. With increasing time, the peak stress decreases in magnitude and moves away from the cavity tip. As can be seen from the figure, a parabolic profile is

achieved as steady state condition ensues. Vitek [6] obtains a variation similar to the one shown in Figure 3 for the transient stress distribution ahead of crack tip arising due to non-uniform deposition of matter from the tip onto the grain boundary. It is also found (but not shown here) that the peak stress away from the cavity tip is higher for larger a/b ratios. This would imply that the chances for nucleation of new cavities, during transient stages, increase with initial cavity radius-to-spacing ratio.

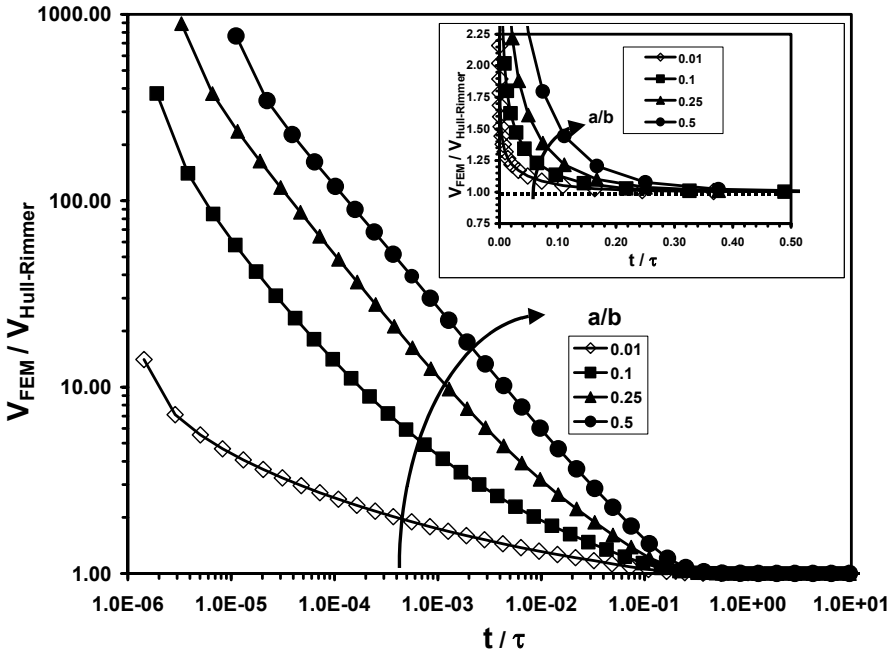

Figure 2. Temporal variation ratio of void growth rate predicted by FEM and by the Hull-Rimmer model for several a/b ratios in γ-Fe. Inset shows the transition from transient to steady state.

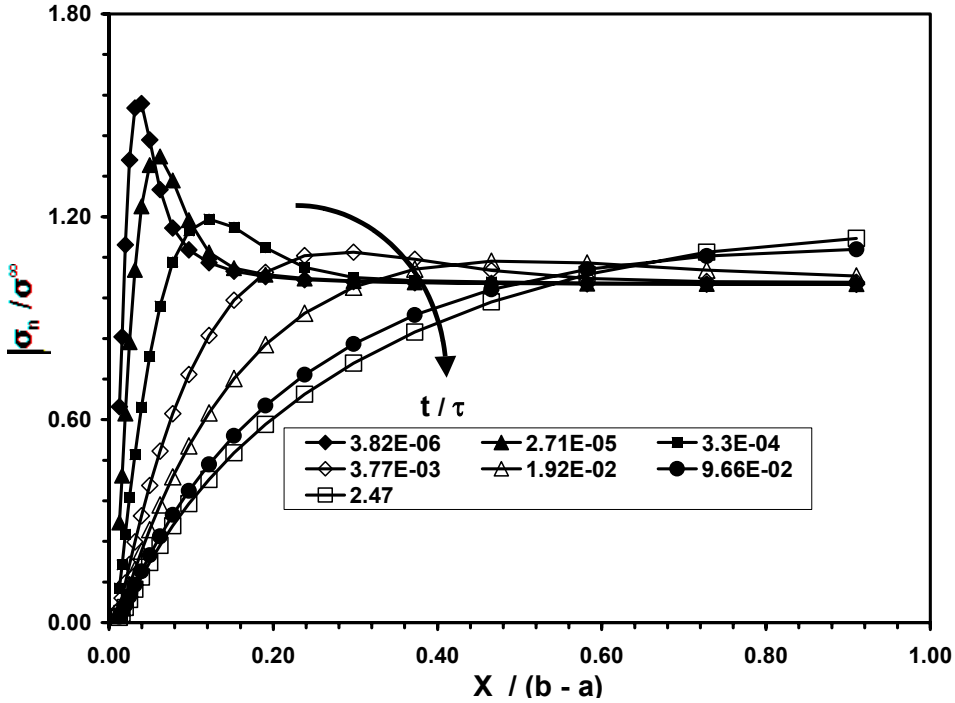

Figure 3. Temporal changes in stress distribution ahead of the cavity tip along the grain boundary in γ-Fe for a/b = 0.1.

The temporal variations of void growth rates normalized with the respective rate predicted by Hull-Rimmer model, are shown in Figure 4 for all the three metals. Indeed, all the curves collapse into a single distribution indicating that the choice of time scale is appropriate. It is worth mentioning that Raj [7] was the first to suggest the appropriate time scale as given in equation (4). It is interesting to note that Trinkaus [8] and Shewmon and Anderson [9] note that in the case of an isolated cavity along a grain boundary, the stress and displacement field expand around the cavity in a self-similar manner in proportion to the cavity radius, with a $\propto t^{1/3}$. They obtained this result assuming rigid grains. In our problem, a wedge of material is introduced ahead of the cavity tip during the transient stage, due to material elasticity. In the work of Trinkaus [8] and Shewmon and Anderson [9] a wedge is introduced because the cavity is isolated (well separated and small). In addition, unlike the Hull and Rimmer model they assume that the grain boundary thickening vanishes at some distance away from the cavity. However, their solution is different from the present in that elasticity and void interactions are not taken into account.

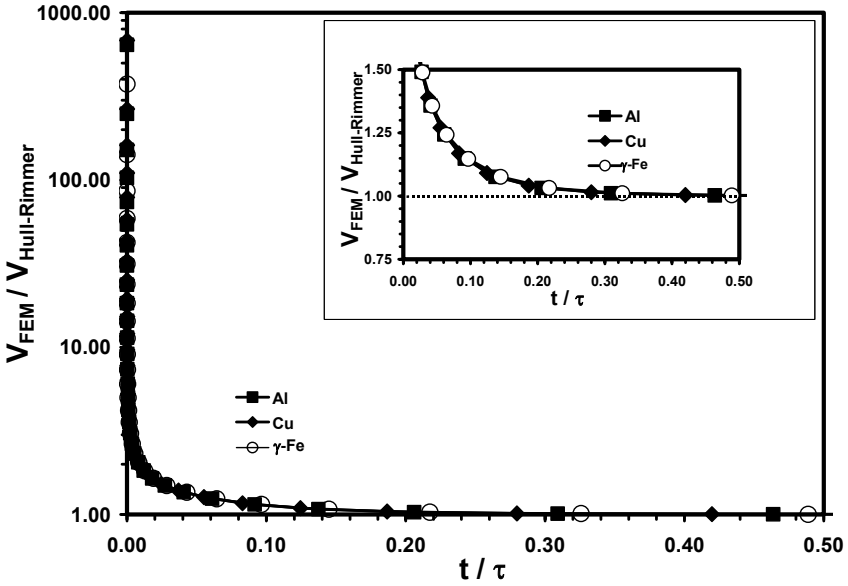

Figure 4. The temporal variations of void growth rates normalized with the respective rate predicted by Hull-Rimmer model for all the three metals.

CONCLUSIONS

The effect of elastic accommodation on the grain boundary diffusion-controlled void growth was analyzed using an axisymmetric unit cell model. In order to accomplish this we have extended the formulation of Needleman and Rice [2] to account for material elasticity. This extension also involved an incremental formulation of the virtual work principle of the boundary value problem involving grain boundary diffusion. The model accounts for void interaction effects. The results of the analyses on void growth rates agree well with the Hull-Rimmer model after the initial transient time for the three different metals considered. During the elastic transient, void growth rates can be several orders of magnitude higher than the steady state growth rate. Using the predictions of finite element analyses for several metals, we demonstrated that the characteristic time is appropriately given by equation (4). Indeed, Raj [7] was the first to suggest a similar form for the characteristic time. It was observed that the transient time is larger for larger a/b values (or larger volume fraction of cavities). Though the elastic transient time may occupy a small portion of the total rupture time, in metallic components experiencing cyclic loading conditions with short hold times, elasticity effects may be important.

ACKNOWLEDGMENT

This work was supported by Department of Energy, Office of Basic Sciences under Grant No. DE-FG02-90ER14135. The authors thank Dr. B. Armaly and R. Price for their support.

REFERENCES

1. Hull, D., and Rimmer, D. E., 1959, “The Growth of Grain Boundary Voids Under Stress” *Philosophical Mag*azine, **4**, pp. 673-687.
2. Needleman, A., and Rice, J. R., 1980, “Plastic Flow Creep Effects in the Diffusive Cavitation of Grain boundaries,” *Acta Metallurgica et Mater*ialia, **28**, pp.
3. Mohan, R., and Brust, F. W., "Effect of Elastic Accommodation on Diffusion Controlled Cavity Growth in Metals" ASME Journal of Engineering Materials and Technology, Volume 122, July 2000, pp. 294-300.
4. ABAQUS Finite Element Software, 1999, User Manual, Ver. 5.8, Hibbitt, Karlsson and Sorenson.
5. Frost, H. J., and Ashby, M. F., 1982, Deformation Mechanism Maps: The Plasticity and Creep of Metals and Ceramics, Pergamon Press, Oxford.
6. Vitek,V.,1978, “A Theory of Diffusion Controlled Intergranular Creep Crack Growth,” Acta Metallurgica et Materialia, **26**, pp. 1345-1356.
7. Raj, R., 1975, “Transient Behavior of Diffusion-Induced Creep and Creep Rupture,” *Metallurgical Trans*ations, **6A**, pp. 1499-1509.
8. Trinkaus, H., 1979, “Drift Diffusion in Grain Boundaries under the Influence of Stress Fields,” physica status solidi, **93**, pp. 293-303.
9. Shewmon, P., and Anderson, P., 1998, Acta Metallurgica et Materialia, **46**, pp. 4861-4872.

ABSTRACT REF NO: ICF100889OR

THE EFFECT OF HYDROGEN-INDUCED SOFTENING ON THE DEFORMATION AT A CRACK TIP: IMPLICATIONS FOR FRACTURE

Y. M. Liang and P. Sofronis

Department of Theoretical and Applied Mechanics,
University of Illinois at Urbana-Champaign,
Urbana, IL 61801, USA

ABSTRACT

The hydrogen concentrations in equilibrium with local stress and plastic straining are studied in conjunction with large elastic-plastic deformation in the neighborhood of a blunting crack tip. The hydrogen effect on material behavior is modeled through the hydrogen-induced volume dilatation and the reduction in the local flow stress. Plane strain finite element analysis shows that stress relaxation due to solute hydrogen decreases the extend of plastic yielding whereas hydrogen-induced material softening causes the deformation to center in the region directly ahead of the crack tip. The consequence of this result on the hydrogen-induced fracture processes is discussed.

KEYWORDS

Hydrogen, diffusion, plasticity, softening, fracture

INTRODUCTION

Of the many suggestions for the explanation of the hydrogen related failures, the mechanism of ***hydrogen-enhanced localized plasticity*** **(HELP***)* appears to be a viable one [1]. Arguments in support of the HELP mechanism are based on experimental observations [2] and theoretical calculations [3] that in a range of temperatures and strain rates, the presence of hydrogen in solid solution decreases the barriers to dislocation motion, thereby increasing the amount of deformation that occurs in a localized region adjacent to the fracture surface [4]. The underlying principle in the HELP mechanism is the shielding of the elastic interactions between dislocations and obstacles by the hydrogen solutes [2, 3]. Reduction of the interaction energies between elastic stress centers results in enhanced dislocation mobility, i.e., decreased material local flow stress [4].

Nonetheless, significant issues remain to be resolved. Among these are: i) what is the detailed mechanism by which the enhanced dislocation mobility causes fracture in bulk specimens? ii) does the fracture occur by microvoid coalescense, formation of a Stroh crack or some other mechanism? iii) can the contribution of the plastic deformation to the fracture energy be established as a function of the hydrogen concentration? In view

of these questions, the prime goal of this paper is to address the effect of hydrogen-induced softening on the stress and deformation fields around a blunting crack tip. In a continuum sense material softening can be described through a local flow stress that decreases with increasing hydrogen concentration. It is important to emphasize that the term "flow stress" denotes the intrinsic flow characteristics of a small volume of material at the microscale around a crack tip where hydrogen concentrates as the material deforms. The amount of hydrogen concentration in the specimen is calculated by considering the effect of plastic straining (trapped hydrogen) and hydrostatic stress (normal interstitial lattice site hydrogen). In view of the very high mobility of the hydrogen solute, hydrogen concentration in trapping sites is assumed always in equilibrium with hydrogen in interstitial sites, which is also assumed to be in equilibrium with local hydrostatic stress. The calculated total hydrogen concentration is then used to estimate the material softening along the lines proposed in the work of Sofronis *et al*. [5] on the basis of the experimental observations of Tabata and Birnbuam [6]. It is emphasized that the present equilibrium calculation of the hydrogen concentrations, stress, and deformation fields is fully coupled. It should also be pointed out that the numerical predictions for our chosen model system, i.e. niobium, turn out to be independent of the amount of trapped hydrogen. Therefore, the present numerical results can be considered as an assessment of the synergism between the local hydrostatic stress and hydrogen-induced softening ahead of a crack tip. However, in view of the generality of the present approach, the current treatment can be easily applied to other systems with different trapping characteristics.

HYDROGEN CONCENTRATION AND CONSTITUTIVE LAW

Hydrogen is assumed to reside either at normal interstitial lattice sites (NILS) or reversible trapping sites at microstructural defects generated by plastic deformation. Hydrogen concentration in NILS is studied under equilibrium conditions with local stress σ_{ij}, and the occupancy of NILS sites, θ_L, is calculated through the Fermi-Dirac form in terms of the stress-free lattice concentration c_0 and stress [5]. Hydrogen atoms at trapping sites are assumed to be always in equilibrium with those at NILS according to Oriani's theory [7], and the trapping site occupancy is given by $\theta_T = \theta_L K/(1-\theta_L+\theta_L K)$, where $K = \exp(W_B/RT)$, W_B is the trap binding energy, R is the gas constant, and T is the temperature. Thus the total hydrogen concentration (in trapping and NILS) measured in hydrogen atoms per solvent atom (H/M) is calculated as $c = \beta\theta_L(\sigma_{kk}) + \alpha\theta_T(\theta_L)N_T(\varepsilon^p)/N_L$, where N_T is the trap density which is a function of the effective plastic strain ε^p, N_L is the number of host metal atoms per unit volume, and α, β are material constants.

Sofronis *et al*. [5] based on the calculations of Sofronis and Birnbaum [3] and on microscopic studies of the effect of hydrogen on dislocation behavior in iron [6] argued that a continuum description of the hydrogen effect on the local flow stress σ_Y can be stated as $\sigma_Y = \sigma_0^H\left(1+\varepsilon^p/\varepsilon_0\right)^{1/n}$, where σ_0^H is the initial yield stress in the presence of hydrogen that decreases with increasing hydrogen concentration, ε_0 is the initial yield strain in the absence of hydrogen, and n is the hardening exponent that is assumed unaffected by hydrogen. In this equation, the hydrogen effect on the local continuum flow characteristics is modeled through the initial yield stress which is assumed to be given by $\sigma_0^H = \phi(c)\sigma_0$, where $\phi(c)$ is a monotonically decreasing function of the local hydrogen concentration c and σ_0 is the initial yield stress in the absence of hydrogen. A possible suggestion for $\phi(c)$ is a linear form $\phi(c) = (\xi-1)c+1$, where the parameter ξ which is less than 1 denotes the ratio of the yield stress in the presence of hydrogen, σ_0^H, to that in the absence of hydrogen, σ_0, at the maximum hydrogen concentration of 1.

The total deformation rate tensor (symmetric part of the velocity gradient in spatial coordinates) is written as the sum of an elastic part (which is modeled as hypo-elastic, linear and isotropic), a part due to the presence of hydrogen, and a plastic part: $D_{ij} = D_{ij}^e + D_{ij}^h + D_{ij}^p$. The mechanical effect of the hydrogen solute atom is purely dilatational and is phrased in terms of the deformation rate tensor as $D_{ij}^h = \Lambda(c)\dot{c}\delta_{ij}/3$, where $\dot{c}$ is the time rate of change of concentration c, $\Lambda(c) = \lambda/\left[1+\lambda(c-c_0)/3\right]$, $\lambda = \Delta v/\Omega$, Δv is the volume change per atom of

hydrogen introduced into solution that is directly related to the partial molar volume of hydrogen $V_H = \Delta v N_A$ in solution, Ω is the mean atomic volume of the host metal atom, c_0 is the corresponding initial concentration in the absence of stress, and δ_{ij} is the Kronecker delta. The material is assumed to be rate independent, flow according to the von Mises J_2 flow theory, and harden isotropically under plastic straining. Thus,

$$D_{ij}^p = \frac{1}{h}\left(\frac{3\sigma'_{kl}}{2\sigma_e} + \mu\delta_{km}\delta_{lm}\right)\frac{3\sigma'_{ij}\overset{\nabla}{\sigma}_{kl}}{2\sigma_e} \tag{1}$$

where $\sigma_e = \left(3\sigma'_{ij}\sigma'_{ij}/2\right)^{1/2}$ is the von Mises equivalent stress, $\sigma'_{ij} = \sigma_{ij} - \sigma_{kk}\delta_{ij}/3$ is the deviatoric stress, $h = \frac{\partial\sigma_Y}{\partial\varepsilon^p} + \frac{\partial\sigma_Y}{\partial c}\frac{\partial c}{\partial\varepsilon^p}$, $\mu = -\frac{\partial\sigma_Y}{\partial c}\frac{\partial c}{\partial\sigma_{kk}}$, $\varepsilon^p = \int\sqrt{2D_{ij}^p D_{ij}^p/3}\,dt$ is the effective plastic strain, and the superposed ∇ denotes the Jaumann stress rate that is spin invariant.

NUMERICAL RESULTS

Solutions to the boundary value problem for the equilibrium hydrogen concentration coupled with material elastoplasticity are presented in the neighborhood of a blunting crack tip under plane strain mode I opening. Small scale yielding conditions were assumed and the system's temperature was 300K. The material used in the simulations was niobium, as this metal is a high H solubility system, suffers from embrittlement at room temperature, and experimental data are readily available. Displacement boundary conditions of the singular linear elastic field were imposed at a circular boundary at a distance $L = 15\text{cm}$ from the tip. The ratio of L/b_0, where b_0 is the initial crack opening displacement, was taken equal to 30,000. The finite element mesh is described in the work of Sofronis and McMeeking [8]. Before the application of the external load, the specimen was assumed to be stress free and at a uniform initial hydrogen concentration c_0. Upon loading, uniform redistribution of the H solute occurs within the solid so that hydrogen is always under quasi-static "local equilibrium" conditions with local stress and plastic strain as discussed in the previous section. Since hydrogen is assumed to be provided by a chemical reservoir, an arrangement corresponding to "far field concentration" kept constant at c_0, the calculation corresponds to a constant chemical potential for the hydrogen solute. Hydrogen was assumed to expand the lattice isotropically and its partial molar volume in solution was $V_H = 1.88\,\text{cm}^3/\text{mole}$ which corresponds to $\lambda = 0.174$. The molar volume of niobium was $10.852\times10^{-6}\,\text{m}^3/\text{mole}$ which implies that the number of the available NILS was $N_L = 5.55\times10^{28}$ solvent lattice atoms per m^3. The hydrogen trap sites were associated with dislocations in the deforming metal. Assuming one trap site per atomic plane threaded by a dislocation, one finds that the trap site density in traps per cubic meter is given by $N_T = \sqrt{2}\rho/a$, where ρ is the dislocation density and a is the lattice parameter. The dislocation density ρ, measured in dislocation line length per cubic meter was considered to vary linearly with logarithmic plastic strain ε^p so that $\rho = \rho_0 + \gamma\varepsilon^p$ for $\varepsilon^p < 0.5$ and $\rho = 10^{16}$ for $\varepsilon^p \geq 0.5$. The parameter $\rho_0 = 10^{10}$ line length/m^3 denotes the dislocation density for the annealed material and $\gamma = 2.0\times10^{16}$ line length/m^3. The trap binding energy was taken equal to $W_B = 29.2\,\text{kJ/mole}$ [5], the parameter β was set equal to 1 and this corresponds to a maximum NILS concentration of 1 H atom per solvent lattice atom, and the parameter α was also set equal to 1 which denotes 1 trapping site per trap. The lattice parameter was $a = 3.3\times10^{-10}\,\text{m}$, Poisson's ratio $\nu = 0.34$, Young's modulus $E = 115\,\text{GPa}$, the yield stress in the absence of hydrogen $\sigma_0 = 400\,\text{MPa}$, the hardening coefficient $n = 10$, and the softening parameter ξ was set equal to 0.1.

In Figure 1, the normalized stress σ_{22}/σ_0 and normalized hydrogen concentration c/c_0 are plotted against normalized distance R/b from the crack tip along the axis of symmetry at an initial hydrogen concentration $c_0 = 0.1\text{H/M}$.

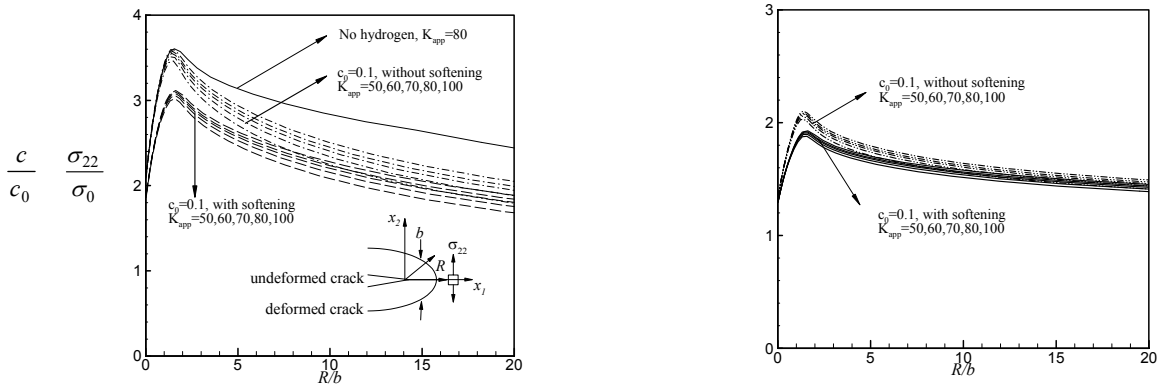

(a) (b)

Figure 1. (a) plot of the normalized stress σ_{22}/σ_0 vs normalized distance R/b along the axis of symmetry ahead of the crack tip for various applied stress intensities measured in $MPa\sqrt{m}$. The parameter R denotes the distance of a point from the notch root in the undeformed configuration and b is the current crack opening displacement; (b) plot of the normalized hydrogen concentration c/c_0 vs normalized distance R/b.

Clearly, at a given initial hydrogen concentration c_0, the hydrogen concentration profiles are shown in Fig. 1b to scale with the applied load in accordance with the formula $c = c\left(\sigma_{kk}, \varepsilon^p\right)$ and the well known corresponding scaling [9] of the stress and effective plastic strain in the small scale yielding solution. Lattice dilatation by H is accompanied with stress relaxation in the area ahead of the tip. As shown in Fig. 1a, this relaxation is more pronounced in the region $R/b > 1.6$ where the plastic strain in the absence of hydrogen is small in comparison to the plastic strain in the region close to the crack tip ($R/b < 1.6$). Hydrogen-induced softening decreases the local flow stress ahead of the crack tip, thus resulting in a reduced hydrostatic stress (Fig. 1a) and increased plastic strain. Since the hydrogen concentration profiles are dominated by the hydrostatic stress, the hydrogen concentration profile ahead of the tip is lower for a material undergoing softening due to hydrogen than for a material in the absence of any softening effect (Fig. 1a). It should also be mentioned here that the reduced hydrogen populations in the softened material are associated with a stronger stress relaxation than in the material without softening under the same applied load. Thus, the overall stress relaxation ahead of a crack tip is dictated by the synergism between material softening and relaxation due to hydrogen-induced dilatation.

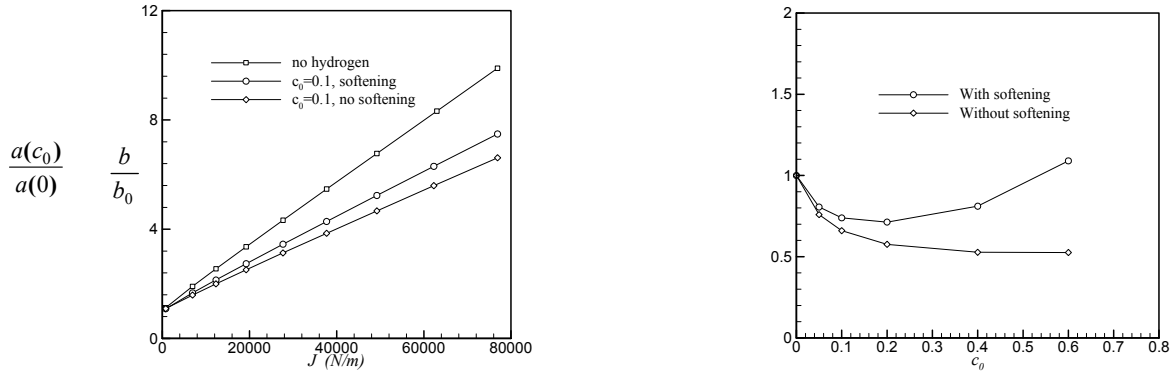

(a) (b)

Figure 2: (a) Plot of normalized crack opening displacement b/b_0 against the applied $J = \left(1-\nu^2\right)K_{app}^2 \Big/ E$ integral. The parameter b_0 denotes the crack opening displacement in the undeformed configuration; (b) Plot of $a(c_0)/a(0)$ against the initial hydrogen concentration c_0, where $a(c)$ is defined through $b/b_0 = a(c)J + 1$

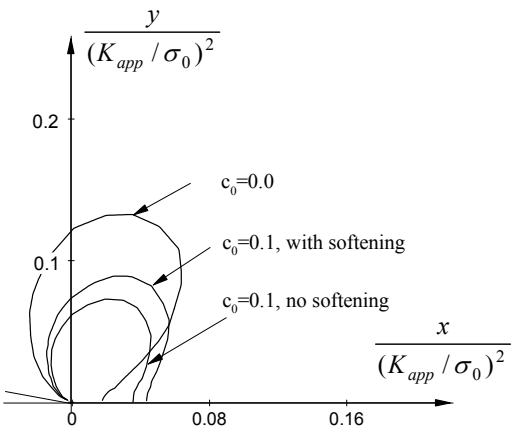

Figure 3: Superposed plastic zones ahead of a crack tip: for the hydrogen free material, $c_0 = 0.1$ and with no softening, and $c_0 = 0.1$ and with softening.

In the absence of hydrogen, there exists a linear relationship between the crack tip opening displacement (CTOD) and the applied J integral, namely $b/b_0 = aJ + 1$ [9], where a is a constant. In the presence of hydrogen, the numerical results of Fig. 2a show that for both hydrogen-induced softening and in the absence of any softening effect, this linear relationship between b and J continues to hold. This is a direct consequence of the fact that scaling of the stress and deformation fields ahead of the tip with the applied load continues to hold in the present case of equilibrium hydrogen concentrations. Figure 2a shows that at a certain applied load and initial hydrogen concentration, hydrogen tends to close the crack, i.e., decrease the parameter a. This is because hydrogen-induced lattice dilatation relaxes the stresses around the crack tip, thus leading to reduced plastic strains behind the tip and smaller plastic zones (see Fig. 3). Furthermore, hydrogen-induced softening causes a to be greater than that without softening because the plastic zone and strains are larger in the former case than in the latter (Fig. 3). It can be deduced that softening increases the parameter a (i.e. increases the CTOD) whereas relaxation due to dilatation decreases (i.e. decreases the CTOD) it. Also, comparing the cases with no hydrogen and hydrogen-induced softening, one sees that the softening effect is overridden by the relaxation effect at the concentration of 0.1 H/M as shown in Fig. 2a.

The dependence of the parameter a (i.e., the CTOD) on the initial hydrogen concentration c_0 is shown in Fig. 2b for the cases with and without hydrogen-induced softening. For the case without softening, a decreases with increasing c_0 and asymptotes a nearly constant value at large initial hydrogen concentrations. This is because for $0 < c_0 < 0.4$, numerical results show that the hydrogen concentration enhancement $\Delta c = c - c_0$ ahead of the crack tip increases with c_0, thereby resulting in increased stress relaxation and in turn, in decreasing $a(c_0)/a(0)$ (CTOD) with increasing c_0. However, for initial concentrations $0.4 < c_0 < 0.6$, Δc is almost insensitive to c_0, in particular for R/b>20, and hence $a(c_0)/a(0)$ is nearly constant.

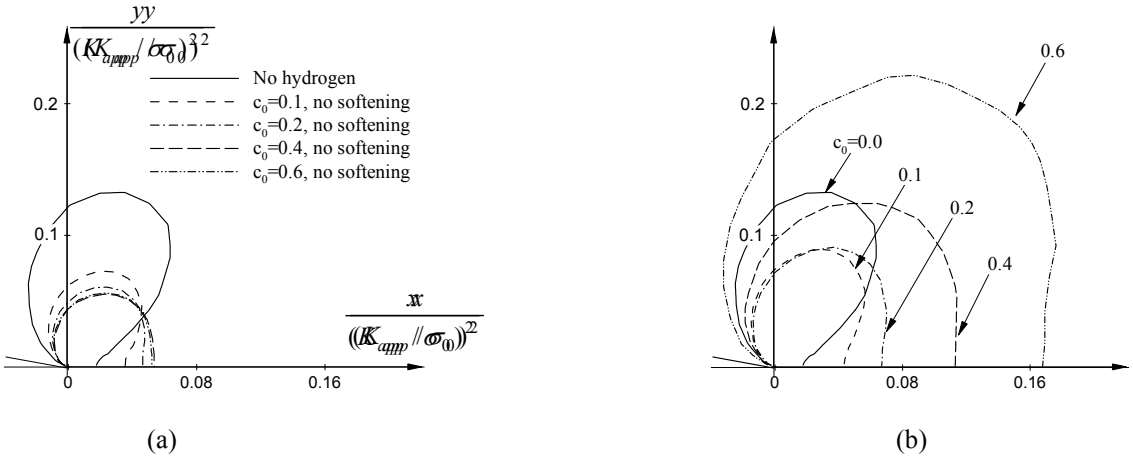

(a) (b)

Figure 4: (a) Superposed plastic zones ahead of the crack tip at various initial hydrogen concentrations c_0 for the case (a) without softening; and (b) with softening.

In the case of hydrogen-induced softening and $c_0 \le 0.2$, $a(c_0)/a(0)$ decreases with increasing c_0 because the relaxation due to $\Delta c = c - c_0$ overrides the relatively small softening effect associated with concentrations $c_0 < 0.2$. In contrast, for $c_0 > 0.2$ the corresponding relaxation is mild due to the small increases in Δc, and

this mild relaxation is overridden by the strong softening effect associated with these large initial concentrations.

The numerical results for the effect of hydrogen on the shape and size of the plastic zone in the neighborhood of the crack tip are shown in Fig. 4. First, hydrogen-induced lattice dilatation relaxes the stresses ahead of the tip and as a result, the plastic zones are shown spread and confined directly ahead of the tip and smaller (Fig. 4a) than in the absence of hydrogen. In the case of no-softening, Figure 4a shows that as the initial hydrogen concentration increases, the plastic flow of the material continues to concentrate in the region ahead of the crack tip while the plastic zone shrinks in the directions along the normal to the axis of symmetry and behind the crack tip. Shrinking of the plastic zone behind the crack tip with increasing initial hydrogen concentration (Fig. 4a) yields reduced crack opening displacements in agreement with the trend shown in Fig. 2b. For $c_0 = 0.4$ and $c_0 = 0.6$, both the plastic zone shape and size are almost the same (Fig. 4a), and this also corresponds to the nearly constant $a(c_0)/a(0)$ shown in Fig. 2b in the absence of softening. In the presence of hydrogen-induced softening, the plastic zones are shown expanding in every direction relative to the case with no softening (Figs. 3, 4b) as the initial concentration increases. Since $c_0 = 0.1$ is a relatively low initial concentration at which the softening effect on spreading the plasticity is dominated by the local expansion and confinement of the plastic flow ahead of the tip due to the dilatation-induced relaxation, the plastic zone size continues to be smaller than that in the absence of hydrogen (Fig. 3). However, at much larger initial concentrations (e.g. $c_0 = 0.6$), the softening effect results in much larger plastically deforming regions (Fig. 4b) and this is in accordance with the behavior of $a(c_0)$ shown in Fig. 2b.

CONCLUDING DISCUSSION

The present finite element calculations of coupled elastoplasticity with hydrogen concentration development in equilibrium with local stress and plastic strain show that that hydrogen concentration profiles ahead of a crack tip scale with the applied load for both hydrogen-induced softening and with no softening effects (Fig. 1). Dilatation-induced relaxation causes the plastic zone to expand and be confined ahead of the crack while it shrinks in all other directions. This reduces the crack tip opening displacement. In contrast, hydrogen-induced softening causes the plastic zone to expand in all directions and the CTOD to increase. At small initial concentrations ($c_0 < 0.2$), stress relaxation dominates whereas softening prevails at larger initial concentrations ($c_0 \geq 0.2$). As a result, the plastic zones are smaller in the former case than in the latter. However, in all cases, there is substantial plastic flow that takes place directly ahead of the crack tip which is not the case in the hydrogen free material (Fig. 4b). Therefore, one may identify the role of hydrogen with promoting intensification of the ductile fracture processes (e.g. void opening and inter-void ligament fracture by shear localization) that occur directly ahead of the crack tip. This is particularly true at small c_o (~0.1H/M) at which the hydrostatic stress, assisting void growth, is not substantially relaxed even in the case with softening.

ACKNOWLEDGEMENTS

This work was supported by NASA through grant NAG 8-1751.

REFERENCES

1. Birnbaum, H.K. and Sofronis, P. (1994) *Mater. Sci. & Eng.* A176, 191.
2. Sirois, E. and Birnbaum, H.K. (1992) *Acta Metall.* 40, 1377.
3. Sofronis, P. and H. K. Birnbaum (1995) *J. Mech. Phys. Solids* 43, 49.
4. Robertson I.M. and Birnbaum, H.K. (1986) *Acta Metall.* 34, 353.
5. Sofronis, P., Liang, Y. M. and Aravas, N. (2001) Submitted to *European Journal of Mechanics A: Solids*.
6. Tabata, T. and Birnbaum, H.K. (1983) *Scripta Metall.* 17, 947.
7. Oriani, R.A. (1970) *Acta Metall.* 18, 147.
8. Sofronis, P. and McMeeking, R.M. (1989) *J. Mech. Phys. Solids* 37, 317.
9. McMeeking, R.M. (1977) *J. Mech. Phys. Solids* 25, 357.

HYDROGEN INDUCED CRACK GROWTH RATE IN STEEL PLATES UNDER UNIAXIAL STRESS

J.L. Gonzalez[1], R. Ramirez[2], F. Fernandez-Lagos[2] and J.M. Hallen[1]
[1]Instituto Politecnico Nacional, ESIQIE, Dep. Ing. Metalurgica
Labs. de Metalurgia, Apdo. Post. 75-872, México, D.F.07300, MEXICO
[2]Subgerencia de Mantenimiento a Ductos e Instalaciones, PEMEX Exploración Producción Región Sur
Edif. 4 Centro Téc. Adm., Av. Carrizal Esq. Campo Saqmaria, Villahermosa, Tabasco, MEXICO

ABSTRACT

The purpose of this work was to determine in a quantitative manner the effect of an external uniaxial stress on the kinetics of the hydrogen induced cracking. In this study, the hydrogen induced cracking was done by cathodic charging of API–5L–X52 steel plates. The growth of the induced cracks was recorded at increasing inspection times by ultrasonic inspection. The external uniaxial stress affected the number of initial cracks in the HIC tests, having more initial cracks as the stress increases. This effect is related with the stress fields interaction from the internal pressure produced by the molecular hydrogen and the applied external stress, which weakens the interface between the matrix and the non-metallic inclusions, thus facilitating the nucleation of cracks by the pressure mechanism. A greater number of individual cracks causes that the number of cracks interconnections to increase, thus affecting the crack shape and growth. The external uniaxial stress, however did not show a significant effect on the hydrogen induced crack growth rate, at least in the interval of the applied stresses used in this work.

KEYWORDS: API-5L-X52 steel, hydrogen induced cracking, crack growth, pipelines

1. INTRODUCTION

There have been a number of failures of line-pipe steels due to the presence of delaminations and blisters which are formed when atomic hydrogen resulting from the corrosion reaction of the steel pipe in the presence of sour gas (H_2S). Although the actual trend in industry is to continue developing and evaluating new steels resistant to hydrogen induced cracking (HIC), there are thousands of kilometers of installed sour gas pipelines that still experience HIC. This facts justifies a need to be able to predict the life span of these pipelines in terms of the extension of HIC. The HIC is due to the absorption of the atomic hydrogen generated by the corrosion reaction between the sour gas and steel, which diffuses towards some internal discontinuities, such as non-metallic inclusions and pre-existing cracks, where it recombines to form molecular hydrogen. The internal pressure in the cavity increases until that the stress intensity in the edge overcomes the toughness of the material and a crack propagates (1). The cracks usually are formed parallel to the surface of the pipe; when they are located approximately at the half thickness, are called delaminations, and when they are located near a free surface, deforming the pipe wall, they are called blisters (1-4). The HIC is possible even in the absence of an external stress, because the stress concentration at the crack tip provides the driving force for the growth (1-4).

Iino (5) found that the manner of extension of the hydrogen induced cracks is considerably influenced by the presence of external stress (pipe hoop stress): in absence of the external stress, cracks extension develops by stepwise linking the hydrogen induced cracks, founding considerable plastic deformation accompanies the stepwise linking. In the presence of an external stress, cracks extension develops by linking the cracks formed in stacked arrays out of a plane approximately perpendicular to the stress axis. The linking between cracks, in this case, is characterized by the absence of plastic deformation. However, recently Zakaria (6) mentions that external stress did not significantly affect the manner of formation and extension of the hydrogen induced cracks. In his investigation, Zakaria found that in the absence of external stress the cracks still form in a stacked array.

Although the actual trend in industry is to continue developing and evaluating new steels resistant to hydrogen induced cracking (HIC), there are thousands of kilometers of installed sour gas pipelines that still experience HIC. This facts justifies a need to be able to predict the life span of these pipelines in terms of the extension of HIC.

Therefore the main aim of the present paper is to determine in a quantitative manner the effect of the external uniaxial stress in the range from zero to $\sigma/\sigma_o = 0.5$ on the kinetics of hydrogen induced cracking.

2. EXPERIMENTAL PROCEDURES

The material used in the experimentation was a carbon steel, type API-5L-X52, from a pipe of 91.4 cm diameter and 2.0 cm thickness. The chemical composition was: 0.14 C, 0.25 Si, 0.99 Mn, 0.01 P and 0.03 S (wt.%). At first, the pipe was inspected with an ultrasonic flaw detector to verify the absence of pre existing cracks and internal defects. Plates of 7.6 cm wide and 17.8 cm long, were cut out from the pipe and ground to get parallel faces and a thickness of 0.9 cm. The greater length of the test plates was parallel to the rolling direction of the pipe. The plate faces were finished with grade 400 SiC grit-paper and cleaned by immersion in an ultrasonic bath for 10 minutes. using a commercial cleaning solution (Ultramet). The plates were stressed using a loading frame as shown in Figure 1. The stress was measured with a strain gauge placed on the face of the plate. Finite element stress field calculation showed that plate exposed test area was under a uniform stress. The applied stress were 15.3, 68.3 and 165.9 MPa, which correspond to a σ/σ_o ratio of 0.05, 0.2 and 0.5 respectively (σ is the applied stress and σ_o is the yield stress of the material).

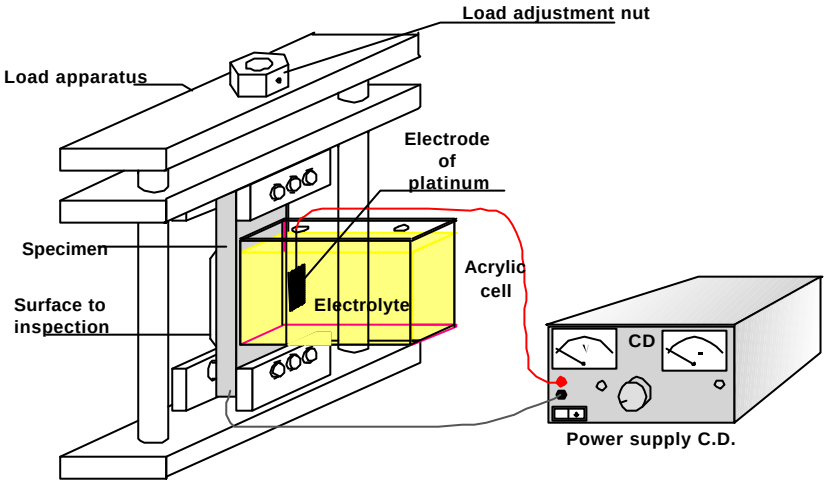

Figure 1. Loading frame and cathodic charging set up.

The cathodic charging set up is shown schematically in Figure 1. This set up, promotes hydrogen absorption through only one face of the plate, just as happens in a pipeline in service. The test solution was 0.4 wt % sulfuric acid in bidistilled water plus five drops of a “poison solution", that consists of 2g of phosphorus dissolved in 40 ml of carbon disulfide. The average pH of the test solution was 2.9. The applied current density was 2.5 mA/cm^2 and the test were ran at ambient temperature (average 22 °C). The solution was changed every six days, adding five drops of the “poison solution” daily. The growth of cracks in the plate was monitored from the free side by ultrasonic inspection. The inspection technique assured a resolution for crack length increments of at least 1 mm. The test were ran until most of the exposed area was cracked.

3. RESULTS AND DISCUSSION

Ultrasonic system used in these studies is a sensitive technique for detecting cracks in samples exposed to hydrogen cathodic charging. Since ultrasonic inspections were conducted before an after to cathodic charging, and those obtained before charging had no defect indications, all defects detected after cathodic charging were due to HIC. Ultrasonic indications were used to identify locations of cracking and quantitative data to characterize the extend of cracking, such as crack length ratios, were obtained. To verify the presence of the cracks, the samples were sectioned for metallographic examination. The cracks observed metallographically were found at the locations indicated from the ultrasonic flaw detector. Figure 2 shows the cracks contours (dashed areas) after the HIC tests at

different stresses and inspection times. It is observed that the crack contours are irregular, showing the tendency to be longer in the rolling direction than in the transverse direction of the plate (an average of 1.3 times).

The meallographic observations showed that most of the cracks were initiated at elongated manganese sulfide inclusions (Figure 3); therefore, the longer crack extension in the rolling direction is attributed mainly to the elongated shape of the non-metallic inclusions.

Figure 4 shows that the initial number of cracks increased with the applied external stress. In the absence of an external stress, the atomic hydrogen generated by the corrosion reaction between the sour gas and steel, diffuses towards elongated MnS inclusions, where it recombines to form molecular hydrogen, reducing the bond strength between inclusion and matrix, which produces the HIC. We suppose that effect of external stresses on the hydrogen induced cracks formation is due to the weakening of the interface between the matrix and the non-metallic inclusions by the superposed stress fields of the molecular hydrogen pressure and the applied external stress in the plate. This will promote the formation of cracks. Figure 2 shows that as charging time increases, linking between cracks takes place to form more complex shapes. This crack linking occurred preferentially in the longitudinal direction, due to the fact that the crack growth was greater in that direction. This preferential growing was more evident at the lowest external stress. Figure 2 shows also the profiles of the cracks in the thickness of the test plates. It is seen that the maximum stepwise cracking was of 10 % of the thickness. During the HIC tests, the crack linking occurred preferentially in the longitudinal direction, due to the fact that crack growth was greater in that direction. This also contributes to make the cracks longer in the longitudinal direction, with a final shape close to a rectangle with round corners. Iino(5) found that in the presence of an external stress (sufficiently high compared to zero and sufficiently low compared to the yield strength of the material) cracks linking developed by stacked arrays in a plane approximately perpendicular to the external stress axis, while in absence of an external stress, the cracks link in a stepwise manner. In the present work, it was found that the external stress did not significantly effect the manner of the formation and extension of the cracks at least in the interval of external stresses used in this work, i.e. in the presence of an external stress the cracks still link in a stepwise manner (Figure 5).

From the crack contours at different inspection times, the crack length and crack growth rates were calculated. Figures 6 and 7 show the average crack growth rate and crack length in the longitudinal direction of the test plates as a function of the exposure time. Figure 6 shows that the crack growth rate decreases with the exposure time and that there is not a significant effect of the external stress on the crack growth rate; however, figure 7 shows that the presence of an external stress increases the final average crack length. This is associated with the effect of the external stress on the crack initiation. and not with the effect of the external stress on the crack growth rate. As the number of initial cracks increases, the interconnection of individual cracks is more frequent and the final crack size is larger.

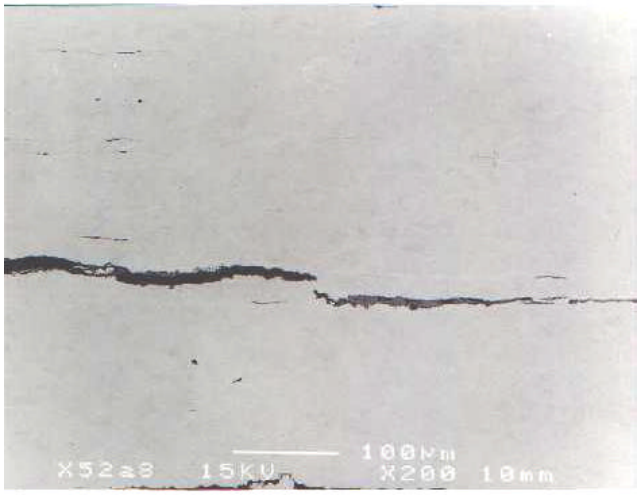

Figure 3. HIC initiating at the MnS inclusions.

5 days

21 days

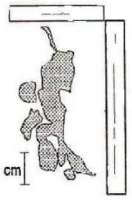

85 days

A)

5 days

12 days

39 days

68 days

95 days

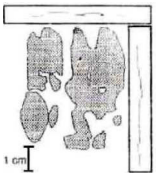

122 days

B)

3 days

13 days

27 days

37 days

64 days

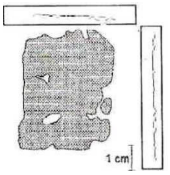

78 days

C)

Figure 2. Figure 2. Crack contours in the steel plates exposed to cathodic charging with uniaxial stress. / $_o$ = 0.052; b) / $_o$ = 0.2 and c) / $_o$ = 0.5

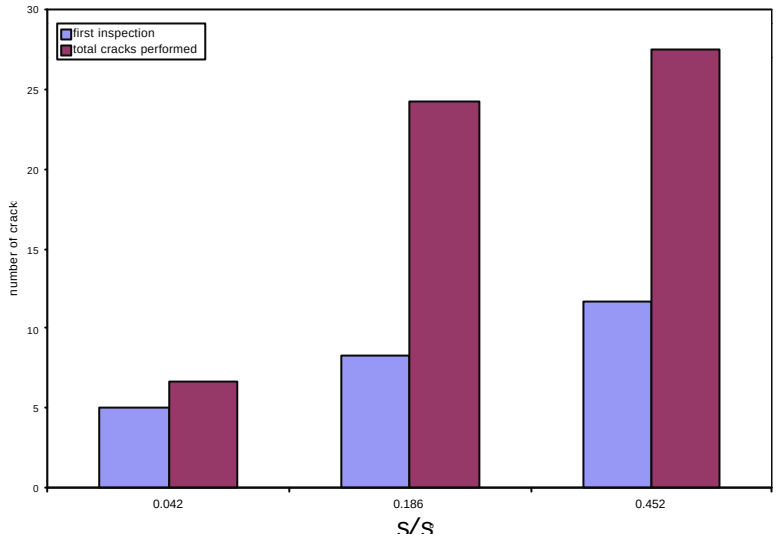

Figure 4. Number of detected cracks during the HIC test.

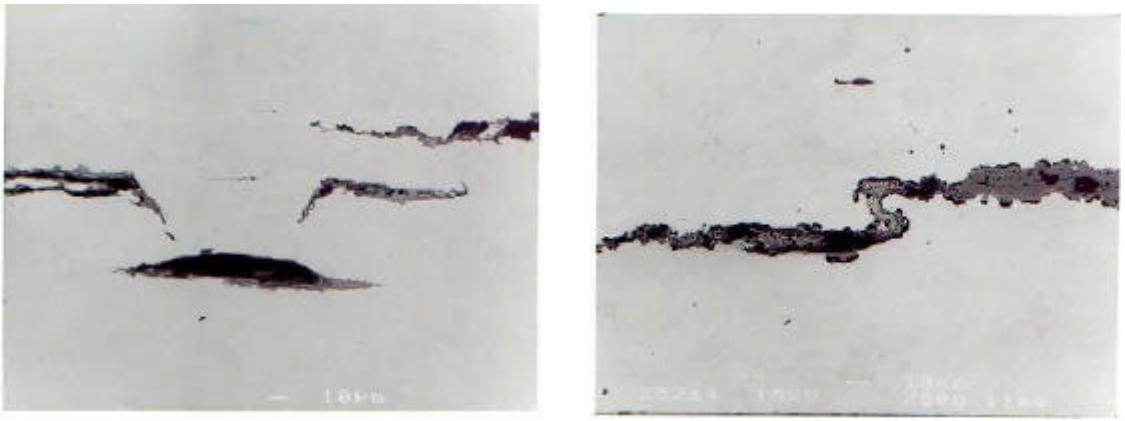

Figure 5. Examples cracks linking in a stepwise manner, observed in the loaded plates.

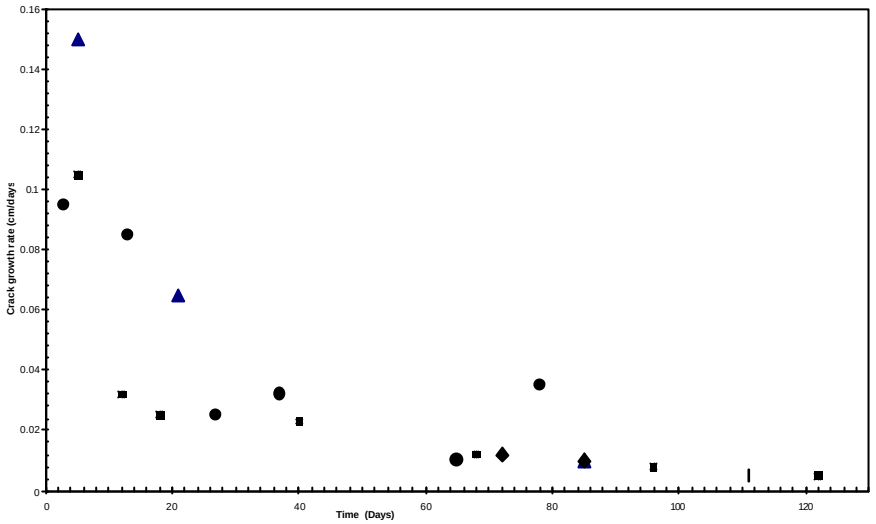

Figure 6. Measured crack growth rates at different external stresses.

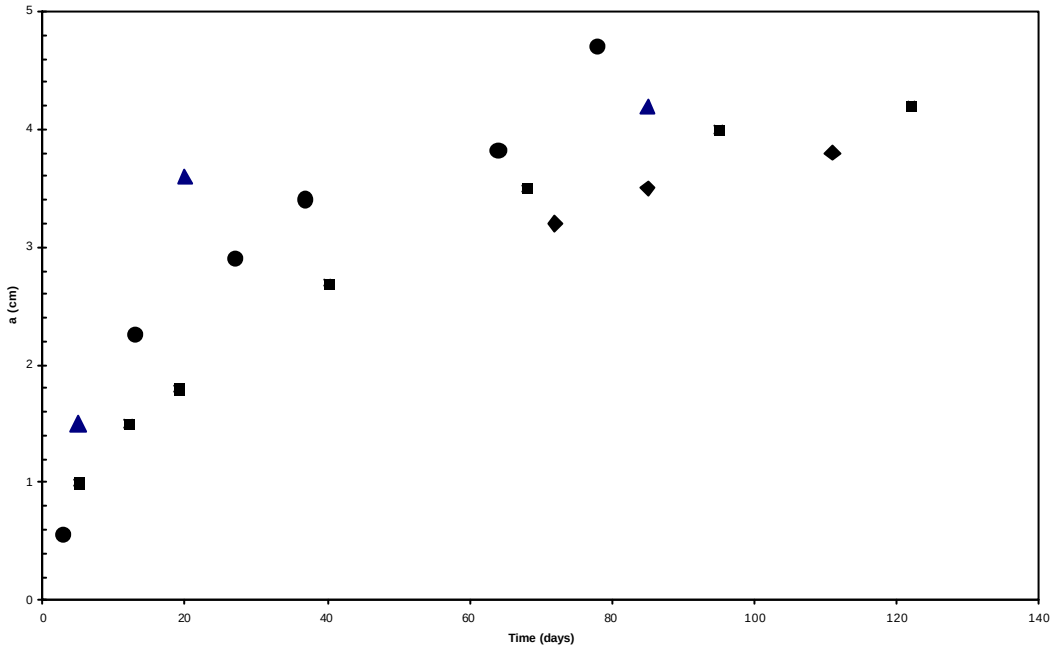

Figure 7. Measured crack lengths at different external stresses.

4. CONCLUSIONS

The effect of a external stress on the hydrogen induced cracking was monitored successfully using an ultrasonic flaw detector.

The presence of an external stress affected the number of initial cracks in the HIC tests, having more initial cracks as the stress increases. This effect is due to the weakening of the interface between the matrix and the non-metallic inclusions by the superposed stress fields of the molecular hydrogen pressure and the applied external stress.

It was found that the total crack length and the number crack interconnections, increased proportionally to the applied uniaxial stress, however little or no effect of the stress was seen on the crack growth rate.

ACKNOWLEDGMENT

Authors tank to the Instituto Politécnico Nacional and PEMEX Exploración Producción Región Sur for their support for the development of this work. This work was financed by PEP Región Sur, grant SRS GCTO 002/00.

REFERENCES

1. T.P. Groeneveld and R.R. Fessler, Hydrogen-Induced Damage in Sour-Gas Gathering Lines, Presented at the NACE Canadian Western Region Conference, Calgary, Alberta, Canada, 1 (1979),
2. R.J. Eiber and J.F. Kiefner,. Battelle's Columbus Laboratories, Failure of Pipelines, Metals Handbook, ASM, Failure Analysis and Prevention. 9th. Edition, 11, 695 (1986).
3. G. Herbsleb, R.K. Poepperling and W. Schwenk, Occurrence and Prevention of Hydrogen Induced Stepwise Cracking and Stress Corrosion Cracking of Low Alloy Pipeline Steels, Corrosion, 36, N 5, 247 (1981).
4. J. Charles, V. Lemoine, G.M. Pressouyre and L. Cadiou, Metallurgical Parameters Covering HIC and SSC Resistance of Low Alloy Steels, Corrosion´86, Albeth Thomas Convention Center, Houston, Texas, paper 164, 1 (1986).Vol. 9A, 1978, pp1581-1590.
5. M. Iino, The Extension of Hydrogen Blister-Crack Array in Linepipe Steel, Met. Trans A, Vol. 9A, 1978, pp1581-159.
6. M.Y.B. Zakaria and T.J. Davies, Formation and Analysis of Stack Cracks in a Pipeline Steel, J. Mat Sci, Vol 28, 1993, pp 3322-3328.

ORAL/POSTER REFERENCE: ICF100891OR

HYDROGEN/LENGTH SCALE INTERACTIONS DURING SMALL VOLUME YIELDING AND FRACTURE

William W. Gerberich and Natalia I. Tymiak

Department of Chemical Engineering and Materials Science
University of Minnesota, Minneapolis, MN 55455

ABSTRACT

Nanoindentation and thin-film decohesion experiments in the presence and absence of hydrogen have revealed a connectivity in terms of size scale. We propose this can be qualitatively interpreted in terms of a volume to length scale which is more precisely connected to the local stand-off distance of the nearest dislocation. The latter controls the local stress. This has ramifications to the ductile-brittle transition, thin-film decohesion and threshold stress intensities for hydrogen embrittlement. Interpretation of threshold stress intensity as a function of test temperature in Fe-3wt%Si single crystals as well as thin film decohesion of Cu from silicon after hydrogen charging are discussed.

KEY WORDS

Hydrogen embrittlement, nanoindentation, size scale, dislocation shielding

INTRODUCTION

Recent findings on two levels of scale have prompted reexamination of our current understanding of hydrogen embrittlement [1-4]. Specifically, at the nanometer/μN scale, nanoindentation measurements of yield points have exhibited a couple of phenomena. One has led to a size scale plasticity dependence often referred to as the indentation size effect. Here the shallower the penetration depth the harder the material as measured by nanoindentation. Elsewhere in this proceedings this is elaborated upon in length. If the same type of experiment is conducted after electrochemically charging the same sample, small penetration depths give a yield point load that strongly increases with increasing hydrogen content. A second level has involved the micron/μN scale where larger indentations into thin films can produce sufficient stored elastic energy that energy release rates can delaminate the film/substrate interface. In addition, we have electrochemically charged such film/substrates system and have shown the critical strain energy release rates associated with interfacial fracture are reduced by as much as a factor of two [4].

In the present paper we propose a connectivity between these two sets of phenomena and as such an interrelationship between two levels of scale. At best, however, we view this as a work in progress because of the complexity of the phenomena and its interpretation. We will emphasize where progress has been made and point out alternative pathways by which hydrogen "embrittlement" might be understood. The research includes a brief review of the indentation size effect on Fe3%Si and W single crystals and its connectivity to a volume to surface area concept. We then briefly review the modified Rice-Thompson model for the brittle to ductile transition applied to Fe3%Si single crystals in the absence and presence of hydrogen. This is all brought together with a length scale that can be measured independently for thin films of Cu/Ti/SiO_2/Si. Applications to film deadhesion with and without hydrogen utilize the Rice-Thompson approach.

THEORETICAL CONNECTIONS

At the smallest scale discussed here, we have found that extremely large enhancements of hardness exist at depths of penetration in the 10–100 nm range [1,2]. Whereas the hardness, H, might be expected to be about three times the bulk yield stress, σ_{ys}, values of (5–20)σ_{ys} were found for indentation into {100} planes of Fe-3wt%Si and W single crystals. Results [1] and interpretation [2] are given elsewhere, examples being given in Figure 1.

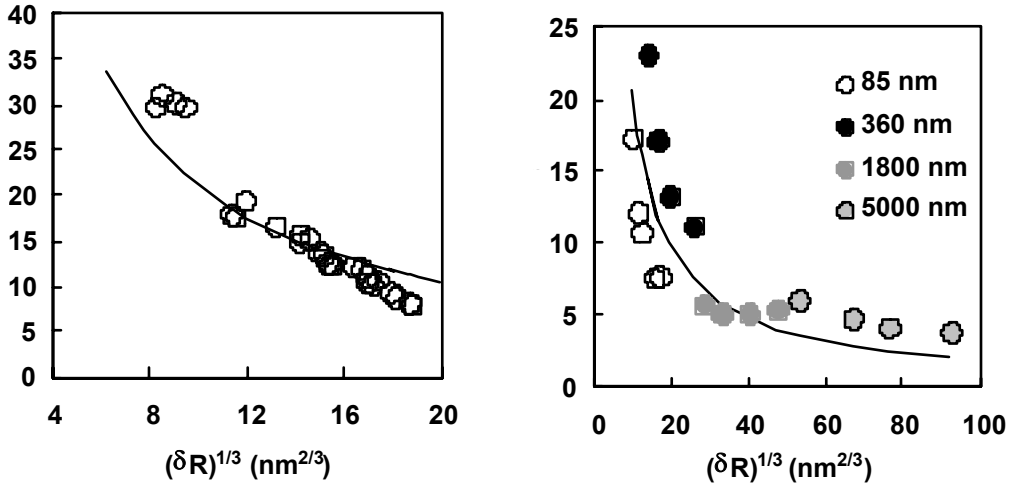

a) b)

Figure 1. Fit of the proposed model [2] for two ⟨100⟩ oriented single crystals. Single tips of 205 nm and 70 nm radii were used in (a) and multiple spherical tips with radii noted were used in (b).

The solid curves in Figures 1(a) and 1(b) represent Eqn. (1) as given by

$$\frac{H}{\sigma_{ys}} = \left\{ \frac{(V/S)^2}{3\delta R} \right\}^{1/3} \tag{1}$$

where V/S is the indent volume to surface ratio, δ is the penetration depth and R is the tip radius of the 90° diamond cones used. For the Fe-3wt%Si this was a 70 nm tip radius while for the W a

variety of tips were used as indicated in Figure 1(b). Tip correction factors were utilized for any penetrations beyond the spherical regime.

In the same study [2] it was noted that *V/S* was constant for the first 100 nm of penetration in a given material. However, it varied from 4.7 to 11.7 μm for four single crystals ranging from tungsten to gold. Since *V/S* is a length scale, this was immediately considered as having a fundamental connectivity to the plasticity process. More details about this are considered in a companion paper as part of this proceedings [5]. We then hypothesized that if this μm-size length scale from nm level experiments represented a microstructural characteristic, might it not be applicable to fracture experiments as well as indentation. While at first glance this might suggest a leap of faith, it is not so strange if you consider the modified Griffith criterion scaling with the relative amount of work associated with crack exposed surface energy and crack-tip plastic volumes. Again, as detailed in the companion paper [5], this analogous behavior for nanoindentation and crack tips is demonstrated. Given that, the step of including hydrogen effects is trivial in concept but complex in detail. That is, hydrogen can be affecting both the surface energy and the plastic work contribution in ways not understood well at all. We [3] and others [6] believe that thin film decohesion, as described in the next section, can provide some of the answers.

In a recent paper and a review, some 25 film/substrate multilayers were evaluated for the effects of film thickness, yield strength, test temperature and interfacial chemistry on delamination toughness [3]. It was concluded that there are brittle to ductile transitions (BDT) in metal films deposited on ceramic or semiconductor substrates. This was analogous to the BDT that occurs when either reducing thickness (increasingly plane stress) or raising test temperature (reducing yield strength) in bulk test specimens. Additional features of this are detailed in the companion paper [5]. One significant feature is that as film thickness decreases, plastic energy dissipation decreases. As shown later under results and discussion, the fracture resistance decreases to the true surface energy of the interface. This allows the local stress intensity ($k_{IG} \equiv \left[2E\gamma_i\right]^{1/2}$) at the Griffith energy level to be established without having to deconvolve the plastic energy dissipation contribution. This may be coupled with a nanometer length scale associated with the distance of the nearest dislocation to the crack tip. Often referred to as a dislocation free zone (DFZ) this leads to the second necessary parameter, *c*. In a series of papers [7], it is shown that if both k_{IG} and *c* are known, use of the Rice-Thomson [8] and Lin-Thomson [9] formalism leads to

$$K_c = \frac{\sigma_{ys} c^{1/2}}{2\exp(4/3)} \exp\left\{\frac{\pi^{3/2} k_{IG}}{6\sqrt{2}\sigma_{ys}(2c)^{1/2}}\right\} \tag{2}$$

Having the yield strength, σ_{ys}, and the Griffith energy which gives k_{IG}, the only unknown is the dislocation stand-off distance, *c*, which controls the local stress and hence the fracture criterion. We believe there is a connectivity between the length scale in nanoindentation, *V/S*, and an approach which should eventually lead to an understanding of the stand-off distance, *c*. While we leave that discussion for the companion paper, a more qualitative argument here is that the number of dislocations in a pile-up follows a similar relationship for cracks and nanoindentations implying the same length scale applies. Approximately six years ago [10] we suggested that observations of crack-tip and nanoindentation-tip emission of dislocations "will eventually lead to more precise mechanisms and solutions for brittle-ductile transition and contact wear phenomena." In a series of papers [7,11,12] we suggested that the number of dislocations in an inverse pile-up might be similar for a yield instability at an indenter or at a crack tip. The number of dislocations in the

respective pile-ups, as calculated elsewhere [5], are shown in Figure 2. This is of some significance and suggests a connectivity of scale over this range as discussed below.

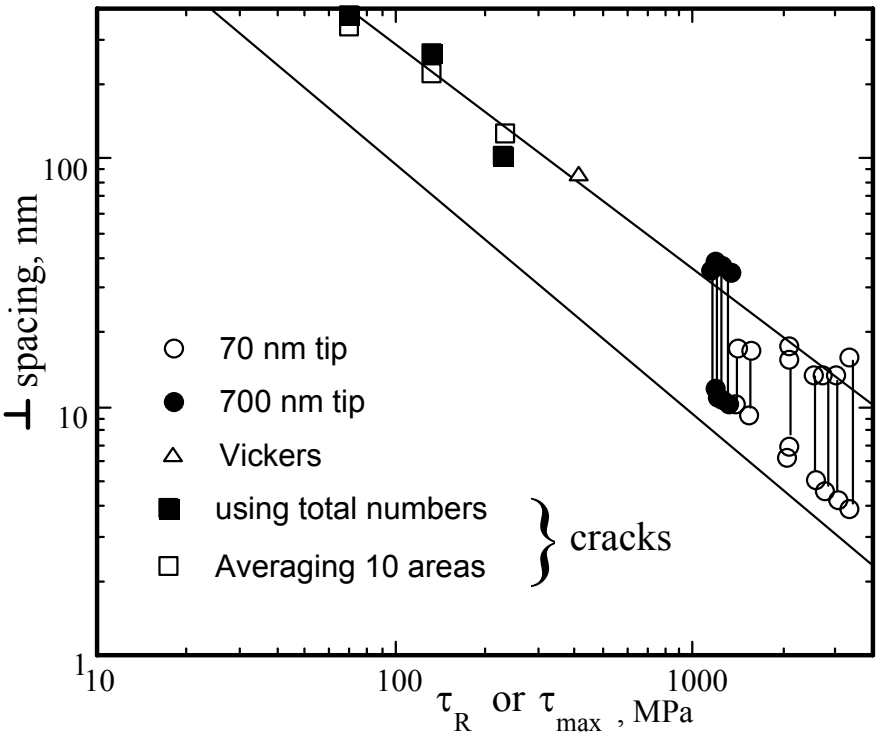

Figure 2. The average dislocation spacing variation with the resolved stress on the slip planes at the crack tips or the maximum shear stress under the indenter. The data range in the 70 and 700 nm tip data are based upon the densest lip band (upper points) and average density of all planes (lower points).

RESULTS AND DISCUSSION

First, we reexamine some hydrogen embrittlement data in Fe-3wt%Si single crystals. We note that this undergoes discontinuous cracking with single forward crack increments of about 0.74 ± 0.12 μm. Such extensions occurred for both externally supplied (1 atm.) or internally supplied (cathodically charged) hydrogen. An example of the latter, not previously published, is shown in Figure 3. Rather than attempting to reexamine kinetics, which is far too complex [14], we will address threshold in the context of the dislocation model presented above.

As discussed elsewhere [5] in this volume, we demonstrate that the lead dislocation for a 22 dislocation pile-up would give a value of 3.2 nm for the "DFZ" which is hardly worth calling a zone. However, Li [15] has recently shown in simulations that additional slip bands emitting can produce a "DFZ" much larger than if a single band is emitting. In fact, a DFZ ranging from 3 to 16 times as large as the distance between the first and second dislocations in front of the DFZ exists. Even though our dislocation arrangements are not identical to the one used [15] we interpreted our 79.5º orientation of slip bands in the context of Li's simulations. From those simulations, it was found that the DFZ could be 15 times as large as our calculated value of 3.2 nm. This would represent a DFZ of 48 nm which is *c* in Eqn. (2). It is important to note that he used 15 emitting slip planes, quantitatively similar to those previously observed. We used this to determine fracture toughness for ‹100›Fe-3wt%Si crystals tested at temperatures from 100 to 298ºK.

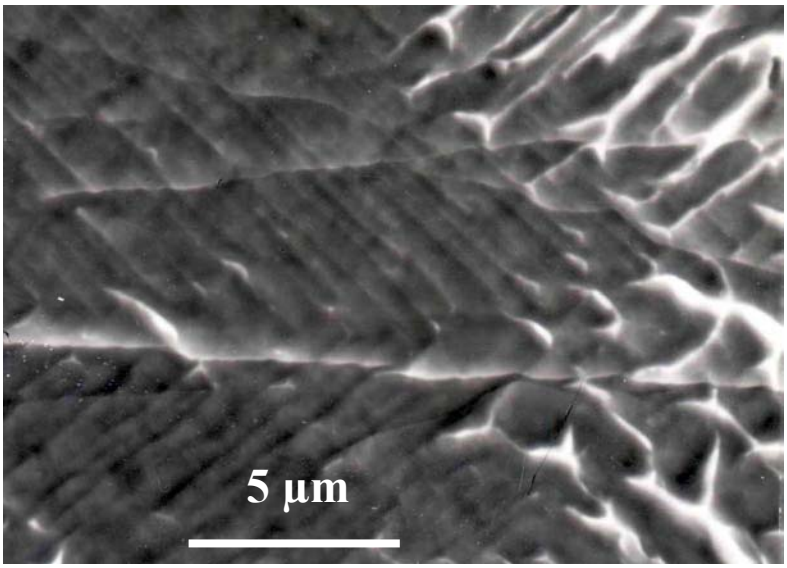

Figure 3. Fracture surface of Fe3%Si indicating discontinuous crack growth during electrolytic hydrogen charging.

The yield strength and average fracture toughness values from the previous study [7] are given in Table 1 for five test temperatures. With a c = 48 nm, the yield strengths observed and a k_{IG} of 0.85 MPa-m$^{1/2}$ as taken from nominal surface energies [7], the agreement is seen to be good between observed and calculated K_{Ic} values.

TABLE 1
Yield strength and fracture toughness, observed and calculated
from Eqn. (2) using a value of c = 48 nm.

T, ºK	100	173	233	298	363
σ_{ys}, MPa	450	395	352	305	285
Obs. K_{Ic}, MPa-m$^{1/2}$	6	23	50	120	> 120
Calc. K_{Ic}, MPa-m$^{1/2}$	11.7	22.7	44.6	118	199

Regarding hydrogen effects, the one simple assumption is that the concentration levels involved do not affect the far field yield strength which dictates pile-up behavior. The second one is *ad hoc* and assumes that k_{IG} through the surface energy is reduced to 0.70 MPa-m$^{1/2}$. This is a slightly greater reduction than was found in a previous analysis [5]. This allows an equally good fit to previously published data [17]as seen in Figure 4.

Returning to small volume behavior as represented by thin films, in a review of 14 metal/interlayer/substrate combinations, it was found that the dislocation stand-off distance scaled with $(k_{IG}/\sigma_{ys})^2$. Taking the Griffith value of 0.85 MPa-m$^{1/2}$, for this Fe-3wt%Si single crystal, this correlation shown elsewhere [3] would give a value of $c \sim 500$ nm, an order of magnitude greater than the 48 nm found. This suggests that the longer length of slip bands available in single crystal or coarse grained solids allows greater shielding compared to nanocrystalline thin films. That is, it is well-documented that regular arrays of dislocations can shield the crack tip from the far-field stress. A balance of forces between the stress field of the dislocation array and the stress field of the stress intensity essentially increases the resistance to crack propagation. In the early stages of nanoindentation, this same balance of forces between tip-emitted dislocations and the stress field of the indenter increases the resistance to penetration. In fact, it has been recently shown [5] that

film thickness which partially controls the nanocrystalline grain size is an integral part of the size scale.

In the thin film review it was found that a Cu/Ti/SiO_2/Si film system had a value of c = 60 nm [3].

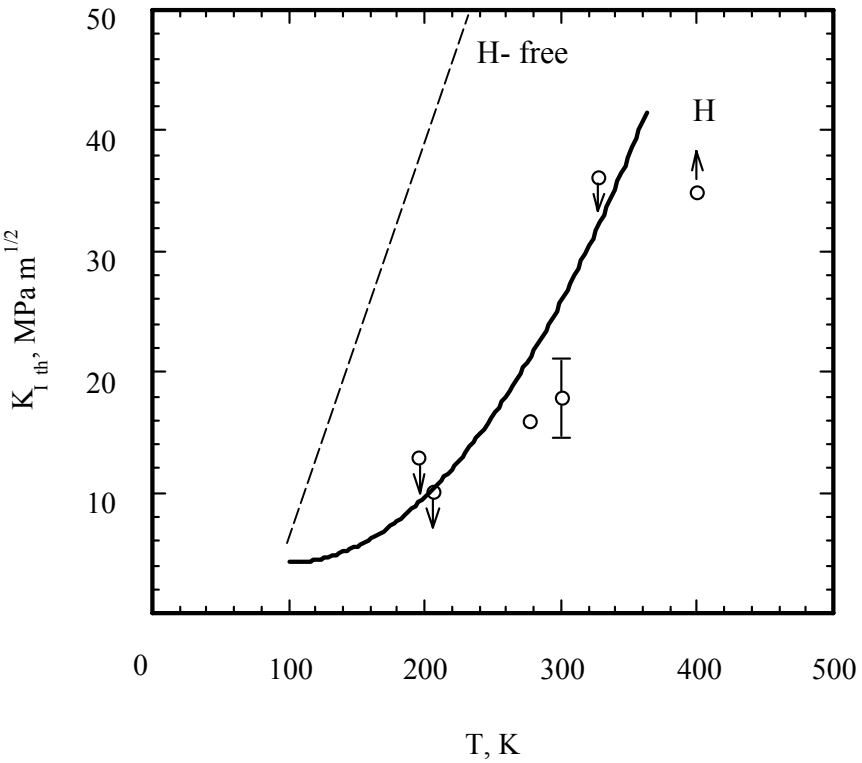

Figure 4. Comparison of Eq. (2) to hydrogen-affected threshold stress intensities for Fe3%Si crystals.

Here, yield strength was given by

$$\sigma_{ys} = \sigma_0\left[1 + \beta h^{-1/2}\right] \tag{3}$$

where σ_0 = 400 MPa, β = 0.287 μm$^{1/2}$ and h = film thickness. With measured values of G_{IG} = 3.6 J/m^2 for interface fracture in Cu/Ti/SiO_2/Si and E = 120 GPa, it was a simple matter to calculate k_{IG} = $(EG_{IG})^{1/2}$ to be 0.66 MPa-m$^{1/2}$ and from that determine c = 60 nm at $K_c = k_{IG}$ using Eqn. (2). The fit to all the data using Eqn. (2) with yield strength varying as a function of thickness from Eqn. (3) is shown in Figure 5. Cathodically charging the same copper films at 60 mA/cm^2 for 70 s in 1 M NaOH reduced the fracture resistance as shown in Figure 5. By allowing a small decrease in the Griffith stress intensity from 0.66 to 0.59 MPa-m$^{1/2}$ due to hydrogen, Eqn. (2) also predicts the decrease in strain energy release rate. For the hydrogen case here, it is seen that a 20% drop in the surface energy can lead to a 50% decrease in the practical work of adhesion for the 1 μm size film in Figure 5.

What does this approach imply for hydrogen embrittlement mechanisms at different levels of scale? Reexamination of Eqn. (2) reveals several aspects perhaps unappreciated prior to recent studies of thin films:

1) At large scale, c can be reasonably small particularly for relatively low yield strength materials such as single crystals or coarse-grain alloys. This can provide large toughness at intermediate temperature in even those materials prone to brittle fracture. At low enough temperatures low energy brittle fracture still prevails in such materials.
2) This does *not* preclude a microscopic fracture mode transition as temperature increases and yield strength decreases. All this implies is that with greater shielding and lower yield strength, $\sigma_{ys}c^{1/2}$ in the denominator of Eqn. (2) decreases with increasing test temperature. This raises K_c exponentially. By elimination of decohesion along either a cleavage plane or an intergranular or bi-material boundary because the necessary K_c is too high (!), the alternative fracture mode is ductile fracture. The same concept applies to hydrogen embrittlement but with additional complexity. Consider stainless steels or superalloys. Does hydrogen reduce k_{IG}, increase σ_{ys} but leave c unaffected? Clearly this does not happen in many stainless steels that fail by microvoid coalescence but perhaps it does in high strength superalloys that fail by intergranular fracture. An intriguing aspect of this is that slip localization would tend to enhance shielding by reducing c. Even if k_{IG} were reduced this could lead to microvoid coalescence as the preferred fracture mode.

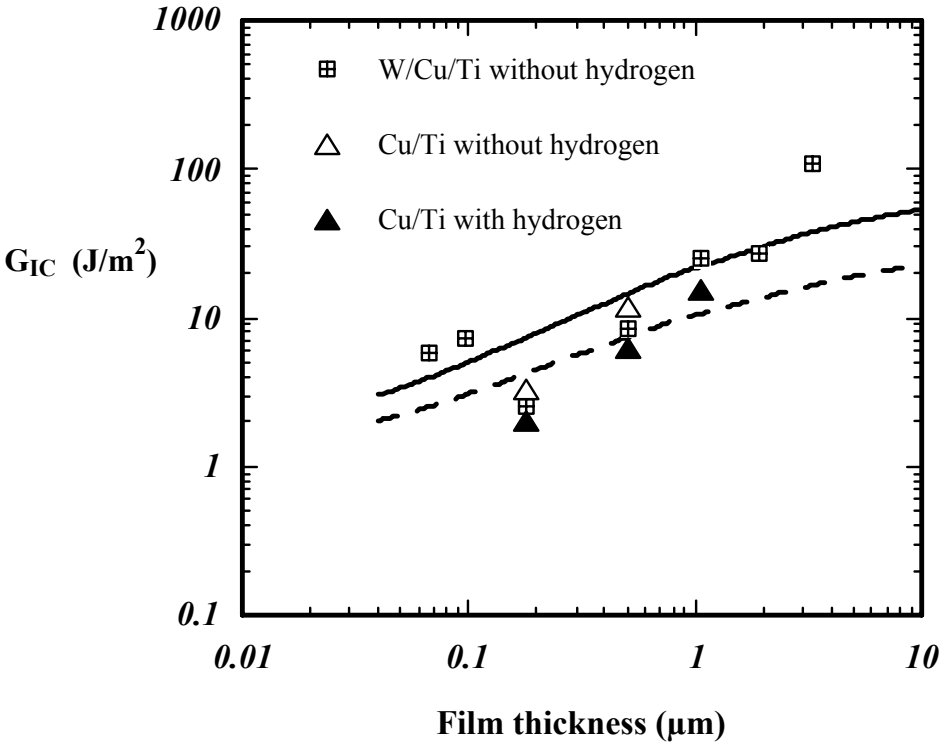

Figure 5. Effect of film thickness on Cu/Ti/SiO2 interfacial fracture resistance with (dashed line) and without hydrogen(solid line).

3) Finally, with respect to small scale, we hypothesize that the values of c can be considerably larger at the same yield strength in thin films compared to larger scale microstructures. The limited shielding available due to restricted lengths of slip bands and numbers of dislocations will tend to give larger values of c and form lower toughness and higher susceptibility to hydrogen embrittlement. This is particularly the case for thin nanocrystalline films with high yield strengths (fine grain size) weakly bonded to a substrate. For such cases it is seen that all three parameters in the exponential, a lower k_{IG} in the numerator and high yield and a larger stand-off distance in the denominator, would favor embrittlement.

SUMMARY

A connectivity of scale in terms of numbers of dislocations emitted at a point source and their average spacing has been established for both nanoindenters and crack tips. Determination of the numbers of parallel slip bands have been indirectly and in some cases directly observed allowing estimates of the number of dislocations per slip band. This gives a crude estimate for the back stress on the source which is surprisingly even much greater for sharp indenter tips than a crack tip. For the same two orders of magnitude displacement scale examined (10–1000 nm), this agreement gives some reason to believe that a consistent length scale is controlling the plastic deformation process. What we have learned with such small scale deformation processes leads to a refined brittle-to-ductile transition model via the Rice-Thomson and Lin-Thomson formalism. This is then easily modified for the hydrogen embrittlement process where either a cleavage plane, a grain boundary or a bi-material thin film interface is degraded. The key here is a length scale dictated by the closest approach of the last dislocation emitted in a shielding array.

ACKNOWLEDGMENTS

This research was supported by the Office of Naval Research under Grant N00014-91-J-1998.

REFERENCES

1. Gerberich, W.W., Tymiak, N.I., Horstemeyer, M. and Baskes, M. (2001) ``Interpretation of Indentation Size Effects," submitted to *J. Appl. Mech.*
2. Tymiak, N.I., Kramer, D.E., Bahr, D.F., Wyrobek, T.J. and Gerberich, W.W. (2001) "Plastic Strain and Strain Gradients at Very Small Indentation Depths," *Acta Mater.* 49, in press.
3. Volinksy, A.A., Moody, N.R., Adhihetty, I. and Gerberich, W.W. (2001) "Interfacial Toughness Measurements of Thin Metal Films," submitted to *Acta Mater.*
4. Katz, Y., Tymiak, N.I. and Gerberich, W.W. (2001) "Nanomechanical Probes as New Approaches to Hydrogen/Deformation Interaction Studies," *Engng. Fract. Mech.*, in press.
5. Gerberich, W.W. (2001) "Scaling Fracture Resistance in Thin Films," submitted to ICF10.
6. Zhuk, A.V., Evans, A.G. and Hutchinson, J.W. (1998) *J. Mater. Res*. 13, No. 2 , 3555.
7. Zielinski, W., Lii, M.J., Marsh, P.G., Huang, H. and Gerberich, W.W. (1992) *Acta Metall. Mater*. 40 Parts I, II, III on pages 1861, 2873, 2883; Huang, H. and Gerberich, W.W., (1994) *Acta Metall*. *Mater*. 42 No. 3, 639; Gerberich, W.W., Volinsky, A.A. and Tymiak, N.I. (2000) MRS Symp. Vol. 594, 351.
8. Rice, J.R. and Thomson, R. (1974) *Phil. Mag*. 29, 73.
9. Lin, I.H. and Thomson, R. (1986) *Acta Metall*. 34, 187.
10. Gerberich, W.W., Lilleodden, E.T., Foecke, T.J. and Wyrobek, J.T. (1995), In *Micromechanics of Advanced Materials*, Chu, S.N.G., *et al*. (Eds.), TMS, Warrendale, PA, p. 29.
11. Harvey, S., Huang, H., Venkataraman, S., Zielinski, W. and Gerberich, W.W. (1993), *J. Materials Research* 8 No. 6, 1291, *ibid*. p. 1300.
12. Gerberich, W.W., Nelson, J.C., Lilleodden, E.T., Anderson, P. and Wyrobek, J.T. (1996) *Acta Materialia* 44, No. 9, 3585.
13. Hull, D. (1975) *Introduction to Dislocations*, 2nd Ed., Pergamon Press, Oxford, p. 224.
14. Chen, X. and Gerberich, W.W. (1991) *Metall. Trans. A* 22A**,** 59.
15. Qian, C.-Fu and Li, J.C.M. (1996) *Mechanics of Materials* 24, 11.

Paper ICF100893OR

Hydrogen, Hydrides, and Crack Tip Deformation in Titanium

C.L. Briant, Z.F. Wang, and K.S. Kumar

Division of Engineering
Brown University
Providence, RI 02912 USA

ABSTRACT

This paper summarizes results obtained in our laboratory on the susceptibility of commercial purity titanium and the α/β titanium alloy Ti-5111 to hydrogen cracking. The tests were run under cathodic polarization in sodium chloride solutions. Cathodic potentials as low as $-1400 mV_{SCE}$ had little effect on the mechanical properties of grade 2 titanium, but grade 3 titanium showed a decrease in the elongation to failure as the electrochemical potential became more cathodic. However, the fracture mode remained ductile with microvoids nucleating at hydrides. Ti-5111 was very susceptible to hydrogen cracking when the pH of the solution was low and the electrochemical potential was cathodic, but hydrides did not appear to play a role in the cracking process.

KEYWORDS

titanium, hydrogen embrittlement, sodium chloride solutions, Ti-5111

INTRODUCTION

The mechanisms of hydrogen embrittlement have been a topic of great debate in past years. One reason for this is that the actual mechanism can vary significantly from one materials system to another [1]. In some materials, such as titanium and zirconium, the primary cause of embrittlement appears to occur through hydride formation. In other materials, such as steel and nickel-base materials, atomic hydrogen appears to be the primary cause of embrittlement. More recent studies of intermetallic compounds have suggested that the source of hydrogen is very important [2]. For example, in FeAl the presence of atomic hydrogen in the environment does not appear to have a great effect on mechanical properties, whereas water vapor can cause a significant decrease in elongation to failure.

Although one single mechanism will not explain hydrogen embrittlement, it is important to have complete descriptions of this problem in all important structural materials. We have recently examined hydrogen embrittlement in various grades of

commercial purity titanium as well as in titanium alloys. The results show that in commercial purity titanium hydrides play a dominant role in causing embrittlement, whereas in the α/β alloys they may play no role at all. By comparing these materials one can understand the different mechanisms that lead to embrittlement.

EXPERIMENTAL

In this paper we will discuss three different materials. Two of the materials were commercial purity titanium and the third was an α/β alloy, Ti5111. Their compositions are listed in Table I along with their basic mechanical properties. All were tested in the as-received condition. The two commercial purity titanium materials had an equiaxed grain structure and the Ti-5111 had a lamellar α/β microstructure.

The mechanical tests for these materials were all performed on single-edge notched sheet tensile samples. The thickness of the grade 2 and grade 3 samples was 1.12 mm and 0.62 mm, respectively, and that of the Ti-5111 was 2.56 mm. The notch had an included angle of 60^{o}. The samples were pulled to failure in a 3.5% solution of sodium chloride under various applied electrochemical potentials. We used the ratio of the elongation to failure in the sodium chloride solution to that in an inert oil held at the same temperature as a measure of susceptibility to hydrogen embrittlement. We will refer to this parameter as the elongation ratio in the text below. All tests were run with the solution at 70^{o}C. The pH of the solution used to test the commercial purity titanium was 1 and that used for the Ti-5111 was either 1 or 8. More details of the testing and post-test examination have been given in references 3 -5.

Table I
Alloy Composition and Mechanical Properties

Alloy	Composition (wt.%)	Yield Strength (MPa)	UTS (MPa)	Elongation to Failure
Grade 2	Ti-0.14O-0.02C-0.008N-0.08Fe	344	506	28
Grade 3	Ti-0.21O-0.01C-0.009N-0.16Fe	489	603	24
Ti-5111	Ti-5Al-1Sn-1Zr-1V-0.08Mo	750 (nominal)	Not Measured	Not Measured

RESULTS

Figure 1a shows the elongation ratio for grades 2 and 3 titanium plotted as a function of electrochemical potential. The results show that there is very little change in the elongation ratio for grade 2 titanium as the electrochemical potential is made more cathodic. This result was obtained, even though other experiments had shown that hydrides begin to form in this material at electrochemical potentials below –600 mV_{SCE} and that thick layers of hydrides are formed at potentials near –1400 mV_{SCE}. In contrast, grade 3 titanium showed a measurable loss in the elongation ratio as the electrochemical potential was made more cathodic. Figure 1b shows the elongation ratio at –1400 mV_{SCE}

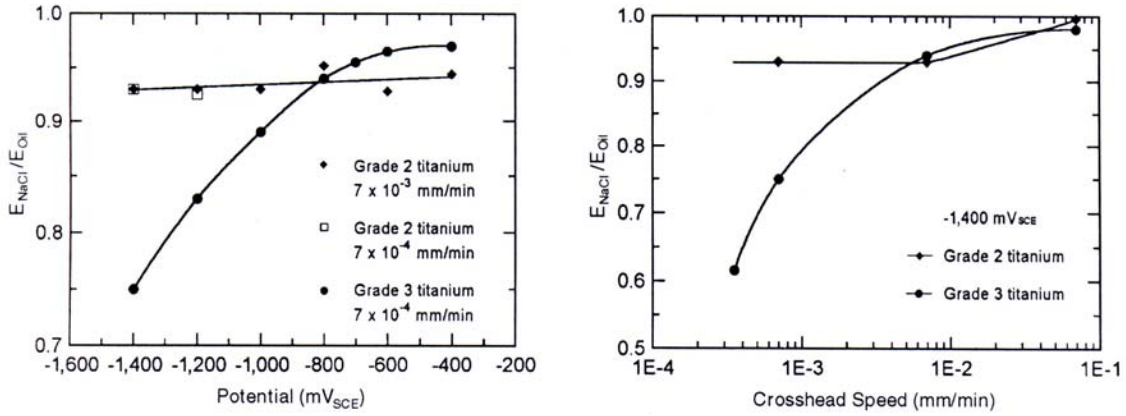

Figure 1: (a.) The elongation ratio plotted as a function of electrochemical potential for grade 2 and grade 3 titanium. The crosshead speeds are given in the figure. (b.) The elongation ratio plotted as a function of crosshead speed for grade 2 and grade 3 titanium.

for both grade 2 and grade 3 titanium plotted as a function of crosshead speed. The results show that as the crosshead speed decreased the elongation ratio stayed approximately constant for grade 2 titanium, whereas the elongation ratio dropped for samples of the grade 3 titanium.

Examination of the fracture surfaces showed that under all conditions the grade 2 titanium underwent ductile failure. An example is shown in Figure 2a. The grade 3 titanium had a similar fracture surface when tested in oil or under anodic conditions. However, as the elongation ratio decreased for the grade 3 titanium, the fracture surface showed new features. These included brittle secondary cracks on the surface, some evidence of large voids on the surface, and evidence of a new population of fine scale voids. A micrograph is shown in Figure 2b. Additional information was obtained by examining the hydride that formed on the surface of a sample after cathodic charging. In the case of the grade 2 titanium, we found that there was a thick layer of hydrides, as shown in Figure 3a, but that beneath this layer few hydrides were observed. In the grade 3 material, this thick layer was also observed, but in addition there were hydrides beneath this thick layer extending into the matrix, as shown in Figure 3b. In flat samples charged for 24 hours at an electrochemical potential of –1000 mVSCE, hydrides extended

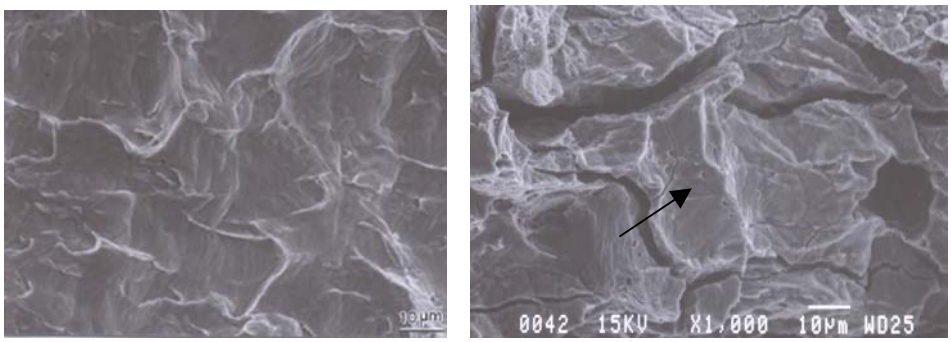

Figure 2: Scanning electron micrographs of (a.) grade 2 titanium tested at –400 mV_{SCE} and (b.) grade 3 titanium tested at –1400 mV_{SCE}. The arrow points out fine microvoids.

approximately 50 μm into the bulk and for an electrochemical potential of –1400 mV_{SCE} the hydrides extended approximately 90 μm into the bulk.

We also examined samples in which the crack had been stopped before proceeding completely through the sample. In the grade 2 material we always found a blunted crack, as shown in Figure 4a, with no evidence of cracking ahead of the rounded crack tip. In contrast, in the grade 3 material we found a sharper crack extending from the blunted crack tip, with evidence that microvoids were forming ahead of this blunted crack and that these microvoids were connecting up to allow the crack to extend.

We now consider the results for Ti-5111. Figure 5 shows the elongation ratio of this material plotted as function of applied potential. In the pH=8 solution, there was no loss in elongation even though the electrochemical potential was very cathodic. In contrast, in the pH=1 solution the elongation ratio was essentially zero when the electrochemical potential was below –1000 mV_{SCE}. The fracture surfaces of the samples that showed no elongation to failure were very brittle, and examination of propagating cracks in these samples showed that they tended to go through the β-phase (5). There was no evidence of hydride formation in these samples, even though in the pH=1 solution the hydrides were found to precipitate at potentials below –500 mV_{SCE}. However, these

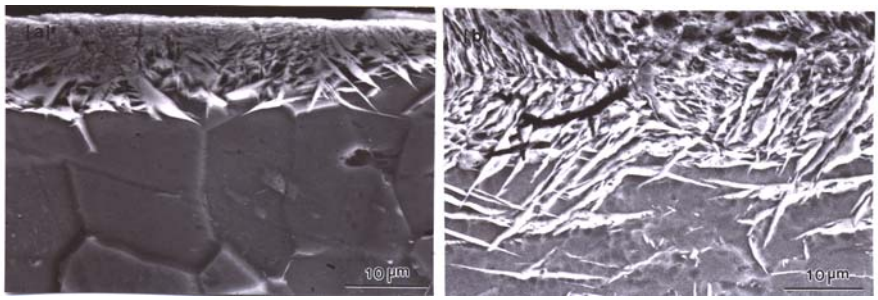

Figure 3 : Scanning electron micrographs of hydrides on the surface of (a.) grade 2 and (b.) grade 3 titanium after cathodic charging.

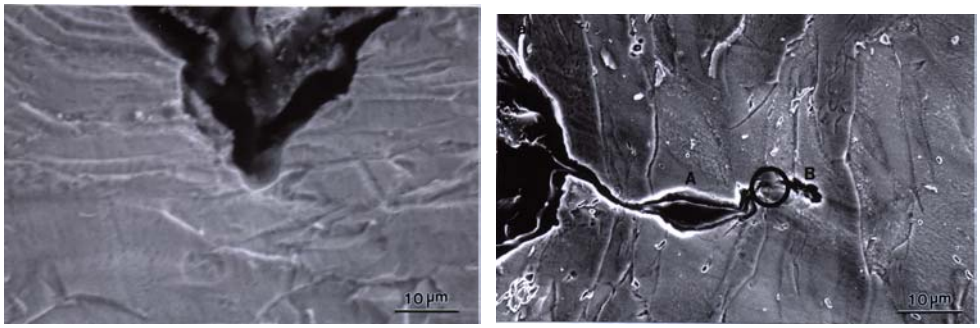

Figure 4 : Scanning electron micrograph of a crack tip in (a.) grade 2 titanium and (b.) grade 3 titanium. Both tests were performed at –1400 mV_{SCE}. The circle in Figure 4b highlights a region where the crack is connecting up between two microvoids.

samples failed so rapidly that there was insufficient times for the hydrides to nucleate and grow to any extent.

DISCUSSION

In general, hydrogen cracking is thought of as a brittle fracture mode. In steels, nickel-base alloys, and intermetallic compounds where atomic hydrogen is the embrittling species, the fracture mode is usually transgranular cleavage or intergranular fracture. Both of these fracture modes are associated with very limited ductility. In systems where hydrides form, the fracture mode is also usually reported to be brittle [1]. The most general models suggest that hydrides form at the crack tip in the tensile field of the crack. These hydrides then fracture in a brittle manner or a crack forms along the hydride-matrix interface.

In our study of the grade 2 and grade 3 titanium, we found no evidence of brittle failure. The fracture mode remained ductile, even though a decrease in the elongation ratio was found for the grade 3 material. Our results suggest that hydrides nucleate in

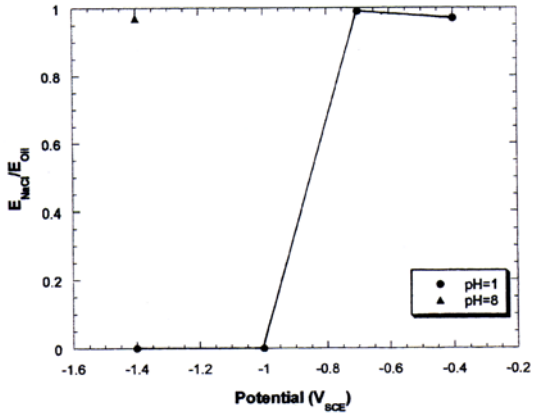

Figure 5: The elongation ratio plotted as a function of the electrochemical potential for Ti-5111. Results are shown for tests run in both pH=1 and pH=8 3.5%NaCl.

the matrix in front of the crack tip. These hydrides then act as sights for microvoid formation. As the stress in front of the crack tip increases, these microvoids connect up, leading to crack advance. New hydrides then form in front of the crack tip and the process is repeated. In the grade 2 material, the hydrides do not form in front of the crack tip and this process does not occur. The reasons why the grade 3 material forms hydrides in front of the crack tip whereas the grade 2 material does not form these hydrides has been discussed in previous publications [4,6]. In short, we propose that the main reason for this difference is the lower solubility of hydrogen in grade 3 material as a result of its higher interstitial content. In addition, the higher yield strength of the grade 3 material may contribute to its greater susceptibility to hydride-induced ductile failure.

When β-phase is present in the material but does not provide a continuous path through the material, the fracture mode should be similar to that reported above. This idea is consistent with the results of Nelson and Williams on Ti-6Al-4V [7,8]. Once the

β-phase forms a continuous pathway, as it does for Ti-5111, the mechanism of hydrogen embrittlement changes significantly. The β-phase has a higher solubility of hydrogen than does the α-phase, and hydrogen will diffuse more rapidly into the β-phase. Thus when the sample is tested in a sodium chloride solution under conditions where hydrogen is generated, the atomic hydrogen will quickly diffuse into the material through this phase and be primarily concentrated there. This high concentration then leads to embrittlement. This result is again similar to that reported by Nelson and Williams for Ti-6Al-4V that had been heat treated to have a continuous β-phase [7,8]. They found cracking along the α/β interfaces and that the fracture mode was a brittle cleavage along the α/β interface.

CONCLUSIONS

This paper has presented results for hydrogen embrittlement in three titanium-base materials. Two were commercial purity titanium in which only the α-phase was present. The third was an α/β alloy. The results showed in the commercial purity titanium that the embrittlement occurred through the formation of hydrides. However, the fracture was completely ductile and the hydrides acted as sights for void nucleation and growth. These voids were then connected up through a fracture process that led to crack advance. Thus, precipitation of hydrides in front of the crack tip is a critical feature of this model. In the α/β material, the fracture was brittle. As shown in reference 5, the crack propagated through the β-phase, which has a higher solubility for hydrogen and also provides a faster diffusion path. Thus by a change in the microstructure of the material, the fracture mode changes significantly.

ACKNOWLEDGMENTS

This research was supported by the United States Office of Naval Research under Grant No. N00014-96-0272. The authors would also like to thank Dr. Jenny Been, TIMET, for providing the Ti-5111 material and for many helpful discussion.

REFERENCES

1. Nelson, H.G. (1984). In: Embrittlement of Engineering Alloys, pp. 275-359, C.L. Briant and S.K. Banerji, (Eds.) Academic Press, New York.
2. Liu, C.T., Lee, E.H., and McKamey, C.G. (1989) Scripta Metall., 23, 875.
3. Wang, Z.F., Briant, C.L., and Kumar, K.S. (1999) Corrosion, 55, 128.
4. Wang, Z.F., Briant, C.L., and Kumar, K.S. (1998) Corrosion, 54, 553.
5. Wang Z.F., Chollocoop, N., Briant, C.L., and Kumar, K.S. (2001) Metall. Trans. to be published
6. Wang, Z.F., Briant, C.L., and Kumar, K.S. (2001) Corrosion 2001, Paper 01239, NACE, Houston, Texas.
7. Nelson, H.G., Williams, D.P., and Stein, J.E. (1972), Metall. Trans. 3, 469.
8. Nelson, H.G (1973) Metall. Trans. 4, 364.

Paper ICF100893OR

Hydrogen, Hydrides, and Crack Tip Deformation in Titanium

C.L. Briant, Z.F. Wang, and K.S. Kumar

Division of Engineering
Brown University
Providence, RI 02912 USA

ABSTRACT

This paper summarizes results obtained in our laboratory on the susceptibility of commercial purity titanium and the α/β titanium alloy Ti-5111 to hydrogen cracking. The tests were run under cathodic polarization in sodium chloride solutions. Cathodic potentials as low as $-1400 mV_{SCE}$ had little effect on the mechanical properties of grade 2 titanium, but grade 3 titanium showed a decrease in the elongation to failure as the electrochemical potential became more cathodic. However, the fracture mode remained ductile with microvoids nucleating at hydrides. Ti-5111 was very susceptible to hydrogen cracking when the pH of the solution was low and the electrochemical potential was cathodic, but hydrides did not appear to play a role in the cracking process.

KEYWORDS

titanium, hydrogen embrittlement, sodium chloride solutions, Ti-5111

INTRODUCTION

The mechanisms of hydrogen embrittlement have been a topic of great debate in past years. One reason for this is that the actual mechanism can vary significantly from one materials system to another [1]. In some materials, such as titanium and zirconium, the primary cause of embrittlement appears to occur through hydride formation. In other materials, such as steel and nickel-base materials, atomic hydrogen appears to be the primary cause of embrittlement. More recent studies of intermetallic compounds have suggested that the source of hydrogen is very important [2]. For example, in FeAl the presence of atomic hydrogen in the environment does not appear to have a great effect on mechanical properties, whereas water vapor can cause a significant decrease in elongation to failure.

Although one single mechanism will not explain hydrogen embrittlement, it is important to have complete descriptions of this problem in all important structural materials. We have recently examined hydrogen embrittlement in various grades of

commercial purity titanium as well as in titanium alloys. The results show that in commercial purity titanium hydrides play a dominant role in causing embrittlement, whereas in the α/β alloys they may play no role at all. By comparing these materials one can understand the different mechanisms that lead to embrittlement.

EXPERIMENTAL

In this paper we will discuss three different materials. Two of the materials were commercial purity titanium and the third was an α/β alloy, Ti5111. Their compositions are listed in Table I along with their basic mechanical properties. All were tested in the as-received condition. The two commercial purity titanium materials had an equiaxed grain structure and the Ti-5111 had a lamellar α/β microstructure.

The mechanical tests for these materials were all performed on single-edge notched sheet tensile samples. The thickness of the grade 2 and grade 3 samples was 1.12 mm and 0.62 mm, respectively, and that of the Ti-5111 was 2.56 mm. The notch had an included angle of 60^{o}. The samples were pulled to failure in a 3.5% solution of sodium chloride under various applied electrochemical potentials. We used the ratio of the elongation to failure in the sodium chloride solution to that in an inert oil held at the same temperature as a measure of susceptibility to hydrogen embrittlement. We will refer to this parameter as the elongation ratio in the text below. All tests were run with the solution at 70^{o}C. The pH of the solution used to test the commercial purity titanium was 1 and that used for the Ti-5111 was either 1 or 8. More details of the testing and post-test examination have been given in references 3 -5.

Table I
Alloy Composition and Mechanical Properties

Alloy	Composition (wt.%)	Yield Strength (MPa)	UTS (MPa)	Elongation to Failure
Grade 2	Ti-0.14O-0.02C-0.008N-0.08Fe	344	506	28
Grade 3	Ti-0.21O-0.01C-0.009N-0.16Fe	489	603	24
Ti-5111	Ti-5Al-1Sn-1Zr-1V-0.08Mo	750 (nominal)	Not Measured	Not Measured

RESULTS

Figure 1a shows the elongation ratio for grades 2 and 3 titanium plotted as a function of electrochemical potential. The results show that there is very little change in the elongation ratio for grade 2 titanium as the electrochemical potential is made more cathodic. This result was obtained, even though other experiments had shown that hydrides begin to form in this material at electrochemical potentials below –600 mV_{SCE} and that thick layers of hydrides are formed at potentials near –1400 mV_{SCE}. In contrast, grade 3 titanium showed a measurable loss in the elongation ratio as the electrochemical potential was made more cathodic. Figure 1b shows the elongation ratio at –1400 mV_{SCE}

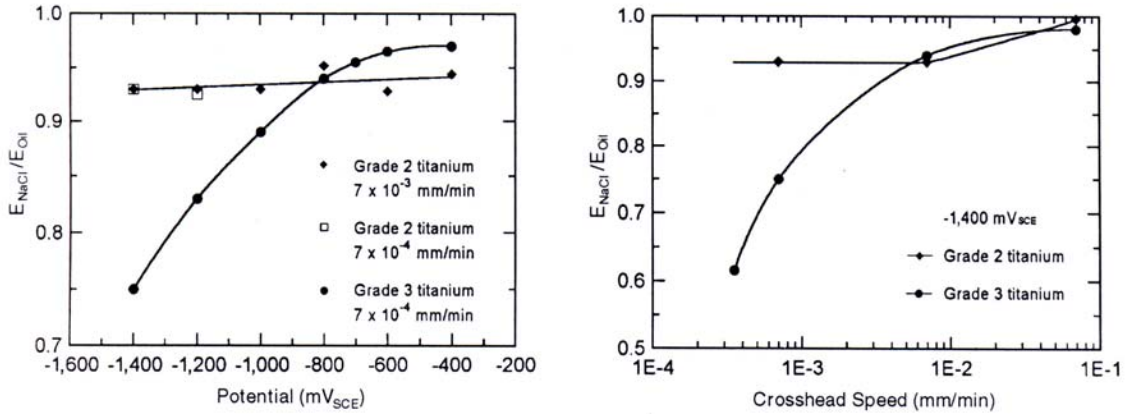

Figure 1: (a.) The elongation ratio plotted as a function of electrochemical potential for grade 2 and grade 3 titanium. The crosshead speeds are given in the figure. (b.) The elongation ratio plotted as a function of crosshead speed for grade 2 and grade 3 titanium.

for both grade 2 and grade 3 titanium plotted as a function of crosshead speed. The results show that as the crosshead speed decreased the elongation ratio stayed approximately constant for grade 2 titanium, whereas the elongation ratio dropped for samples of the grade 3 titanium.

Examination of the fracture surfaces showed that under all conditions the grade 2 titanium underwent ductile failure. An example is shown in Figure 2a. The grade 3 titanium had a similar fracture surface when tested in oil or under anodic conditions. However, as the elongation ratio decreased for the grade 3 titanium, the fracture surface showed new features. These included brittle secondary cracks on the surface, some evidence of large voids on the surface, and evidence of a new population of fine scale voids. A micrograph is shown in Figure 2b. Additional information was obtained by examining the hydride that formed on the surface of a sample after cathodic charging. In the case of the grade 2 titanium, we found that there was a thick layer of hydrides, as shown in Figure 3a, but that beneath this layer few hydrides were observed. In the grade 3 material, this thick layer was also observed, but in addition there were hydrides beneath this thick layer extending into the matrix, as shown in Figure 3b. In flat samples charged for 24 hours at an electrochemical potential of –1000 mVSCE, hydrides extended

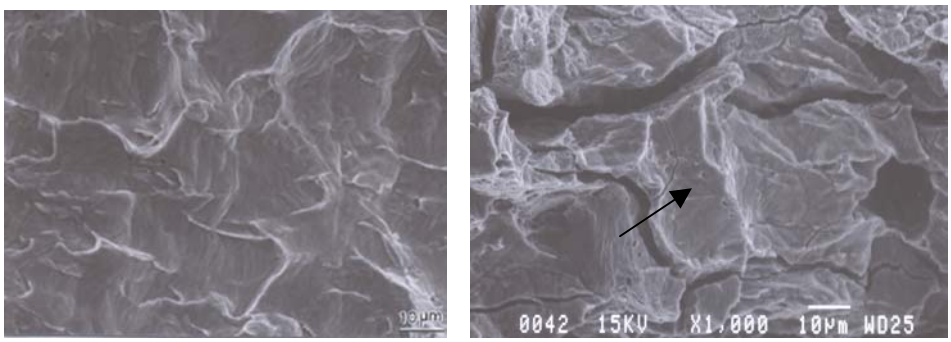

Figure 2: Scanning electron micrographs of (a.) grade 2 titanium tested at –400 mV_{SCE} and (b.) grade 3 titanium tested at –1400 mV_{SCE}. The arrow points out fine microvoids.

approximately 50 μm into the bulk and for an electrochemical potential of –1400 mV_{SCE} the hydrides extended approximately 90 μm into the bulk.

We also examined samples in which the crack had been stopped before proceeding completely through the sample. In the grade 2 material we always found a blunted crack, as shown in Figure 4a, with no evidence of cracking ahead of the rounded crack tip. In contrast, in the grade 3 material we found a sharper crack extending from the blunted crack tip, with evidence that microvoids were forming ahead of this blunted crack and that these microvoids were connecting up to allow the crack to extend.

We now consider the results for Ti-5111. Figure 5 shows the elongation ratio of this material plotted as function of applied potential. In the pH=8 solution, there was no loss in elongation even though the electrochemical potential was very cathodic. In contrast, in the pH=1 solution the elongation ratio was essentially zero when the electrochemical potential was below –1000 mV_{SCE}. The fracture surfaces of the samples that showed no elongation to failure were very brittle, and examination of propagating cracks in these samples showed that they tended to go through the β-phase (5). There was no evidence of hydride formation in these samples, even though in the pH=1 solution the hydrides were found to precipitate at potentials below –500 mV_{SCE}. However, these

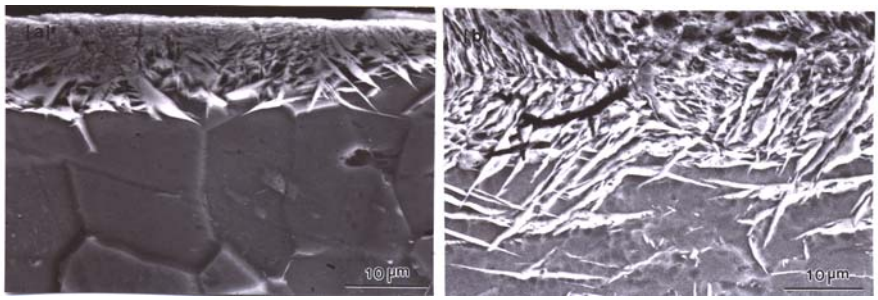

Figure 3 : Scanning electron micrographs of hydrides on the surface of (a.) grade 2 and (b.) grade 3 titanium after cathodic charging.

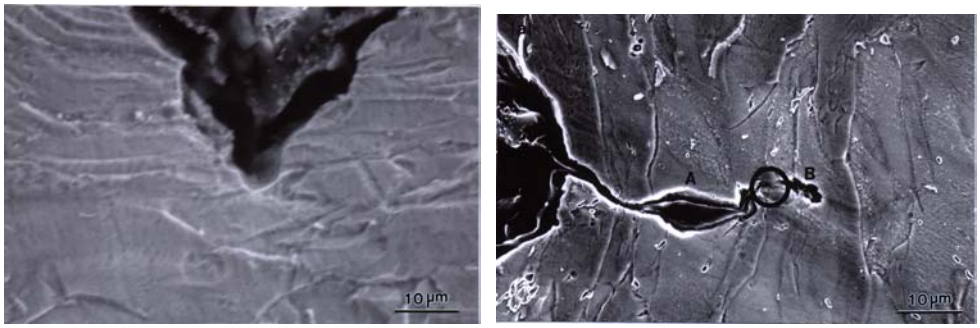

Figure 4 : Scanning electron micrograph of a crack tip in (a.) grade 2 titanium and (b.) grade 3 titanium. Both tests were performed at –1400 mV_{SCE}. The circle in Figure 4b highlights a region where the crack is connecting up between two microvoids.

samples failed so rapidly that there was insufficient times for the hydrides to nucleate and grow to any extent.

DISCUSSION

In general, hydrogen cracking is thought of as a brittle fracture mode. In steels, nickel-base alloys, and intermetallic compounds where atomic hydrogen is the embrittling species, the fracture mode is usually transgranular cleavage or intergranular fracture. Both of these fracture modes are associated with very limited ductility. In systems where hydrides form, the fracture mode is also usually reported to be brittle [1]. The most general models suggest that hydrides form at the crack tip in the tensile field of the crack. These hydrides then fracture in a brittle manner or a crack forms along the hydride-matrix interface.

In our study of the grade 2 and grade 3 titanium, we found no evidence of brittle failure. The fracture mode remained ductile, even though a decrease in the elongation ratio was found for the grade 3 material. Our results suggest that hydrides nucleate in

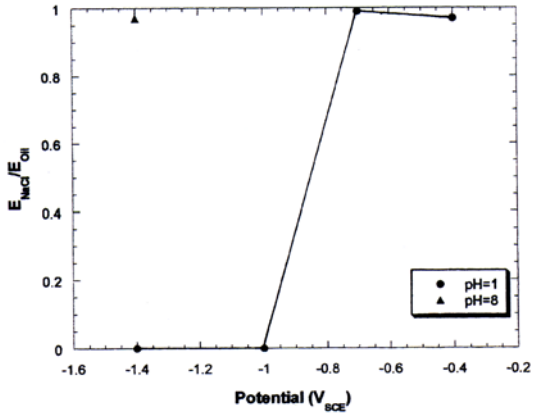

Figure 5: The elongation ratio plotted as a function of the electrochemical potential for Ti-5111. Results are shown for tests run in both pH=1 and pH=8 3.5%NaCl.

the matrix in front of the crack tip. These hydrides then act as sights for microvoid formation. As the stress in front of the crack tip increases, these microvoids connect up, leading to crack advance. New hydrides then form in front of the crack tip and the process is repeated. In the grade 2 material, the hydrides do not form in front of the crack tip and this process does not occur. The reasons why the grade 3 material forms hydrides in front of the crack tip whereas the grade 2 material does not form these hydrides has been discussed in previous publications [4,6]. In short, we propose that the main reason for this difference is the lower solubility of hydrogen in grade 3 material as a result of its higher interstitial content. In addition, the higher yield strength of the grade 3 material may contribute to its greater susceptibility to hydride-induced ductile failure.

When β-phase is present in the material but does not provide a continuous path through the material, the fracture mode should be similar to that reported above. This idea is consistent with the results of Nelson and Williams on Ti-6Al-4V [7,8]. Once the

β-phase forms a continuous pathway, as it does for Ti-5111, the mechanism of hydrogen embrittlement changes significantly. The β-phase has a higher solubility of hydrogen than does the α-phase, and hydrogen will diffuse more rapidly into the β-phase. Thus when the sample is tested in a sodium chloride solution under conditions where hydrogen is generated, the atomic hydrogen will quickly diffuse into the material through this phase and be primarily concentrated there. This high concentration then leads to embrittlement. This result is again similar to that reported by Nelson and Williams for Ti-6Al-4V that had been heat treated to have a continuous β-phase [7,8]. They found cracking along the α/β interfaces and that the fracture mode was a brittle cleavage along the α/β interface.

CONCLUSIONS

This paper has presented results for hydrogen embrittlement in three titanium-base materials. Two were commercial purity titanium in which only the α-phase was present. The third was an α/β alloy. The results showed in the commercial purity titanium that the embrittlement occurred through the formation of hydrides. However, the fracture was completely ductile and the hydrides acted as sights for void nucleation and growth. These voids were then connected up through a fracture process that led to crack advance. Thus, precipitation of hydrides in front of the crack tip is a critical feature of this model. In the α/β material, the fracture was brittle. As shown in reference 5, the crack propagated through the β-phase, which has a higher solubility for hydrogen and also provides a faster diffusion path. Thus by a change in the microstructure of the material, the fracture mode changes significantly.

ACKNOWLEDGMENTS

This research was supported by the United States Office of Naval Research under Grant No. N00014-96-0272. The authors would also like to thank Dr. Jenny Been, TIMET, for providing the Ti-5111 material and for many helpful discussion.

REFERENCES

1. Nelson, H.G. (1984). In: Embrittlement of Engineering Alloys, pp. 275-359, C.L. Briant and S.K. Banerji, (Eds.) Academic Press, New York.
2. Liu, C.T., Lee, E.H., and McKamey, C.G. (1989) Scripta Metall., 23, 875.
3. Wang, Z.F., Briant, C.L., and Kumar, K.S. (1999) Corrosion, 55, 128.
4. Wang, Z.F., Briant, C.L., and Kumar, K.S. (1998) Corrosion, 54, 553.
5. Wang Z.F., Chollocoop, N., Briant, C.L., and Kumar, K.S. (2001) Metall. Trans. to be published
6. Wang, Z.F., Briant, C.L., and Kumar, K.S. (2001) Corrosion 2001, Paper 01239, NACE, Houston, Texas.
7. Nelson, H.G., Williams, D.P., and Stein, J.E. (1972), Metall. Trans. 3, 469.
8. Nelson, H.G (1973) Metall. Trans. 4, 364.

PAPER REFERENCE: ICF100447OR

IMAGE ANALYSIS OF HYDROGEN-ASSISTED MICRO-DAMAGE IN PROGRESSIVELY DRAWN PEARLITIC STEEL

J. Toribio, F.J. Ayaso and E. Ovejero

Department of Materials Science, University of La Coruña,
ETSI Caminos, Campus de Elviña, 15192 La Coruña, Spain

ABSTRACT

This paper analyzes the evolution of hydrogen-assisted damage topography in progressively drawn pearlitic steels. The fractographic analysis revealed changes in the microscopic topographies depending on the fracture propagation mode, with an evolution from pure *tearing topography surface* (TTS) in slightly drawn steels to a kind of *very deformed* TTS (in direction of cold drawing or wire axis) in heavily drawn steels. An image analysis technique was used to analyze the different microscopic fracture modes, thus finding correlations between them. Results showed that the very deformed TTS *really* observed in heavily drawn steels could be *virtually* obtained by deforming –in the drawing direction– the micrograph of slightly drawn steels. This fact provides bases to elucidate the real physical micromechanism of hydrogen-assisted fracture in pearlitic steels.

KEYWORDS

Pearlitic steel, cold drawing degree, hydrogen-assisted micro-damage, fracture micromechanisms

INTRODUCTION

Cold drawn eutectoid steels are high-strength materials used as constituents of prestressed concrete structures in civil engineering. Previous research [1,2] dealt with the fracture of this kind of steel in aggressive environment, showing that heavily drawn prestressing steels exhibit anisotropic fracture behavior associated with changes in the crack propagation direction and transition from mode I to mixed mode propagation approaching the wire axis direction.

In more recent works [3,4] this research line has been developed to analyze steels with intermediate degree of cold drawing, in order to relate –in the materials science manner– the macroscopic behavior of the steels with their microstructure at the two basic microstructural levels of the pearlite colonies [5,6] and the pearlitic lamellar microstructure [7,8], as a function of the cold drawing degree achieved during the manufacturing process to produce the final commercial product.

This paper goes further in the research line and studies –by means of image analysis techniques– the evolution of hydrogen-assisted microdamage topographies at the microscopic levels for the different degrees

of cold drawing, in order to elucidate the physical micromechanisms of fracture of pearlitic steels in hydrogen environments, taking into account the progressively anisotropic fracture behaviour as the strain hardening level produced by cold drawing increases.

MATERIALS AND MICROSTRUCTURE

The materials used in this work were high-strength steels taken from a real manufacturing process at EMESA TREFILERIA, S.A. Wires with different degrees of cold drawing were obtained by stopping the manufacturing chain and taking samples from the intermediate stages. The different steels were named with digits 0 to 6 which indicate the number of cold drawing steps undergone. Table 1 shows the chemical composition common to all steels, and Table 2 includes the diameter (D_i), the yield strength (σ_Y), the ultimate tensile stress (σ_R) and the fracture toughness (K_{IC}).

TABLE 1
CHEMICAL COMPOSITION (wt %) OF THE STEELS

C	Mn	Si	P	S	Cr	V	Al
0.80	0.69	0.23	0.012	0.009	0.265	0.060	0.004

TABLE 2
DIAMETER REDUCTION AND MECHANICAL PROPERTIES OF THE STEELS

Steel	0	1	2	3	4	5	6
D_i (mm)	12.00	10.80	9.75	8.90	8.15	7.50	7.00
σ_Y (GPa)	0.686	1.100	1.157	1.212	1.239	1.271	1.506
σ_R (GPa)	1.175	1.294	1.347	1.509	1.521	1.526	1.762
K_{IC} (MPam$^{1/2}$)	60.1	61.2	70.0	74.4	110.1	106.5	107.9

The microstructural evolution with cold drawing was studied in previous woks [5-8]. Attention was paid to the evolution with cold drawing of the two basic microstructural levels: the pearlite colonies (first level) and the pearlitic lamellae (second level). With regard to the first microstructural level, a progressive elongation and orientation of the pearlitic colonies in the cold drawing direction (wire axis) was observed [5,6]. In the matter of the second microstructural level, the analysis showed an increasing closeness of packing (with decrease of the interlamellar spacing) and a progressive orientation of the pearlitic lamellar microstructure in the cold drawing direction [7,8]. Therefore, both pearlite colonies and pearlitic lamellar microstructure tend to align to a direction quasi-parallel to the wire axis as cold drawing proceeds. Figures 1 and 2 (cf.[8]) show the pearlitic microstructure of steels 0 and 6 respectively, by means of micrographs corresponding to longitudinal metallographic sections of the wires (those sections containing the wire axis). It is seen that, while the microstructure of steel 0 (hot rolled bar which is not cold drawn at all) is randomly oriented, the microstructure of steel 6 (prestressing steel heavily cold drawn) is markedly oriented in the direction of the wire axis (or cold drawing direction) which corresponds to the vertical side of the

micrographs. Figures 3a and 3b plot the quantification of this orientation effect at the levels of colonies and lamellae respectively.

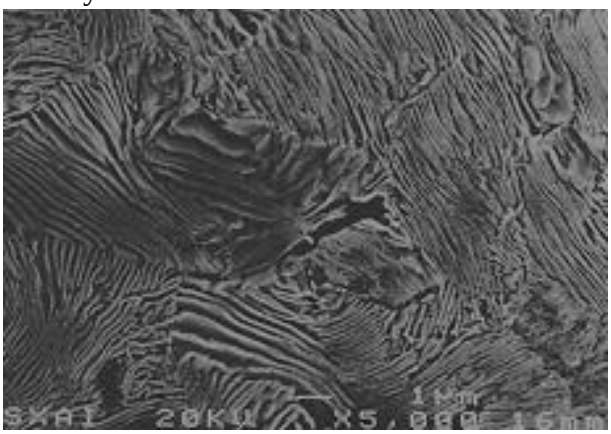

Figure 1: Microstructure of steel 0 (L-section)

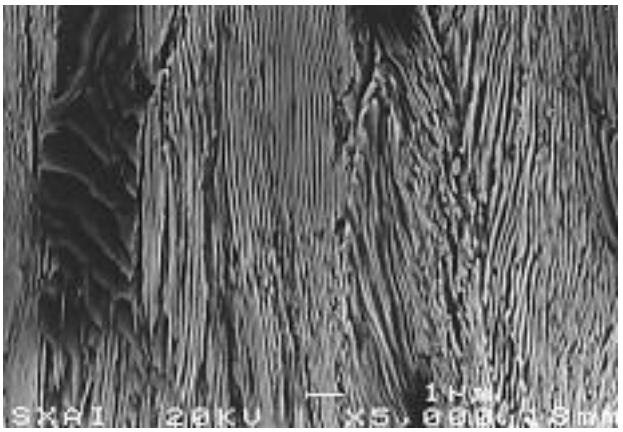

Figure 2: Microstructure of steel 6 (L-section)

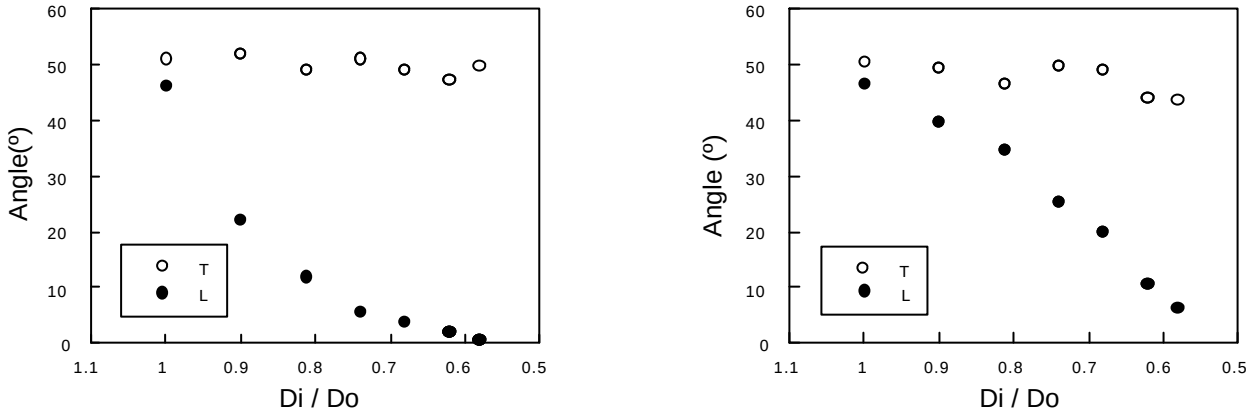

(a) (b)

Figure 3: Evolution with cold drawing of the orientation angles of pearlite colonies (a) and lamellae (b), in the longitudinal (L) and transverse (T) metallographic sections. In (a) the angle was measured between the major axis of the colony (modeled as an ellipsoid) and the axial direction (L section) or the radial one (T section). In (b) the angle was measured between the direction of the lamellae in the metallographic cut and the axial direction (L section) or the radial one (T section).

EXPERIMENTAL PROGRAM

To analyze the hydrogen assisted cracking (HAC) behavior of the different steels, slow strain rate tests were performed on precracked steel wires. Samples were precracked by axial fatigue in the normal laboratory air environment to produce a transverse precrack, so that the maximum stress intensity factor during the last stage of fatigue precracking was $K_{max} = 0.30K_{IC}$, and the crack depth was a = 0.30D in all cases, with D as the wire diameter. After precracking, samples were placed in a corrosion cell containing aqueous solution of 1g/l $Ca(OH)_2$ plus 0.1g/l NaCl (pH=12.5). All tests were conducted under potentiostatic control at –1200 mV vs. SCE at which the environmental mechanism is HAC [1]. The applied displacement rate in axial direction was constant during each test and proportional to each wire diameter: 1.7 $x10^{-3}$ mm/min for steel 6 and 3.0 $x10^{-3}$ mm/min for steel 0.

The experimental results showed an important fact: the HAC behaviour becomes more anisotropic as the cold drawing degree increases, as depicted in Figure 4 by means of the *fracture profile* (macroscopic topography of the fracture surface). Thus a transverse crack tends to change its propagation direction to approach the wire axis or cold

drawing direction and an initial mode I growth evolves towards a mixed mode propagation (*strength anisotropy* with regard to HAC).

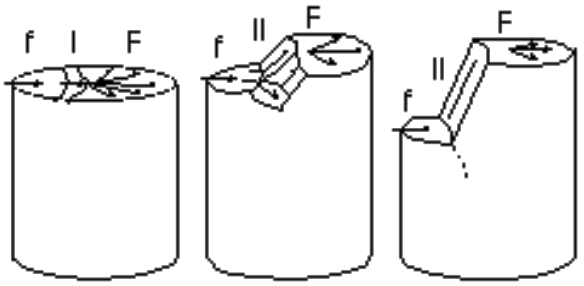

Figure 4: Evolution with cold drawing of fracture surfaces in HAC, from slightly to heavily drawn steels (left to right). Increasingly anisotropic behaviour with cold drawing (f: fatigue; I: mode I propagation; II: mixed mode propagation; F: final fracture by cleavage).

FRACTOGRAPHIC ANALYSIS

A fractographic analysis by scanning electron microscopy (SEM) was carried out on the fracture surfaces to elucidate the microscopic modes of fracture. Figures 5 and 6 offer respectively the microscopic topographies for hot rolled bar (steel 0 which is not cold drawn at all) and for a heavily drawn prestressing steel (steel 6 which has suffered six steps of cold drawing).

In the hot rolled bar (steel 0; cf. Figure 5) there is a subcritical crack growth in mode I by *tearing topography surface* (TTS, cf. [9-12]) before the unstable cleavage-like propagation associated with mechanical final fracture. This special microscopic fracture mode is undoubtedly associated with hydrogen-assisted micro-damage in steels with pearlitic microstructure [11-12].

In the heavily drawn prestressing steel wire (steel 6; cf. Figure 6) the microscopic fracture mode is a kind of *very deformed* TTS, the deformation axis coincident with the cold drawing direction. This topography is produced as a consequence of the macroscopic crack deflection with mode II propagation, *as if* a previous TTS mode had been strained by shear in its own fracture plane (quasi-parallel to the drawing axis).

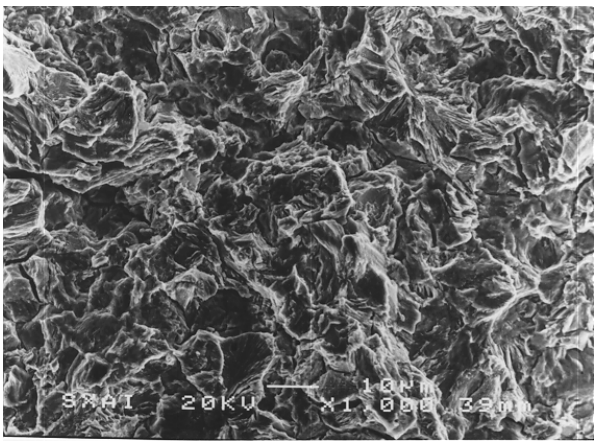

Figure 5: Microscopic fracture mode in steel 0.

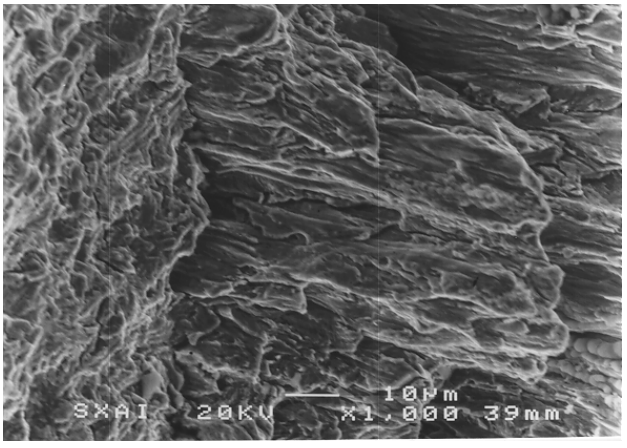

Figure 6: Microscopic fracture mode in steel 6.

The microscopic fracture modes of Figures 5 and 6 may be classified as *hydrogen damage topographies* (HDT). The appearance of this generic topography is a function of the degree of drawing so that it can be noted as $HDT^{(i)}$, where *i* is the number of cold drawing steps undergone by the steel. Thus the topography $HDT^{(i)}$ evolves form pure TTS (which corresponds *exactly* with the mode described in [9-12]) in steel 0 to $HDT^{(6)}$ (a kind of TTS *very*

deformed in the wire axis or cold drawing direction) in steel 6. Between them, a wide range of HDT topographies with intermediate degree of deformation was observed.

DISCUSSION

Form the observation of the fractographs corresponding to $HDT^{(0)}$ (Figure 5) and $HDT^{(6)}$ (Figure 6), the following statements may be drawn:

- All the HDT modes for different degrees of cold drawing are associated to the same HAC mechanism (cathodic potentials and decrease of stress intensity factor).

- A generic $HDT^{(i)}$ exhibits an *apparent deformation* (in the fractograph) which is an increasing function of the degree of cold drawing (represented by the superindex *i* which indicates the number of cold drawing steps undergone by the steel).

- Such a deformation seems to be oriented in the direction of the larger size of the fractograph, i.e., in a direction quasi-parallel to the wire axis or cold drawing direction.

Thus the question arises about whether or not a geometric relationship does exist between the HDT modes so that one can be *virtually* obtained by deformed a previous one (associated with a lower degree of cold drawing). This virtual transformation is sketched in Figure 7, in which the initial fractograph $HDT^{(0)}$ (or pure TTS) in the hot rolled bar is virtually oriented in the direction of HAC in the cold drawn material and deformed by transformations in the radial, hoop and axial directions.

The parameters of the geometric transformations are obtained by the hypothesis of conservation of volume in the Plasticity theory and represent *the virtual deformation* which should be applied to the $HDT^{(i)}$ to obtain other $HDT^{(j)}$ (j > i). Figure 8 shows the results of this virtual deformation process to obtain $HDT^{(6)}$ from $HDT^{(4)}$, where it is seen that this virtual topography really resembles the real one shown in Figure 6, which confirms that the micromechanism of fracture is similar in both cases.

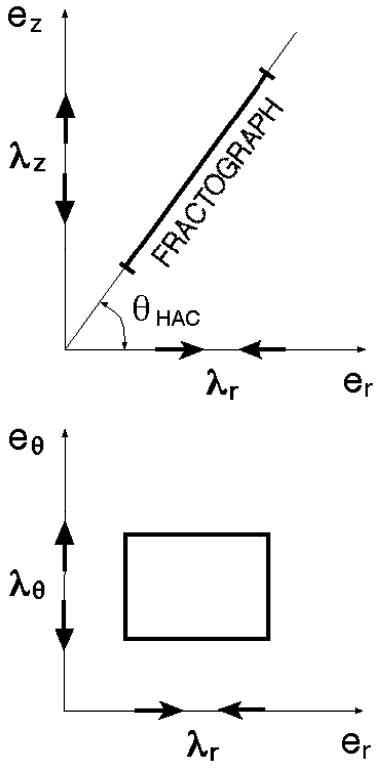

Figure 7: *Virtual* deformation of the fractograph.

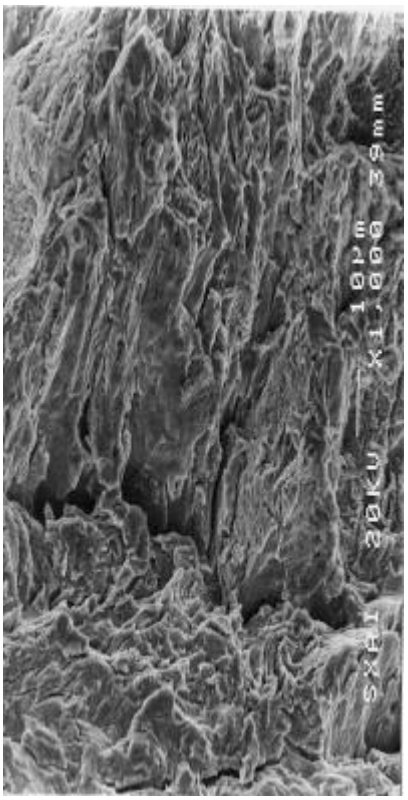

Figure 8: *Virtual* $HDT^{(6)}$ by deformation of $HDT^{(4)}$.

CONCLUSIONS

In eutectoid steels, the microstructural changes produced by the cold drawing process affect the macroscopic behavior with regard to environmentally assisted cracking in general and hydrogen assisted cracking (or hydrogen embrittlement) in particular.

In heavily drawn steels, the microscopic fracture mode is a kind of very deformed tearing topography surface, the deformation axis coincident with the cold drawing direction. This topography is produced as a consequence of the macroscopic crack deflection with mode II propagation.

A proportional relationship was found between the different hydrogen damage topographies (HDT): the very deformed TTS *really* observed in heavily drawn steels could be *virtually* obtained by deforming the micrograph of the pure TTS (associated with the hot rolled material) in the direction of cold drawing.

Acknowledgements
The financial support of this work by the Spanish CICYT (Grant MAT97-0442) and *Xunta de Galicia* (Grant XUGA 11802B97) is gratefully acknowledged. In addition, the authors wish to express their gratitude to EMESA TREFILERIA S.A. (La Coruña, Spain) for providing the steel used in the experimental programme.

REFERENCES

1. Parkins, R.N., Elices, M., Sánchez-Gálvez, V. y Caballero, L. (1982). *Corros. Sci*. **22**, 379.
2. Lancha, A.M. (1987). Ph. D. Thesis, Complutense University of Madrid.
3. Toribio, J. and Ovejero, E. (1998). *Int. J. Fracture* **90**, L21.
4. Toribio, J. and Ovejero, E. (1999). *Scripta Mater* **40**, 943.
5. Toribio, J. and Ovejero, E. (1997). *Mater. Sci. Engng*. **A234-236**, 579.
6. Toribio, J. and Ovejero, E. (1998). *J. Mater. Sci. Lett*. **17**, 1037.
7. Toribio, J. and Ovejero, E. (1998). *Scripta Mater*. **39**, 323.
8. Toribio, J. and Ovejero, E. (1998). *Mech. Time-Dependent Mater*. **1**, 307.
9. Thompson, A. W. and Chesnutt, J.C. (1979). *Metall. Trans*. **10A**, 1193.
10. Costa, J.E. and Thompson, A.W. (1982). *Metall. Trans*. **13A**, 1315.
11. Toribio, J., Lancha, A.M. and Elices, M. (1991) *Scripta Metall. Mater*. **25**, 2239.
12. Toribio, J., Lancha, A.M. and Elices, M. (1992) *Metall. Trans*. **23A**, 1573.

IMPACT STRENGTH OF CRACKED STRUCTURAL MEMBER

I. Maekawa and K. Uda
Kanagawa Institute of Technology
1030 Shimo-Ogino, Atsugi, Kanagawa, Japan

ABSTRACT

Impact tension, bending and torsion experiments are performed using precracked strip and pipe specimens made of polymethyl methacrylate. The dynamic strain concentration factor, $K_{d,\varepsilon}$, is evaluated on the basis of the dynamic strain histories measured at the crack-tip and the smooth portion of each specimen in terms of the strain gauge method. The magnitude of $K_{d,\varepsilon}$ of the short specimen is larger than that of the long one except for the pipe in the case of impact bending. The similar influence of specimen length on the dynamic stress concentration factor $K_{d,\sigma}$ is evaluated by numerical analysis. When the dynamic stress concentration factor is evaluated for the incident stress wave without the influence of reflected waves, it is influenced by the crack-tip geometry. But, the crack-tip geometry dose not influence on the static stress concentration factor, $K_{s,c}$, which is evaluated in a small region at a crack-tip by a new method.

KEYWORDS

Strip, pipe, PMMA, crack, impact experiment, numerical analysis, stress concentration factor.

1. INTRODUCTION

Under a static load, the stress intensity factor is conveniently used to evaluate the integrity of a cracked structural member without regarding for the size effect, if the product of the stress applied and the square root of crack length is equal to that of model for an analogous geometry. However, according to our previous investigations, the fracture strength of a specimen subjected to an impact force showed size dependence, which is named as the mechanical size effect [1,2]. Therefore, it is considered that the investigation on the influence of the length on the impact fracture strength of cracked member is important to secure the safe design. However, no investigations of this type have been reported except for our previous papers[1,2]. Thus, this report intends to clarify the influence of specimen length on the impact fracture strength using cracked strip and pipe specimens made of polymethyl methacrylate (PMMA).

Numerical analyses were also performed to consider the experimental results. Since the influence of the reflected waves is included in these results. Then, the influence of the crack-tip geometry on the dynamic stress concentration factor was also considered without the influence of the reflected waves. Furthermore, it has been pointed out that macroscopic stress analysis for a structural member should be related to the microscopic consideration, taking into account the atomic-level mechanical condition, in order to clarify the fracture mechanism [3]. But, microscopic

investigations do not always consider the loading condition [4,5]. Then, the influence of the crack-tip geometry on the static stress concentration factor is also numerically analyzed by a new method, which enable us to consider the microscopic stress concentration at a crack-tip under a given macroscopic loading condition, and the results were compared with the results of the investigation on the dynamic stress concentration factor.

2. EXPERIMENTAL

2.1 Preparation of Specimens

Long and short strip and pipe specimens made of PMMA were prepared. The Young's modulus and the density of this material are 2.99GPa and $12 \times 10^2 kg/m^3$, respectively. The width and the thickness of strip specimens were 80 and 5mm, respectively. The crack length, which was introduced on one side of each strip using cutter and falling weight, was 10mm. The outer and inner diameters of pipe specimens were 30 and 25mm, respectively, and a partial circumferential precrack was introduced with the length of 16, 12 and 19mm for impact tension, bending and torsion experiments, respectively.

2.2 Experimental Method and the Results

Impact tension, bending and torsion experiments were performed by the falling weight method, as shown in Figs. 1(a) ~ (e). In the case of the impact bending experiment, the cracked side of the specimen was set as for the tensile side, as shown in Figs.1 (b) and (d). Dynamic strains were measured by strain gages cemented at the crack-tip and the smooth portion of every specimen. The distance between a crack-tip and the centerline of the strain gage was 0.5mm. In the case of impact torsion, strain gauges were cemented at the crack-tip and the smooth portion of pipe at an angle of 45° to the axis of pipe, respectively. Every crack extended obliquely to the axis of pipe by an impact torsion. Typical examples of strain history are shown in Figs.2(a) ~ (d).

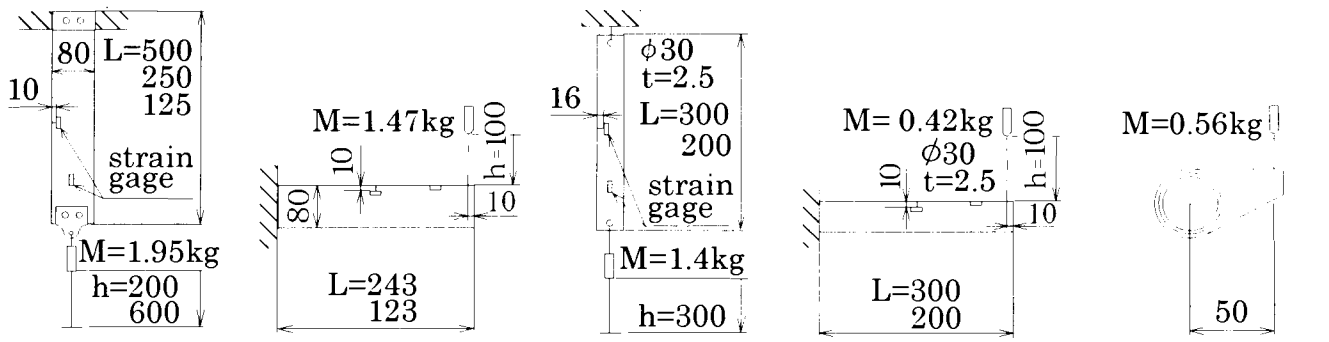

(a)Strip, tension (b)Strip, bending (c)Pipe, tension (d)Pipe, bending (e)Pipe,tortion (φ30,L=300,400)

Fig.1 Schematic illustrations of experiment.

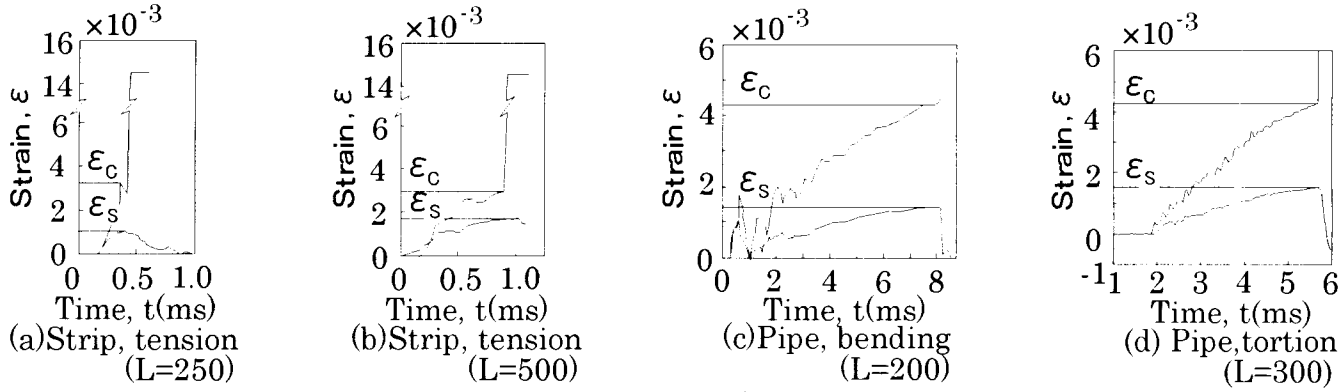

(a)Strip, tension (L=250) (b)Strip, tension (L=500) (c)Pipe, bending (L=200) (d) Pipe,tortion (L=300)

Fig.2 Typical examples of strain history.

Abrupt rise in strain is evident in each strain history measured at the crack-tip. This abrupt rise in strain was caused by the fracture of the strain gage due to the crack extension, and all specimens were fractured in a brittle manner. Thus, the strain, ε_c, at this point was considered to correspond to the impact fracture strength of the cracked specimen. On the other hand, no abrupt rise was observed in the strain history measured at the smooth portion of the specimen, but the maximum strain, ε_s, was observed at almost the same time as the time of the above mentioned abrupt rise in the strain history at the crack-tip. Next, the dynamic strain concentration factor was defined by $K_{d,\varepsilon} = \varepsilon_c / \varepsilon_s$. The influence of specimen length on $K_{d,\varepsilon}$ was shown in Fig.3.

In Fig.3, the magnitude of $K_{d,\varepsilon}$ of the short specimen is larger than that of the long one in all cases, except for the case of the impact bending of the pipe specimen. Comparing Figs.2 (a) and (b), it is evident that the magnitude of ε_c is almost the same, but that ε_s of the long specimen is slightly larger than that of the short one. The time, τ_c, to attain the fracture strain, ε_c, of the long specimen is also longer than that of the short specimen. This result implies that the stress amplitude was increased by the superposition of stress waves reflected at both ends of the specimen. However, in the case of impact bending, the magnitude of $K_{d,\varepsilon}$ of the short pipe specimen is little bit smaller than that of the long one, as shown above. In order to consider the reason for this, numerical analyses were performed by the finite element method (FEM) employing the DYNA3D.

3. NUMERICAL CONSIDERATIONS

3.1. *Influence of Specimen Length on the Dynamic Stress Concentration Factor*

The strip and pipe models were made of PMMA and divided into 400 and 600 elements, respectively. Typical examples of stress history are shown in Figs.4 (a) and (b). The stress wave propagates with the velocity, v, then, it needs the time $\tau_L = L/v$ to travel the specimen length, L. Since the time τ_L is shorter than the time τ_c to attain the maximum stress amplitude, σ_c, after the arrival of wave at the crack-tip, reflected waves were included in the maximum amplitude. Therefore, the dynamic stress concentration factor, $K_{d,\sigma}$, which was defined as the ratio of σ_c to σ_s at the smooth portion of model, was influenced by the length of model as shown in Fig. 5. Where, σ_s is the stress averaged for the time τ_c. Thus, the length dependences of $K_{d,\varepsilon}$ and $K_{d,\sigma}$ are also understood by considering the effect of superposition of mechanical waves, which means both strain and stress waves.

However, in the case of the pipe model, stress waves propagated in spirally between the outer and inner surfaces. Then, it is supposed that the dynamic stress distribution will be very complicated and different from other cases. This is the reason for the different length dependence. But, the computation needs very long time and so an exact analysis shall be performed in the future. In the case of impact torsion, the shearing stress showed very complicated history. And crack extended obliquely for the axis of pipe. Then, the fracture would be caused by the normal stress at the crack-tip. Therefore, the tensile stress component should be used rather than the shearing stress component in order to evaluate the dynamic stress concentration factor. However, the stress concentration factor for the tensile stress was considered in the case of impact tension as described above. Thus, stress history and the stress concentration factor are not described in the case of impact torsion.

3.2. *Influence of Crack-tip Geometry on the Dynamic Stress Concentration Factor*

As described above, reflected waves were included in the maximum amplitude, and the investigation for the microscopic region at a crack-tip is indispensable to clarify the fracture mechanism. Then, the influence of the crack-tip geometry on the dynamic stress concentration factor was numerically investigated for the incident wave without the influence of reflected waves. When an impact tension was imposed with the amplitude of 2MPa on the

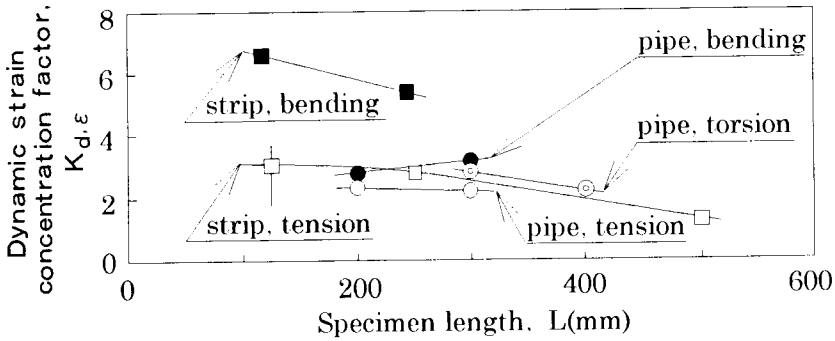

Fig.3 Influence of specimen length on $K_{d,\varepsilon}$.

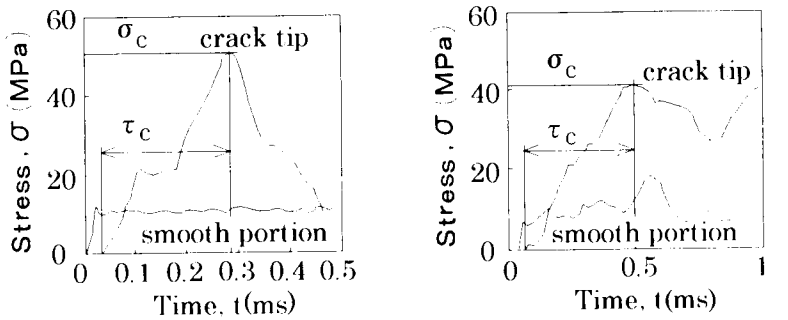

Fig.4 Examples of stress history.

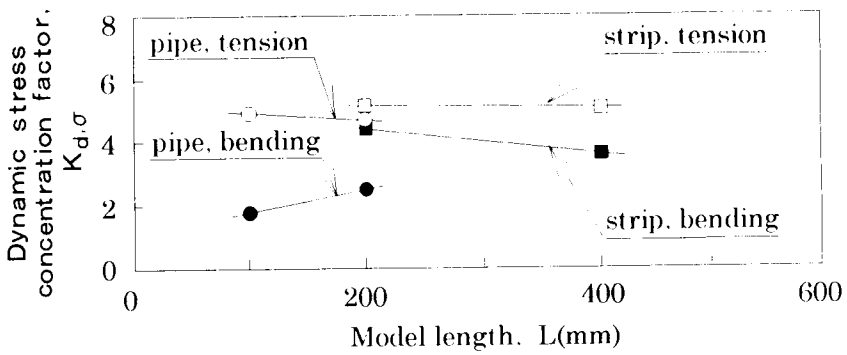

Fig.5 Influence of model length on $K_{d,\sigma}$.

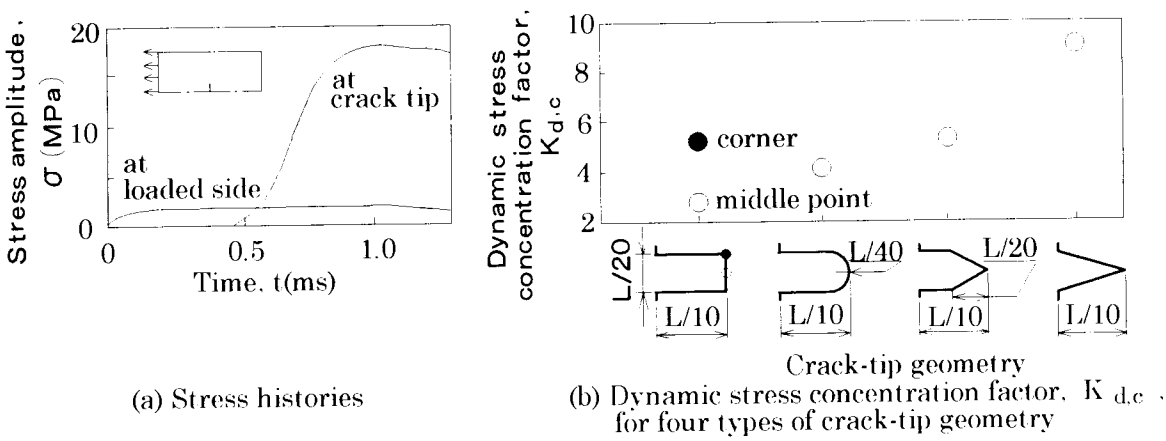

(a) Stress histories

(b) Dynamic stress concentration factor, $K_{d,c}$, for four types of crack-tip geometry

Fig.6 Dynamic stress concentration factor, $K_{d,c}$.

left side of the strip, which has a central crack, the stress histories were recorded at the loaded side and at the crack-tip as shown in Fig.6 (a). In this figure, the peak stress was recorded at the crack-tip. The dynamic stress intensity factor also shows similar peak [6]. In Fig.6 (a), no reflected waves came back to the crack-tip yet until the peak stress was attained. In this case, the dynamic stress concentration factor, $K_{d,c}$ was defined as the ratio of the peak stress to the stress amplitude of incident wave and shown in Fig.6 (b) for five types of crack-tip geometries. According to this figure, the magnitude of $K_{d,c}$ was influenced by the crack geometry.

3.3 *Influence of Crack-tip Geometry on the Static Stress Concentration Factor*

It is also important to determine how the dynamic stress concentration factor is different from static one. Thus, the influence of the crack-tip geometry on the static stress concentration factor was numerically investigated by a new

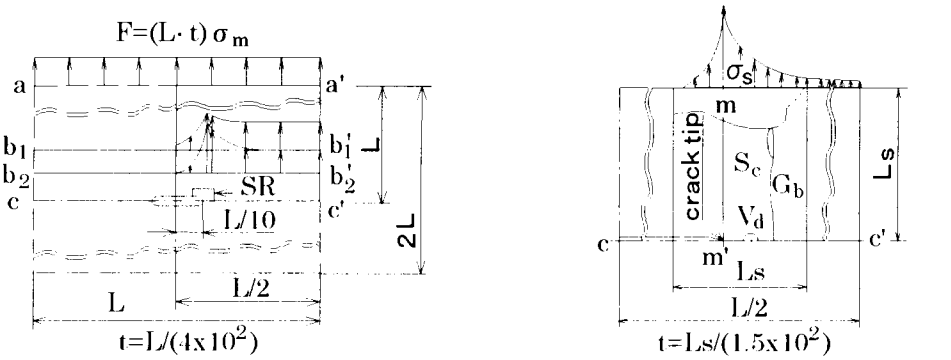

(a) Stress distribution in a (b) Magnified small regin, SR

Fig.7 Model of imaginary magnification method.

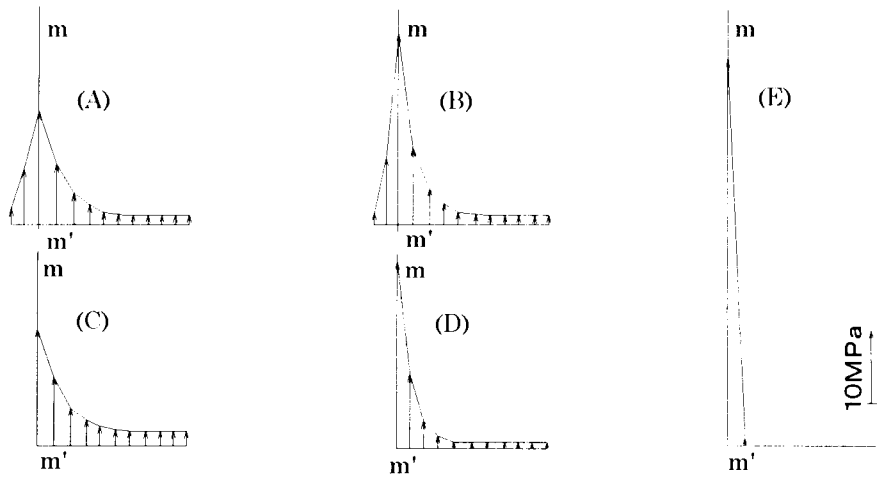

Fig. 8 Five types of the stress distribution on the upper side of magnified region.

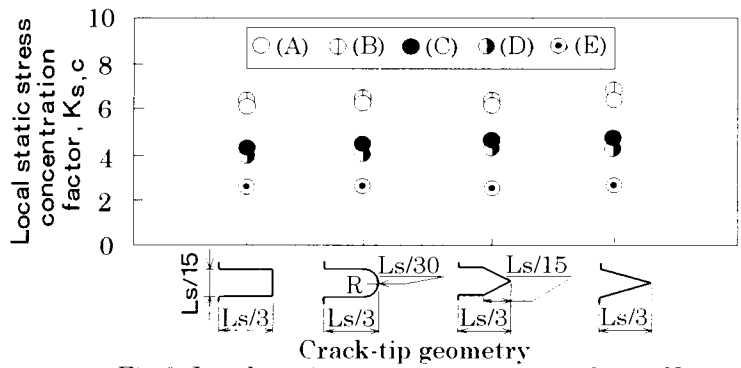

Fig.9 Local static stress concentration factor $K_{s,c}$ for four types of crack-tip geometry.

method. Usually, a crack is considered as a hairline crack. However, the geometry of a crack no longer resembles a hairline crack under the observation by a high magnification microscope [8]. It implies that it needs to change from engineering scale to microscopic one to investigate a microscopic geometry. Similarly, it is considered that the stress distribution in the microscopic region at a crack-tip should be analyzed using a microscopic scale, which is suitable to investigate the influence of microscopic geometry on the stress concentration at a crack-tip in detail, instead of engineering one as follows.

In the first step of this method, the stress distribution around a small region, SR, which includes a crack-tip, was analyzed for a strip with a central crack under a given tension, F. In the second step, the stress distribution was loaded on the boundary of the small region after an imaginary magnification, which is not merely a simple zooming up but also reveals small defects such as short crack, S_c, void, V_d, and grain boundary, G_b. These models are shown in Figs.7 (a) and (b). These models were divided into about 88 and 172 elements for the first and the second steps, respectively, and analyzed by FEM. Since the suitable magnification can not be predicted beforehand, five types of stress distributions are selected to simulate the stress distribution to be applied on the upper side of the small region as shown in Fig.8. The local static stress concentration factor was defined as $K_{s.c} = \sigma_c / \sigma_{m,L}$ in the small region, SR. Where, σ_c and $\sigma_{m,L}$ are the maximum stress at the crack-tip and the mean stress averaged over the length of upper side, L_s, of SR. The influence of crack-tip geometry on $K_{s.c}$ is shown in Fig.9. According to this figure, the crack-tip geometry does not influence on the magnitude of $K_{s.c}$.

4. CONCLUSION

Impact tension, bending and torsion experiments were performed using cracked strip and pipe specimens made of PMMA. Except for pipe specimen in the case of impact bending, the dynamic strain concentration factor of short specimen was slightly larger than that of long one. The similar influence of specimen length on the dynamic stress concentration factor is evaluated by numerical analysis. These size effects can be understood by considering the interference effect of mechanical waves. The dynamic stress concentration factor is also influenced by the crack-tip geometry, when it was evaluated without the influence of reflected waves. But the static stress concentration factor, which was evaluated in the microscopic region at a crack-tip by a new method, was not influenced by the crack-tip geometry.

ACKNOWLEDGEMENTS

The authors wish to express hearty thanks Mr. K. Inoue for his assistance in carrying out the experiments and Honda Metals co. for supplying materials. This work was partly supported by the Grant-in-Aid for Scientific Research of Japan Society for the Promotion of Science.

REFERENCES

1. Maekawa, I. (1997) Proc. of ICF9, Sydney, 6, 2743.
2. Maekawa, I. (1995) JSME Int. J. 38,80.
3. Yokobori, T. (1968) Int. J. Fact. Mech. 4,179.
4. Stroh, A.N. (1955) Proc. Roy. Soc. A232, 548.
5. Mullines, M.(1984)) Acta. Metall, 132, 381.
6. Itou, S. (1988) J. Appl. Mech. 47,801.
7. Bando, Y. (1984) J. Am. Ceram. Soc. C67, 36.

IMPACT WELDING OF ALUMINUM TUBE TO A STAINLESS STEEL TARGET – EFFECT OF DEFORMATION OF TUBE ON BONDING CONDITION -

H. DATE
Department of Mechanical Engineering
Tohoku Gakuin University
1-13-1 Chuo, Tagajo 985-8537, Japan

ABSTRACT

A tubular aluminum projectile, subjected to a longitudinal impact, was impact-welded onto a stainless steel target using a gas gun at impact velocities of 200 m/s or more. The bonded area was estimated using acoustic tomography. The microstructures and element distribution in the joint were analyzed by means of SEM and Energy dispersive X-ray spectroscopy. It appeared that the aluminum projectile was bonded to stainless steel target at an impact velocity from 200 to 300 m/s. The compound layer was observed at the joining interface of aluminum/stainless steel by SEM. The bonding strength of aluminum/stainless steel joint showed a maximum of 190 MPa at 230 m/s and decreased with lower impact velocity. The bonding strength at impact velocities of 220~ 240 m/s was stronger than fracture strength of the aluminum projectile.

KEYWORDS

tube impact-welding, aluminum/stainless steel joint, compound layer, bonding strength

INTRODUCTION

The bonding technique of a tube to a tube or a plate is one of important techniques in mechanical engineering. It has been reported previously by Date and others that a cylindrical projectile with a flat end subjected to a longitudinal impact was bonded to a target plate at impact velocities of 200 m/s or more using a gas gun [1]. A tube was also impact-welded on a flat target using the same gas gun [2]. However the bonding mechanism of the tube could not be deduced by the results of the bar, since the two deformation processes during impact were different. Here, the impact welding of an aluminum tube to a stainless steel target was carried out and the bonding mechanism was examined by the bonding area, deformation process, bonding strength and the compound layer at the joining interface. The differences of the bonding mechanisms of the bar and the tube were clarified with some of the points described above and the proper phenomena about the tube were found out in the experiment.

MATERIALS AND EXPERIMENT

The materials used were stainless steel plates (SUS304) having a diameter of 40 mm and a thickness 5 mm as the target and pure aluminum rods (A1050) having an outer diameter of 11 mm, inner diameter of 6 mm and length 20 mm as the projectile. The aluminum was annealed at 623 K for 3.6 ks. The impact face of target was polished using polishing paper having a mesh of 800 after grinding. An aluminum projectile collided with the stainless steel target at an impact velocity of 200 m/s or more using compressed nitrogen gas [1]. The impact welding was carried out in a vacuum chamber because the air compressed between the target and impact face of the projectile prevented welding. The impact velocity of the projectile was evaluated by a laser beam system. The bonding area was observed and measured using a scanning acoustic tomograph. The microstructure and element distribution in joining interface of the bonded specimen sliced to a thickness of about 3 mm were analyzed by means of SEM and energy dispersive X-ray spectroscopy (EDX). A tension test for measuring the bonding strength of the sliced specimen described above was carried out [1].

BONDED AREA AND DEFORMATION OF PROJECTILE

Two ultrasonic images of the bonded area are shown in Fig. 1 (a) and (b). The impact velocities are 274 m/s and 339 m/s, respectively. The central ring areas in Fig. 1 (a) and (b) are called the inner ring area. Since appearance of the outer ring area shown in Fig.1 (a) depends on the impact velocity as described later, the inner ring area is defined as the bonded area hereafter. The superimposition of a bonded area and a cross-sectional profile of the deformed projectile are given in Fig. 2. Figure 2 shows that the bonded area was not formed at the center of the impact face of the tube wall, but more to the inside. It was clarified that the outer ring area was formed by the folding of the outer wall of the tube because the inner diameters of the outer ring area were larger than the initial outer diameters of the tube. It is observed that the metal of the inner wall flowed in and piled up in the tube. An opening like a crack is observed along the deformed inner wall of the tube.

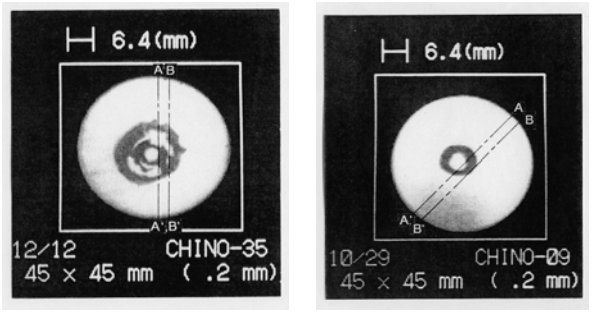

(a) v = 274 m/s (b) v = 339 m/s

Fig. 1 Acoustic images of bonded area

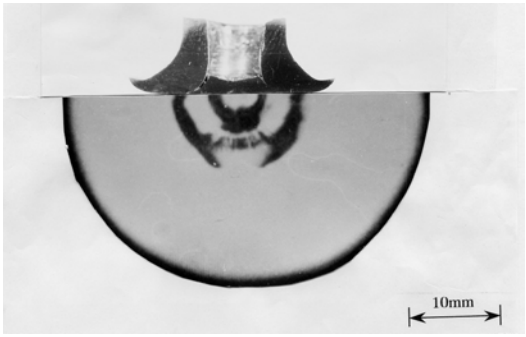

Fig. 2 Deformation profile of projectile and bonded area (v = 254 m/s)

The cross-sections of specimens bonded at the impact velocities of 238 m/s and 339 m/s are shown in Fig. 3(a) and (b). The contour of the outer wall after deformation is similar to the mushrooming profile. However, the profile of the inner wall is complicated as described below. Though the velocity of the metal flowing toward the center of the tube decrease as the inside of the tube is filled with the metal, the metal of the outer wall has continued to flow out during impact. The velocity difference of the two metal flows caused a crack to be initiated, grow and penetrate the wall. Finally the inside metal only is bonded at the target and the other part of the tube is separated from the target. It is clarified from Fig. 3 (a) and (b) that the outer ring area shown in Fig.1 (a) has vanished at a high velocity impact because the outer edge of the impact face of the projectile was lifted up from the target surface and the outer ring area was torn up. The effect of the impact velocity on the bonded area is given in Fig. 4. The size of the area hardly increases with impact velocity unlike the bar [1]. This means that the heat generation on the impact face of the tube is almost constant regardless of impact velocity.

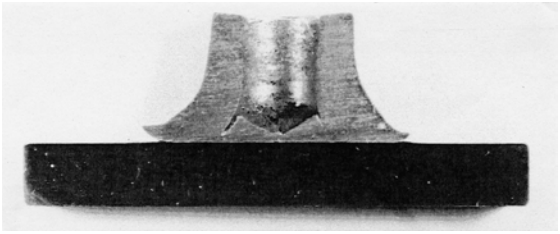

(a) v = 238 m/s

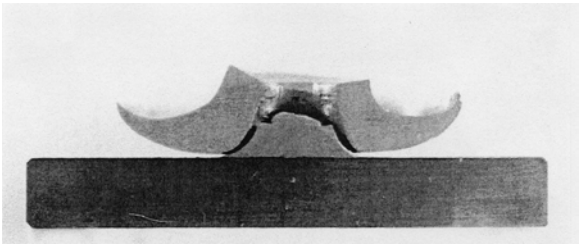

(b) v = 339 m/s

Fig. 3 Deformation process of projectile

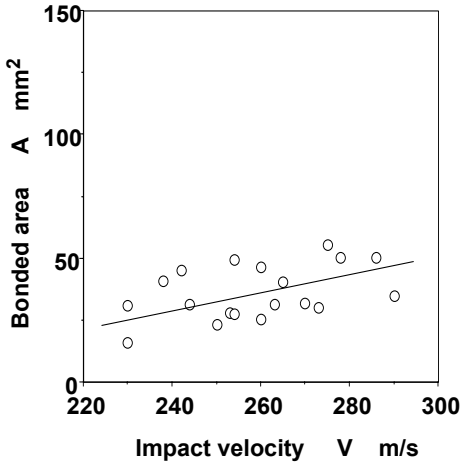

Fig. 4 Effect of impact velocity on bonded area

COMPOUND LAYER AND ELEMENT DISTRIBUTION

The magnified microstructure and X-ray image analysis of elements can be seen in Fig. 5 (a) and (b). Table I gives quantitative analysis of the phase formed at the joining interface in Fig. 5 (a). The maximum thickness of the compound layer was about 8 μm as seen in Fig. 5 (a) and (b). Figure 6 shows the maximum thickness of the compound layer plotted against impact velocities. The thickness hardly increases with impact velocity. The element distribution hardly depends on the position in the compound layer as shown in Table I and the content is almost constant regardless of impact velocity as shown in Fig. 7. The content of aluminum is more than that of Al_3Fe seen in the alloy phase diagram. The lack of dependence of aluminum content on the impact velocity and the position in the layer described above is the same as th

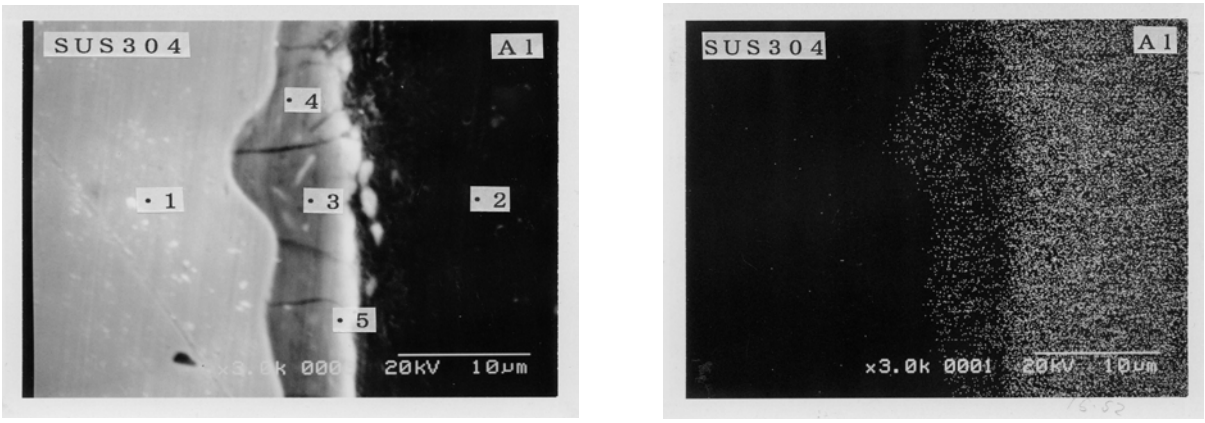

(a) Microstructure (b) X-ray image analysis of Al

Fig. 5 SEM and EDX images of compound layer

Table I Quantitative analysis of elements (at %)

	1	2	3	4	5
Al	2.7	99.7	79.0	78.8	72.8
Cr	19.3	0.0	4.4	4.4	5.4
Fe	69,9	0.3	15.1	15.3	19.7
Ni	8.1	0.0	1.5	1.5	2.1

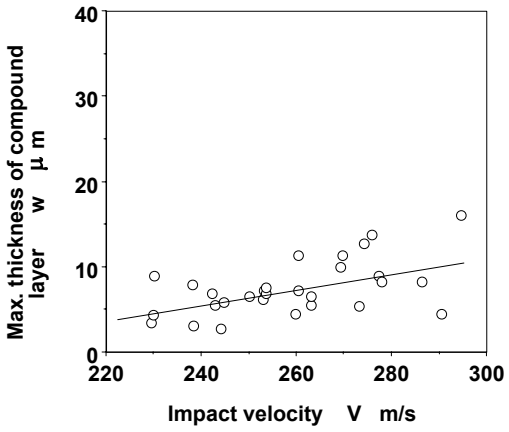

Fig. 6 Maximum thickness of compound layer plotted against impact velocity

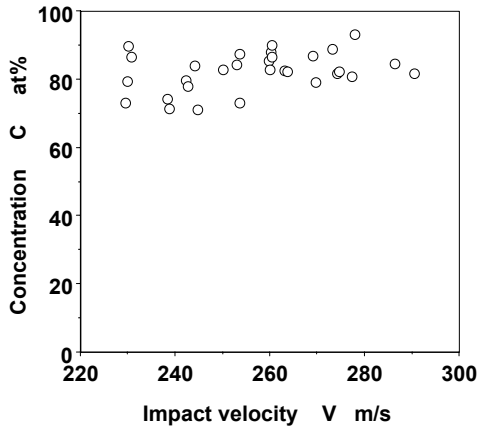

Fig.7 Effect of impact velocity on concentration of Al in compound layer

results for the bar [1]. A mechanical mixing model has been proposed previously by Date for interpreting the formation mechanism of the compound layer by impact welding [3]. The model consists of mixing and solidification of the melting metals. It is deduced from the results obtained using the model that the high content of aluminum in the layer shows much lower heat generation on the impact face than that of explosive welding.

BONDING STRENGTH

Figure 8 shows the dependence of the bonding strength on impact velocity. It was reported previously that the bonding strength of the impact-welded bars is independent of impact velocity because a fracture has not occurred at the joining interface, but on the aluminum projectile. However, as shown in Fig. 8, the bonded strength of the tube decreases with higher impact velocities. The difference of the two tendencies depends on the following difference of the deformation processes of the bar and tube.

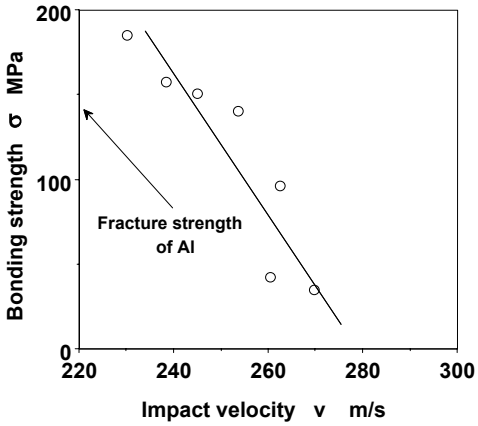

Fig. 8 Effect of impact velocity on bonding strength

The radial deformation was generated at the impact face of the cylindrical projectile subjected to a longitudinal impact. Since the radial displacement increases with the radial distance at symmetric deformation with respect to the axis, the deformation applies a shearing force on the joint. In the case of impact welding of the bar, the compound layer hardly suffers deformation because the layer was formed in the vicinity of the center. However, since the forming position of the compound layer at the impact face of the tube is near the inner wall, a shearing force acts on the interface. It is also clarified that the shearing deformation

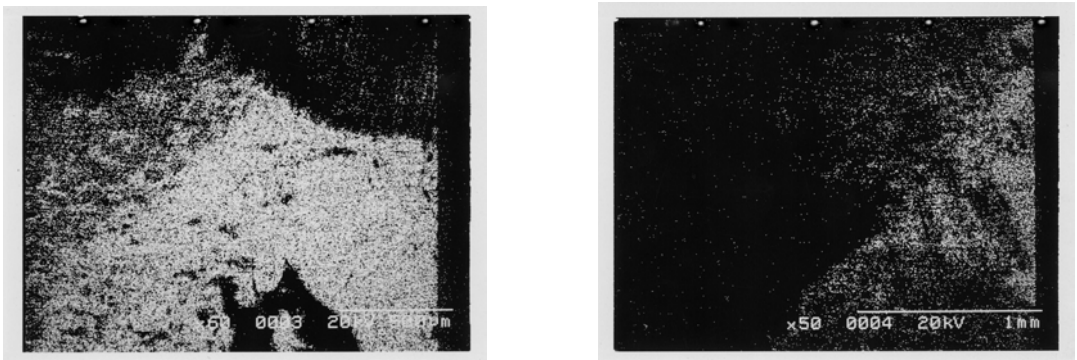

(a) v = 233 m/s (b) v = 260 m/s

Fig. 9 EDX images of fracture surface obtained by tension test

increases with impact velocity. It is conjectured that the deformation initiates a micro-crack in the layer and the increasing of the impact velocity causes the length of the crack to increase. The X-ray image analyses of the fracture surface at the point with the maximum bonding strength in the compound layer after the tension test are shown in Fig. 9 (a) and (b). The impact velocities are 233 m/s and 260 m/s, respectively. Since the white dots show aluminum, a decrease of aluminum is observed with impact velocity. The decrease of aluminum indicates that the fracture surface moves from the aluminum side to the compound layer side with increasing impact velocity. Finally, when impact welding of a tube was carried out with impact velocities of 220 ~ 240 m/s, the bonding strength was stronger than the fracture strength of aluminum.

CONCLUSIONS

An aluminum tube was impact welded onto a stainless steel target and the following results were obtained.

1) Acceptable impact-welding was obtained at impact velocities from 200 m/s to 300 m/s because the inside flow of metal in the tube caused poor welding at impact velocities of 300 m/s or more.
2) Since the temperature generated at the impact face of the tube was lower than that obtained by the impact-welding of the bar, the thickness of the compound layer was thinner than that of the bar and hardly depends on impact velocity.
3) The bonding strength decreased with impact velocity because the bonding surface received shearing deformation with impact velocity.
4) The bonding strength was stronger than the fracture strength of aluminum, when impact welding of a tube was carried out at impact velocities of 230 ~ 250 m/s.

References

[1] Date H., S. Kobayakawa and M. Naka (1999) “ Microstructure and bonding strength of impact-welded aluminum-stainless steel joints”, J. Mater. Process. Technology, 55, 166-170.

[2] Date H. (1998) ” Dynamic Behaviors of Aluminum Tube Subjected to a Longitudinal Impact and Tentative Impact Welding of a Tube”, Trans. of JSME, 64, 1316-1321.

[3] Date H. and M. Naka (2000) ” Formation Mechanism of Compound layer by Impact Welding”, Proc. of PLASTICITY ’00, edited by A.S. Khan, H. Zhang and Y. Yuan, 219-221

IMPORTANCE OF CRACK TUNNELING DURING FRACTURE: EXPERIMENTS AND CTOA ANALYSES

M. A. James[1] and J. C. Newman, Jr.[2]

[1]National Research Council Associate and [2]Senior Scientist
NASA Langley Research Center, Hampton, Virginia, 23681, USA

ABSTRACT

This paper compares experimental crack-front shapes recorded at various stages of crack extension with area-average crack-extension values during fracture tests conducted on 2024-T351 aluminum alloy plate. Crack-front shapes were determined by fracturing the specimen to a predetermined amount of crack extension, and fatigue cycling the specimen for about 2,000 cycles at a high stress ratio (P_{min}/P_{max}) to mark the crack-front location. For each shape, the area-average crack length was determined. The evolution of tunneling was used to create a calibration curve that could be used to adjust surface measured crack length values, for a more representative comparison with analyses that use a straight crack-front approximation. The analysis compares much more favorably with the average crack extension than with the surface measured values near maximum load. However, the area average technique tends to over correct crack extension near the crack initiation load. Crack tunneling results show that the area average technique produces more representative crack-length measurements compared to optical based surface measurements.

KEYWORDS

CTOA, crack extension, unloading compliance, area-average, tunneling, finite-element analysis

INTRODUCTION

During the 1990's, as part of a national aging aircraft program, NASA Langley Research Center (LaRC) conducted intensive research on the fracture behavior of thin sheet aluminum alloys [1]. Some of the products of that research were the constant critical crack-tip-opening-angle (CTOA, Ψ_c) fracture criterion, optical/digital imaging means for measuring CTOA, and optical methods for measuring surface crack extension [2]. Two additional means of measuring crack extension, unloading compliance and area average, were not used in favor of the optical methods. This paper presents a comparison of experimental crack-front shapes recorded at various stages of crack extension with area-average crack extension values, and shows how these various measures compare with surface measured values and typical finite-element predictions.

BACKGROUND

Wells [3] originally proposed the use of the crack-tip-opening displacement (CTOD) or angle (CTOA) during his experimental work. CTOA (Ψ_c) is usually applied as the angle formed by stable tearing material measured at a fixed distance, d, behind the moving crack (typically, d is taken as 1 mm). The fracture methodology developed as part of the NASA program assumes that the critical CTOA is constant and independent of loading and in-plane configuration, as long as the crack length is about 4 times the plate thickness. The criterion has been applied in both two-dimensional (2D) and three-dimensional (3D) finite-element analysis (FEA). Inherent in 2D FEA is the approximation that the crack front is flat and straight through the thickness of the model. However, neither plane stress nor plane strain accurately capture both

the local stress triaxiality near the crack tip and the plane-stress behavior remote from the crack. Three-dimensional analyses with a flat, straight crack-front maintain a straightforward modeling approach, yet capture the complex constraint behavior missing from typical 2D analysis. The methodology is applied by finding Ψ_c such that the analysis matches the average maximum load for coupon tests (typically, compact tension, W = 152 mm, specimen). This angle is used in subsequent analyses for predictions of crack extension and fracture.

Figure 1 shows a schematic of a typical fracture surface. Initially, the material fails in tension, most likely due to micro-void coalescence. Tunneling occurs on the interior, and shear bands start on the surface and eventually join to form a single shear dominated fracture surface.

Recently, a wide variety of fracture tests were conducted on 6.35 mm thick 2024-T351 aluminum alloy [4]. Both C(T) (compact tension) and M(T) (middle-crack tension) specimens were tested. Figure 2 shows selected load-crack extension results, including both test and analysis results. The 152 mm wide C(T) was used to find Ψ_c, the critical value of CTOA, by matching the average maximum load for the tests. This value of Ψ_c was used to predict the behavior of the other C(T) and M(T) configurations. The results show that the constant critical CTOA fracture criterion is transferable between C(T) specimens and M(T) specimens and show that the analysis was able to accurately predict the maximum load for C(T) specimens ranging in size from 50 mm to 152 mm and for M(T) specimens ranging in size from 75 mm to 1016 mm.

A consistent observation made of these load-crack extension curves (and similar curves for other thin sheet and plate materials) is that the straight crack-front analysis generally over-predicts crack extension, before and after maximum load. A number of factors could be contributing to the discrepancies in crack extension, including crack-front tunneling, transition from initially flat fracture to slant fracture after maximum load, and the simplicity of the constant value of CTOA.

CTOA is a local fracture criterion that is always measured a fixed distance from the current crack tip. An alternative fracture criterion is δ_5, which is the displacement measured across the original crack tip location using a 5 mm gauge length. δ_5 is initially a local parameter, but after crack extension behaves more like a remote parameter. Figures 3 (a) and (b) show load-δ_5 plots for the 152 mm wide C(T) and 1016 mm wide M(T), respectively. In contrast to the load-crack extension comparisons, shown in Figure 2, the analysis matches the δ_5 behavior of the tests very well. The δ_5 results compared well before and after maximum load, corresponding respectively to the local and remote stages of crack extension. The results in Figure 3 (b) are somewhat abbreviated because the clip gage measuring δ_5 went out of range near the end of the test. However, data was collected past maximum load.

The results in Figure 3 strongly suggest that the flat, straight crack front in the 3D analysis represents the “average” crack length at any given load. Returning to Figure 2, the amount that the analysis over-predicts crack extension is on the order of the plate thickness. The crack extension was measured on the surface of the specimen during the test using a traveling-stage optical microscope. The surface measured value is the shortest crack length if the specimen is experiencing crack-front tunneling. A more appropriate comparison metric may be to use an average crack length measure, such as unloading compliance or an area average.

TUNNELING TESTS

Experiments and analyses were performed to characterize the crack tunneling for the 6.35 mm thick 2024-T351 aluminum alloy. The typical approach to characterize crack tunneling is to perform a multiple specimen test to obtain one crack-front per specimen [2]. In an effort to obtain more data per specimen, a combined approach was taken here. Three specimens are single crack-front tests, while the final specimen was used as a multiple crack-front specimen test.

A number of methods may be available to mark the crack fronts and measure the tunneling. Dye penetrants could be used while the crack is held open to take advantage of the capillary action at the crack. Radiographic measuring methodologies may be able to characterize the crack extension. Herein the crack front was marked with fatigue cycles at a high stress ratio (R = 0.75 or 0.8) and a relatively high load (80%

of the current fracture load). Typically about 2000 cycles were applied to mark the crack front. The crack front shapes were measured using an optical microscope with X-Y traveling stages.

Three C(T) specimens of width 152 mm were fatigue pre-crack at low stress levels (8 MPa $\sqrt{m}$) to an a/W of 0.4. Each specimen was loaded just enough to cause a predetermined amount of crack extension. Then the fracture crack front was marked using fatigue crack growth. For each specimen, some or all the of the following were collected: load, load-line displacement, crack-mouth-opening displacement, δ_5, unloading compliance, crack extension, and surface field displacements in the vicinity of the original crack tip. The amount of crack extension was based on the desire to characterize the tunneling progression along the crack front for various loading levels. The first specimen was loaded until about 0.25 mm of surface crack extension was visible. Two subsequent specimens were loaded to lower loads based on the unloading compliance load-crack extension curve. Table 1 summarizes the maximum load as well as maximum interior and surface crack extension values. The tunneling magnitude is $T = \Delta a_{max} - \Delta a_s$, where Δa_{max} is the crack extension on the interior, and Δa_s is the crack extension on the surface. The load corresponding to K_{Ic} for this material and configuration is about 10.7 KN.

Figure 4 shows the measured fatigue and fracture crack fronts from the multiple crack front specimen test. Also included in Figure 4 are the area-average (dash-dot) crack lengths for each crack front. Unloading compliance crack extension is somewhat less than area average and is omitted here for clarity. During the early stages of growth, for instance, at the lowest load from Table 1, the crack has some extension along nearly 80% of the fatigue crack-front. This extension was attained at only about 25% above the equivalent K_{Ic} load for this material, indicating that there may be relatively high constraint on the interior of the specimen encouraging growth at such low loads. The estimated plastic zone radius at this load is about 4 mm -- well beyond the limits of LEFM, but still smaller than the thickness. Additionally, this indicates that the crack extension may be retarded on the surface by plasticity, since surface-crack extension does not initiate until significant tunneling has taken place. Tunneling initially increases as the tensile fracture region develops, then as the shear lips form with increasing plasticity, tunneling decreases to an essentially constant value during fully developed slant fracture. The fatigue crack-front tunneling was about 12% of the plate thickness (B). Tunneling increases to about 40% of B when surface growth starts. After the flat-to-slant transition is complete, tunneling stabilizes at about 20% of B.

CRACK EXTENSION CALIBRATION

For tunneling cracks, there are, at least, four crack-length measurements: (1) crack length on the free surface, (2) unloading compliance crack length, (3) area-average crack length, and (4) maximum crack length in the interior. Figures 2 (a) and (b) compare experimentally measured surface values of crack extension with straight crack-front FEA results. Since tunneling does occur, it is desirable to account for the tunneling either in the analysis or in the test data. The most desirable approach is to modify the analysis to include crack-front shapes that match the experimental results [5] or use a modeling methodology that allows the tunneling to evolve naturally as part of the analysis [6]. However, these are cumbersome, time consuming, and not currently practical for industry. The alternative is to consider the experimental data and estimate crack extension using either unloading compliance or area average. Herein, the area-average values, based on the 9-point weighted average procedure [7], will be used, unless otherwise noted. Two situations exist requiring separate calibration curves: specimens that remain flat and specimens that exhibit the flat-to-slant crack transition. The process is essentially the same for the two fracture conditions using different calibration curves.

Figure 5 shows the tunneling magnitude, T, for the two fracture conditions. The tunneling for the flat-to-slant specimens was derived from Figure 4. The tunneling for the flat fracture is adapted from work by Dawicke et al. [5] for a thin sheet 2024-T3 aluminum alloy (scaled from B = 2.3 mm). Dawicke showed through experimental measurements similar to those from Figure 4 that for flat fracture, tunneling increased monotonically until it stabilized at a constant value. The curve for flat fracture in Figure 5 is a curve fit of Dawicke's data.

Figure 6 shows the area-average calibration curves derived from the flat and flat-to-slant crack data in Figure 5. The correction ratio, C_R, is the ratio of area average crack extension to the surface crack extension. The

curves are calculated using the equation for C_R in Figure 6 and the respective tunneling curves from Figure 5. The data points in Figure 6 are the calculated correction ratio based on the area average crack length from the measured tunneling. The f term in the C_R equation indicates what fraction of the tunneling magnitude represents the area average crack extension. For flat fracture the coefficient was determined from the area average crack length of Dawicke's [2] crack front shapes and is 0.64, and for slant fracture the coefficient was determined from the average of the tunneling data as 0.5.

Figure 7 compares data from Figure 2 corrected using the calibration curves for area-average crack extension with the analysis. Only data with $\Delta a > 0.2$ mm were corrected. As expected, both curves shifted significantly, resulting in a better match between the FEA and experimental results near maximum load. However, the analysis now significantly over-predicts the initiation load, indicating that a lower CTOA would be required in the analysis to predict initiation. From Table 1, crack initiation in the interior occurred before 13.3 KN, but the analysis did not initiate until about 19 KN. This is similar to the result by Dawicke et al. [5]. The crack-extension values for the flat specimen were larger than the value for the slant-crack specimens at a given load. Beyond maximum load, the measured surface crack-extension values were approximately the same in Figure 2 for the flat and slant specimens. The differences in the two curves in Figure 7 indicate that the importance of the failure mechanism (tensile versus shear) between the two failure modes may be more significant than was indicated by the surface measured crack-extension data of Figure 2.

CONCLUDING REMARKS

The excellent match between the experimental and analysis data in Figure 3 is compelling, and led us to consider the tunneling issue more carefully. The results in Figure 7 show better correlation between the corrected test data and the analysis results near maximum load, and showed that the constant CTOA fracture criterion transfers well between the fully constrained C(T) specimen and the wide, buckling M(T) specimens. The analysis was able to accurately predict the maximum load for C(T) specimens ranging in size from 50 mm to 152 mm and for M(T) specimens ranging in size from 75 mm to 1016 mm.

Optical measurement methods will likely remain the method of choice for the buckling wide panel tests. Unloading compliance measurements are difficult for buckling panels, and direct current potential difference (area average) can be somewhat difficult to set up and increases the complexity of the test procedure. However, unloading compliance is relatively straight-forward for constrained C(T) and M(T) specimens. If reliable tunneling test procedures can be developed, and if the material shows consistent tunneling behavior, then calibration procedures such as these presented here are viable.

REFERENCES

1. Harris, C.E., Newman, J. C., Jr., Piascik, R. and Starnes, J. H., Jr., "Analytical Methodology for Predicting the Onset of Widespread Fatigue Damage in Fuselage Structure," Journal of Aircraft, Vol. 35, No. 2, pp. 307-317, 1998.
2. Dawicke, D. S. and M. A. Sutton, "CTOA and Crack Tunneling Measurements in Thin Sheet 2024-T3 Aluminum Alloy," *Experimental Mechanics*, Volume 34 No. 4, pp. 357, 1994.
3. Wells, A.A., "Application of Fracture Mechanics at and Beyond General Yielding," *British Welding Journal*, Vol. 11, 1961, pp. 563-570.
4. James, M. A. and Newman, J. C., Jr., "Three Dimensional Analysis of Crack-Tip-Opening Angles and δ_5-Resistance Curves for 2024-T351 Aluminum Alloy," *Fatigue and Fracture Mechanics: 32nd Volume, ASTM STP 1406*, Ravinder Chona, Ed., American Society for Testing and Materials, West Conshohocken, PA, 2000 (in press).
5. Dawicke, D. S., J. C. Newman, Jr., and C. A. Bigelow, "Three-dimensional CTOA and Constraint Effects during Stable Tearing in Thin Sheet Material," *ASTM STP 1256*, W. G. Reuter, J. H. Underwood and J. C. Newman, Jr., Editors, American Society for Testing and Materials, pp. 223-242, 1995.
6. Ortiz, M. and Pandolfi, A., "Finite deformation irreversible cohesive elements for three-dimensional crack-propagation analysis," *Int J Num Meth Engng*, n 44, pp. 1267-1282, 1999.
7. ASTM Standard E1820, Volume 03.01, American Society for Testing and Materials, 2000.

TABLE 1
CRACK EXTENSION AT MAXIMUM APPLIED LOAD

Specimen	Load (KN)	Δa_s (mm)	Δa_{max} (mm)
1	24.4	0.25	2.0
2	17.8	0	0.6
3	13.3	0	0.1

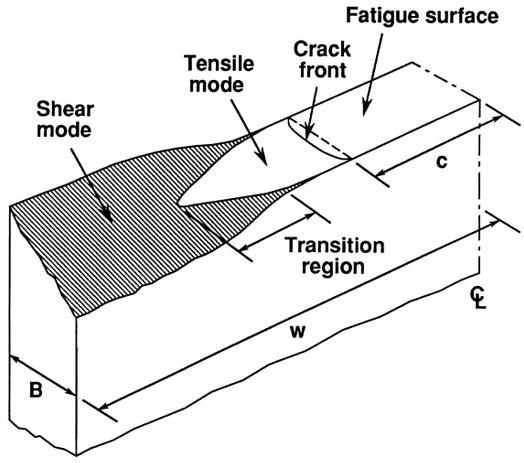

Figure 1: Schematic of a typical fracture surface

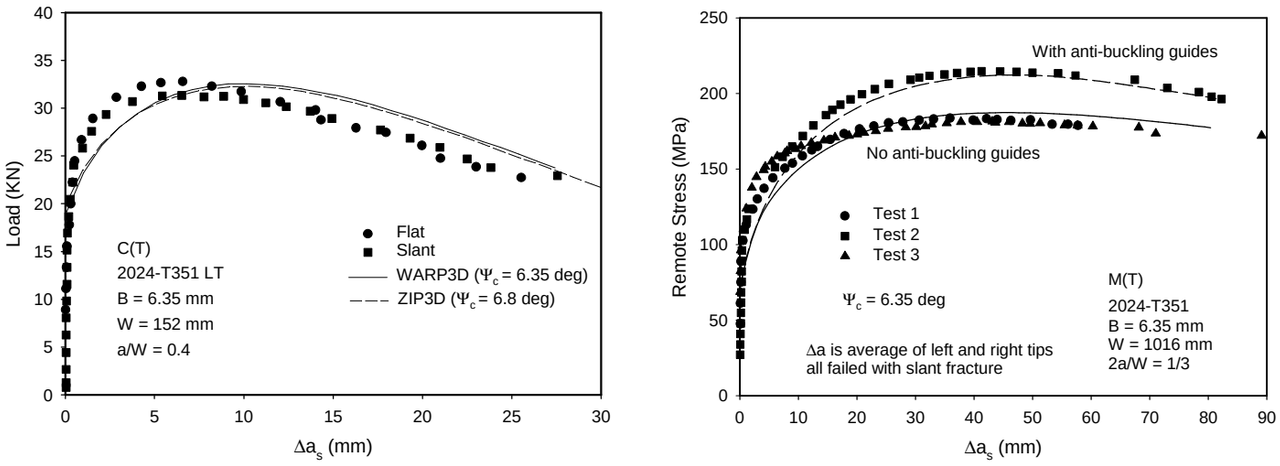

(a) 152 mm C(T) (b) 1016 mm M(T)

Figure 2: Experimental and numerical load-crack extension

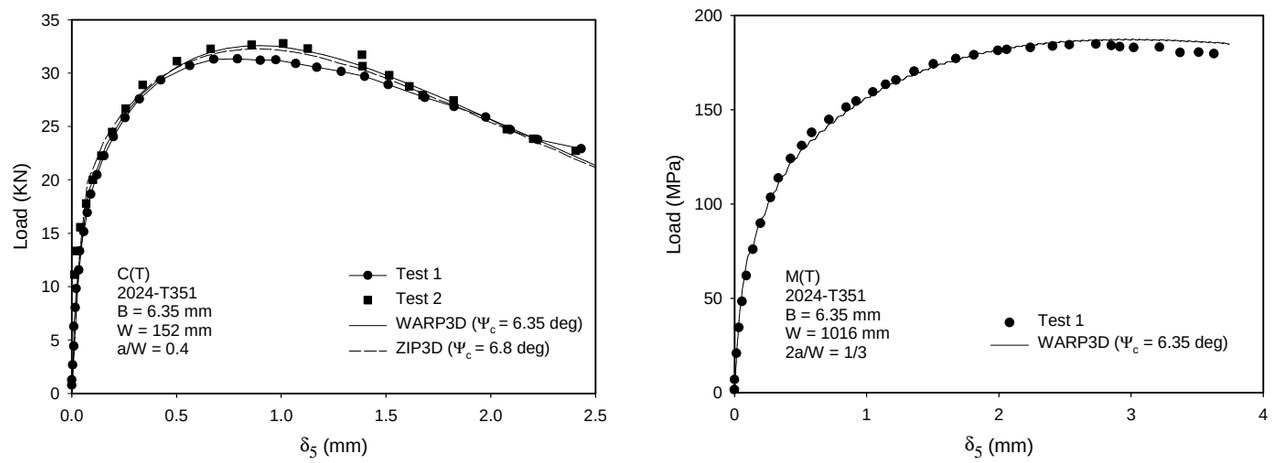

(a) 152 mm C(T) (b) 1016 mm M(T)

Figure 3: Experimental and numerical load- δ_5 results

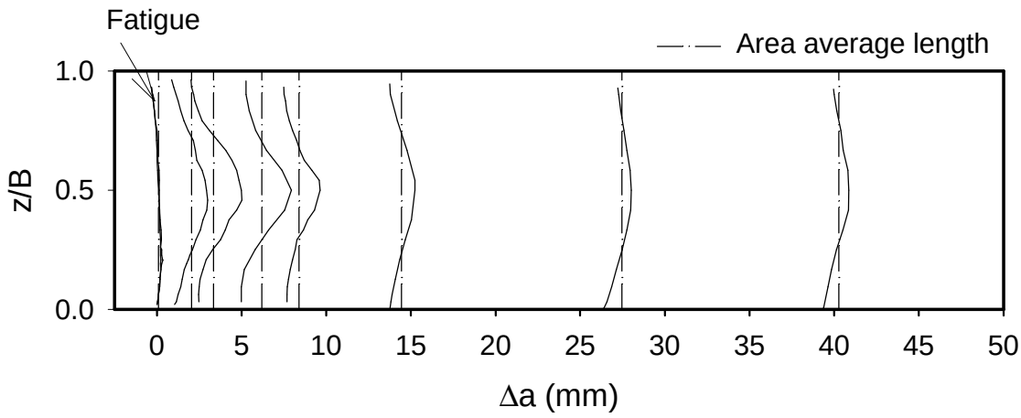

Figure 4: Optically measured fatigue and fracture crack-front shapes

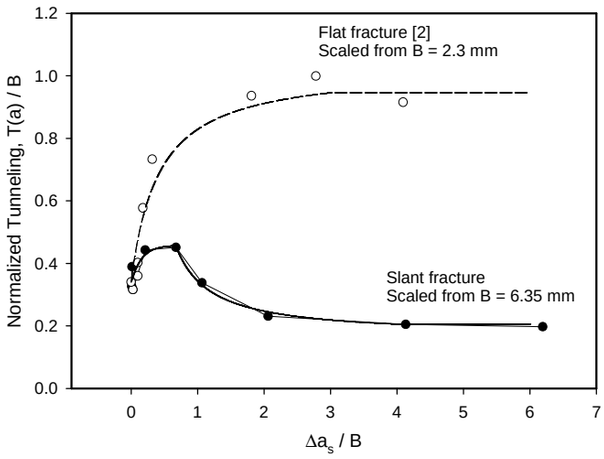

Figure 5: Tunneling magnitude for flat and flat-to-slant fracture surfaces

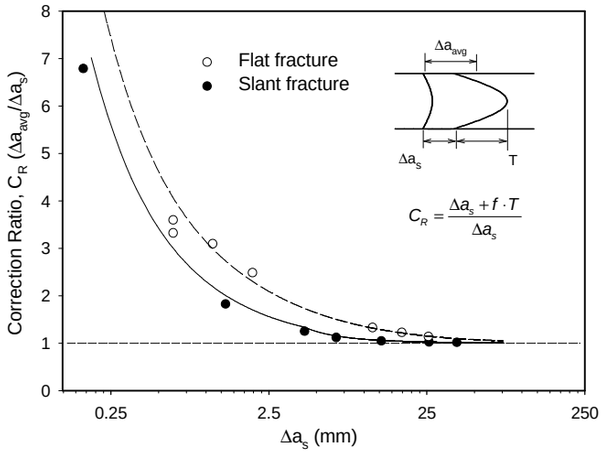

Figure 6: Area average calibration curves for flat and flat-to-slant fracture surfaces

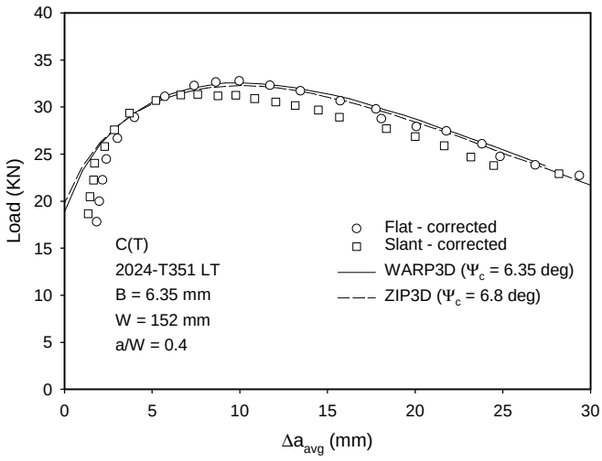

(a) 152 mm C(T)

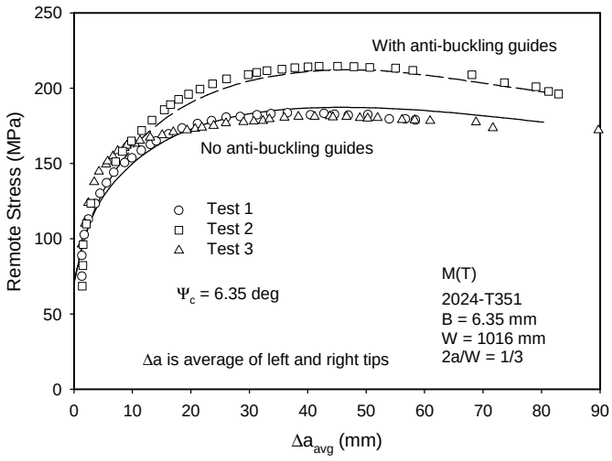

(b) 1016 mm M(T)

Figure 7: Corrected load-crack extension curves

ORAL REFERENCES: ICF100938OR

IMPROVEMENT OF MECHANICAL PROPERTIES OF ALUMINA PARTICULATE COMPOSITES USING POLYCRYSTALLINE ALUMINA POWDER

K. Kageyama, K. Ohi and H. Kato

Department of Mechanical Engineering, Saitama University, Urawa, Saitama, 338-8570, Japan,

ABSTRACT

Alumina particulate zirconia and alumina particulate glass using polycrystalline alumina powder was fabricated by atmospheric sintering to investigate the influence of alumina grain distribution on the mechanical properties of alumina composites. Polycrystalline alumina powder was obtained by quenching and crushing sintered alumina body. Firstly, the fracture toughness of 20% of zirconia particulate alumina was slightly increased with the addition of polycrystalline alumina powder. On the other hand, the bending strength was kept almost constant with the addition of polycrystalline alumina powder. SEM observation of a crack path indicated that a crack propagated into alumina cluster formed by polycrystalline alumina powder and transgranular fracture often occurred in the cluster compared to the other region. Second, 50% of alumina particulate borosilicate glass was sintered using virgin alumina powder or polycrystalline alumina powder. Using polycrystalline alumina powder, sintered body was obtained at lower sintering temperature than that using virgin alumina powder and the average bending strength was improved by the addition of polycrystalline alumina powder, too. Some samples showed that mullite formation occurred during sintering and X-ray analysis indicated that the addition of polycrystalline alumina powder enhanced mullite formation in the samples. These results indicate that the addition of polycrystalline alumina powder can improve fracture toughness, bending strength, mullite formation and/or low temperature sintering of alumina particulate composites.

KEYWORDS

composite, alumina, zirconia, glass and mechanical properties.

INTRODUCTION

Ceramics or glass matrix composites have been studied to improve the poor mechanical reliability of ceramics and glass for the practical use in various industries [1-3]. Conventionally, microstructure of ceramics has been

designed and controlled on a singular scale level. Natural materials (e.g. bamboo), however, consist of complicated structural elements on the several scale level and achieve the excellent combinations of mechanical properties (e.g. flexibility, toughness and stiffness). In the recent studies, synergy ceramics has been proposed and some artificial hyper-organized structure controlling ceramics were fabricated [4]. Nano ceramics composites, for example, exhibited better fracture strength than conventional ceramics [5,6] and the fracture toughness of Si_3N_4 was enhanced by elongated coarse grains [7].

The idea of nano-composites and coarse grain bridging was based on the mixture of dual scale particles. On the other hand, the mixture of dual scale microstructures is also attractive for design of synergy ceramics. Simple example is the composites where clusters of ceramics A are dispersed in matrix of ceramics B. In this case, if the cluster bridging occurs, the toughening by the cluster bridging would be more effective than that by the grain bridging in the conventional ceramics composites because cluster size is much larger than fine singular grain. Though the coarse singular gains dispersed composites can be expected to get the same effect of the toughening by cluster bridging, it usually shows significant decrease in fracture strength caused by inter/trans granular fracture along/in coarse grains. Polycrystalline alumina clusters dispersed composites, however, could maintain the same fracture strength of conventional fine ceramics because the clusters consist of fine singular grains. In this study, alumina polycrystalline powder was obtained by crushing pre-sintered alumina body, mixed with alumina-zirconia composites or Pylex glass. Polycrystalline clusters dispersed composites were obtained by atmospheric sintering and measurements of mechanical properties, observation of microstructure and phase detection by XRD were performed.

EXPERIMENTAL PROCEURE

Commercially available alumina powder (Sumitomo Chemical Co., Ltd., AES-11) was used for polycrystalline powder preparation. Alumina powder was pressed by cold isostatic press under 200 MPa and sintered in air at 1873K for 2h. Sintered alumina body was crashed by a stamp-mill and a automated mortar and sieved through the mesh of which opening size is 32μm. Obtained polycrystalline alumina powder was mixed with virgin alumina powder and commercially available zirconia powder (Tosho Co., Ltd., TZ-3Y) by a wet ball-mill process in ethanol for 24h and dried by a rotary evaporator. The dried powder was pressed and sintered under the same condition mentioned above. The volume fraction of polycrystalline alumina, virgin alumina and virgin zirconia powder was shown in Table1. The volume fraction of total amount of alumina powder (virgin and polycrystalline power) and zirconia powder was set to 80 vol% : 20 vol%. Commercially available Pylex glass powder (Furuya Metal Co., Ltd., 80.9 mol% SiO_2, 12.7 mol% B_2O_3 and 2.3 mol% Al_2O_3) was used for processing of alumina particulate glass matrix composites. The average diameter of Pylex glass powder was 2 μm. Polycrystalline or virgin alumina powder was mixed with Pylex glass powder, dried and pressed and under the same condition mentioned above. The pressed body was sintered in air for 9h. Volume fraction and sintering temperature were shown in Table2. Obtained sintered body was cut to the specimen of 3 x 4 x 40mm and four-point bending test was done. The bending test was performed using a universal testing machine with a cross-head speed of 0.5 mm/min, an upper span of 10 mm and a lower span of 30mm. The microstructure of polished and etched surface of specimens was observed a scanning electron microscope (SEM). Specimens of alumina-zirconia composites were also served for fracture toughness measurement. Vicker's indenter was loaded on the specimen surface under 30kgf for 30sec to induce a crack perpendicular to long axis of a specimen. The four-point bending test was performed to the indented specimens, which were loaded tensile stress on indented surface and the fracture strength was measured. The length and depth of the indented crack on fracture surface was measured by optical microscope and the fracture toughness was calculated using Newman's equation [8]. The path of indented crack on the surface was also observed by SEM. The phases in specimens of alumina-glass composites were identified by X-ray diffraction analysis (XRD) using Cu K□ radiation.

TABLE 1

COMPOSITION OF ALUMINA-ZIRCONIA SAMPLES

Sample	Virgin Alumina Powder (vol%)	Polycrystalline Alumina Powder (vol%)	Virgin Zirconia Powder (vol%)
AZ0	**80**	**0**	**20**
AZ1	**70**	**10**	**20**
AZ2	**60**	**20**	**20**
AZ3	**50**	**30**	**20**

TABLE 2

COMPOSITION OF ALUMINA-GLASS SAMPLES

Sample	Virgin Alumina Powder (vol%)	Polycrystalline Alumina Powder (vol%)	Pylex Glass Powder (vol%)	Sintering Temperature (K)
GV1	**50**	**0**	**50**	**1273-1573**
GP1	**0**	**50**	**50**	**1173-1573**

RESULTS AND DISCUSSION

Alumina Particulate Zirconia Matrix Composites (Alumina-zirconia)

Figure 1 shows the microstructure of alumina-zirconia samples. The samples using only virgin powder shows that fine grains of alumina and zirconia were homogeneously distributed. The samples with the addition of polycrystalline powder show that polycrystalline alumina clusters were dispersed in fine alumina-zirconia matrix and dual scale microstructure was obtained. The coarsening of alumina grains, however, was observed in polycrystalline alumina clusters. Polycrystalline alumina powder was obtained by pre-sintering and thus polycrystalline alumina clusters were suffered double sintering. Such a repeat of sintering caused the coarsening of alumina grains and the further consideration of sintering condition should be needed to obtain fine sintered body. Figure 2 shows the bending strength of alumina-zirconia specimens. The bending strength was slightly increased with the addition up to 20 vol% of polycrystalline alumina powder and dropped with the addition of 30 vol% of that. The decrease in bending strength with the addition of 30 vol% of

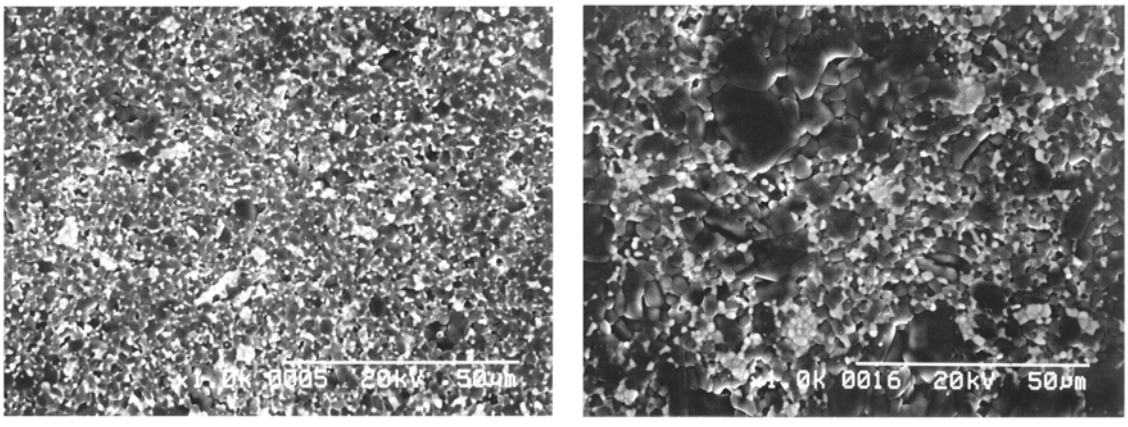

(a) **(b)**

Figure 1: Microstructure of the thermal etched surface of 20 vol% of zirconia particulate alumina. (a) the sample using only virgin alumina powder (b) the sample adding 20 vol% of polycrystalline alumina powder.

polycrystalline alumina powder could be related to the coarsening of polycrystalline alumina clusters due to double sintering mentioned above. On the other hand, the addition up to 20 mol% of polycrystalline alumina powder enhanced or kept constant of the bending strength of the samples regardless of coarsening of polycrystalline alumina clusters. This result indicates that the dual structure formed in alumina-zirconia samples may contribute on the improvement of bending strength.

Figure 3 shows the fracture toughness of alumina-zirconia samples. Fracture toughness was apparently increased with the addition of polycrystalline alumina powder. Figure 4 shows a crack path of samples induced by Vicker's indentation. In the case of the samples using only virgin powder, intergranular fracture largely dominated a crack path. In the case of the sample adding polycrystalline alumina powder, however, both of intergranular and transgranular fracture were observed in the cluster region of polycrystalline alumina grains and intergranular fracture largely dominated in the other region. It is noted that a crack deflection along polycrystalline alumina clusters had never been observed. This fact points out that the cluster bridging by polycrystalline alumina grains unfortunately did not occur in any alumina-zirconia samples although the grain bridging by alumina and zirconia particles were often observed in the mixture region of alumina and zirconia. Possible reason why the fracture toughness was enhanced by the addition of polycrystalline alumina powder is the change of the internal stress distribution in composites. The thermal expansion coefficient of zirconia is higher than that of alumina and consequently the tensile stress occur in the zirconia particles due to thermal residual stress in the case of the samples where zirconia particles are uniformly distributed in the alumina

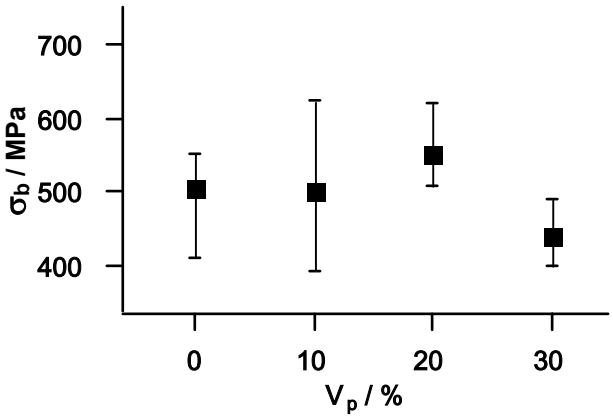

Figure 2: Relationship between bending strength (σ_b) and volume fraction (V_p) of polycrystalline alumina powder.

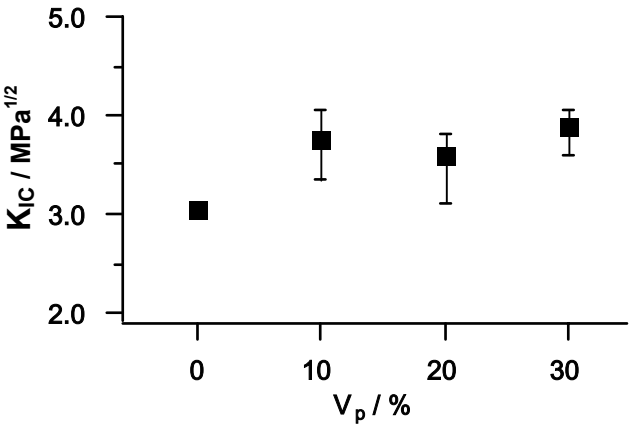

Figure 3: Relationship between fracture toughness (K_{IC}) and volume fraction (V_p) of polycrystalline alumina powder.

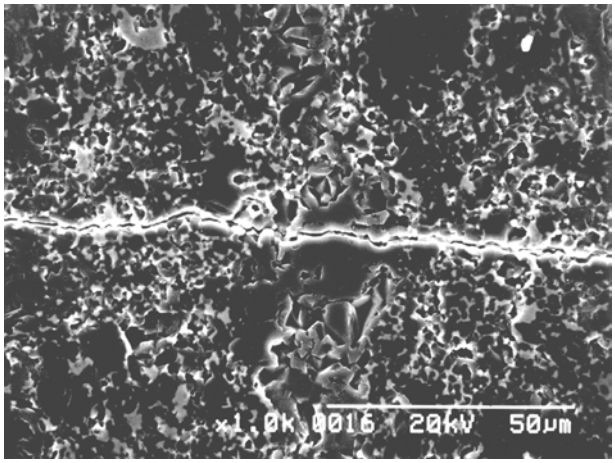

Figure 4: Indented crack path on the etched surface of the sample adding 20 vol% of polycrystalline alumina powder.

matrix. On the other hand, the mixture region of alumina and zirconia has higher macroscopic thermal expansion coefficient than the cluster region of polycrystalline alumina and thus the compressive stress occur in the polycrystalline alumina cluster in the samples where polycrystalline alumina clusters are distributed in the mixture structure of alumina and zirconia. SEM observation indicates that a crack propagated into the polycrystalline alumina cluster. If the compressive stress prevents crack propagation in the polycrystalline alumina cluster, the fracture toughness would be enhanced. Of course, further study is needed because grain size distribution, crack deflection, crack bowing and the other factors should be considered to explain the toughening mechanism by the addition of polycrystalline alumina powder.

Alumina Particulate Glass Matrix Composites (Alumina-glass)

Figure 5 shows typical XRD pattern of the alumina-glass samples. The samples using virgin alumna powder shows that the formation of mullite occurred when sintering temperature was higher than 1473K. On the other hand, the samples using polycrystalline alumina powder shows the mullite formation occurred when sintering temperature was higher than 1373K. The peak ratio of mullite (peak B) to alumina (peak A) exhibits 0.25 for the samples using virgin alumina and 0.46 for the samples using polycrystalline alumina powder when sintering temperature was 1473K. The addition of polycrystalline alumina powder, therefore, enhances mullite formation. Possible reason of enhancement of mullite formation is impurities mixed at preparation of polycrystalline powder. Figure 6 shows microstructure of the samples with mullite formation. Fibrous mullite

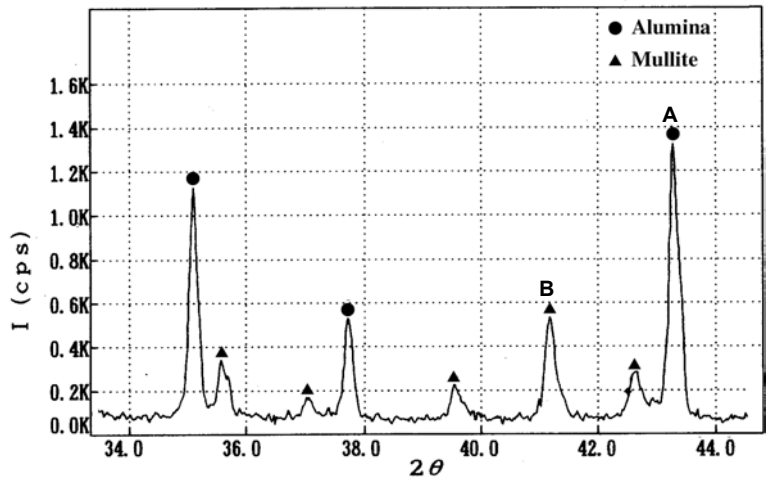

Figure 5: XRD pattern of alumina particulate Pylex glass using polycrystalline alumina powder (sintering temperature is 1473K).

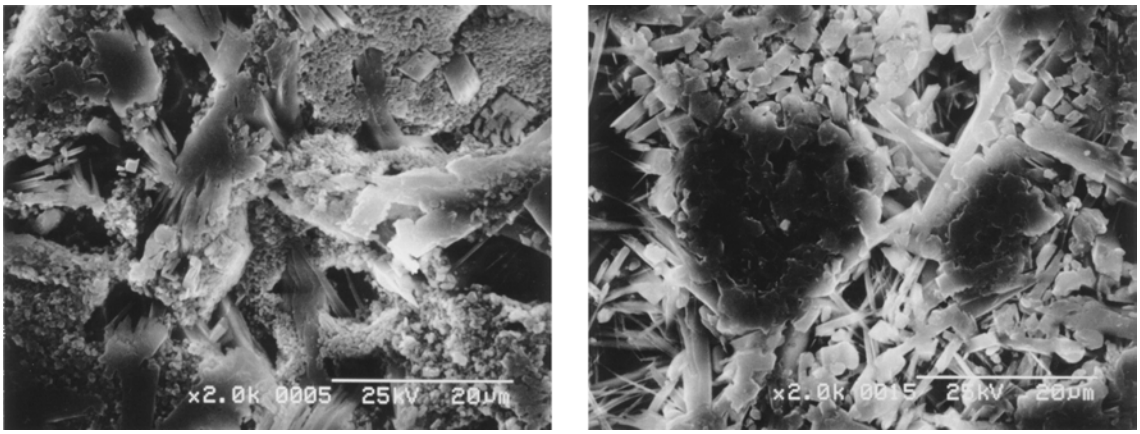

(a) **(b)**

Figure 6: Microstructure of the etched surface of alumina particulate Pylex glass sintered at 1473K. (a) the sample using virgin alumina powders (b) the sample using polycrystalline alumina powder.

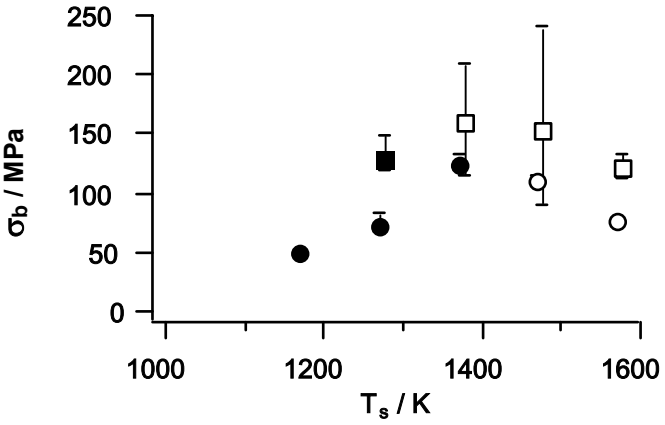

Figure 7: Relationship between bending strength and sintering temperature of alumina particulate Pylex glass. Opened marks show that mullite formation occurred.

crystals were largely formed and polycrystalline alumina clusters still remained in the mixture of glass, alumina and fibrous mullite in the samples, which shows the interested dual structure. Figure 7 shows relationship between the bending strength and sintering temperature of alumina-glass samples. The bending strength was apparently enhanced by the use of polycrystalline alumina powder. Mullite formation usually contributes on the strengthening of glass ceramics but, in this case, the samples with mullite formation tended to have larger scatter of bending strength than those without mullite formation.

CONCLUSIONS

Alumina particulate zirconia and alumina particulate glass using polycrystalline alumina powder was fabricated by atmospheric sintering and composites with dual scale structures were obtained.

The samples of dual scale structures where polycrystalline alumina clusters were distributed in the mixture of alumina and zirconia were obtained though polycrystalline alumina clusters showed coarsening by double sintering. These samples indicated that the addition of polycrystalline alumina powder enhanced the fracture toughness while the bending strength was almost kept constant.

The samples of dual scale structures where polycrystalline alumina clusters were distributed in the glass matrix were obtained. When mullite formation occurred, the polycrystalline alumina clusters were distributed in the mixture of glass and fibrous mullite. The use of polycrystalline alumina powder enhanced the mullite formation and the average bending strength though mullite formation causes the increase in scatter of the bending strength.

References

1. Swearengen, J.C., Beauchamp, E. K., and Eagan, R.J. (1978). Fracture Mechanics of Ceramics vol.4, pp. 973-984, Plenum Press, New York.
2. Taya, M., Hayashi, S., Kobayashi, A.S. and Yoon, H.S. (1990) J. Am. Ceram. Soc. 73, 1382-1391.
3. Evans, A. G. (1986) Acta. Metall. 34, 761-800.
4. Kanzaki, S., Shimada, M., Komeya, K. and Tsuge, A. (1999). Proceedings of the 2nd International Symposium on the Science of Engineering Ceramics, pp. 437-442, Trans Tech Publications, Switzerland.
5. Niihara K. (1990) J.Jpn. Soc. Powder and Powder Metall. 37, 348-351.
6. Niihara K. (1991) Nippoin Seramikkusu Kyokai Gakujutsu Ronbunshi 99, 974-982
7. Hirosaki, N., Ando, M., Akimune, Y. and Mitomo, M. (1992) J. Ceram. Soc. Japan 100, 826-829.
8. Newman, J.R. and Raju, I.S. (1981) Eng. Frac. Mech. 15, 185-192

Improvement of the adhesion strength of PET/PMMA composite by radio frequency plasma treatment

[a]Cioffi, M. O. C., [a]Voorwald, H. J. C. and [b]Mota, R. P
[a] Department of Materials and Technology, [b] Department of Physics and chemistry
State University of São Paulo "Júlio Mesquita Filho",
Av. Ariberto Pereira da Cunha, 333 Cep 12516-410 Guaratinguetá-SP, BRAZIL.

ABSTRACT

The adhesion between polyethylene terephthalate (PET) fibres and polymethyl methacrylate (PMMA) matrix was analysed. The overall goal was to establish mechanical and chemical links between PET and PMMA, in order to increase the adhesion in their composites using cold plasma treatments. PET filaments were treated in a radio frequency (RF) plasma reactor using argon and oxygen as gas fuel. The excitation frequency was 13,56 MHz; the power of the electrical field 50 W, the pressure was set to 0,4 mbar and the treatment times were 5s, 20s, and 100s. Oxygen and argon plasmas were found to promote both chemical and mechanical anchoring by etching and sputtering mechanisms on the surface increasing fibre roughness. The mechanical strength modification of PET fibres was evaluated by pull-out tests of the treated and untreated PET monofilaments. The fibres were subsequently examined by scanning electron microscopy (SEM) to monitor changes of surface roughness. Results obtained showed that the cold plasma causes an increase of the adhesion strength of PET fibre/PMMA matrix and strong modification in the structure of the fibre surface.

Keywords: RF plasma; adhesion, PET/PMMA composite

* Corresponding author. Tel: +55-12-5252800 (r. 306); e-mail: cioffi@feg.unesp.br.

INTRODUCTION

Reinforcement of thermoplastics polymer like PET fibres/PMMA matrix composite results in a material with some improved characteristics such as low embrittlement, stability and high mechanical strength. In addition, the specific gravity of the PET fibres is 1,29 g/cm^3 less, which makes possible to produce a composite material with good mechanical properties and low specific mass. Conversely, it was recognised that the chemical inertness and the low surface energy of the PET fibres will make it difficult to achieve the adequate bond with a polymer to produce the composite[1-2]. The plasma treatment can be effective to improve the interfacial adhesion of the thermoplastics based composites[3]. By using excited-state chemistry in corona discharge, a number of polymers were modified before painting, printing and lamination[4]. Generally, oxidation on the fibre surface etched results in an increase in interfacial bond strength[5]. Gao and Zeng[6] concluded that the adhesion increases by at least four time by plasma treatment and, also, a slight decrease in the surface energy of the treated monofilaments with ageing time is observed. Because of this attractive attributes, plasma treatment of the fibre surface has been considered the prime technique for the control of adhesion in composites. However, the time of treatment is an important parameter to be considered because when it is long the fibers can be degraded and have their mechanical properties reduced. For the plasma treatment, no real increase in pull strength with treatment time was obtained for more than 5-10s[7]. In another work, it was observed that treatment time longer than 180s with argon plasma causes heavy degradation on the poly(tetrafluoroethylene) fiber surface[8]. In this work three different treatment times, 5s 20s, and 100s were used to obtain the adhesion improvement, by objecting, specifically, a treatment time with which there is an increase of the superficial energy without further degradation of the fibers. The oxygen and argon plasma were used to treat the PET in order to promote a perfect interfacial adhesion with the matrix. The experimental design was performed by pull-out test in order to investigate the adhesion of the interface PET/PMMA. SEM analysis of the pull-out specimens after oxygen and argon plasma treatment were realised.

EXPERIMENTAL

Materials

The polymethyl methacrylate resin was polymerized from the methyl methacrylate monomer by a thermal polymerization at 100ºC. The polyethylene therephthalate (PET) fiber provided by Montefiber SpA (Acerra,

Naples-Italy), has a filament diameter about 13 microns and the elastic modulus about 1 GPa.

The PET filaments were treated in a cold plasma reactor using oxygen **or** argon gases, according to the following conditions: excitation frequency was 13,56 MHz, the power of the electrical field was 50 W, the pressure of treatment was 0,3 mbar and the treatment time varied from 5 to 100 s.

For the pull-out tests in tensile mode, an INSTRON 4204 at a constant speed of 12 mm min^{-1} with a 10 N load cell, was used. The pull-out specimens were made according to Gao and Zeng.[6] As shown in Fig. 1, one end of a monofilament with 40cm in length was embedded in a disc of resin that rested in the metal cylindrical support which is attached to a base device; the other end is glued between two cardboard tabs and then fixed in a superior grip attached to the load cell of the equipment.

Figure 1 – Pull-out specimen

The thickness of the disc which determines the immersion length (*l*) of the PET monofilament in the resin disc was 3 mm. The diameter of the monofilament was measured by a scanning electron microscope and the interface area was calculated. The fibre resin adhesion τ was defined according to the expression (1):

$$\tau \equiv \frac{P}{\pi . d . l} \equiv \frac{\text{failure load}}{\text{interface area}} \qquad \textbf{(1)}$$

The surface morphology analysis was developed using a scanning electron microscope LEICA 440S. Gold coating of the samples was carried out using EMSCOPE SC 500.

RESULTS AND DISCUSSION

Adhesion

Table I indicates the results obtained for the pull-out tests with the treated and untreated fibres.

Table1 – Tensile strength and fibre/resin adhesion values of the untreated and treated PET fibres by cold plasma, obtained with pull-out tests.

Treatment	Number of Sample	τ(MPa)	Sdt (MPa)	σmin(MPa)	σmax(MPa)	σu (MPa)
O_2 100”	4	895	116	833	1083	828
O_2 20”	8	862	96	650	975	816
O_2 5”	4	576	87	485	650	545
A_r 100”	6	931	161	668	1167	858
A_r 20”	4	792	139	650	975	748
A_r 5”	5	859	121	730	1048	829

It is possible to observe that the plasma treatments produce a significant effect on the fibre resin adhesion strength. Table I contains the number of specimens tested in each plasma treatment condition, the fibre

average tensile strength and the standard deviation, the minimum and maximum tensile strength and the fibre resin adhesion strength calculated according to equation (1). For the untreated fibre it was impossible to obtain the adhesion strength because the monofilament slighted from the resin disc as soon as the test stated. Experimental tests indicated that for all the treatment conditions the weakest point was the fibre, where the fracture occurred. In other words, the resin adhesion strength is higher than the fibre tensile strength, as shown in the Table 1. For the oxygen plasma treatment, the increase in treatment time from 5s to 20s resulted in an increase in the adhesion strength while for cold plasma treatment, the increase in the treatment time decrease the adhesion strength.

Scanning Electron Microscopy

Fibres surface of oxygen and argon plasma treated PET subsequently exposed to the matrix cure temperature, 100ºC and the roughness profile are represented in the figures 2 to 7.

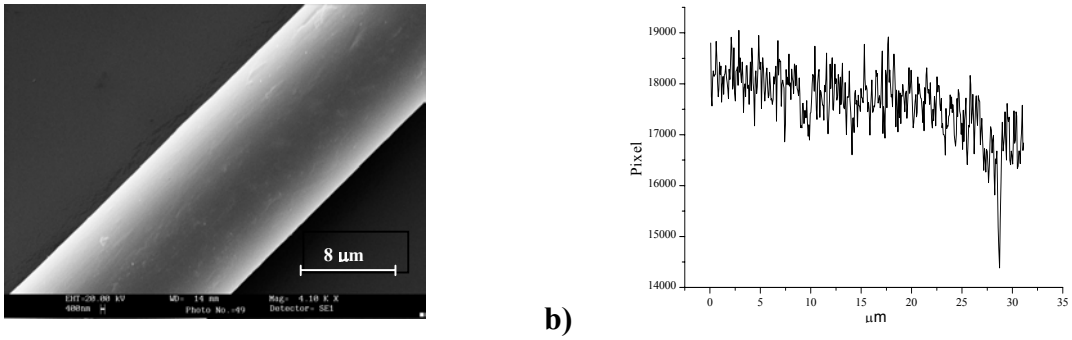

a) **b)**

Fig. 2 – Oxygen plasma treated PET fibres for 5s post heated at 100ºC a) scanning electron microscopy of the fibre surface. b) roughness profile of the PET fibre

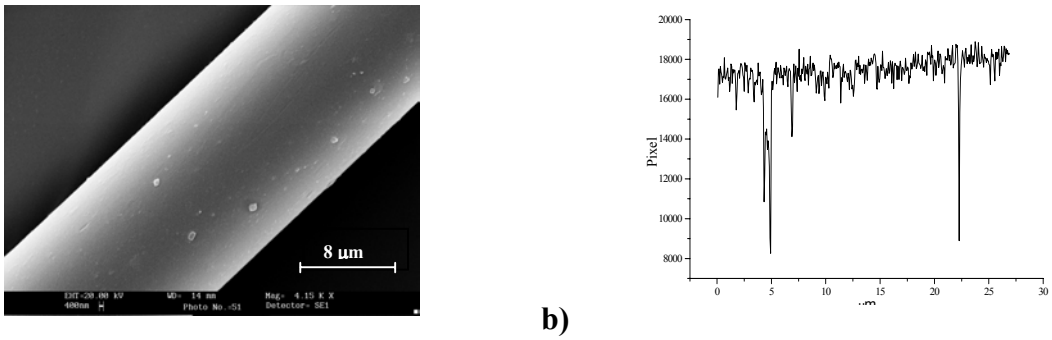

a) **b)**

Fig. 3 – Oxygen plasma treated PET fibres for 20s post heated at 100ºC a) scanning electron microscopy of the fibre surface. b) roughness profile of the PET fibre.

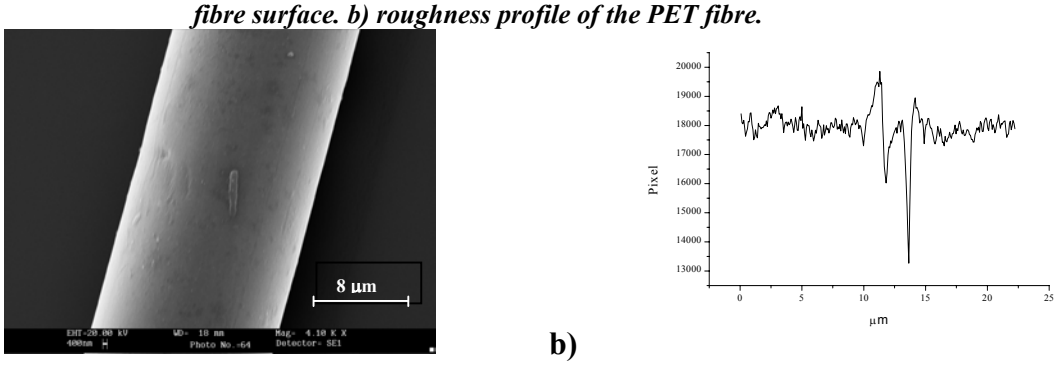

a) **b)**

Fig. 4 – Oxygen plasma treated PET fibres for 100s post heated at 100ºC a) scanning electron microscopy of the fibre surface. b) roughness profile of the PET fibre.

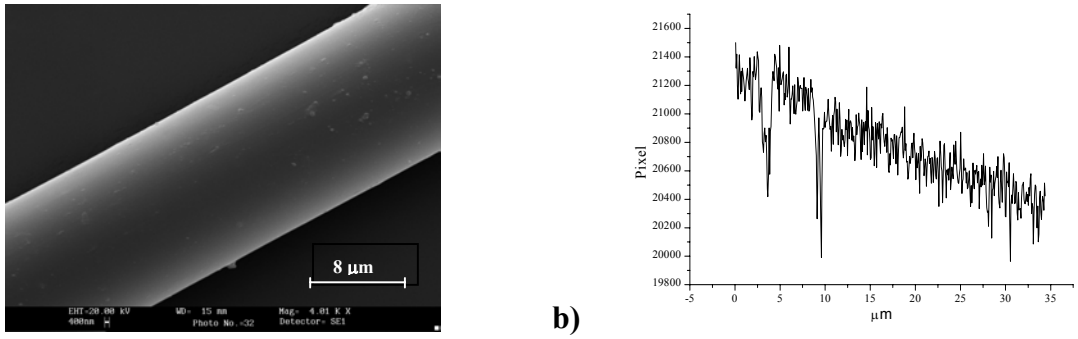

Fig. 5 – Argon plasma treated PET fibre for 5s post heated at 100ºC. a) scanning electron microscopy of the fibre surface. b) roughness profile of the PET fibre.

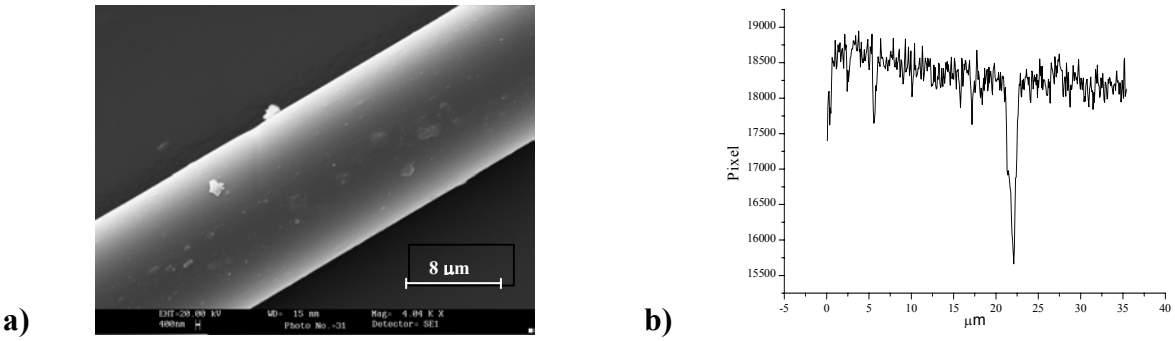

Fig. 6 – Argon plasma treated PET fibre for 20s post heated at 100ºC. a) scanning electron microscopy of the fibre surface. b) roughness profile of the PET fibre.

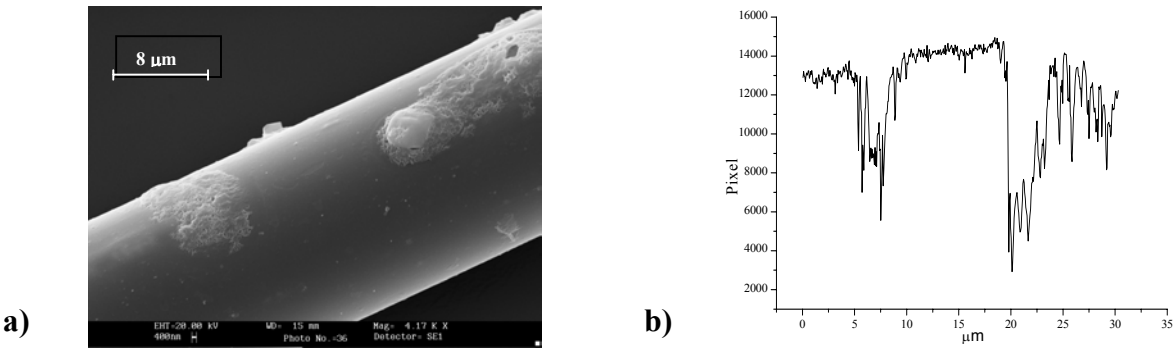

Fig. 7 Argon plasma treated PET fibre for 100s *post heated at 100ºC*. a) scanning electron microscopy of the fibre surface. b) roughness profile of the PET fibre.

Figures 2a to 7a represent the fracture surface of oxygen and argon plasma treated from 5s to 100s and post exposed to the matrix cure temperature, 100ºC. Roughness profile obtained through the scanning line method are represented in figures 2b to 7b and average distances of the roughness interval, for each condition, were calculated. The distances of the roughness interval (D_{ri}) for the oxygen plasma treated PET fibres from 5s to 100s post exposed at 100ºC were 0,44µm, 0,45µm and 0,57µm, respectively and for the argon plasma treated PET fibres from 5s to 100s post exposed at 100ºC were 0,59µm, 0,65µm and 0,99µm. As a comparison parameter, it is important to remember that D_{ri} is equal to 0,55 µm for the untreated fibres. Higher D_{ri} means less roughness peaks in the reference unit length; closely spaced surface defects are associated to low values of D_{ri}. On the other hand, surface analysis from figure 2a to 7a shows an intense

surface degradation on the fibres subjected to argon plasma. Roughness profile represented in figure 7b for argon plasma treatment 100s and post heated at 100°C confirms the significant reduction in the average tensile strength.

CONCLUSIONS

- The plasma treatments produce a significant effect on the fibre resin adhesion strength;
- For the untreated fibre it was impossible to obtain the adhesion strength due to the inertness and the low energy of PET fibres surface;
- For all treatment conditions the weakest point was the fibre, where the fracture occurred attesting that the fibre/resin adhesion strength is higher than the fibre tensile strength;
- The distance of roughness interval (D_{ri}) was a parameter obtained through the use of Scion Image Program and used to associate fibre surface condition after cold plasma treatment and average tensile strength. For oxygen and argon cold plasma treated fibres, D_{ri} is lower in comparison to the untreated fibres which explains decrease in the tensile strength. In some cases, higher roughness depth enhance stress concentration effects and influences mechanical behaviour.

Acknowlegdements

The authors wish to thank the support provided by FAPESP through the process number 97/01160-7.

REFERENCES

1. WEIDNER et al, *J. applied pol. Sci. : Part A: Pol. che,*. 36, (1998) 1639-1648.
2. GOULD, S.A. C., SCHIRALDI, D. A. & OCCELLI, M. L. *J. applied pol. sci.* (1998) 1237-1243.
3. BLACKMAN, B. R. K., KINLOCH, A. J. & WATTS, J. F. *Composites*, 25/5 (1994) 332-341.
4. KILL, G., HUNTER, D. H. & McINTYRE, N. S. *J. pol. sci.: part A pol. che.*, 34 (1996) 2299-2310.
5. JANG, B. Z. *Comp. sci. Tech*. 44 (1992) 333-349.
6. GAO, S. & ZENG, Y. *J. applied pol. sci.* 47, (1993) 2065-2071.
7. OCCHIELLO, E. et. al. *Composites*. 23/3 (1992) 193-200.
8. INAGAKI, N., TASAKA, S. & GOTO, Y. J. applied pol. Sci. 66(1997) 77-84.

REFERENCE: ICF100809OR

IN SEARCH OF A PARAMETER FOR FRETTING FATIGUE

A. L. Hutson[2], T. Nicholas[1], S. Olson[2] and N. Ashbaugh[2]

[1]Air Force Research Laboratory, AFRL/MLLMN, Wright Patterson AFB, OH 45433, USA

[2] University of Dayton Research Institute, Dayton, OH 45469-0128, USA

ABSTRACT

Fretting fatigue experiments were conducted to determine the fatigue limit stress at 10^7 cycles for Ti-6Al-4V. A step-loading procedure was used to determine the fatigue limit stress that, in turn, was applied to the test geometry in numerical simulations using finite elements. Several fretting pad geometries and specimen thicknesses were used to obtain a range of normal and shear forces that produced the stress and displacement fields in the specimen. An evaluation was made of the conditions near the edge of contact where peak stresses occur to deduce parameters which lead to fretting fatigue failures at 10^7 cycles. However, no simple combination of stresses and slip displacements could be used to correlate all of the experimental data. A fracture mechanics methodology was also employed in order to determine the conditions for propagation or non-propagation of cracks that initiate in the edge of contact region. While no parameters were found which could uniquely predict the fretting fatigue failure, adjustment of the coefficient of friction based on computed slip displacements was shown to have a substantial effect on the stress and stress intensity factors. A correlation of friction coefficient with slip displacement is proposed as a possible method for consolidating data from fretting fatigue experiments conducted under different conditions.

KEYWORDS

fretting, fatigue, fracture mechanics, titanium

INTRODUCTION

Fretting fatigue is a type of damage occurring in the presence of contacts in which at least one of the components is subjected to bulk loading. It is normally associated with small magnitudes of relative slip, on the order of tens of microns, and little if any material removal and can lead to premature crack initiation and failure. Such damage has been indicated as the cause of many unanticipated disk and blade failures in turbine engines.

Under laboratory conditions, the synergistic effects of various parameters make determination and modeling of the mechanical behavior of fretting fatigue extremely difficult. The stress state in the contact region involves very high peak stresses, steep stress gradients, multi-axial stresses and differing mean stresses. Further, there is controversy whether the problem is primarily one of crack initiation or a crack propagation

threshold, and whether or not stress states rather than surface conditions play a major role in the observed behavior. The parameters which govern the initiation and subsequent propagation of fretting fatigue cracks is still not well established. Thus the objectives of this investigation are to find several different fretting fatigue conditions analogous to the fatigue limit stress under uniaxial fatigue loading corresponding to a chosen high cycle fatigue (HCF) life. From these, both stress fields and stress intensity factors for specific cases can be obtained in order to find some commonality which may lead to development of parameters having broad application to fretting fatigue.

EXPERIMENTS

Tests were conducted using a high frequency test system to simulate the fretting fatigue loading conditions that occur in turbine engine blade attachments [1,2,3]. The apparatus uses flat fretting pads, with a radius at the edge of contact, against a flat specimen. Normal and shear loads are applied to the specimen as shown in Figure 1. A previous study has shown that the bending moment present in the apparatus is negligible relative to other parameters, and may be disregarded when designing the tests [4].

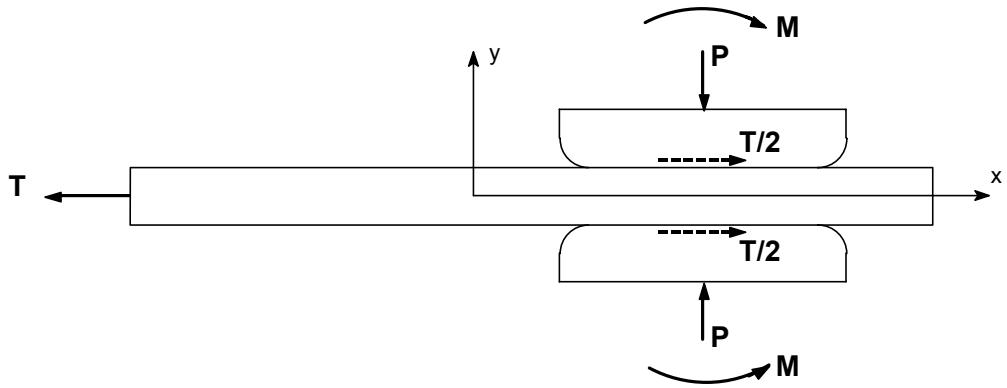

Figure 1: Test geometry and loading schematic.

The test geometry differs from conventional fretting fatigue tests [5,6] in two fundamental ways. First, the axial stress is transferred entirely to the fixture through shear. Resulting stresses in the specimen are zero on one end of the pad, thus the shear force into the pad is determined from the load applied to the specimen. Second, symmetry of the apparatus provides a specimen which breaks on one end, leaving the other end with a fretting scar and damage obtained under nominally identical conditions. As with a conventional fretting fatigue apparatus, the clamping force is constant and only the axial and shear loads are oscillatory.

All tests were conducted at 300 Hz under ambient lab conditions. Specimens and pads were taken from forged Ti-6Al-4V plates used in a series of investigations under a U.S. Air Force sponsored high cycle fatigue program. The processing and microstructure are reviewed in previous work [7,8]. Each specimen was subjected to uniaxial fatigue using a step-loading procedure [9] to determine a fatigue limit stress corresponding to 10^7 cycle fatigue life. Tests were conducted by incrementing the maximum axial stress by five percent of the initial value for various combinations of specimen thickness, pad length, and clamping force. The step loading technique was validated in earlier fretting fatigue studies using the same apparatus [3,10], and is outlined in reference [11].

ANALYSIS

Finite element analysis (FEA) results from a prior investigation [1] and additional computation provided stress fields through the specimen thickness and along the length of the specimen in the vicinity of the edge of contact. Load conditions were selected to cover a range of combinations of pad and specimen geometry, which produce average shear stresses typical of those tested in the experimental portion of the study. Conditions used in the numerical analysis are summarized in Table 1 along with some of the results for comparison. Axial stresses applied to the specimens in the model were taken from experimental

observations. The model included pads with a 3.175 mm blending radius at both ends, resulting in an undeformed contact length of 6.35 mm for the short pad and 19.05 mm for the long pad. In two of the three test conditions simulated numerically [1,3,4], the coefficient of friction, μ, was taken as 0.3. The third case was run with μ=1.0, to allow comparison of results where only μ was changed.

Assuming cracks normal to the specimen surface under pure mode I loading, and using the stresses from the FEA, the stress intensity factor, K, was computed as a function of crack length. The K distributions were calculated using a program developed to model a single edge tension (SE(T)) specimen geometry under a non-constant σ_x stress field [12]. Some success has been reported in modeling fretting fatigue behavior as an edge notch, since both conditions produce similar stress fields [13]. Characterization results from a prior investigation [4] indicated that cracks nucleated at or near the edges of contact in specimens tested in the existing apparatus. The objective of these calculations was to compare the K values from two different cases where the peak stresses were significantly different, yet the stress fields both matched conditions corresponding to failure in 10^7 cycles.

The K solution program required material and crack dimension input parameters in addition to the stress distribution data. 120 GPa was used for the material modulus. The depth position of the final stress value given in the stress distribution, which was equal to half of the specimen thickness, was used for the final crack length. Stress intensity values are only reported for the first 100μm into the specimen thickness, although calculations were performed as far into the model specimen as possible using the available stress data from the FEA simulation.

TABLE 1
SUMMARY OF TEST CONDITIONS AND RESULTS FOR FINITE ELEMENT ANALYSIS.

Specimen thickness (mm)	Pad length (mm)	μ	Clamping Load (kN)	Applied σ_{axial} (MPa)	Average σ_y (MPa)	Average τ_{xy} (MPa)	Peak σ_x (MPa)	Max. Relative Displacement (μm)
1	12.7	0.3	49	275	770	21.6	1300	4.0
4	25.4	0.3	34	275	140	28.9	540	19.0
4	25.4	1.0	34	275	140	28.9	1100	3.4

RESULTS & DISCUSSION

The first results presented are the Haigh stresses corresponding to a 10^7 cycle fatigue life for the 1 mm and 4 mm thick specimens over a range of contact conditions (Figs. 2 and 3). The data are presented as a function of average applied clamping stress, which is taken to be positive. Two contact radii (CR) and two stress ratios are represented, and the baseline uniaxial fatigue limits for this material: 660 MPa @ R=0.5, 558 MPa @ R=0.1, are included. The numerical simulation conditions area also noted.

Much of the data for the 4 mm thick specimens was reported earlier [1] and seemed to indicate no appreciable trend as a function of applied clamping stress. However, the data for the 1 mm thick specimens do show a trend of increasing fatigue strength with decreasing applied clamping stresses, which was not noted in previous investigations [1,4]. The trend is not marked and conducting tests with clamping stresses much below 100 MPa to verify the trend is not possible, since clamping stress has to be applied to keep the specimen from pulling out of the grips in the current test apparatus. Also, the trend is obscured by experimental scatter in tests involving the smaller (0.4 mm) contact radius. Another feature to note in comparing Figures 2 and 3 is an apparent effect of thickness. The 4 mm thick specimens produced much lower fatigue limit stresses than 1 mm thick specimens under similar contact conditions, emphasizing the need for investigators to consider test specimen geometry issues closely in the development of life prediction models for service components.

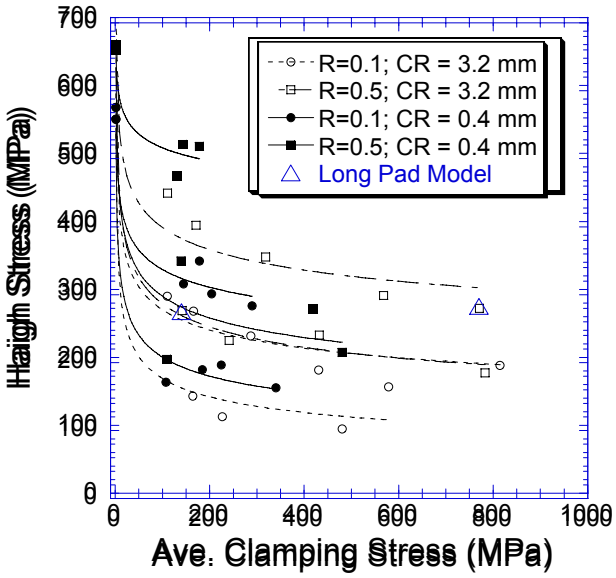

Figure 2: Experimental results for 1 mm thick specimens and unfretted baseline conditions.

Figure 3: Experimental results for 4 mm thick specimens and unfretted baseline conditions.

The next results presented are the K solutions plotted as a function of depth into the specimen (Figs. 4 through 6) for the deformed edge of contact (DEC) location and two adjacent locations 20 μm on either side of the DEC. In Figures 4, 5, and 6, y=0 corresponds to the surface of the specimen in contact with the pad. Each plot also includes the axial stress σ_x, illustrating the extent of the gradients into the specimen thickness for the corresponding K curve. The K values peak at the DEC, as do the stresses on the specimen surface. Other cases (not shown) for locations farther beyond the DEC indicated K values decaying proportional to the stress field. However, K distribution trends at the DEC show a continuous increase in K with crack length, and point to crack propagation to failure and not crack arrest, as reported for other geometries [5].

In comparing the various cases modeled here, we first address the cases where μ is taken as 0.3, a value which represents an average of values corresponding to gross slip over the entire pad length [1]. Data for the 1 mm thick specimen and short pad case are shown in Figure 5; data for the 4 mm thick specimen and long pad are shown in Figure 6. The values of maximum σ_x, shown in Table 1, vary from ~500 MPa for the 4 mm thick long pad case (Fig. 5) to ~1300 MPa for the 1 mm thick short pad case (Fig. 4). Since K depends strongly on the stress field, the calculated K values are higher for the case with the higher stresses, namely the 1 mm thick specimen and short pad case. Variations of stress gradients into the depth from one case to another are not too great and have little effect on the nature of the variation of K with crack length.

The experimental results for these two cases indicate nearly identical fatigue limits (Figs. 2 and 3). One would expect similar peak stresses and stress intensity factors in cases reflecting similar fatigue limits for the same fatigue life. As reported previously [1], differences in applied shear stress and average applied clamping stress at the contact for these two cases do not adequately explain the marked differences in the stresses from the numerical simulations. One possible explanation lies in the value of μ used in the analyses. Work by other researchers has indicated pronounced changes in μ over time under fretting fatigue conditions [14, 15], and as our previous work indicated, overall fretting fatigue behavior is extremely sensitive to μ.

Another observation from the previous work [1] was that the maximum relative displacement (see Table 1) at the edge of contact was considerably different for the two cases studied. This observation, coupled with the observation that increasing the value of μ resulting in increasing values of σ_x, lead to consideration of increasing μ for the case of the 4 mm thick specimen, which showed both lower stresses and higher relative displacements. While there is no physical basis for this assumption, the concept of higher μ for higher slip displacements is not totally without merit. It is also of interest to note that an early fretting parameter [10] contained the product of the stress and relative displacement. Perhaps the theory proposed here has the same

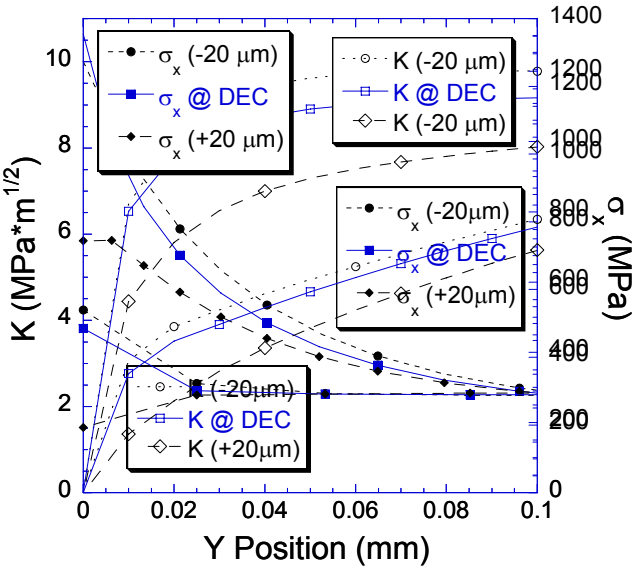

Figure 4: Stress distribution and resulting K solution for 1 mm thick specimen case.

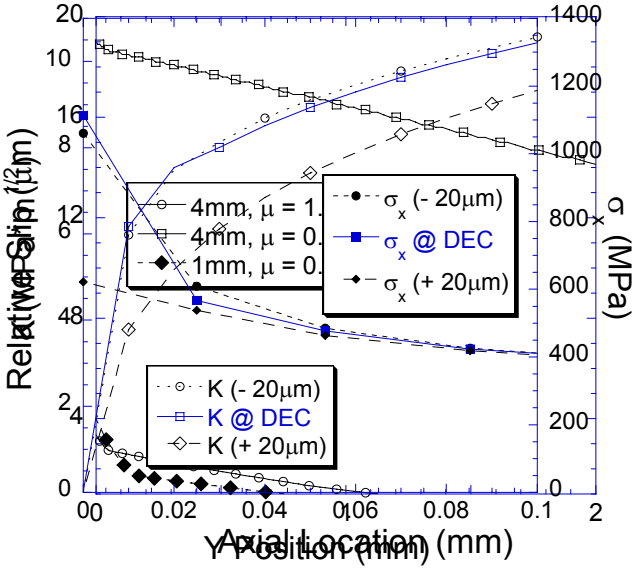

Figure 6: Stress distribution and resulting K solution for 4 mm thick specimen, μ=1.0 case.

Figure 5: Stress distribution and resulting K solution for 4 mm thick specimen, μ=0.3 case.

Figure 7: Comparison of relative displacements along the contact calculated for all three simulation conditions identified in Table 1.

effect by increasing the stress through an increase in μ rather than through multiplying by relative displacement. To explore this concept the next comparison is of the two cases in which a 4 mm thick specimen with a long pad was modeled with two different values of μ. Increasing μ arbitrarily from 0.3 to 1.0 results in an increase in the maximum σ_x from ~ 500 MPa (Fig. 5) to 1100 MPa (Fig. 6). A similar increase was noted in the previous investigation of a 2 mm thick specimen [1]. Corresponding increases in maximum shear stresses were also noted for increases in μ, which are not discussed here. As with the previous comparison, the case with μ=1.0 resulting in higher tensile stresses also produced higher K values.

Changes in μ also produce changes in relative slip between the pad and specimen. In Figure 7, relative slip is plotted from the DEC, denoted by x=0, to x=2.0 mm under the fretting pad. Maximum slip distance occurs at the edge of contact, which is where the maximum tensile stresses occur. For the 4 mm thick specimen and long pad cases discussed above, the maximum slip distances corresponding to maximum tensile stresses is reduced from 19 μm (500 MPa) to 3.4 μm (1100 MPa). By comparison, the 1 mm thick specimen and short pad case produced a maximum relative slip of 4.0 μm (1300 MPa). These results are consistent with findings from the previous investigation, which concluded that stresses and displacements near the edge of contact are very sensitive to the value of μ between pad and specimen [1].

For the conditions modeled here, we hypothesized that initial slip conditions corresponding to μ=0.3 change over time to conditions of increasing μ, and thus increasing σ_x and corresponding K values. As shown above, higher tensile stresses and the resulting K values may be produced either by imposing a high clamping stress or by increasing μ. An equilibrium condition may exist for μ, which is dependent on the resultant relative displacement. If such a condition exists, an iterative method would be required to determine the final condition.

COMMENTS & CONCLUSIONS

Changes in μ over time for various fretting fatigue conditions vastly compound the problem of accurate life prediction for fretting fatigue, since it is very difficult to determine how μ will change over time. Further, such a change will be different for each combination of pad material, specimen material, applied loads, surface modification, and environment. Since fretting fatigue behavior is so profoundly influenced by μ which, in turn, may depend on relative displacements, additional research in how μ changes under fretting fatigue conditions is recommended.

Within the constraints of the geometry and test configuration and loading conditions examined in this investigation and under the assumptions made in the analyses, particularly that of μ being 0.3, the following conclusions can be drawn.

1. High levels of slip may produce increases in μ, which might have to be revised to produce higher stresses and smaller displacements.
2. Stress and relative displacement (slip) fields are very sensitive to the value of μ chosen for analysis.
3. Under the assumption of a Mode I crack normal to the surface, if a crack nucleates, it will continue to propagate to failure.

REFERENCES

1. Hutson, A.L., Nicholas, T., Olson, S.E., and Ashbaugh, N.E. *Submitted to Int. J. Fatigue.*
2. *Fretting Fatigue: Current Technologies and Practices, ASTM STP 1367*(1999). D.W. Hoeppner, V. Chandrasekaran, and C.B. Elliot (Eds). American Society for Testing and Materials, West Conshohocken, PA.
3. Hutson, A., Nicholas, T., and Goodman, R.(1999) *Int. J. Fat.* 21, 7, 663.
4. Hutson, A.L.(2000). MSc Thesis, University of Dayton, USA.
5. *Fretting Fatigue, ESIS 18*(1994). R.B. Waterhouse and T.C. Lindley (Eds). Mechanical Engineering Publications, London.
6. *Standardization of Fretting Fatigue Test Methods and Equipment, ASTM STP 1159*(1992). M. Helmi Attia, and R. B. Waterhouse (Eds). American Society for Testing and Materials, Philadelphia.
7. Peters, J.O. and Ritchie, R.O., *Submitted to Int. J. Fat*.
8. Moshier, M.A., Nicholas, T. and Hillberry, B.M., *Submitted to Int. J. Fat*.
9. Maxwell, D., and Nicholas, T.(1999). In: *Fatigue and Fracture Mechanics: 29th Vol., ASTM STP 1321,* pp. 626-641, T. L. Panotin and S. D. Sheppard (Eds), American Society for Testing and Materials, West Conshohocken, PA.
10. Ruiz, C., Boddington, P. H. B., and Chen, K. C.(1984) *Experimental Mechanics* 24, 208.
11. Thompson, S.R., Ruschau, J.J. and Nicholas, T. *Submitted to Int. J. Fat*.
12. John, R., Weight Function Analysis for a Single Edge Cracked Specimen, Unpublished work, Air Force Research Laboratory (AFRL/MLLN), Wright-Patterson AFB, OH.
13. Giannakopoulos, A.E., Lindley, T.C., Suresh, S., and Chenut, C. *Submitted to Fat. Frac. Eng. Mat. Structures.*
14. Szolwinski, M.P.. Matlik, S.F. and Farris, T.N.(1999). *Int. J. Fat.* 21, 671.
15. Farris, T.N., Harish, G., McVeigh, P.A., and Murthy, H.(2000). In: Proc of the 5th National Turbine Engine High Cycle Fatigue (HCF) Conference on CD, Session 13, Chandler, AZ.

IN VITRO BIOACTIVE FUNCTIONAL OF BIO CERAMICS IN A SIMULATED BODY FLUID

Noriyuki HISAMORI*, Akira NOZUE* Mamoru AIZAWA* and Hiroshi SUEMASU*

* Department of Mechanical Engineering, Sophia University
7-1 Kioi-cho, Chiyoda-ku, Tokyo, 102-8554 Japan
TEL&FAX: +81-3-3238-3318
E-mail : hisamori@me.sophia.ac.jp
http://www.sophia.ac.jp/

ABSTRACT

Apatite ceramics and A-W glass ceramics matrix bonds to living bone through an apatite layer that is formed on its surface in the body. It has been confirmed by SEM observation, thin film X-ray diffraction and FT-IR reflection spectroscopy that the apatite layer can be reproduced on the surface of the hydroxyapatite ceramics and A-W glass ceramics even in an a cellular simulated body fluid with ion concentrations nearly equal to those of human blood plasma. In the present study, structures of bioactive hydroxyapatite ceramics, A-W glass ceramics and the apatite layer formed on its surface in the simulated body fluid were observed under an Atomic Force Microscope (AFM). The apatite layer formed on the substrate apatite ceramics or A-W glass ceramic in the simulated body fluid consisted of the fine apatite particle about 2-3 μ m. The apatite particle in the surface layer was in direct contact with those within the apatite ceramics or A-W glass ceramics without intervention of such hydroxyapatite substrate or A-W glass ceramics substrate.

KEY WORDS

Hydroxyapatite, A-W Glass Ceramics, Bioactive, Simulated Body Fluid, Apatite Layer Form, Fracture resistance, microstructure

INTRODUCTION

Biocompatible materials, such as bioactive ceramics and bioactive glass ceramics can be effective in the repair of bone defects during orthopedics surgery. These materials, calcium phosphates, hydroxyapatite ceramics (HA: $Ca_{10}(PO_4)_6(OH)_2$), tricalcium phosphate (TCP: $Ca_3(PO_4)_2$) etc and A-W glass ceramics [1, 2]. These materials have been found by observation to exhibit varying degrees of osteoconductive behavior. The hydroxyapatite ceramics and bioactive glass ceramics was known as a highly bioactive ceramics, and replacements of lost bone [3, 4]. The same types of the apatite layer was also observed on the surface of hydroxyapatite ceramics and A-W glass ceramics, where as it was not observed on the surface of bioinert ceramics. This indicates that the formation of the apatite layer is prerequisite for the chemical bond of apatite ceramics to living bone. However, detailed structure of the formed apatite layer, such as the size, morphology and composition of the apatite crystal, as well as the detailed microstructure of apatite ceramics and A-W glass ceramics itself has not been revealed yet. The purpose of the present study is to investigate these issues by a high resolution and 3d image AFM.

EXPERIMENTAL PROCEDURE

Preparation of Hydroxyapatite

Submicrometer hydroxyapatite powder (HAp-200 ($Ca_{10}(PO_4)_6(OH)_2$) : 0.3～0.5 μ m average grain size: Taihei chemical industrial Co., Ltd.) were used as starting materials for making hydroxyapatite ceramics. The chemical compositions of this powder were shown in Table1. Pressureless sintering was performed at 1375℃ in O_2 atmosphere using the presintered bodies. And also, A-W glass ceramics, which is commercialized by the name of cerabone A-W, was supplied from Nippon Electric Glass Co., Ltd. (Otsu, Japan). The procedure for preparing the glass-ceramics was previously reported [2]. The dimensions of the soaking specimens used in this study are disk plate size ϕ 16mm×3(t)mm were abraded with the 0.1 μ m diamond paste polished, and washed with pure methanol and distilled water in an ultrasonic cleaner.

TABLE 1
Contents except for hydroxyapatite powder (numerical weight 2000).

Factor	Chloride	Sulfate	Heavy metal (Pb)	Fe
Content [ppm]	20 >	50 >	5 >	10 >
Factor	As	Mg	Mn	
Content [ppm]	1 >	50 >	20 >	

Soaking in Simulated Body Fluid

The hydroxyapatite ceramics specimen were soaking in an a cellular simulated body fluid (SBF) with pH and ion concentration nearly equal to those of human blood plasma [5-8], as given in Table 2, to evaluate their surface bioactivities by examining apatite formation on their surface. The SBF was prepared by dissolving reagent-grade NaCl, $NaHCO_3$, KCl, K_2HPO_4, $3H_2O$, $MgCl_2 \cdot 6H_2O$, $CaCl_2$, and Na_2SO_4 into distilled water, and buffered at pH 7.40 with tris (hydrotymethyl) amminomethane ($(CH_2OH)_3CNH_3$) and hydrochloric acid at 37.0℃. Each specimen was soaked in 30ml of SBF at 37.0℃ foe various periods, and them removed form the fluid and washed with methanol.

TABLE 2
Ion concentrations and pH of simulated body fluid (SBF) and those of human blood plasma.

(mEq/L)

	Na^+	K^+	Ca^{2+}	Mg^{2+}	Cl^-	HCO_3^-	HPO_4^{2-}	SO_4^{2-}	other
Sodium chloride	154.0				154.0				
Ringer fluid	130.4	4.0	2.7		109.4				27.7(Lact.)
Simulated Body Fluid	142.0	5.0	2.5	1.5	147.8	4.2	1.0	0.5	100(Tris)
Blood plasma	142.0	5.0	2.5	1.5	103.0	27.0	1.0	0.5	

Lact : Lactic acid

Tris : Tris-hydroxymethyl - amminomethane

Analysis of Specimen with Surface and SBF

Surface structure changes of the specimens due to the subsequent soaking in SBF were examined by thin film X-ray diffraction [9] (TF-XRD: Model Rint 2000, Ri Rigaku, Japan), FT-IR reflection spectroscopy (FT-IR: Model 8200RH, Shimadzu, Japan) and scanning electron microscopy (SEM: Model JEM6100, JEOL, Japan). Changes in element concentration and pH of SBF due to soaking of the specimens were measured by inductively coupled plasma (ICP) atomic emission spectroscope (Model 7000, Shimadzu, Japan) and pH meter (Model PH82, Yokogawa, Japan). Moreover, higher magnification, nanometric, surface damage and apatite layer evolution is required, instead of traditional micron-order damage evolution by using an in-situ atomic force microscope. Nanometric damage was examined with a scanning atomic force microscopy (AFM) (Model SPM-9500J2, Shimadzu, Japan)

Mechanical Test Methods

Fracture resistance measurements were performed at room temperature, the standard disk-shaped compact specimen is a single edge-notched and fatigue crack disk segment loaded in tension. The general proportions of this specimen configuration are shown Figure 1 and Figure 2.

$$K_C = \frac{P}{Bw^{1/2}} \frac{\left(2+\frac{a}{w}\right)\left\{0.76+4.8\frac{a}{w}-11.58\left(\frac{a}{w}\right)^2+11.43\left(\frac{a}{w}\right)^3-4.08\left(\frac{a}{w}\right)^4\right\}}{\left(1-\frac{a}{w}\right)^{3/2}} \quad \cdots\cdots \quad (1)$$

The fracture resistance (*Kc*) was determining by employing tension testing method (ASTM E399-90). *Kc* values were calculated by using the following equation, where *Kc* is fracture resistance [MPa·$m^{1/2}$], *P* is fracture load [kN], *B* is thickness [cm], *a* is crack length [cm] and w is width [cm] generated in the material tested.

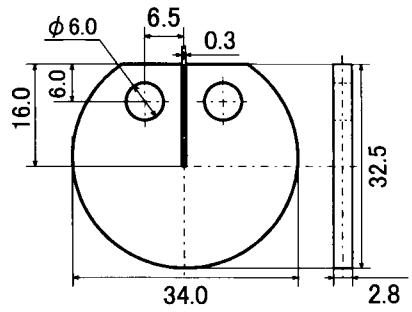

Figure 1 Shape and dimension of specimen

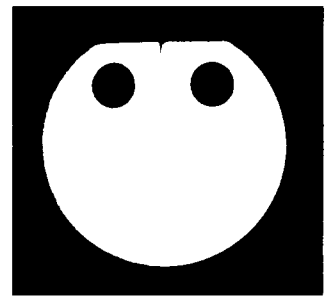

Figure 2 Out looks of Hydroxyapatite CT specimen

RESULTS AND DISCUSSIONS

Bioactive Functional of Apatite Ceramics in a Simulated Body Fluid

Figure 3 shown SEM photographs of sintered surface of apatite ceramics. Figure 4 shown SEM photographs of the cross section of apatite ceramics layer formed that was soaked periods in SBF were (a) 2, (b) 6, and (c) 8weeks. It can be seen from Figure 4 that islandlike substances consisting of particle are formed on all the substrates. Figure 5 shows TF-XRD patterns of the surface of apatite ceramics substrate that were soaked in SBF for 0week and 3weeks. The new XRD peaks appearing after the soaking in SBF are all ascribed to crystalline apatite. Figure 4 show that the islandlike substance formed on the substrate are crystalline apatite and the rate of apatite formation is considerably increased by the soaking periods in SBF for 8weeks. The apatite layer thickness evaluation shown in Figure 6 indicates that the mean thickness increased from 0 μ m to 100 μ m while soaking in SBF for 2,4,6 and 8weeks, respectively.

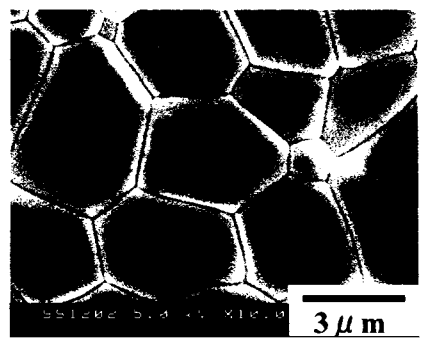

Figure 3 SEM photograph of etched surface of hydroxyapatite ceramic, sintered at 1375℃

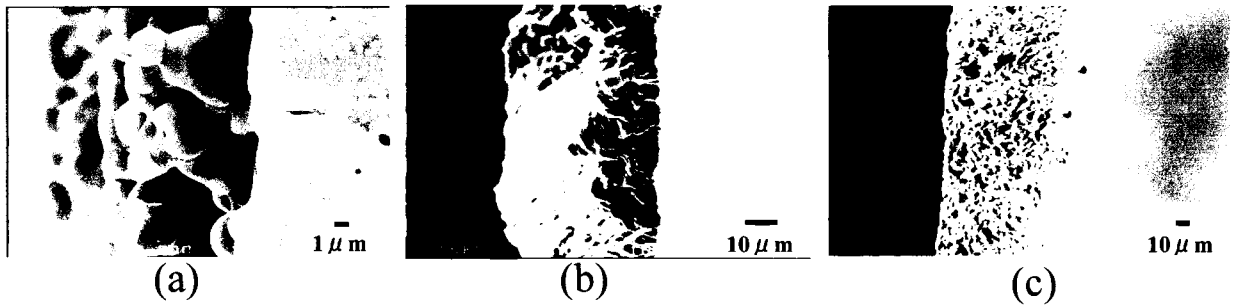

Figure 4 SEM photographs of grown precipitate layer on hydroxyapatite ceramic. ((a) Soaking in SBF for 2weeks, (b) 6weeks, (c) 8weeks)

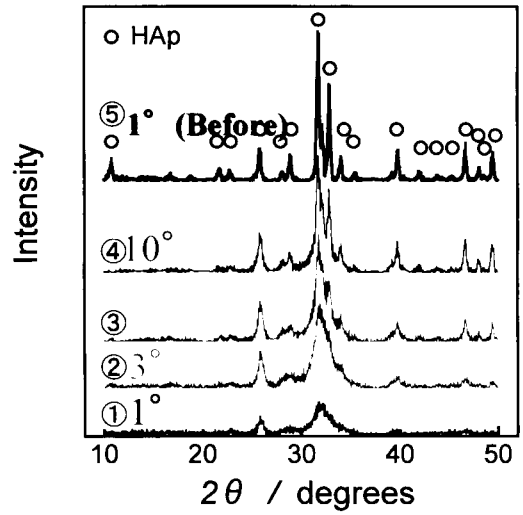

Figure 5 TF-XRD patterns of hydroxyapatite ceramic in SBF (O: hydroxyapatite)

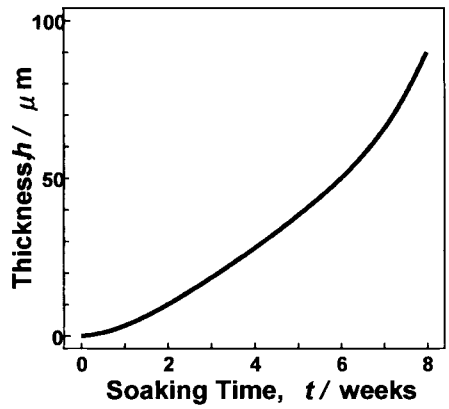

Figure 6 Effects of soaking time on hydroxyapatite particle thickness in SBF

Self-Healing Function of Apatite Ceramics

The room temperature fracture toughness of apatite ceramics, after SBF soaking for from 2 to 8weeks under 37℃, is shown in Figure 7. As a result, corrosion degradation of hydroxyapatite ceramics was preferentially recognized on hydroxyapatite particle after short time immersion into SBF. The general tendency of drastic decrease in fracture toughness was recognized in these materials. In case of materials specimen, most remarkable decrease in fracture toughness after 3weeks immersed into SBF was detected this remarkable degradation in fracture toughness was bought about by the crack propagation behavior of going through into corroded pit (Figure 8). However, the specimens after 4weeks immersion into SBF showed improved fracture toughness compared with those of corroded

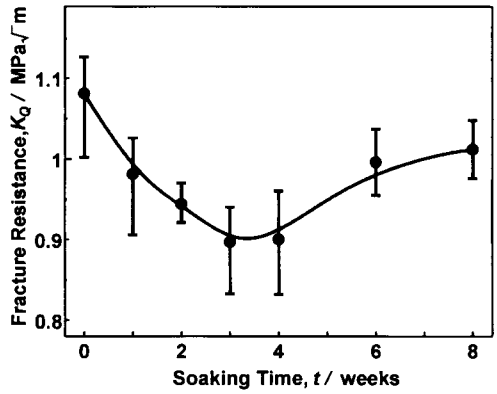

Figure 7. Effects of soaking time on fracture resistance of hydroxyapatite ceramics in SBF

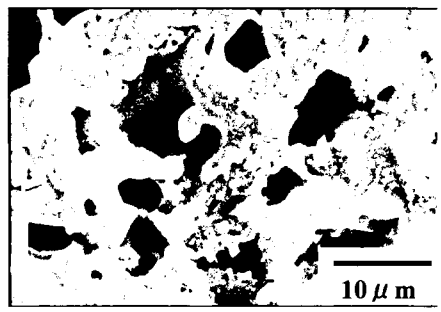

Figure 8 SEM photographs of corroded pits surface of hydroxyapatite ceramics in SBF for 3weeks

hydroxyapatite ceramics (until 3weeks). There improvements in fracture toughness may be brought about through the mechanics was shown to induce the apatite layer formation on it's surface in some areas between 4 and 8weeks by simulated body fluid. The apatite layer formed on the it's hydroxyapatite surface in the SBF consisted of apatite particle about 100 μ m thickness and high interface strength (Figure 6).

In Vitro Bioactive Functional of Apatite Ceramics by In-situ AFM Observation

Through employing AFM analysis, examination of the hydroxyapatite layer formed of the hydroxyapatite ceramics and A-W glass ceramics was conducted. The results are shown in figure 9. Formation of apatite layer was investigated by in-situ AFM observation on the surface of A-W glass ceramics. Effect of apatite layer formed in A-W glass ceramics upon bioactive functional properties were investigated : through examining surface before preconditioned in 37℃ SBF, which were preconditioned in 37℃ SBF solution for 24hr. In case of A-W glass ceramics specimen, most remarkable corrosion pit and grown precipitate was recognized. The specimen of soaking in SBF

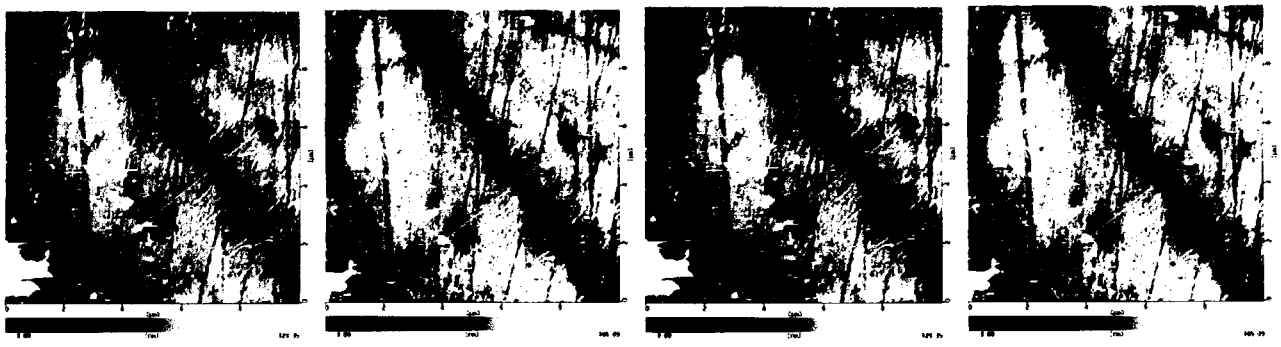

(a) 0min (b) 30min (c) 45min (d) 60min

Figure 9 In-situ visualization of precipitate particle and corrosion products of A-W glass ceramics by AFM in a SBF (1.5) solution, which were preconditioned in 37℃ SBF solution for 24hr.

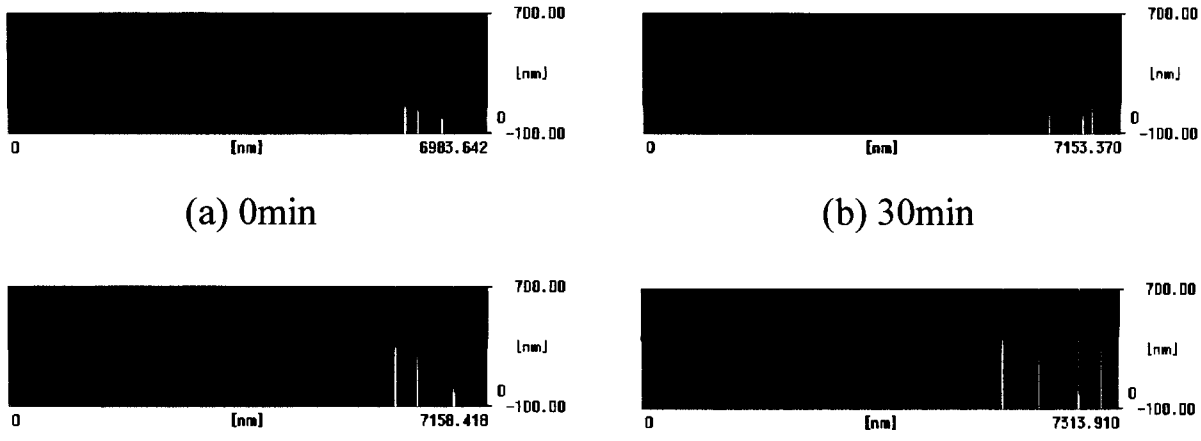

Figure 10 In-situ visualization of precipitate particle and corrosion products of A-W glass ceramics by AFM in a SBF (1.5) solution, which were preconditioned in 37℃ SBF solution for 24hr.

showed the strongest grown precipitate layer and corrosion pit (Figure 10(d)).

SUMMARY

The apatite layer formed on the sintered apatite ceramic in the simulated body fluid consisted of fine needle like apatite particle, which are elongated along C-axis and random oriented. The apatite particles in the surface layer were in direct contact with those within the apatite ceramics substrate without intervention of Ca and P ion. Apatite layer formed in simulated body fluid bought about the fracture resistance changes from corrosion damages to precipitate apatite particle. Nanometreic precipitate apatite particle and corrosion damage is successfully in situ imaged by atomic force microscope.

REFERENCES

1. T.Kokubo, M,Shigematsu, Y.Nagashima, T.Nakamura, T.Yamamuro and S.Higashi, Bull, Inst. Chem., Kyoto Univ., **60**, 260-68 (1982)
2. T.Kokubo, S.Ito, S.Sakka and T.Yamamuro, J.Mater. Sci., **21**, 536-40 (1986)
3. G.Emerwin, Ann.Otil. Rhinol Laryngol. **95**, 76 (1986)
4. J.Wilson, E.douek and K.Rust, Bioceramics, **8**, 235 (1985)
5. C.Ohtsuki, H.Kushitani, T.Kokubo, S.Kotani and T.Yamamuro, J. Biomed. Mater. Res., **25**, 1363-70 (1991)
6. Kokubo, S.Ito, Z.T.Zuang, T.Hayashi, S.Sakka, T.Kitsugi and T.Yamamuro, J. Biomed. Mater. Res., **24**, 331-43 (1990)
7. Y.Ebisawa, T.Kokubo, K.Ohura and and T.Yamamuro, J. Mater. Sic.:Mater Med., **1**, 239-44 (1990)
8. T.Kokubo, Y.Ebisawa, Y.Sugimoto, M.Kiyama, K.Ohura, T.Yamamuro, M.Hiraoka and M.Abe,Terre Haute 213-23 (1992)
9. T.Kitsugi, T.Nakamura, T.Yamamuro, T.Kokubo, M.Shibuya and M.Takagi, J. Biomed. Mater. Res., **21**, 1255-71 (1987)

Oral Reference: ICF100267OR

IN-SITU CHARACTERIZATION OF MATRIX RESPONSE TO FIBER FRACTURES

Jay C. Hanan[1], Irene J. Beyerlein [2], Ersan Üstündag[1], Geoffrey A. Swift[1]
Bjørn Clausen[1], Donald W. Brown[2], and Mark A. M. Bourke[2]

[1] *Department of Materials Science, California Institute of Technology, Pasadena, CA 91125, USA*
[2] *Materials Science and Technology Division, Los Alamos National Laboratory, Los Alamos, NM 87545, USA*

ABSTRACT

Successful application of metal matrix composites often requires strength and lifetime predictions that account for the deformation of each constituent. However, the deformation of individual phases in composites usually differs significantly from their respective monolithic behaviors. For instance, generally little is known about the *in-situ* deformation of the metal matrix and fiber/matrix interface region, other than that it likely differs from the bulk material response. This article describes an approach to quantifying the *in-situ* deformation parameters using neutron diffraction measurements of matrix failure around a fiber fracture in a model composite consisting of an Al matrix and a single Al_2O_3 fiber. We also study the shear sliding resistance as it evolves through fiber fracture upon loading and unloading. Matching the stress/strain distributions predicted from micromechanical models to the measured strain distributions determined by neutron diffraction under applied tensile loading results in an estimate of the typically non-linear, stress-strain behavior of the metal matrix.

KEYWORDS

Metal-matrix composite, neutron diffraction, constitutive behavior, fiber fracture, matrix yielding, Al-Al_2O_3 composite, interface shear strength.

INTRODUCTION

The strength and lifetime of fiber composites are largely governed by the nucleation and interaction of fiber fractures. These fractures unload onto neighboring fibers and matrix, generating strain concentrations which can promote more fiber breaks. The magnitudes and length scales of the strain concentration fields depend on the response of the matrix and interface. Therefore, knowledge on the *in-situ* constitutive behavior of these regions are crucial for determining internal stress states.

Particularly for metal matrix composites (MMCs), the deformation of the matrix material *in-situ* often differs significantly from its respective monolithic, bulk behavior. Generally little is known about the *in-situ* deformation behavior of the metal matrix and fiber/matrix interface region, other than that it likely differs from the bulk material response. There are many possible reasons: (i) microstructural constraints, (ii) localized strain gradients (e.g., near phase boundaries and defects), and (iii)

microstructural features, such as grain size and dislocation densities, of the matrix and interphase, that differ from monolithic features by virtue of the fabrication and consolidation process. The objective of this work is to develop *in-situ* constitutive laws for the matrix and the interface region.

Both single and multiple fiber micromechanical composite models for stress distributions around fiber fracture(s) employ various mathematical forms for the matrix or interface, ranging from rigid plastic to strain hardening, for instance. The simplest model, developed by Kelly and Tyson [1], assumes the matrix or interface deform only in shear and are rigid plastic with a constant shear stress τ_0. The fiber remains elastic and sustains only axial strains. Due to the high shear stress generated in the matrix next to the fracture site, inelastic matrix or interface deformation is assumed to initiate at the fiber fracture site and propagate axially away from the break. The axial length of this inelastic zone is commonly referred to as the slip length, L_s. For an MMC system, perhaps a less reasonable assumption is that axial deformation of the matrix is prohibited. According to [1], slip length L_s is

$$L_s = \frac{DE_f \varepsilon}{4\tau_0} \tag{1}$$

where, D is the fiber diameter, E_f is the Young's modulus of the fiber and ε is the far-field applied strain. The fiber axial coordinate z originates at the fiber fracture. For $z < L_s$ the fiber axial strain is simply ε, but for $z > L_s$ the fiber axial strain ε_f is

$$\varepsilon_f = \frac{4\tau_0 z}{DE_f} \tag{2}$$

This article describes a general approach to quantifying the *in-situ* deformation parameters by linking micromechanical modeling to neutron diffraction measurements of fiber and matrix strain around a fiber fracture. The model fiber composite studied consists of an Al matrix and a single Al_2O_3 fiber. The propagation and relaxation of matrix plasticity induced by the fiber fracture upon loading and unloading is also examined. To illustrate the approach we apply the Kelly-Tyson model [1] to the data. Matching the fiber axial stress distribution predicted from this model in Equation 2 to the neutron measured fiber strains under small applied load increments results in an estimate of the typically non-linear stress-strain behavior of the matrix.

EXPERIMENTAL PROCEDURE

A model composite comprised of a single, polycrystalline Al_2O_3 (alumina) fiber (4.75 mm diameter, from Coors Ceramics, Golden, CO) and an Al alloy (6061, ESPI Metals, Agoura Hills, CA) matrix prepared by casting was used in this study. In order to engineer fiber fracture at the center of the gage section a 0.7 mm thick notch was cut around the circumference of the fiber to a depth of 1 mm using a diamond saw. Prior to casting, the 6061 Al was machined to fit loosely in the mold around the fiber. The sample was cast in a stainless steel mold under vacuum after purging the mold with argon gas. The mold was machined to hold the alumina fiber vertically in a tube furnace while the Al melted around the fiber. Following 30 minutes at 800°C, the entire mold was quenched to room temperature in water. Cylindrical tensile samples were then machined from the cast. The final dimensions of the sample gave a 30 mm long gage length with an 8.23 mm total diameter. X-ray radiography images revealed a continuous matrix with no voids after casting. Reference samples (nominally free of thermal residual stresses) of the matrix and fiber were also prepared using the same technique. For the reference fiber sample, the Al matrix was polished away from the fiber along a 14 mm gage section in order to relieve the thermal residual stresses.

The mechanical behavior of the monolithic Al matrix was determined in tension using a screw-driven Instron load frame at a constant applied strain rate of 0.1 mm/min. The yield stress obtained by finding

the location on the stress/strain curve where it deviates from linear elastic behavior was 75 MPa. On the other hand, the 0.2% offset yield stress was found to be 89 MPa.

The neutron diffraction (ND) experiment was performed on the Neutron Powder Diffractometer (NPD) at the Los Alamos Neutron Scattering Center (LANSCE). Using a hydraulic load frame, the sample was loaded in tension in the presence of the neutron beam as shown in Fig. 1. Data were collected in 20 MPa intervals for approximately one hour at each step. Strain was measured on the sample using an extensometer with a 25 mm gage length. In addition, phase specific elastic strain was determined from the diffraction data via the Rietveld method [2,3]. A 10 mm wide neutron beam struck the entire width of the sample at an angle of 45° resulting in a 14 mm gage length (Fig. 1). Diffraction patterns were collected at $+90^{o}$ and $-90°$ 2θ providing strain information in both the longitudinal and transverse directions.

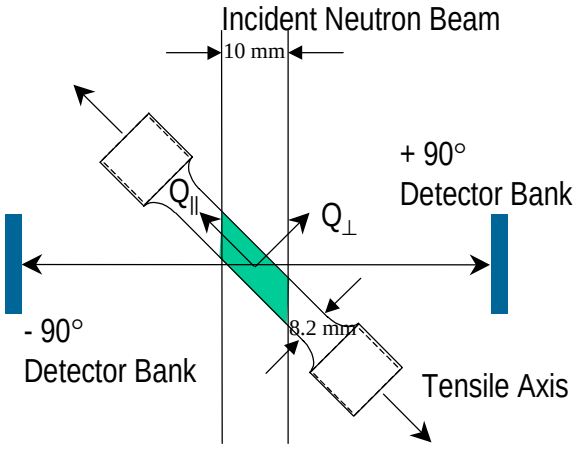

Figure 1. Schematic of the NPD tensile testing geometry. Specimen is at 45° to the incident beam. The scattering (Q) vectors for each detector bank indicate the directions of measured strains.

RESULTS AND DISCUSSION

Neutron Diffraction Measurements

Figs. 2-3 show the applied composite stress vs. axial (longitudinal) strain measured in each phase using ND. Within the error of the ND measurements (±150 με when specimens are changed and ±25 με during a single measurement), the thermal residual strains due to the mismatch of the thermal expansion coefficients of the fiber and the matrix were determined to be roughly relaxed. The reference values for the strains in Figs. 2-3 were taken to be the values measured from the monolithic ("stress-free") versions of the constituents. In other words, the data presented here include the (nearly relaxed) thermal residual strains.

Results shown in Fig. 2 suggest plastic deformation in the matrix during the first loading cycle at an applied composite stress around 60 MPa. A jump in the position of the load frame crosshead at around 55 MPa confirms the fiber broke during the first loading cycle. In addition, the plasticity observed from the extensometer (these data are not shown here) supports an assumption of discontinuity in the fiber, as does the change in slope after 60 MPa for both the fiber and matrix. Upon unloading, residual tensile strain is observed in the fiber and residual compressive strain is seen in the matrix. This is likely a result of the development of plastic strains in the matrix. Subsequent X-ray radiography showed separation of the fiber at the notch, which was not observed before loading.

In Fig. 2, we see further development of tensile residual strains in the fiber and compressive residual strains in the matrix upon fully unloading after each cycle. We suspect that propagation of localized matrix plastic deformation (around the fiber break) is largely responsible for these residual strains. Furthermore, there is a noticeable change in the composite modulus upon loading and unloading during

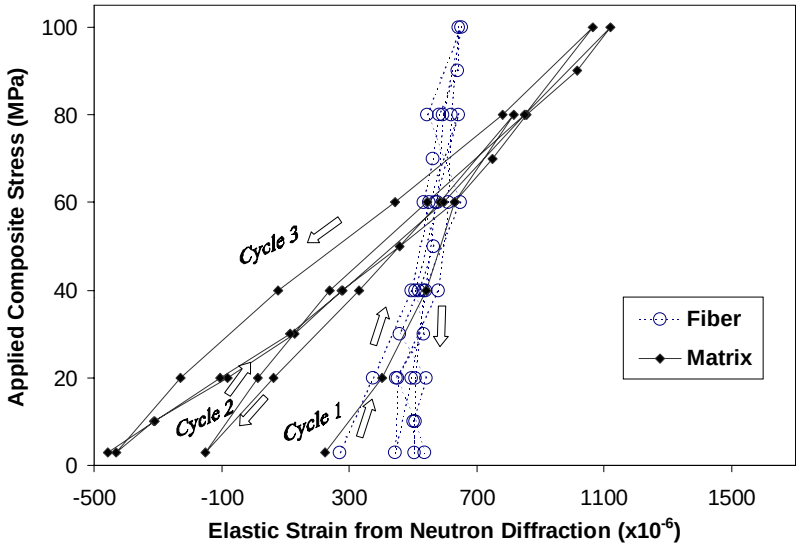

Figure 2. *Axial* strains measured by neutron diffraction in each phase vs. applied composite stress during loading/unloading cycles 1-3.

these first three cycles. For the loading portion of the first cycle, the modulus of the composite is about 156 GPa, nearly the value predicted by the rule of mixtures (~158 GPa). When the sample was unloaded, the composite modulus dropped to about 120 GPa. The modulus dropped again in the second loading cycle by 10 GPa and during the second unloading settled to about 74 GPa (approximately the modulus of the monolithic form of the matrix). The continuous decrease in the composite modulus suggests not only plastic deformation in the matrix, but some fiber pullout as well. In fact, X-ray radiography measurements performed after the ND experiment showed a fiber displacement of 0.15 mm along the axis at the notch. In addition, after completing the cycles, a plastic deformation zone was clearly visible at the surface of the sample in the position of the initial notch.

When Fig. 2 is compared with Fig. 3, marked differences between cycles 1-3, particularly for the matrix, and no significant changes during cycles 3-5 are observed. It is likely that by cycles 3-5, the plastic deformation in the matrix progressed outside the gage section. During the fifth loading/unloading cycle, the sample failed at a final load of 100 MPa after reaching a maximum load of 116 MPa. The matrix failed near the shoulder of the threaded section of the specimen and outside the section sampled by ND. At the failure plane, the fiber remained intact and pulled out of the threaded

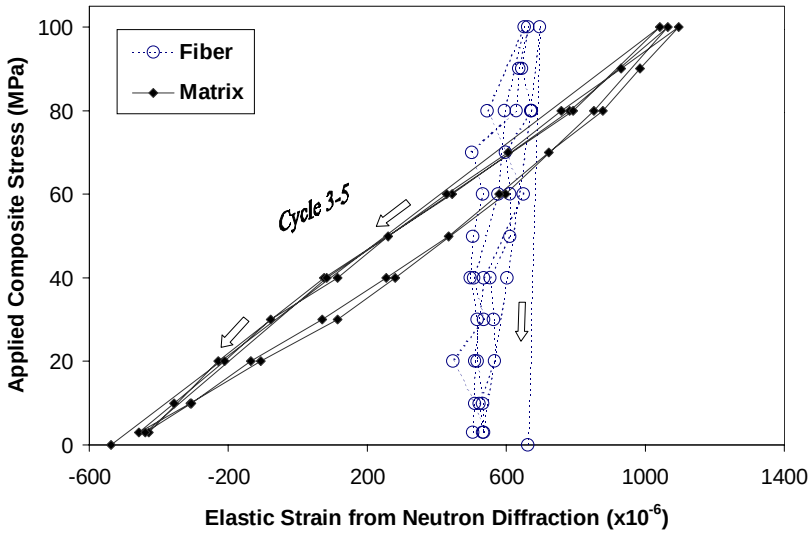

Figure 3. *Axial* strains measured by neutron diffraction in each phase vs. applied stress during loading/unloading cycles 3-5.

end leaving the middle of the gage section intact. The sample was maintained in position after the matrix failure and final residual strain values were recorded: +660 με in the fiber and –540 με in the matrix.

Comparison of Experimental Results with Modeling Predictions

Elastic axial fiber strain data from ND can be used to infer the elastic-plastic deformation response of the matrix. As discussed above, the ND results suggest localized plastic deformation in the matrix around the fiber break. This deformation will alter the elastic strain distribution in the fiber as predicted in several single and multifiber composite models. For instance, we use the simple shear-sliding model presented in [1] for the fiber strain due to a break in a single fiber composite and compare it with the ND data. We find that the slip length, L_s is usually greater than the gage length, z_{max} = 7 mm, at the maximum load of each cycle. Accordingly, Equation 2, when averaged over the length z_{max}, provides a relationship between an average axial fiber strain and the rigid plastic sliding resistance τ_0. This comparison suggests τ_0 varies from 22 to 25 MPa with each cycle when evaluated at its maximum load (Fig. 4). In Fig. 4, the values of applied stress where L_s was less than z_{max} were excluded. The τ_0 values are substantially different than the monolithic shear yield stress of 6061 Al (37 MPa). Such differences between bulk and *in-situ* metal matrix behavior were also observed in Al-Al_2O_3 multifiber composites [4]. Clearly the predicted parameters for *in-situ* matrix parameters depend on the constitutive models used for the fiber and matrix and composite stress analysis. The fact that τ_0 varies significantly during the loading/unloading cycles applied on the specimen suggests that the Kelly-Tyson model is inadequate in describing the behavior of the composite. Current work involves applying other micromechanical models for the matrix constitutive response to interpret the ND results and to obtain better representations of the *in-situ* constitutive behavior of the matrix.

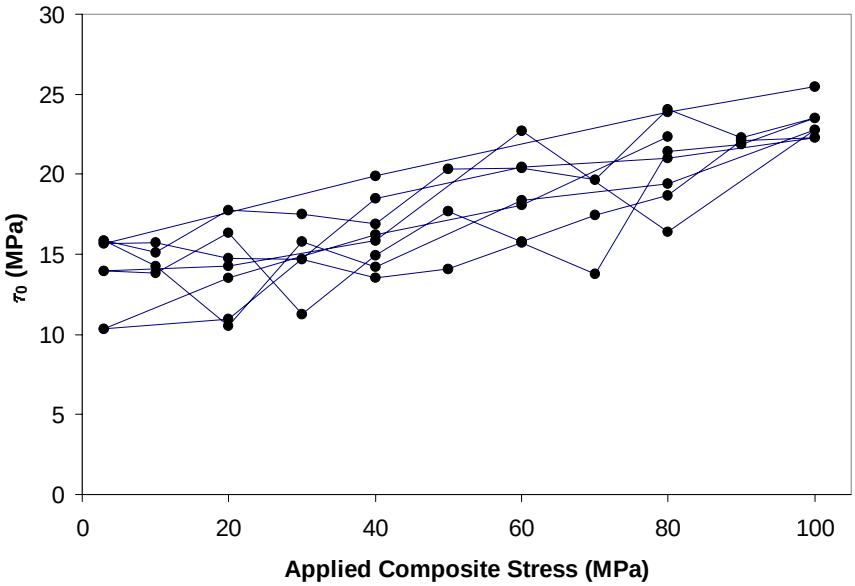

Figure 4. Variation of interface shear strength, τ_0 during loading/unloading cycles as a function of applied composite stress.

CONCLUSIONS

In this study, we examined the consequences of fiber fracture and localized matrix propagation under cyclic loading on the *in-situ* fiber and matrix strains. Even though the matrix fiber bond is strong, after the fiber fracture, the fiber carries only a small fraction of the total load. Plastic deformation in the matrix is observed immediately following fiber failure and increases with increasing applied load. The

shear sliding resistance, τ_0, which is about 30% smaller than the bulk shear yield stress, increases with each cycle.

ACKNOWLEDGEMENTS

This study was supported by the National Science Foundation (CAREER grant no. 9985264) at Caltech and a Laboratory-Directed Research and Development Project (no. 2000043) at Los Alamos. It also benefited from the national user facility at the Lujan Center, LANSCE, supported by the Department of Energy under contract W-7405-ENG-36.

REFERENCES

1. Kelly, A. and Tyson, W., (1965) *J. Mech. Phys. Solids*, 13, 329.
2. Larson, A. C. and von Dreele, R. B., *GSAS-General Structure Analysis System*, LAUR 86-748, Los Alamos National Laboratory, 1986.
3. Rietveld, H. M., (1969) *J. Appl. Cryst*., 2, 65.
4. He, J., Beyerlein, I. J. and Clarke, D. R., (1999) *J. Mech. Phys. Solids*, 47, 465.

IN-SITU ULTRASONIC CHARACTERIZATION OF FATIGUE CRACK INITIATION AND EVOLUTION FROM SURFACE DAMAGE: CRACK CLOSURE EFFECT

S. I. Rokhlin and J.-Y. Kim

The Ohio State University
Nondestructive Evaluation Program
Edison Joining Technology Center
1248 Arthur E. Adams Dr., Columbus, OH 43221

ABSTRACT

A surface acoustic wave method for *in-situ* monitoring of fatigue crack initiation and evolution from a pit-type surface flaw is described. The surface wave signature is acquired continuously during the fatigue cycle without stopping the fatigue test. Crack initiation and propagation are clearly identified from the surface wave reflection signals. The dependence of the ultrasonic surface wave signature on fatigue load reveals the crack opening/closure characteristic continuously displayed during the fatigue cycle. For crack sizing from the ultrasonic signatures, the low frequency scattering theory is employed. The combined effect of the pit and the corner initiated crack on the surface wave reflection is taken into account using an approximate stress-intensity factor. Examples are given for fatigue crack monitoring in 2024-T3 aluminum and nickel base super alloys. The ultrasonic results are supported by fractographs.

KEYWORDS: crack monitoring, crack closure measurement, surface acoustic waves, crack depth measurement

INTRODUCTION

Localized surface damage due to corrosion, foreign object impact or other reasons may cause fatigue crack initiation and failure. A fatigue crack emanating from a surface flaw grows, in general, more rapidly than on a flawless surface. However, the existence of surface damage may result in a damage-induced plastic zone and associated crack closure at a relatively moderate level of applied stress. Thus, experimental results [1] show retardation of crack growth while the crack tip lies in the notch plastic zone. The effect of the crack closure on the fatigue crack growth rate can be considered using the effective stress intensity factor range [2]. Numerical results [3] also verify the dominance of notch plastic deformation over crack tip plastic deformation. Therefore, determination of crack closure (opening) stress becomes important for crack growth analysis and fatigue life prediction.

Numerous techniques have been developed to measure crack closure stress including the ultrasonic surface wave [4,5] method. Most previous work on ultrasonic characterization of surface cracks has been

concerned with a crack on a flawless surface or an artificial saw cut simulating a crack. The existence of surface damage complicates ultrasonic crack detection by masking crack reflection signals. Also, these surface flaws can cause plasticity-induced crack closure. It is known that crack closure adversely affects nondestructive detection of fatigue cracks since when they are tightly closed due to compressional stress, they can remain undetected by nondestructive means. Also, the existence of surface irregularities complicates fatigue crack detection.

In this paper, an experimental method for *in-situ* monitoring of fatigue crack initiation from a surface pit is developed. During fatigue testing surface acoustic wave reflections are measured at different levels of fatigue load. From the measured surface wave reflections, the crack closure (opening) loads are determined. It is also demonstrated that crack closure reduces ultrasonic detectability. The low frequency scattering model is developed to determine small-crack depths. The depths of fully and partially open cracks are predicted from the collected ultrasonic data and compared to those measured from fractographs.

IN-SITU ULTRASONIC MEASUREMENTS

The specimen used in the experiment was a standard dog-bone sample [E-466-96-ASTM] with 1.6 mm thick Al 2024-T3 alloy and Ni base superalloy. A controlled small pit with depth 250 μm and diameter 252 μm was generated by EDM (electrical discharge machine) in the center of sample. Fatigue tests were carried out on the 10 ton servo-hydraulic MTS (mechanical testing system) with 15 Hz cyclic load. The stress range ($\Delta\sigma$) was 231 MPa and the stress ratio R was 0.1 so that the maximum stress level was 75 % of the yield stress. Therefore the fatigue crack may initiate early in fatigue life because of the high stress concentration. This also leads to the development of a pit-induced plastic zone which causes crack closure. Post-fracture surfaces were examined with scanning electron microscope (SEM) fractographs and actual crack and pit sizes were measured.

In order to monitor crack initiation and propagation during the fatigue cycle, ultrasonic surface acoustic wave reflections from the pit and the crack were measured. A commercial wide band longitudinal wave transducer with center frequency 5 MHz was assembled with a specially designed polystyrene wedge for generating and receiving the surface wave signals, as shown in Figure 1. The design of this wedge is critical for acceptable signal-to-noise ratio. For *in-situ* ultrasonic measurements during fatigue, the

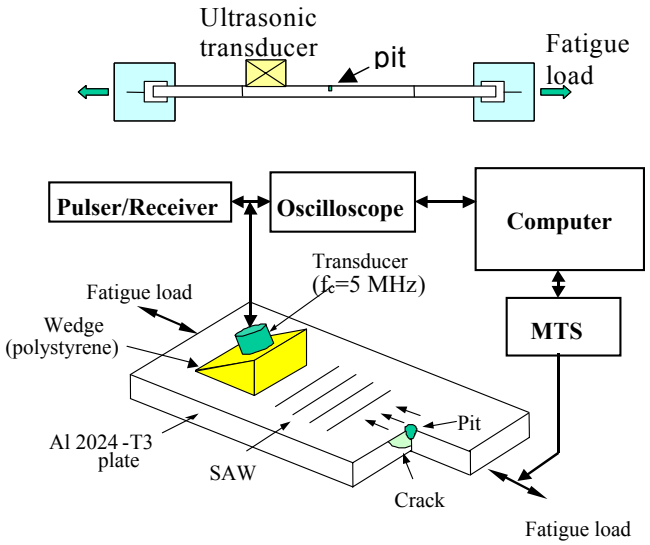

Figure 1: SAW monitoring of surface pit with crack

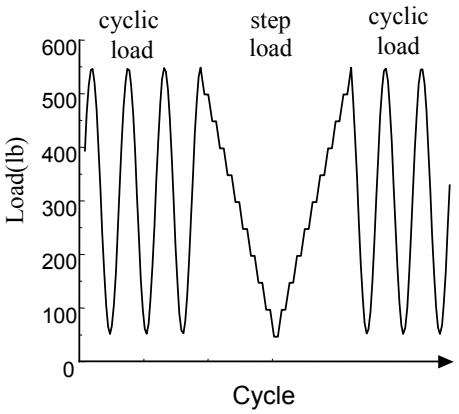

Figure 2: Load patterns to measure crack closure stresses

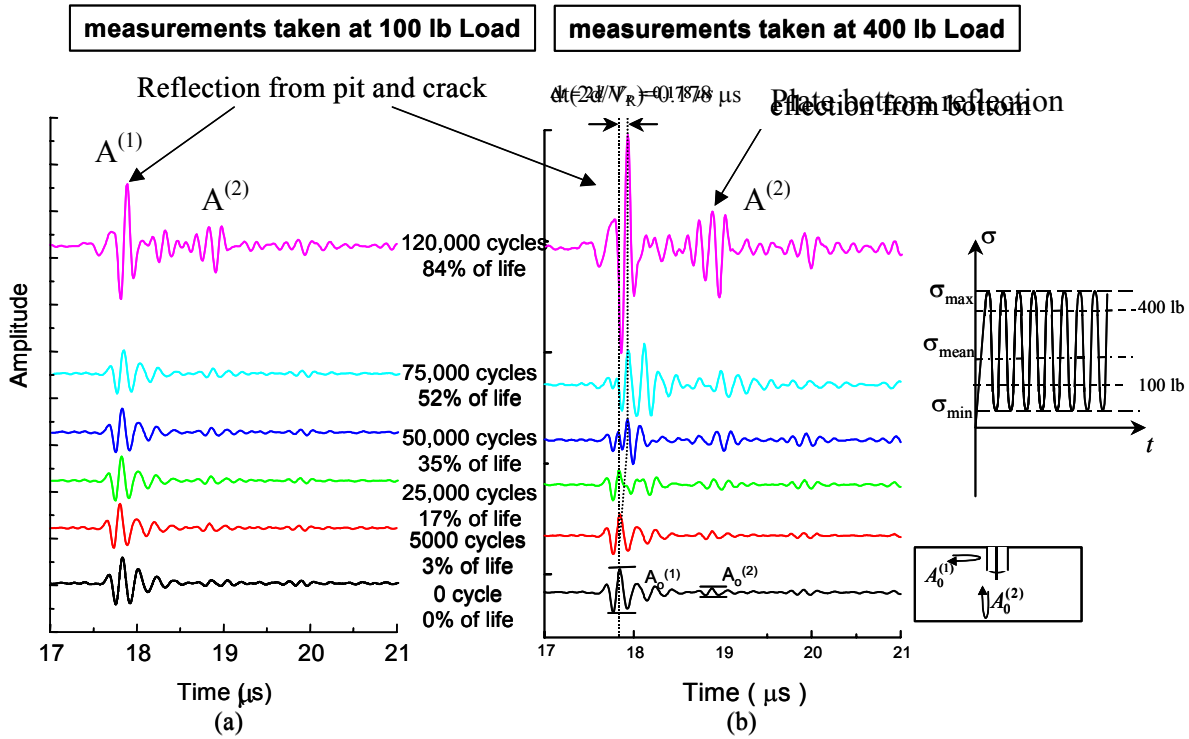

Figure 3: Change of reflection signal at different cycles for two different loads (a) 100 lb, (b) 400 lb.

transducer assembly is attached to the sample undergoing the fatigue test for collection of reflected ultrasonic signals at different load levels during fatigue cycling. The experimental system includes an ultrasonic pulser/receiver oscilloscope and control computer for MTS and ultrasonic data collection. At a predetermined number of cycles the computer controlled cycle fatigue load was changed to a step load (Figure 2) with recording of ultrasonic reflections at each step-load level. More recently the data acquisition system has been improved allowing us to digitize and save the ultrasonic data during the fatigue cycle without need for change of the fatigue load to the step load.

INTERPRETATION OF ULTRASONIC RESULTS

As an example, Figure 3 shows surface wave reflection signals taken for two different load levels (100 lbs on the left (a) and 400 lbs on the right (b)) at different fatigue cycles. The surface wave reflection signal is composed of a backward scattered wave $A^{(1)}$ (first reflection) from the pit and crack, and the plate bottom $A^{(2)}$ (second) reflection of a mode-converted shear wave and the following multiple reflections in the plate (sample). As a result of the crack initiation and growth during the fatigue test the amplitudes of both the first and plate bottom reflections change continuously. It is observed from Figure 3(b) that the signal starts to change due to crack initiation at 25,000 cycles. The signal is shifting in time and growing in amplitude. The SEM fractograph at this number of cycles is shown in Figure 4(a). Whereas the reflection signal recorded at the load level 400 lb changes significantly as the number of cycles increases, no change is observed until 52% of the fatigue life when signals are recorded at 100 lb load. This indicates that at a given number of cycles the ultrasonic signals depend on the cycle load at the moment of signal recording. Detailed interpretation of ultrasonic signals can be found in [6]. The SEM fractographs for cracks at different numbers of fatigue cycles are shown in Figure 4.

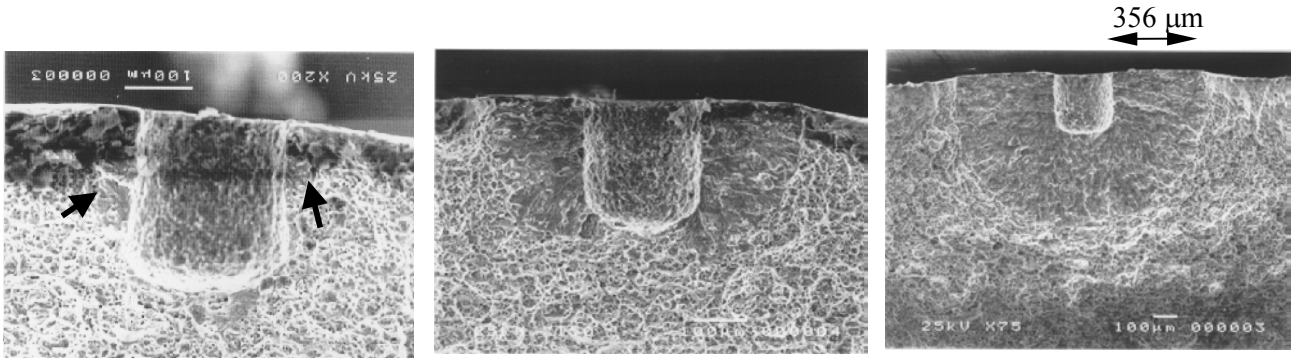

(a) (b) (c)

Figure 4: SEM fractographs at (a) 25,000 cycles, (b) 65,000 cycles, (c) 130,000 cycles

In Figure 5(a) the normalized plate bottom (second) reflection versus the cyclic load is shown. Each curve begins to increase at a certain load level (A) from near zero and then saturates at some load level (B), except for the case at 145,000 cycles when the fatigue crack is so large that it remains open during the whole cycle. The first load level (A) corresponds to the crack mouth opening load and the second (B) to the completely open crack. It is also noted that the crack opening loads change with the number of cycles.

MEASUREMENT OF CRACK CLOSURE LOADS

The loads at the beginning of crack mouth opening (A) and at the completely open crack (B) are determined from the plate bottom reflections and are shown in Figure 5(b). It is noted that the crack mouth opening load (A) is constant until around 100,000 cycles and then decreases, while the complete opening load (B) has its maximum at around 80,000 cycles. This result can be understood by considering the crack transition through the plastic zone caused by the pit under fatigue loading. The pit plastic zone produces the compressive closure force applied to the crack surface while the crack grows in the plastic zone. When the crack is short, the load needed to open the crack completely is just a little higher than the load of the crack mouth opening which is constant at this stage of crack growth. With its growth, the crack-fully-open load increases. When the crack grows out of the pit plastic zone, part of the crack surface is unloaded producing residual stress relief thus reducing the crack closure stresses. For the same reason, the crack-fully-opening load and crack-mouth-opening load decrease when the crack tip lies outside the plastic zone caused by the pit.

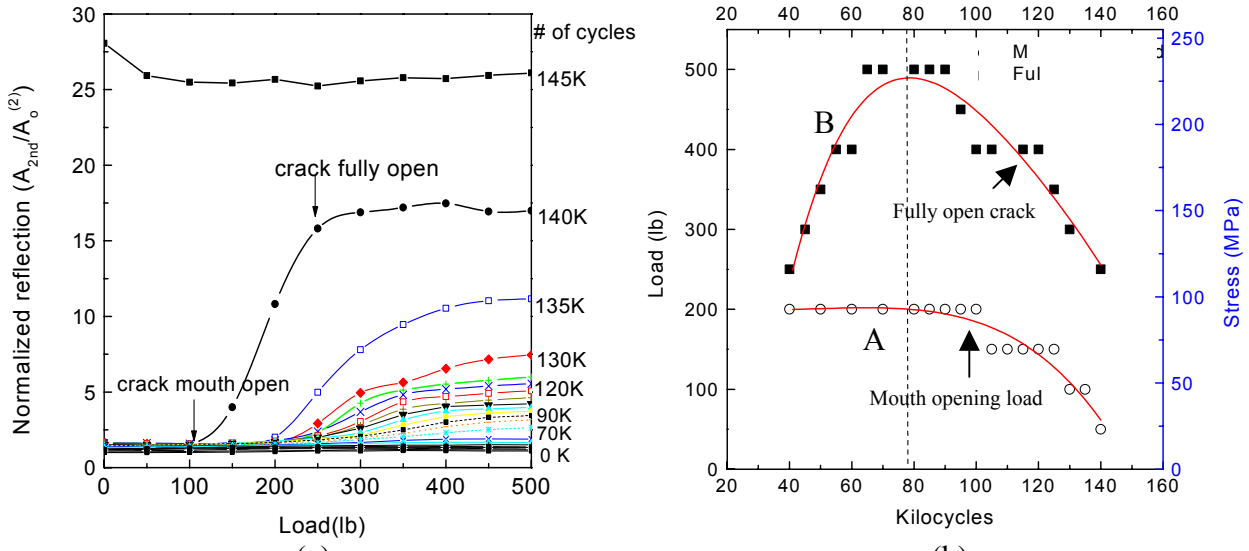

(a) (b)

Figure 5: Determination of crack closure loads. (a) Change of plate bottom reflection vs. cyclic load at different numbers of fatigue cycles, (b) Crack closure (opening) loads vs. number of fatigue cycles.

Assuming that the crack-fully-opening load reaches its maximum when the crack size is equal to the pit-induced plastic zone size, we estimate the plastic zone about 200 μm, which is in reasonable agreement with experiment.

MODEL FOR CRACK DEPTH DETERMINATION

In this section, a model is proposed for determining the depth of a small crack emanating from the surface pit. The low frequency scattering theory [5] is modified to take the effect of the pit into account. For measurements with a single transducer, the ultrasonic reflection coefficient $R(\omega)$ is given by

$$R(\omega) = \frac{i\omega}{4P}\int_S u_I^{(1)}\sigma_{IJ}^{(2)} n_J dS \,, \tag{1}$$

where ω is the angular frequency, i is the unit imaginary number, S is the surface of the flaw, $u_I^{(1)}$ is the scattered displacement field, $\sigma_{IJ}^{(2)}$ is the incident stress field, n_J is the inward normal vector to the flaw surface, and P is the input power to the transducer. Consider the surface wave incident normally to corner cracks developed at the two sides of the pit (Figure 4(b)). The reflection coefficient (Eqn.1) can be represented as a sum of two contributions: integration over the pit surface (S_p) and the crack surface (S_c). Introducing the crack opening displacement and considering only the normal stress on the surface that is dominant in the low frequency range, the reflection coefficient can be expressed as:

$$R(\omega) \approx \frac{i\omega}{4P}\int_{S_p} u_I^{(1)}\sigma_{IJ}^{(2)} n_J dS + \frac{i\omega(1-\nu^2)}{3EP}\int_C \rho(\mathbf{r}) K_I^2 dl \,, \tag{2}$$

where S_c^+ means the front sheet of the crack surface, K_I is the stress intensity factor, ν is Poisson's ratio, E is Young's modulus and $\rho(\mathbf{r})$ is the perpendicular distance from the origin to the line tangential to the crack front C.

To obtain the stress intensity factor, the stress of the incident surface wave is approximated by the bending stress in a plate [5]. Since the stress σ_{zz} changes its sign at the depth $x/\lambda_R \approx 0.3$ we consider the effective thickness of the plate $h^* = 0.6\lambda_R$ and then the bending stress to be $\sigma_{zz} = \sigma_o(1 - 2x/h^*)$. Next, we replace the crack on the pit with that on the through-thickness hole in the plate having the effective thickness (h*) considering the ratio $d/h^* \approx 1$ where d is pit depth. Rokhlin et al. [8] used a similar approximate model for the analysis of fatigue crack initiation and growth from a pit. Raju and Newman [9] analyzed numerically the boundary correction factors for various combinations of geometric parameters. We use their data to calculate interpolated curves for the stress intensity factor at different crack configurations.

To determine the experimental reflection coefficient the surface wave reflection signals were deconvolved with the measurement system frequency response function by measuring the reflection coefficient of a 90^o- step-down corner. In Figure 6(a) the normalized first reflection versus crack depth is presented for samples with different pit diameters D. Due to signal interference between the two terms in Eqn.2, the amplitude of the reflection may increase or decrease depending on the pit diameter. The size of the fully open crack at each number of cycles is determined by comparing the measured and predicted reflection coefficients. The effective crack size of the partially open cracks is determined in the same manner. In Figure 6(b) the typical predicted depths of fully and partially open cracks versus number of cycles are shown. For aluminum samples, the cracks are initiated in the very early stage of fatigue testing. The crack remains closed at low loads (up to 100 lb) while at higher loads (450, 500 lb) the crack is fully open.

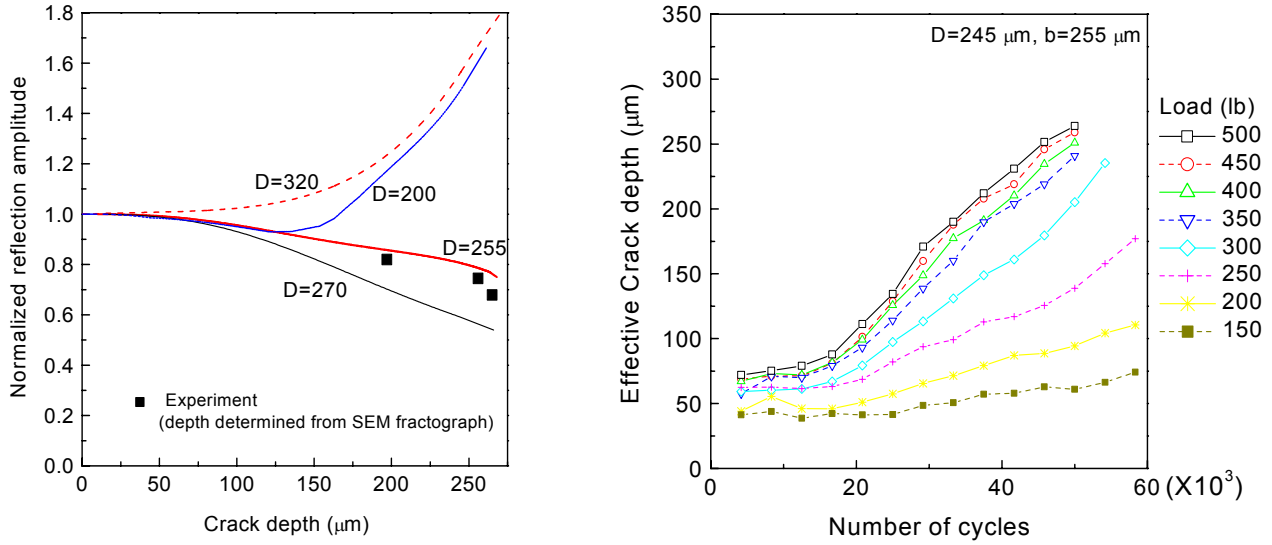

Figure 6: (a) Model prediction of reflection coefficient of the corner cracks. (b) Typical example of crack depths determined at different numbers of fatigue cycle and under different load levels.

CONCLUSION

An experimental method for the evaluation of fatigue cracks emanating from pit-type surface flaws is presented. *In-situ* ultrasonic surface wave measurements have been performed to determine the size and opening/closure loads of the growing fatigue crack during fatigue cycling. By interpreting ultrasonic reflection signals, crack initiation and growth are quantitatively described. The ultrasonic results are verified by SEM fractography by breaking samples in different stages of fatigue life. The complete crack opening process from crack mouth to crack tip is monitored during fatigue cycle loading. The change of crack opening load with crack evolution is attributed to the crack growth through and departure from the plastic zone developed around the pit. The model study is performed for determining crack depth in the small-crack regime.

References

1. Shin, C. S. and Smith, R. A. (1988). *Eng. Frac. Mech.* 29, 301.
2. McEvily, A. J. (1988). In: *Mechanics of Fatigue Crack Closure-ASTM STP 982*, pp.35~43, Newman, J. C., Jr. and Elber, W. (Eds). ASTM, New York.
3. Hou, C.-Y. and Charng, J. J. (1996). *Int. J. Fatigue.* 18, 463.
4. Resch, M. T. and Nelson, D. V. (1992). In: *Small-crack Test Methods-ASTM STP 1149*, pp.169~196, Larsen, J. M. and Allison, J. E. (Eds.). ASTM, New York.
5. Tien, J. J. W., Khuri-Yakub, B. T., Kino, G. S., Marshall, D. B. and Evans, A. G. (1981). *J. Nondestr. Eval.* 2, 219.
6. Dai, W., Kim, J.-Y. and Rokhlin, S. I. (1999). In: *Review of Progress in Quantitative Nondestructive Evaluation*, pp.2225~2233, D. O. Thompson and D. E. Chimenti, (Eds.). Plenum Press, New York.
7. Dowling, N. E. (1979). In: *Fracture Mechanics-ASTM STP 677*, pp.247~273, Smith, C. W., (Ed.). ASTM, New York.
8. Rokhlin, S. I., Kim, J.-Y., Nagy, H. and Zoofan, B. (1999). *Eng. Frac. Mech.* 62, 425.
9. Raju, I. S. and Newman, J. C., Jr. (1979). In: *Fracture Mechanics-ASTM STP 677*, pp.411-430, Smith, C. W. (Ed.). ASTM, New York.

ORAL/POSTER REFERENCE: ICF100540OR

INDENTATION-INDUCED DAMAGE OF THIN-FILMS SUPPORTED ON SUBSTRATES

A.H.W. Ngan and H.P. Ng

**Department of Mechanical Engineering, The University of Hong Kong,
Pokfulam Road, Hong Kong, P.R. China**

ABSTRACT

When indentation is made on a thin film supported on a substrate, the ways by which the indenter's volume can be accommodated are considered here. Depending on the relative strengths of the film and substrate, three regimes are proposed as follows: i) when the film is a lot harder than the substrate, the deformation may be modelled by assuming that the film is rigid; ii) when the film has similar strength as the substrate, the deformation pattern is likely to be spherical as similar to indentation on a homogeneous material; iii) when the film is a lot softer than the substrate, the substrate can be assumed to be rigid. Mechanistic models are proposed for the scenarios ii) and iii).

Keywords Hardness, Coatings, Sputtering, Metal Films

INTRODUCTION

Indentation on thin films supported by substrates has been an important research subject as it is often necessary to know the mechanical properties of, for example, hard protective coatings. When the indentation depth is small, say within 10% of the film thickness, the substrate effect is negligible and hence the measured hardness becomes a sole property of the film material. However, at such small values of indentation depth, the measured hardness is prone to a strong intrinsic size effect (ISE), which we term the *intrinsic* effect here as it refers to the film material alone. When the indentation depth is a significant fraction of the film thickness, the substrate effect becomes significant. To illustrate this, we use data from our recent experiments on deposited metallic alloy films [1-3]. Illustrated in Figure 1(a) are the microhardness values versus indentation depth (h) for three film thickness values (t) obtained from 3Ni/Al alloy films on pure Ni substrates. The h/t ratio is larger than 10% for all the data shown. It can be seen that the measured hardness exhibited a strong negative ISE, and the hardness results for different thickness values fall on distinct curves when plotted against h. However, when plotted against h/t in Figure 1(b), the results fall on a single curve. This indicates that, in this thickness range at least, the ISE obeys geometrical similarity with the film thickness being the characteristic length scale. To distinguish this regime from the intrinsic effect discussed above, we term this the *extrinsic* ISE. When the film remains adhered to the substrate during indentation, one may expect that the extrinsic ISE would be self-similar so that the hardness depends on h/t but not on h alone. This is the situation observed in Figure 1 (b). When film delamination occurs, the interfacial crack length represents another length scale in the problem, and so the indentation may no longer be self-similar.

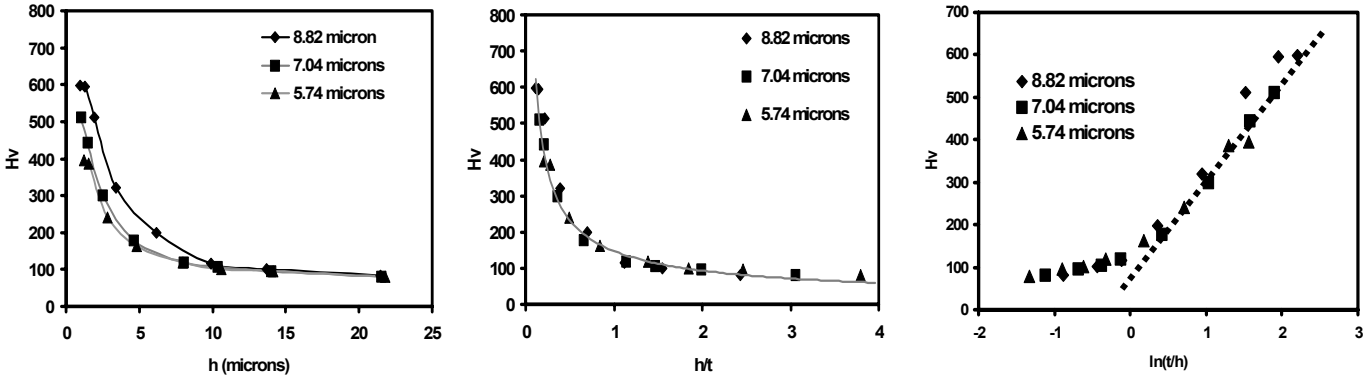

Figure 1: Vickers hardness values against (a) indentation depth h, (b) indentation depth h normalised by film thickness t, (c) ln(t/h) for 3Ni/Al films of three different thickness on pure Ni substrates [2].

If the aim of the experiment is to measure the strength of the film, the strong ISE observed, no matter intrinsic or extrinsic, would certainly make life very difficult as it would not be obvious as to which hardness value on the curve to take, and the measured hardness is no longer roughly three times the yield strength. A reliable model of the ISE would therefore be highly desirable. Since in general the intrinsic effect dominates over quite a narrow range of small indentation depth ratio, we believe it is more useful to make use of the extrinsic ISE to get information about the film strength. It is therefore the aim of this paper to bring some insight into the extrinsic ISE by proposing mechanistic models for this type of ISE.

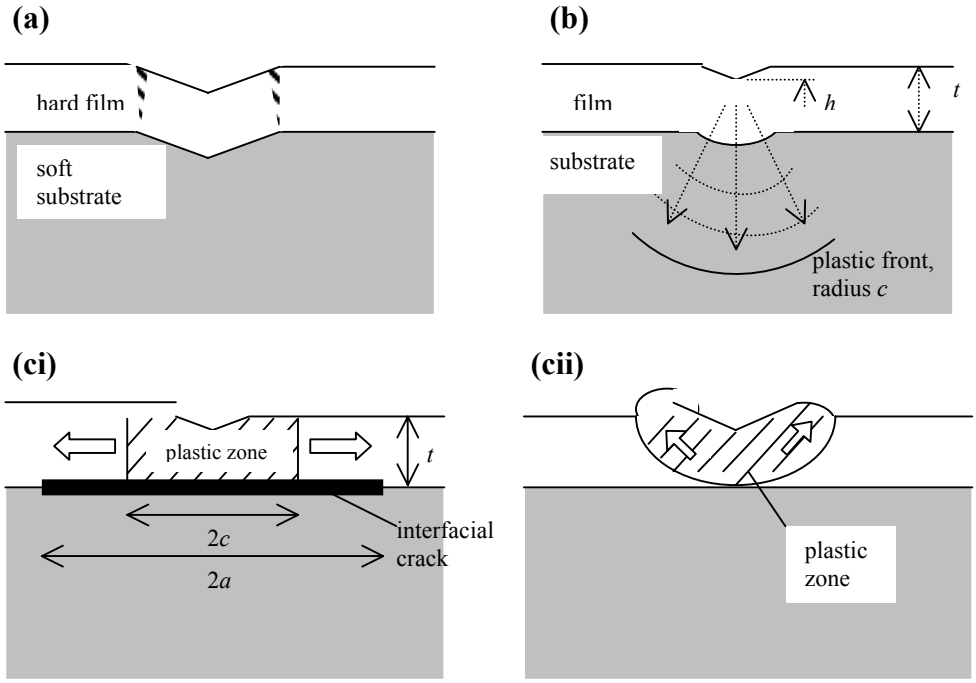

Figure 2: (a) Rigid film mode, (b) radial mode, and (ci,cii) planar modes of plastic deformation accompanying indentation on a thin film supported by substrate.

MECHANISTIC MODELS FOR EXTRINSIC ISE

In a general case of modelling indentation on a film supported by a substrate, it is useful to think of a spectrum of possibilities as shown in Figure 2. One extreme is the *rigid film mode* (Figure 2(a)) in which the film is much harder than the substrate. In this situation, the film will merely deform or crack at the hinges of the indent, and between the indent and the substrate, the film remains rigid. The scenario is therefore similar to that considered by Jönsson and Hogmark [4]. When the film has similar strength as the substrate, the film will deform together with the substrate as shown in Figure 2(b). There is little

tendency of sliding across the film/substrate interface, and depending on the strength of the interface, the film may or may not delaminate, but this should not influence the material flow to a significant extent. We denote this mode as the *radial mode*. The other extreme is to have a very soft film on a hard substrate as shown in Figure 2(c). In this situation, the film material under the indent will be squashed by the indenter, but the substrate will have little deformation. A large shear stress will be set up across the film/substrate interface. If the interface is weak, it will then crack. Once film delamination has occurred, the indentation volume is accommodated mainly by pushing the film material surrounding the indentation core in a more or less co-planar fashion along the film as shown in Figure 2(ci). There will be relative sliding of the film material over the substrate, and when the delamination crack size is large enough, the elastic portion of the delaminated film may buckle upward. This mode is in fact similar to that considered by Evans and Hutchinson [5] who have also provided experimental evidence for its existence. We denote this here as the *planar mode*. If the interface is strong so that the film does not delaminate, the film material is difficult to flow radially outward in a co-planar fashion, so that the only way to accommodate the indenter volume would be to flow upward to as shown in Figure 2(cii). We term this the *pile-up* mode. Since the ISE of the rigid film mode in Figure 2(a) has already been considered by Jönsson and Hogmark [4], and the pile-up mode is difficult to model analytically, we will focus on the remaining two modes in the rest of this paper.

RADIAL MODE

When the film has similar strength as the substrate, the material flow pattern should not differ significantly from that in the indentation on a homogeneous half space. The latter has been modelled rather successfully using the cavity model [6]. For a convenient analytical model for the radial mode in thin-film, we will therefore follow the assumptions of this model. Hence, as a crude approximation, we assume in Figure 2(b) that the mean pressure p_o underneath the indenter creates plastic flow of material residing mainly inside a spherical plastic zone which is a sector of a hemisphere subtended at the centre of the indent. This is more likely the case for blunt indenters like Vickers or Berkovich. Let c be the radius of this plastic zone, and r the radial distance of a point inside this plastic zone. Assuming spherical field inside the plastic zone, equilibrium requires $\partial\sigma_r / \partial r = 2(\sigma_\theta - \sigma_r)/r$, where σ_r and σ_θ are the radial and hoop stresses respectively. With the Tresca criterion σ_θ - $\sigma_r = Y_i$, where Y is yield stress and the subscript i denotes either the film (f) or the substrate (s), the stress solutions are:

$$\sigma_r = \begin{cases} -2Y_f \ln\left(\frac{t}{r}\right) - 2Y_s \ln\left(\frac{c}{t}\right) - \frac{2Y_s}{3} & \text{for } r \leq t \text{ (the film)} \\ -2Y_s \ln\left(\frac{c}{r}\right) - \frac{2Y_s}{3} & \text{for } c > r \geq t \text{ (the substrate).} \end{cases} \quad (1)$$

In deriving eqn. (2), the integration constants are chosen such that the radial stresses are matched across the film/substrate interface, and the boundary between the plastic zone and the elastic outer region for $r > c$ which is also assumed to be spherical. The mean pressure inside the indent core $r < h \tan\Psi$, where h is the depth of the indent and Ψ the semi-angle of the indenter, is given by:

$$p_o = -\sigma_r\big|_{r=h\tan\Psi} = 2Y_f \ln\left(\frac{t}{h\tan\Psi}\right) + 2Y_s \ln\left(\frac{c}{t}\right) + \frac{2Y_s}{3}. \quad (2)$$

The plastic front at $r = c$ can be located by considering compressibility inside the plastic zone in a similar fashion as was done previously [6]. Defining $v = \mathrm{d}u(r)/\mathrm{d}c$ as the rate of change of position u of a material point inside the plastic zone at r with respect to the plastic zone size c, the assumption of incompressibility leads to $\partial v / \partial r + 2v/r = 0$ for $c > r > h \tan\Psi$. Solution to this which matches the elastic region at $r = c$ is

$$\upsilon = \frac{3Y_s c^2}{2E_s r^2}, \quad c > r > h\tan\Psi, \tag{3}$$

where E_s is the Young's modulus of the substrate material. Noting that if the volume of the indent core is to be conserved during a depth increment of dh, $2\pi h^2\tan^2\Psi\,\mathrm{d}u(h\tan\Psi) = \pi h^2\tan^2\Psi\,\mathrm{d}h$. Hence, from eqn. (3),

$$\frac{c}{h} = \left(\frac{E_s\tan^2\Psi}{3Y_s}\right)^{1/3}. \tag{4}$$

Since the measured hardness $H \approx p_o$, substituting eqn. (4) into eqn. (2) gives

$$H = H_o + 2(Y_f - Y_s)\ln\left(\frac{t}{h}\right), \quad H_o = -2Y_f\ln(\tan\Psi) + \frac{2Y_s}{3}\left[\ln\left(\frac{E_s\tan^2\Psi}{3Y_s}\right)+1\right]. \tag{5}$$

H_o is independent of t and h. Eqn. (5) indicates a falling trend of hardness versus indentation depth, i.e. a negative ISE, when $Y_f > Y_s$, and a positive ISE when $Y_f < Y_s$.

In terms of applicability, the radial mode consideration here is subject to two limits. The first is that the indent size must be large enough to make the plastic zone spread well beyond the film/substrate interface, so that the presence of the substrate can be felt. The second limit is that for the cavity model to be a good approximation, the deformation field must stay more or less spherical. This will not be the case when the film and substrate have too different yield properties, or the indent is too deep compared with the film thickness. For the latter, if the indenter penetrates deeply into the substrate, it may be expected that the film profile would conform gradually to the indenter shape even if it does not break, and so the flow field would deviate significantly from being spherical. An intuitive estimate for the field to maintain roughly spherical is that $h/t \ll 1$.

PLANAR MODE

The planar mode is similar to the situation considered by Evans and Hutchinson [5], who have assumed that the plastic and elastic zones reside entirely in the delaminated film. This is likely to be the case when the substrate is non-deformable and the film/substrate interface is weak. Here we follow a similar line of development but focus more on the interaction between the plastic zone and the elastic zone. We assume that the plastic zone surrounding the indent is a disk with radius c as shown in Figure 2(ci). Surrounding this is the elastic zone, which extends from $r = c$ to $r = a$, where a is the radius of the penny shape interfacial crack. From volume conservation of the plastic zone, Evans and Hutchinson [5] showed that the radial displacement at the plastic/elastic boundary, Δ, is given by

$$u(r = c) = \Delta = \frac{\pi h^3\tan^2\Psi}{6ct}. \tag{6}$$

Since the displacement beyond interfacial crack radius may be assumed to be negligible,

$$u(r = a) \approx 0. \tag{7}$$

The elastic stress solutions which satisfy eqns. (6) and (7) are

$$\sigma_r = \frac{cE_f\Delta}{c^2-a^2}\left[\frac{1}{(1-\nu_f)}+\frac{1}{(1+\nu_f)}\frac{a^2}{r^2}\right],\ \sigma_\theta = \frac{cE_f\Delta}{c^2-a^2}\left[\frac{1}{(1-\nu_f)}-\frac{1}{(1+\nu_f)}\frac{a^2}{r^2}\right],\quad a \le r \le c, \tag{8}$$

where E_f and ν_f are respectively Young's modulus and Poisson's ratio for the film material. The elastic energy residing in the elastic region is given by

$$U = -\pi c t \Delta \sigma_r (r = c). \tag{9}$$

The elastic energy release rate $G = -1/(2\pi a)\,(\partial U/\partial a)$ and from eqns. (8) & (9),

$$G = \frac{2c^2 t E_f \Delta^2}{(a^2-c^2)^2}. \tag{10}$$

This expression for G is somewhat different from that of Evans and Hutchinson because here we consider a radial field according to eqn. (8) but in Evans and Hutchinson, a uniform compressive stress state was assumed. A stable crack size will occur when $G = K_{II}^2(1-\nu_f^2)/E_f$, where K_{II} is the mode II critical stress intensity factor of the film/substrate interface. From eqn. (10), this stable crack size is given by:

$$a^2 = c^2 + \frac{cE_f\Delta}{K_{II}}\sqrt{\frac{2t}{1-\nu_f^{\,2}}}. \tag{11}$$

The plastic zone radius is located by noting that at the elastic/plastic boundary at $r = c$, $\sigma_\theta - \sigma_r = Y_f$. From eqns. (6), (8) & (11), this requires

$$\frac{h^3}{c^2 t} = \frac{6(1+\nu_f)}{\pi E_f \tan^2\Psi}\left[\frac{Y_f}{2}-\frac{K_{II}}{\sqrt{t}}\sqrt{\frac{(1-\nu_f)}{2(1+\nu_f)}}\right]. \tag{12}$$

To relate the measured hardness with the plastic zone, a descriptive model must be assumed for the latter. For a blunt indenter, the region outside the indent core but inside the plastic zone, i.e. $c \le r \le h\tan\Psi$, may be assumed to be subject principally to plane stress. The equilibrium condition for this region may therefore be written as $\partial\sigma_r/\partial r = (\sigma_\theta - \sigma_r)/r = Y_f/r$. Solution of this is

$$\sigma_r = Y_f \ln\left(\frac{r}{c}\right) + \sigma_r(r = c), \quad c \le r \le h\tan\Psi. \tag{13}$$

The mean pressure p_o supporting the indenter is approximately equal to $-\sigma_r(r = h\tan\Psi)$. Thus, from eqns. (13), (10), (11) & (12),

$$p_o = \frac{Y_f}{2}\ln\left(\frac{h}{t}\right)+\frac{Y_f}{2}+\frac{K_{II}}{\sqrt{t}}\left[\sqrt{\frac{2}{1-\nu_f^{\,2}}}-\sqrt{\frac{(1-\nu_f)}{2(1+\nu_f)}}\right]-\frac{Y_f}{2}\ln\left[\frac{6(1+\nu_f)}{\pi E_f}\left(\frac{Y_f}{2}-\frac{K_{II}}{\sqrt{t}}\sqrt{\frac{(1-\nu_f)}{2(1+\nu_f)}}\right)\right]. \tag{14}$$

The measured hardness thus has the form

$$H = \frac{Y_f}{2}\ln\left(\frac{h}{t}\right)+H_1 \tag{15}$$

where $H_1 = Y_f f(E_f / Y_f, \nu_f, K_{II} / Y_f \sqrt{t})$ comprises the last three terms in eqn. (14) and is a term independent of *h*. Eqn. (15) indicates that for the planar mode, *H* will increase with the indentation depth, i.e. a positive ISE will result.

As discussed by Evans and Hutchinson [5], buckling of the elastic region $a \leq r \leq c$ may occur for sufficiently large p_o. They have shown using a post-buckling theory that this is equivalent to reducing K_{II} by a factor $\sqrt{\alpha}$, where α (<1) is a parameter indicating the post-buckling stiffness of the film material. With this correction when the film buckles, the form of the depth dependence of *H* in eqn. (15) is unchanged.

COMPARISON WITH EXPERIMENTS

Because of space limitation, we will only discuss the radial mode here. Experimental results involving planar model will be dealt with in a forthcoming publication. For the radial mode, we use the hardness results on 3Ni/Al alloy films on nickel substrates shown in Figure 1(a). These were sputtered films and the experimental procedures have already been described elsewhere [1-3,7]. Being metallic films, they should be deformable and hence such a material system should represent a good prototype for the radial mode. As mentioned earlier, Figure 1(b) shows that the observed ISE obeys geometrical similarity, and one may also notice from eqn. (5) that the predicted ISE for the radial model also obeys similarity. In Figure 1(c) are shown the hardness results plotted against ln(*t*/*h*). It can be seen that the variation is approximately bilinear, with the turning point occurring at $h \approx t$, i.e. at the situation where pierce-through is about to occur. The segment on the left of the turning point corresponds to the post-pierce-through situation and since the apparent hardness at increasing load should approach that of the substrate, this segment should deviate in the long run from the apparent linearity shown in Figure 1(c) when ln(*t*/*h*) becomes increasingly negative. On the right of the turning point, i.e. for the situation before pierce-through occurs, it can be seen that the data fall reasonably accurately on a common straight line in agreement with eqn. (5). The measured slope of this straight line is ~ 2.30 GPa. Hence, from eqn. (5), Y_f should be larger than Y_s by about 1.15 GPa. The hardness of the Ni substrate is 1 GPa, and hence its yield stress is about 0.33 GPa. The estimated yield stress of the 3Ni/Al film is therefore about 1.5 GPa. In ref. [3], more results on alloy thin films are compared with the prediction in eqn. (5). To summarise, by comparing an experimental hardness vs depth variation with eqn. (5), the yield strength of a thin film supported on a substrate can be obtained.

ACKNOWLEDGMENTS

This research was supported by a grant from the Research Grants Council of the Hong Kong Special Administrative Region, China (Project no. HKU 7077/00E), and a CRCG grant from the University of Hong Kong (Project no. 10202005/16180/14500/301/01).

REFERENCES

1. Ng, H.P., Meng, X.K. and Ngan, A.H.W. (1998) *Scripta Mater*. 39, 1737.
2. Ng, H.P. (2000) Ph.D. Thesis, University of Hong Kong.
3. Li, S.Y., Ng, H.P. and Ngan, A.H.W. (2001) to appear in "Fundamentals of Nanoindentation and Nanotribology," ed. S. P. Baker, R. F. Cook, S. G. Corcoran, and N. R. Moody, Mater. Res. Soc. Symp. Proc..
4. Jönsson, B. and Hogmark, S. (1984) *Thin Solid Films* 114, 257.
5. Evans, A.G. and Hutchinson, J.W. (1984) *Int. J. Solids Structures* 20, 455.
6. Johnson, K.L. (1985) *Contact Mechanics*. Cambridge University Press, p. 172.
7. Ng, H.P. and Ngan, A.H.W. (2000) *J. Appl. Phys*. 88, 2609.

ORAL/POSTER REFERENCE: ICF100790OR

INDUCING 'PURE' MODE II SHEAR FAILURES IN LAMINATED COMPOSITES

S. R. Short, Ph.D., P.E.[1] and C.P. Sastry[1]

[1] Department of Mechanical Engineering, Northern Illinois University, DeKalb, IL 60115, USA

ABSTRACT

A thorough knowledge of the resistance to delamination of laminated composite materials requires a test method capable of inducing Mode II fractures. However, pure Mode II (interlaminar shear) failure can be difficult to produce in a test coupon. Several researchers have documented the propensity of the typical flexure-type interlaminar shear test specimen to be adversely affected by a complex stress state near the region of loading and hence exhibit mixed-mode fracture characteristics. In the effort to induce a pure state of shear on the failure plane, a sandwich-coupon, flexure-test specimen has been suggested by the lead author. Such a specimen is capable of producing nearly pure interlaminar shear failures in graphite/epoxy laminates. The current research presents closed-form and finite element analysis results characterizing the stress state within the region of fracture initiation. The resulting shear failures are characterized with respect to fracture pattern, mode of failure, and stress state on the failure plane.

KEYWORDS

Mode II, interlaminar shear, fracture, composites, graphite-epoxy

INTRODUCTION

Strength theories based on failure criteria are essential to composite materials designers to enable prediction of the behavior of structural elements under complex loading. Subsequent to formulation, these strength theories must be verified by comparison with measured strengths. This verification process involves the development of test methods capable of producing a prescribed state of stress and failure mode within a test specimen.

In the past, engineers have relied upon the short-beam shear (SBS) test, as described in ASTM D2344 [1], to interrogate interlaminar shear failures and to provide an estimate of the interlaminar shear strength of composite materials. However, despite its popularity, the short-beam shear test is affected by complications that are not incorporated into the elementary Euler-Bernoulli beam theory upon which interpretation of the test method is based. According to the assumptions associated with this theory, the interlaminar shear stress is parabolically distributed across the face of the specimen with a maximum occurring at the midthickness plane. Unfortunately, the short-beam shear test configuration is deliberately chosen so that the interlaminar shear stress in the beam dominates the stress distribution.

Clearly, the behavior of a short beam deviates from that predicted by the elementary theory [2]. Numerous investigations have indicated the presence of high shear stresses near the concentrated load and supports as depicted in Figure 1 [3,4]. That such complex stress states exist within SBS specimens is corroborated by their typical fracture pattern as shown in Figure 2.

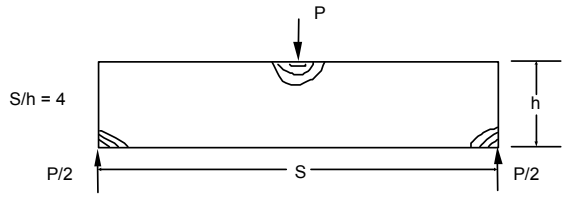

Figure 1: Stress concentrations affecting the short-beam shear (SBS) test

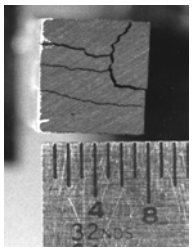

Figure 2: End view of a typical graphite/epoxy SBS test specimen

Analysis shows that the short-beam shear test configuration yields stress concentration effects which are never fully dissipated as St Venant's principle is not satisfied in a highly orthotropic beam of low span-to-depth ratio. While stress concentration effects are reasonably well localized in a standard flexural beam test, the dimensions of the short-beam shear test specimens used to test high-performance composites, such as graphite/epoxy, preclude the dissipation of stress concentration effects. Closer inspection of short-beam shear test specimen failures indicates the presence of microbuckling and microcracking in the region near the load roller. It has been theorized that initial damage in the form of vertical cracks may be necessary to induce the horizontal interlaminar failures observed. Thus, despite its simplicity and popularity, the short-beam shear test method is not appropriate for a general study of interlaminar shear failures of composite materials.

In an attempt to produce true interlaminar shear failure in laminated composite materials, alternatives to the standard short-beam test have been suggested. Some experimenters have proposed the use of thicker short beams; e.g. 50 plies, or the use of a four-point flexure test [5]. Thicker short-beam specimens, however, are still prone to vertical cracking in the load roller region, precluding true interlaminar shear failure. And, investigations have verified that the four-point flexure test is also adversely affected by stress concentrations in the regions of loading resulting in microbuckling and vertical cracking.

The ideal interlaminar shear test method should provide a region of pure, uniform shear stress within the test section of the specimen. Test results should not be affected by the presence of a complex stress state in the region of eventual specimen failure. Toward this goal, a simple test method capable of producing a state of pure interlaminar shear stress within a specified region of a flexure test specimen was developed by the lead author [6]. The test method employed an adhesively bonded test specimen referred to as the steel/composite/steel (SCS) test sample tested in four-point flexure (see Figure 3).

In that research, an SCS test sample was constructed of a coupon of Hercules AS4/3501-6, unidirectional, graphite/epoxy material, bonded between two thin strips of heat-treated steel using an epoxy adhesive. The design of the SCS test sample confined the composite material to the midthickness region of the beam where the stress state approached that of uniform shear. The steel face strips dissipated the stress concentration effects in the vicinity of the load and support points. Interlaminar shear failures along the midplane of the composite test coupon were achieved (see Figure 4). The propagation of the interlaminar shear failures produced by the SCS test sample was monitored using a crack detection device developed by Camping and Short [7]. The interlaminar shear failures of the specimens tested (5 replicates) were all found to follow the same general pattern of propagation, i.e., once the shear failure initiated in the region of pure shear stress between a load and support, it propagated in both directions along the length of the beam, first reaching the end of the specimen closest to the failure initiation site. The shear failure propagated through the zone of compressive stress corresponding to the support region, into the beam overhang region, and out to the end of the specimen.

The failure then propagated in the opposite direction, back into the flexure specimen, through the zone of compressive stress corresponding to the load region, terminating under the load roller farthest away from the failed end. The final interlaminar shear failure appeared as shown in Figure 5.

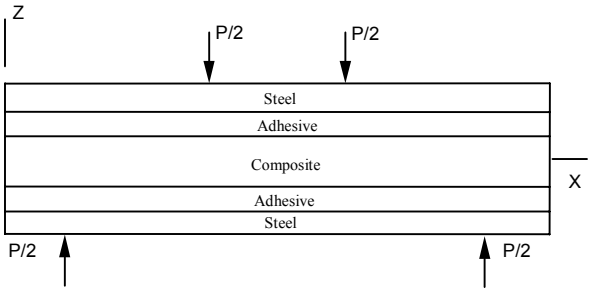

Figure 3: SCS test sample

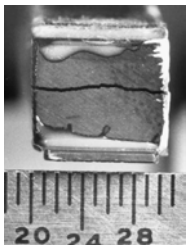

Figure 4: End view of a typical graphite/epoxy SCS test specimen (markings on scale shown are 1/32 in.)

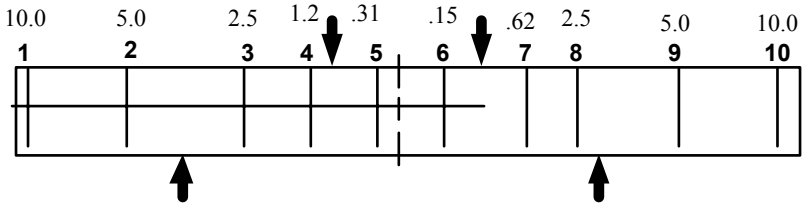

Figure 5: Final location of shear failure in SCS test sample (numbers refer to location of sensors of crack detection device [7]).

Short [6] reasoned that from the results of using the crack detection device, the scanning electron photomicrographs of the fracture surfaces presented for the region between the load and support correspond to that of pure interlaminar shear failure of unidirectional graphite/epoxy material. It was also noted that the fracture surface appearance was somewhat different from that usually reported in the literature as being representative of the pure shear failure of unidirectional graphite/epoxy composites. However, it is noted that in much of the work presented in the literature, the test methods used to produce the shear failures are not reported. Therefore, the question still remained as to whether the interlaminar shear failures produced by the SCS test sample do indeed represent 'pure' Mode II shear failures. Citing the work by Filon [8], Short reasoned that the magnitude of the through-thickness normal stress, σ_z , in the region between the load and supports damps out to such a degree that it can be considered to be fairly negligible on the failure plane (midplane). To answer this question, a more accurate estimate of the stress state on the failure plane between the load and support regions was required.

FINITE ELEMENT STRESS ANALYSIS

The three stress components σ_y , τ_{xy} , τ_{yz} , have little direct effect on the interlaminar shear failure due to the design of the SCS test sample and the nature of the flexure test. Furthermore, since previous research using the crack detection device verified that the shear failures initiate approximately on the midthickness plane of the SCS test sample, between a load and support region, it was assumed that the bending stress, σ_x , also has negligible effect on the failure. Hence, the through-thickness normal stress, σ_z , and the interlaminar shear stress, τ_{xz} , are the only stress components that significantly affect the interlaminar shear failure.

The finite element analysis (FEA) was performed using the software program ANSYS©. A plane stress analysis was performed modeling only half of the SCS test sample due to symmetry. A total of five

areas each representing one of the component layers was created. These areas were subsequently merged.

The composite region was modeled using a "lumped parameter" model based on the work by Post et. al. [9]. This model uses finite elements to represent resin-rich regions within the unidirectional graphite-epoxy laminate. This is consistent with the materialographic inspection of the composite laminate and also with the load-deflection results of the flexural testing. Contact stress elements were used to model the load and support regions.

DISCUSSION OF RESULTS

Excellent agreement was obtained between the FEA and experimental beam deflection and beam strain results as determined via strain gages. Five replicate SCS test samples were tested. Such agreement among the kinematic results supports the position that the corresponding FEA stress analysis results are fairly accurate. The distribution of the interlaminar shear stress, τ_{xz} , along a vertical line midway between the load and support rollers is shown in Figure 6. The abscissa represents the thickness of the SCS test sample with DIST = 0 representing the supported surface of the beam. The maximum value of interlaminar shear stress corresponding to the fracture load experienced by the SCS test sample at the midplane is 101.42 MPa. This compares favorably with the value 99.94 MPa reported by Short [6] using a closed-form analysis.

Figure 7 shows the distribution of the through-thickness normal stress, σ_z , on the midthickness plane between the load and support rollers. The minimum value of the abscissa is representative of a point on the midthickness plane, which lies on a vertical line drawn upward from the center of the support roller. The maximum value indicates a similar point with respect to the load roller. The distance between the two rollers is 15.24 mm. At the midpoint between the load and support rollers, the through-thickness normal (compressive) stress, σ_z , is 1.8 MPa, approximately 5% of the maximum interlaminar shear stress.

Figure 8 shows the distribution of the through-thickness normal stress, σ_z , beneath the load. The abscissa is representative of the beam thickness with the minimum value corresponding to the supported face. The results show that the compressive through-thickness normal stress, σ_z , is mostly dissipated by the top steel strip. The magnitude of this stress at the composite/adhesive interface is approximately 15% of the maximum compressive stress at the top face of the steel strip.

Previous research [6] showed that the SCS interlaminar shear failures initiated within a region of the beam approximately 5-mm wide, located symmetrically about a plane midway between the load and support. The results of the finite element analysis show that the average through-thickness normal stress acting in this region is approximately 5% of the maximum interlaminar shear stress. Therefore, it can be concluded that the crack initiation zone was subjected to a state of relatively pure Mode II interlaminar shear stress. The steel plates in the SCS test sample design proved effective in damping the stress concentration effects of the normal stress due to the load and supports. These stress concentration effects are known to promote failures in standard short-beam shear specimens.

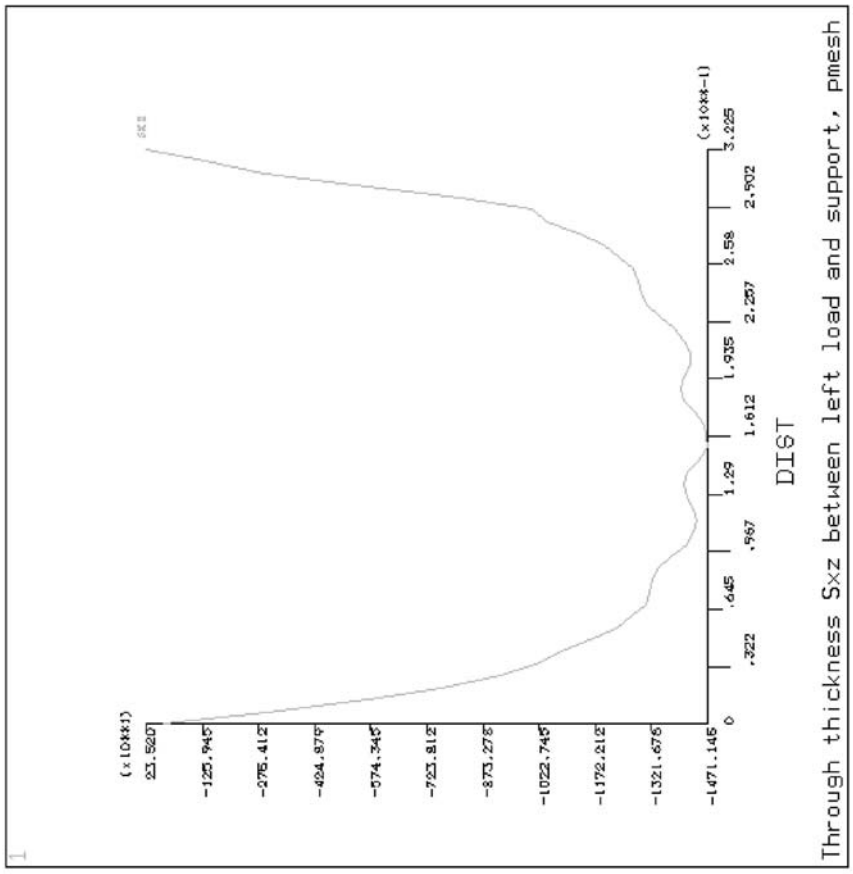

Figure 6: Interlaminar shear stress, τ_{xz} , midway between the load and support

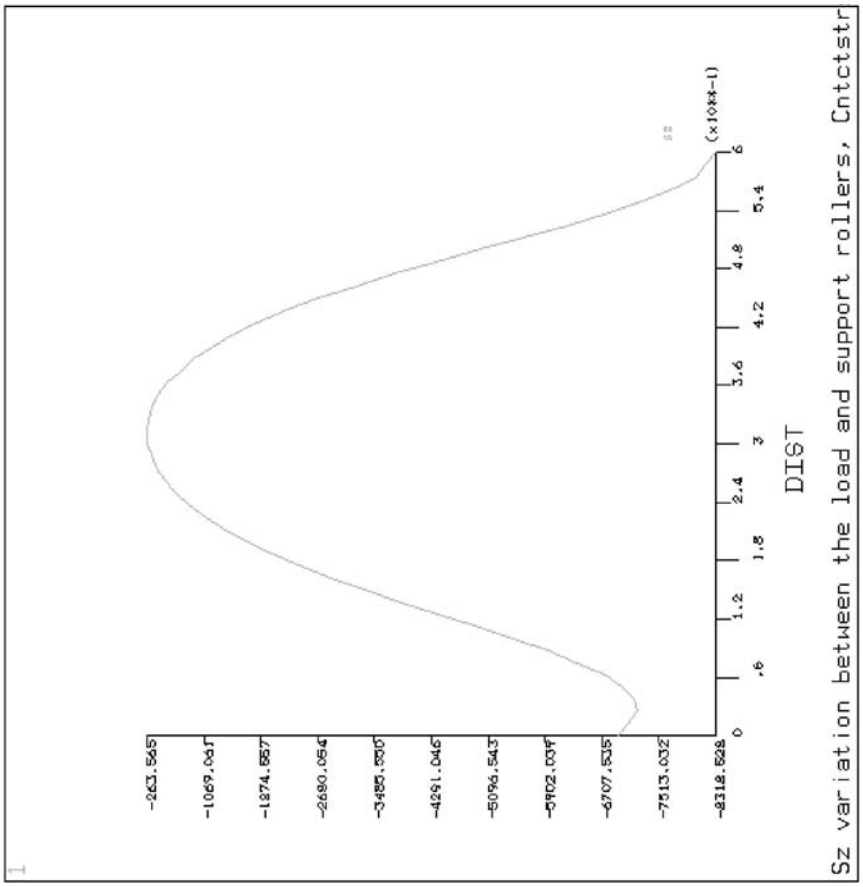

Figure 7: Through-thickness normal stress, σ_z , on midthickness plane between the load and support

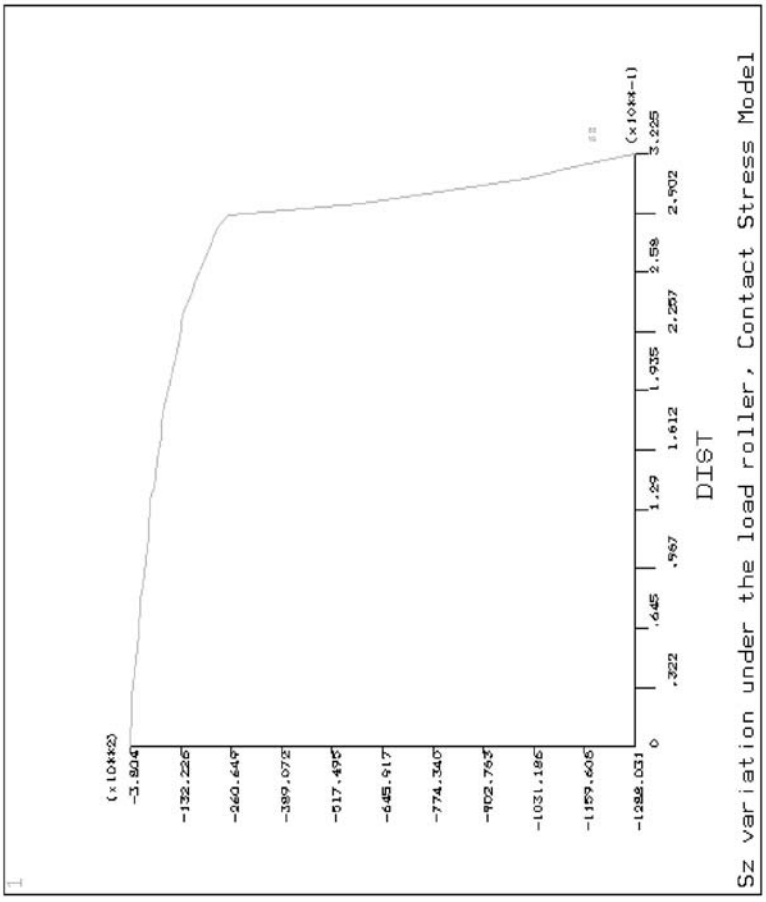

Figure 8: Through-thickness normal stress, σ_z , beneath the load

REFERENCES

1. *ASTM D2344-84,89 Apparent Interlaminar Shear Strength of Parallel Fiber Composites by Short Beam Test*, American Society for Testing Materials, Philadelphia, PA.
2. Whitney, J.M. and Browning, C.E. (1985) *Exp. Mech.* 25, 294.
3. Whitney, J.M. (1985) *Compos. Sci. Technol*. 22, 167.
4. Sandorff, P.E. (1980) *J. Compos. Mater.* 14, 199.
5. Browning, C.E., Abrams, F.L. and Whitney, J.M. (1983) in *Composite Materials: Quality Assurance and Processing, ASTM STP 797,* American Society for Testing and Materials, Philadelphia, PA, pp. 54-74.
6. Short, S.R. (1995) *Composites* 26, 431.
7. Camping, J.D., Short, S.R. (1995) *Exp. Tech.* 19, 15.
8. Filon, L.N.G. (1903) *Trans. Roy. Soc. (London) Ser. A* 201, 63.
9. Post D., Czarnek, R., Joh, D., and Wood, J. (1984) *NASA Contractor Report 3844*.

OPAL/POSTER REFERENCE: ICF100213OR

INELASTIC CYCLIC STRESS-STRAIN RESPONSE IN SILICON-NITRIDE CERAMICS AT ELEVATED TEMPERATURES

K. Hatanaka[1], K. Oshita[1], Y. Ishiga[2] and H. Toyama[1]

[1]Department of Mechanical Engineering, Yamaguchi University
2-16-1 Tokiwadai, Ube-City, Yamaguchi 755-8611, Japan
[2]TOSOH Co., 1-8 Kasumi, Yokkaichi-City, Mie 510-8540, Japan

ABSTRACT

The extensometer was newly developed for measuring axial displacement of ceramics and its composite materials at elevated temperatures. Then the high temperature use-closed loop type push-pull fatigue test system was equipped with this extensometer.

The push-pull cyclic loading tests were performed for silicon nitride ceramics under the controlled triangular and trapezoidal stress wave loadings at 1300°C, and its cyclic stress-strain response was measured. The inelastic strain, which is greatly dependent upon stress rate, was detected in this material at 1300°C. It was found from the shape of the cyclic stress-strain hysteresis loop that inelastic strain was easier to generate under tensile loading than under compressive one; the width in the hysteresis loop was larger on the tensile stress side than on the compressive stress side. Moreover, the cyclic stress-strain hysteresis loop showed that the positive and negative inelastic strains were generated on unloading excursions from the tensile maximum and the compressive minimum stresses as well as on the tensile and compressive loading excursions. The creep strain was also detected during the tensile and compressive stress-hold periods under the trapezoidal stress wave loading. At that time the amount of the creep strain is much larger during the tensile stress-hold period than during the compressive stress-hold one. Another notice is that the cyclic inelastic strain decreases with progress of cyclic loading process, showing that strengthening occurs during cyclic loading at 1300°C in Si_3N_4 ceramics.

KEY WORDS

Si_3N_4 Ceramics, Push-pull Cyclic Loading, Elevated Temperatures, Cyclic Stress-strain Response, Inelastic Strain, Fatigue Life

INTRODUCTION

The basic and practical studies have been extensively carried out for applying ceramics materials, which possess excellent heat-resisting mechanical properties, to high temperature machine components. Fatigue is one of the important mechanical properties to be clarified for actualizing this [1,2].

The cyclic stress-strain response is a fundamental mechanical property for fatigue life prediction. Its

measurement, however, is extremely difficult at so called ultra-high temperatures in ceramics materials; the amount of displacement generating in these materials is quite small, and ultra-high temperature-use extensometer has to be developed to measure such a small displacement. Then the cyclic stress-strain response of ceramics materials has been little examined at elevated temperatures so far.

The inelastic deformation occurs in Si_3N_4 ceramic at elevated temperatures [3,4]. The present study aims at clarifying the inelastic cyclic stress-strain response of Si_3N_4 ceramic at 1300°C, which has not been little examined.

USED MATERIAL AND TEST PROCEDURES

The tested material is sintered silicon nitride ceramic which was fabricated by mixing Y-α sialon and Si_3N_4 particles at ratios of 40 and 60 weight percents, and then sintering the mixed particles in N_2-gas atmosphere at 1750°C. The sintered column was machined into the specimen shown in Fig.1.

The electro-hydraulic type-closed loop type test system was employed for push-pull loading test at 1300°C [2,5], where cyclic triangular stress/strain waves with stress/strain ratios of -1.0 were applied to the specimen, controlling the stress/strain rates. The trapezoidal strain wave with stress-hold time was also used in the cyclic loading test. The displacement was measured in the gauge length of 10mm settled in the parallel part of the specimen by means of the self-designed extensometer.

TEST RESULTS AND DISCUSSION

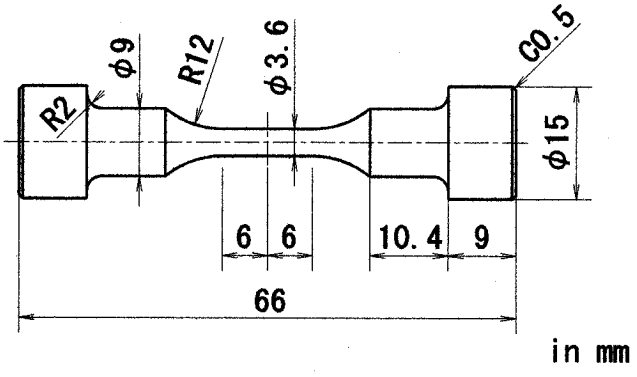

Figure 1: Configuration of test specimen

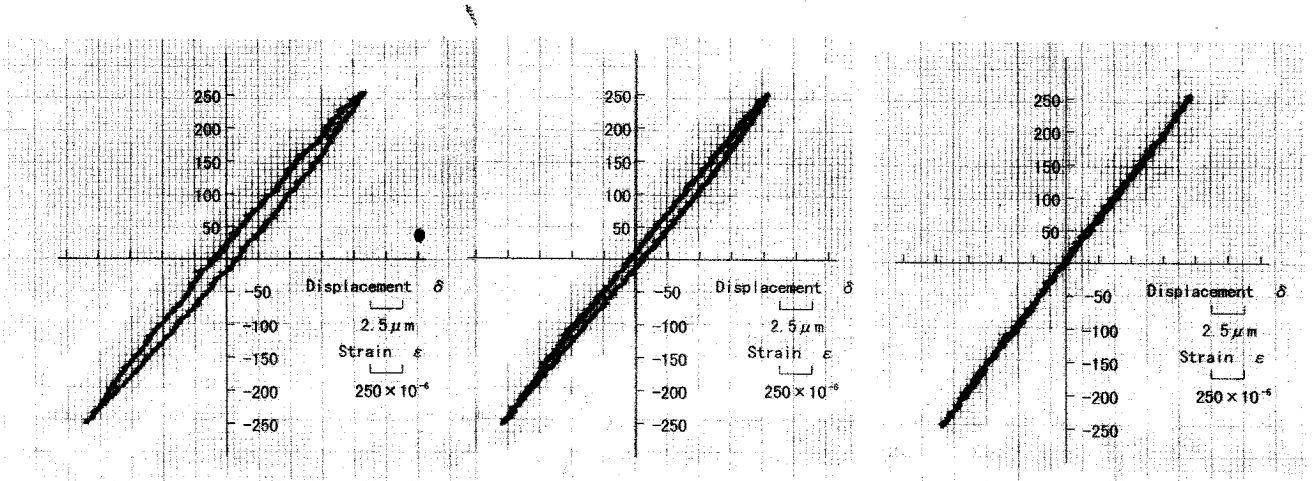

(a) N=1 cycle (t=0 h) (b) N=48 cycles (t=13.3 h) (c) N=807 cycles (t=224.2 h)

Figure 2: Change in cyclic stress-strain response with increase in number of stress cycles at $\Delta\sigma / 2 = 250$ MPa and $\dot{\sigma} = 1.0$ MPa/s at 1300°C in Si_3N_4 ceramic

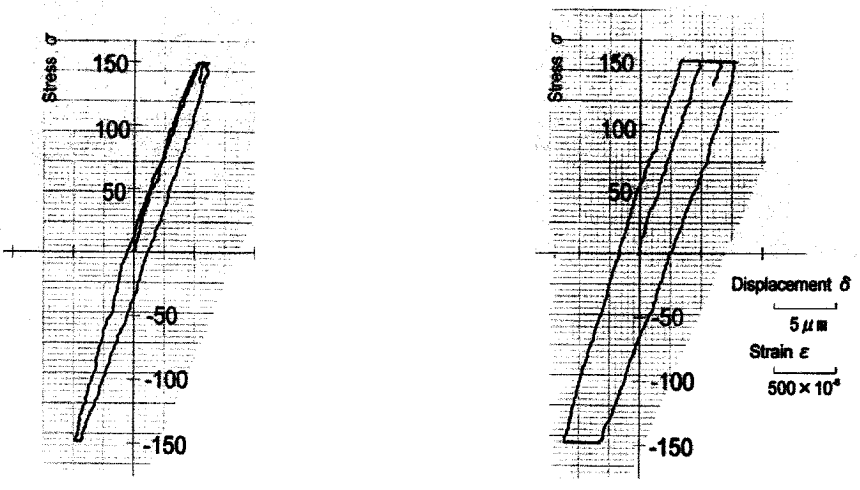

(a) t_h=30 s (b) t_h=10 min

Figure 3: Cyclic stress-strain response under trapezoidal stress wave loading at 1300°C in Si_3N_4 ceramic

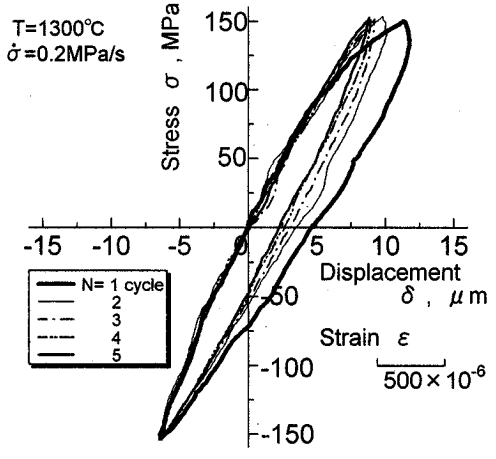

Figure 4: Cyclic stress-strain response at early stage in cyclic triangular stress wave loading process at $\Delta\sigma/2$ =150 MPa and $\dot{\sigma}$ =0.2 MPa/s at 1300°C in Si_3N_4 ceramic

Figure 2 shows the variation in cyclic stress-strain response measured during cyclic loadings at the stress amplitude $\Delta\sigma/2$ = 250 MPa controlled at the stress rate $\dot{\sigma}$ = 1 MPa/s. The inelastic strain detected at N = 1 cycle is gradually reduced with progress of fatigue process, and then almost disappears at N = 807 cycles. This shows the occurrence of the increased resistance against cyclic deformation during cyclic loadings at 1300°C. Figures 2 (a) and (b) also show that much larger inelastic strain is induced by tensile stress than by compressive stress.

Figures 3 (a) and (b) show the cyclic stress-strain response measured for the first one cycle under the cyclic trapezoidal stress wave loadings at $\Delta\sigma/2$ = 150 MPa with the stress rate on loading and unloading excursions, $\dot{\sigma}$ = 2 MPa/s and the stress hold times t_h= 30 s and 10 min. The creep strain is generated for the stress held at $\sigma = \pm 150$ MPa, of which amount is dependent on the hold time t_h and the sign of the stress; the creep strain is much greater for the longer t_h and on the tensile stress side than on the compressive stress one.

The change in the stress-strain hysteresis loop measured under cyclic triangular stress wave loadings at $\Delta\sigma/2$ = 150 MPa and $\dot{\sigma}$ = 0.2 MPa/s is shown in Fig.4. The much larger inelastic strain is shown in the figure than in Fig.2, in which the cyclic stress-strain response is obtained under cyclic loadings at

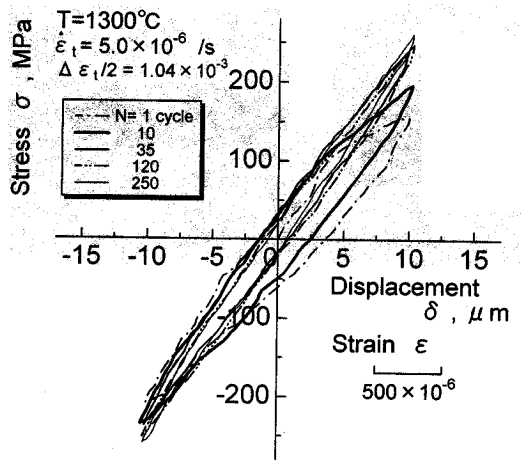

Figure 5: Cyclic stress-strain response at early stage in cyclic triangular strain wave loading process at $\Delta\varepsilon_t/2 = 1.04\times10^{-3}$ and $\dot{\varepsilon}_t = 5.0\times10^{-6}$/s at 1300°C in Si_3N_4 ceramic

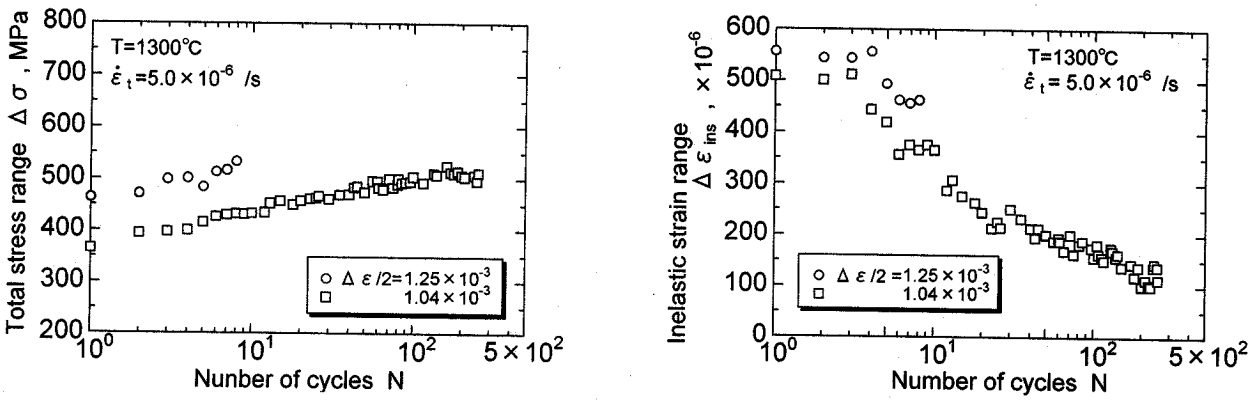

(a) Stress range $\Delta\sigma$ (b) Inelastic strain range $\Delta\varepsilon_{ins}$

Figure 6: Variations in stress and inelastic strain ranges in cyclic triangular strain wave loadings at $\dot{\varepsilon}_t = 5.0\times10^{-6}$/s at 1300°C in Si_3N_4 ceramic

$\Delta\sigma/2 = 150$ MPa and $\dot{\sigma} = 1$ MPa/s. Thus the inelastic strain generated at a given stress amplitude is greatly dependent upon the stress rate, and less at the larger stress rate. The great amount of inelastic strain yields at first tensile loading, and this increases even in the unloading process. Furthermore, the inelastic strain due to compressive stress is much less than that due to tensile stress. The gradual decrease in inelastic strain is also clearly found during stress cycling in the figure, of which the greater part occurs on the tensile stress side. As the result, the difference between the amounts of inelastic strain on the tensile and compressive stress sides is reduced with progress of the stress cycling process.

Figure 5 shows the change in the cyclic stress-strain response obtained from cyclic straining test controlled at strain amplitude $\Delta\varepsilon_t/2 = 1.04\times10^{-3}$ at strain rate $\dot{\varepsilon}_t = 5.0\times10^{-6}$/s. The stress and the inelastic strain increase and decrease with progress of cyclic straining process, respectively, largely on the tensile stress side and slightly on the compressive stress side in the figure. Consequently, the stress-strain hysteresis loop shifts from the configuration with the lower stress and the larger inelastic strain on the tensile stress side from the one with almost the same stress and inelastic strain in absolute value at a given tensile and compressive total strains.

Figures 6 (a) and (b) show the variations in stress and inelastic strain ranges in cyclic straining process at $\dot{\varepsilon}_t = 5.0\times10^{-6}$/s at 1300°C. The figures clearly show that the stress range increases and the inelastic strain range decreases as cyclic straining process progresses, exhibiting the increasing resistance to cyclic

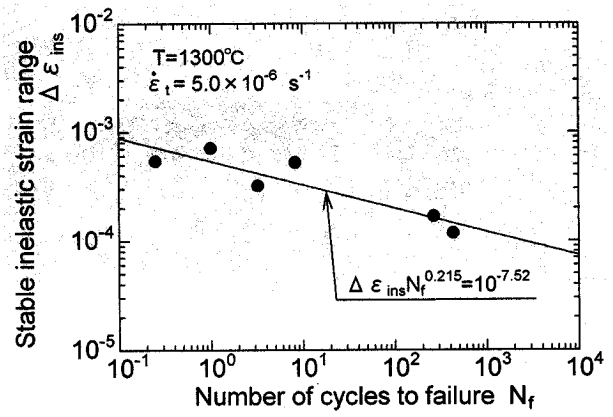

Figure 7: Relationship between inelastic strain range and fatigue life obtained from strain-controlled cyclic loading test at $\dot{\varepsilon}_t$ =5.0× 10^{-6}/s at 1300°C in Si_3N_4 ceramic

deformation during strain cycling. Such phenomena correspond well to the cyclic stress-strain response under stress-controlled cyclic loading, which is shown in Fig.2.

The fatigue life N_f was plotted against the stabilized inelastic strain range $\Delta\varepsilon_{ins}$ in the strain-controlled fatigue test at $\dot{\varepsilon}_t$ = 5.0× 10^{-6}/s, in Fig.7, which was determined at half the number of cycles to failure. The figure shows that the relationship between $\Delta\varepsilon_{ins}$ and N_f is expressed by a linear line on double logarithmic scales, as known in metallic materials. The exponent α in the Manson-Coffin plot [6,7] $\Delta\varepsilon_p \cdot {N_f}^{\alpha} = C$, however, is 0.202 in this material, which is quite small, compared with the one in metallic materials.

CONCLUSIONS

The push-pull cyclic loading tests were performed and cyclic stress-strain response was measured for Si_3N_4 ceramic under the stress- and strain-controlled conditions at 1300°C. The main results obtained are summarized as follows.

(1) The inelastic strain is generated during cyclic loadings, of which amount is much greater at the smaller stress/strain rates, and on the tensile stress side than on the compressive stress side.

(2) The inelastic strain is gradually reduced with progress of the stress- and strain-controlled cyclic loading processes, showing increasing resistance to cyclic deformation in the cyclic loading process.

(3) The Manson-Coffin plot holds in Si_3N_4 ceramic at 1300°C, where the exponent α in $\Delta\varepsilon_{ins} \cdot {N_f}^{\alpha} = C$ is 0.202, being much smaller than the one in metallic materials.

REFERENCES

1. Evans, A.G., (1980). *Int. J. Fract.* 16, 485.
2. Hatanaka, K., Katsuyama, M. and Takagi, H., (1996). *Trans. Jpn. Soc. Mech. Eng. A.* 62, 614.
3. Hatanaka, K., Shiota, H. and Ando, T., (1991). *JSME. Int. J. Ser.I.* 34, 351.
4. Luecke, W.E. and Wiederhorn, S.M., (1999). *J. Am. Ceram. Soc.* 82, 2769.
5. Hatanaka, K., Nishimura, H. and Katsuyama, M., (1994). *Trans. Jpn. Soc. Mech. Eng. A.* 62, 1129.
6. Manson, S.S., (1953). NACA TN-2933.
7. Coffin Jr., L.F., (1954). *Trans. ASME*, 76, 931.

OPAL/POSTER REFERENCE: ICF100213OR

INELASTIC CYCLIC STRESS-STRAIN RESPONSE IN SILICON-NITRIDE CERAMICS AT ELEVATED TEMPERATURES

K. Hatanaka[1], K. Oshita[1], Y. Ishiga[2] and H. Toyama[1]

[1]Department of Mechanical Engineering, Yamaguchi University
2-16-1 Tokiwadai, Ube-City, Yamaguchi 755-8611, Japan
[2]TOSOH Co., 1-8 Kasumi, Yokkaichi-City, Mie 510-8540, Japan

ABSTRACT

The extensometer was newly developed for measuring axial displacement of ceramics and its composite materials at elevated temperatures. Then the high temperature use-closed loop type push-pull fatigue test system was equipped with this extensometer.

The push-pull cyclic loading tests were performed for silicon nitride ceramics under the controlled triangular and trapezoidal stress wave loadings at 1300°C, and its cyclic stress-strain response was measured. The inelastic strain, which is greatly dependent upon stress rate, was detected in this material at 1300°C. It was found from the shape of the cyclic stress-strain hysteresis loop that inelastic strain was easier to generate under tensile loading than under compressive one; the width in the hysteresis loop was larger on the tensile stress side than on the compressive stress side. Moreover, the cyclic stress-strain hysteresis loop showed that the positive and negative inelastic strains were generated on unloading excursions from the tensile maximum and the compressive minimum stresses as well as on the tensile and compressive loading excursions. The creep strain was also detected during the tensile and compressive stress-hold periods under the trapezoidal stress wave loading. At that time the amount of the creep strain is much larger during the tensile stress-hold period than during the compressive stress-hold one. Another notice is that the cyclic inelastic strain decreases with progress of cyclic loading process, showing that strengthening occurs during cyclic loading at 1300°C in Si_3N_4 ceramics.

KEY WORDS

Si_3N_4 Ceramics, Push-pull Cyclic Loading, Elevated Temperatures, Cyclic Stress-strain Response, Inelastic Strain, Fatigue Life

INTRODUCTION

The basic and practical studies have been extensively carried out for applying ceramics materials, which possess excellent heat-resisting mechanical properties, to high temperature machine components. Fatigue is one of the important mechanical properties to be clarified for actualizing this [1,2].

The cyclic stress-strain response is a fundamental mechanical property for fatigue life prediction. Its

measurement, however, is extremely difficult at so called ultra-high temperatures in ceramics materials; the amount of displacement generating in these materials is quite small, and ultra-high temperature-use extensometer has to be developed to measure such a small displacement. Then the cyclic stress-strain response of ceramics materials has been little examined at elevated temperatures so far.

The inelastic deformation occurs in Si_3N_4 ceramic at elevated temperatures [3,4]. The present study aims at clarifying the inelastic cyclic stress-strain response of Si_3N_4 ceramic at 1300°C, which has not been little examined.

USED MATERIAL AND TEST PROCEDURES

The tested material is sintered silicon nitride ceramic which was fabricated by mixing Y-α sialon and Si_3N_4 particles at ratios of 40 and 60 weight percents, and then sintering the mixed particles in N_2-gas atmosphere at 1750°C. The sintered column was machined into the specimen shown in Fig.1.

The electro-hydraulic type-closed loop type test system was employed for push-pull loading test at 1300°C [2,5], where cyclic triangular stress/strain waves with stress/strain ratios of -1.0 were applied to the specimen, controlling the stress/strain rates. The trapezoidal strain wave with stress-hold time was also used in the cyclic loading test. The displacement was measured in the gauge length of 10mm settled in the parallel part of the specimen by means of the self-designed extensometer.

TEST RESULTS AND DISCUSSION

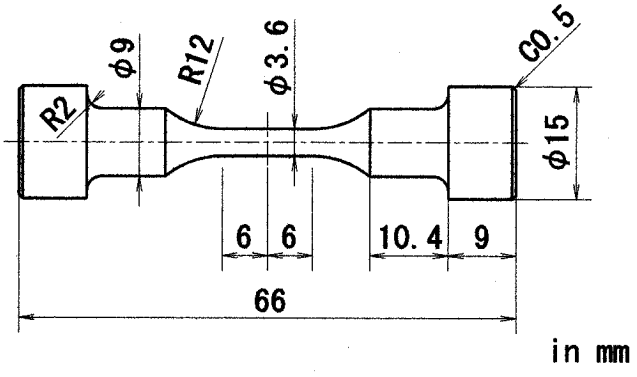

Figure 1: Configuration of test specimen

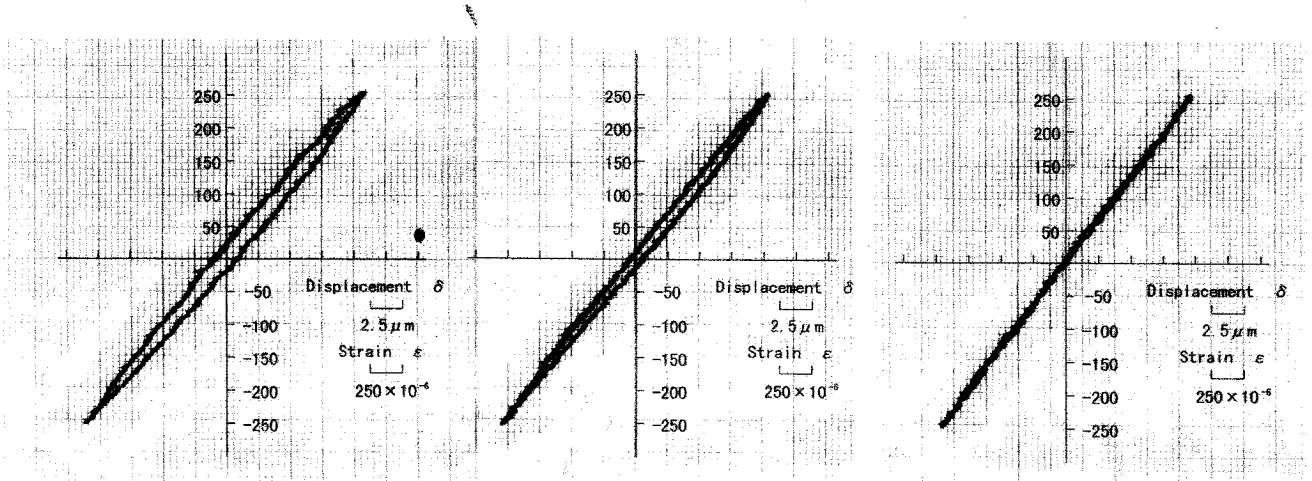

(a) N=1 cycle (t=0 h) (b) N=48 cycles (t=13.3 h) (c) N=807 cycles (t=224.2 h)

Figure 2: Change in cyclic stress-strain response with increase in number of stress cycles at $\Delta\sigma / 2 = 250$ MPa and $\dot{\sigma} = 1.0$ MPa/s at 1300°C in Si_3N_4 ceramic

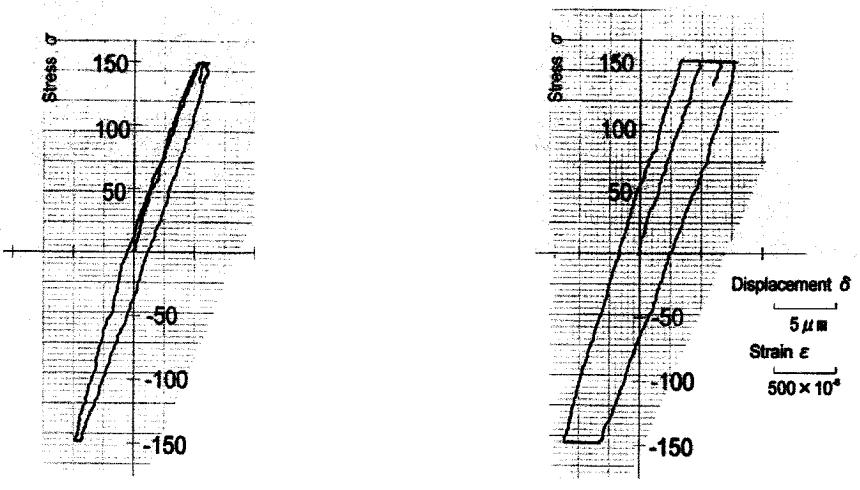

(a) t_h=30 s (b) t_h=10 min

Figure 3: Cyclic stress-strain response under trapezoidal stress wave loading at 1300°C in Si_3N_4 ceramic

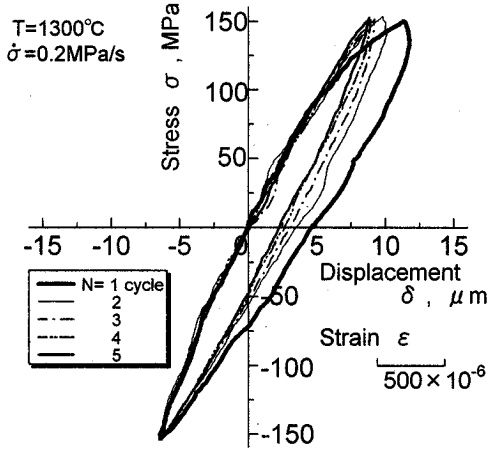

Figure 4: Cyclic stress-strain response at early stage in cyclic triangular stress wave loading process at $\Delta\sigma/2$ =150 MPa and $\dot{\sigma}$ =0.2 MPa/s at 1300°C in Si_3N_4 ceramic

Figure 2 shows the variation in cyclic stress-strain response measured during cyclic loadings at the stress amplitude $\Delta\sigma/2$ = 250 MPa controlled at the stress rate $\dot{\sigma}$ = 1 MPa/s. The inelastic strain detected at N = 1 cycle is gradually reduced with progress of fatigue process, and then almost disappears at N = 807 cycles. This shows the occurrence of the increased resistance against cyclic deformation during cyclic loadings at 1300°C. Figures 2 (a) and (b) also show that much larger inelastic strain is induced by tensile stress than by compressive stress.

Figures 3 (a) and (b) show the cyclic stress-strain response measured for the first one cycle under the cyclic trapezoidal stress wave loadings at $\Delta\sigma/2$ = 150 MPa with the stress rate on loading and unloading excursions, $\dot{\sigma}$ = 2 MPa/s and the stress hold times t_h= 30 s and 10 min. The creep strain is generated for the stress held at $\sigma = \pm 150$ MPa, of which amount is dependent on the hold time t_h and the sign of the stress; the creep strain is much greater for the longer t_h and on the tensile stress side than on the compressive stress one.

The change in the stress-strain hysteresis loop measured under cyclic triangular stress wave loadings at $\Delta\sigma/2$ = 150 MPa and $\dot{\sigma}$ = 0.2 MPa/s is shown in Fig.4. The much larger inelastic strain is shown in the figure than in Fig.2, in which the cyclic stress-strain response is obtained under cyclic loadings at

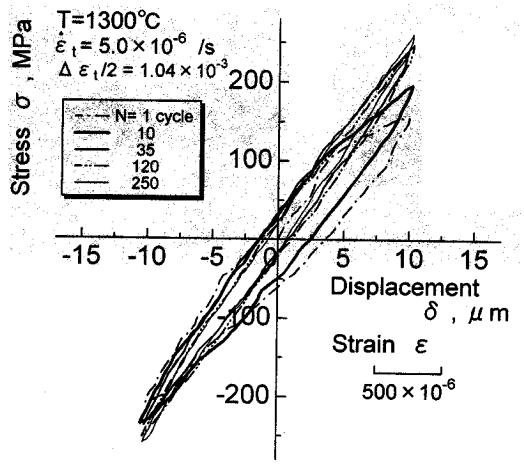

Figure 5: Cyclic stress-strain response at early stage in cyclic triangular strain wave loading process at $\Delta\varepsilon_t/2 = 1.04\times10^{-3}$ and $\dot{\varepsilon}_t = 5.0\times10^{-6}$/s at 1300°C in Si_3N_4 ceramic

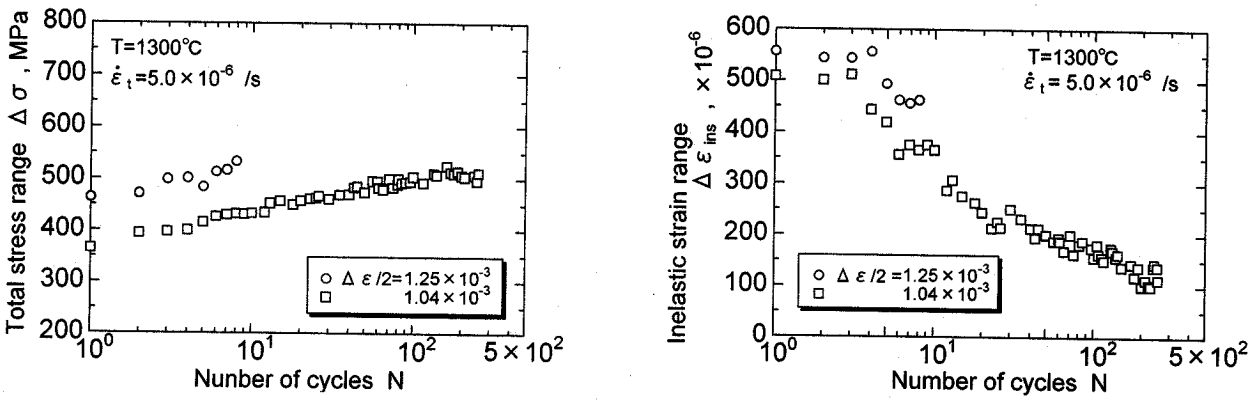

(a) Stress range $\Delta\sigma$ (b) Inelastic strain range $\Delta\varepsilon_{ins}$

Figure 6: Variations in stress and inelastic strain ranges in cyclic triangular strain wave loadings at $\dot{\varepsilon}_t = 5.0\times10^{-6}$/s at 1300°C in Si_3N_4 ceramic

$\Delta\sigma/2 = 150$ MPa and $\dot{\sigma} = 1$ MPa/s. Thus the inelastic strain generated at a given stress amplitude is greatly dependent upon the stress rate, and less at the larger stress rate. The great amount of inelastic strain yields at first tensile loading, and this increases even in the unloading process. Furthermore, the inelastic strain due to compressive stress is much less than that due to tensile stress. The gradual decrease in inelastic strain is also clearly found during stress cycling in the figure, of which the greater part occurs on the tensile stress side. As the result, the difference between the amounts of inelastic strain on the tensile and compressive stress sides is reduced with progress of the stress cycling process.

Figure 5 shows the change in the cyclic stress-strain response obtained from cyclic straining test controlled at strain amplitude $\Delta\varepsilon_t/2 = 1.04\times10^{-3}$ at strain rate $\dot{\varepsilon}_t = 5.0\times10^{-6}$/s. The stress and the inelastic strain increase and decrease with progress of cyclic straining process, respectively, largely on the tensile stress side and slightly on the compressive stress side in the figure. Consequently, the stress-strain hysteresis loop shifts from the configuration with the lower stress and the larger inelastic strain on the tensile stress side from the one with almost the same stress and inelastic strain in absolute value at a given tensile and compressive total strains.

Figures 6 (a) and (b) show the variations in stress and inelastic strain ranges in cyclic straining process at $\dot{\varepsilon}_t = 5.0\times10^{-6}$/s at 1300°C. The figures clearly show that the stress range increases and the inelastic strain range decreases as cyclic straining process progresses, exhibiting the increasing resistance to cyclic

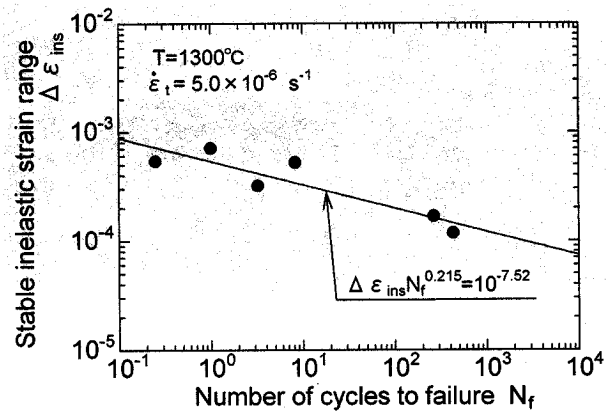

Figure 7: Relationship between inelastic strain range and fatigue life obtained from strain-controlled cyclic loading test at $\dot{\varepsilon}_t$ =5.0× 10^{-6}/s at 1300°C in Si_3N_4 ceramic

deformation during strain cycling. Such phenomena correspond well to the cyclic stress-strain response under stress-controlled cyclic loading, which is shown in Fig.2.

The fatigue life N_f was plotted against the stabilized inelastic strain range $\Delta\varepsilon_{ins}$ in the strain-controlled fatigue test at $\dot{\varepsilon}_t$ = 5.0× 10^{-6}/s, in Fig.7, which was determined at half the number of cycles to failure. The figure shows that the relationship between $\Delta\varepsilon_{ins}$ and N_f is expressed by a linear line on double logarithmic scales, as known in metallic materials. The exponent α in the Manson-Coffin plot [6,7] $\Delta\varepsilon_p \cdot {N_f}^{\alpha} = C$, however, is 0.202 in this material, which is quite small, compared with the one in metallic materials.

CONCLUSIONS

The push-pull cyclic loading tests were performed and cyclic stress-strain response was measured for Si_3N_4 ceramic under the stress- and strain-controlled conditions at 1300°C. The main results obtained are summarized as follows.

(1) The inelastic strain is generated during cyclic loadings, of which amount is much greater at the smaller stress/strain rates, and on the tensile stress side than on the compressive stress side.

(2) The inelastic strain is gradually reduced with progress of the stress- and strain-controlled cyclic loading processes, showing increasing resistance to cyclic deformation in the cyclic loading process.

(3) The Manson-Coffin plot holds in Si_3N_4 ceramic at 1300°C, where the exponent α in $\Delta\varepsilon_{ins} \cdot {N_f}^{\alpha} = C$ is 0.202, being much smaller than the one in metallic materials.

REFERENCES

1. Evans, A.G., (1980). *Int. J. Fract.* 16, 485.
2. Hatanaka, K., Katsuyama, M. and Takagi, H., (1996). *Trans. Jpn. Soc. Mech. Eng. A.* 62, 614.
3. Hatanaka, K., Shiota, H. and Ando, T., (1991). *JSME. Int. J. Ser.I.* 34, 351.
4. Luecke, W.E. and Wiederhorn, S.M., (1999). *J. Am. Ceram. Soc.* 82, 2769.
5. Hatanaka, K., Nishimura, H. and Katsuyama, M., (1994). *Trans. Jpn. Soc. Mech. Eng. A.* 62, 1129.
6. Manson, S.S., (1953). NACA TN-2933.
7. Coffin Jr., L.F., (1954). *Trans. ASME*, 76, 931.

ORAL REFERENCE : ICF100223OR

INFLUENCE COEFFICIENTS TO CALCULATE STRESS INTENSITY FACTORS FOR AN ELLIPTICAL CRACK IN A PLATE

P. Le Delliou[1] and B. Barthelet[2]

[1] Electricité De France R&D, Département MTC, Les Renardières, 77818 Moret s/Loing Cedex, France
[2] Electricité De France, Division Production Nucléaire, 93282 St Denis Cedex, France

ABSTRACT

Crack assessment in engineering structures relies first on accurate evaluation of the stress intensity factors. In recent years, a large work has been conducted in France by the Atomic Energy Commission to develop influence coefficients for surface cracks in pipes. However, the problem of embedded cracks in plates (and pipes) which is also of practical importance has not received so much attention. Presently, solutions for elliptical cracks are available either in infinite solid with a polynomial distribution of normal loading or in plate, but restricted to constant or linearly varying tension.

This paper presents the work conducted at EDF R&D to obtain influence coefficients for plates containing an elliptical crack with a wide range of the parameters : relative size (2a/t ratio), shape (a/c ratio) and crack eccentricity (2e/t ratio where e is the distance from the center of the ellipse to the plate mid plane). These coefficients were developed through extensive 3D finite element calculations : 200 geometrical configurations were modeled, each containing from 18000 to 26000 nodes. The limiting case of the tunnel crack (a/c = 0) was also analyzed with 2D finite element calculation (50 geometrical configurations). The accuracy of the results was checked by comparison with analytical solutions for infinite solids and, when possible, with solutions for finite-thickness plates (generally loaded in constant tension).

These solutions will be introduced in the RSE-M Code that provides rules and requirements for in-service inspection of French PWR components.

KEYWORDS

stress intensity factor (SIF), influence coefficient, elliptical crack, plate

NOMENCLATURE (see figure 1)

a Semi-minor axis of ellipse
c Semi-major axis of ellipse
d Distance from the closest free surface to the center of the ellipse
e Distance from the plate mid plane to the center of the ellipse
E Young's modulus

E(k) Complete elliptic integral of the second kind

i_j Influence coefficient for the *j*th degree $(0 \le j \le 3)$

k Modulus of Jacobian elliptic functions, with $k^2 = 1 - (a/c)^2$

K_I Mode I stress intensity factor

t Plate thickness

ϕ Parametric angle defining a location on the crack front

ν Poisson's ratio

σ_j coefficient for the *j*th degree of the polynomial stress distribution

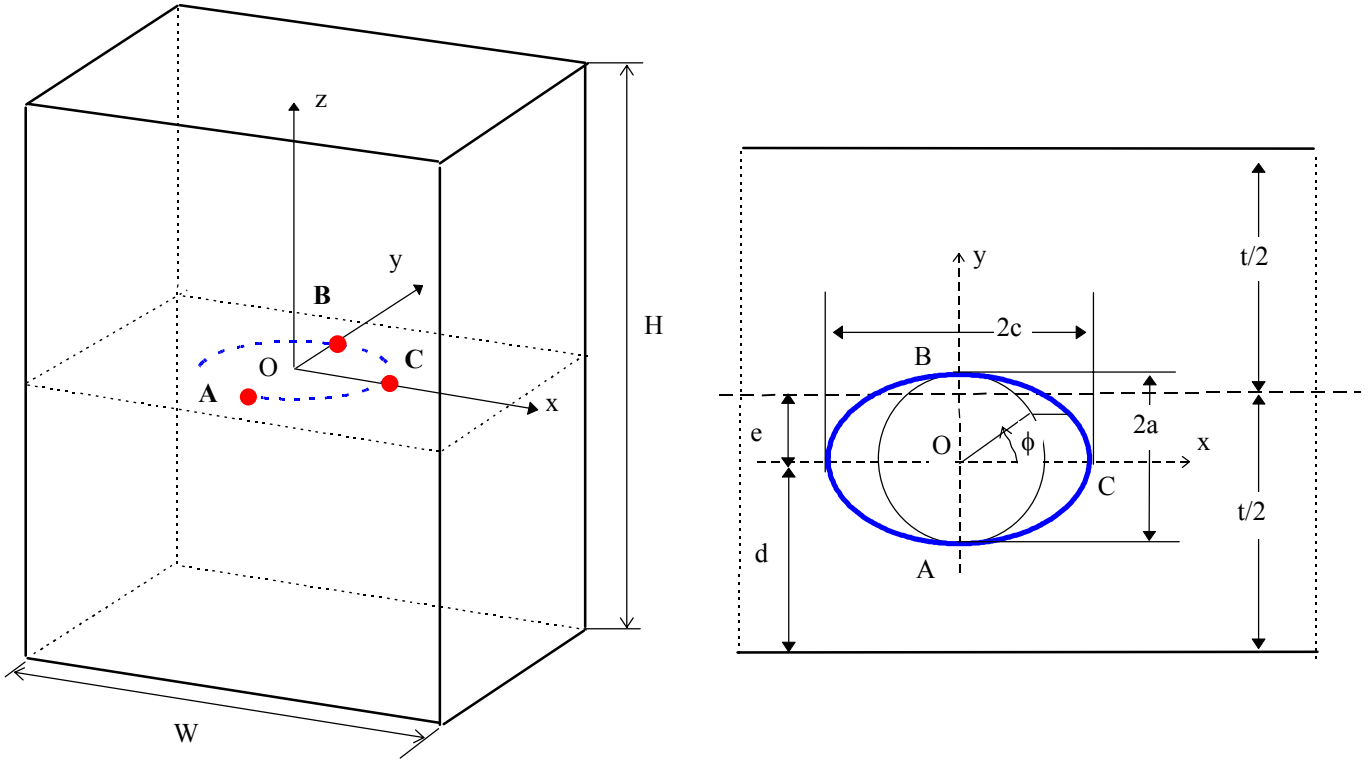

Figure 1 : An elliptical crack in a plate : definition of the geometrical parameters.

INTRODUCTION AND OBJECTIVES

Crack assessment in engineering structures relies first on accurate evaluation of the stress intensity factors. In recent years, a large work has been conducted in France by the Atomic Energy Commission to develop influence coefficients for surface cracks in pipes [1, 2]. These results have been included in the RSE-M Code [3], that provides rules and requirements for in-service inspection of French PWR components. However, the problem of embedded cracks in plates (and pipes) which is also of practical importance has not received so much attention. Presently, solutions for elliptical cracks are available either in infinite solid with a polynomial distribution of normal loading [4-7] or in plate [8-17], but restricted to constant or linearly varying tension. Most of these solutions can be found in the compilation [18].

The objective of this study was to calculate accurate stress intensity factors for embedded elliptical cracks in plates for a wide range of the geometrical parameters defined hereunder :

- the relative crack size (2a/t ratio), ranging from 0.05 to 0.5,
- the shape of the ellipse (a/c ratio), ranging from 1 (penny-shaped crack) to 0 (tunnel crack),
- the crack eccentricity relative to the mid plane of the plate (2e/t ratio), ranging from 0 (centered crack) to a maximum value depending on 2a/t such as : $\frac{2e}{t} + \frac{2a}{t} = 0.95$

The influence coefficients (i_0 to i_3) were developed for a third-order polynomial stress distribution in the thickness direction expressed in the local coordinate system Oxyz (figure 1) as follows :

$$\sigma_{zz}\left(\frac{y}{a}\right) = \sum_{j=0}^{3} \sigma_j \left(\frac{y}{a}\right)^j \quad (1)$$

Then, the stress intensity factor at the point of elliptic angle ϕ is expressed with the coefficients σ_j and the influence coefficients i_j by the relationship :

$$K_I(\phi) = \sqrt{\pi a} \sum_{j=0}^{3} \sigma_j \, i_j(\phi) \quad (2)$$

250 finite element calculations were performed to achieve this goal :

- 200 three-dimensional FE calculations for a/c = 1, 0.5, 0.25 and 0.125,
- 50 two-dimensional FE calculations for a/c = 0 (tunnel cracks).

FINITE ELEMENT ANALYSIS

Mesh generation

The meshes were made with a parametric procedure using Gibi, a powerful meshing software developed by CEA (French Atomic Energy Commission). With this procedure, the generation of a new mesh takes only a few minutes, as the work is limited to the introduction of the geometrical parameters. Isoparametric quadratic elements are used (either 20 node solid elements or 8 node elements depending on the FE model).

The mesh of a plate containing an elliptical crack was derived from a procedure aiming to model a semi-elliptical surface crack in a plate. The mesh of a plate (thickness : t/2 - e) containing a semi-elliptical crack (depth : a and length : 2c) is created. This mesh is duplicated by a symmetry with respect to the plane y = 0. This copy is added to the original mesh and a volume whose thickness is 2e is finally added to complete the mesh. The symmetries are taken into account, so only a quarter of the plate is modeled. The width W and the height H of the plate are chosen large enough to assume that the plate is of infinite size. They are 65 nodes along the crack front. Moreover, these nodes are equally spaced with regard to the parametric angle ϕ, due to the elliptical transformation used to create the crack tip mesh. A typical mesh is shown in figure 2. The meshes contain between 18,000 and 25,000 nodes.

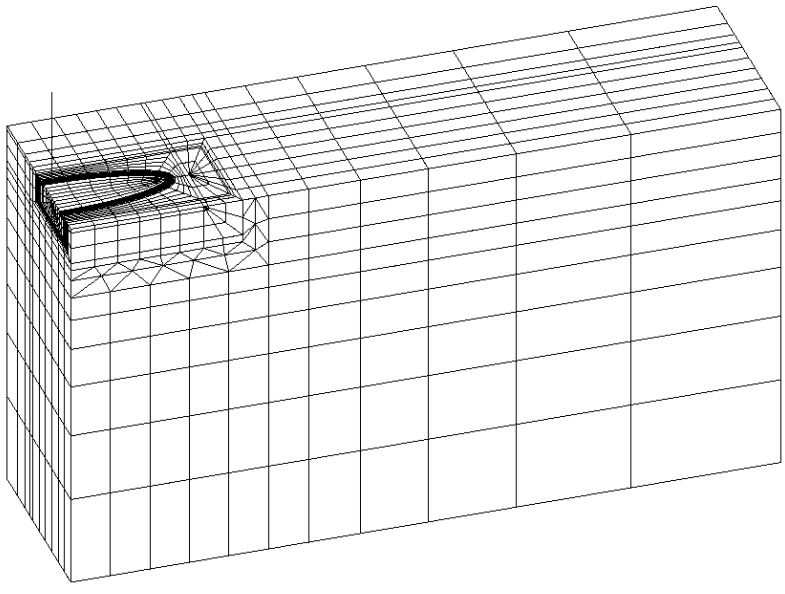

Figure 2 : Typical finite element mesh 2a/t = 0.3, a/c = 0.25, 2e/t = 0.4 (18,669 nodes)

Description of the calculations

The calculations were made with the finite element program *Code_Aster*, developed by EDF. A linear elastic material with a Young's modulus E = 200 GPa and a Poisson's ratio ν = 0,3 was considered. The fixed boundary conditions were applied to the planes x = 0 and y = 0 according to the symmetries involved in the geometry. For each crack geometry, four types of loading were applied directly on the crack surface, with the following pressure distributions :

$$\sigma_{zz}\left(\frac{y}{a}\right) = \sigma_0\left(\frac{y}{a}\right)^j \qquad \text{with } 0 \le j \le 3 \tag{3}$$

The energy release rate G was calculated at each node of the crack front by the G-Theta method, based on a domain integral technique [19]. K_I was calculated from G assuming plane strain conditions and equation (2) was used to derive the influence coefficient from K_I, so the influence coefficient is given by :

$$i_j(\phi) = \frac{1}{\sigma_0}\sqrt{\frac{G_j(\phi)\,E}{\pi\left(1-\nu^2\right)}} \tag{4}$$

RESULTS

Tables of influence coefficients

Influence coefficients have been gathered in twelve tables, i.e. at 3 points of the crack front (A, B and C) and for 4 loading degrees. However, due to space limitations, only two tables corresponding to point A and coefficients i_0 and i_1 are given in this article (Tables 1 and 2).

Validation

The comparison between the present results and those found in the literature [4-18] is made by calculating the relative difference by the relation :

$$\text{Diff}(\%) = 100\left(\frac{i_{\text{Present}}}{i_{\text{Lit}}} - 1\right) \tag{5}$$

For tunnel cracks (a/c = 0), the exact solution [4] for a crack in an infinite solid (2a/t = 0) was used to assess the results for 2a/t = 0.05. The differences range from -0.1 % for i_0 to -0.5 % for i_3. For a crack in a finite-thickness plate, approximate solutions are only available for the constant loading [8] and for a centered crack submitted to a linear loading [9, 10]. For the centered crack, a specific study was conducted for crack sizes up to 2a/t = 0.8. For the constant loading, the maximum difference with [8] was -0.10 %. For the linear loading, the maximum difference with [9] was -1.2 % (for 2a/t = 0.7). The solution [10] seems to give too high values when 2a/t is larger than 0.5.

For elliptical cracks (a/c > 0), the exact solutions [5-7] for a crack in an infinite solid (2a/t = 0) were used to assess the results for 2a/t = 0.05. For the constant loading, the influence coefficient i_0 is given by :

$$i_0(\phi) = \frac{1}{E(k)}\left[\sin^2\phi + \left(\frac{a}{c}\right)^2\cos^2\phi\right]^{\frac{1}{4}} \tag{6}$$

For the linear loading, the influence coefficient i_1 is given by the expression :

$$i_1(\phi) = \frac{1}{3E_2(k)}\sin\phi\left[\sin^2\phi + \left(\frac{a}{c}\right)^2\cos^2\phi\right]^{\frac{1}{4}} \tag{7}$$

where $E_2(k)$ is an elliptic integral defined by :

$$E_2(k) = \frac{1}{3k^2}\left[\left(1+k^2\right)E(k) - \left(1-k^2\right)K(k)\right] \tag{8}$$

in these expressions, K(k) and E(k) are respectively the complete elliptic integrals of the first kind and of the second kind. At point A, the differences were comprised between -0.2 % (constant loading) and -0.4 % (quadratic loading). At point C, the differences were comprised between 0.2 % (constant loading) and -4 % (quadratic loading). At this point, the difference mainly depends on the a/c ratio, as it corresponds to the sharpest curvature of the ellipse. For a crack in a finite-thickness plate, most of the solutions are relative to the constant loading [11, 13, 15] and to the linear loading [12, 14]. Influence coefficients up to the third-degree are given in [16] for a crack with 2a/t = 0.2. The accuracy of all these approximate solutions is difficult to assess. On the overall, the accuracy of the present results is estimated better than 0.5 % at points A and B, and ranging between 0.5 % and 5 % at point C, depending on the loading degree and the a/c ratio.

CONCLUSIONS

Two and three-dimensional finite element analyses have been conducted to calculate influence coefficients up to the third order for elliptical cracks embedded in plates, for a wide range of the geometrical parameters defining the crack : size, shape and eccentricity relative to the mid-plane of the plate. The accuracy of these coefficients has been checked by comparison with exact or approximate solutions available in the literature.

REFERENCES

1. Chapuliot, S. et al (1998) Proc. ASME PVP Conference, Vol. 365, pp. 95-106
2. Chapuliot, S. et al (1999) Proc. ASME PVP Conference, Vol. 388, pp. 3-12
3. RSE-M Code, 1997 Edition and 2000 Addenda, Appendix 5.4-II, AFCEN, Paris
4. Isida, M. (1976) In : *Fracture mechanics and strength of materials 2*, p. 128
5. Irwin, G.R. (1962) Trans. ASME, Ser. E, *J. Appl. Mech.*, Vol. 29, pp. 651-654
6. Green, A.E. and Sneddon, I.N. (1950) *Proc. Camb. Phil. Soc.*, Vol. 46, pp. 159-163
7. Shah, R.C. and Kobayashi, A.S. (1971) *Engineering Fracture Mechanics*, Vol. 3, pp. 71-96
8. Isida, M. (1966) *Trans. ASME*, Ser. E, *J. Appl. Mech.*, Vol. 33, No. 3, pp. 674-675
9. Isida, M. (1956) *Trans. JSME*, Vol. 22, pp. 809-814
10. Benthem, J.P. and Koiter, W.T. (1972) In : *Methods of analysis of crack problems* (Sih , G.C. Ed.),Vol. 3, pp. 131-178
11. Shah, R.C. and Kobayashi, A.S. (1973) *Int. Journal of Fracture*, Vol. 9, No. 2, pp. 133-146
12. Shah, R.C. and Kobayashi, A.S. (1971) Proc. 1971 National Symposium on Fracture Mechanics, Part 1, ASTM STP 513, pp. 3-21
13. Nisitani, H. and Murakami, Y. (1974) *Int. Journal of Fracture*, Vol. 10, No. 3, pp. 353-368
14. Shah, R.C. and Kobayashi, A.S. (1974) *Trans. ASME, J. of Pressure Vessel Technology*, pp. 47-54
15. Isida, M. and Noguchi, H. (1984) *Engineering Fracture Mechanics*, Vol. 20, No. 3, pp. 387-408
16. Shiratori, M., Ogawa, T. and Nishijima, A. (1992) *Trans. JSME*, Vol. 58, No. 545, pp. 48-52
17. ASME Boiler and Pressure Vessel Code (1998), Section XI, Division 1, Article A-3000
18. *Stress intensity factors handbook* in 3 volumes (1992) (Murakami, Y. Ed.), Pergamon Press, Oxford
19. Wadier, Y. and Malak, O. (1989) Proc. SMIRT 10, Vol. G, pp. 13-18

TABLE 1 - INFLUENCE COEFFICIENTS i_0 AT POINT A

		2e/t														
a/c	2a/t	0	0.1	0.2	0.3	0.4	0.45	0.5	0.55	0.6	0.65	0.7	0.75	0.8	0.85	0.9
1	0.5	0.651	0.657	0.667	0.688	0.743	0.823									
	0.4	0.643	0.646	0.650	0.658	0.675		0.721	0.791							
	0.3	0.639	0.640	0.641	0.644	0.649		0.660		0.695	0.754					
	0.2	0.637	0.637	0.637	0.638	0.639		0.642		0.648		0.671	0.714			
	0.1	0.636	0.636	0.636	0.636	0.636		0.636		0.637		0.638		0.646	0.669	
	0.05	0.635	0.635	0.635	0.635	0.635		0.635		0.635		0.636		0.636		0.646
0.5	0.5	0.872	0.886	0.912	0.962	1.082	1.246									
	0.4	0.850	0.856	0.866	0.887	0.927		1.028	1.173							
	0.3	0.835	0.838	0.841	0.848	0.862		0.891		0.970	1.092					
	0.2	0.828	0.829	0.830	0.832	0.835		0.842		0.859		0.913	1.006			
	0.1	0.825	0.825	0.825	0.826	0.826		0.827		0.829		0.833		0.855	0.908	
	0.05	0.825	0.825	0.825	0.825	0.825		0.825		0.825		0.826		0.828		0.854
0.25	0.5	1.026	1.048	1.091	1.173	1.368	1.627									
	0.4	0.983	0.993	1.012	1.047	1.113		1.272	1.496							
	0.3	0.956	0.959	0.967	0.980	1.004		1.053		1.177	1.361					
	0.2	0.940	0.941	0.943	0.947	0.954		0.968		0.997		1.083	1.223			
	0.1	0.933	0.933	0.933	0.934	0.935		0.937		0.940		0.950		0.989	1.071	
	0.05	0.932	0.932	0.932	0.932	0.932		0.932		0.933		0.934		0.939		0.987
0.125	0.5	1.112	1.142	1.201	1.313	1.576	1.940									
	0.4	1.055	1.069	1.095	1.142	1.231		1.442	1.741							
	0.3	1.013	1.019	1.030	1.048	1.081		1.144		1.302	1.534					
	0.2	0.991	0.992	0.996	1.002	1.012		1.031		1.069		1.176	1.348			
	0.1	0.980	0.980	0.981	0.982	0.983		0.986		0.993		1.007		1.058	1.159	
	0.05	0.977	0.977	0.977	0.977	0.978		0.978		0.979		0.981		0.990		1.052
0	0.5	1.186	1.234	1.326	1.503	1.929	2.529									
	0.4	1.109	1.131	1.174	1.248	1.387		1.714	2.173							
	0.3	1.057	1.067	1.085	1.116	1.169		1.265		1.496	1.829					
	0.2	1.024	1.027	1.034	1.045	1.063		1.092		1.147		1.291	1.515			
	0.1	1.005	1.006	1.007	1.009	1.013		1.019		1.029		1.049		1.112	1.232	
	0.05	1.000	1.001	1.001	1.001	1.002		1.004		1.006		1.010		1.022		1.097

TABLE 2 - INFLUENCE COEFFICIENTS i_1 AT POINT A

		2e/t														
a/c	2a/t	0	0.1	0.2	0.3	0.4	0.45	0.5	0.55	0.6	0.65	0.7	0.75	0.8	0.85	0.9
1	0.5	-0.425	-0.426	-0.429	-0.436	-0.459	-0.500									
	0.4	-0.424	-0.424	-0.425	-0.427	-0.431		-0.449	-0.484							
	0.3	-0.423	-0.423	-0.424	-0.424	-0.425		-0.428		-0.439	-0.466					
	0.2	-0.423	-0.423	-0.423	-0.423	-0.423		-0.424		-0.425		-0.431	-0.448			
	0.1	-0.423	-0.423	-0.423	-0.423	-0.423		-0.423		-0.423		-0.423		-0.425	-0.431	
	0.05	-0.423	-0.423	-0.423	-0.423	-0.423		-0.423		-0.423		-0.423		-0.423		-0.425
0.5	0.5	-0.478	-0.481	-0.486	-0.499	-0.538	-0.605									
	0.4	-0.475	-0.476	-0.478	-0.481	-0.490		-0.521	-0.577							
	0.3	-0.474	-0.475	-0.475	-0.476	-0.478		-0.483		-0.504	-0.549					
	0.2	-0.474	-0.474	-0.474	-0.474	-0.474		-0.475		-0.477		-0.489	-0.519			
	0.1	-0.474	-0.474	-0.474	-0.474	-0.474		-0.474		-0.474		-0.474		-0.477	-0.489	
	0.05	-0.473	-0.473	-0.473	-0.473	-0.473		-0.473		-0.473		-0.473		-0.474		-0.477
0.25	0.5	-0.499	-0.504	-0.512	-0.529	-0.582	-0.666									
	0.4	-0.494	-0.496	-0.499	-0.505	-0.517		-0.557	-0.631							
	0.3	-0.493	-0.493	-0.494	-0.496	-0.499		-0.506		-0.535	-0.592					
	0.2	-0.492	-0.492	-0.492	-0.493	-0.493		-0.495		-0.498		-0.515	-0.553			
	0.1	-0.492	-0.492	-0.492	-0.492	-0.492		-0.492		-0.492		-0.493		-0.498	-0.514	
	0.05	-0.492	-0.492	-0.492	-0.492	-0.492		-0.492		-0.492		-0.492		-0.492		-0.498
0.125	0.5	-0.507	-0.513	-0.524	-0.545	-0.607	-0.712									
	0.4	-0.501	-0.503	-0.507	-0.514	-0.529		-0.576	-0.661							
	0.3	-0.499	-0.499	-0.501	-0.502	-0.506		-0.515		-0.548	-0.614					
	0.2	-0.498	-0.498	-0.498	-0.499	-0.499		-0.501		-0.505		-0.524	-0.568			
	0.1	-0.498	-0.498	-0.498	-0.498	-0.498		-0.498		-0.498		-0.499		-0.505	-0.524	
	0.05	-0.498	-0.498	-0.498	-0.498	-0.498		-0.498		-0.498		-0.498		-0.498		-0.505
0	0.5	-0.514	-0.524	-0.539	-0.569	-0.653	-0.794									
	0.4	-0.505	-0.509	-0.515	-0.525	-0.544		-0.605	-0.712							
	0.3	-0.501	-0.503	-0.505	-0.508	-0.513		-0.524		-0.564	-0.642					
	0.2	-0.500	-0.500	-0.501	-0.501	-0.502		-0.505		-0.510		-0.532	-0.582			
	0.1	-0.499	-0.499	-0.499	-0.499	-0.499		-0.499		-0.500		-0.501		-0.508	-0.529	
	0.05	-0.499	-0.499	-0.499	-0.499	-0.499		-0.499		-0.499		-0.499		-0.500		-0.507

ORAL/POSTER REFERENCES: ICF100931OR

INFLUENCE OF ANNEALING PROCESS ON ULTRAFAST CARRIER DYNAMICS FOR AN ION-IMPLANTED SILICON SURFACE

H. Donen, Y. Inagaki, K. Katayama, M. Fujinami and T. Sawada

Department of Advanced Materials Science, Graduate School of Frontier Sciences,
The University of Tokyo, Tokyo 113-0033, Japan

ABSTRACT

We investigated the change of carrier properties in the ultrafast time range during annealing for a Si surface that has an amorphous layer by ion-implantation using a spectroscopic transient reflecting grating method. We observed a drastic change in the carrier properties when a transition from amorphous to crystal occurred. In case that the surface includes an amorphous layer for a short annealing time, carriers were trapped to different energy states according to the annealing time because annealing change the distribution of defect states complicatedly. Furthermore, we found that some defects remained even after crystallization, and that they induced another relaxation channel other than a usual relaxation to a band edge.

KEYWORDS

amorphous, Si, ultrafast carrier dynamics, ion-implantation, anneal, transient reflecting grating, defect states, trap

INTRODUCTION

Ion-implantation techniques play an important role in semiconductor device technology and are widely used in fabrications for many types of devices [1]. In the process of ion-implantation, an as-implanted material has a large amount of defects in its surface region and they induce amorphization in

the surface layer. Postimplantation annealing must be performed for the material to remove implantation-induced defects and to recover the electrical activation of the doped atoms. The recovery process during thermal annealing is technologically important, and so as-implanted and post-annealed surfaces are analyzed mainly by spectroscopic ellipsometry, Raman spectroscopy and Rutherford back scattering for investigating structural, physical and chemical properties of the materials. The methods give information on optical properties, lattice vibration and a spatial distribution of implanted species [2].

For future semiconductor technology, ultrafast carrier dynamics of devices must be clarified for technological innovations, as their fast response and size reduction are needed. Recently, optical pump-probe techniques have clarified carrier properties in the ultrafast time range from femtoseconds to nanoseconds [3-7]. Some such studies paid attention to carrier dynamics for crystalline Si (c-Si) and amorphous Si (a-Si) as representations of device materials. Summarizing the results, for c-Si, carriers photoexcited to extended states initially decay to a band edge in a few picoseconds, and they decrease due to Auger recombination processes in nanoseconds time range [4,5]. Different from the relaxation processes for c-Si, photoexcited carriers in a-Si decay mainly due to bimolecular recombination about a picosecond, while a part of the photoexcited carriers are trapped [6]. It is well known that a-Si shows a phase transition to c-Si by thermal annealing, but it has not been examined how the annealing changes carrier properties in the ultrafast time range during the process.

For the last five years, we have studied ultrafast carrier dynamics at crystalline and as-implanted Si surfaces using ultrafast photothermal methods [7]. Conventional photothermal methods give only one transient response for a single probe wavelength, and thus it is difficult to distinguish some processes occurring at the same time. To get more detailed information, we have improved a transient reflecting grating (TRG) method, one of the photothermal methods, to offer a spectroscopic measurement. The method has a possibility to measure carrier density change directly at each excited state, defect state, and so on. We applied the TRG spectroscopic method to an ion-implanted Si surface after being annealed for different times, and aim at clarifying the influence of annealing process on ultrafast carrier dynamics, focusing on a transition from amorphous to crystal, defect density, and distribution of defect states. Also, we will show the validity of the TRG spectroscopy as a measurement method for ultrafast carrier properties for semiconductor devices.

EXPERIMENTAL

The TRG equipment and principle were described in detail in another paper [8]. A brief explanation is given here. In the TRG technique, two crossed pump pulses are incident at a solid surface and, as a result, the focused spot is irradiated with a pulse of an interference pattern. The complex refractive index ($\tilde{n}$) at the spot changes due to a physical property change. After the pump pulses irradiation, a probe pulse is also incident there, and the complex refractive index change is detected through a diffracted light of the probe light. The signal intensity is theoretically proportional to $(\Delta n)^2+(\Delta k)^2$, where the refractive index of a sample is $\tilde{n}=n+ik$. Using a white light as a probe pulse, carrier density change at various energy states optically coupled to the probe wavelength can be measured. With regard to c-Si, $\Delta\tilde{n}$ is dominated by excited free carriers for longer wavelength, while $\Delta\tilde{n}$ due to a temperature rise is a dominant factor for shorter wavelength.

A regeneratively amplified titanium sapphire laser (CPA-1000: Clark-MXR Inc.) was used as a light source. The pulse train wavelength was 800 nm, with a repetition rate of 1 kHz and a pulse width of 200 fs, in full width at half maximum. The pulse was separated into pump and probe pulses using a partial reflective mirror. The pump pulses were frequency doubled to a wavelength of 400 nm (3.1 eV), and then further divided into two pulses by a half mirror. The two pump pulses were crossed and irradiated onto the same spot of the sample surface, to coincide in time to form an interference pattern. The pump intensity was 1.76 mJ/cm^2. The interval of the interference fringes was 2.13 μm. The probe pulse was focused to heavy water to generate a femtosecond white-light continuum after passing through a computer-controlled optical delay line. Used wavelengths ranged from 450 nm (2.75 eV) to 750 nm (1.91 eV). The probe pulse was irradiated at the center of the spot. The reflected diffracted light with a rainbow of colors spread like a fan due to the diffraction conditions. It was detected with a spectrometer after being collected and focused by a lens. The polarizations of the pump and probe light were cross-polarized to prevent any coherent effects.

The original sample is an Arsenide ion-implanted Si (10^{15}/cm^2) wafer. The sample was annealed at 450 °C in N_2 atmosphere. It was annealed for various time from 0 to 180 minutes. Hereinafter, the original sample and the annealed samples are referred to as "as-implanted Si" and "annealed Si (annealed time)" respectively. To roughly estimate the crystallity of the samples, the reflectance spectra are used. c-Si has two main optical transitions at 370 nm and 270 nm for E_1 and E_2. Generally speaking, the crystallity is increased, as the peak width is narrower.

RESULTS AND DISCUSSION

Reflectance spectra are shown in Fig.1 for a c-Si and the ion-implanted Si annealed for different times. The spectrum for the c-Si showed clear two peaks at 370 nm and 270 nm corresponding to the

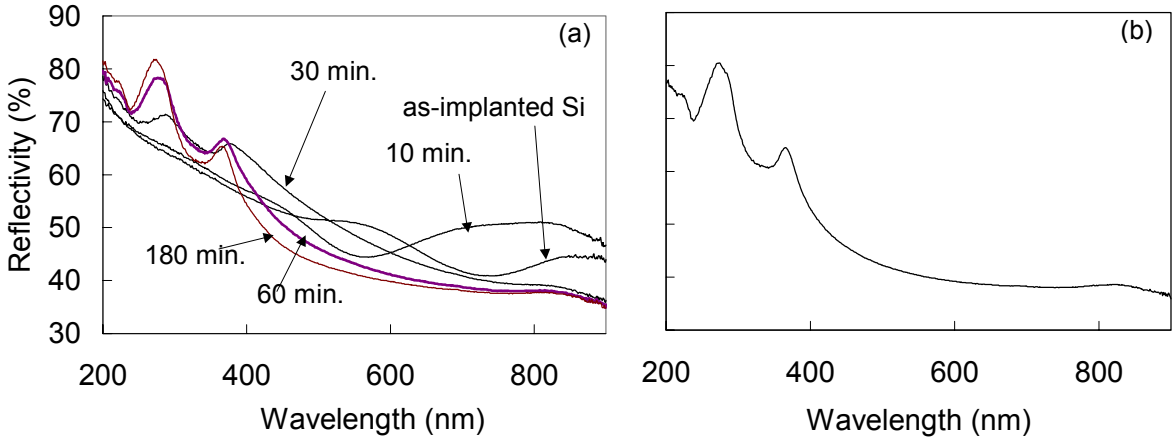

Fig. 1. Reflectance spectra for (a) as-implanted Si and ion-implanted Si annealed for various times and for (b) c-Si

optical transitions for silicon respectively. The spectra for as-implanted and annealed Si (less than 20 min.) didn't show any peaks for E_1 and E_2. These spectra showed a broad peak extending the measured wavelength range. The peaks for the E_1 and E_2 appeared after the annealing time has passed over 30

minutes, and the two peaks got sharper with increasing the annealing time. Considering the spectral change for each annealing time, it was understood that annealing induced the following three-step structural change. 1. Until 20 minutes, some structural changes occurred in the amorphous layer. 2. From 30 to 60 minutes, a phase transition from amorphous to crystal occurred. 3. More than 60 minutes, the crystallized layer gradually got close to a defect-free crystal.

Next, TRG spectra were measured for each sample. Although the transient waveforms depended on the probe wavelength, the mutual relation of the relaxation time among the samples showed similar tendency for every probe wavelength. In this study, we pay attention to the dynamics of photoexcited carriers, not to the temperature rise and fall, and so the transient signals measured at longer wavelength (687nm) are compared (Fig. 2(a).). The relaxation processes of the as-implanted Si and

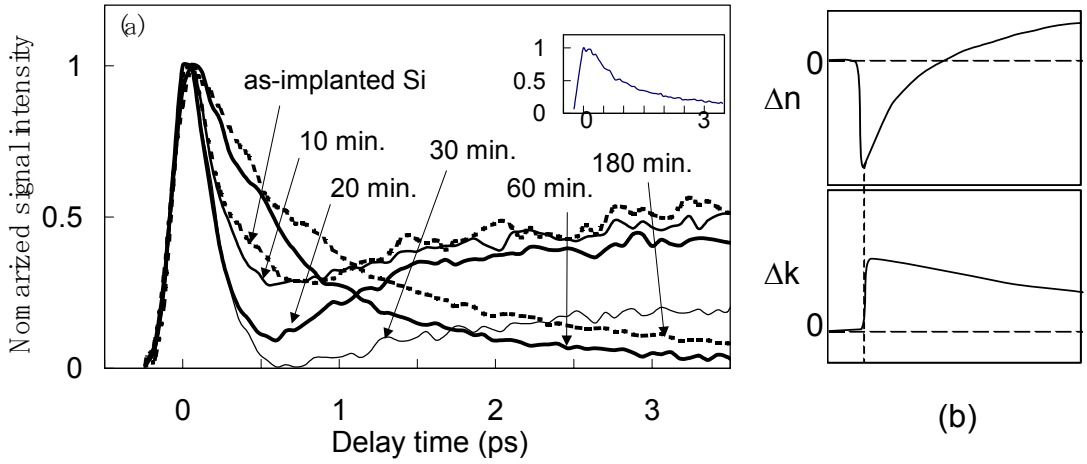

Fig. 2. (a) TRG responses for as implanted Si and ion-implanted Si annealed for various times at the probe wavelength of 687 nm, and the annealed samples are indicated with arrows and annealing times. For reflectance, a transient response for c-Si is shown in the inset. (b) Schematic illustrations for likely behaviors Δn and Δk in this time range in case of a-Si.

annealed Si (less than 30 min.) consisted of mainly two components; the faster one decayed in several hundred femtoseconds and the slower one raised about 1 ps and kept almost constant, while the annealed Si (more than 60 min.) have only a decay component in several pecoseconds. From other reports, for c-Si, it is understood that carriers photoexcited to extended states initially decay to a band edge in several picoseconds [4,5]. While for a-Si, the decay initially occurs due to bimolecular recombination, and a part of the carriers are trapped into defect states and remains there for more than 500 ps [3,9]. Thus, it can be said that the transient responses for the annealing time less than 30 minutes and longer than 60 minutes mainly correspond to those for a-Si and c-Si respectively. Also the results of the reflectance spectra support the consideration. Namely, for the as-implanted Si and the annealed Si (less than 30 min.), the faster and slower components correspond to bimolecular recombination and trapped carriers at defect states. Also the slower component includes a temperature rise effect corresponding to the signal increase after 1 ps. For the annealed Si (more than 60 min.) responses mean a relaxation of carriers from extended to band edge states. Main features of the signals can be explained based on the carrier dynamics for pure c-Si and a-Si, but the change of the transient responses depending on the annealing time is not understood.

Before the consideration, it is necessary to clarify the causes of a refractive index change for silicon in order to understand the TRG signal origin.

In general, a density change of photoexcited carriers and temperature rise are the causes for Δn, while Δk results from an absorption change of the probe light due to free carriers at extended and band edge states, and trapped carriers at defect states [10]. As to a-Si, it is known that Δn is negative for a generation of photoexceted carriers, while it is positive for temperature rise. Then Δn changes from negative to positive as the photoexcited carriers decrease due to bimolecular recombination and consequently the following temperature is raised [11]. Δk is known to be positive due to an absorption change of trapped carriers at defect states, and it monotonously decreases as the trapped carriers

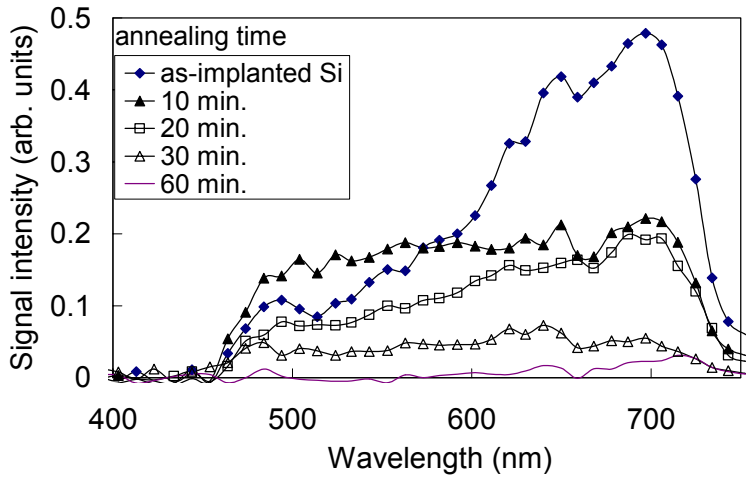

Fig.3 TRG spectra at 3 ps after the pump pulses ware incident, for as-implanted and ion-implanted Si annealed for 10-60 min

recombines [6]. Considering the TRG signal is proportional to $(\Delta n)^2+(\Delta k)^2$, the TRG signals of the as-implanted Si and the annealed Si (less than 30 min.) cannot be explained only by Δn or Δk, and they include both components. (The schematic illustration of typical Δn and Δk responses is shown in Fig. 2(b) for explaining a TRG signal for a-Si.) Fig. 2(a) indicates Δk contribution became weaker with an increase of annealing time. The result means a reduction of the number of trapped carriers due to a decrease in defect states. For c-Si, only Δn is a major component and is induced by a generation of photoexcited carriers. The TRG signals for the annealed Si (more then 60 min.) consist of one component that corresponds to a relaxation of carriers to a band edge. But only the process cannot explain the decay processes because the relaxation time gets longer with an increase of the annealing time. The reflectance spectra showed annealing after 60 minutes still made the sample crystallity change, and the result indicates some structural defects remain even after a phase transition. Thus, we suggest that some carrier trapping processes accelerate the carrier relaxation.

As mentioned above, Δk component for a-Si corresponds to an absorption change due to carriers trapped at defect states for a probe wavelength. It is expected that the wavelength dependent on Δk gives information on the distribution of trapped carriers in energy states. So we show the TRG spectra at 3ps in Fig. 3, when the rate of Δk component is large in the TRG signal.

With an increase of annealing time, the most striking feature is a reduction of the peak around 700 nm until 10 min., and subsequently the spectral waveforms changed complicatedly. We believe that the change

reflect the distribution of trapped carriers in energy states. Although thermally induced Δn component must be subtracted, the main interpretation may be the same because Δn due to a temperature rise does not depend too much on the samples. By initial annealing of 10 minutes, the intensity of the peak around 700 nm decreases remarkably and the peak gets broader. Further annealing made the signal intensity smaller, changing the spectral waveform. These results suggest that the distribution of trap states changed complicatedly, decreasing the whole number of the states, although further exact analysis must be performed on a defect density, a distribution of energy states, a refractive index change due to a temperature rise, and so on, and now we are doing them.

CONCLUSION

We investigated carrier properties in ultrafast time range during annealing for an ion-implanted Si, which causes a phase transition from amorphous to crystal. We observed that carrier properties drastically changed in the transition from amorphous to crystalline and that the defect properties also affect the ultrafast carrier dynamics. When the TRG spectra will be correctly related to a defect density and a distribution of its energy state, the obtained information can provide a useful policy for manufacturing devices where carriers are controlled in the ultrafast time range.

REFERENCES

1. Chevacharoenkul, S., Ilzhoefer, J. R., Feijoo, D. and Gösele, U. (1991) *Appl. Phys. Lett.* **58**, 1434.
2. Boultadakis, S., Logothetidis, S. and Ves, S. (1992) *J. Appl. Phys.* **72**, 3648.
3. Kudrna, J., Pelant, I., Surendran, S., Stuchlík, J., Poruba, A. and Malý, P. (1998) *J. Non-Cryst. Solids* **238**, 57.
4. Goldman, J.R. and Prybyla, J.A. (1994) *Phys. Rev. Lett.* **72**, 1364.
5. Sjodin, T., Petek, H. and Dai, H. L. (1998) *Phys. Rev. Lett.* **81**, 5664.
6. Esser, A., Seibert, K. and Kurz, H., Parsons, G. N., Wang, C., Davidson, B. N., Lucovsky, G. and Nemanich, R. J. (1990) *Phys. Rev. B* **41**, 2879.
7. Tanaka, T., Harata, A. and Sawada, T. (1997) *J. Appl. Phys.* **82**, 4033.
8. Katayama, K., Inagaki, Y. and Sawada, T. (2000) *Phys. Rev. B* **61**, 7332.
9. Kudrna, J., Malý, P., Trojánek, F., Štěpánek, J., Lechner, T., Pelant, I., Meier, J., Kroll, U. (2000) *Mat. Sci. Eng. B* **69-70**, 238.
10. Tanguy, C., Hulin, D., Mourchid, A., Fauchet, P. M. and Wagner, S. (1988) *Appl. Phys. Lett.* **53**, 880.
11. Downer, M. C. and Shank, C. V. (1986) *Phys. Rev. Lett.* **56**, 761.

ICF 100729OR

INFLUENCE OF HYDROSTATIC PRESSURE ON MULTIAXIAL FATIGUE OF NOTCHED COMPONENTS

G. Qilafku, G. Pluvinage

Laboratoire de Fiabilité Mécanique, Université de Metz, France

ABSTRACT:
Tests have been carried out on smooth and notched specimens submitted to cyclic combined tension and torsion loading. The role of the hydrostatic pressureon multiaxial fatigue has been clarified using a volumetric approach The average hydrostatic pressure and shear stress in the fatigue process volume have been computedby Finite Element Method. It has been shown an elliptical dependence between the effective shear stress and the hydrostatic pressure.

KEY WORDS multiaxial fatigue ; notch; volumetric approach ; hydrostatic presure

INTRODUCTION

Hydrostatic pressure has been considered by several authors as an effective parameter on fatigue resistance. The hydrostatic pressure σ_h is defined as the first invariant of the stress tensor. If σ_I, σ_2, σ_3 are the three principal stress, the hydrostatic pressure is given by :

$$\sigma_h = \frac{\sigma_1 + \sigma_2 + \sigma_3}{3} \qquad (1)$$

Two ways are possible :

1) fatigue criterion can be a combination of the second stress invariant J_2 and the hydrostatic pressure acording to Sines (1) Crossland (2) and Kakuno and Kawada (3)

$$\sqrt{J_2} + \kappa\, \sigma_{h,max} \leq \lambda \qquad (2)$$

$$\sqrt{J_2} + \kappa\, \overline{\sigma}_h \leq \lambda \qquad (3)$$

In formulas (2) and (3), κ and λ are material constant, $\sigma_{h,max}$ the maximum value of hydrostatic pressure and $\overline{\sigma}_h$ mean value.

2) fatigue criterion is considered a combination of microscopic shear stress and hydrostatic pressure.

According to Dang Van(4), fatigue crack initiation occurs in critical zones with stress concentrations or near grain plastic sliding which are unfavourably oriented in respect to external loading. Analysing the local stresses and transferring this analysis to a macroscopic scale, Dang Van defined a fatigue initiation criterion at a point and at a time which satisfies the following condition :

$$\tau(t) + A_{DV} \cdot \sigma_h(t) \leq B_{DV} \qquad (4)$$

where A_{DV} and B_{DV} are material constants. The basic mechanism for fatigue crack initiation is the maximum shearing stress which occurs on the mot unfavourably oriented crystallographic plane. The maximal shear stress and the plan of maximal shear stres have to be determined in order to apply this criterion. The influence of hydrostatic pressure increases linearly. The two constant are determined for two particular state of stress : torsion where the fatigue limit is τ_D and hydrostatic pressure equal to zero and alternated tension where the hydrostatic pressure σ_D is and the fatigue limit σ_D :

$$\tau + \left(\frac{\tau_D}{\sigma_D} - \frac{1}{2} \right) . \sigma_h = \tau_D \qquad (5)$$

Dang Van model is the base of Flavenot and Skalli [5] critical layer criterion. Instead of computing the maximal shear stress and hydrostatic pressure on surface , they propose to compute the average values over a" critical layer" which has the same meaning that the effective distance. Examining a large range of experimental data on steel notched specimens, they found that all data fit the fatigue endurance curve $\tau = f(\sigma_h)$determined on smooth specimens. The best value for critical layer is determined by trial and error method and its value is order of material characteristic like grain size. In case of fatigue under combined tension and torsion the relation between shear stress and hydrostatic pressure is given by :

$$\tau + 3 . \frac{2\tau_D - \sigma_D}{2\tau_D . \sigma_D} . \sigma_h = \tau_D \qquad (6)$$

An example of Dang Van diagram is given for a steel (Re = 312 MPa) in figure 1

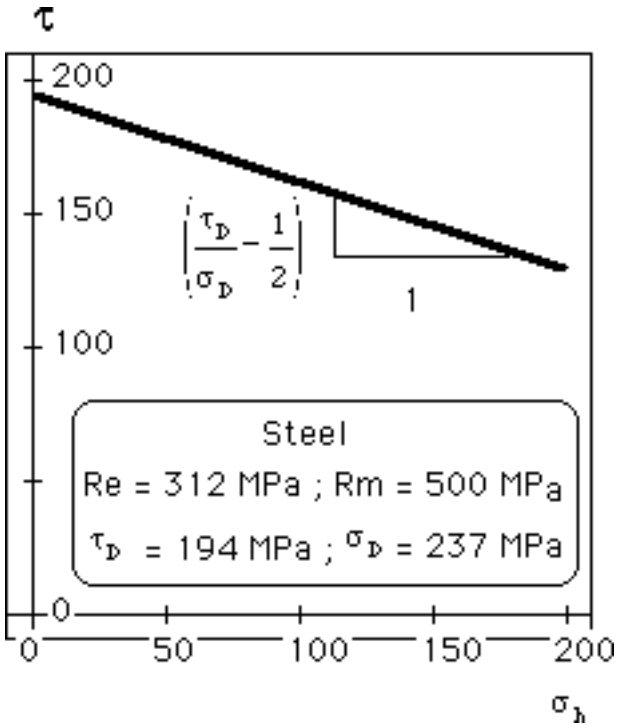

Figure 8.14 : Example of Dang Van diagram for a steel.

PRINCIPLE OF THE VOLUMETRIC METHOD FOR PREDICTING FATIGUE LIFE DURATION

The volumetric approach is an alternative and innovative way of modelling the fatigue failure process emanating from notches. The assumption made in this approach is that the fatigue failure needs a physical volume to occur. Its extent from the notch tip is called the effective distance.

The fatigue process volume is the high stressed region. The choice of the effective distance was made by trial and error method**.** Verifications on different materials and specimen geometry's [6] have shown that the limit between region II and III and corresponds to the minimum of relative stress gradient The fatigue process volume is assumed to be cylindrical with a diameter called X_{ef}. This assumption is based on an analogy with the notch plastic zone which is practically cylindrical. The effective stress range according to the volumetric approach plays the essential role in the fatigue process. It is now defined as the average of the weighted stresses in this volume. This weight stress depends on the relative stress gradient in order to take into account the loading mode and the scale effect in fatigue.

This weighed stress is defined as :

$$\sigma^{*}_{ij} = \sigma_{ij} \,.\, \phi\left(r,\chi\right) \qquad (7)$$

where $\phi\,(x,\chi)$ are the weight function which depends the distance r and the relative stress gradient χ. The weight function is assumed to be unit at notch tip and at point of maximum stress. For this reason, the choice of the weight function has the following linear form :

$$\varphi(r,\chi) = 1 - r.\chi \qquad (8)$$

The effective stress σ_{ef} is defined as the average value of the weighted stress in the fatigue process volume . During fatigue propagation, crack path is always perpendicular to the maximal principal

stress. In tension or bending this stress is conventionally σ_{yy} stress. We can write in bidimensional case :

$$\sigma_{ef} = \frac{1}{X_{ef}} \int_0^{X_{ef}} \sigma_{ij}^{*} \, . \, dr \qquad (9)$$

The validity of volumeric method can be checked by the fact that the effective stress range versus number of cycles to failure coincide with the fatigue reference curve get from smooth specimens
The principle of volumetric method have been applied to tests performed in tension- compression figure 2a and torsion figure 2b on notched specimens (notch radius 0.4mm) made with a low strength steel (yield stress Re = 312 MPa). Experimental Wöhler curve on notch and smooth specimens are presented with the computing data (full square dots). We can notice the good agreement between the prediction of the volumetric method and the fatigue reference curve (smooth specimens curve).

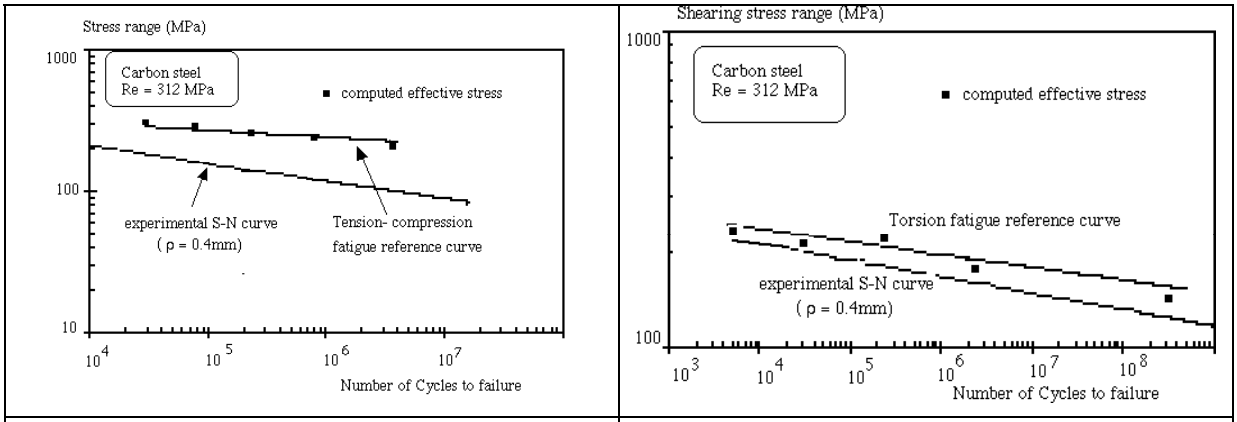

a) Tension- compression | b) Torsion

Figure 2 : Experimental Wöhler curve on notch and smooth specimens presented with the computing data get from the volumetric method.

INFLUENCE OF HYDROSTATIC PRESSURE ON FATIGUE LIFE DURATION OF COMBINED TENSION + TORSION FATIGUE TESTS

Influence of hydrostatic pressure on fatigue life duration is examined on combined tension + torsion tests. The ratio between shear and normal stress gross stress is 2.Specimen are smooth and notched specimens described in figure 8.8.
The material used is a low carbon steel with yield stress Re = 312 MPa and ultimate stress Rm = 500 MPa. The notched specimens are of two types with different notch radius ρ = 0.2 and ρ = 0.4 mm. Basquin's coefficient for Wöhler curves have been determined and reported in table 1.

Specimen	σ'_f (MPa)	b	R^2
	718	-0.066	0.9345
ρ = 0.2 mm	911	-0.1335	0.813
ρ = 0.4 mm	1035	-0.1526	0.8974

Table 1

By Finite Element Method and using elastoplastic behaviour of material, maximal principal stress σ_1, maximal shear stress τ, hydrostatic pressure σ_h and relative stress gradient χ were computed.

Example of such computing is given in figures 2 for (a) a smooth specimen loaded in tension and a notched specimen (ρ = 0.4mm) loaded with combined tension + torsion.

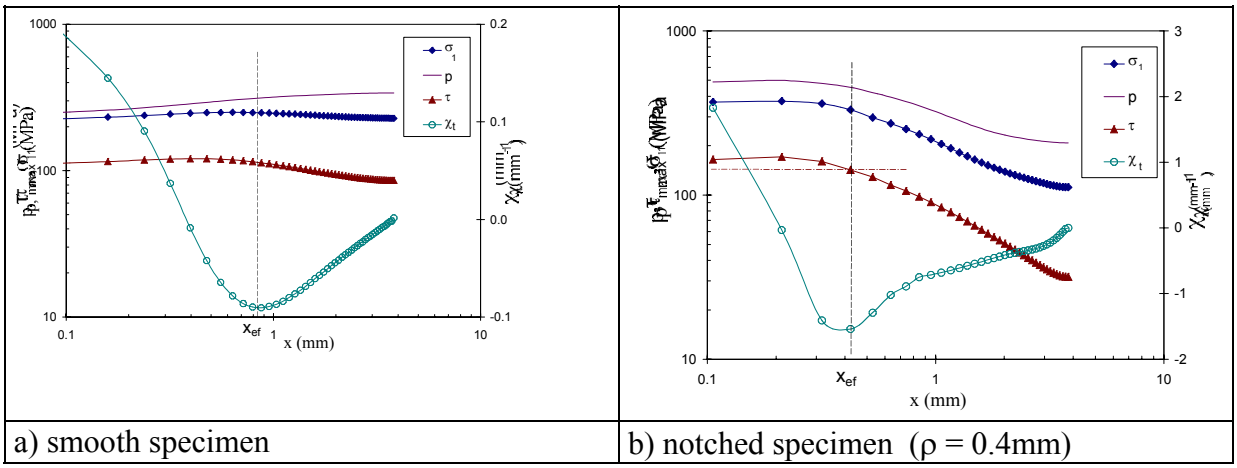

a) smooth specimen | b) notched specimen (ρ = 0.4mm)

Figure 3 : maximal principal stress σ_1, maximal shear stress τ, hydrostatic pressure σ_h and relative stress gradient χ in a bilogarithmic diagram.

We can notice a higher relative stress gradient in presence of torsion loading. In order to take the influence of the stress gradient the effective maximal shear stress and hydostatic pressure are computed; These quantities are defined as the average values of maximum shear stress and hydrostatic pressure over the effective distance which is defined as the distance of minimum relative stress gradient.
The effective shear stress range and hydrostatic are defined as :

$$\Delta\tau_{ef} = \frac{1}{X_{ef}} \cdot \int_0^{X_{ef}} \Delta\tau_{ma} \qquad p_{ef} = \frac{1}{X_{ef}} \cdot \int_0^{X_{ef}} p(x).dx$$

AN ELLIPTICAL CRITERION FOR THE INFLUENCE HYDROSTATIC PRESSURE OF FATIGUE LIFE DURATION

It is assumed in Dang Van and Flavenot and Skalli's models that the influence of hydrostatic pressure is linear. Plotting the effective maximal shear stress τ_{ef} versus effective $\sigma_{h,ef}$ for the previous experimental results, and for different life duration, we can notice that the assumption of linear dependence is not well satisfied. In Figure 14, Dang Van's model is applied for different fatigue life durations. The maximal shear stress τ_{DV} and hydrostatic pressure values p_{DV} according to Dang Van's model are obtained from elasto-plastic finite element computing and chosen as illustrated in Figure 4. It has been found that the correlation coefficients obtained by least square method are very low.

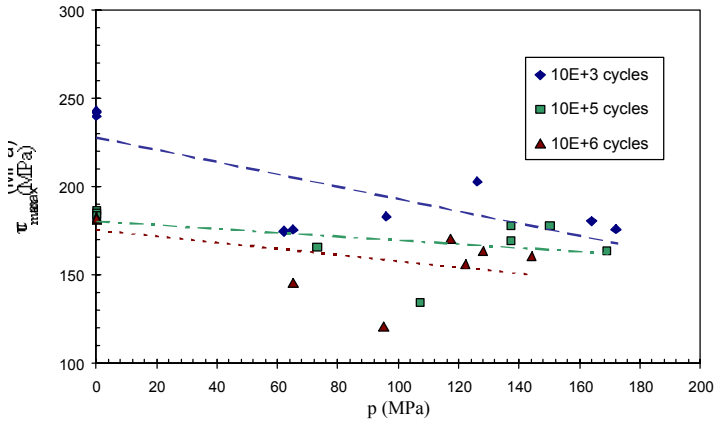

Fig. 4. Application of Dang Van's model for different fatigue life duration

A better representation can be obtained if an elliptical dependence is used (Figure 5). We can that the size parameter of such elliptical representation are not constant but depend on fatigue life duration (figure 6).

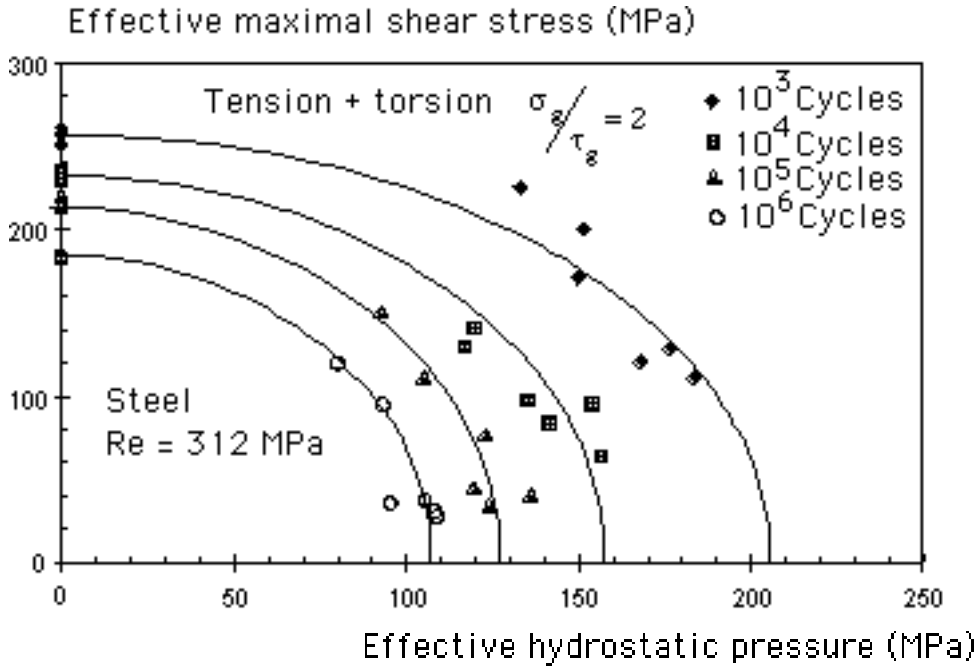

Figure 8.16 : Elliptical representation of the dependence of effective maximal shear stress τ_{ef} versus effective $\sigma_{h,ef}$.

CONCLUSION

In the above study and the experimental results it is shown that the fatigue failure of parts subjected to combined loading, as well as the fatigue under simple loading, has a volumetric character. It depends both on the shear stress and hydrostatic pressure on the most affected material volume.

From the point of view of the state of stress, the torsion loading is the easiest loading mode. The other loading modes can be considered as superposition of hydrostatic pressure to a corresponding simple torsion with the same field of shear stress, here including simple uniaxial loading. From

this fact, the use of two reference curves corresponding to alternated tension-compression and torsion, is quite obvious.

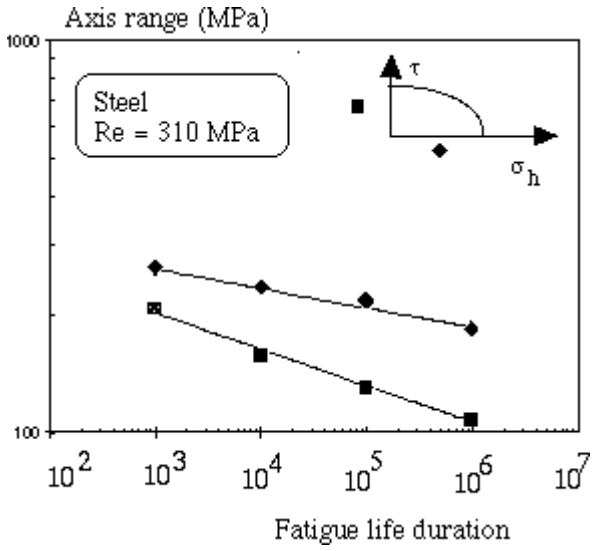

Figure 6 Ellipse axis size versus number of cycles.

REFERENCES

1. Sines.G, ”Behaviour of metals under combined repeated stresses with superimposed static stresses”, National Advisory Committee for Aeronautics Technology, Note3495, Nov, (1995).
2. Crossland.B, 3Effect of large hydrostatic pressure on the torsional fatigue of an alloy steel”, Proceedings of the International Conference of Metals, Institution of Mechanical Engineers,London, (1956).
3. Kakuno.H and Kawada.Y, ” A new criterion for fatigue strength of a round br subjected to combined static nad repeated bending and torsion”, Fatigue of Engineering Materials and Structures, Vol 2, (1979).
4. Dang Van.K, ”High cycle fatigue analysis in mechanical engineering”, Advances in fracture research ICF9,Vol 3, pp 1225-1237, (1997).
5. Flavenot.J.F and Skalli.N ” L’épaisseur de couche critique ; une nouvelle approche du calcul en fatigue des structures soumises à des sollicitations multiaxiales”, Rapport CETIM 12 G 254, Septembre ,pp15-25, (1982).
6. Pluvinage, G. Notch effect in high cycle fatigue, Advances in Fracture Research, ICF9, Fatigue of Metallic and Non-metallic Materials and Structures **3**, Pergamon, Sidney, pp. 1239-1250. (1997)

ORAL REFERENCE: ICF100127OR

Influence of loading changes on the fatigue crack growth

M. Sander and H. A. Richard

Institute of Applied Mechanics, University of Paderborn,
D - 33098 Paderborn, Germany

ABSTRACT

The basis for most of the concepts for predicting the life time of structures generally are tests, which are performed under both constant loading parameters (e.g. amplitude or mean stress) and Mode I conditions. But a component is exposed more or less loading changes during service loadings. Through these loading changes the so called interaction effects are induced, which are not taken into consideration by those standard tests. This means that the prediction of the life time could be too conservative.

In this paper the interaction effects of loading changes (e.g. overloads, block loadings and special service loadings) on the fatigue crack growth are investigated experimentally. The fatigue crack propagation tests have been performed on 7075 T6 aluminium alloy using CT specimens. In these tests the loading changes are interspersed in a basic loading with a constant amplitude. All experiments are controlled by the program system ^{FAM}Control. The experimental results show, that for all investigated loading changes ultimately a strong retardation of the crack growth occurs, which clearly depends on ratio of the loading changes.

KEYWORDS

fatigue crack growth, variable amplitude tests, retardation, acceleration, overload, block-loading, service-loading, Mixed Mode loading

INTRODUCTION

The quality of a product is of increasing importance for industrial applications, because costs arising from missing quality are enormous. Especially the missing quality, which is caused in the early phase of the development of a product are combined with high consequential costs. Not only economic but first of all the safety-engineering factors in this phase are important for a breakproof development of components and structures.
For this purpose the prediction of lifetime is a helpful instrument. The concepts, for example those by Wheeler [1], Willenborg [in 5] or Gray & Gallagher [3], used to predict the fatigue crack growth at variable amplitude loading in components are often based on tests with constant amplitude loadings, in which overloads are interspersed. However structures are exposed service loadings, which are composed of varying loading changes. These loading changes produce both acceleration and retardation, the so-called interaction effects. In this work some loading changes are experimentally investigated to form the basis of concepts for predicting lifetime of structures under real-life-conditions.

LOADING CHANGES DURING SERVICE LOADING

The loadings, under which a fatigue crack grows, can be divided up into two main parts: single-stage loading and service loading. With experiments under single-stage loadings statements can be made about the crack initiation, the crack path and starting of unstable crack growth. But it is impossible to predict the lifetime of a component under real-life conditions with service loadings. The service loadings again consists of single over-/underloads, over-/underloads sequences, block loading and combination loading. All these loading changes alone are interspersed into a single-stage loading. The combination loading is interspersed likewise in an constant amplitude loading, but is composed of the three other loading types. Moreover loading changes can result from a alteration of the load direction, so that all mentioned loading types must be investigated under Mixed Mode. In Figure 1 several loading changes are represented.

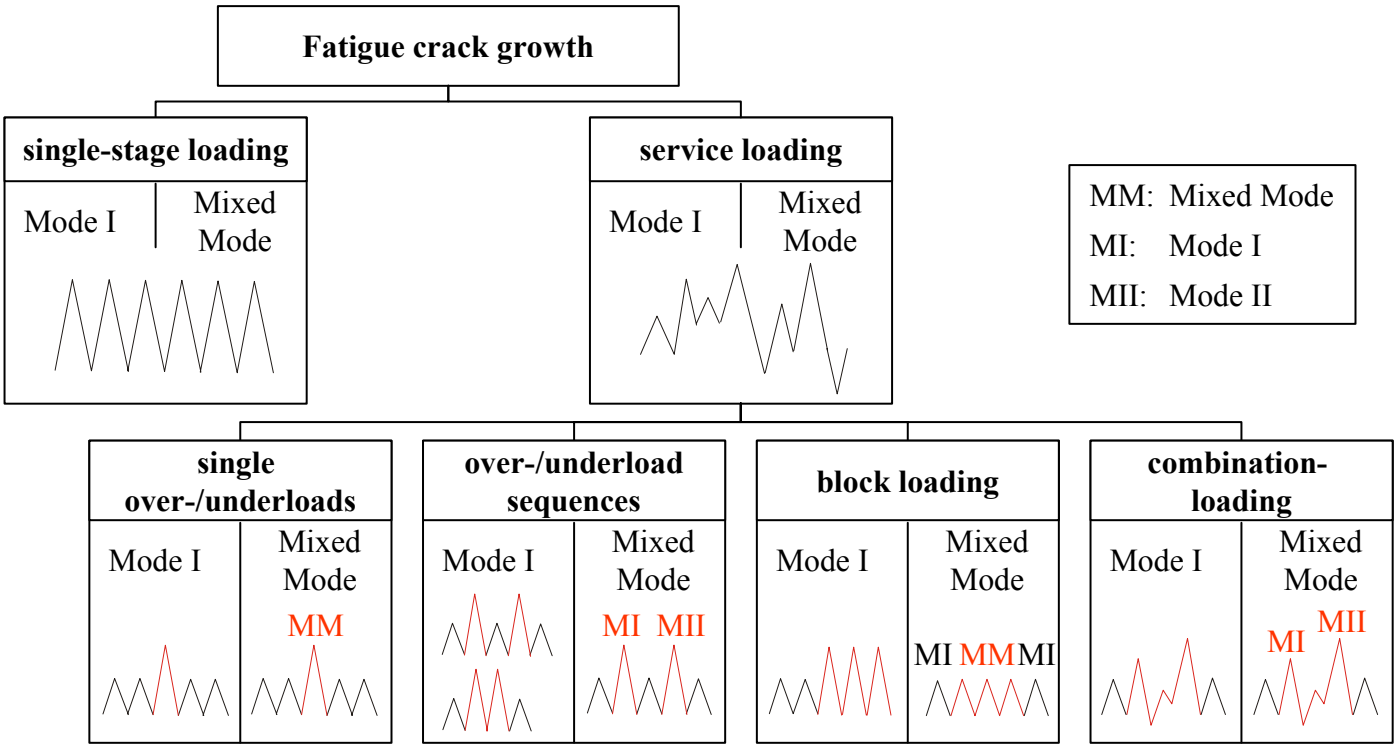

Figure 1: Systematisation of loading cases for fatigue crack growth

In this paper the results of single overloads, overload sequences, block loading and combination-loading under Mode I are presented. The overload ratio is defined as:

$$R_{ol} = \frac{K_{ol}}{K_{max}} \tag{1}$$

and the block loading ratio is defined analogous to the overload ratio as:

$$R_{block} = \frac{K_{block}}{K_{max}} \tag{2}.$$

whereby K_{ol} and K_{block} are the maximum load of the overload resp. the block loading and K_{max} is the maximum load of the constant baseline level of the cyclic stress intensity factor, ΔK_{BI}.

EXPERIMENTAL SETUP

The central unit of the experimental setup (Figure 2) is the servohydraulic testing system. The potential drop method (DC) is used for the measurement of the crack length. For both the measuring data logging and controlling of the experiments the program system ^{FAM}Control is used, which has been developed at the Institute of Applied Mechanics at the University of Paderborn. With ^{FAM}Control it is possible to perform all experiments fully automatic. Figure 3 shows the parameter window of ^{FAM}Control, in which the user can

define all kinds of service loadings. During K-controlled tests, the load will adapted continuously to the crack length.

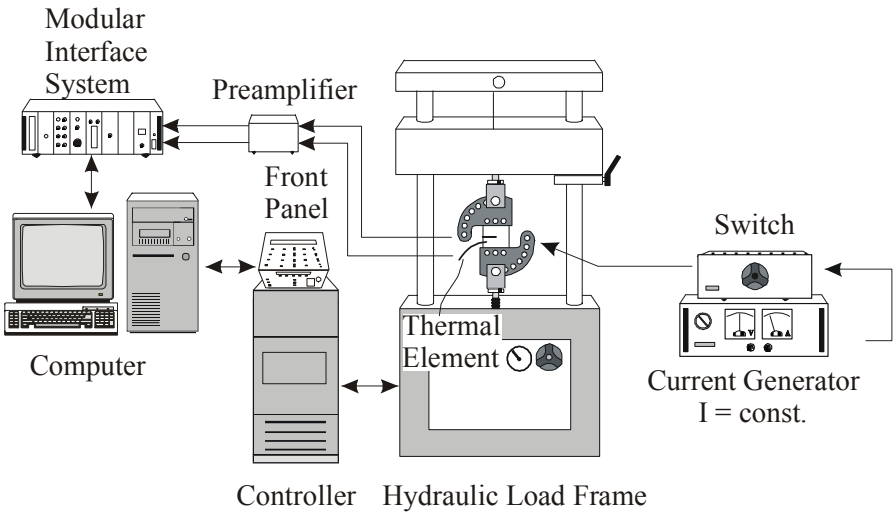

Figure 2: Schematic experimental setup

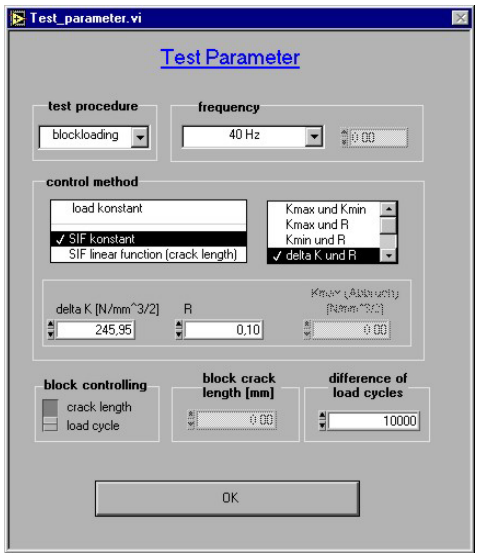

Figure 3: Parameter window of the program system ^{FAM}Control

The experiments have been carried out on the Aluminium alloy AlZnMgCu 1.5 (7075 T651) by means of CT specimens, which have been taken from a plate in T-L direction. The overloads have been interspersed in constant baseline levels, ΔK_{Bl} of 4, 7 and 10 MPam$^{1/2}$ and load ratio of 0.1. The experiments with block loadings and combined loadings have been performed with ΔK_{Bl} = 7 MPam$^{1/2}$ and R = 0.1.

RESULTS OF EXPERIMENTAL INVESTIGATIONS OF LOADING CHANGES

The effects of loading changes become obvious when observing the fatigue crack growth rate (FCGR). All measuring data are evaluated with the incremental polynomial method, as it is described in the ASTM E647 standard. In the transition between the loading changes the secant method has been applied, which results in a direct availability of the crack velocities after a loading change.

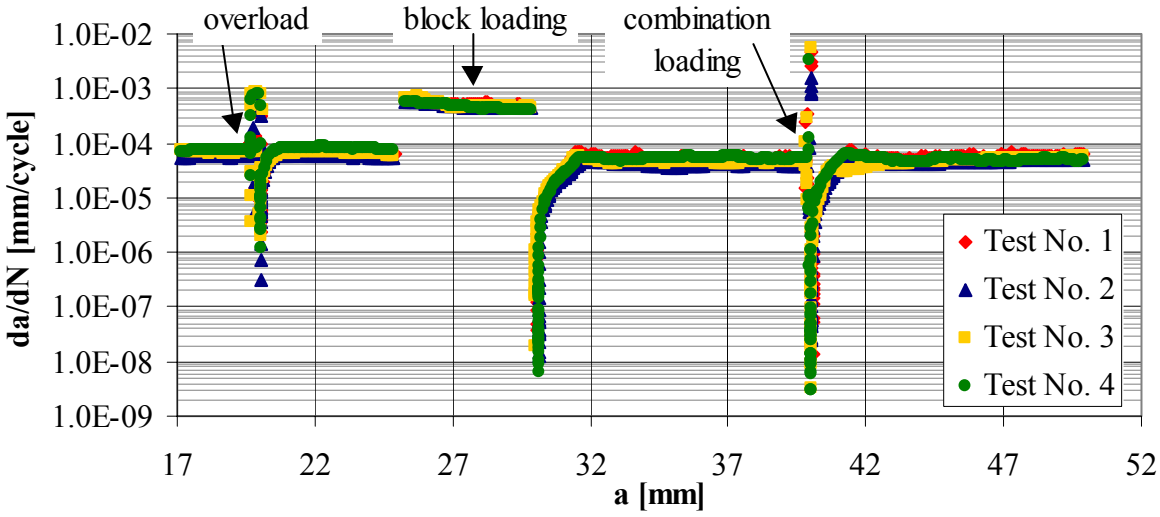

Figure 4: Crack growth rates for different loading changes with acceleration and retardation effects for several tests

Figure 4 illustrates the changes of the FCGR after loading changes with the same loading change ratio R_{ol} and R_{block} of 2.0, which are interspersed in a constant ΔK_{BI}. After a single overload the FCGR initially increases and then the crack growth retards. The block loading has two effects. At the beginning of the block the FCGR accelerates immediately and stays on this level over the whole duration of the block loading. After the block loading the FCGR decreases to a minimum and increases after a while to the base level. The combination loading consists of ten cycles of overloads with different overload ratios, but the maximum overload ratio amounts 2.5. In this case the FCGR increases, too, but decreases to a lower level as the minimum FCGR of the single overload and the block loading.
Figure 5 and Figure 6 show the crack length versus the load cycle curve, in which the typical load interaction effects are illustrated.

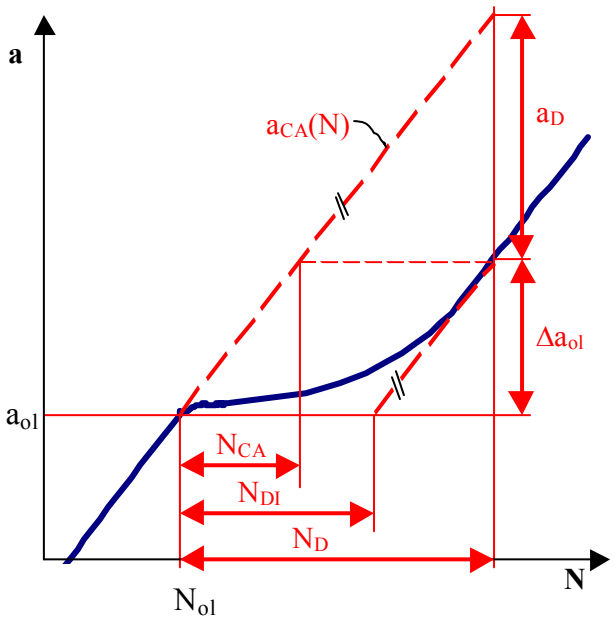

Figure 5: Characteristic parameters of interaction effects following an overload interspersed in a K-controlled-tests

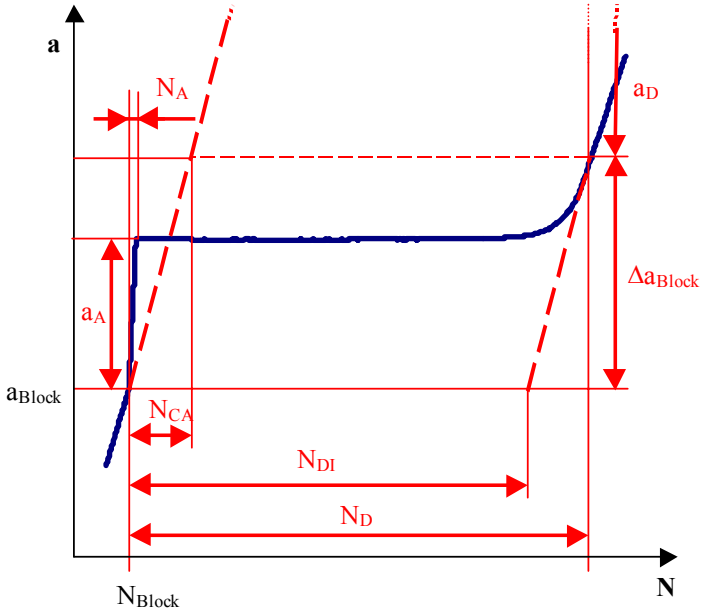

Figure 6: Characteristic parameters of interaction effects following an block loading interspersed in a K-controlled-tests

The magnitude of the retardation after an overload is usually measured by the delay cycles N_D or N_{DI}. N_D is the number of cycles until the FCGR of the constant amplitude loading is reached (comp. Figure 4). The cycle number N_{CA} indicates, how many load cycles are necessary for an overload-affected crack growth increment of Δa_{ol} in the absence of an overload. Instead of the delay cycle N_D sometimes the factor N_{DI} is used. N_{DI} is the number of delay cycles, which is adjusted by the N_{CA}. In addition to the mentioned retardation there exists a phase of acceleration for the block loading. This acceleration is described by the parameters N_A and a_A.
The results of the overload experiments shows, that the retardation effects increase with increasing overload ratios. That means, that the number of delay cycles and the overload-affected crack growth increment increases. This trend is also observed in many other publications [3-6]. Besides that the influence of the baseline level of the cyclic stress intensity factor is investigated. These tests have been performed with the baseline levels 4, 7 and 10 $MPam^{1/2}$. These experiments show, that the retardation effect raises with decreasing ΔK_{BI}.
Moreover Henn, Richard and Linnig [7] have carried out experiments with Mixed Mode overloads using CTS specimens [8]. These experiments prove, that if a Mixed Mode overload is interspersed into a Mode I loading, only the share of Mode I of this overload decides about the amount of retardation.
For the demarcation between tests with Mode I overload sequences and Mode I block loading a series of experiments have been performed. Therefore the number of overloads has been enhanced from a single overload to $n_{ol} = 50$, but the overload ratio is constant. Up to $n_{ol} = 22$ the number of delay cycles increases linearly. At $n_{ol} = 20$, 25 and 50 the fatigue crack arrests and the number of delay cycles reaches the technical

fatigue strength of Aluminium. This means, that from $n_{ol} = 20$ it does not make any difference if any overloads follow, so the limit for block loading has been reached.

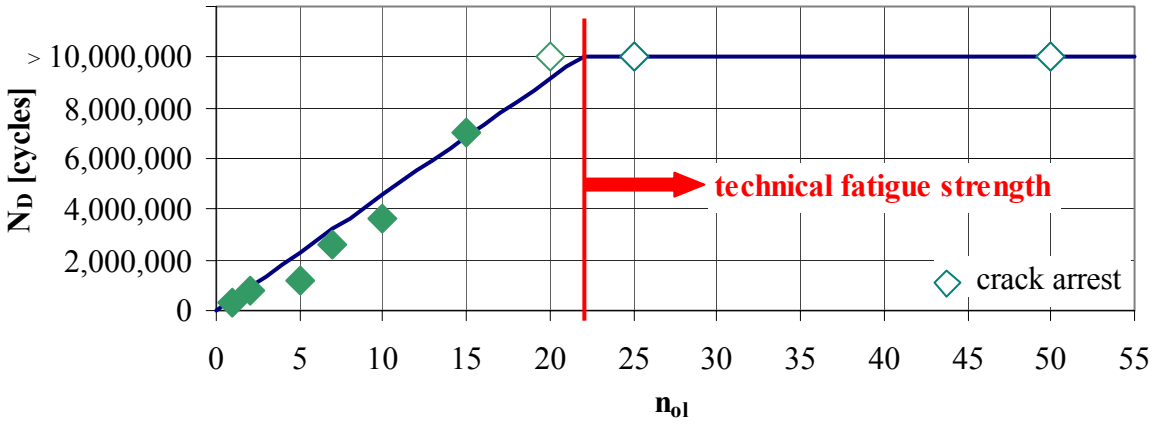

Figure 7: Number of delay cycles N_D over the number of overloads - Comparison between different overload sequences with the same baseline level $\Delta K_{Bl} = 7$ MPam$^{1/2}$ and the same overload ratio of 2.5

In Figure 8 the delay cycles of the experiments are illustrated. Compared to the tests with overloads the experiments with block loadings show a significant bigger retardation effect. From a block loading ratio of 2.2 the retardation is so high, that the technical fatigue strength of Aluminium is reached. The retardation of the combination loading, which consists of ten different load cycles, lies between that one of the overload and that one of the block loading.
Figure 9 shows the overload- resp. block-loading-affected crack growth increments. Both the overload-affected increment and the block-loading-affected increment increase linearly. In contrast to the overload-affected increments the block-loading-affected crack growth increments are much higher.

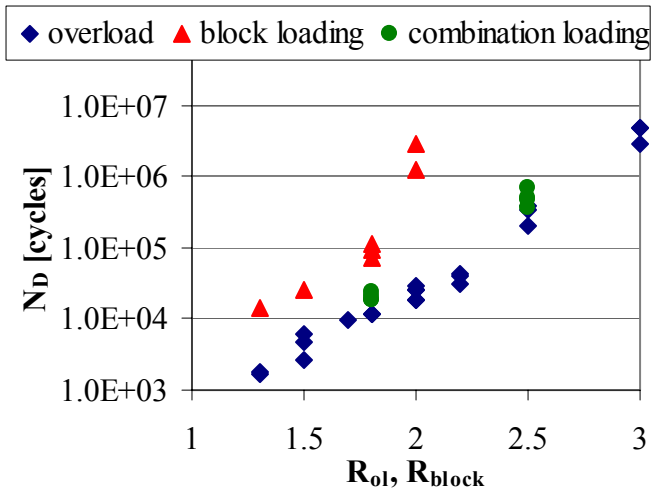

Figure 8: Number of delay cycles depending on the loading change ratio for overload and block loading

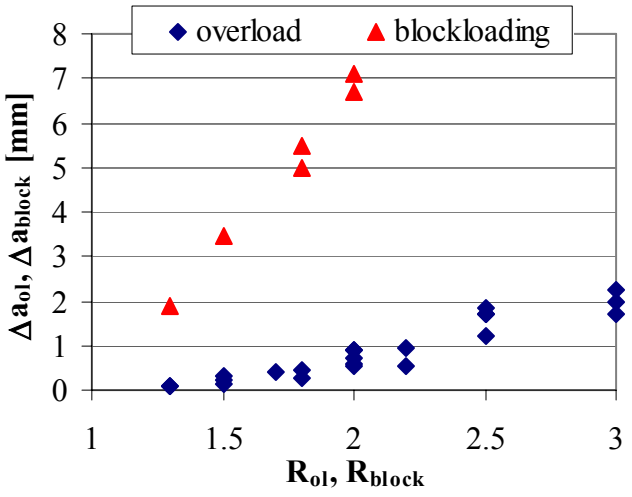

Figure 9: Delay distance depending on the loading change ratio for overload and block loading

The mentioned retardation occurs also under Mixed Mode loading changes. Experiments have been performed, in which the load direction is modified. In opposition to the pure Mode I loading the crack has kinked [9]. However, the crack growth retards after such a loading change from a pure Mode I loading to a Mixed Mode loading [9]. The change in the load direction and the consequences for the stress intensity factors are shown in Figure 10. It is obvious, that it comes up to a block loading. Further studies will be done, with which the influence of the share of Mode II will be investigated.

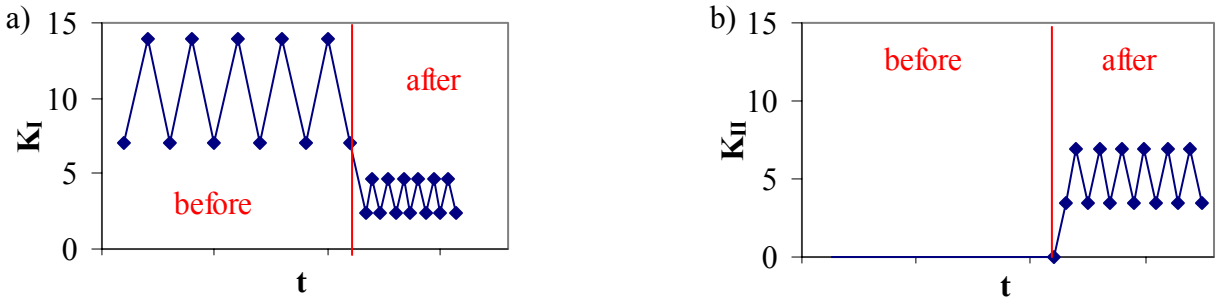

Figure 10: Stress intensity factors K_I (Figure 10a) and K_{II} (Figure 10b) before and after changing the load direction from Mode I to Mixed Mode loading

CONCLUSIONS

From the experiments and literature following conclusion can be drawn:

1. For the presented experiments the program system ^{FAM}Control has been developed. With ^{FAM}Control all experiments can be carried out fully automatic.
2. Loading changes produce both acceleration and retardation. This must be included into concepts for predicting the lifetime of components and structures.
3. The retardation effect of overloads arises with increasing overload ratio and decreasing ΔK_{BI}. Mixed Mode overloads, which are interspersed into a constant Mode I loading, likewise retard the crack growth, but only the share of Mode I of the Mixed Mode overload decides about the amount of the retardation.
4. Interspersed block loadings into a constant amplitude loading leads to acceleration. After block loadings the crack growth retards. The retardation of block loadings are much bigger than the ones of overloads.
5. A change from Mode I to Mixed Mode loading likewise retards the crack growth.
6. If a crack is subjected to either an overload or a block or a service loading the primary propagation direction remains unchanged. But under Mixed Mode fatigue loading a kinking of the cracks according to the K_{II}/K_I ratio can be observed.

REFERENCES

1. Wheeler, O. E. (1972). Journal of Basic Engineering, pp. 181-186
2. Gray, T. D., Gallagher, J. P. (1976). In: Mechanics of Crack Growth. ASTM STP 590, pp. 331-344, Rice, J. R., Paris, C. (Eds.). ASTM, Philadelphia.
3. Skorupa, M. (1996). Empirical trends and prediction models for fatigue crack growth under variable amplitude loading. Netherlands Energy Research Foundation, ECN-R-96-007, Petten.
4. Borrego, L.P., Ferreira, J.M. and Costa, J.M. (2000). In: Fracture Mechanics: Application and Challenges, CD-ROM Proceedings ECF 13, section 5, paper 44, pp. 1-8, Fuentes, M., Martin-Meizoso, A. and Marinez-Esnaola, J.-M. (Eds.). Elsevier, Oxford.
5. Dominguez, J. (1994). In: Handbook of Fatigue Crack Propagation in Metallic Structures, pp. 955-997, Carpinteri, A. (Ed.), Elsevier, Oxford.
6. Schwalbe, K.-H. (1980). Bruchmechanik metallischer Werkstoffe. Carl Hanser Verlag, München.
7. Henn, K., Richard, H. A., Linnig, W. (1990). In: Fatigue 90, pp. 581-587, Kitagawa, H., Tanaka, T. (Eds.), Honolulu.
8. Richard, H. A. (1985). Bruchvorhersagen bei überlagerter Normal- und Schubbeanspruchung von Rissen, VDI-Forschungsheft 631. VDI-Verlag, Düsseldorf.
9. Linnig, W., Richard, H. A., Henn, K. (1990). In: Fatigue 90, pp. 573-579, Kitagawa, H., Tanaka, T. (Eds.), Honolulu.

ORAL/POSTER REFERENCE: ICF10 1096 OR

INFLUENCE OF LOADING RATE ON SHEAR FRACTURE TOUGHNESS FOR FAILURE MODE TRANSITION

J.F. Kalthoff , A. Bürgel

Experimental Mechanics
Ruhr-University Bochum, Germany

ABSTRACT

When subjected to shear loading of sufficiently high rate, many materials do not fail by cracks, but by adiabatic shear bands. Work is reported on investigations for determining the dependence of the impact shear fracture toughness as a function of loading rate, in particular in the regime of failure mode transition from cracks to adiabatic shear bands. For achieving high rate shear loading, edge cracked specimens are asymmetrically impacted at the cracked edge by a projectile accelerated by an air gun to velocities up to 100 m/s. The resulting mode-II stress intensity factors and the times of onset of failure are determined by a specially developed strain gauge measuring technique. Results on shear fracture toughnesses with increasing loading rate are reported for two structural materials, a 1% chromium steel and a high strength aluminum alloy. Whereas decreasing fracture toughnesses are observed with increasing loading rate when failure occurs by tensile cracks, the fracture toughness increases with loading rate when failure occurs by adiabatic shear bands.

KEYWORDS

Fracture toughness, shear loading, rate dependence, adiabatic shear band, failure mode transition

INTRODUCTION

In the regime of linear elastic or small scale yielding fracture mechanics, cracks that are subjected to quasi-static shear mode-II conditions of loading fail by the initiation of tensile mode-I cracks, propagating of an angle of about 70° with respect to the ligament. When the loading is applied dynamically, e.g. by an impact event, a failure mode transition [1,2] is observed when the loading rate exceeds a certain limit value: failure then occurs by an adiabatic shear band propagating almost in the direction of the ligament. These adiabatic shear bands absorb more energy for propagation than cracks. This paper is aimed to investigate the impact shear mode-II fracture toughness K_{IId} as a function of loading rate, in particular in the regime of failure mode transition where the energy dissipation changes from a low to a high energy process [3].

EXPERIMENTAL TECHNIQUES

For achieving high rate shear conditions of loading, edge cracked specimens are asymmetrically impacted at the cracked edge by a projectile accelerated by an air gun to velocities up to 100 m/s (LECEI-technique, see Fig. 1). A compressive wave is initiated to one side of the crack, resulting in a shear-(mode-II)-loading after

the wave has reached the crack tip. The mode-II loading condition gets disturbed after interference of waves reflected at the boundary of the specimen with the crack tip stress distribution. Details of the LECEI-technique are reported in [2].
For determining mode-II stress intensity factors during the phase of loading, a strain gauge measuring technique has been developed [3,4] which is based on a concept introduced by Dally, Sanford [5] for the mode-I case. A strain gauge is mounted on the specimen near the crack tip. The angular position of the strain gauge is specially chosen to eliminate or to minimize the influence of two of the higher order terms of the crack tip stress field. The stress intensity factor is then determined from the measured strain. Two strain gauges are used for extrapolating the measured data against the actual crack tip position. In addition, static precalibration of the strain gauges is applied. Instability, i.e. initiation of failure is indicated by a change of the slope of the strain gauge signal as a function of time: In the case of failure by a crack (which propagates at an angle of about 70° with respect to the ligament - in a downward direction in Fig. 1), the distance between the crack tip and the strain gauge increases and, consequently, the strain gauge signal decreases; in the case of failure by an adiabatic shear band (which propagates almost in the direction of the ligament, i.e. towards the strain gauge), the distance from the failure tip to the strain gauge is decreased and the signal increases. Additional information on the failure event is obtained by direct high speed recordings taken with a Cranz-Schardin 24 spark high speed camera. The stress intensity factor K_{II} derived from the measured strain gauge signal at the moment of instability, i.e. at the time of onset of failure by a crack or by an adiabatic shear band, defines the impact mode-II fracture toughness K^*_{IId}.

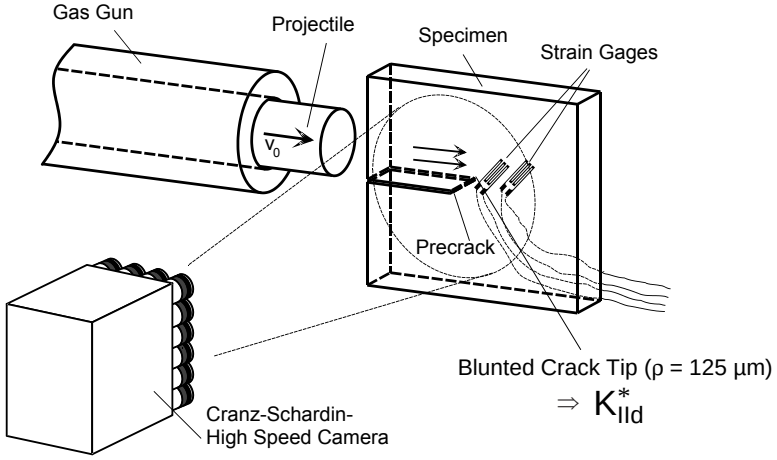

Figure 1: Experimental set-up (schematically)

Two materials are investigated, a 1 % chromium steel and a high strength aluminum alloy. The specimen size used for both series of investigations is 150 mm x 150 mm, the thickness of the specimens is 20 mm. The specimens are prepared with initial cracks/notches of about 60 mm length oriented in TL direction. At its tip the notch/crack is extended by a few mm by a special saw resulting in a finite bluntness at the tip of the crack. The determined fracture toughnesses, thus, are not true fracture toughness values that apply for a sharp pre-crack, but finite bluntness fracture toughnesses are measured, characterized by the symbol K^*_{IId}.

SHEAR FRACTURE TOUGHNESSES

The 1% chromium steel 42 CrMo 4 (German designation) has been investigated. The steel was heat treated at 860 °C (2 h), quenched (oil) and tempered at 160 °C (3 h). In its final condition the steel showed a yield strength σ_Y of about 1570 MPa and a tensile mode-I fracture toughness K^*_{Ic} (ρ = 125 µm) of about 100 $MN/m^{3/2}$.
Series of experiments have been performed with systematic variations of the impact velocity ranging from 20 m/s to 90 m/s. Typical results are given in Fig. 2. Failure paths and failure surfaces are shown on the left hand side of the figure for a low rate experiment (30 m/s impact velocity) and on the right hand side of the figure for a high rate experiment (60 m/s impact velocity). In the low rate experiment, failure occurs by a tensile crack propagating at an angle of about –70° with respect to the ligament (for the beginning of the

failure path); the failure surface is a typical fracture surface with roughness (plus additional indications of delamination in the middle of the specimen) and shear lips at the edges of the specimen, although small in size because of the high yield strength of the material. In the high rate experiment, failure due to an adiabatic shear band is observed propagating almost straight in the direction of the ligament (more precisely in the direction of few degrees to the opposite side of the ligament tensile cracks would propagate). The adiabatic shear band propagates over a considerable length (about 30 mm) and then is arrested. The length of the shear band at the edges of the specimen in all cases is larger than in the middle of the specimen, a behaviour opposite to what is observed for cracks. The failure following the adiabatic shear band is due to late time effects, e.g. due to arbitrary impact events in the catcher tank, when the specimen is decelerated. The adiabatic shear band has a typical shiny, mirror-like appearance, shear lips cannot be identified.

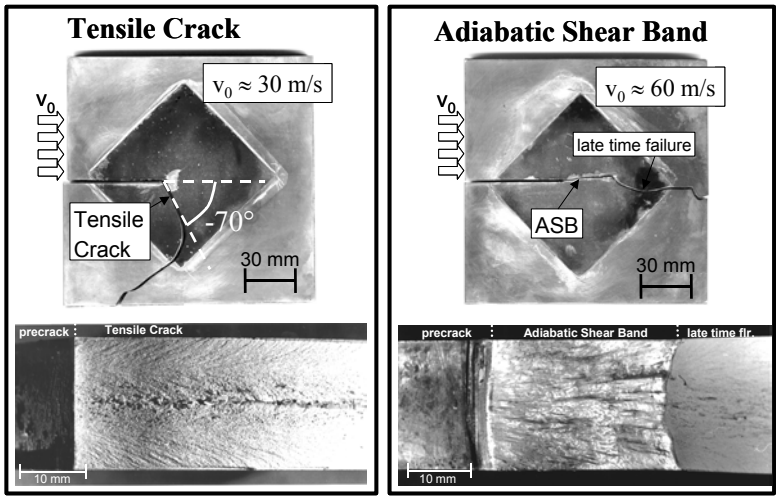

Figure 2: Failure in steel 42 CrMo 4 by tensile cracks or adiabatic shear bands in the low or high rate regime

Figure 3 gives typical strain gauge signals with the strains converted to stress intensity factors obtained in a low and a high rate test. The signals of both strain gauges SG1 and SG2 are shown. In the low rate experiment, an abrupt change of the signal to a decreasing slope is observed, indicating failure by a tensile crack. In the high rate experiment, on the other hand, the slope of the strain gauge signal from a certain time on gets steeper, indicating failure by an adiabatic shear band. The derived times of onset of failure agree with those obtained from high speed photographic recordings of the event.

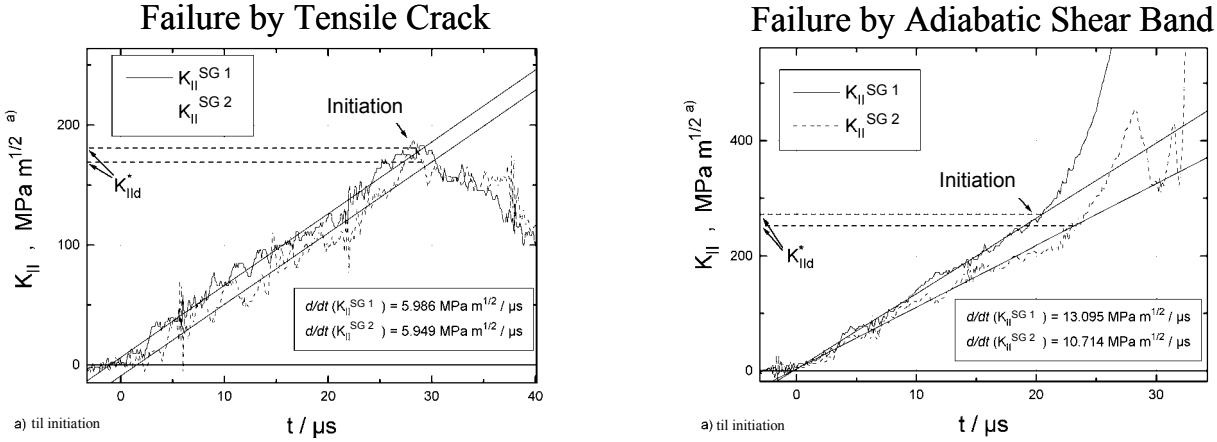

Figure 3: Strain gauge response for failure by tensile cracks and adiabatic shear bands in steel 42 CrMo 4

The shear mode-II fracture toughnesses measured as function of loading rate are shown in Fig. 4. Depending on which failure mode gets activated a different rate dependence is observed: For failure by tensile cracks which is obtained in low rate tests for loading rates $\dot{K}_{II} < 7 \cdot 10^6$ MN/m$^{3/2}$s, the shear mode-II fracture toughness K^*_{IId} decreases with loading rate, a behaviour as it is regularly observed for mode-I loading as well.

But, for failure by adiabatic shear bands, which results in the high rate tests for loading rates $\dot{K}_{II} > 7 \cdot 10^6$ MN/m$^{3/2}$s, the shear mode-II fracture toughness K^*_{IId} shows an increasing trend with loading rate. The transition between the two failure modes is not abrupt, a transition regime is observed for which the one or the other failure mode can become activated. There is no jump of the shear mode-II fracture toughness in this transition regime, the two curves overlap with their individual tendencies maintained.

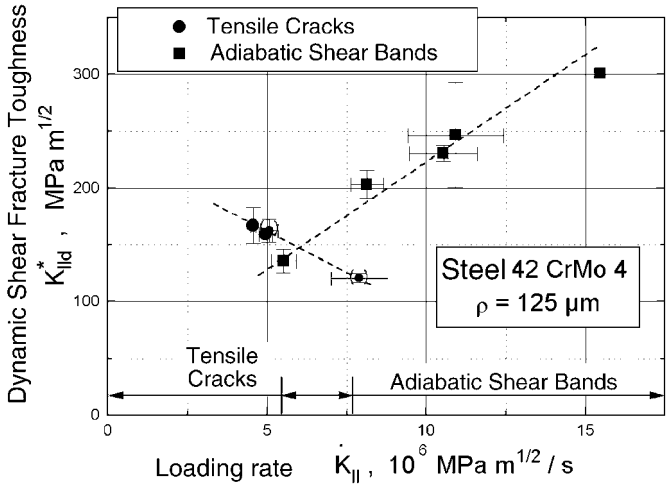

Figure 4: Dependence of shear fracture toughness from loading rate for failure mode transition in steel 42 CrMo 4

The second material investigated is the high strength aluminum alloy Al 7075. The material is used in T6 condition. The relevant material properties were measured to: yield strength σ_Y = 620 MPa, quasi-static pre-crack mode-I fracture toughness $K_{Ic} \approx 27$ MN/m$^{3/2}$.

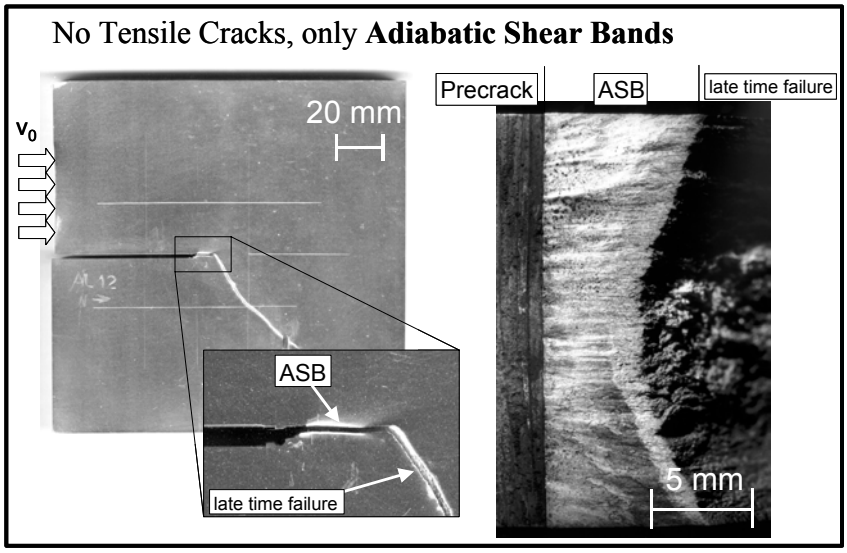

Figure 5: Failure in aluminum alloy Al 7075 by adiabatic shear bands

Results on the failure path and the failure surface are shown in Fig. 5. In all experiments failure by adiabatic shear bands resulted. Failure by tensile cracks at low loading rates could not be observed. In order to further explore this special behaviour, additional experiments have been performed at loading rates reduced down to even quasi-static conditions [6,7]. These experiments showed failure by (adiabatic) shear bands with the same or similar basic characteristics as observed in the dynamic tests. This behaviour is in contradiction to the generally accepted rule that the maximum tangential stress criterion controls the failure path in classical quasi-static linear elastic fracture mechanics. Other researchers have observed the same or a similar behaviour for mode-II or mixed mode loaded cracks in aluminum alloy, see in [7]. This unusual behaviour is not completely understood yet, it is believed that it is a peculiarity of the material aluminum. (In order not to be misunderstood: mode-I tensile crack propagation certainly does exist in aluminum alloy and is observed

in experiments, but for mode-I loading conditions only.) The phenomena and characteristics of adiabatic shear bands observed with the aluminum alloy are the same as observed with steel: The shear bands extend almost straight in the direction of the ligament, they are typically 8 mm long. The length of the band is larger at the edges of the specimen than in the middle of the specimen. The adiabatic shear band has a shiny, mirror-like appearance, shear lips do not exist. Figure 6 gives typical strain gauge signals observed in the aluminum tests. The increase in the slopes of the curves indicates that failure occurred by an adiabatic shear band.

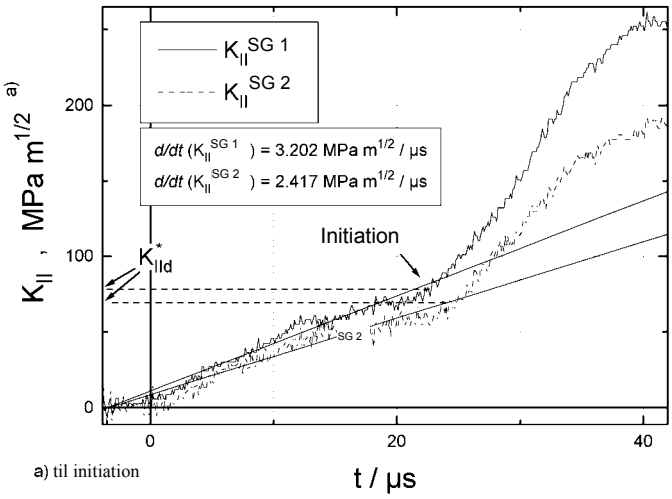

Figure 6: Strain gauge response for failure by adiabatic shear bands in aluminum alloy Al 7075

The shear mode-II fracture toughnesses measured as function of loading rate are shown in Fig. 7. In all the tests which resulted in loading rates $\dot{K}_{II} > 2 \cdot 10^6$ MN/m$^{3/2}$, the shear mode-II fracture toughness K^*_{IId} measured for failure by adiabatic shear bands shows a strongly increasing trend with loading rate, similar as observed in the steel tests.

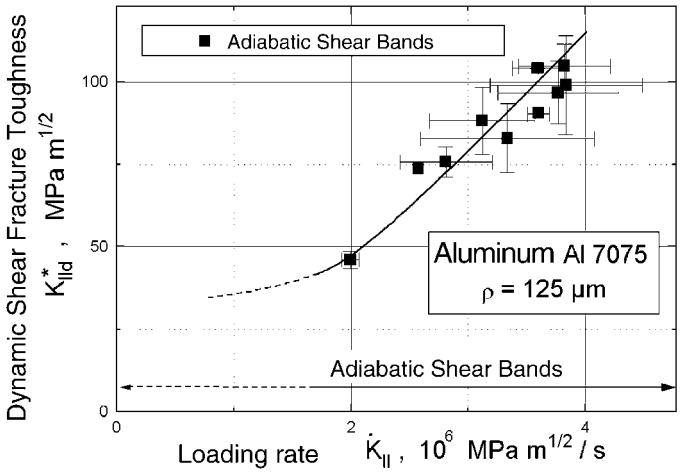

Figure 7: Dependence of shear fracture toughness from loading rate for failure by adiabatic shear bands in aluminum alloy Al 7075

SUMMARY AND DISCUSSION

Shear mode-II fracture toughnesses K^*_{IId} are measured as a function of loading rate. The steel 42 CrMo 4 shows the following behaviour: for failure by tensile cracks at low loading rates the impact fracture toughness decreases with loading rate; for failure by adiabatic shear bands at higher loading rates the fracture toughness increases with loading rate. With the aluminum alloy Al 7075 failure by adiabatic shear bands is observed at all loading rates applied and fracture toughnesses increasing with loading rate result.

The decreasing trend of the fracture toughness with loading rates for crack failure is certainly due to the regular strain rate hardening effects: with increasing loading rate the yield strength of the material increases, i.e. the resulting plastic zone at the crack tip and in turn the fracture toughness decreases. The increasing trend of the fracture toughness with loading rate for failure by adiabatic shear bands is speculated to be caused by thermal softening effects which are a result of the adiabatic conditions and the extreme increases in temperature that control the process of adiabatic shear band failure: yielding of the material and plasticity effects become more pronounced which dissipate more energy, and thus, result in higher fracture toughness values with increasing loading rate. The processes in detail are more complicated in nature of course. Figure 8 shows micrographs of regions underneath the failure surfaces formed by a tensile crack and by an adiabatic shear band. In the case of failure by the tensile crack, the base material with its characteristic structure extends completely up to the failure surface. In the case of failure by the adiabatic shear band, the extreme heating effects result in phase transformations of the shear band zone adjacent to the failure surface which are accompanied by an increase of the hardness of the material.

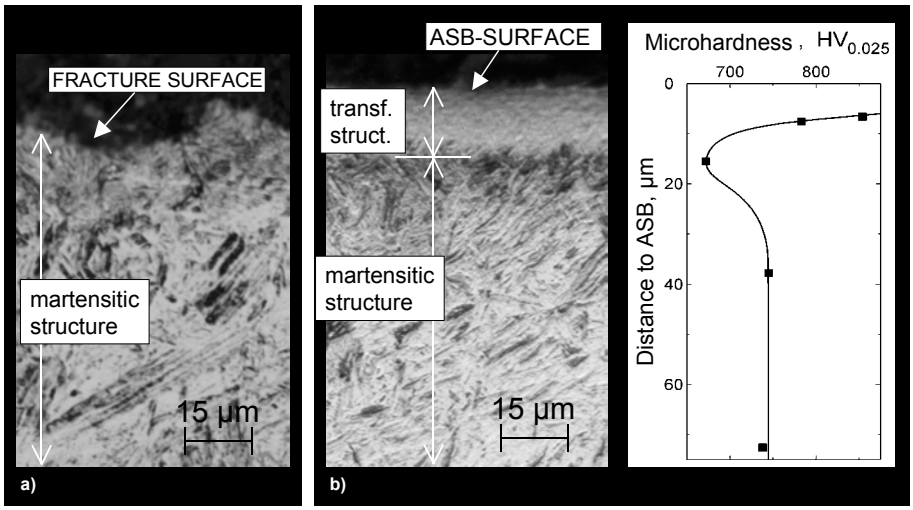

Figure 8: Transformation of the microstructure and increase in micro-hardness in the vicinity of an adiabatic shear band (b) compared to the behaviour near a fracture surface (a)

The above findings and conclusions are essential for establishing optimized conditions for separating material. The general trend that lower amounts of energy are required when the loading rate is increased does not hold anymore and is reversed when the failure mode changes from cracks to adiabatic shear bands.

ACKNOWLEDGEMENT

The research work has been supported by the Office of Naval Research under the technical direction of Dr. Yapa D.S. Rajapakse.

REFERENCES

1. Kalthoff, J.F. (1990) Applied Mechanics Review 43, 247
2. Kalthoff, J.F. (2000) International Journal of Fracture 101, 1
3. Bürgel, A. (2000). Dissertation, Ruhr-Universität Bochum, Germany.
4. Bürgel, A., Shin, H.S., Bergmannshoff, D. and Kalthoff, J.F. (1999). In: Proc. VII. Bilateral Czech/German Symposium: Significance of Hybrid Method for Assessment of Reliability and Durability in Engineering Sciences, 13.-15. April 1999 Liblice, Czech Republic, 11
5. Dally, J.W. and Sanford, R.J. (1987) Exp. Mech. 27, 381
6. Hiese, W. (1999). Dissertation, Ruhr-Universität Bochum, Germany.
7. Hiese, W. and Kalthoff, J.F. (1999) In: Mixed-Mode Crack Behavior, ASTM STP 1359, pp. 74-85, K.J. Miller and D.L. McDowell (Eds.). American Society for Testing and Materials, West Conshohocken, PA

ORAL/POSTER REFERENCE: ICF 100 480 PR

INFLUENCE OF PHASE TRANSFORMATION ON SUBCRITICAL CRACK GROWTH IN NUMERICAL MODELLING OF A CERAMIC COMPOSITE

T. Niezgoda[1], W. Szymczyk[1], J.Żurek[2], J. Jaźwiński[2]

[1] Military University of Technology, 2 Kaliskiego Str., 00-908 Warsaw, Poland
[2] Air Force Institute of Technology, Księcia Janusza Str., 00-908 Warsaw, Poland

ABSTRACT

The aim of the work is to establish the method of numerical simulation of stress induced transformation of ZrO_2 from the tetragonal to monoclinic phase which takes place at the crack tip in two-phase Al_2O_3– ZrO_2 ceramic composite. It is the base for the future crack growth numerical simulations in composite with the use of FEM models with the real grain size distribution and shape. The preliminary analysis allows us to estimate influence of phase transformation of the composite on the cracking resistance.

KEYWORDS

Al_2O_3, ceramic composite, ZrO_2 phase, phase transformation, crack propagation, FEM (Final Elements Method)

INTRODUCTION

Due to their properties, such as high chemical corrosion resistance, high temperature resistance, relatively low density and high hardness as well as shear strength, ceramic materials make a very interesting material for design engineers. They are not widely implemented only because of their brittleness and low cracking resistance. Therefore, many laboratories all over the world have been carrying out intensive research to fully explain the nature of crack formation in ceramic materials. However, this phenomenon still remains far from being explained even in case of single phase Al_2O_3 ceramic material which probably is the most widely tested one.

The issue which attracts researchers' attention is the increase in the material cracking resistance as a function of the crack growth length (R-curve or T-curve). This was observed in case of Al_2O_3 ceramics, Al_2O_3 ceramics with SiC whiskers, corundum ceramics with ZrO_2, stabilized zirconium ceramics, and silicon nitride ceramic materials.

Two theories are used to describe the problem. The first is the theory of bridges created behind the tip of the surface crack. This theory is especially helpful for the description of crack resistance feature of a material which does not undergo stress induced phase transformation. The material which can be best analysed in this way is, for example, pure corundum ceramics.

Another theory used in the analysis of materials containing phases which undergo transformation on the phenomenon of the formation of phase transformation zone surrounding. It is induced by local stress areas developing in front of the crack tip during the crack growth. The direction of tensile stresses is perpendicular to the direction of crack propagation and compressive stresses appear in the direction which is parallel to the crack.

The zirconium dioxide placed in the aluminum oxide matrix with high Young module is compressed in the areas which are distant from the head of the crack. The field of tensile stresses which develops ahead of the developing crack induces the tetragonal zirconium phase and allows for its change into the monoclinic phase with different shape and larger volume. As the result the crack tip stresses are reduced and the cracking resistance increases. This leads to the formation of transformed phase layer along the crack surface.

It is commonly assumed that the thickness of the transformation layer is constant. The thickness is determined by the matrix cracking resistance and the stresses enabling the process of transformation regardless of the tetragonal phase grain size. It is possible that the thickness of the transformation layer depends on the tetragonal phase grain size. There exists a correlation between the growth in the transformation layer and the cracking resistance increase.

The assumption concerning the stress decrease in the area of the crack tip as a result of the process of phase transformation has been used by Evans [1, 2] who has suggested an expression defining the relation between the cracking increase, transformation layer thickness and the crack growth in the transformation zone:

$$\Delta K_I = \frac{E e^T V_f \sqrt{w}}{1-\nu} \kappa(\Delta a / w, \nu) \tag{1}$$

where
E is the Young module of the matrix containing zircon dioxide,
e^T is the transformation strain,
V_f is the volume of the transformed grains,
ν is Poisson's ratio,
κ is the function the value of which increases with the crack growth, describing the material cracking resistance.

Both the ,,zone" and the ,,bridge" theory, lead to the conclusion that the stress intensity coefficient K_{Itip} in the crack tip can be written as follows:

$$K_{Itip} = K_{Ia} - K_{Is} \tag{2}$$

where K_{Ia} is the stress intensity coefficient used, K_{Is} is the ,,shielding" stress intensity coefficient which grows in relation to the crack length until its maximum value $K_{IS_{max}}$ is reached.

The speed of the crack growth is usually described by the following dependence:

$$V = da/dt = A(K_{Itip})^n \tag{3}$$

where A and n are subcritical cracks growth parameters. Because K_{Ia} (where Y is constant depending on the geometry of the analysed system with a fault, σ_a is the stress applied) it may turn out that in some range of values (for $\sigma_a < \sigma_c$, where σ_c is the strength of the material) the increase of the K_{Is} value in the a function will exceed K_{Ia}. This will lead to the retardation of the crack propagation. There is then a possibility of minimizing the phenomenon of subcritical cracks growth which are responsible for the unexpected damage of the ceramic construction elements. If some parameters of the microstructure are known, i.e. the grain size, mechanical properties determined by the Young's module E,

the Poisson's ratio ν, resistance σ_c, cracking resistance K_{Ic} , corresponding to the length of the „natural" flaw, it is possible to calculate numerically the run of the R or T curve. This in turn, allows for defining the range of the flaw sizes if $\sigma_a < \sigma_c$ for which the growth of subcritical cracks is reduced to minimum.

The work on the creation of numerical models, calculation methods, results analysis and evaluation can be basically applied into two areas: the area of ceramic materials without the phases undergoing transformation and the area of materials containing the phase which undergoes transformation. The main stages of the experimental and numerical research within these areas are similar.

On the basis of numerical simulation both the R and T curves as well as the dependence of subcritical cracks growth speed rate V on the stress intensity coefficient can be determined for both types of ceramics. The lifetime, that is the time of use of a given construction element made of the above mentioned type of ceramics including a fault causing stress concentration (such as a crack, cut, Vicker's impression) can also be determined.

PHASE TRANSFORMATION SIMULATION TEST

In earlier works authors established methods for residual stress state numerical assessment and for bridging effect simulations with finite elements method (FEM) [9,10,11,12]. The residual stress state was investigated for the pure Al_2O_3 ceramics as well as for Al_2O_3–ZrO_2 composites with the use of 3D models. For composite containing 20% of ZrO_2 there were obtained values of average residual stresses of ~+700 MPa and ~–250 MPa respectively for ZrO_2 and Al_2O_3 phases (for temperature decrease ΔT = -1150º) which are comparable with example references [7, 8].
The application of numerical modelling results in the creation of the models describing the effect of the phase transformation at the tip of the growing crack.

For the need of phase transformation simulation method establishing 2D models of microscopic volume of two phase polycrystalline material (e. g. composite on base of Al_2O_3 and ZrO_2) were created and tested. The models containing octagon and square grains allow for making simulations for different volume fractions of Al_2O_3 and ZrO_2. As an example the mesh for the model of the material containing 20% of ZrO_2 (simulated by square grains) is presented in Figure 1. Such a mesh containing ideal grains which are uniform for each phase may be treated as "geometrically averaged" (in the sense of size, shape and topology). It is useful for making global observations, which are not affected by a number of factors that take effect in the real material (e. g. distribution of size and shape of grains). This coarse mesh is destined for tests which may answer the question: whether the FEM modeling is able to simulate phase transformation or not.

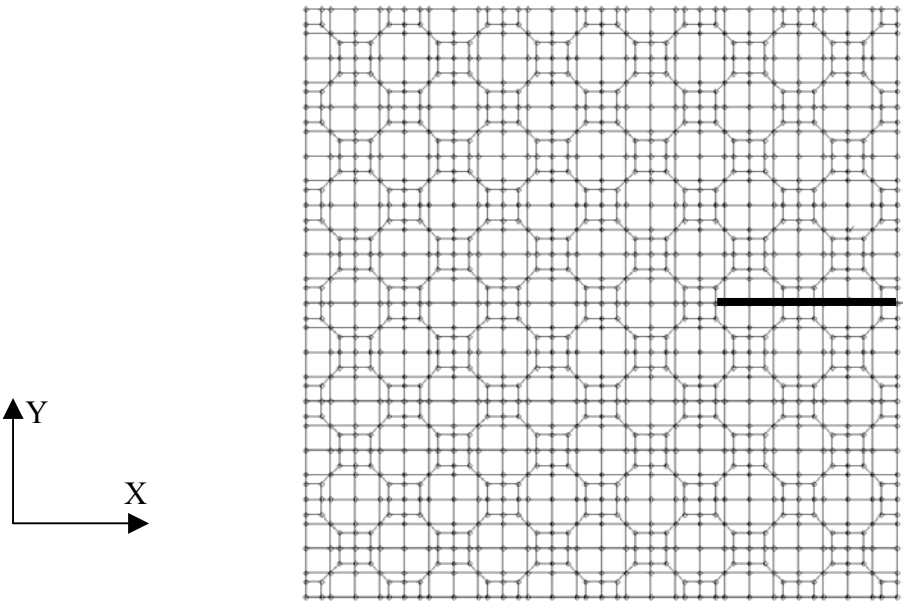

Figure 1: The mesh of the 2D model of two phase polycrystalline material taken for testing calculations. The area fraction of squares is 20%. The bold line shows the crack simulation.

The properties of the phases taken into numerical tests were found mainly in references [13,14]. They are collated in the Table 1. It was assumed that the temperature decrease was $\Delta T = -1500^{o}$. The model is also loaded by displacements of the model boundaries, complying with thermal contraction of surrounding volume of material which in macro scale behaves like isotropic, totally homogeneous one, characterized by thermal expansion coefficient $\alpha_{iso\text{-}MACRO} = 9.3$ placed in Table 2. Values in Table 2 are the weighted sum of appropriate values from Table 1 with respect to volume fractions of Al_2O_3 and ZrO_2.

TABLE 1
MATERIAL PROPERTIES FOR PURE CERAMICS

	Al_2O_3	ZrO_2
E [GPa]	400	200
ν	0.23	0.32
$\alpha_a=\alpha_m$ [K^{-1}]	8.6 e^{-6}	9.2 e^{-6}
α_c [K^{-1}]	9.5 e^{-6}	10.75 e^{-6}
α_{izo} [K^{-1}]	8.9 e^{-6}	10.9 e^{-6}
$\Delta\alpha_{\alpha c-\alpha a}$ [K^{-1}]	0.9 e^{-6}	1.55e^{-6}

TABLE 2
MATERIAL PROPERTIES FOR THE AL_2O_3 + 20% ZRO_2 COMPOSITE - EQUIVALENT FOR MACRO LEVEL

Material	E_{MACRO} [GPa]	ν_{MACRO}	$\alpha_{iso\text{-}MACRO}$ [K^{-1}]
Al_2O_3 + 20% ZrO_2	360	0.25	9.3e^{-6}

In preliminary tests thermal orthotropy of materials is not considered yet. It means that the model grains of Al_2O_3 and ZrO_2 have appropriate isotropic properties ($\alpha_{iso\text{-}MICRO}$) shown in Table 1. This is because the residual stress effect caused by random orientations of material axes in neighboring grains would make it difficult to detect (in the model) the phase transformation phenomenon itself. Random orientation of orthotropy axes in particular model grains - with appropriate orthotropic thermal expansion coefficients - will be then allowed in succeeding simulations.
In preliminary tests an external uniaxial tensile load in the direction perpendicular to the plane of the crack was introduced too. It induces stress σ_y (in the global coordinate frame) on the level of 160 MPa. Such a load causes initial opening of the modeled crack tip.
To recapitulate – the complete set of loads contains: temperature decrease ΔT, displacements of the model borders simulating contraction of the macroscopic environment and the external uniaxial tensile load initializing the crack tip opening.

Figure 2 shows σ_y stress state at the crack tip in the model while the load consists of external uniaxial tension, temperature decrease $\Delta T = -1500$ and the contraction of the macroscopic environment. The crack tip is still open (the scale for displacements: 30:1 – large enough to observe crack tip opening). The stress concentration in the grain of ZrO_2 placed at the crack tip reaches maximum value $\sigma_y \approx +865$ MPa.
Figure 3 shows σ_y stress state at the crack tip in the model while the load consists of uniaxial tension, temperature decrease $\Delta T = -1500$ and the contraction of the macroscopic environment. The phase transformation is simulated in all the grains in the model by the thermal coefficient correction from 10.9e-6 to 10.8e-6 K^{-1}. The crack tip is constrained to be closed. The grain of ZrO_2 placed at the crack tip is then under tensile stress, the maximum value of their concentration decreased to the value $\sigma_y \approx +806$ MPa (the stress relaxation effect induced by phase transformation simulation is visible).

Different shapes and ranges of phase transformation zones were tested to investigate sensitivity of the FEM model: from the case of the zone containing only one monoclinic ZrO_2 grain at the crack tip to the case in which all the grains in the model were transformed. Increasing the dimensions of phase transforming zone in the model produces more and more visible effect of crack tip closing and stress concentrations decrease in transformed grains. The FEM model behaves properly in the qualitative sense.

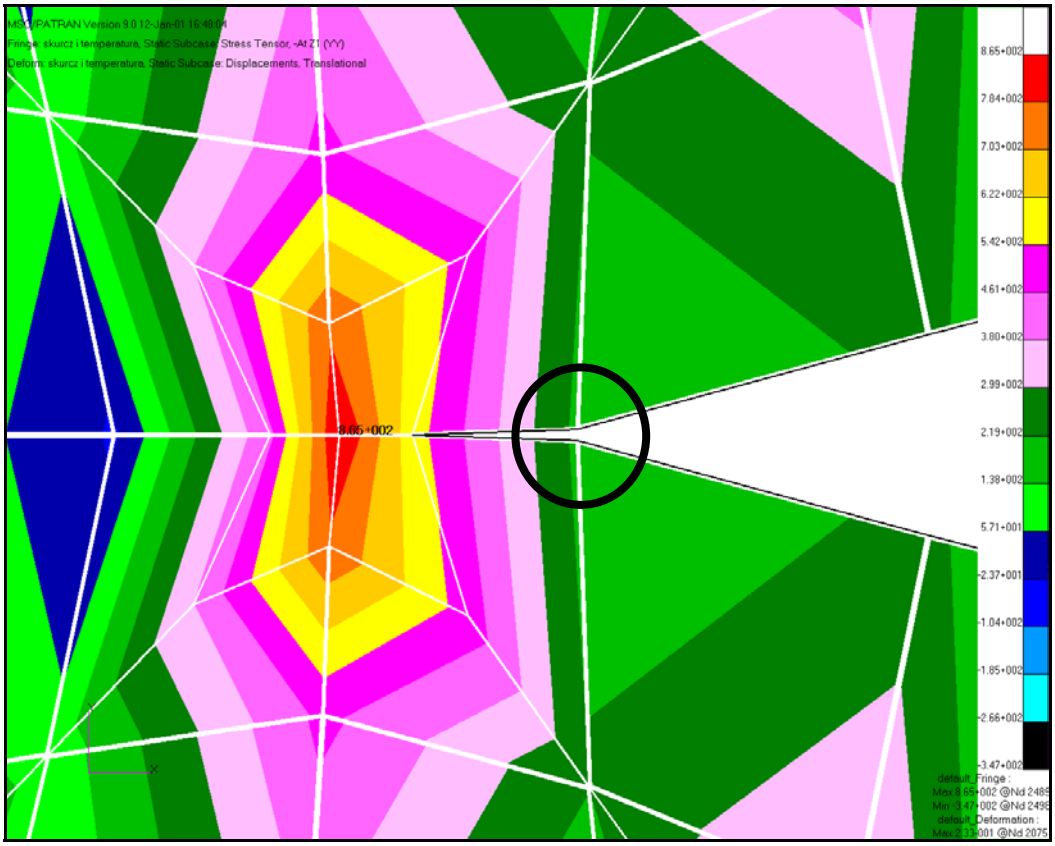

Figure 2: σ_y stresses at the crack tip while the load consists of external uniaxial tension, temperature decrease $\Delta T = -1500$ and the contraction of the macroscopic environment. The crack tip is still opened due to the external uniaxial load (the scale for displacements: 30:1).

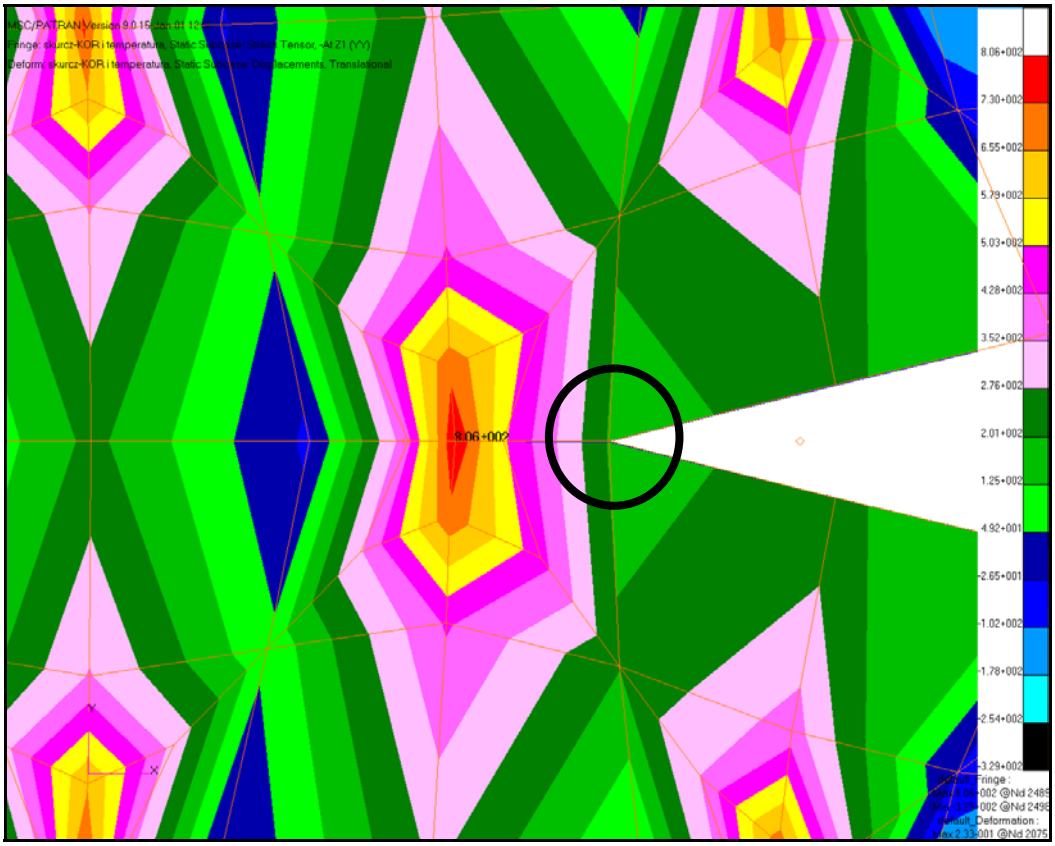

Figure 3: σ_y stresses at the crack tip while the load is the same like in the previous case but the phase transformation is simulated in all the grains in the model. The crack tip is constrained to be closed (the scale for displacements: 30:1).

CONCLUSIONS

The values of stresses obtained for 2D FEM models are comparable with those obtained with the use of 3D ones which were applied earlier for residual stresses assessment [9,10,11,12] and with references [7,8]. Preliminary tests show that FEM modelling of phase transformation phenomenon in $ZrO_2 + Al_2O_3$ ceramic composite is possible. It may be achieved by thermal expansion coefficient correction, equivalent to difference in specific volumes of tetragonal and monoclinic phases of ZrO_2. The tests presented in the paper may be now completed by consideration of random orientations of thermal orthotropy axes in neighboring grains. Presented work is the base for numerical investigations with the use of FEM models with finer meshing, complying with the experimental microscopic observations.

The novelty of this kind research is reflected by the fact that our methods of the numerical simulation will assist the experimental research, speed up the research process and will aid the design of ceramic construction elements while taking into consideration real loads. The results obtained can also reflect the grain size of the ceramic microstructure, the influence of the two types of phenomena on the crack propagation which occur in the crack zone in two kinds of the ceramic material, namely the „bridge" phenomenon (in the pure corundum ceramics) and the phase transformation (in the zircon dioxide ceramics).

The methods which have been worked out and experimentally verified allow for the crack resistance analysis of the real construction elements made of brittle kinds of ceramics used in real conditions and loads (e.g. heat load). The authors of the method believe it will find a wider application in assessing cracking resistance of various kinds of polycrystalline brittle materials with „bridge" or phase transformation effects.
|

REFERENCES

1. Evans A.G., Heuer A.H. (1980), *J. Amer. Ceram. Soc.* 63, pp. 5-6.
2. Mc Meeking R.M., Evans A.G. (1982), *J. Amer. Ceram. Soc.*, 65, 5.
3. Clarke D.R., Adar F. (1982), *J. Amer. Ceram. Soc.*, 65, 6, pp. 284-288.
4. Ma Q., Clarke D.R., (1993), *J. Amer. Ceram. Soc.*, 76, 4, pp. 1433-40.
5. Ma Q., Clarke D.R., (1994), *J. Amer. Ceram. Soc.*, 77, 2, pp. 298-302.
6. He J., Clarke D.R., (1995), *J. Amer. Ceram. Soc.*, 78, 5, pp. 1347-53.
7. Pezzotti G., Sergo V., Sbaziero O., Muraki N., Meriani S., Nishida T., (1999), *J. Eur. Ceram. Soc.*, 19, pp 247-253.
8. Akiniwa Y., Tanaka K., ICRS-6, pp 25-32.
9. Niezgoda T., Szymczyk W., Małachowski J., (1999), *ECERS-6, British Ceramic Proceedings*, 60, pp 475-476.
10. Niezgoda T., Szymczyk W., Małachowski J., (1999), *ECERS-6, British Ceramic Proceedings*, 60, pp 483-484.
11. Niezgoda T., Małachowski J., Szymczyk W., (1999), *ECERS-6, British Ceramic Proceedings*, 60, pp 485-486.
12. Niezgoda T., Małachowski J., Szymczyk W., (1999), *ECERS-6, British Ceramic Proceedings*, 60, pp 486-487.
13. Krell A., Teresiak A., Schläfer D., (1996), *J. Eur. Ceram. Soc*. 16, pp 803-811.
14. R.W.Rice, S.W.Freiman, (1981), *J. Amer. Ceram. Soc.,* 64, 6, 350.

ORAL/POSTER REFERENCE: ICF100985OR

INFLUENCE OF RESIDUAL STRESS ON DUCTILE CRACK INITIATION AND GROWTH IN DISSIMILAR METAL WELD JOINTS

A. H. Sherry, D. P. G. Lidbury and D. W. Beardsmore

AEA Technology plc, Risley, Warrington, WA3 6AT, UK

ABSTRACT

BIMET was a European programme concerned with the structural integrity of components containing dissimilar metal welds. Led by EDF, the BIMET group was composed of eight European partners. Working under the Fourth Framework programme of Nuclear Fission Safety of the European Atomic Energy Community (EURATOM), the group has made significant progress in developing analytical methods for assessing defect behaviour in weldments joining ferritic and austenitic components. These developments have taken place with reference to two benchmark tests. Each test featured a dissimilar metal weld joining austenitic and ferritic pipe material, with the whole assembly tested in four point bending at ambient temperature. An external EDM (electro-discharge-machine) notch was inserted into the SA308 stainless steel weld metal buttering layer, within 2 mm of the ferritic steel pipe and in a region of high weld residual stress. The defect orientation led to combined Mode I and II loading at the crack tip. This paper presents a detailed R6-based analysis of the BIMET 01 and 02 tests, with particular emphasis on the role of residual stress on crack initiation and subsequent crack growth behaviour. The results demonstrate the importance of taking proper account of residual stresses within structural integrity assessments.

KEY WORDS

Dissimilar metal welds, residual stresses, R6, structural integrity, defect assessment

INTRODUCTION

The BIMET (Structural Integrity of Bi-Metallic Components) project was carried out for the European Commission under the Euratom 4th Framework Programme. Eight European partners were involved: EDF (Project Co-ordinator), JRC-IAM Petten, AEA Technology, TWI, GKSS, VTT, Framatome, and CEA. The objective of the project was to contribute to the development and validation of analytical methods used to assess the behaviour of defects located at dissimilar metal welds (DMW). The principal focus was two large-scale benchmark tests, each featuring a 4-point bend test of a nominal 6-inch (152 mm) piping assembly, which contained a ferritic to stainless steel DMW, Figure 1. In each test, a pre-crack was machined within the ferritic/buttering layer to simulate PWR plant experience of cracking in components containing such welds.

Defects in DMWs provide significant challenges to integrity assessment procedures since they include a variation in material properties across the weld, mixed-mode loading and significant residual stresses. This paper presents the results from R6 analyses of the BIMET01 and 02 tests. The R6 procedure [1] includes guidance on the treatment of weld mismatch, mixed-mode loading and residual stresses in defect assessment. Analyses of these tests thus provide a valuable basis on which to validate R6.

BIMET01 AND 02 TESTS

The BIMET01 and 02 test assemblies consisted of 200mm long A508 ferritic steel and type 304 stainless steel sections joined via a DMW carried out to ASME specification, Figure 1. The outside diameter of the specimen was 168mm and the wall thickness (t) was 25mm. Straight-fronted, part-penetrating defects were inserted from the outer surface into the first buttering layer (309L) adjacent to the buttering/ferritic steel interface and inclined to run parallel to it, Figure 2. The defects were 13.6 and 9.2mm in depth for the BIMET01 and 02 specimens respectively. Other geometrical characteristics are included in Figure 2.

Tests were performed in four-point bending at ambient temperature in a 5MN test machine operating under displacement control. Figure 3 illustrates the moment, M_{app}, versus crack-mouth opening displacement (CMOD) behaviour of each test. BIMET01 achieved a maximum bending moment, M_{max}, of 180 kNm prior to unloading whilst that for BIMET02 was 220 kNm. The initiation moment, M_i, was estimated from electrical potential drop data as between 142 and 154 kNm for BIMET01 (Figure 4) and between 155 and 170 kNm for BIMET02. Subsequent ductile tearing of up to 1.4 mm in BIMET01 and up to 8.7 mm in BIMET02 occurred along the buttering/ferritic steel interface. A comprehensive evaluation of residual stresses was performed by measurements of residual strains based on neutron diffraction, Figure 5, and numerical simulation of the DMW fabrication.

R6 ANALYSES

The R6 procedure [1] provides a basis for defect assessment with respect to two failure conditions: fracture and plastic collapse. Assessments are performed with respect to a failure assessment diagram (FAD), in which the abscissa is defined as $L_r = M_{app}/M_L$, where M_L is the limit moment. Under primary and secondary loading, the ordinate, K_r, is defined as

$$K_r = \left\{\left(K^P_{eff} + K^S_{eff}\right)/K_{mat}\right\} + \rho \qquad (1)$$

where K^P_{eff} and K^S_{eff} are effective stress intensity factors, accounting for mixed-mode loading, under primary and secondary loading respectively; K_{mat} is the material fracture toughness and ρ is a plasticity correction parameter. On the FAD, the failure assessment point, plotted for the defect/structure of interest is compared with a failure assessment curve which defines the failure condition. The structure is deemed to be "safe" when the assessment point is located inside the curve. The following sub-sections describe the basis of the R6 analyses performed for the BIMET01 and 02 tests.

Evaluation of K^P_{eff} and K^S_{eff}

The variation of K^P_{eff} with M_{app} was calculated using a weight function solution for a pipe containing an external semi-elliptical defect [2]. This method yielded $K^P_{eff} = 0.635M_{app}$ for BIMET01 and $K^P_{eff} = 0.486M_{app}$ for BIMET02, with K^P_{eff} in MPa$\sqrt{m}$ and M_{app} in kNm. A more accurate solution was obtained from a large-strain elastic-plastic finite element analysis (FEA) of BIMET01 [3]. This gave $K^P_{eff} = 0.652M_{app}$. Since a FEA of BIMET02 was unavailable, the weight function result was scaled by the ratio of BIMET01 solutions to provide a more accurate solution for this test. The value of K^s_{eff} was calculated using measured residual stress data, Figure 5, in conjunction with tabulated weight function coefficients [2]. The Mode I, II and III stress intensity factors thus calculated were combined to give K^s_{eff}

using usual sum-of-squares relationship. This gave K_{eff}^{s} equal to 33.0MPa√m for BIMET01 and 29.2MPa√m for BIMET02.

Evaluation of ρ

The plasticity correction ρ was calculated according to the procedure set out in R6 Section II.6 [1]. Here, ρ is defined according to the following expression:

$$\rho = \Psi - \Phi\left\{\left(K_I^s / K_p^s\right) - 1\right\} \qquad (2)$$

where Ψ and Φ are tabulated functions of the parameter $K_p^s/(K_I^P/L_r)$, K_p^s is the effective stress intensity factor due to secondary loading, K_I^P and K_I^s are the Mode I stress intensity factors due to primary and secondary loading respectively.

Evaluation of K_{mat}

The results of three Mode I fracture toughness tests for the 308L weld metal buttering were used to define a power-law J R-curve as: $J = 262\ \Delta a^{0.4342}$ [4], with J defined in kJ/m^2 and ductile crack extension, Δa, defined in mm. The initiation condition was considered to lie between Δa = 0.2 and 0.5mm, i.e. between J = 130 and 194 kJ/m^2. These values of J were converted to K using the plane strain small-scale yielding expression $K^2 = E'J$, where $E' = E/(1-\nu^2)$, E being Young's modulus and ν being Poisson's ratio. R6 assessments were thus carried out with K_{mat} = 156MPa√m (Δa = 0.2mm) and 190MPa√m (Δa = 0.5mm).

Evaluation of limit moment

The limit moment, M_L for each test was derived in three ways. First, the solution for a part-penetrating circumferential defect under bending in Miller's Limit Load Handbook [5] was used. Here, the limit moment is defined as:

$$ML = m \cdot (4R^2 t\sigma_y) \qquad (3)$$

where m is a function of the crack geometry. The limit moment was calculated with the yield stress, σ_y, equal to that of the 304 base material, giving M_L = 128kNm for BIMET01 and 139kNm for BIMET02. Secondly, a FEA was used to calculate M_L for BIMET01, based on the strength properties of the weaker type 304 stainless steel base material. The limit moment was calculated as 150kNm. This value was scaled by the ratio of Miller limit moments to give a value of 162kNm for BIMET02. Finally, using the ASME 'twice the elastic slope' method alongside a second FEA [2], the mismatch limit moment ($M_{L,mis}$) for BIMET01, incorporating all materials, was estimated to be 160 kNm. This result was again scaled by the ratio of Miller limit moments to give a value of 174kNm for BIMET02.

In the R6 analyses, the base material limit moment, $M_{L,b}$ was taken as either 128 or 150kNm and the mismatch limit moment, $M_{L,mis}$, as 160kNm for BIMET01. For BIMET02, $M_{L,b}$ was taken as either 139 or 162kNm and the mismatch limit moment, $M_{L,mis}$, as 174kNm.

Weld mismatch

The effects of weld mismatch were assessed with reference to the procedures of R6 Section III.8. The stress-strain curve for the equivalent material was calculated using the ratio ($M_{L,mis}/M_{L,b}$) and the 'mismatch' ratio $M = (\sigma_{y,w}/\sigma_{y,b})$. Here $\sigma_{y,w}$ was referred to the 308L-buttering/filler weld, and $\sigma_{y,b}$ to the 304 base material. The ratio of the limit moments was 160/150 = 1.067, and M = 403/297 = 1.36. The resultant equivalent material curve was used to define an Option 2 curve.

Failure assessment curves
R6 assessments were performed with respect to three failure assessment curves: (i) Option 1 curve, (ii) Option 2 curve based on 304 material properties and (iii) Option 2 curve based on the equivalent material properties, Figure 6.

RESULTS

Assessment of crack initiation
BIMET01 (Figure 7): The Option 1 assessment for primary plus secondary loading using the Miller limit moment gives $112 < M_i < 123$kNm for $0.2 < \Delta a < 0.5$mm. This is significantly lower than the experimentally determined range. Reference to the limit moment derived by FE analysis gives M_i in the range 123 to 136kNm while reference to the Option 2 failure assessment curve indicates that the assessed initiation moment lies between 138 and 149 kNm. The equivalent material assessment gives an estimated initiation moment between 144 and 156kNm.

BIMET02 (Figure 8): The Option 1 assessment using the Miller limit moment gives $131 < M_i < 141$kNm for $0.2 < \Delta a < 0.5$mm. This is again lower than the experimentally determined range. Use of the limit moment derived by FE analysis gives M_i in the range 145 to 158kNm while reference to the Option 2 failure assessment curve indicates that the assessed initiation moment lies between 160 and 167kNm. The equivalent material assessment gives an estimated initiation moment between 168 and 175kNm.

Assessment of tearing instability
Tearing instability during each test was assessed via an R6 Category 3 analysis. The solutions for crack driving force and $M_{L,mis}$ were updated for crack growth (Δa) by scaling the original values ($\Delta a = 0$) in terms of the relevant K and limit moment solutions given in [2] and [5], respectively. Values of $K_{mat}(a+\Delta a)$ were based on the tearing toughness curve for the 308L material. The predicted instability moment was 159kNm for BIMET01 and 180kNm for BIMET02. These results underestimate the experimentally observed values of $M_{max} \sim 180$ and 200kNm, respectively.

DISCUSSION

The choice of limit moment has a noticeable influence on the assessed value of M_i. Use of the Miller solution provides a highly conservative assessment of M_i that is more than 20 % below the mean value deduced from EPD measurements. By comparison, use of the FEA solution gives a value of $M_{L,b}$ which is ~ 17 % higher than Miller's solution, and yields a value of M_i which is approximately 15 % below the mean value. The maximum assessed values of M_i correspond to the Option 2 analyses for an equivalent material. The assessments referenced to $J_{0.2}$ fall within the experimentally determined range.

It is evident that the limit moment behaviour of the DMW is controlled by the strength of the weaker material – i.e. the type 304 stainless steel. The effect of weld mismatch is determined primarily by the mismatch in strength between the 308L-buttering and filler weld and the 304 base material.

The choice of failure assessment curve (Option 1 vs. Option 2) has a significant influence on the assessed value of M_i. Whilst the Option 1 curve provides a value of $M_i \sim 15$ % below the mean experimental value, with the Option 2 curve the corresponding reduction is ~ 2 %.

The influence of using equivalent material properties rather than those of the weaker type 304 stainless steel was modest in the present work. A comparison of results from the various Option 2 analyses for primary + secondary loading suggests a 4 % increase in M_i that is mainly attributable to the increase in limit moment from $M_{L,b}$ to $M_{L,mis}$.

Lastly, the R6 analyses suggest that residual stress influenced crack initiation during both tests. This is despite the fact that assessed values of M_i correspond to values of L_r close to unity.

CONCLUSIONS

1. The choice of limit moment has a noticeable influence on the assessed value of M_i. The limit moment behaviour of the DMW is controlled by the strength of the weakest material.
2. The choice of failure assessment curve has a significant influence on the assessed value of M_i, with Option 2 curves providing less conservative assessments.
3. Residual stress influences the initiation of crack growth despite assessed values of M_i corresponding to $L_r \approx 1$ where the influence of such stresses would be expected to be small.
4. The influence of using equivalent material properties rather than those of the weaker type 304 stainless steel base material was found to be modest in the present work.
5. The R6 assessments of initiation (based on 0.2 mm tearing) and tearing instability were conservative with respect to the experimental results for both BIMET01 and 02 tests.

ACKNOWLEDGEMENTS

This work was undertaken within the context of a Euratom Framework Programme 1994-1998. The authors gratefully acknowledge funding from the CEC as well as matching and supplementary funding from the UK Health and Safety Executive. The technical contribution of all BIMET partners and also Dr R A Ainsworth (British Energy Generation Ltd) is also acknowledged.

REFERENCES

1. R/H/R6 Revision 4, “Assessment of the integrity of structures containing defects”, British Energy Generation Ltd, May 2001.
2. B Drubay, S Chapuliot and M Lacire, “A16: Guide for defect assessment and leak before break analysis”, CEA Report, 1999.
3. Goldthorpe, M. R. and Wiesner, C. S., “BIMET – Structural integrity of bi-metallic components: three-dimensional finite element analysis of test BIMET01”, TWI Report No. 8294/3A/99, 1999.
4. P Nevasmaa, “BIMET fracture toughness curves”, email with accompanying spreadsheet to BIMET Task Group 5 participants, VTT Manufacturing Technology, Espoo, Finland, 25 February 1999.
6. A G Miller, “Review of limit loads of structures containing defects”, Int. J. Pres. Vessels Pip, Vol. 32, pp. 197-327, 1988.

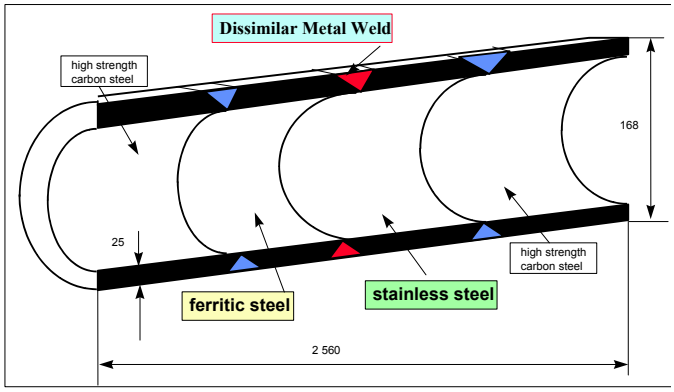

Figure 1: BIMET01 and 02 specimen geometry

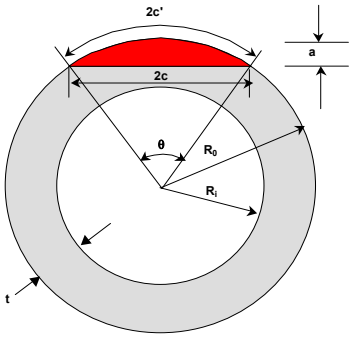

	BIMET01	BIMET02
R_0 (mm)	84	84
R_i (mm)	59	59
t (mm)	25	25
a_{actual} (mm)	13.8	9.28
a (mm)	12.5	8.33
a/ t	0.5	0.33
2c' (mm)	93	75.5
2c (mm)	88.2	73.0
θ (°)	63.3	51.5
R_i/ R_0	0.70	0.70
R_{mean} (mm)	71.5	71.5

Figure 2: BIMET01 and 02 defect geometry

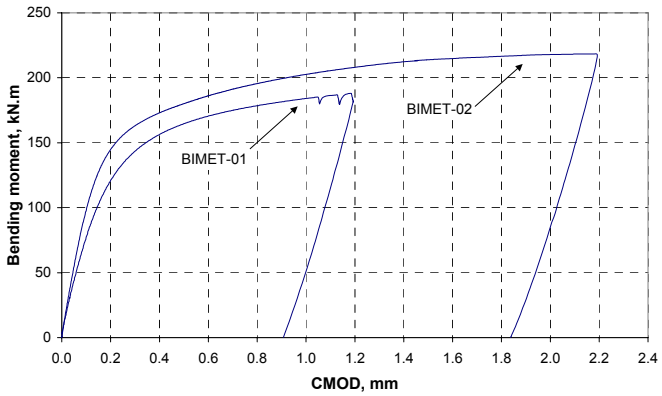

Figure 3: Load-displacement behaviour

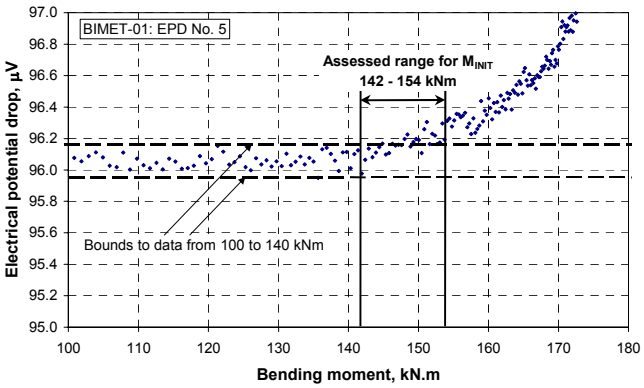

Figure 4: Assessment of initiation moment

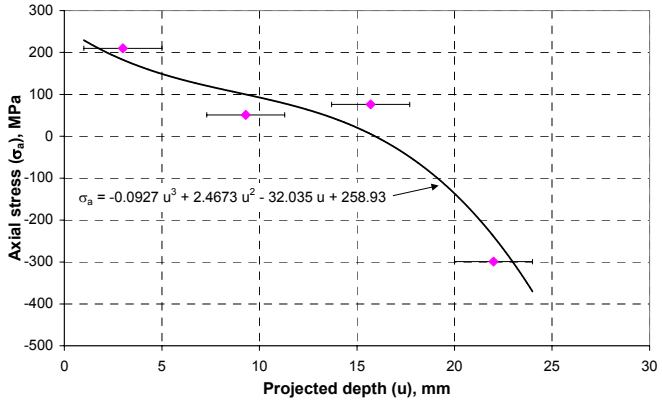

Figure 5: Axial residual stress profile

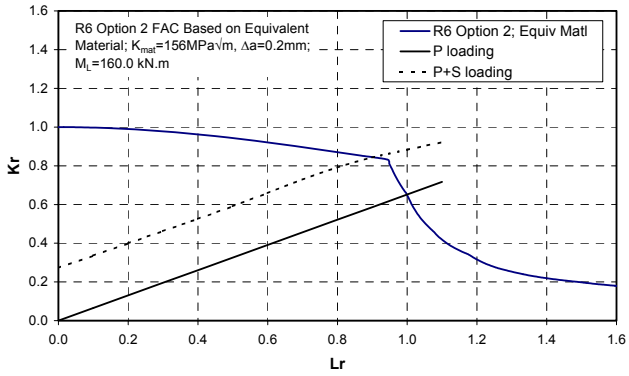

Figure 6: Option 2 FAD for BIMET01

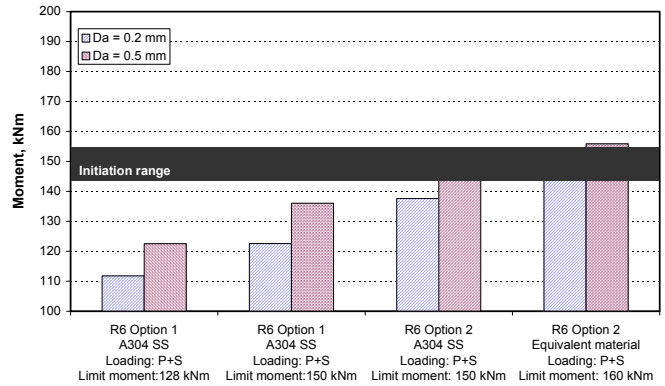

Figure 7: Summary of results of R6 analyses to calculate initiation moment: BIMET01

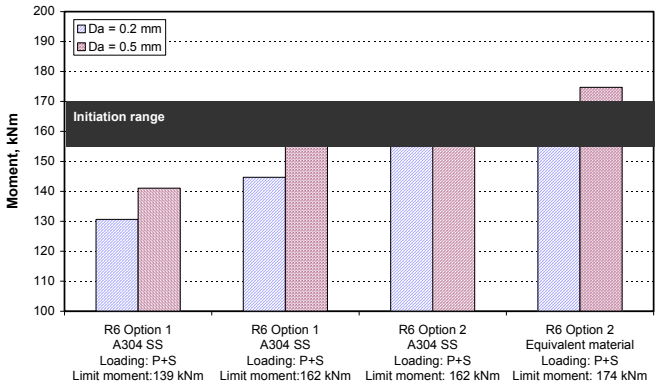

Figure 8: Summary of results of R6 analyses to calculate initiation moment: BIMET02

ORAL REFERENCE: ICF100855OR

INFLUENCE OF RESIDUAL STRESS ON SUPER-LONG LIFE FATIGUE PROPERTIES OF HIGH STRENGTH STEEL SNCM439

T. Matsumura, Y. Ochi, S. Yoshida and K. Masaki

Department of Mechanical Engineering and Intelligent Systems,
University of Electro-Communications,
1-5-1 Chofugaoka, Chofu-shi, Tokyo 182-8585, Japan

ABSTRACT

In recent years, we have been hopeful that life extension engineering will be established to enable the use of machines and structures beyond their design life. Therefore, it is necessary to investigate the fatigue properties of structural components in the super-long life range ($N \geq 1 \times 10^7$). In the case of high strength steels and surface hardened steels with improved strength properties, it has been reported that the *S-N* curve has a tendency to decrease again in the super-long life range ($N \geq 1 \times 10^7$). However, the fatigue fracture mechanism has not yet been clarified.

In the present paper, in order to investigate the fatigue properties of high strength steels and surface hardened steels in the super-long life range ($N \geq 1 \times 10^7$), cantilever type rotating bending fatigue tests were carried out for the SNCM439 high strength steel. For the fatigue tests, the grinding specimen that the notch surface was finished by grinding with a #100 grindstone and the electro-polishing specimen that the notch surface of grinding specimen was removed up to 30μm deep by electro-polishing were prepared. We investigated the fatigue properties and the fracture crack origins. In addition, the residual stresses of surface and inside of specimen were measured using an X-ray diffractometer.

On the notch bottom surface of specimen, the residual stresses in the axial direction and the circumferential direction were -571MPa and -433MPa respectively. It was seen that the compressive residual stress in the axial direction and the circumferential direction on the notch bottom surface rapidly decreased in the section to the about 8μm from the surface and that it approached about -100MPa in the depth over 8μm.

The *S-N* curve clearly has a tendency to decrease again in the super-long life range ($N \geq 1 \times 10^7$) for two kinds of specimen, as previously reported by many researchers. When the results of fatigue test by the grinding specimens are compared with that by the electro-polishing specimens, it is found that the eletctro-polishing specimens are almost equal to the grinding specimen in the fatigue life.

From the results of the observations using a SEM, it was found that the fracture crack origins could be grouped into two classes, the ‘surface crack origin type’ which means that the fracture crack initiate at the grinding flaw on the specimen surface or the pit where the inclusion came off and the ‘internal crack origin type’ which means that the fracture crack initiate at the non-metallic inclusion inside the specimen and that a fish-eye area is found on the fracture surface.

ORAL REFERENCE: ICF100549OR

INFLUENCE ON LOW CYCLE FATIGUE PROPERTIES OF BOND COAT OXIDATION FOR A THERMAL BARRIER COATING

H. Brodin and S. Johansson

Department of Mechanical Engineering, Division of Engineering Materials,
Linköping University, SE-581 83 Linköping, Sweden

ABSTRACT

Influence on the LCF life of a Thermal Barrier Coating has been studied for an air plasma spray (APS) partially stabilised Zirconia (PSZ) top coat together with a NiCoCrAlY APS bond coat sprayed onto a nickel base superalloy. The study has been focused on LCF tests for specimens pre-oxidised to different TGO (thermally grown oxide at the interface between top and bond coat) thicknesses. Comparisons of fatigue behaviour between coated and uncoated materials for both as received and heat treated material has been evaluated. Materials used in the present study are ZrO_2 + 8w/oY_2O_3 top coat, Ni171 bond coat and H230 substrate. The results show a decreasing trend regarding fatigue life when pre-oxidised material is tested. It is also shown that an applied bond coat slightly reduces the fatigue properties in comparison to the uncoated substrate. At 850°C the effect on fatigue life of an oxidised bond coat is significant but at 500°C no large variations regarding fatigue life can be observed. For all cases the Coffin-Manson expression for fatigue life can be used since delamination or spallation do not occur. It is also shown that the crack initiation sites mainly are located to the interface between top coat and bond coat. Regarding the substrate different mechanisms govern the hardening or softening behaviour at various temperatures. At lower temperatures dislocation movement is hindered by small precipitates in the Ni-bas superalloy but at 850°C the dislocations can cross slip and pass by without hardening behavior of the material.

KEYWORDS

thermal barrier coating, NiCoCrAlY, oxide growth, low cycle fatigue, Coffin-Manson law

INTRODUCTION

Thermal barrier coatings (TBC) are important for gas turbine manufacturers when increased efficiency and lower emissions are required from the users of such systems in land based applications. The application in this case is coatings used in gas turbines for power generation. Thermal barrier coatings are already used in aeroplane engines, where military aircraft dominate the market. The differences between land based and airborne turbines are cycle time, fuel type and inspection intervals. These factors sets stronger demands with respect to long time stability and integrity for the materials used in coating systems for land based gas turbines. Therefore ongoing projects aim to develop durable TBC systems and reliable models regarding TBC life in order to fully be able to take advantage of the benefits a TBC can give.

A thermal barrier coating system is normally composed of two layers on a substrate. The top coat is applied in order to serve as a thermal insulator for the underlying material. The drawback is that APS

Zirconia, which is used for its low thermal conductivity, serves as an excellent diffusion path for oxygen. Therefore an oxide forming material has to be applied below the ceramic top coat. This layer is normally composed of one or more of the metals Ni or Co together with Cr, Al and also rare earth metals as Y. Other combinations are present. The alloy can be sprayed in air or vacuum or deposited in other ways on the metallic substrate. The substrate is the load carrying component. It can be a combustor, vane or a turbine blade. The top coat can have a thickness of 350µm up to 2mm, whilst the bond coat normally is sprayed to a thickness between 100µm and 200µm.

The aim of the present study is to clarify what influence a thermal barrier coating will have on the fatigue life for a nickel base superalloy. This is done for material pre-oxidised to interface TGO between 1 and 8 µm in order to achieve results valid for material subjected to conditions experienced in a gas turbine.

EXPERIMENTAL PROCEDURE

The experiments were performed on a material system built up of a 350µm thick PSZ top coat (ZrO_2 + 8w/oY_2O_3) and a 150µm thick bond coat (Ni171 – NiCoCrAlY) both air plasma sprayed onto a nickel base substrate (Haynes 230[1]), see figure 1. After coating at VOLVO AERO[2] the material was heat treated at 1000°C ± 5°C for times sufficiently long to produce thermally grown interface oxides with thickness between 1 and 8µm. Comparisons with previous studies made it possible to predict the oxide growth rates and thus the oxide thickness at different times of oxidation [1]. The material was heat treated in flowing air[3] at a flow rate of 0,5 l/min in order to get a predictable environment. Afterwards the oxide thickness was determined on cut and polished samples using an optical microscope. After heat treatment the material was fatigue tested together with non heat treated material.

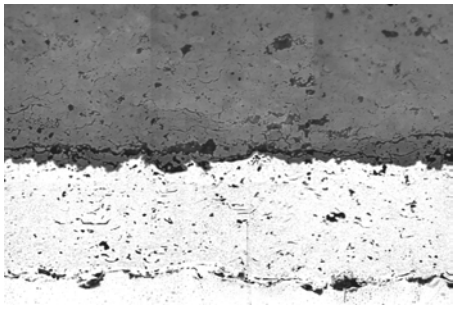

Figure 1: Polished cross section over an air plasma sprayed thermal barrier coating used in the present study. The upper (dark grey) layer is the ceramic top coat. In the middle the metallic NiCoCrAlY bond coat is found. At the bottom the interface between bond coat and the nickel base substrate can be seen. The TC has inherent defects, pores. These are the black spots in the dark grey layer. In the BC an oxide network is present. This is due to the spray process when the molten metal drops are in contact with the surrounding air. Magnification 150x.

Cyclic tests were performed in an MTS 160 kN test rig fitted with the INSTRON 8800 controller, alignment equipment and LCF software together with an MTS high temperature furnace and high temperature extensometer. In order to control the temperatures an external signal from the thermocouple was logged into the computer system via an Eurotherm retransmitter. Low cycle fatigue tests were then performed in strain controlled mode with control of total strain between 0,4 and 1,2%, R = -1 and a strain rate of 0,4 / min. For a total strain range of 0,008 the cyclic frequency is approximately equal to 0.5 Hz. Thermocouple mounting and LCF sample geometry were performed in accordance with ASTM specifications [2, 3]. After testing the specimens were cut and polished for examination with light microscopy and scanning electron microscopy (SEM).

[1] From Haynes International, USA
[2] VOLVO AERO, Trollhättan Sweden. http://www.volvo.com/aero/default
[3] *Technical air,* Trade mark of Air Liquide

RESULTS

Oxide growth

The oxides formed during heat treatment in the present study consist mainly of Alumina. Some Ni, Cr and Co can also be seen in the outer layers for longer oxidation times. This mixture of oxides tends to grow faster than pure Alumina. It has earlier been shown that the oxide formed with time is of spinel type [1, 4]. The oxide thickness after initial oxidation is shown in Table 1.

TABLE 1
RESULTS FROM INITIAL HEAT TREATMENT / OXIDATION OF THE TBC SYSTEM.

Time @ 1000°C [hrs]	Approximate oxide thickness [µm]
0	0,5
100	1
250	4
400	6
1000	8

Fatigue Behaviour

Uncoated material

Uncoated material was tested in order to act as a reference for comparison to the TBC-layer added to a nickel base alloy. The response of HAYNES 230 to mechanical cycling is shown in figure 2. Life responses at the test temperatures are reported in figure 3 and 4. For comparison a separate LCF-test has been performed at room temperature. At this low temperature the material shows a softening behaviour and a fatigue life tenfold higher than at the elevated temperatures.

The hardening response of uncoated material is shown in figure 5. The hardening exponent at 500°C is achieved by fitting a straight line to the measurement data in figure 4. The strain hardening exponent (according to Rahmberg – Osgoods expression) is found to be $n_f = 0,17$. In figure 4 the elastic and inelastic behaviour for HAYNES 230 at 500°C is presented together with regression equations, i.e. data to a Coffin-Manson type of equation.

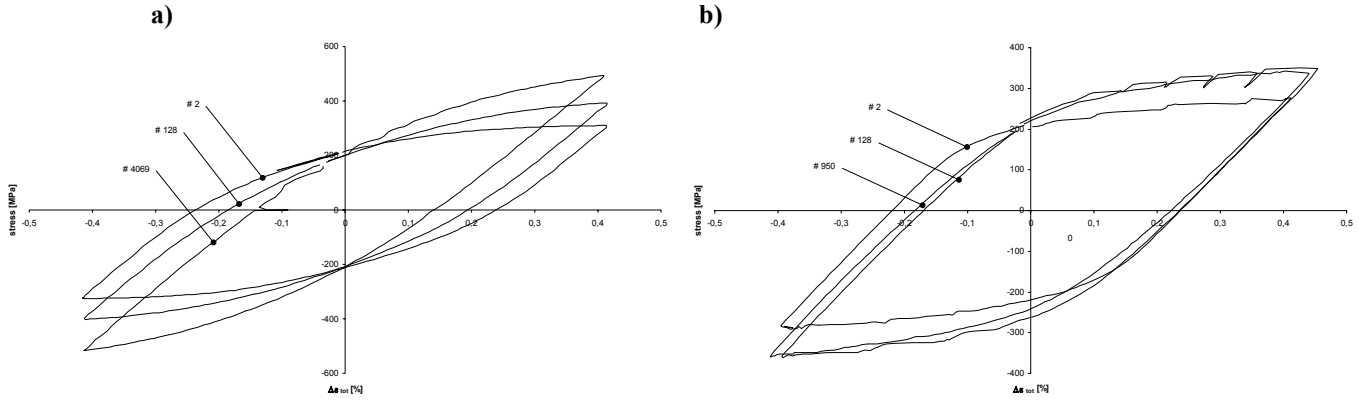

Figure 2: Hysteresis loops for HAYNES alloy 230 at a) 500°C and b) 850°C. It can be seen that the material shows a pronounced hardening behaviour at 500°C whilst at the higher temperature the the hardening of the alloy is not as striking.

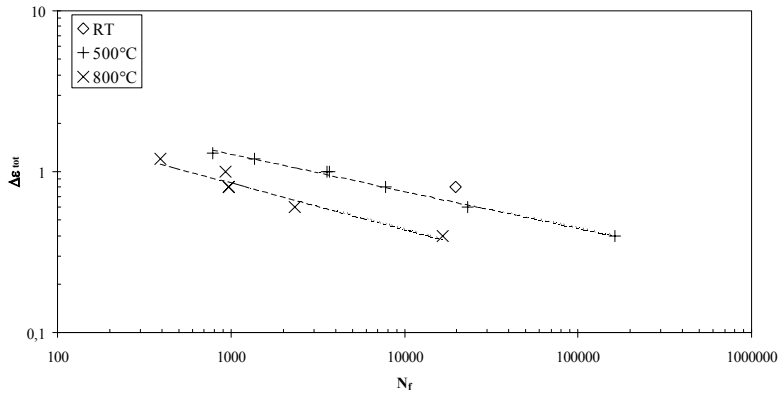

Figure 3: Plot of results for fatigue life versus total strain range of HAYNES alloy 230 at 500°C and 850°C. As a comparison measurements performed at room temperature has been added for $\Delta\varepsilon_{tot} = 0.8\%$.

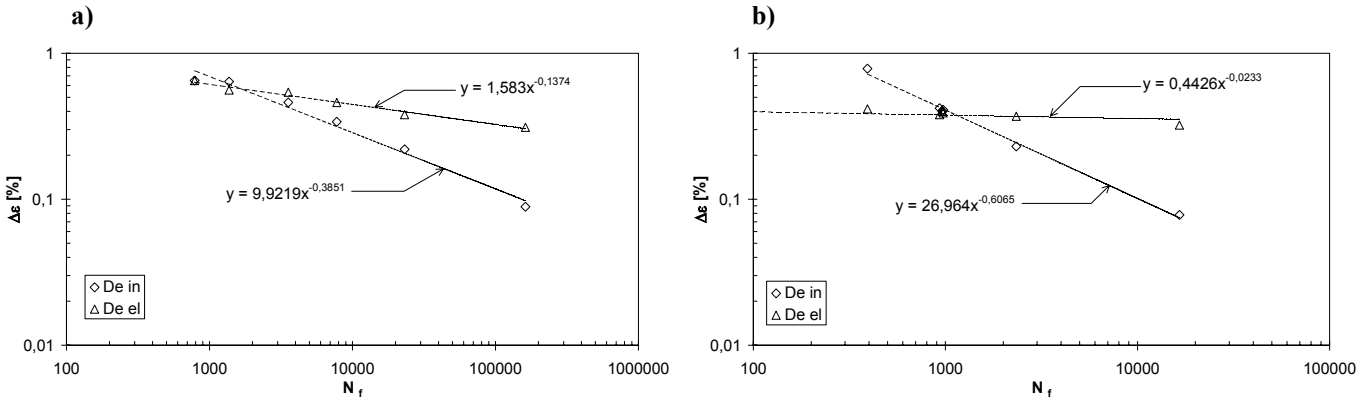

Figure 4: Elastic and inelastic behaviour for uncoated material at a) 500°C and b) 850°C.

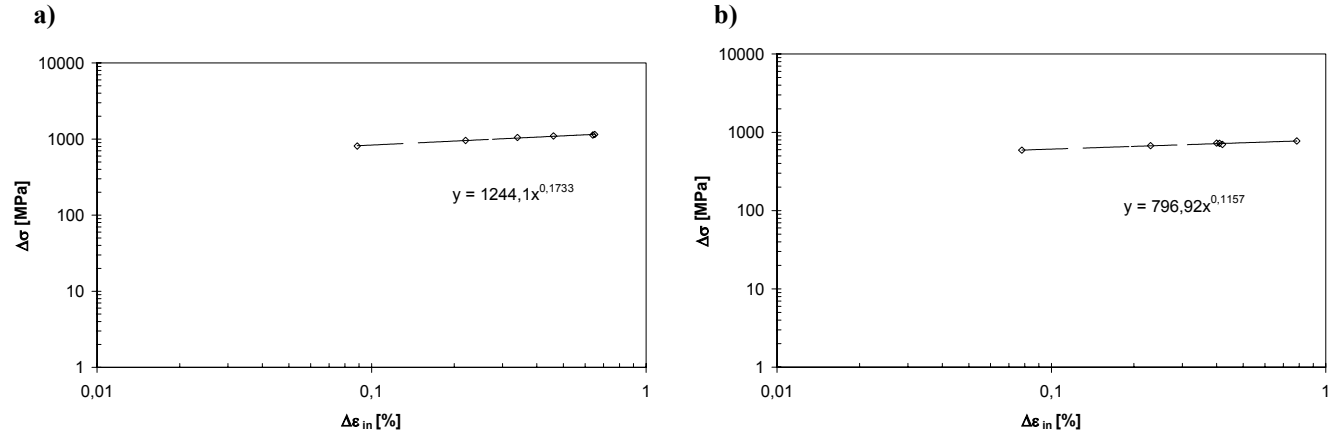

Figure 5: Cyclic stress versus strain response at a) 500°C and b) 850° for HAYNES alloy 230.

At850°C the hardening behaviour is not as significant as for the 500°C case. An analysis similar to the previous case will give a hardening exponent $n_f = 0.116$.

APS PSZ / NiCoCrAlY – coated material

For the coated nickel base alloy the change of fatigue life at $\Delta\varepsilon_{tot} = 0{,}4$ and R = -1 after pre oxidising for times up to 1000h is presented in figure 6. The figure shows data for both test temperatures in the present study (500°C and 850°C). In the figures four different states of TGO thickness are represented. The aim of the heat treatment has been to make an evaluation possible of influence from growth of interfacial and internal oxides on fatigue life. It can be seen that the influence of thermally grown oxides is significant only

at 850°C. At the lower test temperature the results from mechanical testing do not show a clear trend for fatigue life as a function of TGO thickness.

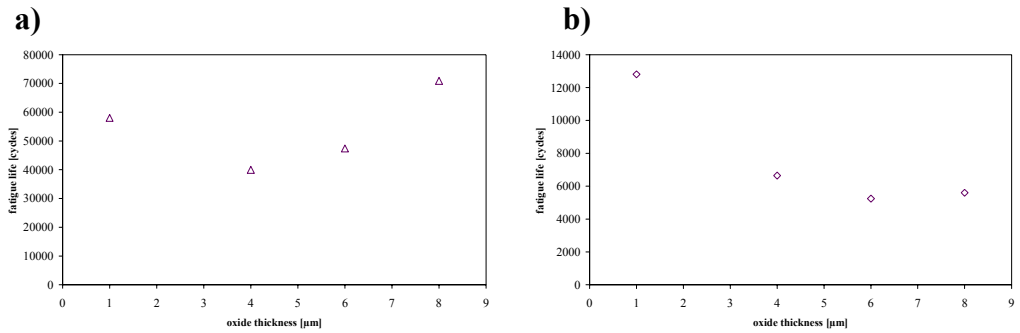

Figure 6: Results from fatigue tests of pre-oxidised TBC on H230. The tests are performed with $\Delta\varepsilon_{tot} = 0,4$ and R = -1. Data stem from LCF tests at a) 500°C and b) 850°C.

Over the test range the fatigue life for uncoated material is superior that of TBC – coated material. This is valid both for variations in temperature and strain range. In most cases when a coating has been added the fatigue cracks initiate at the top coat / bond coat interface or within the bond coat. These findings are in accordance with what previously has been reported [5]. Typical appearance of interface cracks created at the two test temperatures is shown in figure 7. Cracks initiated in the bond coat propagate into the substrate and eventually causes specimen failure after successive load drop for constant strain amplitude. It has earlier been suggested [6] that large compressive stresses are believed to cause buckling of the TBC system if interface cracks are present. In this study no such phenomena are observed.

DISCUSSION

Fatigue of uncoated material

An attempt has been made to evaluate the fatigue performance of the nickel base alloy. It was shown that the material well follows a strain based fatigue model of Coffin-Manson type. This is valid for both coated and uncoated material. For the case of uncoated HAYNES 230 the comparison between model and test will be shown in figure 8. The agreement is good for strain ranges within the frame of the test. Strain ranges larger than those evaluated here are not of great interest, since the fatigue life at higher strain ranges and high temperatures is poor.

The material displays a hardening behaviour at 500°C. At 850°C the hardening behaviour is not as dominant. TEM studies show that the hardening at the lower temperature is due to dislocation pile up at small carbides. A study of material strained at the higher temperature shows a much less dense dislocation structure. Obviously the dislocations now can cross slip and by pass the small particles. In addition some growth of the existing carbides will occur during the fatigue cycle which will reduce the effect of hardening due to entangled dislocations.

Fatigue of coated material

Several authors have discussed the influence of oxides on the integrity of a TBC [6, 7, 8]. Oxidation of thermal barrier coatings is detrimental for the integrity of such a system. Exposure to oxide rich environments at high temperatures for long times causes degradation of the initially aluminium rich bond coat. Earlier studies have shown this and the reason is a combination of aluminium diffusion inwards into the substrate and aluminium consumed at the interface between bond and top coat [1, 9]. The reason for failure is said to be a change in oxide type since the Alumina will be mixed with nickel, cobalt and chromium rich oxides. These oxide types have lower tensile strength than Alumina and also poor fracture toughness.

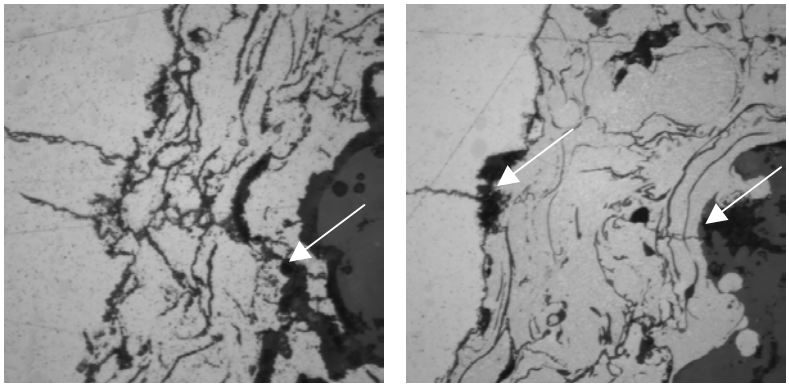

Figure 7: Cut sections of fatigue tested samples. The cracks originate at the interface between top and bond coat or at oxide particles within the bond coat. After this they grow and propagate into the substrate. Arrows indicate origin of cracks.

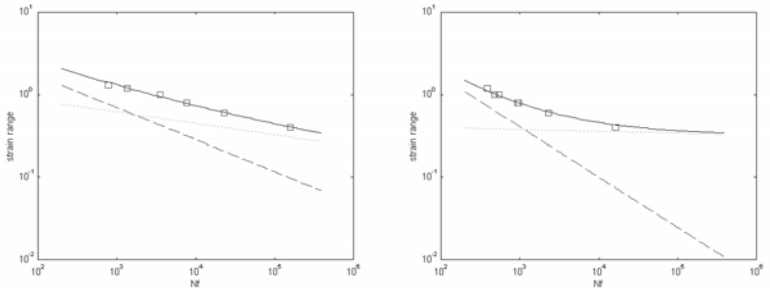

Figure 8: Comparison between model and experiments for a Coffin-Manson type of strain based low cycle fatigue law. Left figure represents 500°C, right 850°C. Open squares indicate experiments, dashed line elastic strain and dash dotted line represents inelastic strains.

After growth of a TGO layer stresses perpendicular to the interface arise, which will be harmful for the coating. The stresses are largest at heating and cooling. Simulations has been performed to show this [10]. The present investigation shows that for compressive stresses in the axial direction, no delamination cracks arise. Probably larger compressive axial stresses need to be present in order to really observe the effect of the low strength oxide types. If the coating system instead had been subjected to thermal cycling then the change in oxide composition would probably have had a detrimental negative effect on fatigue life. This would then also apply to thermomechanical fatigue.

It was earlier shown that the influence of bond coat oxidation on fatigue life was larger at 850°C than at 500°C. This might be explained by the brittle to ductile transition that takes place between 500 and 800°C [11] for the bond coat used in the present study. At the lower temperature the bond coat has mechanical properties more like the oxide since both are brittle. When the temperature is raised the bond coat behaves in a ductile manner and it can be suspected that the by temperature introduced mismatch between the oxide and the metallic bond coat promotes crack initiation.

By adding the TBC to the substrate the curves in figure 8 will be shifted to lower lives. The effect of an added coating is largest for low strain ranges. At high $\Delta\varepsilon$ the measurements from coated material seem to converge with results for the uncoated superalloy. The influence of an added coating is large for low $\Delta\varepsilon$. These findings have also been found by others [12]. This might be influenced by the fact that the fatigue life is more sensible to surface roughness when the strain or stress amplitude is low. In this particular case a coating has been sprayed onto a shot peened surface. This means that both the interface between substrate and bond coat as well as the one between bond coat and top coat is highly irregular. After oxidation the situation might be even worse, since oxide intrusions or protrusions might form at interfaces as the TGO grows thicker.

CONCLUSIONS

In the study a nickel base superalloy has been coated with APS TBC and the effect of this procedure has been investigated. The results can be summarised in the following points:

- For uncoated material the strain hardening exponent is found to be 0,17 at 500°C and 0,12 at 850°C.
- Addition of a thermal barrier coating onto a nickel base superalloy causes fatigue life to decrease for the material system.
- The crack initiates in the bond coat and propagates into the substrate.
- Heat treatment of the material system causes the bond coat to oxidise. The oxidation takes place both at the interface between top- and bond coat and within the bond coat itself. The later is mainly due to that an oxide network is present in the bond coat after manufacturing due to the spray process.
- The oxidation is responsible for the lower resistance to fatigue crack initiation and propagation. When radial fatigue cracks are present these are initiated in the bond coat and propagate into the substrate.
- Severe delamination cracks can not be observed after LCF testing, even though there seem to be some delamination at the interface oxides.
- It is possible to include the lowering of the fatigue life due to bond coat oxidation in a Coffin-Manson type of expression.

ACKNOWLEDGEMENTS

The authors gratefully acknowledge the support provided by ALSTOM POWER Sweden and ELFORSK through the grant KME706.

REFERENCES

1. Brodin, H. and Ericsson, T. *Accepted for publication in HTM*.
2. ASTM E633-95 Standard guide for use of thermocouples.
3. ASTM E606-92 Standard practice for strain controlled fatigue testing.
4. Lee, E. Y. and Sisson, R. D., (1994). In*: Thermal Spray Industrial Applications. Proceedings, 7th National Thermal Spray Conference*. pp.55-59.
5. Li, X. H. et.al. (1997) In: *Sixth International Conference in the Series "Engineering the Surface"*, pp. 141-156.
6. Choi, S. R., Hutchinson J. W. and Evans A. G. (1999) *Mech. of Mater*. 31, pp. 431-447.
7. Tzimas E. et.al. (2000) *Acta Mater*. 48, pp.4699-4707.
8. Rabiei, A. and Evans, A. G. (2000). *Acta Mater*. 48, pp. 3963-3976.
9. Shillington, E. and Clarke, D. (1999). *Acta Mater*. 47, pp. 1297-1305.
10. Jinnestrand, M and Sjöström, S. (2001) *Surf. Coat. Tech*. 135, pp. 188-195.
11. Ashok, K. R., Steinbach, R. W. (1999). *J. Eur. Ceram. Soc*. 19, pp. 2097-2109.
12. Bicego, V., Bontempi P. and Taylor, N. (1998). In: *Low cycle fatigue and elasto-plastic behaviour of materials*, pp. 137-142.

Inhomogeneity effects on crack growth

N. K. Simha[1], F. D. Fischer[2] & O. Kolednik[3]

[1] Department of Mechanical Engineering, University of Miami, P.O. Box 248294, Coral Gables, FL 33124-0624, USA
[2] Institute of Mechanics , Montanuniversität, Franz-Josef-Straβe 18, A-8700 Leoben, Austria
[3] Erich Schmid Institute of Materials Science, Austrian Academy of Sciences and Institute of Metal Physics, University of Leoben, Jahnstrasse 12, A-8700 Leoben, Austria

ABSTRACT

Functionally gradient and composite materials considerably enhance our ability to tailor material properties. However, the inherent inhomogeneities pose new problems for fracture studies of these materials. This article discusses the evaluation of the effect of inhomogeneities on the crack-tip driving force in general inhomogeneous bodies and reports results for bimaterial composites. The theoretical model, based on Gurtin's configurational forces approach, makes no assumptions about the nature of the inhomogeneities or the constitutive properties of the materials. The effect of inhomogeneities on the crack-tip driving force is found by evaluating the difference between the J-integral on a contour close to the crack-tip and the J-integral on a contour in the far-field in a two-dimensional setting.

KEYWORDS

Inhomogeneous materials, functionally gradient materials, composites, crack-driving force, J-integral.

INTRODUCTION

Recent experiments indicate that it is possible to arrest the growth of fatigue cracks. Using bimaterial steel specimens, Suresh et al. [1] have demonstrated that cracks on the side with the lower yield stress seem to stop growing as they approach the bimaterial interface, whereas cracks in the higher yield stress side grow through the interface. Such measurements indicate that it is important to understand the influence of material inhomogeneities on crack growth. Composites and graded materials, which are invariably inhomogeneous, are being increasingly used in engineering applications, and so this issue is of relevance to applications.

One way in which inhomogeneities can influence crack-growth is by altering the nature of the crack-tip stress field. For instance, cracks parallel to a bi-material interface may either grow towards the interface or away from it [2, 3] (kindly see Kolednik [4] for a more comprehensive review). The goal of this article is to examine if there are additional ways in which the inhomogeneities can influence crack growth. We show that the energy release rate is different at the crack-tip and in the far-field, when inhomogeneities are present, and this is a second way in which inhomogeneities can influence crack growth.

CRACK-TIP DRIVING FORCE

The model evaluates the effect of inhomogeneities by finding the difference between the J-integral on two contours - one close to the tip and another along the specimen boundary. The calculation is done in two dimensions and follows Gurtin's configurational forces approach [5, 6]. Since crack growth corresponds to the motion of the crack-tip in the reference configuration, it is best to distinguish the reference and deformed configurations. Hence results are first obtained in a finite deformation setting. Linearized versions are also reported, since the infinitesimal strain setting is widely used in fracture mechanics. For brevity, we only outline the model and refer the reader interested in a full derivation to [7].

In the configurational forces approach, two systems of forces are introduced: the classical deformational forces that act in the current configuration (such as gravity) and a new system of forces called configurational forces that act in the reference configuration. The configurational forces are responsible for kinematic changes in the reference such as the propagation of phase boundaries, thin-film growth and motion of the crack-tip T. Consequently there are separate balance laws for the deformational and configurational forces. Neglecting inertia and heat transfer, we consider the following mechanical setting. In the bulk we choose a deformational stress $\mathbf{S}$ (Piola-Kirchoff), a configurational stress $\mathbf{C}$ and a configurational force $\mathbf{f}$. In addition, a configurational force is taken at the crack-tip $\mathbf{f}_T$.

Consider a region $\mathcal{D}$ containing the crack-tip. The balance of deformational forces requires that

$$\int_{\partial\mathcal{D}} \mathbf{S}\mathbf{n}\, da = \mathbf{0} \qquad \text{for every region } \mathcal{D}$$

where $\mathbf{n}$ is the normal to the boundary $\partial\mathcal{D}$. Note that the only deformational force is due to the contact force from the bulk stress $\mathbf{S}$ acting on the boundary $\partial\mathcal{D}$. On the other hand, the configurational contact force, arising from the bulk stress $\mathbf{C}$ acting on $\partial\mathcal{D}$, the configurational body force as well as the configurational crack-tip force act on the region $\mathcal{D}$. Thus the balance of configurational forces requires that

$$\int_{\mathcal{D}} \mathbf{f}\, da + \int_{\partial\mathcal{D}} \mathbf{C}\mathbf{n}\, dl + \mathbf{f}_T = \mathbf{0}$$

for every region $\mathcal{D}$.

Since the bulk stresses can be singular at the crack-tip, we need to be careful in localizing these balance laws. We remove a circle $\mathcal{B}_r$ of radius r centered at the crack-tip, apply the usual divergence theorem in the domain $\mathcal{D}(t)\backslash\mathcal{B}_r$ and then take the limit $r \to 0$. Please see equations (A1) and (A2) of [8] for details. One can show that the deformational and configurational force balances localize to

$$\nabla\cdot\mathbf{S} = \mathbf{0}\,, \qquad \nabla\cdot\mathbf{C} + \mathbf{f} = \mathbf{0} \quad \text{in the body} \tag{1}$$

$$[[\,\mathbf{S}\,]]\mathbf{p} = \mathbf{0}\,, \qquad [[\,\mathbf{C}\,]]\mathbf{p} = \mathbf{0} \quad \text{on the crack face} \tag{2}$$

$$\lim_{r\to 0}\int_{\partial\mathcal{B}_r} \mathbf{S}\mathbf{n}\, dl = \mathbf{0}\,, \qquad \lim_{r\to 0}\int_{\partial\mathcal{B}_r} \mathbf{C}\mathbf{n}\, dl + \mathbf{f}_T = \mathbf{0} \quad \text{at the crack-tip} \tag{3}$$

Here $\mathbf{p}$ is a normal to the crack (pointing, for instance, from the bottom to the top face) and $\mathbf{n}$ is the outward normal to the boundary of the disk $\partial\mathcal{B}_r$. Equation $(1)_1$ in the bulk is the familiar equilibrium equation of continuum mechanics. Equation $(2)_1$ is trivially satisfied since the crack faces are traction free. The limiting value of the singular bulk stress vanishes at the tip $(3)_1$.

The local forms of the configurational force balance are necessary for finding the crack-tip driving force and the effect of inhomogeneities. It can be shown that the configurational stress in the bulk is nothing but the Eshelby tensor [5]

$$\mathbf{C} = \phi\mathbf{I} - \mathbf{F}^T\mathbf{S}, \tag{4}$$

where ϕ is the stored energy and $\mathbf{F}$ is the deformation gradient. Knowing this we can evaluate the configurational body force $\mathbf{f}$ and the configurational crack-tip force $\mathbf{f}_T$ from relations $(1)_1$ and $(3)_1$ respectively.

The dissipation Γ is defined as the difference between the rate of working and the rate of change of the Helmholtz free energy. The crack-tip dissipation Γ_T can be identified as the limiting value of the dissipation of the region $\mathcal{B}_r$ in the limit as the radius $r \to 0$ [9]. Based on certain conditions on the energy density ϕ, which are satisfied by the linear elastic energy, for instance, Gurtin and Podio-Guidugli [9] show that the crack-tip dissipation is given by

$$\Gamma_T = \mathbf{v}_T \cdot \lim_{r \to 0} \int_{\partial \mathcal{B}_r} (\phi \mathbf{I} - \mathbf{F}^T \mathbf{S})\, \mathbf{m}\, dl \tag{5}$$

where $\mathbf{v}_T$ is the velocity of the crack-tip. The Clausius-Duhem version of the Second Law of Thermodynamics requires that the dissipation Γ_T be non-negative. Then by treating the crack-tip velocity as an internal variable, we can identify the *limiting value* of the integral in (5) as the crack-tip driving force. In fracture mechanics the energy dissipated per unit crack extension is commonly used, and the crack-tip driving force can be written as

$$J_T = \mathbf{e} \cdot \lim_{r \to 0} \int_{\partial \mathcal{B}_r} (\phi \mathbf{I} - \mathbf{F}^T \mathbf{S})\, \mathbf{m}\, dl \tag{6}$$

where the unit vector $\mathbf{e} = \mathbf{v}_T / |\mathbf{v}_T|$ lies along the direction of crack growth. The above integral is the J-integral of fracture mechanics [10]. We reiterate that assumptions about the specific form for the energy ϕ are not necessary to derive the driving force (6), hence it is valid even for non-linear hyperelastic and elasto-plastic materials.

EFFECTS OF INHOMOGENEITIES

Let $\mathcal{D}$ be the region between two circles - one close to the tip $\partial \mathcal{B}_r$ and another in the far-field $\partial \mathcal{B}_{far}$. Note that $\mathcal{D}$ does not include the crack or the disk $\mathcal{B}_r$. Thus only the configurational body force and contact forces act on this region, so the statement of configurational force balance for region $\mathcal{D}$ is

$$\int_{\mathcal{D}} \mathbf{f}\, da + \int_{\partial \mathcal{D}} \mathbf{C}\mathbf{m}\, dl = 0$$

The integral of the configurational contact stress can be decomposed as follows:

$$\int_{\partial \mathcal{D}} \mathbf{C}\mathbf{m}\, dl \; = \int_{\partial \mathcal{B}_{far}} \mathbf{C}\mathbf{m}\, dl \; - \int_{\partial \mathcal{B}_r} \mathbf{C}\mathbf{m}\, dl \; - \int_{C_D} [[\mathbf{C}]]\mathbf{p}\, dl$$

The balance law $(2)_2$ implies that $[[\mathbf{C}]]\mathbf{p} = 0$. In addition, using representation (4) and taking the limit as $r \to 0$, we get

$$\mathbf{e} \cdot \int_{\partial \mathcal{B}_{far}} (\phi \mathbf{I} - \mathbf{F}^T \mathbf{S}) \mathbf{m} dl - \mathbf{e} \cdot \lim_{r \to 0} \int_{\partial \mathcal{B}_r} (\phi \mathbf{I} - \mathbf{F}^T \mathbf{S}) \mathbf{m} dl = -\mathbf{e} \cdot \int_{\mathcal{D}} \mathbf{f} da\ . \tag{7}$$

Inhomogeneities can be modeled by making the free energy ϕ depend on the reference coordinate $\mathbf{x}$, and we take $\phi = \phi(\mathbf{F}, \mathbf{x})$. Note that the balance law $(1)_2$ and representation (4) imply that

$$\mathbf{f} = -\nabla \cdot (\phi \mathbf{I} - \mathbf{F}^T \mathbf{S})$$

Now using (i) $\mathbf{S} = \partial \phi / \partial \mathbf{F}$, (ii) the equilibrium condition $(1)_1$ and (iii) the fact that the order of partial differentiation can be interchanged, one can show that $\mathbf{f} = -\nabla_x \phi(\mathbf{F}, \mathbf{x})$. Thus, identifying the first term in (7) as the far-field J-integral, we get

$$J_{far} - J_T = \mathbf{e} \cdot \int_{\mathcal{D}} \nabla_x \phi(\mathbf{F}, \mathbf{x}) da \tag{8}$$

For homogeneous hyperelastic materials $\phi = \phi(\mathbf{F})$, and equation (7) would imply the path-independence of the J-integral. A similar expression can be obtained when the deformation is infinitesimal, in which

case (4) is replaced by $\mathbf{C} = \phi\mathbf{I} - \nabla\mathbf{u}^T\mathbf{T}$ where $\nabla\mathbf{u}$ is the displacement gradient and $\mathbf{T}$ is the Cauchy stress.

Elastic bimaterial composite. Now consider a composite made of two materials with different stiffness but the same Poisson's ratio. The linear elastic strain energy can be written as $\phi(\lambda, \nu, \mathbf{E}) = \lambda\psi(\nu, \mathbf{E})$ (e.g. see pg. 246 of Timoshenko [11]) where λ denotes the stiffness, ν the Poisson's ratio and the function $\psi \geq 0$ is independent of the stiffness. Thus $\nabla\phi = \psi\nabla\lambda$, and we can rewrite (8) as

$$J_{far} - J_T = \mathbf{e} \cdot \int_{s_1}^{s_2} \left[\psi \int \nabla\lambda \, dn\right] ds$$

where we parametrize the interface with the arc-length s and write the element of area $da = dsdn$ with n denoting the coordinate in the direction normal to the interface. Since the gradient is maximum in the direction normal to the interface, we obtain

$$J_{far} - J_T = (\lambda^+ - \lambda^-) \int_{s_1}^{s_2} (\mathbf{e} \cdot \mathbf{n}) \, \psi(\mathbf{E}) ds \tag{9}$$

where $\lambda^{\pm}$ correspond to the material on the two sides of the interface and the interface normal points from the $-$ to the $+$ side. [Visualizing the interface as being smeared over a distance Δn helps in obtaining (9)]. The limits of integration s_1 and s_2 correspond either to geometrical features of the specimen or can be fixed from the accuracy required for solutions in numerical calculations.

The effect of the jump in the stiffness at the bimaterial interface is given by relation (9). First, recollect that ψ is just the stored elastic energy divided by the stiffness, so it is non-negative. Hence the inhomogeneity will either aid or inhibit crack growth depending on the sign of $(\lambda^+ - \lambda^-)$; positive sign inhibits growth, while negative sign aids growth. Second, the inhomogeneity effects appear only when the bimaterial interface is close to the crack-tip. More precisely, according to the linear elastic K-field, ψ and the integral scale as $1/r$ where r is the distance from the crack-tip.

If the interface is flat and the crack is initially parallel to the interface, then $\mathbf{e} \cdot \mathbf{n} = 0$, and there is no contribution from (9). Notice that the integral in (5) is maximum in the direction $\mathbf{e}$, and this corresponds to the maximum value of J_T. If the presence of the interface causes the maximum dissipation to be in a direction different from the initial crack direction, then we may expect the crack to turn in that direction. Following this, the interface will influence crack growth through (9).

For a crack perpendicular to the bimaterial interface, $\mathbf{e} \cdot \mathbf{n} = 1$. If the crack is on the side with smaller stiffness ($\lambda^+ > \lambda^-$ so $J_{far} > J_T$), then the interface inhibits the crack growth and vice-versa. We now obtain a simple estimate for the integral in (9) by assuming that the usual K-field of LEFM can be used to evaluate the elastic energy. For plane strain [11]

$$\psi(\mathbf{E}, \nu) = \frac{1}{2(1+\nu)} \left[\frac{1-\nu}{1-2\nu}(\epsilon_x^2 + \epsilon_y^2) + \frac{2\nu}{1-2\nu}\epsilon_x\epsilon_y + \frac{1}{2}\gamma_{xy}^2\right]$$

where ϵ_x, ϵ_y are axial strain components and γ_{xy} is the engineering shear strain.

A stress formulation governs the crack-tip equilibrium problem, and solutions are obtained in terms of stresses, not strains. Hence there is a need to write ψ in terms of stresses. Remember the derivative $\mathbf{f} = -\nabla_x\phi(\mathbf{E}, \mathbf{x})$ is taken at fixed strain, but after taking the derivative we can change variables and replace strain with stress. Using the elastic stress-strain relations for plane strain, we obtain

$$\psi = \frac{1+\nu}{2\langle\lambda\rangle^2} \left[(1-\nu)(\sigma_x^2 + \sigma_y^2) - 2\nu\sigma_x\sigma_y + 2\sigma_{xy}^2\right]$$

where σ denotes a linear elastic stress component; however, the Young's modulus is different on either side of the interface, and hence we take the average value ($\langle\lambda\rangle = (\lambda^- + \lambda^+)/2$). Substituting the expressions for the usual mode-I crack-tip K-field stresses we get

$$\psi = \frac{1+\nu}{2\langle\lambda\rangle^2} \left(\frac{K^2}{4\pi}\right) \left[2 - 2\nu - \cos^2(\theta/2)\right] \cos^2(\theta/2)$$

where K is the stress intensity factor, r and θ are polar coordinates, and the origin is at the crack-tip.

Suppose that the bimaterial interface is at a distance of l in front of the crack-tip. Then $cos(\theta) = l/r$ and we can write

$$\psi = \frac{(1+\nu)K^2}{8\pi\langle\lambda\rangle^2}\left[\frac{3-4\nu}{r} + \frac{(2-4\nu)l}{r^2} - \frac{l^2}{r^3}\right]$$

The arc-length is nothing but the (vertical) y-coordinate and noting that $r = \sqrt{l^2+y^2}$, we can evaluate the integral in (9) as

$$\int_{-b}^{b} \psi\, dy = \frac{(1+\nu)K^2}{8\pi\langle\lambda\rangle^2}\left[(3-4\nu)ln\left(\frac{\sqrt{1+\alpha^2}+\alpha}{\sqrt{1+\alpha^2}-\alpha}\right) + 4(1-2\nu)tan^{-1}(\alpha) - \frac{2\alpha}{\sqrt{1+\alpha^2}}\right] \qquad (10)$$

where $\alpha = b/l$ and the limit of integration b either corresponds to the physical dimensions of the specimen or can be chosen depending on the accuracy required for results. For a given value of α the effect of inhomogeneities can be evaluated using (9, 10).

If we treat b as a fixed parameter, then variations in α are due to variations in l. Figure 1 shows Ψ vs. α where

$$\Psi = \left[\int_{-b}^{b} \psi\, dy\right]\left(\frac{8\pi\langle\lambda\rangle^2}{(1+\nu)K^2}\right)$$

The inhomogeneity effect Ψ does not reach an asymptotic value for large values of α, but instead $\Psi \to \infty$ as $\alpha \to \infty$. This means that the inhomogeneity effect Ψ becomes very large as the distance between the crack-tip and the interface becomes vanishingly small. Here we have assumed that the stress-intensity factor K remains constant; however, other studies have found that K changes with α, and hence Figure 1 should be interpreted with this caveat.

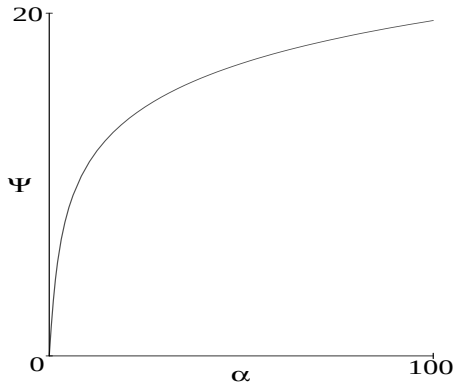

Figure 1: Ψ vs. α

CONCLUSIONS.

1. It is well-known that inhomogeneities can alter the crack-tip stress field. This paper shows that inhomogeneities can influence crack growth in a second way - by causing a difference in the crack-tip and far-field energy release rate [equation (8)].
2. For a bimaterial composite, a crack in the less stiff material is inhibited as it approaches the interface, whereas the growth of a crack in the stiffer material is aided by the interface.

REFERENCES

1. S. Suresh and Y. Sugimura and E. Tschegg. (1992) *Scripta Metallurgica*, 27, 1189.
2. A. Romeo and R. Ballarini. (1995) *J. App. Mech.*, 62, 614.

3. F. Delale and F. Erdogan. (1983) *J. App. Mech.*, 50, 609.
4. O. Kolednik. (2000) *Int. J. Solids Structures*, 37, 781.
5. M. E. Gurtin. (1995) *Arch. Rational Mech. Anal.*, 131, 67.
6. N. K. Simha and K. Bhattacharya. (1998) *J. Mech. Phys. Solids*, 46, 2323.
7. N. K. Simha and F.D. Fischer and O.Kolednik. (2001) *in preparation.*
8. N. K. Simha. (2001) *J. Elasticity*, in print.
9. M. E. Gurtin and P. Podio-Guidugli. (1996) *J. Mech. Phys. Solids*, 44, 905.
10. J. R. Rice. (1968) *J. App. Mech.*, 35, 379.
11. S. Timoshenko. (1959) Theory of Elasticity. McGraw-Hill.

ORAL REFERENCE: ICF100486OR

INITIAL CRACKS IN SATURATED SWELLING SOILS

V.Y. Chertkov
Faculty of Agricultural Engineering, Technion – Israel Institute of Technology
Haifa 32000, Israel

ABSTRACT

Shrinkage cracks in swelling soils determine their transport properties. An available model of shrinkage cracks in a brittle medium, is used for the description of crack growth in water saturated soils undergoing desiccation. The main objective of the work is to validate the model by available data. Available data justify use of the constant elastic, strength, diffusivity, and shrinkage properties of a clay soil. A key point is the existence of a minimum crack capable of developing on the conditions under study. A developing crack passes stages of delay, jump, stable growth at approximately constant velocity, and quick slowing down untill stopping. Relations between the minimum crack dimension and some other characteristic dimensions of soil structure are discussed. The concept of the minimum quasi-brittle crack capable of developing at shrinkage leads to two possible types of shrinkage cracks in clay soils. Checking the model predictions based on the available data shows satisfactory agreement between them.

KEYWORDS

Saturated swelling soil, drying, shrinkage, cracking.

INTRODUCTION

Shrinkage cracks are observable even in saturated clay soils under desiccation in restrained conditions [1-3]. A model of the development of an isolated shrinkage crack under the action of shock drying was earlier considered in the frame of linear elastic fracture mechanics [4]. The objective of this work is to show that the model is in agreement with the available data [1-3] for drying in restrained conditions, but staying saturated was considered to be suddenly placed $\theta = \theta_o$ clay soils. A body with the initial (gravimetric) water content, . The simplest condition of water exchange on the $\theta = \theta_1 < \theta_o$ in a medium with (gravimetric) water content , was assumed. It was supposed that there exists a crack of length l going into $\theta = \theta_1$ boundary of the body, the depth of the body along the z-axis perpendicular to its boundary (the y-axis). The maximum shrinkage (reached on the boundary at z=0) was [4] σ_* stress

, $$(1)\ \sigma_* = \frac{E\alpha}{3(1-\nu)}(\theta_o - \theta_1)$$

where E is Young's modulus; ν is Poisson's ratio; α is the shrinkage coefficient. Dependence of the length l $\beta >> 1$ (D is the hydraulic diffusivity). For $\beta = l/2\sqrt{Dt}$ on the time t was expressed using a parameter

$$(2)\qquad l=\frac{\pi^3\beta^2}{4}l_*,\qquad t=\frac{\pi^6}{64}\frac{\beta^2 l_*^2}{D}=\frac{\pi^3 l_* l}{16D}\qquad \left(l_*=\frac{1}{\pi}\left(\frac{K_{\mathrm{Ic}}}{\sigma_*}\right)^2\right)$$

, and l_* l is close to $\beta<<1$ is the critical stress-intensity factor). For K_{Ic} (

$$(3)\, t=\frac{l_*^2}{4D\beta^2}=\frac{16}{\pi^3 D}\frac{l_*^4}{(l-l_*)^2},\qquad \frac{l-l_*}{l_*}=\frac{8\beta}{\pi^{3/2}}$$

represents the Griffith's formula and is the length of the crack for which the body would fracture if it was l_* . The form of the relation $t(l)$ is given by Fig.1 (except the σ_* loaded by the uniformly distributed stress (Fig.1) will not $l<l_*$ it follows that a crack with l_*). From the meaning of the quantity $l>z_*$ range) after a definite delay time the crack $l>l_*$ (at l_* develop. When the length of the initial crack is close to with a jump goes over into a new moving equilibrium state and further will increase continuously and with time goes into the regime of propagation with a constant velocity. Equalizing asymptotic dependencies $t(l)$ to the right (Eqn. 2) and to the left (Eqn. 3) of the minimum (Fig.1) one can estimate the minimum as

$$(4)\, l_\tau\cong 1.43 l_*,\qquad \tau\cong 2.77 l_*^2/D$$

(Fig.1) [4]. $l_*<l_{\mathrm{O}}<l_\tau$ The initial depth of a quasi-brittle crack developing by jump is in the range Accounting for Eqn. 4 an average initial depth of cracks capable of developing by jump is

$$(5)\, l_{\mathrm{av}}=1.22 l_*$$

L_{av} (Fig.1) and then from Eqn. 2 average crack depth after jump T_{av} From Eqns. 3 and 5 it follows

$$(6)\, L_{\mathrm{av}}\cong 5.72 l_*,\qquad T_{\mathrm{av}}=11.10(l_*^2/D)$$

PROPERTIES OF SATUATED CLAY SOIL AS FUNCTIONS OF WATER CONTENT

). However, at saturated θ_1 and θ_{O}, D, and α can vary in dependence on water content (at given K_{Ic} E, ν, - shrinkage limit) the fracture toughness of the studied clays [5-7] changes with water content $\theta>\theta_{\mathrm{S}}$ state (very little if at all. The same is related to E and ν. The soil water diffusivity of disaggregated clays, D is $\alpha=(1/V)(dV/d\theta)$ nearly constant with soil water content [8]. The shrinkage coefficient α is defined as)). The derivative is at cm^3/g where V is the specific volume of a clay soil (per unit mass of oven-dried soil (a constant pressure. For soils with high clay content the dependence between V and θ is linear [9] and is the water ρ_{W} is the clay particle (or solid phase) density, and ρ_{S} where $\alpha=(1/\rho_{\mathrm{W}})/(1/\rho_{\mathrm{S}}+\theta/\rho_{\mathrm{W}})$ if the absolute value of a relative deflection $\theta''<\theta<\theta'$ value is considered as constant in a range α density. does not surpass 0.1, *i.e.* α'' and α' of corresponding $\bar{\alpha}\equiv(\alpha'+\alpha'')/2$ of the average, $(\alpha''-\alpha')/(\alpha'+\alpha'')<0.1$

OF AN ACTUAL CASE $(\theta_O-\theta_1)$ THE WATER CONTENT DIFFERENCE

decreases (Fig.2) means the $\theta_1 = \theta(0,t)$ surface The fact that the actual water content at the soil existence of small water content differences between the soil surface and a certain superficial layer. To (Fig.2) as a $\Delta\theta \equiv \theta_o - \theta_1 << (\theta' - \theta'')$ estimate these differences one can formally consider a small interval and a θ_o constant small difference between a higher (decreasing) water content within the superficial layer, where $3\delta\theta$ should not surpass $\Delta\theta$. The difference θ_1 lower (decreasing) water content at the soil surface, limit the $\delta\theta$ value [10]. Statistical fluctuations θ is a statistical (thermodynamic) fluctuation of the $\delta\theta$ values from [2, 3, 11] is ~0.001. Therefore in θ value measurements. Absolute error of θ accuracy of is used. $\delta\theta = 0.001$ practical estimation in the following the value

COMPARISON BETWEEN THE MODEL PREDICTION AND THE AVAILABLE DATA

Works [2, 3, 11, 12] were dedicated to studying the different aspects of cracking of intact Saint-Alban sensitive marine clay (80 km west of Quebec City in the Saint Lawrence Valley, Canada) undergoing , $\nu = 0.3$ desiccation and shrinkage in saturated state under restrained conditions. Two sets of data: *E*=4MPa, [3] give the model prediction of $K_{\mathrm{Ic}} = 1.6\mathrm{kPa}\cdot\mathrm{m}^{1/2}$, $\nu = 0.5$ and *E*=6MPa, $K_{\mathrm{Ic}} = 1.35\mathrm{kPa}\cdot\mathrm{m}^{1/2}$. One can conduct a number of comparisons between the model prediction and the data [2, $l_* = 2.00 \pm 1.04\mathrm{cm}$ 3, 11, 12]. It can be shown that: a/ the observable values of the crack length before and after jump, estimate; b/ the model l_* [3] are in agreement with Eqns. 2 and 3 and the $l_{\mathrm{j}} = 8-11\mathrm{cm}$, $l_{\mathrm{o}} = 3-4\mathrm{cm}$ =3-4cm l_{o} estimate, and Eqn. 4; c/ values of l_* [3], the $l_{\mathrm{o}} = 3-4\mathrm{cm}$ is fulfilled with $l_* < l_{\mathrm{o}} < l_\tau$ inequality estimate confirm Eqn. 5 for the average initial depth of cracks before jump; d/ crack length l_* [3] and the =17hours [3] T_{j} [3] and the observable time before jump, $l_{\mathrm{j}} = 8-11\mathrm{cm}$, $l_{\mathrm{o}} = 3-4\mathrm{cm}$ before and after jump, estimate and Eqn. 3. l_* are in agreement with the

RELATIONS BETWEEN l_* AND SOME CHARACTERISTIC DIMENSIONS

$l_* >> \Delta$ Because the crack development is described by the linear elastic fracture mechanics the condition should be carried out, where Δ is the dimension of the structure inhomogeneity (the maximum value of Δ is and the maximum value of l_* the maximum dimension of sand grains in the soil). The above estimate of mm [11] show that the condition is fulfilled. $\Delta \cong 2$

l_* The mean dimension of (surface) cracks developing by the merging of smaller initial cracks of dimension is the critical value of the ratio of the mean linear dimension of an area that one K_* [13] where $(K_* + 1)l_*$ is [14]). In connecting $K_* \cong 5$ initial (surface) crack takes over to the mean crack dimension proper (for soils should coincide $(K_* + 1)l_*$ these enlarged surface cracks and forming the network their mean dimension (data for Saint- $S_{\mathrm{o}} = (K_* + 1)l_* \cong 6l_*$, *i.e.* l_* between initial cracks of dimension S_{o} with the mean spacing, value). Then, using the l_*=20-24cm [2] do not contradict this relation at the estimated S_{o} Alban clay, [15] connecting the thickness of the intensive-cracking layer at the quasi-steady state, $z_{\mathrm{o}} \cong S_{\mathrm{o}}/2$ relation . Then, $z_{\mathrm{o}} \cong 3l_*$ between initial cracks, one can get an estimate of S_{o} [13] and the mean spacing, z_{o} $z_{\mathrm{m}} \cong 30l_*$ [13] (Fig.1) one can get an estimate for the maximum crack depth $z_{\mathrm{o}} \cong 0.1z_{\mathrm{m}}$ accounting for that) and L_{av} estimate, the mean depth of primary cracks after jump (S_{o} . According to Eqn. 6 and the above $L_{\mathrm{av}} \cong S_{\mathrm{o}}$) are of the same order of magnitude, S_{o} their mean spacing at the surface (

. The $z_o < l(t) \le z_m$ and $l(t) \le z_o$ ranges The depth of an actual growing crack, l can be in the passes, on the average, stages (Fig.1) of delay (or forming an z_m development of cracks reaching the depth), and quick $L_{av} \cong < l < z_*$), quasi-stable growth ($l_\tau < l < \cong L_{av}$), crack jump ($l_* < l \le l_\tau$ initial crack) ( ). The first three stages can be described quantitatively based on the $z_* < l \le z_m$ slowing-down and stop (model [4].

TWO POSSIBLE TYPES OF SHRINKAGE CRACKS IN A SWELLING SOIL

The major model concept of the minimum quasi-brittle crack capable of developing at shrinkage, enables one to assume that in saturated clay soils there are cracks of depth $l < l_*$ incapable of developing in dimension in desiccation, and cracks reaching dimension $l > l_*$, that are initial in developing large shrinkage cracks. Observations show, that the network of shrinkage cracks actually consists of larger seasonal macrocracks [16-18] and smaller quasi-steady interaggregate microcracks [19-22].

CONCLUSION

Results of the work demonstrate: a/ the applicability of the linear elastic fracture mechanics for the description of quasi-brittle cracking even in such visco-plastic materials as water saturated swelling clay soils; b/ the connections between the minimum dimension of a quasi-brittle crack capable of developing at shrinkage and other characteristic dimensions of a crack network in a swelling soil; and c/ two possible types of shrinkage cracks in swelling soils.

REFERENCES

1. Konrad, J.-M. and Ayad, R. (1997) *Can. Geotech. J.* 34, 477.
2. Konrad, J.-M. and Ayad, R. (1997) *Can. Geotech. J.* 34, 929.
3. Ayad, R., Konrad, J.-M., and Soulie, M. (1997) *Can. Geotech. J.* 34, 943.
4. Salganik, R.L. and Chertkov, V.Y. (1969) *Mechanics of Solids* (Engl. Transl.). 4, 126.
5. Haberfield, C.M. and Johnston, I.W. (1990) *Can. Geotech. J.* 27, 276.
6. Murdoch, L.C (1993) *Geotechnique*. 43, 267.
7. Harison, J.A., Hardin, B.O., and Mahboub, K. (1994) *J. Geotech. Engng-ASCE.* 120, 872.
8. Kutilek, M., Vogel, T., and Nielsen, D.R. (1985) *Soil Sci.* 139, 497.
9. McGarry, D. and Malafant, K.W. (1987) *Soil Sci. Soc. Am. J.* 51, 290.
10. Landau, L.D. and Lifshitz, E.M. (1980) *Statistical Physics,* Pergamon, Oxford.
11. Konrad, J.-M. and Seto, J.T.C. (1994) *Can. Geotech. J.* 31, 285.
12. Virely, D. (1987) MSc Thesis, Université Laval, Ste. Foy, Quebec, Canada.
13. Chertkov, V.Y. and Ravina, I. (1998) *Soil Sci. Soc. Am. J.* 62, 1162.
14. Zhurkov, S.N., Kuksenko, V.S., and Petrov, V.A. (1981) *Doklady* (Engl. Transl.). 26, 755.
15. Chertkov, V.Y. (2000) *Soil Sci. Soc. Am. J.* 64, 1918.
16. Zein el Abedine, A. and Robinson, G.H. (1971) *Geoderma.* 5, 229.
17. Dasog, G.S., Acton, D.F., Mermut, A.R., and De Jong, E. (1988) *Can. J. Soil Sci*. 68, 251.
18. Morris, P.H., Graham, J., and Williams, D.J. (1992) *Can. Geotech. J*. 29, 263.
19. Guidi, G., Pagliai, M., and Petruzzelli, G. (1978) *Geoderma*. 19, 105.
20. Ringrose-Voase, A.J. and Nys, C. (1990) *J. Soil Sci.* 41, 513.
21. Scott, D.J.T., Webster, R., and Nortcliff, S. (1988) *J. Soil Sci.* 39, 303.
22. Velde, B., Moreau, E., and Terribile, F. (1996) *Geoderma.* 72, 271.

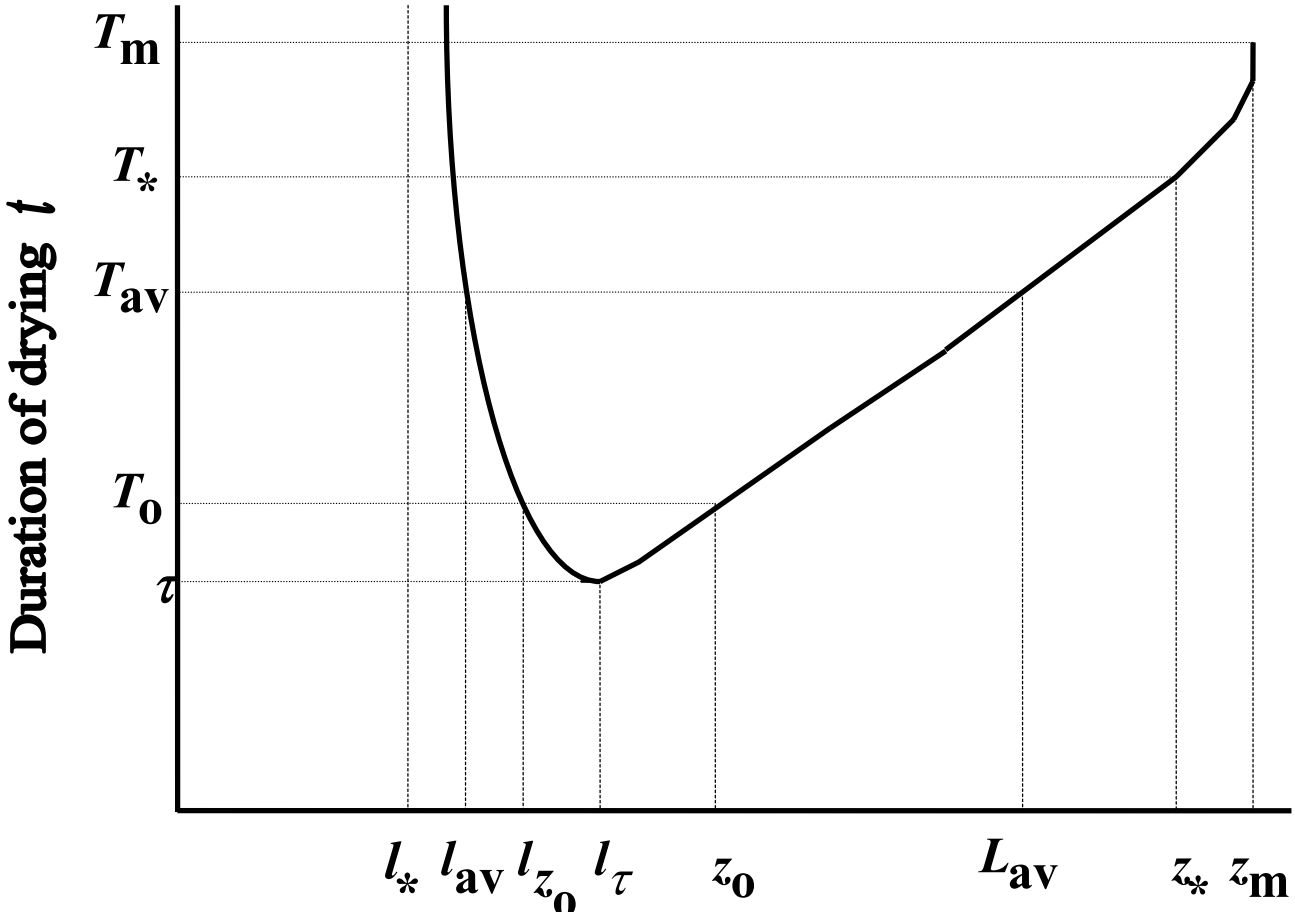

Figure 1: The qualitative appearance of graph of t versus l, characterizing the behaviour of shrinkage crack.

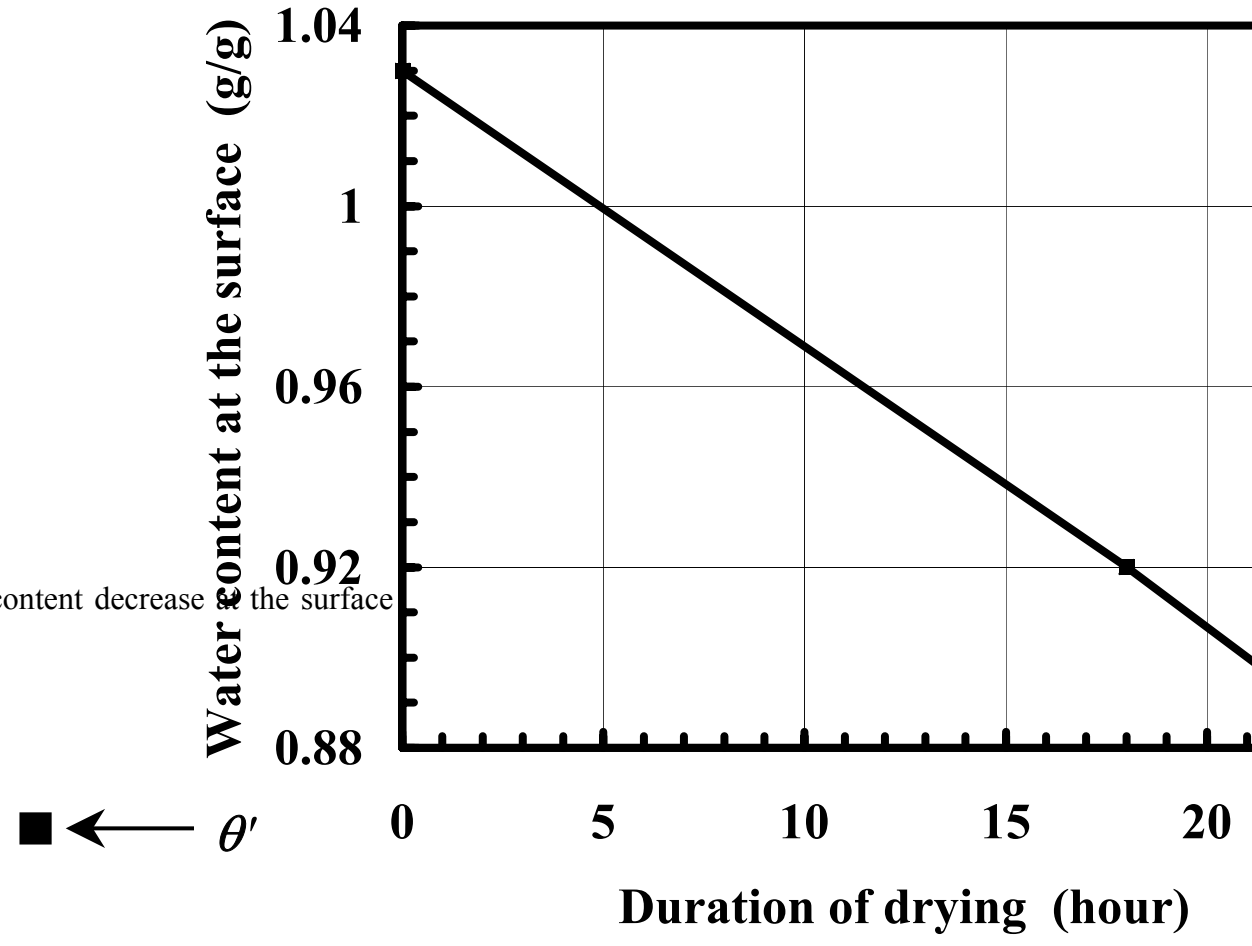

Figure 2: Water content decrease at the surface

INTERFACE CRACK IN PERIODICALLY LAYERED BIMATERIAL COMPOSITE

M. Ryvkin and L. Kucherov

Department of Solid Mechanics, Materials and Systems,
Tel Aviv University, Ramat Aviv 69978, Israel

ABSTRACT

An interface crack in a periodically layered bimaterial composite plane is considered. The solution method is based on the combined using of the representative cell and the dislocation approaches. First, after applying the discrete Fourier transform, the analytical expression of the Green function for a single interface dislocation in a periodically layered media without the crack is derived. Using this result the problem is then reduced to the system of two singular integral equations which are solved numerically. The parametric study of the stress intensity factor and energy release rate revealed new phenomena unlike to the ones observed for the more simple three layered sandwich models of multilayered bodies. It is found that for the case of sufficiently large mismatch in the geometric and elastic characteristics of the layers the stress intensity factor approaches some maximum value which can essentially exceed the corresponding one for a crack on a homogeneous plane.

KEYWORDS: periodically layered composite, interface crack, discrete Fourier transform

1 Introduction

Fracture behavior of periodically layered composite materials for the crack parallel to the interfaces was intensively investigated recently for the cases of antiplane deformation [1], [2], mode I [3], and mixed mode cracks [4]), [5]). The study of the interface crack related to the delamination phenomenon is of special interest. Kaczynsky and Matysiak [6], [7] considered this problem using the non-standard homogenization approach. This approach includes some approximating assumptions and does not give the precise stress distribution required for the fracture analysis. The mathematical technique employed in the present paper hinges on the discrete and integral Fourier transforms and it is free of any homogenization procedure. Hence, it enables to determine the exact values of the stress intensity factor and energy release rate and to carry out the complete parametric study. One of the goals of this study is to compare the results with the ones obtained for the more simple case of an interface crack in a three layered sandwich composite. The latter problem is well investigated, so one will obtain the important information regarding the limits of using sandwich approximation for predicting the fracture properties of a periodically layered composite.

2 Analysis

The plane deformation of a composite consisting of two types of layers arranged periodically is considered (see insert in Fig. 2). The layers of each type are defined by the thickness h_r, shear modulus of the material μ_r and Poisson ratio ν_r $(r = 1, 2)$. The translational symmetry of the composite is violated by an interface crack of length $2a$ subjected to uniform loading

$$\sigma_y + i\tau_{xy} = \sigma_0 + i\tau_0 \ , \qquad |x| < a, \quad y = 0 \ . \tag{1}$$

The solution method is based on the dislocation approach developed by Erdogan and Gupta [8] applied in combination with the representative cell method [9], [1]. The crack is viewed as distributed dislocations with an unknown amplitude $f = f_1 + if_2$

$$\frac{\partial}{\partial x}[\Delta u(x,0) + i\Delta v(x,0)] = (f_1 + if_2)\,\delta(x-t) \ , \tag{2}$$

where $\Delta u(x,0)$ and $\Delta v(x,0)$ are the displacement jumps across the interface in the $x-$ and $y-$directions respectively, and $\delta(x)$ is the delta-function. The Green function for a single dislocation in a periodically layered composite can be found in a closed form by the representative cell method in the same manner as in [2], [3], [5]. To this end the plane is presented as an assemblage of identical cells denoted by the index k $(k = 0, \pm 1, \pm 2, ...)$. After application of the discrete Fourier transform

$$u^* = \sum_{k=-\infty}^{\infty} u^{(k)} e^{i\varphi k} \tag{3}$$

the problem for the plane is reduced to a problem for the representative cell consisting of two dissimilar bonded layers. The values of the components of the stress strain state at the lower $(-)$ and upper $(+)$ edges of the cell are found to be related by the Born-Von Karman type boundary conditions

$$\{u^*, v^*, \tau^*_{xy}, \sigma^*_y\}^+ = e^{i\varphi}\{u^*, v^*, \tau^*_{xy}, \sigma^*_y\}^- \tag{4}$$

including the transform parameter φ. The problem for the representative cell is solved by means of the Fourier integrals. Applying then the inverse discrete Fourier transform one obtains the sought expressions of the Green functions for the stresses in the form of double integrals

$$G^{(k)}_\sigma(x,y,t) = \frac{1}{2\pi}\sum_{j=1}^{2} f_j(t)\int_{-\pi}^{\pi}\int_{-\infty}^{\infty}[A_j e^{-yz} + B_j e^{yz}]e^{i(zx-\varphi k)}dzd\varphi \tag{5}$$

$$G^{(k)}_\tau(x,y,t) = \frac{1}{2\pi}\sum_{j=1}^{2} f_j(t)\int_{-\pi}^{\pi}\int_{-\infty}^{\infty}[C_j e^{-yz} + D_j e^{yz}]e^{i(zx-\varphi k)}dzd\varphi \tag{6}$$

Here k is the number of the cell, t defines the location of the dislocation at the interface within the cell number 0, and A_j, B_j, C_j, D_j are the known functions of the problem parameters and variables t, z, y, φ. The explicit expressions of these functions are obtained by the use of symbolic computation, they are rather cumbersome but observable.

The procedure employed for the conversion of the interface crack problem to a system of two singular integral equations using the Green function is described by Erdogan and Gupta [8]. The solution is obtained as in that work by representation of the unknown dislocation density $f(x)$ as series of Jacobi polynomials.

3 Results

The singular stresses in front of the crack are characterized by the complex stress intensity factor $K = K_1 + iK_2$

$$\sigma_y + i\tau_{xy} = \frac{K}{\sqrt{2\pi r}} r^{i\varepsilon} \ , \tag{7}$$

and the energy release rate

$$G = \frac{(1-\nu_2)(1-\beta^2)}{2\mu_2(1+\alpha)} K\bar{K} \,, \tag{8}$$

where

$$\varepsilon = \frac{1}{2\pi} \ln \frac{1-\beta}{1+\beta} \,. \tag{9}$$

and α and β are the Dundurs parameters. The case of opening normal tractions ($\tau_0 = 0$) is

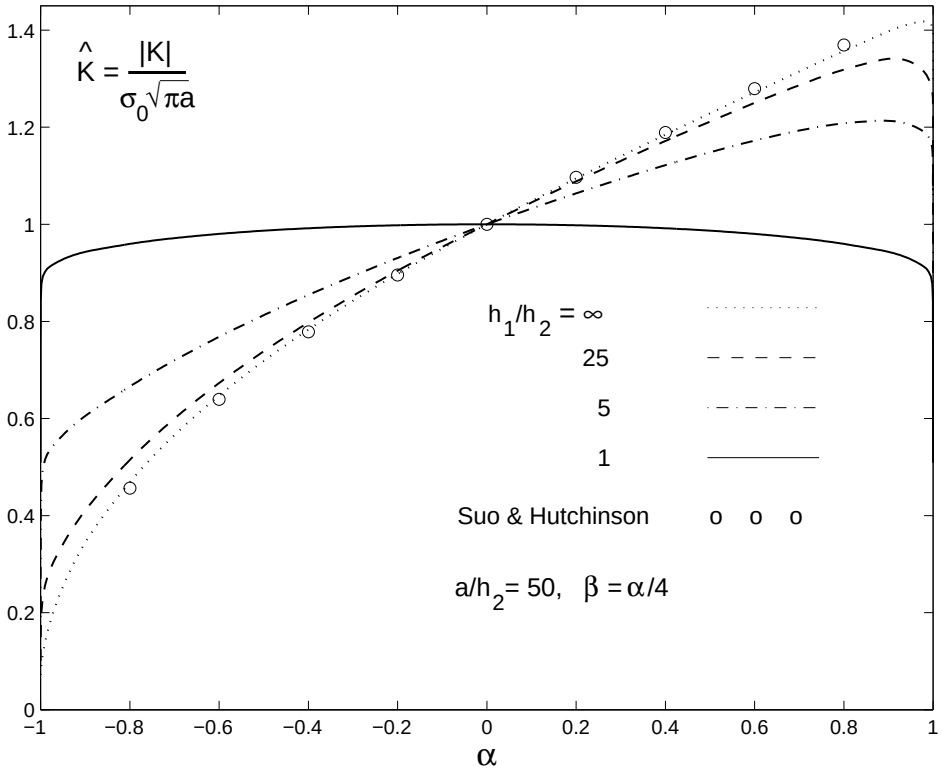

Figure 1: Normalized stress intensity factor vs. elastic mismatch parameter α for $a/h_2 = 50$ and $\beta = \alpha/4$

considered. We will examine first the normalized absolute value of the stress intensity factor

$$|\hat{K}| = \frac{1}{\sigma_0} \left[\frac{K_1^2 + K_2^2}{\pi a} \right]^{1/2} \tag{10}$$

divided by the stress intensity factor for a corresponding crack in a homogeneous plane $K_{hom} = \sigma_0\sqrt{\pi a}$. The dependence of $|\hat{K}|$ upon the mismatch in the elastic properties of the composite constituents is illustrated in Fig. 1. The mismatch is characterized by the value of α and it is assumed that $\beta = \alpha/4$ which is a good approximation for many engineering materials [10]. Three thickness ratios $h_1/h_2 = 1, 5, 25$ are considered, i.e. the layers of the first type with the thickness h_1 are assumed to be not thinner than the layers of the second type. In addition the curve corresponding to the sandwich composite ($h_1/h_2 = \infty$) is depicted for reference. The ratio of the crack length to the thinner layers thickness is taken relatively large $a/h_2 = 50$. Therefore the results for the sandwich composite are very close to the ones obtained from the asymptotic formula for a semi-infinite crack derived in Suo and Hutchinson [11].

Increasing α corresponds to the enhancement of the stiffness of the thinner layers with thickness h_2 relative to the h_1 layers. In the considered case $\beta = \alpha/4$ the thinner layers are more compliant (i.e. $\mu_2 < \mu_1$) for $-1 < \alpha < 0$. For $0 < \alpha < 1$ the situation is reversed, and when $\alpha = 0$ the elastic properties of the composite constituents coincide. Consequently, in view of the accepted

normalization, in the latter case $|K| = 1$. For negative α the general trend observed for periodic composites is the same as for the sandwich. Namely, the behavior of the stress intensity factor is monotonic and its values are less than unity as a result of so called the elastic shielding effect (see, for example, [10]).

For the case of positive α the above similarity does not hold true.

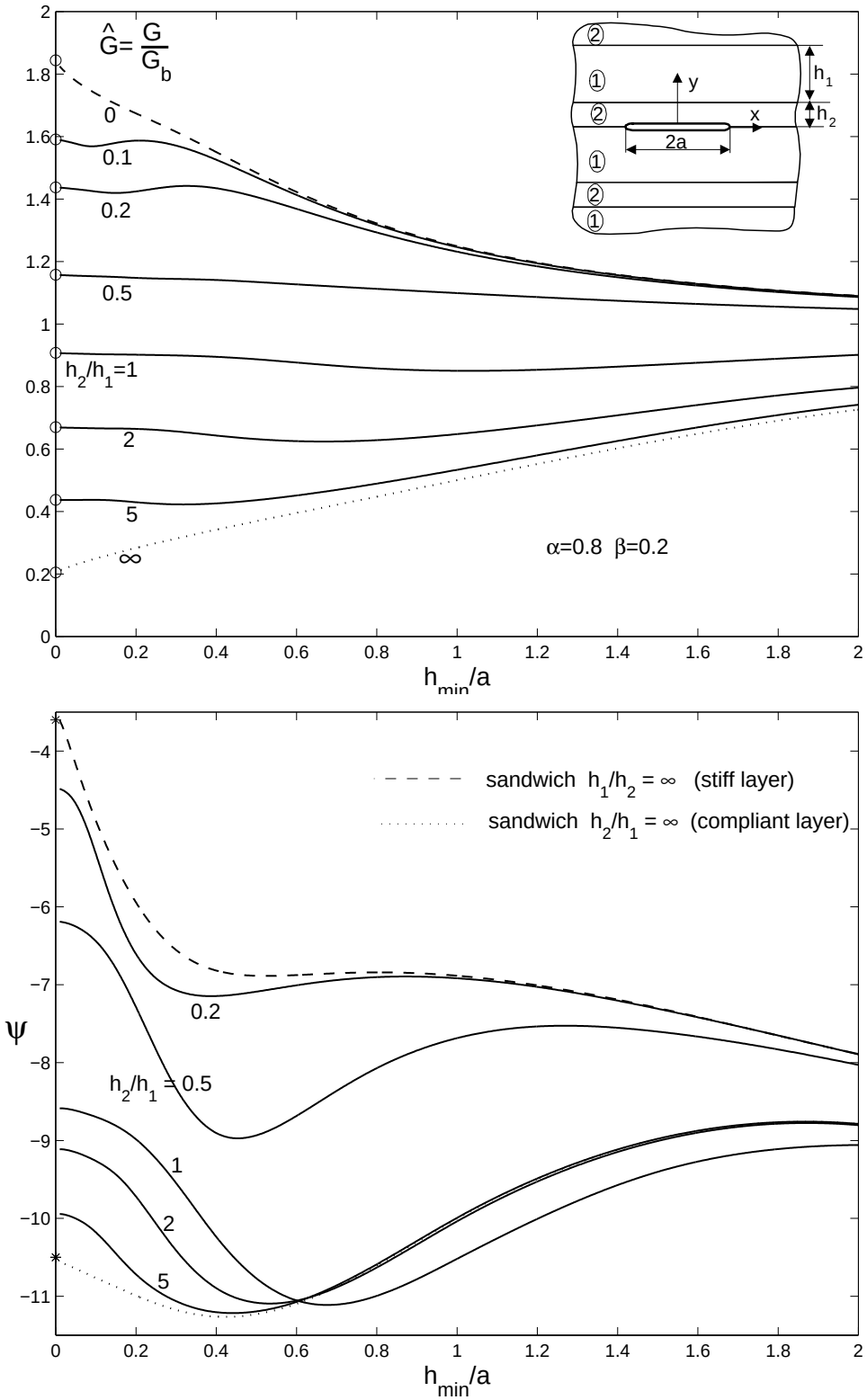

Figure 2: Normalized energy release rate $\hat{G}$ and real phase shift angle $\psi = \mathrm{Arg}[Kh_{min}^{i\varepsilon}]$ (in degrees) vs. crack length parameter h_{min}/a; $h_{min} = min\{h_1, h_2\}$.

The curve for the case of equal thicknesses $h_2/h_1 = 1$ is symmetric with respect to the line $\alpha = 0$

owing to the symmetry of the problem. Therefore the absolute value of the stress intensity factor for an interface crack will be always less than that for the crack in a homogeneous material. On the other hand, for the sandwich composite a monotonic enlargement of the stress intensity factor with increasing α, i.e. with increasing stiffness of the sandwiched layer, is observed which may be referred as the inverse shielding effect. For the bimaterial composites with thin layers $h_1/h_2 = 5,\ 25$ this effect is interfered with an opposite trend induced by the restriction of the displacements of the layered body when the layers of one of the types become stiffer. As a result, the behavior of $|\hat{K}|$ is found to be non-monotonic. This phenomenon is similar to the one observed in the case of a Mode III interface crack [2]. Hence, if we increase stiffness of the thinner layers in a periodic composite it may lead not only to increasing but also to decreasing of the singular stresses in front of the crack tip. Consequently, for some parameter combination the stress intensity factor reaches its maximum value. The magnitude of this value for the given material pair increases with the increasing of the difference in layers thicknesses and can appreciably exceed the value for the crack in homogeneous material.

The influence of the crack length on the energy release rate is presented in the upper part of Fig. 2. It is convenient to consider the normalized quantity

$$\hat{G} = \frac{G}{G_b}\,, \tag{11}$$

where G_b is the energy release rate for the sample problem of a crack at the interface between two half-planes made of the same materials as the layered composite. The crack length is normalized by the value $h_{min} = min\{h_1, h_2\}$ being the thickness of the thinner layers. For the considered elastic materials combination $\alpha = 0.8,\ \beta = 0.2$ the information on all possible thickness ratios is presented. Two reference curves for the sandwich composites with compliant and stiff layers are denoted by the doted and dashed lines respectively.

When the crack is short the layered structure of the composite is not relevant, and, consequently, the asymptote for $h_{min}/a \to \infty$ is unity in view of accepted normalization for all the curves. The increasing of the crack length results in moderate decreasing(increasing) of the energy release rate when the thinner layers are more compliant (stiff). The limiting values of $\hat{G}$ for $h_{min}/a \to 0$ denoted by circles can be evaluated analytically similar to [3]. To this end one has to calculate the energy release rate in terms of the remote stress field. Clearly, for a sufficiently long crack the periodically layered plane composed of isotropic layers can be replaced by an anisotropic one possessing effective elastic properties. For the considered case of normal loading as in the case of mixed mode crack [5]

$$G = \sigma_0^2 \pi a Q\,, \tag{12}$$

the explicit expression of Q in terms of the geometric and elastic parameters of the layers is given in [5].

It may be observed that for the considered elastic mismatch of the materials the analytical limiting values for a semi-infinite crack provide a sufficiently good approximation for the energy release rate in a surprisingly large crack length range. In fact, if the ratio of the thinner layers to the thick ones is more then 0.1, one can use analytic formula in the framework of 5% accuracy for all cracks with $h_{min}/a < 0.4$. The mentioned region, clearly, will extend when the elastic mismatch is diminished i.e. for $\alpha < 0.8$. The case of a large difference in the thickness and the elastic properties of the layers is investigated in [12].

Following [11] we will characterize the argument of the stress intensity factor by a real phase angle $\psi = \mathrm{Arg}[K h_{min}^{i\varepsilon}]$. The dependence of this angle measured in degrees upon the crack length is shown in the lower part of the figure. One can note that the argument of the stress intensity factor is much more sensitive to the crack length than its absolute value related to the energy release. The limiting values for the semi-infinite crack in sandwich composites denoted by asterisks are derived from the asymptotic formula obtained in [11].

In conclusion it should be noted that the behavior of interface cracks in the periodically layered composites is found to be unlike to the one observed for the more simple sandwich models and requiered separate investigation. The employed analysis technique based on the combined use of the representative cell and the dislocation methods provides an exact and convenient mathematical tool for such investigation.

References

[1] Ryvkin, M. (1996) Mode III crack in a laminated medium. *International Journal of Solids and Structures* **33**, No.24, 3611.

[2] Ryvkin, M. (1998) Antiplane deformation of a periodically layered composite with a crack. A non-homogenization approach. *International Journal of Solids and Structures* **35**, 522.

[3] Ryvkin, M.,(1999) A mode I crack paralleling interfaces in a periodically layered composite. *International Journal of Fracture* **99**, No. 3, 173.

[4] Jha, M. and Charalambides, P.G. (1998). Crack-tip micro mechanical fields in layered elastic composites: crack parallel to the interfaces. *International Journal of Solids and Structures* **35**, 149.

[5] Ryvkin, M. and Kucherov, L. (2000) Mixed mode crack in a periodically layered composite, *International Journal of Fracture* **106**, 373.

[6] Kaczynsky, A. and Matysiak, S. (1988) On crack problems in periodic two–layered elastic composites. *International Journal of Fracture* **37**, 31.

[7] Kaczynsky A. and Matysiak S.(1989) A system of interface cracks in a periodically layered composite, *Engineering Fracture Mechanics*, **32**, No.5, 745.

[8] Erdogan F. and Gupta, G.D. (1971) Layered composites with an interface flaw. *International Journal of Solids and Structures* **7**, 1089.

[9] Ryvkin M, Nuller B (1997) Solution of quasi-periodic fracture problems by the representative cell method. *Comp Mech* **20**,145.

[10] Fleck, N.A., Hutchinson, J.W. and Suo, Z. (1991) Crack path selection in a brittle adhesive layer. *International Journal of Solids and Structures* **27**, No. 13, 1683.

[11] Suo, Z. and Hutchinson, J.W (1989) Sandwich test specimens for measuring interface crack toughness. *Materials Science and Engineering* **A107**, 135.

[12] Ryvkin, M. and Kucherov, L. (2001) An inverse shielding effect in a periodically layered composite, submitted to *International Journal of Fracture*.

Interfacial Adhesion and Crack Initiation at Metal/Ceramic Interface

Scott X. Mao and M. Li
Department of Mechanical Engineering,
University of Pittsburgh, Pittsburgh, PA 15261, USA

Abstract - Interface crack initiation in layered materials is investigated for mixed mode I and mode II loadings. The dislocation plasticity in the metal layer is considered, and the energy for initial emission of a dislocation is assumed to be attained before the cleavage of the interface crack. Superdislocation modeling is employed to obtain the critical strain energy release rate, for crack initiation and growth. When a stress separation law is satisfied at the interface crack tip, interface debonding occurs. The strong dependence of fracture energy on mixed mode loading is predicted by this model. The role of the metal layer thickness and interfacial strength is also investigated. In addition, interfacial strength measurement for predicting the toughness is touched.

1. INTRODUCTION

Theoretical work on the elastic-plastic interface crack problem by a number of workers [1-6] has given insight into possible explanations for a strong mixed mode effect due to plasticity. Using a finite element analysis, Tvergaard and Hutchinson [7-8] have calculated the mixed mode toughness of an interface joining an elastic-plastic solid and a non-plastic solid. In their work, a potential function, based on the components of the crack face displacement, was used to generate tractions along the interface where the fracture process caused interface separation occur. Recently, Wei and Hutchinson [9-10] studied the relationship between fracture energy at the interface crack tip and the global toughness under mixed mode loading. Using the SSV model proposed by Suo, Shih and Varias [11] and strain gradient plasticity theory for a metal/ceramic layered material, their FEM analysis showed that plasticity in the metal layer plays an important role in interfacial toughness under the mixed mode loading.

Recent work by Mao and Evans [13] has shown that a growing interface crack in an $Al_2O_3/Au/Al_2O_3$ system does not automatically become sharp. Instead, plastic blunting arises through the activation of slip sources in the metal layer. Using an atomic force microscope (AFM), Mao and Evans also observed that separation still occurs as a result of brittle debonding. In order to model the interface crack growth, a stress criterion (interface separation law) is used in which the interface ruptures when the peak normal stress ahead of the blunt crack exceedes the bond strength at the interface.

This paper develops a stress based approach which predicts mixed mode toughness of an interface joining a solid, which has dislocation plasticity, with another elastic solid that is dislocation-free. We assume that dislocations are emitted from the interface crack tip and that the crack tip will be blunting. The interface ruptures when a nominal stress, which is a function of normal stress and shear stress ahead of the blunted crack, exceeds the strength of the interfacial atomic bonds.

2. ANALYTICAL MODEL

A model of a material with alternating ceramic and metal layers containing a crack on the interface is shown on Fig. 1. The thickness of the metal layer is denoted by h, and

associated materials parameters are: shear modulus μ, Poisson's ratio ν, Burgers vector b and surface energy γ. It is assumed that metal layer has dislocation plasticity and ceramic layers are elastic with no dislocation plasticity. The energy needed for a single dislocation emission from crack tip is assumed to be much smaller than the interface cleavage fracture energy defined by Beltz and Rice [12]. Upon loading, a cluster of dislocations will emit from the crack tip and move along a slip plane in the metal at an angle φ to the interface crack plane, and pile up against the upper interface. The emitted dislocations have two effects on the crack tip. Firstly, if the burgers vector has a component normal to the crack plane, the emitted dislocations blunt the crack tip and a ledge is generated. The blunting reduces the stress concentration at the crack tip such that it is more difficult to reach the cohesive tensile strength. Secondly, the interaction forces between the crack and the emitted dislocations will result in crack tip shielding, giving rise to a crack tip stress intensity lower than the far field applied stress intensity. The detailed relationships are illustrated on Fig. 1.

2.1 Dislocation shielding model

In a layered material, dislocations emitted from the interface crack tip are blocked by the upper interface, sending a back stress to the crack tip which impedes further dislocation emission. For a given applied load and layer thickness, there exists an equilibrium number of dislocations in the pile-ups. Once the equilibrium number is reached, emission of additional dislocations is prevented by the back stress, which hinders further blunting of the crack tip. Considering a group of n dislocations which are blocked by the upper interface as a superdislocation, the total energy of the system, W_T, in the presence of a superdislocation of strength nb is

$$W_T(K_1^{tip'}, K_2^{tip'}, n) = W_d + W_K + W_L \tag{1}$$

where W_d consists of the dislocation self-energy and the interaction energy between dislocations, W_K is energy of interaction between the crack and the dislocations and W_L is the ledge energy and $W_L = nb\gamma$ (γ is the metal surface energy). $K_1^{tip'}$ and $K_2^{tip'}$ are the mode I and mode II components at crack tip, respectively. The equilibrium condition requires that

$$\frac{\partial W_T}{\partial n} = 0, \tag{2}$$

As dislocations are emitted from the crack tip, a cluster of dislocations piles-up against the upper interface and forms a superdislocation. This superdislocation will reduce the crack tip stress to generate dislocation shielding and the relationship between applied and crack tip stress intensity factors can be expressed by (details are given in [14])

$$\begin{bmatrix} K_1^{tip'} \\ K_2^{tip'} \end{bmatrix} = \begin{bmatrix} K_1^{tip} \\ K_2^{tip} \end{bmatrix} + \begin{bmatrix} k_1 \\ k_2 \end{bmatrix}, \tag{3}$$

and the stress intensity factor contributed from the superdislocation is

$$\begin{bmatrix} k_1 \\ k_2 \end{bmatrix} = \frac{3n\mu\sqrt{b}}{2\sqrt{2\pi h}(1-\nu)} \begin{bmatrix} f_1(\varphi) \\ f_2(\varphi) \end{bmatrix}, \tag{4}$$

where the subscripts 1 and 2 denote the mode I and mode II load components. K^{tip} and $K^{tip'}$ are the crack tip stress intensity factor and far field applied stress intensity factor.

K^{tip} and $K^{tip'}$ can also be considered as the stress intensity factor at the crack tip before and after dislocation shielding. k is the stress intensity factor contributed by a superdislocation with strength of nb. The functions f_1 and f_2 are given by the expressions $f_1(\varphi) = (1+\alpha)\sin\varphi\cos\frac{\varphi}{2}$ and $f_2(\varphi) = \frac{1}{3}(1+\alpha)(2\cos\varphi\cos\frac{\varphi}{2} - \sin\varphi\sin\frac{\varphi}{2})$, where α is the Dundurs' parameter.The phase angle at the crack tip after dislocation shielding, can be expressed as

$$\tan\Psi^{tip} = K_2^{tip} / K_1^{tip} . \tag{5}$$

Emitted dislocations also create ledges at the crack tip, and the blunting due to these ledges reduces the maximum tensile stress ahead of the crack tip. For simplicity, we approximate the blunted crack tip by a notch with tip radius Δ, as shown on Fig. 1. The slip step Δ (notch tip radius) is formed due to emission of n dislocations from crack. The components of the slip step, Δ_1 and Δ_2, are given by

$$\begin{aligned} \Delta_1 &= \Delta\sin\varphi \\ \Delta_2 &= \Delta\cos\varphi \end{aligned} \tag{6}$$

where $\Delta = nb$. From [14], the crack tip tensile stress σ^{tip} and shear stress τ^{tip} after dislocation emission can be obtained based on Tada *et al.* [15] as

$$\begin{aligned} \sigma^{tip} &= 2\sqrt{2/\pi}\, K_1^{tip} / \sqrt{\Delta_1}, \\ \tau^{tip} &= 2\sqrt{2/\pi}\, K_2^{tip} / \sqrt{\Delta_2} . \end{aligned} \tag{7}$$

2.2. Interface separation law under mixed mode loadings

As mentioned above, upon loading, dislocations will emit from the crack tip and pile-up against the upper interface. This prevents the further emission of dislocations which impedes blunting of the crack tip. Continuous loading will increase the crack tip stress. It is assumed that interface separation will occur when the combination of the tensile and shear stresses at the interface reaches a critical value. This separation law is expressed as

$$(\frac{\sigma^{tip}}{\sigma_b})^2 + (\frac{\tau^{tip}}{\tau_b})^2 = 1, \tag{8}$$

where, σ_b and τ_b are the tensile strength and shear strength at the interface. We assume that

$$\lambda = \sigma_b / \tau_b , \tag{9}$$

3. CRACK INITIATION TOUGHNESS Γ_i

Based on the analysis presented in section 2, the crack tip stress will be shielded by the superdislocation. Thus, the fracture energy associated with this dislocation shielding will be different from the fracture energy without dislocation emission. In general, the energy release rate at the interface can be expressed by [6]

$$G^{app} = \frac{1-\beta^2}{E^*}[K_1^{tip'2} + K_2^{tip'2}] \tag{10}$$

where $\frac{1}{E^*} = \frac{1}{2}(\frac{1}{\overline{E_1}} + \frac{1}{\overline{E_2}})$, $\overline{E_i} = E_i / (1-\nu_i^2)$ for plane strain and $\overline{E_i} = E_i$ for plane stress. E_1, E_2 and ν_1, ν_2 are the Young's modulus and Poisson's ratios for the metal and the ceramic layers respectively. From Eqs.(2-9) assuming $\beta = 0$, the energy release rate, G^{app}, after dislocation shielding can be expressed by [14]

$$G^{app} = \frac{1}{E^*}\mu^2 b\{[\frac{\sqrt{n\sin\varphi}\,\bar{\sigma}^{tip}}{2\sqrt{2/\pi}} + \frac{3}{2}n\frac{1}{(1-\nu)\sqrt{2\pi\bar{h}}}f_1(\varphi)]^2 + [\frac{\sqrt{n\cos\varphi}\,\bar{\tau}^{tip}}{2\sqrt{2/\pi}} + \frac{3}{2}n\frac{1}{(1-\nu)\sqrt{2\pi\bar{h}}}f_2(\varphi)]^2\} \quad (11)$$

where $\bar{\sigma}^{tip} = \sigma^{tip}/\mu$ and $\bar{\tau}^{tip} = \tau^{tip}/\mu$. n also can be considered as a measure of crack tip opening. With the separation condition expressed by (8), the crack initiation toughness under mixed mode is

$$\Gamma_i(\Psi^{tip}, \bar{h}, \bar{\sigma}_b, \lambda) = \frac{1}{E^*}\mu^2 b\{[\frac{\sqrt{n'}\bar{\sigma}_b}{2\sqrt{2/\pi}\,f} + \frac{3}{2}n'\frac{1}{(1-\nu)\sqrt{2\pi\bar{h}}}f_1(\varphi)]^2 + [\frac{\sqrt{n'}\bar{\sigma}_b\tan\Psi^{tip}}{2\sqrt{2/\pi}\,f} + \frac{3}{2}n'\frac{1}{(1-\nu)\sqrt{2\pi\bar{h}}}f_2(\varphi)]^2\} \quad (12)$$

where $n'(\bar{\sigma}_b, \Psi^{tip}, \bar{h}, \bar{\gamma})$ is a critical dislocation number at crack initiation and can be derived from equations (2, 7-8).

5. RESULTS AND DISCUSSION

In order to demonstrate the theoretical model developed above, an Al_2O_3 / Au / Al_2O_3 system was selected with experimental results obtained by Mao and Evans [13]. With FCC Au as the middle layer[14], the interface crack is on the plane (100) and (111) is the slip plane. The angle between these two planes is 70.5^o, which means that dislocations will emit from the interface crack tip with an angle $\varphi = 70.5^o$. Different values of normalized layer thickness $\bar{h}$ and theoretical tensile stress at the interface crack tip $\bar{\sigma}_b$ are employed to compare the toughness of the material. As also done by Mao and Evans [13], the Burgers vector b is set to $0.286\,nm$ (for Au), h is on the order of a few microns, $\lambda = 1$, $\nu = 0.44$ and $\alpha = 0.58$

A pure mode I loading is obtained if $\Psi^{tip} = 0$. This case was analyzed in detail by Mao and Evans [13], and one important result is shown on Fig. 2. For a fixed layer thickness, the fracture energy needed for the interface crack to initiate cleavage increases when the interfacial tensile strength of the layered material is increased. For fixed interfacial tensile strength, the thicker layer needs more energy to encourage crack cleavage. For $\Psi^{tip} \neq 0$, fracture energy curves for crack initiation are plotted on Fig. 3 as a function of Ψ^{tip} at fixed values of $\bar{\sigma}_b$. Generally, the transition from mode I to mode II increases the difficulty for the interface crack to propagate. Variation of the interfacial tensile strength showed that the stronger the interfacial strength, the metal layer, the more energy that is needed for crack propagation. Fig. 3 shows that there is a large increase in fracture energy when the loading phase is above 60^o. Using Eq (12, interfacial toughness can be predicted if we know the interfacial strength. The interfacial strength σ_b measurement is being developed by Mao recently. Fig. 4 shows an example of the interfacial adhesion force measurement of Au/Al_2O_3 interface by indenting Au coated tip on Al_2O_3 (0001) single crystal substrate.

6. CONCLUSION

In summary, the strong dependence of interface toughness on the relative proportion of mode II to mode I loading, seen in experimental data, is predicted by a dislocation model with an embedded traction separation law that characterizes the fracture process on the interface. The increase in toughness with increasing proportion of mode II to mode I loading is predicted to be a consequence of dislocation shielding outside of the fracture process zone. The dependence of the interfacial fracture toughness on the thickness of metal layer and interfacial strength have been found.

Acknowledgments – The author acknowledges the donors of the Petroleum Research Fund, administered by the ACS, for partial support of this research under (ACS-PRF#35989-AC5).

7. REFERENCE

1. C. F. Shih and R. J. Asaro, *J. Appl. Mech*. **55**, 299 (1988).
2. E. Zywicz and D. M. Parks, *J. Mech. Phys. Solids* **40**, 511 (1992).
3. K. Bose and P. Ponte Castaneda, *J. Mech. Phys. Solids* **40**, 1053 (1992).
4. C. F. Shih, *Mater. Sci. Engng.* **A143**, 77 (1991).
5. K. M. Liechti and Y. S. Chai, *J. Appl. Mech*. **59**, 295 (1992).
6. J. W. Hutchinson and Z. Suo, *Advances in Applied Mechanics* **29**, 63 (1991).
7. V. Tvergaard and J. W. Hutchinson, *J. Mech. Phys. Solids* **41**, 1119 (1993).
8. V. Tvergaard and J. W. Hutchinson, *Phil. Mag.* **70**, 641 (1994).
9. Y. G. Wei and J. W . Hutchinson, *Mat. Res. Soc. Symp*. **409**, 163 (1996).
10. Y. G. Wei and J. W. Hutchinson, *J. Mech. Phys. Solids*, (1996).
11. Z. Suo, C. F. Shih and A. G. Varias, *Acta metall. Mater*. **41**, 1551 (1993).
12. G. R. Beltz and J. R. Rice, *Acta metall. Mater*. **40**, S321 (1992).
13. X. Mao and A. G. Evans, *Acta metall*. Vol.45, No.10, pp4263-4270(1997).
14. S.X. Mao and M. Li, *J. Mech. Phys. Solids*, 47 (1999) 2351-2379.
15. Tada, H., Paris, P. C. and Irwin, G. R. (1985) The stress analysis of crack handbook. 2nd Ed. Paris Productions Incorporated, St Louis, MI.

Figure Caption

Fig. 1. Layered material mode with an interface crack.

Fig. 2. Crack initiation fracture toughness energy.

Fig. 3. Interfacial strength effect on crack initiation energy versus phase angle Ψ^{tip}.

Fig. 4 Example of Interfacial adhesion force measurement by atomic force microscope.

ORAL/REFERENCE:ICF1003040R

INTERFACIAL FORCE MICROSCOPY STUDIES OF γ-APS ON GLASS AND SiO_2

K. M. Liechti[1], K. C.Vajapeyajula[1], M. Wang[1], H. Cabibil[1], H. Celio[1], J.M. White[1] and R.M. Winter[2]

[1]Research Center for the Mechanics of Solids, Structures and Materials, Texas Materials Institute, University of Texas, Austin TX 78712
[2]Department of Chemistry and Chemical Engineering, South Dakota School of Mines and Technology, Rapid City, SD 57701

ABSTRACT

Silane coupling agents are often used as adhesion promoters between polymers and ceramics or metals. They form a thin interphase region whose mechanical properties are thought to differ from those of the bulk polymer. This paper describes the use of an interfacial force microscope to conduct nanoindentation experiments on 50-nm thick layers of γ-APS on glass and SiO_2. The Young's modulus of the γ-APS on glass was one quarter of that on γ-APS on SiO_2. The reasons for this were explored via X-ray photoelectron spectroscopy and Fourier transform infrared spectroscopy. It was found that the Na+ ions in the glass destroyed the cross-links in the γ-APS.

KEYWORDS

Coupling agents, mechanical properties, interfacial force microscope, spectroscopy, interfacial fracture.

INTRODUCTION

Swadener et. al. [1] have shown via X-ray photoelectron spectroscopy (XPS) and atomic force microscopy (AFM) that mixed-mode fracture near a glass/epoxy interface left a 3 nm layer of epoxy on the glass surface. Such a cohesive crack path helped explain why the high intrinsic toughness of the interface was 20 times higher than the thermodynamic work of adhesion of the glass/epoxy interface. Other studies of glass/epoxy interfaces (Drzal [2]; Winter and Houston [3]) have indicated the presence of an interphase region where polymer properties are affected by the substrate so that there is a transition from the substrate to the bulk behavior of the polymer. Presumably, the subinterfacial fracture noted by Swadener et. al. [1] took place in such an interphase region. The traction-separation law of this region was extracted in an iterative manner via a combination of crack opening interferometry and finite element analysis. The objective of this work is to make more direct assessments of traction-separation laws of interphase regions.

EXPERIMENT

One promising instrument for these purposes is the interfacial force microscope (IFM). The IFM (Fig. 1) is unique in that it employs a self-balancing, force feedback sensor which allows force profiles (load vs. displacement data) to be obtained while the sensor remains rigidly fixed in position throughout the measurement (Joyce and Houston [4]; Houston and Michalske [5]).

In this study, the (IFM) was first used to probe the nanomechanical properties of hydrolyzed γ-aminopropyltriethoxysilane γ-APS films fabricated by spin coating on soda glass and SiO_2 surfaces. The γ-APS is widely used as a coupling agent for fiberglass-reinforced composites and as a primer for adhesive joints with thicknesses ranging from a few nanometers to hundreds of nanometers. The film was probed in the IFM apparatus with a Tungsten tip that had a 120-nm radius (Fig. 2).

The Young's modulus of the γ-APS was extracted from the measured load-displacement response from the IFM using Hertzian , JKR [6] and Maugis [7] analyses. The latter two approaches account for surface interactions inside and beyond, respectively, the contact region.

RESULTS

Typical load-displacement responses from the IFM indentation on γ-APS films on SiO_2 are shown in Figure 3. It was found (Table 1) that the modulus of 50 nm thick γ-APS films on glass was a quarter of the modulus values of the γ-APS films on SiO_2. XPS analysis revealed that leaching of Na^+ ions from the glass into the γ-APS destroyed cross-links, making it softer. The moduli listed in Table 1 were extracted on the basis of a Hertzian analysis. Accounting for surface interactions through JKR and Maugis analyses did not significantly alter modulus values.

The moduli of the two γ-APS films were considerably higher than polymers in their glassy state, which at first suggests that the substrates may have had an effect on the results. However, γ-APS the moduli were the same when 75 and 120-nm thick layers were employed and, in all cases, the indentations were less than 10% of the layer thickness. The modulus for glass was in line with typical values, which gave confidence to the operation of the IFM. The modulus for the SiO_2 was high, but was most likely influenced by the Si substrate beneath. As a result, there is a lot of confidence in the quoted modulus values of γ-APS and certainly that the glass substrate affected the chemistry of the γ-APS film. In current work, the modulus of remaining layers of polymer on the glass and SiO_2 fracture surfaces is being probed.

TABLE 1.
YOUNG'S MODULI FROM NANOINDENTATION WITH AN IFM

Film/ Substrate	Poissov Ratio*	Modulus** E_2 (GPa)	Roughness (A˚)
γ-APS/Glass	0.25	8±2	2.2±0.4
γ-APS/Glass	0.25	35±3	2.2±0.5
Glass	0.17	74±6	7.4±2.8
Native SiO_2	0.25	112±17	1.5±0.4

Tungsten tip $E_1 = 400\,\text{GPa},\ \nu_1 = 0.30$.
* Literature values
**Average of 7-10 loading cycles

REFERENCES

1. Swadener, J. G., Liechti, K. M. and de Lozanne, A. L. (1999). J. Mech. & Phys. Solids, 47, 223-258.
2. Drzal, L. T. (1986). Adv. in Polym. Sci., 75, 1-32.
3. Winter, R. M., and Houston, J. E., (1998), Proc. of the SEM Spring Conf. on Exp. and Applied Mechanics, Houston, TX, June 1-3, 1998.
4. Joyce, S. A., and Houston, J. E., (1991), Rev. Sci. Instr., 62 (3), 710 - 715.
5. Houston, J. E., and Michalske, T. A., (1992), Nature, 356, pp. 266 - 267.
6. Johnson, K. L., Kendall, K. and Roberts, A. D. (1971) Proc. R. Soc. London, **A 324**, 301-313.
7. Maugis, D. (1992) J. Colloid and Interface Sci., **150**, 243-269.

ORAL/REFERENCE:ICF1003040R

FIGURES

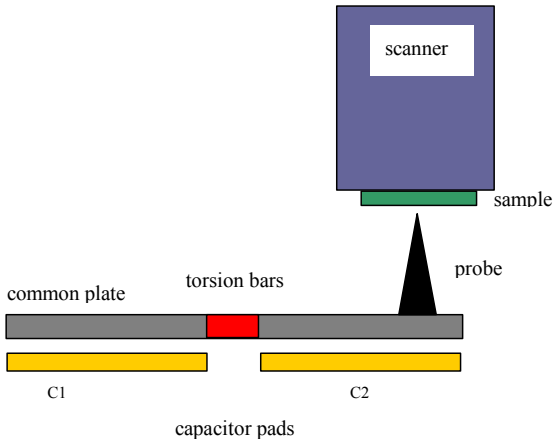

Figure 1. Interfacial force microscope.

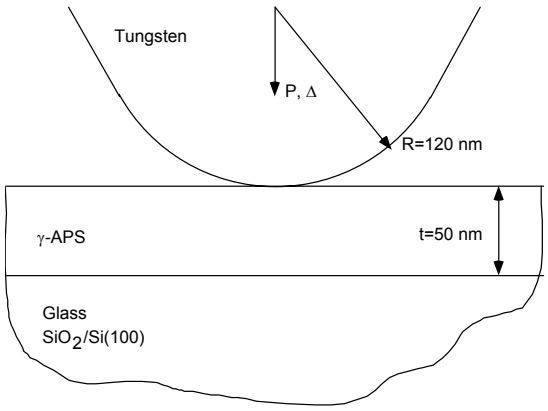

Figure 2. Specimen geometry for the nanoindentation experiment.

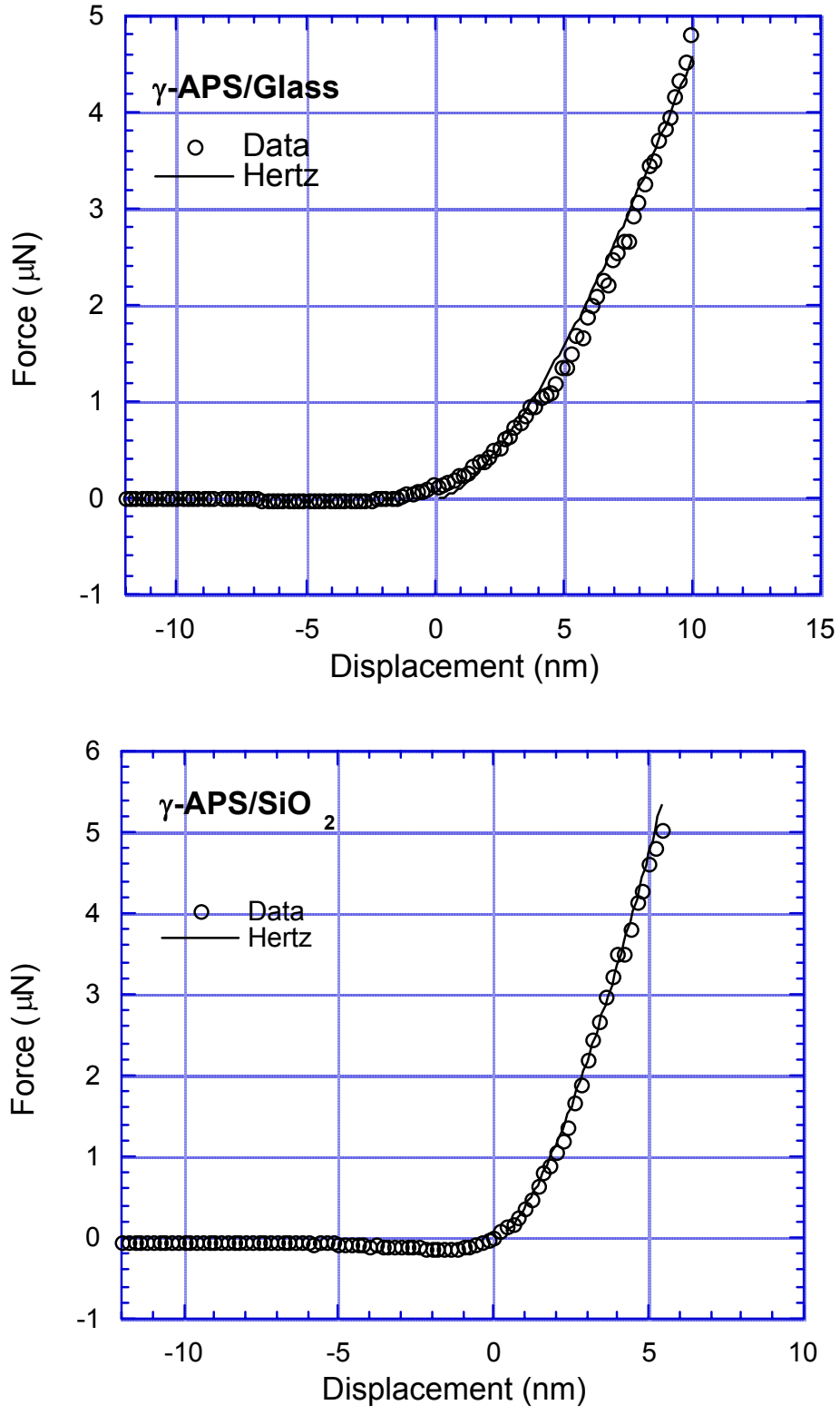

Figure 3. Contact force-displacement responses for γ-APS on glass and SiO_2

INTERNAL DAMAGE TO WIRE ROPES ON CRANE : CASE STUDIES OF FRACTURE ACCIDENTS AND COUNTERMEASURES FOR PREVENTION

M. Tanaka

Mechanical and System Safety Division, National Institute of Industrial Safety,
Ministry of Health, Labor and Welfare, Tokyo, 2040024, Japan

ABSTRACT

Recently in Japan, considerable number of crane accidents due to the fracture of IWRC wire ropes occurred. From the results of the precise analysis of such crane accidents, it was predicted that IWRC wire ropes were prone to internal damage. Therefore, in this study S-bending fatigue tests were conducted on two kinds of IWRC wire rope under a wide range of testing conditions to certify the prediction. The results showed that it was correct. This means that the present situation would be serious, because wire rope inspections are commonly completed by visual observation of external features, which would not reveal internal damage.
To improve such situation, several countermeasures against internal damage inherent in the IWRC wire rope were examined, and two methods were eventually selected as the most practical ones.

KEYWORDS

Wire rope, Crane, Fracture accident, Internal damage, Bending fatigue, Damage inspection.

1. INTRODUCTION

Recently in Japan, IWRC (Independent Wire Rope Core) wire ropes are extensively used for cranes, especially for mobile cranes. Under such situation considerable number of serious crane accidents due to the fracture of wire ropes occurred during the last decade［1］. However, the proper practical countermeasures had not been proposed because the essential cause of this kind of accident has not been clarified,.

Therefore, in this study, accident cases which resulted in casualties (death) were reviewed and the failure properties of IWRC wire ropes were investigated first. Then, to certify the prediction obtained by the first investigation that the wire ropes of this kind are prone to internal damage, a series of S-bending fatigue experiments were conducted on two kinds of IWRC wire ropes under a wide range of conditions, and the problem of the present situation relating to the safety aspects of inspection was pointed out［2］. Finally, several countermeasures against internal damage inherent in the IWRC wire ropes were examined to overcome this serious problem and prevent further accidents.

2. ACCIDENT CASES

2.1 *Case 1: Fracture of Derricking Wire Rope*

a) Description of the accident

When the steel material of about 0.8ton were being hoisted by a 588kN crane in the building construction

site, the wire rope having been used as jib derricking wire rope suddenly broke and the worker near that place was hit by the auxiliary jib and died on the spot.

b) Description of the wire rope and its failure condition

The fractured wire rope has a construction of IWRC 6×Fi (29) shown in **Figure 3** (a) in, with diameter of 16mm,and tensile strength 188kN having been used under the conditions shown in **Figure1**, with D/d =16 (D is the pitch circle diameter of sheave, and d is the rope diameter). The accident occurred eleven months after the wire rope replacement.

At the fractured portion, (1) distinct deformation of wire cross section, (2) internal wear due to the mutual compression and the rubbing between strand wires and core wire rope, and (3) many wire breakings of the cross section type with little elongation or necking are observed. **Figure2** shows an example of this kind of internal damage.

Most wires in core rope, many external wires, some internal wires of strands and all six core wires in them had broken with this type. However, in internal wires and core wires in strands, distinct deformation and wear were not observed. The precise observation by scanning electron microscope (SEM) disclosed that the above mentioned wire breaking of cross section type had occurred by fatigue crack initiation on the surface of wires and the following crack growth due to repeated rope bending at the sheaves.

The wires that kept effective strength until the moment of accident were only one third of internal wires of strands. The" cup and cone "type fracture different from the cross section type shows that they fractured at the accident not in fatigue but in static fracture mode. And the strength of the rope was estimated to be one tenth of the normal one. The external wear and wire breaking were not so extreme in comparison with internal ones. For example, the number of external wire breaking was about one forth of that of internal one at 1.5m from the fractured portion.

c) The cause of accident

The direct cause of this accident was the remarkable decrease of strength of derricking wire rope due to

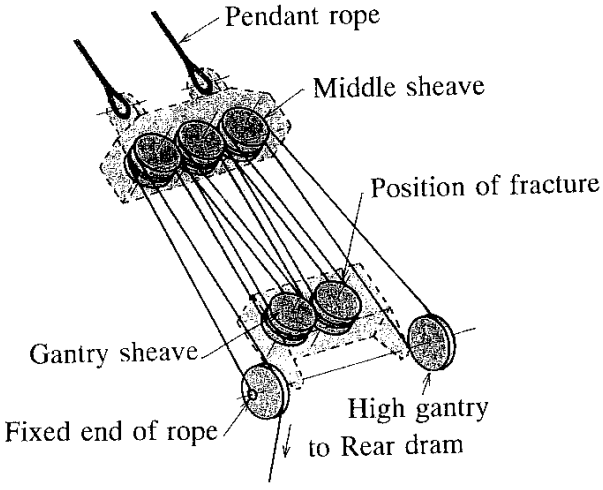

Figure 1: The path of derricking wire rope and fractured position

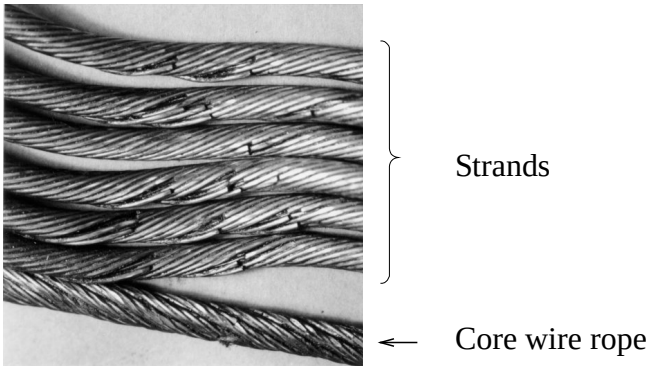

Figure 2: The feature of wire breaking inside the rope near the fractured portion

internal wear and the following fatigue failure. However, the intrinsic cause seemed to be that the damage had proceeded preferentially at internal portion and was very difficult to be found.

2.2 *Case 2: Fracture Accident of Hoisting Wire Rope*

a) Description of accident

The main hoisting wire rope of a crawler crane with a working capacity of 1470kN broke while hoisting a 44ton concrete block to be installed for a water break. The broken wire rope hit a worker on his head and he died instantaneously.

b) Description of the wire rope and working history

The wire rope was also an IWRC 6×Fi(29) with nominal diameter of 28mm and nominal breaking strength of 620kN and had been used for about 1.5 years.

c) The cause of accident

This accident was also caused by the extreme decrease of wire rope strength due to severe wear and excessive corrosion. Therefore, the primary or direct cause was improper management and inspection of the crane. However, almost all grease had been lost from the wire rope near the fractured portion and it was characteristic as a whole that the internal damage was heavier than the external one.

3. CHARACTERISTICS OF DAMAGE TO IWRC WIRE ROPE AND ITS PROBLEMS

3.1 *Characteristics of Damage*

a) Internal wear and fatigue wire breaking

Two examples of accidents due to the fracture of IWRC wire rope used as travelling rope were introduced. The Case1 is a typical example of fatigue failure with considerable wire breaking and the Case 2 is one with heavy corrosion. And both examples show that the internal damage played an important or essential role for the fracture. Similar results has been obtained by the precise investigation by the author on about ten cases and further by the experiment on similar ropes［3］. Taking into account these results and also that the most typical internal wire breaking at the bed portion can’t occur in usual fiber rope core wire ropes, it may be predicted that IWRC wire ropes used as traveling ropes are prone to internal damage.

3.2 *Problems in Maintenance and Inspection*

As to the safe application of crane wire ropes, Japanese standard shows a guideline for the discard of damaged wire ropes. But it does not include the specific method of inspection, and so far the external observation by the naked eyes has been applied practically.

However, if the main damage exists inside the rope, it is impossible to detect them by this method, even if the level of damage exceeds the allowable limit. Therefore this method can't be said the appropriate inspection method as the last resort for safety assurance.

4. CERTIFICATION OF DAMAGE PROPERTIES OF IWRC WIRE ROPES

By the way, it has not been clear whether the prediction described above is correct or not, because the working conditions or history of working loads could not be confirmed for all accidents, and under such situation it would be difficult to focus the target of countermeasures to prevent the similar accidents. To improve such ambiguous situation, the following experiment was conducted at first to certify whether the remarkable internal damage as mentioned above could be formed even under the allowed loading conditions or not, and then to confirm the relations between the damaging conditions and the various testing conditions.

4.1 *Experimental Procedures*

Two kinds of wire ropes; IWRC 6×Fi (29) and IWRC 6×WS (31) were used for this experiment. Both ropes are of Ordinary lay type with red grease without plating, and their nominal ultimate breaking loads are equally 173.6kN. **Figure3** shows their construction. Fatigue tests were conducted mainly under cyclic S-

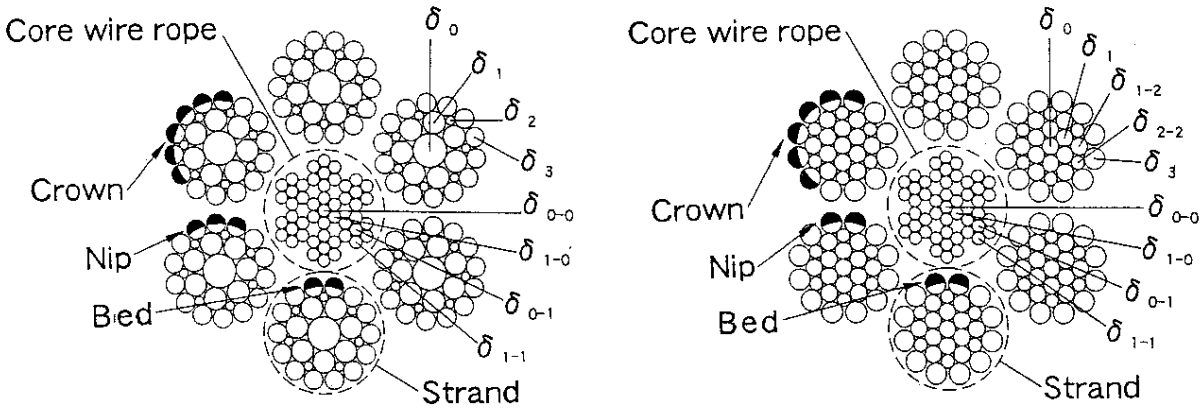

(a) IWRC 6×Fi (29) (b) IWRC 6×WS (31)

Figure 3: Construction of the test wire ropes

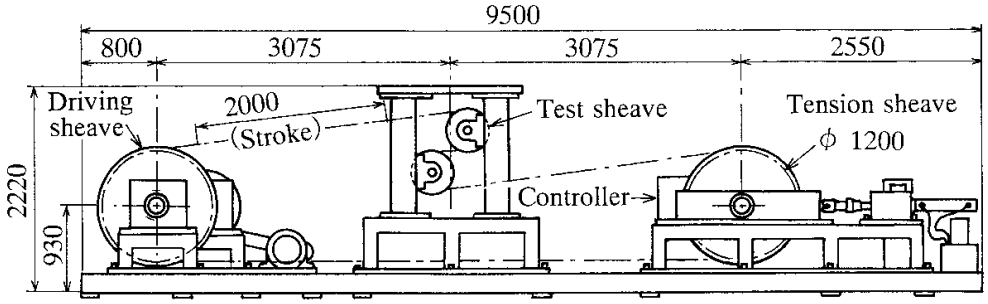

Figure 4: Wire rope fatigue testing machine

bending as shown in **Figure 4**, basically with D/d of 16, rope tension of 34.7kN and cyclic frequency of 10 cycles per minute. Moreover, fatigue tests were conducted with those conditions changed widely to clarify their effect on the rope damaging properties. Fatigue test were stopped when the number of external wire breaking in each rope pitch reached at 10 % of the number of strand wires, and the numbers of wire breaking in various positions (crown ,nip and bed) of strands were counted respectively for 20 pitches in the fatigued portion.

4.2 *Results and Discussion*

Figure 5 shows an example of the wire breaking distribution at various structural positions for IWRC 6×Fi (29) tested under the basic conditions described above. It is clearly that the number of internal wire breaking at bed and nip portions is more than that of visible wire breaking. The similar results were obtained for IWRC 6×WS (31) ropes, although wire breaking at nip portion was dominant in this case.

Figure 6 and **Figure 7** summarize the influence of various mechanical testing conditions including U-bending and some environmental conditions on the wire breaking distributions for both kinds of IWRC ropes, respectively. These results show that the internal damage was dominant or preferential to external ones, excluding for a few rare cases. There is no condition where damage is suppressed concurrently for both

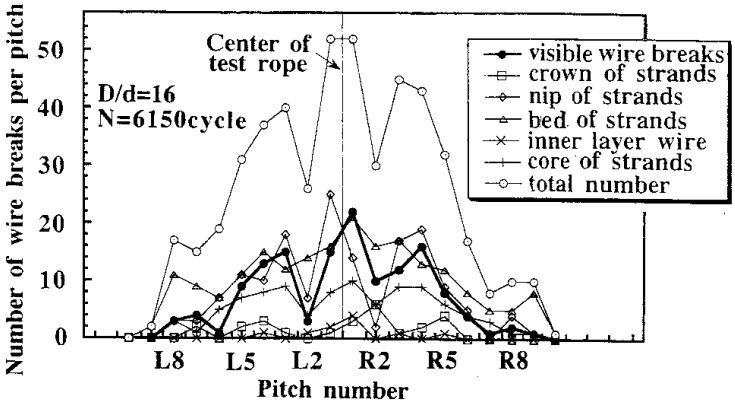

Figure 5: An example of wire breaking at various position in IWRC 6×Fi (29)

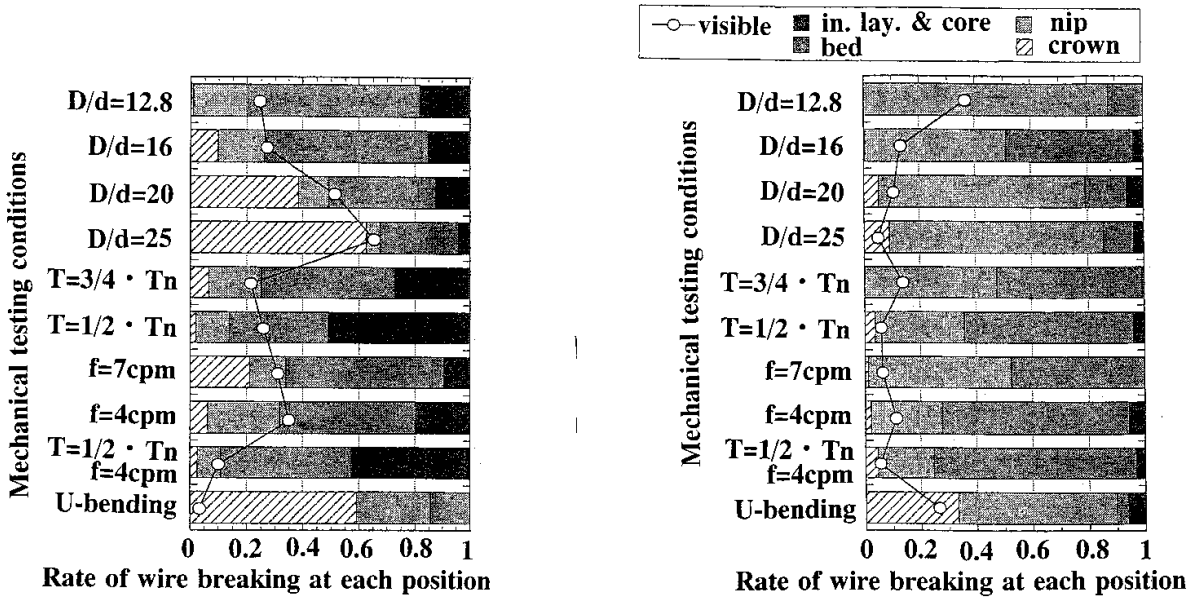

(a) IWRC 6×Fi (29) (b) IWRC 6×WS (31)

Figure 6: Influence of various mechanical conditions on the wire breaking distribution

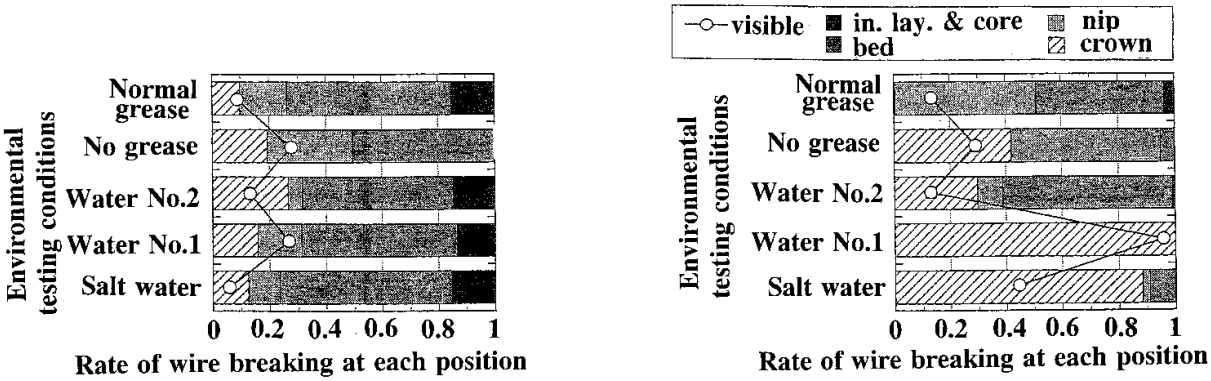

(a) IWRC 6×Fi (29) (b) IWRC 6×WS (31)

Figure 7: Influence of various environmental conditions on the wire breaking distribution

kinds of ropes. From these results, it can be concluded that the prediction described in Section 3.1 is correct and the problem in maintenance and inspection pointed out in Section 3.2 exists actually. Therefore, it is natural to suppose that most of the recent rope fracture accidents as introduced in the section 2 were caused essentially because inspectors had not recognized clearly the significance of such internal damaging property of IWRC ropes.

5. MEASURES FOR THE PREVENTION OF IWRC WIRE ROPE FRACTURE ACCIDENTS

So far, there is no general or decisive countermeasure to prevent fracture accidents of IWRC ropes used as traveling ropes, and some temporary or second best measures have been proposed as followings.

(1) Direct observation of internal portion of the rope
By attaching clamp levers to both sides of the observation point of the rope and loosening the rope by them, the internal damages can be observed directly if there exist distinct ones ［4］ .
(2) Making the discard standard more strict
When only the external inspection is cited inevitably, the rope should be discarded if any or a few, for example, one or two wire breaking was detected.
(3) Shortening of working period
In the case where a rope has been used for a fairly long period and there is no reliable data for working period, the rope should be replaced soon as a temporary measure, and precise damage investigations are

recommended in order to decide the reasonable replacing period for the following wire ropes. It will be more effective if the aforementioned three measures are combined.

(4) Getting rid of factors contributing to the internal damage

Unfavorable factors to prevent the internal damage, such as small D/d, overloading and extreme rope-pattern wear on the surface of sheave groove should be eliminated.

(5) Sufficient grease supply

It is necessary to supply sufficient grease to wire ropes especially of IWRC type when they are used in the corrosive environments such as sea water and so on.

(6) Development of inspection methods and devices

It is strongly expected that new procedures or instruments with the sufficient reliability and theease of treatment for practical use will be developed at low cost.

(7) Standardization of method of wire rope diameter measurement

It seems possible to use the decrement of rope diameter as a measure for discard if the measurement conditions are properly decided, for example, such as "under a constant extension force".

(8) Precise analysis of properties of damage

As decisive or final measures to improve the present situation , it is necessary to investigate the damage properties for this kind of wire ropes systematically.

As the result of the studies by concerning persons (Ministry of Labor, Japan Crane Association, rope makers and crane users) and the performance certification tests by the author on a new commercial rope tester, two concrete countermeasures were selected and recommended as realistic ones.

The first one is "the simple inspection manual for crane wire ropes" proposed by Japan Crane Association. This is a combined method of measure *(2)* and other ones, in which the simple naked eye's observation method with discarding level more strict than usual ones (for example, provided in Crane Structure Code) for various kinds of damages is adapted first, and the rope with higher damage level should be discarded or checked if it can be used further safely, by means of more reliable inspection methods.

The second one is an electro-magnetic damage inspection method using new detecting apparatus developed recently by a rope maker in Japan. According to the study on its detecting ability of internal wire breaking, it has realistically satisfactory performance for checking the safety of IWRC wire ropes.

6. CONCLUDING REMARKS

Damaging properties of IWRC wire ropes were investigated by means of case studies and wide range of S-bending fatigue experiments, and countermeasures were examined to prevent the possible accidents caused by the internal damages of this kind of wire ropes. Main result obtained are summarized as follows.

(1) From the results of the precise analysis of crane accidents caused by the fracture of wire rope, it was predicted that IWRC ropes were prone to internal damage.
(2) The results of extensive fatigue experiments showed that the prediction described above was correct, which means that the present situation would be serious because the wire rope inspections commonly completed by visual observation of external features would not reveal internal damage.
(3) To improve such situation, several countermeasures against internal damage inherent to the IWRC wire ropes were examined, and two practical methods were recommended. The first one is "the simple inspection manual for crane wire ropes", and the second one is the application of electro-magnetic damage detecting apparatus recently developed.

REFERENCES

1. Tanaka, M.(1989). Report on Jib Falling Accident in Dock Crane (in Japanese).
2. Tanaka, M.(1995). Mining and Material '95, Proceeding for Wire Rope (in Japanese), pp.36- 38.
3. Gibson, P. T. et al. (1974). Final Report to Naval Ship System Command.
4. ISO 4340-1990, Annex D, Internal Examination |of Wire Rope, pp. 11-12.

INTRODUCTION OF THE HAMILTONIAN SYSTEM INTO THE ASYMPTOTIC ANALYSIS IN FRACTURE MECHANICS

J. LI

Laboratoire d'Etudes et de Recherches en Mécanique des Structures
Blaise Pascal University of Clermont-Ferrand
Avenue Aristide Briand, 03100 Montluçon, France

ABSTRACT

The asymptotic analysis is a powerful tool in fracture mechanics. The principal criteria of the fracture toughness, such like *K* and *J*, were established on the basis of the asymptotic analysis of the crack-tip fields. In traditional theories, asymptotic analyses are often carried out by using the Airy stress function in establishing high-order differential equations governing the near-tip fields. However, as far as the problems posed in fracture mechanics become complicate, the establishment and the solution of the high-order differential equations become more and more difficult. In this paper, we make use of another philosophy in the asymptotic analysis in fracture mechanics. The key idea is to introduce the Hamiltonian system, usually studied in rational mechanics, into continuum mechanics. We present in this paper the guideline of this method through a simple bi-dimensional elastic problem. The establishment of the governing equations was performed by imitating either the radial coordinate or the angular coordinate as "time". By defining the dual variables in the state space, systems of the first-order differential equations were obtained. The solution methods are also discussed in the frame of eigenvalue computations. It was shown that this method is very efficient and quite simple in establishment and solution of the governing equations of this class of problems. It allows considerations of a large range of problems which are difficult for traditional methods.

KEY WORDS

Near-tip fields, asymptotic analysis, Hamiltonian system, eigenvalue problems

INTRODUCTION

The asymptotic analysis is a powerful tool in fracture mechanics. It permits to write the near-tip fields of a crack or a notch, singular or not, under expansion form. The intensity of these fields can be determined by considering the boundary conditions of the structure by means of some well-chosen parameters. In general, the first term in the expansion suffices to characterize the near-tip fields. If it is not accurate enough, other terms can be added. The principal criteria of the fracture toughness, such like *K* and *J*, were founded on the basis of the asymptotic analysis of the crack-tip fields.

Williams (1957) first carried out asymptotic study near a crack-tip in bi-dimensional elastic material. Airy stress function was used in establishing a fourth order differential equation governing the near-tip fields. Afterward, this method was essentially followed in the asymptotic analysis in fracture mechanics. One can list numerous important results found by using this method. However, as far as the problems posed in the fracture mechanics become complex, the establishment and the solution of the high-order differential

equation become more and more difficult. In certain cases, the stress function may not exist; this makes the traditional method inadequate in these studies.

In this paper, we will make use of another method in the asymptotic analysis in fracture mechanics. The key idea of this new method is to introduce the Hamilton principle, usually used in rational mechanics, into continuum mechanics. Zhong (1995) systematically described this methodology in solving elasticity problems. We believe that it will be helpful to introduce it into fracture mechanics, especially in the asymptotic analysis of the near-tip fields.

Rational mechanics often makes use of the Lagrange function (cinematic energy – potential energy) to describe a dynamic system. It can be represented as function of the generalized displacement vector and its deviation with respect to time, i.e. $L(\boldsymbol{q},\dot{\boldsymbol{q}})$. The Hamilton principle is described as follows: the true movement trajectory from time t_0 to time t_1 of a conservative system makes the action A minimal:

$$\delta A = \delta \int_{t_0}^{t_1} L(\boldsymbol{q},\dot{\boldsymbol{q}})dt = 0 \qquad (1)$$

This variational principle leads to the Langrage equation:

$$\frac{d}{dt}\frac{\partial L}{\partial \dot{\boldsymbol{q}}} - \frac{\partial L}{\partial \boldsymbol{q}} = 0 \qquad (2)$$

By introducing the vector of generalized momentum $\boldsymbol{p} = \dfrac{\partial L}{\partial \dot{\boldsymbol{q}}}$ and the Hamilton function $H(\boldsymbol{q},\boldsymbol{p}) = \boldsymbol{p}^T\boldsymbol{q} - L(\dot{\boldsymbol{q}},\boldsymbol{q})$, the Lagrange equation can equivalently be written under form of the Hamilton canonical equations:

$$\dot{\boldsymbol{q}} = \frac{\partial H}{\partial \boldsymbol{p}} \quad \dot{\boldsymbol{p}} = -\frac{\partial H}{\partial \boldsymbol{q}} \qquad (3)$$

Return back now to fracture mechanics. We can actually write the equations governing the crack tip fields under form of (3). The main idea is to consider one coordinate in the polar system as "time" and take the total potential energy as the Lagrange function. For example, we can consider the radial coordinate r or the angular coordinate θ as time and take the variational principles established in continuum mechanics as the Hamilton variational principle. Then all the procedures currently used in rational mechanics can be translated into continuum mechanics.

Recent studies using this new methodology provided exciting results in asymptotic analysis of crack-tip fields. Not only we can find all existing results in this topic, but also new solutions that may be difficult for classical methods. In order to present clearly the application of the new method, let us consider the most classical problem in this topic, a semi-infinite crack in an elastic plane stress body as studied by Williams (1957).

2: HAMILTONIAN SYSTEM WITH RADIAL COORDINATE TREATED AS "TIME"

Consider the domain $\{-\pi \le \theta \le \pi,\ 0 \le r \le R\}$ in the polar coordinate system. The strain energy in this domain can be represented as function of displacements $\{u_r \quad u_\theta\}$:

$$U = \frac{E}{2(1-\nu^2)}\int_{-\pi}^{\pi}\int_{0}^{R}\left[\left(\frac{\partial u_r}{\partial r}\right)^2 + 2\nu\left(\frac{\partial u_r}{\partial r}\right)\left(\frac{u_r}{r}+\frac{1}{r}\frac{\partial u_\theta}{\partial \theta}\right)+\left(\frac{u_r}{r}+\frac{1}{r}\frac{\partial u_\theta}{\partial \theta}\right)^2 + \frac{1-\nu}{4}\left(\frac{\partial u_\theta}{\partial r}-\frac{u_\theta}{r}+\frac{1}{r}\frac{\partial u_r}{\partial \theta}\right)^2\right] r dr d\theta \qquad (4)$$

where E is the Young modular and ν is the Poisson ratio. For more convenience, we perform the following variable changes:

$$r = e^{\xi} \quad \xi = \ln r \qquad (5)$$

Since the radial coordinate ξ is treated as "time", we note $\dfrac{\partial}{\partial \xi} = (\bullet)$, then (4) becomes

$$U=\frac{E}{2(1-\nu^2)}\int_{-\pi}^{\pi}\int_{-\infty}^{R}\left[(\dot{u}_r)^2+2\nu(\dot{u}_r)\left(u_r+\frac{\partial u_\theta}{\partial\theta}\right)+\left(u_r+\frac{\partial u_\theta}{\partial\theta}\right)^2+\frac{1-\nu}{4}\left(\dot{u}_\theta-u_\theta+\frac{\partial u_r}{\partial\theta}\right)^2\right]d\xi d\theta \tag{6}$$

Without taking the external forces into account, the potential energy of the structure Π=U. We first take the displacement components as the generalized displacement vector $\boldsymbol{q}$.

$$\boldsymbol{q}=\{u_r \quad u_\theta\}^T \tag{7}$$

Then $U=U(\dot{\boldsymbol{q}},\boldsymbol{q})$, the principle of minimum potential energy can be written as:

$$\frac{d}{d\xi}\frac{\partial U}{\partial\dot{\boldsymbol{q}}}-\frac{\partial U}{\partial\boldsymbol{q}}=0 \tag{8}$$

Introducing the generalized momentum vector $\boldsymbol{p}=\dfrac{\partial U}{\partial\dot{\boldsymbol{q}}}$, one obtains:

$$\boldsymbol{p}=\begin{Bmatrix}\dfrac{E}{1-\nu^2}\left[\dfrac{\partial u_r}{\partial\xi}+\nu\left(u_r+\dfrac{\partial u_\theta}{\partial\theta}\right)\right]\\ \dfrac{E}{2(1+\nu)}\left[\dfrac{\partial u_\theta}{\partial\xi}-u_\theta+\dfrac{\partial u_r}{\partial\theta}\right]\end{Bmatrix}=r\begin{Bmatrix}\sigma_{rr}\\ \sigma_{r\theta}\end{Bmatrix} \tag{9}$$

By adopting the notation:

$$S_{rr}=r\sigma_{rr}\quad S_{\theta\theta}=r\sigma_{\theta\theta}\quad S_{r\theta}=r\sigma_{r\theta} \tag{10}$$

the generalized momentum vector becomes:

$$\boldsymbol{p}=\{S_{rr}\quad S_{r\theta}\}^T \tag{11}$$

Equation (9) can be rewritten as:

$$\dot{\boldsymbol{q}}=\boldsymbol{A}\boldsymbol{q}+\boldsymbol{D}\boldsymbol{p} \tag{12}$$

with

$$\boldsymbol{A}=\begin{bmatrix}-\nu & -\nu\dfrac{\partial}{\partial\theta}\\ -\dfrac{\partial}{\partial\theta} & 1\end{bmatrix}\quad \boldsymbol{D}=\begin{bmatrix}\dfrac{1-\nu^2}{E} & 0\\ 0 & \dfrac{2(1-\nu)}{E}\end{bmatrix} \tag{13}$$

Now by substituting $\boldsymbol{p}=\dfrac{\partial U}{\partial\dot{\boldsymbol{q}}}$ into (8) and by using the part integration, we have

$$\dot{\boldsymbol{p}}=\boldsymbol{B}\boldsymbol{q}+\boldsymbol{C}\boldsymbol{p} \tag{14}$$

with

$$\boldsymbol{B}=\begin{bmatrix}E & E\dfrac{\partial}{\partial\theta}\\ -\dfrac{\partial}{\partial\theta}(E\,\cdot) & -\dfrac{\partial}{\partial\theta}\left(E\dfrac{\partial}{\partial\theta}\right)\end{bmatrix}\quad \boldsymbol{C}=\begin{bmatrix}\nu & -\dfrac{\partial}{\partial\theta}\\ -\dfrac{\partial}{\partial\theta}(\nu\,\cdot) & -1\end{bmatrix} \tag{15}$$

Equations (12) and (15) form the dual differential equations governing the posed problem. Moreover, it is more convenient to combine the dual variable $\boldsymbol{q}$ and $\boldsymbol{p}$ into a single vector

$$\boldsymbol{v}=\{\boldsymbol{q}^T\quad \boldsymbol{p}^T\}^T \tag{16}$$

Therefore, the dual equations (12) and (15) are written into a single equation:

$$\dot{\boldsymbol{v}}=\boldsymbol{H}\boldsymbol{v} \tag{17}$$

with

$$\boldsymbol{H}=\begin{bmatrix}\boldsymbol{A} & \boldsymbol{D}\\ \boldsymbol{B} & \boldsymbol{C}\end{bmatrix} \tag{18}$$

Equation (17) is the governing equation obtained in the frame of the Hamiltonian system. The boundary conditions at crack lips are:

$$\begin{aligned}&S_{r\theta}(\theta=\pm\pi)=0\\ &\left(u_r+\frac{\partial u_\theta}{\partial\theta}+\frac{\nu S_r}{E}\right)(\theta=\pm\pi)=0\end{aligned} \tag{19}$$

3: HAMILTONIAN SYSTEM WITH ANGULAR COORDINATE TRATED AS "TIME"

Now we take the angular coordinate θ as "time". Then we note $\frac{\partial}{\partial\theta}=\left(\bullet\right)$. By using the variable changes (5), the strain energy (4) becomes

$$U=\frac{1}{2(1-\nu^2)}\int_{-\pi}^{\pi}\int_{0}^{R}\left[\left(\frac{\partial u_r}{\partial\xi}\right)^2+2\nu\left(\frac{\partial u_r}{\partial\xi}\right)\left(u_r+\dot{u}_\theta\right)+\left(u_r+\dot{u}_\theta\right)^2+\frac{1-\nu}{4}\left(\frac{\partial u_\theta}{\partial\xi}-u_\theta+\dot{u}_r\right)^2\right]d\xi d\theta \quad (20)$$

By following the same procedure as described in the precedent paragraph, we obtain the following system of first-order differential equations:

$$\begin{Bmatrix}\dot{u}_r\\ \dot{u}_\theta\\ \dot{S}_{r\theta}\\ \dot{S}_\theta\end{Bmatrix}=\begin{bmatrix}0 & 1-\partial/\partial\xi & 2(1+\nu)/E & 0\\ -1-\nu\partial/\partial\xi & 0 & 0 & (1-\nu^2)/E\\ -E\partial^2/\partial\xi^2 & 0 & 0 & 1-\nu\partial/\partial\xi\\ 0 & 0 & -(1+\partial/\partial\xi) & 0\end{bmatrix}\begin{Bmatrix}u_r\\ u_\theta\\ S_{r\theta}\\ S_\theta\end{Bmatrix} \quad (21)$$

We write (21) under concise form:

$$\dot{\boldsymbol{v}}=\boldsymbol{H}\boldsymbol{v} \quad (22)$$

where

$$\boldsymbol{v}=\left\{\boldsymbol{q}^T \quad \boldsymbol{p}^T\right\}$$
$$\boldsymbol{q}=\left\{u_{rr} \quad u_{\theta\theta}\right\}^T \quad \boldsymbol{p}=\left\{S_{r\theta} \quad S_{\theta\theta}\right\}^T \quad (23)$$
$$\boldsymbol{H}=\begin{bmatrix}0 & 1-\partial/\partial\xi & 2(1+\nu)/E & 0\\ -1-\nu\partial/\partial\xi & 0 & 0 & (1-\nu^2)/E\\ -E\partial^2/\partial\xi^2 & 0 & 0 & 1-\nu\partial/\partial\xi\\ 0 & 0 & -(1+\partial/\partial\xi) & 0\end{bmatrix}$$

Here we have found the governing equations under the conventional form in the Hamiltonian system. The boundary conditions can be written in a simple form. For the present problem, we have:

$$\boldsymbol{p}(\theta=\pi)=\boldsymbol{p}(\theta=-\pi)=\boldsymbol{0} \quad (24)$$

The governing equation (22) and the boundary conditions (24) allows the solution of the posed problem.

4: THEOREM OF EXPANSION

One can use the method of the separation of variables to solve the governing equations (17) and (22) established in the frame of the Hamiltonian system. We assume that the variable vector $\boldsymbol{v}$ can be written under separable form:

$$\boldsymbol{v}=\exp(\mu\xi)\boldsymbol{\psi}(\theta) \quad (25)$$

where μ is an undetermined eigenvalue, $\boldsymbol{\psi}(\theta)$ is the corresponding eigenvector depending only on θ. The following theorem of expansion has been demonstrated by Zhong (1997):

$\mu=0$ is a multiple eigenvalue of the problem. If μ is an eigenvalue, $-\mu$ is also one. Let $\boldsymbol{\psi}^0_k$, $\boldsymbol{\psi}_i$, and $\boldsymbol{\psi}_{-i}$ be the corresponding eigenvectors respectively. Then any vector $\boldsymbol{v}$ in the solution space can be represented as linear combination of the eigenvectors:

$$\boldsymbol{v}=\sum_{i=1}^{\infty}\left(a_i\exp(\mu_i)\boldsymbol{\psi}_i+b_i\exp(-\mu_i)\boldsymbol{\psi}_{-i}\right)+\sum_{k=1}^{n}a_k^0\boldsymbol{\psi}_k^0 \quad (26)$$

where a_i, b_i and $a^0{}_k$ are the undermined constants.

$$a_i = -\frac{\exp(-\mu_i \xi)\int_{-\pi}^{\pi} \boldsymbol{\psi}_{-i}^T \boldsymbol{J}\boldsymbol{v} d\theta}{\int_{-\pi}^{\pi} \boldsymbol{\psi}_{-i}^T \boldsymbol{J}\boldsymbol{\psi}_i d\theta} \quad b_i = \frac{\exp(\mu_i \xi)\int_{-\pi}^{\pi} \boldsymbol{\psi}_i^T \boldsymbol{J}\boldsymbol{v} d\theta}{\int_{-\pi}^{\pi} \boldsymbol{\psi}_i^T \boldsymbol{J}\boldsymbol{\psi}_{-i} d\theta} \qquad (27)$$

$$with \quad \boldsymbol{J} = \begin{bmatrix} \boldsymbol{0} & \boldsymbol{I} \\ -\boldsymbol{I} & \boldsymbol{0} \end{bmatrix}$$

5: SOLUTION METHODS

We believe there exist many methods, analytical or numerical, to solve the governing equations (17) and (22). We only present here a very explicit method to solve the equation (22). By introducing (25) into (22), we find:

$$\dot{\boldsymbol{\psi}} = \boldsymbol{H}(\mu)\boldsymbol{\psi} \qquad (28)$$

with

$$\boldsymbol{H} = \begin{bmatrix} 0 & 1-\mu & 2(1+\nu)/E & 0 \\ -1-\nu\mu & 0 & 0 & (1-\nu^2)/E \\ -E\mu^2 & 0 & 0 & 1-\nu\mu \\ 0 & 0 & -(1+\mu) & 0 \end{bmatrix} \qquad (29)$$

It is interesting to remark that H is a constant matrix with a parameter μ. For more complicated cases H may be function of θ. In fact, the solution of (28) can be written under following analytical form:

$$\boldsymbol{\psi}(\theta) = \exp\left(\int_{\theta_0}^{\theta} \boldsymbol{H}(\mu) d\theta\right)\boldsymbol{\psi}(\theta_0) \qquad (30)$$

For the present problem, H is a constant matrix, $\theta_0=-\pi$, (30) becomes:

$$\boldsymbol{\psi}(\theta) = \exp\left(\boldsymbol{H}(\mu)(\theta+\pi)\right)\boldsymbol{\psi}(-\pi) \qquad (31)$$

The eigenvalue μ can be determined by the boundary conditions (24). For $\theta=\pi$, we can write:

$$\boldsymbol{\psi}(\pi) = \exp\left(\boldsymbol{H}(\mu)2\pi\right)\boldsymbol{\psi}(-\pi) \qquad (32)$$

Let $\boldsymbol{G} = \exp\left(\boldsymbol{H}(\mu)2\pi\right)$, equation (32) can be rewritten as follows:

$$\begin{Bmatrix} \boldsymbol{q} \\ \boldsymbol{p} \end{Bmatrix}(\theta=\pi) = \begin{bmatrix} \boldsymbol{G}_{11} & \boldsymbol{G}_{12} \\ \boldsymbol{G}_{21} & \boldsymbol{G}_{22} \end{bmatrix} \begin{Bmatrix} \boldsymbol{q} \\ \boldsymbol{p} \end{Bmatrix}(\theta=-\pi) \qquad (33)$$

According to the boundary conditions (24), we have immediately:

$$\det\left|\boldsymbol{G}_{21}\right| = 0 \qquad (34)$$

This is the equation allowing determination of the eigenvalue μ. Iterative procedures can be used in solving (34). Once μ obtained, the vector $\boldsymbol{q}(\theta=\pi)$ can be calculated from the second equation of (33). Then the variable vector $\boldsymbol{\psi}(\theta)$ can straightforwardly be computed from equation (31).

6: MULTI-MATERIAL PROBLEMS

One of the advantages of the approach taking the angular coordinate as "time" is its high capacity to deal with the multi-material problems. Consider a crack formed from several homogeneous elastic materials. The material 1 occupies the sectorial domain $[\theta_0,\theta_1]$, named zone 1; the material 2 occupies the zone 2, bounded by $[\theta_1,\theta_2]$, and so on. This is a general configuration of this class of problems. The cases like a crack lying at an interface between two dissimilar materials or a crack meeting an interface with an arbitrary angle can be regarded as its special cases. We adopt the superscript $^{(i)}$ to indicate the quantities in the zone i , for example, $v^{(i)}$, $H^{(i)}$, etc.. For this problem, one can establish the governing equation (22) for each zone:

$$\dot{\boldsymbol{v}}^{(i)} = \boldsymbol{H}^{(i)}\boldsymbol{v}^{(i)} \qquad (34)$$

The boundary conditions at the two free surfaces of the crack are:

$$\begin{aligned} \boldsymbol{p}^{(1)}(\theta=-\pi) &= \boldsymbol{0} \\ \boldsymbol{p}^{(n)}(\theta=\pi) &= \boldsymbol{0} \end{aligned} \qquad (35)$$

The continuity conditions across the interfaces are:

$$\begin{aligned} &\boldsymbol{v}^{(1)}(\theta=\theta_1)=\boldsymbol{v}^{(2)}(\theta=\theta_1)\\ &\cdots\cdots\\ &\boldsymbol{v}^{(n-1)}(\theta=\theta_{n-1})=\boldsymbol{v}^{(n)}(\theta=\theta_{n-1}) \end{aligned} \tag{36}$$

These relations show the advantage of the choice of the angle coordinate treated as "time": the multi-material problem can be dealt with as a single material problem since the variable vector *v* is continuous across all the interfaces. This makes the resolution of the governing equation (34) much easier.

According to the basic solution (30), we can write the relationship between $\boldsymbol{\psi}^{(i)}(\theta_i)$ and $\boldsymbol{\psi}^{(i)}(\theta_{i-1})$ for each zone:

$$\boldsymbol{\psi}^{(i)}(\theta_i)=\exp\left(\boldsymbol{H}^{(i)}(\mu)(\theta_i-\theta_{i-1})\right)\boldsymbol{\psi}^{(i)}(\theta_{i-1}) \tag{37}$$

Let $\boldsymbol{G}^{(i)}=\exp\left(\boldsymbol{H}^{(i)}(\mu)(\theta_i-\theta_{i-1})\right)$. According to the continuity conditions across the interfaces, we write immediately the relationship between $\boldsymbol{\psi}^{(n)}_{\cdot}(\pi)$ and $\boldsymbol{\psi}^{(1)}_{\cdot}(-\pi)$, namely:

$$\begin{aligned} &\boldsymbol{\Psi}^{(n)}(\pi_i)=\boldsymbol{G}\boldsymbol{\Psi}^{(1)}(-\pi)\\ &\boldsymbol{G}=\prod_{i=n}^{1}\boldsymbol{G}^{(i)} \end{aligned} \tag{38}$$

The eigen-equation is identical as equation (34).

7: CONCLUSIONS

In this paper, we have made a rough draft on the introduction of the Hamiltonian system into the asymptotic analysis in fracture mechanics. We insist on the fact that this approach is not only a new formalism other the traditional methods, but also a real powerful tool to study problems in this topic. By using this new approach, we have successfully investigated some problems that may be difficult for traditional Airy function method (for example, asymptotic analysis for a plane crack formed by several anisotropic materials; asymptotic analysis for cracks in a bending plate formed by several anisotropic materials; residual stress analysis of a crack in elastic-plastic materials etc.). We believe that a large domain can be found in applying this new approach into fracture mechanics.

REFFERENCES

1. Williams, M. L. (1952), *Transitions of the ASME, Journal of Applied Mechanics* 19, 526-528.
2. Zhong, W. X, (1995), *A new systematic methodology for theory of elasticity*, Dalian University of Technology Press (In Chinese)

ORAL REFERENCE: ICF100115OR

INVESTIGATION OF FRACTURE CRITERION FOR COMPOSITE USING CTS SPECIMEN

R. Rikards[1], A. K. Bledzki[2] and F.-G. Buchholz[3]

[1]Institute of Computer Analysis of Structures, Riga Technical University, LV-1658, Riga, Latvia
[2]Institute of Material Science, University of Kassel, D-34109, Kassel, Germany
[3]Institute of Applied Mechanics, University of Paderborn, D-33098, Paderborn, Germany

ABSTRACT

The interlaminar fracture behavior of a unidirectional carbon fiber reinforced composite under full range of in-plane loading conditions has been investigated. Loading conditions from pure mode I through various mixed mode I/II ratios up to pure mode II have been generated by the aid of the compound version of the compact tension shear (CTS) specimen. From the experimentally measured critical loads the mode I, mode II and the various mixed mode I/II critical energy release rates at crack initiation have been determined by the aid of the finite element method and the modified virtual crack closure integral method. Based on these results the parameters of a fracture criterion for the composite under consideration have been determined. It was shown that for the present carbon/epoxy composite the best approximation is achieved employing in criterion a linear function.

KEYWORDS

Laminated composite, interlaminar fracture, mixed mode fracture, fracture criterion.

INTRODUCTION

The main problem of predicting the failure of laminated composite materials is the evaluation of interlaminar fracture toughness properties under mixed mode loading conditions. Various approaches have been chosen in order to develop test specimens for combined loading conditions, but the main research has been conducted on mode I and mode II interlaminar fracture behavior of composite materials. The double cantilever beam (DCB) and the end notched flexure (ENF) specimens have been employed for mode I and mode II tests, respectively. Also for the mixed mode tests mostly beam type specimens were used in order to obtain mixed mode I/II critical energy release rate. For example, a MMB specimen is widely used to determine the mixed mode critical energy release rates for different composites [1-3].

But still the disadvantage of all beam type specimens is that for pure mode I, pure mode II and for the various mixed mode I/II ratios different beam type specimens have to be used. In order to obtain reliable results for interlaminar fracture toughness under different combined or mixed mode loading conditions starting from pure mode I to pure mode II it is desirable that only one type of specimen would be required. Because this was almost impossible to achieve by using beam type specimens also other types of test specimens have been developed. One other type is the Arcan specimen, which was firstly employed for

generating states of plane stress in composite [4], then for fracture tests of isotropic materials [5] and also for mixed mode fracture tests of composites [6,7]. Another type of specimen for studying the interlaminar fracture properties of laminated composites is the Iosipesku specimen [8].

The most recent development [9,10] is a compound version of the compact tension shear (CTS) specimen which covers all in-plane mixed mode loading conditions starting from pure mode I through any mixed mode I/II ratio up to pure mode II loading. The CTS specimen was proposed earlier in [11] for fracture tests of isotropic materials under such general in-plane loading conditions. In the present paper the compound version of the CTS specimen is used for mode I, mixed mode I/II and mode II studies of the interlaminar fracture toughness properties of a carbon/epoxy composite.

EXPERIMENTAL

Material

Unidirectionally reinforced carbon/epoxy laminate was used for interlaminar fracture mixed mode I/II experiments. Volume fracture of the material was 70%. Material is assumed to be transversally isotropic (1 is a fiber direction, 2 and 3 are directions transverse to the fibers). The elastic properties of the material are as follows: E_1=170 GPa, E_2=9.4 GPa, G_{12}=G_{13}=4 GPa, ν_{23}=0.35, ν_{12}=ν_{13}=0.25 and G_{23}=E_2/2(1+ν_{23})=3.5 GPa. These elastic properties were used in the finite element analysis of the CTS specimen. The thickness of the laminate was 2h=1.3 mm.

CTS specimen

The CTS specimen (see Figure 1) was proposed in [11] for mixed mode fracture experiments. The compound version of the CTS specimen (see Figure 2) was proposed in [9,10]. The CTS (compact tension shear) specimen was made by gluing the composite strip in the glassmat/epoxy-Aluminium blocks.

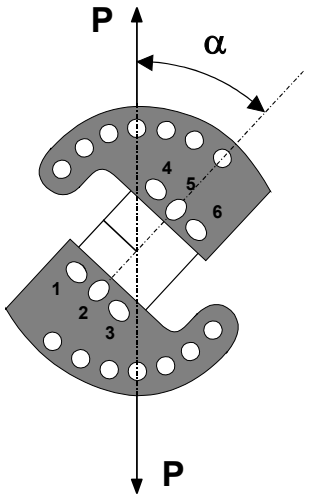

Figure 1: CTS specimen loading device

The load P is applied to the specimen by the loading device under an arbitrary angle α. By this the mixed mode loading of the specimen can be achieved from pure mode I (α=0^0) through mixed mode I/II loading (0^0<α<90^0) up to pure mode II loading (α=90^0). The forces F_i (i=1, 2, ..., 6) acting on the holes of the CTS specimen (see Figure 2) can be calculated by the relations [9]

$$\begin{aligned} F_3 &= F_4 = P\left(\frac{1}{2}\cos\alpha + \frac{c}{b}\sin\alpha\right) \\ F_2 &= F_5 = P\sin\alpha \\ F_1 &= F_6 = P\left(\frac{1}{2}\cos\alpha - \frac{c}{b}\sin\alpha\right) \end{aligned} \qquad (1)$$

where α is the loading angle (see Figure 1). In the finite element analysis these forces are applied at the corresponding nodes of the finite element mesh.

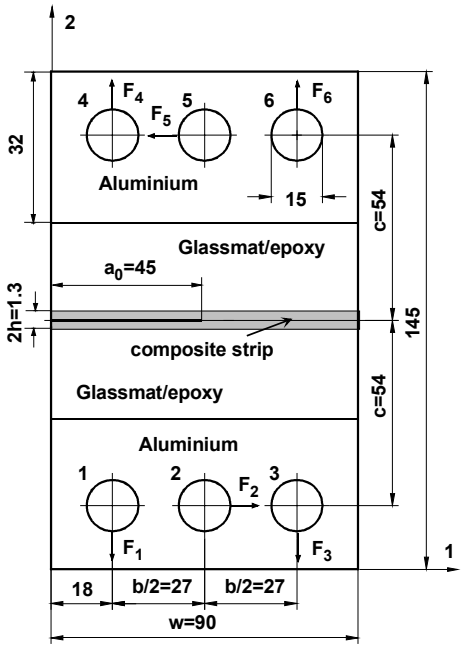

Figure 2: Compound version of the CTS specimen (dimensions are given in mm)

The advantage of the compound version of the CTS specimen is that with the same test specimen all in-plane loading conditions can be generated, starting from pure mode I through all combinations of plane mixed mode I/II ratios and also including pure mode II. In the present investigation experiments have been carried out for pure mode I (α=0^0), pure mode II (α=90^0) and for the mixed mode loading conditions with α=45^0, 60^0, 75^0, 81^0, 84^0 and 87^0.

Testing procedure

The CTS specimens were tested on MTS testing machine. The specimens were loaded with a constant displacement rate 0.5 mm/min and the critical loads P_c at crack initiation were measured. At all 29 samples were tested under various mixed mode ratios.

FINITE ELEMENT ANALYSIS

The finite element model of the specimen consists of quadrilateral plane strain elements with 4 nodal points. The plain strain conditions was used in the finite element analysis. The loads on the specimen were applied according to Figure 2 and were calculated by the expressions (1). The finite element analysis was performed by the program ANSYS [12]. For the calculation of the energy release rates G_I and G_{II} the Modified Virtual Crack Closure Integral (MVCCI) method is utilized so that the separated strain energy release rates are obtained by only one calculation (MVCCI or 1C method) for the actual crack length a as proposed in [13]

$$G_I^{1C}(a) = \frac{1}{t\,\Delta a}\cdot\frac{1}{2}\left[F_y^i(a)\Delta u_y^{i-1}(a)\right];$$
$$G_{II}^{1C}(a) = \frac{1}{t\,\Delta a}\cdot\frac{1}{2}\left[F_x^i(a)\Delta u_x^{i-1}(a)\right], \qquad (2)$$

where $F_x^i(a)$ and $F_y^i(a)$ are the nodal point forces at the crack tip node i in x and y directions, respectively, while $\Delta u_x^{i-1}(a)$ and $\Delta u_y^{i-1}(a)$ are the relative nodal point displacements of the opposite crack faces at node i-

1 in x and y directions, respectively. Therefore $\Delta u_x^{i-1}(a)$ is the relative crack sliding displacement, while $\Delta u_y^{i-1}(a)$ is the relative crack opening displacement at a distance Δa behind the crack tip and t=10 *mm* is the width of the specimen. In the finite element model a crack increment of Δa=0.5 *mm* was used.

The finite element analysis for the CTS specimen with the initial crack a=45 *mm* was carried out. The energy release rates have been calculated by expressions (2). The calculated values by loading of the compound version of the CTS specimen under the applied load P=1000 N are presented in Table 1.

TABLE 1
ENERGY RELEASE RATES AT DIFFERENT LOADING ANGLES

Loading angle α	G_I, kJ/m^2	G_{II}, kJ/m^2
0	0.179799	0
15	0.170867	0.001103
30	0.140009	0.004062
45	0.095687	0.008083
60	0.049916	0.012089
75	0.014946	0.015009
78	0.010161	0.015385
81	0.006249	0.015679
84	0.003261	0.015891
87	0.001224	0.016019
90	0	0.016055

From the values of the separated energy release rates G_I and G_{II} calculated under load P=1000 N easily can be obtained the experimental values of the critical energy release rates. In the experiment for each specimen the critical loads P_c at crack initiation were measured. Since the energy release rate is quadratic function of the applied external load $G=kP^2$ from the Table 1 the corresponding critical energy release rates can be calculated.

RESULTS OF EXPERIMENT

Specimens have been loading under different angles α. The loading angles were chosen in order to obtain different mixed mode ratios giving maximum information about interlaminar fracture behavior of the laminate. In Table 1 it is seen that in the range of loading angles from 0^0 up to 60^{0-} the mode I loading conditions at the crack tip are dominant. At the loading angle 75^0 the mixed mode ratio is G_I/G_{II}=1. For the loading angles from 78^0 to 90^{0-} the mode II loading conditions at the crack tip are dominant. By using the experimental values and the finite element results from Table 1 the critical energy release rates at crack initiation are calculated. The results are presented in Figure 3. Rather large scatter of the results can be observed. Similarly large scatter of the results were obtained in the CTS experiments performed on glass/epoxy laminates [9,10]. One reason of such a large scatter is that width of the specimen is only 10 mm and therefore the influence of edge effects is significant. The loading device was designed for the CTS specimen width 10 mm. It should be noted that for the DCB (double cantilever beam) and ENF (end notched flexure) beam specimens it is recommended the width from 20 to 25 mm. However, as it was investigated in [9] there was no statistically significant difference between the mode II results obtained by the ENF and CTS tests. For some composites the scatter of the results obtained by the DCB tests also is rather large.

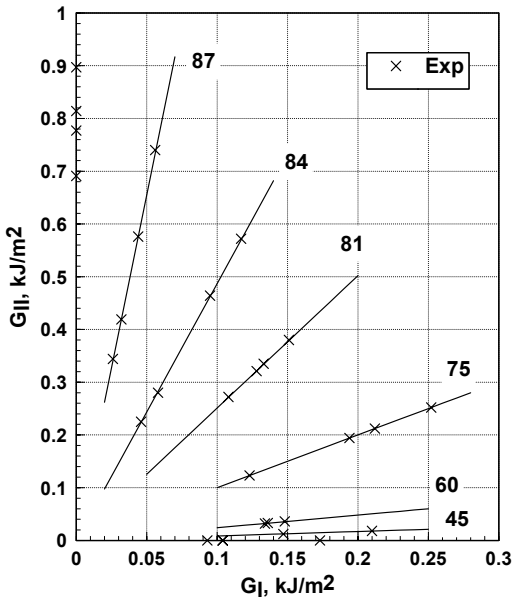

Figure 3: Mixed mode critical energy release rates obtained in the experiment under different loading angles

FRACTURE CRITERION

In the literature a number of mixed mode fracture criteria have been proposed for describing the interlaminar fracture of composites. These criteria are similar to those used for isotropic materials. Fracture criteria can be formulated on the basis of different fracture parameters like stress intensity factor (SIF) or energy release rate for which the critical fracture parameters (K_C or G_C) can be determined experimentally. Previously the stress intensity factors were used preferably as fracture parameters but for composites the energy release rates, which also are used in the present investigation, proved to be more useful and common.

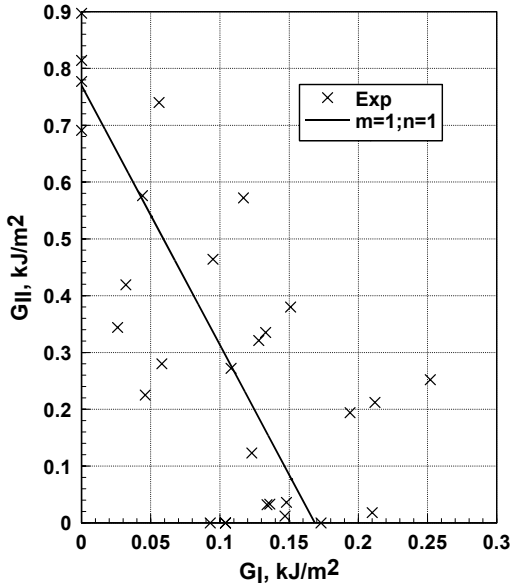

Figure 4: Criterion (3) for the exponents m=1 and n=1

The mixed mode fracture criterion can be written in a general form [14]

$$\left(\frac{G_I}{G_{IC}}\right)^m + \left(\frac{G_{II}}{G_{IIC}}\right)^n = 1 \qquad (3)$$

Here the exponents m, n and parameters G_{IC} and G_{IIC} can be determined by the least squares fit of the experimental data. Employing all combinations of a linear and quadratic terms it was found that the best fit criterion is with the exponents m=1 and n=1, i.e. for the linear criterion

$$\frac{G_I}{G_{IC}} + \frac{G_{II}}{G_{IIC}} = 1 \tag{4}$$

It was found that the best fit for the present material (see Figure 4) is for the parameters G_{IC}=0.168 kJ/m^2 and G_{IIC}=0.770 kJ/m^2.

It should be noted that for the glass/epoxy laminate investigated in [9] the best fit criterion was found with the exponents m=1 and n=2. For the present carbon/epoxy laminate better approximation was obtained employing the linear criterion. Therefore, the criterion (4) can be used to evaluate the interlaminar fracture behavior of the present carbon/epoxy laminate.

CONCLUSIONS

The mixed mode I/II experiments of carbon/epoxy laminate have been performed by using CTS tests. At all 29 samples were tested under different mixed mode ratios starting from pure mode I up to pure mode II loading conditions. By using the experimental results the fracture criterion has been developed. It was found that the best fit criterion is the linear criterion.

REFERENCES

1. Reeder, J.R. and Crews, Jr. J.H. (1990) *AIAA J.* 28, 1270.
2. Kinloch, A.J., Wang, Y., Williams, J.G. and Yayla, P. (1993) *Comp. Sci. Technol.* 47, 225.
3. Zhao, S., Gädke, M. and Prinz, R. (1995) *J. Reinf. Plast. and Comp*. 14, 804.
4. Arcan, M., Hashin, Z. and Voloshin, A. (1978) *Exp. Mech.* 18, 141.
5. Banks-Sills, L., Arcan, M. and Bui, H.D. (1983) *Int. J. Fract.* 22, R9-R14.
6. Jurf, R.A. and Pipes, R.B. (1982) *J. Comp. Mater*. 16, 386.
7. Yoon, S.H. and Hong, C.S. (1990) *Exp. Mech.* 30, 234.
8. Bansal, A. and Kumosa, M. (1995) *Int. J. Fract.* 71, 131.
9. Rikards, R., Buchholz, F.-G., Wang, H., Bledzki, A. K., Korjakin, A. and Richard. H.-A. (1998) *Engng. Fract. Mech.* 61, 325.
10. Rikards, R. (2000) *Computers & Struct.* 76, 11.
11. Richard, H.A. and Benitz, K.A. (1983) *Int. J. Fract.* 22, R55-R58.
12. ANSYS. (1999) *User's manual. Version 5.6.2*. Swanson Analysis System.
13. Rybicki, E.F. and Kanninen, M. F. (1977) *Engng. Fract. Mech*. 9, 931.
14. Di Leonardo, G. (1979) *Int. J. Fract.* 15, 537.

ORAL/POSTER REFERENCE: ICF100635PR

INVESTIGATION ON OBLIQUE IMPACT RESPONSE OF COMPOSITE CYLINDRICAL SHELLS

Walter Z. Nie and Wieslaw K. Binienda

Department of Civil Engineering, The University of Akron,
Akron, OH 44325, USA

ABSTRACT

As the simulation of a subcomponent of jet engine fan case under blade-out loads, the dynamic behavior of a composite cylindrical shell impacted obliquely by a flat projectile has been investigated using explicit numerical method. In order to understand the feasibility of utilizing partial configurations to represent the full subcomponent in experiments and analyses, a half, quarter and half-quarter symmetric FEA models of the shell have been analyzed for both pure elastic and elastic-brittle failure material model. The results suggest that a half configuration of the shell could be well used in place of a full shell for the whole response, while the quarter configuration merely for the impact stage when the evaluation of local damage is the main purpose. In addition, analysis indicates that the damage in the initial impact is not significantly affected by the boundary conditions while the subsequent deformation is strongly influenced by the boundary conditions.

KEYWORDS

Composite laminates, impact, damage and penetration, shell, explicit dynamics, jet engine

INTRODUCTION

The dynamic response of a cylindrical composite shell impacted obliquely by a projectile has a vast practical background in aeronautical engineering. Recently, the impact on composite structures has been a subject of extensive research [1-3]. Lots of factors are involved in impact problems such as the projectile versus target structure mass ratio [4], impact kinetic energy, the shape and length of the projectile, impact angle of obliquity, the dimension of target structure and its boundary conditions etc.

The interest of this research is focused on the influence of structure dimension and boundary condition on the overall dynamic response nature in the oblique impact of cylindrical composite shells. This has obvious practical and economic value in providing guidelines for choosing appropriate simple test models and planning experimental studies. No test data and report were shown to confirm whether a partial configuration of the structure could be used to represent the whole structure in a dynamic impact response test or analysis quantitatively so far. On the other hand, the complexity of impact problems also leads us to choose to combine theoretical, numerical and experimental approaches.

In this research, the numerical analysis of a composite laminate shell, subjected to the oblique impact by a thin flat rigid cylinder with a certain mass, is conducted using explicit dynamic method by ABAQUS. Five cases of analysis are performed for different dimensions of the shell configuration with both free and fully fixed boundary conditions. The strain and kinetic energy transfer and deforming history are examined from the numerical results. Especially, the influence of constraints on the cut boundary of partial configurations taken from the full shell is observed. Only the cases with free and fully fixed boundary condition are studied in consideration that the real constraints on the whole shell should lie between these two extreme situations. Both linear elastic and elastic-brittle failure material model are employed to obtain an understanding of the overall response of the shell and insight into the local damage and mutual influence between them. The localized damage/penetration is simulated using a brittle failure model combined with an element removal mechanism for failed part of the structure.

ANALYSIS MODEL

Illustrated in Figure 1 is a full-ring shell subcomponent proposed for testing of jet engine fan case by NASA Glenn Research Center, to evaluate the performance of a composite structure under blade-out loads. In this research, the transient impact response analysis of the subcomponent was performed using the commercial FEA code ABAQUS/Explicit. The impact velocity was 182.9m/s (600ft/s) and the composite ring was taken to be $7.62X10^{-3}$m (0.3") thick with the following properties, which are representative of a glass/epoxy laminate with a 0°/90° lay-up. $E_{11}=E_{22}=17237$Mpa ($2.5X10^6$ lbf/in^2), $G_{12}=6894.8$Mpa ($1.0X10^6$ lbf/in^2), $G_{13}=G_{23}=4136.9$Mpa ($6.0X10^5$ lbf/in^2), $\upsilon_{12}=\upsilon_{21}=0.14$ and $\rho=1715.6$ kg/m^3 (0.00016 lbf s^2/in^4).

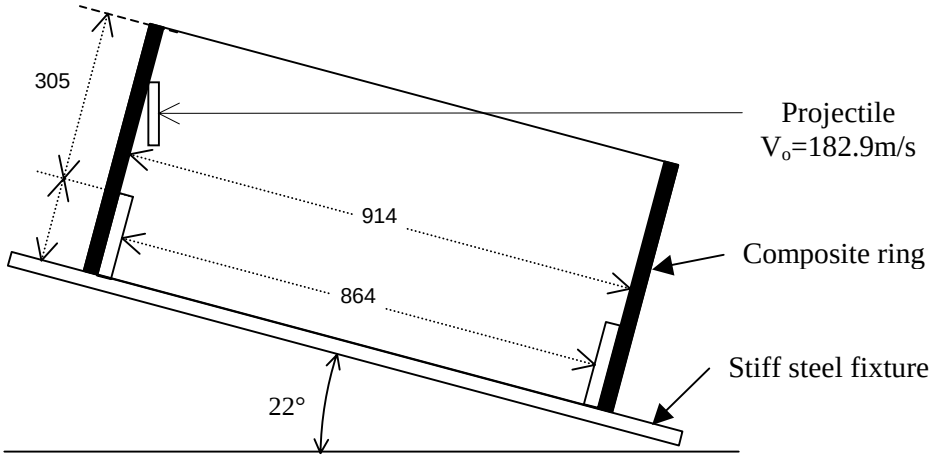

Figure 1: Illustration of the analysis model of the subcomponent (unit: mm)

In addition to the pure elastic model, an elastic-brittle failure model was also included in the analysis to simulate the local damage. The brittle failure model was characterized by a tensile strength σ_t^I =275.8Mpa (40000 lbf/in^2) and a failure strain ε_f =0.023. An element would be removed from the analysis process whenever all of its material points failed. The projectile was a flat circular cylinder with diameter of 114.3mm (4.5"), thickness of 19mm (0.75"), and mass of 0.85kg (1.9lb). It was ideally modeled as a rigid body with a density of 4366.7 kg/m^3 (0.00041 lbf s^2/in^4) since tracking waves and stress distributions in the projectile were not important in the present study. The shell was inclined at an angle of 22° to the horizontal.

In order to examine the effects of the shell dimension and boundary conditions, a half-shell and a quarter-shell model with both free and fixed end conditions at the cut boundary were analyzed in addition to the whole shell, as showed in Figure 2. All the analysis cases are listed in table 1. Because of the symmetry, only half of the structure geometry was modeled for all cases with symmetry condition about mid plane imposed. For simplicity, no friction between the projectile and shell during contact was considered. Four-node thin

shell element S4R was used for the shell, and six-node and eight-node solid element C3D6 and C3D8R for the projectile. In addition, relax stiffness type of hourglass viscosity was used to restrict the element mechanisms, i.e. the zero-energy hourglass deformation mode, due to the degradation of first-order element integration. Also, in order to limit numerical oscillations due to discretization, a linear bulk viscosity with damping coefficient b_1=0.0001 was introduced.

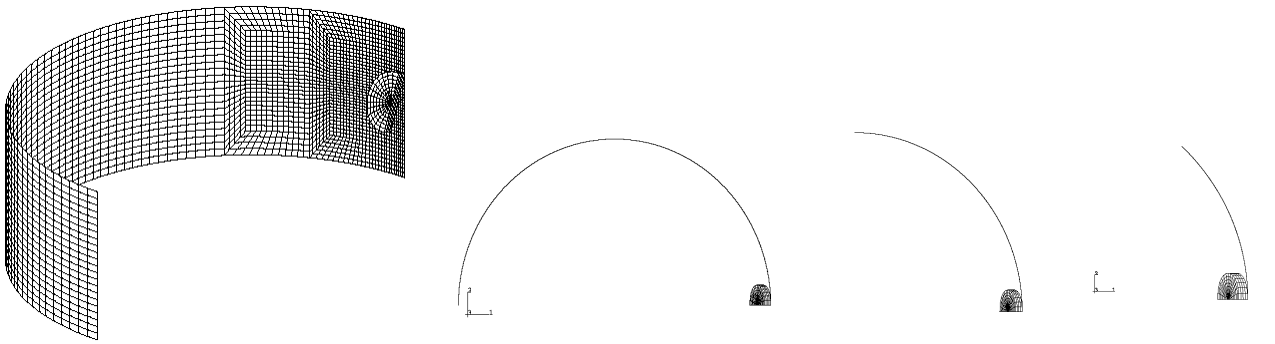

Figure 2: Symmetric FEA models of the structure

TABLE 1
ANALYSIS CASES

Case	Structure	FEA model	Cut-end boundary	Bottom boundary
1	Whole	Half	-	Fixed
2	Half	Quarter	Free	Fixed
3	Half	Quarter	Fixed	Fixed
4	Quarter	Half quarter	Free	Fixed
5	Quarter	Half quarter	Fixed	Fixed

NUMERICAL RESULTS AND DISCUSSION

Deformation

Displacements at the projectile center and top edge of the shell above the impact point are shown in Figures 3(a) and 3(b) for pure elastic analysis of case 1-5. For about the first 1.0ms the projectile is in contact with the shell. For times up to 1.5ms the response is very similar for the full shell and the half-shells with both free and fixed boundary conditions. The response of the quarter-shells is similar to that of the other configurations only for times below about 0.4ms, which corresponds to the initial impact of the upper edge of the projectile. These results suggest that a half-shell configuration could be used in place of a full shell to evaluate local damage; either free or fixed boundary conditions could be used. Figure 4(a) and 4(b) show the displacement history of the projectile center and the impact edge of the shells for all cases 1-5, respectively, when material failure was taken into account. It is seen that the responses for all the 5 cases are almost identical throughout the entire response, indicating that partial configurations could provide perfect approximation to the full model when local failure is involved. The evolution of local damage at the impact area is shown in Figure 5 for case 1 when a brittle-failure model is employed.

It is noticed that for the partial shell configurations (case 2-5), those with free end boundary condition at the cut line provide a more similar response to the full shell (case 1) compared with the fixed end boundary condition. This indicates that the free-end condition provided a better approximation for a partial

configuration to replace the full shell. This is valuable because free boundary is always convenient to be implemented in practice.

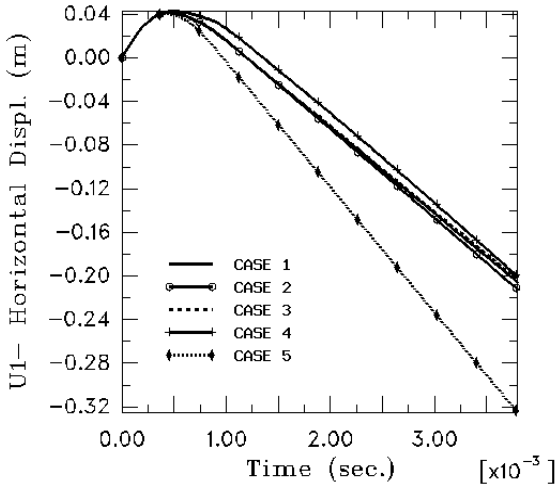

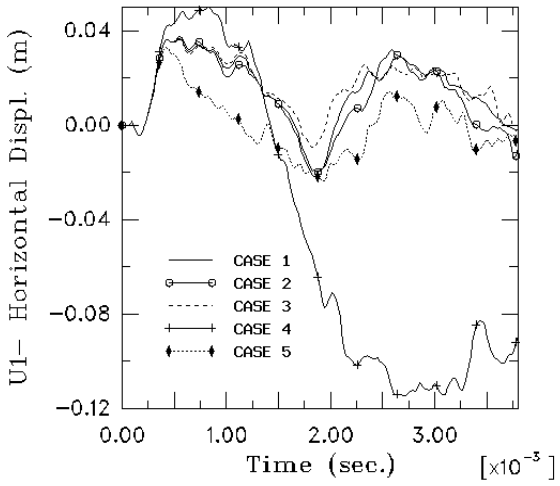

(a): at the projectile center **(b):** at the shell edge above the impact point

Figure 3: Comparison of displacement for case 1-5 (elastic model)

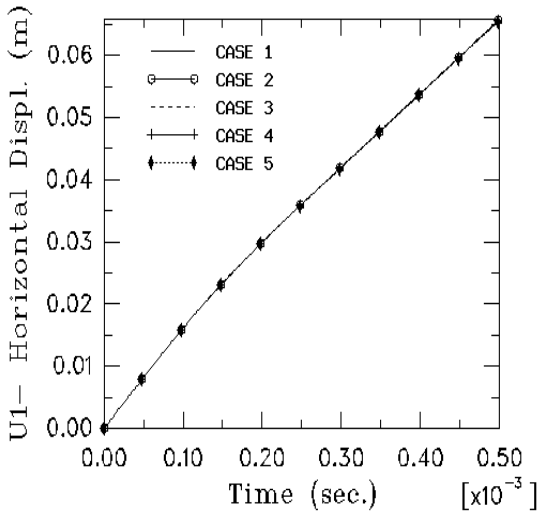

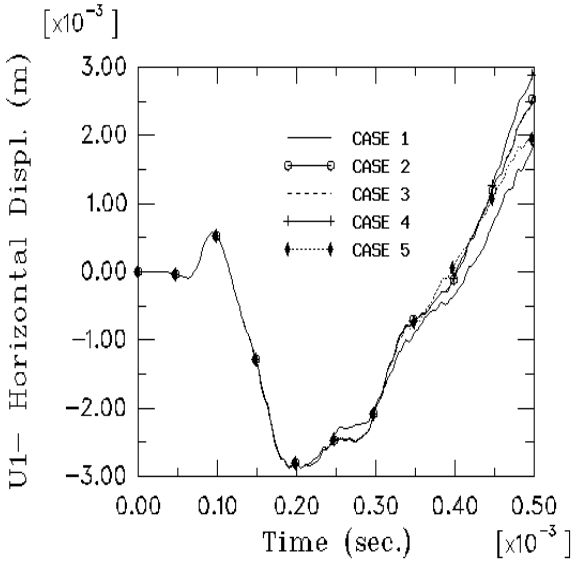

(a): at the projectile center **(b):** at the shell edge above the impact point

Figure 4: comparison of displacement for case 1-5 (elastic-brittle failure model)

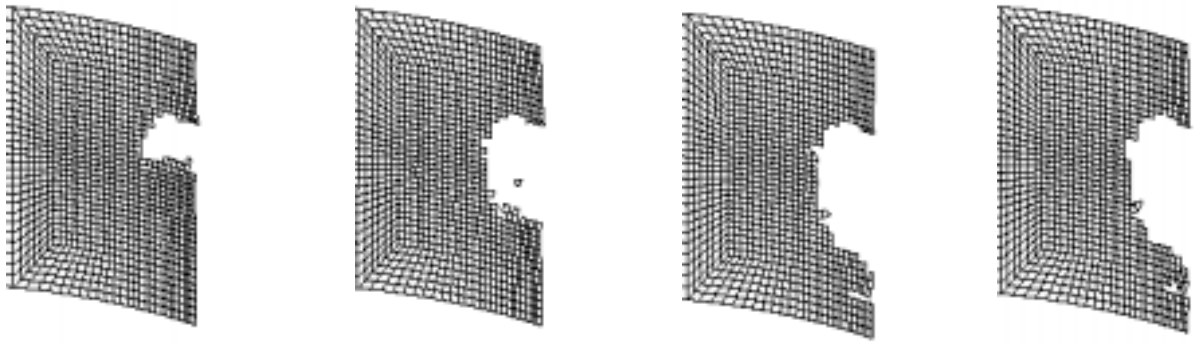

t=0.1 ms t=0.2 ms t=0.5 ms t=1.0 ms

Figure 5: Evolution of local damage and penetration (case 1)

Energy transfer and absorption

An observation of strain and kinetic energy possessed by different portions of the shell helps understand the mechanism of energy transferring and distribution in the structure. Strain energies stored in arcs of various sizes around the impact area are shown in Figure 6 for the pure elastic full-shell configuration. The total energy (strain energy + kinetic energy) is shown in Figure 7. In Figure 6 the strain energy grows to a maximum value at about 0.45ms as the projectile comes into contact with the shell. The maximum strain energy is a little over half of the initial kinetic energy of the projectile. In Figure 7 the total energy in the full shell remains constant after about 1.0ms because the projectile has rebounded from the ring. It is seen that during impact and at the early stage of the later response, the 90^o(half) arc portion of the shell almost possesses all the energy of the whole structure. As the deformation develops, the energy gradually transfers to the rest part of the structure.

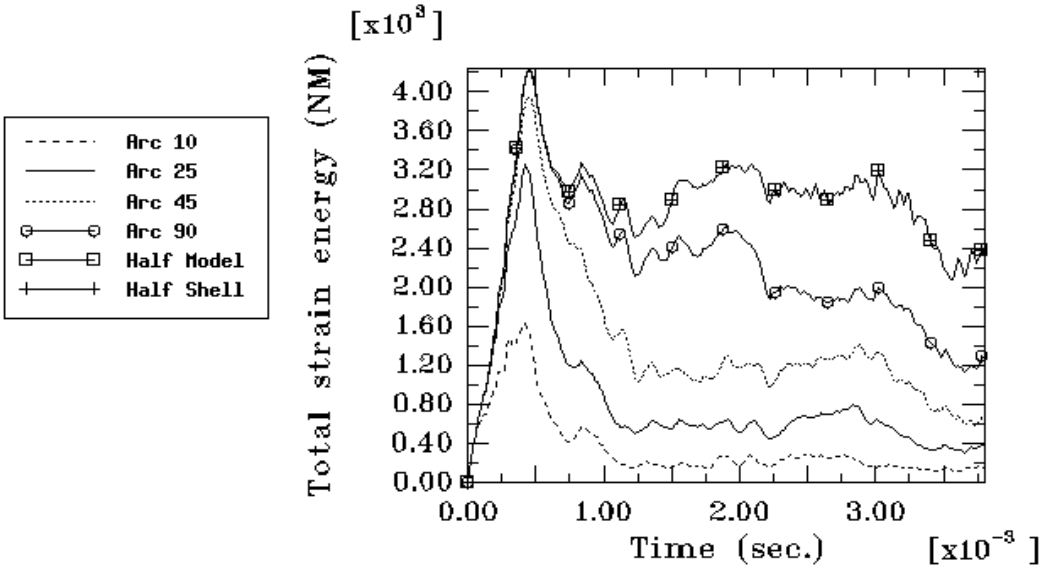

Figure 6: Strain energy in the arc of 10^o, 25^o, 45^o, quarter, and half-shell (without and with the projectile included) for case 1 (elastic model)

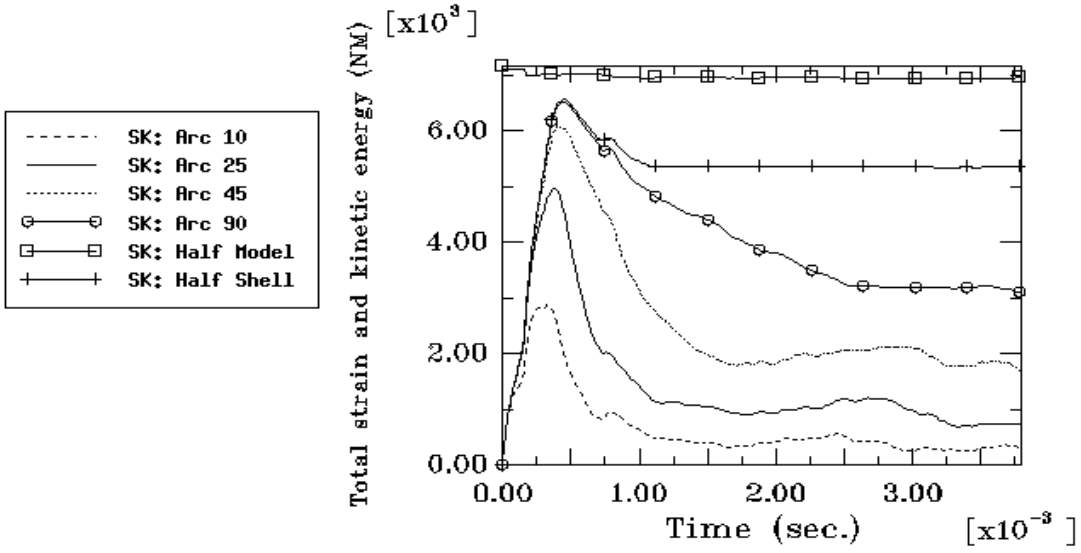

Figure 7: Strain and kinetic energy in the arc of 10 ^{o}, 25 ^{o}, 45 ^{o}, quarter, and Half-shell (without and with the projectile included) for case 1 (elastic model)

CONCLUSIONS

1. The initial local damage is not significantly affected by the boundary conditions while the subsequent deformation is strongly influenced by the boundary conditions.
2. A half shell could be used to replace the full shell when performing an impact experiment or analysis. Especially, an even better approximation could be obtained if local damage is involved.
3. Should a partial configuration be devised to simulate the response of the whole structure as a substitute, a free boundary condition could provide a closer result than a fixed boundary.
4. It is more reliable for a partial configuration to substitute the full shell when the localized damage is mainly concerned. This is because the impact times in the order of transition time for through-the-thickness waves is shorter than that required for the flexural wave reach the boundary [5].

It must be stressed that the projectile versus shell mass ratio drastically changes the response style [6]. Also glass/epoxy composite material is strongly strain-rate dependent. How these factors affect the response characteristics is to be further reported.

REFERENCES

1. Abrate, S. (1994). *Appl. Mech. Rev*. 47(11), 517
2. Collombet, F., Lalbin, X. and Lataillade, J.L. (1998). *Composite Science and Technology*. 58, 463
3. Christoforou, A.P and Yigit, A.SJ. (1998). *Solid and Vibration*. 217(3), 563
4. Nie, Z. and Yang, G. (1990). *Acta Mechanica Solida Sinica*. 3, 375
5. Beks, F-A. (1996). *FFA TN -29*, Bromma, Sweden
6. Olsson, R. (2000). *Composites part A*. 31, 879-887

Reference No. ICF1007090R

ISSUES IN FRACTURE TOUGHNESS AND R-CURVE BEHAVIOR OF PARTICLE REINFORCED METAL MATRIX COMPOSITES

B. S. Majumdar

Department of Materials and Metallurgical Engineering, New Mexico Tech
801 Leroy Place, Socorro, NM 87801

ABSTRACT

Different ASTM procedures were used to estimate the crack initiation toughness and R-curve behavior of SiC-particle reinforced aluminum matrix composites, with both macroscopically homogeneous and heterogeneous microstructures. Although the initiation toughness was similar, the crack resistance behavior varied over a wide range, depending upon the technique used to analyze the load-displacement-crack length data. Analysis showed that the cracks essentially grew under small-scale yielding (SSY) conditions. Aluminum particles had a greater influence on the steady state toughness than the initiation toughness. The implication of crack growth under SSY conditions is further analyzed in the context of development of many brittle systems (such as intermetallics), where an R-curve behavior is suggested as a remedy for low crack initiation toughness. A center cracked tension (CCT) geometry is used to establish that the modest R-curve behavior is of little value when such materials are used under load controlled conditions; i.e., instability occurs immediately on crack initiation, so that the R-curve effect is not realized. Tearing modulus (T) of these materials, as well as many intermetallics are close to unity. Results suggest that an order of magnitude increase in T is necessary before the R-curve behavior can be exploited in component design.

KEYWORDS

Fracture toughness, R-curve, Aluminum, particle, DRA, composite, stability, toughening

INTRODUCTION

Discontinuously reinforced aluminum (DRA) composites possess lower plane strain fracture toughness (K_{Ic} or J_{Ic}) than the aluminum alloys from which they are derived. Consequently, efforts are under way to understand failure mechanisms, and to devise methods to obtain toughness comparable to the Al-alloy matrix.

In this paper, we report results on a model 7093 Al-alloy composite reinforced with SiC particles. Note that the J_{Ic} of DRAs are quite sensitive to the heat treatment, and exhibit a trend of higher toughness with decreasing yield strength, similar to the matrix alloy. The current high strength DRA behaved similarly, and data are available in [1]. In addition to intrinsic toughening mechanisms, DRAs can also be tailored through an extrinsic approach [2]. One such method is to incorporate regions of pure Al or neat matrix alloy, which act as ductile ligaments during fracture. The effectiveness of this method of toughening of DRAs is discussed here. Preliminary data were reported earlier [3].

In this paper, we also focus attention on the engineering application of the R-curve characteristics in materials of limited toughness. This topic is relevant not only for DRAs, but also is important for advanced intermetallic alloys, which possess relatively low toughness (~10-20 $MPa.m^{1/2}$). Microstructural modifications in these systems often produce improved J-R curve, but the effect on the initiation toughness, K_{Ic}/J_{Ic}, is small. Anticipated applications of such

materials in structures are often under load controlled conditions, such as in a fan blade or a turbine blade. In these systems it is important to assess if modest R-curve gains through microstructural design will be adequate for the intended application. Frequently, there is a perceived notion that an R-curve behavior is an insurance against failure. The partially flawed logic is that a higher toughness value generated from the R-curve can be plugged in the stress intensity formula, to obtain a higher critical load or a larger critical crack length than that based on K_{Ic}/J_{Ic}. Clearly this is an incorrect approach, and stability issues must be considered. We report results from our stability analysis.

EXPERIMENTS

Two types of composites were considered in this investigation, and they were all fabricated at Alcoa. The control DRA consisted of 7093 aluminum alloy matrix (7 Zn, 2.2 Mg, 1.5 Cu, 0.14 Zr, 0.1 Ni wt.%,) reinforced with 15 vol.% of SiC particles (average particle size ~10 μm), and prepared through a powder metallurgy route. In addition to the control DRA, ductile phase toughened materials were fabricated with different volume fractions of pure Al particles. The constituents are indicated in Table 1. Two different sizes were considered: aluminum particles of 300 μm (designated small) and 10 mm size (designated large). The global volume fraction of SiC particles was maintained constant at 15 %, so that the presence of a larger volume fraction of Al particles implies that SiC volume fraction was higher in the reinforced region of the toughened composites. In this way, the elastic modulus was held approximately constant at approximately 90 GPa in all the microstructures. All the DRAs were subjected to an underaging (UA) treatment, involving solutionizing at 490 C/4h, water quench, followed by a 120 C/25 min. aging treatment.

Fracture toughness, J_{Ic}, and J-resistance curve of the materials were evaluated using ASTM E-813 and E-561 procedures, and it is shown later why the E-561 procedure is more appropriate for the materials considered here. The compact tension (CT) specimen geometry was employed, with a thickness (B) of 7.6 mm, a width (W) of 20.3 mm, and a notch length of 7.6 mm. All the CT specimens were fatigue precracked according to the standard ASTM procedures to an a/W ratio of approximately 0.5, where 'a' is the crack length.

RESULTS

Figure 1 (a) shows the SEM microstructure of the control DRA in the as-extruded condition and illustrates that the distribution of SiC particles in the aluminum matrix is fairly homogeneous. Figures 1 (b) illustrates the microstructure of ductile phase toughened DRA with small aluminum particles. The tensile properties of the composites are summarized in Table 1:

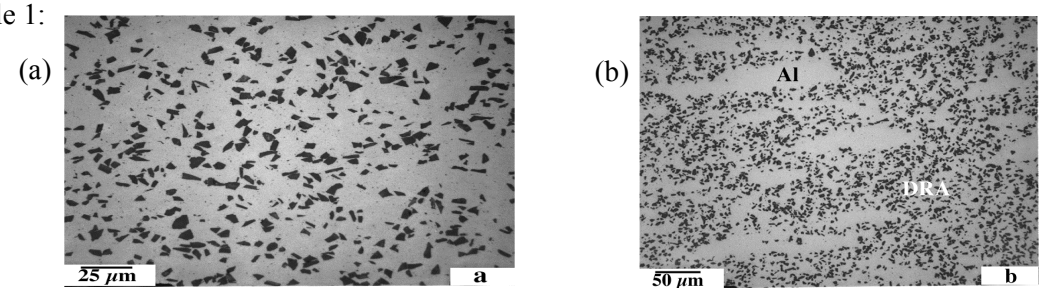

Figure 1. Microstructures of: (a) control DRA, and (b) DRA with 25% small Al-particles

TABLE 1. Results of tension and fracture toughness tests on the composites

Material	Yield Strength, MPa	Tensile Strength, MPa	Elongation, %	N, work hardening exponent	Initiation J_{Ic}, kJ/m^2	Initiation, $K_{a\text{-}eq}$, MPa.m$^{1/2}$	Steady State, K_{ss} MPa.m$^{1/2}$
Control DRA	503	629	5.9	0.089	2.9	16.0	20.0
DRA+10%large Al particles	436	555	4.4	0.087	3.0	16.5	25.2
DRA+25% small Al particles	453	546	4.4	0.075	5.0	24.0	34.6
DRA + 25% large Al particles	466	546	2.2	0.073	4.2	20.5	33.8

Initial analysis of the J-resistance (J-R) curve was conducted as per ASTM E-813, where

$$J_{pl} = \frac{2}{Bb}\int_0^{\Delta} Pd\Delta \qquad (1)$$

where Δ is the plastic part of the load-line displacement, B is the specimen thickness, and b is ligament width. ASTM E-1152 provides a slightly different equation to account for the history of crack growth. However, the difference was small, and did not appear to have a very significant effect on the J-R curve.

In order to assess the load-line displacement record, we used the EPRI estimation scheme of Kumar et al. [4,5] to estimate theoretically the plastic component of the total displacement. Plane strain formulation was used. Experimental data showed that the formulas from Kumar et al's [4,5] scheme severely overestimated the total displacement, by up to a factor of 10. Thus, these data confirmed that small scale yielding (SSY) was operative in our specimens. On the other hand, both ASTM E-813 and E-1152 owe their origin to the classical work of Rice and co-workers [6] who essentially assume full scale yielding of deeply notched specimens. In this work, we have attempted to solve this problem by deriving the J-R curve using the SSY formulation. In the spirit of Irwin's crack length correction approach, the measured displacements were used to derive an effective crack length. This was done by drawing a line from any point in the load-displacement record to the origin, and using the compliance formulas for the compact tension (CT) specimen to derive an effective crack length, a_{eq}. The standard LEFM formula was then used to compute K and hence J. This methodology is essentially what is used in ASTM E-561.

The K-resistance curves for the control DRA are compared in Figure 2, where the J values obtained through E-813 and

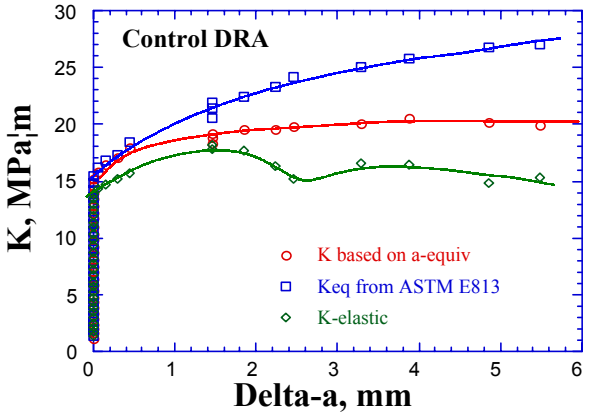

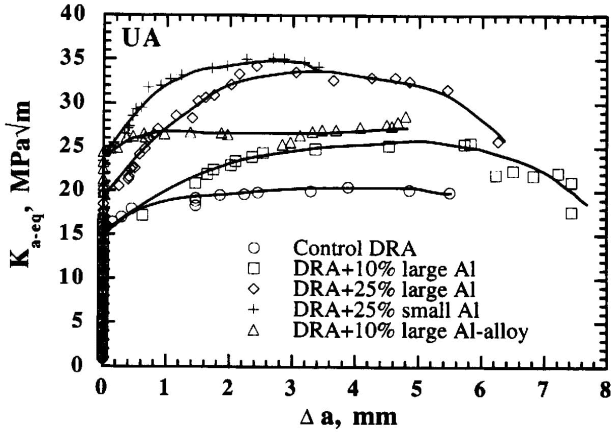

Figure 2. K-equivalent versus crack growth, Δa, using different ASTM procedures for the control DRA.

Figure 3. K-equivalent versus Δa using small-scale yielding approach. Results for the DRAs with different volume percent Al-particles are provided.

E1152 were converted to Ka-eq using Ka-eq=$\{JE/(1-\nu^2)\}^{1/2}$. Figure 2 shows that in the initial 0.5-1 mm of crack growth, the Ka-eq from ASTM E-813 and from the SSY formulation, are very similar. In fact, J_{Ic} results are nearly identical. However, the difference show up for crack growth beyond 1 mm. Figure 2 also shows that Keq based on SSY settles down to a *steady state* value of 20 MPa√m, whereas the data based on ASTM E-813 shows a continuously increasing trend.

The fracture surfaces did not reveal any difference in the crack morphology past the initial stretch zone (< 0.5 mm). Also, as already indicated, the plastic zone size was estimated to be of the order of 1 mm. Thus, there is very little reason why the growing crack should exhibit an ever-increasing trend beyond 1-2 mm of crack growth. The Ka-eq based on SSY indeed is consistent with the expectation of a steady state, K_{ss}, whereas that based on ASTM E-813 is not. Figure 2 also contains a plot of K_{el}, which is the elastic component of J. This plot does indicate drops, but the K value remains at around 15 MPa√m for the entire growth period. Thus, this can be considered with confidence as the lower limit value of K in predicting specimen instability, when previous details of loading are not known.

Figure 3 shows the Ka-eq resistance curves for the control DRA and DRAs containing Al particles in the UA condition. This plot shows that the initiation toughness for the ductile phase toughened materials are generally larger than the control DRA. The steady state toughness for the ductile phase toughened materials reveal a much greater improvement compared with the initiation toughness; an increase of as much as 70%.

MODELING OF FRACTURE TOUGHNESS AND STEADY STATE TOUGHNESS

In a previous paper [7] we modeled the fracture toughness of particulate reinforced composites, and showed that the toughness is quite sensitive to the constraint conditions. Assuming fracture to occur on attainment of a critical strain at one microstructural distance (equated to particle distance) ahead of the crack tip, the following formula was obtained:

$$K_{Ic} = 0.77\left\{\frac{\sigma_o \beta d E}{d_n(1-\nu^2)}\right\}^{1/2} v_p^{-1/6} \qquad (2)$$

where σ_o is the flow stress, v_p is the volume fraction of particles, d is the average particle diameter (10 μm here), and d_n represents the relation between crack tip opening displacement and J ($\delta = d_n J/\sigma_o$), and is given by $d_n = 0.78 - 2.73N + 3.065N^2$, where N is the work hardening exponent. β is 0.5 for a fully constrained crack (i.e., plane strain), and 0.91 for plane stress. Using the material constituent properties (E~90 GPa) and β=0.5, the predicted toughness for the control DRA material in the UA condition (σ_o=503 MPa) is 18.7 MPam$^{1/2}$, which compares favorably with the experimental data. In a separate publication [8], we reported the toughness for a thin specimen (0.76 mm thick) to be 31 MPa.m$^{1/2}$. Using β=0.91 instead of 0.5, the corresponding predicted plane stress toughness is 25.2 MPa.m$^{1/2}$, which is slightly lower than the measured toughness for the thin specimen. Overall, equation (2) appears to have reasonable validity among DRA materials. The only difficulty occurs when predicting the toughness for a peak aged material. In that condition, the material is prone to shear band localization, and an alternate formulation is necessary. The reader is referred to [7] for further details on toughness modeling of DRAs where shear localization is present, under the condition that the DRA has a reasonably uniform distribution of particles.

One can use a crack bridging model with ductile ligaments to model the toughness of the DRA with the ductile Al particles. A simple Dugdale model gives:

$$K_{bridging} = 2f\sigma_y^{Al}\sqrt{2L/\pi} \qquad (3)$$

where f is the volume fraction of the bridging phase, σ_y^{Al} is the flow stress of the Al, and L is the length over which the crack is bridged. At crack initiation, L is small (maximum 0.5 mm). Assuming a flow stress of 100 MPa for the pure Al ligament, the toughness improvements are 0.35 MPam$^{1/2}$ and 0.9 MPam$^{1/2}$ for the materials with 10 volume percent and 25 volume percent Al particles, respectively. The data for the 25 percent particles are clearly greater than the predicted values, and an alternate model is necessary.

A more likely mechanism of toughening of this DRA is crack trapping, which does not require that the crack propagate with isolated islands of ligaments left behind. We use here the model of Bower and Ortiz [9]:

$$\frac{K_{max}}{K_{matrix}} = \left\{(1-\sqrt{f}) + (2.1 + 2.4\sqrt{f})\sqrt{f}\right\}^{1/2} \qquad (4)$$

where K_{max} is the maximum toughening achievable, and K_{matrix} is the toughness of the matrix. Here, we identify K_{matrix} with the toughness of the control DRA (i.e., 16 MPam$^{1/2}$), and f with the volume fraction of the ductile Al phase. The ratio in equation 4 is calculated to be 1.26 and 1.47 for the 10 percent and 25 percent materials, respectively. Equation 4 should certainly be applicable in the steady state domain. Using the steady state toughness (K_{ss}) of 20 MPam$^{1/2}$ for the control DRA, we obtain K_{ss} of 25 MPam$^{1/2}$ and 29.4 MPam$^{1/2}$ for the two volume percent Al particles. These may be compared with experimental values of 25 MPam$^{1/2}$ and 34 MPam$^{1/2}$. The bridging effect also plays a role in K_{ss}. If we assume a total ligamented crack of 3 mm, in keeping with the observed R-curve data, the combined effects from equation (3) and (4) are K_{ss} of 25.9 MPam$^{1/2}$ and 31.6 MPam$^{1/2}$ for the two materials. These are in excellent agreement with the observed data. Overall, the largest contribution to K_{ss} appears to be from crack trapping than crack bridging.

We can extend the crack trapping model to predict initiation toughness. Using the initiation toughness of 16 MPam$^{1/2}$ for the control DRA, we calculate the initiation toughness for the 10% and 25% ductile phase toughened materials as 20 MPam$^{1/2}$ and 23.5 MPam$^{1/2}$, respectively. These may be compared with the experimental data.

STABILITY ANALYSIS

A J-R curve becomes useful only under conditions of stable fracture, when:

$$J_{app}(a) = R(a) \qquad (5a)$$

$$\frac{dJ_{app}}{da} \le \frac{dR}{da} \qquad (5b)$$

where J_{app} is the driving force, obtained from elastic-plastic analysis, and R characterizes the material's resistance to crack growth. While equation 5(a) is independent of whether loading is load or displacement controlled, dJ_{app}/da does depend on the particular type of loading. Displacement control is more stable, since the driving force generally decreases with crack length at constant displacement. This stability aspect has been exploited in leak-before-break calculations of steel pipes used in power generation, where loss of steam pressure through cracked regions of the pipe reduce the diving force for crack growth. Such applications are unlikely with DRA materials.

In order to evaluate the stability of DRA materials, which possess limited J_{Ic} and dR/da, we consider a center cracked tension (CCT) panel under load control. The latter is considered because many anticipated applications are in load control: fan blades and fan exit guide vanes in aerospace turbine engines, ventral fins in fighter planes, door-hatch in airplanes (internal pressure), etc. As indicated earlier, similar load controlled conditions are also likely to be present in applications of high temperature intermetallics, which also possess limited fracture toughness and crack resistance behavior. Thus, the analysis is anticipated to have general usefulness. The reason a CCT panel was considered is because this geometry produces the slowest increase of J with crack length, compared to other geometry. We used a plane stress formulation; to give the specimen added stability.

A CCT specimen with a total width, 2W=20mm, total length L=100 mm, and thickness B=2mm, was considered. Plane stress conditions were assumed. Two different initial crack lengths (total length $2a_o$) were considered: $2a_o$=12 mm and $2a_o$=0.4 mm. The rationale was to vary the plasticity component. Thus, the specimen having the shorter crack length (a_o=0.2 mm) would have a larger plasticity component at crack initiation (i.e., P/P_o closer to unity, where P_o is the limit load equal to the ligament area times the yield strength) compared with the specimen with a_o=6mm. Load-displacement and J values were generated for these two specimens using standard elastic and EPRI's plastic estimation formulas. Effective crack lengths were determined using an iteration method and employing Irwin's plasticity correction. Different crack lengths (a) were considered, starting from the initial a_o and up to a_o+3mm, the typical value where steady-state conditions were observed; see Figure 3. At the loads corresponding to crack initiation for the control DRA (~16 $MPam^{1/2}$) and the DRA with 25 percent large Al particles (~20 $MPam^{1/2}$), dJ/da was computed at constant load.

The applied J versus crack growth (Δa) from elastic plastic computations of the CCT specimen are compared with experimental data in Figure 4. The constant load curves 'a' and 'b' correspond to a_o of 6 mm and 0.2 mm, respectively, and are calculated based on the load at crack initiation (J_{Ic}=2.8 kJ/m^2). The P/Po values at crack initiation were 0.39 and 0.54 for curves 'a' and 'b', respectively. For both these crack lengths, dJ/da at constant P was larger than dR/da (from experimental data). Thus, both the CCT specimens would be unstable at crack initiation.

Figure 5 illustrates the load-elongation curve that would be generated on the CCT specimen with 6 mm crack length, if the material follows the J versus crack length curve generated from the experiments. This plot clearly shows that the maximum load is reached at crack initiation, and that both the load and displacement would have to decrease if the R-curve of the material was to be followed. The maximum load is reached at crack initiation, indicating that instability would ensue at crack initiation, and that the rest of the R-curve would not be of any significant value.

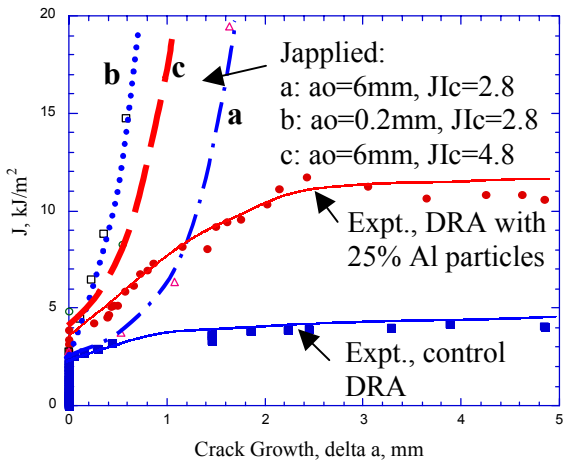

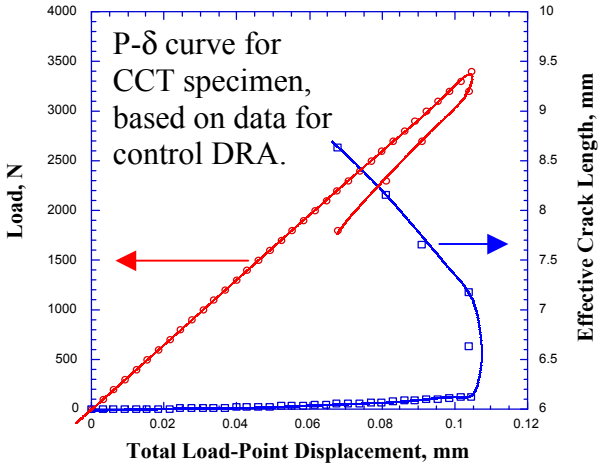

Figure 4. J versus crack growth for a CCT specimen under plane stress, and experimental data (R-curves) for the two DRA materials. The crack lengths used in the calculations are indicated.
Figure 5. Load vs displacement and load vs crack length for the CCT specimen, based on data from the control DRA.

Returning to Figure 4, the curve marked 'c' corresponds to $J_{applied}$ versus Δa at constant load, where the load is based on crack initiation at Keq=20 $MPam^{1/2}$; a_o is 6 mm. This Keq corresponds to the initiation toughness of the ductile phase toughened material with 25 percent large Al particles. Recall from Figure 3 that this material exhibited one of the highest dJ/da. Figure 4 once again illustrates that the $J_{applied}$ curve, 'c', deviates from the R-curve from the point of crack initiation (dJ/da>dR/da), indicative of instability at crack initiation. Thus, although this material had significantly improved crack growth resistance, the enhancement appears to be inadequate for maintaining component integrity under load controlled conditions. Overall, the main problem appears to be the low dJ/da, which results in tearing modulus values $\{T=(E/\sigma_y^2)*dJ/da\}$ in the range of 0.5 to 1.1 for the current composites. These values may be compared with T ranging between 20 and 200 for structural steels. It appears therefore that significant improvements in dJ/da will be necessary before the R-curves can be put to use for DRAs and intermetallics, which have limited ductility.

It is acknowledged that dJ/da at constant load is too stringent in terms of applications, and that a system compliance should be incorporated into the stability analysis. On the other hand, rotating components in turbines are often under load control. Static components offer greater flexibility, and some advantage may be gained from the R-curve behavior. However, we have conducted stability analysis using some typical machine compliance (C_M) values. Although those results are not reported here, they do indicate that the T values are too low to be of much usefulness. Moreover, steady-state toughness values impose added limitations, and these show up better in a plot of T versus J. Our conclusion is that at least an order of magnitude increase in dJ/da is necessary before R-curves become useful for such materials.

CONCLUSIONS

Experiments were conducted on a control DRA, and DRAs toughened extrinsically with Al-particles. The following conclusions are obtained:

a) In these materials, the crack grows primarily under small scale yielding conditions. The appropriate method to determine the J-R curve is discussed.

b) The Al-particles have a greater effect on steady state toughness than the initiation toughness. A good prediction of the toughness of the ductile phase toughened material is obtained through a crack-trapping model.

c) Stability analysis, using the material data and a CCT specimen geometry, indicate that the current dR/da values are insufficient to prevent instability at crack initiation, under load controlled conditions. A significant improvement in the tearing modulus is necessary before the R-curve behavior can be utilized in such materials of limited ductility.

ACKNOWLEDGMENTS

This work was partially funded under a collaborative NUCOR program with the Los Alamos National Laboratory. Part of the work was conducted while the author was at the Wright Laboratories, AFRL, Ohio. Discussions with Dr. A.B. Pandey at Pratt & Whitney, and Dr. D.B. Miracle at AFRL, are gratefully acknowledged.

REFERENCES

1. Pandey, A.B., Majumdar, B.S., and Miracle, D.B. (2000) *Metall. Trans.*, *31A*, pp.921-936
2. Lewandowski, J.J., Liu, C., and Hunt, W.H. Jr. (1989) *Mater. Sci. Eng.*, *107 A*, 241
3. Pandey, A.B., Majumdar, B.S., and Miracle, D.B. (1999) *Mater. Sci. Eng.*, *259 A,* pp.296-307
4. Kumar, V., German, M.D., and Shih, C.F. (1981) *Electric Power Research Institute, EPRI NP 1931*
5. Anderson, T.L. (1995) *Fracture Mechanics: Fundamentals and Applications*, CRC Press LLC
6. Rice, J.R. (1968) *J. Appl. Mech.*, *35*, p. 379
7. Majumdar, B.S., and Pandey, A.B. (2000) *Metall. Trans., Vol. 31A*, pp.937-950
8. Pandey, A.B., Majumdar, B.S. and Miracle, D.B. (1998) *Metall.Trans. A* , *29 A*, pp.1237-1243
9. Bower, A.F., and Ortiz, M. (1990) *J. Mech. Phys. Solids, 38*, p.443

K-R CURVES OF THIN 2195-T8 ALUMINIUM ALLOY PLATE

R. Doglione, D. Firrao

Politecnico di Torino, Italy, C.so Duca degli Abruzzi 24, 10129 Torino, Italy, phone -39-011-5644612, fax -39-011-5644699, e-mail doglione@athena.polito.it

ABSTRACT

The dependence of the raising toughness (R-curves) of a 2195-T8 Al-Cu-Li alloy plate on the microstructure is studied. Large intermetallic particles organised in arrays along the rolling direction serve as nucleation sites of ductile fracture; crack growth occurs mainly by pop-in. The application of Rice and Johnson's criterion for ductile fracture, making appropriate use of the average inclusion spacing along the fracture path in LT and TL direction, leads to satisfactory predictions of the onset of pop-ins and of the R-curves toughness plateaus.

KEYWORDS

Al-Cu-Li-Mg-Zr Plate, K-R Curve, Pop-in, Inclusions.

INTRODUCTION

Among Al-Li alloys, the Weldalite family (Al-Cu-Li-Mg-Ag-Zr) was developed to achieve high strength in the stretched and artificially aged (T8), artificially aged (T6) and naturally aged (T3 and T4) conditions [1]. Compared to other Al alloys, they have a much greater response to natural ageing, as well as being able to achieve high strength and adequate ductility after artificial ageing [2]. The Weldalite alloys are then used in welded structures [3], where a T6 treatment after welding is almost impossible, and in forgings [4], where non uniform stretching could result in undesirable variations in mechanical properties.

The first developed alloy, 2095 (Cu 4.75, Li 1.26, Mg 0.38, Ag 0.38, Zr 0.1 wt. pct.), was characterised in the T8 temper by extremely high tensile strength, often exceeding 700 MPa, but by a rather low fracture toughness, of the order of 20 MPa√m [2]. Alloy 2195 was then developed, with the aim of excellent fracture toughness/strength combinations. To the purpose, both Cu and Li content were lowered, and by T8 temper it was possible to reach a strength exceeding 600 MPa, as well as a fracture toughness of the order of 30 MPa√m or more.

Nowadays, tensile characteristics of rolled, forged and extruded 2195 alloy in the T8 temper are known. On the other hand, fracture toughness K_{Ic} has been reported till now for nominal plane strain conditions, which are appropriate only for thick components; fracture toughness determination for thin plates is actually lacking, mainly because of peculiar R-curve behaviour of thin products. Besides, in damage tolerant applications, the K_{Ic} value is unable to describe the full spreading of the material toughness. In these cases, the K-R curve is the only suitable approach; yet, K-R curves determinations have been scarce for Al-Li alloys, with very few reported data only for 2090 and 8090 alloys [5-13].

Suitable correlations between fracture mechanisms and R-curves, as well as the explanation of the curve on the basis of microstructural parameters have also to be sought. This point is extremely important, because only a thorough knowledge of the influence of the microstructure on the toughness may lead to the optimization process (through chemical composition variations and temper modifications) of the alloys. In order to clarify the problem, it was decided to study the K-R curve behaviour of a 6.35 mm thick 2195-T8 alloy plate and the intervening fracture mechanisms.

EXPERIMENTAL

2195-T8 alloy was received by Reynolds in the form of 6.35 mm thick plate. Details on the chemical composition are given in Table 1. Tension tests were performed in both L and LT directions under strain control at strain rates of 10^{-4} s^{-1}. The average results are reported in Table 2.

TABLE 1
CHEMICAL COMPOSITION OF THE ALLOY (WEIGHT %).

Cu	Li	Mg	Ag	Zr	Si	Fe	Mn	Al
3.94	0.95	0.37	0.39	0.13	0.02	0.03	0.002	bal.

Fracture mechanics tests were performed on C(T) samples 26 mm wide, in the LT and TL crack plane orientations. The single specimen method coupled with the secant reciprocal slope technique was employed, according to the ASTM E561-92 Standard. The tests were performed in crack opening displacement control. It yields decreasing crack growth driving forces, which allow to follow a ductile fracture process entirely, thus limiting the effects of pop-ins and the possibility of global instability.

The microstructure was analyzed by optical microscopy on metallographic samples. Finally, the failure mechanism were studied by microfractographic observations on the fracture surfaces by a Scanning Electron Microscope.

RESULTS

As expected, tensile properties (Table 2) are very high and particularly attractive. A certain anisotropy between L and LT directions is evidenced, pointing out to the presence of crystallographic textures induced by the plate rolling schedule and its subsequent solubilisation treatment. Finally, the strain hardening capabilities are expressed in terms of the Hollomon law in Table 2; owing to the high strength of the alloy, the hardening exponent n is very low, as expected.

With regard to fracture mechanics tests, load-displacement data indicate a classical high strength Al alloy behaviour, i.e. frequent and at times large pop-in steps. Nevertheless, 2195-T8 alloy shows a globally stable behaviour, being possible to control the fracture process along the decreasing part of the load-crack opening displacement diagram. This produced stepped K-R curves, Figure 1.

TABLE 2
TENSILE PROPERTIES OF 2195-T8 ALLOY.

direction	E [GPa]	Re [MPa]	R [MPa]	A%	n	k [MPa]
L	72.8	580	602	8.5	0.022	668
LT	72.6	548	578	10	0.035	682

The microstructure, typical of many high strength aluminium alloys, is made of coarse (several millimeters long) unrecrystallised columnar grains mixed with fine nearly equiaxed recrystallised grains (10 μm ca. diameter). These appear to be located at the boundaries of the large columnar grains, or inside them, when there is a local high concentration of intermetallic particles. These particles are mainly arranged in rows following the rolling direction. The average interparticle spacing inside each inclusion array is of the order of 30 μm, whereas in the long transverse direction the inclusions rows are on the average 480 μm apart.

The fracture mechanism is ductile, mainly transgranular, even if some intergranular character is present. The dimples are developed around the previously cited intermetallics. The cavities are nearly equiaxed around the coarser particles, whereas smaller intermetallics give rise to dimples elongated in the crack growth direction because they encompass several particles. Very elongated dimples are more pronounced and frequent in TL samples.

DISCUSSION

The K-R curves reported in Figure 1 show some peculiar characteristics, namely the grouped distribution of points spaced by pop-ins more visible in the upper part of the curves. Here, after pop-in and crack arrest, new low elevation high K level blunting occurs.

In order to explain the differences in the R-curves and the presence of an approximative toughness plateau in the TL direction, it is necessary to take into account the inclusion distribution, as detailed in the previous paragraph and that, as here reported, fracture is predominantly ductile, by nucleation, growth and coalescence of voids around biggest second phases particles.

Toughness in the TL direction is then related to the inclusion spacing along inclusions rows produced by rolling of the plate. Assuming the validity of the classical fracture criterion proposed by Rice and Johnson [14], critical conditions for fracture are reached when the heavily strained process zone (contained in the plastic zone ahead the crack tip), which scales with the CTOD, reaches the center-to-center spacing λ between bigger intermetallics. This prompted Hahn and Rosenfield [15] to propose a model for the attainment of ductile fracture instability in high strength aluminium alloys:

$$K_{crit} = \sqrt{2 \cdot R_e E \cdot \lambda} \qquad (1)$$

The validity of this model has been questioned by Garret and Knott [16] because it predicts increasing toughness with increasing yield strength, contrary to experiments. However, the same authors recognise that the model correctly reproduces the dependence between toughness and microstructural parameters for peak aged high strength aluminium alloys..

In the present case, being the specimens not in fully plane strain because of insufficient thickness, it is necessary to substitute the factor 2 in equation 1 with a constant k, slightly greater than 2, which accounts for a mixed plane strain-plane stress state. Moreover, the initial part of the R-curve simply represents the enlargement of the plastic zone, without physical crack propagation, what corresponds to the evolution of the stress state from plane strain (at the beginning) to a more relaxed triaxiality. Modified equation 1 should then be correctly interpreted as a condition for the instability at different triaxiality levels, which are represented by different k values. Since R_e, E (Table 2) and λ (30μ, see preceding paragraph) are constant, in a near plane strain state k≈2 and modified equation 1 predict the onset of the instabilities on the R curve nearly at 49 MPa√m, in quite good agreement with the fact that the first significant pop-ins are found on the R-curves (in the TL case) above 40 MPa√m (Fig. 1).

Obviously, the instability is not catastrophic, because tests were conducted under crack opening control and the fracture mechanism is invariant. After crack arrest, further loading produces further stress triaxiality relaxation, an increase of the value of k above 2, and the next instability at K levels above the previous one. The R-curve may then, in average, continue to rise, but only slightly, because with progressive triaxiality

relaxation the increments of k values are small, whereas the short 30 μm inclusion spacing along rows in the L direction dictates the limits of the process zone, and then limits an approximative plateau of the R-curve slightly above 50 MPa√m.

As it regards LT specimens, the previous arguments may be valid to predict the first significant instabilities. At the beginning of loading, in a near plane strain state, some parts of the crack front are located in correspondence with an intermetallic group, where interparticle spacing is still of the order of 30 μm. Again following Hahn and Rosenfield, the onset of the pop-ins may be predicted to lie between 40 and 50 MPA√m, as actually verified on the R curves, e.g. Figure 1. But now the toughness plateau is not easily reached, because after a first momentary unstable crack propagation through the inclusion group, the crack front, in that region of the sample, after arrest will find the next inclusion array at a distance somewhat less (it depends on the arrest distance beyond the first inclusions) than the intermetallics row spacing, 480 μm; such a distance is an order of magnitude larger than the interparticle spacing within the row, 30 μm.

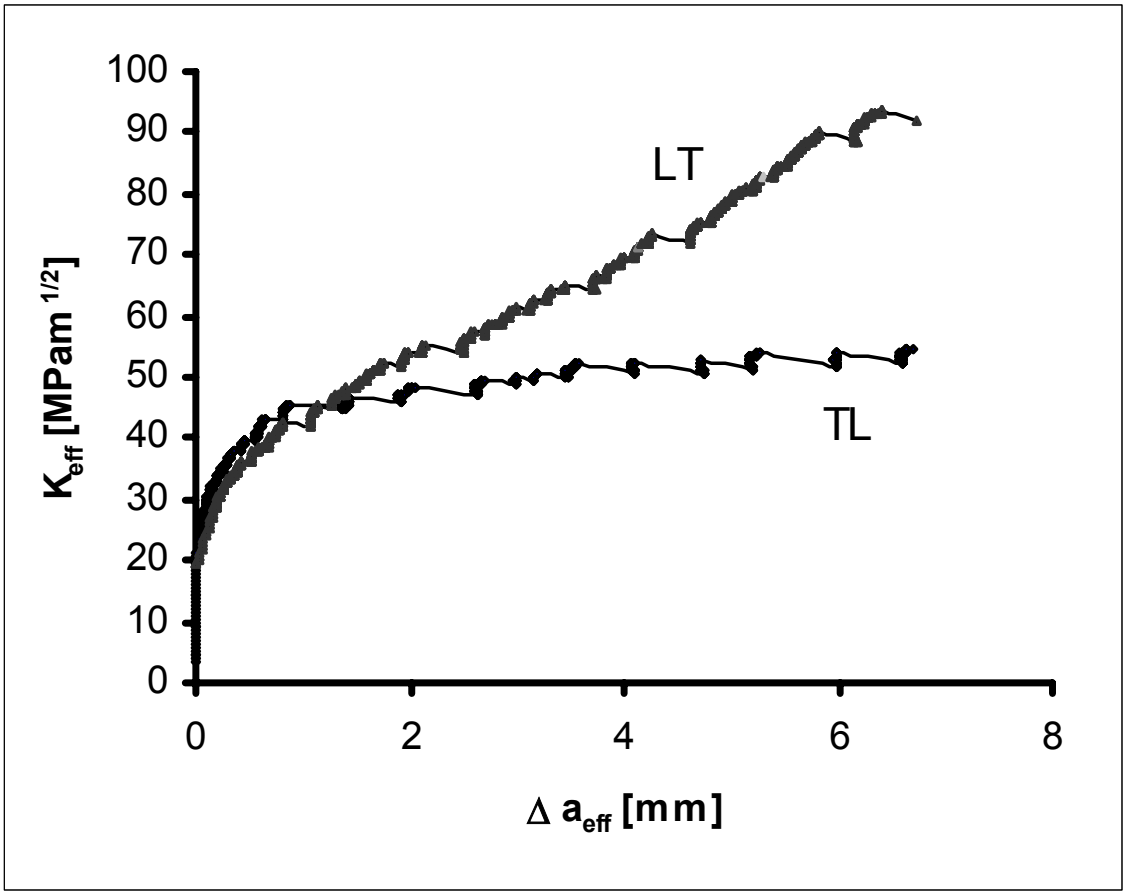

Figure 1: K_{eff}- Δa_{eff} curves for 2195-T8 alloy tested in the TL and LT directions.

Thus, after arrest, new instability conditions are not soon reached in the same region of the sample, and probably critical conditions may be reached easier in another region, where the crack front is closer to the next intermetallics array. The situation corresponds then to an intermittent activation of local instabilities mixed with a progressive loss of constraint and plastic zone enlargement. This explains the long rising of the R curve, and the delay in the attainment of a toughness plateau, which is not reached with the small samples utilised in the present investigation.

However, again equation 1 allows a rough estimate of the order of magnitude of the toughness plateau in the LT direction. Since the average magnitude of crack growth during pop-in in the high part of the R curve is of the order of 230 μm, this means that, in average, the next intermetallics array is at least about 250 from the actual crack front. Again invoking the Rice and Johnson's criterion, and making use of equation 1,

considering that now the sample is far from plane strain conditions, the constant k is above two and the predicted toughness plateau is above 70-80 MPa√m, in good agreement with experimental data, Figure 1.

CONCLUSIONS

Fracture resistance of the Al-Cu-Li-Mg-Zr 2195-T8 6 mm thick plate has been studied following the K-R curve approach. It has been found that 2195-T8 possesses excellent toughness, and this strongly related to the average inclusion spacing. Such parameter induces an important toughness anisotropy between LT and TL directions, the latter being characterised by less attactive performances. It may be concluded that a substantial reduction of the inclusions content, i.e. the coarse intermetallics, might enhance TL fracture toughness because it increases the interparticle spacing, thus postponing the attainement of critical conditions at the crack tip.

ACKNOWLEDGEMENTS

The financial support of Agenzia Spaziale Italiana through the contract no. J97FDA1 is here acknowledged.

REFERENCES

1. Pickens J. R.,. Heubaum F. H, Langan T. J. and Kramer L. S., (1989) In: *Aluminium-Lithium Alloys*, Proc. 5th Int. Aluminium-Lithium Conf., pp. 1397-1414, Sanders T. H. and Starke E. A. eds., MCEP.
2. Edwards M. R., Moore A. and Mustey A. J., (1994) In: *Aluminium Alloys*, Proc. 4th Int. Conf. Aluminium Alloys (ICAA4), Vol. II, pp. 334-341, Sanders T. H. and Starke E. A. eds., Georgia Institute of Technology,.
3. Cross C. E., Loechel L. W. and Braun G. F., (1992) In: *Aluminium-Lithium Alloys*, Proc. 6th Int. Aluminium-Lithium Conf., pp. 1165-1170, Peters M. and Winkler P. J. eds., DGM.
4. McNamara D. K., Pickens J. R. and Heubaum F. H., (1992) In: *Aluminium-Lithium Alloys*, Proc. 6th Int. Aluminium-Lithium Conf., pp. 921-926, Peters M. and Winkler P. J. eds., DGM.
5. Venkateswara Rao K. T. and Ritchie R. O., (1989) In: *Aluminium-Lithium Alloys*, Proc. 5th Int. Aluminium-Lithium Conf., pp. 1501-1512, Sanders T. H. and Starke E. A. eds., MCEP.
6. Barbaux Y., (1989) In: *New Light Alloys*, pp. 8-1, 8-18, AGARD n. 444.
7. Hart G.J., Schra L., McDarmaid D.S. and Peters M., (1989) In: *New Light Alloys*, pp. 5-1, 5-17, AGARD n. 444.
8. Doglione R., Ilia E., Firrao D., (1991) Proc. VII Conv. Naz. Gruppo Italiano Frattura, pp. 57-73, Reale S. ed., Firenze, Italy.
9. R.J.H. Wanhill, L. Schra and W.G.J. Hart, (1992) In: *Aluminium-Lithium Alloys*, Proc. 6th Int. Aluminium-Lithium Conf., pp. 253-258, Peters M. and Winkler P. J. eds., DGM.
10. Doglione R., Ilia E., Marcelli A., Firrao D., (1992), In: *Materials Development in Rail, Tire, Wing, Hull Trasportation*, Vol. 1, pp. 191-200, Associazione Italiana di Metallurgia, Milano, Italy.
11. Firrao D., Doglione R., Ilia E., (1993) In: *Constraint effect in Fracture*, pp. 289-305, Hackett E. M., Schwalbe K.-H. and Dodds R. H. eds., ASTM STP 1171.
12. Doglione R., Ilia E., Firrao D., (1994) In: *Aluminium Alloys*, Proc. 4th Int. Conf. Aluminium Alloys (ICAA4), Vol. II, pp. 374-381, Sanders T. H. and Starke E. A. eds., Georgia Institute of Technology,.
13. Doglione R., Arena F., Firrao D., (1997) In: *Advances in Fracture Research*, Proc. 9th Int. Cong. Fracture, Vol. 1, pp. 259-265, Karihaloo B. L., May Y-W., Ripley M. I. and Ritchie editors R. O., Pergamon Press.
14. Rice J. R. and Johnson M. A., (1970) In: *Inelastic Behaviour of Materials*, pp. 641-672, Kanninen M. F., Adler W. F., Rosenfield A. R. and Jaffee R. I. eds., McGraw Hill.
15. Hahn G. T. and Rosenfield A.R., (1975) *Metallurgical Transactions A*, Vol. 6A, pp. 653-670.
    Garret G. G. and Knott J. F., (1978) *Metallurgical Transactions A*, Vol. 9A, 1978, pp. 1187-1201.

K_{IC} - A NON-MEASURE OF PLANE STRAIN FRACTURE TOUGHNESS

K. R. W. Wallin

VTT Manufacturing Technology
P.O. Box 1704, FIN-02044 VTT, FINLAND

ABSTRACT

The plane-strain fracture toughness, K_{IC}, defined by ASTM E 399, is assumed to represent a size insensitive lower bound value. The interpretation is due to the original work by George Irwin. The materials used for the development of ASTM E 399 were generally aluminum and titanium alloys or maraging steels. The materials had in common that their fracture micro-mechanism was ductile fracture. Even though materials failing by cleavage fracture were not part of the development of the K_{IC} standard, it was soon applied to pressure vessel steels. Also here, it was assumed that valid K_{IC} results are lower bound size insensitive material values showing only little scatter. Based on the present understanding of cleavage fracture, this assumption is known to be incorrect. The misinterpretation is due to the fact that the physical fracture micro-mechanisms were not understood at the time and the developers of the ASTM E 399 testing standard were led astray.

KEYWORDS

Fracture toughness, plane-strain, brittle fracture, ductile fracture.

INTRODUCTION

Structural integrity assessment of structures containing planar flaws (real or postulated) requires the use of fracture mechanics. Fracture mechanics compares in principle two different parameters: the driving force and the material resistance. The driving force is a combination of the flaw size (geometry) and loading conditions, whereas the material resistance describes the materials capability to resist a crack from propagating. Up to date, there exist several different testing standards (and non-standardized procedures) by which it is possible to determine some parameter describing the materials fracture resistance (ASTM E 399, ASTM E 1820, BS 7448, ESIS P2 etc.). Unfortunately, this has lead to a myriad of different parameter definitions and their proper use in fracture assessment may be unclear.

Historically, fracture mechanics evolved from a continuum mechanics understanding of fracture. It was assumed that there existed a single fracture toughness value controlling the materials fracture. If the driving force were less than this fracture toughness, the crack would not propagate and if it exceeded the fracture toughness the crack would propagate. Thus, crack initiation and growth were assumed to occur at a constant driving force value. The only thing assumed to affect this critical value was the constraint of the specimen (or structure). Since at that point of time, there were no quantitative means

to assess the effect of constraint the fracture mechanics, the fracture toughness had to be determined with a specimen showing as high a constraint as possible. This lead to the use of, deeply cracked, bend specimens for the fracture toughness determination.

Historically, the micro-mechanisms of fracture were not considered. It was assumed that the continuum mechanics description of fracture toughness would be valid, regardless of fracture micro-mechanism. This assumption has later been proven to be wrong. Different fracture micro-mechanisms exhibit different physical features that affect the properness of a specific fracture toughness parameter to describe that fracture micro-mechanism.

The common interpretation of the plane-strain fracture toughness K_{IC}, defined by ASTM E 399, is a specimen size insensitive lower bound fracture toughness corresponding to plane-strain stress state. The interpretation is due to the original work by George Irwin where he postulated the expected effect of specimen thickness on fracture toughness (Fig. 1). George Irwin based his conclusions on maximum load toughness behavior of center cracked tension specimens of two aluminium alloys, combined with the specimens macroscopic fracture surface appearance [1]. Even though the experiments did not really correspond to any proper fracture toughness description, nor fracture event, the postulated thickness effect was soon adopted as representing the physical "truth" of fracture behavior. This constituted also the expectations for the development of the ASTM E 399 testing standard.

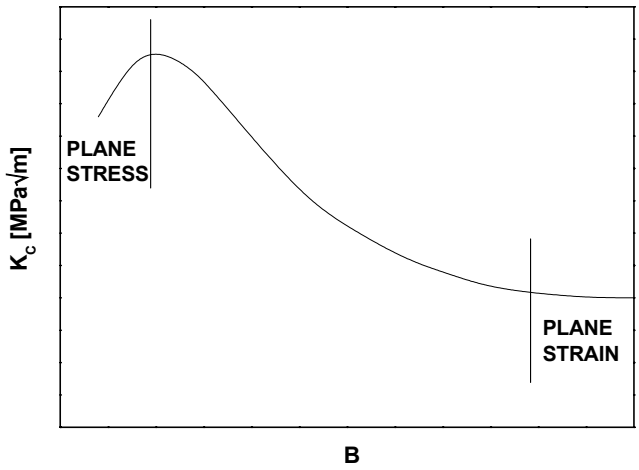

Figure 1: Schematic presentation of the assumption of thickness effect on fracture toughness.

DUCTILE FRACTURE

The materials used for the development of ASTM E 399 were generally aluminum and titanium alloys or maraging steels. The materials had in common that their fracture micro-mechanism was ductile fracture, i.e. the materials showed a rising tearing resistance curve. Unfortunately this was not understood at that time, since the continuum mechanics type of behavior was assumed. This confronted the standard developers with a new problem. Generally, the fracture toughness did not show the expected decreasing trend with increasing specimen size, but the opposite as shown by Fig. 2 [2]. This increasing toughness led to the introduction of the additional demand that $P_{max}/P_Q < 1.1$.

The specimen thickness was still assumed to control the materials fracture toughness as postulated by Irwin. The assumption prevailed, even though the experimental data indicated that it was the specimen ligament size and not thickness that controlled the fracture toughness value (Fig. 3) [2]. The belief in the plane-strain, plane-stress postulate was however so strong that this clear evidence was disregarded.

Also, the plane-strain fracture toughness was assumed to be a lower bound specimen size insensitive material parameter, but the results indicated the reverse, i.e. that K_{IC} increased with specimen size. Since the results were tried to explain solely based on constraint, the real reason for this increase in toughness was never pursued. Based on the present physical understanding of ductile fracture, the increase in fracture toughness is easy to explain.

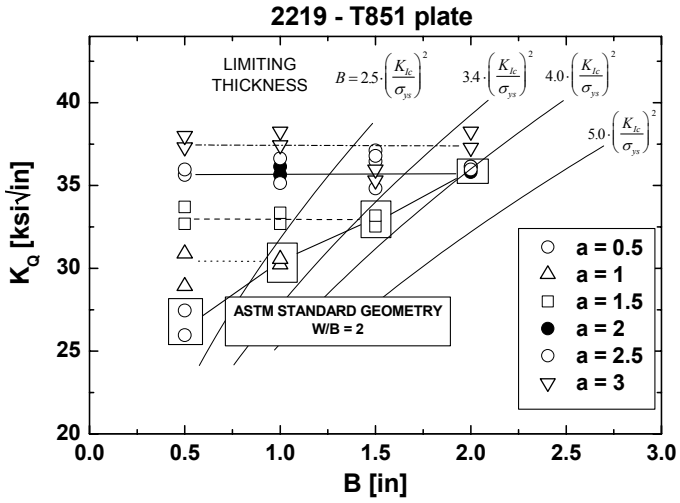

Figure 2: Old K_Q data used to develop ASTM E399 showing increasing toughness with increasing specimen size [2].

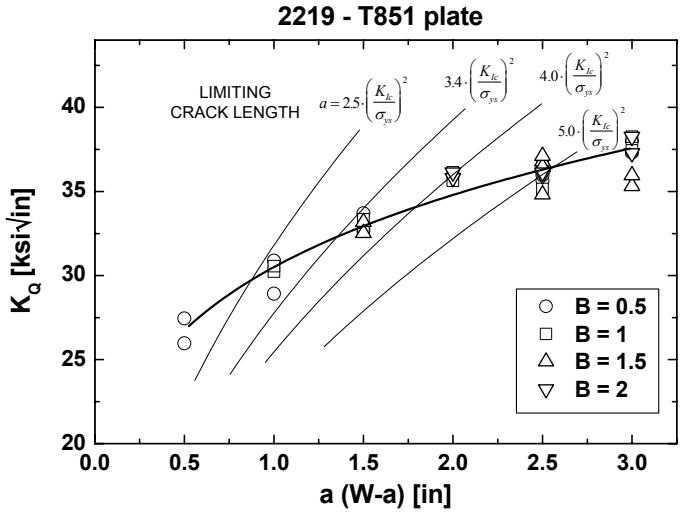

Figure 3: Same data as in Fig. 2 showing ligament size controlling the increasing toughness [2].

At the time of the development of the K_{IC} standard, there was no reliable means of monitoring crack growth during the test and also, crack growth was assumed to occur at a constant value of K_{IC}. This lead to using the 95 % secant method, for the determination of K_Q. If all the non-linearity in a load-displacement curve of a K_{IC} test specimen is due to crack growth, a 95 % secant correspond to a 2 % crack growth with respect to the ligament. With increasing ligament size, also the absolute amount of crack growth, defined by the 95 % secant, will increase. Knowing, like presently is the case, that materials, in the case of ductile crack growth, exhibit rising tearing resistance curves, makes the increasing toughness with increasing specimen size quite understandable. Fig. 4, is a repetition of Fig. 3, including an estimate of the 2 % crack growth, together with a tearing resistance curve fit. It is clear

that the valid K_{IC} values correspond to considerable amounts of crack growth, the value of which is controlled by the ligament size, not specimen thickness. A modern J_{IC} -test would give for the material in Fig. 4 a K_{JIC} of about 23 ksi√in, i.e. clearly less than the valid K_{IC}.

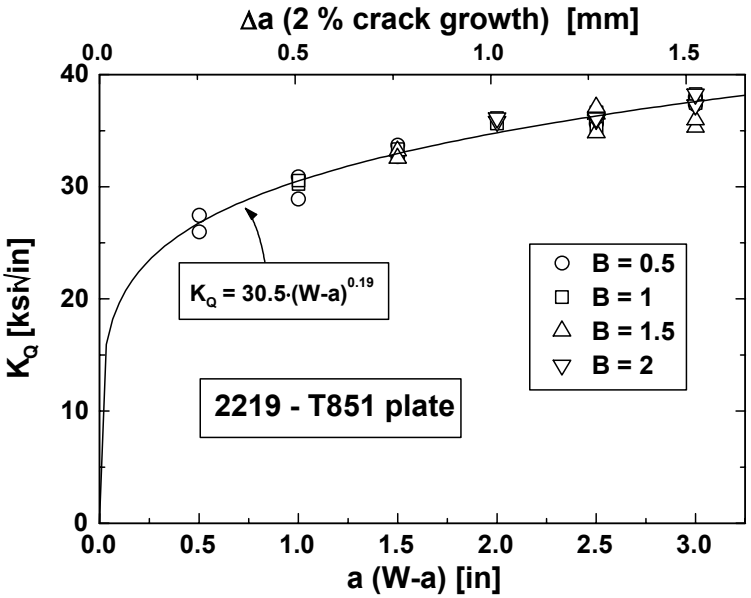

Figure 4: Increasing toughness with increasing ligament size due to increasing tearing resistance curve for ductile tearing.

BRITTLE FRACTURE

Even though materials failing by cleavage fracture were not part of the development of the K_{IC} standard, it soon became applied to testing of nuclear pressure vessel steels. Also here, the original continuum mechanics based philosophy was assumed, i.e. that valid K_{IC} results are lower bound specimen size insensitive material values showing only little scatter. Again, based on the present understanding of the physics of the cleavage fracture micro-mechanism, this philosophical assumption is known to be incorrect.

Based on an interpretation of the physics, the Master Curve method was developed at VTT. Here size effects in brittle fracture toughness are adjusted for, theoretically [3]. Physically, the fracture toughness in temperature space can be divided into three regions, brittle fracture region, transition region and upper shelf. The brittle fracture region is further divided into two separate regions, depending on the way specimen size affects the fracture toughness. In the lower shelf region, size effects are negligible, but at higher toughness values, the brittle fracture toughness will be affected by a statistical size effect. The transition region is defined as the temperature region, where cleavage fracture occurs after some amount of ductile tearing. This region will be specimen size dependent due to the statistical size effect. Finally, the upper shelf is defined as the temperature region where the fracture mechanism is fully ductile. Also the temperature for the onset of upper shelf is specimen size dependent due to the statistical size effect. Besides, statistical size effects, the fracture toughness can be affected by specimen constraint. The basic Master Curve has been standardized by ASTM in ASTM E 1921.

The statistical size effect, due to the weakest link nature of cleavage fracture initiation, is active also for valid K_{IC} results, provided they are above the lower shelf. A good example of this is given by the HSST 02 plate data used originally to develop the ASME K_{IC} reference curve (Fig. 5) [4]. The data, originally known as the "million dollar curve", constituted the first large fracture toughness data set generated for

a single material. Normally, only the valid K_{IC} results are reported, but for clarity, here also the invalid results are included. It is evident that there is a difference between the smaller 1T & 2T specimens and the larger 4T & 6T specimens. This size effect is fully in line with the theoretical statistical size effect as used by the Master Curve methodology [3] (Fig. 6).

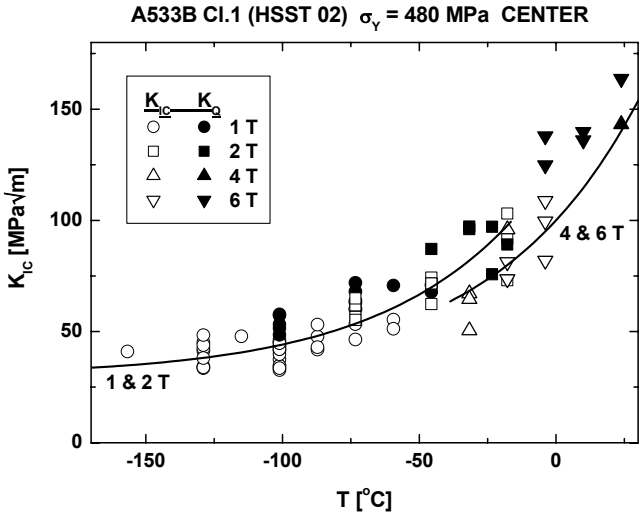

Figure 5: Valid brittle fracture K_{IC} data for the HSST 02 plate indicating decreasing fracture toughness with increasing specimen size.

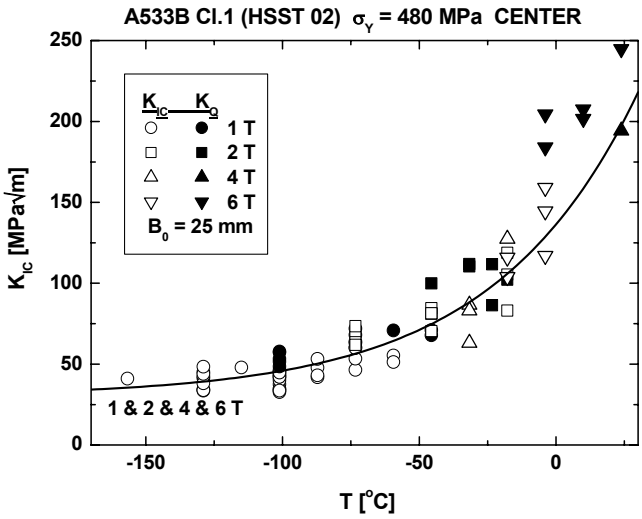

Figure 6: Size effect in valid brittle fracture K_{IC} data for the HSST 02 plate is correctly described with the Master Curve.

Another data set showing the decrease in K_{IC} with increasing specimen size has been presented by MPA (Fig. 7) [5]. Even though the data is limited in number, it clearly indicates decreasing fracture toughness with increasing specimen size, for all valid K_{IC} values. Also in this case, the size effect is in line with the theoretical prediction of the Master Curve. Numerous similar data sets can easily be found in the open literature.

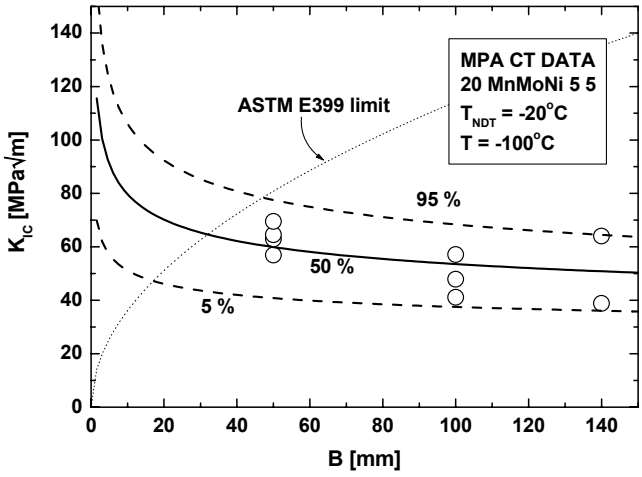

Figure 7: MPA brittle fracture K_{IC} data showing size effect in accordance with the Master Curve [5].

SUMMARY AND CONCLUSIONS

In this work the consistency of the ASTM K_{IC} plane-strain fracture toughness standard (ASTM E399) has been examined based on present knowledge about fracture micromechanisms. Originally the standard was based on continuous mechanics assumptions, which have been found inadequate to describe the real physical fracture process.

It is clear that the classical interpretation of K_{IC} as being a lower bound, specimen size insensitive, fracture toughness value, corresponding to a plane-strain stress state is wrong, both for brittle fracture as well as ductile fracture. The reason for the misinterpretation is due to the fact that the physical fracture micro-mechanisms were not understood at the time and the developers of the ASTM E 399 testing standard were thus led astray. Based on present knowledge, the K_{IC} standard could actually be called a non-measure of plane-strain fracture toughness.

ACKNOWLEDGEMENTS

This work is a part of the Structural Integrity Project (STIN), belonging to the Finnish Research Programme on Nuclear Power Plant Safety (FINNUS), performed at VTT Manufacturing Technology and financed by the Ministry of Trade and Industry in Finland, the Technical Research Centre of Finland (VTT) and the Radiation and Nuclear Safety Authority (STUK).

REFERENCES

1. Irwin, G.R. (1960). *J. Basic Engng ASME*. 82, 417.
2. Kaufman, J.G. (1977). *ASTM STP 632*. 3.
3. Wallin, K. (1999). *Int. J. of Materials and Product Technology*. 14, 342.
4. Marston, T.U. (ed.) (1978). *Flaw Evaluation Procedures - Background and Application of ASME Section XI Appendix A, EPRI NP-719-SR*. Electric Power Research Institute, Palo Alto, California.
5. Kussmaul, K. (1990). Presented at ASTM workshop on historical perspective on the ASTM E 399 K_{IC} standard.

ORAL REFERENCE: ICF101097OR

LENGTH SCALES FOR THE FRACTURE OF NANOSTRUCTURES

William W. Gerberich,[†] John Jungk[†] and Alex A. Volinsky[‡]

[†]Department of Chemical Engineering and Materials Science
University of Minnesota, Minneapolis, MN 55455
[‡]Motorola Corp., Mesa AZ 85202

ABSTRACT

Length scales are essential to the understanding of small volume deformation and fracture in emerging technologies. Recent analysis by two groups at the atomistic [1] and mesoscopic [2] levels have shown the importance of the volume to surface ratio to the indentation size effect (ISE) at small depths of penetration. We have interpreted this in terms of the plastic work under the contact and the surface work associated with the creation of new surface or the excess surface stress. Treating this as a modified Griffith criterion the case is made that this same length scale should apply to the delamination of thin films. By making this simple equivalency in length scales, an *R*-curve analysis for crack growth resistance, G_R, in thin film delamination emerges. This recovers the classic $\sigma_{ys}^2 h/E$ term as well as the fact that interfacial toughness should scale with the square root of incremental crack growth. Here σ_{ys} is yield strength, h is thickness and E is modulus of the film. As applied to thin Cu films bonded to silicon substrates with a thin innerlayer of Ti, the model is in good agreement.

KEY WORDS

Nanoscale lengths, thin films, delamination energy

INTRODUCTION

Current research into nanotechnology is increasingly aware of the limitations of small scales in micromachines, MEMS, microelectric interconnects and magnetic recording heads. One of these limitations is when device reliability is compromised by poor thin film adhesion. The last decade has seen a considerable effort at applying linear elastic fracture mechanics concepts toward film fracture problems [3–5]. To a lesser extent has there been progress in understanding the elastic-plastic thin-film delamination problem particularly on the experimental side of the ledger. This is partly because of a host of possible length scale variables that can be appropriately incorporated to fit any given set of data. The confusion comes in as to how to exactly measure an appropriate length scale and as to which one(s) should be included. To illustrate the problem, we enumerate in

Table 1 some of the possible length scales and evolutionary microstructural features of importance to small volume deformation and fracture. The first five parameters with asterisks are some of the possible fundamental length scales which should be considered in thin film deformation and fracture. We consider interplanar slip band spacing because of possible sub-cell structures which might evolve during a thermal-mechanical processing history. The remaining parameters can easily evolve during the deformation and fracture history, e.g. those associated with nanoindentation induced yield or fracture events.

TABLE 1
POSSIBLE LENGTH SCALES* AND EVOLUTIONARY MICROSTRUCTURAL FEATURES OF IMPORTANCE
IN THE DEFORMATION AND FRACTURE OF SMALL VOLUMES

*	ℓ_s	–	Length of dislocation pile-up
*	ℓ_d	–	Distance between sources (near an indenter or in the vicinity of a crack tip)
*	ℓ_p	–	Interplanar spacing for slip bands
*	d	–	Nanocrystalline grain size
*	h	–	Film thickness
	h_p	–	Pile-up around indentation
	c	–	Nearest approach of $\perp$ to a crack tip
	$N_\perp$	–	Total number of $\perp$'s
	N_s	–	Number of slip bands
	$\ell_\perp$	–	Spacing between $\perp$'s on a slip band
	n_s	–	Number of $\perp$'s on a given slip band

We believe we have fortuitously arrived at a single length scale parameter that controls both small volume deformation and fracture behavior of thin films.

This occurred because of two separate pathways we have been following, one dealing with the indentation size effect (ISE) in bulk crystals and one addressing delamination fracture resistance of thin films. While these seem quite disparate their commonality was that both phenomena were studied by nanoindentation. These included the ISE associated with an abrupt yield excursion in single crystals [2,6] and interfacial fracture resistance from indentation induced blister formation [7,8,16], both of which involved small volume deformation and fracture. For a number of years now we have been drawing a parallel between the point forces associated with a crack tip and an indenter tip [9] and the fact that the driving forces for the two might evolve similar localized dislocation arrangements. In that paper [9] we also noted that the pile-up height around an indentation behaves similarly, as a function of load, for both continuum and discretized models. This further suggested that contact mechanics might provide the connective link between mesoscopic and continuum models. However, it wasn't until we examined the same thin film system using these two approaches that we could convince ourselves that this is truly the case and that the connective link is the length scale that controls deformation and fracture of small volumes. What we have been able to show is that with no unknown constants or parameters, the deformation length scale directly determined from a series of nanoindentations into thin films leads to an *R*-curve analysis for the delamination fracture resistance of those same films. This is currently shown for two Cu films of 120 nm and 3.3 μm thickness bonded with Ti to silicon wafers.

THEORETICAL BACKGROUND

Here we consider in order some theoretical background for length scales as applied to the deformation of bulk material and the deformation and delamination of thin films, all at small scale. Specifically, we address the deformation and fracture response to nanoindentation at the nanometer scale.

Length Scale(s) for Bulk Deformation

Consider a conical tip with a 70 nm tip radius indenting into a surface producing concentric dislocation loops along glide cylinders. When an oxide breakthrough event occurs these travel back to the free surface resulting in pile-up as schematically shown in Figure 1. The sketched semicircle is the calculated "elastic-plastic" boundary from continuum theory. From experimental observations of dislocation rosette patterns, we know that dislocations extend well beyond the continuum estimate. For example, from AFM profiles, we know the rosette pattern extended well beyond the pile-up region observed at the surface, measured to be 500 nm and >3000 nm, respectively [10]. In addition, we now know that dislocations are emitted under the tip prior to the displacement excursion and that these are released commensurate with the yield excursion. Nevertheless, the continuum theory appears to capture the essence of the plastic pile-up process.

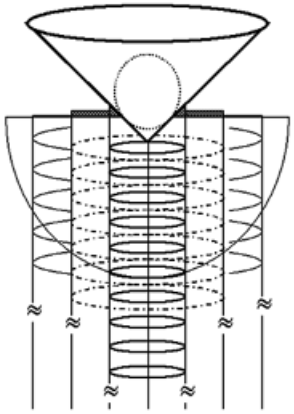

Figure 1: For the sample case of a 70 nm tip radius, the contact radius and plastic zone size are drawn to scale. The corresponding pile-up estimated from Eq. (1) would be 8.8 nm representing 35 dislocation loops.

An example of a yield excursion and the corresponding pile-ups in a <100>Ta single crystal is shown in Figure 2. In a recent paper [10], the continuum representation of pile-up [11] was found to give a good fit to plastic pile-up as determined by AFM measurement. For the contact radius, a being much smaller than the plastic zone size radius, c, plastic pile-up, h_p at the contact edge is given by

$$h_p(a) \cong (1-\nu)\frac{\sigma_{ys}}{E}\left(\frac{c^3}{a^2}\right)\frac{\pi}{2} \qquad (1)$$

as formulated from Johnson's cavity model of contact mechanics [12]. In principal, this maximum pile-up should relate to the release of dislocations forming pile-up, as is idealized in Figure 1. Given that pile-up should be some fraction of the dislocations formed during the yield excursion, δ_{exc}, and that these to first order are δ_{exc}/b dislocations, where b is the Burger's vector, we find

$$h(a) \cong \alpha' n_s b \quad ; \quad \alpha' < 1 \qquad (2)$$

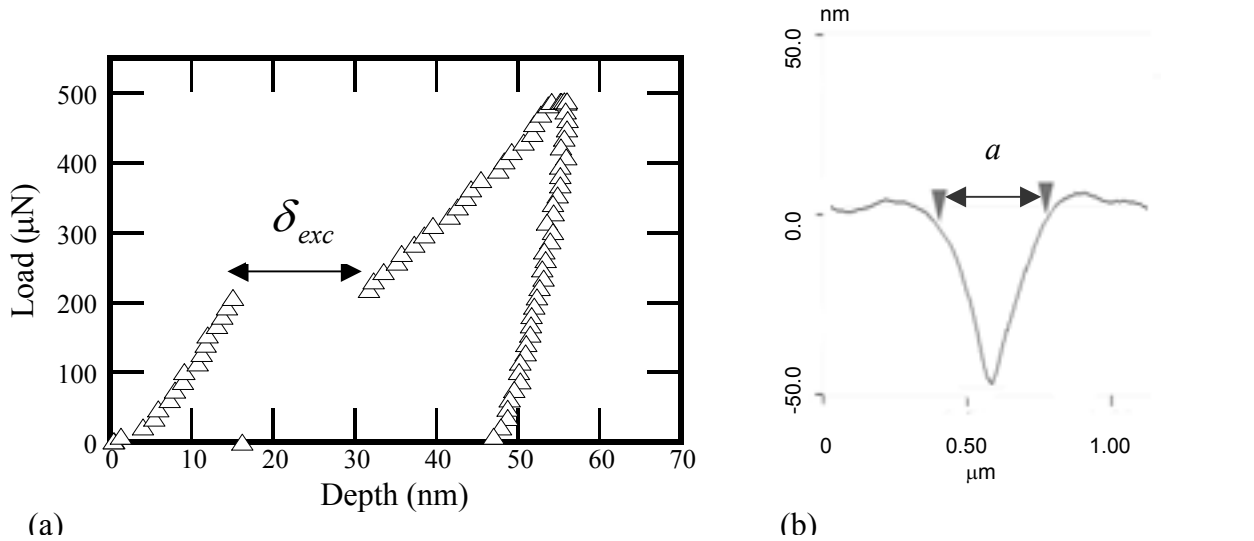

Figure 2: Yield excursion around a 1 μm radius diamond tip showing (a) displacement jump and (b) resulting pile-up measured by AFM.

From previous works [2] on the indentation size effect (ISE) we had shown that the volume to surface ratio could explain the increases in hardnesses observed at very small depths of penetration with $\delta \le 300\,\text{nm}$. The hypothesis was that the surface work was commensurate with the volume work and that this led to a constant volume (V) to surface ratio (S) ratio at small depths. We had previously described this plastic volume under the tip, $2\pi c^2/3$, and contact surface area, πa^2, as a length scale, ℓ_s, giving

$$\ell_s = \frac{V}{S} = \frac{2c^3}{3a^2} \tag{3}$$

in terms of the contact radius, a, and plastic zone radius, c. Furthermore, the volume work of plastic deformation $\tau_{ys} c^2 \delta/2$ and the surface work $\pi a^2 \gamma_s$ gave

$$\frac{W_V}{W_S} = \frac{\tau_{ys} \delta c^2}{\gamma_s \pi a^2} \quad . \tag{4}$$

Combining (3) and (4) gives this work ratio in terms of the length scale to be

$$\frac{W_V}{W_S} = \frac{3\tau_{ys} \delta \ell_s}{4\pi \gamma_s c} \quad . \tag{5}$$

From the data presented elsewhere [6] this ratio is shown for two sets of <100> single crystal data of Al and W where three different tip radii were utilized in each case. A fourth sharpest tip for each was not considered to avoid complications of nonspherical contact. These data in Figure 3 strongly suggest that the surface work is an appreciable portion of the total work for the first several hundred nanometers of penetration. The separation of the data within each material is clearly due to the δ/c ratio with sharper tips producing a greater plastic penetration for the same plastic zone size producing a greater portion of volume work. The separation of the data between the two materials is mostly due to the yield stress to surface energy ratio with the dimensionless parameter $\tau_{ys} \ell_s / \gamma_s$ being 670 for <100> W and 240 for <100> Al. This further suggests that for

small length scales the surface work could become extremely important as this dimensionless parameter drops below 100.

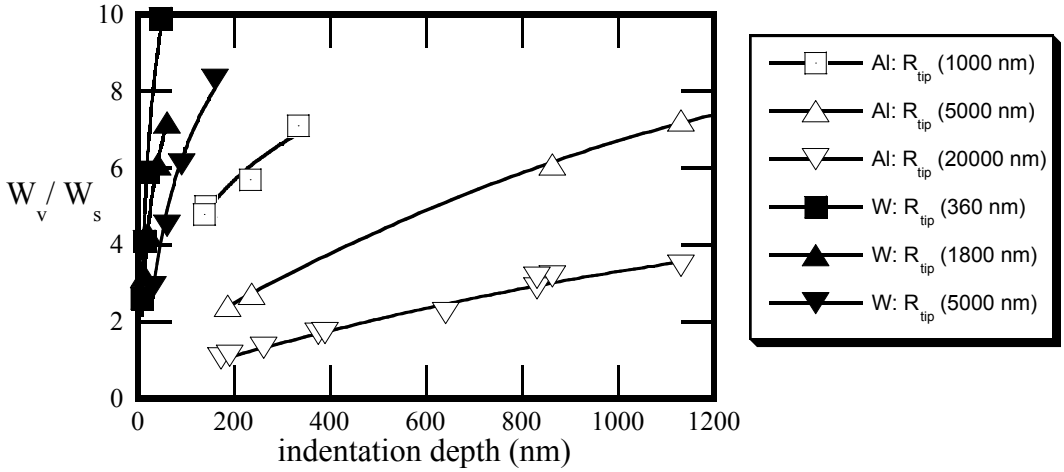

Figure 3: Volume to surface work ratio as a function of depth for a tungsten single crystal with $\ell_s \cong 4700$ nm, τ_{ys} = 400 MPa and γ_s = 2.8 J/m^2 and for an aluminum single crystal with $\ell_s \cong 7900$ nm, τ_{ys} = 30 MPa and γ_s = 1.0 J/m^2. Plastic zone sizes are those reported elsewhere [6].

This prompted us to examine Eqs. (1) and (2) more closely since the plastic pile-up of Eq. (1) is directly related to this length scale as it contains c^3/a^2. As we have recently discussed [10], the number of dislocations emitted, which then form a piled-up slip band, is obtained from Eqs. (1) and (2) eliminating *h(a)* to give

$$n_s = \frac{\pi(1-\nu)\sigma_{ys}c^3}{2\alpha' bEa^2} \quad . \tag{6}$$

Elimination of c^3/a^2 through Eq. (3) and substituting τ_{ys}/μ for σ_{ys}/E gives

$$n_s = \frac{\pi\ell_s(1-\nu)}{2b\alpha}\frac{\tau_{ys}}{\mu} \tag{7}$$

with $\alpha = \alpha' \cdot (3/2)$. Since $\alpha' < 1$, it is tempting to take $\alpha \sim 1$ which then makes Eq. (7) identical to the simple pile-up theory of Eshelby *et al.* [13]. The simplified picture of Figure 1 is that an inverse pile-up forms and at the yield excursion these release into the free surface causing topographical pile-up around the indenter tip. It is significant that Eq. (1) is from continuum theory appropriate to the macroscale while Eq. (7) is from dislocation theory appropriate to the mesoscale.

Because this appeared to work so well for small volume penetration into bulk single crystals, it was decided to apply this to the deformation of thin metal films bonded to and constrained by relatively rigid elastic substrates. Herein then lies the key. When we drastically change the size scale of the component as in thin films, how does this change the length scale(s) appropriate to deformation and fracture. As discussed above, in Table 1 we enumerated the possible length scales and a few of the evolving structural parameters that might be involved in deformation and fracture of thin films. The length scale for a thin film, clearly smaller than that for a corresponding

single crystal, could be a dislocation pile-up length, a nanocrystalline grain size, d, which scales with thickness but not necessarily linearly, or film thickness, h, itself. The other parameters in Table 1 tend to be evolutionary during a point contact process and can eventually lead to friction changes, wear, film fracture or film delamination. Let us first consider definition of the V/S value for thin films as may be important to any of these deformation and fracture processes. This is then followed by application to a film delamination process.

Length Scale for Thin Film Deformation

An in-depth series of tests [14] for four different aluminum films of 0.34, 0.5, 1 and 2 μm thickness gave the relationship between the plastic zone size to indenter contact radius, c/a, and the normalized film thickness to be

$$\left(\frac{c}{a}\right)^2 = \frac{\alpha h}{a} \tag{8}$$

with $\alpha = 5.3$. The extent of plasticity depends on the degree of constraint and the yield stress. For smaller thicknesses, h, the substrate more easily constrains plastic flow coupling with an elevated yield stress to reduce c/a. For greater penetration and hence greater contact radii, a, the constraint factor reduces c/a. For a thin film, it is simple to translate this into a volume to surface ratio for indenters of rotational symmetry, cylinders, spheres or cones. A contact radius, a, giving a surface area of πa^2 and a constrained plastic zone, c, of $\pi c^2 h$ gives

$$\ell_s = \left.\frac{V}{S}\right|_{constrained} = \frac{\pi c^2 h}{\pi a^2} \,. \tag{9}$$

See the schematic of Figure 4(a).

Elimination of c through (8) and (9) gives

$$\ell_s = \frac{\alpha h^2}{a} \quad . \tag{10}$$

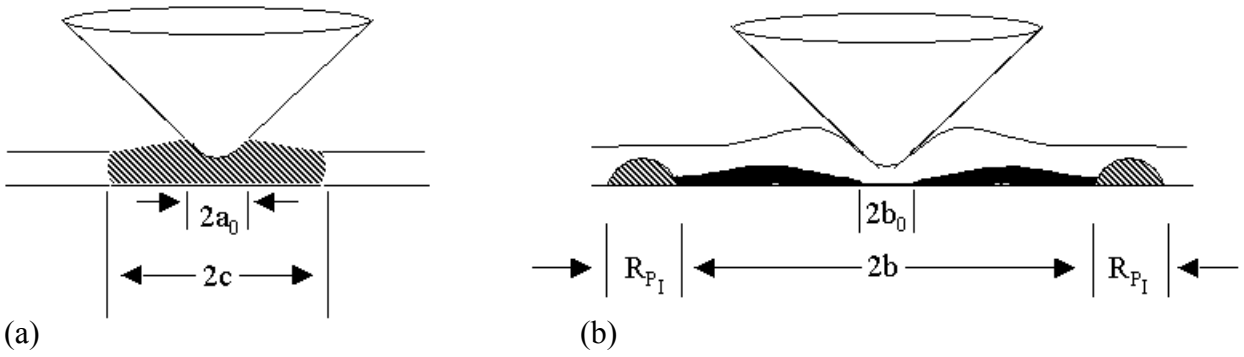

Figure 4: Plastic volumes associated with V/S for (a) a conical indenter into a constrained thin film producing a plastic zone radius of c; (b) a conical indenter producing a contact diameter of $2a_0$ producing an initial crack of ~ $2b_0$ which grows to $2b$ under increasing load forming a plastic zone of R_{P_I}.

In reality this appears to be a mixed length scale since it depends both on the film thickness and the sharpness of the indenter which controls the contact radius for a given penetration depth. One notes that this length scale can be quite small for film thicknesses on the order of 300 nm. Since a 1 μm radius indenter penetrating to the film/substrate interface would give a contact radius of 720 nm, $\ell_s \cong 670\,\text{nm}$ from Eq. (10), about an order of magnitude smaller than the size scale for the corresponding single crystals reported elsewhere [2].

Length Scale Application to Thin Film Delamination

If the volume to surface ratio concept is controlled by the balance of surface work and plastic energy dissipation, clearly it is applicable to thin film delamination which can follow the modified Griffith criterion. This is schematically shown in Figures 4(a) and (b) for indentation and film delamination. With initial indentation only plastic deformation in a zone of length 2*c* forms as addressed above. This defines $\ell_s = V/S$. With the slightest increase of load this could trigger interface cracking at $2b_0$ which then propagates and arrests at 2*b*. Now the plastic energy dissipation of importance to arrest is the deformation in the plane strain plastic zone at the advance of the crack front. We use the plane strain zone for two reasons here. First, we will apply this to films on rigid substrates where the plasticity is constrained. Second, a further constraint is provided by a superlayer of a high modulus material such as tungsten or tantalum nitride which has been applied on top of the ductile film to store elastic energy for the crack propagation process. This superlayer technique has been the subject of a number of recent investigations [15,16]. This constrained plane strain plastic zone size is given by

$$R_{P_I} = \frac{K_I^2}{3\pi\sigma_{ys}^2} \tag{11}$$

where K_I is the applied stress intensity factor. At this point the plastic volume for arrest can be assessed considering a plastic annulus of outer diameter $b + R_{P_I}$, inner diameter *b* and height R_{P_I}, giving

$$V = R_{P_I}\left[\pi[b + R_{P_I}]^2 - \pi b^2 R_{P_I}\right] = 2\pi\left(bR_{P_I}^2 + R_{P_I}^3/2\right). \tag{12}$$

The corresponding surface area created by this event is the film delamination given by

$$S = \pi(b^2 - b_0^2) = \pi\left[(b_0 + \Delta b)^2 - b_0^2\right] \cong 2\pi\Delta b\left(b_0 + \frac{\Delta b}{2}\right) . \tag{13}$$

From (12) and (13) we see that the ratio is

$$\frac{V}{S} = \frac{2R_{P_I}^2 b + R_{P_I}^3}{2\Delta b b_0 + \Delta b^2} \quad . \tag{14}$$

For a number of trials using a sensible range for the incremental crack growth (blister size) and the plastic zone size we calculated *V*/*S* from Eq. (14) to be

$$\frac{25R_{P_I}^2}{16\Delta b} < \ell_s < \frac{10}{3}\frac{R_{P_I}^2}{\Delta b} \quad ; \quad 2b_0 < \left(\Delta b_0, R_{P_I}\right) < 8b_0 \tag{15}$$

which varies by about a factor of two. We're inclined toward the upper limit which represents crack-tip plastic zones smaller than the contact plastic zone. At this point we make two simplifying assumptions, one tenuous and one supported by observation. The first is that the length scale associated with plastic deformation during thin-film indentation is the same as that associated with producing crack-tip plasticity in thin films. Consider a typical thin film delamination fracture with $K_{Ic} \cong 1\,\text{MPa}\cdot\text{m}^{1/2}$ for a 300 nm thick film having a yield strength of 500 MPa. This gives a plane strain plastic zone at the crack tip to be 420 nm from Eq. (11) and compares to the 1000 nm indentation plastic zone calculated from Eq. (8). Since the volume scale of these two zones is similar, we propose that the same length scale should apply. The second assumption, as supported by observations using focused ion-beam machining (FIB) is that the contact radius just prior to delamination, a_0, is the same as the initiation defect size, b_0.

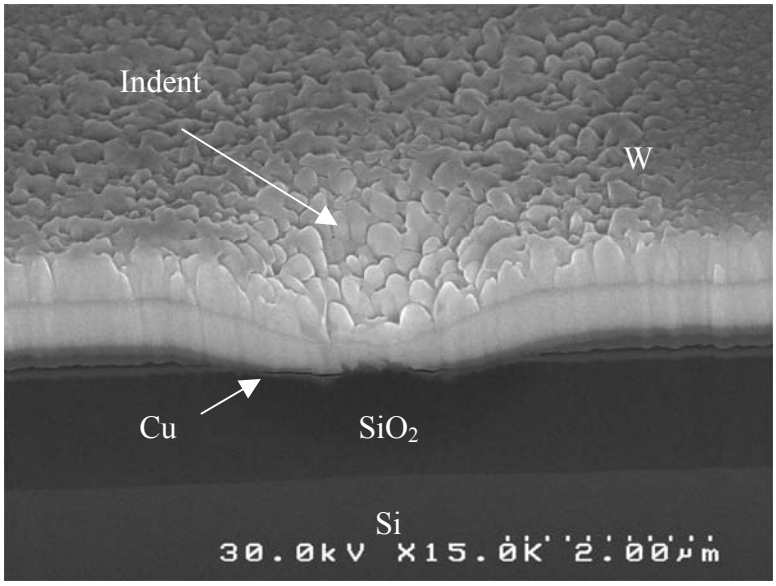

Figure 5: SEM image of the Focused Ion Beam cross-section of a delamination in Cu film.

As seen in Figure 5, a FIB cross-section of a copper film delaminated from a silicon wafer shows this to be reasonable. With $\ell_s^I \sim \ell_s^c$ being the same size scale for indentation (I) and cracking (c) of these films and $a \sim b_0$ one finds from (10), (11) and the approximate upper limit of (15) that

$$\ell_s = \frac{\alpha h^2}{b_0} \cong \frac{3R_{P_I}^2}{\Delta b} \cong \frac{K_I^4}{3\pi^2 \sigma_{ys}^4 \Delta b} \quad . \tag{16a}$$

From the first and fourth equalities this gives

$$K_I = \left(\pi\sqrt{3}\right)^{1/2} \sigma_{ys} \ell_s^{1/4} \Delta b^{1/4} \quad . \tag{16b}$$

From the second and fourth equalities, this reduces to

$$K_I \cong \sigma_{ys} (\pi h)^{1/2} \left(\frac{3\alpha\Delta b}{b_0}\right)^{1/4} \quad . \tag{16c}$$

Given that the strain energy release rate is K_I^2/E, we see that this represents a resistance curve of

$$G_R = \frac{\pi\sigma_{ys}^2 h}{E}\left(\frac{3\alpha\Delta b}{b_0}\right)^{1/2} \tag{17a}$$

where $\Delta b/b_0$ is the ratio of incremental crack extension to the initial defect size and $\sigma_{ys}^2 h/E$ is essentially the leading term in nearly all thin film resistance models involving plasticity. This proposed *R*-curve behavior for forced thin film crack extension is seen to evolve directly from a simple volume to surface length scale. To recapitulate, we propose that both indentation and fracture occurring from small volume deformation are controlled by the same length scale and that this leads to a delamination resistance criteria. Some verification of this proposed model based on existing thin film Cu data follows.

EXPERIMENTAL

A considerable amount of thin-film Cu delamination data exists as derived from superlayer indentation [15,16]. A schematic of this test is shown in Figure 6. This has shown that the thin film fracture energy increases with film thickness, a result consistent with 4-pt. bend data independently determined by Lane and Dauskardt [17]. An example of the blister formed by indenting a 1μm film of W bonded to a Cu film with a Ti underlayer between the Cu and the silicon substrate is shown in Figure 7.

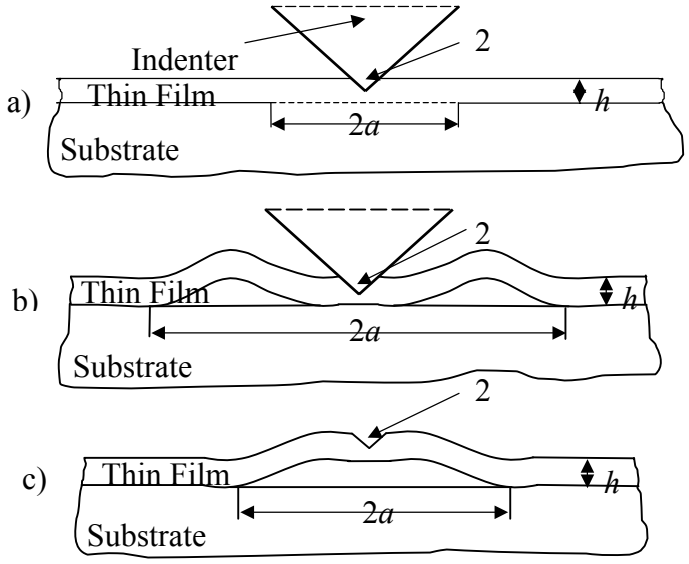

Figure 6: a) No buckling during indentation; b) double-buckling during indentation; c) single-buckling after the indenter tip removal.

At the time we noted a typical factor of three scatter in adhesion energy which we originally attributed to a b/b_0 effect different that that represented by Eq. (17a). Consider then the case for the same film loaded repeatedly to ever increasing loads at different indentation locations as was accomplished here. Assume the crack starts in each case when the penetration reaches a critical

contact radius, say b_0 ~ h, since then the spherical indentation nearly reaches the interface. It is easy to see that if the penetration continues that $\Delta b/b_0$ increases and the resistance must correspondingly increase to support larger stored elastic energy release rates at higher applied loads. This is different from a purely brittle interface where a crack, once triggered, will grow and then arrest with the larger the b/b_0 the lower the fracture resistance. This latter result is obtained from the driving force side of the equation as has been derived by Marshall and Evans [18] and Rosenfeld *et al*. [19]. The analysis associated with Eq. (17a) concerns itself with the resistance side of the equation and what happens if further crack extension along an elastic-plastic interface beyond the initial arrest is driven by ever increasing loads. Equation (17a) is consistent with the slow crack growth observations of Au/Al_2O_3 interfaces [20] and remarkably similar to schematics

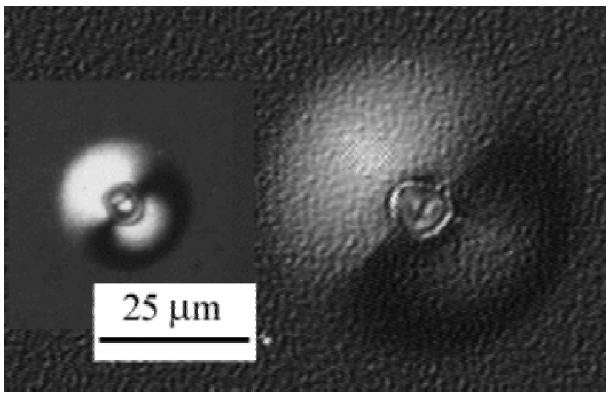

showing resistance curves (Γ_R vs. Δa) for models based upon the embedded process zone [21].

Figure 7: Optical micrographs of indentation iduced blisters with (right) and without (left) a W superlayer.

To ascertain if such a simple length scale model can predict crack growth resistance we reexamined some Cu thin film data based on the superlayer indentation technique. For 120 nm and 3.3 μm thick Cu, data are shown in Table 2. Referring to the schematic of Figure 4, we show the corresponding values of b/b_0, penetration depth, δ, incremental crack extension, Δb, and the measured strain energy release rate from laminate composite analysis [7]. The latter is an extension of the Marshall and Evans analysis [18]. In the tabulation for both thicknesses, it is seen that as $\Delta b/b_0$ increases, G_I generally increases. For a more quantitative comparison, it was necessary to obtain the length scale relationship as had been accomplished for aluminum films and described at Eq. (10). For Cu thicknesses of 200 nm to 2000 nm thick deposited on Si substrates with a TiW innerlayer, we have preliminary results. For these two thicknesses, we find that the form of Eq. (10) is similar with the only difference being the constant α ~ 4.8. This is shown for one thickness in Figure 8. This gives

$$G_R = \frac{12\sigma_{ys}^2 h}{E}\left(\frac{\Delta b}{b_0}\right)^{1/2} \tag{17b}$$

and is seen to correspond well to the data of Table 2 reproduced in Figure 9. Here, we have used σ_{ys} = 600 MPa for the 120 nm film and σ_{ys} = 460 MPa for the 3300 nm film. Equation (17b) slightly underpredicts the thicker films and overpredicts the thinner ones in Figure 9 implying that the factor of 16 difference in toughness predicted is too small. On the other hand, using a 4-pt. bend technique, Lane and Dauskardt observed only a factor of four increase in toughness for the same increase in thickness. Note that this difference in the experimental values could be real due

to differences in bond strengths giving differences in $\Delta b/b_0$ for the same film. In these two sets of data, Volinsky, *et al*. [15,16] used a Ti bond layer while Lane and Dauskardt [17] used a Ta/TaN

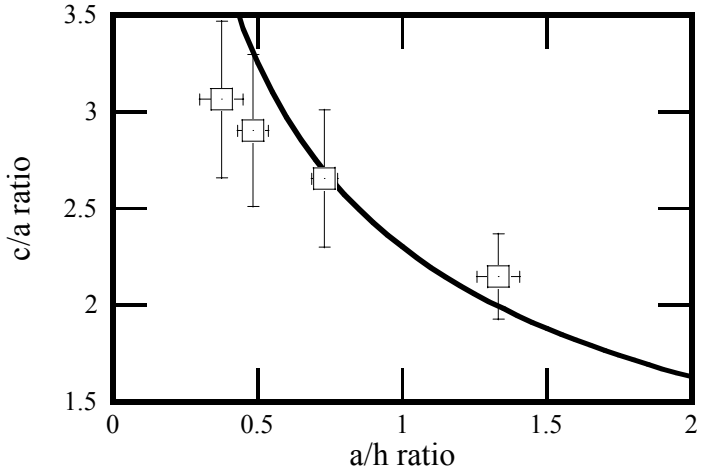

Figure 8: Fit of Eq. (8) to nanoindentation produced plastic zone radii, c, normalized on contact radii, a, as a function of a/h with h being film thickness. For these Cu films, $\alpha \cong 4.8$.

bond layer between the Cu and the substrate. Furthermore, there is a degree of uncertainty about $a_0 \sim b_0$ which could easily account for any difference between prediction and observation. For these reasons we propose that this type of volume/surface approach be a serious candidate for the length scale controlling deformation and fraction of small volumes.

TABLE 2

Cu Thickness, nm	Depth, δ, nm	Delamination Radius, b, nm	$(\Delta b/b_0)^{1/2}$	G_I, obs.
120	546	6800	1.67	2.2
	555	6800	1.67	2.3
	805	8400	1.91	4.5
	819	9000	2.00	3.7
	830	8300	1.90	5.6
	941	10,900	2.25	3.2
	952	11,200	2.29	2.9
	1067	11,900	2.37	3.9
	1083	12,100	2.39	3.9
	1116	11,700	2.35	5.0
	1549	22,300	2.42	9.1
	1869	21,200	3.28	11.9
	1892	31,900	4.09	8.4
	1910	22,300	3.37	9.0
	1915	21.900	3.34	8.95
3300	1767	6500	0.95	59.9
	1783	6700	0.985	57.3
	1811	6700	0.985	60.6
	2344	7700	1.12	131.1
	2351	8200	1.19	101.3
	2412	8200	1.19	115.6
	2818	9900	1.38	123.7
	2853	9600	1.35	146.5
	3091	10,100	1.40	182

SUMMARY

We have first shown a connectivity between mesoscopic and macroscopic deformation theories through plastic pile-up around a nanoindenter. This recovers the classic dislocation pile-up model of Eshelby [13]. To achieve this, a volume (V) to surface (S) ratio model has been invoked, previously shown [2,6] to predict the indentation size effect (ISE) at small penetration depths. The length scale, $\ell_s = V/S$, has then been shown to apply to both small volume deformation and fracture through nanoindentation studies of thin film copper bonded to silicon substrates. This produces a fracture toughness which is proportional to the fourth root of the length scale or, alternatively, a resistance curve with the resistance proportional to the square root of the incremental crack growth. With increasing crack growth it is shown that Cu bonded to silicon substrates with a thin Ti layer increases its fracture resistance by a factor of three.

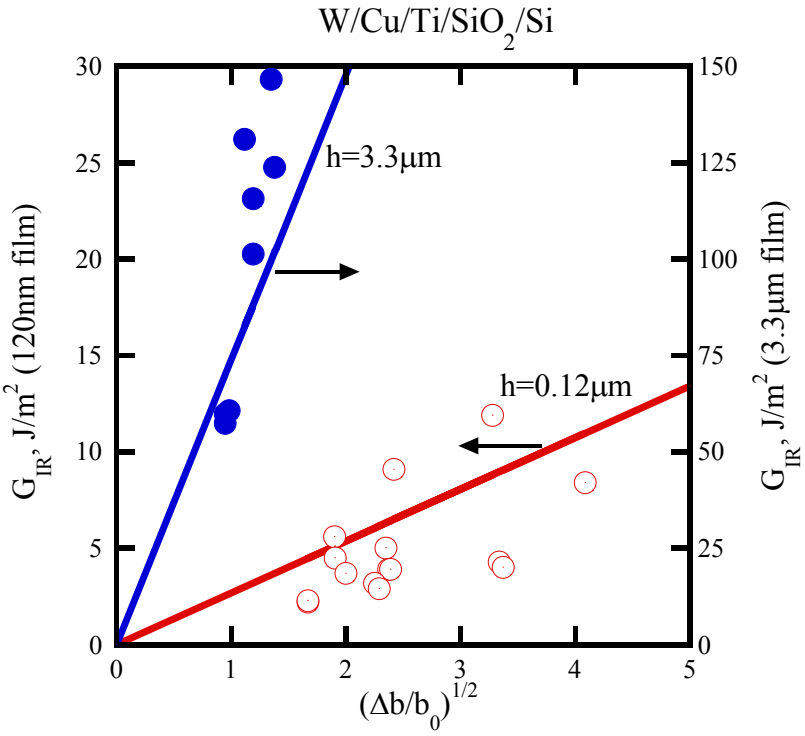

Figure 9: Crack growth resistance of Cu films as a function of incremental crack extension compared to Eq. (17b).

ACKNOWLEDGMENTS

The authors would like to acknowledge support through MINT (The Center for Micromagnetics and Information Technology) via Seagate Technology, Motorola, Inc., and the Department of Energy under DOE contract DE-FG02/96ER45574. We would also like to thank Indira S. Adhihetty, Joseph B. Vella, Robert H. Caprenter and Lester Casoose Jr. of Motorola, Inc. for help with the FIB analysis.

REFERENCES

1. Horstemeyer, M.E. and Baskes, M.I. (1999) *J. Engng. Mater. Tech., Trans. ASME* 121, 114.
2. Gerberich, W.W., Tymiak, N.I., Grunlan, J.C., Horstemeyer, M.F. and Baskes, M.I. (2001) "Interpretations of Indentation Size Effects" *J. Appl. Mech.* submitted.
3. Bagchi, A., Lucas, G., Suo, Z. and Evans, A. (1994) *J. Mater. Res.* 9(7), 1734.
4. Vlassak, J.J., Drory, M.D. and Nix, W.D. (1997) *J. Mater. Res*. 12, 1900.
5. Begley, M.R., Mumm, D.R., Evans, A.G. and Hutchinson, J.W. (2000) *Acta Mater.* 48, 3211.
6. Tymiak, N.I., Kramer, D.E., Bahr, D.F., Wyrobek, T.J. and Gerberich, W.W. (2001) *Acta Mater.* 49, 1021.
7. Kriese, M.D., Moody, N.R. and Gerberich, W.W. (1999) *J. Mater. Res.* 14(7), 3007 (Part I); 3019 (Part II).
8. Volinksy, A.A., Tymiak, N.I., Kriese, M.D., Gerberich, W.W. and Hutchinson, J.W. (1999) *Mater. Res. Soc. Proc.* 539, 277.
9. Gerberich, W.W., Lilleodden, E.T., Foecke, T.J. and Wyrobek, T.J. (1995). In *Micromechanics of Advanced Materials*, pp. 29-35, J.C.M. Li Symposium, TMS, Warrendale, PA.
10. Gerberich, W.W., Tymiak, N.I., Kramer, D.E., Daugela, A., Jungk, J. and Li, M. (2001) "An Approach to Dry Friction and Wear for Small Volumes" *Philos. Mag. A*, submitted.
11. Harvey, S., Huang, H., Venkataraman, S. and Gerberich, W.W., (1993) *J. Mater. Res.* 8(6), 1291.
12. Johnson, K.L. (1970) *J. Mech. Phys. Solids* 18, 115.
13. Eshelby, J.D., Frank, F.C. and Nabarro, F.R.N. (1951) *Philos. Mag.* 42, 351.
14. Kramer, D.E., Volinsky, A.A., Moody, N.R. and Gerberich, W.W. (2000) "Substrate Effects on Indentation Plastic Zone Development in Thin Soft Films," *J. Mater. Res.*, accepted.
15. Tymiak, N.I., Volinksy, A.A., Kriese, M.D., Downs, S.A. and Gerberich, W.W. (1999) *Metall. Mater. Trans.* 31A, 863.
16. Volinksy, A.A., Moody, N.R. and Gerberich, W.W. (2001) "Interfacial Toughness Measurements of Thin Metal Films," *Acta Mater.*, submitted.
17. Lane, M. and Dauskardt, R.H. (2000) *J. Mater. Res.* 15(1), 203.
18. Marshall, D.B. and Evans, A.G. (1984) *J. Appl. Phys.* 56, 2632.
19. Rosenfeld, L.G., Ritter, J.E., Lardner, T.J. and Lin, M.R. (1990) *J. Appl. Phys.* 67(7), 3291.
20. Lipkin, D.M., Clarke, D.R. and Evans, A.G. (1998) *Acta Mater.*47(13), 4835.
21. Evans, A.G., Hutchinson, J.W. and Wei, Y. (1999) *Acta Mater.* 47(15), 4093.

LOADING-RATE DEPENDENCE OF MODE I FRACTURE BEHAVIOR OF RUBBER-TOUGHENED PMMA

M. Todo and K. Takahashi

Research Institute for Applied Mechanics, Kyushu University, Kasuga, Fukuoka 816-8580, Japan

ABSTRACT

Mode I fracture tests of three kinds of rubber-toughened PMMA (RT-PMMA) and a neat PMMA were performed at different loading rates using three testing systems, namely, a servohydraulic testing machine, an instrumented drop weight impact tester and a modified SHPB impact test system. The critical mode I energy release rates, G_{Ic}, were evaluated at the different loading rates and the loading-rate dependences of the G_{Ic} values were examined. Two of the RT-PMMA's exhibited that their G_{Ic} values increased with increase of loading-rate; on the other hand, the G_{Ic} of the other RT-PMMA tended to decrease at the loading-rates higher than 1 m/s. Effects of loading-rate on the damage zones generated in the vicinity of crack-tips were also investigated by optical microscopy. The rate dependence of the G_{Ic} values was then correlated with that of the damage zone formation in terms of energy dissipation process.

KEYWORDS

Rubber toughening, Mode I crack propagation, Toughening mechanisms, Impact testing, Craze formation

INTRODUCTION

To increase the impact resistance of a transparent thermoplastic PMMA, different types of rubber-toughened PMMA (RT-PMMA) have been developed by blending rubbery phases with PMMA matrices, and attempts made to characterize their mechanical properties. The effects of loading-rate on the fracture behavior of RT-PMMA and neat PMMA have been investigated [1-3]. Todo et al. [3] performed mode I fracture tests of two types of RT-PMMA at loading rates from 10^{-4} to 13m/s using a modified servohydraulic testing machine. They found that the maximum mode I stress intensity factor, K_{Imax}, and the maximum mode I energy release rate, G_{Imax}, of one of the RT-PMMA's containing 20wt% rubber particles suddenly decreased at the rates higher than 1 m/s, while the other containing 40wt% rubber particles didn't exhibit such rate dependence. Some attempts have also been made to characterize the deformation and fracture behavior of RT-PMMA from microscopic points of view [4-7]. Todo et al. [7], for example, showed that the toughening mechanism of RT-PMMA is closely related to the microdamage formations such as microcrazing and matrix shear deformation generated in the vicinity of crack-tip.

The aim of the present study is to characterize the effects of loading-rate on the mode I fracture behavior of three types of RT-PMMA by correlating two different aspects, that is, macroscopic fracture property such as the critical mode I energy release rate, G_{Ic}, and microscopic damage formation in the vicinity of crack-tip. To evaluate their G_{Ic} values, mode I fracture tests were performed at different loading-rates from 10^{-5} to 9m/s

using three kinds of testing system. Damage zones developed during crack propagation were also observed using an optical microscope to examine the rate effects on the damage zone formation. A simple model to explain one of the rate dependences observed was then proposed on the basis of the energy dissipation mechanism during crack propagation.

EXPERIMENTAL

Material and Specimen

Three kinds of RT-PMMA were studied: press formed containing 8 wt% butadiene rubber (PM8), extruded containing 20wt% butyl acrylate-co-styrene rubber (EM20) and press formed containing 40wt% butyl acrylate-co-styrene rubber (PM40). A neat PMMA made by cast (CU) was also examined for comparison.

Single edge notch bending (SENB) specimens were prepared for mode I fracture testing. The length L, width W, thickness B and the initial notch length a were 80-90mm, 15mm, 5mm and 7.5mm, respectively. For each specimen, a pre-crack was carefully introduced by drawing a new razor blade along the tip of the machined notch.

Mode I Fracture Testing

Three-point bending fracture tests at low displacement rates from 10^{-5} to 10^{-2}m/s were conducted using a servohydraulic testing machine. The span length was 40mm. Load-time and displacement-time relations were recorded on a digital recorder. The critical mode I energy release rate, G_{Ic}, can be evaluated using the following formula [8]:

$$G_{Ic} = \frac{U}{BWf} \tag{1}$$

where f is the energy calibration factor given as a function of a/W. For each specimen, the critical strain energy U was calculated by integrating the area under its load-displacement curve up to a critical point defined as the point at which the stiffness of the specimen suddenly decreased as a result of the initiation of crack propagation. An example of the SENB test data is shown in Figure 1. It is noted that for the neat PMMA, the critical load was found to be equivalent to the maximum load.

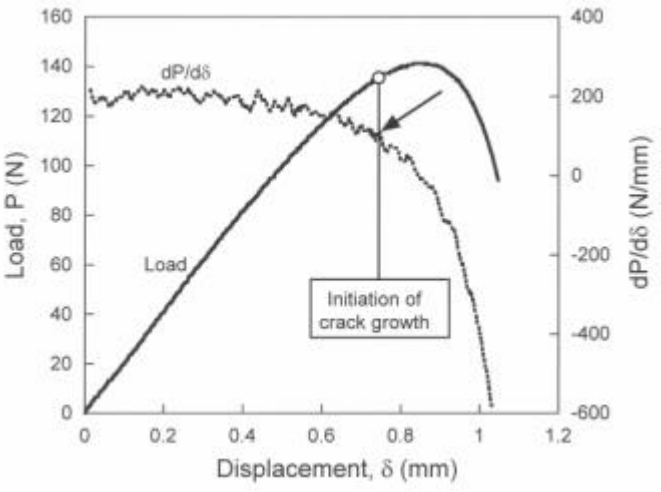

Figure 1: An example of SENB test results. The arrow indicates the initiation of crack growth.

An instrumented drop weight impact test system was used for the fracture tests at the loading rates from 0.5 to 1.6m/s. Displacements at the loading points were measured using an optical displacement measuring device [9]. An example of the test data is shown in Figure 2(a). It is seen that the peaks of the crack-tip strain and the load took place at the same time. It is therefore presumed that the maximum loads were equivalent to the critical loads in this series of impact test. The G_{Ic} values were then evaluated using the same procedure

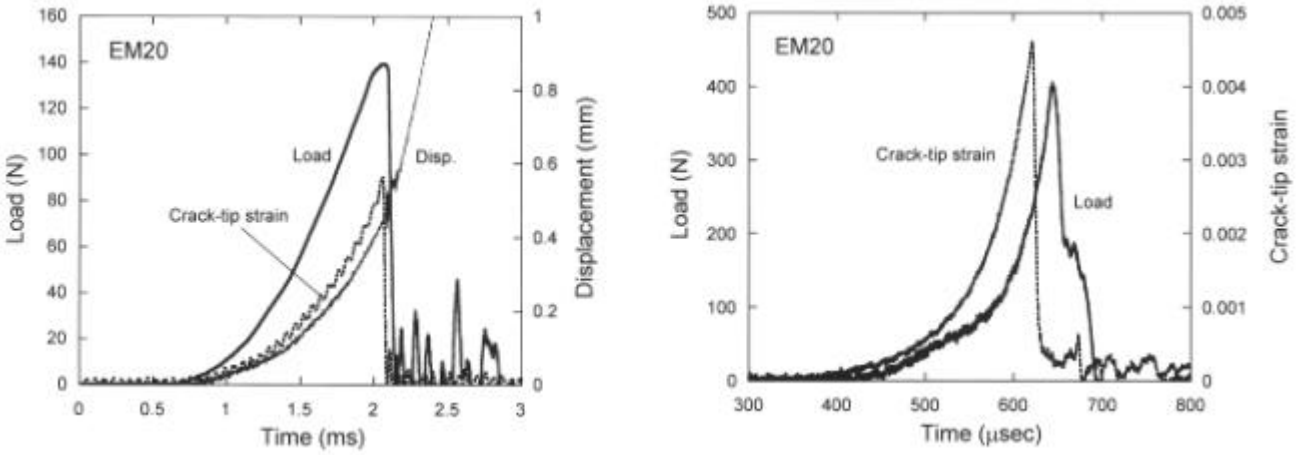

(a) Drop weight impact test (b) SHPB impact test

Figure 2: Examples of impact fracture test data.

as used for the low-rate testing.

Impact fracture tests at the loading rates from 5 to 9m/s were carried out using a SHPB impact bending test system[10]. The SHPB system is shown in Figure 3. For each specimen, strain in the vicinity of the crack-tip was measured to determine the initiation of crack growth. In the present study, to reduce dynamic effects, silicon rubber sheet 1.5mm thick was placed between the striker and the input bar as shown in Figure 3. An example of the test data is shown in Figure 2(b). The load is the sum of the bads measured from the output bars. It appears that dynamic bending effects were dramatically reduced since the initiation of the load was almost identical with that of the crack-tip strain, suggesting the contact between the specimen and the output bars in the initial stage of the loading. It was therefore presumed that the static procedure of G_{Ic} evaluation described above was applicable to the present SHPB test results.

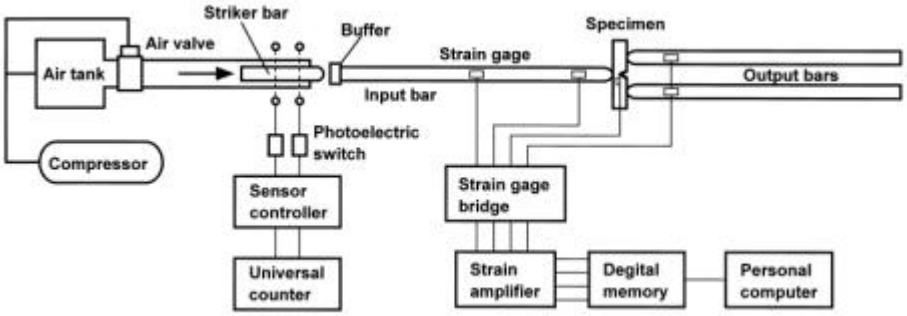

Figure 3: SHPB impact bending test system.

Damage zones generated in the vicinity of crack-tips during crack propagation were observed using an optical microscope. Rectangular sections containing propagating cracks were prepared from the tested specimens at different loading rates. Their surfaces were polished and then observed using the microscope.

RESULTS AND DISCUSSION

Rate Dependence of Critical Mode I Energy Release Rate

The G_{Ic} values obtained are shown as functions of loading rate in Figure 4. The G_{Ic} of CU increased with increase of loading rate up to 10^{-2}m/s and became constant up to 1m/s and then slightly decreased at the higher rates. The G_{Ic} of EM20 was almost independent of loading rate up to 1m/s and then decreased at the higher rates. On the other hand, PM8 and PM40 exhibited similar rate dependences. Their G_{Ic} values were almost independent of loading rate up to 10^{-1}m/s and then increased with increase of loading rate. It is noted that the G_{Ic} of PM8 was the highest of all the materials at every loading rates although PM8 only contains

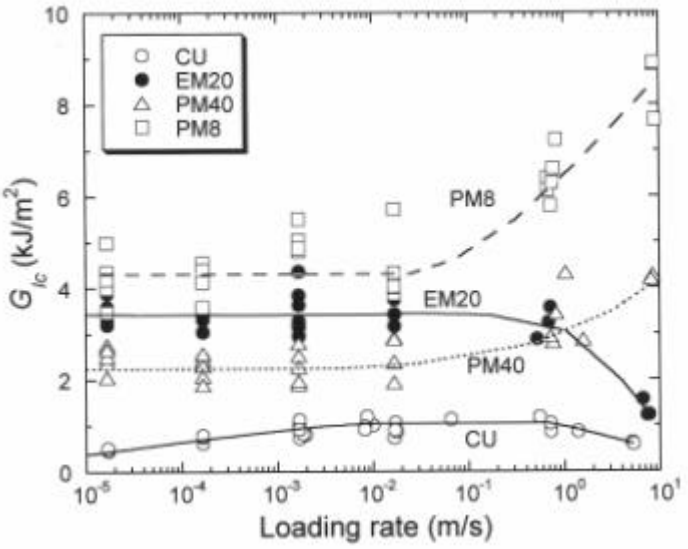

Figure 4: Dependence of loading rate on G_{Ic}.

8wt% rubber particles. It is thus understood that higher toughness can be achieved by blending butadiene rubber even in a relatively low rubber content.

Damage Zone Observation

A propagating crack in CU at a low loading rate and the damage zones developed in PM8 and EM20 at a low and an impact rate are shown in Figure 5 and Figure 6, respectively. It is observed from Figure 5 that there was no damage zone formed in CU. On the other hand, cloud-like damage zones were developed during crack propagation in the RT-PMMA's. It has been known that a collection of microcrazes generated in the surroundings of rubber particles forms a damage zone in the vicinity of a crack-tip [7]. It is noted that PM8 possessing the highest G_{Ic} showed the largest damage zone among the three RT-PMMA's. It has been recognized that the additional energy dissipation due to damage zone formation results in the toughening of RT-PMMA [7]. Thus, larger damage zone corresponds to higher G_{Ic} value. At the high rate, the damage zones of EM20 became very thin, while PM8 still exhibited an extensive damage zone even at the high rate. It is understood that for all the RT-PMMA's, the size of damage zone decreased with increase of loading rate.

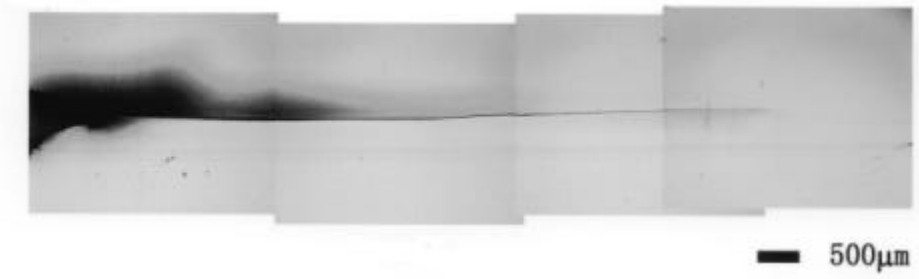

Figure 5: Propagating crack in CU at a low rate.

Mechanism of Rate Dependence of EM20

A crack growth behavior in a RT-PMMA under a steady-state condition is considered to understand the peculiar rate effect observed for EM20. It is assumed that the G_{Ic} of the RT-PMMA can be expressed as [11]:

$$G_{Ic} = G_{Damage} + G_{Surface} \tag{2}$$

where G_{Damage} and $G_{Surface}$ are the contributions of damage zone formation and surface energy to G_{Ic}. It is also assumed that G_{Damage} can be simply approximated by

$$G_{Damage} = w\ddot{O} \tag{3}$$

where w is the energy required to create a unit amount of microcraze and $\boldsymbol{F}$ is the total amount of microcrazes generated in a damage zone during the crack growth. If $G_{Surface}$ is negligibly small compared to G_{Damage}, then Eqns 2 and 3 give

$$G_{Ic} = G_{Damage} = w\ddot{O} \tag{4}$$

The results shown in Figure 6 suggest that $\boldsymbol{F}$ can be expressed as a function of loading rate such that $\boldsymbol{F}$ decreases as loading rate increases as shown in Figure 7. If w is assumed to be expressed as a function of loading rate such that w increases as loading rate increases as shown in Figure 7, then G_{Damage} exhibits a loading rate dependence shown in Figure 7 that is similar to the rate dependence of the G_{Ic} of EM20 shown in Figure 4. Thus, the rate effect on the G_{Ic} of RT-PMMA may be elucidated by correlating the energy dissipation process with microdamage formation during crack growth.

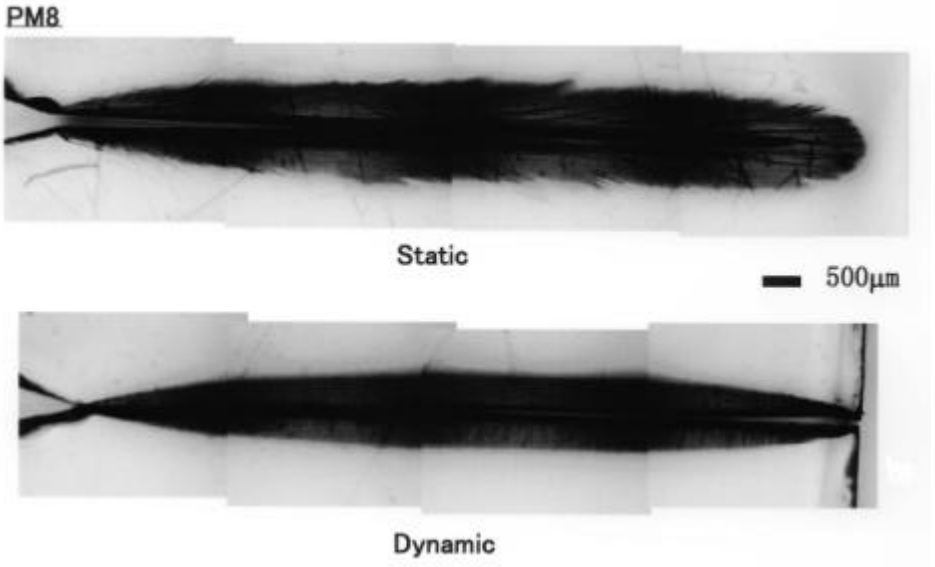

(a) PM8 at a low and an impact rate

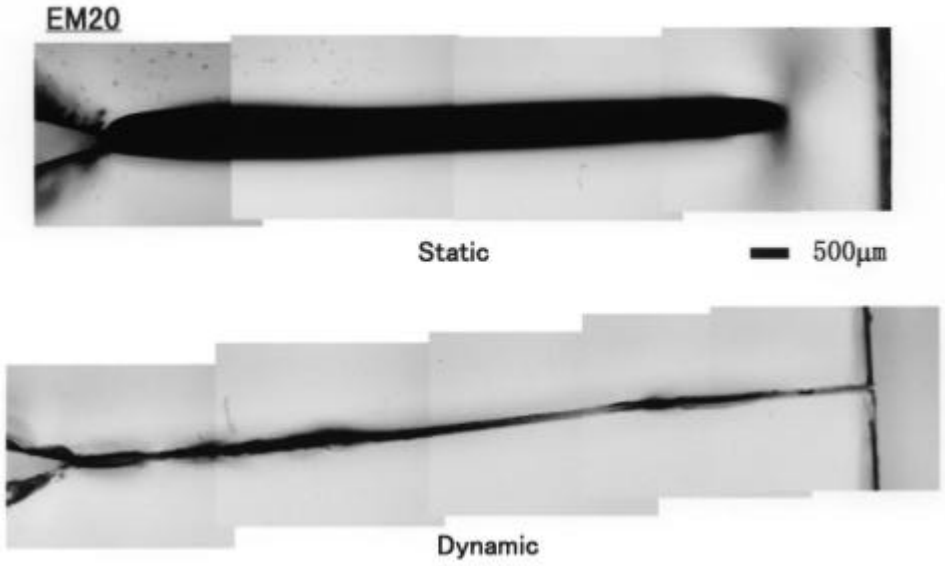

(b) EM20 at a low and an impact rate

Figure 6: Damage zone formation in RT-PMMA.

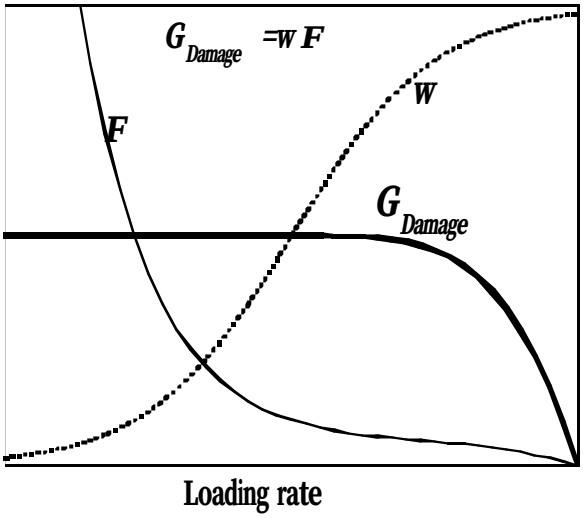

Figure 7: A mechanism of the loading rate dependence of EM20.

CONCLUSIONS

Loading-rate dependences of the critical mode I energy release rates G_{Ic} of three different RT-PMMA and a neat PMMA were investigated in a range of loading rate using three different testing systems. The following conclusions were reached:

(1) The G_{Ic} of CU increased with increase of loading rate up to 10^{-2}m/s and became constant up to 1m/s and then slightly decreased at the higher rates. The G_{Ic} of EM20 was almost independent of loading rate up to 1m/s and then decreased at the higher rates. The G_{Ic} values of PM8 and PM40 were almost independent of loading rate up to 10^{-1}m/s and then increased with increase of loading rate. PM8 exhibited the highest G_{Ic} at every loading rates.

(2) Cloud-like damage zones were developed during crack propagation in the three RT-PMMA's. PM8 showed the largest damage zone corresponding to the highest G_{Ic}. For all the RT-PMMA's, the size of damage zone decreased with increase of loading rate.

(3) The loading rate dependence of the G_{Ic} of RT-PMMA may be correlated with the rate dependence of damage zone formation in terms of the energy dissipation mechanism due to microdamage formation.

REFERENCES

1. Beguelin, Ph., and Kausch, H.H. (1994) *J. Mater. Sci.* 29, 91.
2. Beguelin, Ph., Julien, O., Monnerie, L. and Kausch, H.H. (1994) *Proc. the American Chemical Society Division of Polymeric Materials: Science and Engineering* 70, 147.
3. Todo, M., Takahashi, K., Beguelin, Ph. and Kausch, H.H. (1999) *JSME Inter. Journal (A)* 42, 49.
4. Lovell, P.A., Ryan, A.J., Sherratt, M.N. and Young, R.J. (1994) *Proc. 9th Inter. Conf. on Deformation, Yield and Fracture of Polymers,* 3/1.
5. Plummer, C.J.G., Beguelin, Ph. and Kausch, H.H. (1996) *Polymer* 37, 7.
6. Kausch, H.H., Beguelin, Ph., Lu, A., Plummer, C., Fond, C. and Schirrer, R. (1997) *Proc. 9th Inter, Conf. on Fracture* 6, 2835.
7. Todo, M., Takahashi, K., Jar, P.-Y.B. and Beguelin, Ph. (1999) *JSME Inter. Journal (A)* 42, 585.
8. ASTM D 5045-91a: Standard Test Methods for Plane-Strain Fracture Toughness and Strain Energy Release Rate of Plastic Materials.
9. Todo, M., Nakamura, T., Mada, T. and Takahashi, K. (1998) *Advanced Comp. Mater.* 7, 285.
10. Todo, M. and Takahashi, K. (1999) *Proc. the ASC 14th Tech. Conf.,* 131.
11. Tohdoh, M., Chaturvedi, S.K. and Sierakowski, R.L. (1996) *Inter. J. Fracture* 75, 285.

ORAL/POSTER REFERENCE: ICF100410OR

LOCAL FRACTURE PROPERTIES IN MMCS

O. Kolednik and I. Sabirov

Erich Schmid Institute of Materials Science, Austrian Academy of Sciences,
A - 8700 Leoben, Austria

ABSTRACT

The purpose of this paper is to explore the effect of the local microstructure near the crack tip on the local fracture properties of an aluminum based metal matrix composite with a varying volume fraction of alumina particles. It is investigated how parameters, such as the distance and the position of the first particle from the crack tip, the particle size, or the distance to neighbour particles, influence the local fracture initiation toughness. Furthermore, the local conditions for void initiation by either particle fracture or matrix-particle decohesion are studied. A new digital image analysis system is applied to perform a quantitative analysis of the fracture surfaces from stereo image pairs. The critical crack tip opening displacement, COD_i, and the crack tip opening displacement in the moment of void initiation, COD_{vi}, are determined as a function of the distance and the angle of the nearest alumina particles from the pre-fatigue crack front. The maximum normal stresses, $\sigma_{max,vi}$, that are necessary to initiate voids at the different individual particle locations are roughly estimated and compared. It is found that most critical are not the particles located directly in front of the crack tip but those that lie in the direction of the maximum extension of the plastic zone.

KEYWORDS

metal matrix composite, automatic fracture surface analysis, critical crack tip opening displacement, void initiation, stereophotogrammetry, local fracture toughness, microstructure

INTRODUCTION

A new automatic fracture surface analysis system has been recently developed that is capable of analyzing automatically stereo image pairs taken in the scanning electron microscope (SEM) [1,2]. Compared to a predecessor version [3,4], the system has been improved appreciably. The key part of the system is a matching algorithm which is able to find very accurately homologue, i.e. identical, points in the stereo image pair. The system generates a digital elevation model of the depicted region consisting of about 10.000 to 30.000 points. Important capabilities of the system are the automatic extraction of profile and surface roughness parameters and the determination of fractal dimensions [5], as well as the measurement of the critical crack tip opening displacement, COD_i, or the crack tip opening angle, *CTOA*, [4,6]. By this way, the fracture toughness of a material can be determined locally because COD_i is a measure of the local fracture initiation toughness, and *CTOA* a measure of the local crack propagation toughness [6].
With this system, we have now the tool to investigate how the local microstructure of a material influence its local fracture properties. In this paper, this idea is demonstrated on an aluminum based metal matrix composite (MMC) with alumina particles. It is studied how parameters, such as the distance and the position of the first particle from the crack tip, the particle size, or the distance to neighbour particles, influence the local conditions for void initiation and the fracture initiation toughness.

MATERIAL, EXPERIMENTAL PROCEDURE, AND RESULTS

The determination of global tensile and fracture properties

The material is a cast and extruded MMC with an Al-6061 matrix with Al_2O_3 particles. The chemical composition is given in Table 1. The particle volume fraction is varied: f_{Al2O3} = *10, 15,* and *20%*. The material was annealed 30 minutes at 560°C, quenched in water and aged at room temperature. Compact tension (CT) specimens with a thickness B = *12.5* mm, a width of W = *40* mm and an initial crack length of $a \approx 20$ mm were machined; the specimens had an LT crack plane orientation. Fracture mechanics tests are conducted on the pre-fatigued specimens according to the ESIS standard [7]. (In a forthcoming paper, the investigation is extended where materials with different aging conditions are studied; the influence of the global constraint of the specimen is checked by testing center cracked tension specimens, too.) The results of the tests are collected in Table 2; the fracture initiation toughness is given in terms of the J-integral, $J_{0.2/Bl}$, and in terms of the critical stress intensity, K_{IC}. In the table, the tensile testing data are also listed: the Young's modulus, E, the yield stress, σ_y, the ultimate tensile strength, σ_u, and the strain hardening coefficient, N. The values for the Al-6061 matrix material are given for comparison.

TABLE 1
CHEMICAL COMPOSITION OF THE AL 6061 ALLOY

Si	Fe	Cu	Mn	Mg	Zn	Cr	Ti
0.4÷0.8	0.7	0.15÷0.4	0.15	0.8÷1.2	0.25	0.04÷0.35	0.15

TABLE 2
GLOBAL MATERIAL PROPERTIES

% Al_2O_3	E [GPa]	σ_y [MPa]	σ_u [MPa]	N [MPa]	$J_{0.2/Bl}$ [kJ/m^2]	K_{IC} [MPa$\sqrt{m}$]	σ_0 [MPa]	d_n [1]
0	71	97	183	5.0	150	109	79	0.28
10	86	159	265	6.25	10.4	32	138	0.36
15	95	158	256	6.67	6.5	26	137	0.38
20	104	172	261	7.14	6.5	26	151	0.40

Stereophotogrammetric studies

Stereo image pairs of the midsection region are taken in the SEM by tilting the specimen. Corresponding regions on both halves of the broken fracture mechanics specimens are analyzed by our automatic fracture surface analysis system. From the digital elevation models of the corresponding regions, crack profiles are extracted perpendicular to the pre-fatigue crack front. From the crack profiles, the critical crack tip opening displacement, COD_i, and the crack tip opening in the moment of void initiation, COD_{vi}, are determined.

Figure 1 shows corresponding regions near the midsection on the two specimen halves of the specimen with f_{Al2O3} = *10 %*. The pre-fatigue region (at the midsection of the page) and the region of micro-ductile fracture can be clearly distinguished. In the SEM images, corresponding profiles are indicated. The profiles are drawn so that each crosses an alumina particle that is located close to the crack front. Sometimes the paths have a zigzag shape to find easier the corresponding path on the second specimen half.

In Figure 2a, the two corresponding profiles of Particle 10 are arranged so that the moment of fracture initiation is depicted, i.e., the first void in front of the tip coalesces with the blunted crack. COD_i is easily measured, COD_i = *16* µm. The location of Particle 10 is marked in each profile. If the upper profile is shifted vertically so that the two profiles touch at this location, we get a sketch of the crack in the moment of void initiation, Figure 2b, and the crack tip opening displacement in the moment of void initiation, COD_{vi} = *10* µm. The size of the particle is measured from the SEM images, and the polar coordinates, r and θ, of the particle center with respect to the crack tip are determined from Figure 2b. All these values are collected in Table 3, together with the data of other profiles. A few COD_i-values cannot be exactly determined; they are marked by a "?" sign.

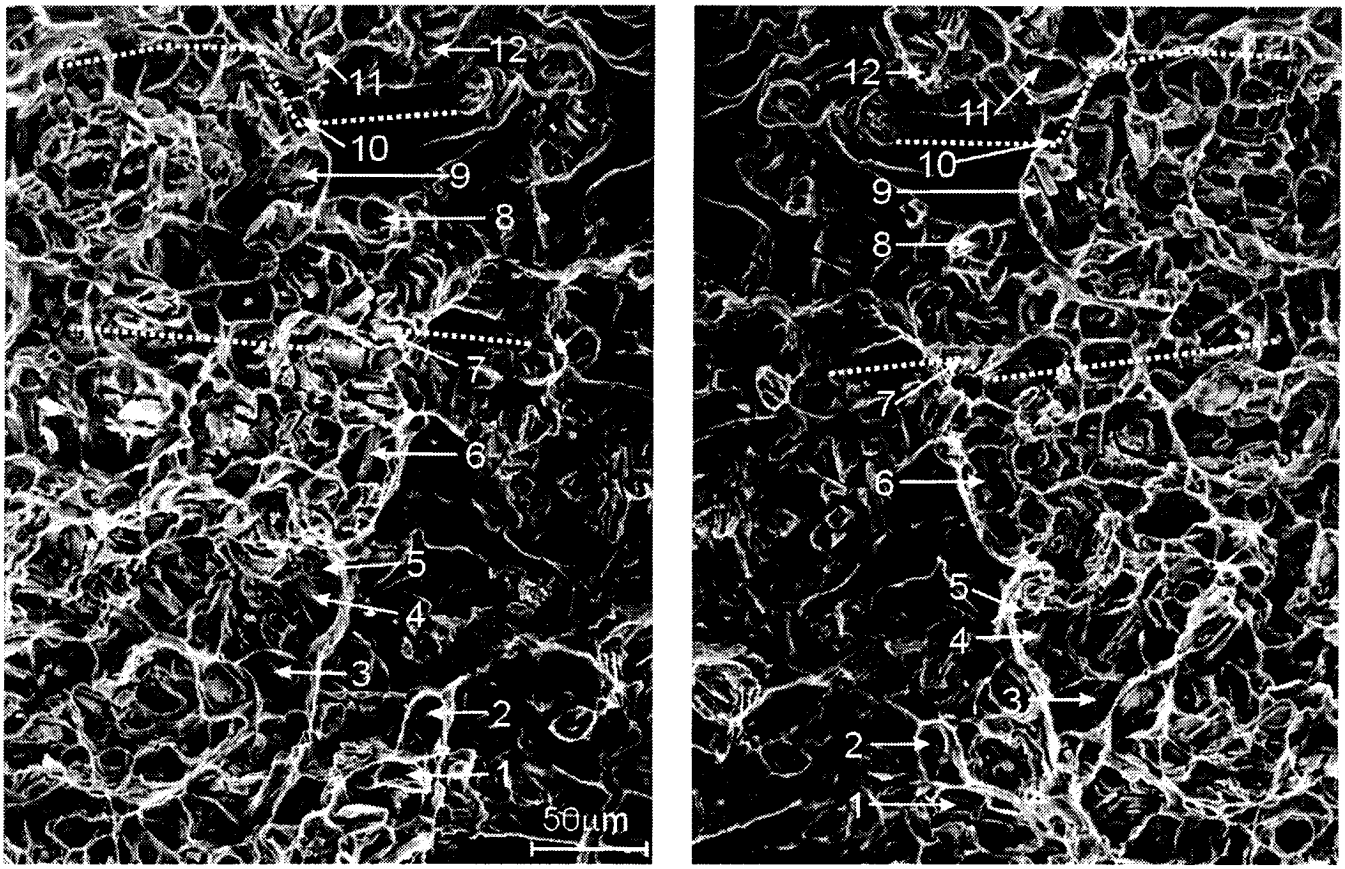

Figure 1: SEM images of corresponding midsection regions of the specimen with f_{Al2O3} = *10 %*

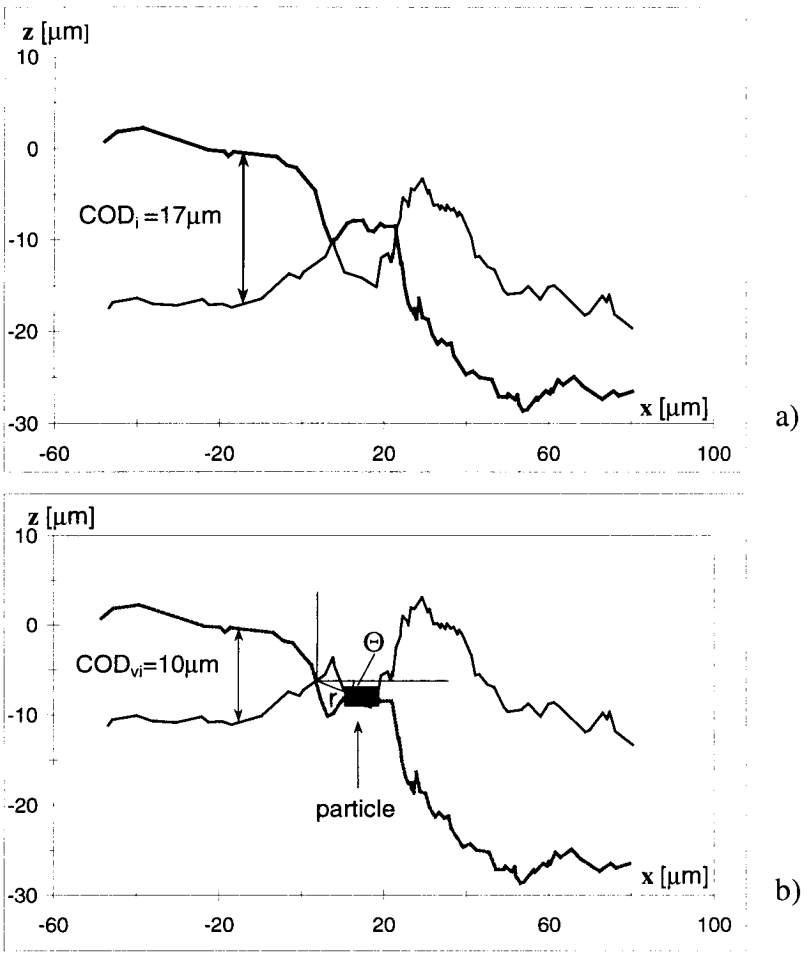

Figure 2: Crack profile through Particle 10, a) in the moment of fracture initiation, b) in the moment of void initiation at the location of the particle

TABLE 3

RESULTS OF THE STEREOPHOTOGRAMMETIC ANALYSIS FOR THE SPECIMEN WITH $f_{Al2O3} = 10\ \%$

Particle	Size [μm]	r [μm]	θ [°]	COD_{vi} [μm]	COD_i [μm]	σ^{max}_{vi} [MPa]	COD_I [μm]	Δa_I [μm]	Mecha-nism
1	3 x 12	15.6	-40	12	16.5	716	28.5	36	dec.
2	8 x 8	17.2	-31	6	6.5	644	18	17	fr.
3	12 x 3	43.2	35	7	12	571	20	65	fr.
4	20 x 9	30.5	32	7	9 ?	608	16	30	fr.
5	8 x 4	27.1	55	5	5	557	14	34	fr.
6	23 x 4	33.8	-71	≈2	13	436	19	25	fr.
7	15 x 6	30.4	-47	≈0	≈0	small	5	23	fr.
8	10 x 3	11.0	55	≈0	≈0	small	5	14	fr.
9	17 x 4	11.7	-20	6	11.5	665		>65	fr.
10	4 x 2	7.5	21	10	17	758	19.5	17	dec.
11	12 x 7	13.2	-11	9.5	16	686		>40	fr.
12	4 x 2	11.9	45	1.5	1.5 ?	549	12.5	40	fr.

Very interesting are the profiles through Particle 7, as the moments of void initiation and fracture initiation occur simultaneously at a very low value of $COD_{vi} \approx COD_i \approx 0$, Figure 3. Particle 7 fractures at a very low external loading and the crack immediately extends locally by a value of $\Delta a_I = 23$ μm. This is the first step of local crack extension. The upper profile must be shifted vertically to $COD_I = 5$ μm to produce the next step of crack extension. At a given position along the crack front, crack growth is a discontinuous process consisting of a series of local blunting and extension steps. The values of COD_k plotted against Δa_k, for $k = 1...n$, form a local crack growth resistance curve as was described in [6]. The values of the first extension step are included in Table 3.

In the region depicted in Figure 1, the crack tip opening displacement at fracture initiation varies between 0 and 17 μm, the scatter is extremely high. The mean value is $COD_i \approx (9.0 \pm 6.3)$ μm. For conventional engineering materials, such as steels, a much lower scatter of $\pm 15\%$ would be common [4,8]. On positions where COD_i is close to zero, the crack will locally extend at very low loads and stop after a crack extension, Δa_I. Against further extension, the crack will feel a much higher resistance, namely COD_I. Therefore, it is reasonable to replace at those positions COD_i by the value of COD_I, when the local average of COD_i should be compared to the global fracture initiation toughness, $J_{0.2/BI}$ or K_{IC}, measured in a fracture mechanics test. This corrected average is denoted COD_i^*. For the region of Figure 1, we get $COD_i^* \approx (10.8 \pm 4.2)$ μm.

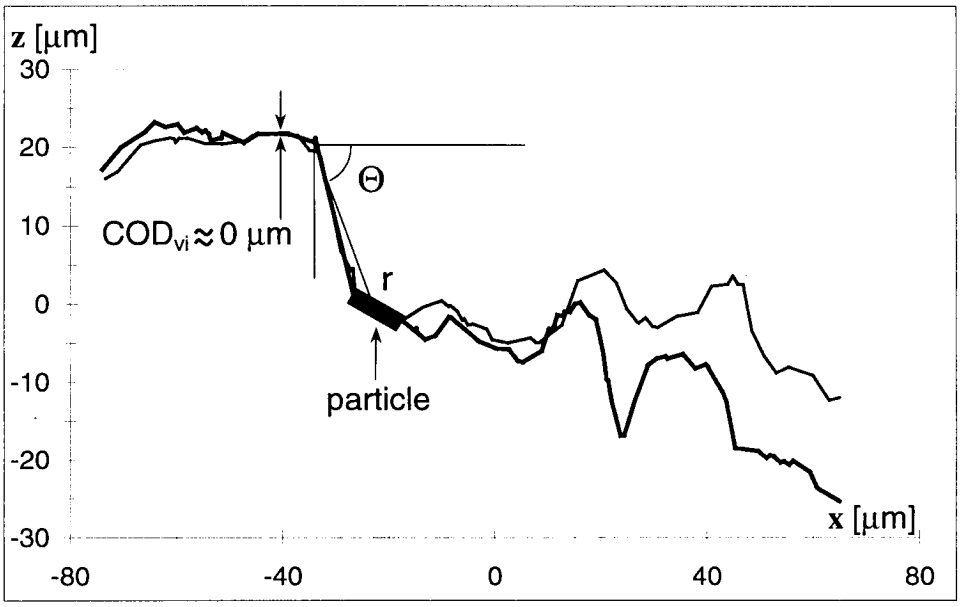

Figure 3: Crack profile through Particle 7 in the moment of void initiation; $COD_{vi} \approx COD_i \approx 0$

The mechanism of void initiation is either particle fracture, designated "fr." in the table, or matrix-particle decohesion designated "dec." For example, the broken parts of Particles 7 are found on both specimen halves, therefore particle fracture can be assumed. Void initiation by matrix/particle decohesion appears in two cases, only; most particles are fractured. The COD_{vi}-values scatter strongly, from *0* to *12* μm. No simple influence of the distance, *r*, between tip and particle is seen. As an example, Particle 8, with $COD_{vi} \approx 0$, is located close to the tip. In contrary, Particle 9 which has the same size and distance from the tip exhibits large values of COD_{vi} and COD_i. Very low COD_{vi}-values are also found for Particles 7 and 6 which are much more distant from the tip. It should be noticed that, with the exemption of Particle 5, the particles with a large deviation from the crack plane, i.e. a large angle θ, show very small COD_{vi}-values.

Estimate of the maximum stress at void initiation

For the individual particles, the maximum normal stress at the moment of void initiation is estimated from the solution of the HRR field which gives the stress field around a crack tip as, [9,10],

$$\sigma_{ij} = \sigma_0 \left[\frac{E\,J}{\alpha \sigma_0{}^2 I_N\, r} \right]^{1/(N+1)} \tilde{\sigma}_{ij}(N,\Theta) \tag{1}$$

The J-integral which determines the intensity of the stress field is substituted by the relation, [11],

$$J = \frac{1}{d_N} \sigma_0\, COD \tag{2}$$

In the two equations, *r* and θ are the polar coordinates, I_N and d_N are dimensionless constants both depending on the strain hardening coefficient, *N*, and on σ_0 /E (for d_N) [11]. *N*, α and σ_0 determine the standard power-law work hardening behavior of the material, with $\alpha = 1$. The reference stress, σ_0, is evaluated from the tensile testing data, following the procedure outlined in Appendix 6 of the ESIS Standard [7]. The values of d_N and σ_0 are listed in Table 1.

To evaluate the stress tensor at the moment of void initiation, $\sigma_{ij,vi}$, for each individual particle, the COD_{vi}-values of Table 3 are inserted into Eqn. 2 and Eqn. 1. The values of the dimensionless function, $\sigma_{ij}(N,\theta)$, are taken from [12]. The general stress tensor $\sigma_{ij,vi}$ is transformed to get $\sigma^{max}{}_{vi}$; the results are given in Table 3. Finite element analyses have shown that, although Eqn.1 is strictly valid only for applying a small strain theory and a sharp crack, the values are valid for distances of $r \geq 2\ COD$ [13]. This condition is fulfilled for most particles. However, due to the inhomogeneity of the material the real maximum particle stresses will be higher. The $\sigma^{max}{}_{vi}$-values of Table 3 should be taken, therefore, as rough estimates that are useful only for a comparison among the different particles.

No systematic influence of the particle size on the maximum normal stress is deduced from the table. The two particles that fail by decohesion have the largest $\sigma^{max}{}_{vi}$-values. $\sigma^{max}{}_{vi}$ does not seem to be the decisive parameter, as some particles, i.e., those located at high angle θ, fail at very low maximum normal stresses.

Comparison of the different specimens

For the specimen with f_{Al2O3} = *10* %, a second region, where the SEM images are taken at a higher magnification, is analyzed in a similar way. In total, 16 near-tip alumina particles are considered. In Table 4, the average values of COD_{vi}, COD_i, and $\sigma^{max}{}_{vi}$ are collected. For the other specimens, similar analyses are performed. In the specimen with f_{Al2O3} = *15* %, 14 particles are analyzed. 3 particles had a $COD_{vi} \leq 1$ μm. In the specimen with f_{Al2O3} = *20* %, 10 particles are analyzed; 5 particles had a $COD_{vi} \leq 1$ μm. The averaged results of these specimens also listed in Table 4.

DISCUSSION

It is plausible that plastic straining induce high stresses in the particle because of the misfit strains. It can be, therefore, assumed that for void initiation the plastic strain at the position of a particle must exceed a critical value [14]. For plane strain conditions which prevail in the specimen midsection, the plastic zone has a

TABLE 4

CONDITIONS FOR VOID AND FRACTURE INITIATION AT ALUMINA PARTICLES NEAR THE CRACK FRONT (AVERAGE VALUES)

% Al_2O_3	COD_{vi} [μm]	COD_i [μm]	COD_i^* [μm]	σ^{max}_{vi} [MPa]
10	5.5	10.7	12	546
15	4.4	6.4	8.0	442
20	1.5	6.1	6.1	324

maximum extension at an angle of about $\theta = 70°$ with respect to the crack plane. In that direction, the plastic zone size is by a factor 4.4 larger than directly in the crack plane, [15],

$$\omega_{70} = 0.157 \frac{K^2}{\sigma_y^{\,2}} \approx 0.16 \frac{J E}{\sigma_y^{\,2}} \approx \frac{0.16}{d_N} \frac{E \sigma_o \, COD}{\sigma_y^{\,2}} \tag{3}$$

This explains that most critical are not the particles located directly in front of the crack tip but those that lie in the direction of the maximum extension of the plastic zone. Even for a very low COD of 0.5 μm, the maximum extension of the plastic zone becomes already very large compared to the distance to the nearest particle: $\omega_{70} \approx 104$ μm (for the specimen with $f_{Al2O3} = 10$ %). Void initiation is induced due to the plastic strain, mostly by particle fracture, and the crack growth is initiated by the formation and failure of a shear band from the crack tip to the pre-crack.

For higher particle volume fractions, the plastic zone size decreases slightly because of the increased flow stress; however, this is more than compensated by the decreased distance of the tip to the next particle in a location favorable for void initiation, Therefore, more and more particles fracture at a very low loading, as has been found in the analysis, and the average values of COD_{vi}, COD_i, and σ^{max}_{vi} (which is the hypothetical maximum normal stress for a homogeneous material) decrease.

ACKNOWLEDGEMENTS

The authors acknowledge gratefully the financial support of this work by the Austrian Fonds zur Förderung der wissenschaftlichen Forschung under the project number P14333-PHY.

REFERENCES

1 Scherer, S., Werth, P., Pinz, A., Tatschl, A. and Kolednik, O. (1999) In: *Electron Microscopy and Analysis 1999,* pp. 107-110, Kiely, C.J. (Ed.). Institute of Physics Publishing, Bristol, U.K.

2 Scherer, S. and Kolednik, O. (2001) *Microscopy and Analysis* 70, in press.

3 Stampfl, J., Scherer, S., Gruber, M. and Kolednik, O. (1996) *Appl. Physics* A63, 341.

4 Stampfl, J., Scherer, S., Berchthaler, M., Gruber, M. and Kolednik, O. (1996) *Int. J. Fracture* 78, 35.

5 Kolednik, O. and Schwarzböck, P. (2000) In: *Fracture Mechanics: Applications and Challanges, Proc. of ECF13,* Paper 1U.60., Fuentes, M., Elices, M. (Eds). Elsevier, Amsterdam.

6 Stampfl, J. and Kolednik, O. (2000) *Int. J. Fracture* 101, 321.

7 ESIS P2-92 (1992) ESIS Procedure for Determining the Fracture Behaviour of Materials. European Structural Integrity Society, Delft, The Netherlands.

8 Kolednik, O. and Stüwe, H.P. (1985) *Engng Fracture Mech.* **21,** 145.

9 Hutchinson, J.W. (1968) *J. Mech. Phys. Solids* 16, 13.

10 Rice, J.R. and Rosengren, G.F. (1968) *J. Mech. Phys. Solids* 16, 1.

11 Shih, C.F. (1981) *J. Mech. Phys. Solids* 29, 305.

12 Shih, C.F. (1983) Tables of HRR Singular Field Quantities, MRL E-147. Materials Research Laboratory, Brown University, Providence, RI, USA.

13 McMeeking, R.M. and Parks, D.M. (1979) *ASTM STP* 668, 175.

14 Thomason, P.F. (1990) Ductile Fracture of Metals. Pergamon Press, Oxford.

15 Levy, N., Marcal, P.V., Ostergren, W.J. and Rice, J.R. (1971) *Int. Journ. Fracture Mech.* 7, 143.

ICF1001055

LONG TERM PREDICTION OF FATIGUE LIFE FOR FRP JOINT SYSTEMS

Y. Miyano[1], M. Nakada[1], N. Sekine[2], and S. W. Tsai[3]

[1]Materials System Research Laboratory, Kanazawa Institute of Technology,
Yatsukaho, Matto, Ishikawa 924-0838, Japan
[2]Graduate Student, Kanazawa Institute of Technology,
Ohgigaoka, Nonoichi, Ishikawa 921-8501, Japan
[3]Department of Aeronautics & Astronautics, Stanford University,
Stanford, CA 94305-4035, USA

ABSTRACT

The tensile constant elongation-rate (CER) and fatigue tests for GFRP/metal conical shaped joint, adhesive joint using a ductile PMMA adhesive, and bolted joint were carried out under various loading rates and temperatures. The fatigue failure loads as well as CER failure loads for these three types of GFRP joint depend clearly on loading rate and temperature. The time-temperature superposition principle holds for fatigue failure loads as well as CER failure loads for these GFRP joints, therefore the master curves for fatigue failure load can be obtained from these results. The dependence of these fatigue failure loads upon number of cycles to failure as well as time to failure and temperature can be characterized from the master curves for these GFRP joints.

KEY WORDS

GFRP, Conical shaped joint, Adhesive joint, Bolted joint, Tensile behavior, Fatigue, Life prediction, Time-temperature superposition principle

INTRODUCTION

The mechanical behavior of polymer resins exhibits time and temperature dependence, called viscoelastic behavior, not only above the glass transition temperature T_g but also below T_g. Thus, it can be presumed that the mechanical behavior of polymer composites also significantly depends on time and temperature even below T_g which is within the normal operating temperature range.

The time-temperature dependence of the tensile and flexural strengths under constant strain-rate (CSR) and fatigue loadings for various kinds of FRP has been studied in our previous papers [1-8]. It was observed that the fracture modes are almost identical under two types of loading over a wide range of time and temperature, and the same time-temperature superposition principle holds for CSR and fatigue strengths. Therefore, the master curves of fatigue strength for these FRP were obtained.

In this paper, the tensile fatigue tests as well as tensile constant elongation-rate (CER) tests for GFRP/metal conical shaped joint, GFRP/metal adhesive joint using a ductile PMMA adhesive, and GFRP/metal bolted joint are carried out under various loading rates and temperatures. The time and temperature dependencies of tensile fatigue behavior for these three GFRP joints are discussed.

EXPERIMENTAL PROCEDURE

Preparation of GFRP joints

The conical shaped joint is made from a unidirectional GFRP rod, metal end fittings (42CrMo4), and bonding resin as shown in Fig.1. The unidirectional GFRP rod consists of E-glass fibers and epoxy resin, and is produced by pultrusion molding. The bonding resin consists of epoxy resin and silica. The bonding resin taper and the bonding length are respectively 6° and 25mm.

The adhesive joint is made from a GFRP pipe, ductile cast iron rod (600-3), and adhesive resin as shown in Fig.2. The GFRP pipe consists of glass cloth and epoxy resin, and is produced by tape winding method. An adhesive resin is a ductile PMMA resin. The adhesive resin thickness and length are respectively 4 mm and 28 mm.

The bolted joint is constructed from a GFRP pipe, steel rod (C45), and bolt as shown in Fig.3. The GFRP pipe is the same to that for adhesive joint. The GFRP pipe is joined to steel rod by two bolts. One is ¼-20UNC bolt with small washer, where the thickness of GFRP pipe is 3mm. The other is M8×1.25 bolt with large washer, where the thickness of GFRP pipe is 5mm.

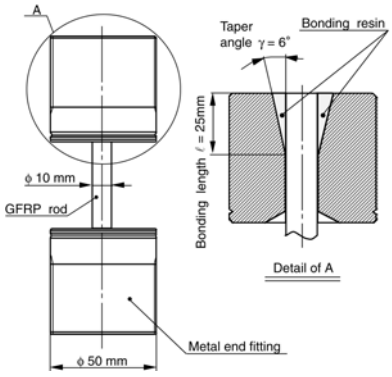

Fig.1 Conical shaped joint

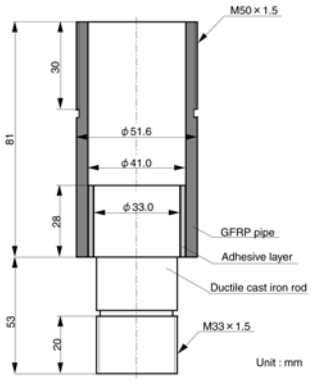

Fig.2 Adhesive joint

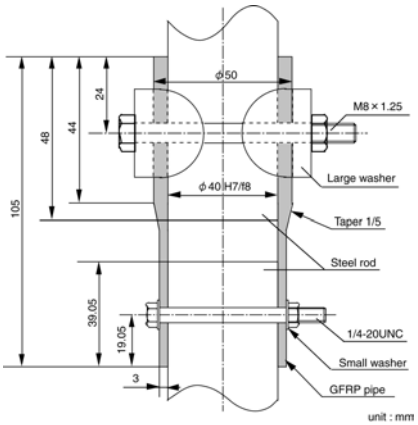

Fig.3 Bolted joint

Test procedure

The tensile CER tests were carried out under various loading rates and temperatures using an Instron type testing machine. The loading rates were 0.01, 1 and 100mm/min. The tensile fatigue tests were carried out under various temperatures at two frequencies f=5 and 0.05Hz using an electro-hydraulic servo testing machine. Load ratio R (minimum load/maximum load) was 0.05.

RESULTS AND DISCUSSION

Master curve of CER failure load

Figures 4 and 5 show the master curves of tensile CER failure load and time-temperature shift factors for three cases: (a) conical shaped joint, (b) adhesive joint, and (c) bolted joint.

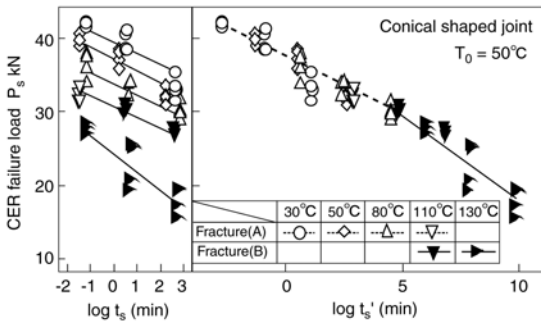

(a) Conical shaped joint

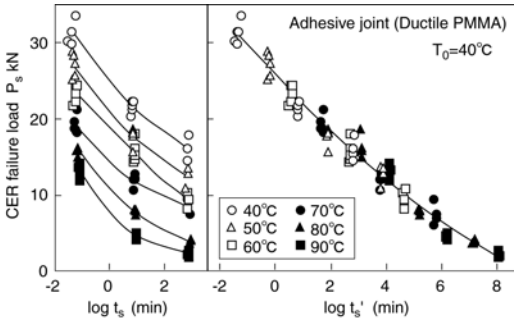

(b) Adhesive joint

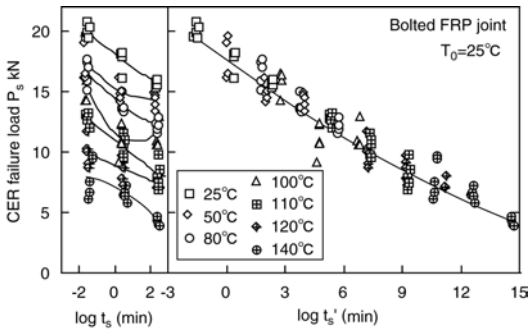

(c) Bolted joint

Fig.4 Master curves of CER failure load for three types of GFRP joint

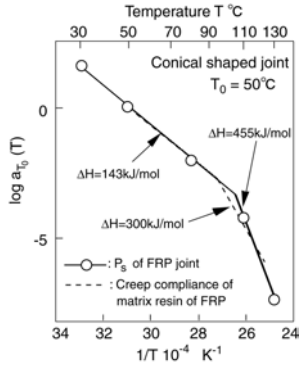

(a) Conical shaped joint

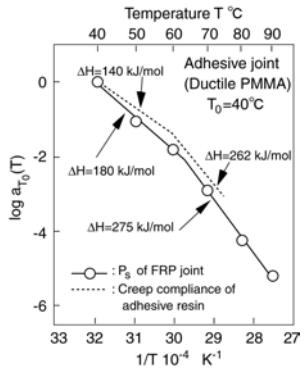

(b) Adhesive joint

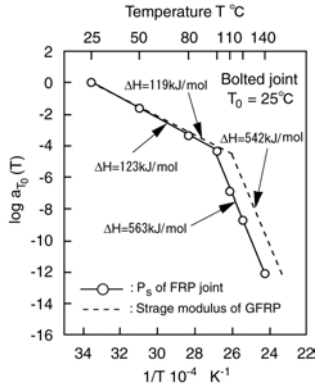

(c) Bolted joint

Fig.5 Time-temperature shift factors of CER failure load for three types of GFRP joint

The left sides of Fig.4 show the CER failure load P_s versus time to failure t_s, the time period from initial loading to maximum load. The master curves for each P_s were constructed by shifting P_s at various constant temperatures along the log scale of t_s so that they overlap on P_s at the reference temperature T_0 or on each other to form a single smooth curve as shown in the right sides of this figure. Since the smooth master curves for each P_s can be obtained, the time-temperature superposition principle is applicable for

each P_s.

The time-temperature shift factors $a_{To}(T)$ for each P_s obtained experimentally in Fig.4 are plotted respectively in Fig.5. These $a_{To}(T)$ agree with those for the viscoelastic stress-strain relationship of the matrix resin of GFRP or adhesive resin for the corresponding GFRP joint indicated by dotted lines, which are described by two Arrhenius' equations with different activation energies ΔH.

The fracture of conical shaped joint occurs at the GFRP rod within the contact area of the bonding resin. The failure mode changed with temperature. In the region of low temperature, this joint fails coaxially at the surface of GFRP rod, and then the shearing crack propagates transversely in the GFRP rod (Fracture A). In the region of high temperature, this joint also fails coaxially at the surface of GFRP rod, and then the shearing crack propagates longitudinally in the GFRP rod (Fracture B). The fracture modes A and B for this conical shaped joint can be classified clearly on the master curve as shown in Fig.4 (a). The fracture of adhesive joint occurred in the adhesive resin nearby the interface between cast iron rod and adhesive resin in all region of temperature tested. The fracture of bolted joint occurs at GFRP pipe in the vicinity of ¼-20UNC bolt in all region of temperature tested. The bearing failure of GFRP pipe was observed initially, and then cracks occurred along circumference direction of GFRP pipe from the right and left edges of hole.

From these results, the time-temperature dependence of CER failure load for the conical shaped joint, adhesive joint, and bolted joint is controlled by the viscoelastic behavior of the matrix resin of GFRP or adhesive resin for the corresponding GFRP joint.

Master curve of fatigue failure load

We turn now the fatigue failure load P_f and regard it either as a function of the number of cycles to failure N_f or of the time to failure $t_f=N_f/f$ for a combination of frequency f, temperature T and denote them by $P_f(N_f, f, T)$ or $P_f(t_f, f, T)$. Further, we consider the CER failure load $P_s(t_f, T)$ as the fatigue failure load at $N_f=1/2$, R=0, and $t_f=1/(2f)$.

To describe the master curve of P_f, we need the reduced frequency f' in addition to the reduced time to failure t_f', each defined by

$$f' = f \cdot a_{T_0}(T), \quad t_f' = \frac{t_f}{a_{T_0}(T)} = \frac{N_f}{f'} \qquad (1)$$

We introduce two alternative expressions for the master curve: $P_f(t_f', f', T_0)$ and $P_f(t_f', N_f, T_0)$. In the latter expression, the explicit reference to frequency is suppressed in favor of N_f. Note that the master curve of fatigue failure load at $N_f=1/2$ is regarded as the master curve of CER failure load. Equation (1) enables one to construct the master curve for an arbitrary frequency from the tests at a single frequency under various temperatures.

Figure 6 displays the fatigue failure load P_f versus the number of cycles to failure N_f (P_f-N_f) curves at a frequency f=5Hz for three cases: (a) conical shaped joint, (b) adhesive joint, and (c) bolted joint. The CER failure loads regarded as the fatigue failure load at $N_f=1/2$ are included in these figures. The fracture mode of conical shaped joint is also classified into two modes on the P_f-N_f curves as shown in Fig.6 (a).

In Fig.7, P_f versus the reduced time to failure t_f' curves for several reduced frequencies f' at the reference temperature T_0 are depicted by thin lines, which are obtained by converting N_f of Fig.6 into t_f' using Eq.(1) and the shift factor for CER failure load. The master curves of P_f for fixed N_f indicated by thick lines are constructed by connecting the points of the same N_f on the curves of each f' indicated by thin lines in these figures.

The P_f-N_f curves at f=0.05Hz predicted from Fig.7 are displayed in Fig.8 together with test data. Since the P_f-N_f curves predicted on the basis of the superposition principle capture test data satisfactorily, the time-temperature superposition principle for CER failure load also holds for fatigue failure load. Therefore, the validity for the construction of master curves of fatigue failure load using the time-temperature shift factor for CER failure load is confirmed.

Comparison of the master curves of fatigue failure load

From the master curves of tensile fatigue failure load for three types of GFRP joint as shown in Fig.7, the time-temperature dependent fatigue behavior for these three types of GFRP joint can be characterized. The tensile fatigue failure load for conical shaped joint depends slightly on time to failure and temperature, however the fatigue failure load decreases clearly with increasing N_f. The fatigue failure loads for adhesive joint and for bolted joint depend clearly on time to failure and temperature, however these fatigue failure loads decrease scarcely with increasing N_f.

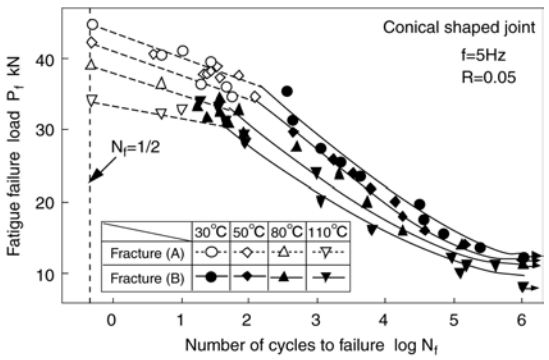

(a) Conical shaped joint

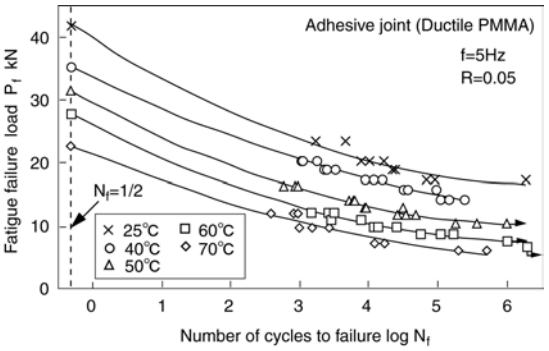

(b) Adhesive joint

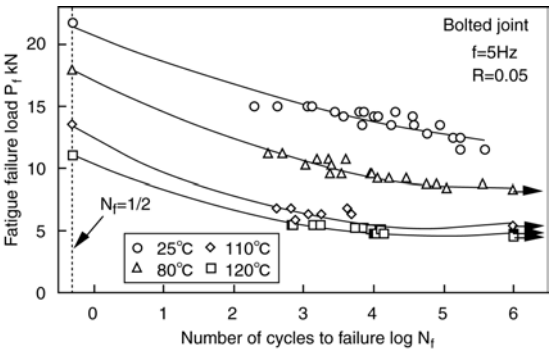

(c) Bolted joint

Fig.6 P_f-N_f curves for three types of GFRP joint at frequency f=5Hz

CONCLUSION

The time and temperature dependence of tensile fatigue behavior for GFRP/metal conical shaped joint, adhesive joint using a ductile PMMA adhesive, and bolted joint are determined experimentally. The time-temperature superposition principle holds for the tensile fatigue failure loads as well as CER failure loads for all of these GFRP joints, therefore, the master curves of fatigue failure load for these GFRP joints can be obtained. The master curves of fatigue failure load show very characteristic behavior due to the structure and the combination of materials of GFRP joints.

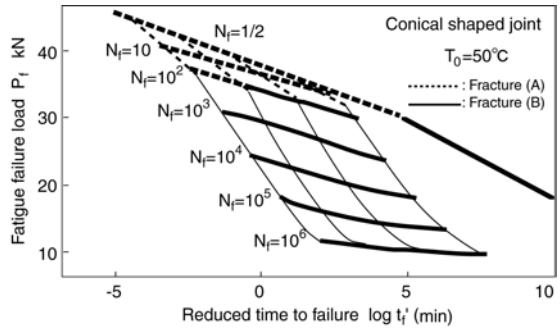

(a) Conical shaped joint

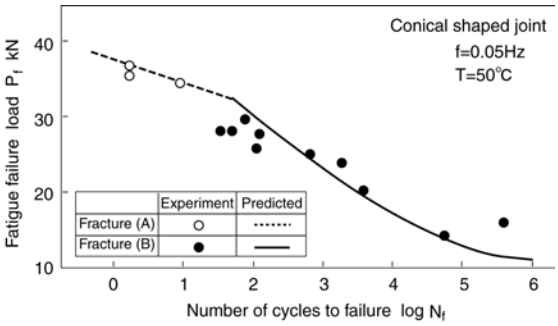

(a) Conical shaped joint

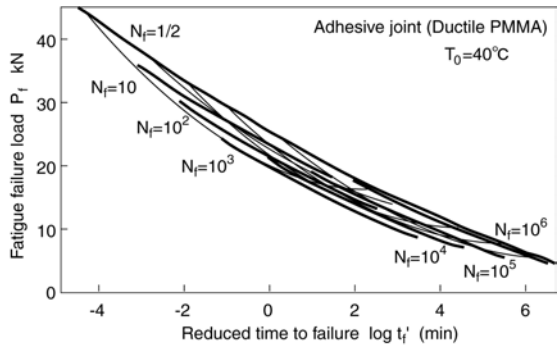

(b) Adhesive joint

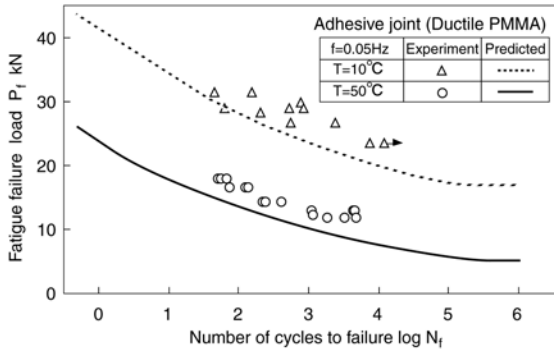

(b) Adhesive joint

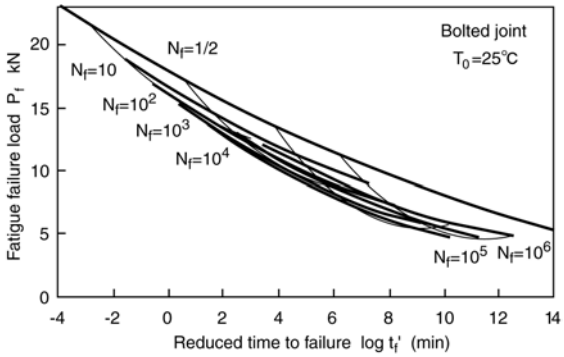

(c) Bolted joint

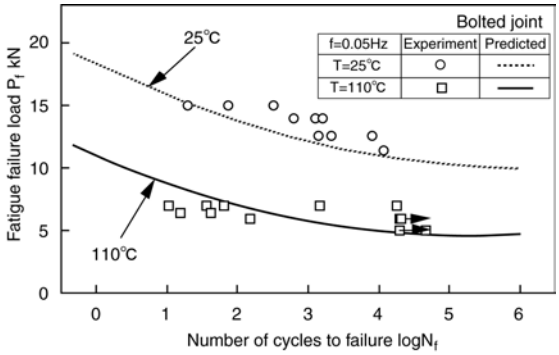

(c) Bolted joint

Fig.7 Master curves of fatigue failure load for three types of GFRP joint

Fig.8 P_f-N_f curves for three types of GFRP joint at frequency f=0.05Hz

REFERENCES

1. Aboudi, J. and Cederbaum, G. (1989). Composite Structures, 12, p.243.
2. Ha, S. K. and Springer, G. S. (1989). J. Composite Materials, 23, p.1159.
3. Sullivan, J.L. (1990). Composite Science and Technology, 39, p.207.
4. Miyano, Y., Kanemitsu, M., Kunio, T. and Kuhn, H.J. (1986). Composite Materials, 20, p.520.
5. Miyano, Y., McMurray, M. K., Enyama, J. and Nakada, M. (1994). J. Composite Materials, 28, p.1250.
6. Miyano, Y., McMurray, M. K., Kitade, N., Nakada, M. and Mohri, M. (1994). Advanced Composite Materials, 4, p.87.
7. Miyano, Y., Nakada, M. and McMurray, M. K. (1995). J. Composite Materials, 29, p.1808.
8. Miyano, Y., M. Nakada, M. K. McMurray, and R. Muki, J. Composite Materials, 31 (1997), p.619.

MODELING OF GRAIN PULLOUT IN FATIGUED POLYCRYSTALLINE ALUMINA

M.T. Kokaly[1], A.S. Kobayashi[1] and K.W. White[2]

[1]University of Washington, Department of Mechanical Engineering, Seattle, WA 98195-2600, USA
[2]University of Houston, Department of Mechanical Engineering, Houston, TX 77204-4792, USA

ABSTRACT

A second generation, 2-D finite element (FE) model of grain pull-out and push-in in an alumina wedge-opening double cantilever beam (WL-DCB) specimen was constructed using observations and measurements from photomicrographs of the specimen surface. The FE model consisted of an idealized structure of quadrilateral elements corresponding to three different grain sizes. Frictional sliding, intact elastic grains, and cantilever grains were modeled in the interface. The observed intragranular fracture sites and appearance of detached grains indicative of broken elastic grain bridges and rotated grains were included in the model by removing the relevant elements. An iterative inverse process was used to match the experimental cyclic load/unload test results of the WL-DCB specimen.

KEYWORDS

Inverse analysis, hybrid experimental-numerical analysis, ceramic fracture, low cycle fatigue, fracture process zone.

INTRODUCTION

Since the earlier work of Knehans et. al. [1], numerous work on the toughening effects generated by grain bridging in the trailing fracture process zone (FPZ) have been published, especially over the last decade. Unfortunately, the controlling factor, the grain bridging force was only inferred in the majority of studies. Hay and White [2] used a "post fracture tension" (PFT) specimen to directly measure the crack closure stresses (CCS) in the trailing wake of a stably grown crack in a high purity alumina double cantilever beam (WL-DCB) specimen. The PFT results provided an excellent platform for modeling the grain-bridging force due to frictional sliding since other grain bridging mechanisms such as elastic grain bridging and cantilevered grain rotation occur only immediately in front of the crack tip. A zero order finite element (FE) model of the PFT specimen subjected to monotonic loading by Tran, et. al. [3] provided the load versus displacement results which were in remarkable agreement with the measured results of [2]. This modeling was followed by a first order FE model [4] of a cyclically loaded PFT specimen based on the newer results of Hay and White
[5]. In this paper, we present a second order FE model of grain bridging in a cyclically wedge-loaded double cantilever beam (WL-DCB) specimen.

EXPERIMENTAL BACKGROUND

WL-DCB Specimen

A high purity alumina (Coors AD998), WL-DCB specimen was cyclically loaded under displacement control at room temperature, 600, and 800°C. The applied load and the crack opening displacement (COD) profile, determined through moiré interferometry, were recorded during the loading and unloading processes. Details of the experimental procedure and results are given in [6].

The crack opening profiles at the maximum and minimum loads during the first loading cycle at room temperature are shown in Fig. 1. Comparison of the loaded and unloaded crack opening profiles revealed not only a residual crack opening along the length of the crack but a residual crack opening larger than that at the maximum load in the area near the crack tip. The residual crack opening was attributed to a cantilever effect from the interference of completely pulled out grain bridges during unloading. The residual COD at unloading was found to increase after the next cycle of loading. This increase in residual COD and the related decrease in sliding distance between frictional grains was the probable cause of the lack of fatigue damage and hence fatigue crack extension in tension-tension cycling of monolithic structural ceramics in an inert environment.

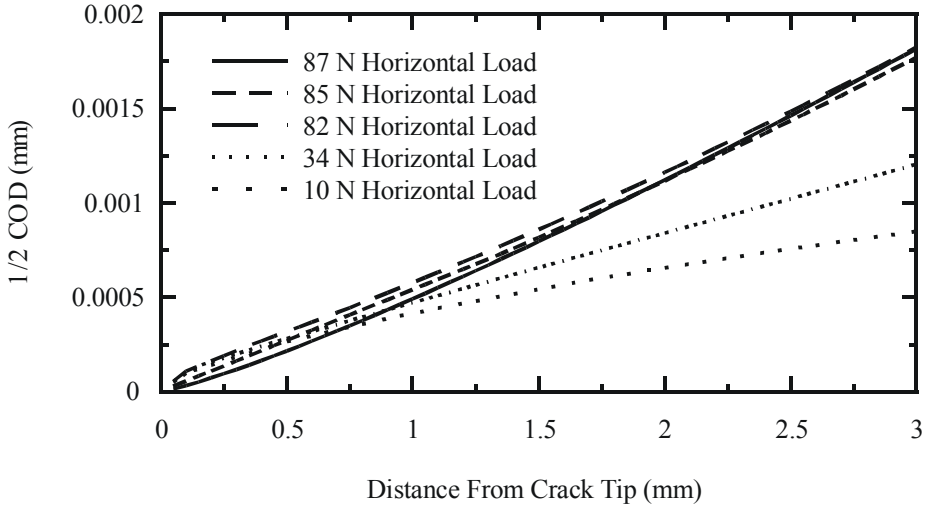

Fig. 1. Crack profiles at 1st loading cycle. .

Side-surface Micrograph

Figures 2 and 3 show the micrographs along a crack in the side surface of a WL-DCB specimen at unloading after 25 cycles of loading. Intergranular fracture dominated the crack interface and was interspersed with transgranular fracture (in the brackets) in Fig. 2. Although the crack paths in Fig. 3 suggest locations of possible angled grain rotation, most angled grains failed by intergranular fracture prior to an appreciable crack opening. Crack opening at the peak load was resisted by elastic bridges, cantilevered grains, and frictional bridging grains. Elastic grain bridges and cantilevered grains fractured transgranularly or detached from surrounding grains at a small COD after which frictional bridges dominated the resistance to crack opening. An example of a transgranularly fractured grain is given in the highlighted section of Fig. 3. The frictional forces were generated by the residual compressive stresses caused by the anisotropic thermal contraction in the grains during cool down from the processing temperature of 1500°C.

FPZ MICROMECHANICS

Crack Closing (Bridging) Stress

Abundant experimental evidence [1-6] show that the dominant fracture energy dissipation mechanism in structural ceramics is the crack opening resistance in the trailing FPZ of a crack. The FE model described in [3, 4] simplifies the complex micro-mechanics governing grain separation along the opening crack in order to determine the CCS versus COD relation using the experimentally determined load and displacement boundary conditions. A slightly different version of this hybrid analysis was performed to determine the

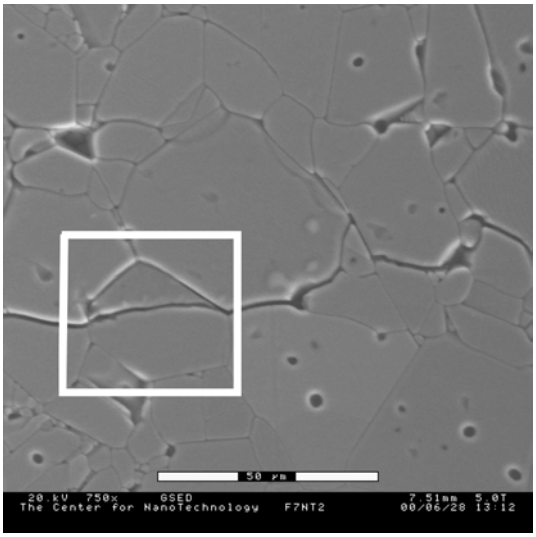

Fig. 2. Intergranular and transgranular cracks.

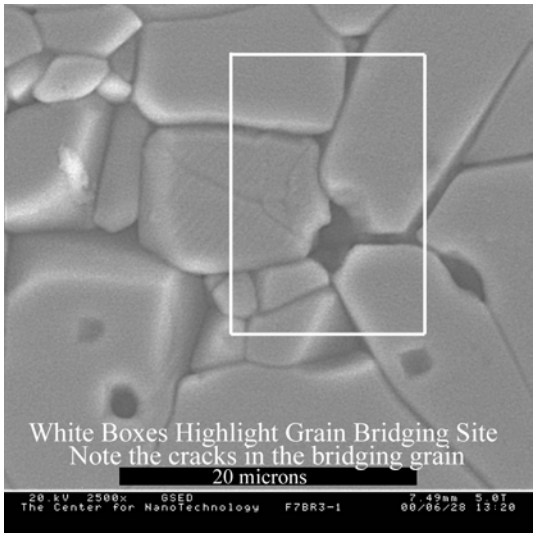

Fig. 3. Fractured bridging grain.

crack closing stress during periods of loading and unloading [6]. Figure 4 shows the difference between the experimentally determined CCS versus COD relations at the maximum applied load at both room temperature and 800°C. The decrease in the crack bridging force at 800°C is attributed to both the decrease in viscosity of the glassy grain interface and the partial relieving of the residual compressive stresses, hence, the decrease in the resistance to grain pullout.

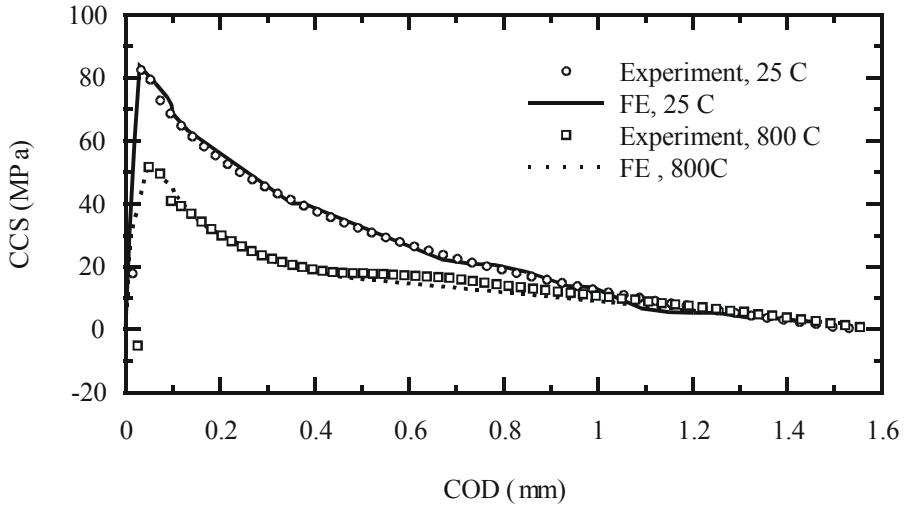

Fig. 4. CCS versus COD relations at maximum load.

FE MODEL

A micromechanical model based on all three grain bridging mechanisms mentioned previously was subjected to the loading cycle. The disposable parameters in the model were the relative contributions of elastic grain bridges, cantilevered grains, and frictional bridging to the grain bridging force [7]. By necessity, the model was a highly idealized assembly of quadrilateral elements. At the interface, elastic grain bridges were modeled by constraining the coincident nodes on the opposite side of the crack to have the same displacement. Angled, cantilevered grains were modeled by adjusting the nodal points of the initial mesh to provide an angled interaction surface. Frictional bridges were modeled, as in the previous cases, with the frictional properties defined at the crack interface. Examples of each type of bridge is given in Fig. 5. Lacking any prior analysis of the behavior of the grain bridges during loading, a time consuming trial-and-

error, iterative inverse analysis was used to match the meso-responses of the micro-mechanical model and the experimental data, primarily the applied load, COD profile and CCS vs. COD relation.

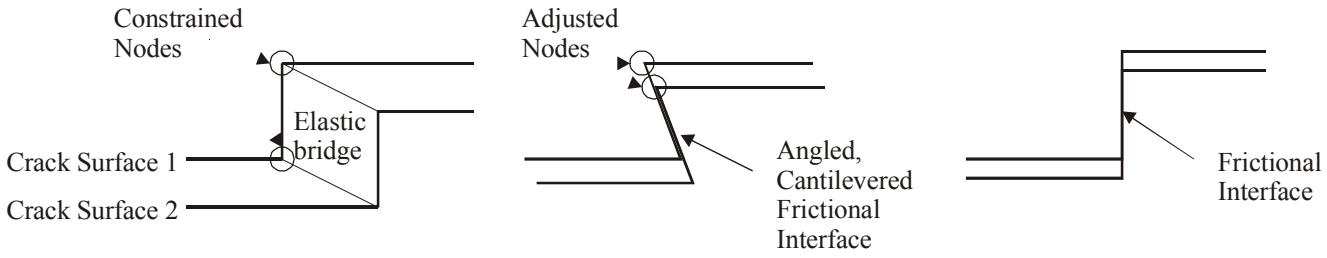

Fig. 5. Modeling of Three Types of Grain Bridges.

The FE model used in this study accounted for the random grain size distribution and the random orientation of the axes of thermal expansion. Unlike previous studies [3, 4], as shown in Fig. 6, this is a two-dimensional idealization of the complex three-dimensional complex distribution of grains through the thickness of the WL-DCB specimen. Since the model was a slice through the thickness of the WL-DCB specimen, the width of the FE model was equal to the thickness of the WL-DCB specimen minus the side groove or 2.4mm. The thickness of the model was equated to the average grain size of 15 μm. A Matlab preprocessor randomly distributed the principal thermal expansion directions from 0 to 160^{o} in 15^{o} increments. The compressive residual stress, which caused frictional resistance to the grain pullout, was generated by the mismatch in grain shrinkage during the cool down from the processing temperature. The complex distributions of irregular grains of various sizes were replaced by trapezoidal and rectangular grains of varying sizes in the region adjacent to the fracture surface as shown in Fig. 6. In order to conserve computing time, three layers of increasingly larger elements with randomly orientated anisotropic thermal coefficients of expansion, were used outside of the fracture region. Grain sizes under 3 μm were considered too small for effective grain bridging in the WL-DCB specimen.

The grain size distribution was incorporated into the model by manipulating the coefficients of thermal expansion. The coefficients were scaled by the ratio of the assigned grain size to the average grain size of 15 μm. This allowed the model to maintain a reasonable residual thermal strains and hence residual compressive stresses between grains while using a simple mesh. Since the goal of the model involved the interactions between grains, a surface area grain distribution was used. This retained the distribution of expansion mismatch between grains as in the real material and hence, residual stress at the interface.

Material Properties

The linear coefficients of thermal expansion in the two principle directions were assumed to be 8.62×10^{-6} in the (0001) plane and 9.38×10^{-6} mm/^{o}C in the [0001] direction. Because of the existence of a symmetry plane, 1/3 of the grains were assigned an isotropic thermal expansion equal to the expansion in the (0001) plane. An isotropic modulus of elasticity of 350 GPa and a Poisson ratio of 0.23 were used. The elastic isotropy assumption was based justified on the basis of [8], which showed, by a numerical experiment, that the effect of elastic anisotropy of the alumina grains had negligible effect on the average residual stresses, which were generated by thermal anisotropy.

In the absence of any micro-mechanical data, the friction coefficient for estimating the resistance to the subsequent intergranular sliding was assumed to be 0.7. The Coulomb friction coefficient was an educated average of the bulk friction coefficients given by Jahanmir and Dong [9 and was adjusted to account for the rougher surfaces due to the presence of the interstitial phase.

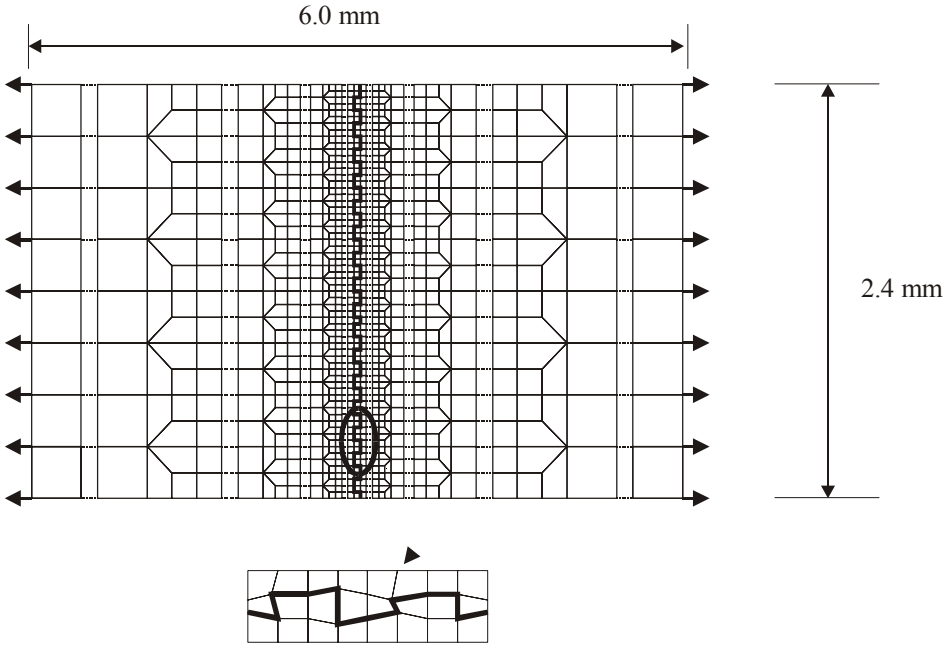

Fig. 6. FE model of the fracture surface.

RESULTS

Initially, the FE model was subjected to a cool down process from 1500^{o}C to 25^{o}C or 800^{o}C. The model was then subjected to a cyclic loading. The relative contributions of the various bridging mechanisms to the CCS were adjusted to match the CCS versus COD relation. The resulting CCS vs. COD relations generated by the FE model are shown in Fig. 4 together with the corresponding experimental data. The computed and measured unloading CCS vs. COD relations at locations 0.1, 1.0 and 2.0 mm from the crack tip are also shown in Figs. 7 and 8. In all cases, the COD did not return to zero. These results show that additional compressive force is required to return the grains to their original uncracked position. Furthermore, the good agreement of the FE results and the experimental data indicates that the assumptions and modeling techniques used were successful in representing the micro-mechanics of grain bridging in alumina during loading and unloading.

CONCLUSION

A micro-mechanical FE model, which is based on grain pullout and push-in of a WL-DCB specimen has been presented. The FE model, which was developed through an inverse process, successfully replicated the measured cyclic load and unload relations of an alumina WL-DCB specimen.

ACKNOWLEDGMENT

The work reported here is supported by an AFOSR grant F49620-96-1-0451, Dr. Ozden Ochoa, was the grant monitor.

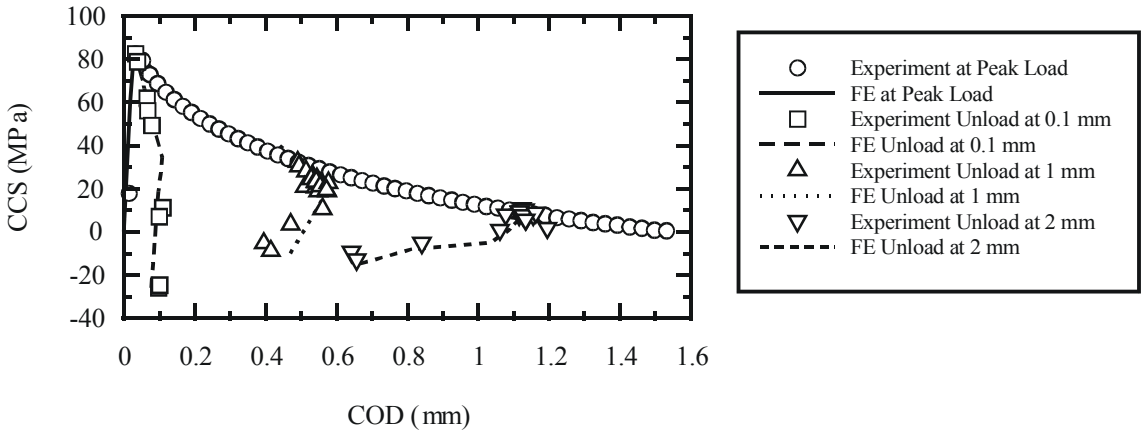

Fig. 7. CCS vs. COD relations during the first loading and unloading at room temperature.

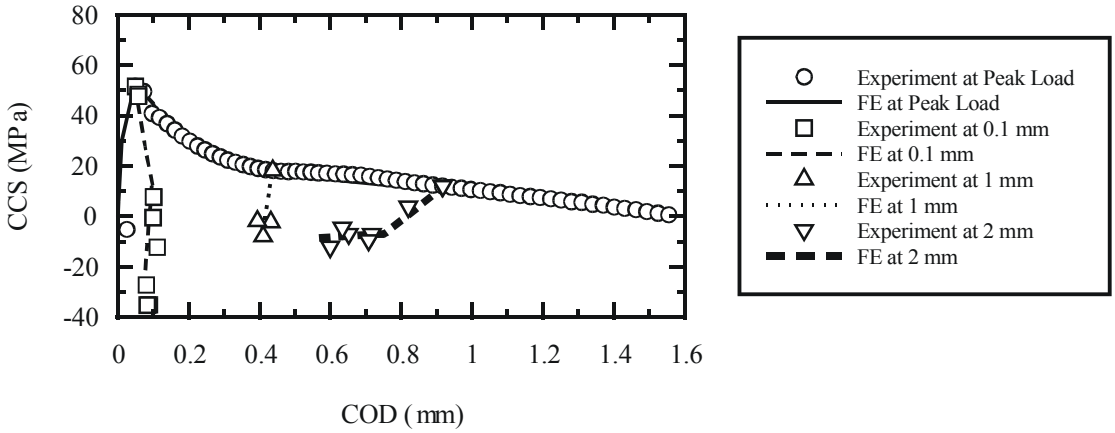

Fig. 8. CCS vs. COD relations during the first loading and unloading at 800^{o} C.

REFERENCES

[1] R. Knehans and R.W. Steinbrech, *J. Matr. Sci. Lett.* **1** (8) (1982), 327.

[2] J.C. Hay. and K.W. White, *J. Am. Ceram. Soc.* **78** (1995), 1025-1032.

[3] D.T. Tran, C.T. Yu, J.C. Hay, K.W.White and A.S. Kobayashi, in *Fracture Mechanics of Ceramics 11*, R.C. Bradt, D.P.H. Hasselman, D. Munz, M. Sakai and V. Ya Shevchenko, eds, Plenum Publishing Corp. (1996), 29.

[4] M.T. Kokaly, D.K. Tran, A.S. Kobayashi, X. Dai, K. Patel and K.W. White, *Mat'l Sci. Eng.* A285 (2000), 151.

[5] J.C. Hay and K.W.White, *Acta mater.* **45** (9) (1997), 3625.

[6] Kokaly, M.T., Kobayashi, A.S. and White, K.W. in *Proc. of Int'l. Conf. Fracture 10*, Honolulu, HI, Dec. 3-7, 2001.

[7] G. Vekinis,M.F. Ashby and P.W.R. Beumont, *Acta. Metall. Mater.*, **38** (600, 1151-1162.

[8] A.F. Bower and M. Ortiz, *ASME J. Engr. Mater. Techn.* **115** (2) (1993), 230.

[9] S. Jahanmir and X. Dong, *J. Tribology* **114** (1992), 403.

ORAL/POSTER REFERENCE:00845

LRM CONSTITUTIVE MODEL FOR DESCRIBING FUNCTIONALLY GRADED MATERIAL WITH FAST PROPAGATING CRACK

Michihiko NAKAGAKI[1] and Yadong WU[1]
[1] Department of Mechanical Systems Engineering, Kyushu Institute of Technology,
Iizuka-City, Fukuoka, JAPAN 820-8502

ABSTRACT

This paper treats a computational procedure to analyse a fast crack propagating transversely in a heat shield type functionally graded material(FGM). The constituents of the FGM vary from a 100 percent zirconia to a 100 percent ceramic. To best describe the severity of the propagating crack in such an inhomogeneously varying material, the T* crack-tip integral parameter is used. The FGM is assumed to be a particle dispersed composite material in elasto-plastic regime. The material constitutive modeling for the composite is performed by using authors' Localized Rigidity Model(LRM) on the basis of Self-consistent Compliance(SCC) scheme. Also a Neuro-Fuzzy technique is used to describe a constitutive law for the FGM in the same regime. The constitutive models are incorporated in a dynamic finite element code to study the crack propagation in the FGM with various grading patterns across the cracked plate. A fuzzy technique is utilized to perform a T* controlled crack propagation, thus predicted crack speed during the natural propagation in the varying toughness medium.

KEYWORDS

Functionally Graded Material, Self-consistent Scheme, Equivalent Inclusion Method, Localized Rigidity Model, Fracture, T*-integral

INTRODUCTION

In meso-mechanical point of view, the Functionally Graded Material(FGM) is a composite, in which the material composition continuously varies with location. A heat shield type FGM employs a ceramic material in combination with some metals for its counterpart. It is designated to have high resistance to very high temperature and also to have effective removal of the transmitted heat on the other side. If the composite is thin, a very high temperature gradient will occur accompanying extensive thermal stress causing meso-scopic damage as well as macroscopic defects. Assuming the most probable mode of the macro-failure for the FGM will be of fracture, the fracture resistibility is requested as another important function for the FGM. Cracks may emanate from the high temperature side surface in the ceramic, followed by possible propagation into the depth of the material. Hopefully, relatively high toughness of the metal material as counterpart may prevent the crack propagating into the depth, where the fracture toughness would continuously vary with the variation of the volume fraction of the mixed materials. Thus predicting the crack propagation speed in the FGM is important for estimating the performance of the fracture resistibility.

In the present, a theoretical/computational methodology for the analysis of the FGM is introduced, and its

application is made to a dynamically propagating crack running transversely in the FGM, where the intensity of the estimated crack-tip severity is managed to keep in valance with the graded material toughness in the FGM during the propagation. To detect the crack-tip severity, an integral fracture parameter, T*[1], is used. Emphasis is placed on the use of a fuzzy inference algorithm to control the crack speed deduced from the T* values preceding the current crack position.

As to describing the constitutive rule for the FGM, spherical particles of arbitrary size in mesoscale are supposed to be randomly dispersed in the matrix medium. By assuming that the volume fraction of the inclusion is continuously varied, the grading is modeled. Authors have attempted modeling the constitutive law for the graded particle dispersed composite media of thermo-elastoplasticity by neural network scheme[2]. In the present effort, a closed form constitutive model[3] describing the nonlinear material mechanics of the particle dispersed medium is employed.

MODELING

Functionally Graded Material

One of the manufacturing process of the FGM is sintering the powder constituents in the hot isostatic pressure condition. Consider for simplicity the case when the FGM consists of the material of two phases. A schematic representation of such may be depicted in Figure 1(a), where two materials grade from 0 to 100 percent from one to another. On one side, the inclusions of the meso-structure are isolated with each other and suspended in the matrix material. On the other side, the same situation holds, but the constituent materials are reversed. Regarding the inclusion suspended medium as a particle dispersed composite material, the suspended spherical grain model by Kerner[4] was used to describe the constitutive law to evaluate elastic crack in the FGM under a quasi-static thermal shock load[5]. Treating a thermo-elastoplastic FGM, Nakagaki et al[6] devised a neural network procedure to model the constitutive law.

Since the dissemination of Eshelby's equivalent inclusion theory[7] with eigen strain concept and the mean field theory by Mori-Tanaka[8] opened the way to the recent developments of particle dispersed composites. Those are the works represented by Tandon-Weng[9]. Calling their model by EMT, it hypothesize that the constitutive relation between the average stress and average strain in phase is same as that of the monolith material. However, it is found that when the plastic deformation occurs, average stress-strain behavior in the phase is greatly influenced by the volume fraction of particles. This is due to the interaction between particles, which causes localized plastic deformations even at a low global load level. This nonlinearity in the microscopic level is directly reflected to the macroscopic stress and strain behavior of the composite. Thus, the averaged stress and strain in each phase is not constituted by the plastic state of the monolith material.

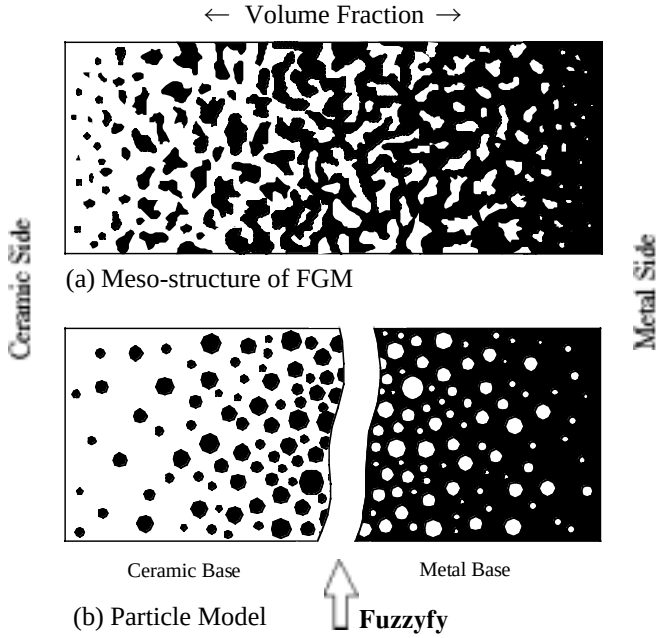

Figure 1: Schematics of (a)FGM and (b)Modeled particle domain

In this paper, we use the Localized Rigidity Method (LRM), in which meso-scopically localized plasticity due to interaction between particles is treated by means of a statistical scheme. Description of the present LRM model with elliptical equivalent inclusions and the pertinent mathematical treatment is given with the use of Gaussian distribution function. Upon relating the stress and the strain at the distributed meso-local level in each phase, the state variables and the constitutive law for the composite is derived.

Localized Rigidity Modeling(LRM)

In order to define precisely the distributed local stress, the entire range of the distributed stress over the phases is divided into a number of segments, in each of which an appropriate elastoplastic constitutive law can be used. Denote the stress in a segment in the matrix phase by $i, (i = 1, 2 \cdots)$, and for the inclusion by $j, (j = 1, 2 \cdots)$. Define the distribution functions over the normalized stress ρ_1^i and ρ_2^j, by $P_1(\rho_1^i)$ and $P_2(\rho_2^j)$ respectively. The stress segment corresponds to some number of small domains in which the stress is ς_1^i or ς_2^j. The volume fractions of the area and can be represented in terms of the distribution function.

$$\Delta c_i = (1 - f)\, P_1(\rho_1^i)\, \Delta\rho_1^i \tag{1}$$

$$\Delta c_j = f\, P_2(\rho_2^j)\, \Delta\rho_2^j \tag{2}$$

The sum of the volume fraction of the segments in the matrix and the particles should be equal to their total volume fraction of the matrix and the inclusions. The distribution function will be defined such that the sum of the segments are unity. Therefore we have,

$$\sum_{i=1}^{n} \Delta c_i = 1 - f \tag{3}$$

$$\sum_{j=1}^{m} \Delta c_j = f \tag{4}$$

Since the inclusions are thought to be randomly located in the medium, a Gaussian type regular distribution function is assumed for the stress in the matrix

$$P_1(\rho_1^i) = \frac{1}{\sqrt{2\pi}\phi} e^{-\frac{1}{2\phi^2}(\rho_1^i - 1)^2} \tag{5}$$

where, ϕ is the variance. According to the theory of statistics, 99.7% of the stress distribution between the maximum and the minimum in the matrix will fall within the limits such that,

$$(1 - 3\phi) \le \rho_1^i \le (1 + 3\phi) \tag{6}$$

Therefore, an approximation is made to define the normalized minimum and the maximum stresses such that

$$\rho_1^{\min} = (1 - 3\phi) \qquad \text{and} \qquad \rho_1^{\max} = (1 + 3\phi) \tag{7}$$

Since a stress concentration often occurs at the interface between the matrix and the inclusions, the stress distribution along the surface of the inclusion must be known. Utilizing the works by Mura-Cheng[10] and Tandon-Weng[9] for an ellipsoidal inclusion under the uni-axial stretch, the variance in the present model can be defined.

$$\phi = \frac{f\,|g_1 - g_2|}{6} \tag{8}$$

where, and are the parameters of the minimum and the maximum stresses such that,

$$g_1 = \sqrt{\frac{1}{2}\left[\left(q_1 - \frac{p_1 + \hat{\gamma} p_2}{1 - \hat{\gamma}^2} - q_2\right)^2 + \left(q_1 - \frac{p_1 + \hat{\gamma} p_2}{1 - \hat{\gamma}^2}\right)^2 + (q_2)^2\right]} \tag{9}$$

$$g_2 = \sqrt{\frac{1}{2}[(q_1 - \frac{p_2}{1-\hat{\gamma}} - q_2)^2 + (q_1)^2 + (\frac{p_2}{1-\hat{\gamma}} + q_2)^2]} \tag{10}$$

and further where, p_1, p_2, p_2 and q_2 are the parameters given in Tandon-Weng's.

At the local stress segment level, it is assumed that the stress and the strain are incrementally related in the homogeneous material fashion, so that the stress and the strain increments are related such that,

$$d\underset{\sim}{\varepsilon}_1^i = \underset{\sim}{\Gamma}_1^i : d\underset{\sim}{\sigma}_1^i \qquad \text{and} \qquad d\underset{\sim}{\varepsilon}_2^j = \underset{\sim}{\Gamma}_2^j : d\underset{\sim}{\sigma}_2^j \tag{11}$$

The average strain increment over the macro composite will be

$$d\underset{\sim}{\varepsilon}_0 = \sum_{i=1}^{n} \Delta c_i \, \underset{\sim}{\Gamma}_1^i : d\underset{\sim}{\sigma}_1^i + \sum_{j=1}^{m} \Delta c_j \, \underset{\sim}{\Gamma}_2^j : d\underset{\sim}{\sigma}_2^j \tag{12}$$

On the basis of the self-consistency concept, the final incremental form of the macro average constitutive relation for the nonlinear composite will be given as in the following:

$$d\underset{\sim}{\varepsilon}_0 = \hat{\underset{\sim}{\Gamma}} : d\underset{\sim}{\sigma}_0 \tag{13}$$

where,

$$\hat{\underset{\sim}{\Gamma}} = \sum_{i=1}^{n} \Delta c_i \, \underset{\sim}{\Gamma}_1^i : \underset{\sim}{C}_0^i + \sum_{j=1}^{m} \Delta c_j \, \underset{\sim}{\Gamma}_2^j : (\underset{\sim}{I} \otimes \underset{\sim}{I} + \underset{\sim}{A}_0^j : \hat{\underset{\sim}{E}}_0) \tag{14}$$

Since the quantities with hat in both the hands of the above are the global quantities and are unknown, the equations must be solved by some numerical scheme. Detail of the LRM constitutive model is found in Ref. [11].

Fuzzy Treatment

As it was mentioned earlier, the constituent material of the FGM's meso-scopic phase structure reverses from one end to the other, as depicted in Figure 1(a). For the heat shield type FGM, candidate constituents are a ceramic and a metal. On one end, the metal particles are suspended in the ceramic medium, and vice versa on the other end. In between, a type of bone mellow structure, which dominates the most of the domain, exists, and it is difficult to say which constituent takes the role of the matrix or the inclusion. Thus, suggested in Figure 1(b) shows a meso-structure model for the FGM, in which two sets of particle dispersed domains are considered, one with the ceramic as matrix and one with the metal as matrix. In both the cases, the inclusions are of spherical or ellipsoidal geometry so that the LRM equivalent inclusion model can be utilized. Between these two cases, considerable discrepancy will be seen in the material nonlinear stress-strain behaviors even when the distribution pattern of the volume fraction of the constituents are identical each other. In order for modeling the FGM composites of such an ambiguous meso-structural media, the present paper suggests the use of a fuzzy algorithm as one of an appropriate mean.

In the real FGM, the dominant volume fraction of, say, the ceramic does not warrant that the ceramic should takes the role of the matrix. Thus, the crisp data of the volume fraction are selected to be an input in the present fuzzy scheme, to be processed to determine its fuzzy membership grade via a membership function such that,

$$F(x) = \exp\,[-\frac{1}{a^2}(x-b)^2] \tag{15}$$

The membership grade of the counterpart is also calculated to be added to the former by Max-min scheme. The results are de-fuzzified to estimate a weight between the two estimates by the LRM constitutive law.

In the present work, the fuzzy scheme is used in twofold. One is for the aforementioned FGM grade modeling. Another is for controlling the fast crack speed running transversely in the FGM plate, where the material composition as well as the fracture toughness are varying. The mixing rule for the fracture toughness has not been established. Hence, known values for the toughness of each constituent were mixed in the linear mixing rule along the volume fraction of the constituents to be converted to obtain the critical . For the latter, the fuzzy

is used to minimize the gap between the material parameter and the calculated T* from the previous load step to predict the most probable time increment at the current step. Thus the scheme for the T* controlled crack propagation in the FGM is established.

RESULTS

An edge cracked plate of a transversely graded FGM at 800ºC is under tension on the top and the bottom edges of the plate. The FGM is assumed to be composed of a ceramic and a titanium alloy. Figure 2(a) depicts the plate geometry and the loading condition. The metal is thermo-elastoplastic while the ceramic is considered to behave merely elastic. The plate was statically loaded until the crack-tip attain the criticality.
Analysis of the problem was performed with the use of a finite element method, where the constitutive law for the FGM is mathematically described by the LRM model and the fuzzy inference scheme as shown in the above.
To evaluate the crack severity, the crack-tip parameter, T* contour integral, is employed such that,

$$T^* = \int [(W + T)n_1 - n_j \sigma_{ij} u_{i,1}]ds - \int_{V-V_\rho} [W_{,1} + \gamma \dot{u}_i \dot{u}_{i,1} (G_i - \gamma \ddot{u}_i) u_{i,1} - \sigma_{ij} \varepsilon_{ij,1}]dV \qquad (16)$$

At the moment when the estimated T* reaches the critical value, the crack was set to dynamically propagate across the plate. During the propagation, the crack running speed was controlled by the fuzzy algorithm so that the T* keeps agreement with its varying critical values during the propagation described in the above.

The results shown in the rest are those for a linearly graded FGM plate. Figure 2(b) shows the calculated T* values versus crack depth during the crack propagation compared with the critical , which is a unique material property graded along the material design for the FGM plate. Reasonable agreements between the two in average over the entire propagation indicate a successful simulation of the present T* based natural crack propagation in the graded FGM with the fuzzy procedure. Some difficulty was encountered at the incipient crack propagation resulting over estimate of T*. It was because the crack speed was zero in the preceding time step. It may not be difficult to find some remedial procedure to fix the misfit.

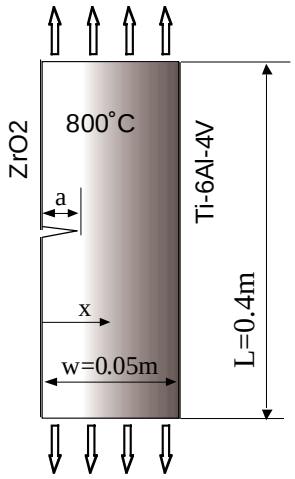

(a)

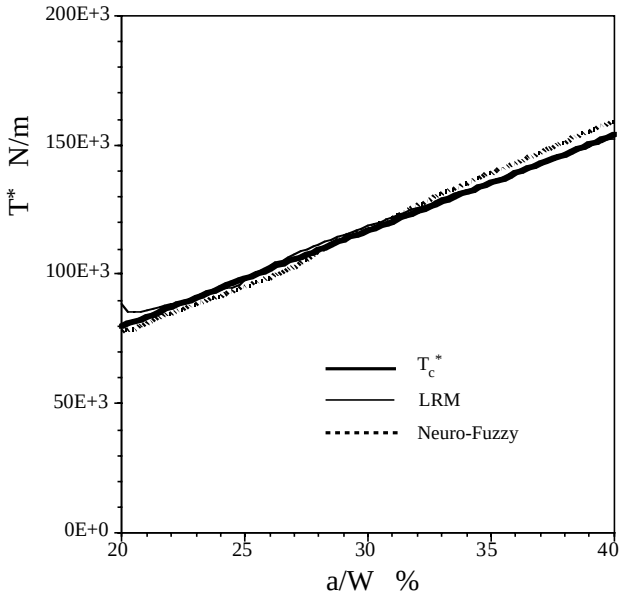

(b)

Figure 2: (a) Cracked FGM plate under tension and (b) Fuzzy controlled T* results

Shown together in the figure is the result for the same problem with the same procedure but calculated using the constitutive model obtained by a neural network scheme[2]. In this case also a reasonable simulation is seen to be performed.

Figure 3(a) shows the predicted crack speeds during the T* controlled crack propagation in the FGM plate thus simulated. In this result, the starting speed with LRM constitutive law much differs from that by the Neuro-Fuzzy calculation.

Shown together in the figure is another estimate of the crack speed where the FGM constitutive law was modeled by a neural network scheme instead of the closed form LRM. Although the incipient misfit in T* might cause in the LRM result the unreasonably high value of predicted crack speed, overall discrepancy between the two results are quite different. Far field quantities such as the remote stress at the plate ends do not observe a quite discrepancy between the two cases, but the propagation speed is sensitive and reflects the material description model. Therefore the present study warns the significance of the proper description of the constitutive law especially predicting the possible crack arrest in the very inhomogeneous material such as FGM.

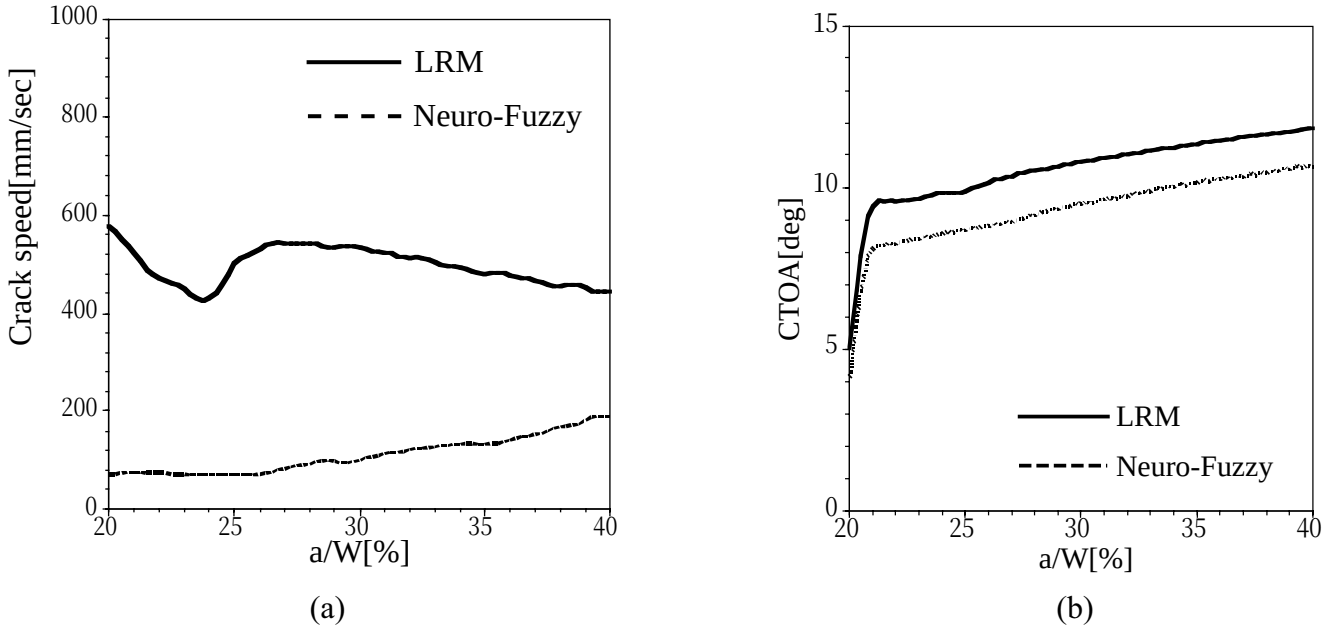

Figure 3: (a) Predicted crack speed and (b) Crack-tip opening angle during T* controlled propagation

During the crack propagation, the crack-tip opening angle is calculated and shown in Figure 3(b) for the two procedure. Continuous increase of CTOA indicates possible ductile fracture in the area.

REFERENCES

1. Atluri, S. N., Nishioka, T., Nakagaki, M.(1984): *Engineering Fracture Mechanics,* 20-2, pp209- 244.
2. Nakagaki, M.,Wu Y., Hagihara,S.(1998): *Key Engineering Materials*, 145-149, I, pp.333-342.
3. Nakagaki, M.,Wu Y., Brust, F. W.(1999):*Computer Modeling and Simulation in Engineering*, Vol 4, No.3, pp186-192.
4. Kerner, E. H.(1956): *Proc. of Phys. Soc.*, 69 B, pp802-807.
5. Nakagaki, M., Matsukawa, M., Inaba, T., and Kuranari, R.(1993): *Proc. of Asian Pacific Conference on Fracture and Strength* 93, pp683-688.
6. Nakagaki, M., Wu, Y., Shibata, Y., Hagihara, S (1996): *Proceedings of Localized Damage* IV, pp543 -550.
7. Eshelby, J.D.(1957): *Proc. of the Royal Society of London*, Series A, Vol.241A, pp.376-396.
8. Mori,T., Tanaka,K.(1973): *Acta Metallurgica*, Vol.21, p.571-574.
9. Tandon,G.P.,Weng, G.J.(1988):*J. of Applied Mechanics, Transaction of ASME*, Vol.55, p.126-135.
10. Mura, T., Cheng, P.C. (1977):*J. of Applied Mechanics, Transactions of the ASME*, Vol.44, pp.591-594.
11. Wu, Y. , Nakagaki, M. (1998): *Transaction of JSME* , Vol. 64, No.622, pp.1646-1653.

ORAL REFERENCE: ICF100132OR

Major aspects of Mixed-Mode problems

H.A. Richard

Institute of Applied Mechanics, University of Paderborn
D – 33098 Paderborn, Germany

ABSTRACT

In this paper a survey on Mixed-Mode fracture and fatigue problems is carried out. At first the overlapping of fractures Modes I and II will be considered. For such loading situations both the occurrence of unstable crack growth and the kinking angle of the crack can be predicted by different fracture criterions. For the case of an unstable propagation of a crack under superimposed Mode I and Mode II loading those criteria have proven their reliability for homogenous materials, which has already been shown by various experimental research. If an existing crack is subjected to a Mixed-Mode loading, the direction of crack propagation changes. The kinking angle for such a crack can be predicted very well by the existing criteria. It is notable, that a delayed crack growth can be observed when a kinking of a fatigue crack takes place.
The three-dimensional crack growth in arbitrary structures and components can generally be characterized by the occurrence of all the crack Modes I, II and III. For all these Mixed-Mode loading situations this paper will present the theoretical fundamentals, experimental research and concepts for the prediction of their effects.

KEYWORDS

Mixed-Mode fracture, fatigue crack growth, fracture criteria, prediction concepts, All-fracture-modes-specimen

INTRODUCTION

In various fields of engineering a large number of crack problems can be found, that are caused by Mixed-Mode loading at the crack tip. These loading conditions may occur e.g. as a result of superimposed stresses on construction components, oblique or curved cracks, multiple cracks or cracks in the vicinity of notches.
In the past 2D-problems of crack growth under Mixed-Mode I and II loading conditions have attracted much attention. A number of fracture criteria for predicting the onset of fracture and its direction are well established [1-5]. In particular the CTS-specimen together with the related special loading device [5,6] and detailed theoretical, experimental and computational investigations have contributed to the current state in the field [7-9]. So this problem is now almost understood. In contrast to this, for the more general 3D Mixed-Mode problems only a few approaches are known and there is still a lack of understanding. Indeed in some recent papers [10-12] investigations regarding superimposed Mode I and Mode III can be found, but those results can not be applied to cases of Mode II and III and can especially not be generalised to cases, where all basic fracture modes I, II and III are involved.

TWO-DIMENSIONAL MIXED MODE FRACTURE AND FATIGUE

In 2D or plane Mixed-Mode cases the basic relations can be presented in the form of a fracture curve and a threshold curve in a K_I-K_{II}-diagram (see the grey region in the K-diagram Figure 1). Unstable fracture will occur, when the loading condition at the crack tip, characterised by the stress intensity factors K_I and K_{II} reach any point of the 2D-fracture curve [5,13]. For Mixed-Mode and Mode II fracture the crack will kink off form its initial direction (see Figure 2). For isotropic materials the kinking angle φ_0 is a function of the K_{II}/K_I ratio only (Figure 3).
Besides other criteria [1-4], the K_I-K_{II}-fracture curve can be described by the following relation

$$K_V = \frac{K_I}{2} + \frac{1}{2}\sqrt{K_I^2 + 4(\alpha_1 K_{II})^2} \le K_{IC} \tag{1}$$

In Eqn. 1 K_V is the effective stress intensity factor and the parameter α_1 is the ratio K_{Ic}/K_{IIc} of the fracture toughness values for pure Mode I and pure Mode II loading. For some materials the value α_1 is determined: AlCuMg1: α_1=1.05; PMMA: α_1=1.08; PVC: α_1=0.93. The well established maximum tangential stress criterion [1] and the maximum energy release criterion [3] can be well approximated by this formula with α_1=1.15. The related kinking angle can be predicted by the following relation[5]

$$\varphi_0 = \pm\left[155{,}5° \frac{|K_{II}|}{|K_I| + |K_{II}|}\right] - 83{,}4° \left[\frac{|K_{II}|}{|K_I| + |K_{II}|}\right]^2 \tag{2}$$

in which $\varphi_0>0$ has to be considered for $K_{II}<0$. A comparison of Eqn. 2 with experimental findings is given in Figure 3 (continuous line: Eqn. 2).

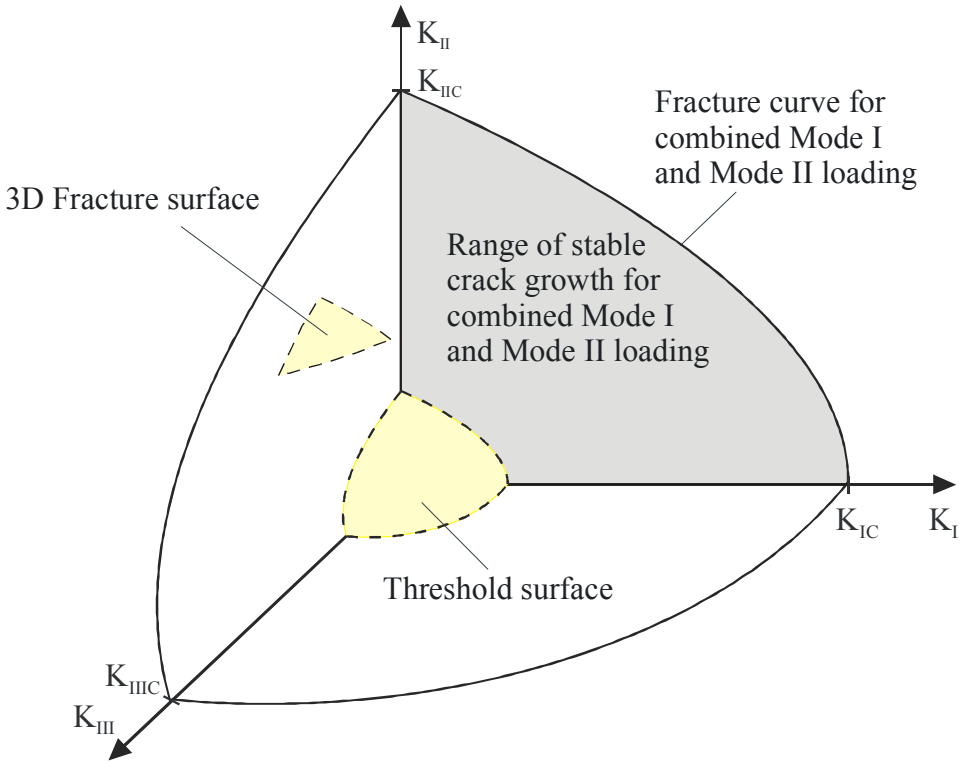

Figure 1: K-diagram for Mixed-Mode I+II+III loading

For plane Mixed-Mode cases fatigue crack growth (stable crack growth) can only develop, if the crack tip loading conditions are characterised by a point lying between the threshold curve and the fracture curve (Figure 1). In that case the effective cyclic stress intensity factor

$$\Delta K_V = \frac{\Delta K_I}{2} + \frac{1}{2}\sqrt{\Delta K_I^2 + 6\Delta K_{II}^2} \tag{3}$$

is characterising the stable crack growth, which means that the crack growth rate da/dN is a function of ΔK_v.

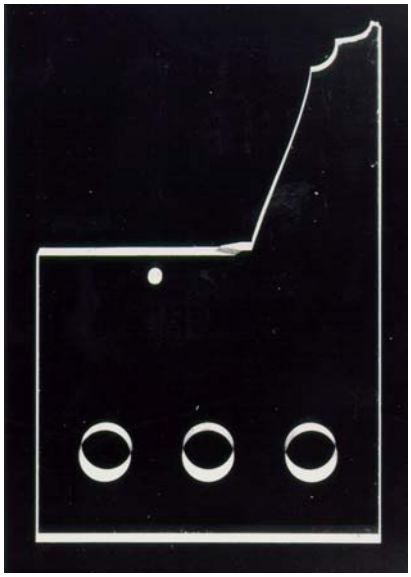

Figure 2: CTS-specimen broken under pure Mode II loading

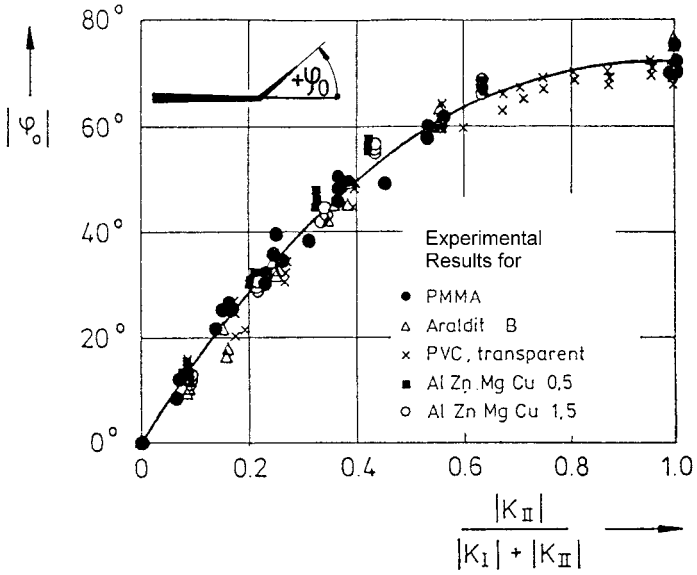

Figure 3: Measured crack deflection angels for Mixed-Mode-I+II loading

Also under fatigue loading conditions the kinking of the crack as described above can be observed. After the kinking the ratio $\Delta K_{II}/\Delta K_I$ tends towards 0, which means, that the crack propagates after the kinking without any abrupt change of direction as long as no further loading change occurs. The process of kinking results in a notable retardation of the crack growth, which can be seen in Figure 4.

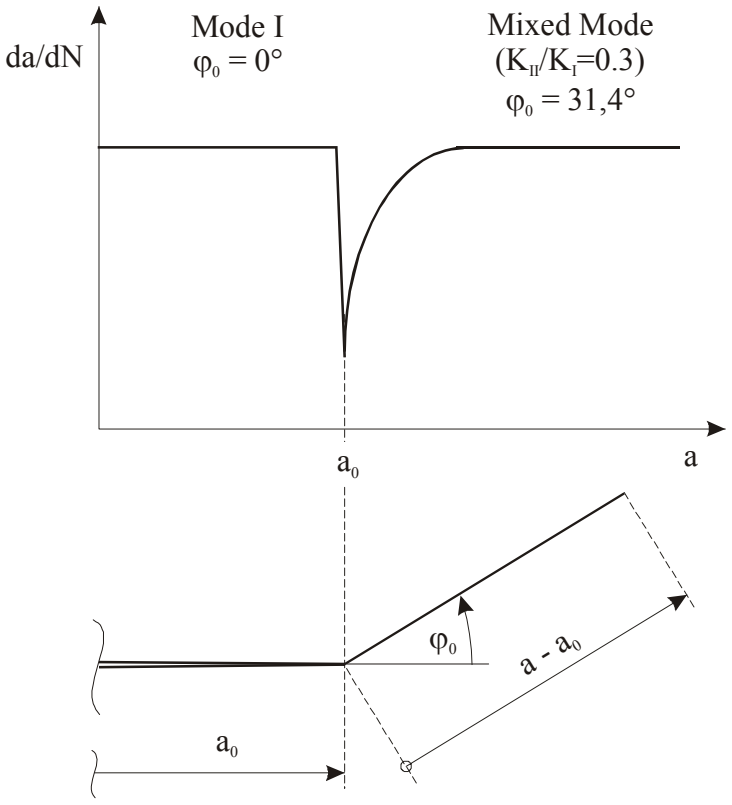

Figure 4: Retardation of crack growth rate during the kinking process after a Mode I to Mixed Mode load change

THREE-DIMESIONAL MIXED MODE FRACTURE AND FATIGUE

In 3D-Mixed-Mode cases, where all basic fracture Modes I, II and III are involved, the situation can be explained by the aid of Figure 1.
Unstable crack growth will occur, if a local loading condition along the crack front reaches a point of the fracture surface, which expands between the fracture limit curves for Mode I and II, Mode I and III and Mode II and III. This fracture surface can be described by the following relation [14]

$$\left(\frac{K_I}{K_{IC}}\right)^u + \left(\frac{K_{II}}{K_{IIC}}\right)^v + \left(\frac{K_{III}}{K_{IIIC}}\right)^w = 1. \tag{4}$$

With u=1, v=w=2 and $\alpha_1=K_{Ic}/K_{IIc}$ and $\alpha_2=K_{Ic}/K_{IIIc}$ by Eqn. 4 a fracture criterion

$$K_V = \frac{K_I}{2} + \frac{1}{2}\sqrt{K_I^2 + 4(\alpha_1 K_{II})^2 + 4(\alpha_2 K_{III})^2} \le K_{IC} \tag{5}$$

can be established, which covers also most of the general cases, in which all fundamental fracture modes are superimposed. Whereas for plane Mixed-Mode problems the fracture limit curve is well established with $\alpha_1=1.155$, the value to be taken for α_2 has not yet been fixed. In three-dimensional Mixed-Mode cases fatigue crack propagation can be observed, if the local crack tip loading conditions, characterised by the stress intensity factors K_I, K_{II} and K_{III} can be found in between the treshold-surface and fracture surface in the K-diagram (Figure 1).

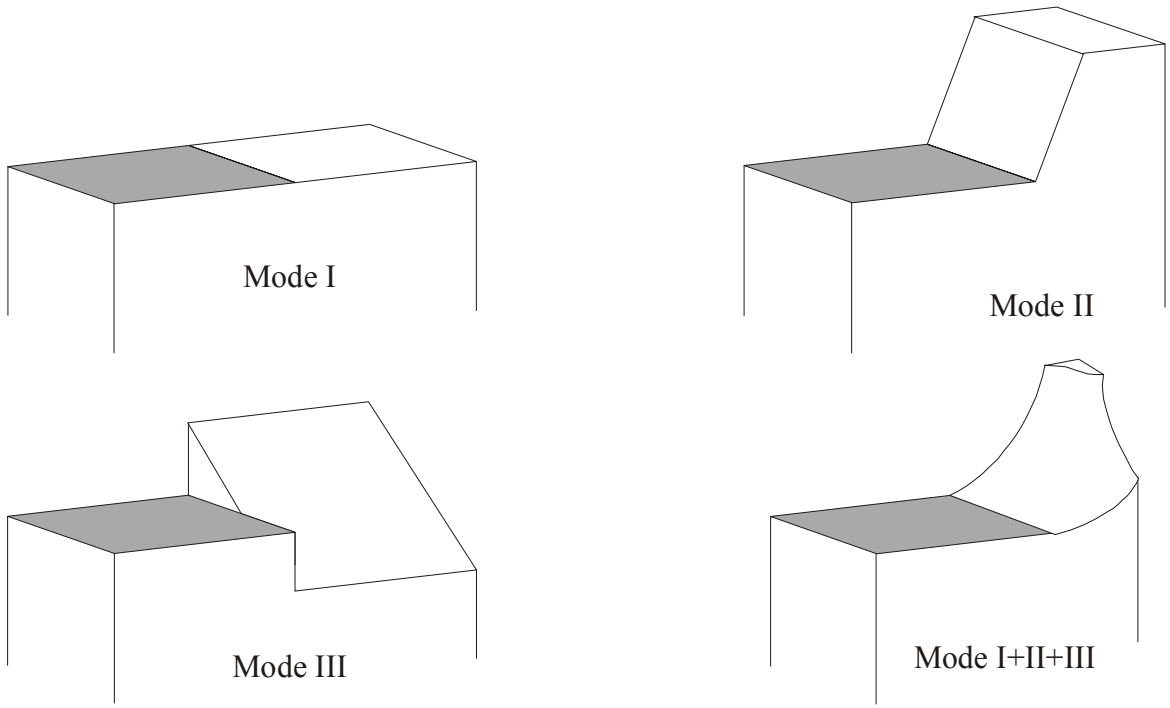

Figure 5: Principle orientation of the fracture surfaces for different fracture modes

The prediction of fracture surfaces, that describe stable and unstable crack growth (see Figure 5) is widely open. Theoretical approaches e.g. in [2,11] need to be experimentally verified [15]. This is also true for the recently published new criterion [16], which allows a 3D-Finite Element simulation of arbitrary crack problems [17,18].

For experimental investigations of crack growth and fatigue under different Mixed-Mode loading conditions several types of specimens are available [1,5,10]. But in fact none of theses specimens covers neither the full range of all basic fractures modes nor all combinations thereof. These requirements are fulfilled so far only by the AFM-specimen [14,15] in combination with the special loading device (Figure 6). After an optimisation of the AFM-specimen (Figure 7) many fatigue and fracture experiments are necessary to verify

the theoretical concepts and criteria and the results of the numerical studies already performed as well as to investigate the so far unsolved Mixed-Mode problems.

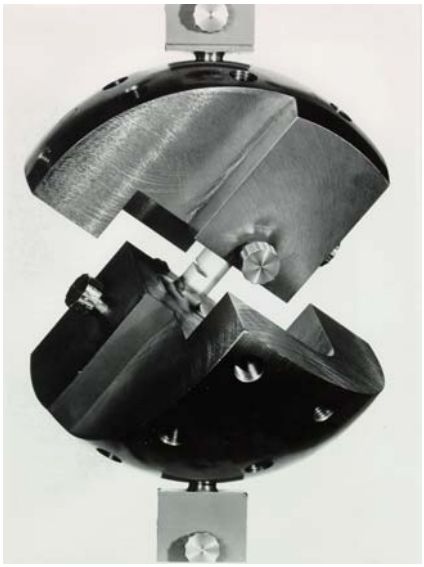

Figure 6: Loading device for the AFM-specimen developed for the superposition of Mode-I+II+III

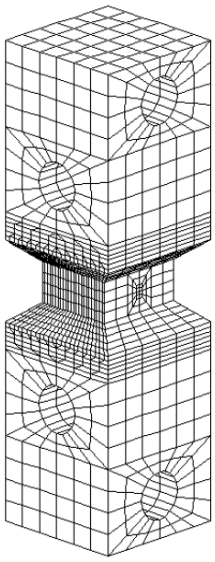

Figure 7: Finite Element model for a modified AFM-specimen

CONCLUSIONS

In this paper major aspects of Mixed-Mode crack problems are described, that are of especial relevance for industrial components and structures. It becomes apparent, that two-dimensional fracture problems in isotropic materials are widely solved. In contrast to this, further investigations of fatigue crack propagation problems especially in regions near the threshold value have to be carried out.
For three-dimensional fracture and fatigue cases many further experimental and numerical studies have to performed.

REFERENCES

1. Erdogan, F. and Sih, G.C. (1963). *Journal of Basic Engineering* 85, 519.
2. Sih, G.C. (1974). *International Journal of Fracture* 10, 305.
3. Nuismer, R.J. (1975). *International Journal of Fracture* 11, 245.
4. Amestoy, M., Bui, H.D., and Dang-Van, K. (1981). In: *Advances in Fracture Research,* pp. 107-113, Francois, D. (Ed).
5. Richard, H.A. (1985), Bruchvorhersagen bei überlagerter Normal- und Schubbeanspruchung von Rissen. *VDI-Forschungsheft* 631, VDI-Verlag, Düsseldorf.
6. Richard, H.A. and Benitz, K. (1983). *International Journal of Fracture* 22**,** R55.
7. Aoki, S., Kishimoto, K., Yoshida, T., Sakata, M. and Richard, H.A. (1990) *J. of Mechanics and Physics of Solids* 38**,** 195.
8. Richard, H.A., Linning, W. and Henn, K. (1991). *Forensic Engineering*, Vol. 3, Nos. 2/3, 99.
9. Richard, H.A. and Schöllmann, M. (1999). In: *Fatigue `99,* Vol. 2, pp. 839-844, Wu, X.-R. and Wang Z.-G. (Eds.). Higher Education Press, Peking.
10. Davenport, J.C.W. and Smith, D.J. (1993). *Fat. Fract. Engng. Mater. Struct*., 16, 10, 1125.
11. Pook, L.P. (1995). *Int. J. Fatigue* Vol. 17, No. 1**,** 5.
12. Hull, D. (1995). *Int. J. Fracture* 70, 59.
13. Richard, H.A. (1984). In: *Application of Fracture Mechanics to Materials and Structures*, pp. 309-316, Sih, G.C. et al., The Hague.
14. Richard, H.A. and Kuna, M. (1990). *Engng. Fracture Mech*. 35, 949.

15. Buchholz, F.G. and Richard, H.A. (2000). In: *Meso-mechanical aspects of material behaviour, Proceedings of the special symposium, Yufuin, Oita,* pp. 1-17, Kishimoto, K., Nakamura, T. and Amaya, K. (Eds). Tokyo Institute of Technology, Tokyo.
16. Schöllmann, M., Kullmer, G., Fulland, M. and Richard, H.A (2001). *6th International Conference on Biaxial and Multiaxial Fatigue and Fracture,* NN.
17. Fulland, M., Schöllmann, M. and Richard, H.A. (2000). In: *Advances in Computational Engineering & Sciences*, Vol. 1, pp. 948-953, Atluri, S.N. and Brust, F. (Eds). Tech Science Press, Palmdale.
18. Richard, H.A., Schöllmann, M., Fulland, M. and Sander, M. (2001). *6th International Conference on Biaxial and Multiaxial Fatigue and Fracture,* NN.

ORAL REFERENCE: ICF100825OR

MATERIAL RESPONSE WITH THE CELL METHOD

F. Cosmi

Department of Energetics, University of Trieste,
via A. Valerio 10, 34127 Trieste, IT

ABSTRACT

A new numerical model estimating the effect of randomly located micro-cracks on the structural response of a material is presented. Both heterogeneities of the structure and stress concentrations are taken into account by the model, that makes use of an homogeneous matrix in which randomly distributed cracks are present. The Cell Method is a recently developed numerical method that can be used to solve such a model. Both elastic and elastic-plastic behaviours can be included in the model. The Cell Method is presented and results of simulations from tests in both the elastic and plastic fields are discussed.

KEYWORDS

Damage, structural response, numerical method, cells.

INTRODUCTION

A lot of work has been done in the past in order to estimate the effect on the material properties of a low concentration of elliptical and circular voids. A self-consistent approximation of a material with identical polygonal randomly oriented voids has been proposed in [1]. In the crossover regime beam lattice models [2] along with interpolation functions [3] have been proposed. Finite element models have also been used to estimate the stiffness of a 2D initially elastic continuum containing square perforations [4]. A new model for the investigation of the effect of randomly located voids on the structural response of a material is presented in this paper. The discrete model makes use of a homogeneous matrix, in which randomly distributed cracks are present, as shown in Figure 1.

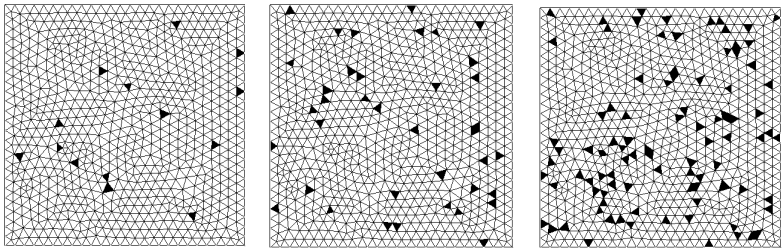

Figure 1: Randomly distributed void cells in homogeneous matrixes.

The Cell Method concept is deeply different from that of other widely used numerical methods such as FEM, and brings some advantages with it. As will be shown, CM is a "real" discrete method, in the sense that field equations are directly written for a whole region and no differentiation is needed to form the field equations. CM is thus applicable in all those cases in which variables cannot be differentiated, for example when the displacement field undergoes large variations, i.e. when the size of the heterogeneities is the same scale of that of the mesh [5]. A model such as the mentioned homogeneous matrix with distributed heterogeneities can be then solved with the Cell Method leading to consistent results.

It must be also mentioned that some aspects of the Cell Method may recall the Finite Volumes Method or the so-called *direct* – or *physical* – approach [6]. These methods did not have much success, maybe due to an intrinsic difficulty to develop higher order elements. On the contrary, higher order interpolation functions are easily implemented in CM.

When compared, CM results agree with those obtainable with other numerical methods, although convergence and accuracy are better than those obtained with FEM with the same interpolation order [7].

The present research makes uses only of linear interpolation functions and focuses on the other mentioned peculiar aspect of the Cell Method: the possibility to have heterogeneities the same size of that of the mesh.

THE CELL METHOD FOR PLANE ELASTICITY

The Cell Method has been recently introduced by E. Tonti [8, 9] and is currently being applied in several fields, such as thermal conduction, electromagnetism, mechanics of porous materials, and fracture mechanics. Application of the method to high porosity materials such as sintered alloys has been discussed in [10], where the Young modulus of four sintered alloys was computed and simulation showed a good agreement with experimental results.

In order to describe the Cell Method for plane elasticity, let us consider a body of constant thickness t, loaded in a plane. The variables used in the problem can be classified in

- *Configuration variables*, that is kinematic variables such as nodal coordinates and displacements, strain tensor, etc.,
- *Source variables*, that is static and dynamic variables such as forces, torques, momenta, etc.
- *Energy variables*, which result from the product of a configuration and a source variable, and which we are not going to use in the following.

According to this classification, the method implies the use of two staggered meshes: configuration variables are to be associated with a primal complex of cells, in this case a Delaunay triangles complex, while source variables are associated with a dual complex, the Voronoi tessellation associated with the primal mesh. Other choices for the dual complex are possible. Each node of the primal cell will be surrounded by a dual cell, which can be regarded as an influence region for the inner node.

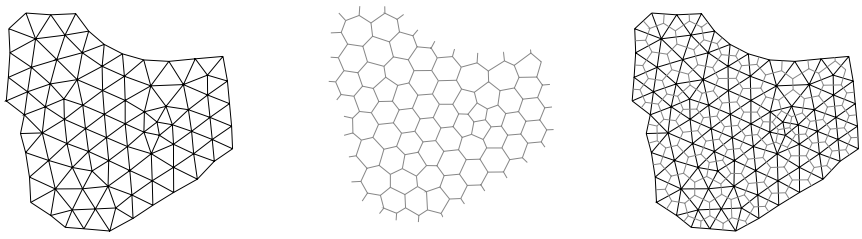

Figure 2: Primal (Delaunay), dual (Voronoi) complexes of cells and their ensemble.

If a Delaunay 3-nodes primal cell is used, the displacement field over the primal cell will be interpolated by a linear function. Strain components in a point inside a cell are given by

$$\{\varepsilon\}_c = [B]_c \{u\}_c$$

where

$$\{\varepsilon\}_c = \{\varepsilon_x \quad \varepsilon_y \quad \gamma_y\}^T, \quad [B]_c = -\frac{1}{2A_c t}\begin{bmatrix} A_{1x} & 0 & A_{2x} & 0 & A_{3x} & 0 \\ 0 & A_{1y} & 0 & A_{2y} & 0 & A_{3y} \\ A_{1y} & A_{1x} & A_{2y} & A_{2x} & A_{3y} & A_{3x} \end{bmatrix}, \quad \{u\}_c = \{u_1 \quad v_1 \quad u_2 \quad v_2 \quad u_3 \quad v_3\}^T,$$

t is the thickness of the sample, A_c the area of the cell, and the meaning of A_{ij} is shown in Figure 3.

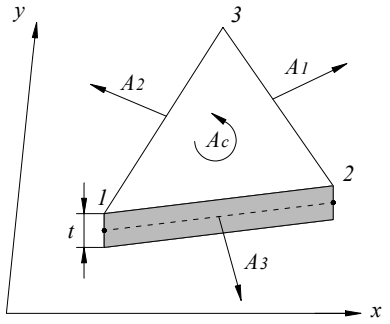

Figure 3: Geometrical quantities.

Introducing the constitutive matrix for the primal cell $[D]_c$ we may write the constitutive equation in the usual form

$$\{\sigma\}_c = [D]_c \{\varepsilon\}_c = [D]_c [B]_c \{u\}_c$$

In order to write equilibrium equations for the influence region of the node, we shall now need to express the forces acting through each side of the dual polyhedron surrounding the node.

As expected using a linear interpolation of the displacement field, strain and stress tensor components are constant within each primal cell. As a consequence, the surface force $\boldsymbol{T}$ (see Figure 4) will be given by

$$\begin{Bmatrix} T_{1x} \\ T_{1y} \end{Bmatrix} = \frac{1}{2}\begin{bmatrix} A_{1x} & 0 & A_{1y} \\ 0 & A_{1y} & A_{1x} \end{bmatrix}\begin{Bmatrix} \sigma_x \\ \sigma_y \\ \tau_{xy} \end{Bmatrix}$$

and for the three nodes of a cell

$$\{T\}_c = -tA_c [B]_c^T [D]_c [B]_c \{u\}_c = -[K]_c \{u\}_c \tag{1}$$

where $\{T\}_c = \{T_{1x} \quad T_{1y} \quad T_{2x} \quad T_{2y} \quad T_{3x} \quad T_{3y}\}^T$ and $[K]$ represents the 6x6 stiffness matrix for the cell.

We shall call $\tilde{U}_h$ the dual cell surrounding node h (see Figure 5), $\boldsymbol{T}_h$ the total force acting on the boundary of $\tilde{U}_h$ - due to all the cells that surround node h-, $\boldsymbol{F}_h$ the resultant of volume forces and of external forces acting on $\tilde{U}_h$ through the boundary cells:

$$\boldsymbol{T}_h = \sum_c \boldsymbol{T}_h^c, \quad \boldsymbol{F}_h = \sum_c \boldsymbol{F}_h^c + \sum_c \boldsymbol{B}_h^c.$$

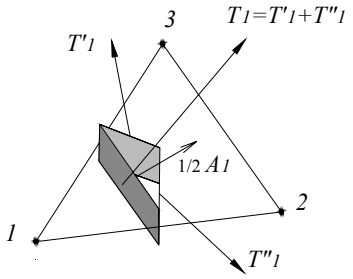

Figure 4: Forces acting through the sides of the dual cell of node *1*.

Equilibrium can be then written for region $\tilde{U}_h$:

$$\boldsymbol{T_h} + \boldsymbol{F_h} = 0$$

that is a set of $2n$ linear equations in the $2n$ unknowns u_{ix}, u_{iy} (i=1,…,n) which can be also written as

$$[K]\{u\} = \{F\} \tag{2}$$

and solved with the usual methods.

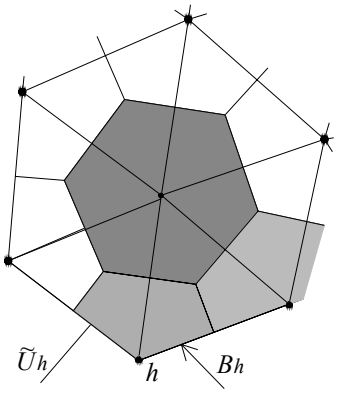

Figure 5: Equilibrium of the dual cell of node *h*.

SIMULATIONS AND DISCUSSIONS

It can be easily seen that the constitutive matrix may vary freely from one cell to the neighbour. As a consequence, the size of the heterogeneities can be the size of the mesh.

In a first set of simulations a 1498 cells matrix was tested in the elastic field. A number n of cells (see Figure 1) was set to void in each simulation and a tensile test was performed imposing a displacement on the right end of the sample, while the left end was constrained, though allowing lateral contractions of the sample. Figure 6 shows the ratio between computed Young modulus and the unimpaired one E^*/E vs. f, where $f=n/N$, n= number of void cells, N=total number of cells, E=210 GPa. For each void density 5 simulations were run. Porosity being equal, fluctuations of Young modulus can be observed in the graph, due to different distributions of the void cells, whose location varies randomly from one simulation to another. The plotted line corresponds to the linear fit with slope –2.47. The decrease in stiffness is similar to that reported in [1, pp.360-361] for FEM simulations with square perforations, although less pronounced. Figure 7 shows the stress concentrations near the void cells (black) in one of the simulations.

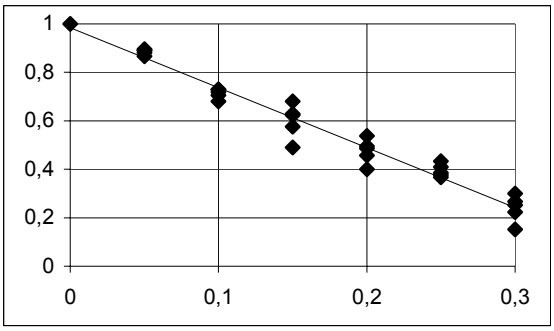

Figure 6: Cell method estimates of stiffness *E*/E* vs. *f*.

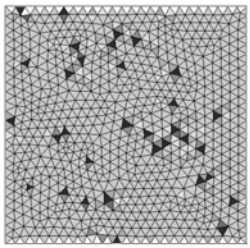

Figure 7: Stress concentrations near the void cells (black) in one of the simulations.

The ratio *E*/E* vs. *f* with low void concentrations is shown in Figure 8 for 25 simulations on a 1498 cells matrix. Small fluctuations of Young modulus can be observed in the graph. The plotted line corresponds to the self-consistent model proposed in [2], which assumes a quicker decrease of stiffness (slope –4.2) than the one computed with the proposed method.

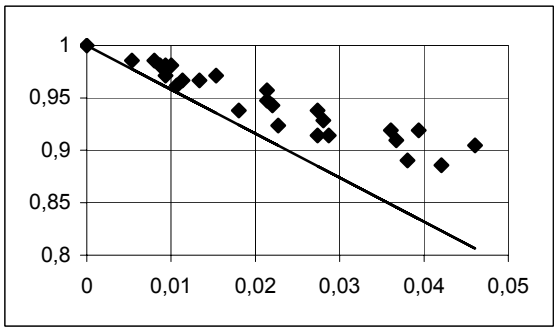

Figure 8: Young modulus *E*/E* vs. *f*.

PLASTICITY

Plasticity may also be implemented in the framework of the Cell Method. An elastic perfectly plastic material and von Mises yield condition have been assumed. For a primal cell

$$\{\sigma\}_c = [D]_c[\{\varepsilon\}_c - \{\lambda\}_c]$$

where $\{\lambda\}_c$ represents the homogeneous inelastic strain tensor for cell *c*. Equation (1) becomes now

$$\{T\}_c = -[K]_c\{u\}_c + \frac{1}{2}[A]_c^T[D]_c\{\lambda\}_c = -[K]_c\{u\}_c + [L]_c\{\lambda\}_c \tag{3}$$

and the fundamental equation (2) in incremental terms is

$$[K]\{\Delta u\} = \{\Delta F\} + [L]\{\Delta\lambda\} \tag{4}$$

The non-linear incremental problem is solved dividing the load history into steps, at the beginning of which displacements and internal stresses are known, and considering a backward difference integration scheme. Equation (4) can be solved for $\{\Delta u\}$, the second invariant of the deviatoric stress computed, and von Mises condition used to update $\{\Delta\lambda\}$. The process is repeated until convergence is obtained, then a new step is considered. Figure 9 shows the progressive plasticization of a 1498 cells matrix with 33 void cells, yield strength Ry = 430 MPa. From simulations, E^* = 195 GPa in the initial, elastic, part of the diagram.

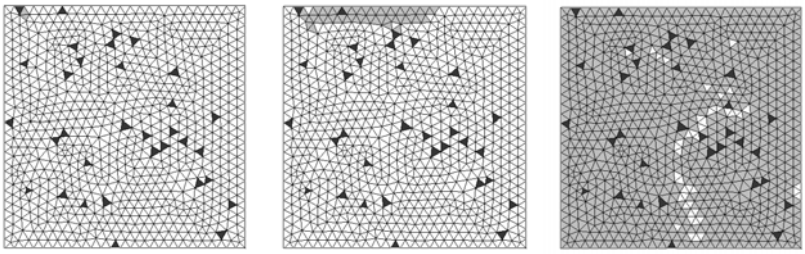

Figure 9: The model with void cells (black), initial and progressive plasticization (grey).

The result of the simulation is reported in Figure 10 in the form of a stress-strain plot. Figure 10 shows also the stress-strain curve obtained from simulation running an unimpaired matrix (E = 210 GPa).

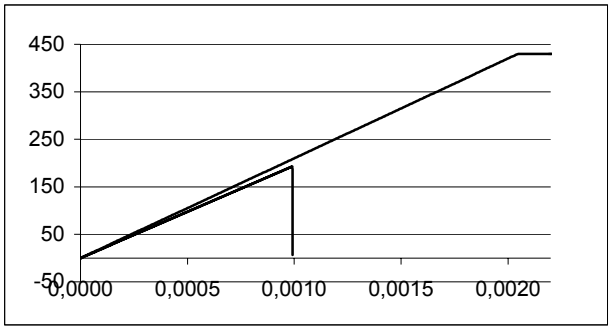

Figure 10: Stress-strain curve of 4198 cells matrix, with 33 and without void cells.

CONCLUSIONS

A new numerical model, consisting of a homogeneous matrix in which randomly distributed cracks are present, has been employed to estimate the effect of randomly located micro-cracks on the structural response of a material. The model considers both heterogeneities of the structure and stress concentrations, and may be solved with the Cell Method. Both elastic and elastic-plastic behaviours have been included in the model, and results of simulations from tests in both the elastic and plastic fields have been discussed.

REFERENCES

1. Jasiuk, I., Chen, J. and Thorpe, M.F. (1994), *Appl. Mech. Rev*., Vol.47, pp. S18-S28
2. Day, A.R., Snyder, K.A., Garboczi, E.J. and Thorpe, M.F. (1992), *J. Mech. Phys. Solids*, Vol. 40, pp. 1031-1051
3. Thorpe, M.F., Jasiuk, I., (1992), *Proc. Royal Soc. London*, Vol. A 438, pp.531-544
4. Krajcinovic, D. (1996) *Damage Mechanics*, Elsevier, North Holland
5. Roux, S. (1990). In *Statistical Models for the Fracture of Disordered Media*, pp. 109-113, Herrmann H.J., and Roux, S. (Eds). Elsevier, North Holland
6. Huebner, K.H. (1995) *The finite element method for Engineers*, John Wiley & Sons, pp. 39-59
7. Cosmi, F. *Computer Modeling in Engineering and Sciences*, to be published
8. Tonti, E., (2000) In *Atti del XIII Convegno Italiano di Meccanica Computazionale*, pp. 1-41, Brescia (IT).
9. Tonti, E., (2001) *Computer Modeling in Engineering and Sciences*, Vol.2, N.2
10. Cosmi, F., Di Marino, F. (2000) In *Proc. of 17th Danubia Adria Symposium on Experimental Methods in Solid Mechanics*, pp. 75-78, Prague, Czech Republic

ORAL REFERENCE: ICF100594OR

MATERIALS WITH CRACKS AND PORES: MICROMECHANICS, CROSS-PROPERTY CORRELATIONS AND APPLICATIONS

Mark Kachanov [1] and Igor Sevostianov [2]

[1] Department of Mechanical Engineering, Tufts University
Medford, MA 02155, U.S.A.

[2] Department of Mechanical Engineering, New Mexico State University
Las Cruces, NM 88003, U.S.A.

ABSTRACT

Explicit correlations between two groups of anisotropic effective properties - conductivity and elasticity - are established for porous materials with anisotropic microstructures (non-randomly oriented pores of non-spherical shapes). In the present work, the correlations are derived in the framework of the non-interaction approximation. The elasticity tensor is expressed in terms of the conductivity tensor in the closed form.. Applications to realistic microstructures, containing mixtures of diverse pore shapes are discussed.

KEYWORDS

Elasticity, conductivity, effective properties, porous, cross-property

INTRODUCTION

An intriguing fundamental, as well as practical, question concerning anisotropic porous materials is the following one: can different effective physical properties be explicitly linked to one another? Such cross-property correlations become especially important for applications if one property (say, electric conductivity) is more easily measured than another property (full set of anisotropic elastic constants). The importance of such correlation has been pointed out by Berryman and Milton [1] and was particularly emphasized by Gibiansky and Torquato [2].

We consider solids with anisotropic microstructures formed by non-randomly oriented pores of non-spherical shapes, including mixtures of diverse shapes. The matrix material is assumed isotropic. The microstructures of this kind are relevant for many realistic materials, both man-made and naturally occurring. We examine cross-property correlations between two groups of anisotropic effective properties: elastic compliances and thermal conductivities. Note, that the problem of thermal conductivity is mathematically equivalent to the ones of electric conductivity, dielectric and

magnetic permeabilities or diffusion coefficients; therefore, our results apply to the mentioned physical properties as well.

We show that the correlations can be established in the explicit form that directly express the tensor of effective elastic compliances in terms of the conductivity tensor. These expressions are approximate, with the accuracy that remains good for a wide range of pore geometries.

Cross-property correlations between various effective properties of heterogeneous materials have been examined in several works. The most relevant for the present work is the classical paper of Bristow [3] in which an explicit connection between the effective conductivity and effective elastic moduli of a solid with cracks was derived. The derivation was done in the framework of the non-interaction approximation and for the case of random crack orientations (overall isotropy).

The conductivity – elasticity correlations were further investigated in the work of Berryman and Milton [1] on the two-phase composites, where the cross-property bounds (that are narrower than the classical Hashin-Shtrikman's ones) were established. The cross-property bounds were substantially advanced by Gibiansky and Torquato [4,5], who narrowed them under additional restrictions on the composite microgeometry and on the properties of constituents. Gibiansky and Torquato [4] also considered the transversely isotropic material (fiber reinforced composite) and established bounds for two of the five effective elastic constants in terms of the effective conductivities. Gibiansky and Torquato [5] established the cross-property bounds for the isotropic solid with cracks; this result is particularly valuable since neither upper nor lower non-trivial bounds for the effective elastic constants of cracked solids in the classical sense (i.e. in terms of the crack density) cannot be established [6].

It should be mentioned that correlations between other pairs of effective properties were considered in a number of works. Levin [7] interrelated the effective bulk modulus and the effective thermal expansion coefficient of the two phase isotropic composites. Milton [8] established cross-property bounds for the transport and the optical constants of isotropic composites. Similar bounds for the electrical and the magnetic properties were given by Cherkaev and Gibiansky [9]. The general approach to establishing various cross-property correlations was outlined by Milton [10], see also the recent review of Markov [11].

The present work focuses on the conductivity-elasticity correlations for the anisotropic porous materials (an isotropic matrix containing spheroidal pores of arbitrary orientational distribution and generally diverse aspect ratios). In contrast with the works that focus on bounds, our work derives the explicit cross-property correlations for the full set of effective anisotropic constants. In this sense, the present work can be viewed as an extension of Bristow's [3] explicit cross-property correlation for the isotropic cracked media.

The results of the present work are derived in the non-interaction approximation. Strictly speaking, it applies to the case of low concentration of pores (although, as far as materials with cracks are concerned, computer simulations of Kachanov [6] show that the predictions of the non-interaction approximation remain valid at relatively high crack densities). The key to our analysis is the recent finding of Shafiro and Kachanov [12] that the fourth rank effective elasticity tensor S_{ijkl} for the anisotropic porous microstructures can be represented, with good accuracy, in terms of a certain symmetric second rank tensor ω_{ij} and unit tensor δ_{ij}. The present work establishes a connection between ω_{ij} and the effective conductivity tensor.

ON THE EFFECTIVE ELASTIC PROPERTIES OF POROUS MATERIALS.

We briefly summarize the results on the effective elasticity of materials with pores of diverse shapes and orientations that are relevant for our analyses (see [12,13] for details).

Cavity compliance tensors. For a solid of volume V containing *one* cavity, the total strain per V under remotely applied stress tensor $\boldsymbol{\sigma}$ is a sum:

$$\boldsymbol{\varepsilon} = \boldsymbol{S}^0 \boldsymbol{:} \boldsymbol{\sigma} + \Delta\boldsymbol{\varepsilon} \tag{1}$$

where $\boldsymbol{S}^0$ is the compliance tensor of the matrix (a colon denotes contraction over two indices). In the case of the isotropic matrix, $S^0_{ijkl} = \frac{1}{2G_0}\left\{\frac{1}{2}\left(\delta_{ik}\delta_{jl} + \delta_{il}\delta_{jk}\right) - \frac{\nu_0}{1+\nu_0}\delta_{ij}\delta_{kl}\right\}$.

Due to linear elasticity, strain $\Delta\boldsymbol{\varepsilon}$ is a linear function of the applied stress:

$$\Delta\boldsymbol{\varepsilon} = \boldsymbol{H}^E \boldsymbol{:} \boldsymbol{\sigma} \tag{2}$$

where fourth rank tensor $\boldsymbol{H}^E$ - a *cavity compliance tensor* - was calculated for *3-D* ellipsoidal pores by Kachanov *et al* (1994). Superscript "E" indicates the elasticity problem (in contrast with $\boldsymbol{H}^C$, introduced in Section 3 in connection with the conductivity problem).

Let us consider a *3-D* cavity of the shape that possesses three mutually orthogonal planes of geometric symmetry, with unit normals $\boldsymbol{l}, \boldsymbol{m}, \boldsymbol{n}$ (this case covers ellipsoids but is not restricted to them). Cavity compliance tensor $\boldsymbol{H}^E$ has, due to symmetry, the following structure:

$$\begin{aligned}\boldsymbol{H}^E = \frac{2V_{cav}}{VE_0}\big[& \xi_1 \boldsymbol{llll} + \xi_2 \boldsymbol{mmmm} + \xi_3 \boldsymbol{nnnn} + \eta_1 (\boldsymbol{lm}+\boldsymbol{ml})(\boldsymbol{lm}+\boldsymbol{ml}) \\ & + \eta_2 (\boldsymbol{mn}+\boldsymbol{nm})(\boldsymbol{mn}+\boldsymbol{nm}) + \eta_3 (\boldsymbol{nl}+\boldsymbol{ln})(\boldsymbol{nl}+\boldsymbol{ln}) + \\ & + \zeta_1 (\boldsymbol{llmm}+\boldsymbol{mmll}) + \zeta_2 (\boldsymbol{mmnn}+\boldsymbol{nnmm}) + \zeta_3 (\boldsymbol{nnll}+\boldsymbol{llnn})\big]\end{aligned} \tag{3}$$

where the three groups of components of $\boldsymbol{H}^E$-tensor - dimensionless coefficients ξ_i, η_i, ζ_i - represent the normal, shear and Poisson's ratio compliances of the cavity. For the ellipsoidal shape, they are given in the appendix in terms of Eshelby's tensor.

Further analysis is best done in terms of the *elastic potential,* rather than compliances: for a solid with many cavities, such a formulation identifies the proper parameters of pore density (that may not reduce to porosity if pores are non-spherical) and establishes the overall anisotropy in the cases of non-random pore orientations.

For volume V containing a cavity, the potential in stresses - such a function $f(\boldsymbol{\sigma})$ that (1) can be written as $\varepsilon_{ij} = \partial f / \partial \sigma_{ij}$ - is a sum of two terms:

$$f(\boldsymbol{\sigma}) = (1/2)\boldsymbol{\sigma}:\boldsymbol{\varepsilon}(\boldsymbol{\sigma}) = (1/2)\boldsymbol{\sigma}:\boldsymbol{S}^0:\boldsymbol{\sigma} + (1/2)\boldsymbol{\sigma}:\boldsymbol{H}^E:\boldsymbol{\sigma} \equiv f_0 + \Delta f \tag{4}$$

where f_0 is the potential in the absence of cavity In the case of the isotropic matrix $f_0 = (1/2E_0)\left\{(1+\nu_0)tr(\boldsymbol{\sigma}\cdot\boldsymbol{\sigma}) - \nu_0(tr\boldsymbol{\sigma})^2\right\}$ and Δf is the change due to cavity.

For a solid with *many* cavities,

$$\Delta f = (1/2)\boldsymbol{\sigma}:\sum_k \Delta\boldsymbol{\varepsilon}^{(k)} \tag{5}$$

where $\Delta\boldsymbol{\varepsilon}^{(k)}$ are linear functions of applied stress $\boldsymbol{\sigma}$. These functions reflect pore shapes, as well as elastic interactions between pores; their determination constitutes the most difficult part of the problem. Provided the mentioned functions are specified, the effective compliances S_{ijkl} are found from the relation

$$\varepsilon_{ij} = \partial f/\partial\sigma_{ij} = S^0_{ijkl}\sigma_{kl} + \partial(\Delta f)/\partial\sigma_{ij} \equiv S_{ijkl}\sigma_{kl} \tag{6}$$

We consider the approximation of non-interacting cavities. It is of the fundamental importance: besides being rigorous at small defect densities, it is the basic building block for various effective field methods. In this approximation, each cavity is placed in remotely applied stress $\boldsymbol{\sigma}$ and is not influenced by other cavities. Then, $\Delta\varepsilon_{ij}^{(m)} = H^{E(m)}_{ijkl}\sigma_{kl}$ and

$$\Delta f = \sum_k \Delta f^{(k)} = \frac{1}{2}\boldsymbol{\sigma}:\sum_k \boldsymbol{H}^{E(k)}:\boldsymbol{\sigma} \tag{7}$$

where summation over cavities may be replaced by integration over orientations,

Representation of a cavity compliance tensor in terms of a second rank symmetric tensor.

For certain shapes of a cavity, its characterization by $\boldsymbol{H}^E$ - tensor can be reduced, with sufficient accuracy, to the one in terms of a certain second rank symmetric tensor $\boldsymbol{\Omega}$. Namely, we seek to approximate (uniformly with respect to all stress states) the potential change due to cavity $\Delta f = (1/2)\,\boldsymbol{\sigma}:\boldsymbol{H}^E:\boldsymbol{\sigma}$ by the expression:

$$2\Delta f = \underbrace{B_1(tr\boldsymbol{\sigma})^2 + B_2 tr(\boldsymbol{\sigma}\cdot\boldsymbol{\sigma})}_{\text{isotropic terms}} + \left[B_3\boldsymbol{\sigma}\cdot\boldsymbol{\sigma} + B_4(tr\boldsymbol{\sigma})\boldsymbol{\sigma}\right]:\boldsymbol{\Omega} \tag{8}$$

where B_i are scalar coefficients that depend on the cavity shape and on ν_0 (they are given in the Appendix and illustrated in Fig.2) and where $\boldsymbol{I}$ and $\boldsymbol{J}$ are the second rank and fourth rank unit tensors, respectively ($I_{ij} = \delta_{ij}$ and $2J_{ijkl} = \delta_{ik}\delta_{jl} + \delta_{il}\delta_{jk}$). The "isotropic terms" in (8) are expressed in terms of stress invariants and do not depend on the cavity orientation. Symbols $\boldsymbol{nn}$ and $\boldsymbol{II}$ denote hereafter tensor (dyadic) products of vectors or tensors.

The condition for reduction of (3) to the simplified form (8) reduce to certain restrictions on components of tensor $\boldsymbol{H}^E$; see [12] for details. With the exception of a sphere, these conditions do not hold exactly, but they are satisfied, with good accuracy, for *spheroids*. In the case of a solid containing *many* pores, a similar condition is also satisfied.

EFFECTIVE CONDUCTIVITIES OF A MATERIAL WITH SPHEROIDAL PORES

We consider reference volume V of a material with the isotropic thermal conductivity k_0 containing an insulating ellipsoidal pore; a_1, a_2, a_3 are semi-axes of the pore and $\boldsymbol{l}, \boldsymbol{m}, \boldsymbol{n}$ are unit vectors along them. The change of heat flux vector $\Delta\boldsymbol{Q}$ (per volume V) due to the cavity is a linear function of the far-field temperature gradient $\boldsymbol{G}^0$ and hence can be written in the form:

$$\Delta\boldsymbol{Q} = \boldsymbol{H}^C \cdot \boldsymbol{G}^0 \tag{9}$$

where second rank tensor $\boldsymbol{H}^C$ is a function of the inclusion shape (superscript "C" indicates the conductivity problem). It has been derived in[14]. In the framework of the non-interaction approximation (each inclusion is subject to the same far-field temperature gradient, unperturbed by the presence of other inclusions), the effective conductivity tensor $\boldsymbol{K}$ is expressed in terms of a sum (or integral over orientations) $\sum_i \boldsymbol{H}^{C(i)}$ over individual inclusions:

$$\boldsymbol{K} = k_0 \boldsymbol{I} + \sum_i \boldsymbol{H}^{C(i)} \tag{10}$$

where $k_0\boldsymbol{I}$ is the tensor of (isotropic) conductivity of the matrix.

CROSS-PROPERTY CORRELATIONS BETWEEN ANISOTROPIC COMPLIANCES AND CONDUCTIVITIES

Utilizing the above results we obtain the following explicit cross-property correlations that apply to an arbitrary mixture of pores of diverse aspect ratios – the central result of the present work::

$$E_0(\boldsymbol{S} - \boldsymbol{S}_0) = \left[\frac{b_1 a_2 - b_4 a_1}{a_2(a_2 + 3a_1)}\boldsymbol{II} + \frac{b_2 a_2 - b_3 a_1}{a_2(a_2 + 3a_1)}\boldsymbol{J}\right]\frac{tr(\boldsymbol{K}_0 - \boldsymbol{K})}{k_0}$$
$$+ \frac{b_3}{a_2}\frac{1}{k_0}[(\boldsymbol{K}_0 - \boldsymbol{K})\cdot\boldsymbol{J} + \boldsymbol{J}\cdot(\boldsymbol{K}_0 - \boldsymbol{K})] + \frac{b_4}{a_2}\frac{1}{k_0}[(\boldsymbol{K}_0 - \boldsymbol{K})\boldsymbol{I} + \boldsymbol{I}(\boldsymbol{K}_0 - \boldsymbol{K})] \tag{11}$$

This relation covers all pore shapes (including mixtures of diverse shapes) and orientational distributions of pores in a unified way. It contains the matrix constants (elastic constants and conductivity) and does not contain any adjustable parameters. The shape dependent coefficients at tensorial terms in this basic relation are plotted in [13].

The presence of shape factors – coefficients at the tensorial terms in (11) – reflects the fact that pore shapes affect the elastic and the conductive properties differently. However, this difference is relatively mild, as seen from a relatively mild variation of these factors in the entire range of

possible shapes and vanishes altogether in the limiting cases of strongly oblate (aspect ratio smaller than 0.15) and strongly prolate (aspect ratio larger than 10) pores.

References

1. Berryman, J.G. and Milton, G.W. (1988) Microgeometry of random composites and porous media. *J. Phys.*, **D 21**, 87-94.
2. Gibiansky, L.V. and Torquato, S. (1995) Connection between the conductivity and bulk modulus of isotropic composite materials. *Phyl. Trans. Roy. Soc .L.*, **A353**, 243-278.
3. Bristow, J.R. (1960) Microcracks, and the static and dynamic elastic constants of annealed heavily cold-worked metals. *British J. Appl. Phys*, **11**, 81-85.
4. Gibiansky, L.V. and Torquato, S. (1996a) Rigorous link between the conductivity and elastic moduli of fiber reinforced materials. *Proc. Roy. Soc.* **A452**, 253-283.
5. Gibiansky, L.V. and Torquato, S. (1996b) Bounds on the effective moduli of cracked materials. *J Mech Phys Solids*, **44**, 233-242.
6. Kachanov, M. (1992) Effective elastic properties of cracked solids: critical review of some basic concepts. *Appl. Mech. Reviews* **45**(8), 304-335.
7. Levin, V.M. (1967) On the coefficients of thermal expansion of heterogeneous material, Mechanics of Solids, **2**, 58-61
8. Milton, G.W. (1981) Bounds on the electromagnetic, elastic and other properties of two-component composites. *Phys. Rev. Lett*., **46**, 542-545.
9. Cherkaev, A.V. and Gibiansky, L.V. (1992) The exact coupled bounds for effective tensors of electrical and magnetic properties of two-component two-dimensional composites. *Proc. Roy. Soc. Edinburgh*, **A122**, 93-125.
10. Milton, G.W. (1997) Composites: a myriad of microstructure independent relations. In: *Theoretical and Applied Mechanics 1996*, Ed.:Tatsumi, T. *et al*, Elsevier, 443-459.
11. Markov, K.Z. (1999) Elementary micromechanics of heterogeneous media. In: *Heterogeneous Media: Micromechanics Modeling Methods and Simulations*, Ed.: Markov, K.Z and Preziosi, L., Birkhauser, 1-162.
12. Shafiro, B. and Kachanov, M. (1999) Solids with non-spherical cavities:simplified representations of cavity compliance tensors and the overall anisotropy, *J. Mech. Phys. Solids* **47**, 877-898.
13. Kachanov, M., Tsukrov, I. and Shafiro, B. (1994) Effective moduli of solids with cavities of various shapes. *Appl. Mech. Reviews* **47**(1), S151-S174.
14. Shafiro, B. and Kachanov, M. (2000) Anisotropic effective conductivity of materials with non-randomly oriented inclusions of diverse ellipsoidal shapes, *J. Appl. Phys.* (submitted).

MATHEMATICAL MODEL OF A CRACK ON AN IMPERFECT INTERFACE

Y.A.Antipov[1] and A.B.Movchan[2]

[1]Department of Mathematical Sciences, The University of Bath,
Bath BA2 7AY, UK
[2]Department of Mathematical Sciences, The University of Liverpool,
Liverpool L69 3BX, UK

ABSTRACT

A mathematical model of a crack along a thin soft interface layer is studied in this paper. This type of interface could arise in a ceramic support that has been coated with a layer of high surface area material which contains the dispersed catalyst. Asymptotic analysis is applied to replace the interface layer with a set of effective contact conditions. We use the words "imperfect interface" to emphasise that the solution (the displacement field) is allowed to have a non-zero jump across the interface. Compared to classical formulations for cracks in dissimilar media (where ideal contact conditions are specified outside the crack), in our case the gradient field for the displacement is characterised by a weak logarithmic singularity. The scalar case for the Laplacian operator as well as the vector elasticity problem are considered. Numerical results are presented for a two-phase elastic strip containing a finite crack on an imperfect interface.

KEYWORDS

Imperfect interface, crack, Wiener-Hopf problem, integral equation

INTRODUCTION

Motivation for this work arises from the study of the fracture of ceramic catalytic monolith combustors that are being incorporated into new proto-type designs of gas turbines. The ceramic monolith consists of an extruded structure that contains a large number of parallel channels, e.g. consisting of: 62 cells/cm^2, each cell 1.1mm$\times$1.1mm square, with an open frontal area of 66%. The ceramic surface is coated with a high surface area material (e.g. γ-Al_2O_3) which contains the dispersed catalyst. It is in the catalytic layer (also known as the wash-coat), where the combustion reactions take place (e.g. $CH_4 + 2O_2 \rightarrow CO_2 + 2H_2O$), and the energy associated with this highly exothermic reaction is released. In the application in a gas turbine combustor, temperatures of the catalyst layer could vary from ambient conditions (when the turbine is not working) up to 1100°C. It is important that the catalyst layer remains firmly bound to the ceramic support structure during this process. If it cracks and shears, then catalyst will be lost from the monolith which would a) result in a lost in performance of the combustor, and b) lead to possible damage of components downstream of the combustor. Further information on catalytic combustion and

layer of catalyst, this gives a two-phase structure. In examining the surface, cracks are clearly visible in the layer. The cracks would have occurred as a result of a) shrinkage of the coated layer (after drying and calcining), and b) differences in coefficients of thermal expansion as the material was exposed to a wide range of temperatures. The presence of a crack on the surface is not considered necessarily to be a problem, however, if the crack propagates and the interface is sheared then this will lead to catalyst loss.

It is documented in engineering literature that the damage of ceramic structures is accompanied by "crack bridging". In the model presented here we assume that the bridging effect exists along the whole interface surface between the substrate and the layer of catalyst (we shall also use the words "imperfect interface" or "soft adhesive"), and, in addition, a crack with zero tractions on its faces is introduced along the interface contour. We study the problems of anti-plane shear and elasticity problems for this two-phase structure. Mathematical models of interfacial cracks are well-developed in the literature for the cases when ideal contact conditions prevail on an interface surface outside a crack. Asymptotic models of elastic adhesive joints were introduced in [2]. The adhesive was modelled as a thin soft layer where effective contact conditions involve continuity of tractions and a linear relation between the traction components and the displacement jump across the adhesive. Laminated structures with linear interfaces were also studied in [3].

In the present work we analyse mathematical models of cracks along imperfect interface boundaries and make an emphasis on the asymptotic behaviour of the solution and its derivatives near the crack ends and at infinity. In contrast to the results already published in the literature, on the interface boundary (outside the crack) we allow for a non-zero displacement jump specified as a function of traction components. The presence of this condition affects the asymptotics of the displacement and stress components in the vicinity of the crack ends.

ANTI-PLANE PROBLEM FOR A STRIP WITH A SEMI-INFINITE CRACK ALONG AN IMPERFECT INTERFACE

Consider two bodies Ω_+ and Ω_- connected through a thin interface layer Ω_0 of thickness ϵ. Assume that the material occupying Ω_+,Ω_- and Ω_0 is characterised by the shear moduli μ_+, μ_- and $\mu_0 = \epsilon\mu$ respectively, where μ is of the same order as μ_+ and μ_-. For the case of anti-plane shear, the displacements u^+, u^- and $u^{(0)}$ in Ω_+,Ω_- and Ω_0 satisfy the Laplace equation in the corresponding strips and the following boundary conditions

$$u^{\pm} = u^{(0)}, \quad \mu_{\pm}\frac{\partial u^{\pm}}{\partial y} = \mu_0\frac{\partial u^{(0)}}{\partial y} \quad \text{on} \quad \Gamma_{\pm} = \{(x,y) : y = \pm\epsilon/2\}\,.$$

Let $t = \epsilon^{-1}y$, so that within Ω_0, $|y| < \epsilon/2$, and hence $|t| < 1/2$. In terms of x and t

$$\nabla^2 u^{(0)} = \epsilon^{-2}\frac{\partial^2 u^{(0)}}{\partial t^2} + \frac{\partial^2 u^{(0)}}{\partial x^2} = 0.$$

Denote by $u_0^{(0)}$ the leading term of $u^{(0)}$. Then to leading order, the tractions are continuous across the interface layer and proportional to the displacement jump $\chi(x) = u(x,+0) - u(x,-0)$:

$$\mu_+\frac{\partial u}{\partial y}|_{y=+0} = \mu_-\frac{\partial u}{\partial y}|_{y=-0} = \mu\chi(x), \quad |x| < \infty.$$

First, we analyse the Dirichlet problem. Assume that a three-phase strip contains a semi-infinite delamination crack $\{-\infty < x < 0, y = \pm 0\}$. Ahead of the crack, there exists a thin layer of soft adhesive.

Formally, the problem is set as follows

$$\nabla^2 u(x,y)=0, \quad |x|<\infty, \quad -b<y<0, \quad 0<y<a,$$

$$u(x,a)=u(x,-b)=0, \quad |x|<\infty,$$

$$\mu_{\pm}\frac{\partial u}{\partial y}|_{y=\pm 0}=\mu\chi(x), \quad x>0; \quad \mu_{\pm}\frac{\partial u}{\partial y}|_{y=\pm 0}=p(x), \quad x<0. \tag{1}$$

where $p(x)$ characterises the shear load applied to the crack faces. To reduce the boundary-value problem (1) to a Wiener-Hopf functional equation, we extend the second boundary condition in (1) to the whole real axis:

$$\mu_{\pm}\frac{\partial u}{\partial y}(x,\pm 0)=\mu\chi(x)+\psi(x), \quad |x|<\infty, \tag{2}$$

where $\psi(x)$ is unknown as $x<0$ and $\psi(x)=0$ as $x>0$. Applying the Fourier transform to the problem (1), using the condition (2) and introducing the integrals

$$\Phi^-(\alpha)=\int_{-\infty}^{0}\psi(\xi)e^{i\alpha\xi}d\xi, \quad \Phi^+(\alpha)=\int_0^{\infty}\chi(\xi)e^{i\alpha\xi}d\xi, \quad P^-(\alpha)=\int_{-\infty}^{0}p(\xi)e^{i\alpha\xi}d\xi,$$

we get the following Wiener-Hopf equation

$$\Phi^-(\alpha)=G(\alpha)[\mu\Phi^+(\alpha)+P^-(\alpha)], \quad -\infty<\alpha<+\infty, \tag{3}$$

$$G(\alpha)=1+\frac{\mu}{\alpha}\left(\frac{\tanh\alpha a}{\mu_+}+\frac{\tanh\alpha b}{\mu_-}\right).$$

Since the function $G(\alpha)$ is even and has zero increment of $\arg G(\alpha)$ along the real axis, the solution of the problem (3) is defined by the following formulae

$$\Phi^-(\alpha)=-\frac{\Psi^-(\alpha)}{X^-(\alpha)}, \quad \alpha\in\mathbb{C}^- \quad , \quad \Phi^+(\alpha)=-\frac{\Psi^+(\alpha)}{\mu X^+(\alpha)}, \quad \alpha\in\mathbb{C}^+,$$

where $\mathbb{C}^+=\{\alpha:\mathrm{Im}(\alpha)>0\}$, $\mathbb{C}^-=\{\alpha:\mathrm{Im}(\alpha)<0\}$, $\Psi^{\pm}(\alpha)$ and $X^{\pm}(\alpha)$ are the limit values of the functions

$$\Psi(\alpha)=\frac{1}{2\pi i}\int_{-\infty}^{+\infty}\frac{X^+(\beta)P^-(\beta)}{\beta-\alpha}d\beta,$$

$$X(\alpha)=\exp\left\{\frac{1}{2\pi i}\int_{-\infty}^{+\infty}\ln G(\beta)\frac{d\beta}{\beta-\alpha}\right\}=\exp\left\{\frac{\alpha}{\pi i}\int_0^{+\infty}\ln G(\beta)\frac{d\beta}{\beta^2-\alpha^2}\right\}, \quad \alpha\in\mathbb{C}\backslash\mathbb{R}^1.$$

Note that the function $G(\alpha)$ is bounded at the origin and tends to 1 as $\alpha\to\pm\infty$. Assume that the load $p(x)$ is given by

$$p(x)=\sum_{k=1}^{N}d_k e^{\alpha_k x}, \quad x<0, \tag{4}$$

where d_k, α_k are constant coefficients and $0<\alpha_1<\alpha_2<\ldots<\alpha_N$. Then the displacement jump admits the following series-representation

$$\chi(x)=\frac{1}{\mu}\sum_{k=1}^{N}d_k X_k\sum_{n=1}^{\infty}\frac{e^{-\sigma_n x}}{X^-(-i\sigma_n)iG'(-i\sigma_n)(\sigma_n+\alpha_k)},$$

where

$$X_k=X^+(i\alpha_k)=\exp\{\frac{\alpha_k}{\pi}\int_0^{\infty}\ln G(\beta)\frac{d\beta}{\beta^2+\alpha_k^2}\}, \quad \mathrm{Im}(X_k)=0,$$

$-i\sigma_n$ ($\sigma_n>0$) are the elements of the countable set of roots of $G(\alpha)$ in $\mathbb{C}^-$. We note that $\mathrm{Im}\{X^{\pm}(\pm i\tau)\}=0$, $\tau>0$ and $\mathrm{Im}\{iG'(-i\sigma_n)\}=0$. Thus, the displacement jump decays exponentially as $x\to+\infty$. It

$\psi(x) = O(e^{\lambda_0 x})$, where $\lambda_0 = \min\{\frac{\pi}{2a}, \frac{\pi}{2b}, \alpha_1\}$. Analysis of the solution in a neighbourhood of the crack tip yields that the displacement jump $\chi(x)$ is continuous and the function $\psi(x)$ is discontinuous at $x = 0$: $\chi(x) = \Lambda_0 + O(x)$, $x \to 0$; $\psi(x) = M_0 + O(x)$, $x \to -0$, $\psi(x) = 0$, $x > 0$. Here

$$\Lambda_0 = \frac{1}{\mu}\sum_{k=1}^{N} d_k(1 - X_k), \quad M_0 = \sum_{k=1}^{N} d_k X_k.$$

These formulae and the relation (2) indicate that the traction $\sigma_{zy}(x, 0)$ is bounded but discontinuous at the crack tip and its jump is

$$[\sigma_{zy}(x, 0)]_{x=-0}^{x=+0} = -\psi(-0) = -M_0.$$

The stress component $\sigma_{zx}(x, 0)$ has a logarithmic singularity at $x = 0$.

Next, we analyse the Neumann problem. Its formulation is similar to the previous problem, with the Dirichlet boundary conditions on the upper and lower parts of the strip being replaced by the homogeneous Neumann data. The unknown function $u(x, y)$ satisfies the equation and the contact conditions (1). Instead of the second relation in (1), we assume that

$$\frac{\partial u}{\partial y}(x, a) = \frac{\partial u}{\partial y}(x, -b) = 0, \quad |x| < \infty.$$

We seek the solution in the class of functions with the finite energy integral and with the following behaviour at infinity

$$|u(x, y)| < C_1, \quad x \to -\infty, \qquad |u(x, y)| < C_2 e^{-\delta x}, \quad x \to +\infty,$$

uniformly with respect to $-b < y < a$, where C_1, C_2 and δ are positive constants. To specify the solution uniquely, we impose the following orthogonality condition

$$\int_{-\infty}^{\infty} \frac{\partial u}{\partial y}(x, \pm 0)dx = 0. \tag{5}$$

The corresponding Wiener-Hopf problem becomes

$$\Phi^-(\alpha) = G(\alpha)[\mu\Phi^+(\alpha) + P^-(\alpha)], \ \alpha \in \Gamma, \quad \Gamma = \{\alpha : \mathrm{Im}(\alpha) = -\delta_0 \in (-\delta, 0)\}, \tag{6}$$

$$G(\alpha) = 1 + \frac{\mu}{\alpha}\left(\frac{\coth \alpha a}{\mu_+} + \frac{\coth \alpha b}{\mu_-}\right).$$

Here $\Phi^+(\alpha)$ is an analytic function in D^+, and the functions $\Phi^-(\alpha), P^-(\alpha)$ are analytic in D^-, where $D^+ = \{\alpha : \mathrm{Im}(\alpha) > -\delta_0\}$, $D^- = \{\alpha : \mathrm{Im}(\alpha) < -\delta_0\}$. The solution of the problem (6) is not unique:

$$\Phi^+(\alpha) = \frac{C - \Psi^+(\alpha)}{\mu(\alpha + i)X^+(\alpha)}, \quad \alpha \in D^+, \quad \Phi^-(\alpha) = \frac{C - \Psi^-(\alpha)}{(\alpha - i)X^-(\alpha)}, \quad \alpha \in D^-,$$

where C is an arbitrary constant,

$$\Psi^{\pm}(\alpha) = \frac{1}{2\pi i}\int_{\Gamma} \frac{(t + i)X^+(t)P^-(t)}{t - \alpha}dt, \ \alpha \in D^{\pm},$$

$$X^{\pm}(\alpha) = \exp\left\{\frac{1}{2\pi i}\int_{\Gamma} \ln\left(\frac{t - i}{t + i}G(t)\right)\frac{dt}{t - \alpha}\right\}, \quad \alpha \in D^{\pm}.$$

However, the original Neumann boundary value problem is solvable uniquely, and constant C is determined by the condition (5) as follows $C = \Psi^+(0) - iX^+(0)P^-(0)$. Further, assuming as before that the load has the form (4) and analysing the behaviour of the solution at infinity, we get

$$\psi(x) = A + O(e^{\lambda_1 x}), \quad \chi(x) = -\frac{1}{\mu}A + O(e^{\lambda_1 x}), \quad x \to -\infty,$$

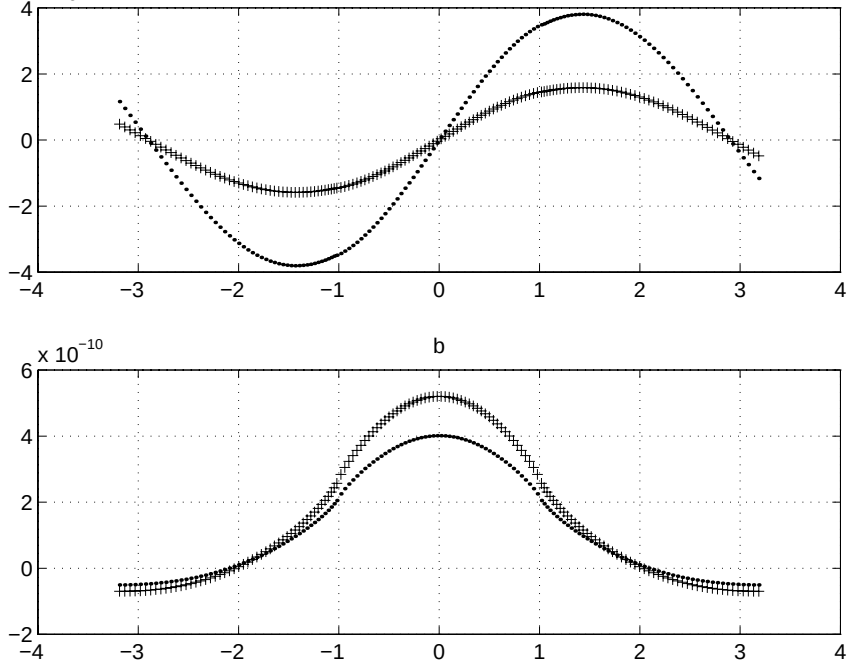

Figure 1: The displacement jumps $\chi_1(x)$ (a) and $\chi_2(x)$ (b) vs. x for the lower material brass $(+++)$ and CFRP (...).

where

$$\lambda_1 = \min\{\alpha_1, \frac{\pi}{a}, \frac{\pi}{b}\}, \quad A = \frac{\mu_1}{X^+(0)} \sum_{k=1}^{N} \frac{d_k(\alpha_k + 1)X^+(i\alpha_k)}{\alpha_k^2}.$$

Thus, in contrast to the Dirichlet problem studied in the previous section, the functions $\psi(x)$ and $\chi(x)$ do not vanish as $x \to -\infty$. For positive x, the function ψ vanish, and the displacement jump decays exponentially $\chi(x) = O(e^{-\sigma_1^{(0)} x}), \quad x \to +\infty$ ($-i\sigma_1^{(0)}$ is the first root of the function $G(\alpha)$ in D^- and $\sigma_1^{(0)} > 0$).

PLANE STRAIN PROBLEM FOR A STRIP WITH A FINITE CRACK ALONG AN IMPERFECT INTERFACE

Consider the domain with the same geometry as before but with the crack along the imperfect interface being finite. The displacement vector $\boldsymbol{u} = (u, v)$ satisfies the Lame equation

$$\nabla^2 \boldsymbol{u} + \frac{1}{1 - 2\nu_\pm} \nabla \nabla \cdot \boldsymbol{u} = 0.$$

The traction conditions are posed on the upper and lower parts of the boundary of the strip and on the crack faces $\tau_{xy} = f_1(x),\ \sigma_y = f_2(x)$ as $|x| < c,\ y = 0$. The interface conditions outside the crack are

$$\tau_{xy}(x, 0) = \alpha_{11}\chi_1(x) + \alpha_{12}\chi_2(x), \quad \sigma_y(x, 0) = \alpha_{12}\chi_1(x) + \alpha_{22}\chi_2(x), \quad |x| > c, \ \ y = \pm 0.$$

Here $\chi_1(x) = u|_{y=+0} - u|_{y=-0},\ \chi_2(x) = v|_{y=+0} - v|_{y=-0}$ are the displacement jumps. The constants α_{kj} are given. For an isotropic interface layer, $\alpha_{11} = \mu, \alpha_{22} = \lambda + 2\mu, \alpha_{12} = \alpha_{21} = 0,\ \epsilon\lambda, \epsilon\mu$ are the Lamé elastic moduli. We seek the solution with finite elastic energy, and assume that the displacement field decays at infinity. Introduce new functions $\Psi_1,\ \Psi_2$ such that

$$\tau_{xy}(x, 0) = \alpha_{11}\chi_1(x) + \alpha_{12}\chi_2(x) + \Psi_1(x),$$

$$\sigma_y(x, 0) = \alpha_{12}\chi_1(x) + \alpha_{22}\chi_2(x) + \Psi_2(x), \quad |x| < \infty,$$

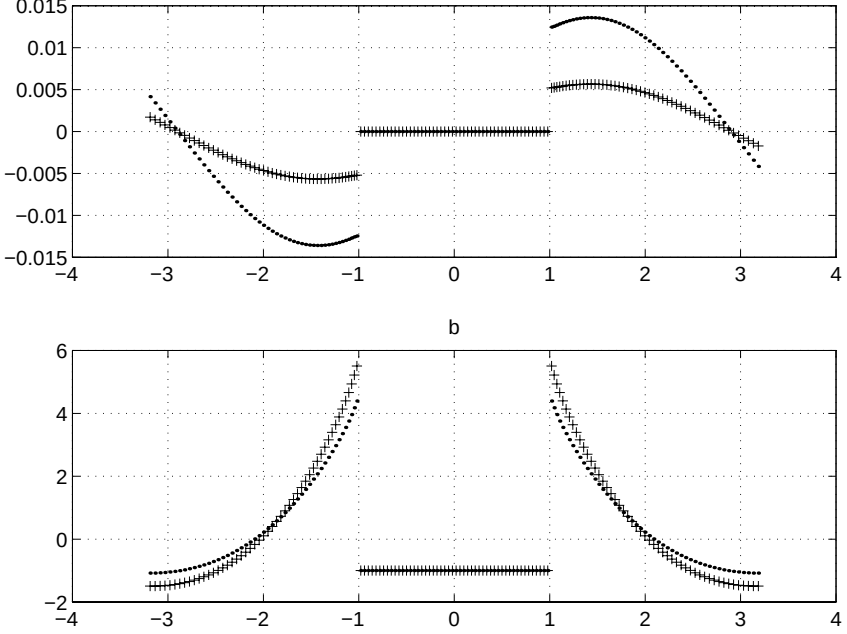

Figure 2: The stress components τ_{xy} (a) and σ_y (b) along the interface vs. x for the lower material brass $(+++)$ and CFRP (...).

where $\Psi_j(x) = 0$ outside the crack. By the method of integral transforms, the original problem is reducible to the following Fredholm system of the second order

$$\Psi_k(cx) + \frac{\beta_{kj}}{\pi} \sum_{j=1}^{2} \int_{-1}^{1} \{\log|\xi - x| + K_{kj}(\xi - x)\} \Psi_j(c\xi) d\xi = f_k(cx), \quad |x| < 1, \quad k = 1,\ 2, \tag{7}$$

where $\beta_{kj} = c\alpha_{kj}[(1-\nu_+)/\mu_+ + (1-\nu_-)/\mu_-]$, $\mu_\pm, \nu_\pm$ are the shear modulus and Poisson's ratio of the upper (lower) part of the composite strip. The function $K_{kj}(\xi - x)$ is bounded at $\xi = x$ and its first derivative has a logarithmic singularity. Analysis of the system (7) shows that the displacement jumps $\chi_1(x),\ \chi_2(x)$ are continuous at the points $x = \pm c$ and the stress components $\sigma_y(x,0), \tau_{xy}(x,0)$ are bounded and discontinuous at the ends $x = \pm c$. The system of integral equations (7) is solved numerically. Figures 1 and 2 show the displacement jumps and the stress components along the interface for the case $f_1 = 0, f_2 = -1, a = b = c = 1$. The upper material is aluminium with the elastic modulus $E_+ = 70\,GPa$ and Poisson's ratio $\nu_+ = 0.3$. The lower material is either $CFRP$: $E_{-(CFRP)} = 135\,GPa,\ \nu_{-(CFRP)} = 0.3$, or brass: $E_{-(Br)} = 100\,GPa,\ \nu_{-(Br)} = 0.25$. The interface layer is assumed to be made of FM 1000 and characterised by the normalised moduli, $E = 10\,GPa, \nu_0 = 0.41$ whereas the real values are given by $E_0 = 1.24\,GPa, \nu_0 = 0.41$, and thus here $\epsilon = 0.124$. The parameters that are involved in the interface condition in this case have the following values, $\alpha_{11} = 0.35\,GPa$; $\alpha_{22} = 2.3\,GPa$, and $\alpha_{12} = \alpha_{21} = 0$.

ACKNOWLEDGEMENTS

The work was supported by U.K. Engineering and Physics Sciences Research Council (EPSRC).

REFERENCES

1. Hayes, R.E. and Kolaczkowski, S.T. (1997) *Introduction to catalytic combustion.* Gordon and Breach Publishers.
2. Klarbring, A. (1991) *Int. J. Engng. Sci.* 29, 493.
3. Bigoni, D., Ortiz, M. and Needleman, A. (1997). *Int. J. Solids Structures* 34, 4305.

ORAL REFERENCE: ICF100114OR

MEASURING CRACK TIP DEFORMATION IN NANOSCOPIC RESOLUTION

Y. M. Xing[1,2] and W. Yang[1]

[1] FML, Department of Engineering Mechanics, University of Tsinghua, Beijing, 100084, China
[2]Department of Basic Science, Inner Mongolia Polytechnic University, Hohhot, 010062, China

ABSTRACT

Interference of HREM image of deformed crystal with unidirectional reference gratings leads to direct measurement of displacements and strains of nanoscopic resolution. The fringe contrast is enhanced by an optical filtering technique. Using the HREM moiré method, we measure the near tip nanoscopic deformation on the {111} plane of single crystal silicon with a loaded quasi-cleavage crack running in the [110] direction. The measured strain distribution ahead of the crack tip agrees with the linear elastic fracture mechanics prediction up to 10nm from the crack tip. Dislocations of Peierls type are detected and they extend from the crack tip over a length of hundreds of Burgers vectors.

KEYWORDS

Crack tip, nanoscopic deformation, measurement, dislocation,

INTRODUCTION

Dislocation nucleation from a crack tip underlies the mechanism of brittle versus ductile transition [1]. In a pioneering work for the competition between cleavage crack growth and dislocation emission from a crack tip, Rice and Thomson [2] performed an activation analysis in which the total energy change due to the formation of a dislocation half loop at the crack tip was calculated as a function of the loop radius and the dislocation core cut-off radius. Later on, the concept of Peierls-dislocation [3] was introduced to remove the uncertainty of the dislocation core cut-off radius and to formulate the concept of unstable stacking energy [4]. The competition between cleavage and dislocation emission can be revealed in microscopic details by testing single crystals. With known dopant level and sharp transition temperature, silicon or iron-silicon crystal is a frequent choice for the observation of dislocation emission from a crack tip [5].

Optical techniques have been used extensively in the direct determination of crack tip deformation fields. Current moiré technology, from moiré interferometry to electron beam moiré, has a grating frequency

from 1200 to 10000 lines/mm [6]. Recently, the authors proposed the HREM-moiré method [7]. The fundamental limitation on a perfect crystal is the constancy of its lattice spacing with respect to thermal vibration at room temperature. Silicon single crystal has a lattice structure with a period of 0.304nm, which represents a grating with a frequency of 3289474 lines/mm. Such a high-frequency grating allows measurement with atom-size sensitivity and nanoscopic resolution. When the specimen is loaded, the deformation alters the spacing of lattice and may cause dislocation emission. The changes in the microstructure are recorded by the HREM image. The principle of moiré formation is the same as the one in geometric moiré. The HREM image of the crystal lattice acts as a specimen grating. The optical grating with standard spacing acts as a reference grating. Under a proper magnification, the specimen grating is superimposed onto the reference grating and moiré patterns emerge that reveal displacements, strains and lattice defects.

Since the crystal lattice is commonly packed in non-orthogonal array, the uni-directional reference grating, rather than the cross-line gratings in the geometric moiré method, is used. The moiré fringes represent the displacement components normal to the reference-grating lines. One can align the reference-grating lines exactly with the lattice lines in *y*-direction to measure the displacement component u_x, then rotates the reference-grating an angle θ to another set of lattice lines to obtain the displacement component u_r. If there is no mismatch between the reference grating and the non-deformed crystal lattice under amplification, the displacements u_x and u_r can be expressed by

$$u_x = \frac{N_x p}{M}, \quad u_r = \frac{N_r p}{M} \quad (N_x、N_r=0，1，2\bullet\bullet\bullet) \qquad (1)$$

where p denotes the reference-grating pitch, M the magnification of TEM, and N_x and N_r the fringe orders in the x and r directions. The in-plane strain components are determined by

$$\varepsilon_x = \frac{p}{Mf_{xx}}, \quad \varepsilon_r = \frac{p}{Mf_{rr}}, \quad \gamma_{xy} = \frac{p}{Mf_{xy}} + \frac{p}{Mf_{rx}}\sin\theta \qquad (2)$$

The values f_{xx} , f_{rr}, f_{rx}, and f_{xy} are the intervals between adjacent fringes, the first index represents the normal of the reference grating and the second index the measuring direction of the fringe interval. For a valid measurement, the specimens must be thin enough so that the weak-phase-body hypothesis is valid, and the adjustment of object glass of TEM must satisfy Scherzer's under-focus condition [8]. One can modify the reference grating by slight rotation mismatch (characterized by a rigid body rotation angle α) and/or stretching mismatch (characterized by a constant strain ε) to obtain subtle features of the deformation field.

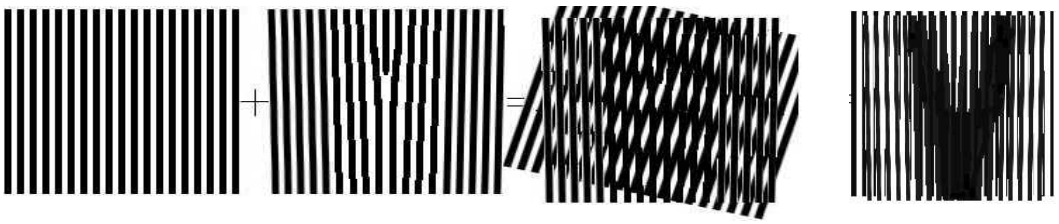

Angular mismatch moiré Parallel moiré

Figure 1 Illustration of moiré patterns for dislocation

Moiré fringes can also be used to measure the lattice slip δ and to identifythe dislocation. Dislocations occur at the places where fringes join or drop. The joining fringes are formed by aligning the reference-grating lines parallel to the specimen-grating lines; and dropped ones by placing the reference grating lines in an inclined angle with the specimen grating, as simulated in Figure 1. Even the incomplete or Peierls dislocation can be identified by the shearing of moire fringes. Moiré patterns with

these signatures are easy to be identified from the HREM image and reference grating interference.

The fringes produced by direct superposition of HREM image of crystal lattices and reference grating are hardly visible. But they can be transformed into fringes of high contrast by an optical filtering process as illustrated in Figure 2. The light that passes through the grating structure is diffracted into several diffraction orders, while the light that passes through the gray continuous-tone areas does not diffract. The field lens converges the transmitted beams to separate points in its focal plane, corresponding to diffraction orders from the striped areas. The light from the continuous-tone areas converges to point 0. The camera only admits light of one nonzero diffraction order, the image on the camera screen is bright at all points corresponding to striped areas, and dark elsewhere. Both coherent and non-coherent lights can be chosen as the light source in the filtering apparatus. We use laser here to obtain higher fringe contrast and resolution, at the risk of speckle noise. A Panasonic WV-BP310/G CCD video camera connected to a microcomputer collects all images.

Initial fringes may occur due to either initial lattice defects or the mismatch between lattice image and reference grating. We recorded the specimen-lattice images before and after loading. The actual results are delivered by subtracting the initial data from the final ones. A reference area is selected. It should be free of defects, unloaded or with diminishing stress. The fringes in that area characterize the mismatch between the magnified lattice spacing and the reference grating. The mismatch fringes are then subtracted from the final results.

The testing samples were cut from a Si sheet in the primary cleavage plane {111} so that the lattice image can be easily recorded. The loading device and the specimen geometry are shown in Figure 3. The specimen was ground mechanically into a sheet of diameter d = 2mm and thickness h = 30 μm. The central area for the TEM analysis was thinned out by ionic bombardment till punching. A pre-compressed copper ring of diameter 2mm and thickness 0.4mm was glued on one side of the specimen, with the compression axis normal to the [110] direction. When the glue solidified, the copper ring was unloaded to exert tensile force onto the specimen. That process resembles displacement-controlled loading and creates a stable and atomistically sharp crack in the most cleavable direction of [110]. The crack arrests after propagating a limited distance.

A transmission electronic microscope (JEM-200cx) was used to take the lattice image and the moiré fringes were produced by the method mentioned above. The magnification is 200,000 times. The magnified lattice lines in [110] direction have a frequency of about 16 lines/mm. Accordingly, adjacent fringes roughly represent the difference of one Burgers vector in the normal displacements. Figure 4(a) is the fringe pattern without rigid-rotation mismatch. The nano-crack approximately lies in the horizontal direction. Symbols D and A label the locations of the crack tip before and after loading. The discontinuity of the out-of-plane displacement along the crack makes the focusing on both sides of the crack difficult, so we only present the fringe pattern above the crack. The fringe pattern represents the contour map of the displacement in y-direction, though includes initial mismatch fringes between lattice image and reference grating.

Direct measurement of the strain distribution ahead of a crack tip is instrumental to understand the microscopic failure mechanism of brittle materials. In the present test, the distribution of strain in y-direction along the line AX was obtained from the fringe pattern in Figure 4(a). Up to now all crack tip strain measurements can only reach a resolution of about 0.1micron [9]. The measurements (with the initial fringes subtracted) shown by the square dots in Figure 5, however, provides data points as close as 4nm from the crack tip. The measured strain distribution was compared to the solid curve plotted under the linear elastic fracture mechanics (LEFM) prediction $\varepsilon_y = K(1-\nu)/(E\sqrt{2\pi x})$ under the plane stress case, where $K \approx 1.21\text{MPa}\sqrt{\text{m}}$ is the correlated mode I stress intensity factor. A Young's modulus of

107GPa and a Poisson's ratio of 0.3 are used for silicon in that correlation. The HREM-moiré measurements on strain agree perfectly with the LEFM prediction up to 10nm from the crack tip. Within the 10nm range, the measured strain is somewhat lower than the LEFM prediction. The strain at the crack tip may reach 5%, indicting an in-plane equal-biaxial stress as high as 7.6GPa.

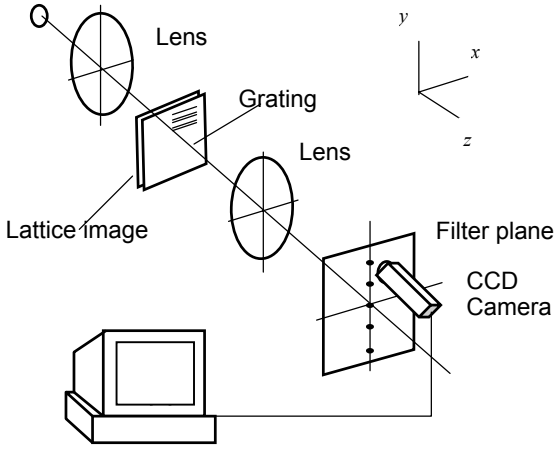

Figure 2 Optical filtering apparatus

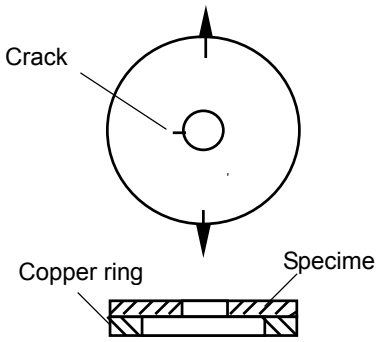

Figure 3 Specimen and loading device

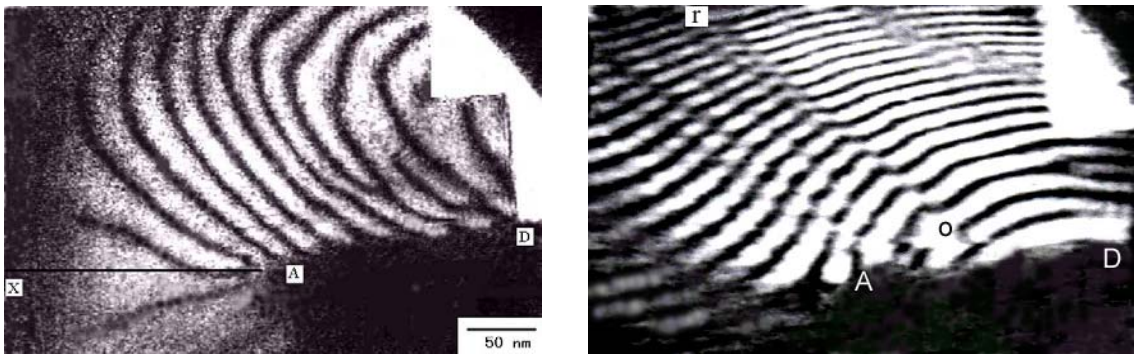

(a) (b)

Figure 4 Moiré fringe patterns near a crack tip: (a) without rigid-body-rotation mismatch, and (b) with rigid-body-rotation (α =0.011 rad) and constant strain ($\varepsilon = -0.035$) mismatch.

Figure 4(b) shows the moiré fringes that were deliberately taken to reveal dislocation emission from the crack tip. A slightly coarser reference grating was designed to get denser moiré fringes, and the reference grating was rotated slightly to resolve the kinking of moiré fringes across the dislocation planes. Through calibration at the location remote from the crack tip, we found those operations rotate the reference grating by $\alpha = 0.011$ radians and superpose a uniform strain of $\varepsilon = -0.035$ in the y direction. The fringes join or drop at a few places near the crack line. The amount of dislocation emissions is less than the previous observation [6]. The reasons may be listed as follows: (1) the current test was carried out in single crystal silicon at room temperature ($T = 24.5^{\circ}\mathrm{C}$); (2) the crack extends in the most cleavable plane of [110] while the dislocations emit from the non-primary glide plane; and (3) the deformation field for closely packed dislocations or dislocation dipoles are hardly resolvable at nanoscopic scale.

Figure 4(a) shows that more dislocations nucleate near point D than point A. Accordingly, cleavage proceeds after dislocations emit, and the spread deformation field associated with a running crack suppresses the further dislocation emission. Only incomplete dislocations are observed near the cracking path, as indicated in Figure 4(b) by several slip traces in about 45° direction with respect to the crack.

The moiré fringes kink along these lines. These slip traces are nearly parallel to each other, suggesting that a crack propagated in step-by-step manner, as illustrated in Figure 6.

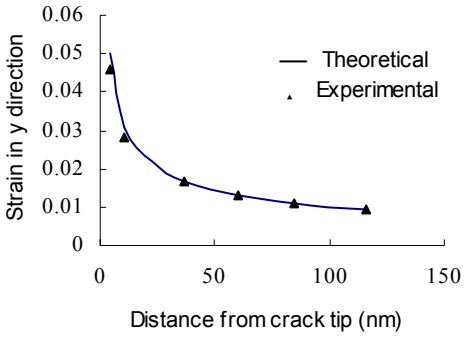

Figure 5 Strain distribution in *y* direction ahead of the crack tip.

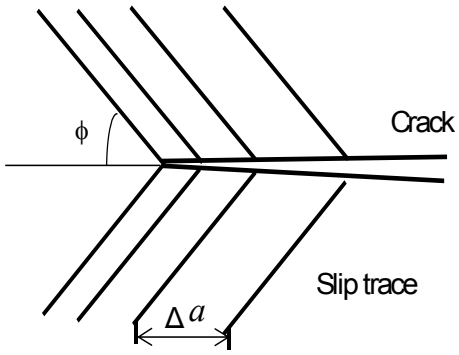

Figure 6 Schematics of crack growth in step-by-step manner

Zielinski *et al.* [10] reported step-by-step crack growth for Fe-2wt%Si and showed that the cleavage crack left 3.5 slip traces of residual dislocations for every 100nm crack growth, with an average of 18.6 dislocations per trace. Zhu *et al.* [11] defined a crack tip opening angle (CTOA) as $\mathrm{CTOA} = 2\tan^{-1}\left(nb\sin\phi/\Delta a\right)$, where b denotes the amplitude of Burgers vector, Δa the step size of cracking and n the number of dislocations emanated during each cracking step. In the present case, the incomplete dislocations has to be included as:

$$\mathrm{CTOA} = 2\tan^{-1}\left(\frac{nb+\delta_r}{\Delta a}\sin\phi\right) \qquad (3)$$

Where δ_r represents the slip in radial direction due to incomplete dislocations. The non-mismatched moiré fringes in Figure 4(a) can be used to determine the CTOA as $b/\Delta f$, where Δf is the fringe interval along AD nearest to the current crack tip. The CTOA is evaluated as $0.014\mathrm{rad}$. Near the current crack tip, no complete dislocation have been formed, thus one has $n = 0$. The measurement from Figure 4(b) gives $\phi \approx \pi/4$ and $\Delta a = 20\sim30\mathrm{nm}$. Equation (3) then estimates the value of δ_r from 0.2 to 0.3nm, less than the lattice spacing 0.304nm of silicon.

Two kinds of dislocations can be observed from the fringe pattern. Three complete dislocations, whose moiré fringes share the similar features with Figure 1, can be observed near the point D of Figure 4(a). The other kind is the incomplete or Peierls-dislocations, one of them is along the line *or* in Figure 4(b). The moiré fringes are sheared along this line. They represent slip between lattice layers. The amount of slip gradually changes along the line *or*, as recorded in Figure 7. The slip of lattice is zero at the point far from the crack tip and is one Burgers vector at the tip. This type of lattice slip assembles the structure of a nucleated Peierls dislocation [3] from a crack tip that provides direct experimental support for the Peierls framework concept [4].

The slip range represents the width of a dislocation. Based on the Frenkel sinusoidal shear stress-slip relation, Beltz and Rice estimated the width of a Peierls dislocation from a crack tip as $R = 0.0628Eb^2/[(1-\nu^2)\gamma_{us}]$, where γ_{us} denotes the unstable stacking energy [4]. For silicon, $\gamma_{us} = 0.16Eb$, consequently $R \approx 4.36b$. The present test, however, suggests a much larger value of

$R \approx 600b$, as evidenced in Figure 7. Explanation is needed for such a long extension of dislocation slip from a crack tip.

AKNOWLEGEMENT

The authors greatfully acknowledge the support by the National Natural Science Foundation of China (19962001).

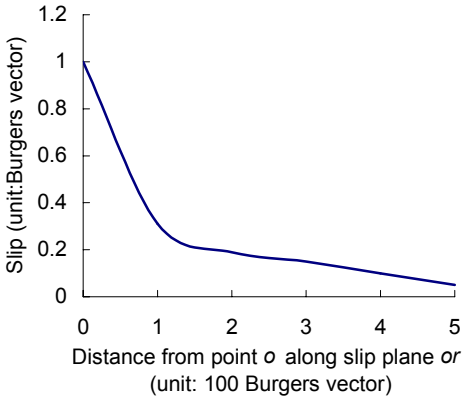

Figure 7 Slip distribution along a Peierls dislocation

REFERENCE

1. Ashby, M.F. and Embury(1985), J.D. Spripta Metall. 19, 557; Argon, A.S., Acta Metall(1987). 35, 185; Brede M. and Haasen, P.(1988) Acta Metall. 36, 2003; Hirsch, P.B. and Roberts, S.G. Phil. Mag. (1991) A64, 55; Hsia, K.J. and Argon, A.S. (1994), Mater. Sci. & Eng. A176, 111.
2. Rice, J.R. and Thomson, R.(1974), Phil. Mag., 29, 73.
3. Peierls R.E. (1940), Proc. Phys. Soc. 52, 23.
4. Argon, A.S.(1987), Acta Metall. 35, 185; Chiao,Y.H. and Clark, D.R.(1989) Acta Metall. 37, 203; Schoeck, G.(1991), Phil. Mag. A63, 111; Rice, J.R.(1992), J. Mech. Phys Solids 40, 239; Beltz G.E.and Rice, J.R. (1992), Acta Metall. Mater. 40, 321; Rice, J.R. and Beltz, G.E. (1994), J. Mech. Phys. Solids 42, 333; Schoeck, G. (1994), Phil. Mag. A69, 1085.
5. John, C.S., (1975),Phil. Mag. 32, 1193; Brede, M. K., Hsia J.and Argon, A.S., J.(1991)Appl. Phys. 70, 758; Mesarovic, S.D.J. (1997), J. Mech. Phys. Solids, 211.
6. Post, D.(1980), Mechanics of Nondestructive Testing, ed. Stinchcomb, W.W., Plenum Press, NY,; Kishimoto, S. *et al.*, Proceedings of 6th International Conference on Mechanical Behavior of Materials, ed. Jones(1991), M.,4, 661; Dally, J.W. and Read, D.T.(1993)., Experimental Mechanics 33, 2704
7. Dai, F.L and Xing, Y.M.(1999), Acta Mechanica Sinica 15, 283.
8. Hirsch, P., Howie, A., Nicholson, R., Pashley, D.W. and Whelan, M.J.(1977), Electron Microscopy of Thin Crystals, Krieger, Malabar, FL.
9. Mao T.H. *et al*(1983), J. Materials Sci. Letter, 2, 613; Shield T. W.and Kim, K.S. (1994), J. Mech. Phys. of Solids, 42, 845; Shi Y. Q., *et al.*(1996), Experimental Mechanics, 36, 193.
10. Zielinski, W., Lii, M.J.and Gerberich, W.W. (1992), Acta Metall. Mater. 40, 2861.
11. Zhu, T. Yang, W.and Guo, T. (1996), Acta Metall. Mater. 44, 3049.

Mechanical and Fracture Properties of Methacrylic Particle-Modified PVC

Y. Nakamura[1], E. Takekuni[1], Y. Kinugawa[1], and T. Iida[1]

[1] Department of Applied Chemistry, Osaka Institute of Technology,
5-16-1, Ohmiya, Asahi-ku, Osaka, 535-8585 Japan

ABSTRUCT

The effect of interfacial structure on the mechanical properties of an incompatible polymer blend have been investigated. For this purpose, uncrosslinked and crosslinked poly(methyl methacrylate) particles having the mean size of about 0.8 μm are prepared by a seeded emulsion polymerization, and then the amount and the distribution of crosslink points in the particles are varied. The obtained emulsion particles are powdered by a freeze dry method and dispersed into poly(vinyl chloride) matrix by a melt blending. The uncrosslinked particles are completely dissolved in the matrix due to a good compatibility of poly(methyl methacrylate) with poly(vinyl chloride). In the case of the crosslinked particles, the mutual diffusion of the polymer molecules is restricted within the particle/matrix interfacial regions by the crosslink points. The interfacial structures with different concentration slope dependent upon the amount and the distribution of inner crosslink points are developed with the same particle size. It is found that the yield stress decreases with a decrease in the interfacial adhesion. When the interfacial adhesion is sufficient, the yield stress was never lower than those of their components.

KEY WORDS

Poly(vinyl Chloride) / Compatibility/ Interphase/ Emulsion Polymerization / Poly(methyl Methacrylate)

INTRODUCTION

In this study, the effect of interfacial adhesion on the mechanical and fracture properties were investigated using a model system. For this purpose, uncrosslinked and crosslinked PMMA particles, which have the same particle size, were prepared by a seeded emulsion polymerization. The amount and the distribution of the crosslink points in the particles were controlled by varying the addition period and the concentration of the crosslinking monomer. These emulsions were dried, and the obtained powder was dispersed into the PVC matrix by melt blending. It is well known that PMMA has a good compatibility

with PVC. Thus, uncrosslinked PMMA particles can be compatible completely in the PVC matrix[1,2]. On the other hand, in the cases of the crosslinked PMMA particles, the crosslink points restricted the mutual diffusion of the polymer molecules within the interfacial regions. As a result, it was expected that the interfacial structures with different "concentration gradience" dependent upon both the amount and the distribution of inner crosslink points would be developed at the interphase with the same particle size. The interfacial structure was characterized, and the investigation of the effects on the mechanical and fracture properties was carried out. And the effect of particle size was also investigated in the particle diameter range of 0.3 – 0.8 μm with the same interfacial adhesion level.

EXPERIMENTAL

Materials

Commercial grade methyl methacrylate (MMA) and ethylene glycol dimethacrylate (EGDMA) monomers were purified by distillation under reduced pressure in a nitrogen atmosphere and they were stored in a refrigerator. Analytical grade potassium peroxodisulfate (KPS) and sodium lauryl sulfate (SLS) were used without further purification as initiator and surfactant, respectively. Commercial grade PVC (Geon 103 EP, Nippon Zeon Co., Ltd., polymerization degree: 1050) and lead stearate (Katayama Chemical Industries Co., Ltd.) as a stabilizer for PVC were used.

Table 1 Recipe of seeded emulsion polymerization [a].

Emulsion No.	1	2	3	4	5	6	7	8
Emulsion No. 1	–	62.70	–	–	–	–	63.15	–
Emulsion No. 2	–	–	10.27	10.30	10.20	10.10	–	–
Emulsion No. 7	–	–	–	–	–	–	–	11.38
MMA [b] (g)	100.70	87.50	127.8	128.53	123.81	118.04	81.41	128.38
EGDMA [c] (g)	–	–	–	1.40	6.37	12.34	6.19	–
SLS [d] (g)	0.40	–	0.40	0.40	0.40	0.40	–	0.40
KPS [e] (g)	0.40	0.35	0.50	0.50	0.50	0.50	0.35	0.50
Water (g)	400.2	350.0	512.0	510.7	512.5	510.0	350.1	498.7
Polymerization stage	1st	2nd	3rd	3rd	3rd	3rd	2nd	3rd
MMA/EGDMA [f]			100/0	99.5/0.5	97.5/2.5	95/5		97.5/2.5
Concentration of crosslinked points [g]			No		Higher in the surface layer			Higher in the inner part
Code [h]			Type A	Type B-0.5	Type B-2.5	Type B-5		Type C-2.5

[a] Polymerization temperature: 70°C. Atmosphere: N_2.
[b] Methyl methacrylate.
[c] Ethylene glycol dimethacrylate.
[d] Sodium lauryl sulfate.
[e] Potassium peroxodisulfate.
[f] Mol fraction in the finally obtained particles.
[g] Expected from the added stage of EGDMA during seeded emulsion polymerization.
[h] Mol fraction of EGDMA was shown at the end of each Type.

Seeded Emulsion Polymerization

Table 1 shows the recipes of seeded emulsion polymerization. The concentration of surfactant (SLS) was lower than the critical micelle concentration. The No.1 PMMA emulsion was used as a common seed particle. EGDMA was used as a crosslinking monomer. The seeded emulsion polymerization with three stages was carried out to make the particle size larger. In the second and third stage, the monomer was added dropwise during the polymerization process. The obtained PMMA particle (No. 3) without EGDMA is called Type A. In the preparation processes for Nos. 4 – 6 emulsions, EGDMA was added

during the third stage, and then the amount was varied from 0.5 to 5 mol % in the final particle. They are called Type B. EGDMA was added in the second stage for the No. 8 emulsion at the content of 2.5 mol %. The particle is called Type C. The EGDMA content in the final obtained particles is shown at the end of each Type (ex. Type B-5). All polymerizations were continued until the conversion reached above 98 %. The obtained emulsions were powdered by a freeze-dry method using a freeze-dryer (FDU-506, Tokyo Rikakikai Co., Ltd.). The mean particle size was about 0.8 μm for all the samples described above, which was determined using scanning electron microscopy (SEM).

The Types B-2.5 and B-5 particles having the mean diameter of 0.6 μm were prepared by changing the amount of added monomers in the third stage. Those having the mean diameter of 0.3 μm were prepared by the seeded emulsion polymerization with two stages. That is, the MMA and EGDMA monomers were added to the common seed particles (No. 1) in the second (final) stage.

Sample Preparation

PVC, lead stearate (3 parts per hundred parts of resin by weight, phr) and PMMA particles (10 - 50 phr) were mixed using a mixing roll at 200 ± 5°C for 10 min. About 0.8 mm-thickness sheets were prepared by compressing the mixed compounds at 200°C under a pressure of 19.6 MPa for 2 min. The prepared sheets were quenched by a cold press.

The conventional PVC/PMMA blend was also prepared to make a comparison with the particle-modified PVCs, and it was called "PMMA blended PVC" in this paper. For this purpose, the PMMA was prepared from Type A particles by the dissolution in acetone and the precipitation in water.

Mechanical Properties and Fracture Toughness

Mechanical properties and J_c, as fracture toughness for ductile polymer were measured in the same way as the previous articles[3-6].

RESULTS AND DISCUSSIONS

In this study, the crosslinked PMMA particles were prepared by the seeded emulsion polymerization with three stages. The crosslinking monomer (EGDMA) was added in the third (final) stage for the Type B particles, whereas in the second stage for the Type C particles as shown in Table 1. As a result, the different concentration gradience of the crosslink points is expected to be formed in the particle as follows:

Type A: No crosslink points.

Type B: Higher in the surface layer.

Type C: Higher in the inner part.

In the Type B particles, the amount of the crosslink points in the particle should be increased with an increase in the concentration of added EGDMA. And the different interfacial structures with concentration gradience with the same particle size should be formed in the PVCs modified with the Types B and C particles.

Firstly, the effect of interfacial structure on the mechanical properties was investigated.

Figure 1 shows the yield stress of particle-modified PVCs. The yield stress increased with an increase in the particle content in the Type A particle-modified PVC. The similar tendencies were observed in the

PMMA blended and the Type C-2.5 particle-modified PVCs. In the Type B particle-modified PVCs, whereas the yield stress was lower than Type A above 30 phr in the order of Type B-0.5 > B-2.5 > B-5.

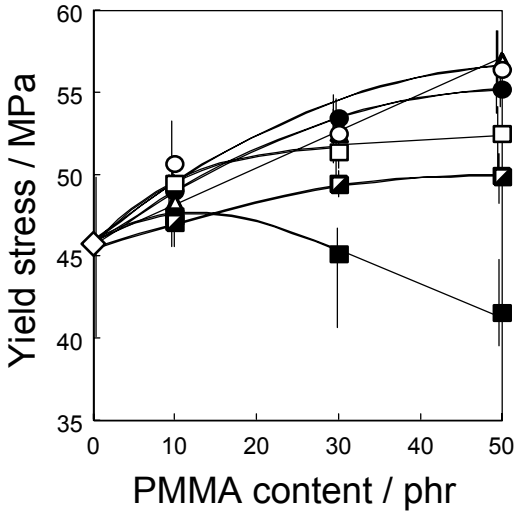

Figure 1 Yield stress of PVC modified with uncrosslinked (◇) and crosslinked PMMA particles and blended with PMMA (●). Modified particles: ○ ; Type A, □ ; Type B-0.5, ◪; Type B-2.5, ■ ; Type B-5,△ ; Type C-2.5.

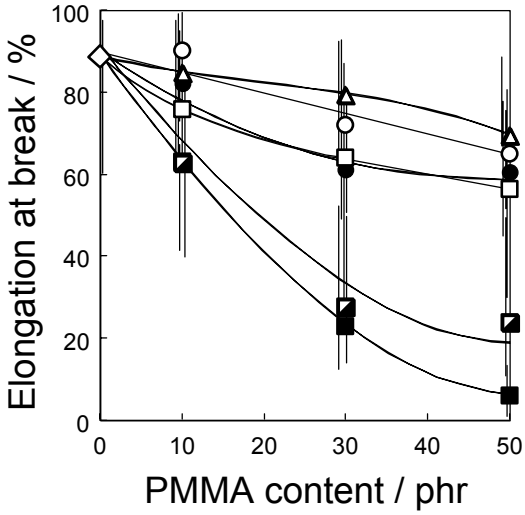

Figure 2 Elongation at break of PVC modified wi uncrosslinked (◇) and crosslinked PMMA particle and blended with PMMA (●). Modified particles: ○ ; Type A, □ ; Type B-0.5, ◪; Type B-2.5, ■ ; Type B-5,△ ; Type C-2.5.

Figure 2 shows the elongation at break of particle-modified PVCs. The elongation decreased gradually with the increase in the PMMA content for the Types A, B-0.5 and C-2.5 particle-modified and the PMMA blended PVCs. However, it became clear that the elongation was far lower in the Types B-2.5 and B-5 particle-modified than in the other PVCs.

From the results above, it was clarified that the yield stress and the elongation at break were strongly affected by both the amount and the distribution of crosslink points in the particles. And, the mechanical properties developed with a decrease in the amount of crosslink points within the Type B particle-modified PVCs. And then, the better mechanical properties were obtained in the modified PVC with particles having the crosslink points at the inner part (Type C) than those at the outer layer (Type B).

Figure 3 shows the tensile fractured surfaces observed by SEM. In the Type A (a), no particles were observed on the surface. This indicated that the PMMA was dissolved in the PVC matrix, because PMMA have a good compatibility with PVC. The similar result was obtained in the PMMA blended PVC (The data doe not appear in Figure 3).

On the other hand, in the Type B-5 (c), the mixed particles were clearly observed on the fractured surface, and the interfaces were completely debonded. They had almost the same sizes of the modified Type B-5 particles. The particles were also observed in the Type B-0.5 (b); however, the interfaces became more unclear. The interface of Type B-2.5 was intermediate between Types B-0.5 (b) and B-5 (c). That is, it was found that the interfacial adhesion was stronger in the order of Type B-0.5 > B-2.5 > B-5. In the Type C (d), no particles were observed on the surface, and the surface was similar to that of Type A (a). These results show that the interfacial adhesion was stronger in the Type C-2.5 than in the all Type B.

From the results above, the concentration gradience of both polymers at the interfacial layer is expected to be higher in the order of Type B-5 > B-2.5 > B-0.5 > C-2.5. The similar aspects of above observations were also obtained from the dynamic mechanical analysis.

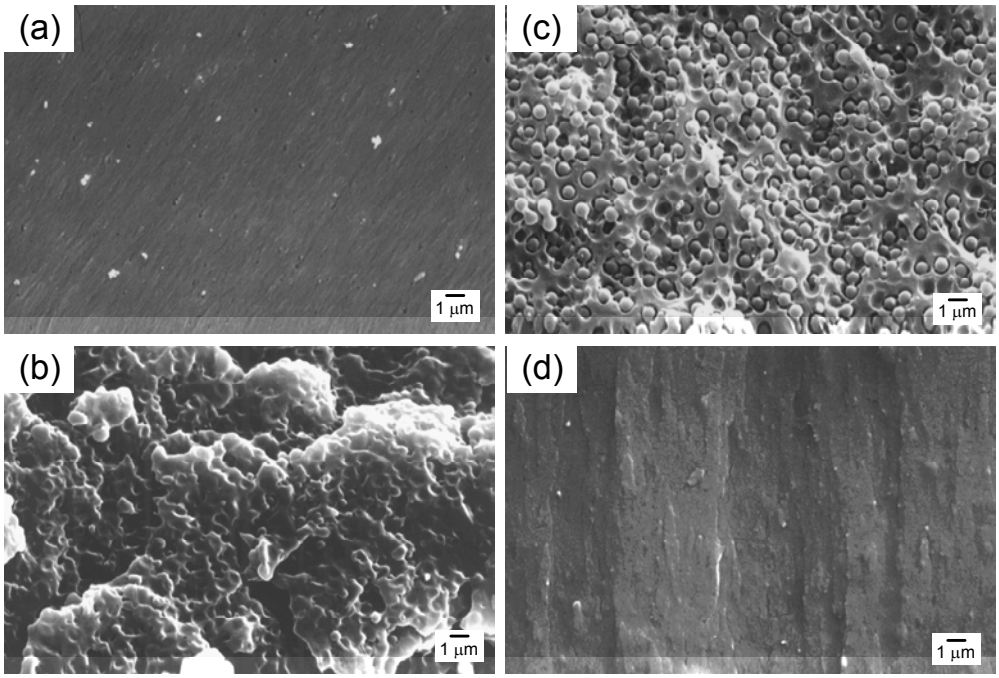

Figure 3 Fractured surfaces after tensile test observed by SEM of PVC modified with uncrosslinked (a) and crosslinked (b-d) PMMA particles at a particle content of 50 phr. Modified particles: (a) Type A, (b) Type B-0.5, (c) Type B-5, (d) Type C-2.5.

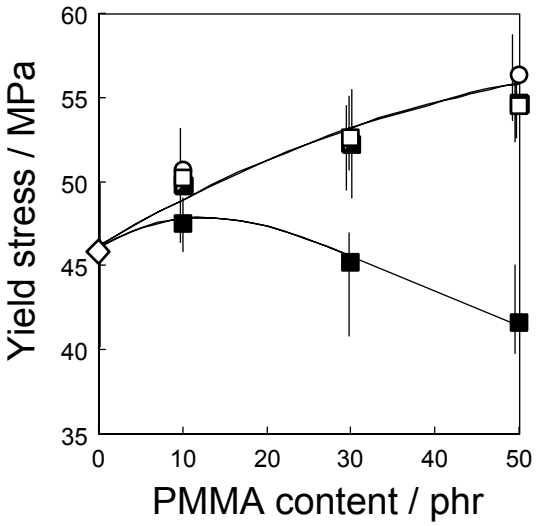

Figure 4 Yield stress of PVC modified with uncrosslinked (○ , Type-A) and crosslinked PMMA particles. Mean particle size: ○ ; 0.8 μm, □ ; 0.3 μm, ◪; 0.6 μm, ■ ; 0.8 μm.

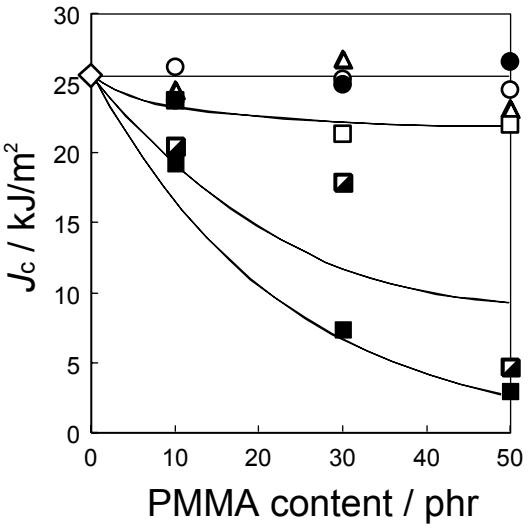

Figure 5 Fracture energy J_c of PVC modified with uncrosslinked (◇) and crosslinked PMMA particle and blended with PMMA (●). Modified particles: ○ ; Type A, □ ; Type B-0.5, ◪; Type B-2.5, ■ ; Type B-5, △ ; Type C-2.5.

Secondly, the effect of particle size on the mechanical properties was investigated in the particle diameter range of 0.3 – 0.8 μm in the Type B-5 particle-modified PVC having the weakest interfacial adhesion. The results of their yield stress is shown in Figure 4. The decrease of yield stress was never observed when the particle size was 0.6 μm and below in both modified PVCs. The following facts were confirmed; (i) the particles were well dispersed in the PVC matrix; and (ii) there was no influence of particle size on the interfacial adhesion from the SEM observation for the fractured surfaces and the AFM observation for the polished stress-whitened surfaces of the tensile specimen after test. As Figure 4 indicates, it is clear that the yield stress never decreased when the particle size is effectively small, despite having weaker interfacial adhesion.

Figure 5 shows the J_c of particle-modified PVCs with the same particle size (0.8 μm). There was no decrease in the J_c for the Types A and C particle-modified and the PMMA blended PVCs with an increase in the PMMA content. The J_c values for the Type B-0.5 particle-modified was almost the same level as those of above PVCs. On the other hand, the J_c of the Types B-2.5 and B-5 particle-modified PVCs were different and decreased significantly with an increase in the particle content in the modified PVC and the amount of crosslink points in the particles.

From the results above, it seems reasonable to suppose that the interfacial gradience would bring the effective blend or particle-filled composite without sacrificing anything in their mechanical and fracture properties.

CONCLUSIONS

It was an investigation of the effects of interfacial adhesion and particle size on the mechanical properties and fracture toughness in the PVC modified with crosslinked PMMA particles prepared by a seeded emulsion polymerization having different amount and distribution of crosslink points. Following results were obtained.

i) The interfacial structures with different concentration gradience which is dependent upon the amount and the distribution of inner crosslink points seemed to be developed.
ii) The yield stress and the fracture toughness decreased with a decrease in the interfacial adhesion, namely an increase in the concentration gradience.
iii) The decreasing of particle size with a weaker interfacial adhesion has the effect on the improvement of the yield stress.
iv) When the interfacial adhesion is sufficient, it never occurred that the level was lower than those of their components in the mechanical properties and the fracture toughness.

REFERENCES

1. S. Havriliak, and J. Shortridge, *Polymer*, **29**, 70 (1988).
2. R. Flores, J. Perez, P. Cassagnau, A. Michel, and J. Y. Cavaillé, *J. Appl. Polym. Sci.*, **60**, 1439 (1996).
3. Y. Nakamura, Y. Fukuoka, and T. Iida, *J. Appl. Polym. Sci.*, **70**, 311 (1998).
4. Y. Nakamura, M. Kanbe, and T. Iida, *J. Adhes. Soc. Jpn.*, **36**, 338 (2000).
5. Y. Nakamura, K. Nagata, N. Yoshimoto, H. Okumura, S. Okabe, H. Nigo, and T. Iida, *J. Adhes. Soc. Jpn.*, **36**, 53 (2000).
6. Y. Nakamura, H. Okumura, N. Yoshimoto, T. Iida, K. Nagata, H. Nigo, H.Yoshitani, T. Nishino, and K. Nakamae, *Polym. Polym. Compos.*, **8**, 123 (2000).

ORAL REFERENCE: 978

MECHANICAL BEHAVIOR AND ELECTRICAL RESISTANCE CHANGE IN CARBON PARTICLE DISPERSED PLASTIC COMPOSITE

D-Y. Song , Y. Hirata and N. Takeda

Graduate School of Frontier Science, The University of Tokyo c/o Komaba Open Laboratory (KOL), The University of Tokyo, 4-6-1 Komaba, Meguro-ku, Tokyo 153-8904, Japan

ABSTRACT

Mechanical behavior and electrical resistance change of CPDP (carbon particle dispersed plastic) composite consisting of epoxy resin and conductive carbon particle were investigated under monotonic loading and repeated loading-unloading. The electrical resistance almost linearly increased with increasing strain during loading and the residual electrical resistance was observed even after removing load. The value of the residual electrical resistance was dependent on the maximum strain under the applied stress. This result suggests that the estimation of maximum strain (i.e., damage) is possible by the measuring electrical resistance of composite. The behavior of electrical resistance change during and after loading was discussed on the basis of the results of microscopic deformation and fracture observation. Moreover, the relationship between the volume fraction of carbon particle and the electrical resistivity of CPDP was investigated in relation to the percolation theory. Simulation model of percolation structure was established by Monte Carlo method and the simulation result was compared to the experimental results. The electrical resistance change under applied loading was analyzed quantitatively using the percolation equation and a simple model for the critical volume fraction of carbon particle as a function of the mechanical stress. It was revealed that the prediction was in good agreement with the experimental result except in the region near the failure of material.

KEYWORDS

Carbon particle , Mechanical behavior , Damage , Electrical resistance change, Percolation

INTRODUCTION

The electrical resistance method is expected to be effective for foreseeing damage and preventing fatal fracture of composite material structure. Recently, the relationship between the mechanical parameters (i.e., stress and strain) and the changes in electrical resistance of CFRP composite has been experimentally demonstrated [1-2]. Moreover, the damage detection utilizing the percolation structure of conductive particle instead of carbon fiber has been made [3], but this study was limited to the qualitative evaluation, and the systematic evaluation

with regard to the correlation between mechanical behavior and electrical resistance change is not yet made. In the present study, the relationship between mechanical behavior and the change of electrical resistance for CPDP (carbon particle dispersed plastic) composite was evaluated using both experimental and theoretical methods. To this end, the monotonic loading and repeated loading-unloading tensile tests were carried out using CPDP with epoxy resin and conductive carbon particle, and its microscopic deformation and fracture were observed. Moreover, the relationship between the volume fraction of carbon particle and the electrical resistivity of CPDP was investigated in relation to the percolation theory. Simulation model of percolation structure was established by Monte Carlo method and this result was compared to the experimental results. Finally, the electrical resistance cha nge under applied load was analyzed quantitatively using the percolation equation and a simple model for the critical volume fraction of carbon particle as a function of the mechanical stress (strain).

EXPERIMENTAL PROCEDURE

The materials used were the conducting carbon particle with the flake shape of average size 5μm and an insulting epoxy matrix (Epikote 828 Yuka Shell Co.). Specimens were prepared as follows: firstly, carbon particle and epoxy resin were mixed in a given proportion and pores in this mixture was removed under vacuum. Then, the mixture was injected into the teflon-made mold of dumbbell shape and cured in the electrical furnace under the condition of precure at 50°C, 80min, and aftercure at 100°C, 60min (hereafter, this composite was referred to CPDP). The electrodes for measuring electrical resistance were attached on the opposite surfaces, which were first polished to suppress the insulating matrix surface layer, within the gage length of specimen using silver paste. The dimensions of specimens were 105mm in length, 10mm in width and 1mm in thickness. Tensile tests were conducted at the crosshead speed of 0.5mm/min. The electrical resistance was measured using two-probe DC method. A constant current of 0.1μA was applied on the specimen, and the changes in electrical resistance under loading and unloading were measured simultaneously with stress and strain. Microscopic deformation on specimen surfaces was observed using polarization microscope under loading and fracture surfaces were also observed using scanning electron microscope (SEM) after tensile test.

EXPERIMENTAL RESULTS AND DISCUSSION

Figure 1 shows the electrical resistance change/strain and stress/strain curves for CPDP with 10vol.% carbon particle. The change in electrical resistance exhibited nearly linear behavior up to the final failure of specimen

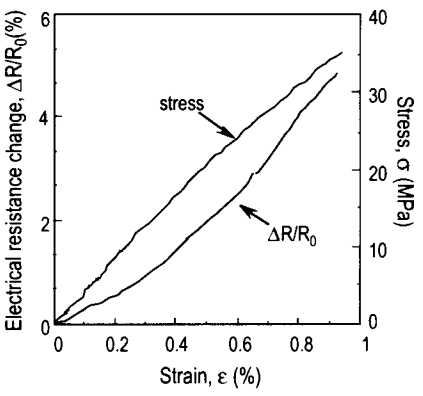

Figure 1: Relations of $\Delta R/R_0$ vs. ε and σ vs. ε for CPDP with 10 vol. % carbon particle

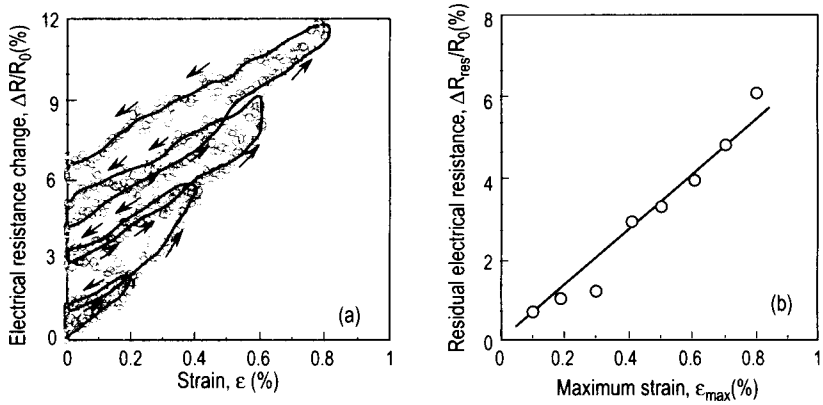

Figure 2: Relations of (a) $\Delta R/R_0$ vs. ε and (b) $\Delta R_{res}/R_0$ vs. ε_{max} for CPDP with 15 vol. % carbon particle

with increasing strain. In particular, CPDP indicated the change in electrical resistance from a considerably small strain level compared to the case of CFRP showing electrical resistance change due to the fracture of carbon fiber mainly. This was the reason why the percolation structure formed with carbon particle showed the sensitive response (i.e., the change of conduction path) against applied loading. Figure 2(a) shows the electrical resistance change/strain curve for CPDP with 15vol.% carbon particle obtained from repeated loading and unloading test. It was seen that the change in electrical resistance was left after unloading at a relatively small 0.2% strain and increases with increasing strain. Figure 2(b) shows the relation between maximum strain applied in the past and residual electrical resistance. The value of residual resistance was dependent on the maximum strain under the applied load. This means that the CPDP has the ability to memorize the maximum strain applied in the past as a residual electrical resistance. This change in electrical resistance under applied load is considered to be caused by the rearrangement of carbon particles with percolation structure due to the microdeformation and cracking of matrix. Figure 3 shows a SEM micrograph of a fracture surface of the CPDP specimen with 15vol.% carbon particle. It was seen that matrix cracking and plastic deformation were significantly observed on the fracture surface, but carbon particles were not observed on the fracture surface. It can be considered that most of carbon particles dropped out when the final fracture of specimen occurred because of the weak adhesion between particle and matrix. Figure 4 shows a polarization micrograph for the surface of CPDP specimen with 0.1vol.% carbon particle. The plastic deformation of matrix surrounding carbon particles was clearly observed as indicated by arrows in this figure. Therefore, the existence of residual electrical resistance as described above is considered to be attributed to this plastic deformation of matrix, leading to the change of geometrical arrangement of carbon particle from its initial state (i.e., the change of conduction path).

Figure 3: SEM micrograph of fracture surface of specimen with 15 vol. % carbon particle

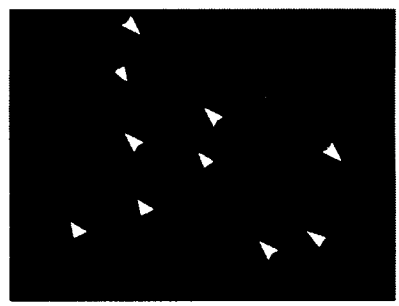

Figure 4: Polarization micrograph of specimen with 0.1 vol. % carbon particle

THEORETICAL ANALYSIS OF ELECTROMECHANICAL PROPERTY OF CPDP

Percolation theory

The property of composite system composed of conductive carbon particle dispersed in insulting polymer matrix are explained as percolation phenomena i.e., when the amount of carbon particle is sufficiently high, the composite transforms from an insulator to a conductor as the result of continuous contacts betweencarbon particles (i.e., percolation) within the polymer matrix. Generally, close to the percolation threshold, the concentration dependence of resistivity in a conductor-insulator composite has been well expressed with percolation theory [4-6].

$$\rho(V) = A(V - V_c)^{-t} \tag{1}$$

where, V_c is the critical carbon volume fraction required to form a continuous conduction path, ρ (V) is the resistivity at carbon volume fraction,V, A and t are the constants. According to literature [7-9], t was found to exist between 1.65 and 2.0 for three dimensional system. Figure 5 shows the variation of resistivity with volume fraction of 5μm carbon particle. It is seen that the resistivity decrease abruptly when the carbon volume

fraction exceeds a critical value. This suggests that the percolation theory can hold in the present experimental results. The constants in Eqn. 1 were obtained using a least square fit to the experimental data. The obtained values are V_c= 0.065, t= 1.9, A = 0.003 MΩ mm The curve calculated with these values is also plotted in Figure 5, showing a good agreement with experiments.

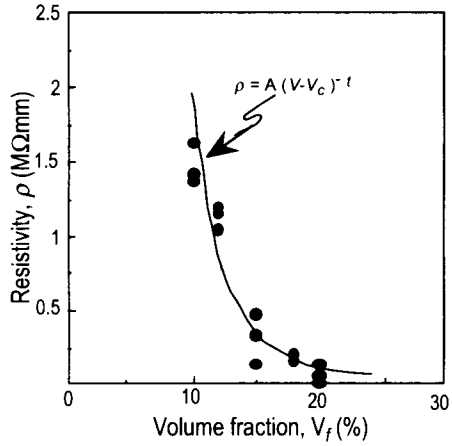

Figure 5: Relations of ρ vs. V_f for 5 μm carbon particle

Simulation Model of Percolation Structure

A simulation model of percolation structure was established by Monte Carlo method. Here, two dimensional random array problem was simulated as follows: At first, the sites of n =1000, which correspond to carbon particles, were randomly arranged in a square of side unity. In order to satisfy the normal distribution with the standard deviation of 0.2R, the circles of the radius, R=1/ (π n)$^{0.5}$ were randomly assigned to each site. Next, for the constructed sites, we examined whether the conduction path between any two sites was formed. Here, we firstly introduced the distance between sites as follows:

$$d_{ij} = [(x_i - x_j)^2 + (y_i - y_j)^2]^{0.5} \tag{2}$$

where, x_i and y_i, x_j and y_j are the coordinates at sites i and j. Then, setting $R_{ij} = R_i + R_j$, the conduction path between sites could be judged by the following equation:

$$H(x) = R_{ij} - d_{ij} \tag{3}$$

where, $H(x)$ is Heaviside function ($H(x)$ =0: $x < 0$, $H(x)$ =1: $x \geq 0$). Thus, $H(x)$ = 1 is the formation condition of conduction path between sites. The condition that two sites exists in the same cluster connected by conduction path was given by

$$B_{ij} = \prod_{a=1}^{A} H_a(x) = 1 \tag{4}$$

where, A is the number of Heaviside functions between sites i and j.

Thus, as the check of the overall percolation in the square, when at least one site having the same cluster number exists at the edges of both directions of x and y in a square (i.e., spanning state), we regard this state as the starting point of percolation. However, during the entire conduction path was not identified, the same way as described above was repeated until the percolation reaches as the radius R increases at the rate of 0.05R. The radius of site at percolation state was referred to the critical radius R_c.

Simulation Result

The process of percolation formation obtained by two dimensional simulation is shown in Figure 6. The critical volume fraction, V_c obtained from the simulation was about 48 vol.%. This value is very high compared to the

value of about 7 vol.% obtained from the experimental results. This difference can be explained by the tunneling effect of conductive particles. For conductive particle-polymer composites, it has been recognized that although the particles were not completely interconnected, the conductive phase was activated and the electrical network was formed (that is, tunneling effect) [10-12]. Considering such a tunneling effect, it can be seen that the site area of this simulation is not the area of particle but corresponds to the region affected by the tunneling effect. Thus, it was simply assumed that the tunneling effect existed to a certain distance on the particle size. That is, for the particle of radius R, if the tunneling effect was effective to the range of kR, the value of k, which might be a constant representing the extent of tunneling effect, was found to be about 2.71 using the average critical volume fraction of 48 vol.%. Thus, it can be said that the tunneling effect existed to the distance of about 8.3μm from the surfaces of particles for the particle of average diameter 5μm.

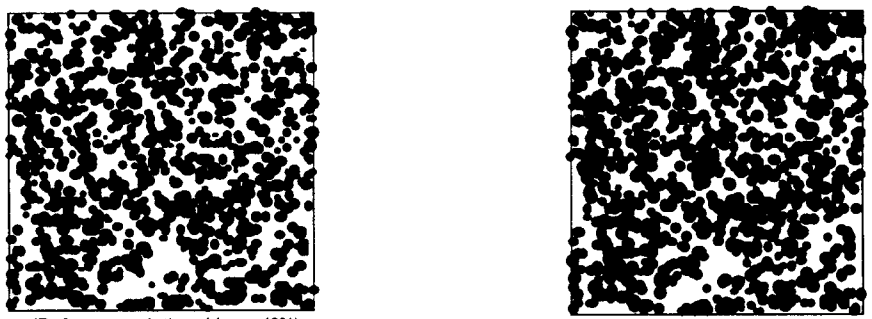

Figure 6: Process of percolation formation

Approximate Analysis of Electrical Resistance Change Under Applied load

The change of electrical resistance of CPDP with tensile loading will be developed using Eqn. 1. Here, the critical volume fraction, V_c, as a first approximation, was assumed to change linearly with applied stress. Moreover, in the case of conductive particle-polymer composite the average number of contacts per particle changes linearly with stress, and was known to be inversely proportional to the critical volume fraction [13, 14]. Thus, the critical volume fraction with stress can be expressed as a simple form as follows:

$$V_c(\sigma) = \frac{V_c(0)}{1 - \alpha\,\sigma} \tag{5}$$

where, $V_c(0)$ was 0.065, the critical volume fraction when the applied stress was absent. This value was obtained from the relationship between the resistivity and the volume fraction described in Figure 5. α is a constant. Then, substituting Eqn. 5 into the percolation Eqn. 1, the resistivity and its change of CPDP under applied stress were finally determined from the following Eqns. 6 and 7.

$$\rho = A\,[V - \frac{V_c(0)}{1 - \alpha\,\sigma}]^{-t} \tag{6}$$

$$\frac{\Delta\rho}{\rho_0} \approx \frac{\Delta R}{R_0} = \left[\frac{V - \dfrac{V_c(0)}{1 - \alpha\,\sigma}}{V - V_c(0)}\right]^{-t} - 1 = \left[\frac{V - \dfrac{V_c(0)}{1 - \alpha\,E\,\varepsilon}}{V - V_c(0)}\right]^{-t} - 1 \tag{7}$$

Figure 7 shows a comparison between the analysis result by Eqn. 7 and experimental result for the CPDP of 5μm carbon particle (in this study the resistivity of CPDP is equivalent to the its resistance, i.e., $\rho \approx R$). Here, the constant α was obtained by fitting Eqn. 7 to the experimental result and its value was 0.008. The predicted result agreed well with the experimental result below 0.6% strain near the failure of material, where damage and electrical resistance greatly changed. It can be therefore said that the electrical resistance change under applied loading is evaluated approximately using the percolation equation and an appropriate model for the

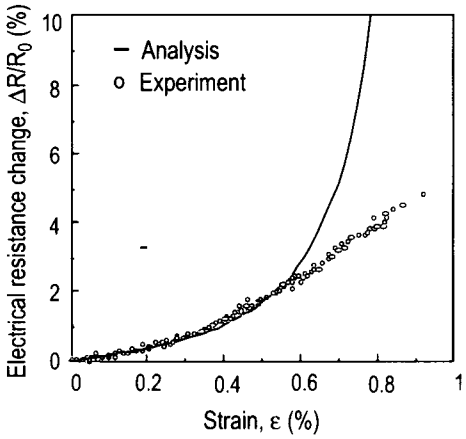

Figure 7: Comparison between analysis and experimental results

critical volume fraction of carbon particle as a function of the stress (or strain).

CONCLUSIONS

Mechanical behavior and electrical resistance change for CPDP (carbon particle dispersed plastic) composite were characterized under tensile loading and repeated loading-unloading. The electrical resistance almost linearly increased with increasing strain during loading and the residual electrical resistance was observed even after removing load. The value of the residual electrical resistance was dependent on the maximum strain under the applied stress. These results suggest that estimation of the maximum strain (damage state) is possible by measuring electrical resistance of composites. The electrical resistance change during loading was attributed to geometrical rearrangement (i.e., the separation of conduction path) of carbon particles with percolation structure due to the plastic deformation and/or the cracking of matrix. The residual resistance was found to be due to the plastic deformation of matrix remaining after removing loading. The relation between the volume fraction of carbon particle and the electrical resistivity of CPDP was well expressed by the percolation equation. Percolation process was simulated by Monte Carlo method. The electrical resistance change of CPDP under applied loading could be approximately analyzed using the percolation equation and a simple model for the critical volume fraction as a function of the stress. This electrical resistance method using the conductive carbon particle is considered to be effective for damage estimation of composite material and structure.

REFERENCES

1. Ceysson, O. et al. (1996) *Scripta Mater.* 34-8,1273.
2. Schulte, K. et al. (1995) *Proc. ICCM,* 349.
3. Takada, M. et al. (1999) *J. Japan Soc. Comp. Mater.* 25, 225.
4. McLachlan, D. S. et al. (1990) *J. Am. Ceram. Soc.*73-8, 2187.
5. Kirkpatrik, S. (1973) *Rev. Mod. Phys.* 45, 574.
6. Pike, G. E. et al. (1974) *Phys. Rev.* B10,1421.
7. Abeles, B. et al. (1975) *Phys. Rev. Lett.* 35, 247.
8. Carmona, F. et al. (1987) *J. Appl. Phys.* 61-7, 2550.
9. Zallen, R. (1983). *The Physics of Amorphous Solids*; Ch.4., Willey New York.
10. Balberg, I. (1987) *Phys. Rev. Lett.* 59-12, 1305.
11. Sichel, E. K. et al. (1978) *Phys. Rev. B.*18-10, 5712.
12. Ruschau, G. R. et al. (1992) *J. Appl. Phys.* 72-3, 953.
13. Gurland, J. (1966) *Trans. Metall. Soc.* AIME. 236, 642.
14. Aharoni, S. M. (1972) *J. Appl. Phys.* 43,2463.

MECHANICAL PROPERTIES OF IONOMER/CLAY NANOCOMPOSITE-MODIFIED EPOXY

S. Matsuda[1], H. Akimoto[1] and A. Murakami[1]

[1] Department of Chemical Engineering, Himeji Institute of Technology,
Shosha, Himeji 671-2201 JAPAN

ABSTRACT

Epoxy resin was modified with ionomer / clay nanocomposite. The hardener (DDM) content was controlled from 5 to 26phr because ionomer is expected to react with epoxy resin. Effect of DDM content on mechanical properties was investigated. The dynamic viscoelastic tests showed that the glass transition temperature increased with decreasing the DDM content. For the epoxy with 7 and 9phr DDM, there is no apparent grass transition temperature, and thermal resistance was considerably improved. Fracture toughness decreased with decreasing the DDM content. Whereas the fracture toughness value of the modified epoxy with 26phr DDM was 20% higher than that of the unmodified one, that with 9phr DDM was 40% less. These results can be explained by increase of crosslink in epoxy matrix which were caused by the reaction with epoxy and ionomer.

KEYWORDS

Epoxy, Ionomer, Nanocomposite, Thermal resistance, Dynamic viscoelasticity, Fracture toughness

INTRODUCTION

Epoxy resin which is a representative network polymer has been widely used because of its high thermal resistant property and easy processing. The epoxy resin has been modified by inserting various types of the additives to improve mechanical, electrical and the other properties; carboxyl-terminated butadiene acrylonitrile (CTBN) rubber was very effective in the enhancement of the fracture toughness of the epoxy resin[1-4]. Recently, some researchers reported on the addition of clay into the polymeric materials to enhance the thermal resistance and the elastic modulus[5,6]. Addition of newly developed ionomer / clay nanocomposite is expected to give some special properties to epoxy resin. In this study, the epoxy resin was modified by the addition of the ionomer / clay nanocomposite particles. Effect of the addition of the nanocomposite on the thermal property and the fracture toughness was investigated.

EXPERIMENTAL PROCEDURE

Materials

The epoxy resin used in this study was diglicydyl ether of bisphenol A epoxy, Epikote 828. Curing agent was 4-4' diaminodiphenylmethane (DDM). Nanocomposite particles (Mitsui Du-pont polychemicals Co.Ltd.) which had 10μm diameter were used as additives. The nanocomposite particles were splay-dried from the dispersion

of clay (montmorillonite) and thermoplastic resin, ethylene ionomer, in which 77% of carboxyl acids were neutralized with Zinc ion. The chemical structure of the ionomer was shown in Figure 1.

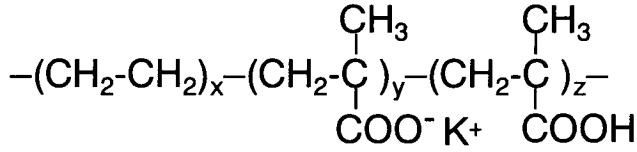

Figure 1: Chemical structure of ethylene ionomer.

The nanocomposite particles were added to the epoxy resin and mixed with a homogenizer. After degassing, this mixture was added to the DDM and mixed by hand. Curing condition was 120°C for 2hours and 180°C for 8hours. The formulation of the resins is given in Table1. As the ionomer can react with the epoxy resin, the ionomer content was varied from 5phr to stoichiometry, 26phr.

TABLE1
FORMULATIONS OF EPOXY MATERIALS

	Epoxy	Curing agent DDM	Clay / ionomer nanocomposite
Unmodified	100	26	0
Nanocomposite-modified	100	26	10
	100	20	10
	100	15	10
	100	9	10
	100	7	10
	100	5	10
	100	0	20

Dynamic viscoelasticity

Dynamic viscoelastic behavior was measured using rectangular specimens, 85 x 10 x 1mm, which were machined from the molded blocks. A specimen was mounted vertically in a testing machine, and the upper fixture was oscillated in torsion. The specimen was cooled to -50°C, and then heated to 300°C at constant heating rate, 1.38°C/min. Glass transition temperatures were defined as the temperature at the peak of the loss modulus, G".

Fracture toughness

Fracture toughness tests were conducted according to ASTM D5045 using compact tension specimens, 62 x 60 x 6mm, which were machined from the molded plates. Notches were introduced with a saw, and sharp precracks were formed by tapping a razor blade into the notch. Load in opening mode was applied through drilled holes in the specimen at displacement rate of 0.5mm/min. Testing temperature was 23°C. Fracture toughness values were calculated from the maximum load.

RESULTS AND DISCUSSIONS

Dynamic viscoelasticity

Effect of DDM content on dynamic shear modulus was shown in Figure 2. The shear modulus of the unmodified epoxy resin decreased gently with increasing temperature, and suddenly dropped to $2x10^7$Pa at 180°C, the glass transition temperature. For the nanocomposite-modified epoxy with 26phr DDM, the behavior was similar to that of the unmodified one. The glass transition temperature and the modulus at rubbery plateau region above the glass transition temperature was increasing with decreasing the content of DDM. For the modified epoxy with 7 and 9phr DDM, the shear modulus decreased gradually over whole temperature range and there is no apparent peak in the loss modulus. This fact shows that the glass transition doesn't occur in this epoxy system. When DDM content is 5phr, the shear modulus decreased largely from 100 to 200°C but the modulus at rubbery plateau region was much higher than the unmodified epoxy, which was similar to that of epoxy / ionomer resin

system without DDM. The glass transition region and the rubbery plateau modulus has relations closely to the microstructure of the polymer, and the following suggestions are to be discussed. There is no significant difference in the network structure of the epoxy matrix between the stoichiometric epoxy with and without the nanocomposite. This means that DDM can react with the epoxy resin faster than ionomer. For the modified epoxy resin, ionomer can react with the unreacted epoxy matrix which remain after DDM reacted with epoxy, and the crosslink density rises in the epoxy matrix. Lower DDM content lead to higher crosslink density because an amount of reaction sites between ionomer and epoxy increases. For the epoxy with 7 or 9phr DDM, the densest network (almost perfect) may be achieved. In addition, each clay piece may restrained the movement of the molecular chains. When the content is less than 7phr, the property of the ionomer-epoxy product is superior to the other properties.

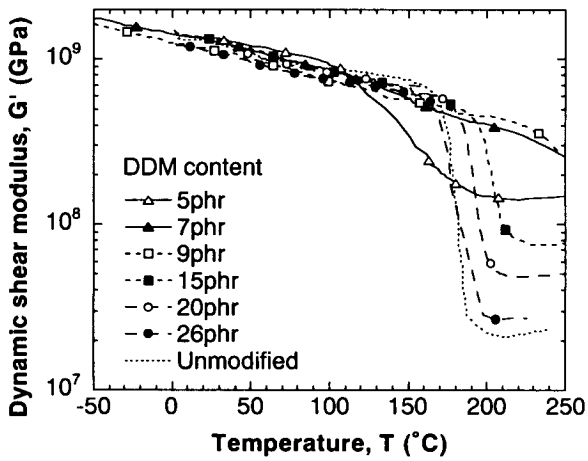

Figure 2: Effect of DDM content on dynamic shear modulus for nanocomposite-modified epoxy.

Fracture toughness

The fracture toughness values of unmodified and modified epoxies are shown as a function of DDM content in Figure 3. For the epoxy with stoichiometry DDM, the toughness value of the modified epoxy was 20% higher than that of the unmodified one. As to the modified epoxies, the fracture toughness was increasing with increasing DDM content. In particular, the toughness of the epoxy with lower DDM content was 40% less than that of the unmodified one.

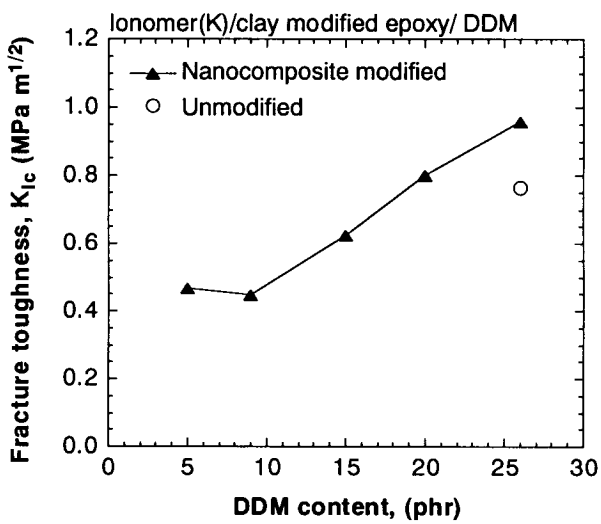

Figure 3: Fracture toughness of nanocomposite-modified epoxy.

Fractographic observations are shown in Figure 4. The particles were dispersed on the surfaces of all the epoxy system, and the size the particle after curing was larger than the original size. It is suggested that epoxy penetrated into ionomer rich region in the particles. For the modified epoxy with 26phr DDM, the crack propagated along

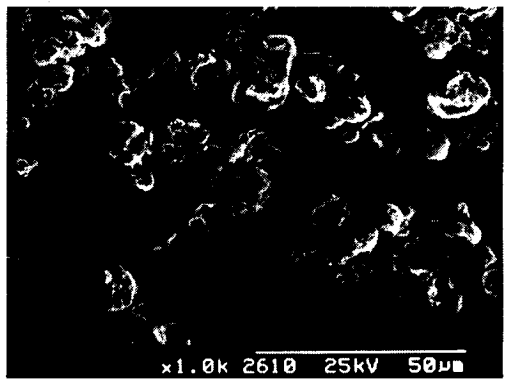

(a) DDM content, 26phr

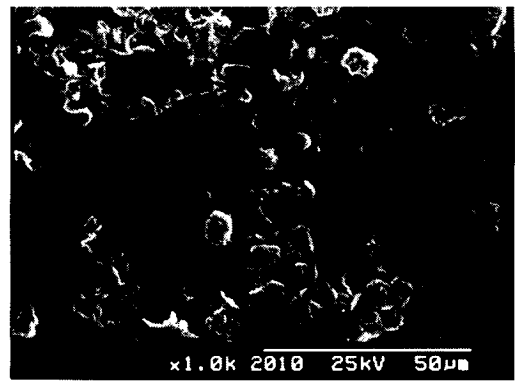

(b) DDM content, 20phr

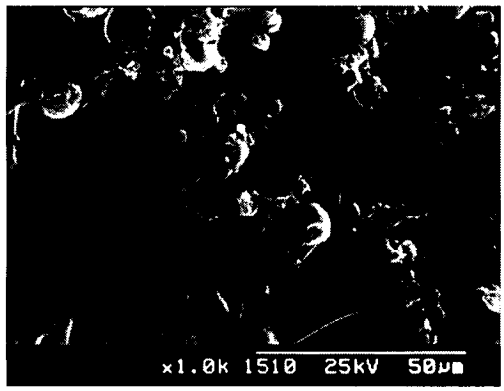

(c) DDM content, 15phr

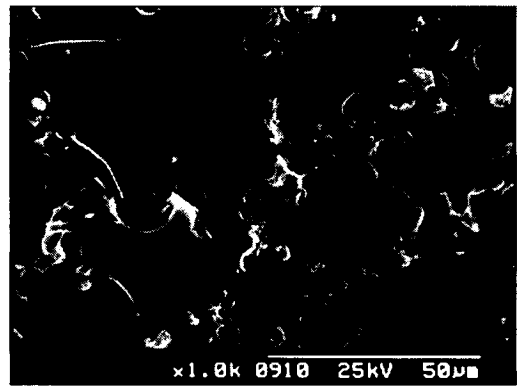

(d) DDM content, 9phr

Figure 4: Scanning electron micrographs of fracture surfaces for nanocomposite-modified epoxy.

the particle / epoxy interfaces. For that with 20phr DDM, the crack propagated partly inside the particles. The rate of the fracture inside the particle increased with decreasing the DDM content. When DDM content is 9phr, the crack propagated mostly inside the particles. These facts show that high thermal resistant epoxy (9phr DDM) has strong interfaces where ionomer reacted enough with epoxy, and that the epoxy with higher DDM content has poor interfaces.

Fracture mechanism were discussed on the basis of the fractographic observation. For the modified epoxy with 26phr DDM, because the interfacial debonding by poor interfaces causes the crack blunt, stress intensity in the vicinity of the crack tip is lowered and the fracture toughness increases. On the other hand, the epoxy with lower DDM which has high crosslink density become brittle because high crosslink restrain the region of the plastic deformation. In addition, the crack blunt cannot be expected because of strong interfaces.

CONCLUSIONS

Epoxy resin was modified with ionomer / clay nanocomposite particles. Effect of hardener (DDM) content on mechanical properties was investigated. The dynamic viscoelastic tests showed that the glass transition temperature increased with decreasing the DDM content. For the epoxy with 7 and 9phr DDM, there is no apparent glass transition temperature, and thermal resistance was considerably improved. The fracture toughness decreased with decreasing the DDM content.

Reference

1. Kunz, S.C., Sayre, J.A. and Assink, R.A. (1982) *Polymer* 23, 1897.
2. Kinloch, A.J., Shaw, S.J., Tod, D.A. and Hunston, D.L. (1983) *Polymer* 24, 1341.
3. Sultan, J.N. and McGarry, F.J. (1973) *J. Polym. Eng. Sci.* 13, 29.
4. Yee, A.F. and Pearson, R.A. (1986) *J. Mater. Sci.* 21, 2475.
5. Usuki, A., Kojima, Y., Kawasumi, M., Okada, A., Fukushima, Y., Kurauchi, T. and Kamigaito, O. (1993) *J. Mater. Res.* 8, 1179.
6. Wang, Z. and Pinnavaia, T.J., (1998), *Chem. Mater.* 10, 1820.

Mechanical Properties of Tungsten Fiber Reinforced Ti-6A1-4V Alloy by HIP Fabrication

S.Y. SON[*1], S. NISHIDA[*2], N. HATTORI[*2], K. HAYASHI[*2] and K. NAKANO[*3]

[*1] Graduate school of Saga University, Dept. of Mechanical Engineeting,
Honjo-machi 1, Saga City, 840-8502, JAPAN
[*2] Saga University, Dept. of Mechanical Engineering
[*3] Takata Engineering Ltd. Co., Kitakyushu 808-0143, JAPAN

ABSTRACT

Tungsten short fiber reinforced Ti-6Al-4V alloy (W/Ti-6A1-4V) was processed by Hot Isostatic Pressing (HlP) and it's mechanical properties were investigated and compared with those of conventional Ti-6Al-4V alloy and HlP treated Ti-6Al-4V.

According to the results in the present study, the average hardness of diffusion phase between fibers and Ti-6Al-4V matrix shows a value of about 20-30% higher than that of the conventional Ti-6Al-4V and also the hardness value increased with an increase in the volume fraction of tungsten fibers. The tensile strength of the composite material was about 15% higher than that of the conventional Ti-6Al-4V.

However, the fatigue limit of the composite materials was unexpectedly deteriorated in comparison with that of the conventional ones. The deterioration of the fatigue limit could be attributed to the defects in the microstructure of the composites such as clustering of fibers, micro-cracks and porosity.

KEYWORDS

Tungsten Fiber Reinforced Ti-6Al-4V Alloy, HlP Fabrication, Hardness number, Tensile Strength, Fatigue Limits, Defects

1. INTRODUCTION

Metal-matrix composites (MMCs) have been continuously developed to provide a mutual solution between an advanced property and cost saving. Several kinds of MMCs containing particles, whiskers or fibers as reinforcements have been increasingly employed in industry where specialized properties of materials with extremely high fatigue limits, high stiffness and low coefficient of thermal expansion, etc. are demanded [1,2,3].

Conventional Ti-6Al-4V alloy is widely employed in several engineering applications and the MMCs using this alloy for the matrix have been studied and expected to be one of the most currently advanced materials [4,5]. Most research on Ti-based MMCs has concentrated on ceramic reinforcement composites whose fabrication is expensive and complicated. Recently, tungsten (W) fiber, which possesses high a melting point and excellent mechanical strength has been attempted to be used as an alternative metallic reinforcement in developing a new type of W/Ti-6Al-4V MMC.

The subject of this paper is to investigate the mechanical and fatigue properties of a tungsten fiber reinforced Ti-6Al-4V (W/ Ti-6Al-4V) processed by a powder metallurgy method employing HIP, following by a secondary treatment using free forging and rotary swaging.

2. EXPERIMENTAL PROCEDURE

2.1 Materials and specimen

Table 1. Chemical compositions of Ti-6Al-4V alloy

Al	V	Fe	O	C	N	H
6.14	3.93	0.17	0.19	0.011	0.014	0.009

mass%

Table 2. Tensile strength and aspect ratio of W fiber

Fiber diameter d (μ m)	Tensile strength σ_B (MPa)	Aspect ratio l*/d		
		Max.	Min.	Ave.
20	3430	135	7.0	47.9

*l: Fiber length, d: Fiber diameter

Table 3. Specimens and fiber contents by HIP conditions and second process

Materials	HIP	Second process	Volume fraction of W fiber (vol.%)
Con.*	-	-	0
H1-9	1	FF	9
H2-0	2	RS	0
H2-6			6
H2-9			9
H2-12			12

FF: free forging, RS: rotary swaging
Con.* : conventional Ti-6AL-4V

Table 4. Results of Vickers hardness test

Materials	Average	Surface*	Core*	Matrix**	Interface**
Con.	316.9	320.5	313.2	-	-
H1-9	446.0	457.1	435.0	394.0	464.3
H2-0	-	334.3	345.0	-	-
H2-6	381.0	410.0	373.0	359.5	424.6
H2-9	405.5	421.3	379.9	382.2	453.5
H2-12	418.2	431.3	396.0	406.0	437.5

*: HV(1.96N) **: HV(0.049N)

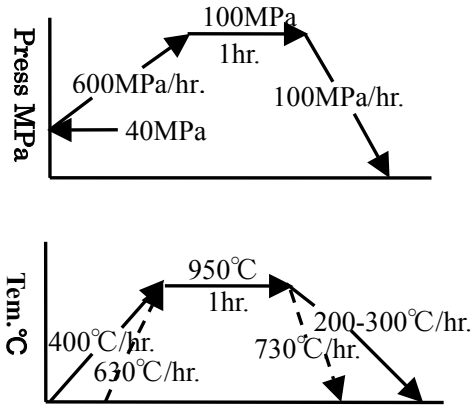

Fig. 1 HIP treatment conditions HIP1(—), HIP2(··)

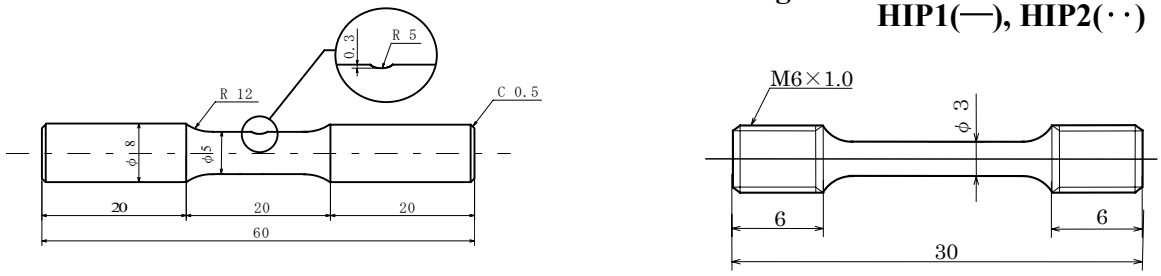

(a) Fatigue specimen **(b) Tensile specimen**

Fig. 2. Shape and dimensions of specimen

Atomized Ti-6Al-4V powder, with grains of an average size of 100μm, and tungsten short fibers were mixed (using a V milling machine, operating at 60 rpm for 0.5hr) and then the composites were processed by HIP[6,7]. Table 1 lists the chemical composition of Ti-6Al-4V alloy and Table 2 lists the tensile strength, density and aspect ratio of W short fiber, respectively.

Two conditions of HIP were used as depicted in Fig. 1. In order to improve the homogeneity of fiber-distribution in the matrix, a secondary process employing free- forging (FF) or rotary swaging (RS) was performed after the HIP process. Table 3 lists the specification of the specimens.

Configurations of tensile and fatigue test specimens are shown in Fig. 2.

2.2 Test procedure

All of specimens were annealed at 600°C for 0.5hr in a vacuum furnace. After annealing, the specimens were mechanically polished with emery paper (#400~3000) then with polishing powder (Al_2O_3/0.1 μm), and then etched with a solution of 10%HF + 20%HNO_3. To assess the effects of the polishing method on the testing results, one additional group of HIP-2 treated specimens was prepared by extensive electro-polishing after mechanically polishing.

The Vickers Hardness number was measured in accordance to JIS-Z2244 at the loads of 1.96N and 0.245N, respectively.

The tensile tests were carried out using a hydraulic universal testing machine（with a capacity of 98kN）and the fatigue tests were conducted by an Ono-type rotating bending machine operating at 3000rpm at room temperature. The surface of the fatigue specimens was monitored by

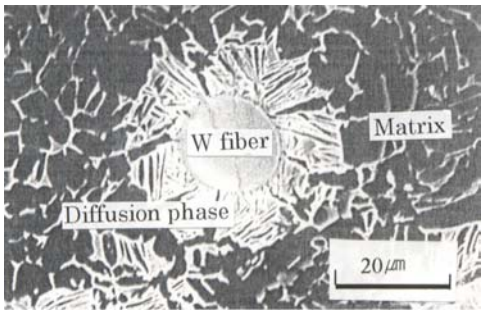

(a) Microstructure of composite

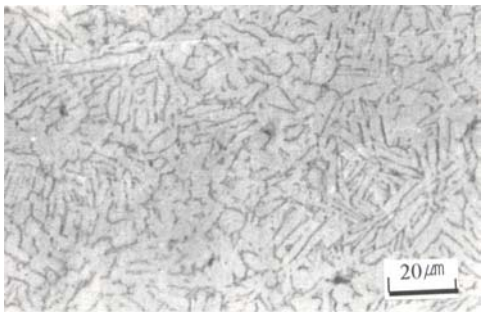

(b) HIP2-0

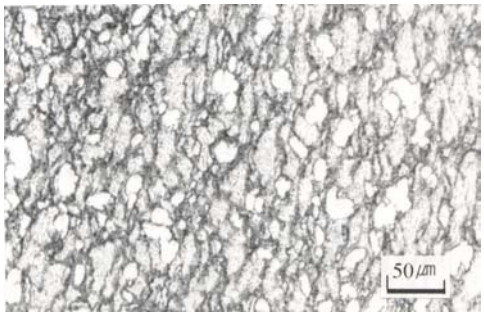

(c) HIP1-9

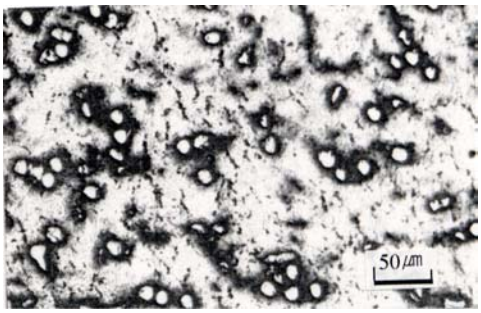

(d) HIP2-9

Fig.3 Optical microstructure

Table 5. Tensile strength of W / Ti-6Al-4V

Materials	Tensile strength MPa
Con.	980
H2-0	1088
H2-6	1144
H2-9	1520
H2-12	1288

plastic-replica method and the successively taken replicas were observed with an optical microscope. The fracture surface of the tensile and fatigue specimens was investigated using scanning electro microscope (SEM).

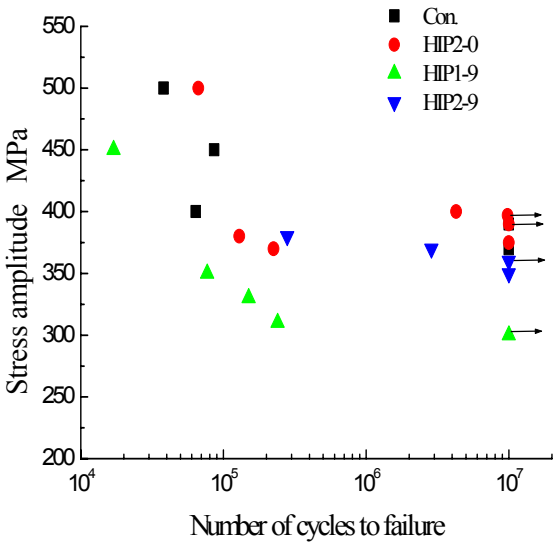

Fig. 4 S-N curves of HIP1 and HIP2 specimens

3. RESULTS

Fig. 3 shows the microstructure of HIP-Ti-6Al-4V alloy and HIP1-W/Ti-6Al-4V and HIP2-W/Ti-6Al-4V, respectively [Fig.3]. An interphase structure was observed between the fibers and the matrix [Fig.3 (a)]. By EPMA analysis, it is suggested that the interphase could be a diffusion phase in which the W atom diffused into the Ti-6Al-4V matrix. Table 4 lists the result of the hardness test. The hardness number of HIP1 showed higher value than HIP2 by about 12%. The hardness numbers of the diffusion phase in MMCs showed a value by about 20-30% more than that of conventional Ti-6Al-4V alloy. It increased with an increase in volume fraction of W fiber.

Table 5 lists the results of the tensile test of HIP2-W/Ti-6Al-4V specimens. The tensile strength of the MMCs showed a higher value in comparison with the tensile strength of the conventional Ti-alloy. It tended to improve with an increase in the volume fraction of the W fibers. The maximum value of the tensile strength in this work was 1520 MPa, which was achieved for the MMC reinforced with 9 vol.% W fibers.

Fig. 4 representatively illustrates the S-N curves of HIP1-9, HIP2-9, HIP2-0and conventional Ti-6Al-4V specimens. The fatigue limit of HIP1-9 and HIP2-9 were lower than that of the conventional Ti-6Al-4V by approximately 25% and 10% respectively. On the contrary HIP2-0

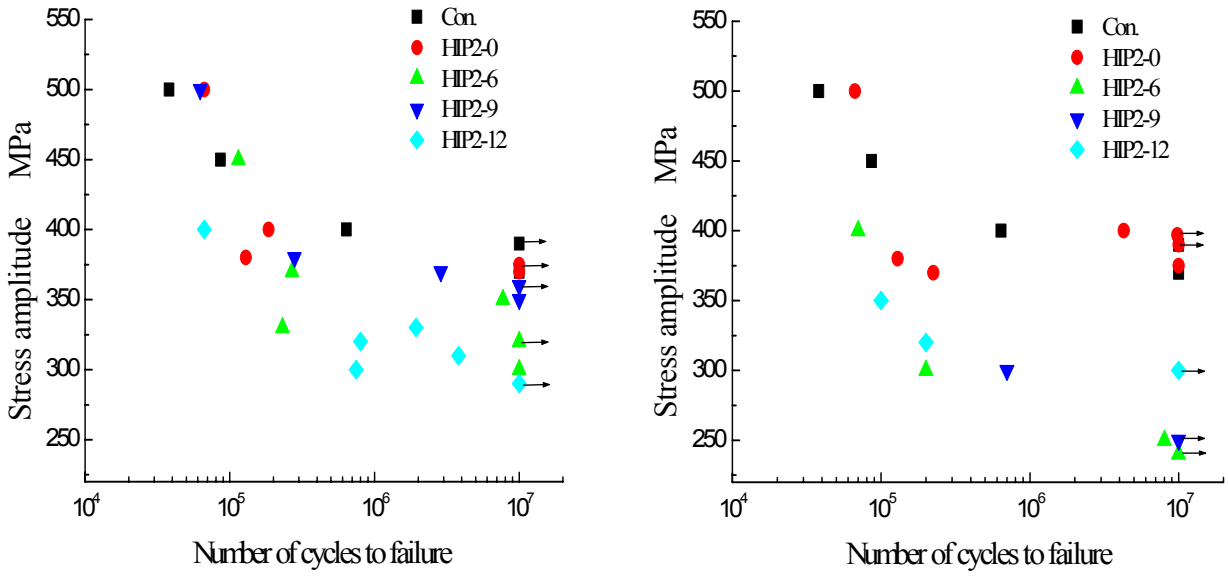

(a) Mechanically polished materials **(b) Electro-polished materials**

Fig.5 S-N curves of HIP-2 specimen to various fiber content ratios

exhibited the same or higher value fatigue limit in comparing with that of the conventional Ti alloy.

Fig. 5 shows some typical S-N curves of HIP2 treated specimens followed by mechanical [Fig.5 (a)] and electro-polishing [Fig.5 (b)]. The fatigue limit of the MMCs was about 40% lower than that of the conventional Ti-6Al-4V specimens. Considering the volume fraction of W-fibers, the fatigue limit decreased in the order of 12,9,6 vol.% for the electro-polished specimens, but it decreased in the order of 9,6,2 vol.% for the mechanically polished ones. Generally, the overall fatigue limits of the mechanically polished specimens were higher.

4. DISCUSSIONS

4.1 W-fibers/matrix diffusion layers and improvement of tensile strength:

According to the foregoing test results, tensile strength of W/Ti-6Al-4V showed a remarkable improvement with the addition of the tungsten fibers. The interface layer between the W fiber and the Ti-6Al-4V matrix was a diffusion layer as shown in Fig.3 (c) and (d). The HIP1 specimen exhibited relatively larger areas of diffusion phase than those of the HIP2 one. The difference may be caused by the difference of heating and cooling rate in each HIP process, where the slower rate in the HIP1 process might result in a larger amount of diffusing of W atoms into the matrix.

The results of hardness test shown in Table 4 also suggested that the average hardness increases proportionally to the area of the diffusion phase in the matrix.

The existence of the diffusion phase improved the local strength of the interfaces between the reinforcing fibers and surrounding matrix materials, resulting in a good reinforcing effect of the W fibers on the overall static strength of the MMC. The observation of a fracture surface of a tensile specimen shown in Fig.6 exhibits the vast majority of broken fibers, where as “pull-out fibers” were hardly found. That suggested a strong interface was achieved in the present MMC.

4.2 Deterioration of fatigue limit:

From a simple empirical relation between fatigue limit σ_W and Vickers hardness number HV, expressed as $\sigma_W \fallingdotseq 1.6HV$, the fatigue limit of the composite was expected to be improved according to the increase of hardness number. However, the fatigue limit of the MMC in this work actually deteriorated: The reasons for this might be attributed to the low ductility of the matrix associated by defects, such as, clustering of fibers, micro-cracks and porosity. Particularly, fiber-clusters seemed to reduce the crack initiation resistance of this MMC.

Fig.7 (a) shows the observation of crack initiation in a HIP1-W/ Ti-6Al-4V specimen started from a cluster of fibers [see Fig.7 (b) for details] and secondary micro-cracks (mostly inter-granular) were frequently observed on the fatigue fracture zone [see Fig. 7 (c)].

The fracture surface of HIP2 showed multi initiation cracks and porosity [view Fig.7 (d) an (e)].

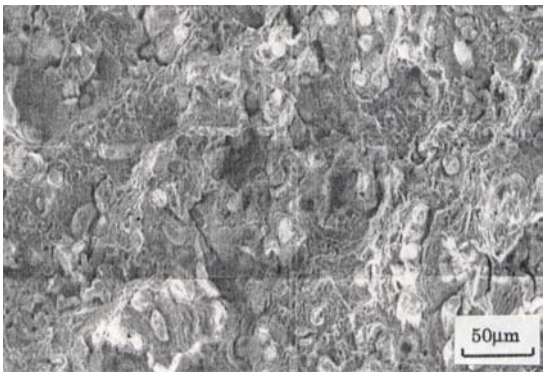

Fig.6 Tensile fracture surface observed with SEM

Table 6. The density of porosity

Materials	Porosity density (%)
H2-0	-
H2-6	3.26
H2-9	3.55
H2-12	4.01

Several cracks initiating from the surface of the fatigue specimen and then coalescing to propagate were observed. The results of quantitative analysis of the density of porosity in the HIP2-specimens, represented by the percentage of area exposed on a specified area are shown in Table 6. The porosity density seems to increase with an increase in the fibers volume fraction.

The fatigue limit of the HIP2-0%W/Ti-6Al-4V specimens without fibers exhibited an excellent result; even better than that of the conventional Ti-6Al-4V specimen. Consequently, the existence of defects caused by the addition of fibers into the Ti-6Al-4V matrix seems to be the major problem in order to improve the fatigue properties of the MMCs. To assess the influence of the effects of the distribution of fibers on the fatigue properties of W/Ti-6Al-4V, much more rigorous studies on this subject are required. Within the limitation of the present work, it was found that rotary swaging (RS) treatment gave a better result to the fatigue limit than the free forging (FF) one. The improvement of fatigue property might be expected when an adequate HIP process associated with a secondary process such as RS is developed to overcome with the problems understood by the present study.

In addition, the polishing process of the fatigue specimen may also have an affect on the fatigue limit of the MMCs specimen. As shown in Fig. 7 (f), the electro-polished specimens' surface exhibits W-fiber-extrusion (resulted from the fact that W-fibers were relatively cathodic with respect to the Ti-6Al-4V matrix in electro-polishing process) and the difference of stress concentration at

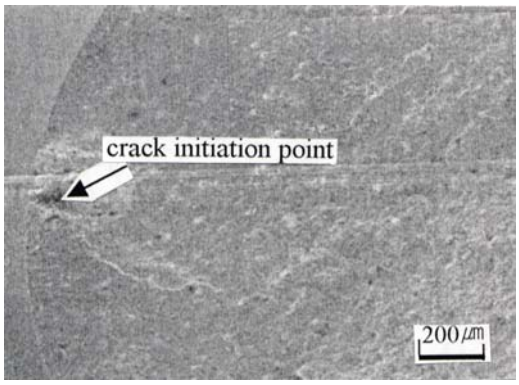

(a) Crack initiation point HIP1-9

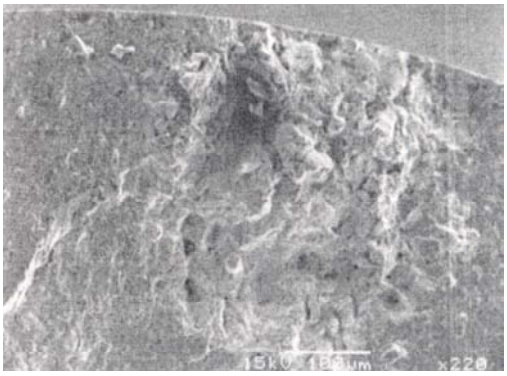

(b) Magnificent crack initiation point

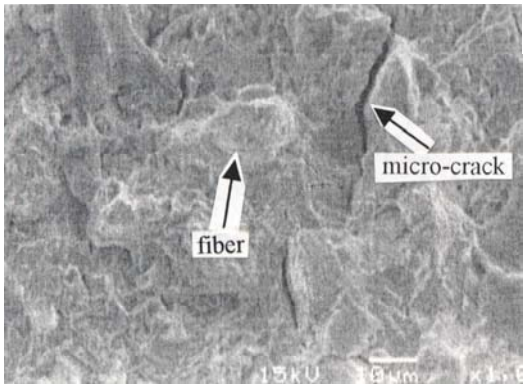

(c) Micro-cracks in the matrix HIP1-9

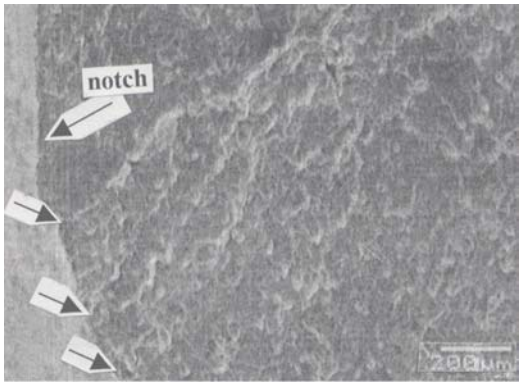

(d) Multi cracks initiation points HIP2-9

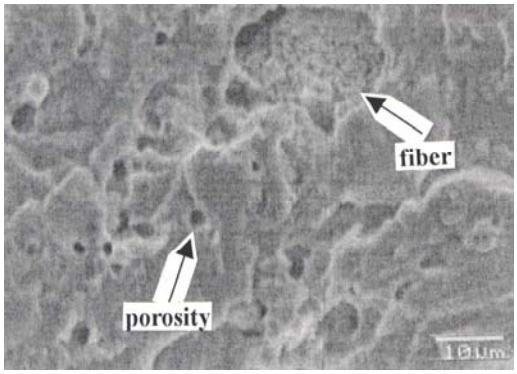

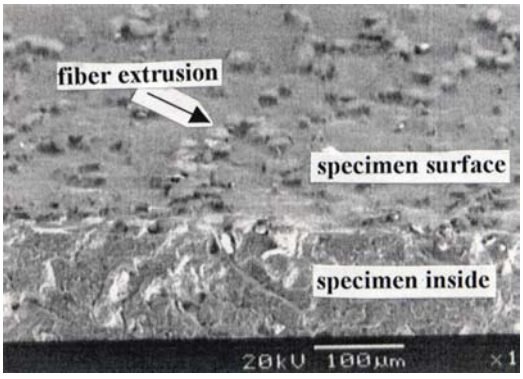

(e) Porosity in the matrix HIP2-9 **(f) Fiber extrusion HIP2-9**

Fig.7 Fatigue fracture surface observed with SEM

the interphaces of W-fibers/matrix may be attributed to the reason why the fatigue limit of the electro-polished specimens was lower than that of the mechanically polished ones.

5. RESULTS

The testing results on HIP fabricated W/Ti-6Al-4V MMCs have been reported and discussed. The main conclusions are follows;

1. W-fibers reinforced Ti-6Al-4V matrix composite could be produced by the HIP process used in this work.
2. The hardness number and the tensile strength of MMCs produced by the above process showed higher values in comparison with those of conventional Ti-6Al-4V by about 20-30% and 15% respectively. Both hardness and tensile strength with tended to increase the increase of in volume fraction of tungsten fibers.
3. However, fatigue limit of the MMCs unexpectedly deteriorated. The defects such as clustering of fiber, micro-cracks and porosity, etc. were considered to be the major reson.
4. Within the present work, the employment of high heating and cooling rates in the HIP process led to the better property of the composite. HIP2 process is found to be comparatively better than HIP1 for producing W/Ti-6Al-4V MMCs.

REFERENCES

(1) T.Hayashi , The composite material engineering, (1980), p1173-1181
(2) R.O.Ritchie, R.H.Dauskardt and B.N.Cox., Fatigue of Advanced Materials, MEPE Ltd, (1991), 315.9
(3) H,Ochiai et al.: Journal of the Japan Society for Composite Materials, 21-2, (1995), p37-46.
(4) W.F.Smith., Structure and Properties of Engineering Alloys, McGraw-Hill Book Co., (1994)
(5) M.J.Donachie,Jr., Titanium a technical guide, ASM international, (1988)
(6) T.Kimura et al.: Journal of the Japan Society of Mechanical Engineers, 28-11, (1998), p897-901.
(7) Titanium material researchers, Present aspect of Titanium materials research in Japan, (1989), p81

ORAL REFERENCE: ICF1001077

MECHANICAL PROPERTIES, ADHESION, AND FRACTURE TOUGHNESS OF LOW-K DIELECTRIC THIN FILMS FOR MICROELECTRONIC APPLICATIONS

Indira S. Adhihetty[1], Joseph B. Vella[1], Alex A. Volinsky[1], Cindy Goldberg[2], and William W. Gerberich[3]

[1] Motorola, Digital DNA™ Labs, Process and Materials Characterization Lab, Mesa, AZ.
[2] Motorola, Digital DNA™ Labs, APRDL, Austin, TX.
[3] University of Minnesota, Dept. of Chem. Eng. and Materials Science, Minneapolis, MN.

ABSTRACT

Due to the radical compromise in thermal and/or mechanical properties that the migration from silicon dioxide to novel low-k dielectric films necessarily incurs, the IC industry is motivated to better understand the failure modes of low-k dielectric films. These failure modes include thermal instability, poor mechanical strength, and chemical-mechanical polishing (CMP) failure due to low cohesive and adhesive fracture toughness. By developing a methodology to predict failure modes, we are able to screen multiple candidate low-K materials. The following study is a discussion of some of the experimental approaches that Motorola has taken to understand and mitigate some of these failure mechanisms.

KEYWORDS

Low-K dielectrics, thin films, adhesion, fracture toughness, mechanical properties

INTRODUCTION

The semiconductor industry is gradually moving from well-established SiO_2/Al interconnects to Cu/low-K to meet the next generation device requirements. Increased device speed, reduced power and heat dissipation requirements and reduced interline cross talk are many benefits driving device manufacturers to move to low-K materials. However the transition is challenging since these new material systems will introduce a number of integration and reliability issues. During the last few years industry has been looking into two major categories of low-K materials namely organic spin-on dielectric (SOD) film and hybrid organic/inorganic silicate films made by a CVD or spin-on process. Each has their advantages and disadvantages. Silicate films are extremely

thermally stable and reasonably hard, but they are fragile. On the other hand organic materials have reasonable thermal stability and are tough, but are soft.

A viable low-K material must be compatible with dual-damascene lithography, etching, stripping and cleaning processes, and especially CMP and device packaging methods. The reliability of devices containing these multi-layer dual-damascene stacks depends on several factors including device mechanical stability, adhesion of the barrier metal to the low-K film, adhesion of etch stop, hard mask and capping layers to the low-K film and barriers and the ability to polish the Cu and package device without failure. Since the dual-damascene stack is exposed to high shear stresses during the CMP process, any flaws at the interfaces or in the low-K film itself can lead to long term reliability problems. Thus detailed reliability and compatibility tests are required to integrate new low-K dielectric materials and Cu interconnects.

For the above-mentioned mechanical device stability four material properties of the device components are important: elastic modulus, hardness, interfacial adhesion, and film fracture toughness.

Mechanical properties of thin films often differ from those of the bulk materials. This can be partially explained by the nanostructure of thin films and the fact that these films are attached to a substrate. Due to typically high yield strengths, thin films can support very high residual stresses. This residual stress can be relieved later during processing or in the actual device operation through plastic deformation, thin film fracture, or interfacial delamination.

Both elastic and plastic properties are important for thin film characterization. Thin film mechanical properties can be measured by tensile testing of freestanding films [1] and by the microbeam cantilever deflection technique [2-4], but the easiest way is by means of nanoindentation, since no special sample preparation is required and tests can be performed quickly and inexpensively.

Nanoindentation is a versatile technique for measuring films mechanical properties (elastic modulus, hardness, interfacial adhesion, and film fracture toughness). It works using the same principals as conventional hardness tests, but is performed on a smaller scale using sensitive load and displacement sensing equipment. During the measurement a sharp diamond indenter is forced into the tested material while continuously recording both the force and the indentation depth. Mechanical properties are measured by either analyzing the continuous load-displacement profile or by measuring the material response to a frequency modulated force oscillation that is imposed on the indentation tip during indentation. Both elastic modulus and hardness can be readily extracted directly from the nanoindentation curve [4-7]. Since the depth resolution is on the order of nanometers, it is possible to indent even very thin (100 nm) films. Indentation has been also used to measure thin film adhesion [8-13], where the mechanical energy release rate, or practical work of adhesion is calculated based on the delamination size. Similar fracture properties such as fracture toughness or adhesion strength are derived from the continuous load-displacement profile and an independently measured geometrical scale parameter, which results from indentation, such as crack length or delamination radius.

Indentation techniques could also be used for measuring fracture toughness. When a sharp tip such as Vickers, Berkovich or a cube corner diamond is indented into bulk brittle materials, radial cracking usually occurs after a critical load has been reached,

which allows ones to calculate fracture toughness based on the maximum indentation load and the crack length [14-16]. This method of analysis in complicated in the case of thin film radial fracture because of the half penny crack shape perturbation by the substrate, film densification, and residual stresses in the film. Current studies have yielded promising developments in this area however.

The objective of this study is to identify proper techniques to characterize low-K materials, and, if feasible, to propose a correlation between the mechanical properties of low-k dielectric thin films and their reliability.

RESULTS AND DISCUSSION

One challenge facing the IC industry lies in generating a low-k film that can withstand chemical mechanical polishing without fracturing or delaminating. Researchers have been putting considerable emphasis on determining hardness or Young's modulus threshold that corresponds with a materials ability to endure CMP, wire bonding or bump processes. According to recent studies at Sematech there appeared to be a correlation between elastic modulus and the films ability to withstand chemical-mechanical polishing. However because these films' mechanical properties are intimately linked with their porosity, trends in hardness often correspond to trends in modulus. Correlation with CMP failure can be just as easily made with the film hardness. Figure 1 shows the relationship of hardness and modulus that stems from the variation in porosity of a group of silicate films. Furthermore, one must be careful not to make the conceptual leap from correlation to causation. Studies at Motorola have shown that it is not just modulus, hardness, adhesion or toughness, but more likely a combination of all of these mechanical properties that cause CMP related failure.

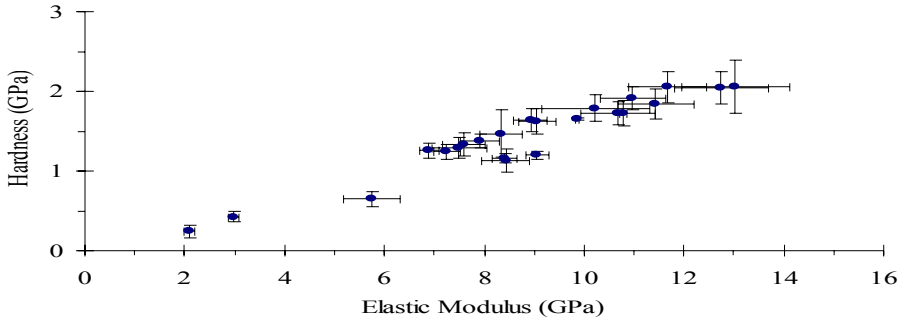

Figure 1. Linear plot of representative silicate low-k dielectric film hardness versus modulus, demonstrating the interrelated mechanical properties of these films that stem largely from their porosity.

Elastic modulus and hardness of different low-K materials from different vendors were measured using nanoindentation. These studies were carried out using a NanoIndenter XP dynamic contact module. Frequency and tip displacement modulated continuous stiffness measurements were made at a frequency of 75 Hz and an oscillation amplitude of 1 nm. Mechanical properties were extracted from hardness and modulus versus displacement profile minima or approximately at a depth of 10% of the film thickness. All films were deposited on thin metallic adhesion/barrier layer to a thickness

of approximately 1 μm. Schematic of a typical low-K test structure is shown in Figure 2. Typical hardness and modulus profiles as a function of indentation depth are shown in Figure 3. Presently it is not well understood whether the increase in modulus and hardness at low depth is an effect of adhesion or an intrinsic indentation size effect [17]. It is important to note that many low-k films exhibit viscoelastic and viscoplastic (creep) behavior, which significantly complicates the measurement of their mechanical properties. These properties from indentation measurements are strain rate and tip oscillation frequency dependent. Progress has been made in techniques utilizing spherical indentation to measure these time dependent properties. However the use of blunt indentation tips often precludes the use of very thin films because of the inability to localize the plastic zone beneath the tip. Furthermore techniques of tip frequency sweep to determine storage and loss modulus in thin films requires that these films adhere to linear viscoelastic theory.

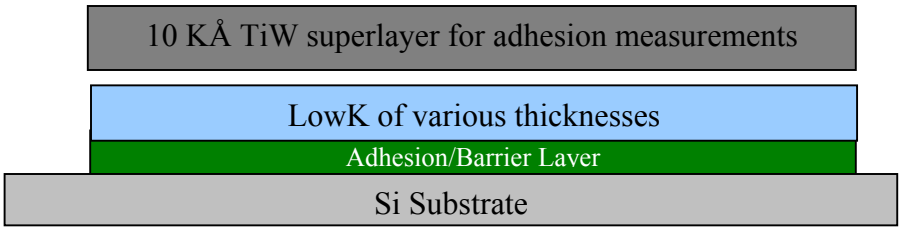

Figure 2. Schematic of a typical Low-K test structure.

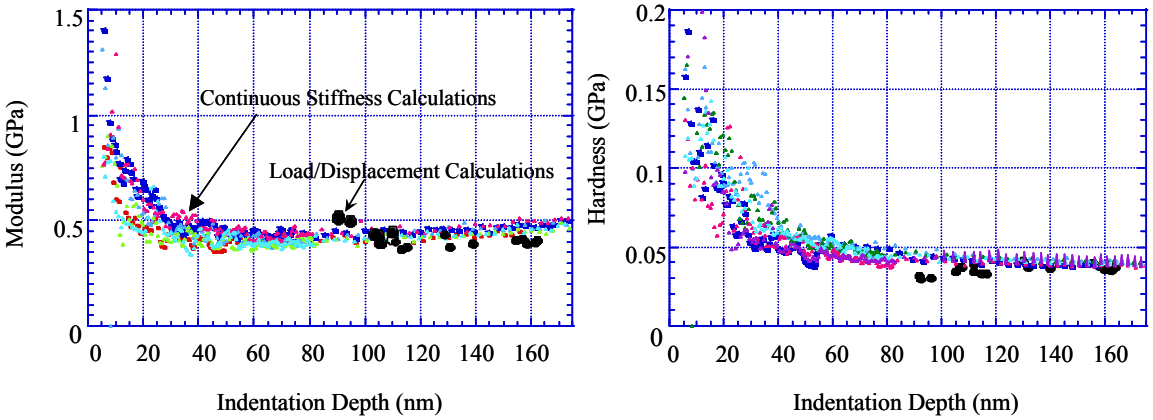

Figure 3. Elastic modulus and hardness profiles as a function of indentation depth.

Beyond measuring the mechanical properties significant advances have been made recently in measuring the adhesion strength of thin films using nanoindentaiton. With the high hardness to modulus ratios one may expect low fracture toughness and adhesion of these materials. Adhesion of low-K dielectric films was measured by means of a superlayer indentation technique [10-13]. Most well-adhered or low modulus thin films can not be delaminated by means of regular indentation and would rather deform plastically around the indenter by forming pileup, or they would not be able to carry the indentation stress to the crack tip. To prevent these problems a high modulus hard superlayer, capable of supporting and storing large amounts of elastic energy is deposited

on top of the film of interest. Upon indentation a delamination blister forms around the indent, and its area is used to calculate the strain energy release rate (practical work of adhesion). Several delamination blisters have been cross-sectioned using Focused Ion Beam (FIB), and it showed that in most cases low-K fracture is cohesive, so what is really measured is the fracture toughness of the low-K film, not the interfacial adhesion.

Knowledge of the elastic modulus and hardness are also required to calculate fracture toughness. Fracture toughness of a bulk brittle material can be calculated based on the maximum indentation depth, P_{max} and the crack length, c [15,16]:

$$K_C = \alpha\left(\frac{E}{H}\right)^{1/2}\left(\frac{P_{\max}}{c^{3/2}}\right) \tag{1}$$

where α is an empirical constant which depends on the geometry of the indenter, E is the elastic modulus, and H is the mean hardness. This expression can not be directly applied in the case of a thin film, since typically the crack shape is no longer halfpenny shape anymore. It was also noted that the maximum indentation load scales linearly with the crack length to the 3/2 power, so as a first order approximation equation 1 can be used to estimate low-K films fracture toughness.

An additional method utilized for measuring toughness involves a lateral scratch, which causes a tangential stress at the trailing edge of the scribe. This has been utilized by both Ostartage, et al [18] and Hoehn, et al [19], noting that

$$K_C = 2\sigma_{\theta\theta}\sqrt{\frac{c}{\pi}\sin^{-1}\left(\frac{a}{c}\right)} \tag{2},$$

where a is the contact radius and c is the half crack. Since a/c is almost always less than ½, $\sin^{-1}(x) \sim x$ and with $\sigma_{\theta\theta} = P_{\max}/\pi a$, one finds that equation (2) reduces to:

$$K_c \approx \frac{2P_{\max}}{\pi^{3/2}}\cdot\frac{1}{ac^{1/2}} \approx const\cdot\left(\frac{P_{\max}}{c^{3/2}}\right) \tag{3}$$

with the latter approximation coming if $c/a \sim$ constant. This then is the same as equation (1), since $(E/H)^{1/2}$ is nearly constant in Figure 1. However, both equation (1) and (3) have inherent composite yield strength, modulus and strain energy release rate built into a laminate system needing detailed analysis.

It is important to understand how low-K films fracture toughness changes with the film thickness. For several low-K materials there a is a critical thickness of approximately 3 μm at which the film fractures due to the residual stress relief. For the low-K brittle films fracture toughness is most likely to decrease with the film thickness due to the higher residual stress and larger flaw size/porosity. Similar or opposite trends have been described in other thin film/substrate systems. For example, thicker W films on steel are tougher, but W(C) film toughness decreases with the film thickness due to the limited crack tip plasticity [20]. We have made initial attempts to employ ellipsometry to measure low-K film porosity [21], but at this point more thorough theoretical analysis is

required to accurately assess thin film fracture toughness using the nanoindentation technique.

CONCLUSIONS

This report describes a methodology to use nanoindentation to measure modulus, hardness, and adhesion and fracture toughness of various classes of low-K materials. These properties are used to predict mechanical reliability of advanced IC devices. By correlating mechanical properties to mechanical reliability we have an effective approach to screening new dielectric materials.

REFERENCES

1. Read D. T., Dally J. W., (1993), *J. Mater. Res*., **8**(7), pp. 1542-1549
2. Weihs T. P., Hong S., Bravman J. C., and Nix W. D., (1998), *J. Mater. Res*. **3**(5), pp. 931-942
3. Baker S. P. and Nix W. D., (1994), *J. Mater. Res*. **9**(12), pp. 3131-3144
4. Baker S. P. and Nix W. D., (1994), *J. Mater. Res*. ***9***(12), pp. 3145-3152
5. Doerner M. and Nix W., (1986), *J. Mater. Res*. **1**, p. 601
6. Pharr G. M., Oliver W. C., Brotzen F., (1992), *J. Mater. Res*., **7** (3), pp. 613-617
7. Oliver W. C. and Pharr G. M., (1992), *J. Mater. Res*., **7**, pp.1564-1583
8. Marshall D. B. and Evans, A.G., (1984), *J. Appl. Phys*., **56**, 2632
9. Vlassak J. J., Drory M. D. and Nix W. D., (1997), *J. Mater. Res*., Vol. **12**, No. **7**, p. 1900
10. Kriese M. D. and Gerberich W. W., (1999), *J. Mater. Res.,* **14** (**7**), 3007
11. Kriese M. D., Gerberich W. W., Moody N. R., (1999), *J. Mater. Res.*, **14** (**7**), 3019
12. Volinsky A. A., Tymiak N. I., Kriese M. D., Gerberich W. W. and Hutchinson J. W., (1999), *Materials Research Society Symposium Proceedings*, Vol. 539, (Pittsburgh, Pennsylvania: Materials Research Society), p. 277
13. Volinsky A. A., (2000), Ph.D. Dissertation, University of Minnesota, Minneapolis
14. Antis, G. R., Chantikol P., Lawn B. R., and Marshall D. B. (1981), J. of Amer. Ceram. Soc., Vol. **64**, No. 9, pp. 533-538
15. Pharr G. M., Harding D. S., Oliver W. C., (1993), *Mechanical Properties and Deformation Behavior of Materials Having Ultra-Fine Microstructures*, M. Nastasi et al. (eds.), Kluwer Academic Press, pp. 449-461,
16. Harding D., Oliver W., Pharr G., (1995), MRS Symp. Proc. Vol. 356, pp. 663-668,
17. Grunlan J. C., Xia X., Rowenhost D, and W. W. Gerberich, (2001), *Rev. of Sci Instr*., **72 (6)**
18. Ostartage C. P., Churalambides P. C., and Evans A. G., (1989), *Acta Mater*. **37(7)**, p. 2077
19. Hoehn J. W., Venkataraman S. K., Huang H., and Gerberich W. W., (1995), *Mat. Sci and Engng*., **A192/193**, p. 306
20. Harry E., Rouzaud A., Ignat M., Juliet P., (1998), *Thin Solid Films*, **332**, pp. 195-201
21. Vella, J .B., Xie, Q., Edwards, N. V., Kulik, J., Junker, K. (2001), submitted to *Materials Research Society Proceedings*, Fall, Symposium L. Thin Film Stresses and Mechanical Properties IX.

Oral/Poster Reference: ICF10645OR

MECHANICS-BASED MODELING OF DYNAMIC FRAGMENTATION AND COMPARISON WITH EXPERIMENTS

W. J. Drugan

Department of Engineering Physics
University of Wisconsin–Madison
1500 Engineering Drive
Madison, WI 53706 USA

ABSTRACT

We describe a new, largely analytical model of the dynamic fragmentation of brittle materials that accounts for the mechanics of the ongoing dynamic deformation and the development of material failure. The model predicts fragment size and time to fragmentation initiation in terms of fundamental material properties and the applied strain rate, in situations where the deformation rate prior to fragmentation initiation can be treated as being uniform. The predictions of the model are compared to some recent careful experiments on dynamic fragmentation; the agreement is shown to be quite good, significantly better than that of two widely-adopted analytical models of dynamic fragmentation that are based on energy balance arguments and which treat dynamic fragmentation as an instantaneous event. Although more extensive theoretical-experimental comparisons are needed, for a wider range of materials and strain rates, the present initial comparisons imply that accounting for the mechanics of the ongoing dynamic deformation and development of material failure in dynamic fragmentation leads to more accurate predictions, and that such modeling need not be heavily numerically-based.

KEYWORDS

dynamic fragmentation; dynamic failure; brittle material; stress waves; characteristics.

INTRODUCTION

If a solid body is subjected to rapid energy input by, for example, impact with or by another body, impingement of a laser or x-ray beam, rapid temperature change, etc., it is often observed that the body will shatter into numerous pieces. Reliable safety assessments of structural components that may be subject to such rapid energy input demand accurate models of this dynamic fragmentation phenomenon, so that key information such as fragment size can be predicted. To date, the most widely applied theoretical models of dynamic fragmentation appear to be based on relatively simple global energy balance arguments to predict

fragment size, such as the pioneering study of Grady [1] or its improvement by Glenn and Chudnovsky [2]. Such models assume that the fragmentation event occurs instantaneously, and thus are expected to be limited in validity to situations involving extremely high strain rates.

We are interested in developing models of the dynamic fragmentation process that are analytical to the extent possible, but which also account for the actual time-varying dynamic deformation and the mechanics of the development of material failure that occurs before the final fragmentation event. Not only should such models be applicable over a wider range of applied strain rates, but they should reflect more accurately the actual mechanics of the failure process and hence provide more accurate predictions of fragment size and other pertinent quantities.

The present paper describes one such mechanics-based model of the dynamic fragmentation process for brittle materials that we have recently developed (Drugan [3]), and compares its predictions, together with those of the Grady [1] and Glenn and Chudnovsky [2] models, with the results of the careful impact fragmentation experiments of Piekutowski [4].

MECHANICS-BASED DYNAMIC FRAGMENTATION MODEL

Drugan [3] proposed and analyzed two models of the dynamic fragmentation process in brittle materials: one that treats initially "unflawed" material, and one that treats material containing a distribution of flaws. Here we review the simpler "unflawed" material model. As will be seen, this model assumes that flaws develop at the locations and times predicted by a dynamic instability analysis.

We begin with perhaps the simplest realistic assumption for dynamic fragmentation analysis, as proposed by Grady [1]: a body that is experiencing, due to a rapid energy input that has just occurred, a uniform constant volumetric strain rate that persists until fragmentation initiates. We focus attention on a prospective fragment inside this straining body, perform a dynamic analysis of the ongoing stress and deformation state in the prospective fragment and ask when this deformation becomes unstable, signaling the initiation of fragmentation and thus determining the critical fragment size and time of fragmentation initiation as a function of material properties.

Since we here restrict analysis to brittle fragmentation, we model the material as being homogeneous, isotropic linear elastic but, in addition, we model the surfaces that will become the fracture surfaces by cohesive zones which incorporate a realistic traction-separation relation for fracturing brittle material. For simplicity, we idealize the prospective fragment as being a cube that is connected to the surrounding material in the body by cohesive zones, as illustrated in Figure 1. The advantage of doing this is that, given our assumption of a uniform volumetric strain rate until fragmentation initiation, one observes that the stress and deformation history in each of the three cube normal directions will be identical, and therefore it is sufficient to analyze one of these – i.e., the three-dimensional problem is reduced to being one-dimensional.

We begin by analyzing the dynamic stress and deformation fields within the elastic cube. The three-dimensional version of Hooke's law for a homogeneous, isotropic linear elastic solid is

$$\sigma_{ij} = \frac{E}{1+\nu}\left(\varepsilon_{ij} + \frac{\nu}{1-2\nu}\varepsilon_{kk}\delta_{ij}\right), \tag{1}$$

where E is Young's modulus, ν is Poisson's ratio, σ_{ij} and ε_{ij} are components of the stress and infinitesimal strain tensors, respectively, δ_{ij} is the Kronecker delta, and a repeated index implies summation. Using the fact that $\varepsilon_{11} = \varepsilon_{22} = \varepsilon_{33}$ and the shear strains are all zero, due to our uniform volumetric strain rate assumption, the normal stress-normal strain relation parallel to any cube axis has the form, from (1),

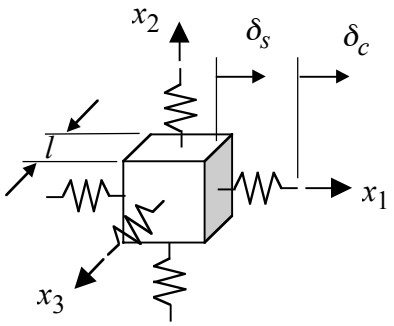

Figure 1. A prospective fragment, consisting of an elastic cube with (initially undetermined) side length l, and half cohesive zones that connect it to the remainder of the body. Displacement of the cube edge relative to its center is denoted by δ_s, and of the half cohesive zone relative to the cube edge by δ_c.

choosing the x_1-direction without loss of generality

$$\sigma_{11} = \hat{E}\varepsilon_{11} = \hat{E}\frac{\partial u_1}{\partial x_1}, \quad \text{where} \quad \hat{E} \equiv \frac{E(1-\nu)}{(1+\nu)(1-2\nu)}, \tag{2}$$

an effective one-dimensional tensile modulus $\hat{E}$ being defined as indicated, and we have employed the relation of the normal infinitesimal strain component to the spatial derivative of the displacement. Substitution of (2) into the x_1-direction equation of conservation of linear momentum gives (when no body forces act) the governing equation for the u_1-component of the displacement field in the elastic cube:

$$c^2\frac{\partial^2 u_1}{\partial x_1^2} = \frac{\partial^2 u_1}{\partial t^2}, \quad \text{where} \quad c \equiv \sqrt{\frac{\hat{E}}{\rho}}, \tag{3}$$

and ρ is mass density. Identical equations apply for the other two coordinate directions, so as observed earlier, it is sufficient to analyze this one direction. Equation (3) has the general solution

$$u_1(x_1,t) = f(x_1 - ct) + g(x_1 + ct), \tag{4}$$

where f and g are arbitrary functions, to be determined by the boundary and initial conditions, and c is the elastic wave speed defined in (3).

We seek the equation governing the half cohesive zone displacement δ_c; this is accomplished by enforcing on (4) the initial conditions in accord with our assumption of a constant and uniform strain rate $\dot{\varepsilon}_0$, and the boundary conditions of normal stress and displacement continuity, at the cube edges, with the cohesive zones. The latter make use of our assumption that the total strain rate (in each direction) of the elastic cube plus its half cohesive zones remains the constant $\dot{\varepsilon}_0$ before fragmentation. One can eliminate all other unknowns to obtain the following governing equation for δ_c (see Drugan [3] for details of the analysis):

$$\boxed{\delta_c'(t) + \frac{1}{\tau}\delta_c(t)\exp\left[1 - \frac{2}{\delta^*}\delta_c(t)\right] = c\,\dot{\varepsilon}_0\,t, \quad \delta_c(0) = 0, \quad \text{valid for } 0 \le t \le \frac{l}{c}}, \tag{5}$$

where $\tau \equiv \delta^*\hat{E}/\left(2c\sigma_{\max}\right)$ is a constant having time dimensions. In deriving (5), we have employed the normal traction/normal separation relation for the cohesive zones suggested by the *ab initio* atomistic calculations of Rose et al. [5,6]:

$$\sigma_c\left(2\delta_c\right) = \sigma_{\max}\frac{2\delta_c}{\delta^*}\exp\left(1 - \frac{2\delta_c}{\delta^*}\right), \tag{6}$$

where σ_{max} is the strength of the cohesive surface, which is attained when $2\delta_c = \delta^*$. Observe that (5) is valid only for times sufficiently short that an elastic wave reflection does not take place; in situations where fragmentation initiation takes longer than this, wave reflections must be accounted for and (5) is modified; see Drugan [3] for details. We here restrict discussion to situations (i.e., to sufficiently high strain rates) in which fragmentation initiation occurs before any elastic wave reflections occur, so that (5) is valid.

There are two unknowns to be determined: the time to fragmentation initiation, and the minimum fragment size. We thus impose two conditions to determine these unknowns: First, we hypothesize that fragmentation initiation will occur at the time t_{cr} when the stress level in the cohesive zone has just attained the cohesive strength σ_{max}. In terms of the cohesive zone displacement, this requires [see (6)]

$$2\delta_c(t_{cr}) = \delta^*. \tag{7}$$

Second, the instability condition determining the minimum possible fragment size, $l_{\min}$, is the condition that at time t_{cr}, the prospective brittle fragment, which is the elastic cube, has just stopped expanding. This requires, using the assumption of uniform strain rate until fragmentation initiation $\delta_s'(t) + \delta_c'(t) = \dot{\varepsilon}_o l/2$:

$$\delta_s'(t_{cr}) = 0 \quad \Rightarrow \quad \delta_c'(t_{cr}) = \tfrac{1}{2}\dot{\varepsilon}_o l_{\min}. \tag{8}$$

For the very high strain rate regime considered here, defined by the condition that fragmentation initiates for $t_{cr} \le l_{\min}/c$, (5) applies. [For lower strain rates not satisfying this condition, the modified analysis is given in Drugan [3].] Thus, combining (7) and (8) and using (5) to express $\delta_c'(t)$, we find the minimum fragment size to be:

$$l_{\min} = 2c\left(t_{cr} - \frac{1}{\dot{\varepsilon}_o}\frac{\sigma_{\max}}{\hat{E}}\right), \qquad \text{valid for } 0 \le t_{cr} \le \frac{l_{\min}}{c}, \tag{9}$$

where t_{cr} is obtained by solution of (7) [which in turn requires the numerical solution of (5)]. This can be done once and for all in terms of nondimensionalized quantities; Drugan [3] did this, and found that the resulting predictions for minimum fragment size and time to fragmentation initiation are very accurately fit by the following equations in the very high strain rate regime:

$$\boxed{\tilde{l}_{\min} = 2.1395\,\tilde{\dot{\varepsilon}}_o^{-0.4264}, \quad \tilde{t}_{cr} = 2.0184\,\tilde{\dot{\varepsilon}}_o^{-0.60016}, \quad \text{valid for } 0 \le \tilde{t}_{cr} \le \tilde{l}_{\min}.} \tag{10}$$

Here, the nondimensionalized quantities are defined as:

$$\tilde{l}_{\min} = \frac{2(1-2\nu)e\sigma_{\max}^2}{(1-\nu)^2 K_{Ic}^2} l_{\min}, \quad \tilde{t}_{cr} = \frac{2(1-2\nu)ce\sigma_{\max}^2}{(1-\nu)^2 K_{Ic}^2} t_{cr}, \quad \tilde{\dot{\varepsilon}}_o = \frac{(1-\nu)^2 \hat{E} K_{Ic}^2}{2(1-2\nu)ce\sigma_{\max}^3}\dot{\varepsilon}_o, \tag{11}$$

where all quantities are defined previously except K_{Ic}, the plane strain fracture toughness and e, the natural logarithm base.

REVIEW OF PREVIOUS ENERGY-BALANCE MODELS

A pioneering and widely adopted model of dynamic fragmentation in brittle materials is due to Grady [1]. One postulate of this model, which we have adopted here as noted above, is that a body is initially in a state of rapid uniform expansion – i.e., the strain rate is constant throughout the body. Grady focused attention on

a body portion that would ultimately become a fragment, and decomposed its total kinetic energy into two parts: that of the total mass moving with the center of mass of the body portion, and that associated with relative motion of material particles with respect to the body portion's mass center. He postulated that the latter part of kinetic energy is available to drive fragmentation, and predicted fragment size by equating this energy to that required for the total surface energy to form a new fragment, tacitly assuming fragmentation to be instantaneous. For cubic fragments as modeled here, the Grady prediction of fragment size is

$$l = 24^{\frac{1}{3}}\left(\frac{K_{Ic}}{\rho c \dot{\varepsilon}_o}\right)^{\frac{2}{3}}. \tag{12}$$

Glenn and Chudnovsky [2] improved the Grady [1] model by noting that in addition to the local kinetic energy of a prospective fragment, its stored elastic energy is also available for new fracture surface formation. Application of this more complete energy balance argument demands the additional requirement that no fragmentation occurs until the stress state attains a critical value, $\sigma_{\max}$, at which level instantaneous fragmentation is postulated to occur. The Glenn and Chudnovsky [2] prediction of fragment size is

$$l = 4\sqrt{\frac{\alpha}{3}}\sinh\left(\frac{\phi}{3}\right), \tag{13}$$

where

$$\alpha \equiv \frac{3\sigma_{\max}^2}{\hat{E}\rho\dot{\varepsilon}_o^2}, \qquad \beta \equiv \frac{3}{2}\left(\frac{K_{Ic}}{\rho c \dot{\varepsilon}_o}\right)^2, \qquad \phi \equiv \sinh^{-1}\left[\beta(3/\alpha)^{\frac{3}{2}}\right]. \tag{14}$$

COMPARISON OF THE PRESENT AND ENERGY BALANCE MODELS WITH EXPERIMENT

It should first be observed that it would be difficult to conduct an experiment in which the assumption made by all the analytical models discussed here, namely that a body experiences a uniform and constant strain rate until fragmentation initiation, was precisely met everywhere. However, a set of careful experimental results exist which appear, on the basis of the flash radiographic records, to correspond to a quite uniform fragmentation event, so that our assumption should be met at least in a large portion of the fragmenting body. These are the experimental results of Piekutowski [4]. The experiments involved the high-speed impact of 2017-T4 aluminum spheres with 6061-T6 aluminum plates, causing dynamic fragmentation of the aluminum spheres. Here we compare the measured fragment sizes from the experiments with the predictions of the energy-based models and our new model. The material properties for the 2017-T4 aluminum spheres are:

$$E = 73 \text{ GPa}, \quad \nu = 0.33, \quad \rho = 2791 \text{ kg/m}^3, \quad \sigma_{\max} = 430 \text{ MPa}, \quad K_{Ic} = 20 \text{ MPa}\sqrt{\text{m}}. \tag{15}$$

(The material property values are from Kishida and Nakagawa [7], whose dynamic fracture experiments showed a substantial reduction in fracture toughness of this alloy at high strain rates; $K_{Ic} \approx 20$ MPa$\sqrt{\text{m}}$ is a lower bound to their high-strain-rate data.) The strain rates in the experiments of Piekutowski [4] ranged from 0.9 to 2.6 × 10^5/s; he reported only the strain rates for these two extreme tests. Table 1 shows the experimental results from these two tests, together with the predictions of the present model [Equations (10) and (11)], the Grady model [Equation (12)], and the Glenn and Chudnovsky model [Equations (13) and (14)]. Note that, although the present model predicts minimum fragment size, when the strain rate is uniform and material properties variation is neglected, as assumed, all fragments are the same size, so the minimum and average fragment sizes coincide. (The fact that all fragments are not the same size in the experiments shows that our two assumptions are not precisely met.) Also, it is easy to verify that the strain rates in the experiments are in the "high strain rate regime", that is, they satisfy the needed inequality in (10).

$\dot{\varepsilon}_o$, s^{-1}	l, mm (Piekutowski experiments)	l, mm (present model)	l, mm (Grady model)	l, mm (Glenn & Chudnovsky model)
0.9×10^5	0.814	0.853	1.58	1.39
2.6×10^5	0.506	0.543	0.778	0.731

Table 1. Comparison of experimental results of Piekutowski [4] for the average measured fragment size with the theoretical predictions of the present model [Equations (10), (11)], the Grady model [Equation (12)], and the Glenn and Chudnovsky model [Equations (13), (14)].

DISCUSSION

The comparison in Table 1 of the three dynamic fragmentation models with the experimental data of Piekutowski [4] shows that the present, mechanics-based dynamic fragmentation model agrees much more closely with the experimental measurements than do the two energy-based models which ignore the mechanics of the dynamic fragmentation process. As noted above, the energy-based models assume an instantaneous fragmentation event, so their predictions would be expected to be less accurate the lower the applied strain rate; this is clearly reflected in the comparisons in Table 1, which also shows that the accuracy of the present model changes little with changing strain rate. It should be emphasized that none of these three models involves any "free" parameters: all make specific predictions based only on the set of material constants listed above. Although the comparisons presented here involve a limited set of experimental results, restricted to a single material and a somewhat limited range of strain rates, and much further experimental-theoretical comparison should be conducted, these initial comparisons indeed appear to confirm the importance of accounting for the actual time-varying dynamic deformation and the mechanics of the dynamic failure process in the accurate modeling of dynamic fragmentation.

ACKNOWLEDGEMENTS

This research was supported by Lawrence Livermore National Laboratory under contract No. W-7405-ENG-48 with the Department of Energy, and by Contract BB-3609 with Sandia National Laboratories.

REFERENCES

1. Grady, D. E. (1982) *Journal of Applied Physics* 53, 322-325.
2. Glenn, L. A., Chudnovsky, A. (1986) *Journal of Applied Physics* 59, 1379-1380.
3. Drugan, W. J. (2001) "Dynamic Fragmentation of Brittle Materials: Analytical Mechanics-Based Models." *Journal of the Mechanics and Physics of Solids* 49, 1181-1208.
4. Piekutowski, A. J. (1996). In: *High-Pressure Shock Compression of Solids II*, pp. 150-175, Davison, L., Grady, D. E., Shahinpoor, M. (Eds.). Springer, New York.
5. Rose, J. H., Ferrante, J. and Smith, J. R. (1981) *Physical Review Letters* 47, 675-678.
6. Rose, J. H., Smith, J. R. and Ferrante, J. (1983) *Physical Review B* 28, 1835-1845.
7. Kishida, K., Nakagawa, K. (1983), *Zairyo*. 32, 1096-1101.

PAPER REFERENCE: ICF100450OR

MECHANISMS OF FRACTURE IN PEARLITIC STEELS WITH DIFFERENT DEGREES OF COLD DRAWING

J. Toribio, F. J. Ayaso and M. Toledano

Department of Materials Science, University of La Coruña,
ETSI Caminos, Campus de Elviña, 15192 La Coruña, Spain

ABSTRACT

In this paper the fracture process of steels with different levels of cold drawing is studied. Results demonstrated that progressive drawing affects the fracture behavior, so that heavily drawn steels exhibit anisotropic fracture behavior with a change in crack propagation direction which approaches the wire axis or cold drawing direction. A micromechanical model of fracture is proposed to rationalize the results on the basis of the microstructural evolution in the steels as a consequence of the drawing process which produces a progressive orientation, along the drawing axis, of the two basic microstructural levels: the pearlite colonies and the pearlitic lamellae. In slightly drawn steels, the Miller-Smith model of shear cracking in pearlite seems to be adequate to describe the fracture process. In heavily drawn steels, a fracture propagation step appears, and it may be caused by extremely slender *pearlitic pseudocolonies* aligned in the drawing direction, with very high *local* interlamellar spacing which makes them preferential fracture paths with minimum local resistance.

KEYWORDS

Pearlitic steel, cold drawing degree, fracture micromechanisms, microstructure-based modeling.

INTRODUCTION

Manufacturing of pearlitic steels to obtain prestressing steel wires to be used in prestressed concrete structures consists of cold drawing a hot rolled bar in several passes to increase the yield strength by producing strong plastic deformations in the material. Thus the manufacturing process in the form of increasing cold drawing —with the subsequent progressive plastic deformation— produces important microstructural changes in the steel which could influence its ulterior fracture performance.

Previous research on this topic dealt *only* with the first and last steps of the cold drawing manufacturing process, i.e., the hot rolled bar (base material) and the commercial cold drawn prestressing steel wire (high-strength material to be used in prestressed concrete). Ref [1] presents a general overview, while [2] studies the anisotropic fracture behavior of the fully drawn wire. This paper analyzes the fracture phenomenon in wires of eutectoid pearlitic steel with *intermediate* degrees of cold drawing.

EXPERIMENTAL PROGRAM

Samples from a real manufacturing process were supplied by EMESA TREFILERIA. The manufacture chain was stopped in the course of the process, and samples of five intermediate stages were extracted, apart from the original material or base product (hot rolled bar: not cold drawn at all) and the final commercial product (prestressing steel wire: heavily cold drawn). Thus the *drawing intensity* (or straining level) is treated as the fundamental variable to elucidate the consequences of manufacturing on the posterior fracture behavior. The different steels were named with digits 0 to 6 which indicate the number of cold drawing steps undergone. Table 1 shows the chemical composition common to all steels, and Table 2 includes the diameter (D_i), the yield strength (σ_Y), the ultimate tensile stress (σ_R) and the fracture toughness (K_{IC}), cf [3].

TABLE 1
CHEMICAL COMPOSITION (wt %) OF THE STEELS

C	Mn	Si	P	S	Cr	V	Al
0.80	0.69	0.23	0.012	0.009	0.265	0.060	0.004

TABLE 2
DIAMETER REDUCTION AND MECHANICAL PROPERTIES OF THE STEELS

Steel	0	1	2	3	4	5	6
D_i (mm)	12.00	10.80	9.75	8.90	8.15	7.50	7.00
σ_Y (GPa)	0.686	1.100	1.157	1.212	1.239	1.271	1.506
σ_R (GPa)	1.175	1.294	1.347	1.509	1.521	1.526	1.762
K_{IC} (MPam$^{1/2}$)	60.1	61.2	70.0	74.4	110.1	106.5	107.9

Cold drawing produces changes in the pearlite colony (first microstructural unit) in the form of slenderizing [4] and progressive orientation parallel to the wire axis or cold drawing direction [5]. Drawing also produces changes in the lamellae in the form of decrease of interlamellar spacing [6] and orientation parallel to the wire axis [7]. Figures 1 and 2 (cf.[5,7]) show the pearlitic microstructure of steel 6 at the levels of pearlite colonies and pearlitic lamellae respectively, by means of optical and scanning electron micrographs corresponding to longitudinal metallographic sections of the wires (those sections containing the wire axis). It is seen that the microstructure of steel 6 (prestressing steel heavily cold drawn) is markedly oriented in the direction of the wire axis (or cold drawing direction) which corresponds to the vertical side of the two micrographs.

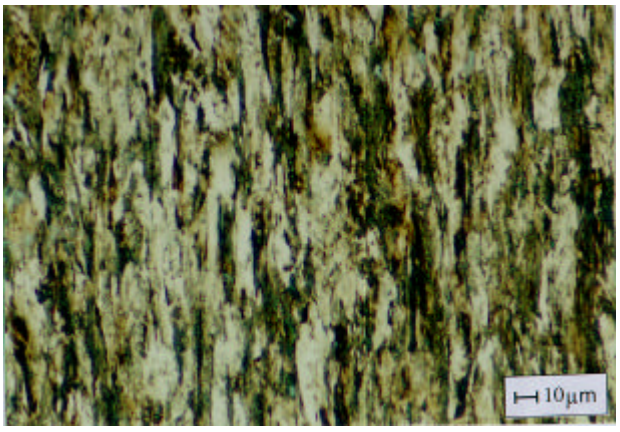

Figure 1: Optical micrograph (steel 6).

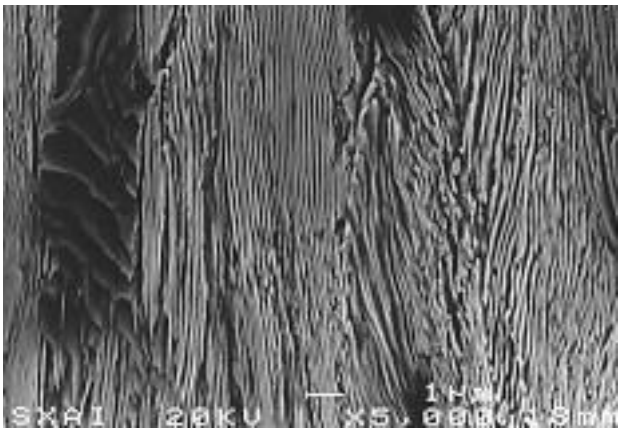

Figure 2: Scanning electron micrograph (steel 6).

In addition, in the most heavily drawn steels there are some exceptional *pearlitic pseudocolonies* (cf. [8]) which are extremely slender, aligned quasi-parallel to the drawing direction and whose *local interlamellar*

spacing is clearly anomalous —specially high— in comparison with the average (or global) spacing because the cementite plates are not oriented along the wire axis direction so that they are pre-fractured by shear during manufacture, as shown in the left part of Figure 2. The characteristics of these pseudocolonies make them local precursors of micro-cracking, i.e., preferential fracture paths with minimum local fracture resistance [9].

To analyze the fracture mechanisms in the steels with different degrees of cold drawing, two sets of tests were performed: (i) fracture tests on cylindrical precracked samples; (ii) fracture tests on axisymmetric notched specimens with a circumferentially-shaped notch. In the latter case, four notch geometries were used, with the following dimensions: notch A : R/D = 0.03, A/D = 0.10, notch B : R/D = 0.05, A/D = 0.30, notch C : R/D = 0.40, A/D = 0.10, notch D : R/D = 0.40, A/D = 0.30, where A is the notch depth and R the notch radius.

RESULTS

Figure 3 shows the fracture modes in precracked samples. The initial hot rolled material (steel 0) and the slightly drawn steels (steels 1-3) behave isotropically, i.e., cracking develops in mode I following the initial plane of fatigue crack growth (Figure 3a). The most heavily drawn steels (steels 4-6) exhibit a clearly anisotropic fracture behavior in the form of crack deflection after the fatigue precrack with a deviation angle of almost 90º from the initial crack plane and further propagation in a direction close to the initial one (Figure 3b).

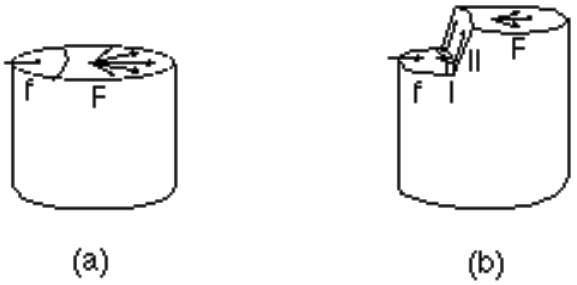

Figure 3: Fracture modes: (a) slightly drawn steels 0-3; (b) heavily drawn steels 4-6; f: fatigue precracking; I: mode I subcritical cracking, II: 90º propagation step; F: final fast fracture.

The fractographic analysis by scanning electron microscopy showed *predominant* appearances from brittle cleavage (C) in the slightly drawn steels (Figure 4: steel 1) to ductile micro-void coalescence (MVC) in the heavily drawn steels (Figure 5: steel 5). The 90º-step appears at a distance x_S from the fatigue precrack tip, and this distance decreases as the cold drawing degree increases, i.e., the step gets closer to the fatigue precrack as the drawing becomes heavier, and in the fully drawn material (steel 6) the step is located just at the fatigue precrack tip (x_S=0). The fibrous appearance of the described step is shown in Figure 6 at two different scales.

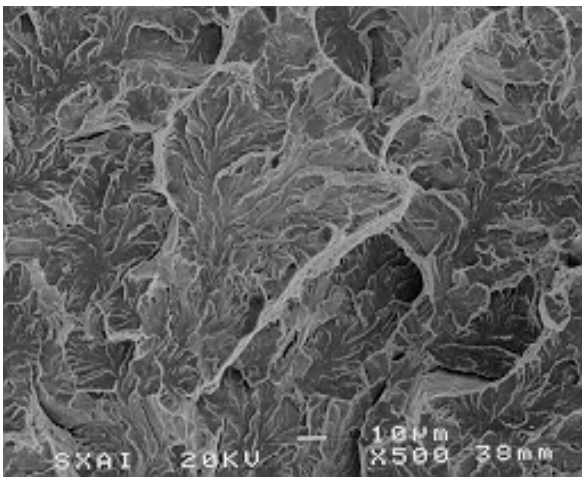

Figure 4: Fracture by cleavage in steel 1.

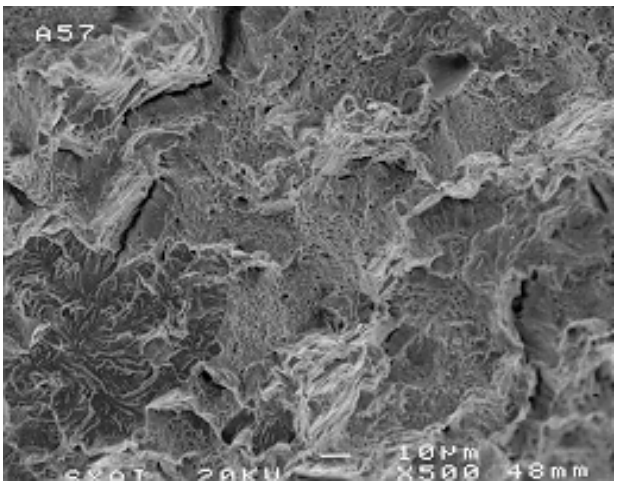

Figure 5: Fracture by MVC in steel 5.

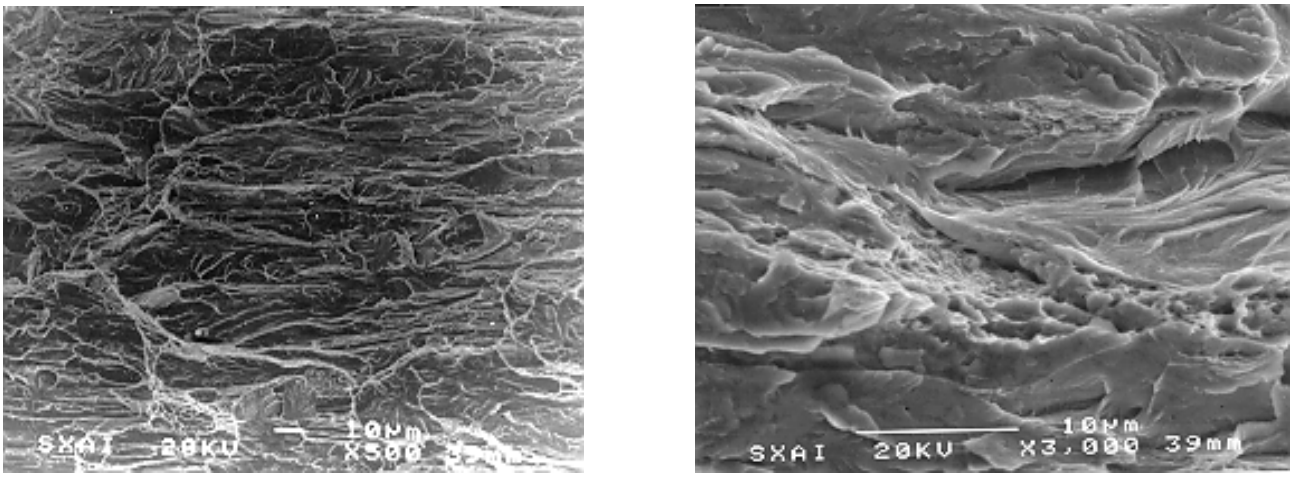

Figure 6: Fractographic appearance of the 90º-step in steel 6, at two different scales

Figure 7 shows two fracture profiles obtained in notched samples (in notch B of maximum stress triaxiality). The fracture profile becomes more stepped as the microstructural orientation in the direction of the wire axis increases as a consequence of cold drawing. This fact explains why specimen 3B (left) exhibits a slightly stepped fracture profile, whereas in the fracture profile of specimen 4B (right) there is a macroscopic step perpendicular to the initial propagation direction transverse to the wire axis. The step is oriented parallel to the wire axis, as in the case of precracked samples of heavily drawn steel.

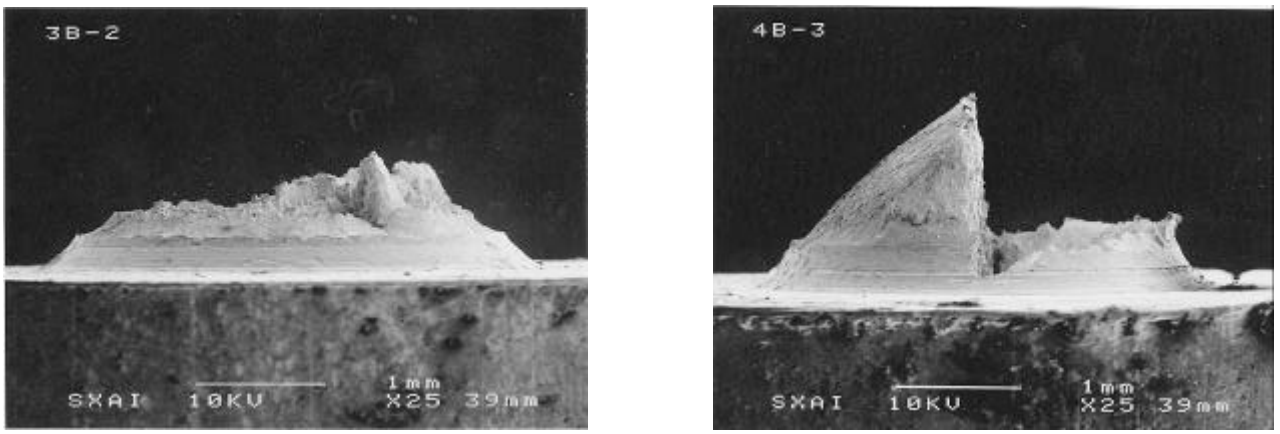

Figure 7: Fracture profile of notch B (maximum depth; minimum radius) and steels 3 (left) and 4 (right).

MICROMECHANICAL MODELLING

Hot Rolled and Slightly Drawn Steels

Since hot rolled and slightly drawn steels exhibit isotropic fracture behavior, a classical micromechanical model for this kind of microstructure allows a rationalization of the fracture behavior. In this framework, the most commonly accepted model is that proposed by Miller and Smith [10] on the basis of a micromechanism of shear cracking in pearlite. It has been used many times in the scientific literature to explain the fracture process in different types of pearlitic microstructures, cf. [11-15].

The model is illustrated in Figure 8 which suggests that micro-cracks are formed by *shear cracking*. First of all, slip takes place in ferrite when the material is stressed. Secondly, due to the stress concentration at the ferrite/cementite interfaces along the ferrite slip plane, the cementite plates become fractured and promote shear. When the shear becomes large enough, there is a final phase of link-up of the holes to form a macroscopic crack which promotes final fracture.

The model by Miller and Smith is able to explain different fracture processes of pearlitic microstructures in air environments (cf. [12]), ranging from ductile MVC to brittle cleavage catastrophic failure. Many times, there is a dimple fracture initiation (ductile region of certain microstructural size) followed by cleavage propagation. The critical size for final fracture depends on the temperature, strain rate and stress triaxiality in the local fracture region [12].

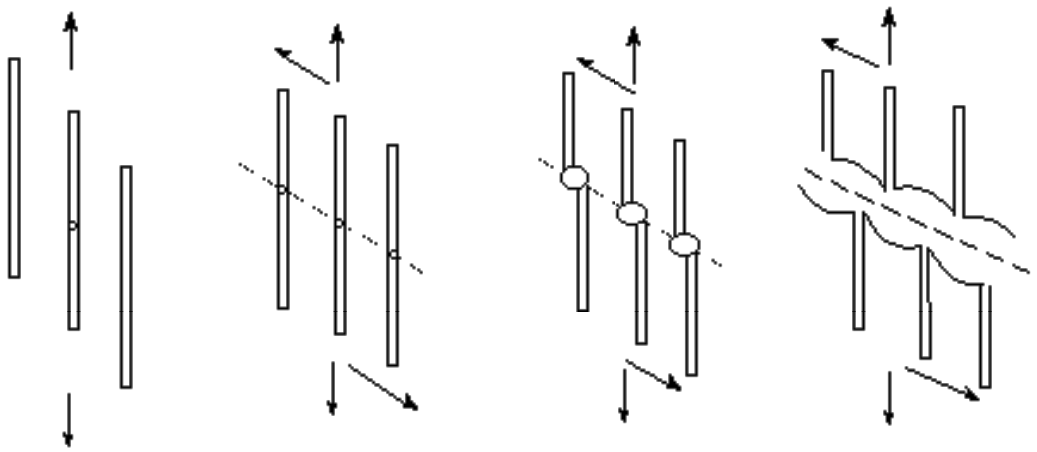

Figure 8: Micromechanical model of fracture by shear cracking in pearlitic microstructures (after Miller and Smith [10]) applicable to fracture in hot rolled and slightly drawn steels.

Heavily Drawn Steels

The anisotropic fracture behavior in heavily drawn steels can be rationalized on the basis of the oriented pearlitic microstructure of the steels. In the metallographic analysis on these steels, some pearlitic pseudocolonies appear aligned to the cold drawing direction and they are potential fracture sites for two reasons:

(i) the very high local interlamellar spacing which makes them weaker or potentially fracturable by shear cracking of pearlitic plates according to the mechanism of *shear cracking* in pearlitic microstructures proposed by Miller and Smith [10].

(ii) the presence of some microcracks and defects consisting of plates prefractured in the pseudocolony during the manufacturing process (cold drawing) as a consequence of the very high stresses applied on the wire (mechanical pre-damage)

Thus the pearlitic pseudocolonies act as local micro-crack precursors, and their presence could explain the fracture path in heavily drawn steels (Figure 3b). Figure 9 offers a scheme showing the formation of the 90º-step when the macro-crack (starting from the precrack or from the notch tip) reaches the location of the pearlitic pseudocolony (Figure 9a), and then the pearlitic plates are fractured by a mechanism of shear cracking (shown in Figure 9b) according to the model proposed by Miller and Smith [10].

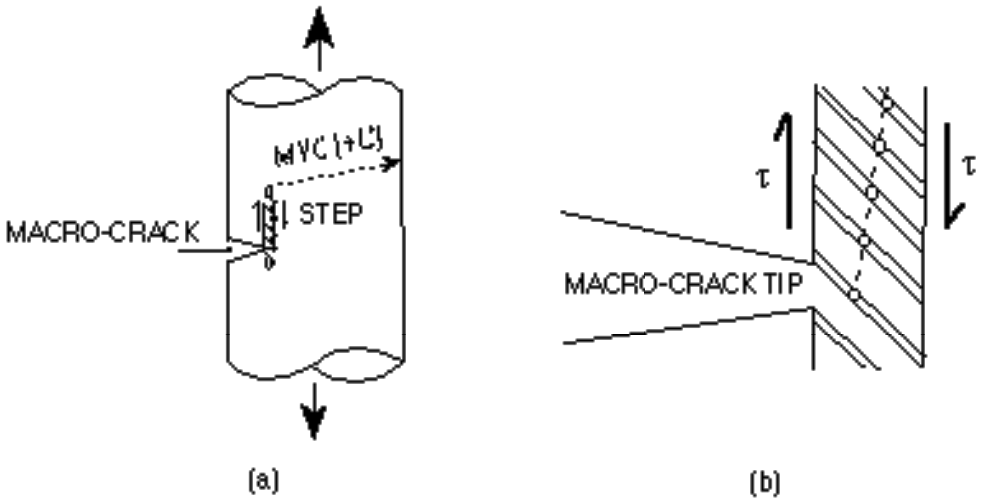

Figure 9: Micromechanics of final fracture in heavily drawn steels: (a) the 90º-step appears when the macro-crack reaches an extremely slender *pearlitic pseudocolony* with anomalous (very high) local interlamellar spacing; (b) the pseudocolony fails very easily by shear cracking of pearlite, according to the model proposed by Miller and Smith [10].

Finally, Figure 10 offers a general sketch of the fracture process in heavily drawn steels, with a first stage of propagation by MVC over a distance x_S up to the appearance of the 90º-step The distance x_S (i.e., the mode I propagation length) is a decreasing function of the drawing degree, a consequence of the frequency of appearance of pseudocolonies which is higher when drawing becomes heavier, i.e., the average distance between these microstructural units is a decreasing function of the level of drawing. The heavier the drawing, the higher the probability of change in crack propagation direction.

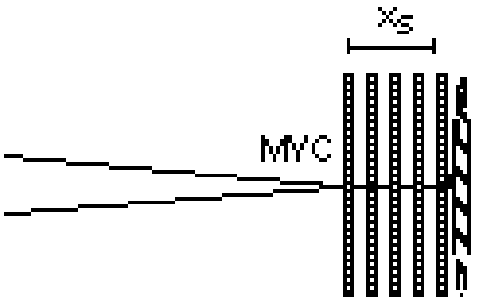

Figure 10: Micromechanical model of initiation and final fracture in heavily drawn steels. The microstructure is assumed to be totally oriented in the cold drawing direction.

CONCLUSIONS

While the fracture behavior of slightly drawn steels is isotropic (mode I propagation), the heavily drawn steels exhibit anisotropy and crack deflection (mixed mode propagation).

In slightly drawn steels, the fracture micromechanism consists of shear cracking in the pearlitic microstructure according to the model proposed by Miller and Smith.

In heavily drawn steels, crack deflection takes place when the macrocrack reaches the position of a pearlitic pseudocolony which represents a local fracture precursor.

Acknowledgements
The financial support of this work by the Spanish CICYT (Grant MAT97-0442) and *Xunta de Galicia* (Grant XUGA 11802B97) is gratefully acknowledged. In addition, the authors wish to express their gratitude to EMESA TREFILERIA S.A. (La Coruña, Spain) for providing the steel used in the experimental programme.

REFERENCES

1. Elices M. (1985). In: *Fracture Mechanics of Concrete: Structural Application and Numerical Calculation*, pp. 226-271, Sih, G.C. and DiTommaso, A. (Eds.). Martinus Nijhoff Publishers, Dordrecht.
2. Astiz, M.A., Valiente, A., Elices, M and Bui, H.D. (1984). In: *Life Assessment of Dynamically Loaded Materials and Structures-ECF5*, p. 385, Faria L.O. (Ed). EMAS, West Midlands, 1984,.
3. Toribio, J. and Toledano, M. (2000) *Constr. Building Mater*. **14**, 47.
4. Toribio, J. and Ovejero, E. (1997) *Mater. Sci. Engng.* **A234-236**, 579.
5. Toribio, J. and Ovejero, E. (1998) *J. Mater. Sci. Lett.* **17**, 1037.
6. Toribio, J. and Ovejero, E. (1998) *Scripta Mater.* **39**, 323.
7. Toribio, J. and Ovejero, E. (1998) *Mech. Time-Dependent Mater.* **1**, 307.
8. Ovejero, E. (1998). Ph. D. Thesis, University of La Coruña.
9. Toledano, M. (1998). Ph. D. Thesis, University of La Coruña.
10. Miller, L.E., Smith, G.C. (1979) *J. Iron Steel Inst.* **208**, 998.
11. Porter, D.A., Easterling, K.E. and Smith, G.D.W. (1978). *Acta Metall*. **26**, 1405.
12. Park, Y.J. and Bernstein, I.M. (1979) *Metall. Trans*. **10A**, 1653.
13. Lewandowski, J.J. and Thompson, A.W. (1986) *Metall. Trans.* **17A**, 461.
14. Lewandowski, J.J. and Thompson, A.W. (1986) *Metall. Trans.* **17A**, 1769.
15. Nakase, K. and Bernstein, I.M. (1988) *Metall. Trans.* **19A**, 2819.

ORAL REFERENCE: 978

MECHANICAL BEHAVIOR AND ELECTRICAL RESISTANCE CHANGE IN CARBON PARTICLE DISPERSED PLASTIC COMPOSITE

D-Y. Song , Y. Hirata and N. Takeda

Graduate School of Frontier Science, The University of Tokyo c/o Komaba Open Laboratory (KOL), The University of Tokyo, 4-6-1 Komaba, Meguro-ku, Tokyo 153-8904, Japan

ABSTRACT

Mechanical behavior and electrical resistance change of CPDP (carbon particle dispersed plastic) composite consisting of epoxy resin and conductive carbon particle were investigated under monotonic loading and repeated loading-unloading. The electrical resistance almost linearly increased with increasing strain during loading and the residual electrical resistance was observed even after removing load. The value of the residual electrical resistance was dependent on the maximum strain under the applied stress. This result suggests that the estimation of maximum strain (i.e., damage) is possible by the measuring electrical resistance of composite. The behavior of electrical resistance change during and after loading was discussed on the basis of the results of microscopic deformation and fracture observation. Moreover, the relationship between the volume fraction of carbon particle and the electrical resistivity of CPDP was investigated in relation to the percolation theory. Simulation model of percolation structure was established by Monte Carlo method and the simulation result was compared to the experimental results. The electrical resistance change under applied loading was analyzed quantitatively using the percolation equation and a simple model for the critical volume fraction of carbon particle as a function of the mechanical stress. It was revealed that the prediction was in good agreement with the experimental result except in the region near the failure of material.

KEYWORDS

Carbon particle , Mechanical behavior , Damage , Electrical resistance change, Percolation

INTRODUCTION

The electrical resistance method is expected to be effective for foreseeing damage and preventing fatal fracture of composite material structure. Recently, the relationship between the mechanical parameters (i.e., stress and strain) and the changes in electrical resistance of CFRP composite has been experimentally demonstrated [1-2]. Moreover, the damage detection utilizing the percolation structure of conductive particle instead of carbon fiber has been made [3], but this study was limited to the qualitative evaluation, and the systematic evaluation

with regard to the correlation between mechanical behavior and electrical resistance change is not yet made. In the present study, the relationship between mechanical behavior and the change of electrical resistance for CPDP (carbon particle dispersed plastic) composite was evaluated using both experimental and theoretical methods. To this end, the monotonic loading and repeated loading-unloading tensile tests were carried out using CPDP with epoxy resin and conductive carbon particle, and its microscopic deformation and fracture were observed. Moreover, the relationship between the volume fraction of carbon particle and the electrical resistivity of CPDP was investigated in relation to the percolation theory. Simulation model of percolation structure was established by Monte Carlo method and this result was compared to the experimental results. Finally, the electrical resistance cha nge under applied load was analyzed quantitatively using the percolation equation and a simple model for the critical volume fraction of carbon particle as a function of the mechanical stress (strain).

EXPERIMENTAL PROCEDURE

The materials used were the conducting carbon particle with the flake shape of average size 5μm and an insulting epoxy matrix (Epikote 828 Yuka Shell Co.). Specimens were prepared as follows: firstly, carbon particle and epoxy resin were mixed in a given proportion and pores in this mixture was removed under vacuum. Then, the mixture was injected into the teflon-made mold of dumbbell shape and cured in the electrical furnace under the condition of precure at 50°C, 80min, and aftercure at 100°C, 60min (hereafter, this composite was referred to CPDP). The electrodes for measuring electrical resistance were attached on the opposite surfaces, which were first polished to suppress the insulating matrix surface layer, within the gage length of specimen using silver paste. The dimensions of specimens were 105mm in length, 10mm in width and 1mm in thickness. Tensile tests were conducted at the crosshead speed of 0.5mm/min. The electrical resistance was measured using two-probe DC method. A constant current of 0.1μA was applied on the specimen, and the changes in electrical resistance under loading and unloading were measured simultaneously with stress and strain. Microscopic deformation on specimen surfaces was observed using polarization microscope under loading and fracture surfaces were also observed using scanning electron microscope (SEM) after tensile test.

EXPERIMENTAL RESULTS AND DISCUSSION

Figure 1 shows the electrical resistance change/strain and stress/strain curves for CPDP with 10vol.% carbon particle. The change in electrical resistance exhibited nearly linear behavior up to the final failure of specimen

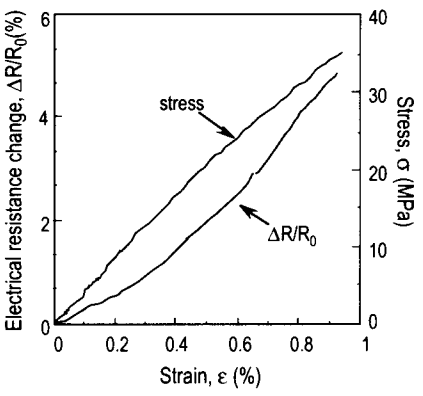

Figure 1: Relations of $\Delta R/R_0$ vs. ε and σ vs. ε for CPDP with 10 vol. % carbon particle

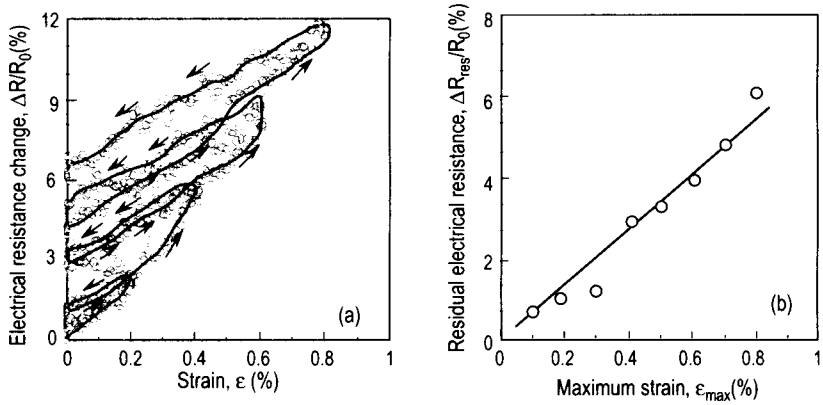

Figure 2: Relations of (a) $\Delta R/R_0$ vs. ε and (b) $\Delta R_{res}/R_0$ vs. ε_{max} for CPDP with 15 vol. % carbon particle

with increasing strain. In particular, CPDP indicated the change in electrical resistance from a considerably small strain level compared to the case of CFRP showing electrical resistance change due to the fracture of carbon fiber mainly. This was the reason why the percolation structure formed with carbon particle showed the sensitive response (i.e., the change of conduction path) against applied loading. Figure 2(a) shows the electrical resistance change/strain curve for CPDP with 15vol.% carbon particle obtained from repeated loading and unloading test. It was seen that the change in electrical resistance was left after unloading at a relatively small 0.2% strain and increases with increasing strain. Figure 2(b) shows the relation between maximum strain applied in the past and residual electrical resistance. The value of residual resistance was dependent on the maximum strain under the applied load. This means that the CPDP has the ability to memorize the maximum strain applied in the past as a residual electrical resistance. This change in electrical resistance under applied load is considered to be caused by the rearrangement of carbon particles with percolation structure due to the microdeformation and cracking of matrix. Figure 3 shows a SEM micrograph of a fracture surface of the CPDP specimen with 15vol.% carbon particle. It was seen that matrix cracking and plastic deformation were significantly observed on the fracture surface, but carbon particles were not observed on the fracture surface. It can be considered that most of carbon particles dropped out when the final fracture of specimen occurred because of the weak adhesion between particle and matrix. Figure 4 shows a polarization micrograph for the surface of CPDP specimen with 0.1vol.% carbon particle. The plastic deformation of matrix surrounding carbon particles was clearly observed as indicated by arrows in this figure. Therefore, the existence of residual electrical resistance as described above is considered to be attributed to this plastic deformation of matrix, leading to the change of geometrical arrangement of carbon particle from its initial state (i.e., the change of conduction path).

Figure 3: SEM micrograph of fracture surface of specimen with 15 vol. % carbon particle

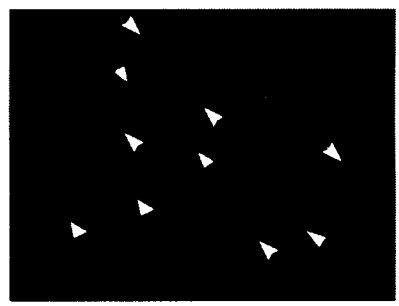

Figure 4: Polarization micrograph of specimen with 0.1 vol. % carbon particle

THEORETICAL ANALYSIS OF ELECTROMECHANICAL PROPERTY OF CPDP

Percolation theory

The property of composite system composed of conductive carbon particle dispersed in insulting polymer matrix are explained as percolation phenomena i.e., when the amount of carbon particle is sufficiently high, the composite transforms from an insulator to a conductor as the result of continuous contacts betweencarbon particles (i.e., percolation) within the polymer matrix. Generally, close to the percolation threshold, the concentration dependence of resistivity in a conductor-insulator composite has been well expressed with percolation theory [4-6].

$$\rho(V) = A(V - V_c)^{-t} \tag{1}$$

where, V_c is the critical carbon volume fraction required to form a continuous conduction path, ρ (V) is the resistivity at carbon volume fraction,V, A and t are the constants. According to literature [7-9], t was found to exist between 1.65 and 2.0 for three dimensional system. Figure 5 shows the variation of resistivity with volume fraction of 5μm carbon particle. It is seen that the resistivity decrease abruptly when the carbon volume

fraction exceeds a critical value. This suggests that the percolation theory can hold in the present experimental results. The constants in Eqn. 1 were obtained using a least square fit to the experimental data. The obtained values are V_c= 0.065, t= 1.9, A = 0.003 MΩ mm The curve calculated with these values is also plotted in Figure 5, showing a good agreement with experiments.

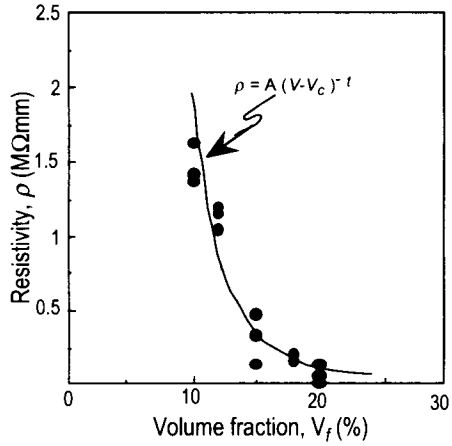

Figure 5: Relations of ρ vs. V_f for 5 μm carbon particle

Simulation Model of Percolation Structure

A simulation model of percolation structure was established by Monte Carlo method. Here, two dimensional random array problem was simulated as follows: At first, the sites of n =1000, which correspond to carbon particles, were randomly arranged in a square of side unity. In order to satisfy the normal distribution with the standard deviation of 0.2R, the circles of the radius, R=1/ (π n)$^{0.5}$ were randomly assigned to each site. Next, for the constructed sites, we examined whether the conduction path between any two sites was formed. Here, we firstly introduced the distance between sites as follows:

$$d_{ij} = [(x_i - x_j)^2 + (y_i - y_j)^2]^{0.5} \tag{2}$$

where, x_i and y_i, x_j and y_j are the coordinates at sites i and j. Then, setting $R_{ij} = R_i + R_j$, the conduction path between sites could be judged by the following equation:

$$H(x) = R_{ij} - d_{ij} \tag{3}$$

where, $H(x)$ is Heaviside function ($H(x)$ =0: $x < 0$, $H(x)$ =1: $x \geq 0$). Thus, $H(x)$ = 1 is the formation condition of conduction path between sites. The condition that two sites exists in the same cluster connected by conduction path was given by

$$B_{ij} = \prod_{a=1}^{A} H_a(x) = 1 \tag{4}$$

where, A is the number of Heaviside functions between sites i and j.

Thus, as the check of the overall percolation in the square, when at least one site having the same cluster number exists at the edges of both directions of x and y in a square (i.e., spanning state), we regard this state as the starting point of percolation. However, during the entire conduction path was not identified, the same way as described above was repeated until the percolation reaches as the radius R increases at the rate of 0.05R. The radius of site at percolation state was referred to the critical radius R_c.

Simulation Result

The process of percolation formation obtained by two dimensional simulation is shown in Figure 6. The critical volume fraction, V_c obtained from the simulation was about 48 vol.%. This value is very high compared to the

value of about 7 vol.% obtained from the experimental results. This difference can be explained by the tunneling effect of conductive particles. For conductive particle-polymer composites, it has been recognized that although the particles were not completely interconnected, the conductive phase was activated and the electrical network was formed (that is, tunneling effect) [10-12]. Considering such a tunneling effect, it can be seen that the site area of this simulation is not the area of particle but corresponds to the region affected by the tunneling effect. Thus, it was simply assumed that the tunneling effect existed to a certain distance on the particle size. That is, for the particle of radius R, if the tunneling effect was effective to the range of kR, the value of k, which might be a constant representing the extent of tunneling effect, was found to be about 2.71 using the average critical volume fraction of 48 vol.%. Thus, it can be said that the tunneling effect existed to the distance of about 8.3μm from the surfaces of particles for the particle of average diameter 5μm.

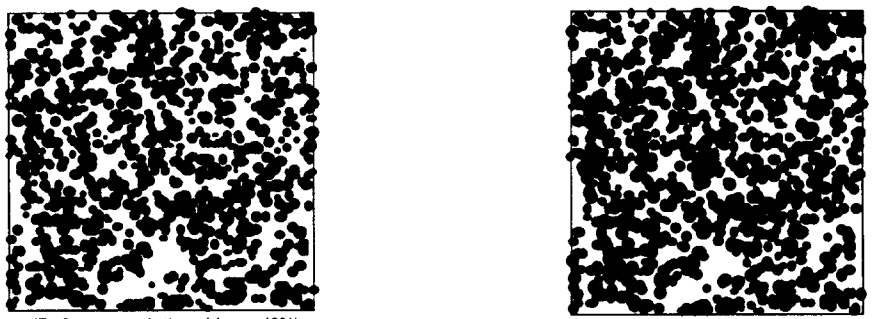

Figure 6: Process of percolation formation

Approximate Analysis of Electrical Resistance Change Under Applied load

The change of electrical resistance of CPDP with tensile loading will be developed using Eqn. 1. Here, the critical volume fraction, V_c, as a first approximation, was assumed to change linearly with applied stress. Moreover, in the case of conductive particle-polymer composite the average number of contacts per particle changes linearly with stress, and was known to be inversely proportional to the critical volume fraction [13, 14]. Thus, the critical volume fraction with stress can be expressed as a simple form as follows:

$$V_c(\sigma) = \frac{V_c(0)}{1 - \alpha\,\sigma} \tag{5}$$

where, $V_c(0)$ was 0.065, the critical volume fraction when the applied stress was absent. This value was obtained from the relationship between the resistivity and the volume fraction described in Figure 5. α is a constant. Then, substituting Eqn. 5 into the percolation Eqn. 1, the resistivity and its change of CPDP under applied stress were finally determined from the following Eqns. 6 and 7.

$$\rho = A\,[V - \frac{V_c(0)}{1 - \alpha\,\sigma}]^{-t} \tag{6}$$

$$\frac{\Delta\rho}{\rho_0} \approx \frac{\Delta R}{R_0} = \left[\frac{V - \dfrac{V_c(0)}{1 - \alpha\,\sigma}}{V - V_c(0)}\right]^{-t} - 1 = \left[\frac{V - \dfrac{V_c(0)}{1 - \alpha\,E\,\varepsilon}}{V - V_c(0)}\right]^{-t} - 1 \tag{7}$$

Figure 7 shows a comparison between the analysis result by Eqn. 7 and experimental result for the CPDP of 5μm carbon particle (in this study the resistivity of CPDP is equivalent to the its resistance, i.e., $\rho \approx R$). Here, the constant α was obtained by fitting Eqn. 7 to the experimental result and its value was 0.008. The predicted result agreed well with the experimental result below 0.6% strain near the failure of material, where damage and electrical resistance greatly changed. It can be therefore said that the electrical resistance change under applied loading is evaluated approximately using the percolation equation and an appropriate model for the

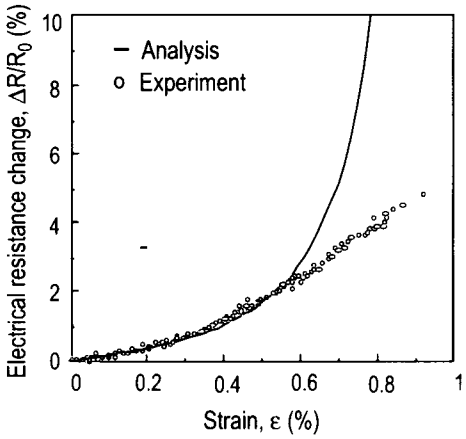

Figure 7: Comparison between analysis and experimental results

critical volume fraction of carbon particle as a function of the stress (or strain).

CONCLUSIONS

Mechanical behavior and electrical resistance change for CPDP (carbon particle dispersed plastic) composite were characterized under tensile loading and repeated loading-unloading. The electrical resistance almost linearly increased with increasing strain during loading and the residual electrical resistance was observed even after removing load. The value of the residual electrical resistance was dependent on the maximum strain under the applied stress. These results suggest that estimation of the maximum strain (damage state) is possible by measuring electrical resistance of composites. The electrical resistance change during loading was attributed to geometrical rearrangement (i.e., the separation of conduction path) of carbon particles with percolation structure due to the plastic deformation and/or the cracking of matrix. The residual resistance was found to be due to the plastic deformation of matrix remaining after removing loading. The relation between the volume fraction of carbon particle and the electrical resistivity of CPDP was well expressed by the percolation equation. Percolation process was simulated by Monte Carlo method. The electrical resistance change of CPDP under applied loading could be approximately analyzed using the percolation equation and a simple model for the critical volume fraction as a function of the stress. This electrical resistance method using the conductive carbon particle is considered to be effective for damage estimation of composite material and structure.

REFERENCES

1. Ceysson, O. et al. (1996) *Scripta Mater.* 34-8,1273.
2. Schulte, K. et al. (1995) *Proc. ICCM,* 349.
3. Takada, M. et al. (1999) *J. Japan Soc. Comp. Mater.* 25, 225.
4. McLachlan, D. S. et al. (1990) *J. Am. Ceram. Soc.*73-8, 2187.
5. Kirkpatrik, S. (1973) *Rev. Mod. Phys.* 45, 574.
6. Pike, G. E. et al. (1974) *Phys. Rev.* B10,1421.
7. Abeles, B. et al. (1975) *Phys. Rev. Lett.* 35, 247.
8. Carmona, F. et al. (1987) *J. Appl. Phys.* 61-7, 2550.
9. Zallen, R. (1983). *The Physics of Amorphous Solids*; Ch.4., Willey New York.
10. Balberg, I. (1987) *Phys. Rev. Lett.* 59-12, 1305.
11. Sichel, E. K. et al. (1978) *Phys. Rev. B.*18-10, 5712.
12. Ruschau, G. R. et al. (1992) *J. Appl. Phys.* 72-3, 953.
13. Gurland, J. (1966) *Trans. Metall. Soc.* AIME. 236, 642.
14. Aharoni, S. M. (1972) *J. Appl. Phys.* 43,2463.

For oral presentation in Session "MesoFracture Mechanics" organized by GC Sih

Meso-fracture of Metal Matrix Composites Reinforced by Particles of Large Volume Fraction

Wei YANG, Chouwei ZHOU and Daining FANG

Department of Engineering Mechanics, Tsinghua University

Beijing, 100084, China

ABSTRACT: Meso-fracture process for metal matrix composites (MMC) reinforced by particles of large volume fraction is pursued in this paper. Particle reinforced Al_2O_3/Al MMC is made under a pressure-less filtration technique. Samples are tested in uniaxial tension, compression and three-point bending, and their fracture patterns and fractography are recorded. The micromechanics model of the composite is composed of identical elastic spheres linked by columns of elastic perfectly plastic matrix. The metallic matrix is treated in two categories: the elastic perfectly plastic von Mises columns linking various particles are actively engaged in forming the skeleton of the MMC; while the rest of the matrix is inactive and only serves to constrain the radial deformation of linking columns. The failure of the interface is governed by the interfacial energy release rate, the matrix damage by the Rice-Tracey void evolution law, and the particle breaking by the largest principal stress. The macroscopic stress-strain relation is derived from the normal and tangential moduli of the two-particle linkages by averaging over a statistical assembly of three packing patterns. Two random variables are adopted for the fluctuations of local stresses in particles and along particle/matrix interfaces. The simulated overall constitutive responses agree with the experiments for the uniaxial tensile, uniaxial compression and three-point bending specimens. The simulated meso-fracture patterns under three testing configurations reproduce the experimental results. Simulated proportions of failure by interface debonding, matrix voiding and particle breaking also agree with the experiments.

KEY WORDS: meso-fracture, particle reinforcement, metal matrix composite, FEM simulation.

MESODAMAGE OF 2024-T3 ALUMINUM ALLOY SPECIMEN DUE TO CORROSION-INDUCED LOCALIZED HYDROGEN EMBRITTLEMENT

Al. Th. Kermanidis[1], P. Papanikos[2] and Sp. G. Pantelakis[1]

[1] Laboratory of Technology & Strength of Materials, Department of Mechanical Engineering & Aeronautics, University of Patras, 26500 Patras, Greece
[2] Institute of Structures and Advanced Materials, ISTRAM, 57 Patron-Athinon Road, Patras 26441, Greece

ABSTRACT

For the evaluation of the structural integrity of ageing aircraft components the effect of corrosion has to be accounted for. In recent years it has been recognized that corrosion of 2024-T3-aluminium alloy is associated to localized hydrogen embrittlement. Obtained damage is location, size, time and temperature dependent. Macroscopically it is reflected through a dramatic reduction of tensile ductility and fracture toughness. A mesodamage concept is adopted to provide the missing link between atomic-and macro-scale level. The proposed model is based on the assumption that different exposure times of thin specimens can yield for the average properties of a number of prospective meso-volumes at a certain distance from the corrosion attacked location of a real aircraft component. The reduction of fracture toughness was associated with the reduction of strain energy density obtained from tension tests of corroded and non-corroded specimens. It was shown that the developed model could be used to evaluate the fracture toughness of the corroded alloy and, thus, the residual strength of corroded aircraft component.

KEYWORDS

Meso-damage, corrosion, hydrogen embrittlement, fracture toughness, aluminium alloys, aging aircraft.

INTRODUCTION

Corrosion and the associated hydrogen embrittlement of high strength aluminium alloys present a major threat to the structural integrity of aging aircraft structures. The potential interaction of corrosion with other forms of damage such as a single fatigue crack or multiple site damage can lead to loss of structural integrity and catastrophic failure [1]. Numerous committees and international conferences have been organized [2-3] to ponder on the problem of material degradation in older aircraft and one important issue is corrosion [4-5]. Currently, corrosion and hydrogen damage mechanisms of aluminium alloys are far from being understood. Involved damage processes occur in atomic scale. Corrosion attack of aluminium alloys has been attributed to the complex process of oxidation [e.g. 1, 6]. Yet, it has been recognized that additionally to oxidation processes, hydrogen produced during the corrosion process may diffuse to the material interior and lead to hydrogen-metal interaction [e.g. 7]. The hydrogen trapping sides depend on the alloy system [7-14]. In [9] the determined embrittlement of the Al-Mg and Al-Zn-Mg aluminium alloy systems was explained as the result of the formation of magnesium hydrides on the grain boundaries. Yet, a dramatic embrittlement of the

alloys 2024 following exposure in several corrosive environments has been reported in [7, 10-12]; 2024 belongs to the Al-Cu system. The same behavior was observed for the 6013, 8090 and 2091 alloys as well. In [13] hydrogen trapping sides for the Al-Cu alloy 2024 are identified. Currently no reliable methodologies exist to link the corrosion and hydrogen damage processes which occur in atomic level to the macroscopic material properties, which are required for structural integrity calculations. In the present work a meso-damage approach is introduced to obtain the missing link between atomic-and macro-scale level. The location, size and time dependency of damage is accounted for. The approach is based on the simplification that different exposure times of thin large scale specimens can yield for the average properties of a number of prospective meso-volumes at a certain distance from the attacked area of a real aircraft component. The approach has been utilized to overcome the need for performing experiments on specimen size reduced to microns. The experiments were used to assess the significantly reduced values of fracture toughness and tensile ductility at meso-volumes lying ahead of the corrosion attacked surface. The investigation is carried out for the Aluminium alloy 2024-T3. The reduction of fracture toughness at meso-volumes is assessed from the reduction of strain energy density obtained from tension tests of corroded and non-corroded specimens.

MESODAMAGE APPROACH

Corrosion is the result of complex oxidation processes at atomic scale. Hydrogen embrittlement is a diffusion controlled process and it is associated with the concentration and trapping of hydrogen at preferable trapping sides. The process takes place at atomic scale as well. The severity of the hydrogen damage depends on location and time. As such a process, embrittlement evolution in a thick specimen or component is linked to the concentration of hydrogen atoms, as shown typically in Figure 1. Distance zero in figure 1 represents the hydrogen source which is the corrosion attacked area (e.g. the tip of a crack at a rivet. The crack acts as hydrogen channel). Embrittlement reaches its maximum value at the surface layer, which is saturated with trapped hydrogen and decreases gradually with decreasing concentration of hydrogen.

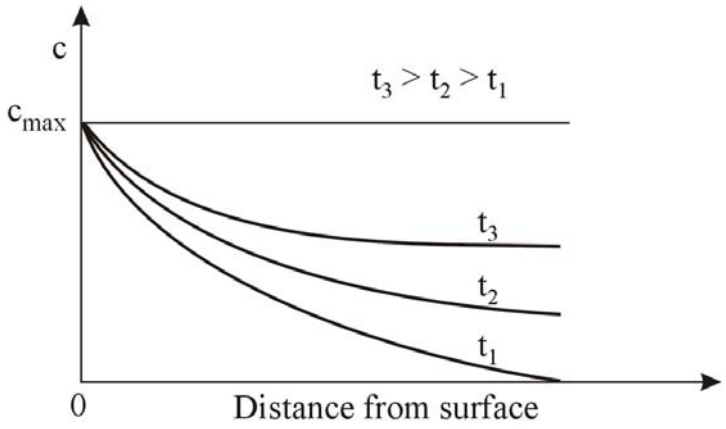

Figure 1: Hydrogen concentration along thickness for different exposure times (schematically)

This process may be interpreted as the embrittlement of three-dimensional meso-volumes, which exhibit different degree of embrittlement. It yields to varying mechanical properties and fracture toughness at the meso-level. The tensile tests described underneath can be used to evaluate these varying tensile properties and fracture toughness. In diffusion controlled processes same concentration of the diffusing medium can be achieved at short distances from the source of the diffusing medium and short diffusion times or at long distances from the source and long times. Thus, the properties of specimens subjected to different exposure times can be interpreted to reflect the average properties of a number of prospective meso-volumes at different distances from the surface. Early experimental results [5, 14] indicate that hydrogen diffusion is very low from the front and back surface of the specimens and high from the edges and through the thickness cuts. Obviously the specimen thickness of 1,6mm is too large as compared to the size of meso-volumes typically not exceeding a few microns. Yet, as shown in [14] the hydrogen may diffuse at distances larger than 25mm. Thus, the properties of the meso-volumes lying along the path of hydrogen diffusion may

be approximated through prospective average values derived each time for a number of meso-volumes involved in 1.6mm distance. With regard to the diffusion controlled embrittlement process the varying degree of embrittlement at different distances from the hydrogen source may be simulated through the exposure of specimens of same thickness (here 1,6mm) for different times at same corrosive environment.

EXPERIMENTS

The experiments included firstly the exposure of specimens to corrosive environments as they are specified in the respective standards for accelerated laboratory corrosion tests for a number of different exposure times. Then the corroded specimens were subjected to mechanical testing.

Materials and Specimen Preparation

The investigation was performed on the aluminium alloy 2024-T3 with the following chemical composition: 0.10% Si, 0.18% Fe, 4.35% Cu, 0.67% Mn, 1.36% Mg, 0.02% Cr, 0.07% Zn, 0.03% Ti, 0.01% Zr. The alloy was received in sheet form of 1.6mm nominal thickness. Tensile and fracture toughness specimens were prepared. Tensile specimens were machined according to ASTM E8m-94a; specimens were cut in both longitudinal (L) and long transverse (LT) direction. Fracture toughness specimens were cut in (L) direction following the ASTM E561-94 specification. More details about the corrosion tests can be found in [12].

Mechanical Testing

The tensile tests aim to provide information on the gradual decrease of the tensile properties during exfoliation corrosion exposure and to assess the degree of properties with increasing distance from the hydrogen source. All tensile tests were performed according to ASTM E8m-94a specification using a 200 KN Zwick universal testing machine and a servohydraulic MTS 250 KN machine by a deformation rate of 10 mm/min. Fracture toughness tests were conducted according to the ASTM 561-94 specification.

RESULTS AND DISCUSSION

Mechanical Characterization

The tensile properties of the reference material are summarized in Table 1. The energy density is evaluated by the area under the true stress-strain curve.

TABLE 1
TENSILE PROPERTIES FOR REFERENCE MATERIALS

Material	Yield stress, S_y (MPa)		Ultimate tensile stress, R_m (MPa)		Elongation to failure, A_{50} (%)		Energy density, W (MJ/m^3)	
	L	LT	L	LT	L	LT	L	LT
2024-T3	396	339	520	488	18.0	18.0	86.7	81.7

The residual mechanical properties as a percentage of the properties of the reference material are shown in Figure 2 for the L (a) and LT (b) directions. The figure shows the property decrease trend versus exposure time in exfoliation corrosion solution. All properties decreased non-linearly with exposure time. It is clear from Figure 1 that yield and ultimate tensile stress have been practically not affected. On the contrary, a clear trend of an appreciable tensile ductility decrease has been observed. Obtained yield and ultimate tensile stress decrease is caused by corrosion induced material surface degradation. It was found that after machining of the corrosion attacked material surface layer, yield and ultimate tensile stress increase again almost to their initial values. Yet, tensile ductility drop is volumetric. Machining of the corrosion attacked surface layer had practically no influence on the determined tensile ductility values although the tensile tests were performed on the “non-corroded” material core after the removal of the corrosion-attacked layer. In [13], the observed bulk embrittlement has been associated to hydrogen penetration and absorption.

Fracture Toughness

Figure 3 shows the fracture surfaces of a non-corroded (a) and a corroded fracture toughness specimen (b). It is clear from the figures that the mode of final failure is different for the two cases. In the non-corroded specimen, a typical ductile fracture is observed. However, a brittle fracture is observed in the corroded specimen indicating that the corrosion-induced embrittlement goes far beyond the corroded layer of the material, which for the specimen showing in Figure 3(b) has a depth of 200 μm. The failure surface indicates the gradual change from a brittle to a ductility failure with increasing distance from the corroded area. Table 2 shows the fracture toughness tests conducted and the values of fracture toughness obtained. For the case of protected specimens (anodizing and sealing), no corrosion effect was observed. The small decrease of the fracture toughness as compared to the un-protected reference specimens might be attributed to the fact that the process of anodization leads to material embrittlement. The results for the un-protected specimens indicate that corrosion leads to a significant decrease in fracture toughness (27%). Yet, the dimensions of the specimen are by far larger as the distance within hydrogen may diffuse. Obtained fracture toughens values reflect specimens which are partially fully embrittled, in certain locations only partially embrittled to different degrees of embrittlement and, far from the hydrogen source, not embrittled at all. The approach described underneath will be utilized to yield to local fracture toughness values. Following to the work in [15], the strain energy density evaluated from the stress-strain curve of the material can be associated to the fracture toughness with the relation:

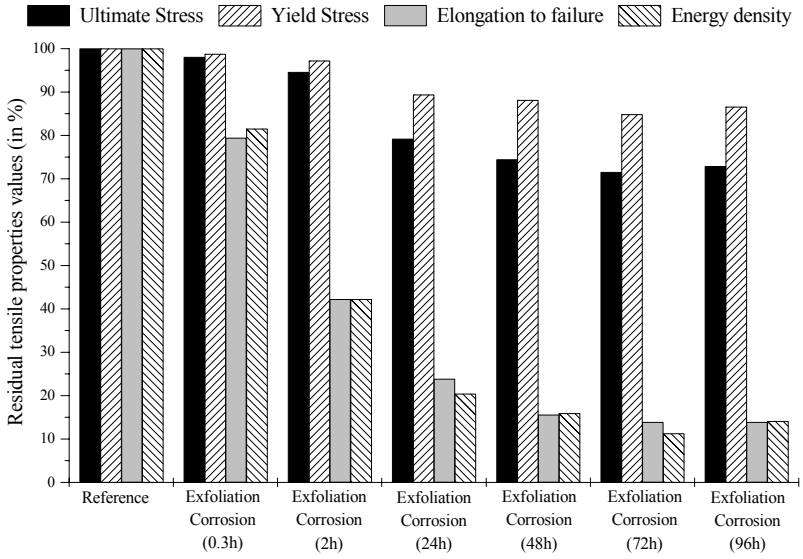

(a)

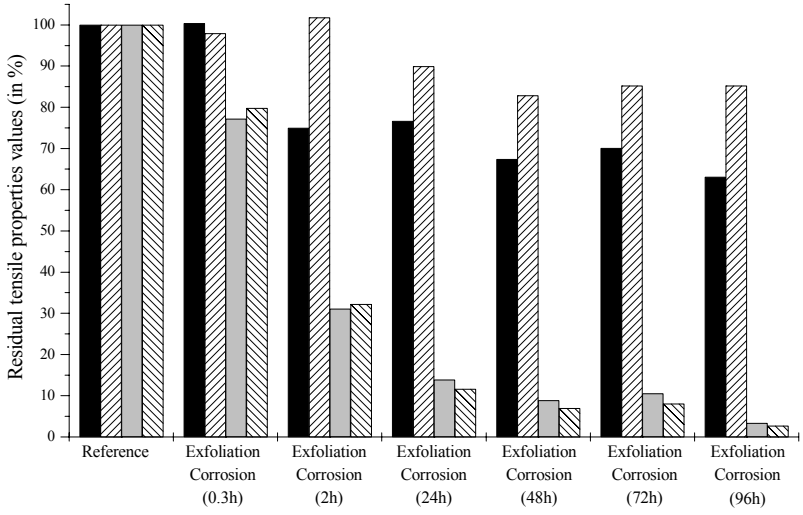

(b)

Figure 2: Gradual tensile property degradation for the alloy 2024 during exposure in exfoliation corrosion solution: (a) L direction, (b) LT direction.

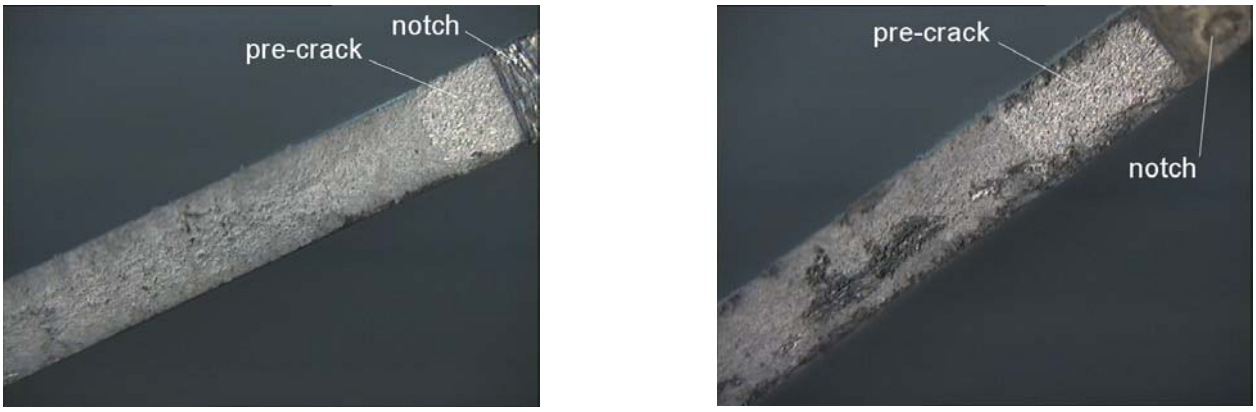

(a) (b)

Figure 3: Fracture surfaces of a (a) non-corroded and (b) corroded (EXCO 36 h) fracture toughness specimens

TABLE 2
FRACTURE TOUGHNESS TEST RESULTS

Material 2024-T3	Corrosion exposure	Direction/ number of tests	$K_c\,(MPa\sqrt{m})$
Reference	None	L/2	134.6
Corroded	EXCO 36 h	L/2	97.8
Reference (anodized and sealed)	None	L/2	126.5
Corroded (anodized and sealed)	EXCO 36 h	L/2	125.2

$$K_c^2 = \beta W \tag{1}$$

where K_c is the fracture toughness, W the strain energy density and β a function of the elastic properties of the material. The quantity β will be considered constant with corrosion exposure. Eqn. 1 can be used to estimate the value of K_c for an embrittled material due to corrosion since it suggests that

$$K_c^2(cor)/K_c^2 = W(cor)/W \tag{2}$$

Using the values of Table 1 and the results of Figure 1(a) it can be estimated that the value of energy density for 36 h exfoliation corrosion is $W(36h) = 14.7\,MJ/m^3$. From Tables 1 and 2 we have that $K_c = 134.6\,MPa\sqrt{m}$ and $W = 86.7\,MJ/m^3$. Therefore, Eqn. 2 gives $K_c(36h) = 55.4\,MPa\sqrt{m}$. This value is however much smaller than the measured value of $97.8\,MPa\sqrt{m}$. The reason for this discrepancy is that the fracture toughness specimen does not experience volumetric embrittlement as the tensile specimen used to obtain the strain energy density. The above observation is very important as far as the structural integrity of a corroded aircraft structure is concerned. It indicates that the use of the virgin material fracture toughness for assessing the structural integrity of aged and corroded components may result to essential overestimation of residual strength, which could lead to fatal consequences. On the other hand, the use of the value of fracture toughness evaluated assuming volumetric embrittlement of the material can be very conservative and lead to over sizing. It is therefore necessary for a specific problem to use a local fracture toughness, which will range from the minimum value (volumetric embrittlement) to the maximum value of the virgin material. This is especially true for MSD problems where the distance of the rivet holes is such that allows local volumetric embrittlement of the material. This work is currently extended to investigate this issue.

CONCLUSIONS

A mesodamage concept is proposed to evaluate the location, size and time dependent embrittlement as a result of hydrogen diffusion and trapping during the corrosion process. The investigation was carried out for the Aluminium alloy 2024-T3. The work indicates the following:

- Corrosion-induced degradation of mechanical properties occurs gradually with the exposure time or the distance from the attacked surface. Tensile ductility decreases exponentially to extremely low final values.
- Tensile test results can be used to evaluate the varying material properties and fracture toughness of a component at any depth and level of embrittlement.
- The fracture toughness of the corroded material decreases significantly. It is necessary to evaluate a local fracture toughness associated with the reduction of strain energy density.
- Adoption of the proposed mesomechanics approach has been proven very efficient for facing the complex interactive corrosion-hydrogen embrittlement process.

ACKNOWLEDGMENTS

This work was partially supported by the Greek General Secretariat for Research and Technology (project PENED99 /649).

REFERENCES

1. Inman, M.E., Kelly, R.G., Willard, S.A. and Piascik R.S. (1997). In: *Proceedings of the FAA-NASA Symposium on the Continued Airworthiness of Aircraft Structures*, pp. 129-146, Springfiled, Virginia.
2. FAA-NASA Symposium on the Continued Airworthiness of Aircraft Structures, FAA Center of Excellence in Computational Modeling of Aircraft Structures, Atlanta, USA, 1996.
3. AGARD Workshop, *Fatigue in the Presence of Corrosion*, RTO Meeting Proceedings 18, Corfu, Greece, 1999.
4. BRITE/EURAM 1053, Structural Maintenance of Aging Aircraft (SMAAC), CEC Brussels, Final Report, 1999.
5. EPETII/30 (1999). *Damage Tolerance Behavior of Corroded Aluminum Structures.* Final Report, General Secretariat for Research and Technology, Greece.
6. Smiyan, O.D., Koval, M.V. and Melehkov, R.K. (1983*) Soviet Mater. Sci*. 19, 422.
7. Pantelakis, Sp.G., Vassilas, N.I. and Daglaras, P.G. (1993*) Metall* 47, 135.
8. Scaman, G.M., Alani, R. and Swann, P.R. (1976) *Corrosion Science* 16, 443.
9. Tuck, C.D.S. (1980). In: *Proceedings of the 3rd Int. Conference of Hydrogen on the Behavior of Materials*, pp. 503-510, Jackson, USA.
10. BRITE/EURAM BE92-3250, Investigation on Aluminium-Lithium Alloys for Damage Tolerance Applications, Final Report, CEC Brussels, 1993.
11. Pantelakis, Sp.G., Kermanidis, Th.B., Daglaras, P.G. and Apostolopoulos, Ch.Alk. (1998). In: *Fatigue in the Presence of Corrosion*, AGARD Workshop, Corfu, Greece.
12. Pantelakis, Sp.G., Daglaras, P.G. and Apostolopoulos, Ch.Alk. (2000) *J. Theor. Appl. Fract. Mech*. 33, 117.
13. Haidemenopoulos, G.N., Hassiotis, N., Papapolymerou G. and Bontozoglou V. (1998) *Corrosion* 54, 73.
14. PENED99/649 (2000). *Corrosion and Hydrogen Embrittlement of Aircraft Aluminum Alloys.* Mid Term Assessment Report, General Secretariat for Research and Technology, Greece.
15. Jeong, D.Y., Orringen, O. and Sih, G.C. (1995) *J. Theor. Appl. Fract. Mech*. 22, 127.

METHOD FOR ESTIMATING SERVICE LOAD FROM STRIATION WIDTH AND HEIGHT

Katsuaki FURUKAWA

Second Forensic Division, First Mechanical Section
National Research Institute of Police Science
6-3-1 Kashiwanoha , Kashiwa-shi, Chiba 277-0882, Japan

ABSTRACT

A case-study method is proposed to determine service loading from fracture surface striations. Although it is well known that striation spacing relates to the crack growth rate, it is considered impossible to determine maximum and minimum loads under service loading conditions, and to define the stress ratio R from an analysis of the striation spacing. This paper presents a new method of measuring the figure of striation using a laser microscope.

KEYWORDS

Fatigue fracture, striation configuration, laser microscope, three dimensional measurement, Stress ratio.

INTRODUCTION

More than 80% of machine structure fractures originate in fatigue. Consequently, to prevent recurrence, it is important to analyze the fracture surface in order to ascertain the cause of the fracture and to estimate the service load. In relation to a PL law that took effective on July 1, 1995, it is predicted that investigation into the cause of accidents will become an important social issue and it is thought that post-accidental analysis of the fracture surface will be important for investigating the cause of accidents.

Striations are commonly observed on fatigue-fractured surfaces and most of these correspond to the load cycle. The fact that crack growth rates (da/dN) correspond to striation spacing (s) is also well known.

Because the relationship between da/dN, s, and ΔK (stress intensity factors range = $K_{max} - K_{min}$) or ΔK_{eff} (effective stress intensity factors range = $K_{max} - K_{op}$), satisfies Paris' law, attempts have been made to estimate the service load from the striation spacing (s) on the fracture surface [(1) – (3)] .

However it is impossible to estimate maximum (P_{max}) or minimum (P_{min}) loads at the

time of accident from the relationship between da/dN, s, and ΔK . This is because even when ΔK is constant, the da/dN – ΔK relationship changes completely if P_{max} and P_{min} differ (that is, if the stress ratio $R = P_{min}/P_{max}$ varies). Thus, most important thing is whether the stress ratio R can be determined from the configuration and dimensions of the striations. Until now, it has been difficult to estimate R during service load from the fracture surface; the author, however, using 2017-T4 aluminum alloy and type 304 stainless steel, have found that the difference in R is evident mainly in differences in striation configuration, particularly the differences in the ratio between height (H) and width (s) .

As a result, it becomes clear that there is almost a one-to-one correspondence between H/s (the striation height-width ratio) and stress ratio R, and that the relationship between H/s and R for 2017-T4 aluminum alloy is the same as that of type 304 stainless steel . Even when stress ratio R remains constant, the H/s values for many of the striations on the fracture surface are actually scattered over a wide range, necessitating statistical analysis of the measured H/s data in order to accurately estimate R.

For this reason it is important to measure the H/s value for as many striations as possible, then investigate the trends of scattering. H/s is usually measured by obliquely slicing a mountain of striation, but it is possible to obtain a valid H/s only if the cutting planes are exceedingly sharp.

Therefore, the author have improved the method used in previous studies and developed a method that greatly increases the amount of valid measured data, thereby improving the reliability of service load estimates. This method, which will be discussed below, can be applied to the analysis of actual accidents.

Materials, Configuration of Specimen

The material used here was an 2017-T4 Al alloy. Table 1 shows its mechanical properties and Table 2 shows its chemical composition. Fig. 1 shows the configuration of a

Table 1. Mechanical properties of Al alloy.

$\sigma_{0.2}$	σ_B	Ψ(%)
270	435	23.8

Table 2. Chemical composition of Al alloy.

Al	Cu	Mg	Mn	Si
94.9	3.7	0.6	0.4	0.4

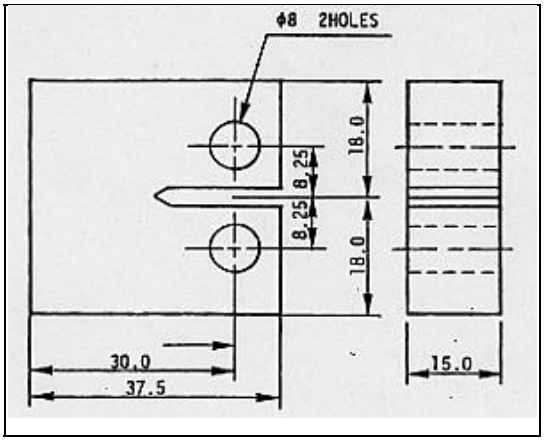

Fig. 1. Configuration of CT specimen.

CT specimen. In the fatigue-crack growth tests, a servo-hydraulic testing system was used under various combinations of R and P_{max}. The fatigue fracture surfaces formed in this manner were observed by means of a scanning electron microscope (SEM), and striation width (s) and striation configuration (H/s) were measured by a laser microscope.

Measuring Striation Configuration

The observed striations are quite difficult to measure because the width is only 0.1 - 2 μm and the height even smaller. Resolving this difficulty, therefore, becomes a key point.

As a highly accurate method for measuring the shape of a cross section of a striation, the author previously proposed a method for polishing after embedding specimens in plastic. This method, however, had the disadvantage that it dulls the edge of the polishing plane. The author then proposed a method of using a microtome to cut specimens embedded in plastic .

This method magnifies the striation, particularly the height, by cutting the striation at an angle. Thereby, this method enable us to measure the height of striation accurately. The quality of the cutting method affects the accuracy of the measurement. The drawback to this method is that relatively few valid measured values can be obtained, since the fracture surface of the specimen embedded in plastic might be damaged during the cutting process. Therefore, the author decided to test the method proposed here, wherein the problem is resolved by using a laser microscope method in which the specimen is not embedded in plastic ,but is measured directly by the laser microscope and 3-D equipment with SEM. This improved method is explained below.

When specimens are analyzed with the laser microscope, at first fracture surfaces of specimens are observed with a optical microscope and then a plateau on a fracture surface, which was horizontal to the optical axis, is selected as a measurement plane. Because if the measurement face inclined to optical axis , reflective efficiency of laser decreased and therefore the reliability of measurement data decreased.

Then 50 square μm of a horizontal fault plane on fracture surface was used as a measurement plane. These plane images were formed every 50 nm in perpendicular direction and a three dimensional image was formed by piling up twenty images as shown in Fig. 2. At last a perpendicular fault image was formed from this three dimensional image. Striation spacing (s) and height (H) was measured with a definition shown in Fig. 3.

The measurement condition by 3-D equipment with SEM are indicated below. Acceleration voltage is 20 kV, sample current is 1 nA and the magnification on scanning area is 3000 – 10000. As shown Fig. 4, 6 pieces of back scattered electron detectors are used in this measurement and each detector is fixed and height is calculated from data obtained by 6 pieces of back scattered electron detectors .

Experimental results and observations

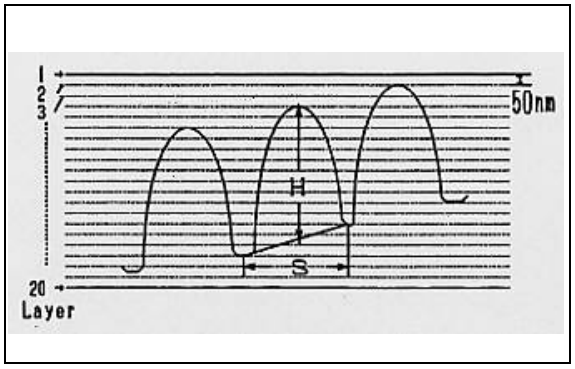

Fig. 2. Measuring method using a laser Microscope.

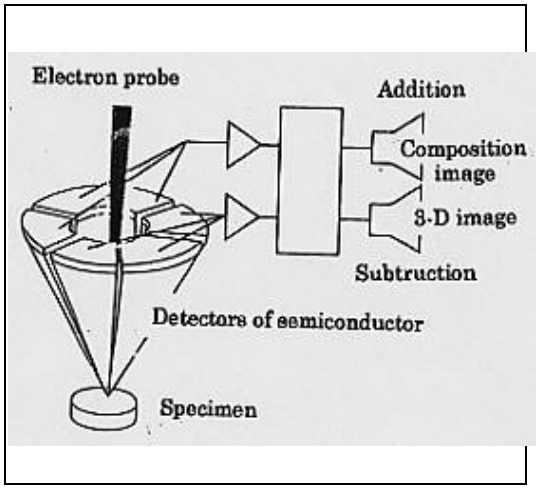

Fig. 4. The 3D analysis equipment attached With SEM.

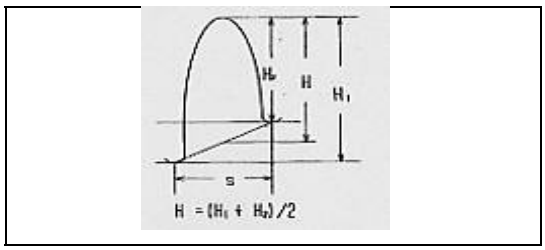

Fig. 3 Definition of Striation width and height .

(1) The relationship between crack growth rate (da/dn and s) and ΔK under various values of stress ratio R

The relationship between da/dN measured by the replica method and ΔK is shown in Fig. 5 and also that between striation spacing s measured by SEM and ΔK in Fig. 6. These figures indicate that crack growth rate is influenced not only by ΔK but also by R and that there is no one-to-one correspondence between the crack growth rate and ΔK. Therefore,

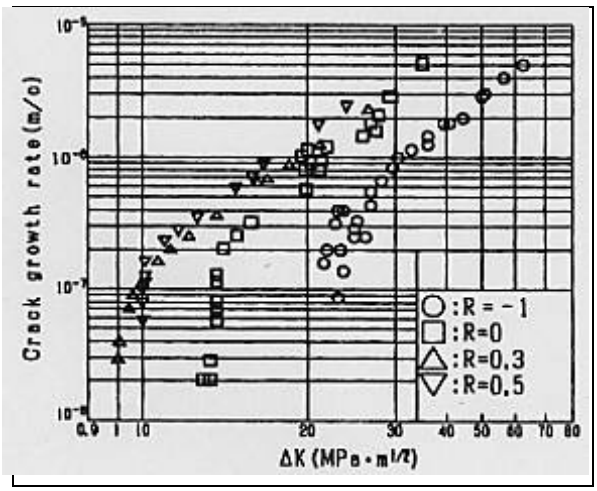

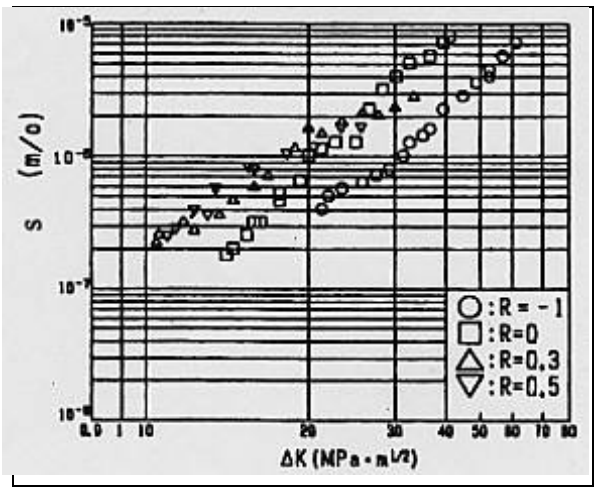

Fig. 5. Relationship between ΔK and da/dN.

Fig. 6. Relationship between ΔK and s.

in order to determine service loading from fractured structures, not only crack growth rate (da/dN or s) but also stress ratio R must be determined from the fracture surface.

(2) Influence of R on H/s

As a image of the laser microscope is shown Fig. 7, in the present study after assembling data from nearly 100 data in order to understand the overall tendencies, the distribution trends for those values were studied. As noted above, the results revealed a considerable range of distribution .

Furthermore, the average values of 100 data were compared. As it is equally true in the case of measuring with the laser microscope and 3-D equipment, the same method was adopted.

Fig. 8 shows the plotted data. Fig. 8 clearly shows that the values of H/s on each stress ratio R obtained by microtome method are nearly as same as those obtained by the methods using the laser microscope and 3-D equipment. Therefore, it was found that stress ratio R could be measured from fracture surface by the methods of measuring striation figure with laser microscope and 3-D equipment. By both methods, striation can be easily searched because striation can be observed by optical microscope and SEM respectively.

Thus, as the height of striation is measured directly by using laser microscope and 3-D equipment with SEM, striation figure became able to be measured with ease and simplicity.

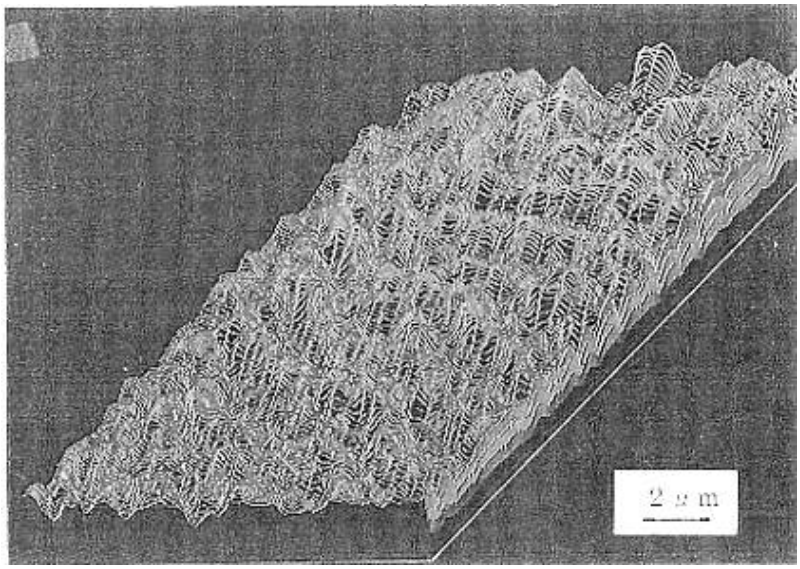

Fig. 7. A image of the laser microscope.

Conclusion

In this investigation the figure of striation were measured with laser microscope and

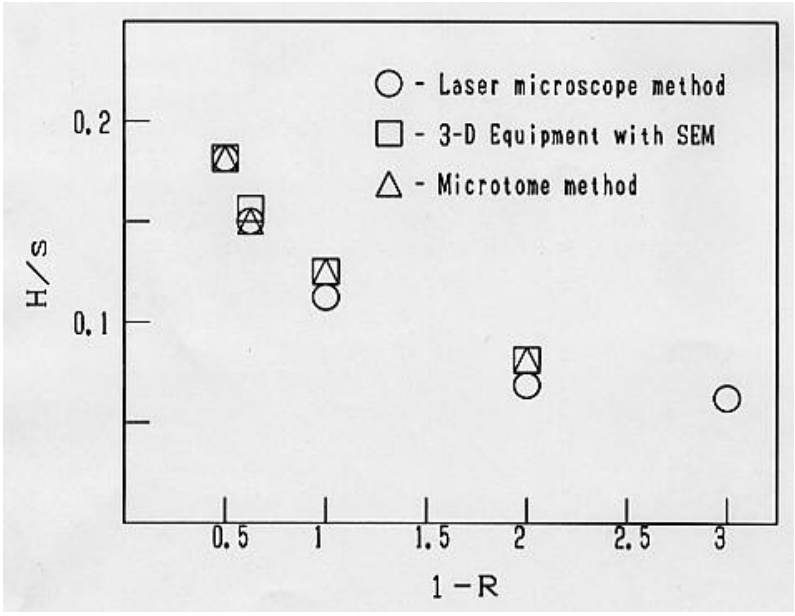

Fig. 8. The relationship between H/s and R.

3-D equipment with SEM. Striation can be easily searched with a microscope and SEM. Therefore, the figure can be easily measured with laser microscope and 3-D equipment. In this report the new methods, which are that the figure of striation are directly measured with laser microscope and 3-D equipment, were developed. Therefore, this new methods led us to measure the figure of striations more accurately and easily.

The results obtained through the present investigation are as follows.

(1) The methods that the figure of striations are directly measured with laser microscope and 3-D equipment without making section with a microtome are developed. By both methods, the figure of striations at every point can be easily measured.

(2) Determining the stress ratio R from the average values of 100 data can be recommended as a practical and valid method. The correlation between H/s and R measured with laser microscope and 3-D equipment are the same as that with measured by sectioning.

Therefore, it was found that the stress ratio R can be estimated with accurate and ease by the method with laser microscope and 3-D equipment.

REFERENCES

(1) Trans. Jap. Soc. Mater. Engng. Sci. Fract. Meeting., J. Jap. Soc. Mech. Engng. 76, 1973, pp.1203-1208 (in Japanese).

(2) R. Koterazawa, Lecture Fractography (5), J. Soi. Mater. Sci. 23, 1974, pp.803-813 (in Japanese).

(3) K. Furukawa, Y. Murakami, A Method for Predicting Service Load from the Width and Height of Striation. J. Soc. Mater. Sci. Vol.45, 1996, 340-345(in Japanese).

ICF100217OR

MICROELECTROMECHANICAL STRUCTURES FOR MULTIAXIAL FATIGUE TESTING

K. Komvopoulos

Department of Mechanical Engineering, University of California, Berkeley, CA 94720, USA

ABSTRACT

Recent advances in micromachine devices have increased the need for information about the dynamic material behavior at scales relevant to microelectromechanical systems (MEMS). However, the present understanding of fatigue at MEMS scales is relatively sparse. The review of the literature indicates that there is a significant scatter in the fatigue strength of silicon, the basic structural material of MEMS. In addition, most of the previous work has been performed with very simple devices that do not simulate fatigue under multiaxial loading conditions, similar to those occurring during micromachine operation. The aim of this publication, therefore, is to introduce novel microstructures, fabricated by standard surface micromachining, that enable fatigue testing under conditions typical of most MEMS devices. Cyclic loading is generated by interdigitized comb drives, arranged along radial "spokes" extending from a suspended ring held in place by thin flexures (fatigue specimens) attached to an anchor at the center of the device. The test structures are excited at resonance using on-chip actuation to generate the forces required to produce fatigue damage. The fabrication process for obtaining such microstructures and preliminary results from fatigue experiments performed at atmospheric conditions are presented and discussed in the context of damage accumulation in polycrystalline silicon microstructures subjected to cyclic loading.

KEYWORDS

Microelectromechanical Systems (MEMS), Multi-axial loading, Fatigue, Damage

INTRODUCTION

Monitoring the movement, position, actuation, and signaling of microelectromechanical systems (MEMS) has been increasingly used to sense chemical, electrical, mechanical, and thermal processes. Developments in this emerging field have been based on a technological basis derived from the integrated circuitry industry and have led to the design, fabrication, and implementation of microsystems spanning a wide range of industrial and medical applications [1,2]. With an estimated compound annual growth rate of 50%, predictions suggest that MEMS device revenues will exceed approximately US$10 billion in the near future. Due to increasing demands for versatile microsystems, dramatic changes have been encountered in fabrication techniques, materials, and device dimensions, with ultimate goal to enhance micromachine sensitivity and endurance. Despite early indications suggesting that significant

opportunities exist for MEMS, a large number of challenging issues presently inhibit rapid evolution of micromachines from the laboratory to the application world. For such small devices, a number of physical effects have a different significance at the micrometer scale than at macroscopic scales. Consequently, the identification of the effects of process parameters on the microstructure and material behavior at the microscale and the development of testing methods yielding information about micromachine performance over a wide range of application conditions are of scientific and industrial significance.

The mechanical behavior of polycrystalline silicon (polysilicon) has attracted significant attention since it is considered to be the building block of integrated circuitry technology. However, most of the research has been concentrated on the static fracture strength of polysilicon. Greek and Johansson [3] performed a Weibull analysis and found polysilicon fracture strength between 1.0 and 1.25 GPa for tension loading. Sharpe et al. [4] used laser interferometry to measure the strain in microfabricated tensile specimens and determined a tensile strength of about 1.2 GPa. Koskinen et al. [5] performed tensile tests on polysilicon samples of varying grain size and measured fracture strength in the range of 2.86-3.37 GPa. Kapels et al. [6] tested 4 μm thick polysilicon structures and reported fracture strength values of approximately 3.4 and 2.9 GPa for bending and tension loading, respectively. Kahn et al. [7] used a probe tip to separate the end tips of a deeply notched cantilever specimen, and based on the stress at the crack tip (determined from the probe tip position at the instant of fracture) they found the fracture toughness to be equal to 2.3 $MPa \cdot m^{1/2}$, independent of specimen thickness and doping. Tsuchiya et al. [8] reported that the fracture strength of polysilicon crystallized from amorphous silicon is in the range of 2.0-2.7 GPa and decreases with increasing specimen length, whereas the effect of the specimen width is insignificant. It was observed that fracture initiated mostly from defects produced from sacrificial HF wet etching on the side surface and edge of the specimen and argued about the fracture dependence on surface defect density and the independence of fracture on the volumetric defect density. However, a comparison of the data given in some of the previous studies shows that the two lowest tensile strength values correspond to the specimens with the largest widths. Fracture of flexure elements due to the combined effects of tensile and bending cyclic stresses may exhibit a dependence on specimen width, and thus the conclusion drawn by Tsuchiya et al. [8] might not be applicable to different types of loading. Furthermore, even though in-plane tensile loading may be appropriate for devices having a thin membrane in tension (e.g., pressure sensors and strain gages), load bearing elements in most MEMS devices (e.g., accelerometers and actuators) are flexure systems usually subjected to in-plane bending, similar to the conditions in the tests performed by Jones at al. [9], Connally and Brown [10], and Van Arsdell and Brown [11].

From the above discussion, it is evident that new testing devices and methods are needed to reliably evaluate the micromechanical properties and dynamic performance of thin-film microstructures. The objective of this research, therefore, was the establishment of a standard methodology for mechanical property testing at the microscale using thin-film microstructures fabricated by surface micromachining. Preliminary results are presented to demonstrate the initial development of fatigue damage in polysilicon microstructures subjected to cyclic loading under ambient conditions.

EXPERIMENTAL

Significant errors in force measurements are often encountered with probe tips or load cells used to apply forces on microfabricated test specimens used for mechanical property characterization. This is mainly due to the difficulty to accurately determine the microscopic displacement of a macroscopic device. Hence, it is more advantageous to use on-chip electrostatic actuation generated from inderdigitized comb drives [10,11. This method of actuation was adopted in the design of the fatigue devices of this work.

Basic Characteristics of Fatigue Microstructures

The mask design and process flow were designed to allow some control over the dimensions of the test specimens. The height of the beams was controlled by the amount of a single polysilicon deposition and the width of the beams was defined by the anisotropic etch of the polysilicon with an oxide mask. A schematic of a microstructure for fatigue testing is shown in Fig. 1. The main design features of this design are summarized below.

(a) On-chip actuation by comb drives is used to generate an electrostatic force to fatigue the test specimen. This approach is superior to the charged parallel-plate method because the force produced is independent of position.

(b) Cyclic loading is generated by interdigitized comb drives arranged along radial "spokes" extending from a suspended ring held in place by thin flexure beams (fatigue specimens) that are attached to an anchor at the center of the device. Two fatigue specimens can be seen in Fig. 1.

(c) Movement is obtained by applying a potential difference between the suspended and stationary comb teeth using an electrical connection made to the specimen. Both test specimens were charged such that current flows no matter which one fractures. In addition to the bending stress, axial and transverse forces are exerted to the fatigue specimens by the rotating ring, leading to multi-axial loading conditions. This is a unique feature of the present design compared to previous similar devices [10,11].

(d) A vernier is used to estimate the rotation of the ring during actuation. A matching set of stationary indicator marks was placed near the end to allow measurement of angular displacements as small as 0.2^{o}, in order to correlate the movement and, in turn, the stress (or strain) amplitude due to the applied voltage, and to determine whether the compliance of the test specimens changed during testing. Since measurable displacements can only be obtained under dynamic conditions, determination of the maximum deflection based on the blurred edge of the resonating microstructure is approximate.

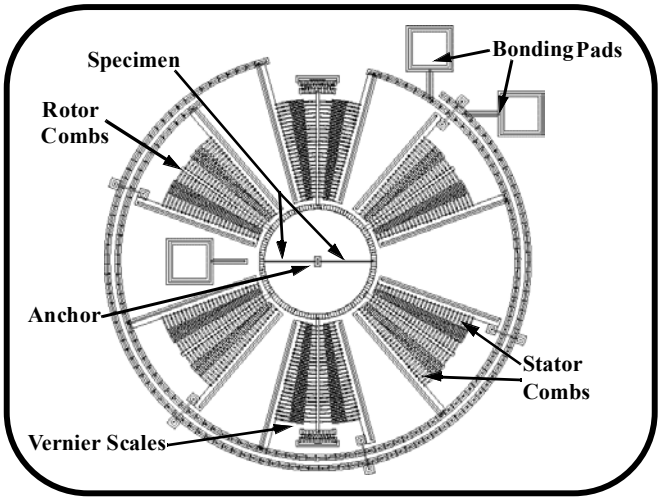

Figure 1: Schematic of fatigue test microstructure with two flexure beams (fatigue specimens).

Fatigue Microstructures

The fatigue specimens were excited at resonance by a sinusoidal electrostatic force generated by the rotary actuators. The evolution of fatigue damage was studied by observing the time it takes for the stiffness to decrease or equivalently the resonant frequency to change. The spring constant was determined based on Rayleigh's method. This involved equating the potential energy of the flexures at their extreme positions to the sum of the kinetic energy of the flexures and the rotational kinetic energy of the actuator. Thus, the natural frequency of the system was monitored, and any deterioration (aside from drift effects) was attributed to fatigue damage accumulation in the flexure beams. The strain amplitude was determined from the specimen rotation (between 0.5^{o} and 3.5^{o}). To maintain the fatigue test structure at resonance, the natural frequency and amplitude must be controlled and tracked continuously over the range of anticipated frequency shifts. A phase detector can be used to measure the difference in phase between the driving

voltage applied to the forcing electrode and the output voltage of the sensor. Implementation of such control system requires circuitry that can sense motion based on the change of the system's capacitance, determine if the device is at resonance, and accordingly correct the driving frequency [12].

Fabrication Process

The fabrication process comprised doping a 100 μm thick p-type silicon wafer of 1-2 Ω·cm resistivity with phosphorus in a standard diffusion furnace using $POCl_3$ as the dopant source in order to prevent the occurrence of feed through charges to the substrate from the electrostatic devices on the surface. A 0.3 μm thick thermal oxide layer (1050°C) and a 0.6 μm low-stress LPCVD silicon nitride layer (835°C) were then deposited to produce an electrical isolation layer. This was followed by the deposition of a 0.5 μm LPCVD polysilicon film, which was patterned to obtain the anchor at the center of the structure. Subsequently, a 2 μm thick PSG sacrificial layer was deposited by LPCVD and annealed at 1050°C for 1 h in N_2. This sacrificial layer was patterned lithographically, and the anchors were transferred into the sacrificial PSG layer by plasma etching. The structural layer was deposited to a thickness of 2 μm. Then, the structural layer was coated with a thin (0.2 μm) PSG layer, and the wafer was annealed at 1050°C for 1 h. The anneal dopes the polysilicon with phosphorus from the PSG layers above and below it and also reduces the residual stress. The polysilicon and PSG masking layer were patterned using a mask designed to form the structural layer. The PSG layer was etched to produce a hard mask for subsequent polysilicon etch. After etching the polysilicon, the photoresist was stripped off and the remaining oxide hard mask was removed by plasma etching. Finally, diced wafers were immersed in a bath of 49% HF at room temperature for ~1.5 min, rinsed with DI water and methyl alcohol for several minutes, and successfully released by CO_2 supercritical drying performed at ~40 ^{o}C under pressure of ~1350 psi for 10 min. Figure 2 shows a scanning electron micrograph of a microdevice with two flexure (fatigue) specimens fixed to an anchor at the center of the device and an inner ring that can be rotated by the attached comb drives.

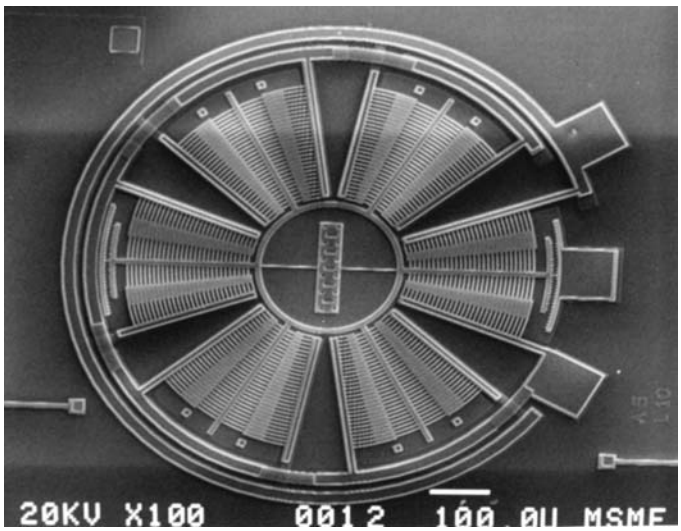

Figure 2: Scanning electron micrograph of a released microstructure with two flexure (fatigue) beams.

RESULTS AND DISCUSSION

From a dynamic analysis, the resonance frequency of the in-plane rotation of the specimens was predicted to be in the range of 8-60 kHz, depending of the number, length, and width of flexure beams. Figure 3 shows vibration results obtained from an experiment performed at atmospheric conditions with a microstructure having two flexure beams of 2 μm thickness, 4 μm width, and 100 μm length excited at different frequencies by an in-plane driving force. The motion of the oscillating device was captured by a

strobe-like system. The displacement was determined by a motion detection technique of image processing. The frequency response of the device was obtained by frequency sweeping. Sixteen frequency points specified in a certain range around the natural frequency were swept one by one and the amplitude and phase of the oscillation at each frequency was measured. To determine the resonant frequency more accurately, a second measurement was performed and the frequency points were specified in such a way that the points were denser close to the resonant frequency and sparser away from the resonant frequency. The results for the amplitude of the displacement and the phase shift, shown in Figs. 3(a) and 3(b), respectively, indicate that the resonance frequency of the in-plane rotation is equal to 14.2 kHz. Considering the unknown damping characteristics of the system, the measured resonance frequency is in close agreement with the value of 15.5 kHz predicted from the dynamic analysis. This suggests that the analytical model (not described here for brevity) captures the dynamic behavior of the actual fatigue microstructures fairly accurately. It should be pointed out that finite element simulation results confirmed that the in-plane rotation of the microstructures with two and three flexure beams were significantly

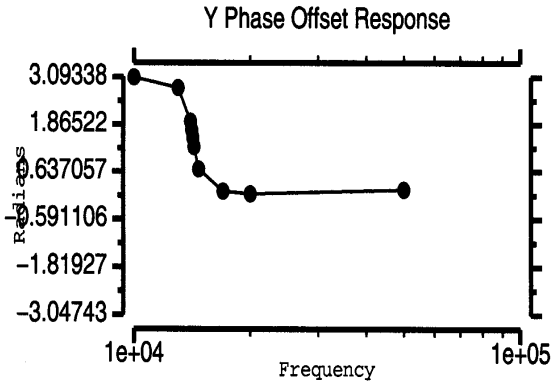

different from those of other fundamental modes. In addition, the electrostatic force used to actuate the specimens is in the plane of motion and the damping for vertical motion of the microdevice is much higher than that for in-plane motion. Thus, actuating the specimens at the desired frequency is fairly straightforward.

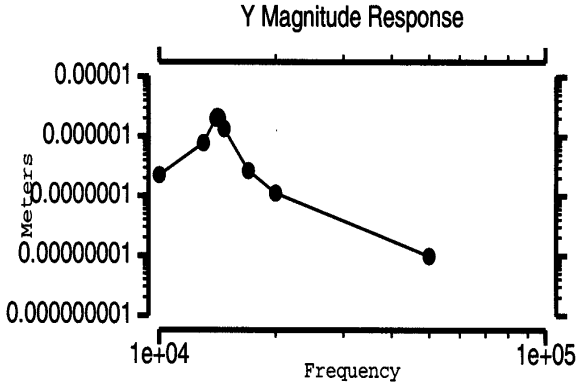

(a) (b)

Figure 3: Frequency response of a fatigue microstructure with two flexure beams of 100 μm length, 2 μm thickness, and 4 μm width: (a) amplitude of in-plane displacement versus frequency and (b) phase shift from the driving force versus frequency.

Figure 4 shows results from short-term fatigue tests performed with different devices having two or three flexure beams of 2 μm thickness, width equal to 2 or 4 μm, and length in the range of 50-90 μm. The microstructures were placed in a multi-probe station and were actuated at resonance by a sinusoidal force

generated by applying a 10 V DC voltage and a 30 V bias voltage at a driving frequency corresponding to the fundamental resonance frequency of the in-plane rotation of the microstructures. In each experiment, the stress amplitude was varied in the range of 0.1-1.0 GPa, but the loading was almost fully reversed, i.e., stress ratio close to –1. However, the stress amplitude was variable since it depends on the device dimensions. All the resonance frequencies of the different specimens are shown to decrease with time, suggesting a reduction in stiffness. Since all the tests were performed in a clean-air laboratory environment under atmospheric conditions and the frequency change is fairly significant, the change in the dynamic response of the devices is attributed to the onset of fatigue damage. Due to the very small dimensions of MEMS, crack initiation mechanisms control the fatigue life. While the mechanism(s) associated with the changes of the dynamic response of the tested microstructures require further investigation, it may be speculated that the observed stiffness degradation is a manifestation of microscopic processes involving intra-/trans-granular microfracture, which cannot be observed macroscopically. It has been reported that subcritical crack growth in polysilicon follows a transgranular path and is due to the synergistic effects of water and stress [11]. The preliminary results shown in Fig. 4 demonstrate the high sensitivity of the present fatigue microstructures to capture extremely small damage levels encountered with the onset of cyclic loading, not possible with conventional testing techniques employing macroscopic bending specimens.

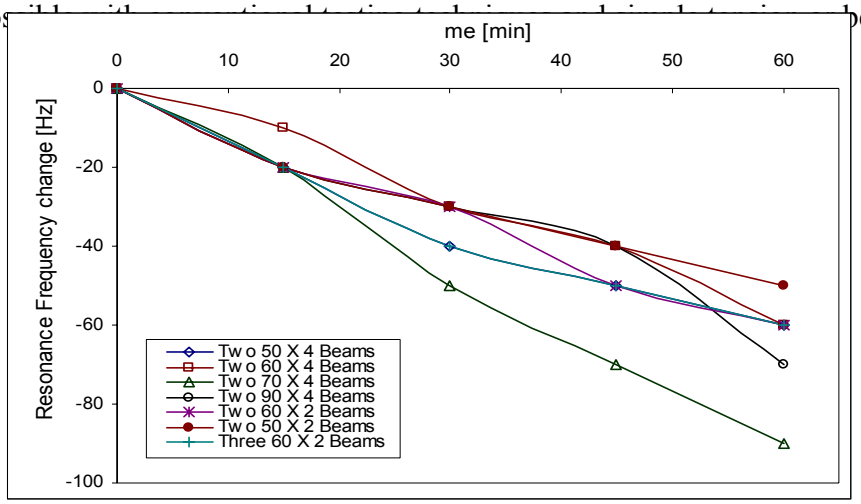

Figure 4. Change of resonant frequency of fatigue microstructures revealing fatigue damage evolution.

CONCLUSIONS

The microfabrication and basic characteristics of MEMS structures for multi-axial fatigue testing were presented along with preliminary results revealing the evolution of fatigue damage. The results demonstrate the feasibility of the adopted testing scheme and the high sensitivity of the microdevices to track small-scale fatigue damage.

ACKNOWLEDGMENTS

This research was supported by the National Science Foundation under Grant No. DMI-9872324 and the Defense Advanced Research Projects Agency/Microelectromechanical Systems (DARPA/MEMS) under Grant No. DABT63-98-1-0011. The author is grateful to P. Stupar and C. Belu for discussions on the design of the specimens and A. Choy and X. Sun for assistance in microfabrication and testing.

REFERENCES

1. Wise, K. D. (1991) *Proc. IEEE Micro Electro Mechanical Systems*, pp. 33-38.

2. Fujita, H. (1997) *Proc. IEEE Micro Electro Mechanical Systems*, pp. 1-8.
3. Greek, S. and Johansson, S. (1997) *Proc. SPIE*, Vol. 3224, pp. 344-351.
4. Sharpe, W. N., Yuan, B., Vaidyanathan, R. and Edwards, B. L. (1997) *Proc. IEEE Micro Electro Mechanical Systems*, pp. 424-429.
5. Koskinen, J., Steinwall, J. E., Soave, R. and Johnson, H. H. (1993) *J. Micromechanics and Microengineering*, Vol. 3, pp. 13-17.
6. Kapels, H., Aigner, R. and Binder, J. (2000) *IEEE Trans. Electron Devices*, Vol. 47, pp. 1522-1528.
7. Kahn, H., Stemmer, S., Nandahumar, K., Heuer, A. H., Mullen, R. L., Ballarini, R. and Huff, M. A. (1996), *Proc. IEEE Micro Electro Mechanical Systems*, pp. 343-348.
8. Tsuchiya, T., Tabata, O., Sakata, J. and Taga, Y. (1997) *Proc. IEEE Micro Electro Mechanical Systems*, pp. 529-534.
9. Jones, P. T., Johnson, G. C. and Howe, R. T. (1996) *Micro Electo Mechanical Systems*, ASME, DSC-Vol. 59, pp. 325-330.
10. Connally, J. A. and Brown, S. B. (1993) *Exper. Mech*. 33, pp. 81-90.
11. Van Arsdell, W. W. and Brown, S. B. (1999) *J. Microelectromechanical Systems*, Vol. 8, pp. 319-327
12. Sun, X., Horowitz, R. and Komvopoulos, K. (2001) *Proc. MEMS Symposium, Int. Mech. Eng. Congress and Exposition*, in press.

ORAL/POSTER REFERENCE: ICF108920R

MICROMECHANICAL MODELING OF HYDROGEN-INDUCED FRACTURE MODES IN IN903

B.P. Somerday and N. R. Moody

Sandia National Laboratories, Livermore, CA 94550, USA

ABSTRACT

Previous slow crack growth results for the austenitic Fe-Ni-Co superalloy IN903 in hydrogen gas demonstrated that the near-threshold fracture mode was a function of grain size. For grain sizes of 23 μm and 49 μm, hydrogen-induced fracture was intergranular. At larger grain sizes of 114 μm, 172 μm, and 200 μm the hydrogen-induced fracture mode changed to slip-band cracking. This transition in fracture mode from intergranular cracking to slip-band failure with increasing grain size results from competing hydrogen-induced fracture mechanisms. A stress-based micromechanical fracture model predicts that the resistance to intergranular cracking increases with increasing grain size. In addition, a strain-based model predicts that the grain size-independent slip-band fracture resistance is of the same order as the intergranular cracking resistance. The predicted fracture-resistance trends intersect at a grain size of about 100 μm, which supports the observed fracture-mode transition between grain sizes of 49 μm and 114 μm.

KEYWORDS

Hydrogen, fracture, superalloys, micromechanical modeling

INTRODUCTION

Results for the austenitic Fe-Ni-Co superalloy IN903 demonstrated that the mode of hydrogen-induced slow crack growth was sensitive to changes in both microstructure and magnitude of the applied stress-intensity factor (K). Constant-displacement experiments on wedge-opening load specimens in 207 MPa hydrogen gas at 25^{o}C showed that stage II cracking at high K levels was intergranular and independent of grain size from 23 μm to 200 μm (Figures 1(a) and 1(c)) [1, 2]. As K approached threshold (stage I) in specimens having grain sizes of 114 μm, 172 μm, and 200 μm, hydrogen-induced fracture transitioned to a mixed mode with slip-band failure predominating over intergranular cracking (Figure 1(d)). In contrast, stage I cracking in specimens having grain sizes of 23 μm and 49 μm remained intergranular (Figure 1(b)).

The transition in near-threshold fracture mode from intergranular to slip-band cracking as grain size increased (Figure 1(b) compared to Figure 1(d)) can be viewed in terms of either competing hydrogen transport paths or competing hydrogen-induced fracture mechanisms. Considering the former scenario, hydrogen is likely transported from the crack-tip surface to process-zone fracture sites through both transgranular and intergranular mechanisms. Hydrogen accumulates at transgranular sites *via* numerous lattice transport paths intersecting the crack-tip surface. While the number of transport paths is more limited along grain boundaries compared to the lattice, hydrogen may diffuse more rapidly along grain-

boundary paths [3, 4]. Assuming that hydrogen must diffuse over a distance that scales with grain size to enable grain-boundary fracture, relatively short diffusion distances in small-grain-size IN903 coupled with rapid hydrogen transport along grain boundaries may have promoted near-threshold intergranular cracking. As grain size increased, diffusion distances for grain-boundary fracture became greater and sufficient time was allowed for hydrogen accumulation at transgranular sites to promote slip-band cracking.

Hydrogen-induced fracture was intergranular in large-grain-size IN903 during stage II cracking (Figure 1(c)), which indicates that hydrogen readily diffused along grain boundaries in these microstructures. These stage II results suggest that hydrogen should be similarly supplied to grain boundaries in stage I to allow intergranular cracking in large-grain-size IN903, assuming that hydrogen-diffusion distances in stage I are comparable to those in stage II. This argument opposes the idea that competing hydrogen-transport mechanisms govern the grain size-dependent fracture-mode transition in stage I. Alternately, the transition from intergranular fracture to predominantly slip-band cracking as grain size increased (Figure 1(b) compared to Figure 1(d)) can be attributed to crack-tip mechanics and microstructure.

Micromechanical fracture models can provide insight into the roles of crack-tip mechanics and microstructure in governing hydrogen-induced fracture modes. Threshold K (K_{TH}) for intergranular slow crack growth in IN903 exposed to hydrogen gas was well-described using a stress-based micromechanical model, which proposes that fracture proceeds when the crack-tip normal stress exceeds the local fracture stress over a characteristic distance [1, 2]. This distance, related to microstructure, was associated with the grain size in IN903 [5]. In addition, slip-band cracking in hydrogen-charged IN903 during rising-displacement fracture toughness tests was accurately modeled using a strain-based micromechanical approach [1, 2, 6]. The premise of this model is similar to the stress-based model, *viz*, fracture proceeds when the crack-tip effective plastic strain exceeds the local fracture strain over a characteristic distance. For hydrogen-induced slip-band cracking in IN903, application of the strain-based model to rising-displacement fracture toughness data (K_{IH}) suggested that matrix carbide particles defined the characteristic distance [1, 2, 6].

The objective of this work is to apply stress- and strain-based micromechanical fracture models to understand the grain size-dependent transition from intergranular cracking to slip-band failure in IN903 during stage I slow crack growth in hydrogen gas. These models are analyzed using tensile data as well as rising-displacement fracture toughness and slow crack growth results from previous hydrogen-induced fracture studies of IN903.

RESULTS AND DISCUSSION

Micromechanical models are applied to near-threshold slow crack growth in IN903 to assess whether fracture-mode transitions are due to a competition between stress-based intergranular fracture and strain-based slip-band cracking. The stress-based model requires a solution for crack-tip normal stress, data for the local grain-boundary fracture stress, the characteristic microstructural fracture distance, and material deformation properties. Formulation of this model is based on elastic-plastic crack-tip stress solutions from Tracey [7] and Schwalbe [8] as described elsewhere [1, 2]. Local grain-boundary fracture stresses were estimated from hydrogen-induced tensile fracture data, which yielded values that were pertinent to the crack-tip hydrogen concentration during slow crack growth [1, 2]. These values are given in Table 1 and show that fracture stress depends on grain size. The characteristic fracture distance is assumed to equal the grain size. Deformation properties include a yield stress of 1100 MPa and strain-hardening exponent of 0.15 [1].

Model predictions of K_{TH}, assuming stress-controlled intergranular slow crack growth at all grain sizes, are shown in Figure 2. This model demonstrates that K_{TH} for stress-controlled intergranular fracture increases as grain size increases. (The trend line in Figure 2 does not include calculated K_{TH} at a grain size of 23 μm. This value equaled 37 MPa√m and was judged to be erratically high.)

TABLE 1
LOCAL FRACTURE STRESS FOR IN903 AS A FUNCTION OF GRAIN SIZE

Grain Size (μm)	Fracture Stress (MPa)
23	3007
49	2170
114	1543
172	1321
200	1251

A simple expression was derived for strain-controlled K_{TH} from crack-tip effective plastic strain, local fracture strain (ε_f^*), characteristic microstructural fracture distance (l^*), and material deformation properties (flow stress, σ_o, and elastic modulus, E), i.e., $K_{TH}=6[\sigma_o E \varepsilon_f^* l^*]^{1/2}$ [1, 2, 6, 9-11]. This model accurately described slip-band fracture in hydrogen-charged fracture toughness specimens of IN903.

To apply the strain-based model to the case of slip-band fracture during slow crack growth, estimates of ε_f^* are needed as a function of grain size and for the crack-tip hydrogen concentration that develops from exposure to 207 MPa hydrogen gas. Crack-tip fracture strains are assumed to be independent of grain size since rising-displacement fracture toughness, K_{IH}, and fracture modes for hydrogen-charged specimens were constant as a function of grain size [1, 2, 6]. Local fracture strain as a function of hydrogen concentration up to 5000 appm was estimated using void dimensions measured from hydrogen-charged fracture toughness specimens coupled with a void-growth model [2, 6]. These values are listed in Table 2. The fracture strain for slow crack growth in 207 MPa hydrogen gas is determined from extrapolating the results in Table 2 to the estimated crack-tip hydrogen concentration of 11,200 appm ($\varepsilon_f^*=0.006$) [2]. The values of σ_o (1198 MPa) and E (147.5 GPa) used to model K_{IH} [2, 11] are used in this study. In addition, the characteristic distance, l^*, is assumed to equal the average carbide spacing (35 μm), since this feature governed hydrogen-induced slip-band fracture for both hydrogen-charged fracture toughness tests and slow crack growth tests at low gas pressures [2, 11].

Model predictions of K_{TH}, assuming strain-controlled slip-band fracture at all grain sizes, are shown in Figure 2. Predicted values of K_{TH} are constant since ε_f^* was assumed to be independent of grain size. This trend parallels that measured for K_{IH} [2, 6], but predicted K_{TH} values are lower because of the elevated crack-tip hydrogen concentration.

TABLE 2
LOCAL FRACTURE STRAIN FOR IN903 AS A FUNCTION OF HYDROGEN CONCENTRATION

Hydrogen Concentration (appm)	Fracture Strain, ε_f^*
0	0.045
770	0.033
1876	0.030
2900	0.021
5000	0.016
$11{,}200^{+}$	0.006^{++}

$^{+}$Estimated for crack tip exposed to 207 MPa H_2 gas
$^{++}$Extrapolated from values at 0 to 5000 appm hydrogen

Comparing predictions from the strain-controlled slip-band cracking model to those based on the stress-controlled intergranular fracture model in Figure 2 indicate that a fracture-mode transition is possible. Predicted K_{TH} values are lower for the stress-based model at grain sizes up to about 100 μm. Above a grain size of 100 μm, predicted K_{TH} values are lower for the strain-based model. These model results suggest that the resistance to stress-based intergranular cracking is lower than the resistance to strain-based slip-band fracture at small grain sizes. The trend is inverted at larger grain sizes; i.e., the resistance to slip-band fracture is lower than the resistance to intergranular cracking. The fracture-mode trend predicted from K_{TH} modeling in Figure 2 is consistent with observations of near-threshold slow crack growth, as slip-band cracking predominated over intergranular fracture at large grain sizes (Figure 1(d)). In addition, measured K_{TH} values follow the lower-bound model predictions (Figure 2), *viz*, K_{TH} increases as grain size increases from 23 μm then appears to reach a plateau value at larger grain sizes.

Analysis of near-threshold slow crack growth results using micromechanical models shows that fracture-mode transitions in IN903 exposed to hydrogen gas can be attributed to competing hydrogen-induced fracture mechanisms. The transition from intergranular cracking to slip-band fracture (Figure 1(b) compared to Figure 1(d)) resulted from the governing effect of the characteristic microstructural distance for intergranular fracture. As the characteristic microstructural distance (grain size) in the stress-based model increased, higher K levels were predicted for intergranular cracking. This increase in intergranular cracking resistance allowed slip-band fracture to proceed preferentially.

The idea that the characteristic microstructural distance for intergranular fracture governs the grain size-dependent fracture mode in stage I can be applied to understand the K-dependent fracture transition in large-grain-size IN903. Specifically, the fracture mode transitions from intergranular cracking in stage II (Figure 1(c)) to slip-band failure in stage I (Figure 1(d)). Assuming that grain size defines the salient distance for intergranular cracking, this transition can be explained because changes in K affect the volume of material at the crack tip that is enveloped by high stress and strain. At low K levels near threshold, the distance over which high stress and strain are sustained may be less than the fracture distance (grain size), which allows slip-band fracture to preempt intergranular cracking. As K increases, high stress and strain are sustained over larger distances that may be comparable to the grain size; intergranular fracture can then be activated.

The idea that fracture-mode transitions in large-grain-size IN903 are due to the interplay between K-dependent crack-tip stress and strain fields and an invariant characteristic distance for intergranular fracture is not supported by analysis of stage II crack growth kinetics. A recent review of hydrogen-induced crack growth rate data in stage II suggests that hydrogen penetration ahead of the crack tip and the associated fracture distances are well less than 1 μm [12]. Included in this analysis are stage II slow crack growth results for IN903 in high-pressure hydrogen gas. This analysis contradicts the assumption that fracture distances on the order of the grain size can account for K-dependent fracture-mode transitions in large-grain-size IN903. Reconciling the contradictory views that near-threshold fracture can be characterized by micrometer-sized, microstructure-relevant fracture distances, while stage II crack growth kinetics require sub-micrometer fracture distances, is a topic that will be addressed in future work.

CONCLUSIONS

The near-threshold fracture mode of IN903 exposed to hydrogen gas exhibits a transition from intergranular cracking to slip-band failure as grain size increases, which results from competing hydrogen-induced fracture mechanisms. A stress-based micromechanical fracture model predicts that the resistance to intergranular cracking increases with increasing grain size. In addition, a strain-based model predicts that the grain size-independent slip-band fracture resistance is of the same order as the intergranular cracking resistance. The predicted fracture-resistance trends intersect at a grain size of about 100 μm, which supports the observed fracture-mode transition between grain sizes of 49 μm and 114 μm.

ACKNOWLEDGEMENTS

The authors are grateful to R.P. Gangloff for critically reviewing the manuscript. This work was supported by the U.S. Department of Energy under contract DE-AC04-94AL85000.

REFERENCES

1. Moody, N.R., Stoltz, R.E. and Perra, M.W. (1986). In: *Corrosion Cracking*, pp. 43-53, Goel, V.S. (Ed). ASM, Metals Park, OH.
2. Moody, N.R., Robinson, S.L. and Garrison, W.M. (1990) *Res Mechanica* 30, 143.
3. Harris, T.M. and Latanision, R.M. (1990). In: *Hydrogen Effects on Material Behavior*, pp. 133-142, Moody, N.R. and Thompson, A.W. (Eds). TMS,Warrendale, PA.
4. Tsuru, T. and Latanision, R.M. (1982) *Scripta Metall.* 16, 575.
5. Moody, N.R., Perra, M.W. and Robinson, S.L. (1988) *Scripta Metall.* 22, 1261.
6. Moody, N.R., Stoltz, R.E. and Perra, M.W. (1987) *Metall. Trans. A* 18A, 1469.
7. Tracey, D.M. (1976) *J. Eng. Mat. Tech. Trans. ASME* 98, 146.
8. Schwalbe, K.-H. (1977) *J. Eng. Mat. Tech. Trans. ASME* 99, 186.
9. Ritchie, R.O. and Thompson, A.W. (1985) *Metall. Trans. A* 16A, 233.
10. Lee, S., Majno, L. and Asaro, R.J. (1985) *Metall. Trans. A*, 16A, 1633.
11. Moody, N.R., Perra, M.W. and Robinson, S.L. (1990). In: *Hydrogen Effects on Material Behavior*, pp. 625-635, Moody, N.R. and Thompson, A.W. (Eds). TMS, Warrendale, PA.
12. Gangloff, R.P. (2001) "Diffusion Control of Hydrogen Environment Embrittlement in High Strength Alloys," submitted to *International Conference on Hydrogen Effects on Material Behavior and Corrosion Deformation Interactions*.

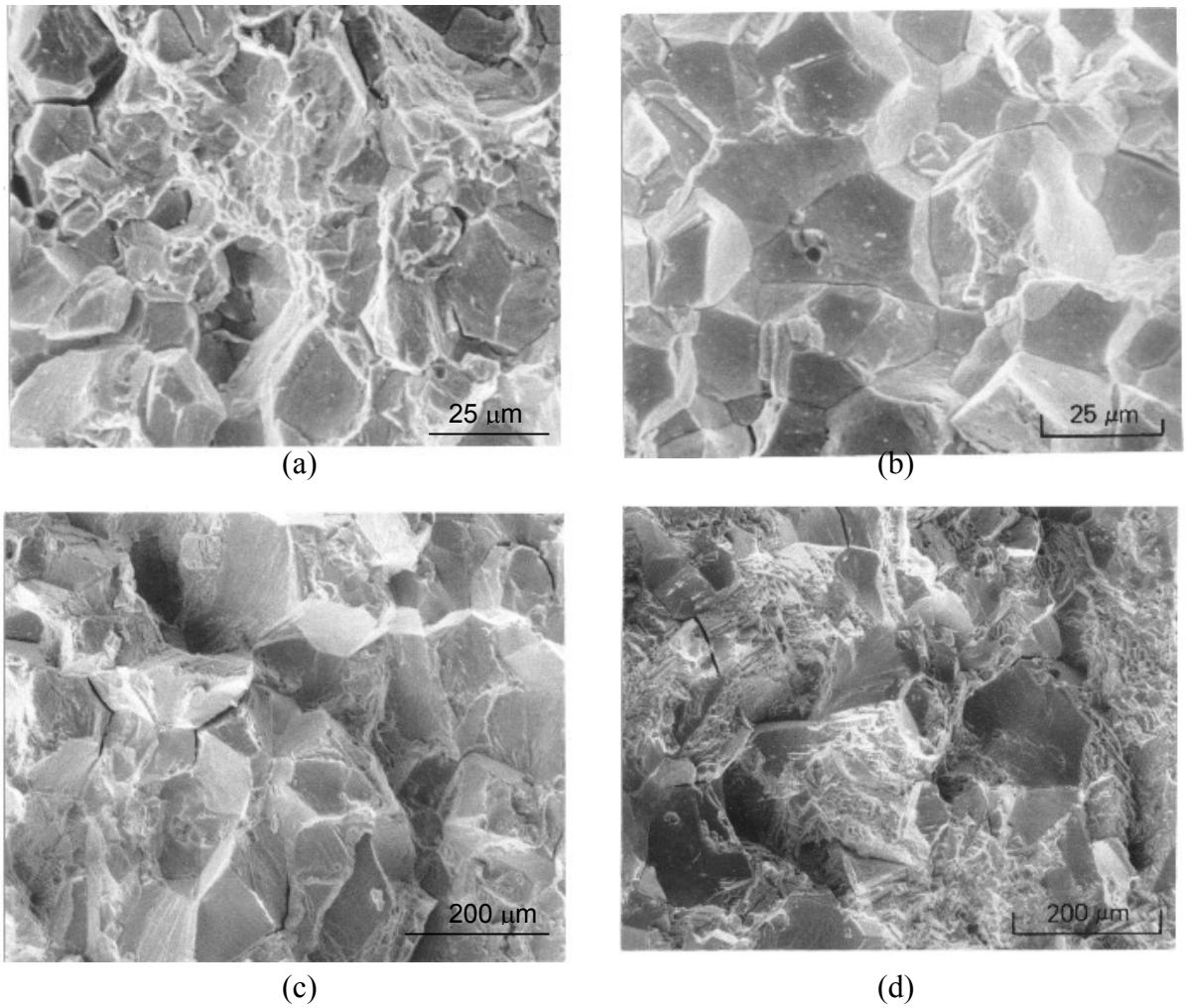

Figure 1: Fracture surfaces for IN903 in 207 MPa hydrogen gas at 25°C: (a) intergranular cracking for 23 μm grain size at K=70 MPa√m, (b) intergranular cracking for 23 μm grain size at K=30 MPa√m, (c) intergranular cracking for 172 μm grain size at K=70 MPa√m, and (d) slip-band and intergranular cracking for 172 μm grain size at K=41 MPa√m.

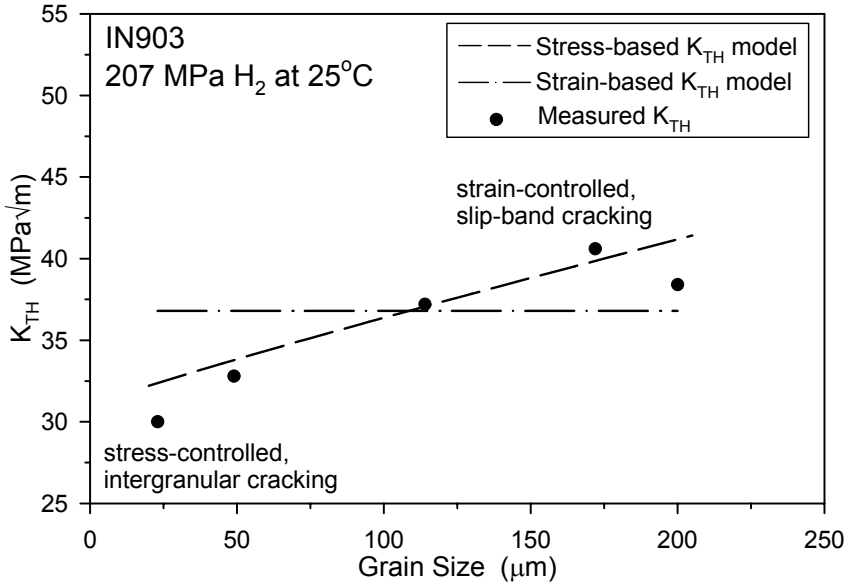

Figure 2: Comparison of K_{TH} from stress-based and strain-based micromechanical fracture models to measured values of K_{TH} for IN903 in 207 MPa hydrogen gas at 25°C.

ORAL POSTER REFERENCE : ICF100966OR

DAMAGE AND ULTIMATE FAILURE OF TEXTILE CERAMIC MATRIX COMPOSITES

J. Lamon

Laboratoire des Composites Thermostructuraux
UMR 5801 (CNRS-SNECMA-CEA-UB1)
3, Allée de la Boétie, 33600 Pessac, France

ABSTRACT

Composites are heterogeneous materials. Brittle matrix composites combine brittle constituents. As a consequence, damage and failure exhibit typical features that influence the response under load. A large amount of data on the mechanical behavior of unidirectionnally reinforced ceramic matrix composites can be found in the literature. The present paper examines the ultimate failure and damage mechanisms in 2D woven SiC/SiC composites. The failure mechanisms as well as features of ultimate failure are addressed. In particular, it is emphasized that ultimate failure and matrix damage are successive and separate phenomena and that the statistical distribution of strength data exhibit a limited scatter and a very limited dependence on the stressed volume.

KEYWORDS

Ceramic-matrix composites, fracture, interface, non-linear behavior, probabilistic methods.

INTRODUCTION

The concept of composite materials is very interesting. It covers a wide variety of materials of which one can tailor the properties with respect to end use applications, by playing with the combination of constituents. A large variety of respective properties and arrangement can be devised.
Models of the mechanical behavior are required to design either structures or materials. Those approaches aimed at predicting the stress-strain behavior from constituent properties are based on micromechanics (see for instance [1-2]). They are essentially appropriate for material design purposes. Those aimed at designing structures are based on continuum damage mechanics. The composite is considered to be a continuous medium (or an homogeneous material) at macroscopic or an intermediate mesoscopic scale (see for instance [3]).
The mechanical behavior of ceramic matrix composites displays several typical features that differentiate them from the other materials, including the other classes of composites as well

as homogeneous (monolithic) materials. With a view to developing appropriate models, it is required that the basic phenomena that determine composite mechanical behavior be well understood and properly described. A lot of papers have been devoted to unidirectionnally reinforced composites. The mechanical behavior is essentially *damage sensitive.* It consists in a non-linear response as a result of transverse cracking in the matrix. Cracks are arrested by fibers and they are deflected at fiber/matrix interfaces causing fiber debonding. Ultimate failure is dictated by fibers. Matrix cracking and fiber failure are random brittle failure phenomena, as a result of the presence of populations of fracture-inducing flaws distributed randomly [1, 2, 4, 5].

In those textile composites (i.e. those composites reinforced with fabrics of fiber bundles), damage and ultimate failure are influenced by microstructure [6, 7]. The 2D SiC/SiC composites manufactured by Chemical Vapor Infiltration provide an excellent illustration of these effects. Their microstructure is highly heterogeneous, as a result of the presence of woven infiltrated tows that behave as physical entities, large pores (referred to as macropores) located between the plies or at yarn intersections within the plies and a uniform layer of matrix over the fiber preform (referred to as the intertow matrix). Much smaller pores are also present within the tows. Extensive inspection of these composites under tensile loads using a microscope, and acoustic emission recording allowed damage and failure mechanisms to be identified [7, 8].

The paper discusses typical features of damage and ultimate failure and in a textile ceramic matrix composite (2D SiC/SiC).

DAMAGE IN 2 D WOVEN SiC/SiC COMPOSITES

Damage in 2D woven SiC/SiC consists essentially in transverse cracks in the matrix and associated interface cracks resulting from deviation of the matrix cracks by the tows and the fibers within the tows (also referred to as debonding). Three main steps can be distinguished during tensile tests under incremental loads, using a microscope mounted on the testing machine (figure 1) [7] :
Step 1: cracks initiate first in the intertow matrix at macropores where stress concentrations exist (strains between 0.025 % and 0.12 %).
Step 2: cracks appear then in the transverse tows (strains between 0.12 % and 0.2 %).
Step 3: transverse microcracks initiate in the longitudinal tows for strains larger than 0.2 %. These microcracks remain localized within the longitudinal tows. They do not propagate within the rest of the composite. The matrix in the longitudinal tows experiences a fragmentation process and the crack spacing decreases as the load increases.
For both first families of cracks deflection occurs at the periphery of longitudinal tows, whereas for the third family of cracks it occurs at the fiber/matrix interfaces within the tows [7, 9].
The significant Young's modulus decreases that are generally observed during tensile tests [7, 9] (figure 2) illustrate the dependence of damage on the heterogeneous microstructure of composite. Young's modulus refers to the tangent modulus determined from the linear portion of the reloading curve obtained on unloading-reloading cycles. The major modulus loss (70 %) is caused by both the first families of cracks (strains < 0.2 %). Microcracks within the longitudinal tows are responsible for only a 10 % loss. The 70 % modulus loss reflects big changes in load sharing: the load becomes carried essentially by matrix infiltrated longitudinal tows (tow overloading). During microcracking in the longitudinal tows, load sharing is affected further, and the load becomes carried essentially by the fibers within the

tows (fiber overloading). The elastic modulus reaches a minimum value described by the following equation :

$$E_{min} = \frac{1}{2} E_f V_f \qquad (1)$$

Eqn. (1) implies that the matrix contribution in load carrying is negligible. At this stage matrix damage and debonding are complete. Saturation of matrix cracking is generally observed for a 0.8% strain. At this stage, fibers are fully loaded. The mechanical behavior is controlled now by the fiber tows oriented in the direction of loading.

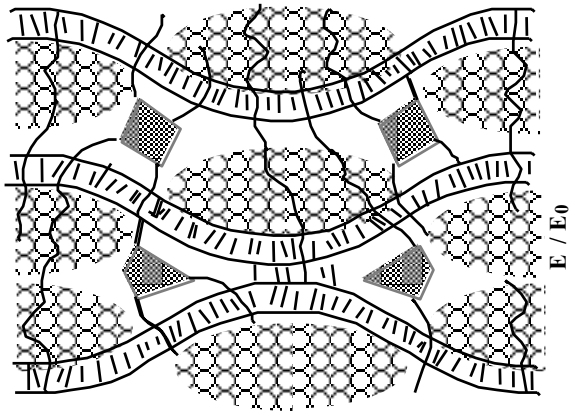

Figure 1 : Schematic diagram showing microstructure and matrix cracking in a 2D SiC/SiC composite during a tensile test (longitudinal strain = 0.8 %)

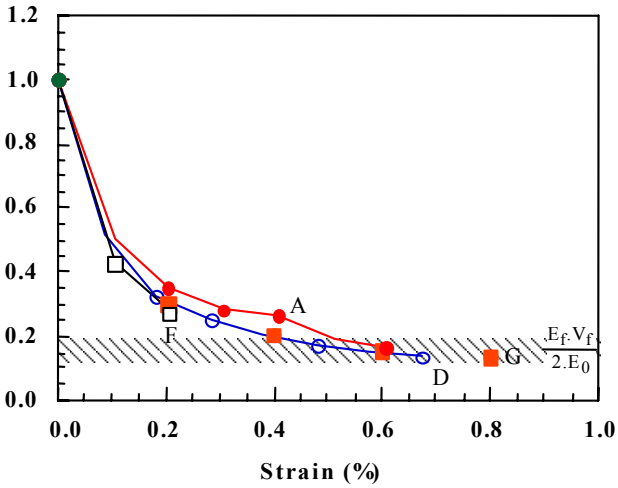

Figure 2 : Relative elastic modulus versus applied strain during tensile tests on various 2D woven SiC/SiC composites reinforced with treated fibers : (A) Nicalon/$(PyC_{20}/SiC_{50})_{10}$/SiC, (D) Nicalon/PyC_{100}/SiC, (F) Hi-Nicalon/PyC_{100}/SiC, (G) Hi-Nicalon/ $(PyC_{20}/SiC_{50})_{10}$/SiC

ULTIMATE FAILURE

Failure mechanisms

Under a tensile load, ultimate failure of a tow of parallel fibers involves two steps [10, 11]:
- a first step of stable failure,
- a second step of unstable failure.

During the first step, fibers fail individually as the load increases. The applied load is carried by the surviving fibers only. In the absence of fiber interactions, there is no load transfer from the surviving fibers to the broken fibers. The load on the surviving fibers increases when a fiber fails. The load that was carried by the broken fibers is shared by the surviving ones (global load sharing).

The unstable failure (second step) occurs when the surviving fibers cannot tolerate the load increment resulting from a fiber failure. At this stage, a critical number of fibers have been broken.

Ultimate failure of matrix infiltrated tows also involves a two-step mechanism and a global load sharing when a fiber fails [1, 12]. In the presence of multiple cracks across the matrix and the associated interfacial debonds, the load carrying capacity of the matrix is tremendously reduced or annihilated. The load is taken up equally by the remaining intact

fibers, and the fibers fail only once [1, 12]. The matrix infiltrated tows can be assimilated to bundles of fibers subject to the specific stress field induced by the presence of multiple cracks across the matrix. Ultimate failure occurs when a critical number of fibers have failed.

This mechanism also dictates ultimate failure in textile ceramic matrix composites. Ultimate failure is caused by the failure of a critical number of broken tows (≥ 1).

This mechanism is at variance with that observed in polymer matrix impregnated tows, where a local load sharing occurs when a fiber fails [4]. In these composites, the fibers fail first. Therefore, the uncracked matrix is able to transfer the load to the broken fibers.

Features of ultimate failure

In SiC/SiC composites, ultimate failure generally occurs after matrix cracking saturation. The fibers break under loads close to the maximum at ultimate failure [2, 7, 9]. Matrix damage and ultimate failure thus appear to be successive and separate phenomena. They may be regarded as independent phenomena when one considers that the load is carried by the fibers and there is no contribution of the matrix during fiber failures. They may be also regarded as dependent when one considers that the stress-state that operates on the fibers at ultimate failure results from matrix cracking. Both viewpoints can be accounted for in micromechanics- based models.

Ultimate failure is highly influenced by stochastic features. Since fibers are brittle, they are highly sensitive to the presence of flaws (stress concentrators), that are distributed randomly. As a consequence, the strength data exhibit a significant scatter, as illustrated by figure 3 [13]. Figure 3 shows the relationship between various sets of strength data measured respectively on single fibers, tows, matrix infiltrated tows and textile composites. It can be noticed that the strength magnitude and the strength interval decrease when considering successively single fibers, tows, matrix infiltrated tows and textile composites. As a result of the previously mentioned two step mechanism, the ultimate failure becomes dictated by the lowest strength extreme of the distributions, i.e. the lowest strength extreme of the distribution of fiber strengths for the failure of tows and infiltrated tows, and that of infiltrated tow strengths for the 2D composites failure. These strength extremes correspond respectively to the critical number of individual fiber breaks (≈ 17% for SiC Nicalon fibers [1]) and to the critical number of tow failures (≥ 1). The gap between the respective magnitudes of the strengths pertinent to the tows and to the matrix infiltrated tows results from the method of strength determination. The critical number of individual fiber breaks was taken into account in the tow strength only. The strength of the infiltrated tows and the textile composites was derived from the area of the cross section of specimens.

Figure 4 illustrates the scatter in strengths observed on 2D woven SiC/SiC composites tested under tensile loading conditions [14]. The specimens were loaded parallel to a tow direction. Tests were performed on two batches of 12 dog-bone shaped-specimens each, including small and large specimens. The statistical distributions of strength data were determined using ranking statistics. Ordering the strengths from smallest to largest and assigning a ranking number i, the probabilities of failure were then assigned by the following relationship :

$$P(\sigma_i) = (i-0.5)/N \qquad (2)$$

where N is the sample size.

The scatter in ultimate strengths can be characterized using the Weibull modulus m. Assuming that the stress-state is uniform :

$$P(\sigma) = 1 - \exp\,(V/V_0)(\sigma/\sigma_0)^m \qquad (3)$$

Where V is the stressed volume, $V_0 = 1mm^3$, σ is the applied stress and σ_0 is a scale factor.
The estimates of m obtained using the maximum likelihood method are rather high: m = 17 for the smaller specimens, and m = 20 for the larger ones.
Figure 4 also shows that the strength data exhibit a very limited dependence on the stressed volume. It can be noticed that, at low stresses, the higher strengths were obtained for the larger volumes.
Assuming that the tensile strengths of the composite follow weakest-link scaling, the ultimate strengths of the large specimens were predicted from the failure data of the small specimens, using the following equation derived from (1):

$$\sigma_1/\sigma_2 = (V_2/V_1)^m \qquad (4)$$

where $\sigma_1(P,V_1)$ and $\sigma_2(P,V_2)$ are ultimate strengths for a given failure probability P and for stressed volumes V_1 and V_2.
Figure 4 shows that the calculated strengths for the large specimens are underestimated significantly. The Weibull model thus predicts a great scale effect which is at variance with the trend shown by experimental results. This indicates that the Weibull approach is not appropriate to the description of ultimate failure of brittle matrix composites.

According to the Weibull predictions, a significantly larger size effect would be observed on an equivalent monolithic material. This result as well as the fiber-composite relations depicted on figure 3 suggest that the flaw sensitivity was tremendously reduced in the 2D SiC/SiC composite, as a result of the damage mechanism and the individual failure breaks that cause a truncating of the populations of pre-existing flaws. Those flaws that become responsible for ultimate failure are located in the previously mentioned critical fibers of which failure leads to catastrophic failure of composites [1, 14].

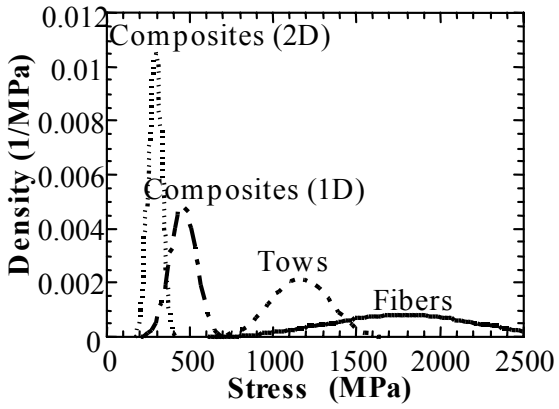

Figure 3 : Strength density functions for SiC fibers (NLM 202), SiC fiber tows, SiC/SiC (1D) minicomposites and 2D SiC/SiC composites.

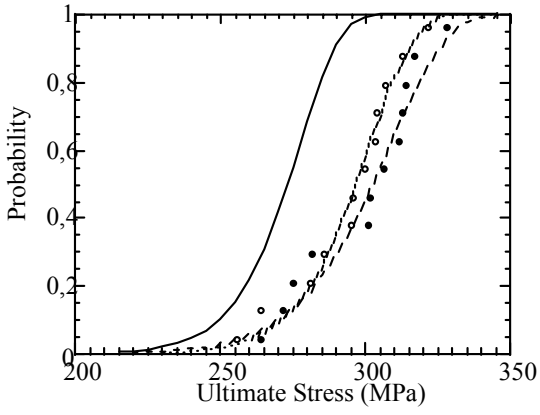

Figure 4 : Scale effects in 2D woven SiC/SiC composites. Influence of specimen dimensions on ultimate failure in tension : (•) V_1 = 8 x 30 x 3 mm^3, (o) V_2 = 160 x 120 x 3 mm^3, solid line : prediction of failure of larger specimens (volume V_2) using the Weibull's model.

Conclusions

In 2D woven SiC/SiC composites, ultimate failure generally occurs after matrix cracking saturation, under longitudinal strain ≥ 0.8%. Matrix damage and ultimate failure thus appear to be successive and separate phenomena. However under incremental loading, the load becomes progressively carried by the fibers only after matrix cracking saturation. Ultimate failure becomes controlled by the longitudinal tows. Fiber breaks initiate under high loads close to ultimate failure. Ultimate failure exhibits several interesting features including a small scatter in strength data and a very limited dependence on the stressed volume. These features can be related to the failure mechanisms that involve tow failures. They indicate a limited sensitivity to the flaw populations.

6- Acknowledgements

The author gratefully acknowledges support of SNECMA and CNRS through grants obtained by the Ph.D students involved in the generation of the results reported here (Ph. Forio, V. Calard, N. Lissart, L. Guillaumat). J. Forget and C. Dupouy are also acknowledged for their assistance with manuscript preparation.

7- References

1. N. Lissart and Lamon J. (1997) *Acta Mater*. 45, 1025.
2. Curtin W.A. (1991) *J. Am. Ceram. Soc*. 74, 2837.
3. Ladevèze P. (1992) *J. Computers and Structures*. 44, 79.
4. Batdorf S.B. (1985) in Probabilistic methods in the mechanics of solids and structures: Proc. IUTAM Symposium, Springer-Verlag. p. 299-305.
5. Sutcu M. (1989) *Acta Metal*. 37, 2567.
6. Karandikar P., Chou T.W. (1993). *Composites Science and Technology*, 46, 253.
7. Guillaumat L. and Lamon J. (1999) *Revue des Composites et des Matériaux Avancés*. 9, 183.
8. Forio Ph., Lamon J. (1999) in : Proc. The Twelfth International Conference on Composite Materials (ICCM 12), CD-ROM, Paris, France.
9. Forio Ph.(2000) *PhD Thesis*, University of Bordeaux, France.
10. Daniels H. E. (1944) *Proc. Roy. Soc. London*. 183, 405.
11. Coleman B. D. (1958) *J. Mech. Phys. Solids*. 7, 60.
12. Cao H., Thouless M.D. (1990) *J. Am. Ceram. Soc*. 73, 2091.
13. Calard V. (1998) *PhD Thesis*, University of Bordeaux, France.
14. Calard V. and Lamon J. (2001) to be published.

ORAL REFERNCE: ICF100261OR

MICROMECHANICS IN CONTINOUS GRAPHITE FIBER/EPOXY COMPOSITES DURING CREEP

C.H. Zhou[1], I. J. Beyerlein[2], and L. S. Schadler[1]

[1]Materials Science and Engineering, Rensselaer Polytechnic Institute
Troy, NY12180, USA
[2]Los Alamos National Laboratory, Los Alamos, MS G755, NM 87545, USA.

ABSTRACT: Micro Raman spectroscopy and classic composite shear-lag models were used to analyze the evolution with time of fiber and matrix strain/stress around fiber breaks in planar model graphite fiber-epoxy matrix composites. Impressive agreements were found between the model predictions and the experimental results. The local matrix creep leads to an increase in the load transfer length around the break under a constant load. This increases the chance of fiber breakage in the neighboring intact fibers.

KEYWORDS: Micromechanics, polymer composites, creep, Raman spectroscopy, modeling

1.INTRODUCTION

An important issue in the design of polymer composite structures is prediction of their time dependent performance and lifetime. The macroscopic failure of polymer composites is believed to start from localized damage zones (fiber breaks, matrix cracks, etc.), which inevitably form during fabrication or initial loading. Under a constant load, these initially harmless damage zones may grow in time and interact with each other, due to the time dependent nature of the polymer matrix. When one of these damage zones grows beyond a critical size, final failure of the structure takes place without any visible warning. Because failure of the composite is the result of a series of micro-events, a powerful experimental tool is required to investigate the creep-failure process at the micro scale, instead of the traditional macro-scale tests, in order to build an effective lifetime-predicting model.

In recent years, micro Raman spectroscopy (MRS) has been used to directly measure the axial strain along the fibers in composites [1-3]. Since many high performance fibers have great Raman sensitivity to strain, no other technique is comparable to MRS in strain measurements at micro scale in fiber-reinforced composites. However, most work in this area has been done on the time independent response. In this work, micro Raman spectroscopy was used to investigate the strain/stress evolution along a broken fiber in multi-fiber model composites during creep at room temperature. Predictions from a viscous break interaction (VBI) model [4] based on classic shear-lag concepts were compared with the experimental data.

2. VISCOUS BREAK INTERACTION (VBI) MODEL

VBI is a shear-lag analysis for a multi-fiber composite. The details of the 2D version used here can be found in Beyerlein et al. [4]. Figure 1 shows a region in a composite lamina of evenly spaced fibers and matrix regions and containing a couple of fiber breaks. As indicated, E is the fiber Young's modulus, w is the inter-fiber spacing (surface-to-surface), d is the fiber diameter, A is the fiber cross-sectional area, and b is the out-

of-plane thickness of the model. Here b is set equal to d. In the fiber axial direction x, a constant far field strain per fiber, denoted ε^*, is applied.

The time dependent compliance of the matrix $J(t)$ is well described with a common three parameter expression we term the "complete power law" compliance model, which is

$$J(t) = J_1 [1+(t/t_C)^{\alpha}] \tag{1a}$$

where t is time, t_C is the relaxation time, α is the power law exponent and J_1 is the initial compliance. For long times, i.e. $t \to \infty$, $J(t)$, apart from the initial elastic response, can also be well represented using the following "incomplete power law" function in time, where J_e is a compliance constant,

$$J(t) = J_e(t/t_C)^{\alpha} \tag{1b}$$

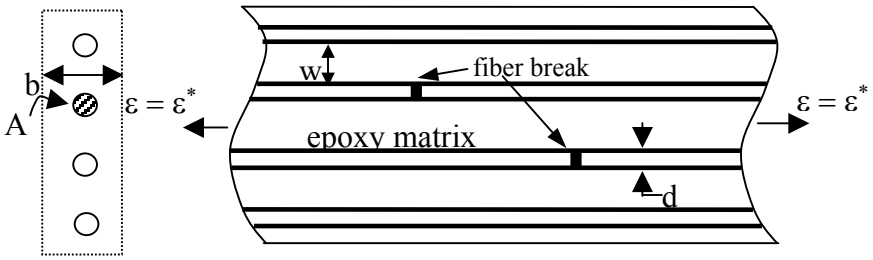

Figure 1: Illustration of the geometry of the 2-D array of fibers used in the VBI model

Consider an isolated fiber break in a 2D lamina (see Figure 1) with a matrix viscoelastic compliance following the power law function (Eqn.1b). Let $\varepsilon_r^* = \varepsilon_r/\varepsilon^*$ be the constant residual axial strain in the fiber normalized by the far field fiber strain ε^*. According to the model [4], the axial fiber strain $\varepsilon_0(z)$ along a fiber with a break at $x = 0$ is,

$$\varepsilon_0(z)/\varepsilon^* \approx 1 - \frac{\left(1-\varepsilon_r^*\right)}{2} C_\theta [\exp\{-2C_\theta\beta_0|z|\}]\, d\theta - \kappa_1(\alpha)|z| \int_0^{\pi} C_\theta^{\,2} [\exp\{-2C_\theta\beta_0|z|\}] d\theta, \tag{2}$$

where $C_\theta = \sin(\theta/2)$, $z = (x/\delta)/(t/t_c)^{\alpha/2}$, $\delta = \sqrt{EAwJ_e/d}$, and

$$\beta_0 = \Gamma(1+\alpha/2)/\sqrt{\Gamma(1+\alpha)}\ ,\ \kappa_1(\alpha) = \frac{(\pi\alpha/2)^2}{6}\ \beta_0 \tag{3}$$

Use of Eqn.1b for $J(t)$ not only simplifies the analysis such that we are able to obtain the closed form result but the fiber strain depends only on the parameter $z = (x/\delta)(t_C/t)^{\alpha/2}$, which couples space and time. Similarly for $\varepsilon_1(z)$, the axial strain in the intact fibers adjacent to the break at $x = 0$, the model predicts

$$\varepsilon_1(z)/\varepsilon^* \approx 1 - \frac{\left(1-\varepsilon_r^*\right)}{2} \int_0^{\pi} \cos(\theta) C_\theta [\exp\{-2C_\theta\beta_0|z|\}] d\theta - \kappa_1(\alpha)|z| \int_0^{\pi} \cos(\theta) C_\theta^{\,2} \exp\{-2C_\theta\beta_0|z|\}]\, d\theta, \tag{4}$$

3. EXPERIMENTAL DETAILS

Figure 2 shows the geometry of the model fiber composite specimens fabricated for this MRS (micro Raman spectroscopy) experiment. The matrix is an epoxy (Epon 828+ Epi-Cure 3234 curing agent at 1:0.129 ratio) with a modulus of 3.3 GPa, a shear modulus of 1.26 GPa and a Poisson's ratio of 0.33. The fiber is a Toray M4O high modulus graphite fiber with an axial modulus of E=390 GPa, a shear modulus of 147 GPa, and an average fiber diameter of 6.6 μm. A planar array of 5~8 fibers was placed with relatively uniform spacing in the middle of the dog-bone shaped mold. Bordering this fiber array were graphite fiber tows to reduce the macroscopic creep during the test. The composite samples were cured at room temperature for 12 hrs and post-cured at 100^0C for 2 hrs.

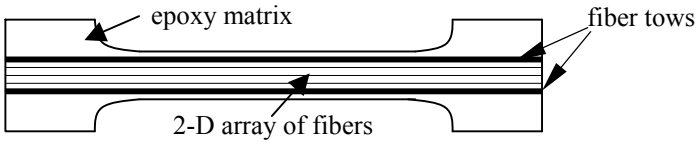

Figure 2: Schematic showing the geometry of the model composites

A constant uniform load was applied to the samples using custom-built jigs. A strain gauge was attached directly to the sample surface to monitor the macro-strain. Load was applied until a break was observed in a fiber and was then held constant. The macroscopic creep was negligible during the test period. Raman spectra were recorded along the broken fiber at periodic time intervals for several weeks, using a Renishaw Ramanscope System 2000, and a 514 nm Argon ion laser which has a spatial resolution of approximately ± 1 μm. The strain in the fibers was calculated from the shift in the second order A_{1g} mode. From the fiber strain data, the interfacial shear stress (ISS) was calculated using a simple force balance

$$\text{ISS} = E\,(d/4)\,\mathrm{d}\varepsilon/\mathrm{d}x \qquad (5)$$

4. RESULTS AND DISCUSSION

4.1 Bulk Matrix Creep Tests

In order to obtain the time dependent response of the matrix, long-term creep tests (~20 days) were performed on the bulk epoxy matrix. Figure 3 shows the change in matrix shear compliance with time at room temperature for the bulk epoxy at two different stress levels (10MPa and 20MPa). The power law functions (Eqn.1a) and (Eqn.1b) were used to fit the data. As shown in Figure 3, Eqn.1a provides a good description of the data, while Eqn.1b can only be used to describe the long-term behavior.

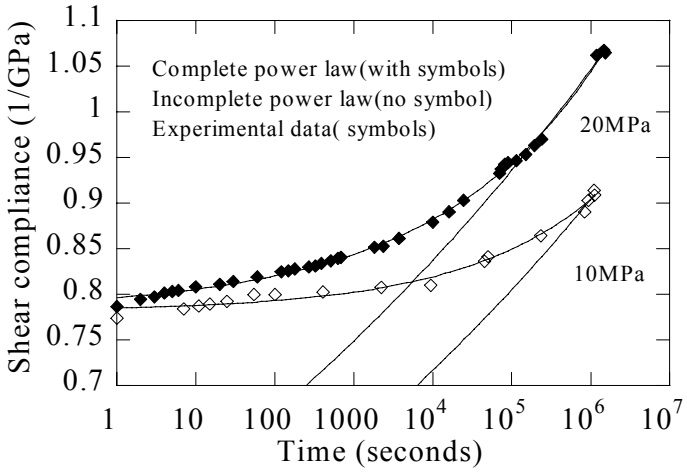

Figure 3: A plot of creep compliance $J(t)$ versus time of the bulk matrix

TABLE 1
COMPARISON OF THE PARAMETERS ASSOCIATED WITH DIFFERENT CREEP FUNCTIONS FOR THE EPOXY MATRIX

Parameters	Compliance constant J_1, or J_e, (1/GPa)		Relaxation time t_C (seconds)		Shape parameter α	
Stress (MPa)	10	20	10	20	10	20
Complete Power Law $J(t) = J_1 + J_1(t/t_C)^{\alpha}$	0.78	0.78	1.4×10^{9}	1.9×10^{8}	0.26	0.21
Incomplete Power Law $J(t) = J_e\,(t/t_C)^{\alpha}$	0.93	1.03	1.7×10^{6}	7×10^{5}	0.05	0.048

Table 1 lists the values for the parameters associated with these two different functions. The shape parameter α did not change significantly with the stress level, especially for the incomplete power law. However, for both laws, the relaxation time τ_c tends to decrease with increasing applied stress.

4.2 MRS Data and Model Predictions for Multi-fiber Composite

In this section, the measured axial strain distributions and the calculated interfacial stress (ISS) at different times are compared with VBI model predictions using parameters from Eqn.1a or Eqn.1b, as listed in Table.1. In one of our multi-fiber model samples, two fibers were very close to each other with an inter-fiber spacing of 13μm. A break was found in one fiber when the applied macroscopic strain was 1%. Figure 4 shows the strain along the two fibers with model predictions at two different times, τ =3.6x10^4 and τ = 2.5x10^6 seconds after the fiber broke.

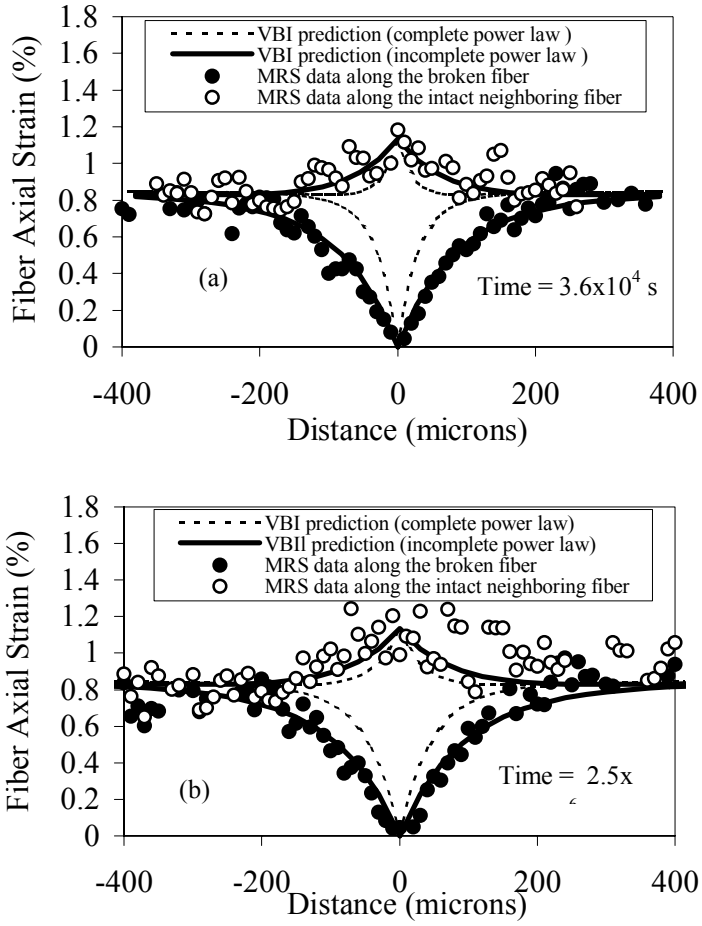

Figure 4: A comparison of the experimental axial strain data and the model predictions using complete power law parameters or incomplete power law parameters at 1% macrostrain at (a) 3.6x10^4 s; (b) 2.5x10^{6}s

The VBI model predictions using incomplete power law parameters are in very good agreement with the experimental data, while the predictions with complete power law parameters only give qualitative descriptions of the strain profiles. This is not surprising because the model solutions are derived using the incomplete power law function for the matrix shear creep compliance. In fact, the parameters from both stress levels (10MPa and 20MPa) were used to calculate the strain distributions. It was found that the predictions were almost identical for the two sets of parameters despite the difference in τ_c. An important feature in Figure 4 is the scattering of the axial strain data along the neighboring intact fiber. As described in Beyerlein's work [5], a fiber break will produce a stress concentration along the nearby fibers. In the ideal elastic case, the stress concentration appears as a sharp peak located at the fiber break. This peak would be

obscured and broadened if there is any matrix yielding or interfacial debonding near the break. Figure 4 suggests the presence of inelastic zones near the fiber break and possible growth of the inelastic zone during the creep.

In Figure 5 and Figure 6, only predictions from the incomplete power law are compared with the MRS results. The interfacial shear stress (ISS) distributions along the right part of the broken fiber are illustrated in Figure 5. The feature of the experimentally derived ISS curve at 3.6×10^4 seconds suggests some local matrix yielding might have occurred near the fiber break. As defined by Beyerlein et al [6], the load recovery length is the distance between the ISS_{max} (usually located at the fiber end) and the point where the ISS asymptotically approaches zero. The ISS profiles from MRS data show an increase of the load recovery length, while the peak value for the ISS did not change much over the time period. For the neighboring intact fiber, we define the positively affected length as the distance between the two points where the ISS approaches zero symmetric to the break. Corresponding to the increase in the load transfer length in Figure 5, the positively affected length in the intact neighboring fiber also expanded in time, as shown in Figure 6. This increases the chance of failure in the neighboring fiber, as was observed in this sample when a break occurred in the neighboring fiber at 112μm from the original break after 3×10^6 seconds. Although the model also predicts a similar increase in the load recovery length, the predicted change is smaller than that shown from the experimental results.

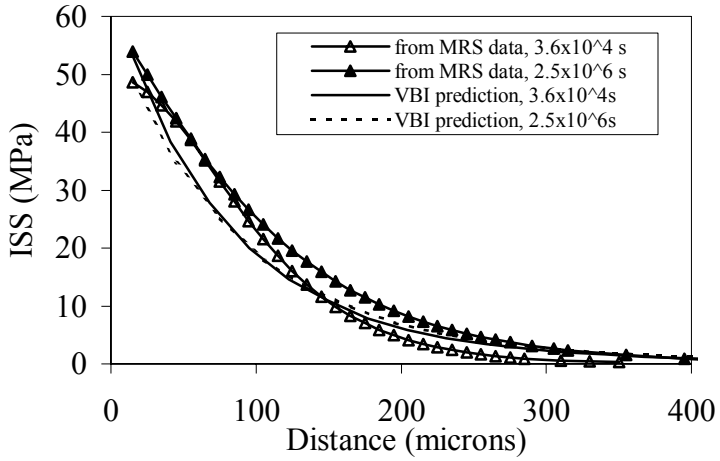

Figure 5: A comparison of the ISS derived from the experimental data and the model predictions using incomplete power law parameters at 1% macrostrain for the right part of the broken fiber at two different times

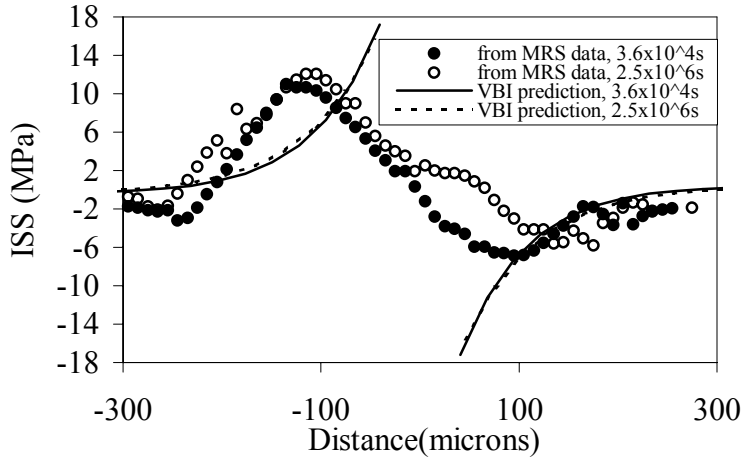

Figure 6: A comparison of the experimentally derived ISS and the model predictions using incomplete power law parameters for the intact neighboring fiber at two different times

For this composite sample, the solutions using the complete power law parameters did not show very good agreement with the MRS results. Although the incomplete law (Eqn.1b) works well only for the long-term creep of the polymer matrix, the VBI predictions using its parameters show excellent agreement with the MRS data, especially the axial strain profiles along the broken fiber. The smaller change in the predicted ISS profiles might partly result from the difference between the idealized model and the real composite sample. In the sample the fibers were not strictly evenly spaced. Two fibers were 13 μm apart, while other fibers were 25~30 μm away from them. Since the model considers evenly spaced fibers, it is very likely that the model predicts changes smaller than that in the real sample where the local matrix volume fraction is higher. As described in the previous section, this model does not include the possible plastic deformation and the interfacial debonding near the fiber break. For graphite reinforced epoxy composites, interfacial debonding or matrix yielding is common near the fiber break at relatively high strains. Therefore, it will be necessary to take into account these non-linear phenomena in future models.

5. CONCLUSIONS

The stress/strain redistribution during the creep of graphite fiber reinforced epoxy composites was investigated experimentally with Micro Raman spectroscopy and theoretically with a simple but effective viscoelastic shear lag model using VBI technique. Model predictions using the incomplete power law for the matrix creep showed good agreement with the experimental results. It was confirmed that the load transfer length increased due to the local matrix creep near fiber breaks under a constant load. This can explain why new fiber fractures occur later in time and are usually offset from the plane of the original break.

REFERENCE:

1. Melanitis, N., Galiotis, C., Tetlow, P.L.and Davies, K.L. (1993) *J.Mater. Sci*., **28**, 1648
2. Schadler, L. S. and Galiotis, C. (1995) *Int.l Mater. Rev.*, **40**, 116
3. Thomsen J.S. and Pyrz R. (2000) *Compos. Sci. Technol*. **60,** 1791
4. Beyerlein, I.J., Phoenix, S.L. & Raj, R. (1998) *Int. J. Solids Strucutres* **35**, 3177
5. Beyerlein, I. J., Amer, M., Schadler, L. S. and Phoenix, S. L. (1998) *Sci. Eng.Compos. Mater.*, **7,** 151
6. Beyerlein, I. J., Zhou, C. H., and Schadler, L. S. (2001) Proceedings of the ICOSSAR conference, June 2001, New Port Beach, California.

MICROMECHANISMS OF FATIGUE IN POLYSILICON MEMS STRUCTURES

S. M. Allameh[+], P. Shrotriya[+], B. Gally[x], S. Brown[x] and W.O. Soboyejo[+]

[+]The Princeton Materials Institute and Department of Mechanical and Aerospace Engineering, Princeton University, 1 Olden Street, Princeton, NJ 08544
[x]Exponent Failure Analysis and Associates, 21 Strathmore Road, Natick, MA 01760

ABSTRACT

This paper presents the results of a combined experimental and computational study of crack nucleation and surface topology evolution during the cyclic actuation of polysilicon MEMS structures. The evolution in surface topology observed during the crack nucleation stage is related to the underlying notch-tip stress distributions calculated using finite element analysis. Measured changes in surface topology due to the stress-assisted dissolution of silica are shown to be predicted by linear stability analysis.

KEYWORDS

Polysilicon MEMS, fatigue, surface reaction, stress-assisted dissolution, surface topology evolution, linear stability analysis

INTRODUCTION

Micro-Electro-Mechanical Systems (MEMS) fabricated from polysilicon are extensively used in a wide range of applications in which fatigue failure is possible [1-9]. These include applications ranging from accelerometers, actuators and pressure sensors [1,2], in which cyclic loads can ultimately lead to the nucleation and propagation of cracks. Unfortunately, however, the current understanding of fatigue in polysilicon is still limited.

The initial work on the fatigue of silicon MEMS structures was done by Brown and co-workers [3-5]. They obtained stress-life and fatigue crack growth rate data that suggested a strong influence of water vapor on the fatigue of polysilicon. More recently, Kahn et al. [6], Muhlstein et al. [7], Sharpe et al. [8] and Allameh et al. [9] have also reported the result of experimental studies of fatigue in polysilicon. Most of these studies have suggested that the overall fatigue life in polysilicon MEMS is dominated by the crack nucleation stage [3-9].

The paper presents the results of a combined experimental and computational/analytical study of the possible role of surface topology evolution in the nucleation of fatigue cracks in notched polysilicon MEMS structures.

Evidence of surface topology evolution obtained from atomic force microscopy is analyzed using Fourier analysis techniques. Evidence of surface topology evolution is presented along with finite element analysis of the notch-tip stress distributions that suggest a strong influence of stress state on the topology evolution. The measured surface topologies obtained using atomic force microscopy (AFM) are also compared with predictions from linear perturbation analysis of the stability of surface topology that evolves during stress-assisted dissolution of the silica layer that is present due to the surface oxidation of Si.

MATERIAL

The polysilicon MEMS structures that were used in this study were supplied by Cronos Integrated Microsystems (formerly MCNC) of Raleigh-Durham, NC. The MEMS structures were fabricated in batch runs at Cronos. Details of the micromachining processing schemes are given in Ref. [2]. The polysilicon MEMS structures consist of a capacitive comb-drive attached to the end of a notched sample as shown in Fig.1 (a). The devices were sealed under a topical SiO_2 layer that was removed before actuation. The release process consisted of rinsing in acetone, dissolving topical SiO_2 in concentrated (49.6%) hydrofluoric acid, rinsing in distilled water, followed by rinsing in propanol and drying in air at 110^{o}C. The surface of the structures was studied initially in a scanning electron microscope (SEM) to examine the microstructure, grain size and porosity. A secondary electron image of the polysilicon is presented in Fig. 1(b). This shows an equiaxed microstructure consisting of nano-size grains, with an average grain size of ~200 nm, and distributed porosity at the triple points.

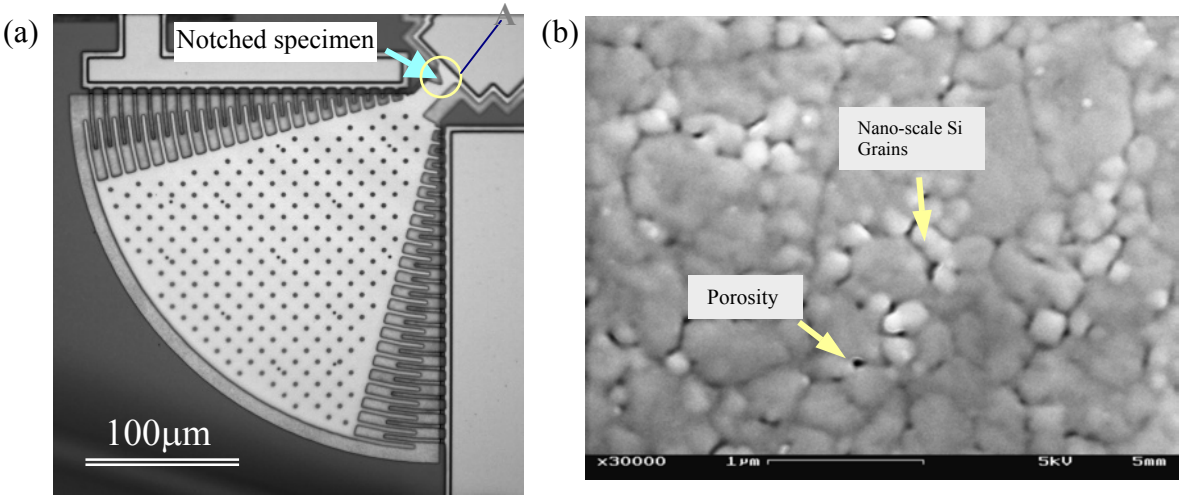

Figure 1 Notched polysilicon sample: (a) Photograph of a notched comb drive structure, (b) Scanning electron micrograph of polysilicon MEMS structure before actuation.

EXPERIMENTAL PROCEDURE

Atomic force microscopy (AFM) was used to characterize the surface morphology of the polysilicon sample before, during, and after cyclic actuation. The characterization included scanning of the specimen surface (labeled A in Fig. 1) immediately below the bottom of the notch where tensile stresses are highest during actuation. Two scan sizes (2µm x 2µm and 5µm x 5µm) were chosen to study both the extent and magnitude of the superficial morphological changes that occur during cyclic actuation. Following specimen calibration using techniques described by Van Arsdell et al. [5], the polysilicon structures were actuated at a constant actuation

voltage of 145 V through the application of an alternating direct current that was generated from a programmable wave function generator and amplified. The angular displacements of the actuating structures were examined using an optical microscope that was connected to a video recorder, and a microvision system [10]. AFM images were obtained during the cyclic actuation of the polysilicon MEMS structures. These were used to measure the morphological changes in the areas of highest tensile stress in the vicinity of the notches. The measured changes in surface topology were then analyzed using Fourier analysis techniques [11,12].

Polysilicon structures tested in this study show significant surface changes that occur after cyclic actuations for 2×10^9 cycles with a constant angular displacement of 1.44 degrees. AFM images obtained from the area at the bottom of the notch before and after actuation are presented in Fig. 2. There is a significant change in the surface topology before actuation (Fig. 2a) and after actuation (Fig. 2b) in an area of 5 μm x 5 μm. The observed changes in the surface topology may be ascribed to a stress assisted dissolution of SiO_2 that can give rise to the evolution of grooves and ultimately to the nucleation of fatigue cracks [11,12].

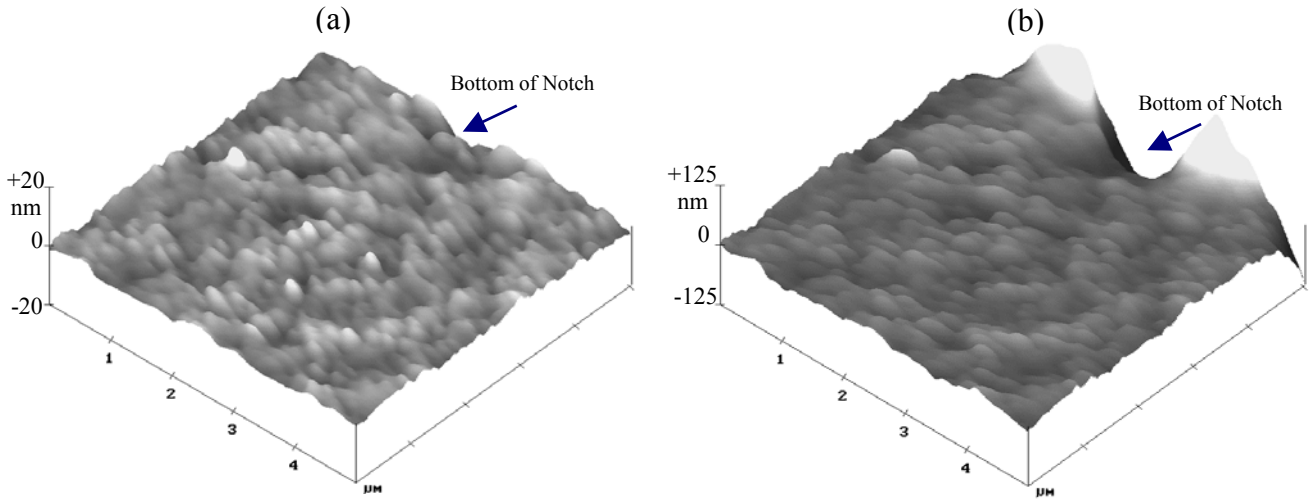

Figure 2 AFM images showing surface evolution of the silicon MEMS sample under cyclic loading conditions. (a) Before actuation and (b) after actuation.

MODELING

Finite element Analysis

The stress distribution at notch-tip corresponding to the measured angular displacement was modeled using finite-element analysis in order to determine the relationship between the observed angular displacement and maximum principal stress, σ_{max}. The geometry of the notch was determined from the measured values, while the dimensions of the specimen were taken from the nominal design. The model was constructed from the 6,200 six-noded plane stress triangular elements. The mesh density was determined by a study of the numerical convergence of stress distribution with the number of elements. For the analysis, Young's modulus and Poisson's ratio of polysilicon were assumed to be 147 GPa and 0.22, respectively and a linear elastic small strain formulation was used. The finite element analysis was performed using ABAQUS. The typical results of the finite element analysis are presented in Fig. 3. Figure 3(a) shows the details of the discretization near the notch-tip and Fig. 3(b) shows the contour of maximum principal stress in the region surrounding the notch-tip corresponding to an angular displacement of 1.44°.

Linear Perturbation Analysis

Kim et al. [11] and Yu and Suo [12] have used linear perturbation analysis to study the dissolution of a stressed solid surface and related the change in surface profile to the stress state. A similar analysis is utilized here to study the observed roughening of the SiO_2 layer on the polysilicon MEMS structures. Following Yu and Suo [12], a linear perturbation analysis is utilized in order to correlate the time evolution of individual Fourier components of the surface roughness to applied stress state. The perturbation analysis is performed by assuming that the surface mobility is independent of the stress state [11, 12]. The time evolution of the amplitude of a Fourier component, $q(\omega,t)$, at an angle θ to the principal axes, *is* expressed as [11, 12]:

$$\ln \frac{q(\omega,t)}{q(\omega,0)} = M\alpha t \,. \tag{1}$$

Where M is the surface mobility associated with the dissolution reaction, t is the time and α is given by [11,12]:

$$\alpha = \frac{2(1+\nu)}{E}\left[(1-\nu)\left(\sigma_1 \cos^2\theta + \sigma_2 \sin^2\theta\right)^2 + \left(\sigma_1 - \sigma_2\right)^2 \cos^2\theta \sin^2\theta\right]\omega - \gamma\omega^2 \,. \tag{2}$$

E is the Young's modulus, ν is the Poisson's ratio, γ is the surface energy per unit area and σ_1 and σ_2 are the in-plane principal stresses.

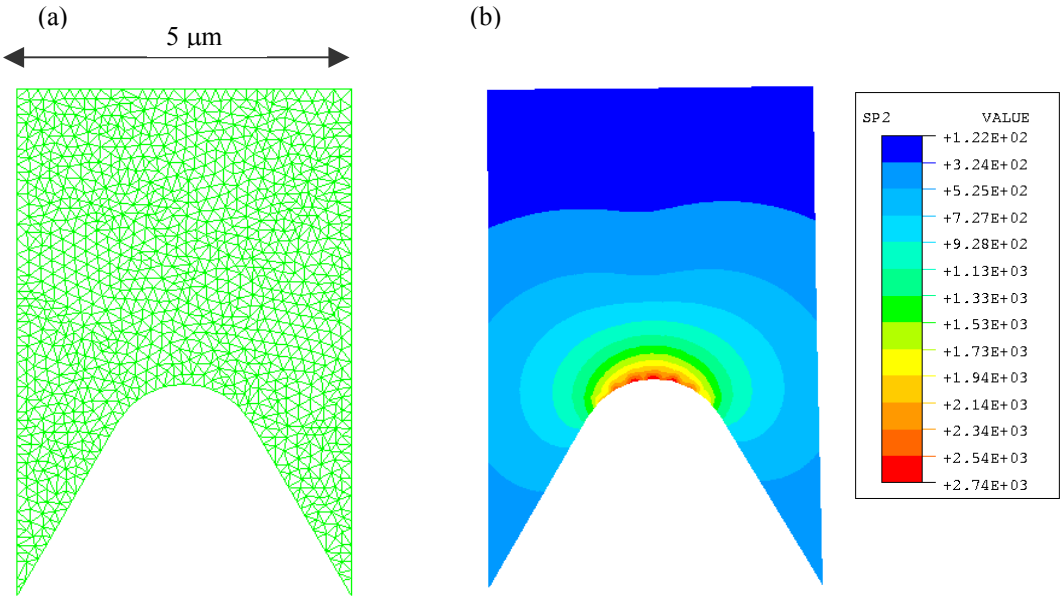

Figure 3 Finite element calculations: (a) Details of the discretization near the notch-tip, (b) Principal stress distribution near the notch-tip corresponding to angular displacement of 1.44°.

The quantity, α, corresponding to stress state at base of the notch, is evaluated for the different Fourier components in order to study the influence of the stress-assisted surface reaction. During the experiments, the MEMS structure was loaded under cyclic loading hence the root mean square (RMS) average of principal stresses is utilized in the calculations. The RMS average of the in-plane stresses at the base of the notch are

computed to be σ_{11} = 1990 MPa, σ_{22} = 141 MPa and σ_{12} = 0. The interfacial energy of the SiO_2 and water system is reported equal to 4.8 Jm^{-2} (46 ergs cm^{-2}) [13]. The contour plot of α corresponding to the stress state is presented in Fig. 4. The dark thick contour line on the plots corresponds to $\alpha = 0$ and α is positive for all the wave numbers enclosed by it.

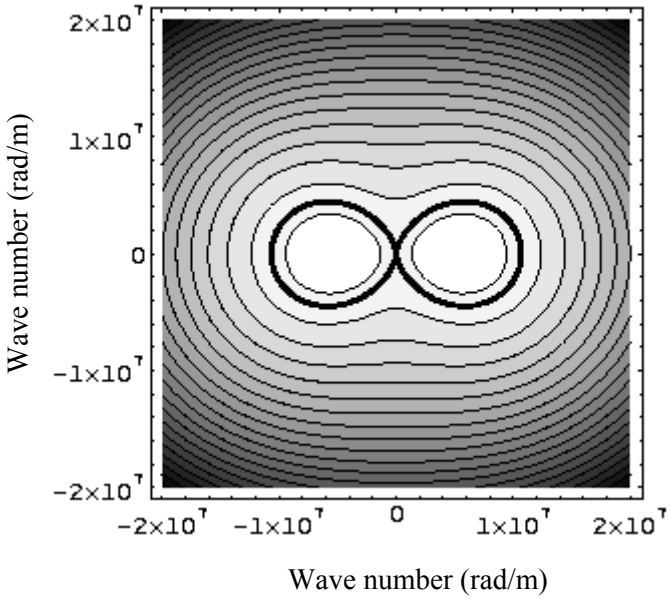

Figure 4 Contours of a corresponding to the stress state at the notch-tip

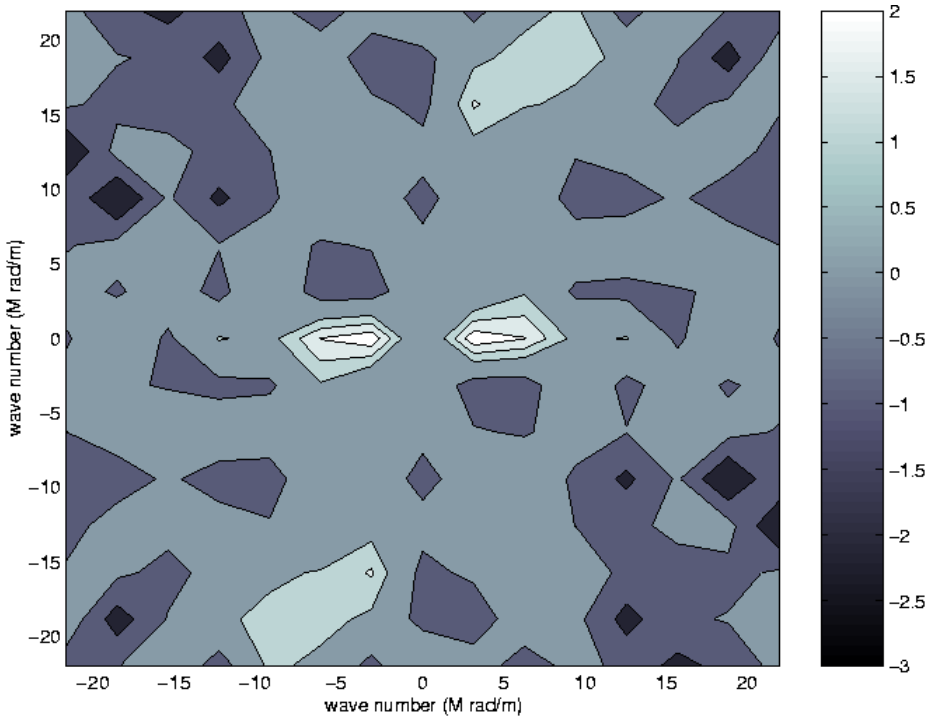

Figure 5 Contours of $\ln q(\omega,t)/q(\omega,0)$ corresponding to an area of 2 μm x 2 μm near the notch-tip.

Following the procedure described by Kim et al. [11], the quantity on the left hand side of Eq. (1) was evaluated using the measured surface morphologies of the MEMS structure before and after the cyclic actuation. The contours of $\ln q(\omega,t)/q(\omega,0)$ corresponding to the areas of 2μm x 2μm area, near the notch-tip are plotted in Fig. 5. Comparison of the contour plots of $\ln q(\omega,t)/q(\omega,0)$ and α indicates that the shape of the contours is similar. Additionally, the magnitude of the wave numbers predicted to grow by linear perturbation analysis compare remarkably well with the experimental measurements.

SUMMARY AND CONCLUDING REMARKS

1. AFM images obtained from 2x2μm and 5x5μm of the area located on the surface of the structure at the bottom of the notch show that significant changes in surface topology occur in polysilicon during cyclic actuation.
2. The finite element analysis shows that the highest principal stress levels occur in the regions where the evolution of surface topology results in formation of deep grooves.
3. Time evolution of the surface roughness indicates that amplitudes of a few wave numbers grow with time during cyclic actuation. This effect may be attributed to stress-assisted interactions between water molecules and the SiO_2 layer on the surfaces of the notched specimens in the regions at the bottom of the notch.

ACKNOWLEDGEMENTS

The research was supported by the Division of Materials Research of The National Science Foundation (NSF) and The Defense Arms Research Projects Agency (DARPA). WOS, PS and SA are grateful to Dr. Jorn Larsen-Basse, the program manager at NSF, for his encouragement and support. Appreciation is also extended to Alex Butterwick and Hadi Allameh for assistance with experimental techniques.

REFERENCES

1. K.D. Wise and K. Najafi (1991) *Science*, 254, 1335.
2. M. Madou (1997) *Fundamentals of Microfabrication*, CRC Press, New York.
3. J.A. Connally and S.B. Brown (1992) *Science*, 256, 1537.
4. J.A. Connally and S.B. Brown (1993) *Experimental Mechanics*, 33, 81.
5. W. Van Arsdell and S. Brown (1999) *J. Microelectromech. Syst.,* 46, 320.
6. H. Kahn, R. Ballarini, R. L. Mullen and A. H. Heuer (1990) *Proc. Roy. Soc., Series A* 455, 3807.
7. C. Muhlstein, S. Brown and R. O. Ritchie (2001) In: *Mechanical properties of structural films,* STP 1413, C. Muhlstein and S. Brown (Eds). American society for testing and materials, West Conshohocken. (in press).
8. W. N. Sharpe Jr., B. Yuan and R. L. Edwards (1999). In: *Proc. Fatigue'99*, pp. 1837-1844.
9. Allameh, S. M. Gally, B. Brown, and W. O. Soboyejo (2001). In: *Mechanical properties of structural films,* STP 1413, C. Muhlstein and S. Brown (Eds). American society for testing and materials, West Conshohocken. (in press)
10. D. M. Freeman, A. J. Aranyosi, M. J. Gordon (1998), In: *Proc. Solid-State Sensor and Actuator Workshop, Hilton Head Island, SC*. 150-155.
11. K. S. Kim, J. A. Hurtado and H. Tan (1999) *Phys Rev. Lett.*, 83, 3872.
12. H. H. Yu and Z. Suo (2000) *J. Appl. Phys.*, 87, 1211.
13. R. K. Iler (1979). *Chemistry of Silica*, John Wiley & Sons, New York.

MICROSTRUCTURAL FEATURES OF SHORT CRACK GROWTH IN A BETA TITANIUM ALLOY

U. Krupp, W. Floer, H.-J. Christ, A. Schick* and C.-P. Fritzen*

Institut für Werkstofftechnik, Universität Siegen, D-57068 Siegen, Germany
*Institut für Mechanik und Regelungstechnik Universität Siegen, D-57068 Siegen, Germany

ABSTRACT

Initiation and early growth of short cracks during fatigue loading are strongly affected by the local microstructural arrangement, e.g. grain geometry and crystallographic orientation. In the case of the beta-titanium alloy Ti-6.8Mo-4.5Fe-1.5Al (TIMETAL®LCB) used in this study, even under macroscopically elastic loading slip bands and small cracks are generated at highly misoriented grains due to the elastic anisotropy. While high-misorientation conditions promote crack initiation, the propagation of short cracks is hindered by crack path deflection at high-angle grain boundaries or possibly crack closure effects. In the present paper this could be shown by fatigue tests which were carried out in combination with the measurement of local displacement by means of a laser interferometric strain/displacement gauge (ISDG) and the determination of individual crystallographic orientations by means of electron back-scattered diffraction (EBSD) in the scanning electron microscope (SEM). The experimental results were proved by FE modelling of exemplary details of the deformed microstructure.

KEYWORDS

short cracks, crack closure, elastic anisotropy, EBSD, ISDG, beta-titanium alloys

INTRODUCTION

While the growth of long fatigue cracks can be described in a uniform manner by the well-known sigmoidal function of the crack growth rate (log da/dN) versus the stress-intensity factor (log ΔK), the behaviour of short cracks is characterised by the lack of uniformity, which involves the risk of non-conservative design [1]. By observing individual microstructural short cracks it can be found that (1) cracks grow at ΔK values much lower than the threshold value for long cracks ΔK_{th}, (2) crack propagation rates decrease or even stop, or (3) cracks propagate at higher rates than predicted for the long crack curve [1]. This behaviour is due to the fact that the growth rate of microstructurally short cracks is determined by both, the shear stress on the operating slip planes as a consequence of local Schmid factor variations and dislocation pile-up in front of barriers like grain boundaries (GBs) or precipitates [2-4]. Crack blocking at GBs is often followed by a rapid increase of the crack propagation rate leading to oscillating crack growth kinetics, which Navarro and de los Rios attributed to the activation of dislocation sources in a grain i+1 by the dislocation pile up in the neighbouring grain i at the barrier [5]. The blocking effect of GBs as well as the geometrical arrangement of the slip systems are closely related to the crystallographic orientation and the geometry of individual grains.

High-misorientation conditions and low multiplicity of slip promotes plastic incompatibility of neighboured grains and intergranular crack propagation [6,7], while low angle GBs can easily be crossed by slip and therefore by propagating transgranular cracks [8]. Once a short crack begins to grow it suffers further microstructural interactions by crack coalescence and crack closure which speed it up or slow it down [1,9]. Although plasticity-induced crack closure, which plays a considerable role for the growth mechanisms of long cracks, should be negligible for short cracks due to the small plastic wake behind the crack tip [10], roughness-induced crack closure effects and plastic displacement in front of the crack tip might be important factors influencing short crack propagation [11].
Stimulated by the knowledge that life of dynamically loaded components is often determined by the propagation of short cracks, the present study deals with the quantification of microstructural features, which are responsible for stress localisation, crack initiation and early crack growth kinetics, and is focussed on the objective to develop a model for mechanism-oriented life-time prediction.

EXPERIMENTAL DETAILS

The studies on the short crack propagation mechanisms were carried out on the metastable beta-titanium alloy TIMETAL®LCB (low cost beta, Ti-6.8Mo-4.5Fe-1.5Al), which was developed as a relatively cheap and light-weight alternative to high-strength steel in the automotive industry (e.g. for suspension springs). The results presented in this paper are restricted to fatigue tests in the solution heat-treated condition, exclusively consisting of b.c.c. beta grains with an average grain size of 102µm. Shallow-notched (in the gauge length) cylindrical specimens, which were machined from hot-rolled rods and vacuum heat treated (830°C, 5h, water-quenched) were electropolished and fatigued in a SCHENCK S31 servohydraulic testing system using symmetrical pull-push loading conditions at room temperature under stress control. During fatigue testing, initiation and early growth of fatigue cracks was observed by an optical microscope which is attached to the testing system and connected to a digital image analysis system to generate individual crack propagation vs. crack length plots (*da/dN* vs. *a*, see ref. [12]).
In order to estimate the contribution of crack closure effects to the propagation behaviour of short cracks the testing system is equipped with an self-made laser interferometric strain displacement gauge (ISDG), according to Sharpe's concept [13], which allows high-resolved determination (theoretical resolution: 1.85nm) of local strain. Data is produced by moveable photodiodes which follow the displacement of an interference pattern generated by a laser beam, which is reflected at two Vickers microhardness indentations in the specimen surface (Fig. 1). The shift of the microhardness indentations, placed approx. 50µm above and below a growing short crack, yields the crack opening displacement COD, which contains information e.g. about local crack closure effects.

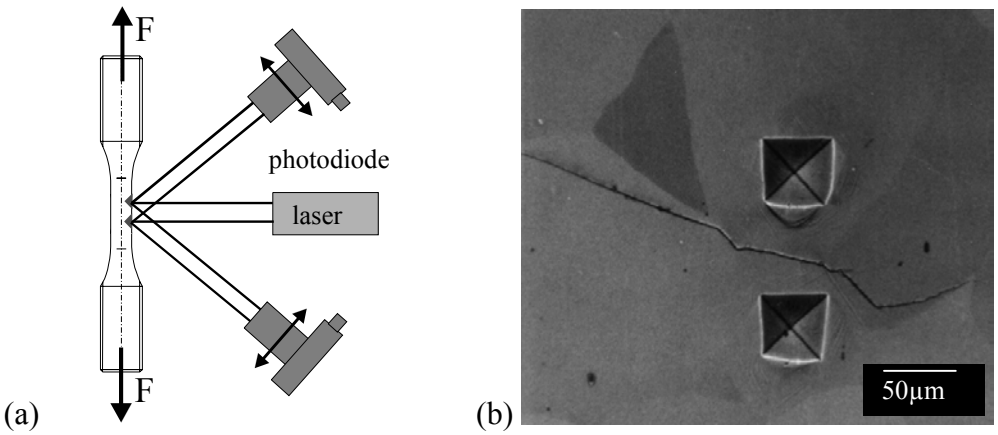

Figure 1: Measurement of local displacement by an ISDG system: schematic representation (a) and Vickers microhardness indentations above and below a growing short crack ($\Delta\sigma/2$=600MPa ⇳)(b)

To carry out microstructural examinations, the specimens were removed from the fatigue testing machine after certain numbers of cycles. Due to the smooth electropolished surface, the grains are observable in electron channeling contrast (ECC) in the SEM (PHILIPS XL30 LaB_6). The individual crystallographic

orientations of the grains participating in cracking processes on the surface and the corresponding misorientation angles were evaluated by an EBSD system (TSL). The physical principle and the evaluation methods are described in detail in [14].

RESULTS AND DISCUSSION

Crack Initiation

Fatigue tests, carried out at a stress amplitude of $\Delta\sigma/2$=600MPa (approx. 50% of the yield stress σ_Y of LCB in the solution heat treated condition) and a stress ratio of R=-1, were interrupted several times during the fatigue life of approx. N_f=5000 cycles to characterise the initiation sites of microstructural short cracks. Fig. 2 represents that predominantly cracks originate at GBs either intergranularly (Fig. 2a) or transgranularly along slip bands (Fig. 2b). EBSD measurements of more than 600 grains reveal that during fatigue life (1) approx. 80% of all the cracks initiate transgranularly and (2) intergranular cracking is restricted to high-angle GBs, which are defined by misorientation angles Θ>15° [8]. Analogously to the results Zhang and Wang obtained for Cu bicrystals in [6], high-angle GBs seem to prevent slip across the boundary, hence they give rise to plastic incompatibility and therefore crack initiation.

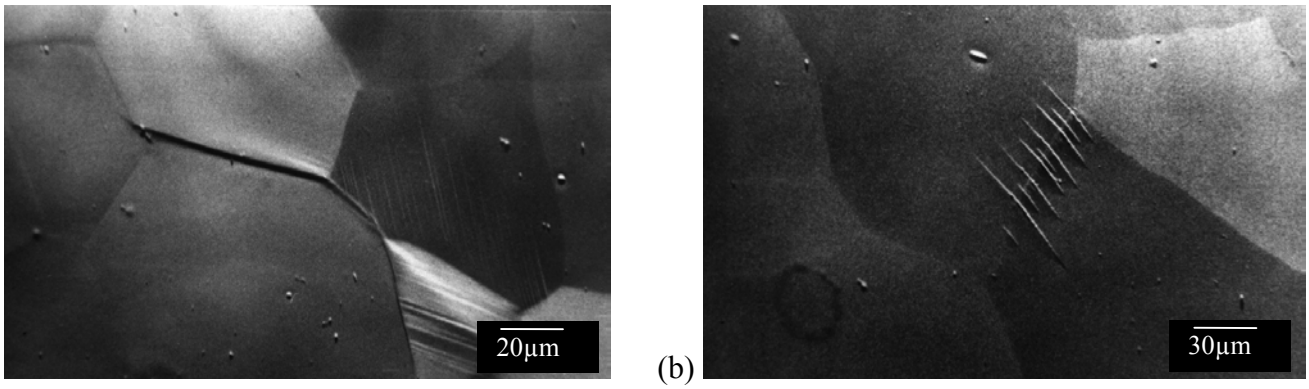

Figure 2: Intergranular (a) and transgranular crack initiation (b) at high-angle GBs ($\Delta\sigma/2$=600MPa ⇔)

Since nearly all the cracks observed initiated at GBs without any interactions with precipitates, pores etc., it can fairly be assumed that elastic anisotropy creates high stress levels in the vicinity of highly-misoriented grains. A mechanical confirmation requires the three-dimensional stiffness matrix of the test material LCB. Due to the lacking of such data in literature, a method has been developed to calculate the anisotropy on the base of local displacement measurements (by means of ISDG) and crystallographic orientation determination (applying EBSD) [15]. By FE modelling of several real cracked microstructures as it is shown exemplary in Fig. 3 using the determined anisotropy value of A≈0.7 it was demonstrated, that local stress reaches maximal values at exactly those GBs which cracked during fatigue loading.

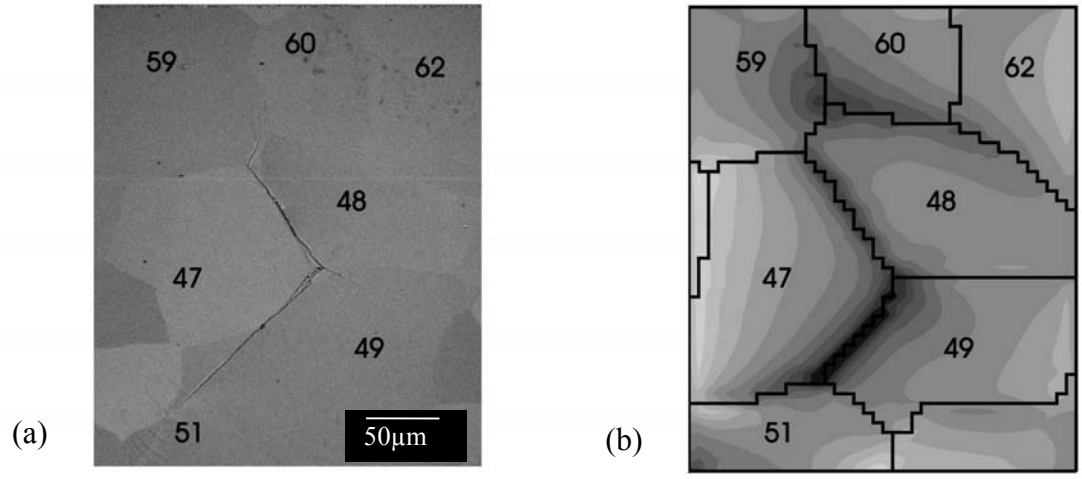

Figure 3: Intergranular crack initiation: SEM micrograph (a) and corresponding calculated stress distribution (b) (maximum mean stresses: high stress values = dark) ($\Delta\sigma/2$=600MPa ⇔)

Crack Propagation

Once a short crack has been initiated its propagation rate and direction depends on (1) the direction of the operating slip planes with regard to the loading axis and the GBs, (2) the crystallographic misorientation of neighbouring grains, (3) crack closure effects, and (4) mutual interactions and coalescence of short cracks. Fig. 4a shows several microstructurally short cracks on the surface of the beta-titanium alloy LCB. The one marked with a solid arrow follows slip planes inclined 45° with regard to the loading axis, i.e. in direction of the maximum shear stresses. It could be observed that high deflection of the crack path at a barrier is in most cases connected with a temporary arrest, while dislocation pile-up activate crack continuation in the neighbouring grain, as proposed in the model of Navarro and de los Rios [5]. On the contrary, at high constrained GBs (e.g. in Fig. 4a, dashed arrow) many slip bands are activated leading to high back stresses towards the GB which fails by slip-step cracking instead of growing slip band cracks. The observation of several growing cracks during fatigue testing by an optical microscope supplemented by SEM/EBSD examinations reveals, that in particular low-angle GBs or low intersection angles between slip planes of neighboured grains or intergranular cracks as well as slip band cracks parallel to the maximum shear stress are prone to short crack propagation.

Furthermore it might be mentioned that fatigue damage cannot be attributed to a single short crack. Fig. 4b demonstrates the intensified plasticity in the vicinity of two approaching crack tips. By applying the replica technique the following coalescence events were identified as the substantial mechanisms leading to the transition from short to long crack behavior. It is worth mentioning that modelling of crack coalescence requires a statistical approach, which has been done by a promising microstructure simulation in combination with the short crack growth model of Navarro and de los Rios in [16].

(a) 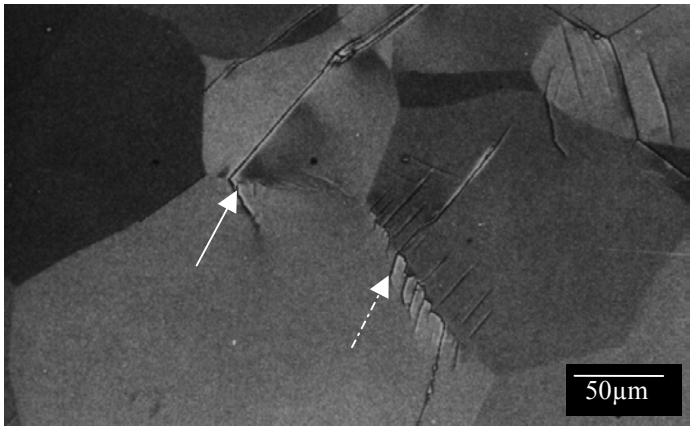

(b) 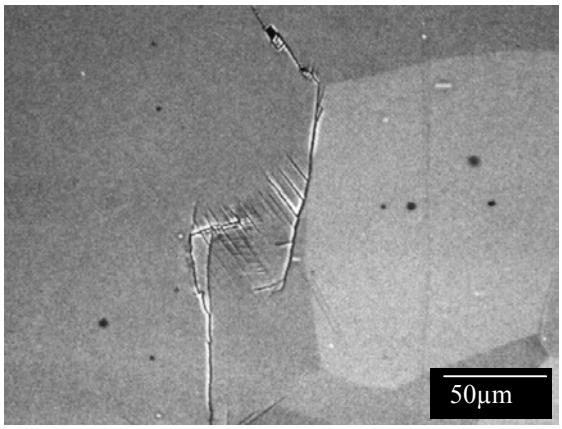

Figure 4: Crack deflection and plastic incompatibility at a high-angle GB (a) and plastic distortion in the vicinity of two coalescent cracks (b) ($\Delta\sigma/2$=600MPa $\Leftrightarrow$)

Since direct observation of short cracks is restricted to the two-dimensional surface, the crack shape is often assumed to be semicircular or semi-elliptical. For long cracks, which are almost independent of microstructural features, this simplification might be true, the depth of short cracks however tends to be dictated by the crystallographic orientation and the GB arrangement in a similar way than it was shown for surface crack propagation. The local aspect ratio *a/c* (crack depth / half surface crack length) was determined by preparing and evaluating metallographically various cross sections along selected surface cracks. It was found, that early short crack growth into the material is slower than at the surface. This can be derived from an average aspect ratio of approx. *a/c*=0.5 (for more details see ref. [12]).

The studies of short cracks on the surface of the beta-titanium alloy LCB gave rise to the assumption, that shear stresses in the slip planes are the predominant driving force for crack propagation and GBs act as crack growth retarding barriers (or in some cases as intergranular crack initiation sites). For long cracks it is generally accepted that crack propagation depends strongly on crack closure effects, originally reported by Elber in [17]. He established, that the plastic zone formed during tensile loading at the tip of a growing crack leads to a premature contact of the crack surface during unloading. Therefore the part of the cycle in which the crack is open is reduced by plasticity-induced crack closure, i.e. the crack driving stress intensity factor range ΔK is reduced to an effective stress intensity factor ΔK_{eff} by the closure stress intensity factor ΔK_{cl}:

$\Delta K_{eff} = \Delta K - \Delta K_{cl}$. Furthermore, a jagged crack surface in combination with a displacement of the opposite crack areas result in a premature crack closure, which is known as roughness-induced crack closure.
Although there are numerous studies on crack closure effects during the propagation of long fatigue cracks, there is a lack of data concerning the impact of crack closure on the propagation of microstructurally short cracks. Since the length of the plastic wake behind the tip of a short crack, which is responsible for plasticity-induced crack closure, as well as the extent of roughness are assumed to be quite small, a transient behavior from short to long crack closure might be expected, according to [18]. Fig. 5 shows exemplary results and the evaluation of the COD measurements for two stress amplitudes at a stress ratio of R=-1. The closure stress σ_{cl} (defined by the intersection point of the tangents on the parts of the hysteresis loop where the crack is fully closed and fully open, resp.) for the lower stress amplitude is appreciable for surface crack lengths of more than approx. 50µm and lies in the tensile part of the cyclic loading (Fig. 5b). Since no plastic deformation could be observed at the crack tip, the positive closure stress is attributed to roughness-induced crack closure. For higher stresses, the crack becomes fully closed in the compressive part of the loading cycle. Following the remarks given in Liaw's review article [19] about crack closure at near-threshold fatigue crack growth levels, higher plastic strain at the crack tip of short cracks as compared to long cracks and the simultaneous absence of a plastic wake can explain the negative crack closure stress at higher stress amplitude. This assumption is supported by the plastic opening of the hysteresis loop for the higher stress amplitude in Fig. 5a (both curves represent surface crack lengths of approx. 300µm). Crack closure effects, which extend the part of the loading cycle when the crack is open, might additionally rise to higher propagation rates of short cracks compared to long cracks (based on the usual assumption, that K_{min} is set to zero if σ_{min} is negative). Concerning such comparisons it should be mentioned, that the application of the ΔK concept to microstructurally short cracks implies a violation of the assumption of continuum mechanics and linear elastic fracture mechanics, respectively.

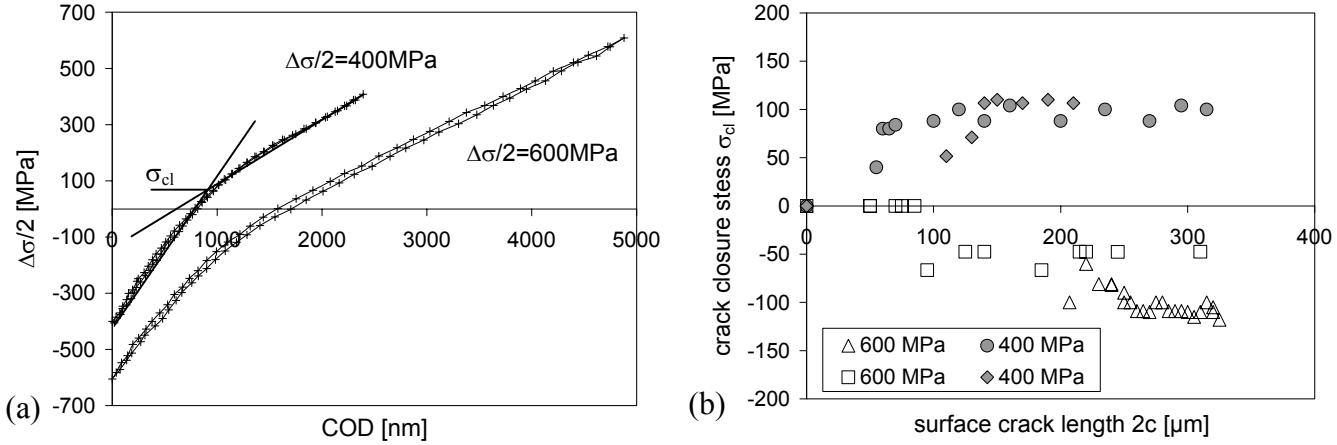

Figure 5: Evaluation of crack closure effects: stress vs. crack opening displacement (a) and crack closure stress vs. crack length (b)

CONCLUSIONS

The behaviour of short cracks in the beta-titanium alloy LCB in the solution heat treated condition is strongly dependent on the local crystallographic orientation. In-situ observation of growing cracks by an optical microscope during fatigue testing in combination with SEM examinations using the EBSD technique to determine local crystallographic orientations revealed that cracks initiate exclusively at high-angle grain boundaries either trans- or intergranularly. FE calculations of the microstructure on the base of the experimentally estimated value of the elastic anisotropy of A=0.7 yielded the highest stresses at these grain boundaries, which were actually observed to be cracked. Generally, favourable conditions/sites for crack propagation are:

- low angle grain boundaries,
- low angles between operative slip systems of neighbouring grains or intergranular cracks,
- slip planes parallel to the maximum shear stress (45° inclined to the loading axis).

The transition from short to long crack behaviour is substantially influenced by interactions and coalescence of short cracks. Measurements of the crack opening displacement by an ISDG system showed, that crack closure effects do not only influence the driving force for long cracks but also affect the propagation of microstructurally short cracks. Particularly if the applied stress amplitude exceeds approx. 50% of the yield stress of about 1200 MPa (at a stress ratio of R=-1) cracks tend to stay open in the beginning of the compression phase of the loading cycle. This can be attributed to the high crack tip deformation of short cracks as compared to long cracks and might be an additional reason, why short cracks frequently propagate much faster and at (nominally) lower stress intensity factors than the threshold value of the stress intensity factor of long cracks.

Achnowledgment

The financial support by Deutsche Forschungsgemeinschaft (DFG) in the framework of the priority program on mechanism-based life prediction is gratefully acknowledged. The authors wish to acknowledge the theoretical and experimental contribution particularly the numerous EBSD measurements by Dr. Yunming Hu, who stayed with the Institut für Werkstofftechnik at the Universität Siegen from 1998 to 2000 and is now a research associate at the department of materials science at the University of Toronto.

REFERENCES

1. Taylor, D. (1989) *Fatigue Thresholds* Butterworth, London.
2. Suresh, S., Ritchie, R.O. (1984) *Int. Met. Rev.* 29, 445-475.
3. Long, M., Crooks, R., Rack, H.J. (1999) *Acta mater.* 47, 661-669.
4. Kaynak, C., Ankara, A., Baker, T.J. (1996) *Int. J. Fatigue* 18, 25-31.
5. Navarro, A., Los Rios, E.R. (1988) *Phil. Mag. A* 57, 15-36.
6. Zhang, Z.F., Wang, Z.G. (2000) *Mat. Sci. Eng. A* A284, 285-291.
7. Peralta, P., Laird, C. (1999) *Mat. Sci. Eng. A* A264, 215-231.
8. Hu, Y.M., Floer, W., Krupp, U., Christ, H.-J. (2000) *Mat. Sci. Eng. A* A278, 170-180.
9. Stolarz, J. (1997) *Mat. Sci. Eng. A* A234-236, 861-864.
10. Ritchie, R.O., Suresh, S. (1982) In: *Proc. AGARD 55th SMP Meeting, Toronto*, pp. 1.1-1.14.
11. Nakajima, K., Terao, K., Miyata, T. (1998) *Mat. Sci. Eng. A* A243, 176-181.
12. Floer, W., Krupp, U., Christ, H.-J., Schick, A., Fritzen, C.-P. (2000) In: *Proc. 13th European Conference on Fracture, San Sebastian, Spain* (on CD ROM).
13. Sharpe Jr., W.N., Grandt Jr., A.F. (1976) *Mechanics of Crack Growth, ASTM STP 590*, 302-320
14. Randle, V. (1993) *The Measurement of Grain Boundray Geometry,* Inst. of Physics Publishing, London
15. Schick, A., Fritzen, C.-P., Floer, W., Hu, Y.M., Krupp, U., Christ, H.-J. (2000) In: *Proc. Damage and Fracture Mechanics*, pp. 393-402, A.P.S. Selvadurai, C.A. Brebbia (Eds), WIT Press, Southampton
16. Olfe, J., Zimmermann, A., Rie, K.-T., (2000) In: *Proc. Mechanismenorientierte Lebensdauervorhersage, Kolloquium der Deutschen Forschungsgemeinschaft, DVM*, pp. 97-105.
17. Elber, W. (1970) *Engng. Fract. Mech.* 2, 37-45.
18. Larsen, J.M., Williams, J.C., Thompson, A.W. (1988) In: *Mechanics of Ftaigue Crack Closure, ASTM STP 982*, pp. 62-92, J.C.Newman Jr., W. Elber (Eds).
19. Liaw, P.K. (1988) In: *Mechanics of Ftaigue Crack Closure, ASTM STP 982*, pp. 149-167, J.C.Newman Jr., W. Elber (Eds).

Microstructure and Mechanical Properties of Laser Cladded Steel Plates

S. Niederhauser and B. Karlsson

Department of Engineering Metals, Chalmers University of Technology, SE-412 96 Göteborg, Sweden

Abstract

A low alloyed hypo-eutectoid steel plate was cladded with a cobalt-chrome alloy by means of a laser. Subsequently, the layered structure was examined by metallographic inspection, by hardness measurement, and mecanically. The latter consisted of tensile tests and low-cycle-fatigue. The cladding resulted in a structure with high interfacial strength and good ductility.

Key words: Laser cladding, Co-Cr, carbon steel, microstructure, deformation behaviour, fatigue properties.

1 Introduction

The process of laser cladding consists of the injection of powder into the meltpool created by a laser beam on the surface of a substrate material. The laser beam and, thus, the meltpool are scanned over the surface, resulting in a single track of a surface layer on the substrate. By applying the process in several passes (or multipass), one beside the other, the whole surface can be coated. The clad is metallurgically bonded to the substrate with a very small intermixing zone between the clad and the substrate. During cladding the substrate is heated and subsequently cooled with high rates, as it acts as heat sink. This leads to the so-called heat affected zone (HAZ) under the clad. The HAZ can change its microstructure owing to e.g. a phase transformation within the temperature range that is encountered. In addition, during multipass cladding several thermal cycles can change the newly created phases further.

Clads produced by means of laser possess unique properties compared to other techniques. First, they are very compact without noticeable porosity. Second, the bonding between the clad and the substrate is very strong owing to the metallurgical bonding. Third, the high heating and cooling rates often results

Table 1
Composition of the clad powder and the substrate in [wt.%]

Element	Fe	C	Co	Cr	Mo	Ni	Si	S & P	Mn	V
Clad	0.35	0.125	bal	25.5	5.6	2.15	1.01			
Sub	bal	0.51		0.13	0.029	0.11	0.32	<0.03	0.72	0.051

in non equilibrium phases. In addition, the process is fast and can easily be automated. In recent years laser cladding has attracted more and more attention. Microstructure, phase identification, and hardness measurement were the fundamental interests of such studies [1,2]. This paper additionally deals with mecanical behaviour.

2 Experiments

First, a test plate of plain carbon steel (commercial name SURA B82) was cut and ground to the dimension of 200 mm x 10 mm x 20 mm. The clad was applied on the top surface by moving the laser beam in the longitudinal direction. Successive passes were introduced by parallel runs in the same direction with 2 mm displacements (transversal). After cladding of the whole surface a second layer was put on top of the first one, resulting in about a 2 mm thick clad on top of the substrate. Underlying the clad a 1 mm thick HAZ has developed. From this test plate all the samples and specimens were taken. Table 1 shows the chemical composition of the two materials. The fatigue properties of this material and variants of it was recently studied by Ahlström [3].

Next, metallographic examination and hardness measurements of the test plate were done perpendicular to the direction of the passes. Samples from the plate were ground, polished, and finally etched, using a 2 % Nital solution in order to show the microstructure in the HAZ and the substrate. Vickers hardness was measured at two positions using a load of 10 kg. One position was in the middle of a cladding pass, the other between two subsequent passes.

Then, tensile testing was performed on specimens both in the longitudinal and transversal directions. The specimen had a nearly squared cross section of about 4 mm side, with a clad thickness of about 1.6 mm. Before conducting the tests, the specimen were ground in the tensile direction down to paper 1200 in order to minimize surface effects. The test itself was conducted using a strain rate of 10^{-4} s^{-1}.

For fatigue testing total strain control was employed with a triangular wave shape and symmetric loading ($R_\epsilon = -1$) at $\dot{\epsilon} = 10^{-2}$ s^{-1}. The test specimens had a thickness of around 7.5 mm, whereof the clad is about 1.8 mm, and

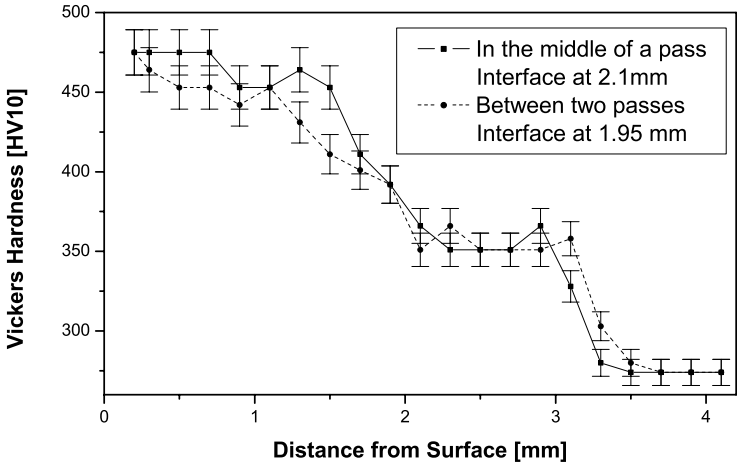

Fig. 1. Hardness evolution in the clad, HAZ, and the substrate along two symmetry lines

a width of about 6 mm. They were ground in the tensile direction down to paper size 2400. Two levels of total strain amplitude were employed, namely 0.4 and 0.6 %.

3 Results and Discussion

The microstructure of the substrate material consists of fine lamellar pearlite with some 10 % of ferrite in the previous austenite grain boundaries. Laser coating austenitised the closest underlying substrate, followed by formation of martensite. Later heating owing to the next parallel pass and to the second layer lead to tempering of the martensite, resulting in a microstructure of small carbides in a ferritic matrix, evenly distributed and also decorating previous austenite grain boundaries.

The hardness curves shown in Figure 1 demonstrate the variation of the hardness with respect to the depth under the surface. The clad shows declining hardness values inwards, reflecting grain coarsening and softening of the inner clad layer during application of the outer layer. The hardness plateau in the HAZ reveals a uniform carbide distribution. The short transition zone to the unaffected substrate material reflects a partial austenitisation in the first run. The slight differences of the two hardness profile positions indicate a difference in annealing influenced by succeeding passes. However, the hardness profiles through the coating and HAZ are fairly even over the whole layer.

Figure 2 shows stress-strain relations of cladded material in longitudinal and transversal direction and of substrate material for comparison. Apart from slightly different flow stress levels caused by different thickness of the cladded layer, the specimens exhibit no dependence on straining direction. However,

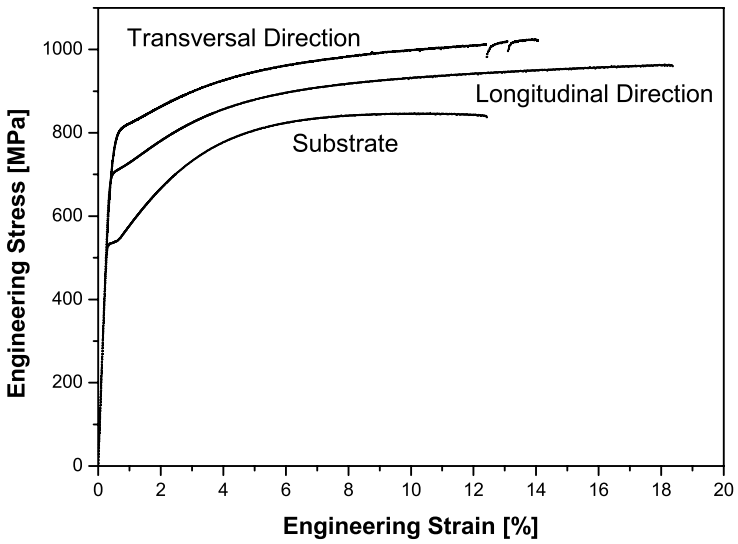

Fig. 2. Stress-Strain relations for cladded and substrate materials

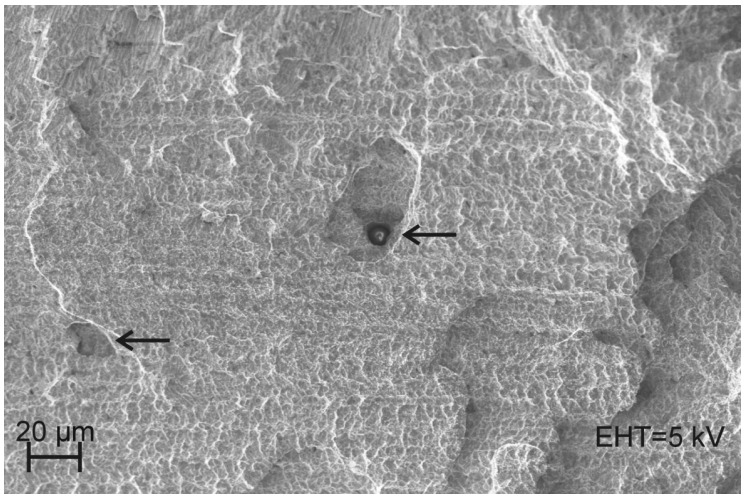

Fig. 3. Fracture surface from a transversal tensile test bar, showing an unmelted particle and pre-fracture (arrows)

the elongation to fracture turns out to be somewhat lower in the transversal direction. It is interesting to note that cladding leads to higher elongation to fracture compared with the substrate material. The fracture behaviour of the cladded material is essentially the same for both directions, i.e. the clad shows a brittle fracture (Fig. 3), the HAZ a ductile, and the unaltered substrate is in mixed mode, depending on local grain size and orientation. The only difference between the two fracture surfaces is the presence of small particles in the transversal fracture surface (Figure 3), initiating earlier fracture and, thus, lower elongation to fracture. The high elongation as well as the fracture surface topography reveal a good interfacial bond strength between the coated layer and underlying substrate material.

The fatigue tests with duplicate specimens in each case showed lifetimes of

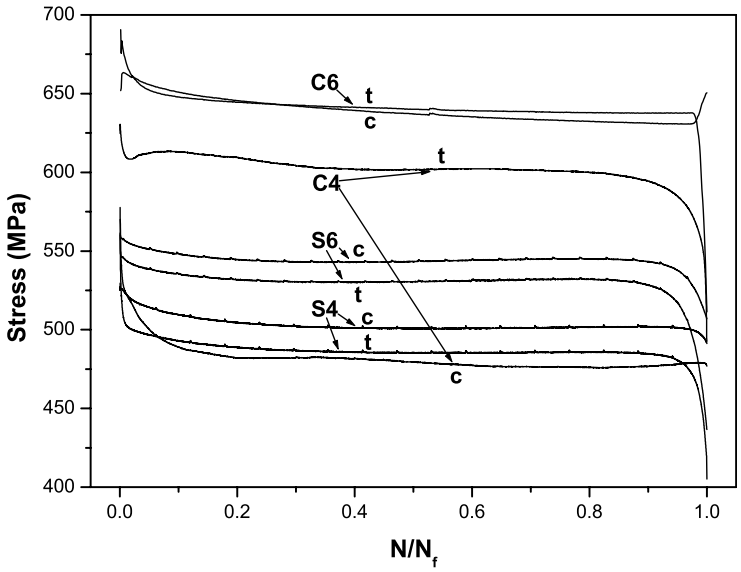

Fig. 4. Peak tensile (t) and absolute values of peak compressive (c) stresses of fatigue tests for the substrate (S) only and cladded (C) material, 4 and 6 indicate the strain amplitudes 0.4 and 0.6 % of the different curves respectively

$N_f = 10,000$ and $3,500$ at total strain amplitudes 0.6 and 0.4 % respectively for the substrate material. Cladded materials showed corresponding lifetimes of $N_f = 6,000$ and $1,500$. Obviously, the coating leads to some shortening of the lifetime, somewhat more pronounced at higher strain amplitudes. By normalising the lifetime, stress-lifetime diagrams as shown in Figure 4 can be drawn. Evidently, the stress levels are higher for the cladded material for the same strain amplitudes. A fairly limited softening takes place during strain cycling for all cases, independent of strain amplitude and material. While the substrate material exhibits essentially equal stress amplitudes in tension and compression, there is a very deviating picture for the the cladded material at the low strain amplitude 0.4 %. In this case, the highest peak stress levels are in the tensile direction and are much larger than the stresses in compression. This strong directionality in the peak stress levels vanishes for the strain amplitude of 0.6 %. As usually found in the this kind of fatigue behaviour representation, unloading due to cracking does not occur until after some 80 % of the whole lifetime. Such cracking leads to more unloading in tension than in compression.

The strong anisotropy in the peak stresses during cyclic straining of the cladded material at the low strain amplitude can qualitatively be understood as follows. Recent measurements of retained stresses (elastic strains) in a stellite laser coating (similar alloy) on austenitic stainless steels [4] revealed compressive stresses of the order of 80 MPa in the coating, while the underlying material had balancing but lower tensile stresses, which diminshed inwards into the material. This compressive stress in the coating corresponds to an elastic strain of approximately 0.04 %. In the present case, however, the martensite formation in HAZ leads to stress/strain reversal so that tensile retained

stresses would result in the the surface coating. Further, considering the maximum elastic strain in the coating of about 0.5 %, it means that the imposed total strain amplitude of 0.4 % would slightly plastically deform the coating in tension while the compressive loading would not yield plastic straining. Therefore, the peak stresses would be higher in tension than in compression. On the other hand, a total strain amplitude of 0.6 % leads to plastic straining in both tension and compression with approximately similar peak stresses in both directions. Measurements of retained stresses/strains in the present case with accompanying analysis of the fatigue stresses are under planning in this project. The important issue, however, is the influence of retained strains on the the peak stess levels in tension and compression at strain amplitudes where the coating is only elastically deformed, but the substrate also plastically.

4 Conclusion

The interface region between the clad and the HAZ shows a good metallurgical bonding and thus, a high strength. The clad has a weakness zone between two subsequent passes, which could be solved by putting two subsequent passes closer together (partial overlapping). The cladded material shows only slightly shorter fatigue lifetimes than those of the substrate material, yet with considerably higher stress amplitudes. Internal stresses created during cladding causes asymmetry in the peak loads at small strain amplitudes.

Acknowledgements

The authors express their gratitude for the financal support of Duroc AB, which also cladded the steel plate. This work was performed within the centre of excellence Charmec (CHAlmers Railway MEChanics).

References

[1] De Mol van Otterloo, J.L. and De Hosson, J.Th.M (1997) Acta mater. 45, 3.

[2] Hidouci, A., Pelletier, J.M., Ducoin, F., Dezert, D. and El Guerjouma, R. (2000) Surf. Coat. Tech. 123, 1.

[3] Ahlström, J. (2000), PhD Thesis, Chalmers University of Technology, Sweden.

[4] Hosseini, M. and Ericsson, T. (2000) Presented at: Heat Treatment 2000, Göteborg, Sweden.

ORAL reference : 99

MIXED MODE I/III FRACTURE TOUGHNESS OF MILD STEEL

M.Srinivas[1], S.V.Kamat[1] and P. Rama Rao[2]

[1] Defence Metallurgical Research Laboratory, Kanchanbagh, HYDERABAD- 500058, INDIA
[2] University of Hyderabad, Gachi Bowli, HYDERABAD-500046,INDIA

ABSTRACT

One of the main limitations of the mixed mode fracture toughness evaluation is the lack of standard test procedures especially for ductile materials. The objective of the present work was to establish the slope of the blunting line under mixed mode I/III loading using stretch zone width measurements and to study the effect of mixed mode I/III loading on the fracture toughness of mild steel. Mild steel was chosen as the test material as it is a widely used structural material. Fracture toughness tests were carried out employing modified single edge notched three point bend specimens with initial crack orientation angles of 0, 30 and 45°. A crack with a notch root radius of 110 μm was introduced to a depth of 0.5 W, where W is the width of the specimen, using wire cut electrical discharge machining. A multiple specimen technique similar to that recommended by ASTM E-813 was used for determining the mixed mode I/III fracture toughness. The blunting line slope for the different crack orientations was determined using stretch zone width measurements and was superimposed on the respective J-R curves to determine the mixed mode I/III fracture toughness. The mixed mode I/III fracture toughness of mild steel was found to decrease significantly with increasing mode III loading component. The effect of mixed mode I/III loading on fracture toughness of mild steel was explained on the basis of the fracture mechanism as well as the nature of the deformation fields ahead of the crack tip under mixed mode I/III loading.

Key words: Mixed mode I/III fracture toughness, mild steel, stretch zone width, blunting line

INTRODUCTION

Mixed mode fracture toughness evaluation is gaining importance, as the loading experienced at the tip of the crack in a structure in most practical applications could be very complex resulting in mixed mode fracture. One of the main limitations of the mixed mode fracture evaluation is the lack of standard test procedures. In recent years, test procedures for the determination of mixed mode I/III fracture toughness has been suggested for both brittle [1] and ductile [2] materials. In the procedure for evaluation of mixed mode I/III fracture toughness for ductile materials (J_{tc}), Manoharan et. al.[2] have suggested an empirical relation for the determination of the slope of the blunting line which is as follows

$$m_{i/iii} = \frac{m_i \cos\phi + m_{iii} \sin\phi}{\cos\phi + \sin\phi} \qquad \text{--- (1)}$$

where $m_i = 2\,\sigma_{yt}$, $m_{iii} = 2\,\tau_{yt}$ and ϕ is the crack orientation angle with respect to the mode I crack. Kamat et. al. [3] in their study on mixed mode I/III fracture toughness on Armco iron have shown that the experimentally measured blunting line slope under mixed mode I/III loading was significantly greater than that predicted by expression (1) suggested by Manoharan et.al. [2]. They have also obtained an expression for blunting line for Armco iron, which is given below

$$m_{i/iii} = 4\,\sigma_{yt}\,(1.005 - 0.00524\,\phi) \qquad \text{--- (2)}$$

The present investigation is aimed at establishing the slope of the blunting line under mixed mode I/III loading using stretch zone width measurements as well as to study the effect of mixed mode I/III loading on the fracture toughness in mild steel. Mild steel was chosen as the test material as it is a widely used construction material.

EXPERIMENTAL PROCEDURE

Mild steel, containing in weight percent, 0.23C,1.6Mn, 0.035S and 0.03P in the form of 15 x 30 mm^2 rectangular cross-sectional bars was used in the present study. The microstructure consisted of 65 vol.% ferrite with a mean linear intercept grain size of around 20 μm and 35 vol.% pearlite. The mechanical properties of mild steel are given in Table 1.

A multiple specimen technique similar to that recommended by ASTM E 813 [4] was used for determining the mixed mode I/III fracture toughness. The modified single edge notched 3-point bend specimen geometry is shown in fig.1. Fracture toughness tests were performed at ϕ =30° and 45°. Fracture toughness results for pure mode loading (ϕ =0°) were taken from an earlier study [5]. Fatigue pre cracking is precluded in specimen with ϕ =30° and 45° because of the proclivity of the fatigue pre-crack to rotate towards mode I orientation. Hence, pre-cracking was done for all specimens by means of wire cut electrical discharge machining (EDM). A 0.2 mm diameter wire, which resulted in a notch root radius of 110 μm was used for this purpose.

All fracture toughness tests were carried out on an Instron 8500+ servo hydraulic testing machine at a displacement rate of 1mm /min. The specimens were post-cracked by fatigue to delineate the stretch zone and stable crack extension. To measure the stretch zone width, the fractured surfaces were examined under Scanning Electron Microscope (SEM) with the fracture surfaces tilted at an angle of 45° with respect to the incident beam about an axis parallel to the machined notch. SEM pictures were recorded at magnifications of 50-100X within the range of 3/8 to 5/8 of specimen thickness, six measurements were taken and averaged.

RESULTS

Load Vs Load line displacements for ϕ =0°, 30° and 45° exhibit a load drop immediately after the linear portion similar to yield drop in tensile tests. The load drop in fracture toughness tests, known as pop-in, is attributed to the yielding phenomenon [6] as there is no evidence of unstable crack extension either prior to or after the formation of stretch zone width (fig.2).

The J_t value for each specimen was determined using the following expression

$$J_t = \frac{2\,U}{b\,B_{eff}} \qquad \text{---3}$$

where U is the total energy under load Vs load line displacement plot, b is the ligament ahead of the crack and $B_{eff} = B/\cos\phi$ where B is the thickness and ϕ is the loading angle. The J_t value thus obtained is plotted as a function of crack extension as shown in figs. 3 and 4 for ϕ = 30 and 45 ° respectively. The plot of J- Δa for ϕ = 0 is reproduced from an earlier study [5] in fig. 5 for fatigue precracked specimen. Blunting line having a slope given by expression (1) intersects the J – Δa curve yielding J_{tc} values of 140 and 90 kJ/m^2 for ϕ = 30 and 45°, respectively.

An alternative method for J_{tc} calculation, based on stretch zone width measurements was also employed. Representative scanning electron micrograph illustrating the critical stretch zone width for ϕ = 30 and 45° are given in fig. 2. The critical stretch zone width values for all three loading angles are given in

table 2 along with the corresponding J_{tc} data. The J_t vs szw_c, assuming $szw_c = \Delta a$, is superimposed on the respective J-Δa plots in fig.3 and 4 for the two loading angles. The plot J_t Vs szw_c is nominally a straight line parallel to the y-axis and the point where it intersects the J - Δa regression line is then the initiation fracture toughness J_{tc}. Also, the straight line joining the above intersection point and the origin describe the blunting behaviour of the material. The J_{tc} values obtained using this method are also given in Table 2.

DISCUSSION

Blunting Line

Table 3 shows that the experimentally measured blunting line slopes under mixed mode I/III loading conditions agree reasonably well with that predicted by expression (1) suggested by Manoharan et.al. However, an empirical fit to the data results in the following equation for the blunting line slope under mixed mode I/III loading

$$m_{i/iii} = 2\sigma_{yt} (1.005 - 0.00524\,\phi) \qquad -- 4$$

This condition is very similar to that found earlier for Armco iron [3].

The only difference between the two equations is the constraint factor. Several investigators [7-10] have found that the constraint factor is a function of the work hardening exponent, n. For Armco iron which has $n > 0.2$ the constraint factor is 2 whereas for mild steel where $n = 0.15$ the constraint factor is 1. Thus it appears that a generalized expression for blunting line slope under mixed mode I/III loading can be written as

$$m_{i/iii} = 2\,(C.F.)\,\sigma_{yt} (1.005 - 0.00524\,\phi) \qquad -- 5$$

Currently studies are underway, to verify the applicability of the above expression to other materials.

Mixed Mode Fracture Toughness

The variation in the measured fracture toughness with loading angle ϕ is shown in fig. 6. The fracture toughness decreases with increasing ϕ. Srinivas et.al. [11] have suggested a technique for the estimation of initiation fracture toughness J_{Ic} for ductile materials using blunt notch specimens. Their study showed that critical stretch zone width in the fatigue-precracked condition and blunt notch condition are related and could be expressed as

$$SZW_c^{fp} = (SZW_c^{\rho} - \rho) \qquad --6$$

where SZW_c^{fp} is the critical stretch zone width in the fatigue-cracked specimen, SZW_c^{ρ} the measured critical stretch zone width for blunt notch specimen have notch root radius ρ. Thus it is possible to estimate the notch root independent fracture toughness (that is the fracture toughness determined using fatigue – precracked specimens) from the measured SZW_c^{ρ} by means of the following expression

$$Jtc = 2\,(C.F.)\,\sigma_{yt}\, f(\phi)\, (SZW_c^{\rho} - \rho) \qquad --7$$

where $f(\phi) = (1.005 - 0.00524\phi)$ with ϕ in degrees.

The corrected stretch zone width and the calculated notch root independent fracture toughness for different loading angles are given in Table 4. The variation of notch root independent toughness under mixed J_{tc}, as a function of ϕ is included in fig.6. The fracture toughness decreases significantly with increasing ϕ. The decrease in fracture toughness with increasing loading angle is similar to that found in

other ductile materials which fails by classical void nucleation and growth mechanism and has been attributed by Kamat and Hirth [12] to a autocatalytic shear localization-void nucleation model.

CONCLUSIONS

1. The experimentally measured blunting line slope under mixed mode I/III loading was found to nearly match with that predicted by expression (1) suggested by Manoharan et.al.
2. The fracture toughness of mild steel decreased significantly with increased mode III loading.

ACKNOWLEDGEMENTS

DRDO is thanked for providing funding and the facilities to carry out this research.

REFERENCES

1. A.M.Kumar, J.P Hirth, R.G.Hoagland and X.Feng., J. Test. and eval. 1994, **22**,327
2. M.Manoharan, J.P.Hirth and A.R.Rosenfield, J.Test. eval. 1990, **18**, 106
3. S.V.Kamat, M.Srinivas, P.Rama Rao, Acta Meter, 1998, **46**, 4985
4. Annual Book of Standards Vol. 3.01 ASTM E-813, American Society for Testing Materials 1994, 628
5. M.Srinivas and S.V.Kamat, Mater. Sci. & Technol., (in print)
6. M.Srinivas, G.Malakondiah & P.Rama Rao, Scripta metall. 1989,**23**,1627
7. W.J.Mills, J. Test. eval., 1981, **9**,56
8. P.Doig, R.F.Smith and P.E.J.Felwitt, Engng fract. mech., 1984, **19**,653
9. M.Srinivas, G.Malakondiah and P.Rama Rao, Engng Fract. Mech. 1987, **28**, 561
10. S.W.Yin, R.A.Gerbrands and M.Hartevelt, Engng.Fract. Mech., 1983, **18**, 1025
11. M.Srinivas, S.V.Kamat and P.Rama Rao, J Test. eval., 1994, **22**,302
12. S.V.Kamat and J.P.Hirth, J.Engng mater. Technol., 1995,**117**,391

Table –1 Mechanical Properties of mild steel.

Properties	Value
Lower Yield Strength, MPa	300
U.T.S, MPa	477
Elongation in 25 mm GL	31
n	0.15

Table –2 Critical szw and J_{tc} values for mild steel

Loading angle ϕ degrees	szw_c measured μm	J_{tc} from empirical blunting line kJ/m^2	J_{tc} from szw_c measurement kJ/m^2
0	318	--	247
30	187	140	135
45	137	90	85

Table –3 Blunting line slopes for mild steel under mixed mode I/III loading

Loading angle ϕ degrees	Blunting line slope calculated using expression (1) (MPa)	Blunting line slope measured experimentally (MPa)
30	635	658
45	582	590

Table-4 Corrected values of szw & J_{tc} for mild steel

Loading angle ϕ degrees	Notch root radius μm	Measured szw_c μm	Corrected szw_c μm	J_{tc} (calculated from corrected szw_c) kJ/m^2
0	110	318	208	162
30	110	187	77	51
45	110	138	28	16

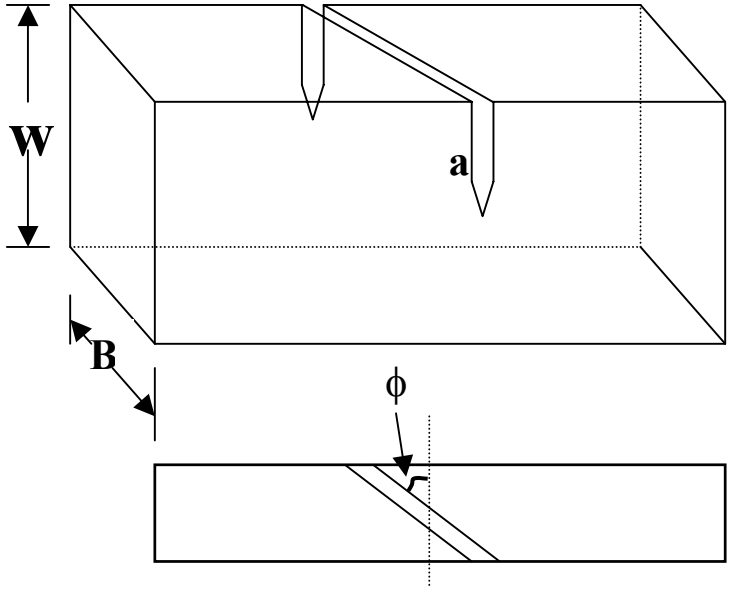

Fig.1. SENB specimen geometry used for mixed mode I/III fracture toughness evaluation of mild steel

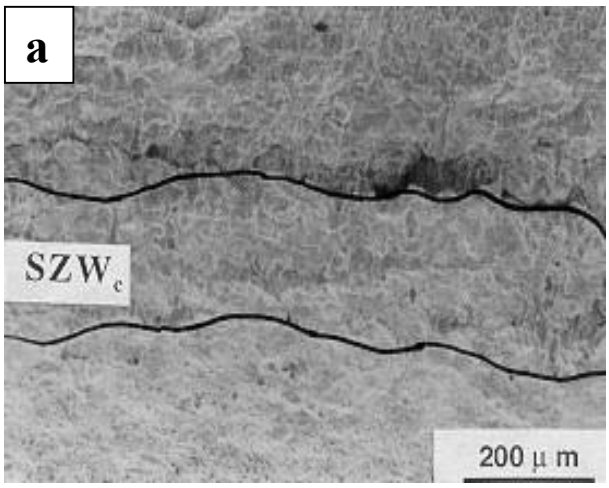

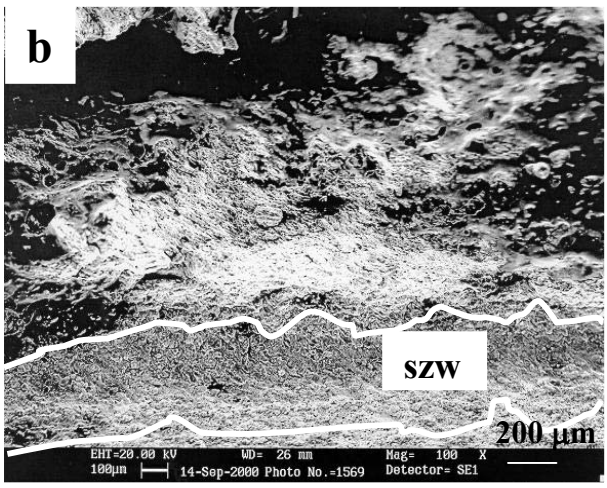

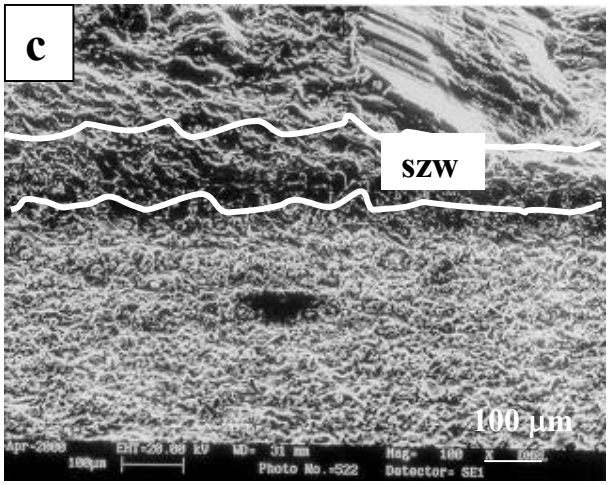

Fig.2.SEM fractograph illustrating szw_c for (a) ϕ=0°, (b) ϕ=30°, (c) ϕ=45° for load line displacement corresponding to 6.0 mm displacement.

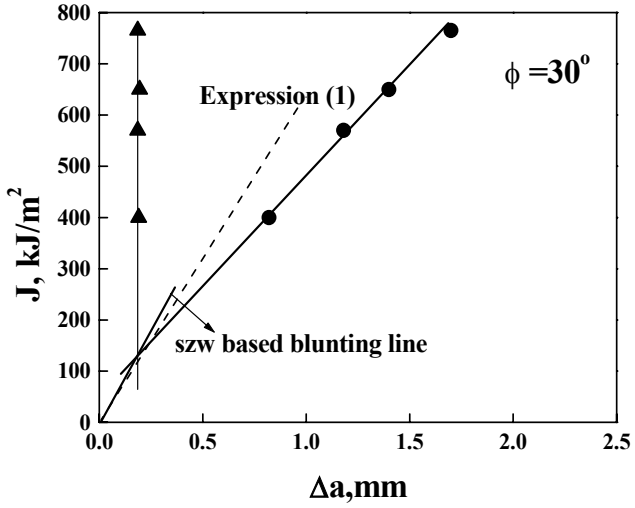

Fig.3 J - Δa plot of mild steel for $\phi = 30^o$

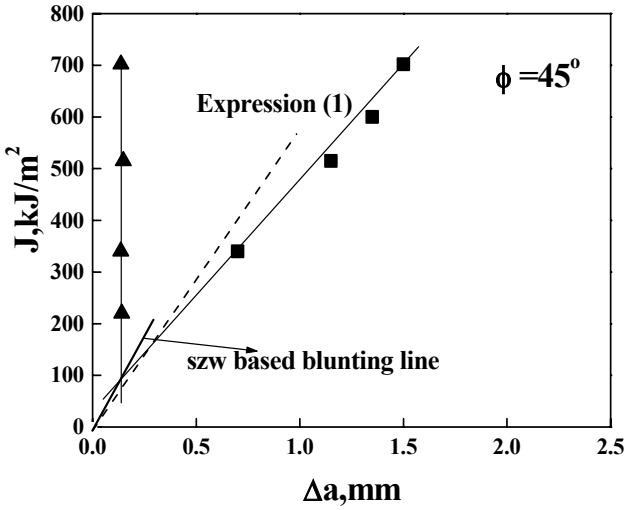

Fig.4. J - Δa plot of mild steel for $\phi = 45^o$

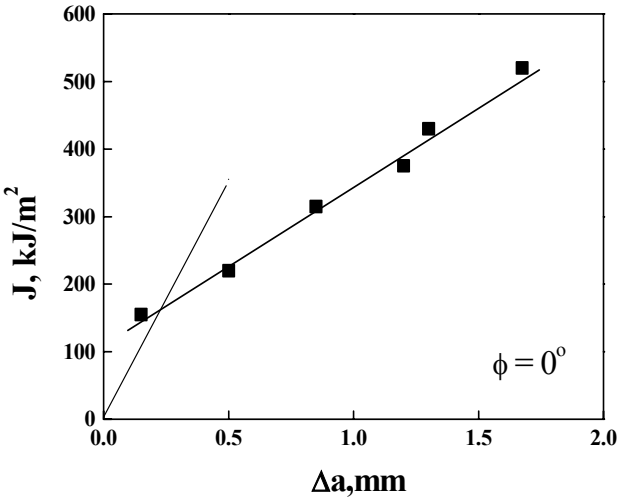

Fig. 5 J - Δa plot of mild steel for $\phi = 0^o$

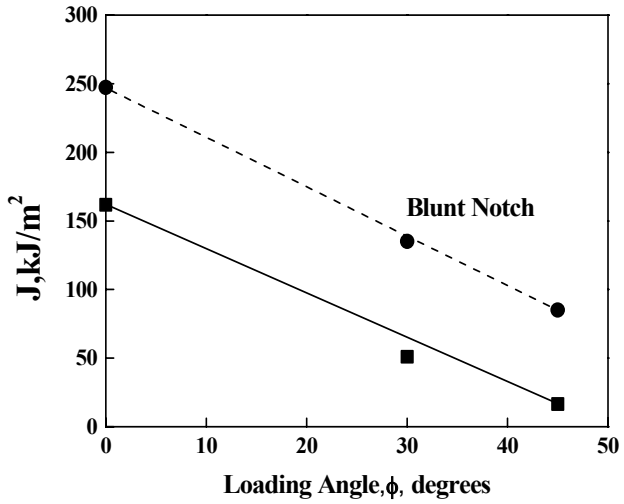

Fig.6. Variation of mixed mode I/III fracture toughness with loading angle

ORAL/POSTER REFERENCE: ICF100381OR

MODE-I DELAMINATION CHARACTERISATION OF CROSS-PLY FIBER-METAL LAMINATES

J. Laliberté[1], P. V. Straznicky[1], and C. Poon[2]

[1]Department of Mechanical and Aerospace Engineering, Carleton University, 1125 Colonel By Drive, Ottawa, ON, K1S 5B6 CAN
[2]Institute for Aerospace Research, National Research Council of Canada, 1500 Montreal Road, BLDG M-14, Ottawa, ON, K1A 0R6 CAN

ABSTRACT

A series of delamination characterisation tests have been carried out on cross-ply fiber-metal laminates (FMLs). These tests were carried out to improve the accuracy of low-velocity impact finite element simulations with a potential new aircraft material. Three variants of the commercially available material known as GLARE (GLAss REinforced) aluminum laminates were employed. These tests were conducted using a modified double-cantilever beam (DCB) test specimen. The results showed that the Mode-I energy release rate (G_{IC}) has limited dependence on the lay-up of the FML. A modified data reduction scheme was developed to reduce the static load data to G_{IC} values. This scheme gave lower values than several other data-reduction methods because it accounted for the deformation of the adherends in the DCB specimens. Fiber-bridging was observed during the DCB tests, however, since the same phenomenon is observed in the impact simulations the G_{IC} data could still be applied to the simulations.

KEYWORDS

Fiber-metal laminate, delamination, finite element modelling, fiber-bridging, GLARE, energy release rate

INTRODUCTION

Fiber-metal laminates (FMLs) are a relatively new class of aerospace materials that consist of metal layers and fiber-reinforced polymer layers bonded together [1, 2 and 3]. Structures manufactured from these materials can benefit greatly from the laminates' increased strength, reduced density and increased resistance to different forms of damage compared to monolithic aluminum. Carleton University, in partnership with the National Research Council of Canada's (NRCC) Institute for Aerospace Research (IAR) and Bombardier Aerospace has been investigating the impact damage resistance of traditional composites and these new hybrid materials [4, 5 and 6]. Currently a finite element (FE) model of low-velocity impact damage in FMLs is being developed. Figure 1 shows the behaviour of the LS-DYNA explicit FE simulation without accounting for the effect of fiber bridging. As can be seen, there is exaggerated deformation and delamination damage. Although there is some data available in literature on the Mode I delamination behaviour of unidirectional FMLs [7] there is none on the behaviour of cross-ply FMLs. Finite element simulations have shown that Mode I behaviour dominates the propagation of the delamination damage in low velocity impact of GLARE. The subsequent sections of this paper will describe the characterisation of the Mode I (opening) delamination behaviour of cross-ply GLARE variants.

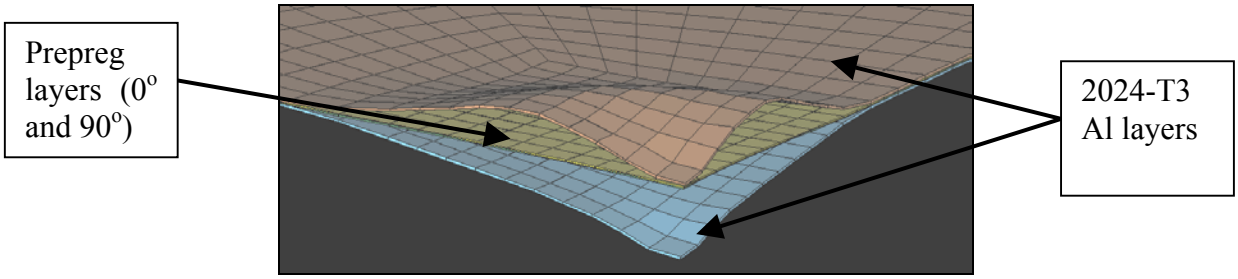

Figure 1: Low velocity impact simulation of GLARE without fiber-bridging correction.

DELAMINATION TESTING OF FIBER-METAL LAMINATES

Interlaminar cracking or delamination is a significant failure mode in fiber-metal laminates. The presence of delamination has been shown to influence the initiation and propagation of fatigue damage [8 and 9]. Delamination propagation in FMLs can be influenced by geometry, material discontinuities and typically consists of coupled Mode I, II and III fracture behaviours defined as opening, in-plane shear and transverse in-plane shear. Finite element modelling of the full structural situation can then provide estimates of the relative contributions of each damage mode. For instance, in FML impact simulations Mode II dominates at the outset of impact and Mode I dominates during the impactor rebound phase. Thus Mode II properties are important for initiation and Mode I behaviour influences the ensuing delamination propagation. It is therefore important to study each mode separately before attempting to combine them in an FE model.

While delamination testing has been carried out on traditional composite materials by numerous other researchers comparatively little work has been conducted with FMLs. This research has mainly centred on delamination in adhesively bonded FML splice joints as well as delamination resulting from crack propagation [7, 10, 11, 12, 13 and 14]. A modified double cantilever beam (DCB) test specimen (Figure 2) was employed by Vlot and van Ingen [7] to determine the Mode I G_{IC} properties of unidirectional variants of GLARE. The data reduction method used by Vlot and van Ingen was based on classical beam bending theory combined with considerations for the rotation of the two arms at the delamination crack tip. Several other schemes for determining the value of G_{IC} from experiments are summarised in Table 1. The area method and modified area method use the area enclosed by the segments of the load-displacement curve shown in Figure 3. The modified area method contains corrections that are explained below. The displacement method uses the crosshead displacement and the crack opening displacement to find G_{IC}. Finally the compliance method uses the relationship between the compliance (C) of the specimen and the crack tip displacement (a). Readers are directed to the references for the full derivation of the formulae.

TABLE 1
SUMMARY OF DCB DATA REDUCTION METHODS.

Method	G_{IC} Formula	Ref.
Modified Area Method	$G_{IC} = \frac{P^2}{bE_{11}^* I^*}\left[a^2 + \frac{2a}{\lambda} + \frac{1}{\lambda^2}\right]$ (1)	15
Area method	$G_{IC} = \frac{4P^2 a^2}{bE_x I_x}$ (2)	15
Displacement Method	$G_{IC} = \frac{3P\delta}{2ba}$ (3)	16
Compliance Method	$G_{IC} = \frac{P^2}{2b}\frac{dC}{da}$ (4)	16

In Table1 P is the applied load, a is the crack length, I_x is the moment of inertia in the axial direction of the beam, I^* is the modified moment of inertia calculated using the constituent properties, E is the modulus of the material under consideration, E_{11}^* is the modified modulus calculated from the constituent properties, C is the compliance of the specimen (also δ/P), δ is the crosshead displacement, λ is defined below, and b is the width of the specimen.

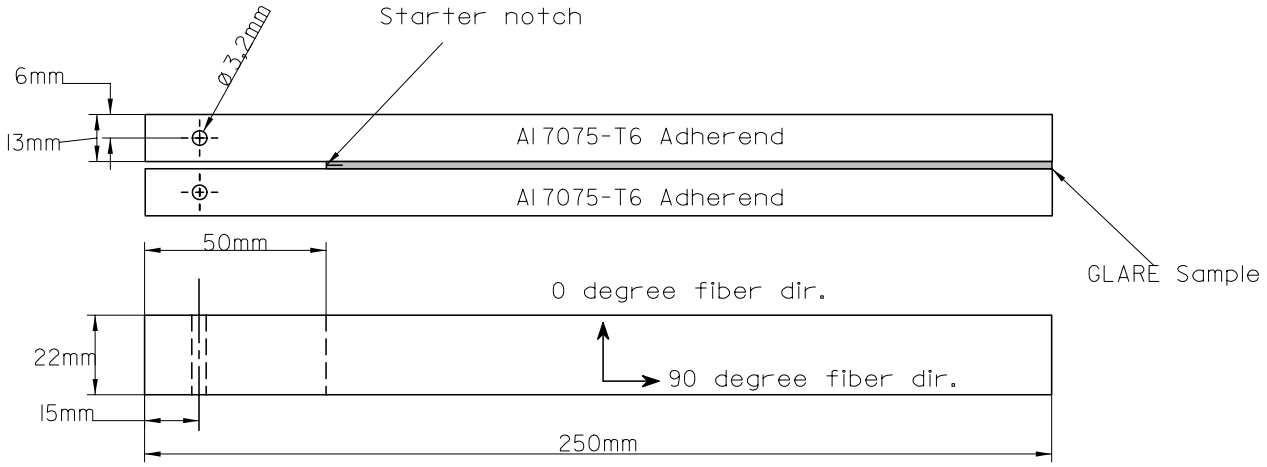

Figure 2: DCB specimen configuration.

The modified area method was developed by Kanninen [15] and presented in terms of the stress intensity factor. This relationship can be further modified to yield the Mode I energy release rate, G_{IC}. Vlot and van Ingen [7] applied this relationship to the results of their experimental testing. The test method employed for the tests described herein employs repeated loading and unloading cycles, which is different than that employed by Vlot and van Ingen. The modified area method is then used to calculate the energy released during the delamination propagation. This method takes into account the curvature of the DCB arms through the application of simple beam theory. The governing differential equation for the deflection, w, of the beam is:

$$\frac{d^4 w}{dx^4} + 4\lambda^4 H(x) w = 0 \tag{5}$$

where

$$H(x) = \begin{cases} 1, x > 0 \\ 0, x < 0 \end{cases}, \quad \lambda = \left[\frac{k}{4E_{11}^* I^*} \right]^{1/4} \text{ and } k = \frac{2bE_{22}}{h}$$

Where E_{22} is the modulus is the transverse modulus and h is the height of the specimen. From the solution of this differential Eqn. 5 a relationship for the specimen compliance can be developed that leads to the strain energy for the specimen, W. The stress intensity factor, K, can be related to the energy release rate for constant displacement as (Crews and Reeder [17]):

$$K^2 = -\frac{E}{b}\frac{dW}{da} = -2EG_{IC} \tag{6}$$

Substituting in the solution of Eqn. 5 and simplifying yields the relationship shown in Eqn. 1 in Table 1.

EXPERIMENTAL TESTING

Apparatus and DCB Specimen

Three variants GLARE were employed for these tests. The lay-ups were GLARE-3-2/1 [Al/(0^o/90^o)/Al], GLARE-4-2/1 [Al/(0^o/90^o/0^o)/Al] and GLARE-5-2/1 [Al/(0^o/90^o/90^o/0^o)/Al]. The ply angles are relative to the long axis of the DCB specimen (Figure 2). These particular variants of GLARE were selected in order to study the effect of lay-ups on Mode-I delamination behaviour. Also, there was a lack of published data concerning the Mode-I behaviour of these materials and LS-DYNA impact modelling required this data to accurately simulate the impact events. Earlier durability testing at NRCC made extensive use of these materials [3]. The specimens were prepared as shown in Figure 2. The specimen was loaded in an MTS hydraulic load frame through pins inserted in the holes near the end of the specimen. A 5 mm starter notch was introduced in the FML specimen using a diamond saw. They were then loaded quasi-statically at a rate of 5 mm/min under displacement control until the first evidence of cracking occurred on the load curve. The load was then reduced to zero at the same rate. This procedure was repeated several times for each specimen until complete failure. The amount of crack propagation during each loading step was recorded.

Results

A sample load versus crosshead displacement curve is shown in Figure 3. Each loading repetition is shown on the graph. The initial and final crack tip displacement was recorded for each load step. The final G_{IC} results are summarised in Table 2 for all of the GLARE variants, averaged for each specimen group (5 specimens per group). The differences in the values calculated using the three different methods will be discussed in the subsequent section.

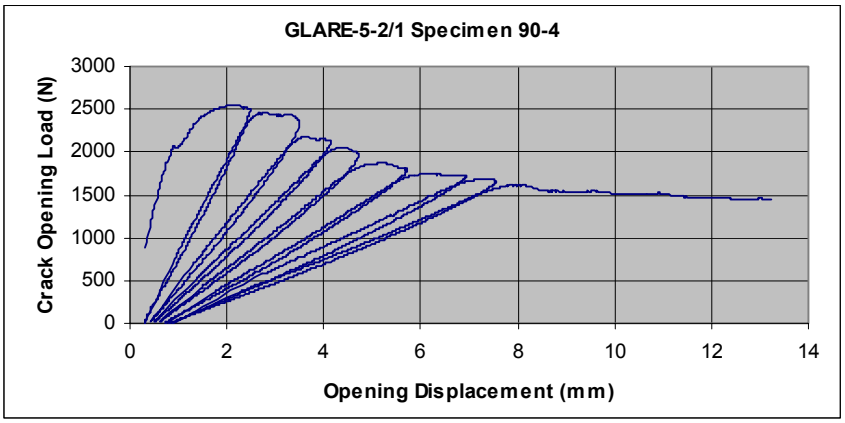

Figure 3: Sample load curve from Mode-I delamination characterisation test.

TABLE 2
MEASURED OF G_{IC} VALUES

Material	Average Measured G_{IC} Values		
	Modified Area [17]	Area [16]	Displacement [16]
	N/mm	N/mm	N/mm
GLARE-3	1.71	2.50	2.55
GLARE-4	2.24	3.13	2.46
GLARE-5	2.34	3.48	3.54

Extensive fiber bridging was also noted following examinations of the fracture surface of the specimens (Figure 4 and Figure 5a). The delamination cracks propagated in prepreg layers with the fiber oriented parallel to the delamination direction. Each of the three types of GLARE exhibited the same behaviour. This indicates that the "path of least resistance" through the prepreg layer is parallel to the fibers rather than perpendicular. The fibers pull away from the matrix and produce the fracture surface shown in Figure 4.

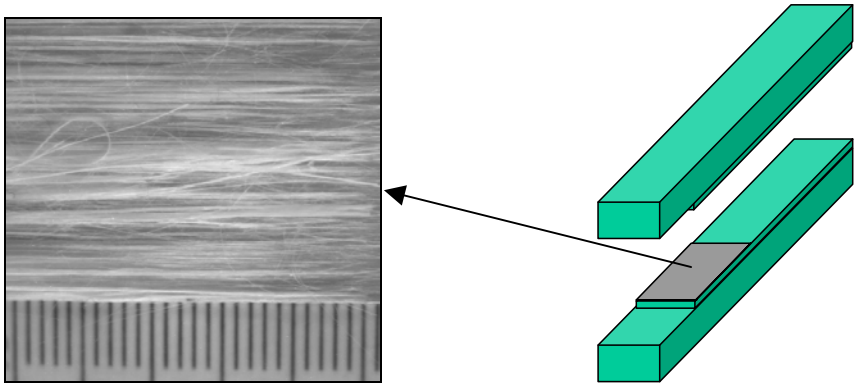

Figure 4: Optical micrograph of the "hairy" failure surface in a typical FML DCB specimen**.**

It is well documented that fiber bridging affects the measured G_{IC}. Other phenomena, such as crack jumping between layers influence this property as well. However, if the material exhibits the same damage modes in its final application as observed in coupon tests then the results can be applied to the full-scale structure.

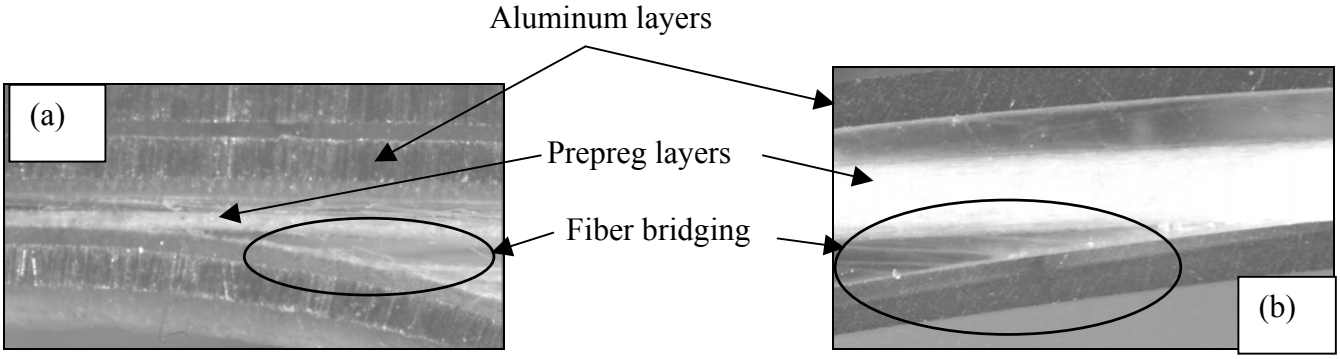

Figure 5: (a) Fiber bridging in a typical FML DCB specimen and (b) in an impacted FML specimen.

Discussion of Results

The differences between the G_{IC} values calculated by each of the methods in Table 2 can be attributed to the assumptions made in the development of the data reduction methods, specifically:

- The modified area method contains corrections for the bending of the adherends. The flexibility of the adherends affects the measured load-displacement response of the DCB specimen. Also, some of the energy stored in the specimen is stored as elastic strain energy in the aluminum adherends.
- The area method does not take the specimen flexibility into consideration and thus produces a higher calculated value of G_{IC}.
- The displacement method is based on the measured crack opening displacement of the specimen. There is no direct accounting for the stiffness of the specimen or the adherends. As with the area method this results in a G_{IC} that includes strain energy effects of the specimen and also the load frame if an extensometer is not used to measure the crack opening displacement.

MODELLING OF DELAMINATION DAMAGE IN FMLS

Following the completion of the DCB testing the results were then employed to generate crack opening load curves that relate the crack opening stress to the displacement. This information was used to improve the LS-DYNA low velocity impact simulations described earlier. The resulting behaviour more closely resembles that observed in the experimental low-velocity impact tests (Figure 6a and Figure 6b). LS-DYNA simulations were generated of the DCB specimens. By applying the load values measured during the DCB experiments to the FE simulations it was possible to develop a preliminary load versus displacement curve incorporating the effects of fiber bridging.

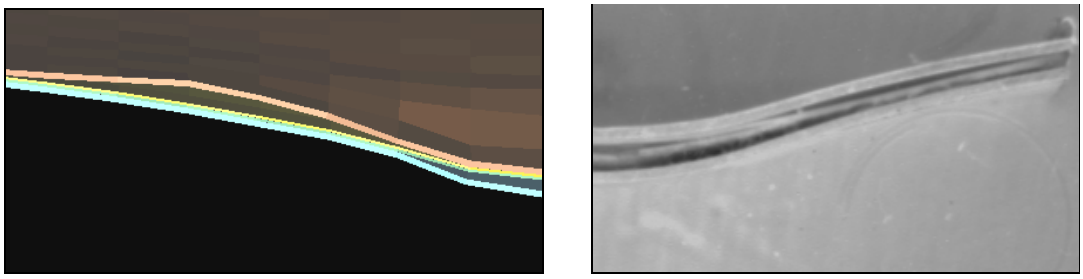

Figure 6: (a) Corrected low velocity impact simulation result (b) impacted FML specimen.

CONCLUSIONS AND FUTURE WORK

The Mode-I delamination behaviour of several GLARE cross-ply laminates has been investigated using double cantilever beam specimens. The data from the tests were reduced to G_{IC} using three different techniques. Differences between the G_{IC} results were explained based on the formulation of the data reduction methods. Fiber bridging was noted in the DCB specimens, however the same damage mode was observed in impacted specimens. Therefore, the G_{IC} data is valid provided the damage modes between the coupon tests and the final structure are the same. Since this is the case with the experimental impact simulations the DCB test results are applicable to the LS-DYNA simulations. The LS-DYNA simulations were successfully improved in accuracy using the DCB test data.

The next phase in this research will involve estimating the energy released during impact by measuring the delaminated area. Knowing the G_{IC} for the material will allow a comparison between the experimental value of absorbed energy and the FE derived value.

ACKNOWLEDGEMENTS

The authors would like to thank Tom Benak and Tony Marincak of NRCC for their invaluable and dedicated technical assistance with the experimental test portion of this project. Sincere gratitude is also due Katherine McCuaig, a senior undergraduate student from Carleton University who provided much assistance to the development of the DCB specimens and test methodology. Bombardier Aerospace also provided financial assistance through the NRC-Bombardier Collaborative FML Durability Project (NRC Project number 46-QJO_18).

REFERENCES

1. Lawcock, G., Ye, L. and Mai, Y-W. (1995) *SAMPE Journal* 31, 23.
2. Asundi, A. and Choi, Alta Y.N. (1997) *J. Mat. Processing Technology* 63, 386.
3. Laliberté, J., Poon, C. and Straznicky, P.V. (1999) IAR LTR-ST-2231, NRC Canada.
4. Veitinghoff, H. E. (1994) MEng Thesis, Carleton University, Canada.
5. Majeed, R. O. (1995) MEng Thesis, Carleton University, Canada.
6. Fouss, E. O. (1996) MEng Thesis, Carleton University, Canada.
7. Vlot, A. and van Ingen, J. W. (1998) *J. Composite Mat.* 32, 1805.
8. Li, K., Chudnovosky, A., Kin, Y and Macheret, J. (1995) *Poly. Composites* 15, 52.
9. Li, E. and Johnson, W. S. (1998) *J. Composites Tech. and Research* 20, 3.
10. Yeh, J. R. (1988) *Eng. Fract. Mech.* 30, 827.
11. Vries, T.J. de, Vlot, A. and Hashagen, F. (1999) *Composite Struct.* 46, 131.
12. Lin, C.T. and Kao, P.W. (1996) *Acta Materialia* 44, 1181.
13. Hashagen, F., de Borst, R. and de Vries, T. (1999) *Composite Struct.* 46, 147.
14. Guo, Y.J., Wu, X.R. and Zhang, Z.L. (1997) *Fatigue Fract. Eng. Mat. Struct.* 20, 1699.
15. Kanninen, M. F. (1973) *Int. J. Fract.* 9, 83.
16. Hashemi, S., Kinloch, A., Williams, J. (1989) *J. Mat. Sci. Letters* 8, 125.
17. Crews, J.H. and Reeder, J. R., NASA TM 100662, 1988.

ORAL/POSTER REFERENCE: ICF100247PR

MODEL OF MECHANICS FOR FIBER REINFORCED TI ALLOY MATRIX COMPOSITES UNDER THERMOMECHANICAL LOADING

Li-Sha Niu[1], Qi-Yang Hu[1], Hui-Ji Shi[1] and Claude Robin[2]

[1]Department of Engineering Mechanics, Tsinghua University,
Beijing 100084 P. R. China

[2]Mechanical Depqrtment, Ecole des Mines de Douai, Douai 59500 France

ABSTRACT

A micromechanical model of fiber-reinforced metal matrix composites is established with considering the coating effects. During the investigation, the coatings and fibers are assumed to have a linearly elastic behavior, and the matrix respond viscoplastically with temperature. Micro-mechanics theories using the concepts of average stress and strain are adopted and developed to integrate matrix, coating and fiber properties for predicting the stress-strain response under thermomechanical loading. Considering the viscoplastic behavior of metal matrix, the Bodner-Partom unified theory is used as the basic constitutive equations of metal matrix. The main problem is reduced to a set of the ordinary differential equations of one order that can be resolved by numerical solution algorithms. In the application, three-layer model is applied to analyze the stress-strain response of a titanium matrix composite. Through the calculation, first, the thermo-residual stresses in the constituents of the material are obtained, then, the mechanical behaviors are estimated under the loading of thermomechanical cycles in the in-phase and out-of-phase cases.

KEYWORDS

thermomechanical loading, metal matrix composite, coating effects, temperature cycle, viscoplasticity

INTRODUCTION

The use of fiber-reinforced metal matrix composites in design has increased significantly in recent years with the development of aerospace industry [1,2]. Therefore, the knowledge of thermomechanical behavior of the materials is very important for designing the structures of the materials. In the past, several of these studies were limited to two-layer models that paid relatively less attention to the effects of coatings on the residual stress and assumed only two linking types: bonding and slipping, existing between metal matrix and fiber. However, the effect of coating could not be ignored, as some relevant investigations indicated [3].

During the investigation, a micromechaical model for fiber-reinforced metal matrix composites with coating materials is presented. The model considers that the coating and fibers have a linearly elastic behavior, but the matrix responds viscoplastically with temperature. Micromechanical theories using the concepts of average stress and strain are adopted and developed to integrate fibers and matrix properties for predicting the response

of unidirectional composites. The stress-strain equations are used to the basic three-layer models of metal matrix composites. Then the main problem is reduced to a set of ordinary differential equations. Numerical solution algorithms are developed to achieve the mechanical behavior of the composites by varying thermal and mechanical loading. The thermo-residual stress in fabrication of a fiber-reinforced titanium matrix composite is analyzed and the stress-strain response under the loading of thermomechanical cycles is emphatically estimated in this investigation.

MICRO-MECHANICAL MODEL WITH COATING CONCEPT

The Representative Volume Element (RVE) of unidirectional fiber-reinforced matrix composites is used to describe the stress-strain state. The selection of the RVE and the coordination is shown in Figure 1.

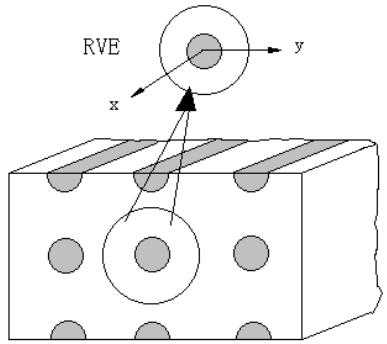

Figure 1: Selection of the RVE and the coordination

The concepts of average stress and strain are adopted in the model [4]. Suppose the stress field in a representative volume, V, of a unidirectional composite is denoted as σ_v. The volume average stress σ of the composite are defines by

$$\sigma = \frac{1}{V}\int_V \sigma_v dV = \frac{1}{V}\left(\int_{V^m} \sigma_v dV + \int_{V^c} \sigma_v dV + \int_{V^f} \sigma_v dV\right) \tag{1}$$

where V^f, V^c and V^m are the fiber, coating and matrix volume, respectively. The volume average stresses of the matrix, coating and fibers are described as follows

$$\sigma^m = \frac{1}{V^m}\int_{V^m} \sigma_v dV \ , \quad \sigma^c = \frac{1}{V^c}\int_{V^c} \sigma_v dV \ , \quad \sigma^f = \frac{1}{V^f}\int_{V^f} \sigma_v dV \tag{2}$$

Similarly to the stresses, by introducing $\boldsymbol{\varepsilon}^m$, $\boldsymbol{\varepsilon}^c$ and $\boldsymbol{\varepsilon}^f$ as the volume average strains of the matrix, coating and fibers, respectively, the stresses $\boldsymbol{\sigma}$ and the strains $\boldsymbol{\varepsilon}$ of the composite can be expressed as

$$\begin{cases} \sigma = v^m\sigma^m + v^c\sigma^c + v^f\sigma^f \\ \varepsilon = v^m\varepsilon^m + v^c\varepsilon^c + v^f\varepsilon^f \end{cases} \tag{3}$$

The superscripts *m, c* and *f* indicate the matrix, coating and fiber, and v^m, v^c and v^f are the volume fractions of the matrix, coating and fiber, respectively.

Assuming that the deformation of the RVE is infinitesimal and the total strain can be decomposed into elastic, thermal and plastic components, and the fibers exhibit transverse-isotropic thermoelastic behaviors and the matrix has thermo-elasto-viscoplastic behaviors. Then, we have the incremental stress-strain relationship for the matrix

$$d\boldsymbol{\varepsilon}^m = \underline{S}^{me} d\boldsymbol{\sigma}^m + d\boldsymbol{\varepsilon}^{mT} + d\boldsymbol{\varepsilon}^{mp} \tag{4}$$

and the linear elastic stress-strain relationship for the fiber and coating

$$d\boldsymbol{\varepsilon}^c = \underline{S}^{ce} d\boldsymbol{\sigma}^c + d\boldsymbol{\varepsilon}^{cT} \tag{5}$$

$$d\boldsymbol{\varepsilon}^f = \underline{S}^{fe} d\boldsymbol{\sigma}^f + d\boldsymbol{\varepsilon}^{fT} \tag{6}$$

The superscript *e*, *p*, and *T* denote the elastic, plastic (inelastic) related components and temperature, respectively. S^{me}, S^{ce} and S^{fe} are the elastic compliance matrices of matrix, coating and fiber, respectively, which read for the plane stress case.

The matrix, coating and fiber thermal strains in Equations (5), (6) and (7) are assumed to be linearly dependent upon the temperature difference ΔT and can be written as

$$\boldsymbol{\varepsilon}^{mT} = \boldsymbol{\lambda}^m \Delta T \ , \ \boldsymbol{\varepsilon}^{cT} = \boldsymbol{\lambda}^c \Delta T \ , \ \boldsymbol{\varepsilon}^{fT} = \boldsymbol{\lambda}^f \Delta T \tag{7}$$

where $\boldsymbol{\lambda}$ are the thermal expansion coefficients. The strains of the matrix, coating and fiber within a layer along the fiber direction can be considered as:

$$\varepsilon_x^m = \varepsilon_x^c = \varepsilon_x^f \tag{8}$$

In the three-layer model, the transverse matrix stress can be related to the fiber stress and coating stress in a form

$$\sigma_y^m = \eta_y^{mc} \sigma_y^c + \eta_{yx}^{mc} \sigma_x^c \tag{9}$$

$$\sigma_y^c = \eta_y^{cf} \sigma_y^f + \eta_{yx}^{cf} \sigma_x^f \tag{10}$$

where the subscript *x* and *y* denote the direction parallel and normal to the fibers, respectively. η_y^{mc}, η_{yx}^{mc}, η_y^{cf} and η_{yx}^{cf} are the stress partitioning factors.

Combining Equations above, we can obtain the expression for the relationship between matrix stress and coating stress in an incremental form as

$$d\boldsymbol{\sigma}^m = \underline{C}_1 d\boldsymbol{\sigma}^c + \underline{C}_2 \left(d\boldsymbol{\varepsilon}^{cT} - d\boldsymbol{\varepsilon}^{mT} - d\boldsymbol{\varepsilon}^{mp} \right) \tag{11}$$

and the relationship between coating stress and fiber stress as

$$d\boldsymbol{\sigma}^c = \underline{B}_1 d\boldsymbol{\sigma}^f + \underline{B}_2 \left(d\boldsymbol{\varepsilon}^{fT} - d\boldsymbol{\varepsilon}^{cT} \right) \tag{12}$$

and the relationship between matrix stress and fiber stress as

$$d\boldsymbol{\sigma}^m = \underline{A}_1 d\boldsymbol{\sigma}^f + \underline{A}_2 d\boldsymbol{\varepsilon}^{cT} + \underline{A}_3 d\boldsymbol{\varepsilon}^{fT} + \underline{A}_4 \left(d\boldsymbol{\varepsilon}^{mT} + d\boldsymbol{\varepsilon}^{mp} \right) \tag{13}$$

where C_1 , C_2 , B_1 and B_2 are the coefficients related to the Young's modulus, volume percentage and stress partitioning factors of each constituent, and $\underline{A}_1 = \underline{C}_1 \underline{B}_1$, $\underline{A}_2 = -\underline{C}_1 \underline{B}_2 + \underline{C}_2$, $\underline{A}_3 = \underline{C}_1 \underline{B}_2$, and $\underline{A}_4 = -\underline{C}_2$.

The Bodner-Partom unified theory of viscoplasticity is used to establish the basic constitutive models of metal matrix.

(a) Flow law is described as

$$\varepsilon_{ij}^{\ p} = \lambda S_{ij} \tag{14}$$

where S_{ij} is the deviatoric stress related to the stress tensor by $S_{ij} = \sigma_{ij} - \frac{1}{3}\delta_{ij}\sigma_{kk}$.

(b) Scalar kinetic equation is described as

$$D_2^{\ p} = D_0^{\ 2} \exp\left\{-\left[\frac{(Z)^2}{3J_2}\right]^n\right\} \tag{15}$$

with $D_2^{\ p} = \frac{1}{2}\dot{\varepsilon}_{ij}^{\ p}\dot{\varepsilon}_{ij}^{\ p}$, $J_2^{\ p} = \frac{1}{2}S_{ij}S_{ij}$, $Z = Z^I + Z^D$, $\lambda^2 = D_2^{\ p}/J_2$, and J_2^p is the second invariant of the deviatoric stress, and Z^I and Z^D represent the hardening due to isotropic and directional characteristics, respectively.

(c) Isotropic hardening relationship is described as

$$\dot{Z}^I = m_1\dot{W}_p\left(Z_1 - Z^I\right) - R_1 Z_1\left(\frac{Z^I - Z_2}{Z_1}\right)^{r_1} + \dot{T}\left[\left(\frac{Z^I - Z_2}{Z_1 - Z_2}\right)\frac{\partial Z_1}{\partial T} + \left(\frac{Z_1 - Z^I}{Z_1 - Z_2}\right)\frac{\partial Z_2}{\partial T}\right] \tag{16}$$

with W_p is the inelastic work per volume, and $\dot{W}_p = \sigma_{ij}\dot{\varepsilon}'_{ij}$, $Z^I(0) = Z_0$, $\dot{W}_p(0) = 0$.

(d) Kinematic hardening relationship is described as

$$Z^D = \beta_{ij}u_{ij} \tag{17}$$

$$\dot{\beta}_{ij} = m_2\dot{W}_p\left(Z_3 u_{ij} - \beta_{ij}\right) - R_2 Z_1\frac{\beta_{ij}}{\sqrt{\beta_{kl}\beta_{kl}}}\left(\frac{\sqrt{\beta_{kl}\beta_{kl}}}{Z_1}\right)^{r_2} + \dot{T}\frac{\beta_{ij}}{Z_3}\frac{\partial Z_3}{\partial T} \tag{18}$$

$$u_{ij} = \frac{\sigma_{ij}}{\sqrt{\sigma_{kl}\sigma_{kl}}} \tag{19}$$

In the equations presented, the quantities D_0, n, m_1, m_2, Z_1, Z_2, Z_3, R_1, R_2, r_1 and r_2 are material parameters to be determined. D_0 is a parameter representing the limiting value of the plastic strain rate under shear, usually assumed to be equal to 10^{-4} sec^{-1}, except for cases of very high strain values. n is a parameter related to the viscosity of dislocation motion and controlling the strain rate sensitively. m_1 and m_2 are material parameters controlling the hardening recovery rate; Z_1 is the saturation value for Z for high inelastic work, i.e. the maximum value of Z (a material constant). Z_2 is a parameter corresponding to the state of full thermal recovery. Z_3 is a variable characterizing the directional (anisotropic) hardening; R_1 and R_2 are parameters characterizing the hardening recovery rate; r_1 and r_2 are indices of the hardening recovery rate.

From equation (14) and (15), we can obtain:

$$\dot{\varepsilon}_{ij}^{\ p} = D_0\exp\left[-\frac{1}{2}\left(\frac{\left(Z^I + Z^D\right)^2}{3J_2}\right)^n\right]\frac{\sigma'_{ij}}{\sqrt{J_2}} \tag{20}$$

Substituting the relationship between matrix stress and the plastic strain in equation (16)-(19) into equation

(20), we can get the independent differential equations about the metal matrix stress. Then the main problem is reduced to three variables: matrix stress, the isotropic hardening variable and the directional-hardening variable. The equation (16), (18) and (20) that are related to these three variables can constitute a set of ordinary differential equations:

$$\begin{cases} \dot{\sigma}^m = f\left(\sigma^m, Z^I, \beta, T\right) \\ \dot{Z}^I = g^I\left(\sigma^m, Z^I, T\right) \\ \dot{\beta} = g^D\left(\sigma^m, \beta, T\right) \end{cases} \tag{21}$$

Given initial conditions, boundary conditions and a superposition of thermal and mechanical loads, equation (21) can be solved based on the classic fourth order Runge-Kutta method.

STRESS ANALYSIS OF TI MMCS UNDER THERMOMECHANICAL LOADING

A Ti-6Al-4V matrix composite reinforced with SCS-6 carborundum fibers was assumed to be stress free at a fabrication temperature of 900°C and then cooled down to room temperature, 25°C. The composite system analyzed consists of the titanium-based-alloy matrix with a 0.66 volume fraction, the fiber with 0.339 and the coating with 0.001. The coating behaviors are assumed as: the elastic modulus is equal to 200 GPa; the coefficient of thermal expansion is equal to 7.0×10^{-6}/°C. When the temperature drops from 900°C to 25°C, different thermo-residual stresses arise in the constituents of the material. The longitudinal stress in the matrix and coating is positive, and in the fiber is negative. The transverse stress in the matrix is positive, and in the coating and fiber is negative. The shearing stress is the highest in the fiber. For example, Figure 2 gives the variation of the longitudinal residual stress along with the temperature in different constituents of the material.

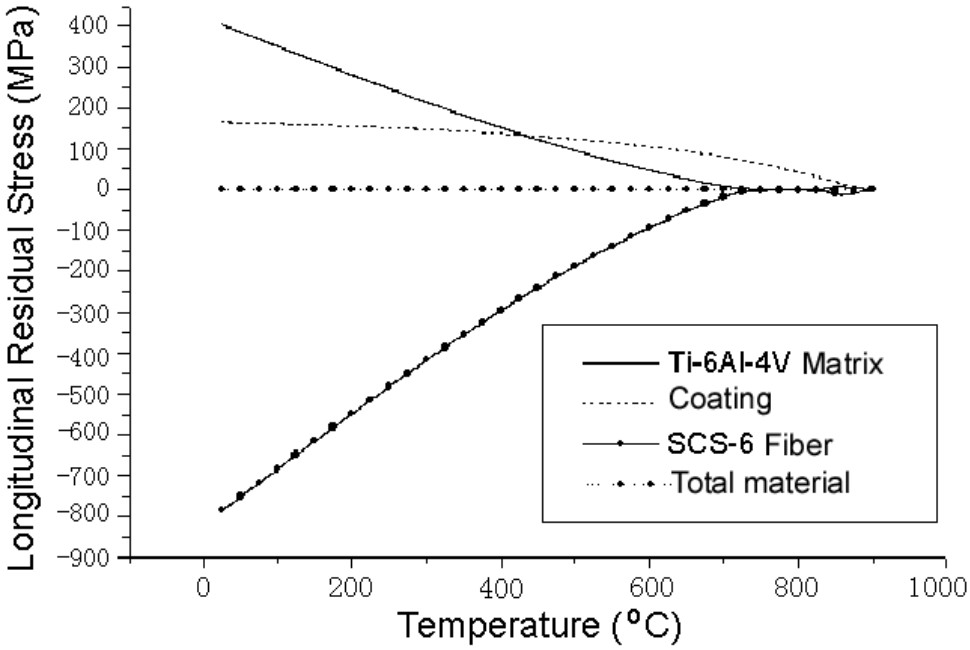

Figure 2: Variation of the residual stress along with the temperature

The mechanical behaviors of the material under thermomechanical loading are obtained by composing tow cycles in in-phase or out-of-phase: temperature cycle of 150~650°C and mechanical strain cycle of -0.004~0.004 in longitudinal direction. In the in-phase case, the maximum tensile strain coincides with maximum temperature. In the out-of-phase case, the maximum compressive strain occurs at maximum temperature. Three cycles are performed in calculation. Before le first cycle, the material is considered at the temperature of 25°C and the thermo-residual stress has exhibited in it. The results of calculation show that in the first cycle of loading there is an inelastic stage because of the thermo-residual stress in the material. The

stability of stress-strain response emerged from the second cycle of loading since the plastic deformation is not great in the first cycle. Comparing the in-phase case with the out-of-phase case, one finds that the stresses of the material in the out-of-phase case are greater than that in the in-phase case. Figure 3a shows the longitudinal stress-strain response of the metal matrix from the first cycle to the third cycle in the out-of-phase case. Figure 3b shows the response of the total material in the same case.

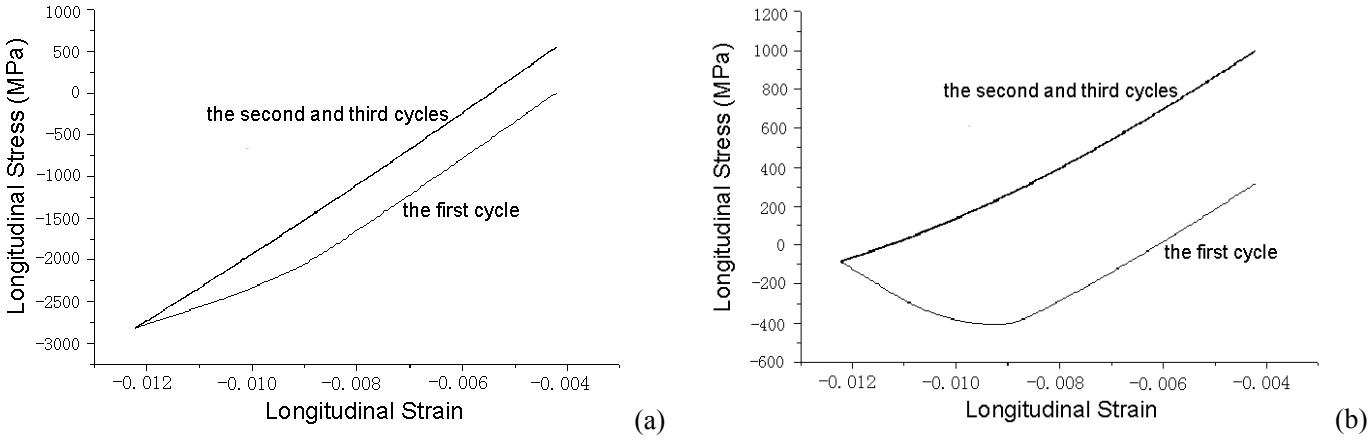

Figure 3: The stress-strain response in the out-of-phase case, (a) matal matrix, (b) total material

CONCLUSIONS

A three-layer micromechanical model of matrix/coat/fiber is used to analyze the stress-strain relationship of fiber-reinforces metal matrix composites under a superposition of thermal and mechanical loads. The concepts of average stress and strain are adopted and developed to integrate matrix, coating and fiber properties for predicting the response of unidirectional composites. The Bodner-Partom unified theory of viscoplasticity is applied to establish the basic constitutive models of metal matrix. The main problem then is reduced to a set of ordinary differential equations. In the application, three-layer model has adopted to analyze the stress-strain response of a titanium matrix composite. Through the calculation, first, the thermo-residual stresses in the constituents of the material are obtained, then, the mechanical behaviors are estimated under the loading of thermomechanical cycles in the in-phase and out-of-phase cases. The results should encourage the utilization of this model in the interface stress analysis and design of composite structures.

ACKNOWLEDGMENTS

We are grateful for the financial support provided by the Special Funds for the Major State Basic Research Projects G19990650 and the Chinese National Natural Science Foundation No. 59871022, as well as the Research Fund of the Nord-Pas de Calais Region of France.

REFERENCES

1. Neu, R., Coker, W.D. and Nicholas, T. (1996) *International Journal of Plasticity*, 12, 361.
2. Robertson, D.D. and Mall, S. (1994) *Composites Science and Technology,* 50, 483.
3. Warwick, C.M. and Clyne, T.W. (1991) *Acta. Met. et Mat.,* 39, 437.
4. Ha, S.K., Wang,Q. and Chang F.K. (1991) *Journal of Composites Materials,* 25, 334.
5. Brayshaw, J.B. and Pindera, M.J. (1996) *Journal of Engineering Materials and Technology*, 116, 505.

Ref No: ICF100221OR

Modeling of Crack-Opening Stress Levels under Different Service Loading Spectra and Stress Levels for a 1045 Annealed Steel

M. Khalil*, T. H. Topper and K. Soudki
University of Waterloo, Waterloo, Ontario, Canada

ABSTRACT

The crack opening stresses of a crack emanating from an edge notch in a 1045 annealed steel specimen were measured under three different Society of Automotive Engineers (SAE) standard service load histories having different average mean stress levels. The three spectra are the SAE Grapple Skidder history (GSH) which has a positive average mean stress, the Log Skidder history (LSH) which has a zero average mean stress, and the Inverse of the GSH (IGSH) which has a negative average mean stress. In order to capture the actual behavior of the crack opening stress in the material, the crack opening stress levels were measured using a 900X optical video microscope at frequent intervals for each set of histories scaled to two different maximum stress ranges.

The crack opening stresses were modeled assuming that the crack opening stress when it is not at the constant amplitude steady state level for a given stress cycle builds up as an exponential function of the difference between the current crack opening stress and the steady state crack opening stress of the given cycle unless this cycle is below the intrinsic stress range for crack growth or the maximum stress in the cycle is below zero in which case the crack opening stress does not change.

The crack opening stress model was implemented in a fatigue notch model and the fatigue lives of notched annealed 1045 steel specimens under the three different spectra scaled to several maximum stress levels were estimated. The average measured crack opening stresses were within between 8 and 13 percent of the average calculated crack opening stresses. The fatigue life predictions based on the modeled crack opening stresses and the fatigue notch model were in good agreement with the experimentally determined fatigue data.

KEYWORDS

Service spectrum – Crack-opening stress – Effective strain intensity factor – Steady state crack-opening stress.

INTRODUCTION

An empirical model for the steady state crack opening stress S_{op} under constant amplitude loading by DuQuesnay [*1*] gave good predictions of measured crack opening stress levels. Many researchers have documented the effects of variable amplitude loading on crack closure [*2-8*]. The application of a tensile overload can cause either an acceleration or a delay in crack growth. A post overload increase in crack closure level and crack growth retardation occurs when the applied overload is less than approximately one half the yield stress of the material [6, *9, 10,*]. An overload of much more than one half the yield stress of the material will decrease the crack closure level and accelerate crack growth. Applying an underload causes a flattening of the asperities in the crack wake, which decreases the crack closure level and in turn increases the effective stress intensity factor and accelerates crack propagation.

This research is aimed at providing crack closure inputs for modeling fatigue damage or crack growth in a specimen under service loading spectra. The crack opening stress behavior of cracked specimens under service loading spectra is modeled and the accuracy of the model is evaluated experimentally using measured crack closure data. This paper is a continuation to research previously presented by the authors [*11*] using the same load spectra in tests on a 2024-T351 aluminum alloy.

MATERIAL AND EXPERIMENTAL METHODS

The material used in this study is a SAE 1045 as received steel which is commonly used in the automotive industry. The chemical composition and mechanical properties of the material are given in Tables 1 and 2 respectively. All testing was carried out on round threaded specimens with a rectangular gauge length profile. The geometry and dimensions are shown in Figure 1. An edge notch of 0.6 mm diameter was machined into one side of the specimen, at mid length as shown in (Figure 1). Using a notched specimen allows the stresses to exceed the material yield stress at the notch root without buckling or tensile yielding of the whole specimen. This notch size was small enough that, once initiated, the crack rapidly grew out of the zone of influence of the notch.

The crack opening stress was measured using a 900x power short focal length optical video microscope at given cycles before and after an overload occurred. The procedure for measuring the crack opening stress was to stop the test at the maximum stress of the required cycle and then to decrease the load manually while observing the crack tip region in the monitor attached to the optical video until the crack surfaces start to touch each other. Two sets of readings were recorded for each given cyclic stress level, and the average were calculated.

Table 1 – Chemical Composition (percentage by weight)

Steel	C	Si	P	Mn	S	Fe
1045	0.46	0.17	0.027	0.81	0.023	rest

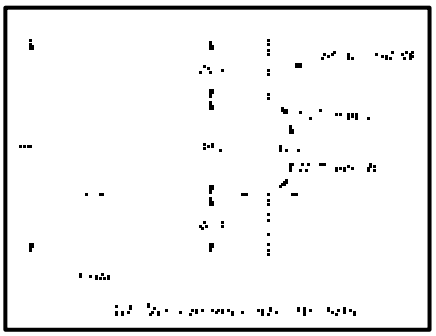

Figure 1 Specimen Geometry

Table 2 – Mechanical Properties of 1045 As-Received Steel

Mechanical Properties	Units	Magnitude
Modulus of Elasticity	MPa	206000
Tensile Yield Stress (0.2% offset)	MPa	761
Cyclic Yield Stress (0.2% offset)	MPa	580
Ultimate Tensile Stress	MPa	781
True Fracture Stress	MPa	647
Area Reduction	%	40

Crack opening stress model

Dabayeh and Topper [*12*] measured crack opening stress changes for various levels of tensile and compressive overloads followed by constant amplitude cycles having a variety of R-ratios.

The crack opening stress after being reduced by the overload increased to its steady state level in an approximately exponential manner. They showed that when normalized all the closure stress versus cycles, data fell onto a single curve. However, the application of their relationship to complex load histories is complicated. The present authors have applied a simpler relationship suggested by Vormwald and Seeger [*13*] relating the change in crack opening stress in a given cycle to the difference between the current opening stress S_{cu} and the steady state opening stress S_{ss}.

$$\Delta S_{op} = m(S_{ss} - S_{cu}) \qquad (1)$$

where ΔS_{op} is the increase in crack opening stress during a load cycle and m is a material constant produced by fitting equation (1) to crack-opening stress build-up measurements. A value of m equal to 0.002 gives a good fit to the measured crack-opening stress data. The constants for DuQuesnay's steady state crack opening stress model were calibrated by measuring crack opening stress during a load history consisting of different maximum and minimum stresses. The two constants were found to be 0.55 and 0.23 for a and b respectively.
Using equation 1 the crack-opening stress levels were modeled assuming that the crack-opening stress for a given cycle instantaneously decreases to the constant amplitude steady state level for that cycle if this steady state crack opening stress is lower than the current opening stress. Otherwise it follows the exponential build-up formula of equation 1 unless the cycle is below the intrinsic stress range, or the maximum stress is below zero in which case it doesn't change.

Crack growth analysis

A crack growth analysis based on a fracture mechanics approach as presented by Dabayeh et al. [*14*] was used to model the fatigue behavior of the 1045 as received steel specimens for the given load spectra and stress ranges. The crack growth analysis was based on an effective strain-based intensity factor as presented by Dabayeh et al. [*14*], a crack growth rate curve obtained during closure-free loading cycles, and a local notch strain calculation based on Neuber's rule [*14*].

Experimental measurements

The three load spectra were scaled to various maximum stress ranges. The upper limit of these ranges was set so the maximum and minimum stresses did not cause large scale notch plasticity as the fatigue crack grew out of the notch while the lower limit was set so that fatigue lives did not exceed fifteen hundred blocks. In order to obtain the fatigue life curves the three spectra mentioned above were scaled to various stress ranges and applied to the 1045 notched steel specimens till failure.

Results for the SAE Grapple Skidder Load History

For the experimental crack closure measurements the torsion channel of the Grapple Skidder spectrum which has a positive mean stress was scaled to two different stress levels, a maximum nominal stress range of 910 MPa and a maximum nominal stress range of 751 MPa. The measured crack opening stresses for the two different maximum stress levels are shown in Figures 2 and 3 respectively. The figures show the applied nominal stress spectrum for each load history, the calculated crack opening stresses using the crack opening stress model and the experimentally measured crack opening stresses. Figure 4 is an expanded view of a portion of Figure 2 that shows the modeled and experimental crack opening stress. As expected, the crack opening stress decreases when the specimen is subjected to a large overload then starts to build-up again during subsequent smaller cycles. The average measured crack opening stresses were

within 8 and 9 percent of the average calculated crack opening stresses for the two different maximum stress levels. Figure 5 shows a plot of the measured fatigue lives versus the maximum stress range of the Grapple Skidder load spectrum and the lives predicted using the crack opening stress model in the fatigue crack growth program. The estimated fatigue lives are in good agreement with the experimental observations.

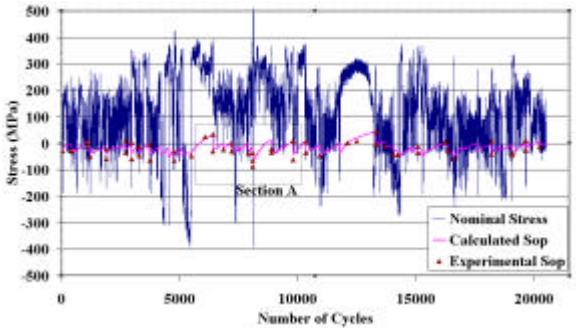

Figure 2. GSH Maximum Stress 910 MPa

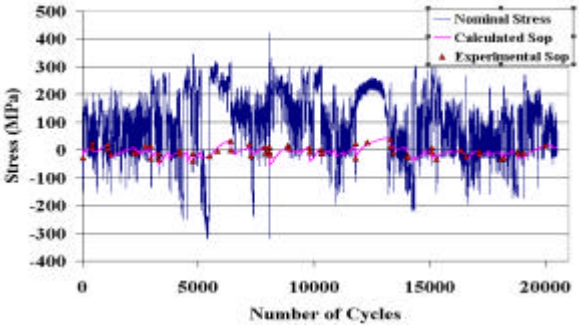

Figure 3. GSH Maximum Stress 751 MPa

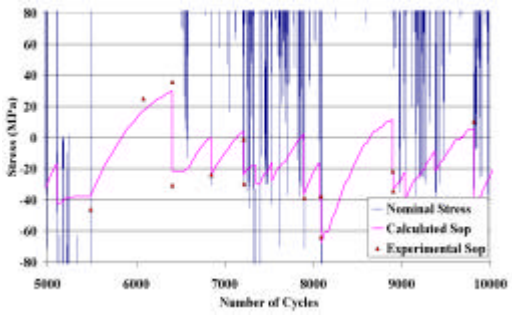

Figure 4. Section A

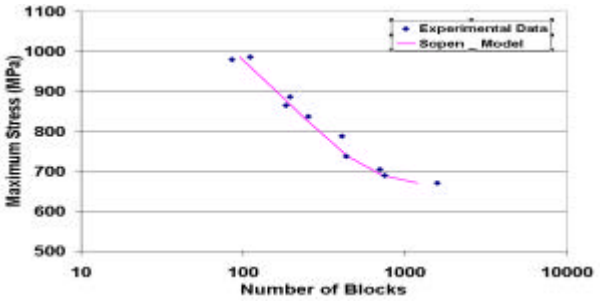

Figure 5. Fatigue Life vs. maximum stress (GSH)

Results for the SAE Log Skidder Load History

The cable channel of the Log Skidder spectrum which had an average mean stress of zero was scaled to two different stress levels. These stress levels were: a maximum nominal stress range of 887 MPa and a maximum nominal stress range of 675 MPa. The crack opening stresses for the maximum stress ranges are shown in Figures 6 and 7 respectively. The figures show the nominal applied spectrum for maximum stress ranges of 887 MPa and 675 MPa, the calculated crack opening stresses using the crack opening stress model and the experimentally measured crack opening stresses. Figure 8 is an expanded view of a portion of Figure 6 that shows the modeled and experimental crack opening stress. The average measured crack opening stress were within 9 and 11 percent of the average calculated crack opening stress for the two different maximum stress levels respectively. Figure 9 shows the measured fatigue lives versus the maximum stress range of the Log Skidder load Spectrum. The estimated fatigue lives are in good agreement with the experimental values.

Results for the Inverse Grapple Skidder Load History

The inverse of the torsion channel of the Grapple Skidder spectrum which had a negative mean stress was scaled to two different maximum stress levels. These stress levels are: A maximum

nominal stress range of 1008 MPa and a maximum nominal stress range of 675 MPa. The crack opening stresses for the two maximum stress ranges are shown in Figures 10 and 11 respectively. Figure 12 is an expanded view of portion of Figure 7 that shows the modeled and experimental crack opening stress. The average measured crack opening stresses were within 13 and 10 percent of the average calculated crack opening stress for the two different maximum stresses levels respectively. Figure 13 shows the measured fatigue lives versus the maximum stress range of the inverse Grapple Skidder Spectrum. The estimated fatigue lives are in good agreement with the experimental values.

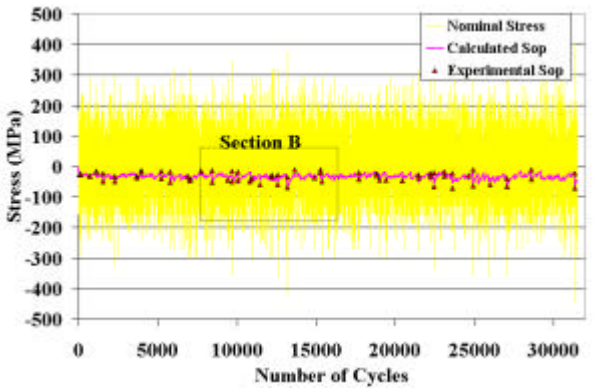

Figure 6. LSH Maximum Stress 887 Mpa

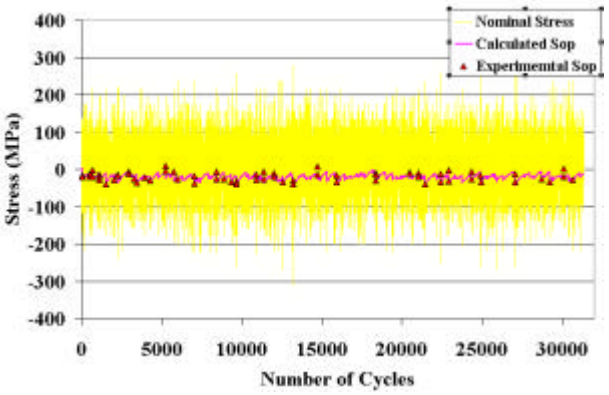

Figure 7. LSH Maximum Stress 675 MPa

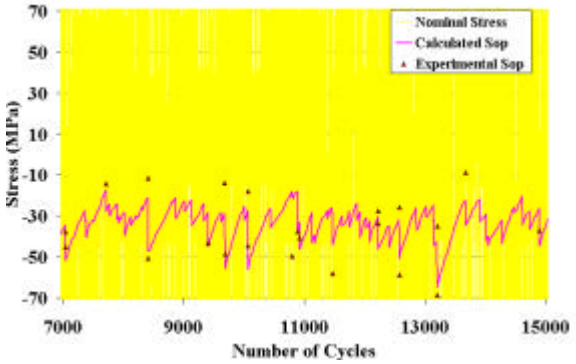

Figure 8. Section B

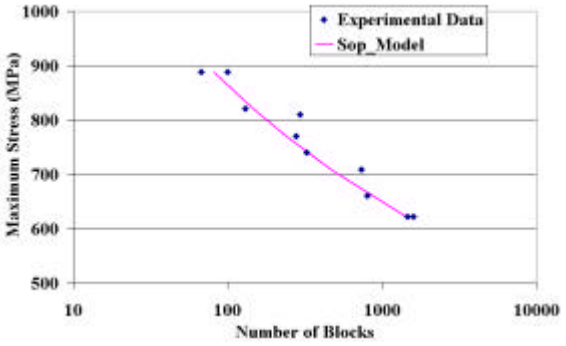

Figure 9. Fatigue Life vs. maximum stress (LSH)

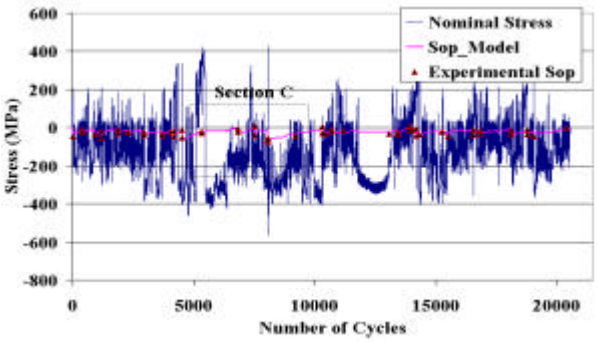

Figure 10. IGSH Maximum Stress 1008 Mpa

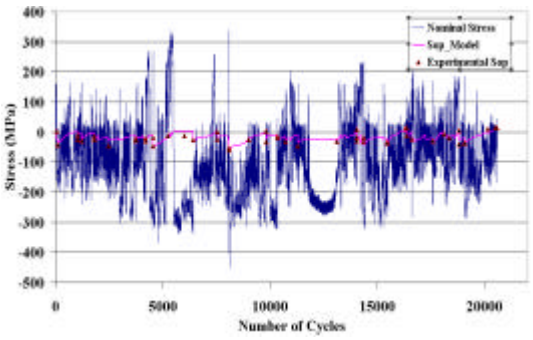

Figure 11. IGSH Maximum Stress 675 MPa

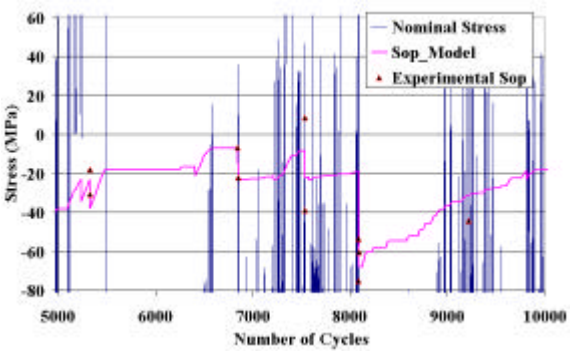

Figure 12. Section C

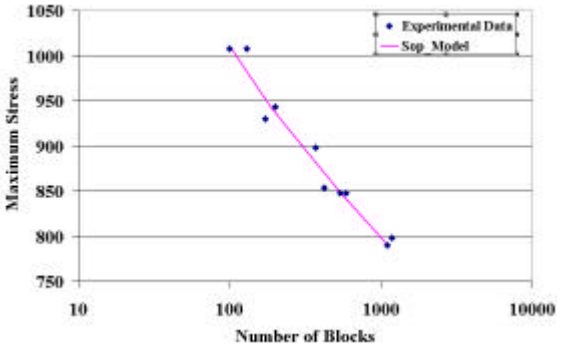

Figure 13. Fatigue Life vs. maximum stress (IGSH)

CONCLUSIONS

1. The crack-opening stress level dropped immediately after the application of an overload and then gradually increased with subsequent small cycles.
2. The crack opening stress can be modeled using an exponential build-up formula which is a function of the difference between the current crack opening stress and the steady state crack opening stress of the given cycle.

REFERENCES

1....DuQuesnay, D. L.," Fatigue Damage Accumulation in Metals Subjected to High Mean Stress and Overload Cycles, Ph.D. Thesis ", *University of Waterloo*, Waterloo, ON, Canada, 1991.

2....Bernard, P. J. and Lindley T. C. and Richards, C. E., " Mechanics of Overload Retardation During Fatigue Crack Propagation ", *ASTM STP 595*, pp. 78 - 97, 1976.

3....Wheeler, O. E., " Spectrum Loading and Crack Growth ", *J. Basic Eng. Trans. Am. Soc. Mech. Eng*, Vol. 4, pp. 181 - 186, 1972.

4....Matsouks, S. and Tanaka, K., "Delayed Retardation Phenomena of Fatigue Crack Growth in Various Steels and Alloys ", *J. Master Sci.*, Vol. 13, pp. 1335 - 1353, 1978.

5....Shin, C. S. and Fleck, N. A., "Overload Retardation in a Structural Steel", *Fatigue Fract. Eng. Mater Struct.*, Vol. 9, pp. 379 - 393, 1987.

6....Ward-Close, C. M. and Blom, A. F. and Ritchie, R. O., " Mechanisms Associated with Transient Fatigue Crack Growth Under Variable Amplitude Loading ", *Eng. Fract. Mech.*, Vol. 32, pp. 613 - 638, 1989.

7....Suresh, S., "Micromechanisms of Fatigue Crack Retardation Following Overloads ", *ASTM STP 595*, Vol. 18, pp. 577 - 593, 1983.

8....Schijve, J., " The Accumulation of Fatigue Damage in Aircraft materials", *AGARD*, No. 157, 1972.

9....Topper, T. H. and Yu, M. T., " The Effect of Overloads on the Threshold and Crack Closure ", *Int. J. Fatigue*, Vol. 7(3), pp. 159 - 164, 1985.

10..Alzeo, W. X. and Skatjr, A. C. and Hillberry, B. M., " Effect of Single Overload/Underload Cycles on Fatigue Crack Propagation ", *ASTM STP 595*, pp. 41 - 60, 1976.

11..Khalil, M., DuQuesnay, D., and Topper, T. H., **"**Prediction of Crack-Opening Stress Levels for Service Loading Spectra" *Application of Automation Technology in Fatigue and Fracture Testing and Analysis, ASTM STP 1411*, A. A. Braun, P. C. McKeighan, M. A. Niclson, and P. R. Lohr, Eds., American Society for Testing and Materials, West Conshohocken, PA, 2002

12..Dabayeh, A. And T.H. Topper, " Changes in Crack-Opening Stress after Underloads and Overloads in a 2024-T351 Aluminum Alloy.", *Int. J. Fatigue*, pp. 261-269, Vol. 17, No. 4, 1995.

13..Vormwald, M. and T. Seeger, "The Consequences of Short Crack Closure on Fatigue Crack Growth Under Variable Amplitude Loading", *Fatigue Fract. Eng. Mater. Struct.*, Vol. 14, No. 3, 1991, pp. 205 – 225.

14..Dabayeh, A. A., Xu, R. X., Du, B. P., and Topper, T. H., "Fatigue of Cast Aluminum Alloys under Constant and Variable-amplitude Loading", *Int. J. Fatigue*, Vol. 18, No. 2, pp. 95 – 104, 1996.

MODELING OF RESIDUAL STRESS EFFECTS USING EIGENSTRAIN

Michael R. Hill

Mechanical and Aeronautical Engineering, University of California,
One Shields Avenue, Davis, CA 95616, USA, mrhill@ucdavis.edu

ABSTRACT

This paper discusses the modelling of residual stresses in fracture problems. Historically, residual stress effects in fracture have focused on the crack driving force, so that solely opening mode residual stresses are assumed to influence fracture. However, residual stresses can effect all components of stress at the crack-tip, and can thereby alter crack-tip constraint and influence material toughness. This paper discusses a modelling approach capable of revealing the effects of residual stress on both driving force and constraint. The modelling employs non-linear finite element analyses in which residual stresses are treated using eigenstrain. Eigenstrain is imposed to induce residual stress as an initial condition in a cracked geometry. Under subsequent applied loading, the stress fields due to applied and residual loadings are free to interact, with residual stress being potentially reduced by gross plasticity. In order to predict fracture independent from the level of crack driving force, the evolution of the crack-tip stress and strain with applied loading is monitored using any of various micromechanical fracture prediction schemes, which depend directly on the crack-tip conditions. Domain integral solutions for J, derived from the FEM results and properly corrected for the presence of initial eigenstrain, are computed. Constraint is quantified using J-Q theory. Together, J and Q allow comparison between the modelling approach pursued and more traditional global parameter approaches.

KEYWORDS

residual stress, fracture, eigenstrain, finite element method

INTRODUCTION

Recent research in micromechanical modeling has made progress toward the accurate prediction of fracture under various crack-tip constraint conditions. Historically, fracture prediction has focused on determining a global fracture parameter (e.g., the J-integral, J, or the Mode-I stress intensity factor, K_I) as a function of applied load, and finding the load at which the parameter exceeds a critical level for fracture. This approach rests on the assumption that the fracture parameter alone controls the crack-tip stress and strain. Unfortunately, in application, material non-linearity (i.e., yielding) at the crack-tip invalidates this assumption. Yielding is a function of the triaxial state of stress, and the crack-tip stress state has a range of variation in real structures. In fact, it is well known that differences in crack-tip triaxiality (or, more commonly “constraint”) can exist in structures due to differences in geometry and applied loading (e.g., thick versus thin, or tension versus bending). Further, different crack-tip stresses lead to fracture at different levels

of the global fracture parameter. An alternative method to parameter-based approaches, micromechanical methods directly examine the crack-tip stress and strain state to provide an estimate of fracture propensity. Implementation of the micromechanical approach therefore requires the prediction of crack-tip stress and strain, and its history with applied loading. In practice, finite element methods (FEM) are used to compute the crack-tip conditions, as a function of applied loading.

Application of the micromechanical approach to predict fracture in residual stress bearing structures provides some surprising results. The traditional approach to predict fracture of residual stress (RS) bearing, flawed components involves linear superposition. This approach assumes that only opening mode RS will impact the fracture process, when, in fact, residual stresses are often triaxial. Triaxial RS will influence non-linear material behavior at the crack-tip, a process not accounted for by superposition. Including RS in a micromechanical approach, however, does allow the residual stress field to affect the behavior of material at the crack-tip. Accordingly, the micromechanical approach offers a more complete accounting of RS effects in fracture, and gives insight to the fracture process when RS is present. An example application of this approach is briefly described, which illustrates the alteration of driving force and constraint due to residual stress, and their effect on fracture prediction.

FRAMEWORK

This section describes a computational and analytical framework for predicting fracture in flawed, RS bearing structures using micromechanics. We first lay out the general finite element procedures employed. Next, we describe methods for introducing RS into the computation. The computational results provide the crack-tip stress and strain history as a function of applied load, which serve as input to a micromechanical fracture prediction model. The RKR model for brittle fracture is described, and later used to illustrate the approach. Finally, *J-Q* analysis is described, which helps to interpret the stress and strain history at the crack-tip, and to compare the results of micromechanics to those that would be obtained using a traditional global parameter approach.

General analysis techniques

Elastic-plastic finite element computation is used to simulate the response of a structure of interest to both applied and residual stresses simultaneously. The finite element solutions employ a non-linear, finite strain formulation. Plasticity is assumed to follow isotropic, incremental J_2 flow theory with a piece-wise linear Cauchy-stress logarithmic-strain curve obtained from tensile testing. Commercial codes can be used to perform these analyses. Mesh refinement in the crack-tip region is critical, and must assure that stress and strain are accurately captured in the near crack-tip region. Time-stepping in the analysis provides a means to capture the developing crack-tip state with increasing applied load, which serves as input to the fracture prediction scheme.

Inclusion of residual stress

Residual stress is included in the finite element computation using eigenstrain, ε^*. Eigenstrain is a combination of all the non-elastic, incompatible strains set up during processing of a material [1]. In welding, the eigenstrain is a combination of thermal, plastic, and transformation strains; in coining or autofrettage, the eigenstrain is due to plasticity. The eigenstrain field is defined with reference to *elastic* deformation of the structure, and reproduces the entire RS state when the material behavior is *elastic*; therefore, eigenstrain is *not* merely a sum of the various non-linear strains. For a particular process, the eigenstrain field is a tensor with spatial dependence, and can be found experimentally [2] or by modeling [3]. If a process model is used to determine the residual stress field in a given body, σ^{RS}, or if residual stress is measured at enough points to provide a spatial distribution of the residual stress field, the eigenstrain field can be found from the residual stress field using

$$\varepsilon^*_{ij} = -C^{-1}_{ijkl}\sigma^{RS}_{kl} \tag{1}$$

where C is the usual elastic tensor giving stress from elastic strain.

The use of an eigenstrain distribution in modeling offers several advantages for further analysis. First, the residual stress present can be determined by imposing the eigenstrain distribution in a linear elastic finite element model of the geometry. (Note that residual stresses, by their nature, do not result in active yielding, and a valid eigenstrain field must impose stresses that satisfy the yield criterion). Although an eigenstrain analysis is complicated by the spatial variation of each component of the eigenstrain tensor, a general-purpose finite element program can be used to produce the RS field. Further, when the eigenstrain field is known, the entire, full-field, triaxial RS state is known at every point within the structure.

When the eigenstrain field is known for the unflawed structure, the analysis of a flawed structure can be performed. The addition of a crack introduces new surfaces, and the RS state in the flawed body depends on these surfaces. If the structure is linear elastic, the state is found simply by modeling the traction-free surfaces. In non-linear materials, crack-tip yielding must be allowed when introducing the flaw. To handle this situation, the eigenstrain distribution is first imposed in the body with crack-face nodes restrained, and the equilibrium RS state found (this step is elastic). Then, the crack-face nodes are released in succession, so that the crack gradually extends from the free surface to simulate fatigue (this step can be elastic-plastic). The rate at which the crack is extended will have a bearing on the crack-tip fields, and one must ensure that the opening is gradual enough (e.g., so subsequent fracture analysis is not affected). When properly executed, this process redistributes the original RS field, allowing for crack-tip yielding, and resulting in a flawed RS bearing structure.

Once RS is introduced into the computation, applied loading is simulated. During this subsequent loading phase, the residual and applied stresses act together at the material level. Any new plastic deformation is the result of both stress types. Therefore, this analysis technique allows for the non-linear interaction of RS and applied loading, which is not accounted for when applying global approaches.

An alternative to using eigenstrain is direct simulation the process causing the residual stress field. Results of the simulation can then be used as an initial condition for the simulation of crack introduction and applied loading. However, direct simulation can only be readily pursued for simple problems, with small amounts of plasticity or other incompatible strain.

Micromechanical fracture prediction

Since the analysis technique just described provides a complete description of the material state in the presence of residual and applied loading, the crack-tip material history can be used within a micromechanical scheme to predict fracture. The physical phenomena occurring in the fracture process vary, and it is generally useful to consider brittle and ductile fracture processes separately [4]. Here we briefly describe one model for predicting brittle fracture, and this is used later to illustrate the general computational approach. In principle, other micromechanical models could be employed.

Initiation of cleavage fracture in mild steels can be predicted using the RKR micromechanical model [5]. This simple model predicts fracture when the opening stress, σ_{yy}, ahead of the crack-tip exceeds a fracture stress, σ_f^*, over a microstructurally relevant distance, l^*. In applying this model, one monitors the progress of the opening stress ahead of the crack-tip due to residual and applied loading. Once the RKR criterion is satisfied, fracture is predicted. The parameters in the RKR model are typically found through laboratory testing for a given material and reported ranges for steels are 2 to 5 grain diameters for l^*, and 2 to 4 times the yield strength for σ_f^* [5]. When the micromechanics condition for fracture initiation is satisfied, the associated applied load and global fracture parameters (e.g., *J*-integral) can be found from the FEM results.

Characterization of crack-tip behavior

When the above procedures are used to predict fracture, none of the traditional global fracture parameters are used. Nevertheless, it is useful to compare the micromechanical predictions with those that might be made using a traditional approach. To perform this comparison, we utilize two parameters, one related to driving force and one to constraint. Specifically, we invoke *J-Q* theory, which was developed from simulation of crack-tip fields in finite and infinite size bodies [6,7].

During the non-linear analysis, the *J*-integral is estimated at each increment of applied loading using the domain integral technique. As such, the computed value of *J* includes the contribution of residual stress within the material. Calculation of *J* in the presence of RS and eigenstrain requires special attention. Recent work [8,9,10] has found that domain-independent values of *J* can be obtained if two corrections are made to the usual domain integral formulation for *J*. The first of these involves the spatial derivative of the residual stress or eigenstrain field with respect to the crack driving direction (assumed to be x_1 here, for simplicity) [8]. The second involves a modification of the work density of the material, *W*, to account for plastic dissipation present at a crack-free initial state, which follows residual stress introduction, $W^p_{\text{initial state}}$ [9]. The first correction term is required to obtain domain independence in any modelling approach that involves residual stress or eigenstrain. The second term is needed, for example, when the residual stress state is found through process modeling which causes plastic straining and dissipation unrelated to subsequent fracture loading. The domain integral including these two additional terms can be written as [10]

$$J = \frac{1}{A_q}\left(\int_V \left(\sigma_{ij}\frac{\partial u_j}{\partial x_1}\frac{\partial q}{\partial x_i} - W\frac{\partial q}{\partial x_1}\right)dV + \int_V \left(\sigma_{ij}\frac{\partial(\varepsilon^*_{ij} - C^{-1}_{ijkl}\sigma^{RS}_{kl})}{\partial x_1}\right)q\,dV + \int_V \left(W^p_{\text{initial state}}\frac{\partial q}{\partial x_1}\right)dV\right) \qquad (2)$$

where the first integral is the usual domain integral formulation for *J*, and the second and third integrals are the first and second correction terms described above; these three terms, including the leading factor $1/A_q$, will be referred to as J_1, J_2, and J_3. The quantities in the integrals not yet defined are the stress tensor, σ_{ij}, the displacement vector, u_j, the spatial coordinates, x_i, a scalar weight function representing a virtual displacement, *q*, the material work density, *W*, and the crack-front area of the virtual displacement, A_q (see, e.g., [11]).

In a number of cases, the values of *J* computed from the usual formulation (i.e., J_1 alone) are highly inaccurate. Consider, for example, the cold-expanded hole with a radial crack shown in Figure 1(a) which was recently studied in [12]. In that study, the uncracked hole was expanded radially by 4%, then allowed to relax to form a compressive residual stress field at the hole periphery. The radial cracks shown in the figure were then introduced, and far-field loading applied. Because the residual stress varied strongly near the hole, and because the plasticity caused by the expansion process introduces plastic dissipation unrelated to the fracture problem, the *J* values published in [12] were highly domain-dependent. Reproducing the simulations, and computing the three terms in Eqn. 2, provides the results shown in Figure 1(b) [10]. Clearly the correction terms in Eqn. 2 are important for obtaining domain independence of *J* in such problems.

For a given level of *J*, the constraint conditions at the crack-tip are represented by the parameter *Q*. *Q* has been shown to characterize the magnitude of the hydrostatic stress over the forward sector ahead of the crack-tip to a good approximation. *Q* is formally defined as

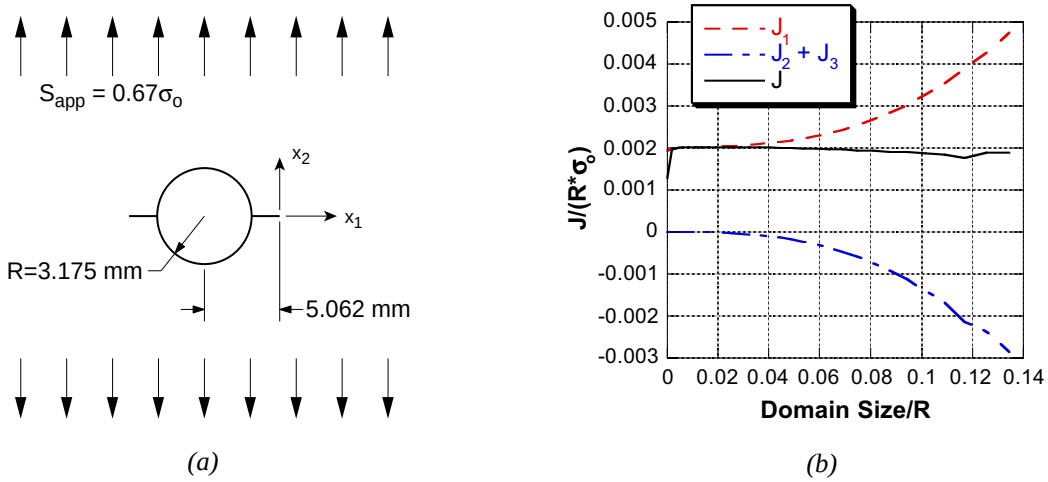

(a) *(b)*

Figure 1: Cold expanded hole with radial crack: (a) geometry, and (b) domain integral results

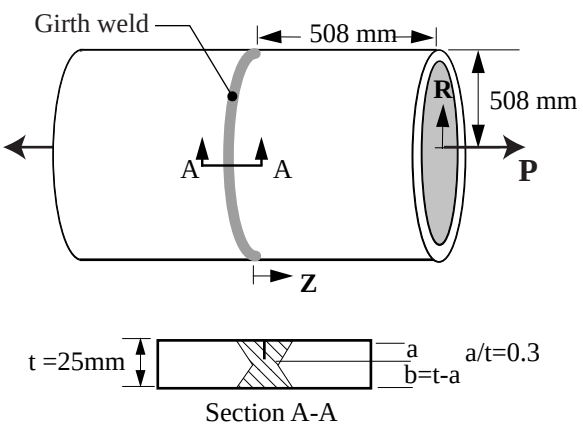

(a)

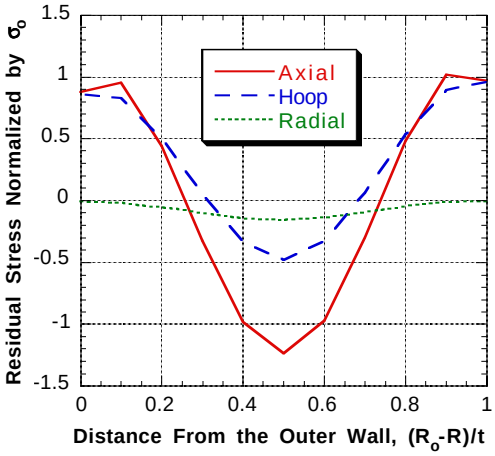

(b)

Figure 2: (a) Girth-welded pressure shell, (b) RS in the unflawed condition

$$Q = \left(\frac{\sigma_{\theta\theta} - \sigma_{\theta\theta}\big|_{\mathrm{SSY};T=0}}{\sigma_o} \right) \text{ at } \theta = 0, \left(\frac{r\sigma_o}{J} \right) = n \tag{3}$$

where, σ_o is the material yield strength, and n is a constant usually taken in the range 2 to 4 [6,7]. Q depends on the crack-tip stress state in the body of interest, $\sigma_{\theta\theta}$, and on the stress state in a plane-strain, Mode I loaded, small-scale yielding reference solution, $\sigma_{\theta\theta}\big|_{\mathrm{SSY};T=0}$, where both exhibit the same J.

Because Q is a constraint parameter, it provides insight into the fracture process. Q near zero suggests that a body is in small-scale yielding. As deformation levels increase in finite specimens, the hydrostatic stresses at the crack-tip are relieved, producing a negative Q value, and signaling a loss in constraint. A negative value of Q indicates lower crack-tip stress compared to a body in small-scale yielding and, therefore, a reduced propensity for cleavage fracture at a given value of J. A positive Q-value indicates that high constraint exists for a particular crack-tip state.

TRIAXIAL STRESS EFFECTS IN BRITTLE FRACTURE

This section serves as an example to illustrate the approach described above. It focuses on the prediction of brittle fracture of the axially loaded, girth-welded shell shown in Figure 2(a), initiating from a circumferential external flaw. Details of the study can be found in [13]. The properties assumed are those of A516-70, a high hardening, ferritic, pressure vessel steel with uniaxial yield strength of 303 MPa. The RKR parameters for this material are assumed to be $\sigma_f^* = 3.5\sigma_o$ and $l^* = 0.15$ mm, or about 3 ferritic grain diameters.

This analysis makes use of an assumed eigenstrain distribution. This distribution gives rise to residual stresses that are typical of a continuously welded, double-sided joint in mild steel plate [14]. The nature of continuous welding allows the assumption of an eigenstrain field that depends on the transverse and through-thickness welding directions, but is independent of position along the weld. Further, the eigenstrain field is assumed symmetric about both the centerline of the weld and the mid-wall of the shell. The residual stress field computed when the assumed eigenstrain field is imposed in the un-flawed geometry is shown in Figure 2(b), on the plane where the crack will be introduced. For the flaw orientation shown in Figure 2(a), axial stresses correspond to the opening mode, and over the length of defect considered (from 0 to 0.3 in Figure 2(b)), the axial RS is tensile. Accordingly, RS will tend to increase the crack-driving force and therefore decrease the fracture load.

Fracture predictions using the RKR model show a strong constraint effect caused by RS. Fracture loads are predicted to be 21.3 MN and 9.83 MN without and with RS, respectively. Because RKR is satisfied at these loads, crack-tip opening stresses are nearly the same in each loading case. However, this occurs at markedly

different values of J, 36.7 kN/m without RS and 13.5 kN/m with RS. Recall that these values of J are computed using the domain integral, so they include the influence of RS on driving force. As shown in Figure 3(a), the significant change in J at fracture is due to high constraint imposed by the RS field. Figure 3(b) shows that this additional constraint suppresses plastic strain formation compared with the non-residual stress bearing case. These interesting results demonstrate that RS can cause a significant change in crack-tip constraint. Figure 3(a) shows that the tension loaded shell has quite low constraint when RS is absent, but behaves like a body in small-scale yield when RS is present. If the RS bearing shell were assumed to have constraint similar to the RS-free shell, the superposition approach would lead to an erroneous and non-conservative fracture assessment. This observation gives credence to codified assumptions of high constraint, as RS can combine with applied loads to produce highly constrained crack-tip fields in a geometry and loading condition that would otherwise exhibit low constraint.

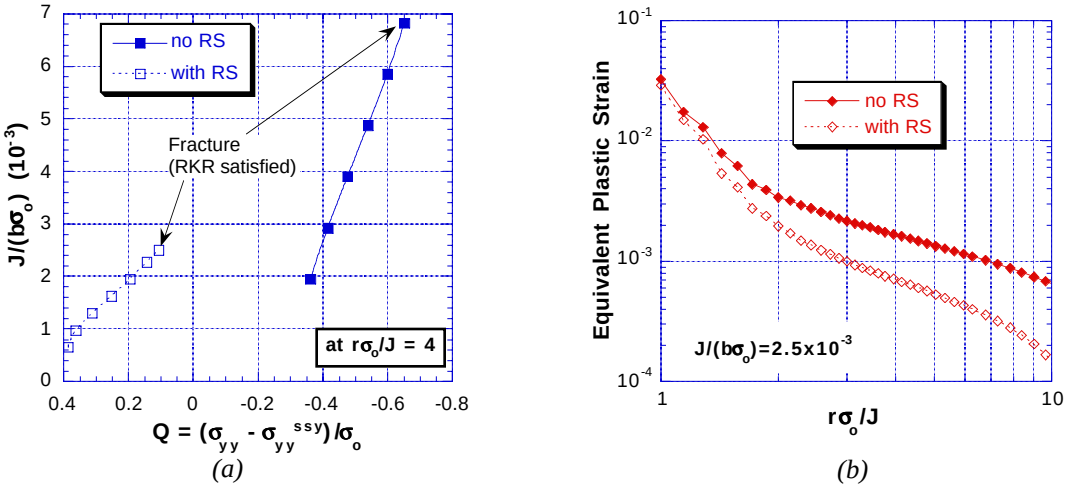

Figure 3: (a) *J-Q* trajectories and (b) plastic strain for the shell

REFERENCES

1. Mura, T. (1987). *Micromechanics of Defects in Solids*. Dordrecht, Netherlands.
2. Hill, M.R. (1996). Ph.D. Thesis, Stanford University.
3. Goldak, J.A., and Patel, B. (1985). In: *Advanced Joining of Materials (AGARD CP-398)*, pp. 1-1 - 1-32. AGARD.
4. Shih, C.F. (1999). In: *Fatigue and Fracture Mechanics, 29th Volume*, pp. 9-14, Panontin, T.L., and Sheppard, S.D., Eds. ASTM, West Conshohocken, PA.
5. Ritchie, R.O., Server, W.L., and Wullarert, R.A. (1979) *Met Trans A* 10, 1557.
6. O'Dowd, N.P., and Shih, C.F. (1991) *J Mech Phys Solids* 39, 989.
7. O'Dowd, N.P., and Shih, C.F. (1992) *J Mech Phys Solids* 40, 939.
8. Matos, C.G., and R. H. Dodds, Jr. (2000) *Eng Struct* 22, 1103.
9. Lei, Y., O'Dowd, N.P., and Webster, G.A. (2000) *Int J Fract* 106, 195.
10. Meith, W.A. (2001). MSc Thesis, University of California, Davis.
11. Shih, C.F., Moran, B., and Nakamura, T. (1986) *Int J Fract* 30, 79.
12. Pavier, M.J., Poussard, C.G.C., and Smith, D.J. (1999) *Eng Fract Mech* 63, 751.
13. Panontin, T.L., and Hill, M.R. (1996) *Int J Fract* 82, 317.
14. Gunnert, R. (1961). In: *Proceedings of the Special Symposium on the Behavior of Welded Structures*, pp. 164-201, Kingery, R.A., Ed. University of Illinois Engineering Experiment Station, Urbana, IL.

MODELLING THE EFFECTS OF RESIDUAL STRESSES ON CLEAVAGE FRACTURE IN WELDED STEEL FRAMES

C. G. Matos and R. H. Dodds, Jr.*

Department of Civil & Environmental Engineering, University of Illinois, Urbana, IL 61801, U.S.A.

ABSTRACT

This study applies an advanced micro-mechanics model of cleavage fracture in ferritic steels to examine the fracture behavior of welded, moment resistant steel frames of the type widely constructed prior to the Northridge earthquake. The Weibull stress model for cleavage, coupled with 3-D analyses of connections containing crack-like defects, provides a quantitative estimate of the cumulative failure probabilities with increasing beam moment. The 3-D models incorporate the complex geometry of a typical welded joint. A set of previously conducted, 15 full-scale tests on T–connections of the pre-Northridge design provide fracture moments to calibrate parameters of the Weibull stress model. Once calibrated, the model is used to examine the importance of welding induced residual stresses in the lower-flange. The model predicts the cumulative failure probability as a function of beam moment.

Keywords: Residual stresses, Cleavage, Eigenstrain, Northridge earthquake

1. INTRODUCTION

Fractures in the connections of welded steel moment resistant frames (WSMFs) during the 1994 Northridge earthquake prompted new research efforts to understand the causes and to develop improved designs [1]. WSMFs constructed prior to the Northridge event often have large rolled sections of A36 (beams) and A572 (columns) steels with flux-core field welds to connect the beam flanges with the column face (see Fig. 1). The geometry of the connection includes an access hole in the beam web, backup bars left in-place, bolted shear tabs, continuity plates in the columns at the beam flange locations, etc. Post-quake field surveys and laboratory tests of full-scale connections indicate the existence of relatively long, shallow defects in the lower-flange weld [2,3]. Fractures initiate at this location and propagate in a very rapid, brittle mode possibly preceded by a small amount of stable ductile tearing ($\lesssim$1–2 mm) [4]. The full-scale connection tests often exhibit limited macroscopic plastic deformation as measured by the plastic rotation (θ_p) prior to the brittle fracture event [5].

This work focuses on understanding and characterizing the brittle fracture behavior for the existing inventory WSMFs having the pre-Northridge design. The approach combines a probabilistic, micro-mechanical model to describe the cleavage fracture process with large-scale, 3-D finite element analyses of the full connections to compute the crack-front stress fields that capture local variations of the fracture parameters and constraint. Applications of this analysis capability examine the relative importance of welding induced residual stresses on the probability for cleavage fracture initiation at the interface of the beam flange and column face.

2. STATISTICAL ANALYSIS OF FULL JOINT TESTS

The tests of pre-Northridge style connections [5] define a set of fifteen specimens having very similar construction. Each of the fifteen specimens reportedly failed in a brittle fracture mode, with fracture initiating in the lower-flange beam-to-column weld. The individual test reports include overall specimen geometry and the measured load at fracture, *P*. This information enables computation of a nominal fracture moment, M_f, at the location where the lower-flange weld connects to the adjacent column flange. Despite the nominal specification of A36 steel for the beams, measured yield strengths from beam flange coupons varied widely. To accommodate the variations in beam sizes and yield strengths in the statistical analysis, fracture moments are normalized by the plastic moment of the section

$$\frac{M_f}{M_P} = \frac{P\ell}{Z\sigma_{ys}} \tag{1}$$

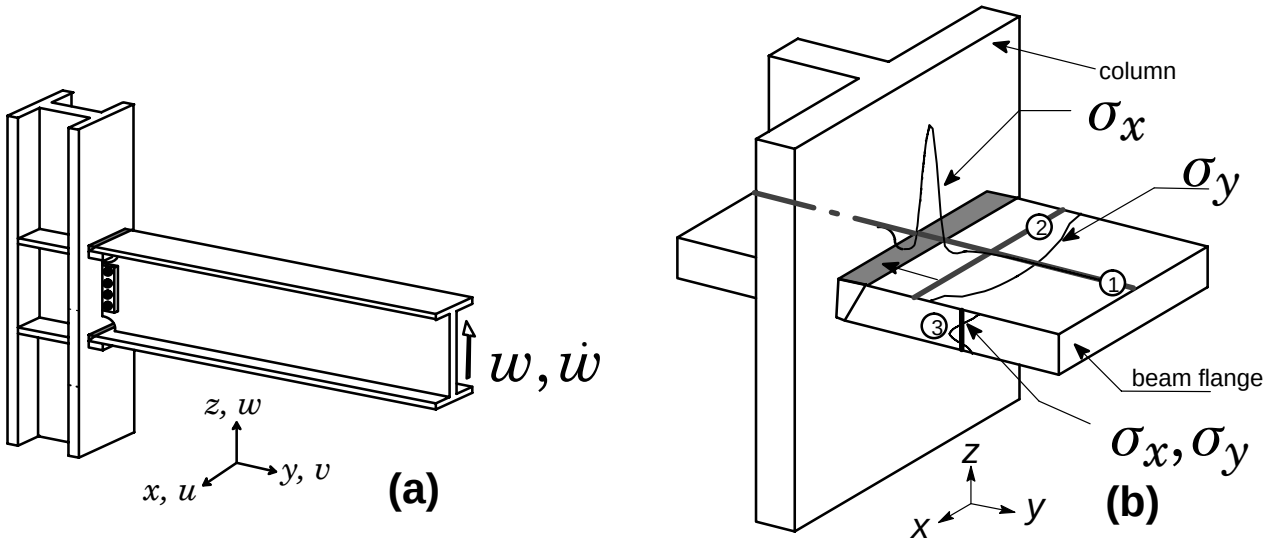

Fig. 1. (a) Schematic of typical pre-Northridge beam-column connection. (b) Typical patterns of residual stresses

where ℓ denotes the reported distance from the centerline of the load actuator to the column face, σ_{ys} defines the reported (coupon) yield stress of the beam flange for each test specimen and *Z* denotes the plastic modulus of the beam cross section. The very strong similarity of geometry and fabrication in these test specimens leads to the postulate that the large variation in values for the normalized fracture moment arises from the expected statistical scatter of toughness values for cleavage fracture in the ductile-to-brittle transition (DBT) region (combined with observed scatter of flaw sizes). Median estimates for the rank failure probability of normalized fracture moment, M_f/M_P, are given by $\mathcal{P}_f = (j - 0.3)/(n + 0.4)$, where *j* denotes the rank (failure) order by increasing M_f/M_P and *n* denotes the sample size (in this case $n = 15$). Normalized values of fracture moment should follow a Weibull distribution as do toughness values for cleavage fracture [6]. The simple, two-parameter Weibull distribution for the cumulative failure probability (median rank) has the form described in Fig. 2a.

3. THE WEIBULL STRESS MODEL

In the DBT region of ferritic steels, the cumulative failure probability follows a three-parameter Weibull distribution in terms of the Weibull stress [7]),

$$P_f(\sigma_w) = 1 - \exp\left[- \left(\frac{\sigma_w - \sigma_{w-\min}}{\sigma_u - \sigma_{w-\min}} \right)^m \right]. \tag{2}$$

where σ_w represents the Weibull stress defined as the integral of a weighted value of the maximum principal (tensile) stress (σ_1) over the process zone of cleavage fracture (i.e., the crack front plastic zone),

$$\sigma_w = \left[\frac{1}{V_0} \int_{\overline{V}} \sigma_1^m dV \right]^{1/m} \tag{3}$$

where $\overline{V}$ represents the volume of the cleavage fracture process zone and *m* denotes the Weibull modulus which defines the shape of the probability density function for microcrack size in the fracture process zone. The parameters σ_u and $\sigma_{w-\min}$ appearing in Eq. (2) denote the scale parameter of the Weibull distribution and the threshold σ_w-value for cleavage fracture respectively. Cleavage fracture cannot occur if $\sigma_w < \sigma_{w-\min}$. Under SSY conditions, $\sigma_{w-\min}$ is σ_w for an experimentally estimated value of $K_{I-\min} \approx 20$ MPa$\sqrt{\text{m}}$ for common ferritic steels..

4. NUMERICAL PROCEDURES

4.1. Modeling of Residual Stresses

The eigenstrain approach [11] used here proves especially convenient to introduce residual stresses in 3-D finite element models. Matos and Dodds [12] developed a field of eigenstrains to generate residual stresses in single-V

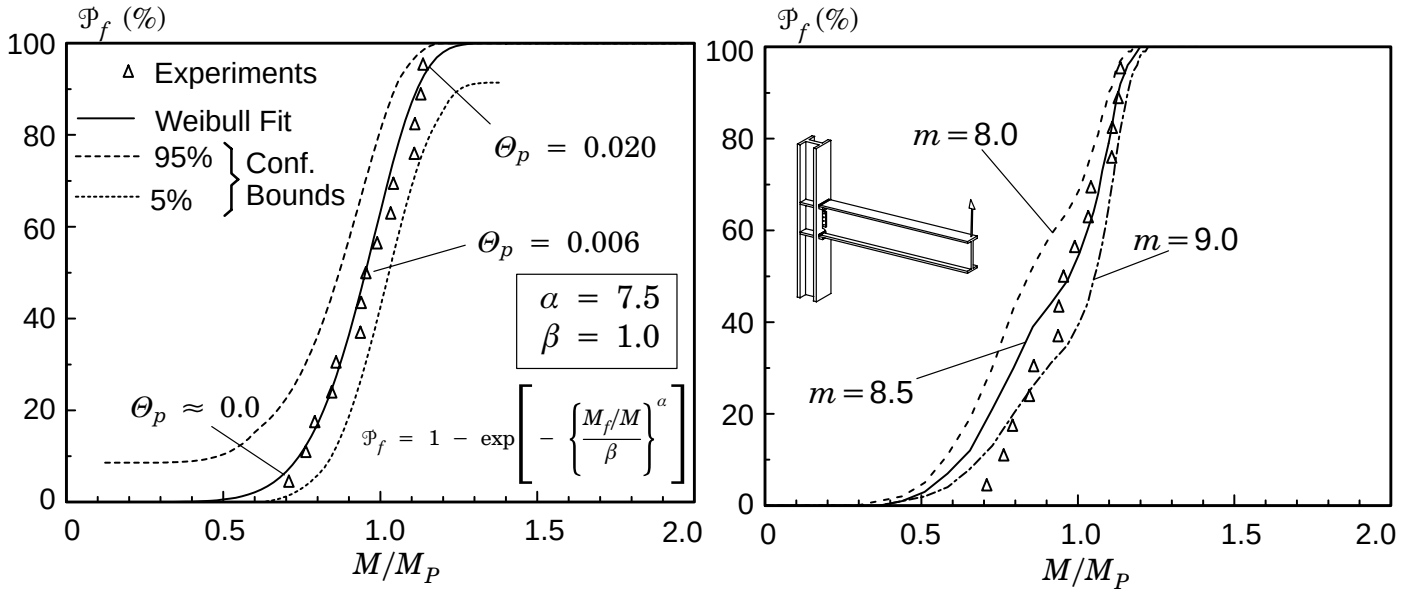

Fig. 2. (a) Weibull fit of experimental tests. (b) Weibull stress calibration of full-joint connections.

groove welds used to join the lower beam flange to the column flange. The residual stress field generated by these eigenstrain functions closely matches the field computed using thermomechanical simulation of a multi-pass welding process for this configuration [13]. Figure 1b depicts key features of this residual stress field. The weld longitudinal stresses (σ_{xx}) along line 1 reach values of the weld metal yield stress (σ_{ys}^{wm}) but decay rapidly to zero outside the weld. Weld transverse stresses (σ_{yy}) along line 2 have a smaller magnitude. Distributions of σ_{xx} and σ_{yy} over the beam flange thickness (along line 3) have tensile stresses at the surfaces and compression at the center. The eigenstrain functions to generate these residual stresses have the form:

$$\epsilon_{ij}^{*} = -\frac{\sigma^{*}}{E} f_{ij}(x,y,z) \tag{4}$$

where $\sigma^{*} = \sigma_{ys}^{wm}$ scales the stress amplitudes defined by the normalized functions $f_{ij}(x,y,z)$. A unit temperature change coupled with anisotropic thermal expansion coefficients, α_{ij}, equal to the ϵ_{ij}^{*} values sampled at element centers provides a simple mechanism to introduce these eigenstrains into the computational model [12].

4.2. Specimen Configurations and Materials

The finite element analyses of the full connection use a non-AISC standard section for the beam with depth $d = 762$ mm, flange width $b_f = 152$ mm, web thickness $t_w = 13$ mm, and flange thickness $t_f = 25$ mm. The column corresponds to a W14 × 176 section. Inspections of welded connections in buildings and in full-scale joints fabricated under laboratory conditions [2] reveal a range of crack-like defects along the root pass of the welds. Lack-of-fusion type defects of variable depth can extend the full width of the weld. These observations led to the adoption in this study of a uniform depth, sharp crack that extends the full width of the beam flange. The crack "depth" equals the applicable backup bar dimension (9.5 or 3.2 mm), plus an additional $a_0 = 5.7$ mm to reflect a typical bead size for the weld root pass. Symmetry of the geometry and loading permits modeling of only one-half of the specimen. The mesh has 34 focused rings of elements in the radial direction surrounding the crack front and 20 elements along the crack front length (half of the beam flange width). The crack tip has a small, initial radius of 20 μm to enhance convergence of the finite-strain solutions.

Stress-strain curves for quasi-static loading rates are constructed from the engineering strain-stress curves reported by Kaufmann *et al.* [17]. The finite element analyses thus have three different materials (beam A36, column A572 and weld metal E70T-4).

4.3. Loading and Boundary Conditions

The loading protocol for quasi-static analyses follows this sequence: 1. Apply the eigenstrains to introduce residual stresses through a total temperature increase of 1°. The temperature increase acts with specified anisotropic thermal expansion coefficients for each element in the weld region to generate the eigenstrains. Use ten, uniform increments of 0.1° to resolve the small amount of resulting plastic deformation. 2. Increase the beam tip

deflection monotonically (quasi-static) through 500 variably sized increments to reach a maximum tip deflection of 254 mm.

4.4. Finite Element Models

Models for fracture analyses are constructed using three-dimensional, 8-node elements with $\overline{B}$ formulation. *J*-integral values are evaluated with a domain integral procedure [14] using domains defined outside the material having non-proportional strain histories at the crack front. The computed *J*-values reflect finite strain effects and thermal strains used to produce the residual stresses. With the inclusion of additional terms that arise from the anisotropic thermal expansion coefficients to model the eigenstrains [12], the *J*-values maintain a strong path independence. The WARP3D [15] code supports computation of crack front average *J*-values and pointwise *J*-values at each node location along the crack front.

5. RESULTS AND DISCUSSION

5.1. Calibration of Weibull Stress Parameters

A two-parameter Weibull distribution, with moments normalized by the beam plastic moment, describes very well the measured distribution of fracture moments in the 15 nearly identical tests conducted on the pre-Northridge design (A36 beams, A572 columns, E70T-4 welds). Fig.2a shows the fit of $\mathcal{P}_f = 1 - exp(-\left\{(M/M_f)/\beta\right\}^{\alpha})$ where the the Weibull modulus is 7.5 with a scale factor of 1.0. The most ductile of the 15 tests reached a total (joint) plastic rotation (Θ_p) of 0.021 radians [16]. Post-processing of the 3-D, nonlinear finite element analyses (including residual stresses) to compute the evolution of Weibull stress values with beam moments at the column face enables calibration of parameters for the recently modified Weibull stress model: $m = 8.5$, $\sigma_u = 2.4\sigma_{ys}$, and $\sigma_{w-\min} = 1.25\sigma_{ys}$. Fig. 2b shows the calibrated Weibull distribution from the finite element analyses which lies well within the 90% confidence bounds for the experimental data. Other curves illustrate the strong sensitivity to the fit value of *m*.

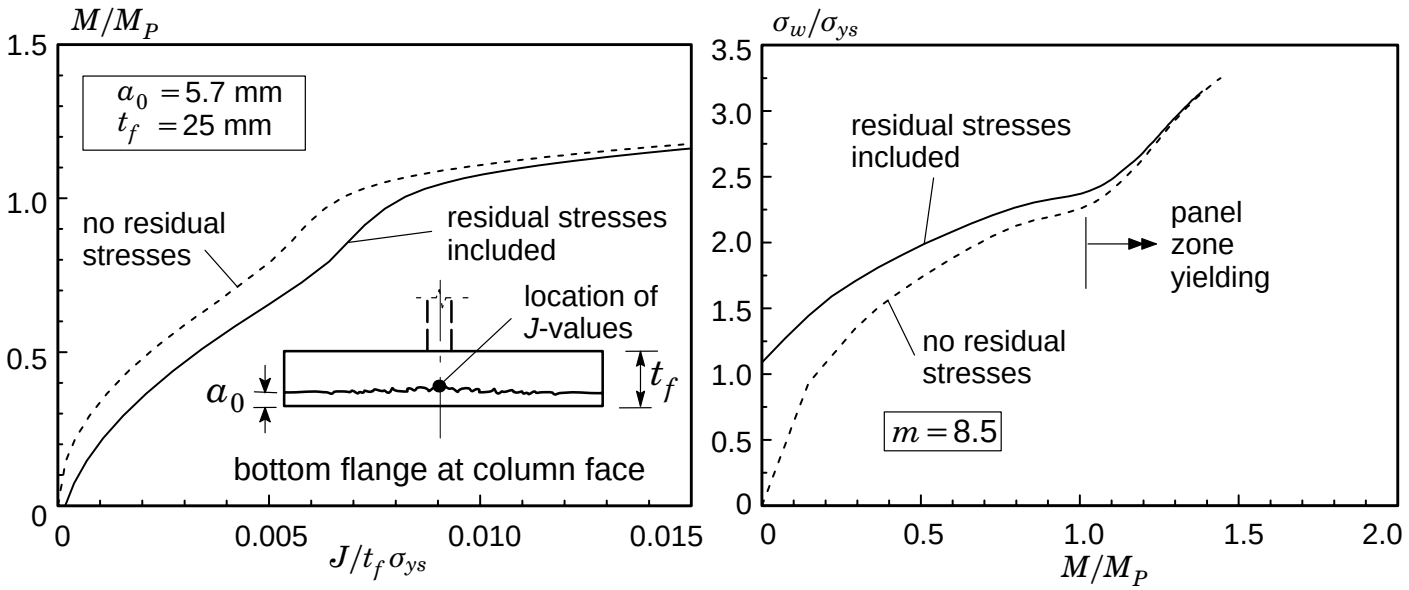

Fig. 3. (a) Development of *J* at center of beam flange. (b) Weibull stress vs. moment at the column face.

5.2. Effects of Residual Stresses: Pre-Northridge Connection

Figure 3a quantifies the impact of residual stresses on the development of *J*-values under increased moment at the column face. These locally computed *J*-values refer to the center of the beam flange as indicated on the figure, where the largest values occur across the full-width of the crack. Early in the loading, the residual stresses increase *J*-values by approximately 20% or equivalently about 15 MPa$\sqrt{m}$ in terms of the stress intensity factor. This essentially fixed increment of crack front loading remains effective throughout but decreases in relative magnitude as the total *J*-values increase rapidly once the connection progresses toward formation of a plastic

hinge. Figure 3b shows a similar influence of residual stresses on the Weibull stress. The strong upswing in σ_w values at $M/M_P \approx 1$ for both curves corresponds to the onset of panel zone yielding in the column. The relatively large σ_w values early in the loading caused by the residual stresses indicate a substantially larger probability for cleavage fracture. Again, once the plastic deformation leads to increased σ_w values later in the loading, the relative importance of the residual stress effect diminishes rapidly. These observations agree with the conventional tenet that residual stress effects decrease in significance under large scale yielding.

Figure 4 shows the effects of residual stresses on the probability of cleavage fracture with moment at the column face as the loading parameter. The residual stresses increase the crack front constraint slightly (in terms of the Weibull stress) for M/M_P values < 0.6. When inserted in the Weibull stress model and combined with the applied load, residual stresses increase the (absolute) cumulative fracture probabilities by 10% for M/M_P values < 0.75, and by 20% for M/M_P values > 0.9.

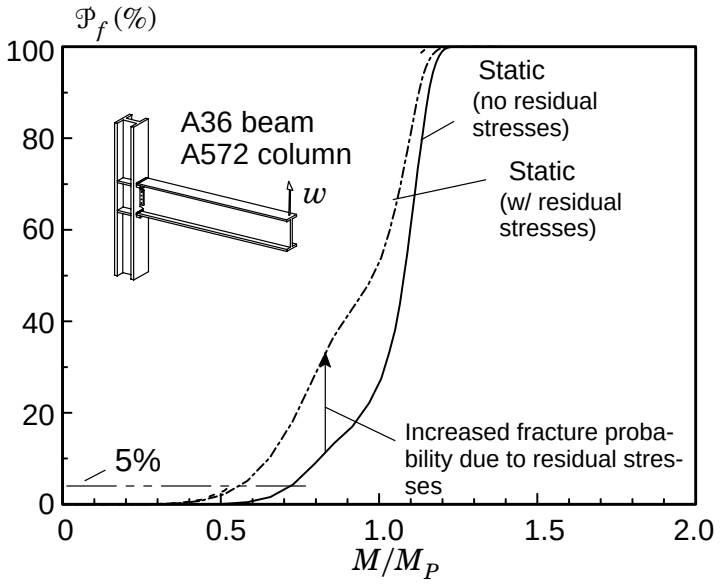

Fig. 4. Cumulative failure probabilities predicted by Weibull stress model.

6. CONCLUDING REMARKS

This study describes probabilistic modeling of the nonlinear fracture behavior in the beam lower-flange to column welds found in moment resistant frames of the design commonly used prior to the Northridge earthquake. 3-D finite element analyses, coupled with an advanced micro-mechanical fracture model based on the Weibull stress, are used to assess the relative significance of residual stresses. The present work considers only the initiation of *brittle fracture* triggered by a *transgranular cleavage* mechanism typical of that exhibited by ferritic steels (and welds) operating in the DBT region.

The finite element models represent the commonly used T-configuration tested in laboratories to simulate exterior connections. Loading takes place through specified displacements imposed at the end of the beam. A realistic residual stress field is introduced using an eigenstrain approach. Measured fracture loads from 15 earlier tests conducted as part of the SAC-Steel and other programs on nearly identical, full-scale T-connections of the pre-Northridge design provide a statistically significant data set to enable calibration of the micro-mechanical model. The computational studies here focus on comparison of the various configurations through the cumulative failure probabilities predicted by the Weibull stress model with loading expressed in terms of the normalized beam moment at the column flange.

REFERENCES

[1] The SAC Joint Venture is a partnership of the Structural Engineers Association of California, the Applied Technology Council, and the California State Universities for Earthquake Engineering.

[2] Kauffmann E. J., Fisher J. *Fracture analysis of failed moment frame weld joints produced in full-scale laboratory tests and buildings damaged in the Northridge earthquake. SAC* 95-08, part 2, 1996;1-1 – 1-21.

[3] Interim Guidelines: *Evaluation, Repair, Modification and Design of Welded Steel Moment Frame Structures*. FEMA-267, Federal Emergency Management Agency, 1995.

[4] Barson J., Pellegrino J. *Failure analysis of welded steel moment–resisting frame connections.* Part II*: pre–Northridge welded steel moment frame connections.* SAC/BD–99/23,2000.

[5] Connection Test Summaries. *Program to reduce the earthquake hazards of steel moment frame structures.* FEMA-289, 1997.

[6] Beremin FM. *A local criterion for cleavage fracture of a nuclear pressure vessel steel. Metall. Trans.* 1983;11:2277-2287.

[7] Gao X, Dodds R. H. Jr. *A Weibull stress model to predict cleavage fracture in plates containing surface cracks. Fatigue & Fracture of Engineering Materials and Structures* 1999;22:481–493.

[8] Gao X, Dodds R. H., Tregoning RL, Joyce JA. *Effects of loading rate on the Weibull stress model for simulation of cleavage fracture in ferritic steels.* Submitted to *Fatigue Fracture Engng Mater Struct* 2000.

[9] Minami F., Ochiai T., Kubo T., Shimanuki H, Arimochi K, *Evaluation of pre-straining and dynamic loading effects on fracture toughness of structural steels by the local approach.* ASME 2000; *PVP Conference*.

[10] Minami F., Ochiai T., Hashida T., Arimochi K, Konda N. *Local approach to dynamics fracture toughness evaluation*. To appear in *ASTM STP* 31st National symposium on *Fatigue and Fracture Mechanics*, 2001.

[11] Mura T. *Micromechanics of Defects in Solids.* Kluwer Academy Publishers. The Netherlands, 1991.

[12] Matos C. G., Dodds R.H. Jr. *Modeling the effects of residual stresses on defects in welds of steel frame connections. Engng Struct* 2000;22:1103–1120.

[13] Zhang J., Dong P. *Residual stresses in welded moment frames and implications on structural performance. J Struct Engng* 2000;126:306–315.

[14] Moran B., Shih C..F. *A general treatment of crack tip contour integrals. International Journal of Fracture* 1987; 35:295-310.

[15] Koppenhoefer K., Gullerud A., Ruggieri C, Dodds R, Healy B. *WARP3D. Structural Research Series* (SRS) 596, UILU-ENG-94-2017, University of Illinois at Urbana-Champaign, 1998.

[16] Matos C. G., Dodds R. H. *Probabilistic fracture modeling of welds in steel frame connections.* Part I*: Quasi-static loading.* Engng Struct, 2000 (in press).

[17] Ricles J, Mao C, Kaufmann E, Lu L, Fisher J. *Dynamic tension test of simulated welded beam flange connection.* SAC Task 7.05, Preliminary Report, 1999.

ORAL/POSTER REFERENCE: ICF100275OR

MODELING CRACK PROPAGATION: A PHASE FIELD APPROACH

L. O. Eastgate[1], J. P. Sethna[1], M. Rauscher[1], T. Cretegny[1],
C. R. Myers[2], and C.-S. Chen[2].

[1]Laboratory of Atomic and Solid State Physics, Department of Physics,
Cornell University, Ithaca, NY 14853, USA.
[2]Cornell Theory Center, Cornell University, Ithaca, NY 14853, USA.

ABSTRACT

We present a continuum phase field model for crack propagation. It includes a phase field that is proportional to the mass density and a displacement field that is governed by linear elastic theory.

The phase field smoothes the sharp interface, enabling us to use equations of motion for the material rather than for the interface and thus avoiding front tracking. The interface dynamics thus emerges naturally, without making phenomenological assumptions about the crack dynamics. Our model is physically motivated, yet it avoids being specific; it does not focus on a particular material, which makes it easier to identify the basic principles of crack behavior.

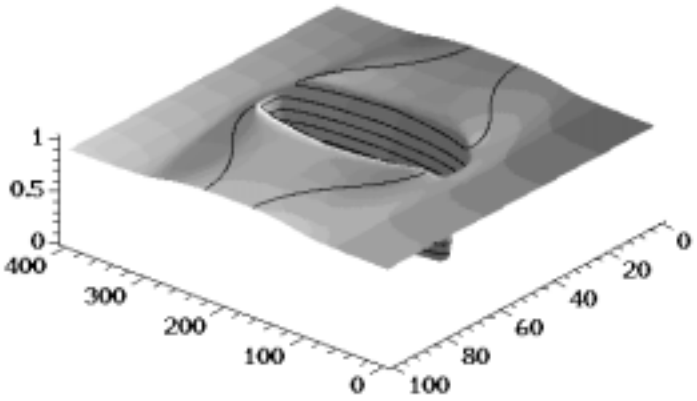

Figure 1: *A surface plot of a phase field with a growing double-ended crack.*

KEYWORDS

Fracture, phase field, multiscale, finite difference.

INTRODUCTION

The study of fracture is usually approached using mathematical descriptions and numerical simulations based on empirical observations. Finite element methods are commonly used to investigate the behavior of fractured materials on a large scale. Though these methods work well in most cases, the equations are mainly based on experimental observations.

We present a continuum description starting from basic theoretical assumptions. We introduce a phase field model, originally used to describe thermodynamic phase transitions and widely used to model solidification[1], and combine it with a displacement field. The phase field serves two main purposes. First, it smears out any sharp interfaces, averaging out microscopic detail and leaving only the necessary macroscopic variables. Second, the model gives equations of motion for the material rather than the boundaries, thus front-tracking is avoided. One of our main goals is to find macroscopic fracture laws.

The next section gives an outline of the theoretical model, presenting the main equations. This is followed by a discussion of the numerical implementation. We then describe our procedures for measuring the Griffith's threshold, before giving some concluding remarks.

THE FRACTURE MODEL

The model consists of a phase field ϕ and a displacement field $\mathbf{u}$. The former is interpreted as the normalized mass density, and typically has values between zero and one. The latter, through its derivatives, represents strain in the material. The model is based on a free energy $\mathcal{F}$ that is constructed so that the equations of motion (2–3) minimize the energy $\mathcal{F}$ with respect to time (that is, $d\mathcal{F}/dt < 0$). The free energy is given by

$$\mathcal{F} = \int_V \left(\frac{w^2}{2} |\nabla \phi|^2 + \frac{h^2}{4} \phi^2 (1 - \phi - \nabla \cdot \mathbf{u})^2 + \phi^2 \mathcal{E}(\epsilon) \right) dV \,, \tag{1}$$

where V is the volume of the system. The first term in the integrand is a gradient term discouraging spatial fluctuations in the phase field. The parameter w is proportional to the interface width. The second term is a Ginzburg-Landau double well potential, favoring values of ϕ at zero and $1 - \nabla \cdot \mathbf{u}$, representing the two phases vacuum and solid, respectively. If the material is completely unstrained, then $\nabla \cdot \mathbf{u} \equiv 0$ and the upper value is one, otherwise this value is either somewhat higher (for a compressed material) or lower (for a stretched material). The factor $1 - \phi - \nabla \cdot \mathbf{u}$ can be thought of as a density of vacancies or interstitials. The parameter h controls the height of the barrier between the vacuum and solid phases. The last term is the elastic strain energy density $\mathcal{E}(\epsilon) = (1/2) C_{ijkl} \epsilon_{kl} \epsilon_{ij}$. For a homogeneous, isotropic material, the tensor C_{ijkl} can be described by the two Lamé constants μ (the shear modulus) and λ by $C_{ijkl} \epsilon_{kl} \epsilon_{ij} = (\lambda \epsilon_{mm} \delta_{ij} + 2\mu \epsilon_{ij}) \epsilon_{ij}$. Since the elastic energy is only defined in the material (that is, $\phi \neq 0$), $\mathcal{E}(\epsilon)$ is multiplied by a factor of ϕ^2; thus the strain energy will go to zero in the vacuum. The strain is related to the displacement field by $\epsilon_{ij} = (\partial_j u_i + \partial_i u_j)/2$. This means that the divergence of the displacement field is just the trace of the strain, $\nabla \cdot \mathbf{u} = \epsilon_{mm}$.

The equations of motion for the phase field ϕ and displacement field $\mathbf{u}$ are

$$\frac{\partial \mathbf{u}}{\partial t} = -\frac{1}{\eta} \left(\frac{\delta \mathcal{F}}{\delta \mathbf{u}} + \phi \nabla \frac{\delta \mathcal{F}}{\delta \phi} \right) \tag{2}$$

$$\frac{\partial \phi}{\partial t} = -\nabla \cdot \mathbf{J} \qquad \mathbf{J} = -D \nabla \frac{\delta \mathcal{F}}{\delta \phi} + \phi \frac{\partial \mathbf{u}}{\partial t} \tag{3}$$

where η and D are the viscosity and the diffusion constant, respectively. Note that Equation (3) is the continuity equation. This means that total ϕ, or mass, is conserved. The first term in $\mathbf{J}$ is a diffusion

term, while the second term makes sure that the mass follows the motion of the displacement field. The evolution of the fields are constructed to be over-damped and downhill in the free energy.

The Lamé constants are connected through Poisson's ratio ν by $\lambda = 2\mu\nu/(1-2\nu)$ [2]. In the case of plane strain, the $\nabla \cdot \mathbf{u}$ term in the double well potential turns out to be crucial to preserve this relation.

NUMERICS

We have implemented Equations (2) and (3) for a plane strain system. Thus we can perform our simulations on a two-dimensional regular finite difference grid with periodic boundary conditions in both directions. We have investigated both single-ended and double-ended cracks under mode I loading, see Figure 2.

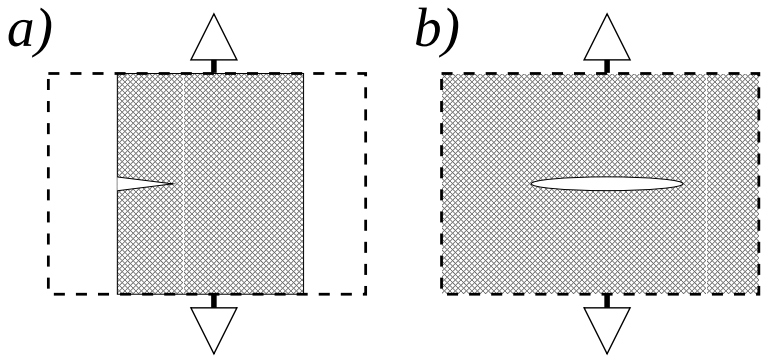

Figure 2: *A strained material with a (a) single-ended or a (b) double-ended crack. The arrows indicate the loading direction, the dashed lines the periodic boundaries.*

The system is initially strained in the y-direction with a uniform constant strain s. The strain is represented through the spatial derivatives of the displacement field $\mathbf{u}$, which means that there is an inherent discontinuity in the strain field at the y-boundary. This problem has been resolved using "skew-periodic" boundary conditions. In essence, we identify $\mathbf{u}$ on the bottom with $\mathbf{u} + \Delta\mathbf{u}$ on the top where $\Delta\mathbf{u}$ parameterizes the applied strain. Thus the strain remains continuous across the boundary. In addition to inserting a constant-slope displacement field in the y-direction, the phase field is altered from 1 to $1 - \nabla \cdot \mathbf{u}$. This is to account for the change in mass density if a material is stretched or compressed.

After straining the sample in the y-direction, a double ended crack, or slit, is inserted by removing mass (that is, setting the phase field to zero) in an elongated rectangular area in the center. The crack will grow if the strain is above some threshold value as given by the Griffith's criterion. One of our first tasks was to find this threshold value (see below).

The model described above has two different mechanisms for moving mass. One is a very slow process, which we identify as diffusion. The other is more rapid, where the phase field moves with the displacement field.

The periodic boundary conditions of the finite-difference grid allows the use of Fourier methods. To increase stability, we implemented a semi-implicit scheme[3]. The implicit parts can be solved analytically in Fourier space, which increases efficiency considerably.

MEASURING GRIFFITH'S CRITERION

One way of finding the Griffith's threshold is to measure the energy density (per unit length) of a cracked, relaxed system (that is, find the surface energy), and compare it to the energy density of a strained unfractured material. A small concern is that the measured surface energy can vary significantly if the crack is too narrow or the energy is measured too soon after the crack tip has passed. The energy of the unfractured material is just a special case of Equation (1) with $\partial_y u_y = s = \text{constant}$, $\partial_x u_x = -\nu s$ and $\phi = 1 - \nabla \cdot \mathbf{u}$; using $\lambda = 2\mu\nu/(1-2\nu)$, we get the relation

$$\mathcal{F} \approx \mu(1+\nu)s^2\,, \qquad \text{for } s \ll 1\,. \tag{4}$$

Taking the difference between the energy density in front of and behind the crack gives the energy released as a strained material is fractured and relaxed. The Griffith's criterion is reached when the strain is so low that the energy on both sides of the crack tip are the same. In our model, this happens at around 4% strain with our current choice of parameters.

Another way of finding the Griffith's criterion is by comparing the crack velocity to the energy release rate $\mathcal{G}$. This can be done using the J-integral[4]. The J-integral must be positive for the crack to grow. If the crack is parallel to the x-axis, the energy release rate $\mathcal{G}$ is equivalent to the x-component of the J-integral, J_x. Instead of performing the contour line-integral, it is common to convert it to an area-integral for increased accuracy when doing the integral numerically. The area integral is defined as

$$J_x = -\int_A \Omega(x,y)\,dx\,dy \tag{5}$$

where $\Omega(x,y) = W\partial_x q - \sigma_{ij}\partial_x u_i \partial_{x_j} q$ and $W = \phi^2 \mathcal{E}(\epsilon)$. Here q is a function that is unity around the crack tip and zero outside. Notice that if q is constant in a region, $\Omega(x,y) \equiv 0$, so in effect the line integral is replaced by a "thick line" contour integral, where the "thick line" exists everywhere q has a gradient.

CONCLUSION

We have presented a continuum phase field model of fracture, where the free energy and equations of motion are based on basic descriptions of thermodynamics. The fracture interfaces emerge and evolve naturally, avoiding the need for front tracking and phenomenological assumptions of crack growth laws. One of our main goals is to find macroscopic fracture laws.

Future work may include general three dimensional simulations, and spatial and temporal noise to represent inhomogeneities and plasticity.

References

[1] See e.g. Warren, J. A. (1995). *IEEE Comput. Sci. Eng.*, 2, 38, or Karma, A. and Rappel, W.-J. (1998). *Phys. Rev. E*, 57, 4323.

[2] See e.g. Zienkiewicz, O. C. and Taylor, R. L. (1989). *The Finite Element Method*, McGraw-Hill, London.

[3] Eyre, D. J. (1998). In: *Computational and Mathematical Models of Microstructural Evolution*, (eds. J. W. Bullard, R. Kalia, M. Stoneham, L.-Q. Chen), The Materials Research Society, 1998.

[4] Rice, J. R. (1968). In: *Fracture: An Advanced Treatise*, Vol. 2 (Mathematical Fundamentals), pp. 191–311, (ed. H. Liebowitz), Academic Press, N.Y.

MODELING OF DAMAGE EVOLUTION EQUATION OF PZT CERAMICS AND ITS APPLICATION TO CRACK GROWTH ANALYSIS

M. Mizuno [1], Y. Honda [2] and H. Kato [2]

1 Department of Machine Intelligence and Systems Engineering, Akita Prefectural University, Tsuchiya, Honjo, Akita 015-0055, Japan
2 Department of Mechanical Engineering, Graduate School of Nagoya University, Chikusa-ku, Nagoya, Aichi 464-8603, Japan

ABSTRACT

In order to describe damage of $PbZrO_3$-$PbTiO_3$ (PZT) ceramics, a damage variable based on the continuum damage mechanics is introduced, and an evolution equation of the damage variable for PZT ceramics is formulated by taking into account effects of mechanical and electrical loads on the damage development. On the other hand, the damage variable is introduced into piezoelectric constitutive equations of PZT ceramics by using a modified cubes model; i.e. material constants in the constitutive equations are expressed as a function of the damage variable. Then, a set of the piezoelectric constitutive equations and the evolution equation of damage variable are employed to predict fatigue life under various mechanical and electrical loading conditions, and the validity of the modeling is discussed by comparing the predictions with experimental results. Finally, as an example of applications, the constitutive equations and the damage evolution equation are applied to a crack growth analysis by using a double cantilever beam (DCB) model, and the effects of electric field on the crack growth are discussed.

KEYWORDS

Damage mechanics, Piezoelectric ceramics, Evolution equation of damage variable, Constitutive equation, Modified cubes model, Crack growth analysis, Double cantilever beam model

INTRODUCTION

Piezoelectric ceramics are used in sensors and actuators because of their fast electromechanical response, relatively high power of generating force and small size. In the operation of actuators, the piezoelectric ceramics are subjected to mechanical and electrical loads cyclically, and damage such as cavities and microscopic cracks in the ceramics develops by both loads. Since the damage causes change in mechanical and piezoelectric properties and causes fracture of the ceramics finally, mathematical description of the damage development is necessary to predict fracture of the ceramics as well as to control actuators precisely.

Researches on description of the damage of piezoelectric ceramics in the framework of the continuum damage mechanics have been published, so far. Chuang et al. [1] predicted fatigue life of a 4-point bend

PZT ($PbZrO_3$-$PbTiO_3$) ceramics by a finite element model. Jain and Sirkis [2] modeled the damage by the micromechanics and discussed the effects of the damage on mechanical and piezoelectric properties. On the other hand, Sun and Jiang [3] discussed fatigue crack growth under mechanical and electrical loads and estimated it by the fracture mechanics. Moreover, the effects of electric field on fatigue life and crack growth were discussed by other researchers [4, 5]. However, any damage evolution equation has not been formulated appropriately by taking into account the effects of electric field on the damage.

In the present paper, a damage variable is introduced into piezoelectric constitutive equations by using a modified cubes mdel [6]; i.e. material constants in the constitutive equations are expressed as a function of the damage variable. An evolution equation of the damage variable is formulated by taking into account the effects of electric field on fatigue life. In order to confirm the validity of the formulation, fatigue life is simulated by using the constitutive equations and the evolution equation in comparison with experimental results [7, 8]. Finally, as an application of the constitutive equations and the evolution equation, those equations are applied to a double cantilever beam (DCB) model [9], and the effect of electric field on the crack growth is discussed.

PIEZOELECTRIC CONSTITUTIVE EQUATION AND DAMAGE EVOLUTION EQUATION

Piezoelectric Constitutive Equations by Taking into Account Damage

In general, piezoelectric constitutive equations are given as follows:

$$\sigma_{ij} = C_{ijkl}\varepsilon_{kl} - e_{mij}E_m, \tag{1}$$

$$D_i = e_{ikl}\varepsilon_{kl} + \kappa_m E_m, \tag{2}$$

where $\sigma_{ij}, \varepsilon_{ij}$, E_i and D_i are stress, strain, electric field and electric displacement, respectively, while C_{ijkl}, e_{mij} and κ_m represent elastic moduli, piezoelectric moduli and permittivity, respectively. The material constants are affected by damage such as cavities and microscopic cracks. Thus, if the damage is expressed by a damage variable ω based on the continuum damage mechanics, the material constants are given as a material function of ω:

$$C_{ijkl} = C_{ijkl}(\omega),\ e_{mij} = e_{mij}(\omega),\ \kappa_m = \kappa_m(\omega). \tag{3}$$

In the present paper, the damage is assumed to be isotropic for the sake of simplification.

Modified Cubes Model

If an isolated cavity in the material is assumed to be represented by a cube, it is classified into 3-0 type connectivity introduced by Newnham et al. [10]. Since representative material constants of ceramics including cavities are derived as material constants of two-phase composites by combining a series model and a parallel model [6], the material constants are defined as a function of volume fraction of cavity easily.

The material constants in Eqns 1 and 2 in the poling direction of piezoelectric ceramics are given as follows:

$$\overline{C} = (1-a^2)C_0, \tag{4}$$

$$\overline{\kappa} = (1-a^2)\kappa_0 + \frac{a^2\kappa_{air}\kappa_0}{a\kappa_0 + (1-a)\kappa_{air}}, \tag{5}$$

$$\overline{e} = (1-a^2)e_0, \tag{6}$$

where $\overline{C}$, $\overline{\kappa}$ and $\overline{e}$ are representative elastic, dielectric and piezoelectric constants, respectively, while C_0, κ_0 and e_0 are elastic, dielectric and piezoelectric constant of the ceramics without cavity, respectively. κ_{air} represents permittivity of air and a is a dimension of a unit cell in the modified cubes

model.

Introduction of Damage Variable

If the damage variable is interpreted as reduction of load-carrying net area caused by cavities [11], the damage variable ω is given by

$$\omega = 1 - \frac{S^*}{S} = 1 - \frac{1-a^2}{1} = a^2, \tag{7}$$

where S and S^* are cross-sectional area and effective load-carrying area of a unit cell in the modified cubes model. Therefore, representative elastic, dielectric and piezoelectric constants in Eqns 4-6 are expressed as a function of damage variable ω as follows:

$$\overline{C} = (1-\omega)C_0, \tag{8}$$

$$\overline{\kappa} = (1-\omega)\kappa_0 + \frac{\omega\kappa_{air}\kappa_0}{\sqrt{\omega}\kappa_0 + (1-\sqrt{\omega})\kappa_{air}}, \tag{9}$$

$$\overline{e} = (1-\omega)e_0. \tag{10}$$

The piezoelectric constitutive equations in the uniaxial state in the poling direction are given as follows:

$$\sigma = \overline{C}(\omega)\varepsilon - \overline{e}(\omega)E, \tag{11}$$

$$D = \overline{e}(\omega)\varepsilon + \overline{\kappa}(\omega)E. \tag{12}$$

Evolution Equation of Damage Variable

In the present paper, the effect of electric field on the damage is assumed to be introduced into the evolution equation of damage variable through internal stress caused by piezoelectric effect [4, 5, 7, 8]. Since the constitutive equations 11 and 12 are not taken into account domain switching, the application of the equations is restricted within lower electric field than coercive field. Since, in general, ceramics tensile strength is lower than compressive and shear strength, reference stress for damage criterion is expressed by linear combination of the maximum principal stress σ^1 and the equivalent stress σ^{EQ}. Accordingly, the evolution equation of damage variable is formulated by

$$\frac{d\omega}{dt} = A\left[\frac{\alpha\sigma^1 + (1-\alpha)\sigma^{EQ}}{1-\omega}\right]^k, \tag{13}$$

where A, k, α are material constants, and they are determined by different experiments in stress states.

Figure 1 and 2 show simulations of fatigue life of PZT ceramics by using the constitutive equations 8-12 and the damage evolution equation 13 in comparison with experimental results [7, 8].

SIMPLIFIED ANALYSIS OF CRACK GROWTH

As an application of the constitutive equations 8-12 and the damage evolution equation 13, a simplified analysis of crack growth in steady state is performed by using a double cantilever beam (DCB) model [9].

Formulation of DCB Model

In the DCB model, a plate with a crack is divided into three zones as shown in Figure 3; i.e. elastic zone Ω_e, fractured zone Ω_f and damaging zone Ω_D. The elastic zone is treated as a cantilever beam in which elastic shear deformation is dominant, while a crack is included in the fractured zone where any deformation is not considered. The constitutive equations and the damage evolution equation are applied

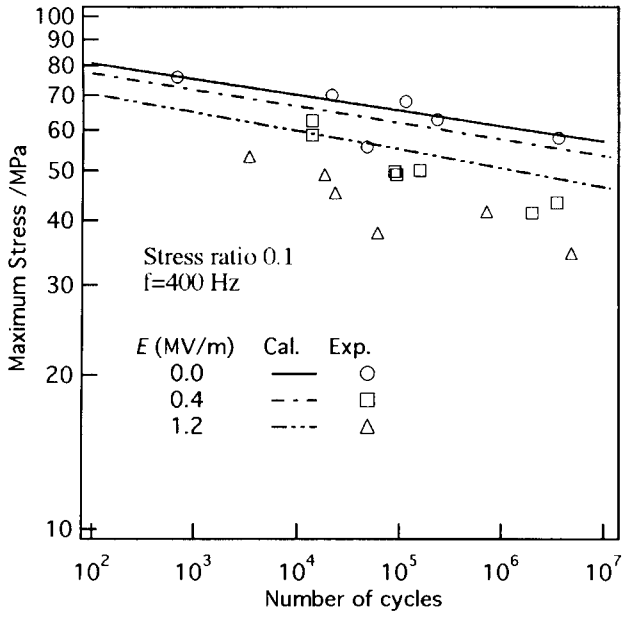

Figure 1: Fatigue life under DC electric field

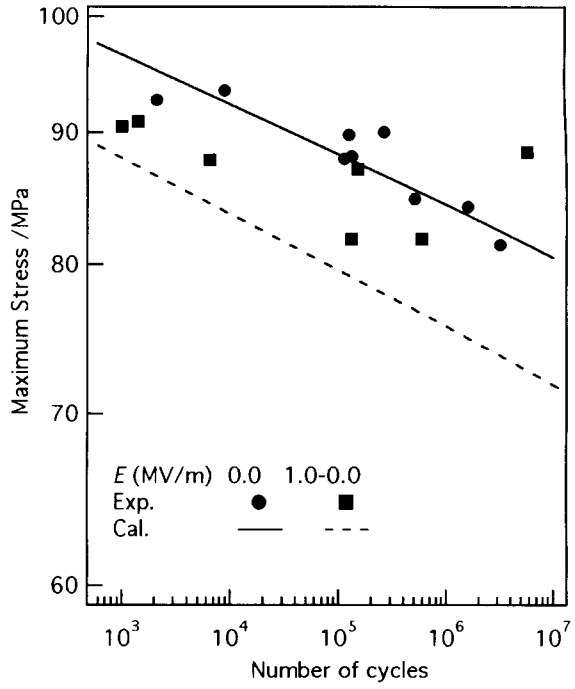

Figure 2: Fatigue life under AC electric field

to the damaging zone, in which stress state is assumed to be uniaxial. In the model, poling direction coincides with axis y in the coordinate system $o-xy$, and electric field in the same direction as the poling direction is positive.

Furthermore, for the sake of the simplification, crack growth in steady state at constant rate v and a concentrated load W at $x=0$ are considered. Then, if the Galilean transformation, which transforms the crack tip to the origin $z=0$ in the new coordinate system $o'-zy$, is introduced, Eqn 13 and the relation between displacement and stress in the elastic zone are given as follows:

$$-v\frac{d\omega}{dz}=A\left[\frac{\sigma}{1-\omega}\right]^{k}, \tag{14}$$

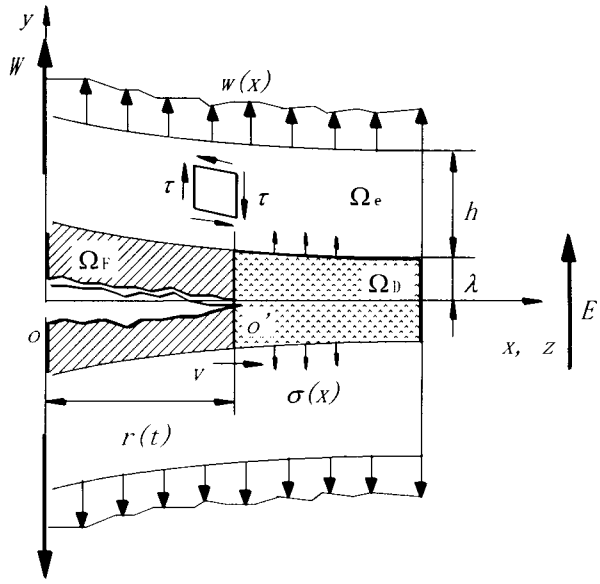

Figure 3: Double cantilever beam model

$$G_0 h\lambda \frac{d^2\varepsilon}{dz^2} = \sigma, \tag{15}$$

where G_0, h and λ are the shear modulus, width of the elastic zone and width of damaging zone, respectively.

Boundary Condition

In the present paper, $w(x) = 0$ since a concentrated load W at $x = 0$ are considered, and considering the fracture condition at the crack tip, $z = 0$, boundary conditions are represented as follows:

$$\frac{d\varepsilon}{dz}(0) = -\frac{W}{G_0 h\lambda}, \tag{16}$$

$$\omega(0) = 1, \tag{17}$$

$$\varepsilon(0) = \varepsilon_R, \tag{18}$$

where ε_R is fracture strain.

On the other hand, since the shearing force at infinity, $z = \infty$, may vanish and the strain generates due to piezoelectric effect by electric field, boundary conditions at $z = \infty$ are depicted as follows:

$$\frac{d\varepsilon}{dz}(\infty) = 0, \tag{19}$$

$$\varepsilon(\infty) = \frac{e_0}{C_0} E. \tag{20}$$

Eqns 11, 14 and 15 are solved under initial conditions 16-18, then, distribution of stress, strain and damage variable in front of the crack tip in the steady state of crack growth can be obtained. In the system of differential equations, since the crack growth rate v and the fracture strain ε_R are unknown, v and ε_R are determined so that the boundary conditions 19 and 20 are satisfied.

Results of Analysis

In the present paper, crack growth of PZT ($PbZrO_3$-$PbTiO_3$) ceramics is analyzed and following material constants are employed:

$$C_0 = 16.3\ \mathrm{N/m^2},\ e_0 = 7.1\ \mathrm{C/m^2},\ \kappa_0 = 34.0\times10^{-10}\ \mathrm{C/Vm},\ G_0 = 6.0\times10^{10}\ \mathrm{N/m^2},$$
$$A = 7.4\times10^{-103},\ k = 51,\ h = 0.05\ \mathrm{m},\ \lambda = 0.005\ \mathrm{m}. \tag{21}$$

Figures 4 and 5 show distributions of stress σ and strain ε in front of the crack tip under various electric fields E, and Figure 6 shows the effect of electric field on the crack growth rate v.

CONCLUDING REMARKS

In the present paper, damage such as cavities and microscopic crack in PZT ceramics was represented by the damage variable based on the continuum damage mechanics, and introduction of the damage variable into the piezoelectric constitutive equation and formulation of evolution equation of damage variable were performed. Then, as an application of those equations, they were applied to the DCB model to analyze the crack growth in the steady state, and the effect of electric field on the crack growth was discussed.

Since it is found that concentration of stress and electric field around the crack tip causes domain switching which generates internal stress and affects the damage development, it is necessary to take into account the domain switching in the constitutive equations and the damage evolution equation and to consider the

distribution of electric field around the crack tip in the analysis of crack growth. In order to perform coupling analysis of stress-electric-damage field, the local approach based on the continuum damage mechanics by using a finite element method is useful.

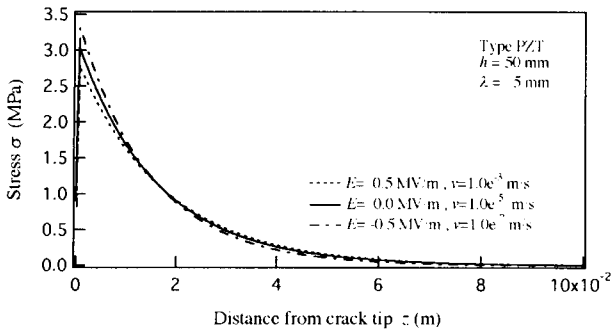

Figure 4: Distribution of stress in front of crack tip

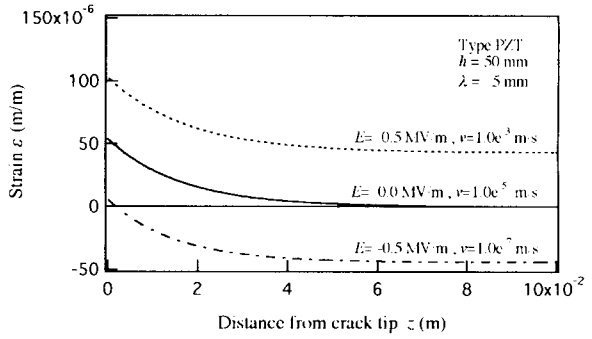

Figure 5: Distribution of strain in front of crack tip

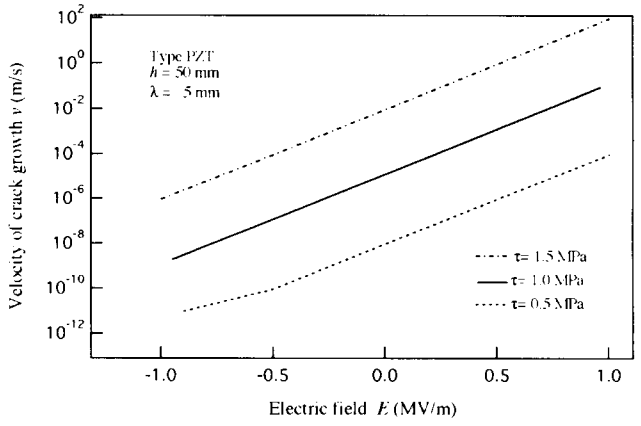

Figure 6: Effect of electric field on crack growth rate

REFERENCES

1. Chuang, T., Wang, Z., Hill, M. and White, G. (1996) *Fract. Mech. Ceramics* 12, 135.
2. Jain, A. K. and Sirkis, J. S. (1995) *SPIE* 2443, 374.
3. Sun, C. T. and Jiang, L. Z. (1997) *SPIE* 3040, 129.
4. McHenry, K. D. and Koepke, B. G. (1978) *Fract. Mech. Ceramics* 5, 337.
5. Wang, D., Fotinich, Y. and Carman, G. P. (1998) *J. Appl. Phys.* 83, 5342.
6. Banno, H. (1987) *Ceramic Bulletin* 66, 1332.
7. H. Makino and N. Kamiya (1994) *Jpn. J. Appl. Phys.* 33, 5323.
8. H. Makino and N. Kamiya (1998) *Jpn. J. Appl. Phys.* 37, 5301.
9. S. Murakami, K. Hayakawa and M. Mizuno (1993) *Eur. J. Mech., A/Solids* 12, 249.
10. R. E. Newnham, D. P. Skinner and L. E. Cross (1978) *Mater. Res. Bull.* 13, 525.
11. S. Murakami (1988) *J. Appl. Mech.* 110, 280.

ORAL/POSTER REFERENCE: ICF100471OR

MODELLING OF PLASTIC EFFECTS DURING SMALL FATIGUE-CRACK GROWTH

O.Ye. Andreykiv[1], V.V. Panasyuk[1], R.O. Ritchie[2] and O.I. Darchuk[1]

[1]Karpenko Physico-Mechanical Institute, 5 Naukova St., 72601 Lviv, Ukraine
[2]Department of Materials Science and Mineral Engineering, University of California, Berkeley, CA 94720-1760, USA

ABSTRACT

A method is presented for assessment of effects of main plastic factors – reversed plastic yielding of the material and plasticity-induced crack closure – on small fatigue crack behavior. The method uses the closed form analytical solution of the elastic-plastic problem for a rectilinear crack in a plate on the basis of plastic-strip model. This allowed to simplify significantly the calculation of the stress-strain parameters at the crack tip (the effective stress intensity factor range and crack tip opening displacement range). It was shown that the calculated results agree well with those obtained by the more complicated methods, including a method of finite elements. Using the proposed method, the dependence of the small crack growth rate on the loading amplitude and stress ratio, initial crack size and other parameters, has been analyzed. The revealed regularities and tendencies are proved experimentally. In particular, the method is successfully utilized to predict the small fatigue crack growth rate in Fe-3% Si alloy under high amplitude loading.

KEYWORDS

Small fatigue cracks, crack closure, plastic strip model, singular integral equation method, crack tip opening displacement.

INTRODUCTION

Small fatigue crack behavior greatly depends on the plasticity effects. At the relatively high stress level that are usually required to grow small cracks, the criterion of small scale plasticity at the crack tip, relative to the overall size of the crack, is violated. Therefore, conventional methods of linear-elastic fracture mechanics can not be used and the crack growth rate dl/dN should be evaluated from deformation or energetic parameters, e.g. crack tip opening displacement range $\Delta\delta$:

$$dl/dN = v(\Delta\delta) \tag{1}$$

The value of $\Delta\delta$ is significantly dependent on the plastic-induced crack closure, that is differently manifested for small and long cracks. To consider these factors, it is necessary to analyze the elastic-plastic situation at the crack tip under cyclic loading. Approximate analysis can be done by known plastic-strip model (Dugdale [1], Panasyuk [2]). This approach was advanced by Budiansky and Hutchinson [3], Newman [4-5], Wang and Blom [6-7] and others authors. A rather simple method of an analytical solution on the basis of strip-model of elastic-plastic problems about fatigue crack growth by its reduction to a singular integral equation,

has been proposed earlier by Panasyuk et al [8-9]. This method allows us to decrease the complexity and instability of calculations, typical of numerical methods. The mentioned method is used in this paper to assessment of the stress-strain state near small fatigue crack and prediction of crack growth rate from equation (1).

DEVELOPMENT OF THE MODEL

We consider an internal rectilinear crack of length $2l$ in a plate subjected to cyclic loading ($p=p_{min} \sim p_{max}$), as shown in Figure 1. According to plastic-strip model, plastic zones at the crack tip are replaced by the additional cuts where the boundary normal stresses are equal to flow stress. At $p=p_{max}$ these stresses are taken as equal to $\alpha\sigma_0$, where σ_0 is average between yield stress and ultimate tensile strength of material, α is plastic constraint factor, the accounts for the influence of stress state on tensile yielding at the crack front in accordance with Newman [4]. For plane stress conditions $\alpha=1$, and for simulated plane strain conditions $\alpha=3$. At $p=p_{min}$ the stresses within the cyclic plastic zone are equal to $-\sigma_0$. In the analysis the crack closure, caused by plastic stretches of thickness $h(x)$ on the fatigue crack surfaces, is accounted for. These plastic stretches are the result of the residual plastic deformation formed in the near-surface layers as the crack grows through plastic zone ahead of the crack tip. During unloading, the crack surfaces contact each other along the entire crack length or in specific sections ($l_c < |x| < l$) near the crack tip. Contact stresses are denoted as $\sigma_{con}(x)$.

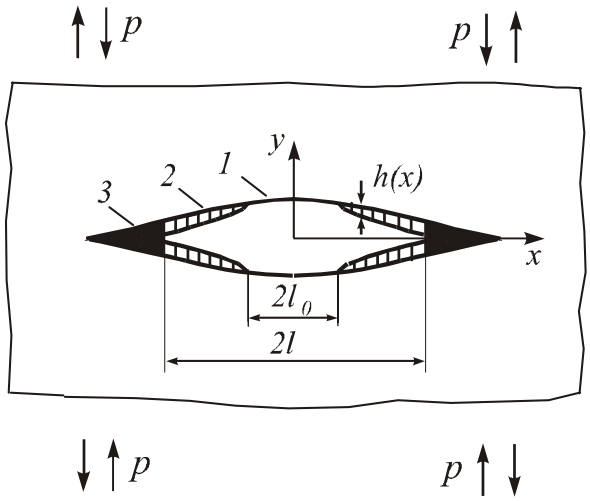

Figure 1: A rectilinear fatigue crack in plate: 1- crack; 2-plastic stretch; 3-plastic zone

Analytical solutions to the corresponding boundary-value problem for a plate with model cuts (crack + plastic zones) have been obtained on the basis of results in [2] (details are given in Panasyuk et al [10]). Specifically, normal displacements of the crack edges at the maximum and minimum loads are found to be:

$$u_{max}(x) = p_{max}\int_0^{l+l_p} H(l+l_p,x,\xi)d\xi - \alpha\sigma_0\int_l^{l+l_p} H(l+l_p,x,\xi)d\xi \tag{2}$$

$$u_{min}(x) = u_{max}(x) - (p_{max}-p_{min})\int_0^{l+l_{pf}} H(l+l_{pf},x,\xi)d\xi + (1+\alpha)\sigma_0\int_l^{l+l_{pf}} H(l+l_{pf},x,\xi)d\xi + \int_{l_c}^{l}\sigma_{con}(\xi)H(l+l_{pf},x,\xi)d\xi \tag{3}$$

where $H(l,x,\xi) = \frac{2}{\pi E} ln \frac{\sqrt{l^2-x^2}+\sqrt{l^2-\xi^2}}{\sqrt{l^2-x^2}-\sqrt{l^2-\xi^2}} d\xi$; l_p, l_{pf} is the length of monotone and cyclic plastic zone, respectively; E is the elastic modulus of the material.

Together with the condition of crack edge closing in the contact region

$$u_{min}(x) = h(x) \qquad l_c \le |x| \le l \tag{4}$$

dependence (3) forms equation to estimate the unknown contact stresses $\sigma_{con}(x)$. By differentiation with respect to x, this equation is reduced to singular integral equation:

$$\int_{l_c}^{l} \frac{\sigma_{con}(\xi)\sqrt{(l+l_{pf})^2-\xi^2}}{x^2-\xi^2}d\xi = \frac{\pi E}{4}\frac{\sqrt{(l+l_{pf})^2-x^2}}{x} f(x) \qquad l_c \le |x| \le l \tag{5}$$

where

$$f(x) = \frac{\sigma_s}{\pi E}\left\{H(l+l_p,x,l) - H(l+l_p,x,-l) - 2H(l+l_{pf},x,l) + 2H(l+l_{pf},x,-l) + \left(\frac{\pi}{4}\frac{p_{max}-p_{min}}{\sigma_s} - arccos\frac{l}{l+l_{pf}}\right)\frac{8x}{\sqrt{(l+l_{pf})^2-x^2}}\right\} - \frac{d}{dx}u_{res}(x)$$

Solution of equation (5), according to Muskhelishvili [11], gives the following formula for $\sigma_{con}(x)$:

$$\sigma_{con}(x) = \frac{E}{\pi}\frac{x\sqrt{l^2-x^2}}{\sqrt{x^2-l_c^2}\sqrt{(l+l_{pf})^2-x^2}}\int_{l_c}^{l}\frac{\sqrt{(l+l_{pf})^2-\xi^2}\sqrt{\xi^2-l_c^2}}{\sqrt{l^2-\xi^2}}\frac{f(\xi)}{\xi^2-x^2}d\xi\,. \tag{6}$$

The tensile plastic zone length l_p and cyclic plastic zone length l_{pf} are determined from the conditions that the stress at the point just ahead of the plastic zone is elastic and infinitely approaches the yield stress. Parameter l_c is determined from the condition that the contact stress approaches zero at the end of contact zone.

The developed solution is used for assessment of the parameters of elastic-plastic situation at the fatigue crack tip. Main parameters are as follows: maximum and minimum crack tip opening displacement $\delta_{max}=2u_{max}(l)$; $\delta_{min}=2u_{min}(l)$; and the crack opening stress p_{op}, which is defined at the external load $p=p_{op}$ at which crack surfaces are fully open and process of active deformation of the material immediately ahead of the crack tip begins. The mentioned parameters determine the effective stress intensity factor range $\Delta K_{eff} = (p_{max} - p_{op})\sqrt{\pi l}$ and cyclic crack tip opening displacement range $\Delta\delta=\delta_{max} - \delta_{min}$, which are the basic values for calculating fatigue crack growth rate from linear and nonlinear criteria of fracture mechanics.

NUMERICAL RESULTS AND DISCUSSION

The proposed model is applied to a fatigue crack emanating from a rectilinear defect of length $2l_0$. The defect thickness is assumed to be sufficient to prevent contact of the opposite crack faces even under symmetrical tension-compression loading. Thus, at the initial moment there is no closure effect. Further growth of a fatigue crack is accompanied by the fracture of plastically deformed material ahead of the crack tip and formation of plastic stretches on its surfaces. Their thickness are unknown but are evaluated by step-by-step analysis of crack extension. Specifically, at each step, the size of a stretch formed on the fresh crack surface is assumed to be equal to the value of crack edge displacement $u_{min}(x)$ immediately ahead of the crack tip. This value is calculated by the mentioned above model.

Some of the predicted results for plane stresses ($\alpha=1$) at two stress ratio $R=0$ and $R=-1$ and several operating stress p_{max}/σ_0 are presented in Figures 2-4.

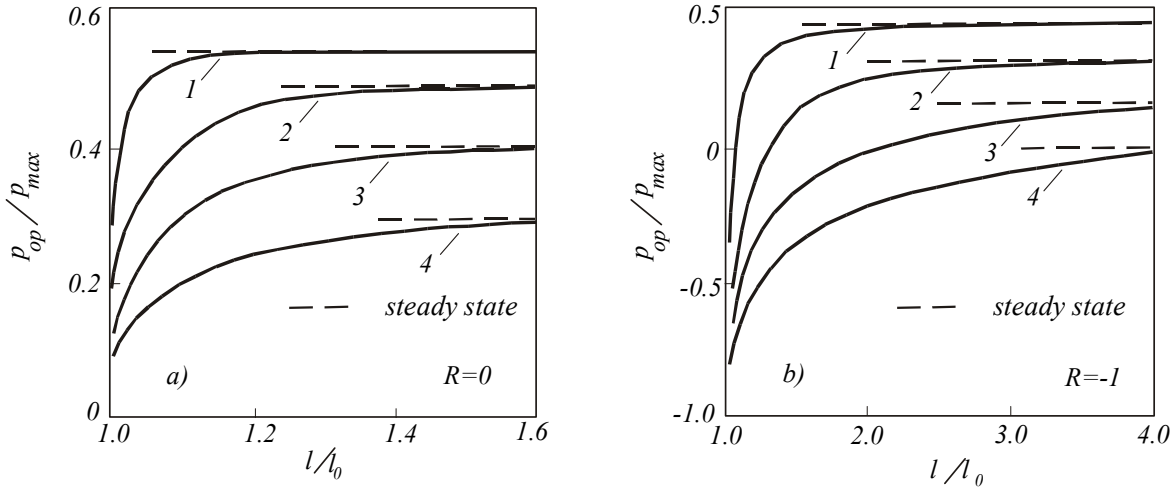

Figure 2: Predicted variation of normalized crack closure loads p_{op}/p_{max} with a crack length: (a) $R=0$; (b) $R=-1$; 1- $p_{max}/\sigma_0=0.2$; 2- $p_{max}/\sigma_0=0.4$; 3- $p_{max}/\sigma_0=0.6$; 4- $p_{max}/\sigma_0=0.8$

With the crack length extension, the thickness of plastic stretch on the crack surfaces increased and this induced a higher crack closure level (see Figure 2). After some increment of a crack length the process stabilizes itself and crack closure ratio p_{op}/p_{max} approaches constant «steady-state» values, which pertain to those for long cracks. These steady-state values are shown in Figure 3 as functions of the maximum stresses p_{max}/σ_0. These results indicate that level of plasticity-induced crack closure becomes lower with increase of the operating loads magnitude, especially at negative load ratios.

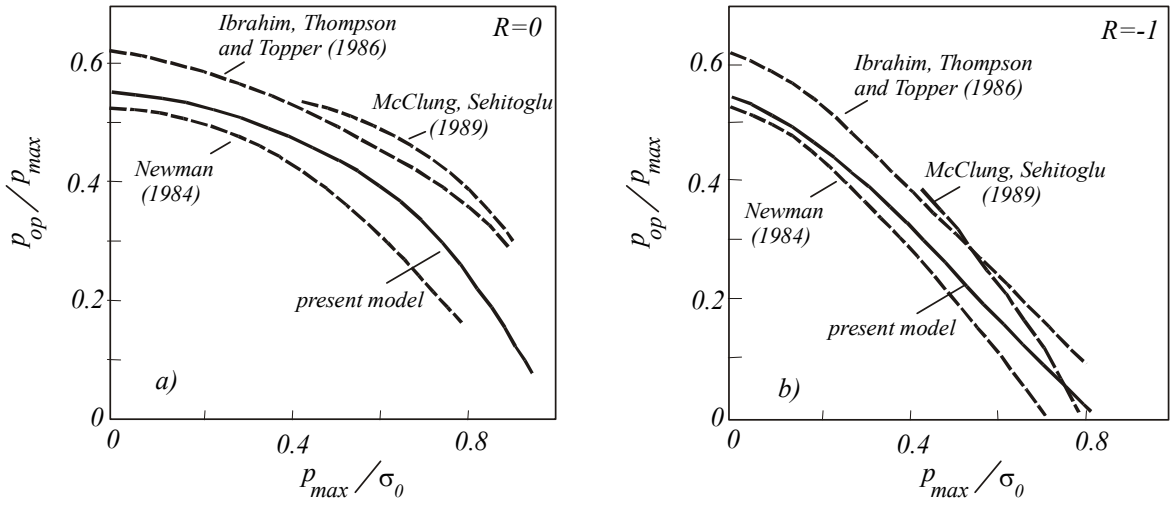

Figure 3: Predicted values of the closure ratio p_{op}/p_{max} as a function of the cyclic loading level p_{max}/σ_0 for a steadily growing crack and comparison of the present results with other models: (a) $R=0$; (b) $R=-1$

In Figure 3 the presented results are compared with several other previous models. The curves p_{op}/p_{max}~p_{max}/σ_0 for a steadily growing crack, which were obtained earlier using the method of finite element (McClung. and Sehitoglu [12]) or generalized plastic strip model (Newman [13], Ibrahim, Thompson and Topper [14]), are also presented. These results agree well for both stress ratio and various loading amplitudes.

The predicted values of normalized cyclic crack tip opening displacement range $\Delta\delta$ are shown as a function

of the maximum stress intensity factor K_{max} in Figure 4. Based on presented data, the following conclusions as to behavior of small fatigue crack can be draw.

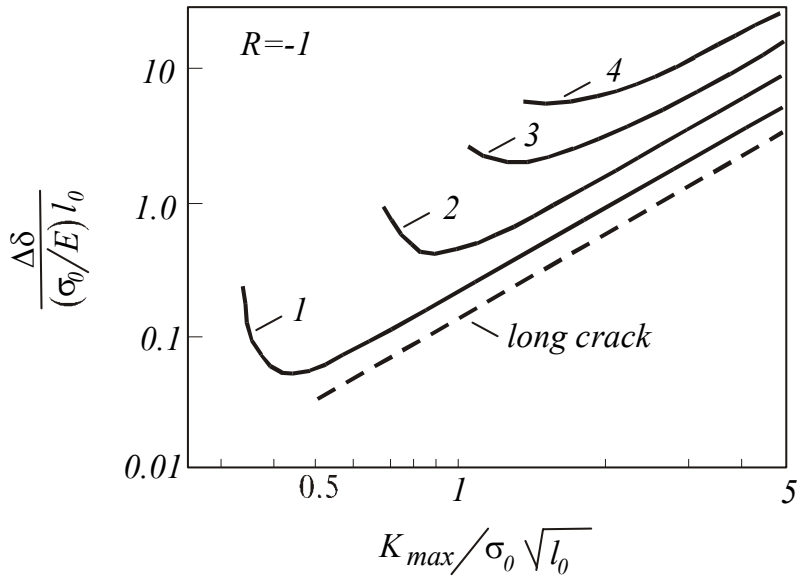

Figure 4: Dependence of normalized crack tip displacement range on maximum stress intensity factor in a cycle

Firstly, the level of plasticity-induced crack closure is lower for small cracks, compared to the steady-state values pertaining to long cracks. Similarly, at the commencement of crack growth, cyclic crack tip opening displacement for the small crack exceed the corresponding steady-state (long crack) values. As a result the growth rate for the small crack would be expected to be higher.

Secondly, as a crack grows, a gradual increase in the magnitude of plastic deformation near crack tip takes place; this promotes the crack growth. At the same time, a gradual increase in the level of plasticity-induced crack closure occurs; this retards the crack growth. The interaction of this two factors caused the non-monotone variation of «crack driving force»: a value of $\Delta\delta$ at first decreases and then increases with the crack growth (see Figure 4). This could causes both retardation and sometimes complete arrest of small cracks, what has been observed frequently by experiment.

Finally, the presented data indicate that for small cracks the actual value of $\Delta\delta$ is determined not only by current magnitude of the external cyclic loading, as is the case for long crack growth, but is significantly dependent on the crack length. We thus conclude that small crack growth rates cannot be predicted without considering the history of their initiation.

EXPERIMENTAL VERIFICATION OF THE MODEL

The proposed model has been used for calculating small fatigue crack growth rate in Fe-3% Si alloy and to compare predicted results with the earlier known experimental data [15]. Nisitani, Kawagoishi and Goto [15] tested cylindrical specimens of diameter 5mm in rotating bending. Maximum bending stresses on the specimen surface were 0.54 ~ 0.86 of the yield strength. The surface cracks initiated from a small blind hole (diameter and depth are 0.3 mm). Figure 5(a) shows relation between the crack growth rate and the stress intensity factor range. Only at low values of loading amplitude (σ_a = 560 ÷ 640 MPa) these relations are described by a unique dependence. At high stress levels, the ΔK -based criterion is unsuitable for evaluating the crack growth rate.

On the basis of the presented model calculation of cyclic crack tip opening displacement range $\Delta\delta$ was carried at the following values of the parameters: $p_{max}=\sigma_a$, $R=-1$; $\sigma_0 = 1300$ *MPa;* $\alpha = 1.8$. The initial defect

size was taken equal to the hole diameter $2l_0 = 0.3$ *mm*. The reason of that was the fact that experimental data correspond to the crack lengths that at least two-fold exceed the hole sizes ($2l \geq 0.6$ *mm*). Under such conditions, the elastic-plastic situation at the crack tip slightly depends on the initial defect geometry.

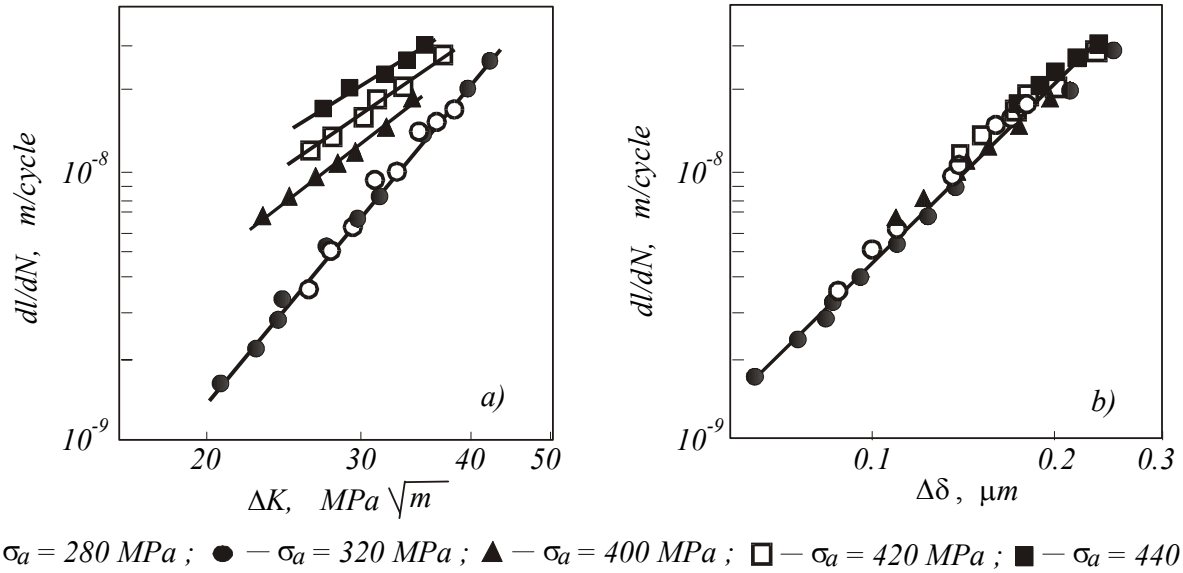

Figure 5: Crack growth rate in Fe-3% Si alloy: (a) depending on ΔK [12], (b) depending on $\Delta\delta$

In Figure 5(b) the dependence of the crack growth rate on $\Delta\delta$ is illustrated. All experimental data are described by a unique dependence. Thus, in this case crack growth can be predicted by the proposed model and deformation fatigue criterion in form equation (1).

REFERENCES

1. Dugdale, D.S. (1960) *J. Mech. Phys. Solids.* 8, 100.
2. Panasyuk, V.V. (1971). *Limiting Equilibrium of Brittle Solids with Cracks.* Manag. Inform. Serv., Detroit.
3. Budiansky, B. and Hutchinson, J.H. (1978) *J. Appl. Mech.* 45, 267.
4. Newman, J.C., Jr. (1981). In *Methods and Models for Predicting Fatigue Crack Growth under Random Loading, ASTM STP 748,* pp. 53-84, Chang, J.B. and Hudson, C.M. (Eds.). American Society for Testing and Materials, Philadelphia.
5. Newman, J.C., Jr. (1994) *Fatigue Fract. Engng Mater. Struct.* 17, 429.
6. Wang, G.S. and Blom, A.F. (1991) *Eng. Fract. Mech.* 40, 507.
7. Wang, G.S. (1993) *Eng. Fract. Mech.* 46, 909.
8. Panasyuk, V.V, Andreykiv, O.Ye., Darchuk, O.I. and Kun, P.S. (1994). In *Structural Integrity: Experiments, Models and Applications*, pp. 1271-1276, Schwalbe, K.-H., Berger, C. (Eds). EMAS, Warley.
9. Panasyuk, V.V, Andreykiv, O.Ye., Darchuk, O.I. (1998). In *Fracture from Defects*, pp. 229-234, Brown, M.W., de los Rios, E.R. and Miller, K.J. (Eds.). EMAS, Warley.
10. Panasyuk, V.V, Andreykiv, O.Ye., Ritchie, R.O. and Darchuk, O.I. (2001) *Int. J. Fracture* 107, 99.
11. Muskhelishvili, N.I. (1966). *Some Basic Problems of the Mathematical Theory of Elasticity.* Nauka, Moscow.
12. McClung, R.C. and Sehitoglu, H. (1989) *Eng. Fract. Mech.* 33, 237.
13. Newman, J.C., Jr. (1984) *Int. J. Fracture* 24, R131.
14. Ibrahim, F.K., Thompson, J.C.and Topper, T.H. (1986) *Int. J Fatigue* 8, 135.
15. Nisitani, H., Kawagoishi, N. and Goto, M. (1994). In *Handbook of Fatigue Crack Propagation in Metallic Structures*, pp. 773-778, Carpinteri, A. (Ed.). Elsevier, Oxford.

ORAL/POSTER REFERENCE: ICF100916OR

MODELLING OF SIZE EFFECTS ON FRACTURE IN THE BRITTLE-TO-DUCTILE TRANSITION REGIME

A H Sherry[1], D P G Lidbury[1], D C Connors[2] and A R Dowling[2]

[1]AEA Technology plc, Risley, Warrington, WA3 6AT, UK
[2]BNFL Magnox Generation, Berkeley, Gloucestershire, GL13 9PB, United Kingdom

ABSTRACT

Measurements of toughness in the ductile-to-brittle fracture regime exhibit an effect of test-piece size. For a given level of toughness (K_{JC}), this may be considered as a positive shift in the transition temperature (ΔT) with increasing specimen thickness for a particular geometry. This Paper describes a numerical programme undertaken to investigate the influence of specimen size on the fracture toughness behaviour of submerged-arc weld material in the ductile-to-brittle transition regime. The influences of sampling volume and constraint on ΔT have been assessed for 10 mm thick CT (CT-10) and 20 % side-grooved pre-cracked Charpy specimens (PC-CVN) relative to 25 mm thick standard plane-sided compact-tension (CT-25) specimens. Three-dimensional, elastic-plastic finite element analyses have been used to assess the constraint behaviour of these specimens, and the BEREMIN model has been applied to predict ΔT. The analyses have indicated a loss of constraint over a significant proportion of the crack front for both CT-10 and PC-CVN specimens at toughness levels greater than approximately 100 MPa$\sqrt{m}$. For CT-10 specimens, constraint-loss is most significant towards the outer edges of the specimen whilst high constraint conditions are initially maintained over the central region of the crack-front. This high constraint region may be viewed as an effective crack-front width that reduces with increasing deformation. For side-grooved PC-CVN specimens, constraint loss occurs uniformly across the crack front. Statistical models, based on empirical data, give a value of ΔT = 18 ºC for this material at a mean reference toughness of 100 MPa$\sqrt{m}$. The BEREMIN model tends to over-predict this value by ~ 35 ºC for CT-10 specimens and ~ 55 ºC for side-grooved PC-CVN specimens.

KEY WORDS

Fracture toughness, constraint, size effect, Local Approach

INTRODUCTION

Fracture toughness measurements made within the ductile-to-brittle transition temperature regime are influenced by specimen size. For a given level of toughness, K_{JC}, this may be thought of in terms of a positive shift in the transition temperature, ΔT, with increasing specimen thickness, B. Alternatively, with temperature fixed, the mean toughness derived from tests on small specimens is greater than that obtained from corresponding tests on larger specimens. There are two principal reasons for this size effect.

First, cleavage initiation in ferritic steel is associated with the pile-up of dislocations against brittle second-phase particles. The volume of the crack-tip plastic zone is therefore an important factor in the cleavage process since the greater the volume, the more likely it is that a favourable brittle particle will be sampled. Under LEFM conditions, the volume of the plastic zone is proportional to $K^4 \cdot B$, where K is the stress intensity factor and B is the crack front length (equal to the specimen thickness in standard fracture toughness specimens). The size effect on transition toughness may thus be approximately described by $K_{JC} \propto 1/B^{0.25}$. Statistical models of transition behaviour broadly reflect this scaling relationship:

- Moscovic [2]: $K_{JC} \cdot B^{0.179}$ or $K_{JC} \cdot B^{0.391}$ = constant
- Master Curve [3]: $K_{JC} \cdot B^{0.25}$ = constant

Secondly, the transition between small and large-scale yielding leads to a reduction in crack-tip constraint and a lowering of the hydrostatic stress field. This transition, which leads to an increase in effective toughness, occurs at lower crack driving forces in small compared with large specimens since at the same applied K the radius of the plastic zone is a greater proportion of the uncracked ligament. At a given temperature, constraint loss leads to an increase in the critical value of K required to initiate cleavage. The constraint parameter Q, quantifying the extent to which the actual hydrostatic stress field diverges from that corresponding to small-scale yielding (SSY) conditions, can be defined as [4]:

$$Q = \frac{\sigma_H - (\sigma_H)_{SSY}}{\sigma_0}, \qquad \text{at } \theta = 0, r\sigma_0 / J_z = 2 \tag{1}$$

where r and θ denote polar co-ordinates centred at the crack-tip, J is the J-integral and σ_0 is the yield stress. At low levels of K, the plastic zone is small and Q remains close to zero, but under large-scale yielding, Q becomes negative.

The influences of both sampling volume and constraint loss on cleavage toughness in the transition regime may be simulated using appropriate fracture models. The BEREMIN Local Approach uses a two-parameter Weibull model to describe the influence of crack-tip stress on cleavage probability, p [5]

$$p = 1 - \exp\left\{-\left(\frac{\sigma_W}{\sigma_u}\right)^m\right\} \tag{2}$$

The Weibull stress, σ_W, is defined as a volume integral taken over the fracture process zone, Ω

$$\sigma_W = \left\{ \frac{1}{V_u} \iiint_{\Omega} \sigma_q^m \, d\Omega \right\}^{\frac{1}{m}} \quad (3)$$

The constants, V_u (the characteristic volume), σ_u (the scale parameter) and m (the Weibull modulus) are the parameters of the model. The scalar field, σ_q conventionally represents the distribution of maximum principal stress, σ_1, within the plastic zone.

This Paper describes a numerical programme undertaken to investigate the influences of specimen size (sampling volume and constraint loss) on transition toughness behaviour. In particular, the behaviour of 10 mm thick compact-tension specimens (CT-10) and 20 % side-grooved pre-cracked Charpy specimens (PC-CVN) are assessed relative to standard 25 mm thick compact-tension specimens (CT-25).

MATERIAL

The material of interest is a submerged arc weld (SAW) metal. Tensile properties and BEREMIN parameters are summarised in Table 1, fracture toughness behaviour is illustrated in Fig. 1 [1]. A comparison of the calibrated model with the base-line toughness data is included in Fig. 1.

TABLE 1
TENSILE PROPERTIES AND BEREMIN PARAMETERS FOR SAW MATERIAL

T, ºC	E, GPa	σ_0, MPa	V_u, μm^3	m	σ_u, MPa
-110	216	569	$(50)^3$	13.17	3,733
-70	214	498	$(50)^3$	13.17	3,836
-50	213	470	$(50)^3$	13.17	3,859
-25	211	442	$(50)^3$	13.17	3,877
0	210	419	$(50)^3$	13.17	4,097
25	209	400	$(50)^3$	13.17	4,675

NUMERICAL ANALYSIS

Three-dimensional finite element models of the CT-10 and PC-CVN specimens were developed. Each model consisted of eight-noded full-integration brick elements arranged into planar layers. The thickest layer was towards the centre of the specimen and the thinnest towards the outer surface. In both models, the crack tip was modelled by a series of square-section brick elements of in-plane dimension 50 μm. Figure 2 illustrates the PC-CVN model.

A series of small-strain elastic-plastic finite element analyses were performed with stress-strain data appropriate to fourteen temperatures in the range –150 to +25 ºC. A series of SSY analyses were also performed within the framework of a boundary layer model to simulate the behaviour of a crack in an infinite body under high constraint plane strain conditions. The

crack-tip stress and strain fields derived from these analyses were post-processed to define the variation of Q as a function of increasing load using Eqn. (1), and p as a function of K_J and temperature using Eqns. (2) and (3).

RESULTS

Crack driving force

Figures 3 and 4 illustrate the variation of K_J across the crack front for CT-10 and PC-CVN specimens respectively. Here, the deformation level has been indexed by the parameter M, where $M = b\sigma_0/J$. Here b is the ligament size. M decreases with increasing deformation. Current validity limits in fracture toughness testing require that $M \geq 30$ at cleavage for fracture toughness data to be valid.

For the CT-10 specimen, the peak value of K_J is located at the centre of the specimen and reduces towards the outer surface for all load levels. For the PC-CVN specimen, the peak value of K_J is located at the root of the side-grooves, which act as a stress-concentrating feature. These results are similar to those presented elsewhere for plane and side-grooved specimens [6]. In order to define a crack-tip loading parameter applicable to the full width of the specimen, an average value of K_J ($K_{J,ave}$) has been calculated.

Crack-tip constraint

Figure 5 shows the variation of Q across the CT-10 specimen at different load levels. For low loads, a large proportion of the crack front is under high constraint (here defined as $Q \geq -0.1$), but Q decreases towards the outer surface. As the load level increases, the proportion of the crack front under high constraint reduces. Figure 6 shows similar results for the PC-CVN specimen. Again, at low loads, most of the crack front is under high constraint, but Q decreases slightly towards the root of the side grooves. As loading increases, constraint reduces uniformly across the crack front.

Predicted transition behaviour

Predicted transition curves using Eqns. (2) and (3) and p = 5, 50 and 95 % for CT-10 and PC-CVN specimens are compared with base-line CT-25 data in Figs. 7 and 8 respectively. Also shown are loci of constant M (30 and 80). Relative to the base-line data at 100 MPa√m, the predicted curves for the CT-10 and PC-CVN specimens exhibit a shift of approximately 55 º and 75 ºC respectively. These values are larger than that of 18 ºC derived from statistical analysis of actual data [2]. The model predictions show an increase in scatter compared with the base-line data. At –75 ºC, the base-line data indicate a scatter between the 5^{th} and 95^{th} percentiles of ~ 100 MPa√m, whereas that predicted for the CT-10 and PC-CVN specimens is greater than 200 and 300 MPa√m respectively.

DISCUSSION

The elastic and elastic-plastic stress intensity factor calculations emphasise the three-dimensional nature of deformation in fracture toughness specimens. The Q-stress profiles plotted in Figs. 5 and 6 illustrate the variation of constraint conditions through the thickness of fracture specimens.

For the CT-10 specimen, crack-tip constraint is reduced at the outer surfaces of the specimen at moderate loading levels, Fig. 5. As the loading level increases, the low constraint region progressively extends towards the centre of the specimen until, at M ≈ 30, low constraint conditions dominate across almost the full crack front. This observation leads to two important implications.

Sampling volume: the volume of highly stressed (i.e. high constraint) material ahead of the crack-tip may be smaller than that assumed by the $B^{0.25}$ scaling law, particularly for high load levels. Under these conditions, such scaling laws may under-predict the size effect since they inherently assume high constraint to extends across the full thickness. This observation has led Nevalainen and Dodds [6] to calculate effective specimen thicknesses (B_{eff}) for both CT-10 and plane-sided PC-CVN specimens based on the areas enclosed within the principal stress contour $\sigma_1/\sigma_0 = 3$. For a CT-10 specimen with a work hardening exponent n = 5 to 10, $B_{eff} \approx 0.5B$ for M < 90. This is consistent with the Q-stress data presented in Fig. 5. For a plane-sided PC-CVN specimen, $B_{eff} \approx 0.65B$ for M < 125.

Constraint effects: at fracture, the level of crack-tip constraint across the specimen width may be somewhat less than that under SSY leading to an enhancement in cleavage fracture toughness. To ensure fracture toughness data relate to high constraint conditions across a significant proportion of the crack front width, the results presented in Figs. 5 and 6 suggest that the value of M at fracture should be greater than 100 for CT-10 specimens and greater than 60 for side-grooved PC-CVN specimens.

For the CT-10 and PC-CVN specimens, the Local Approach model predicts significantly higher values of ΔT, by margins of 35 º and 55 ºC, than that derived from the $B^{0.25}$ scaling law. A difference has been observed in using small specimens to measure the Master Curve parameter T_0 [3]. For some materials there appears to be a difference between the value of T_0 derived from tests on 10 mm thick specimens and that for larger specimens. Size-dependent values of T_0 were obtained from specimen data relating to a range of nuclear pressure vessel steels [8]. As the deformation index M decreases the values of T_0 derived from PC-CVN specimens tend to reduce below those obtained from larger specimens. Work by Tregoning [9] shows that this effect may be material dependent and even negligible for some materials. Thus, it is clear that there can be an influence of specimen size different from that predicted by a $B^{0.25}$ scaling law. The Local Approach model results presented in this paper tend to over-predict the magnitude of this difference.

CONCLUSIONS

1. The finite element analyses have indicated a loss of constraint over a significant proportion of the crack front for M < ~100 for CT-10 and M < ~60 for side-grooved PC-CVN specimens.
2. For CT-10 specimens, constraint loss is most significant towards the outer edges of the specimen. High constraint conditions are maintained over the central 50 % of the crack-front for M > 100.
3. For side-grooved PC-CVN specimens, constraint loss occurs uniformly across the crack front. High constraint conditions are maintained over 90 % of the crack front for M > 60.
4. To ensure fracture toughness data relate to high constraint conditions across a significant proportion of the crack front width, the current results suggest that the value of M at

fracture should be greater than 100 for CT-10 specimens and greater than 60 for side-grooved PC-CVN specimens.

5. Statistical models, based on empirical data, give a value of ΔT of 18 ºC at a mean toughness of 100 MPa√m. The BEREMIN model over-predicts this by ~ 35 ºC for CT-10 specimens and 55 ºC for side-grooved PC-CVN specimens.
6. A review of experimental data relating to RPV steel sub-sized specimens has revealed a difference in ΔT values predicted by the $B^{0.25}$ scaling law and those derived from sub-sized specimens. The magnitude of this difference, at a mean toughness level of 100 MPa√m, may be up to 30 ºC for some materials.

ACKNOWLEDGEMENTS

This work was funded by, and is published with the permission of BNFL Magnox Generation. The authors are grateful to Prof. R H Dodds (University of Illinois) and Dr M T Kirk (USNRC) for informal technical discussions during the course of the work.

REFERENCES

[1] A R Dowling and D P G Lidbury, "Local Approach modelling of constraint contributions to the ductile to brittle transition", in *Fracture, Plastic Flow and Structural Integrity*, Proceedings of the 7th Symposium organised by the Technical Advisory Group on Structural Integrity of Nuclear Plant, Eds. P Hirsch and D Lidbury, 2000.

[2] R Moskovic, "Statistical Analysis of censored fracture toughness data in the ductile to brittle transition temperature region", Engng Fract. Mech., Vol. 44, pp. 21-41, 1993.

[3] K Wallin, "Fracture toughness transition curve shape for ferritic structural steels", in *Fracture of Engineering Materials and Structures*, Edited by S T Teoh and K H Lee, Elsevier Applied Science, pp. 83-88, 1991.

[4] N P O'Dowd and C F Shih, "Two-parameter fracture mechanics: theory and application", NUREG/CR-5958, 1993.

[5] F M BEREMIN, "A Local Criterion for Cleavage Fracture of Nuclear Pressure vessel Steels", Metallurgical Transactions, Vol. 14A, pp. 2277-2287, 1983.

[6] M Nevalainen and R H Dodds, "Numerical investigation of 3-D constraint effects on brittle fracture in SE(C) and C(T) specimens", *Int. J. Fract.*, Vol. 74, pp. 131-161, 1995.

[7] J D S Sumpter and J W Hancock, "Status review of the J plus T stress", presented at the 10th European Conference on Fracture, Berlin, 20-23 September 1994.

[8] M T Kirk, private communication, August 2000.

[9] R L Tregoning, "Application of Master Curve approach for design and structural integrity assessment", presented at IG-RDM8 Open Workshop on Fracture Toughness Master Curve for Reactor Pressure Vessel Steels, Nashville, January 22, 1999.

[10] C Ruggieri, R H Dodds and K Wallin, "Constraint effects on reference temperature, T_0, for ferritic steels in the transition region", *Engng Fract. Mech.*, Vol. 60, pp. 19-36, 1998.

[11] M T Kirk and M Mitchell, "A review of technical and regulatory developments needed to enable application of Master Curve technology to the fracture integrity assessment of commercial nuclear power reactors", ASME PVP- Vol. 412, pp. 187-195, 2000.

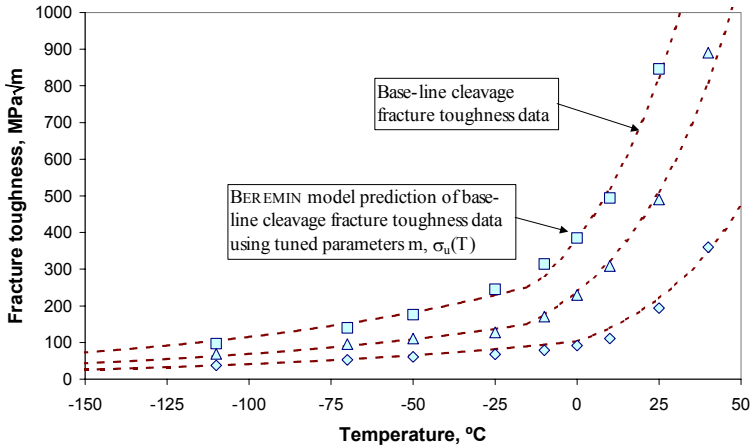

Figure 1:. SAW baseline fracture toughness data for CT-25 specimens. Statistical model and BEREMIN model prediction.

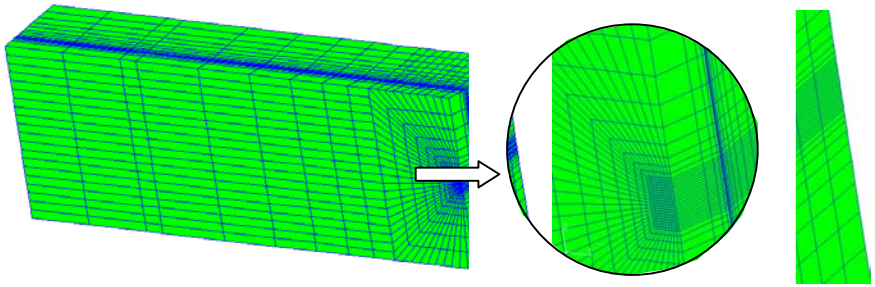

Figure 2: Finite element model of PC-CVN specimen. B = 10mm; W = 10 mm; a/W = 0.5; SG = 20%

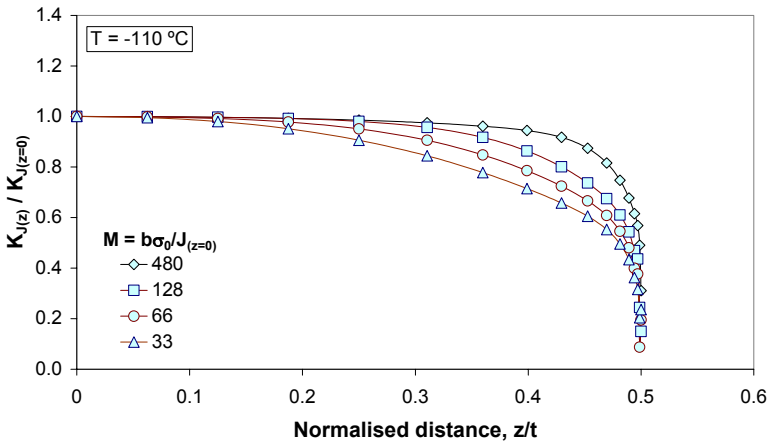

Figure 3: Normalised K_J as a function of distance along the crack front. CT-10 specimen.

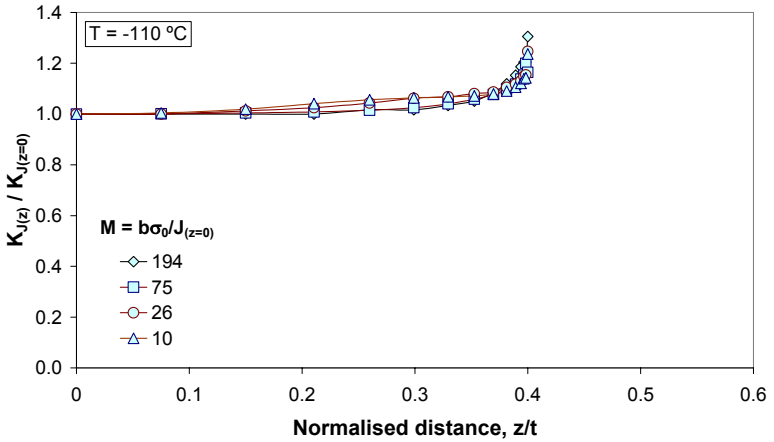

Figure 4: Normalised K_J as a function of distance along the crack front. PC-CVN specimen.

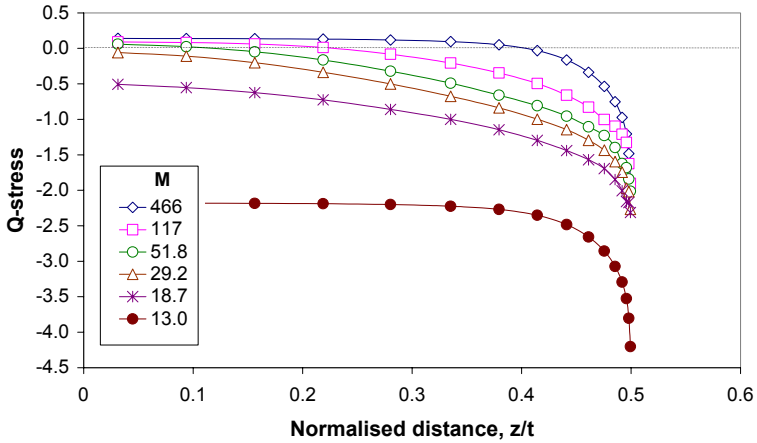

Figure 5: Q as a function of distance along the crack front. CT-10 specimen.

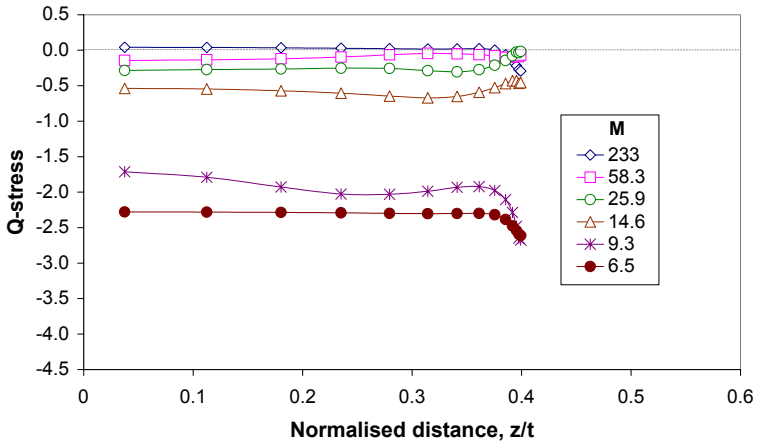

Figure 6: Q as a function of distance along the crack front. PC-CVN specimen.

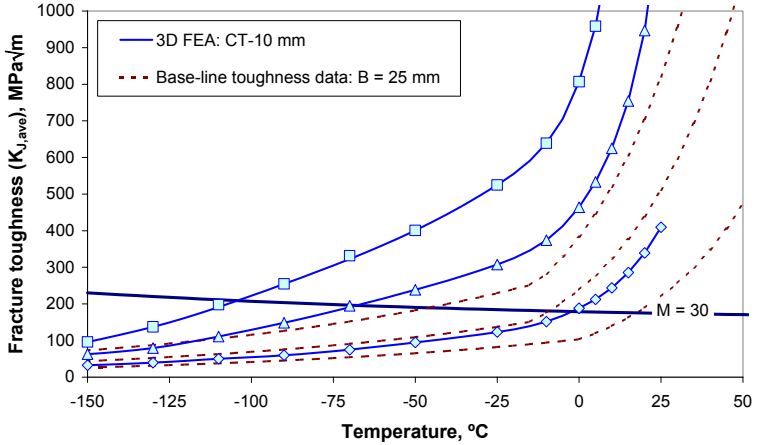

Figure 7: Predicted transition behaviour for CT-10 specimen.

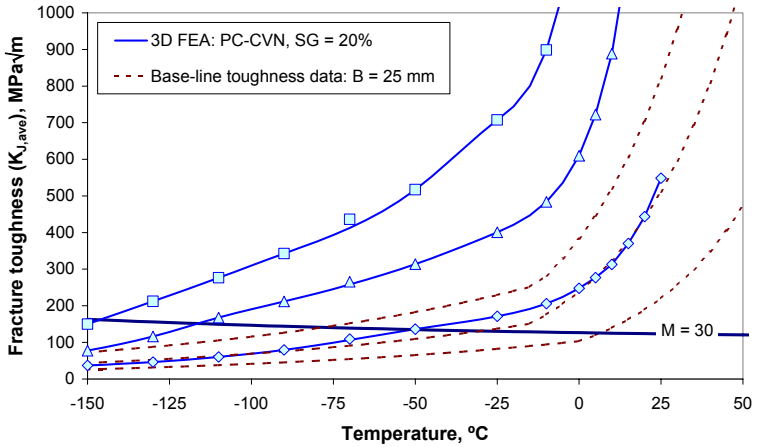

Figure 8: Predicted transition behaviour for PC-CVN specimen.

MODELLING OF TRANSVERSELY ISOTROPIC BLISTER TEST SPECIMEN

F. Suat Kadıoğlu

Middle East Technical University, Mechanical Eng. Dept.,06531, Ankara, TURKEY

ABSTRACT

In this study, a transversely isotropic elastic layer bonded to a rigid substrate is considered, with the intent of modelling the blister test. The motivation for the study is to incorporate the effect of anisotropy of the layer on the energy release rate associated with the debonding of the layer. A linear elasticity approach is adopted rather than plate theory so the results will be applicable to relatively thick films. In addition to being a model for the blister test, the assumed geometry and loading can also represent the problem of a composite cover plate. The problem is reduced to the solution of a system of singular integral equations of the second kind by using Hankel transforms. These equations are solved for sample cases and numerical results for energy release rates are given.

KEYWORDS

Blister Test, Transversely Isotropic, Energy Release Rate, Singular Integral Equation

INTRODUCTION

Structures consisting of two or more bonded layers are frequently encountered in many engineering applications. Films grown on substrates by different methods such as PVD or CVD can also be regarded to be in this category. It is known that such structures may suffer delamination because of residual or thermal stresses. Bonding strength between the film and the substrate is therefore very important. Williams' Blister test [1] is a method which can be used to determine the bonding strength. Blister test specimen consists of a thin layer bonded to a substrate. In the test, a blister is formed by applying a certain pressure on the lower surface of the layer through an opening in the substrate. The layer is made to separate from the substrate in a controlled manner through the spreading of the circular boundary between the bonded and already separated parts. By calculating the energy release rate associated with this process it is possible to obtain quantitative information on the bonding strength of the layer substrate pair. Many aspects of this test and its variations has been investigated by various researchers. To name a few, Updike [2] who studied the effect of adhesive layer elasticity on bonding strength, Farris and Keer [3] who analyzed Williams' blister test as an interface crack problem and Jensen and Cochelin [4] who studied constrained blister test can be mentioned. In this study (which is based on [6]) a model is constructed to calculate the energy release rate for Williams' blister test applied to a transversely isotropic layer. By virtue of the theory of elasticity approach adopted (which is very similar to that in [7]), the singular nature of stresses at the debonding front are taken into account.

FORMULATION OF THE PROBLEM

Geometry of the problem is given in Figure 1. It was shown in earlier studies (See for example Dahan and Predeleanu [5]) that the solution of axisymmetric elasticity problems for transversely isotropic media can be obtained through the use of a potential function of the Love type.

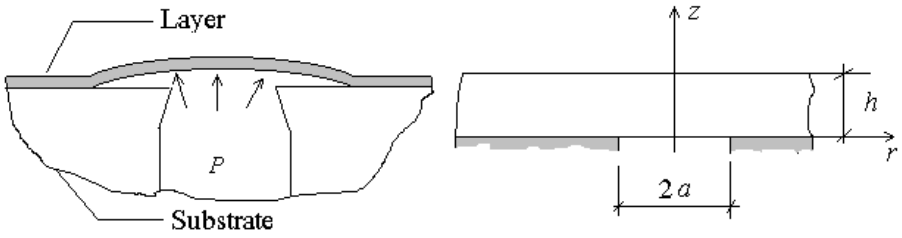

Figure 1: Blister test and test specimen model

This potential function, φ, for the problem under consideration is given as follows:

$$\varphi(r,z)=\int_0^\infty \lambda\left(B_1e^{m_1\lambda z}+B_2e^{m_2\lambda z}+B_3e^{m_3\lambda z}+B_4e^{m_4\lambda z}\right)J_0(\lambda r)d\lambda\,, \tag{1}$$

where $B_k(\lambda)$ are unkowns to be determined by using boundary conditions,

$$m_{1,3}=\left[\frac{(a+c)\pm\sqrt{(a+c)^2-4d}}{2d}\right]^{1/2},\ m_{2,4}=-\left[\frac{(a+c)\pm\sqrt{(a+c)^2-4d}}{2d}\right]^{1/2}, \tag{2}$$

$$a=a_{13}\frac{a_{11}-a_{12}}{a_{11}a_{33}-a_{13}^{\ 2}},\ b=\frac{a_{13}(a_{13}+a_{44})-a_{12}a_{33}}{a_{11}a_{33}-a_{13}^{\ 2}},c=\frac{a_{13}(a_{11}-a_{12})+a_{11}a_{44}}{a_{11}a_{33}-a_{13}^{\ 2}},d=\frac{a_{11}^{\ 2}-a_{12}^{\ 2}}{a_{11}a_{33}-a_{13}^{\ 2}}. \tag{3}$$

a_{ij} are the compliances defined by

$$\begin{bmatrix}\varepsilon_{rr}\\ \varepsilon_{\theta\theta}\\ \varepsilon_{zz}\\ \gamma_{rz}\end{bmatrix}=\begin{bmatrix}a_{11}&a_{12}&a_{13}&0\\ a_{12}&a_{11}&a_{13}&0\\ a_{13}&a_{13}&a_{33}&0\\ 0&0&0&a_{44}\end{bmatrix}\begin{bmatrix}\sigma_{rr}\\ \sigma_{\theta\theta}\\ \sigma_{zz}\\ \tau_{rz}\end{bmatrix}, \tag{4}$$

Then the non-zero stresses and displacements of interest are given as

$$\sigma_{zz}=\frac{\partial}{\partial z}\left(c\frac{\partial^2\varphi}{\partial r^2}+\frac{c}{r}\frac{\partial\varphi}{\partial r}+d\frac{\partial^2\varphi}{\partial z^2}\right),\tau_{rz}=\frac{\partial}{\partial r}\left(\frac{\partial^2\varphi}{\partial r^2}+\frac{1}{r}\frac{\partial\varphi}{\partial r}+a\frac{\partial^2\varphi}{\partial z^2}\right), \tag{5}$$

$$u=-(1-b)(a_{11}-a_{12})\frac{\partial^2\varphi}{\partial r\partial z},w=a_{44}\left(\frac{\partial^2\varphi}{\partial r^2}+\frac{1}{r}\frac{\partial\varphi}{\partial r}\right)+(a_{33}d-2a_{13}a)\frac{\partial^2\varphi}{\partial z^2}. \tag{6}$$

Boundary conditions of the problem are

$$\sigma_{zz}(r,h)=0,\ \sigma_{rz}(r,h)=0, \tag{7}$$

$$u(r,0)=0,\ w(r,0)=0,\ r\geq a, \tag{8}$$

$$\sigma_{rz}(r,0)=0,\ \sigma_{zz}(r,0)=-P,\ r\leq a. \tag{9}$$

The problem is subjected to mixed boundary conditions on z=0 surface. In order to reduce the problem to solution of a system of singular integral equations the following auxiliary functions have been defined.

$$G_1(r)=\frac{\partial w}{\partial r}(r,0)\ ,\quad G_2(r)=\frac{1}{r}\frac{\partial(ur)}{\partial r}(r,0). \tag{10}$$

By using equations (1), (5), (6), the homogeneous boundary conditions (7), (8) and the definitions of the auxiliary functions, (10), the unknown $B_k(\lambda)$ functions can be expressed in terms of the auxiliary functions. Then by using the mixed boundary condition (9) the following integral equations can be obtained.

$$\int_0^a \rho G_1(\rho)\int_0^\infty d_{11}(\lambda)\lambda J_0(\lambda r)J_1(\lambda\rho)d\lambda d\rho+\int_0^a \rho G_2(\rho)\int_0^\infty d_{12}(\lambda)\lambda J_0(\lambda r)J_0(\lambda\rho)d\lambda d\rho=P\ , \tag{11}$$

$$\int_0^a \rho G_1(\rho)\int_0^\infty d_{21}(\lambda)\lambda J_1(\lambda r)J_1(\lambda\rho)d\lambda d\rho+\int_0^a \rho G_2(\rho)\int_0^\infty d_{22}(\lambda)\lambda J_1(\lambda r)J_0(\lambda\rho)d\lambda d\rho=0\ , \tag{12}$$

where functions $d_{ij}(\lambda)$ are given in the appendix.

In order to solve these integral equations the asymptotic values of the functions $d_{ij}(\lambda)$ must be determined as λ goes to infinity. After a long analysis these values are found to be as follows:

$$d_{11}^{\ \infty}=-d_{22}^{\ \infty}=\frac{M_2m_4(M_3N_1-M_1N_3)+M_4m_2(M_1N_3-M_3N_1)}{(a_{44}-Cm_2^{\ 2})m_4(M_3N_1-M_1N_3)+(a_{44}-Cm_4^{\ 2})m_2(M_1N_3-M_3N_1)}, \tag{13}$$

$$d_{12}^{\ \infty}=-d_{21}^{\ \infty}=\frac{M_2(a_{44}-Cm_4^{\ 2})(M_1N_3-M_3N_1)+M_4(a_{44}-Cm_2^{\ 2})(M_3N_1-M_1N_3)}{A\left[(a_{44}-Cm_2^{\ 2})m_4(M_3N_1-M_1N_3)+(a_{44}-Cm_4^{\ 2})m_2(M_1N_3-M_3N_1)\right]}, \tag{14}$$

$$A=(1-b)(a_{11}-a_{12}),\ C=(a_{33}d-2a_{13}a),\ t_i=m_i\lambda\ ,M_i=m_i(m_i^{\ 2}d-c),\ N_{\rm i}=(1-m_i^{\ 2}a),(i=1,2,3,4) \tag{15}$$

By using these asymptotic values the singularities in equations (11) and (12) can be extracted. Further, one can extend the range of outer integrals into the negative range $(-a,0)$ by observing that $G_1(r)=-G_1(\mathrm{r})$ and $G_2(r)=G_2(-r)$. Doing so the final form of integral equations can be obtained as follows.

$$C_iG_{3-i}(\rho)+\frac{L_i}{\pi}\int_{-a}^{a}G_i(\rho)\left[\frac{1}{\rho-r}+H_i(r,\rho)\right]d\rho+$$

$$\sum_{j=1}^{2}\int_0^a\frac{|\rho|}{2}G_j(\rho)\int_0^\infty\left[d_{ij}(\lambda)-d_{ij}^{\ \infty}\right]\lambda J_{i-1}(\lambda r)J_{2-j}(\lambda\rho)d\lambda d\rho=Q_i\ ,(i=1,2). \tag{16}$$

where

$$C_1=d_{12}^{\ \infty},\ C_2=d_{21}^{\ \infty}\ ,L_1=d_{11}^{\ \infty}\ ,\ L_2=-d_{22}^{\ \infty}\ ,\ H_i=\frac{h_k(r,\rho)-1}{\rho-r},\ (k=1,2) \tag{17}$$

$$h_1(r,\rho)=\begin{cases}\dfrac{\rho^2-r^2}{|r\rho|}K\left(\dfrac{\rho}{r}\right)+\dfrac{r}{\rho}E\left(\dfrac{\rho}{r}\right),\ |\rho|<|r|\\ E\left(\dfrac{r}{\rho}\right),\ |\rho|>|r|\end{cases},\ h_1(r,\rho)=\begin{cases}\left|\dfrac{\rho}{r}\right|E\left(\dfrac{\rho}{r}\right),\ |\rho|<|r|\\ \left(\dfrac{\rho}{r}\right)^2E\left(\dfrac{r}{\rho}\right)-\dfrac{\rho^2-r^2}{r^2}K\left(\dfrac{r}{\rho}\right),\ |\rho|>|r|\end{cases}. \tag{18}$$

This system of singular integral equations can be solved by defining

$$G_2(r)+iG_1(r)=(1-r)^{\alpha}(1+r)^{\beta}F(r),\ \alpha=-\frac{1}{2}-i\omega,\ \beta=-\frac{1}{2}+i\omega,\ \omega=\frac{1}{2\pi}\log\left(\frac{1+\gamma}{1-\gamma}\right)\ \gamma=\frac{d_{12}^{\infty}}{d_{11}^{\infty}}, \tag{19}$$

and following the method given in [6,7]. After solving the unknown function $F(r)$, the stress intensity factors and the energy release rate (ERR) associated with the debonding of the elastic layer can be obtained as;

$$k_1+ik_2=id_{11}^{\infty}\sqrt{1-\gamma^2}F(1),\quad G=\frac{\partial U}{\partial a}=\pi\frac{k_1^{\,2}+k_2^{\,2}}{4d_{11}^{\infty}}. \tag{20}$$

SAMPLE RESULTS AND DISCUSSION

Figure 2 shows the sample calculation for energy release rate (henceforth ERR) of an epoxy layer, (E=3.1 GPa, ν=0.35), bonded to a rigid substrate. Since a transversely isotropic formulation is done, a slight anisotropy is introduced by reducing the compliances a_{13} and a_{33} by 5%, to obtain numerical results. Also given on this figure are the ERRs for the two limiting cases of the blister test,

$$G_0=\frac{2(1-\nu^2)}{\pi E}P^2a,\quad G_1=\frac{3(1-\nu^2)}{256\pi E}\frac{1}{(h/2a)^3}P^2a. \tag{21}$$

In Eqn. (21) G_0 is the ERR associated with an isotropic infinitely thick layer and G_1 is the ERR associated with an isotropic thin film, bonded to a rigid substrate [1].

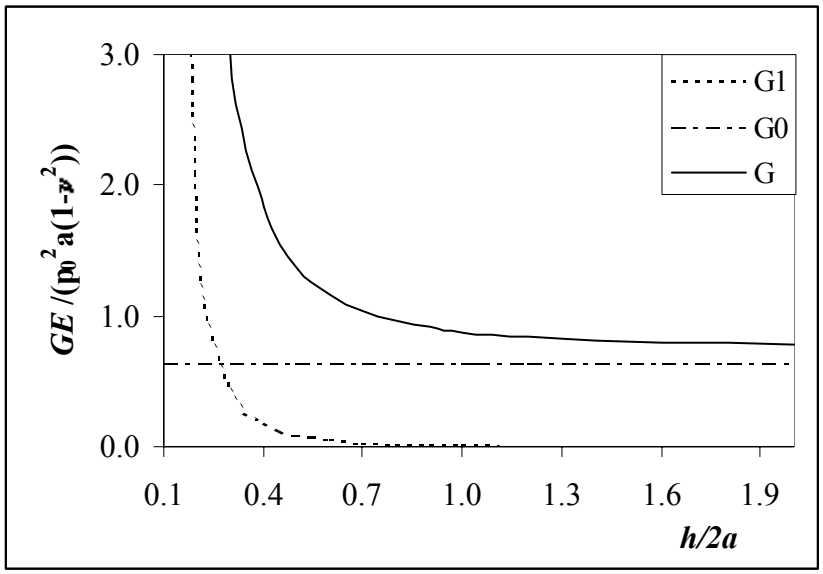

Figure 2: Energy release rates for an isotropic material

In the derivation of G_0 the complex nature of singularity has not been taken into account [1] and the contribution of shear stresses are not considered. On the other hand G_1 is derived by using the classical plate theory and it is a good approximation for small $h/(2a)$ ratios (such as $h/(2a) < 0.1$). The elasticity approach adopted in this study (and in [3]) is most useful in the range between these two extreme cases, where the film thickness is too large to apply classical plate theory but too small to be assumed as infinitely thick.

For $h/(2a) < 0.2$, difficulties are encountered in the numerical solution of the singular integral equations. Because of this, convergence of G value obtained from equation (20) and G_1 value obtained from equation (21) can not be clearly demonstrated. For the other limiting case (large $h/(2a)$), the asymptotic solution is

recovered albeit it does not match exactly with G_0. The difference is attributed to omission of the complex singularity and the contribution of shear stresses in the derivation of G_0. The results, however, agree well with those given in [7] for an epoxy layer bonded to an aluminum substrate which is much stiffer than the epoxy.

Figure 3 shows the sample calculations for non-dimensional energy release rate ratio which is defined as

$$G_r = \frac{G}{G_0}. \tag{22}$$

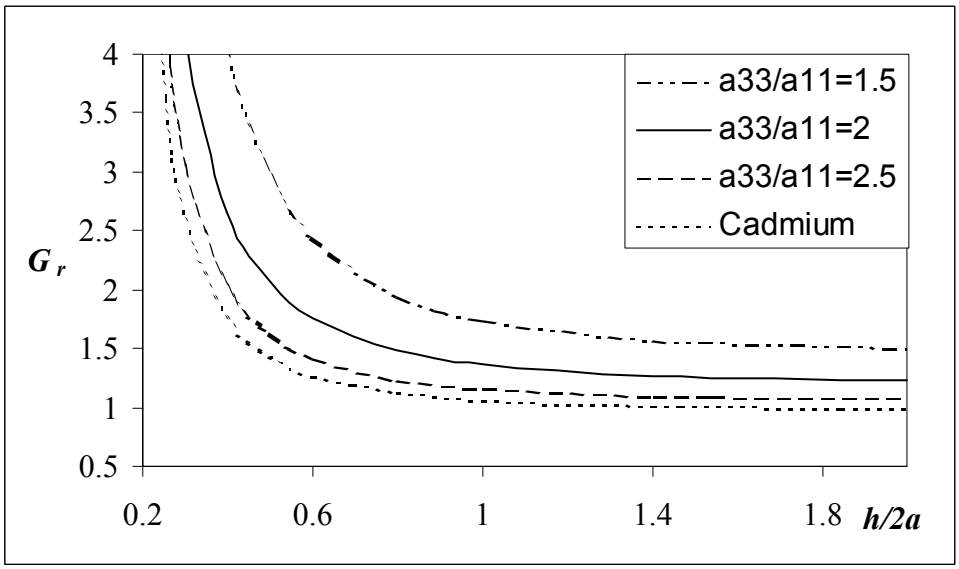

Figure 3: Energy release rate ratio

In these sample calculations cadmium (a_{11}=0.0129, a_{12}=−1.5×10^{-3}, a_{13}=−9.3×10^{-3}, a_{33}=0.0369, a_{44}=0.0640 all in units of GPa^{-1}) and three hypothetical materials are considered. Material properties of hypothetical materials are taken to be equal to those of cadmium except a_{33} which is varied as shown in the legend of Figure 2. The isotropic material is taken to have a Young's modulus of E=77.52 GPa, and a Poisson's ratio of ν=0.116 .These are the in-plane Young's modulus and Poisson ratio of Cadmium.

The results indicate that ERR depends strongly on the elastic constants of a transversely isotropic material. Dependence is stronger when the layer thickness is small compared to the hole diameter. (For layer thicknesses much smaller than the hole diameter, difficulties are encountered in the numerical solution. For such layer thicknesses a thick (or thin plate formulation) could be attempted.) On the other hand, when the layer thickness is greater than 1.25 times the hole diameter, the dependence of ERR on layer thickness practically disappears and infinitely thick layer solutions can be used.

The problem considered in this paper can be extended in several directions. For example the residual stresses in the layer and the elasticity of the substrate can be taken into account. One can also include an adhesive layer between the upper layer and the substrate.

REFERENCES

1. Williams, M.L. (1969) *J. Appl. Polym. Sci*. 13, 29.
2. Updike, D.P. (1976) *Int. J. Frac.*12, 815.
3. Farris, T.N. and Keer, L.M. (1985) *Int. J. Frac.* 27, 91.
4. Jensen, H.M. and Cochelin, B. (1994) *J. Adhesion*, 47, 231.
5. Dahan, M. and Predeleanu M. (1980) *Lett. Appl. Engng. Sci.* 18, 1067.
6. Bilici, M.A. (2000). MSc Thesis, Middle East Technical University, Ankara, Turkey.

7. Arın, K. and Erdogan, F. (1971) *Int. J. Engng. Sci.* 9, 213.

APPENDIX

$$B_i = \sum_{j=3}^{4} \frac{\Delta_{ij}}{\Delta} R_j \ (i=1,2,3,4),$$

$$H = \begin{bmatrix} M_1 e^{t_1 h} & M_2 e^{t_2 h} & M_3 e^{t_3 h} & M_4 e^{t_4 h} \\ N_1 e^{t_1 h} & N_2 e^{t_2 h} & N_3 e^{t_3 h} & N_4 e^{t_4 h} \\ a_{44} - Cm_1^{\,2} & a_{44} - Cm_2^{\,2} & a_{44} - Cm_3^{\,2} & a_{44} - Cm_4^{\,2} \\ Am_1 & Am_1 & Am_1 & Am_1 \end{bmatrix},$$ h_{ij} are elements of the matrix H.

$$\begin{aligned}
\Delta_{13} &= -h_{14}h_{23}h_{42} + h_{13}h_{24}h_{42} + h_{14}h_{22}h_{43} - h_{12}h_{24}h_{43} - h_{13}h_{22}h_{44} + h_{12}h_{23}h_{44} \\
\Delta_{14} &= h_{14}h_{23}h_{32} - h_{13}h_{24}h_{32} - h_{14}h_{22}h_{33} + h_{12}h_{24}h_{33} + h_{13}h_{22}h_{34} - h_{12}h_{23}h_{34} \\
\Delta_{23} &= h_{14}h_{23}h_{41} - h_{13}h_{24}h_{41} - h_{14}h_{21}h_{43} + h_{11}h_{24}h_{43} + h_{13}h_{21}h_{44} - h_{11}h_{23}h_{44} \\
\Delta_{24} &= -h_{14}h_{23}h_{31} + h_{13}h_{24}h_{31} + h_{14}h_{21}h_{33} - h_{11}h_{24}h_{33} - h_{13}h_{21}h_{34} + h_{11}h_{23}h_{34} \\
\Delta_{33} &= -h_{14}h_{22}h_{41} + h_{12}h_{24}h_{41} + h_{14}h_{21}h_{42} - h_{11}h_{24}h_{42} - h_{12}h_{21}h_{44} + h_{11}h_{22}h_{44} \\
\Delta_{34} &= h_{14}h_{22}h_{31} - h_{12}h_{24}h_{31} - h_{14}h_{21}h_{32} + h_{11}h_{24}h_{32} + h_{12}h_{21}h_{34} - h_{11}h_{22}h_{34} \\
\Delta_{43} &= h_{13}h_{22}h_{41} - h_{12}h_{23}h_{41} - h_{13}h_{21}h_{42} + h_{11}h_{23}h_{42} + h_{12}h_{21}h_{43} - h_{11}h_{22}h_{43} \\
\Delta_{44} &= -h_{13}h_{22}h_{31} + h_{12}h_{23}h_{31} + h_{13}h_{21}h_{32} - h_{11}h_{23}h_{32} - h_{12}h_{21}h_{33} + h_{11}h_{22}h_{33}
\end{aligned}$$

$$\begin{aligned}
\Delta = {} & h_{41}(\ h_{14}h_{23}h_{32} - h_{13}h_{24}h_{32} - h_{14}h_{22}h_{33} + h_{12}h_{24}h_{33} + h_{13}h_{22}h_{34} - h_{12}h_{23}h_{34}) + \\
& h_{31}(-h_{14}h_{23}h_{42} + h_{13}h_{24}h_{42} + h_{14}h_{22}h_{43} - h_{12}h_{24}h_{43} - h_{13}h_{22}h_{44} + h_{12}h_{23}h_{44}) + \\
& h_{21}(\ h_{14}h_{33}h_{42} - h_{13}h_{34}h_{42} - h_{14}h_{32}h_{43} + h_{12}h_{34}h_{43} + h_{13}h_{32}h_{44} - h_{12}h_{33}h_{44}) + \\
& h_{11}(-h_{24}h_{33}h_{42} + h_{23}h_{34}h_{42} + h_{24}h_{32}h_{43} - h_{22}h_{34}h_{43} - h_{23}h_{32}h_{44} + h_{22}h_{33}h_{44})
\end{aligned}$$

$$\begin{aligned}
d_{11} &= (\Delta_{13}M_1 + \Delta_{23}M_2 + \Delta_{33}M_3 + \Delta_{43}M_4) / \Delta \\
d_{12} &= (\Delta_{14}M_1 + \Delta_{24}M_2 + \Delta_{34}M_3 + \Delta_{44}M_4) / \Delta \\
d_{21} &= (\Delta_{13}N_1 + \Delta_{23}N_2 + \Delta_{33}N_3 + \Delta_{43}N_4) / \Delta \\
d_{22} &= (\Delta_{14}N_1 + \Delta_{24}N_2 + \Delta_{34}N_3 + \Delta_{44}N_4) / \Delta
\end{aligned}$$

MODELLING THE EFFECTS OF MICROSTRUCTURE AND MICROTEXTURE ON THE STATISTICS OF SHORT FATIGUE CRACK GROWTH

Angus J. Wilkinson

Department of Materials, University of Oxford,
Parks Road, Oxford, OX1 3PH, UK
angus.wilkinson@materials.oxford.ac.uk

ABSTRACT

A physically based model for the growth of short fatigue cracks through a local grain structure will be presented. The growth rate is evaluated using an existing solution for the distribution of dislocations ahead of a crack in a slip band that is blocked by a grain boundary. Probability functions describing the grain size and grain orientation distributions are used within a Monte-Carlo framework so as to calculate the growth rates of many individual cracks passing through different local microtextures. The grain size controls the distance to the next barrier through which the slip band and crack must propagate. The grain orientations control the resolution of the far field tensile loading into shear stresses on local slip systems. It is assumed that the cracks grow along slip planes driven by the local mode II loading at rates that are proportional to the cyclic mode II displacement at the crack tip. Experiments show that the twist component of the crack plane deflection at a grain boundary is also of significance, since the crack retardation tends to be more marked for large twist deflections. The strengths of the microstructural barriers are thus controlled by the misorientation between the two neighbouring grains. The spatial distribution of grain orientations thus also enters the simulation. The simulations allow probabilistic descriptions of the microstructure and microtexture to be incorporated in a model that evaluates not only the average behaviour of the short cracks, but also the statistical variation in the behaviour. Curves showing the probability of propagating cracks reaching a given crack length in a given number of cycles will be presented.

KEYWORDS

Fatigue, short fatigue cracks, texture, statistics

INTRODUCTION

The number of cycles required for a naturally initiated fatigue crack to grow to a size at which it threatens the structural integrity of an engineering component is often dominated by its early growth rate in a regime where the stress intensity factor range is low and the crack length is short. Extrapolation of data and/or models that adequately describe the behaviour of long fatigue cracks into the short crack regime generally results in non-conservative predictions due to the faster growth of short cracks under the same nominal driving force (ΔK). Additionally, short fatigue cracks show increased sensitivity to local material

microstructure, there being many reports of crack growth rates rising and falling as a grain boundary (or other microstructural feature) is approached and then passed by the crack tip [see 1 for examples].

Evidence that the crack growth rate of short fatigue cracks tends to be reduced when plastic deformation ahead of the crack is blocked by a grain boundary was provided by selected area channelling pattern studies [2]. Such an effect has been modelled by Navarro and de los Rios and co-workers [3, 4] who extended the BCS dislocation modelling approach of Bilby, Cottrell and Swinden [5] in which the crack and the plastic zone ahead of it are represented by continuous distributions of dislocations. The extensive work of Navarro and de los Rios [6] analysed the retardation of the fatigue crack growth rate caused by the reduced amount of slip available when the plastic zone was blocked by a grain boundary. Such models successfully produce the observed pattern of rapid growth across a grain and retardation at the grain boundaries.

The scatter observed in the fatigue lives of samples that are nominally the same and cycled under the same loading conditions is in part due to the sensitivity of short fatigue crack growth rates to the local details of the microstructure. Boyd-Lee and King [7] have observed such effects in Ni-based superalloys, and developed empirical probabilistic laws to describe the of short fatigue crack growth that they could then use to predict the evolution of crack length populations through the fatigue life of a sample.

This paper examines the effect of preferred grain orientations (texture) on the statistics of short fatigue crack growth. The NR solutions given by Navarro and de los Rios [3] are used within a Monte-Carlo framework to follow the individual growth behaviour of many virtual cracks each sampling different possible local microtextures. From this the probability of a crack reaching a given length is obtained as a function of the number of load cycles.

THE MODEL

A schematic diagram illustrates the components of the model in figure (1). The sample is taken to be polycrystalline and subjected to a far field uniaxial cyclic loading (σ). In a plastically soft grain a crack forms on the active slip plane. The crack growth is assumed to result from irreversible shear deformation at the crack tip caused by the mode II component of the loading. The shear stress on the crack plane is assumed to be given simply by

$$\tau = \left(\frac{1}{1 + i_p - i_c}\right) \sum_{i=i_c}^{i=i_p} \frac{\sigma}{m_i} \qquad \text{eq 1}$$

where m_i is the Sachs (single slip) orientation factor for the ith grain in the polycrystal. i_c and i_p are the grain numbers of grains containing the crack tip and head of the plastic zone respectively. The spatial distribution of grain orientations (relative to the loading axis) thus enters the model through equation 1.

The plastic zone ahead of the crack is described by BCS theory if the zone does not impinge upon the next grain boundary and by NR theory when the plastic zone is blocked by the next grain boundary. The crack growth rate is taken to be proportional to the cyclic displacement at the crack tip (Φ) for which equations 2a and 2b give results from the BCS and NR theories respectively.

$$\Phi_{BCS} = \frac{4b\tau_f c_{BCS}}{\pi^2 A} n_{BCS} \ln\left(\frac{1}{n_{BCS}}\right) \qquad \text{eq 2a}$$

$$\Phi_{NR} = \frac{4b\tau_f c_{NR}}{\pi^2 A}\left\{ n_{NR} \ln\left(\frac{1}{n_{NR}}\right) + \sqrt{1 - n_{NR}^2}\left[\frac{\pi[1-R]\tau}{4\ \tau_f} - \arccos\left(n_{NR}\right)\right]\right\} \qquad \text{eq 2b}$$

where b is the Burgers vector, τ_f is the friction stress resisting the forward motion of the dislocations within the grain (which is, of

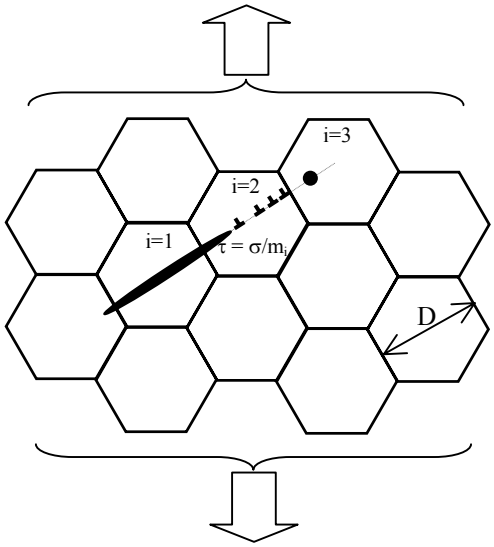

Figure 1: schematic diagram of the model

course, less than the macroscopic yield stress of the polycrystal), A is an elastic constant for the material ($A=\frac{\mu b}{2\pi(1-\nu)}$, with μ the shear modulus, and ν Poissons ratio). The applied stress (τ) and the load ratio (R) enter both theories through the parameter n, which is the ratio of crack length (a) to plastic zone size (c) as shown in figure 1. For the unblocked plastic zone the BCS theory gives

$$\frac{a}{c_{BCS}}=n_{BCS}=\cos\left(\frac{\pi[1-R]\tau}{4\tau_f}\right) \qquad \text{eq 3}$$

while when the plastic zone is blocked its size is controlled by the position of grain boundaries, so

$$c_{NR}=\frac{D_1}{2}+\sum_{i=2}^{i=i_p} D_i \quad \text{and} \quad \frac{a}{c_{NR}}=n_{NR} \qquad \text{eq 4}$$

where D_i are the diameters of the grains through which the crack has grown.
The plastic zone remains blocked at a given grain boundary until the stress $S(r_0)$ on a source a small distance r_0 into the next grain is sufficient to activate it, i.e slip is transferred when

$$S(r_0)\frac{m_i}{m_{i+1}}\geq S_{crit} \qquad \text{eq 5}$$

The factor m_i/m_{i+1} is included to crudely accounts for the tilting of the slip plane in grain i+1 from that in grain i.
Calculation of the crack growth rate as a function of crack length a proceeds as follows:

(i) calculate c_{BCS} and c_{NR} [eqs. 3 and 4]
(ii) if $c_{BCS} > c_{NR}$ then calculate $S(r_0)$ and if condition [eq. 5] is satisfied increase i by 1 and start again from step (i)
(iii) if $n_{BCS} < n_{NR}$ then growth rate is given by $\lambda\,\Phi_{BCS}$ [eq. 4] otherwise use $\lambda\,\Phi_{NR}$ [eq. 8]
(iv) increase a to new value and repeat from step (i)

The parameter λ varies from 1 for completely irreversible slip, to 0 if slip is completely reversible.
As the crack grows from one grain to the next, sizes and orientations are assigned to the new grains using random numbers and probability laws that describe the overall grain size and orientation distributions for the polycrystal. The process is repeated for a large number of cracks so as to assess how the statistics of microstructure and texture impact on the scatter in fatigue behaviour.

RESULTS

Materials parameters typical of a peak aged Al-Li alloy (8090) will be used in the following illustration of the model. The values of the main parameters given in table 1 will be used unless explicitly stated otherwise. In all cases the simulations followed the growth of virtual cracks from an initial flaw size of 1 μm to a final length of 500 μm which typifies short crack growth leading to 'initiation' of an engineering crack.

TABLE 1
MATERIALS PARAMETERS USED IN THE CALCULATIONS

Parameter	Symbol	Value
Shear modulus	μ	29.6 GPa
Poisson ratio	ν	0.3
Burgers vector	b	0.286 nm
grain diameter	D	100 μm
Source position	r_0	1 μm
Source strength	S_{crit}	400 MPa
friction stress	τ_f	50 MPa
Slip reversibility	λ	0.05

Grain Size Distribution Effects

In polycrystalline metals and alloys the average grain size is a basic parameter often used to quantify the scale of the microstructure. However, considerable scatter in grain size about this average is often present, and more detailed quantified analysis typically leads to the representation of the population of grain sizes through a log-normal distribution. Figure 2a shows the cumulative fraction of cracks that have grown to a size of at least 500 µm as a function of number of applied cycles at a stress amplitude of 200 MPa (R=0), for simulated polycrystals with different grain size distributions shown in figure 2b. For each of these cases the crystal orientations have been assign completely random orientations. Increasing the width of the grain size distribution from zero (thin line) is seen to cause increased spread in the fatigue behaviour as would intuitively be expected. Importantly the pronounced tail on the large grain size side of the log-normal distribution leads to the greatest changes being observed on the critical low-life part of the fatigue life distributions. Similar effects of an extended tail at low fatigue life are observed when the grain size distribution is altered to include a small fraction of 'blown' grains with markedly larger size outside the main distribution.

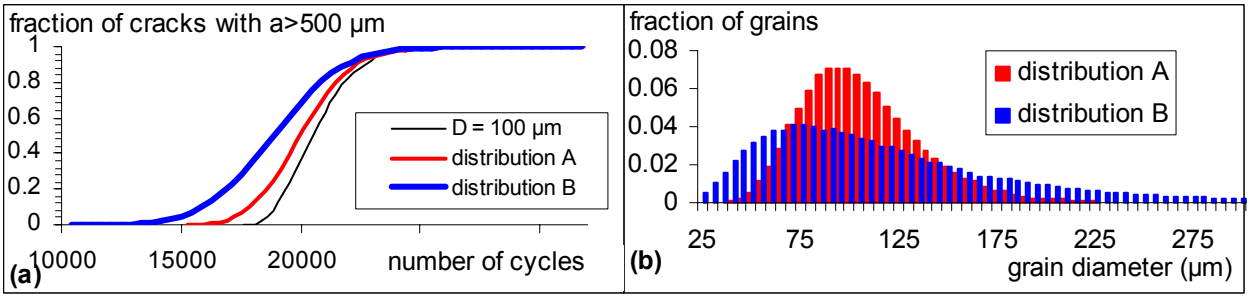

Figure 2: (a) distributions of fatigue cycles required to grow short fatigue crack to 500 µm through grains with size distributions given in (b).

Grain Orientation Distribution Effects

The thin line in figure 2a shows that the specific grain orientations selected along a given crack path lead to a spread in the fatigue life even when the grain size is constant. The manufacture of the vast majority of engineering components involves some form of deformation processing (rolling, extrusion etc) and as a result quite marked preferred orientations or textures are imparted. In fcc metals textures involving the alignment of either <100> or <111> axes along the extrusion or rolling direction is relatively common. Figure 3a shows how these simple fibre textures affect the statistics of short fatigue crack growth. In each case the distributions of the misalignment angles between the <100> or <111> fibre axis and the loading axis was taken to be of gaussian form with a standard deviation of 10°. As before a stress amplitude of 200 MPa (R=0), was used and the grain size was held constant at 100 µm. The differing preferred orientations result in considerable differences in both the average and the scatter in the fatigue life. The effects are more marked than those imparted by varying the grain size distribution (figure 2). Figure 3b shows how the variation in fatigue response is based on the Sachs factor (m_i) distributions present in the differently textured polycrystals. The randomly oriented (untextured) crystals have the lowest average Sachs factor and correspondingly the shortest average fatigue life, while the <111> fibre texture has the highest average Sachs factor (i.e. is plastically harder) and the longest fatigue life. The shape of the Sachs factor distribution also affects the calculated fatigue life distribution. For example, the untexted polycrystal results in a relatively small spread in Sachs factors with a pronounced tail towards the higher (plastically hard) Sachs factors and this results in a relatively narrow range of fatigue lives with a considerable part of this range taken up by the slowest 10% of the cracks. By contrast the wider range of Sachs factors present in the <111> fibre results in a broader range of fatigue lives.

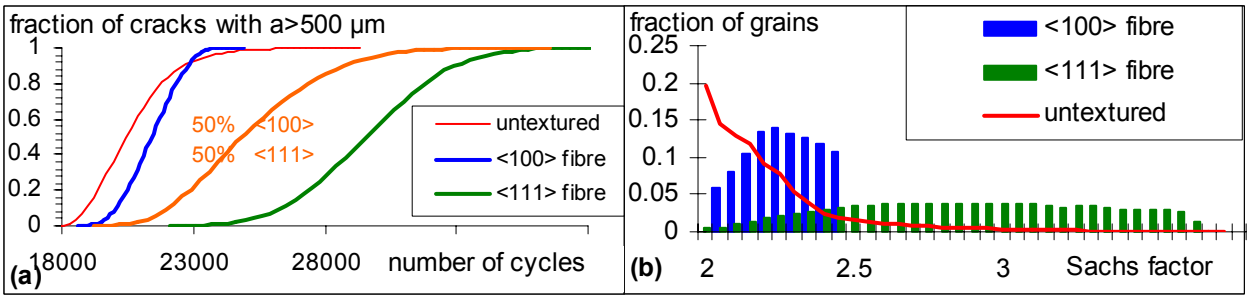

Figure 3: (a) distributions of fatigue cycles required to grow short fatigue crack to 500 µm through grains with different orientation distributions. (b) distributions of Sachs factors for different assumed textures.

Neighbouring Grain Orientation Effects

So far the calculations have been made on the basis that each grain boundary presents a barrier to the transfer of slip that is of the same strength. However, in reality the strength of the barrier will vary as a function of the grain boundary geometry, which leads to the observation that some grain boundaries cause a strong retardation (or even arrest) of short fatigue cracks while others have minimal effect. Recent experiments on Al-Li alloys [8] in which slip is highly planar and the cracks grow along {111} slip planes have indicated that the crack propagation across a grain boundary tends to select the slip plane that will minimise the extent of crack plane twisting. Furthermore the strength of the crack retardation is greater at grain boundaries for which the minimum available twist deflection is relatively large. Here we define the twist angle $\Delta\Psi$ as the acute angle between the traces on the grain boundary of the slip planes in the two neighbouring grains.

The program was modified to incorporate such effects by rewriting equation 5 as

$$S(r_0)\frac{m_i}{m_{i+1}} \geq \left[1+\frac{\Delta\Psi}{\Psi_0}\right]\frac{S_{crit}}{2} \qquad \text{eq 6}$$

where Ψ_0 was set as 25°.

Furthermore, the slip system onto which the crack transferred across a grain boundary was selected by minimising

$$m_{i+1}\left[1+\frac{\Delta\Psi}{\Psi_0}\right]$$

rather than simply minimising m_{i+1}, as was done in the previous calculations.

Any orientation coherence (i.e. any preferred spatial arrangement of the grain orientations) in the material would thus enter the model through two point correlations in the orientations which affect the distribution of $\Delta\Psi$ values in equation 6. However, in this work we will assume no such orientation coherence.

The effects of incorporating the sensitivity of grain boundary strength on the twist deflection of the crack plane is illustrated in figure 4. For a polycrystal with a <100> fibre texture the deflection of the crack plane as it crosses grain boundaries is generally rather limited since the grains all share similar orientation and as a result only a small increase in the width of the fatigue life distribution occurs. However, for an untextured polycrystal, the random sequence of grain orientations leads to more significant crack plane deflections at the grain boundaries and hence a wider range of grain boundary strengths. In this case the increased variability of the strength of crack retardation at the grain boundaries causes a marked widening of the fatigue life distribution. Furthermore, inclusion of the neighbouring grain orientation effect generally makes it easier for cracks to propagate through the <100> fibre textured material than the untextured material despite the <100> oriented grains being plastically harder.

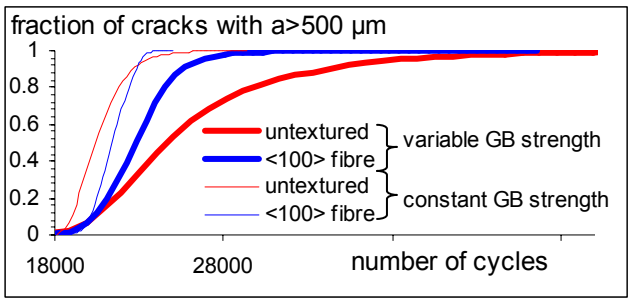

Figure 4: effects of variable grain boundary strength on the distributions of fatigue cycles required to grow short fatigue crack to 500 µm through grains with different orientation distributions.

CONCLUDING REMARKS

The characterisation of materials has seen a significant advance in the development of the automated electron back scatter diffraction technique [9], which allows the spatial distributions of grain orientations to be determined in a statistically significant way. It is important that models aimed at linking microstructure to material properties adopt frameworks allowing incorporation of statistical information describing grain size and grain orientation distributions and any spatial or other correlations between them. The modelling described in this paper is a simple step in this direction.

The physically based model for the growth of short fatigue cracks developed here allows the effects of grain size, grain orientation and neighbouring grain orientation distributions to be simulated within a Monte-Carlo framework. The simulations track the growth of many individual cracks through different possible paths through the microstructure and allow not only the average crack behaviour but also the statistical variation in the crack behaviour to be examined.

ACKNOWLEDGMENTS

I am grateful to the EPSRC for funding this work (GR/L48669) and to the Royal Society for their continuing support through the University Research Fellowship scheme. My thanks go to Drs Tongguang Zhai and John W Martin for insightful discussions about short fatigue crack growth.

REFERENCES

1 Suresh, S. and Ritchie, R. O. (1984) *Int. Metals Rev.*, **29**, 445-476.
2 Edwards, L. and Zhang, Y. H. (1994) *Acta Metall. Mater.*, **42**, 1423-1431.
3 Navarro, A. and de los Rios, E. R. (1988) *Phil. Mag. A*, **57**, 37-42.
4 de los Rios, E. R. and Navarro, A. (1990) *Phil. Mag. A*, **61**, 425-449.
5 Bilby, B. A., Cottrell A. H. and K. H. Swinden (1963) *Proc. Roy. Soc. Lond. A* **272**, 304.
6 de los Rios, E. R., Xin, X. J. and Navarro, A. (1994) *Proc. Roy. Soc. Lond. A*, **447**, 111-134.
7 Boyd-Lee, A. and King, J. (1993). In: *Fatigue Design (ESIS Publication 16)*, pp283-296, Solin, J., Marquis, G., Siljander, A. and Sipila, S., (Eds). Mechanical Engineering Publications, London.
8 Zhai, T, Wilkinson, A. J. and Martin, J. W. (2000) *Acta Mater.* **48**, 4917-4927.
9 "Electron Backscatter Diffraction in Materials Science" eds. Adams B. L., Schwarz A. J. and Kumar M., (Kluwer Academic/Plenum Publishers)

ORAL/POSTER REFERENCE: ICF100341OR

MODELING ELECTROMIGRATION AND MICROPORES FORMATION IN THIN-FILM IC INTERCONNECTS

R.V. Goldstein[1], M.E. Sarychev[2], D.B. Shirabaikin[2], A.S. Vladimirov[2], Yu.V. Zhitnikov[1]

[1]Institute for Problems in Mechanics of the Russian Academy of Sciences,
117526, Vernadskogo prt. 101-1, Moscow, Russia
[2]Institute of Physics and Technology of the Russian Academy of Sciences,
117218, Nakhimovsky prt. 34, Moscow, Russia

ABSTRACT

The modern tendency for increasing the productivity of microelectronic devices at the expense of the size shrinkage and the development of densely packed multilevel microelectronic structures stipulates the rising concern for the reliability of integrated circuits (IC). In this work the summary of general physical models of electromigration, the stress generation, and the void formation is given. On the basis of the models mentioned the simulation of the void nucleation in a triple point of the interconnect polycrystalline structure, as well as modeling the fracture of a two-level metallization in the plug region is performed. For both cases characteristic sizes of voids and times to their nucleation are calculated numerically.

KEYWORDS

Integrated circuits failure, electromigration, mechanical stresses, void nucleation.

INTRODUCTION

The IC failures are mainly caused by the fracture of interconnects. Interconnect is a thin-film metal line deposited on a silicon substrate and covered with a passivation layer. Its characteristic sizes in a cross-section vary from approximately 0.1 μm to several microns, while length lies within 10-1000 μm. In microelectronic devices of today interconnects are generally arranged in multilevel metallizations. The neighboring layers are connected by vertical plugs.

The fracture of interconnects is initiated by the nucleation of micropores in the regions supersaturated by vacancies. The rise of supersaturation is caused by the current-induced vacancy transfer (electromigration). The fundamental role of electromigration is stipulated by extremely high current densities ($\sim 10^{10}$-10^{12} A/m^2) used in modern microelectronics. Numerous experiments reveal that electromigration in thin films proceeds predominantly along grain boundaries. Therefore, the crystalline structure heterogeneities like triple points, inclusions, intersections of grain boundaries with the line lateral surface are preferable sites for the void nucleation, since they invoke strong vacancy flux divergence leading, in turn, to the supersaturation evolving. Subsequent growth of micropores, resulting from the vacancy inflow, causes the interconnect fracture. In multilevel metallization voids also form in the vicinity of a plug where the spatial distribution of the electric current is strongly non-uniform. In this case the void nucleation competes with the line edge depletion conditioned by intensive vacancy outflow.

Redistribution of vacancies under the electric current impact causes the rise of spatially non-uniform volume deformations in an interconnect, which, in turn, lead to the generation of the heterogeneous mechanical

stress field. Stresses influence both electromigration and the void nucleation. One of the main features of the interconnect deforming consists in the presence of a constraint from a substrate and a passivation cover, which are stiffer than a line.
Therefore, the goal of this study is the development of non-linear self-consistent models for the vacancy electromigration, the mechanical stress evolution, and the void nucleation. In the next section the model for the kinetics of electromigration-induced mechanical stresses is described briefly. In the third section a summary of the void nucleation kinetic model is given. In the fourth section results of calculations for the void formation in a triple point of the interconnect crystalline structure and for the damage of a two-level metallization in the plug region are presented.

MODELING THE VACANCY DIFFUSION AND THE MECHANICALSTRESSES RISE UNDER THE ELECTRIC CURRENT IMPACT

The spatio-temporal distribution of vacancies satisfies the following diffusion equation [1]

$$\dot{C} + q_{i,i} = -\tau_s^{-1}\left(C - C_e\right), \tag{1}$$

where $C(x_1, x_2, x_3, t)$ is the concentration of vacancies; $\dot{C} \equiv \partial C/\partial t$; $q_i(x_1, x_2, x_3, t)$ is the i-the component of the vacancy flux; $q_{i,i} \equiv \partial q_i/\partial x_i$, $i = 1, 2, 3$ (here and below repeated indices denote summation); τ_s is the characteristic time of the vacancy generation/annihilation; $C_e(x_1, x_2, x_3, t)$ is the equilibrium concentration of vacancies determined as [1]

$$C_e = C_0 \exp\left(f_r'\Omega\sigma/k_B T\right), \tag{2}$$

where C_0 is the equilibrium concentration for lack of stresses; Ω is the atomic volume; $f_r' = 1 - f_r$, f_r is a parameter determining the relative contraction of an atomic cell on substituting an atom with a vacancy; $\sigma(x_1, x_2, x_3, t)$ is a spherical part of the mechanical stress tensor σ_{ij}; T is temperature; k_B is Boltzmann's constant. In general, when electromigration proceeds concurrently with the action of mechanical stresses, the vacancy flux has the following form [1]

$$q_i = D\left(-C_{,i} + Z^*\rho_0 j_i C/k_B T - f_r\Omega\sigma_{,i}C/k_B T\right), \tag{3}$$

where D is the vacancy diffusivity; $C_{,i} \equiv \partial C/\partial x_i$; $\sigma_{,i} \equiv \partial\sigma/\partial x_i$; Z^* is the effective charge of a vacancy; ρ_0 is the interconnect specific resistivity; $j_i(x_1, x_2, x_3)$ is the i-th component of the current density vector.
The rise of mechanical stresses in an interconnect is conditioned by heterogeneous volume deformations induced by electromigration of vacancies. As shown in [1,2], in the case considered the deformation rate $\dot{\varepsilon}_{ij}$ is determined as

$$\dot{\varepsilon}_{ij} = \dot{\varepsilon}_{ij}^{\sigma} + \dot{\varepsilon}_{ij}^{c} = C_{ijkl}\dot{\sigma}_{kl} + \Phi\delta_{ij}\,, \tag{4}$$

where $\dot{\varepsilon}_{ij}^{\sigma}$ is the deformation rate caused by mechanical stresses under fixed vacancy concentration; $\dot{\varepsilon}_{ij}^{c}$ is the deformation rate conditioned by the vacancy migration and the generation/annihilation processes for lack of stresses; C_{ijkl} is the compliance tensor; $\dot{\sigma}_{kl} \equiv \partial\sigma_{kl}/\partial t$; δ_{ij} is the Kronecker delta; $i, j, k, l = 1, 2, 3$;

$$\Phi = \Omega\left\{f_r q_{i,i} - f_r'\tau_s^{-1}\left(C - C_e\right)\right\}/3\,.$$

From Eqn. 4 it follows that

$$\dot{\sigma}_{kl} = C_{ijkl}^{-1}\left(\dot{\varepsilon}_{ij} - \Phi\delta_{ij}\right). \tag{5}$$

Applying the quasi-static approach, we may write [3]

$$\sigma_{kl,l} \equiv \partial\sigma_{kl}/\partial x_l = 0\,. \tag{6}$$

Lets assume the line isotropic. Differentiating Eqn. 5 with respect to x_l and taking Eqn. 6 into account we obtain an equation describing the electromigration-induced deformation of an interconnect [2]

$$V_{k,ki} + (1-2\nu)V_{i,kk} = 2(1+\nu)\Phi_{,i}\,, \tag{7}$$

where V_i is the i-th component of the displacement velocity vector; $V_{k,ki} \equiv \partial^2 V_k/\partial x_k \partial x_i$; $V_{i,kk} \equiv \partial^2 V_i/\partial x_k^2$; ν is the Poisson ratio; $\Phi_{,i} \equiv \partial\Phi/\partial x_i$; $i, k = 1, 2, 3$. Kinetics of the stress tensor components satisfies the following equation [2]

$$\dot{\sigma}_{ij} = \lambda V_{k,k}\delta_{ij} + \mu(V_{i,j} + V_{j,i}) - 3(3\lambda+\mu)\Phi\delta_{ij}\,, \tag{8}$$

where λ and μ are the Lame constants; $V_{i,j} \equiv \partial V_i/\partial x_j$; $i, j, k = 1, 2, 3$. Therefore, Eqns. 1-3 and Eqns. 7-8 form a system of 3D differential equations describing the vacancy transport and the stress field evolution under the electric current impact.

A KINETIC MODEL FOR THE VOID NUCLEATION

Owing to electromigration the distribution of vacancies in a line deviates from equilibrium. In the sites where their concentration exceeds equilibrium (supersaturation) the fluctuational clusterization of vacancies becomes thermodynamically advantageous. This process can be described by the classical nucleation theory [4]. According to its fundamentals, only the clusters, which size (the number n of vacancies forming a cluster) exceeds a certain critical value n^*, are thermodynamically stable and, therefore, able for subsequent growth. The critical cluster size is determined from the condition of maximum for the Gibbs free energy change on clusterization ΔG_n:

$$\left(\partial\Delta G_n/\partial n\right)_{n=n^*} = 0\,.$$

Hereinafter the void nucleation is treated as the formation of a vacancy cluster of the critical size.
Using equations of the classical nucleation theory, we derive an equation for the time to the void nucleation $t_i(t')$ under fixed values of the vacancy concentration and stresses attained by the time moment t' [5]:

$$\int_{t'}^{t_i(t')} \exp\left(-\frac{\tau(t')}{\tilde{t}-t'}\right) d\tilde{t} = \frac{1}{V_N J_S^*(t')}\,, \tag{9}$$

where V_N is the characteristic volume of the region where the void formation takes place; J_S^* is a steady-state value of the nucleation rate (the net number of voids forming per unit volume and time); τ is the incubation time characterizing the time interval, during which the nucleation rate attains by order of magnitude its steady-state value. Expressions for J_S^* and τ are given in [5,6].
Since the current time of electromigration satisfies $0 \le t' < \infty$ and the probability of nucleation exists at any time moment, the probability of nucleation per unit time equals $[t_i(t') - t']^{-1}$. Then, the value

$$dP(t') = dt'/[t_i(t') - t']$$

is the probability of the void formation within the time interval $[t'; t' + dt']$. Hence, the time t_n to the void nucleation with regard to contributions $dP(t')$ from $t' = 0$ is determined as the time for which the net probability becomes equal to unity, i.e. from the integral equation

$$\int dP = \int_0^{t_n} \frac{dt'}{t_i(t') - t'} = 1 . \qquad (10)$$

The time t_n is calculated by solving the integral Eqns. 9-10, determining the void nucleation kinetics, jointly with the differential Eqns. 1-3 and 7-8, describing electromigration and the stress field evolution.

RESULTS OF CALCULATIONS FOR THE VOID NUCLEATION IN A TRIPLE POINT AND FOR THE DAMAGE OF A TWO-LEVEL METALLIZATION

Within the framework of the models developed we have performed numerical calculations for the void nucleation in a triple point of the interconnect crystalline structure [6] and in the plug region of a two-level metallization [7]. Since in the latter case the void formation competes with the line edge depletion [7], we have also taken that fracture mechanism into account. The results for a triple point are presented in Figures 1-2 and for a two-level metallization – in Figures 3-5.

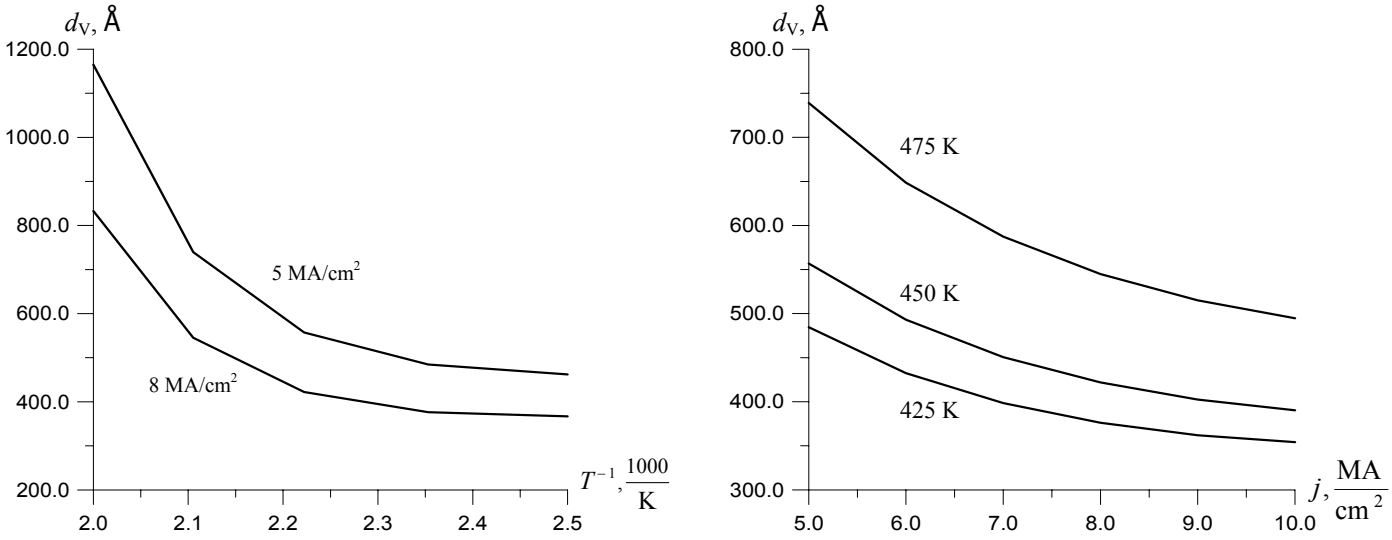

Figure 1: The void characteristic size as a function of temperature and current density

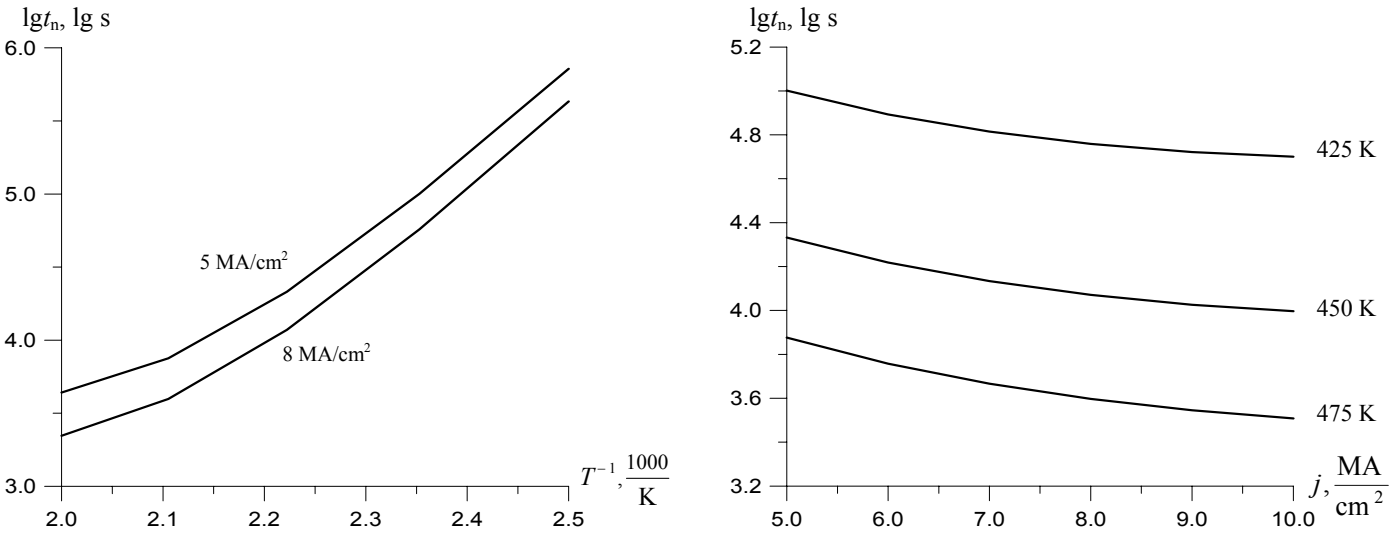

Figure 2: The time to the void nucleation as a function of temperature and current density

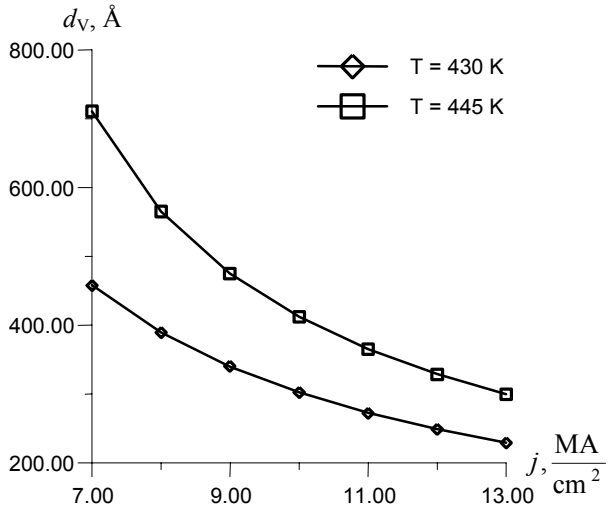

Figure 3: The void characteristic size as a function of current density

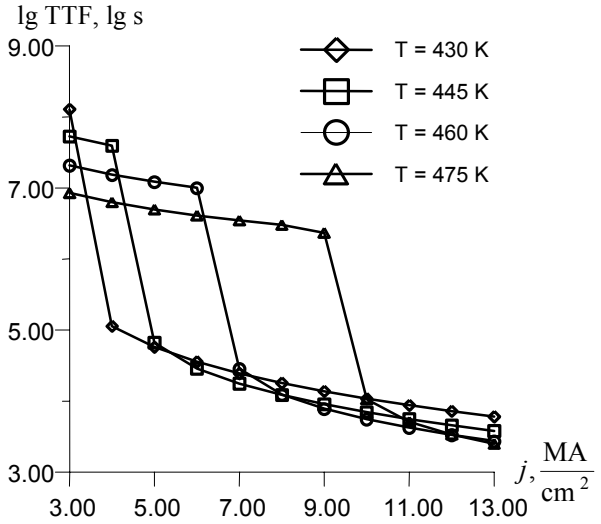

Figure 4: TTF as a function of current density

In Figure 4 the time to fracture (TTF) of a two-level metallization is presented, at that the line is considered to be damaged if a void nucleates or the edge erosion (see Figure 5) exceeds a certain critical value [7]. A bimodal character of the metallization fracture is seen: for low current densities the edge depletion takes place, while for high currents the void nucleation occurs. The results obtained agree well with experimental data [5-7].

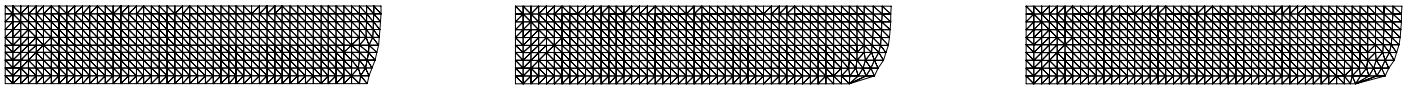

1.9×10^7 s $\quad$ 5.7×10^7 s $\quad$ 7.6×10^7 s

Figure 5: Evolution of the line edge depletion (T = 445 K, j = 4 MA/cm^2)

CONCLUSION

In this study we give a summary of non-linear self-consistent models for the vacancy electromigration, the mechanical stress evolution, and the void nucleation in thin-film IC interconnects. Within the framework of the models developed we have performed numerical calculations for the void formation in a triple point of the interconnect crystalline structure and for the damage of a two-level metallization in the plug region. In

the latter case fracture is caused either by the void nucleation, or by the line edge depletion. The results obtained agree well with experimental data.

REFERENCES

1. Goldstein, R.V., Makhviladze, T.M., Sarychev, M.E., Vladimirov, A.S., Shirabaikin, D.B., Zhitnikov, Yu.V. (1996). *Proceedings of IPT RAS*. 11, 61.
2. Sarychev, M.E., Zhitnikov, Yu.V., Borucki, L., Liu C.-L., Makhviladze, T.M. (2000). *Thin Solid Films*. 365(2), 211.
3. Timoshenko, S.P. and Goodier, J.N. (1970). *Theory of Elasticity.* McGraw-Hill, Tokyo.
4. Feder, J., Russell, K.C., Lothe, J., Pound, G.M. (1966). *Advances in Physics*. 15, 111.
5. Makhviladze, T.M., Sarychev, M.E., Zhitnikov, Yu.V. (1997). *Proceedings of IPT RAS*. 13, 98.
6. Goldstein, R.V., Vladimirov, A.S., Zhitnikov, Yu.V. (2000). In: *Proceedings of the 3rd International Conference on Single Crystal Growth, Strength Problems, and Heat Mass Transfer*, pp. 541-552, Ginkin, V.P. (Ed). IPPE, Obninsk.
7. Goldstein, R.V., Shirabaikin, D.B., Zhitnikov, Yu.V. (2000). In: *Proceedings of the 3rd International Conference on Single Crystal Growth, Strength Problems, and Heat Mass Transfer*, pp. 456-468, Ginkin, V.P. (Ed). IPPE, Obninsk.

ORAL REFERENCE : ICF100347OR

MODIFIED ELECTROCHEMICAL EMISSION SPECTROSCOPY(MEES) AS NDT METHOD OF DETECTION OF SCC OF METALLIC GLASSES

K. Habib

Materials Science Lab, Department of Advanced Systems
K I S R , P. O. Box 24885 SAFAT, 13109 Kuwait

ABSTRACT

A preliminary study on the susceptibility of various iron-boron-silicon metallic glasses to stress-corrosion cracking (SCC) has been conducted. Testing was carried out on thin metallic ribbons of $Fe_{78}B_{13}Si_9$, $Fe_{81}B_{13.5}Si_{3.5}C_2$, $Fe_{66}Co_{18}B_{15}Si_1$, $Fe_{77}B_{16}Cr_2Si_5$, and $Fe_{40}Ni_{38}Mo_4B_{18}$, in 0%, 25%, 50%, 75%, and 100% hydrochloric acid solutions at the open circuit potential of the metallic glasses in solutions, at room temperature. The tests were performed under constant-strain conditions in the various solutions until complete separation of the ribbons occurred. The preliminary results indicated that the susceptibility of the glasses $Fe_{78}B_{13}Si_9$, $Fe_{81}B_{13.5}Si_{3.5}C_2$, $Fe_{66}Co_{18}B_{15}Si_1$, and $Fe_{77}B_{16}Cr_2Si_5$, to stress-corrosion cracking varies only as a function of the amplitude of the strain. The susceptibility to SCC is independent of the solution concentration and the addition of carbon, chromium, and cobalt to the glass. However, the results indicated that $Fe_{40}Ni_{38}Mo_4B_{18}$ glass is not susceptible to stress-corrosion cracking in HCl solutions at different strain amplitudes.

In addition, an early stage of stress corrosion cracking (SCC) of the same metallic glasses in the same solutions was investigated in situ by a new non-destructive testing (NDT) method. The new method of SCC detection is based on the optical corrosion-meter for measuring the corrosion current density (J) and on a modified electrochemical noise technique for determining the corrosion admittance (Ac) at the open circuit potential of the alloys in solutions, at room temperature. A comparison between the two techniques of SCC study indicates that the new method has many advantages relatives to the constant-strain method.

KEYWORDS : Stress Corrosion Cracking (SCC), Metallic Glass, Electrochemical Noise, Constant Strain, Non-Destructive Method, Corrosion Admittance, Holographic interferometry , and HCl Solution.

INTRODUCTION

It has been known for some time that thin films of metallic glasses have many practical values owing to their extremely homogeneous and disordered atomic structures [1]. For instance, Allied Chemical Inc., has recently reported results on a $Fe_{78}B_{13}Si_9$ metallic thin film, known commercially as Metglass 2605S [2], indicating that the film has excellent physical and magnetic properties as compared to the crystalline alloy. The film was found suitable for extremely low core loss in distribution, power transformers, and motors. It combines high induction and superb magnetic properties at frequencies, induction, and operating temperatures of these devices. Furthermore, the film can be used in inductors, current transformers and other devices requiring high permeability and low core loss at low frequencies.

Subsequently, Allied Chemical succeeded in developing three new metallic films ($Fe_{81}B_{13.5}Si_{3.5}C_2$ known as Metglas 2605SC, $Fe_{66}Co_{18}B_{15}Si_1$ known as Metglas 2605Co, and $Fe_{77}Cr_2B_{16}Si_5$ known as Metglas 2605 S3-A) with improved physical and magnetic properties. Detailed information on these films has been well documented elsewhere [3]. In addition to the Fe-B-Si glasses, an Fe-Ni glass, $Fe_{40}Ni_{38}Mo_4B_{18}$ known as Metglas 2826 MB, was among the first Metglas alloys developed by Allied Chemical. The $Fe_{40}Ni_{38}Mo_4B_{18}$ glass has a high content of corrosion resistant elements (Ni and Mo) in a comparison with the other glasses. Information on the internal structures and properties of the Fe_{40} Ni_{38} Mo_4 B_{18}, are reported elsewhere [4 & 5].

Specifically, the properties of the Fe_{81} $B_{13.5}$ $Si_{3.5}$ C_2, are balanced in a way that may lend the films useful in pulse transformers, magnetic amplifiers, power transformers, current transducers and other devices requiring a square-loop high saturation material. The film also offers a unique combination of high resistivity, high saturation induction, and very low core loss, making it suitable for use from low to high frequencies. Fe_{66} Co_{18} B_{15} Si_1 exhibits the highest saturation induction of any amorphous alloy commercially available. In addition, it possesses very low core loss and it is designed ideally for pulse applications where maximum flux swing is desired. However, Fe_{77} Cr_2 B_{16} Si_5 is found to exhibit very low core loss at high frequencies (>1 KHz) when annealed to obtain a rounded B-H Loop. Its saturation induction is much higher than ferrites and can be used at elevated temperatures without cracking or showing large drops in usable flux density. In torodial losses are reduced as temperature increases.

In general, the properties of Fe_{77} Cr_2 B_{16} Si_5 can be substantially tailored by annealing treatment. In addition, the alloy offers an improved high frequency annealing cycle which makes field annealing optional. High frequency losses can be lowered without use of a field while field annealing will increase permeability. Other anneals for low frequencies yield exceptionally high (60 Hz) permeabilities which are useful in current transformers or ground fault protection devices.

On the other hand, the $Fe_{40}Ni_{38}Mo_4B_{18}$ alloy has medium saturation induction. Also, it has lower magnetostriction and higher corrosion resistance than the Fe-B-Si alloys [4 & 5]. The alloy can be annealed for very high DC permeability, and use of the alloy in field sensors and shielding applications is possible. Furthermore, magnetic properties of the alloy can be altered through selective field annealing. Finally, applications for the alloy in manufacturing devices requiring rounded or square B-H Loops are suggested.

In the present investigation, $Fe_{78}B_{13}Si_9$, $Fe_{81}B_{13.5}Si_{3.5}C_2$, $Fe_{66}Co_{18}B_{15}Si_1$ and $Fe_{77}B_{16}Cr_2Si_5$,a$Fe_{40}Ni_{38}Mo_4B_{18}$ glasses were examined for their practical applications as electronic materials [6-8], to the susceptibility of the alloys to stress-corrosion cracking in HCl solutions under a bending stress test [9] and a new non-destructive testing (NDT) method. The new method of SCC detection is based on the optical corrosion-meter [10-20] for measuring the corrosion current density (J) and on a modified electrochemical noise technique for determining the corrosion admittance (Ac) [21-22] at the open circuit potential of the alloys in solutions. The observations of SCC were basically interferometric perturbations detected by the optical corrosion-meter. The interferometric perturbations interpreted as a combined action of a deformation and an electrochemical attack, localized corrosion, in a form of an early stage of SCC, of a deformation ranged between 0.3 μm to several micrometers, of the metallic glasses. Also, the early stage of localized corrosion, i.e., corrosion current corresponding to the deformation, of the same metallic glasses in same conditions was determined in situ by a modified electrochemical noise (EN) technique, called the modified electrochemical emission spectroscopy (MEES) technique, simultaneously during the optical interferometry measurements of the SCC. Determinations of localized corrosion by the MEES technique were electrochemical noise spectra detected on corrosion admittance (Ac)-time plots of the metallic glasses in solutions. The corrosion admittance parameter, Ac=(dJ/dV), which defined the MEES technique, is capable of indicating localized corrosion, as a result of SCC, and uniform corrosion activities. In this investigation, the parameter Ac was modified in which that the change of the corrosion current density (dJ) was measured by the optical corrosion-meter rather than by the zero resistance ammeter,which is usually used for measuring the dJ in electrochemical noise technique.

The modified form is defined as follows:

$$Ac = dJ_O/dV \qquad (1)$$

Where, dJ_O is the difference between the corrosion current density (J) of two subsequent values, and measured by the optical corrosion-meter [18], an electromagnetic method.

dV is the difference between the open circuit potential (V) of two subsequent values [21- 22], normally measured by a potentiometer , an electronic method.

According to (Equ.1), It is generally accepted that the break down passive film (initiation of SCC) will cause a potential drop and a current rise at the same time, and the repassivation of passive film (repassivation of SCC) will cause the potential to increase and the current to decrease. Therefore the Ac parameter , is defined as follows to reflect SCC, passivation or repassivation, and uniform corrosion:

If $A_C < 0$, this indicates that the working electrode under SCC.
If $A_C > 0$, this indicates that the working electrode under uniform corrosion.
If $A_C = 0$, this indicates that the working electrode under passivation or repassivation.

In this way all the corrosion activities (either SCC or uniform corrosion) are clearly revealed in the Ac spectra. Consequently, results of the present work indicate that the optical corrosion-meter as an electromagnetic method of measuring the SCC , and MEES technique, as an electronic method for determining the Ac, are very useful techniques as non-destructive methods for detection of SCC of metallic glasses at the initiation stage of the phenomenon .

EXPERIMENTAL DETAILS

For the bending stress test [9], corrosion samples were prepared from thin foils of the $Fe_{78}B_{13}Si_9$, $Fe_{81}B_{13.5}Si_{3.5}C_2$, $Fe_{66}Co_{18}B_{15}Si_1$, $Fe_{77}Cr_2B_{16}Si_5$, and $Fe_{40}Ni_{38}Mo_4B_{18}$ glasses in a rectangular shape. The length of each sample was approximately 25 mm. The width of the samples varied from one sample to another based on the amplitude of the bending strain during the application of stress to each sample. The thickness of the foils was approximately 16.7 μm for $Fe_{78}B13Si9$, 23.1 μm for $Fe_{81}B_{13.5}Si_{3.5}C_2$, 20 μm for $Fe_{66}Co_{18}B_{15}Si_1$, 16.7 μm for $Fe_{77}Cr_2B_{16}Si_5$, and 16.7 μm for $Fe_{40}Ni_{38}Mo_4B_{18}$ glasses.

The samples were tested as-received and not subjected to any prior heat treatment because of the difficulty in retaining ductility [3]. Stress corrosion tests were conducted in HCl solutions with concentrations in the range of 0-100% HCl until the samples failed. The ribbon samples were bent inside glass tubes of different sizes with each tube size corresponding to a different bending strain (see fig.1). The procedures for calculating the bending strain was based on the following formula [10]:

$$\Sigma = \frac{h/2}{r} \qquad (2)$$

where h stands for the thickness of the ribbon , and r is the internal radius of the glass tube.

It should be noted that because of the thickness of the samples used in the present work, failure criterion was the complete separation of the glasses into two pieces. In the case of the MEES technique for

detecting the susceptibility of SCC of the metallic glasses, experimental details will be given in the presentation.

RESULTS AND DISCUSSION

In the case of the bending stress test, the results indicated that $Fe_{78}B_{13}Si_9$, $Fe_{81}B_{13.5}Si_{3.5}C_2$, $Fe_{66}Co_{18}B_{15}Si_1$, and $Fe_{77}Cr_2B_{16}Si_5$ glasses were found susceptible to stress-corrosion cracking in HCl solutions. Samples of the same alloys tested in 0% HCl (distilled water) suffered only from general corrosion attack, rust, during the stress-corrosion tests. Data on strain amplitudes versus time to failure of the different alloys in 25%, 50%, 75% and 100% HCl are presented in tables 1-4. In general, results indicate that the higher the strain, the shorter the life of the samples. All of the samples failed within five hours of immersion in the HCl solutions regardless of the different concentrations of HCl and the additions of the alloying elements (C, Co, Cr) to the Fe-B-Si glass. Consequently, it can be concluded that $Fe_{78}B_{13}Si_9$, $Fe_{81}B_{13.5}Si_{3.5}C_2$, $Fe_{66}Co_{18}B_{15}Si_1$, and $Fe_{77}B_{16}Cr_2Si_5$ glasses have low stress corrosion resistance in HCl solutions.

In addition, results indicated that $Fe_{40}Ni_{38}Mo_4B_{18}$ glass is not susceptible to stress-corrosion cracking in any of the HCl solutions. The alloy has good stress-corrosion resistance in HCl solutions and 0% HCl (distilled water). In fact, in a previous study [9], $Fe_{40}Ni_{38}Mo_4B_{18}$ alloy was found only susceptible to stress-corrosion cracking in 100% H_2SO_4. This is probably attributed to the presence of enough passive alloying elements, Ni and Mo, in the glass as compared to the Fe-B-Si glasses. In the case of the MEES technique for detecting the susceptibility of SCC of the metallic glasse, detailed results will be given in the presentation.

Figure 1: Schematic diagram of ribbon sample bent in the glass tubes.

TABLE 1
Stress corrosion of the $Fe_{78}B_{13}Si_9$ glass

strain x 10^{-3} (mm/mm)	Time to failure (hrs) 25% HCl	50% HCl	75% HCl	100% HCl
3.34	≤ 2.5	≤ 1.5	≤ 1	≤ 3.5
4.0	≤1.5	≤ 1.5	≤ 1	≤ 3.5
8.35	≤ 1.5	≤ 1	≤ 0.25	≤ 3.5
11.13	≤ 1	≤ 1	≤ 0.25	≤ 3.5

TABLE 2
Stress corrosion data of the $Fe_{81}B_{13.5}Si_{3.5}C_2$ glass.

strain x 10^{-3} (mm/mm)	Time to failure (hrs) 25% HCl	50% HCl	75% HCl	100% HCl
4.62	≤ 1.5	≤ 5.5	≤ 0.25	≤ 3.5
5.8	≤ 1.5	≤ 5.5	≤ 0.25	≤ 3.5
11.55	≤ 1	≤ 1	≤ 0.25	≤ 3.5
15.4	≤ 1	≤ 1	≤ 0.25	≤ 3.5

TABLE 3
Stress corrosion data of the $Fe_{66}Co_{18}B_{15}Si_1$ glass

strain x 10^{-3} (mm/mm)	Time to failure (hrs) 25% HCl	50% HCl	75% HCl	100% HCl
4.0	≤ 1.5	≤ 5.5	≤ 1	≤ 3.5
5.0	≤ 1.5	≤ 5.5	≤ 1	≤ 3.5
10.0	≤ 1.5	≤ 5.5	≤ 0.25	≤ 3.5
13.3	≤ 1	≤ 1.5	≤ 0.25	≤ 3.5

TABLE 4
Stress corrosion data of the $Fe_{77}B_{16}Cr_2Si_5$ glass

strain x 10^{-3} (mm/mm)	Time to failure (hrs) 25% HCl	50% HCl	75% HCl	100% HCl
3.34	≤ 2	≤ 1.5	≤ 1	≤ 3.5
4.8	≤ 2	≤ 1.5	≤ 1	≤ 3.5
8.35	≤ 1	≤ 1.5	≤ 0.25	≤ 3.5
11.13	≤ 1	≤ 1.5	≤ 0.25	≤ 3.5

REFERENCES

1.Beck .,H and Guntherodt.,H, Glassy Metal II, (1983), p.169, 343, Spring Verlag, Berlin .

2.Metglas: "Magnetic Alloys" Data Sheet on Magnetic Alloys, (1989) Allied Chemical Incorporated .

3.Habib.,K, Eling.,V, Wu., C, Moore.,K, and Mihalik.,R, (1990), Scripta Metallurgica et Materiala, vol. **24**, pp.1057-1062 .

4. Habib,K., Moore.,K, Fritz., P, (1990), Journal of Materials Science Letters, vol.**9**, p.852 .

5.Habib,.K, (1992), Journal of Materials Science Letters, Vo.**11**,No.2, P.162.

6.Mas.,J, (1988), Metallic Glasses as Electronic Materials, Proc. Power Electronic Specialists Conference, IEEE, New York, pp.68-75.

7.Smith.,C, (1982),Magnetic Shielding to Multi-Gigawatt Magnetic Switches: Ten Years of Amorphous Magnetic Applications, IEEE Trans. Magn., vol.**18**, pp.1376-1381.

8.Metglas Filter Metals, (1991), Brochure on Brazing Foils, Allied Chemical Inc.,.

9.Habib., K, Carmichael., and G,Lakes,R., (1990), Materials Characterization, vol. **24**, pp. 41-47.

10.Habib K.J., (1990), Applied Optics , **29** (13), pp.867-869.

11.Habib., K, (1990), Experimental Techniques of Physics, **38** (5/6) , pp. 535-538.

12. Habib., K, Carmichael G., Lakes R. , Stwalley W. , (1990), Corrosion Journal, **49** (5), pp.354-362.

13 . Habib., K,(1994), Optics and Lasers in Engineering, **20**, pp.81-85.

14. Habib., K, (1995), Optics and Lasers in Engineering, **23**,pp.65-70.

15 .Habib., K, (1990), Proc. SPIE, **1230** , pp. 293-6.

16. Habib., K, (1993), Optics and Lasers in Engineering, **18**, , pp.115-20.

17. Habib., K, F. Al Sabti, and H. Al- mazeedi, (1997),Optics and Lasers in Engineering ,Vol.**27**, No.2,PP.227-233.

18.Habib., K. and F.Al-Sabti,(1997), Corrosion Journal, **53**.(9) PP. 680-685.

19. Habib., K., (1998), " , Corrosion Science, **40**.(8) PP. 1435-1440.

20.Habib., K., (1995) , Optics and Lasers in Engineering ,Vol.**23** PP.213-219.

21.Chen., F,.andW.F.Bogaets,(1996),,Corrosion Iournal,Vol.**52**,P.753.

22.Chen ., F, J.Shadley,and E.F.Rybicki,(1999),, NACE 99, paper No.193.

ORAL/POSTER REFERENCE: ICF100870OR

MOLECULAR DYNAMICS SIMULATION OF CRACK PROPAGATION IN HCP CRYSTALS

S. Ando[1], H. Tonda[1] and K. Takashima[2]

[1]*Department of Materials Science and Mechanical Engineering, Faculty of Engineering, Kumamoto University, Kumamoto, 860-8555, Japan*
[2]*Precision and Intelligence Laboratory, Tokyo Institute of Technology, Yokohama, 226-0026, Japan*

ABSTRACT

The crack propagation behavior of hcp single crystals has been simulated by molecular dynamics method using Lennard-Jones type potential. A definite dependence of crystallographic orientation on crack propagation behavior was obtained. In a model crystal with initial crack plane and direction were $(10\bar{1}0)$ and $[1\bar{2}10]$, the crack propagated parallel to $(10\bar{1}0)$ $[1\bar{2}10]$ and two sets of prismatic slips were occurred at the crack tip. Therefore, the crack in this crystal is deduced to extend by alternating shear on two intersecting prismatic slip systems. In a model crystal with (0001) $[1\bar{2}10]$ initial crack, the crack propagated parallel to (0001) and small twinning region was occurred in front of the crack. The crack propagation rate in the twin region is lower than those in the matrix region. In the model crystal with $(10\bar{1}0)[0001]$ initial crack, the crack propagate parallel to notch plane with some basal slips and prismatic slips were occurred in front of the crack.

KEYWORDS

HCP, crack propagation, Lenard-Jones potential, molecular dynamics.

INTRODUCTION

Fatigue crack growth in crystalline metals and alloys are fundamentally based on cyclic plastic deformation at the crack tip. The crack growth increment for each cyclic loading (*da/dN*) in such materials often occurs in the range of 10^{-6} to 10^{-3} mm, and this extension is usually smaller than the grain size of such materials. Therefore, it is extremely important to know the fatigue crack growth mechanisms that may occur in singe crystals to promote increased understanding of the intrinsic fatigue crack growth resistance of materials.

Among hcp crystals, α-titanium and its alloys have been applied to aerospace structures and engine components because of their excellent specific strength and corrosion resistance. However, there have been few studies on fatigue crack growth mechanisms in titanium crystals. This may be partly due to the fact that the slip systems of hcp crystals have not yet been identified precisely. In addition, mechanical twinning may occur in hcp crystals. This may make it difficult to clarify fatigue crack growth mechanisms in hcp metals. Therefore, it is important to evaluate the crack propagation mechanism of such materials.

The crack propagation process is subjected to the behavior of atoms near the crack tip. Microscopic analysis using the molecular dynamics has, therefore, advantages over macroscopic analysis. In the present study, the atomic structure at the crack tip in α-titanium single crystals with different orientations has been investigated by method of molecular dynamics simulation.

CALCULATING METHOD

In the present simulation, Lennard-Jones type interatomic potential (Minonishi *et al.*[1], 1981),

$$V(r) = \varepsilon_0\{(d/r)^{12}-2(d/r)^6\} \quad (1)$$

was used, where $\varepsilon_0 = 0.16$ eV, $d = 1.021522a$ (a is the lattice parameter in (0001)) and r is the distance between atoms.

Figure 1 shows the atom arrangement of model crystals used in this study. Every initial crack was set perpendicular to y-axis and its direction was parallel to x-axis. The crystallographic orientations of initial crack plane and direction in the Crystal 1 were $(10\bar{1}0)$ and $[1\bar{2}10]$, those in the Crystal 3 were (0001) and $[10\bar{1}0]$, those in the Crystal 4 were (0001) and $[1\bar{2}10]$ and those in the Crystal 5 were $(10\bar{1}0)$ and [0001], respectively. These models were applied fixed boundary condition along x- and y-axes and periodic boundary condition along z-axis. The number of atoms contained in each model crystals are listed in Table 1. The initial cracks were introduced to the model crystals by terminating interaction between atoms along crack plane. The external load to propagate crack was added on the x- and y- fixed boundary atoms by their displacement, which was estimated by an isotropic elastic field with stress intensity factor K singularity.

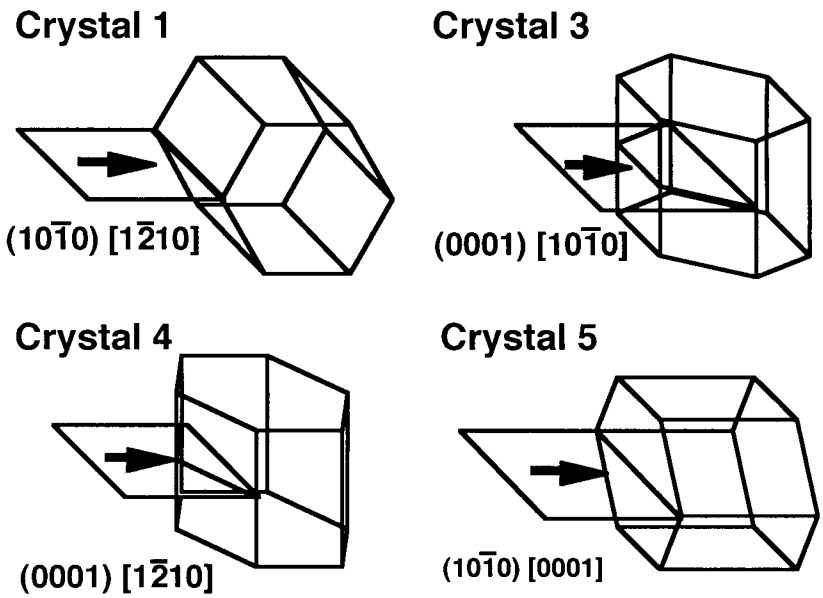

Figure 1: Model hcp crystals and initial crack orientation.

TABLE 1
Size of model crystals.

	X atoms	Y atoms	Z atoms	Total
Specimen-1	44	48	2	4224
Specimen-3	26	50	2	2600
Specimen-4	42	50	2	4200
Specimen-5	54	24	2	2592

The magnitude of time step used in integration of the equation of motion was $2x10^{-16}$ s and the increment in external field is K = 0.01MPam$^{1/2}$ every 5000 time steps. The initial temperature of the crystals were set to 293K.

RESULTS AND DISCUSSION

All of the crystals consist from two atomic layers. The atoms of each layer are represented by circles and squares, respectively. Figure 2 shows the atomic structure at the crack tip in Crystal 1. The arrows in the figure show the y-component of relative displacement between atoms according to Vitek's method (Vitek *et al.*[2], 1970). Crack propagation in Crystal 1 was occurred at K = 0.56 MPam$^{1/2}$, and the dislocations were emitted upward and downward of the crack. Each directions of emitting dislocations were inclined 60 degree to the initial crack plane. This indicates that two intersecting prismatic slip systems ($(1\bar{1}00)$ $[11\bar{2}0]$ and $(01\bar{1}0)$ $[\bar{2}110]$) were activated at the crack tip. As a result, the crack in Crystal 1 was propagated parallel to $(10\bar{1}0)$ $[1\bar{2}10]$ initial crack.

In the fatigue crack growth in real titanium single crystals (Mine *et al.*[3], 1998), many slip trace of prismatic slips were observed near crack surfaces. The result of Crystal 1 is similar to that of real titanium single crystals. Therefore, as shown in Fig. 3, the slip-off model of crack propagation in titanium single crystals is deduced from present simulation result.

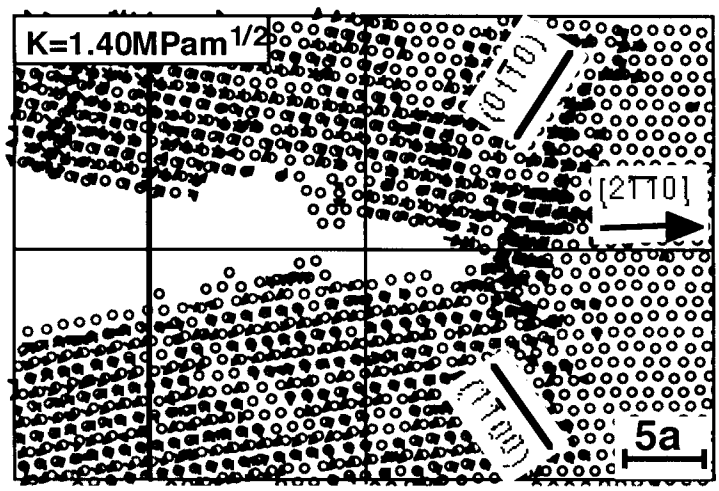

Figure 2: Atomistic structure of crack tip results in Crystal 1 at K = 1.40MPam$^{1/2}$.

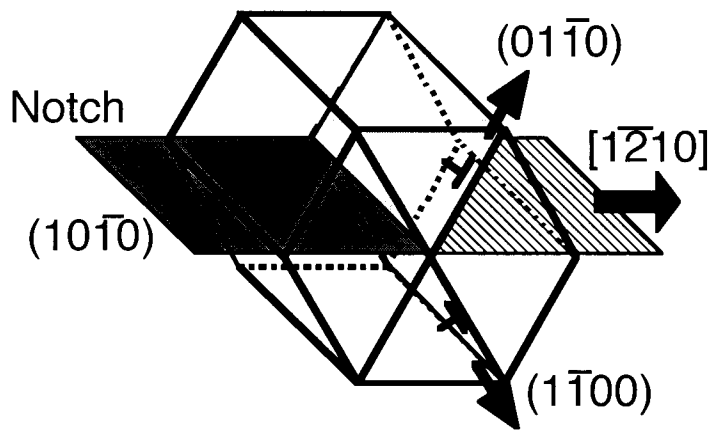

Figure 3: Slip-off model activated in Crystal 1.

In the case of Crystal 3, the initial crack started to propagate at K = 0.50 MPam$^{1/2}$ and, as shown in Fig. 4 by solid lines, $\{10\bar{1}1\}$ twins occurred at the crack tip with increasing K. In the case of Crystal 4, the initial crack propagated parallel to (0001) with increasing K as brittle manner. In this crystal, as shown in Fig. 5, a region which shows different atomic orientation to the matrix was developed. Since the atomic orientation of that region corresponds to (0001) plane, it can be seen that $\{10\bar{1}2\}$ deformation twin occurred in front of the crack tip at K=1.03 MPam$^{1/2}$. After that, the crack was propagated through this twin region.

Figure 6 shows a crack tip structure in Crystal 5. The initial crack started to propagate at K = 0.67 MPam$^{1/2}$, and the crack became blunt with emittion of many partial dislocations parallel to the basal planes from the crack tip.

Figure 7 shows relationships between the crack growth length and the stress intensity factor in each model crystals. A slope of the curve for Crystal 4 is larger than that of Crystal 1 and Crystal 3 below K = 1.1 MPam$^{1/2}$. This indicates that the crack parallel to (0001) plane propagates easily than in the case of Crystal 1 and Crystal 3. The crack in Crystal 3 propagated through $\{10\bar{1}2\}$ twin region above K = 1.1 MPam$^{1/2}$, then the slope of the curve in Fig. 7 becomes small. This indicates that the crack growth rate in the twin region is low than that of the matrix. In real titanium single crystals with a crack parallel to (0001), fatigue cracks were propagated with many $\{10\bar{1}2\}$ twins and fatigue crack propagation resistance on (0001) crack is higher than the case of crack propagation with alternating shear of prismatic slips[3]. From above simulation results, it is suggested that because of the crack growth rate is low in the $\{10\bar{1}2\}$ twin occurred in front of the crack, fatigue crack propagation resistance with respect to (0001) crack in titanium single crystal becomes high.

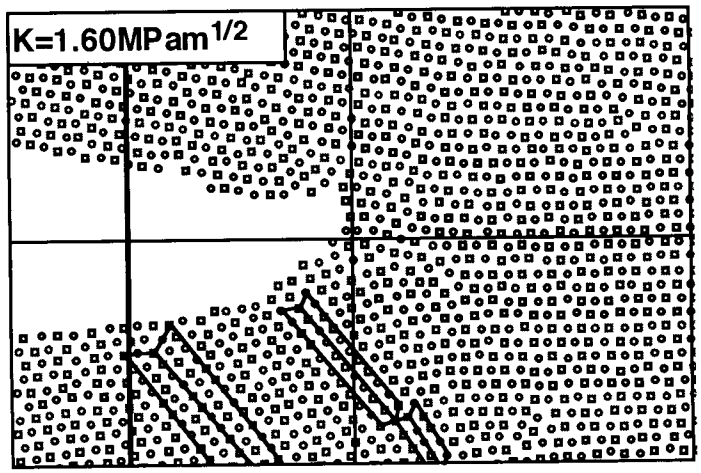

Figure 4: Atomistic structure of crack tip results in Crystal 3 at K = 1.60MPam$^{1/2}$.

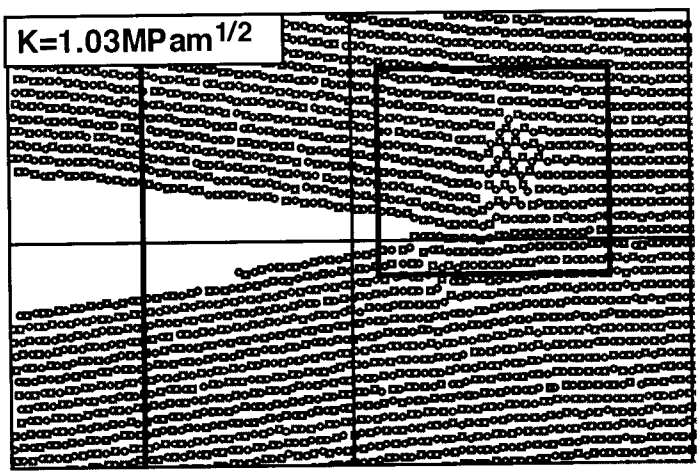

Figure 5: Atomistic structure of crack tip results in Crystal 4 at K = 1.03MPam$^{1/2}$.

In the case of Crystal 5 with crack propagates [0001], the threshold value of stress intensity factor for crack propagation is higher than other three crystals and the curve of crack growth rate is lowest. In the case of titanium single crystal, a fatigue crack normal to (0001) propagates to [0001] when high stress intensity factor range is applied (Yamada *et al.*[4], 1999). This shows that crack propagation resistance with respect to [0001] is heigest and this is agreement with the simulation result in Crystal 5. It was also reported that the fatigue crack normal to (0001) inclined (0001) and propagated at low stress intensity factor range[4]. In Crystal 5, it was not seen such a behavior at low stress intensity factor. We need more investigation about this point.

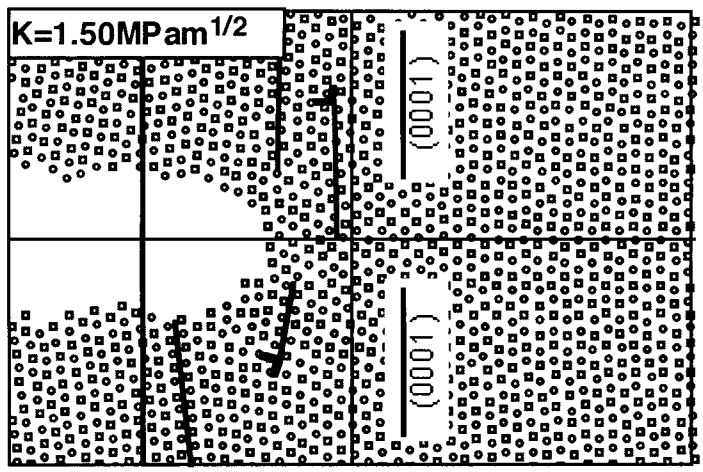

Figure 6: Atomistic structure of crack tip results in Crystal 5 at K = 1.50MPam$^{1/2}$.

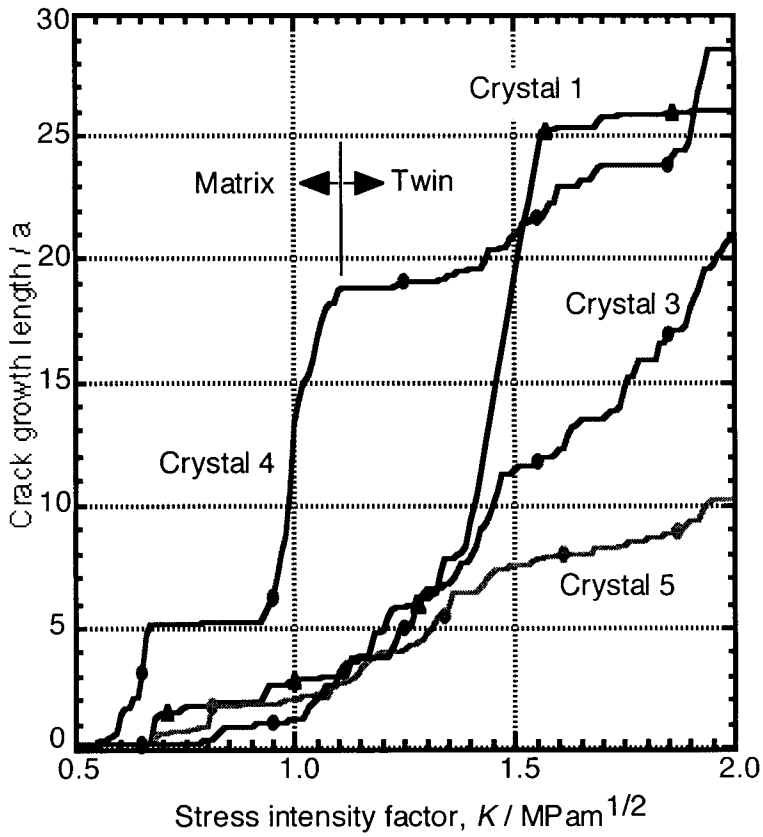

Figure 7: Relationship between crack grwoth length vs. stress intensity factor.

CONCLUSION

The crack growth behavior of a-titanium single crystals has been investigated by molecular dynamics simulation using Lennard-Jones type potential. Results are summarized as follows:

1. In the model crystals with the initial crack plane and direction were $(10\bar{1}0)$ and $[1\bar{2}10]$, a crack propagated parallel to $(10\bar{1}0)[1\bar{2}10]$ by alternating shear on two intersecting prismatic slip systems. This behaviors are similar to those of real α-titanium single crystals. From this result, the slip-off model consist of two intersecting prismatic slip systems was proposed.

2. In the model crystals with the initial crack plane and direction were (0001) and $[10\bar{1}0]$, $\{10\bar{1}1\}$ twins occured at the crack tip.

3. In the model crystals with the initial crack plane and direction were (0001) and $[1\bar{2}10]$, a brittle crack propagated and$\{10\bar{1}2\}$twin occurred in front of the crack. The crack growth rate in the twin region was lower than in the matrix.

4. In the model crystals with the initial crack plane and direction were $(10\bar{1}0)$ and [0001], a crack propagated to [0001] with many partial dislocations. The crack growth rate is lowest than other three crystals.

REFERENCES

1. Minonishi, Y. Ishioka, S. Koiwa, M. Morozumi, S. and Yamaguchi, M. (1981). The Core Structure of $1/3\langle\bar{1}\bar{1}23\rangle\{11\bar{2}2\}$ edge dislocations in h. c. p. metals. *Philosophical Magazine A*, **43**, 1017-1026.
2. Vitek, V. Perrin, C. and Bowen, D. K. (1970). The Core Structure of $1/2\langle111\rangle$ Screw Dislocation in B. C. C. Crystals. *Philosophical Magazine*, **21**, 1049-1073.
3. Mine, Y. Yamada, T. Ando, S. Takashima, K. Tonda, H. Higo, Y. and Bowen, P. (1998), Fatigue Crack Propagation in Titanium Single Crystals. *Key Engineering Materials*, **145-149**, 721-726.
4. Yamada, T. Mine, Y. Tateishi, Y. Ando, S. Tonda, H. and Takashima, K. (1999). Orientation Dependence of Crack Propagation Behavior in Titanium Single Crystals. *Abstracts of the Japan Institute of Metals*, **38**, 415.

Oral/Poster Reference: ICF10054PR

MONITORING PART-THROUGH CRACK GROWTH USING COMPLIANCE TECHNIQUE

N. Parida and S. Tarafder

National Metallurgical Laboratory, Jamshedpur, India, 831007

ABSTRACT

Specimens with part-through crack were obtained by fatiguing ridged specimens. These specimens were then fatigue tested while simultaneously monitoring crack opening displacement (COD) using a clip on COD gauge.. The depth 'a' and the surface length '2c' of the cracks were measured by ultrasonic testing and beach marking technique, and the data obtained from this were compared with COD data. The results showed that automatic monitoring of 'a' and '2c' could be carried out through COD.

KEY WORDS

Part-through crack, compliance technique, ultrasonic, beach marking.

INTRODUCTION

One of the most important and essential aspects of fatigue crack growth rate (FCGR) test with part-through cracks is accurate monitoring of crack shape development as the test progresses. The ratio of the depth to half the surface length (a/c) can be used to describe the shape of the cracks and is referred to as aspect ratio of the crack. As the aspect ratio varies with increase of crack length, it is necessary to monitor both 'a' and 'c' during the experiment. Generally 'a' and 'c' are measured by beach marking technique, and 'a' by potential drop method. On the other hand the on-line crack extension of a through crack can be monitored by a number of methods, e.g., ACPD, DCPD or compliance technique. Of these the compliance technique has proven to be the most popular because it tends itself to easy automation using a clip on crack opening displacement (COD) gauge interfaced to a computer. In this method, displacement, V, at any location of the specimen usually at external knife edges fixed over the crack mouth is monitored continuously along with the load, P. From the (V,P) data obtained during a particular load cycle, the compliance V/P of the specimen is computed. The length of the crack at the instant of the load cycle can be correlated to the compliance through a relation of the form

$$\frac{a}{W} = F(u) \tag{1}$$

$$u = \frac{1}{\sqrt{\frac{EBV}{P} + 1}} \tag{2}$$

where W,B are the width and thickness of the specimen, *E* is the Young's' modulus, and F is polynomial function. Such relations are known as compliance crack length (CCL) relations. CCL relations are available for different specimens such as TPB, 4PB, CT, AT, and DCT [1-3]. These relations are not only specific to specimen geometry, but, for a given specimen, to the location of measurement of displacement or compliance. In this paper we have attempted to explore the use of this method for on-line monitoring of both 'a' and 'c' of part-through cracks, through comparison of different techniques such as ultrasonic and beach marking.

EXPERIMENTAL

The material used in testing was A-537 class-I steel , a widely used material for construction of LPG Horton spheres. The chemical composition and the mechanical properties of the steel are given in Tables 1 & 2 respectively.

TABLE 1
CHEMICAL COMPOSITION OF THE STEEL (%WT).

C	Mn	Si	P	S	Cu	Ni	Cr	Mo	V	Nb
0.22	1.26	0.45	0.015	0.003	0.065	0.018	0.026	0.002	0.005	0.003

TABLE 2
MECHANICAL PROPERTIES OF THE STEEL

YS [MPa]	UTS [MPa]	%El
359	555	32

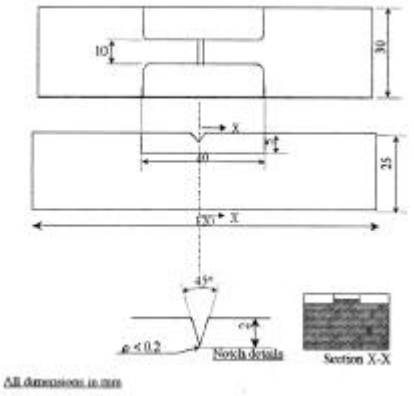

Figure 1: Specimen drawing

Specimens with semi-elliptical cracks were obtained by fatiguing ridged specimens (Fig.1) using a 50 KN Instron servohydraulic testing machine. The surface length (2c) and depth (a) of the cracks were measured by optical microscope, and ultrasonic testing. The specimens were then fatigue tested at different load amplitudes till the crack became through. By changing the amplitude of the load during the tests, beach marks were produced in the specimen. For a few specimens, the tests were stopped in between to measure the length and depth of the cracks by optical microscope and ultrasonic testing. After completion of the tests 'a' and '2c' were measured from the beach marks and the data obtained from this were compared with that of obtained from ultrasonic testing and optical microscope (Table 3). For conducting the ultrasonic tests an Ecchograph 1030 test system from M/s. Karl Deutsch, Germany was employed. The probes used in the test were a normal beam probe of 6mm diameter and 1 MHz frequency; and a 45 angle beam probe of 2 MHz frequency. During the fatigue testing, using a clip on crack

opening displacement (COD) gauge, the crack opening displacement 'V' at external knife edges fixed over the crack mouth were monitored continuously along with the load, P. These V/P data were then correlated with the data of 'a' and '2c' obtained from beach marking technique.

RESULTS AND DISCUSSION

A comparison of 'a' and '2c' data obtained from different techniques was made. The data are presented in Table3. The results show that the data obtained from beach marking technique are on the higher side whereas the values obtained from the ultrasonic testing are on the lower side. This is because after unloading, a part of the crack gets closed and as the crack is very fine, the ultrasonic probes are not detecting the actual crack tip. However, the beach marking data are similar to the data obtained from optical microscope. This indicates that beach marking technique is very reliable technique for measuring the surface length and depth of a part-through crack during fatigue tests. It gives a conservative estimation of these values. Moreover it can measure both 'a' and 'c', whereas optical microscopy can measure only 'c'. We, therefore, used the beach marking technique for measuring 'a' and 'c' during the fatigue tests and used these data for correlating them with V/P obtained from COD gauge.

TABLE 3

VALUES OF '2C' AND 'A' MEASURED FROM DIFFERENT TECHNIQUES

Sl.No.	ΔP [KN]	N [cycles]	a [mm]		2C [mm]	
			Ultrasonic	Beach Marking	Microscope	Beach Marking
0	30	396,000	6.3	8.6	14.5	14.9
1	22.5	20,000	6.9	9.03	15.3	15.4
2	30	16,465	10.6	10.8	18.5	19.02
3	20	43,533	13.2	13.45	-	28.24
4	25	33,673	-	14.77	Through	Through

As mentioned above, the on-line crack extension of a through crack can be monitored by a number of methods, e.g., ACPD, DCPD or compliance technique. Of these the compliance technique has proven to be the most popular because it tends itself to easy automation using a clip on crack opening displacement (COD) gauge interfaced to a computer. We, therefore, explored here the use of this method for on-line monitoring of both 'a' and 'c' of part-through cracks during fatigue tests. The values of 'a' and '2c' obtained from beach marking technique and their corresponding V/P values obtained from COD gauge for three different specimens are given in Table 4. These results were then plotted as (a, 2c) vs. V/P, and are shown in Fig 2 for two specimens.. As can be seen from these figures that there exists an almost linear relationship between (a,2c) and V/P. This indicates that COD gauge can be used for continuous monitoring of 'a' and '2c' during fatigue experiments. However, to find a general empirical relation more work has to be carried out.

TABLE 4

VALUES OF 'A' AND '2C' MEASURED BY BEACH MARKING TECHNIQUE AND THEIR CORRESPONDING 'V/P' VALUES FOR THREE SPECIMENS FATIGUE TESTED AT DIFFERENT LOADS.

specimen Id .No.	Fatigue crack growth stage	a (mm)	2c (mm)	V/P (mm/MN)
PTC 1	0 (initial)	2.66	11.66	2.228
	1	5	16.66	2.763
	2	7.33	25.33	3.855
PTC 2	0 (initial)	2.33	12	2.398
	1	5	16	2.929
	2	7.33	21.68	3.615

	3	8.33	26.33	4.487
PTC3	0 (initial)	1.66	10.33	1.564
	1	4	13.33	1.927
	2	6.66	18.33	2.362
	3	8	23.33	2.930
	4	9	26.66	3.619

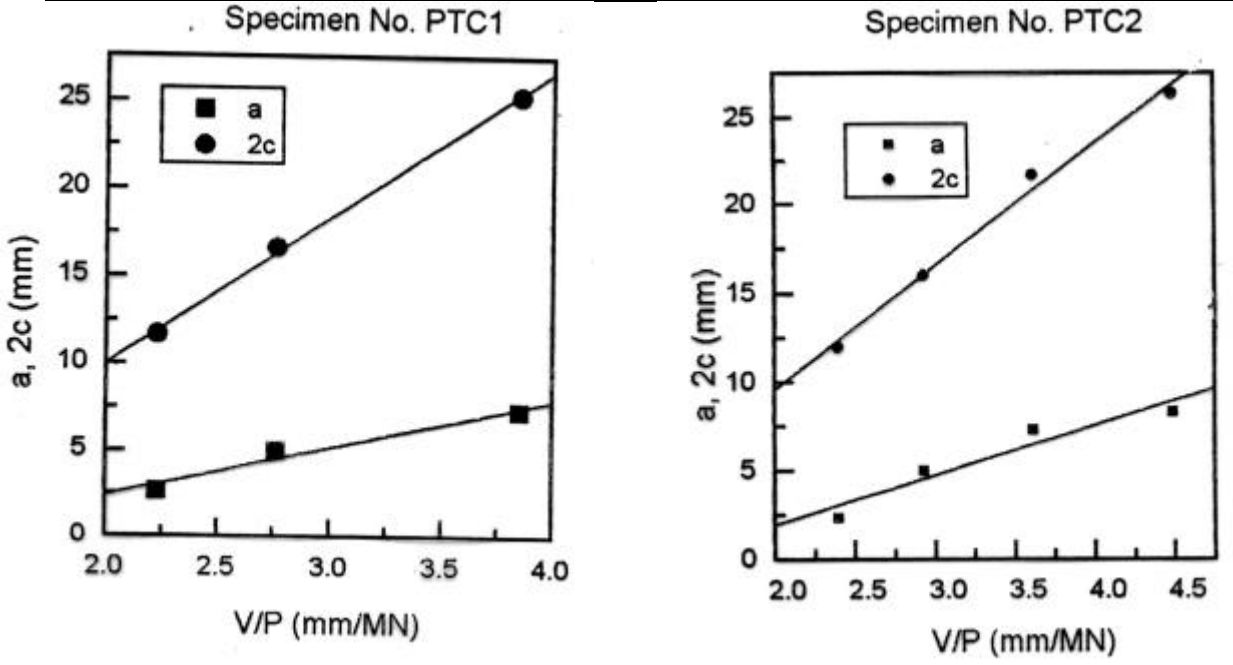

Figure 2: a, 2c vs. V/P for two specimens

CONCLUSIONS

From the above the following conclusions can be drawn.

1. Beach marking technique is the most reliable technique for the measurement of 'a' and '2c'
2. Automatic monitoring of 'a' and '2c' can be carried out through COD.

ACKNOWLEDGMENT

The authors wish to thank Prof. P. Ramachandra Rao, Director National Metallurgical Laboratory, Jamshedpur for his kind permission to publish these results.

REFERENCES

1. Saxena, A and Hudak, S. J, "Review and Extension of Compliance Information for Common Crack Growth Specimens", *Int. J. of Fracture*, 14, (1978), pp. 453-468.
2. E399-90, Test method for plane –strain fracture toughness of metallic materials, Annual Book of ASTM Standards, (1994), pp. 407-437.
3. E647-91, Standard Test method for measurement of fatigue crack growth rate, Annual Book of ASTM Standards, (1992), pp. 407-437.

CRACK PROPAGATION AND DAMAGE IN METALLIC ALLOYS

E. Bouchaud [1] and F. Paun [2]

[1]DSM/DRECAM/SPCSI, CEA-Saclay
91191 Gif-Sur-Yvette Cedex, France
[2]DMMP, ONERA
B.P. 72, 29 Av. du Général Leclerc,
92322 Châtillon Cedex

ABSTRACT

The morphology of damage cavities in an aluminium alloy is investigated with an Atomic Force Microscope (AFM) and shown to be the same as the one exhibited at small length scales by fracture surfaces. These observations support a scenario of crack propagation which takes explicitely damage into account.

KEYWORDS

Scaling, Roughness, Quantitative fractography, Atomic Force Microscopy, Damage.

INTRODUCTION

The renewed interest for the morphology of fracture surfaces and crack fronts [1-4] has given rise to a considerable theoretical effort [5-12]. However, no model to this day is entirely satisfactory. Among the various questions one can ask about the basic hypothesis of these models, the question of damage appears to be crucial. The central point of the present paper is to show that damage has to be explicitely taken into account to be able to predict the observed scaling properties.

As a matter of fact, fracture surfaces of various materials have been shown to be self-affine, sometimes on more than five decades of length scales [2-4,13]. They actually exhibit two self-affine regimes, observed both on metallic alloys and on glass, with exponents $\zeta_c \simeq 0.5$ at small length scales, and $\zeta \simeq 0.8$ at larger length scales [2-4,13,14]. The crossover length ξ_c separating the two regimes has been observed to decrease with the average crack front velocity [2,4]. Although models of lines propagating through randomly distributed microstructural heterogeneities are in principle able to predict such a behaviour, the most refined of them [9] fails to reproduce the experimental observations.

The basic hypothesis of these models which is questioned here is relative to damage: can one define a crack front at all scales of observation within the scaling domain ? The answer is yes as long as the scale of observation is smaller than the size of independent damage cavities. It does not make any sense at larger length scales.

The scenario we have in mind both for the ductile fracture of metals and plausibly, at very different length scales, for the fracture of amorphous materials [15-17], is the following: cavities nucleated on the sites of the material heterogeneities extend giving rise to a roughness exponent close to 0.5 as long as they are isolated. The 0.8 roughness exponent is the result of the coalescence of these cavities (small cavities merge together and also join the main crack), which are likely to be intercorrelated.

To test this idea, actually inspired by the results obtained from Molecular Dynamics simulations on amorphous ceramics [15-17, we have investigated the morphology of damage cavities appearing during fracture in an aluminium alloy.

Material and experimental techniques

The material is an Al-Cr-Zr alloy, constituted by flakes of rapidly quenched ribbons consolidated by extrusion. The microstructure is shown [18,19] to be quite anisotropic, for the flakes align in the direction of extrusion, which happens to be also the direction of crack propagation in this case. The alloy is made of elongated strips of material parallel to this direction, with alternately coarse intermetallic precipitates (diameter 0.5-1 μm)and much finer ones (diameter 0.1μm). In the strips containing fine precipitates, the grains of the α matrix are elongated in the direction of extrusion, and flattened along the plane of the plate. Their thickness is of order 1μm, and their length can reach several tens of micrometers. In the strips containing coarse precipitates, the grains are rather equiaxed, and the smallest ones are of the order of 1μm. Two types of intermetallic phases are identified, one is $Al_{13}Cr_2$ with precipitates sizes in the range 40-300 nm, and the other one, Al_3Zr (metastable), appears in the form of extremely fine precipitates about 10nm in size. No porosity is detected in the material prior to fracture, although, because of the poor consolidation (the extrusion temperature remains moderate in order to avoid a coarsening of the fine hardening precipitates as well as a return to thermodynamic equilibrium of the metastable phases), it cannot be excluded.

Chevron notched bar specimens are submitted to mode I tension. The geometry of the specimen is such that the crack actually progresses between the flakes. Crack propagation is stopped before complete failure. The sample is cut and polished as shown in Fig. 1 to allow for two sets of observations (at different depths of cut) of the damaged zone ahead of the crack tip. The distance between the two planes of cut is 0.5mm, larger than all the microstructural lengths.

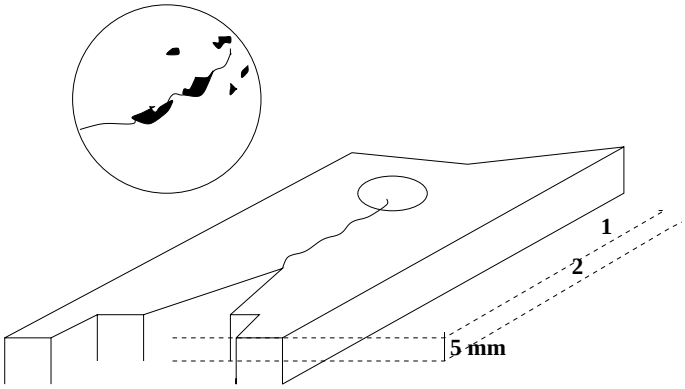

Figure 1: Sample preparation for the observation of the damaged zone ahead of the main crack tip. The two cuts (planes 1 and 2) are distant by 0.5 mm. The damaged zone ahead of the crack tip is explored in Atomic Force Microscopy.

Experimental results

The observations are performed with an Atomic Force Microscope (AFM). An AFM image of the crack tip zone is shown in Fig. 2.

In what follows we distinguish “large” and “small” cavities. The large cavities are quite anisotropic in shape (see Fig. 2, these cavities are elongated in the direction of the main crack), with dimensions 10-100μm. Furthermore, they are visibly linked to the main crack. Small cavities are much more isotropic in shape, and their dimensions are close to 3-5μm. They seem to be independent of the main crack.

Large and small cavities have a very different structure at a fine scale, as shown in Fig. 3. We will see later that this qualitative difference actually reflects a quantitative difference in roughness.

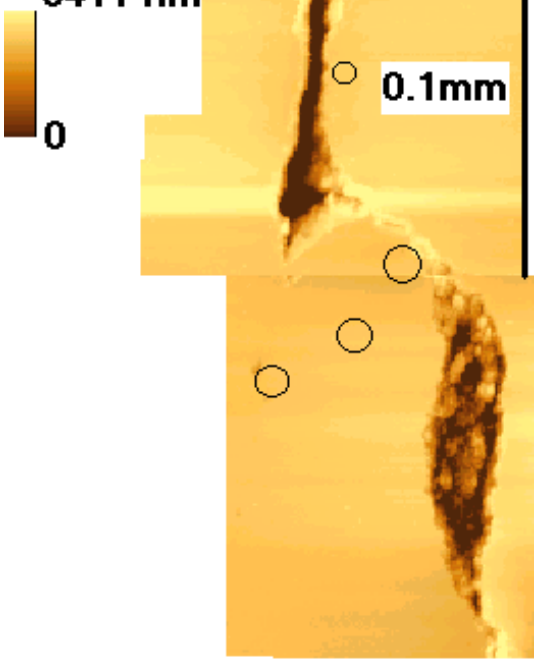

Figure 2: AFM image of the crack tip. One can observe a large cavity visibly related to the main crack. The circles indicate the location of small cavities which seem independant of the main crack.

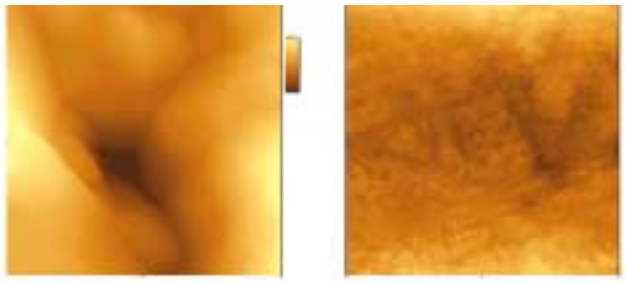

Figure 3: AFM image of a large (left, image size) and a small cavity (right 1.02μmx1.02μm, image size 2.5μmx2.5μm) at a comparable magnification, showing the difference in structure.

In each explored cavity 10 profiles containing 1000 points (corresponding to distances ranging from 1.13 to 10 micrometers) are registered in two directions (parallel and perpendicular to the direction of crack propagation). In each case, these profiles are analysed with two different methods - namely the Hurst method and the power spectrum method [20] - in order to determine the roughness exponent. For each cavity, an average of both the min-max difference $\Delta Z_{max}(r)$ and the power spectrum $P(q)$ is performed, with consistent results.

In both cases, contrary to what can be observed for their shape, large cavities appear to be isotropic, while small ones present an anisotropy between the parallel and perpendicular directions.

As an example, an average of the power spectrums of 10 parallel profiles and 10 perpendicular profiles are shown in Fig. 4 for one large cavity. The best fit is a power law with exponent 2.53, corresponding to a roughness index ζ equal to 0.77. This is consistent with the result of the Hurst analysis, for which a roughness exponent 0.79 is measured.

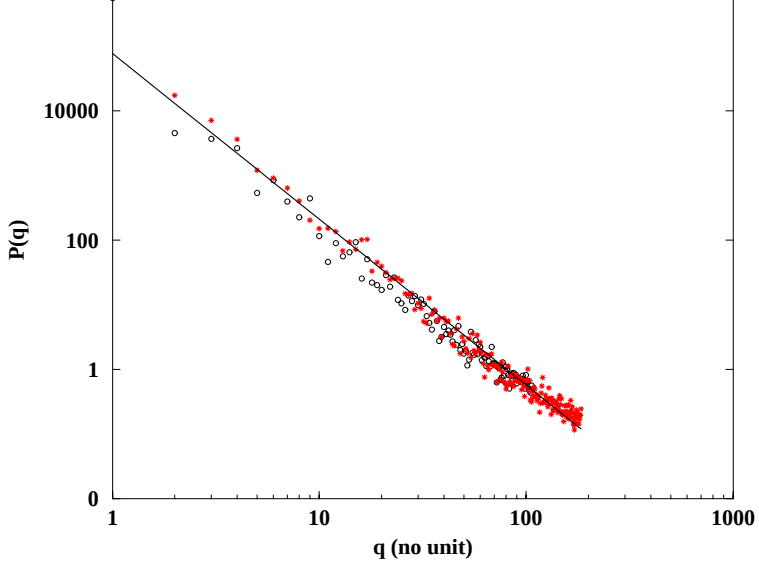

Figure 4: Average over the power spectra of 10 parallel (o) and 10 perpendicular ($\star$) profiles. The best fit is a power law with exponent -2.53 in both cases (solid line).

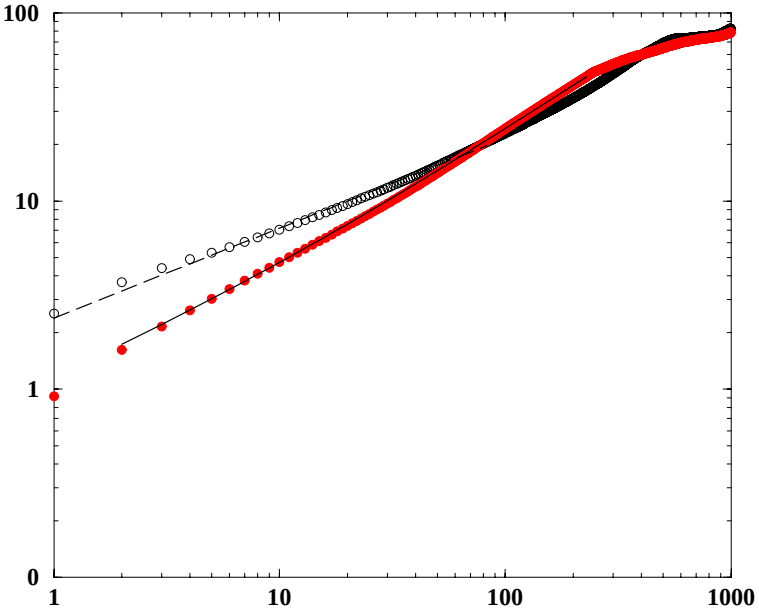

Figure 5: Average over the power spectra of 10 parallel ($\bullet$) and 10 perpendicular (o) profiles. The best fits correspond to one power law with exponent 0.48 (dashed line) in the case of perpendicular profiles and to a function corresponding to two asymptotic regimes (0.5 at small length scales, 0.78 at larger ones, with a crossover at 6 nm) in the case of parallel profiles (solid line).

The structure of small cavities is more complex, since they do not only exhibit the two regimes self-affine regimes (0.5 and 0.8), but are also anisotropic. Fig. 5 shows the evolution of $\Delta Z_{max}(r)$ for 10 parallel and 10 perpendicular profiles in the case of a small cavity in the AlCrZr alloy. For profiles parallel to the direction of crack propagation, one can see the two asymptotic regimes (roughness exponents 0.5 and 0.8), while along the perpendicular direction, only the 0.5 regime is present. This behaviour is reproduced in all the small cavities we observe, for the two planes of cut.

We have shown that “large” cavities, linked to the main crack are isotropic and reveal only, in the present case, the roughness index 0.8. On the contrary, “small” independent cavities have a more complex structure: they only exhibit the 0.5 regime in a direction perpendicular to crack propagation, and the two regimes in the direction of the main crack.

This supports the following scenario [21] for crack propagation: when cavities grow by themselves, their acquire a roughness characterized by a 0.5 exponent. The 0.8 exponent exhibitted at larger length scales is directly linked to the coalescence of such cavities.

The fact that the 0.8 exponent is also observed at larger length scales in small cavities may be the sign that these damage defects are the result of the coalescence of smaller cavities. This is true only in the direction of crack propagation, where coalescence is as a matter of fact more likely to occur. Note that this is not the case for the Molecular Dynamics simulations results however [15-17], where only the 0.5 exponent is observed. It might be due to the smaller sample sizes, and to the higher crack speeds (coalescence has no time to occur before the cavity joins the main crack).

At length scales smaller than a cavity size before coalescence, a crack front can perfectly be defined. In principle, line models [8-11] might be able to predict the 0.5 roughness in this case. However, an other hypothesis has been made elsewhere [22], suggesting that crack front waves [23-25] might be responsible for the roughening at these small length scales. This model leads as a matter of fact to a 1/2 roughness index independently of the microstructure, and to material-dependent length scales.

At larger length scales, one cannot define a crack front, because of the very existence of the assembly of damage cavities. These cavities, growing in mutual interaction under the action of a high stress triaxiality due to the presence of the main crack, are probably strongly correlated “geometrically”: the presence of a given cavity will favour or prevent the opening of an other one in a certain domain, and probably influence its growth rate. Our conjecture is that these correlations are at the origin of the non-trivial 0.8 exponent observed on various types of materials (see [2] and references therein). One has now to address the question of universality of this exponent, when damage correlations of different natures must be considered. The similarity of the crack growth mode and the differences in the scales at which this phenomenon occurs might however be a clue to understand universality in exponents and differences in relevant length scales [2].

It has been shown in the case of fracture surfaces that the crossover length decreases with the average crack velocity. In the new scenario imagined here, this crossover length is the size of cavities at coalescence, and cavities have more time to grow before coalescence if the average crack velocity is smaller.

One can also wonder why only the 0.8 exponent is seen in large cavities. This may be due to the intensity of the local stress field: cavities joining the main crack are very likely in zones of higher stresses than cavities which are not crossed by the crack. These cavities coalesce more rapidly than cavities located in regions of lower stresses, and hence, having less time to grow before coalescence takes place, reach a size ξ_c at coalescence which is significantly smaller, and might be unreachable at our scales of observation.

Finally, it has been shown elsewhere [13] that the self-affine correlation length, i.e. the upper bound of the scaling domain, is of the order of the grain size for metallic materials. Damage correlations are likely to disappear when there is a change in the crystalline orientation, and hence, we believe that this self-affine correlation length might as well be viewed as a damage correlation length.

One limitation of our study, however, concerns the direction of the observed profiles in cavities as compared to the direction of profiles observed on fracture surfaces. Cavities can be explored either in a direction parallel to crack growth or perpendicular to it, but they can only be studied within a plane containing the tensile direction (see Fig. 1). On the contrary, fracture profiles on post mortem specimens are both perpendicular to the direction of crack propagation and to the tensile axis. In other words, the roughness exponents measured on fracture surfaces are inaccessible as far as cavities are concerned.

However, the clear differences in morphology exhibitted by the independent cavities and the ones linked to the main crack strongly support the idea of two relevant processes, one being linked to the growth of isolated damage defects, and the other one to their coalescence.

1. B.B. Mandelbrot, D.E. Passoja, A.J. Paullay, Nature **308** 721 (1984).
2. E. Bouchaud, J. Phys./ Condens. Matter **9**, 4319 (1997).
3. P. Daguier, S. Hénaux, E. Bouchaud and F. Creuzet, Phys.Rev. E **53**, 5637 (1996).
4. P. Daguier, B. Nghiem, E. Bouchaud, F. Creuzet, Phys. Rev. Lett. **78**, 1062 (1997).
5. J. Schmittbuhl, S. Roux, J.-P. Vilotte, K. J. Maloy, Phys. Rev. Lett. **74**, 1787 (1995).
6. G. G. Batrouni, A. Hansen, Phys. Rev. Lett. **80**, 325 (1998).
7. V. I. Räisänen, E. T. Seppala, M. J. Alava, P. M. Duxburry, Phys. Rev. Lett. **80**, 329 (1998).
8. J.-P. Bouchaud, E. Bouchaud, G. Lapasset, J. Planès, Phys. Rev. Lett., **71**, 2240, (1993) ; E. Bouchaud, J.-P. Bouchaud, J. Planès, G. Lapasset, Fractals, **1**, 1051, (1993).
9. S. Ramanathan, D. Ertaş, D. S. Fisher, Phys. Rev. Lett. **79**, 873 (1997).
10. S. Ramanathan, D. S. Fisher, Phys. Rev. Lett. **79**, 877 (1997).
11. S. Ramanathan, D. S. Fisher, Phys. Rev. B **58**, 6026 (1998).
12. D. Ertaş, M. Kardar, Phys. Rev. Lett. **69**, 929 (1992); D. Ertaş, M. Kardar, Phys. Rev. E **48**, 1228 (1993).
13. E. Bouchaud,P. Daguier, M. Hinojosa, B. Nghiem, Bulletin Mecamat (1998).
14. E. Bouchaud, S. Navéos, J. Physique I **5**, 547 (1995).
15. A. Nakano, R. K. Kalia, P. Vashishta, Phys. Rev. Lett. **73** , 2336 (1994).
16. A. Nakano, R. K. Kalia, P. Vashishta, Phys. Rev. Lett. **75** , 3138 (1995).
17. P. Vashishta, R. Kalia, A. Nakano, Computing in Science and Engineering, p. 56, september/october (1999).
18. E. Bouchaud, L. Kubin, H. Octor, Metall. Trans. A, **22A**, 1021 (1991).
19. E. Bouchaud, H. Octor, T. Khan, Materials and Design **14**, 29 (1993).
20. J. Schmittbuhl, J.P. Vilotte, S. Roux, Phys. Rev. E **51**, 131 (1995).
21. E. Bouchaud, F. Paun, Computing in Science and Engineering, p. 32, september/october (1999).
22. E. Bouchaud, J.-P. Bouchaud, D. S. Fisher, S. Ramanathan, J. R. Rice, in preparation.
23. J. W. Morrissey, J. R. Rice, EOS Trans. Amer. Geophys. Un. **77**, F485 (1996).
24. J. W. Morrissey, J. R. Rice, J. Mech. Phys. Solids **46**, 467 (1998).
25. J. W. Morrissey, J. R. Rice, J. Mech. Phys. Solids **48**, 1229 (2000).
26. E. Bouchaud, G. Lapasset, J. Planès, Europhys. Lett. **13**, 73 (1990).
27. K. J. Maloy, A. Hansen, E.L. Hinrichsen, S. Roux, Phys. Rev. Lett. **68**, 213 (1992).

ICF100140OR

MULTI-SCALE FATIGUE OF AS-CAST LIGHTWEIGHT STRUCTURAL METALS

Ken Gall[1], Mark Horstemeyer[2], David L. McDowell[3], Jinghong Fan[3], and Nancy Yang[2]

[1]Department of Mechanical Engineering, University of Colorado, Boulder, CO, 80309 USA
[2]Materials & Engineering Sciences Center, Sandia National Laboratories, Livermore, CA 94550 USA
[3]GWW School of Mechanical Engineering, Georgia Institute of Technology, Atlanta, GA 30332 USA

ABSTRACT

We present an overview of a multiscale modeling approach whereby we examine basic mechanisms of fatigue deformation at length scales ranging from nanometers to millimeters, as necessary to treat hierarchical heterogeneous microstructural features in castings. A coordinated numerical and experimental effort is outlined that employs atomistic simulations, finite element modeling, electron microscopy, and mechanical testing. Atomistic and realistic micro-mechanical simulations of representative microstructural features are used to elucidate the role of different microstructural constituents such as Si particles, pores, and oxides on fatigue crack nucleation and growth. Ultimately, we demonstrate that fatigue life prediction methodologies can be developed that explicitly incorporate features of the cast microstructures.

KEYWORDS

Cast Al-Si, Defects, SEM, modeling, finite element, atomistic, fatigue life predictions.

INTRODUCTION

Current fuel consumption and cost demands in the automotive industry are facilitating the widespread use of lightweight cast materials for structural components. Although cast components have always enjoyed certain economic advantages compared to wrought materials, they are usually over-designed due to processing related variability within and between components. Most existing fatigue life prediction approaches have been primarily developed in the context of wrought materials, and they do not provide clear paths for optimal casting design. The present paper overviews a methodology developed to understand and predict the fatigue of cast materials over multiple length scales. The techniques are only summarized here, and interested readers should consult the papers referenced within for details. A similar approach was also employed to understand and predict the monotonic failure of cast Al-Si alloys [1].

FATIGUE MECHANISMS

Extensive Scanning Electron Microscope (SEM) observations of the fracture surfaces of fatigued cast A356 aluminum samples has been performed to characterize the critical mechanisms of fatigue crack nucleation and growth [2, 3]. Following Figure 1, fatigue cracks

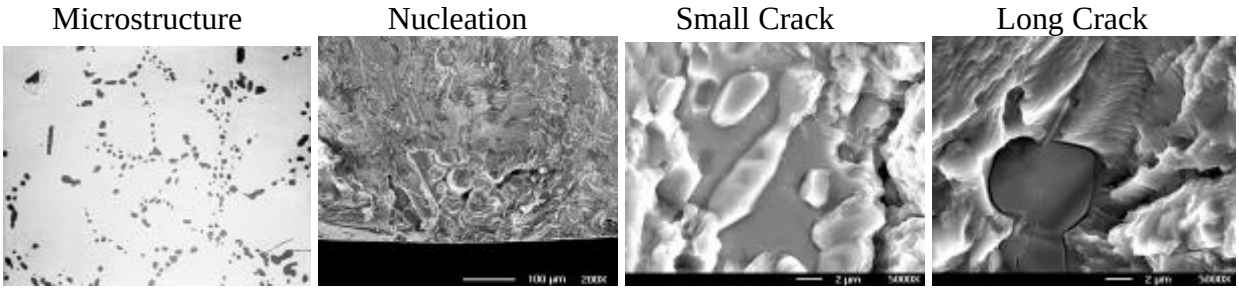

Figure 1: SEM images of the microstructure and progression of fatigue damage in cast Al-Si subjected to high cyclic fatigue loading conditions [2,3].

are found to preferentially nucleate at inhomogeneities such as voids or trapped oxide inclusions. Subsequent to nucleation, the cracks typically progress as microstructurally small cracks whereby the Si particles act as barriers and the cracks can only pass them by debonding (Figure 1). If the nucleation site is large enough, the crack may bypass the microstructurally short stage. On the other hand, longer cracks propagate through the Si particle laden microstructure via the fracture of large irregular particles (Figure 1). From SEM observations, it is clear that the Si particles can act as barriers or weak links to fatigue crack propagation, depending on the crack tip driving force [2, 3]. To develop a physically-based model, one must account for the critical roles of the Si particles, voids, and other inhomogeneties on fatigue crack nucleation and growth.

ATOMISTIC AND MICRO-MECHANICAL MODELING

Atomic level simulations [4] were used to ascertain the local strength of the Al-Si interface in the as-cast material since this quantity was not easily measured experimentally. Figure 2 is an image from a Modified Embedded Atom Method (MEAM) simulation showing the debonding of a composite aluminum and silicon block attached at a $[100]_{Al}||[100]_{Si}$

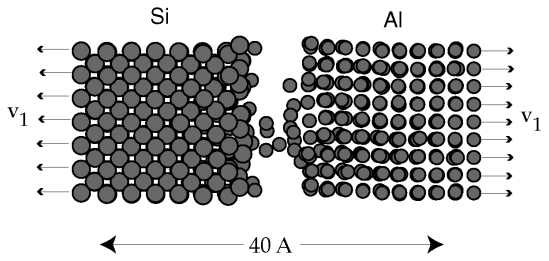

Figure 2: MEAM simulation on the debonding of an Al-Si interface [4].

interface, and subjected to far field velocities. The results of [4] demonstrated that the interface debonds at about 2/3 the stress before the bulk Al material fails. In the absence of vacancies, dislocations, impurities, and mechanical defects, the nucleation of interfacial fracture occurs at the atomic positions where the local displacement of interface atoms creates a rippled structure. Moreover, the debonding of the interface was found to behave nearly identical to continuum-based traction separation models. In terms of higher scale modeling, the atomic level

simulations provided knowledge on the relative strength of the interface compared to the bulk materials, and support for using traction-separation laws in micro-mechanical finite element simulations. Micro-mechanical finite element simulations were conducted to study the local plastic shear strains near voids and inclusions [5] and stress distributions near Si particle clusters [6]. Figure 3 is a representative example demonstrating local cyclic plasticity near a debonded inclusion [5]. The contour plot on the left in Figure 3 shows the development of local plastic

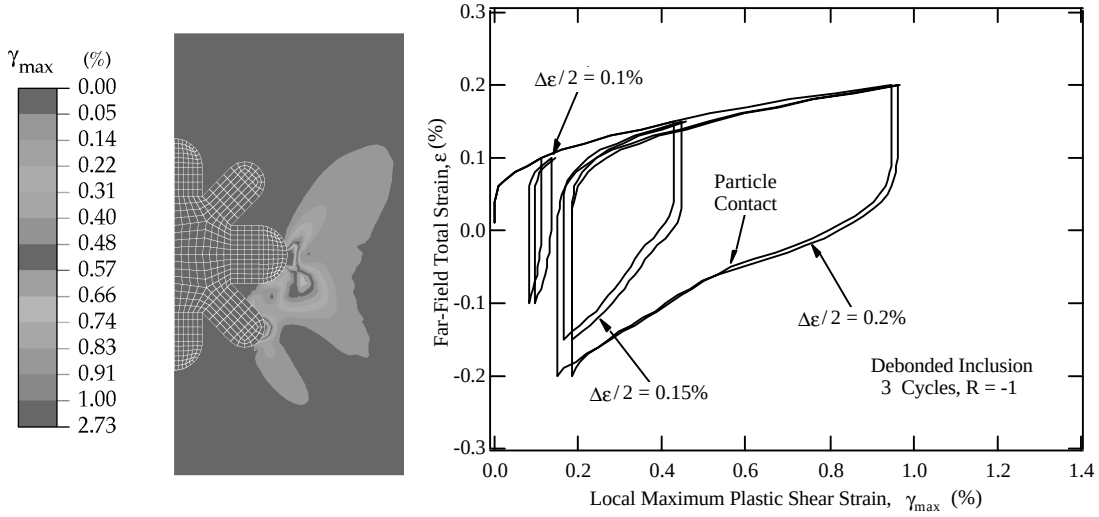

Figure 3: Local plastic shear strains near a debonded inclusion [5].

shear strains on the order of a few percent near a debonded star shaped inclusion under an applied far-field strain of 0.2 %. The plot on the right in Figure 3 shows the relationship between the far-field strain and the local maximum plastic shear strain, γ_{max}, averaged over a finite area [5]. Although the far-field strain is fully reversed (R = -1), the local plastic shear strain does not reverse itself. Furthermore, the local plastic shear strain range is as high a 1 % even when the far-field strain range is nominally elastic (0.2 %). The results in [5] quantified the plastic strain levels as a function of inhomogeneity type, shape, and size, and external factors such as R-ratio and applied far-field strain range. Debonded inclusions and voids were predicted to be the critical inhomogeneities for fatigue crack formation. Furthermore, for voids and debonded inclusions, shape has a negligible effect on fatigue crack formation compared to other significant effects such as inhomogeneity size and R ratio. Increasing the size of an inclusion by a factor of four increases $\Delta\gamma_{max}$ by about a factor of two. At low R ratios (-1) equivalent sized voids and debonded inclusions have comparable $\Delta\gamma_{max}$ values. At higher R ratios (0, 0.5) debonded inclusions have $\Delta\gamma_{max}$ values twice that of voids. Such results are critical for developing a mechanism and microstructure based fatigue crack nucleation model, as discussed later.

We also employed micro-mechanical finite element simulations to model the advancement of microstructurally small cracks in a Si particle laden microstructure [7]. The cracks were simulated to grow through the Al-rich matrix and through the silicon particles by successive particle-matrix interface debonding, commensurate with SEM observations. Figure 4 is an example result showing the fluctuation in the crack tip opening displacement as the crack approaches and grows around Si particles. The results show that as the crack approaches a particle, the maximum plastic shear strain range at the crack tip element decreases. However, as the crack impinges directly on the particle, the plastic shear strain range rapidly increases. The increase in the plastic shear strain range has been interpreted in terms of geometrically necessary

dislocations. The effects of initial crack length, applied strain amplitude, and crack closure on crack tip behavior show very strong effects of particles on the growth behavior of microstructurally small cracks. Although the crack opening displacement with a long initial crack length is much greater than a short one, once both cracks have engaged 2-3 silicon particles their difference is reduced and they follow a common retardation pattern. As the dendrite cell spacing increases, the crack closure period decreases. In the presence of particles, to a good approximation the crack is open only under tensile load.

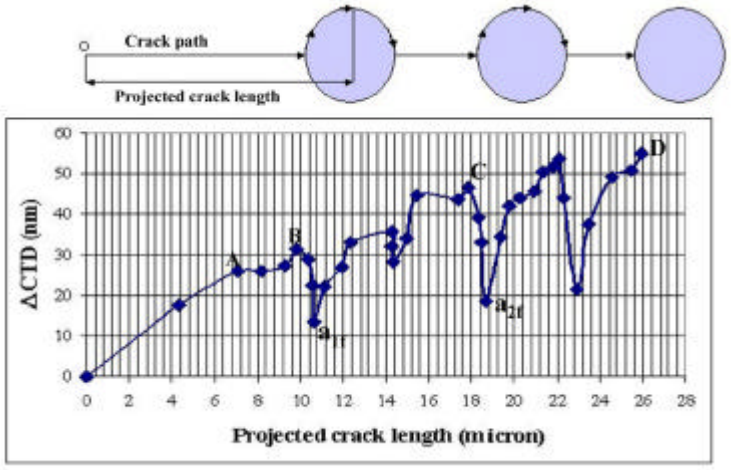

Figure 4: Finite element model of fatigue crack growth through a field of Si particles [7].

FATIGUE MODEL

Based on the foregoing computational results, along with experimental motivation from this study and other literature, a fatigue model was developed that is sensitive to the scale of initial inclusions and the dendrite cell size (DCS), e.g., Si particles and no significant pores or oxides, no large pores or oxides (length scale of < 3DCS), large pores within the bulk, large pores near the surface and large folded oxides. The fatigue life (for crack nucleation and growth up to about 1 mm, at which point the crack has transitioned to long crack status governed by ΔK_{eff} (LEFM), is governed by a set of relations that describes formation of cracks at micronotches such as gas pores or Si particles, followed by growth in the microstructurally sensitive regime characterized by a relatively small crack tip cyclic plastic zone and damage process zone compared to the mean Si particle size and spacing. The total fatigue lifetime is given by:

$$N_T = N_{inc} + N_{MSC} + N_{PSC} + N_{LC} = N_{inc} + N_{MSC/PSC} + N_{LC} \quad (1)$$

where N_{inc} is the number of cycles to incubation (nucleation plus small crack growth through the notch root influence) of a micronotch root scale crack with initial length, a_i, on the order of 1/2 the maximum Si particle diameter, $\hat{D}_{part}$, or pore size, $\hat{D}_p$. Here, N_{MSC} is the number of cycles required for propagation of a microstructurally small crack (MSC) with length $a_i < a < k$ DCS, where k is a non-dimensional factor that is typically in the range of 3-5. Further, N_{PSC} is the number of cycles required for propagation of a physically small crack (PSC) during the transition from microstructurally small crack status to that of a dominant, long crack which then propagates according to LEFM with an associated number of cycles N_{LC}. Since the DCS is typically on the order of 30 to 100 μm, depending upon the solidification rate, the PSC regime may conservatively extend up to 300-800 μm.

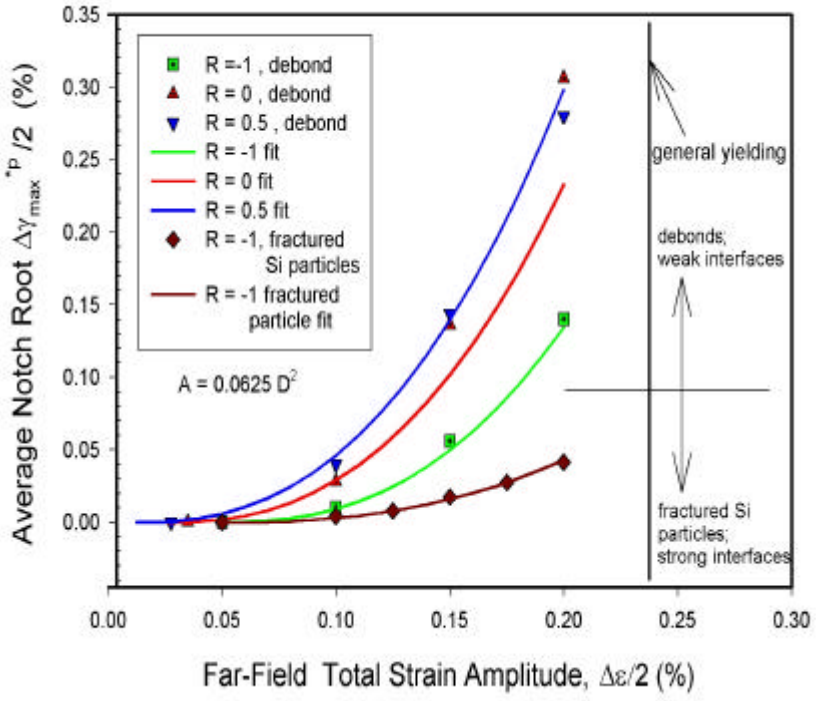

Figure 5: Relation between average notch root maximum plastic shear strain amplitude and applied total strain amplitude for micronotches (debonded or fractured Si particles or pores).

Using finite-element based transfer functions between remote applied strain and micronotch root strain, as shown in Figure 5, a local Coffin-Manson law is applied to determine the number of cycles required to form a crack and grow it outside the domain of influence of the notch root, N_{inc}. Then, using the MSC/PSC growth law

$$\left(\frac{da}{dN}\right)_{MSC/PSC} = G(\Delta CTD - \Delta CTD_{th}),$$
$$\Delta CTD = f(\bar{\varphi})C_{II}\left(\frac{DCS}{DCS_o}\right)\left[\frac{U\Delta\hat{\sigma}}{S_u}\right]^n a + C_I\left(\frac{DCS}{DCS_o}\right)(\Delta\gamma^p_{max}/2|_{macro})^2 \quad (2)$$

the MSC/PSC component of lifetime is computed, where $\bar{\varphi}$ is the average porosity, $U\Delta\hat{\sigma}$ is an effective normal stress range, and S_u is ultimate strength. DCS and DCS_o are the current and reference dendrite cell size and $\Delta\gamma^p_{max}$ is the maximum plastic shear strain range over all possible shear planes. The second term governs fully plastic growth of small cracks. It is found that the HCF-LCF transition occurs at the point of percolation of cyclic microplasticity through the interdendritic eutectic regions, and nucleation lifetime is negligible above this effective strain amplitude (0.23% at R = -1). The transition to long crack LEFM-governed behavior is defined by the point where the crack growth rate in Equation (2) crosses over the da/dN data based on long crack ΔK_{eff}. Effects of coalescence of multiple small cracks that nucleate at various inclusions (Si particles and pores) in the microstructure are important to address in the LCF regime and result in a crossover of fatigue resistance; low porosity is essential to superior HCF resistance, whilst large, widely spaced pores actually assist the LCF resistance. The scatter in fatigue data for cast A356-T6 alloy can essentially be fully

described by the typical range of microstructure inclusions that are present in laboratory specimens (see Figure 6 below).

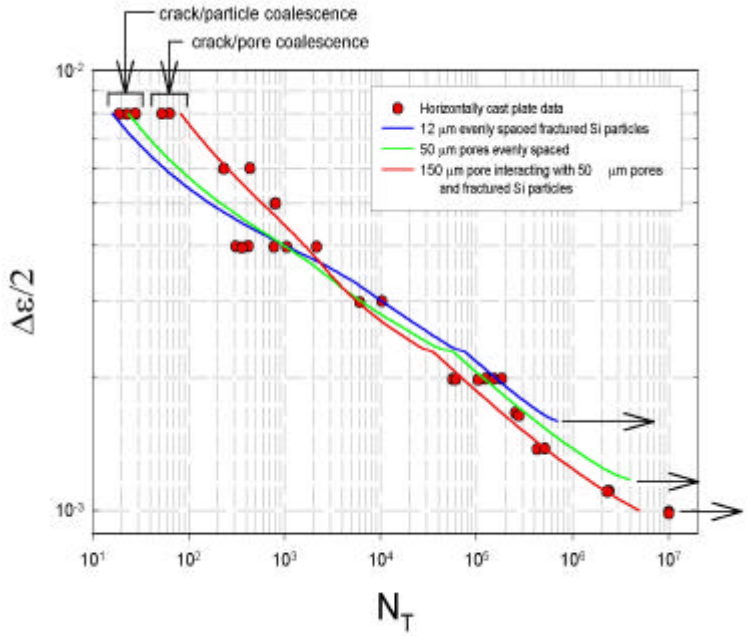

Figure 6: Variation in completely reversed, uniaxial strain-life behavior as a function of maximum inclusion size for horizontally cast plate, including LCF coalescence effects.

ACKNOWLEDGMENTS

This work has been sponsored by the U.S. Department of Energy, Sandia National Laboratories under contract DE-AC04-94AL85000. This work was performed under the leadership of Dick Osborne and Don Penrod for the USCAR Lightweight Metals Group. We would like to thank Gerry Shulke for providing the material and Westmoreland Mechanical Testing and Research for conducting the fatigue tests.

REFERENCES

[1] Gall, K. and Horstemeyer, M. F. (2000) *J. Eng. Mat. Tech.*. 122, 355.

[2] Gall, K. Yang, N., Horstemeyer, M. F., McDowell, D. L. and Fan, J. (1999) *Metall. Trans.*, 30A, 3079.

[3] Gall, K. Yang, N., Horstemeyer, M. F., McDowell, D. L. and Fan, J. (2000) *Fat. Frac. Eng. Mat. Struc*, 23, 159.

[4] Gall, K., Horstemeyer, M. F., Baskes, M. I., and Van Schilfgaarde, M. (2000) *J. Mech. Phys. Solids*, 48, 2183.

[5] Gall, K., Horstemeyer, M. F., McDowell, D. L., and Fan, J (2001) In Press *Int. J. Frac.*

[6] Gall, K., Horstemeyer, M. F., McDowell, D. L., and Fan, J (2000) *Mech. Mat.* 32, 277.

[7] Fan, J., McDowell, D. L., Horstemeyer, D. L., Gall, K., (2001) Submitted *Eng. Frac. Mech.*

ORAL/POSTER REFERENCE: ICF100399PR

MULTI-PASS WELDING SIMULATION OF TIG WELDED AISI 316LN

C.H.L.J. ten Horn[1], G.W. Medendorp[1], J. Zuidema[1], A. Bakker[1], P.G. de Heij[2], D. d'Hulst[2]

[1] Materials Science, Delft University of Technology, Rotterdamseweg 137, 2628 AL Delft, The Netherlands
[2]NRG Petten, PO Box 25, 1755 ZG Petten, The Netherlands

ABSTRACT

Residual stresses may have considerable effects on the behaviour of a welded structure. However, these stresses are difficult to measure on site, therefore a numerical tool may provide a suitable means to predict these residual stresses. When dealing with multi-pass welds, numerical procedures found in literature suggest that the user must change the mesh after each weld pass. In doing so, the prediction of the residual stresses becomes quite labour intensive. Therefore, a new approach for the prediction of residual stresses due to multi-pass welding is desirable. In this new approach the plate and the filler material of all the weld passes are present from the start of the analysis. The plate and filler material is modelled using contact bodies. In the thermal analysis the bodies can be (de)activated. The results from the thermal analysis are used for the mechanical analysis, i.e. an uncoupled analysis is performed. At temperatures above the melting point, sliding of the contact bodies is allowed while below the melting point the bodies are effectively glued to their surroundings. For comparison with the thermal analysis, experiments were performed to measure the temperatures in an AISI 316 LN stainless steel plate during the Tungsten Inert Gas (TIG) welding process. The temperatures obtained from the calculations are too high and cooling of the plate is too fast, in comparison with the measurements. The deformation and the residual stresses obtained by the mechanical analysis are found to be too small. However, the approach used here to model a multi-pass weld process can be used with minor adjustments.

KEYWORDS

Welding, numerical simulation, residual stress, AISI 316 LN

INTRODUCTION

When working with welded structures, the residual stresses are a force to be reckoned with. However, these stresses are hard to measure on site, therefore a numerical tool may provide a suitable means to predict these residual stresses. Following the procedures found in literature, the user has to change the mesh after each weld pass, which makes it quite labour intensive. Therefore, a new approach is needed. The new procedure described here allows the use of one finite element mesh and one calculation run for the entire multi-pass weld, thereby making it less labour intensive. The commercial finite element program MARC was used.
For the validation of the numerical results, experiments were performed. A 10mm thick AISI 316 LN plate with a U-butt groove was clamped on a rigid platform to restrain the movement during welding. The groove

was filled using 9 TIG weld passes with filler material SMA 16-8-2 SP. During the welding experiment, the temperature of the plate was monitored at several places.

EXPERIMENTS

An automated welding experiment was carried out to obtain the temperature fields caused by the TIG welding process in a 120x90x10-mm AISI 316LN stainless steel plate. These temperature fields were used to verify the calculations. During the welding process the plate was clamped on an aluminium platform for extra cooling and to restrain the movement of the plate. Figure 1 shows a schematic illustration of the clamp, the stainless steel plate and their dimensions. Prior to the welding, the stainless steel plate was annealed in order to ensure a stress-free initial condition for the residual stress measurements to be performed later.

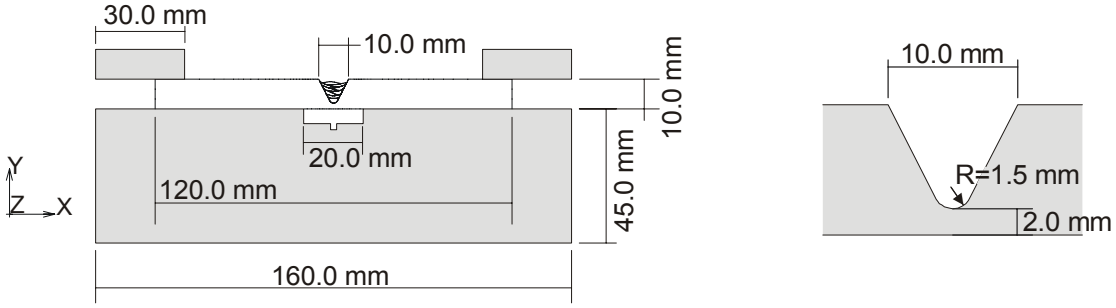

Figure 1: Schematic illustration of the clamp, the plate (a.) and the weld groove and their dimensions.

Ten thermocouples (Chromel-Alumel with an Inconel mantle) were placed on the bottom side of the plate to measure the temperatures. The placement was such that the distance to the weld centre line was 0, 2, 4, 6, 16 and 24 mm.

FINITE ELEMENT MODEL

Argyris [1] has shown that mechanical generated heat has a marginal influence on the temperature field during the welding process. He concluded that the temperature field and the mechanical field during the welding process could be calculated in two separate analyses. First a transient thermal analysis was performed, in which the temperature history of the stainless steel plate was computed. Secondly, a transient thermo-elastic-plastic analysis is performed to compute transient and residual stresses and strains using the results of the thermal analysis.
The filler material of the different weld passes are modelled as individual contact bodies. For the thermal analysis these bodies are linked to each other to obtain the thermal interaction, while utilising the contact bodies during the mechanical analysis.
The final mesh consists of 11 contact bodies, containing 2320 isoparametric, arbitrary quadrilateral generalised plane strain elements, with 4 integration points, and 2717 nodes.

The Thermal Analysis

The temperature distribution during the welding process is a result of the heat input of the welding arc, conduction of heat through the material, surface heat losses and the thermal properties of the material.
The amount of heat supplied to the stainless steel plate by the welding arc can be expressed as:

$$Q = \eta_a UI \tag{1}$$

where Q is the energy of the welding arc, U is the arc voltage, I is the arc current and η_a is the arc efficiency. The arc efficiency is taken to be 90%.
Part of the heat of the welding arc is used to melt the filler material while the remainder of the heat is introduced to the plate as a spatially distributed surface heat flux (figure 2), which shape is determined by equation (2):

$$q(x,t) = \frac{\eta_a Q}{v} \cdot \frac{C}{0.95 \cdot \sigma \cdot \sqrt{2\pi}} \cdot e^{\frac{-(x-m)^2}{2\sigma^2}} \cdot e^{\frac{-v\cdot(\tau-t)^2}{a^2}} \quad (2)$$

where v is the travel velocity of the torch, x is the distance from the weld centre, m is the position of the centre of the weld in relation to the centre of the groove, t is the time, τ is the time at which the torch centre enters the analysis plane, C, a and σ are constants.

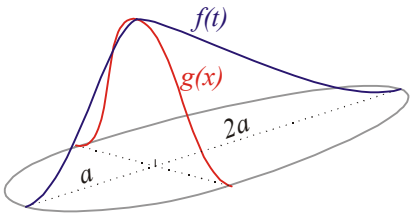

Figure 2: Illustration of the distribution functions for the surface heat flux.

Heat losses from the surface of the plate are modelled using Fourier's law of heat transfer. The heat transfer coefficient for convection was modified to account for the losses of heat due to radiation.

The filler material in the thermal analysis

The deposition of filler material is simulated using the DEACTIVATE/ACTIVATE procedure of MARC [2]. With this procedure it is possible to turn elements on and off to effectively remove material from or add material to the model.

The body representing the filler material of one weld is divided into six rows all being deactivated at the beginning of the analysis. During the analysis, one by one the rows are activated again, simulating the deposition of the filler material. Once a row is activated, the surface heat flux is repositioned so that the surface heat flux always works on top of the activated elements.

The filler material is added hot to the model. The thermal properties of the stainless steel plate and the filler material are assumed to be the same and are temperature dependent, see figure 3. As the temperatures in the aluminium clamp will not be very high, the thermal properties are taken as constants.

To account for the convective heat transfer in the weld pool, the thermal conductivity of the material above melting point is increased. The latent heat used in the analyses is 330 kJ/kg, the solidus temperature is taken as 1400 °C and the liquidus temperature is 1459 °C.

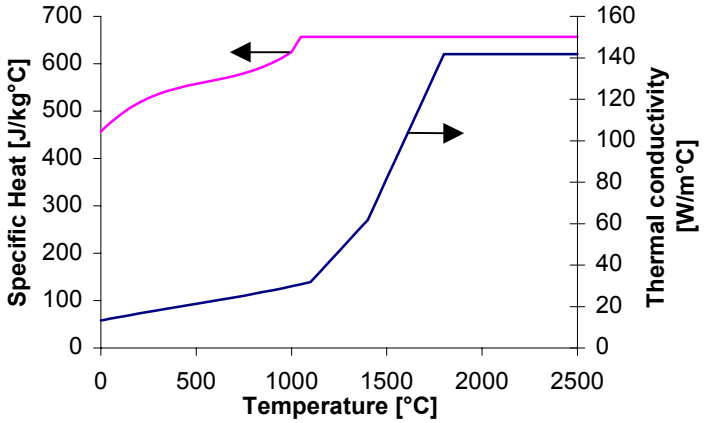

Figure 3: Temperature dependent thermal conductivity and specific heat of the stainless steel.

The mechanical analysis

Rate-independent elastic-plastic equations included with the thermal strain effects are used for the mechanical model. Creep strains are neglected, given that the time period at which the plate is at high temperatures is very short. The von Mises yield criterion is used with the kinematic hardening rule to model

the Bauschinger effect and reverse plasticity, which by many researchers is believed to take place during the welding process [3].

The filler material in the mechanical analysis
For the mechanical analysis it is not possible to use the DEACTIVATE/ACTIVATE options to simulate the deposition of the filler material as it would result in unrealistic deformations and severe numerical problems. In this study, the contact analysis option in MARC is used. During the analysis, the contact bodies cannot separate from each other as this would create cavities. Once a body is above melting temperature, the body is allowed to slide with no friction over its surrounding contact bodies. At temperatures below melting point, no sliding is allowed and the body is effectively glued to its surroundings.
The elements representing the part of the plate between the clamping parts of the aluminium platform are rigidly tied to the clamp. The rest of the plate is allowed to separate from the clamp. Between the plate and the clamp, the friction coefficient is taken to be 0.25 [4].
The mechanical properties of the stainless steel plate and filler material are also taken temperature dependent [5]. While the properties of the aluminium clamp are again taken as constants. Furthermore, the clamp is modelled as a linear elastic material. The temperature dependent Young's modulus, yield stress, linear thermal expansion coefficient and the Poisson's ratio of the stainless steel used for the computations are shown in figure 4. The Young's modulus above melting point is taken to be constant. The value corresponds to the value of the Young's modulus just before melting. To avoid numerical problems the Poisson's ratio may not become 0.5 and the yield stresses at high temperatures must have low, but non-zero, values.

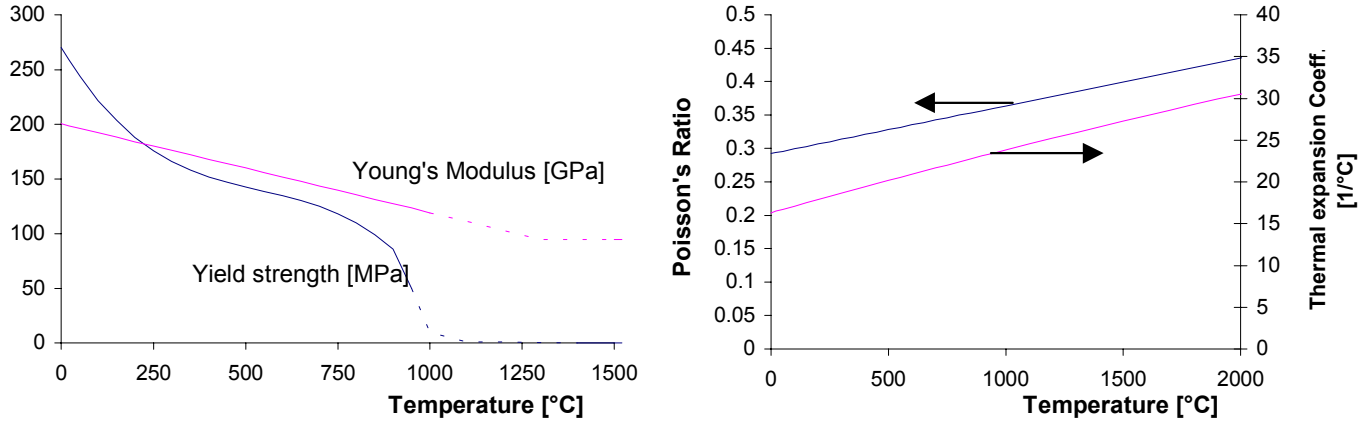

a. b.

Figure 4: Temperature dependent yield stress, Young's modulus, thermal expansion and Poisson's ratio [5].

In reality the plastic strains are relieved when the stainless steel is at a sufficiently high temperature. The presence of nonzero material properties above melting temperature would cause the plastic strains not only to continue accumulating but also to reach artificially high values owing to the very low magnitude of the mechanical properties at these temperatures. Therefore a total relief of stresses and plastic strain is used during the mechanical analyses when the material is above 1150 °C. This is achieved using of the user subroutine UACTIVE. The temperature of 1150 °C is chosen, since this is approximately the temperature at which stress free annealing takes place in seconds.

RESULTS

Thermal analysis
The temperature history for the first weld pass can be seen in figure 5. It shows both the experimentally measured (5a) and the calculated (5b) temperature histories for 4 thermocouples located at 0, 2, 4 and 6 mm respectively from the weld centre.

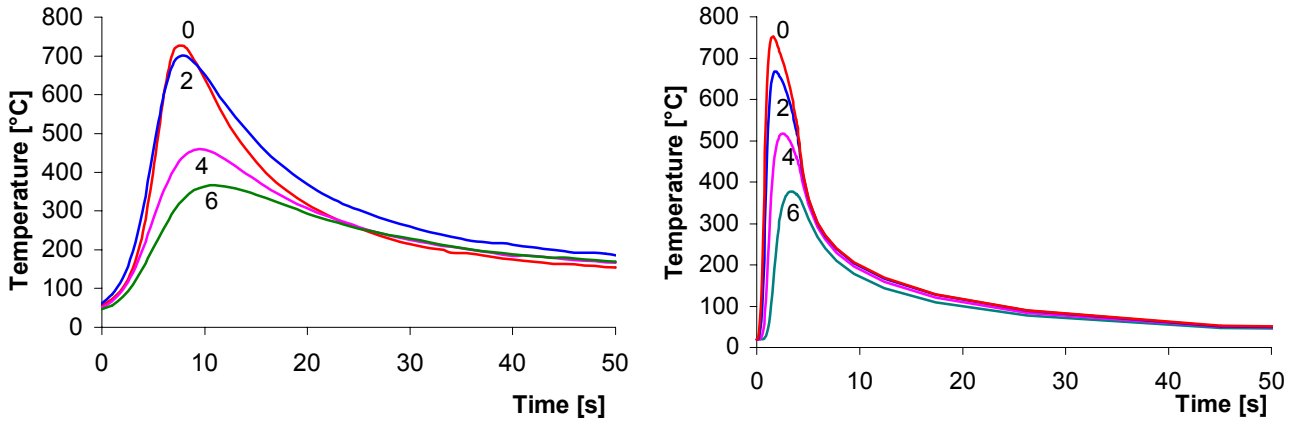

Figure 5: The measured (a.) and the calculated (b.) temperature history for the first weld at 0, 2, 4 and 6 mm from the weld centre line.

The computed temperatures rise and fall too fast in comparison with the measured values. This is most likely caused by a too steep distribution function used for the surface heat flux. The calculated cooling rate that is observed after the weld pass has been completed, is also too high, this is probably caused by a too high convective heat transfer coefficient. Figure 6 shows both the measured and the calculated peak temperatures for two thermocouples. It can be seen that the first weld pass is accurately calculated while for the other weld passes the peak temperatures are too high. Given that the peaks are to high for all thermocouples and that the cooling is too fast, it is most likely that the area of the surface heat flux is too small. The efficiency of the arc is assumed to be 90 %, which is most likely to be too high for the TIG welding process.
From the calculations it followed that re-melting of part of the previous welds and the plate occurred.

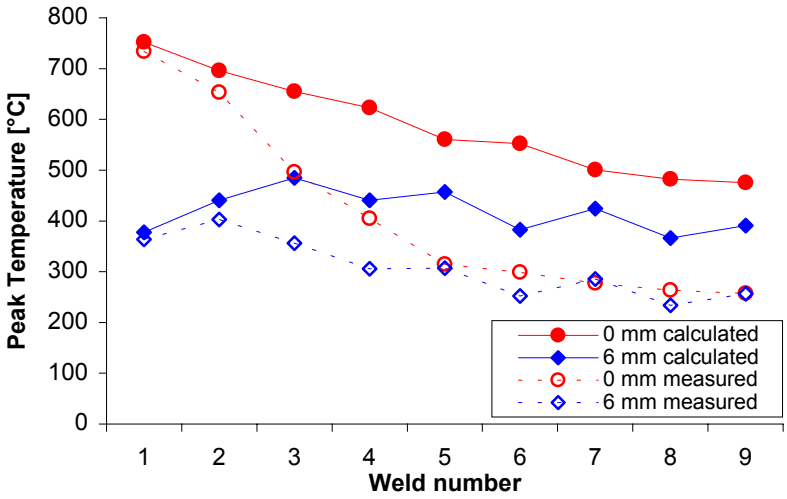

Figure 6: Peak temperatures for the different weld passes for two thermocouples.

Mechanical analysis
The stresses that are present in the plate after completion of the 9 weld passes, can be seen in figures 7a and 7b. The figures show the stresses along the bottom side of the plate before and after the release of the clamp. It is clear that the clamp mainly restrains the plate in the direction perpendicular to the weld (σ_{xx}).
These figures also show that the stresses directly under the weld are approximately 200 MPa, whereas the stresses further from the weld are quite low, approximately 40 MPa.
Figure 8 shows the undeformed plate and the deformed plate after the welding has been completed and the clamp has been released. The majority of the deformation of the plate is located directly underneath the weld zone. This localisation was also seen in the thermal analysis and the residual stresses and may be due to the poor thermal conductivity of the stainless steel. But two other effects may play a role. Firstly, it is believed that the low stresses may also be due to a too low temperature for stress relieve; most stresses generated by

previous welds disappear due to the next welding pass. And secondly, the manner of clamping the plate as implemented in the model is probably too rigid.

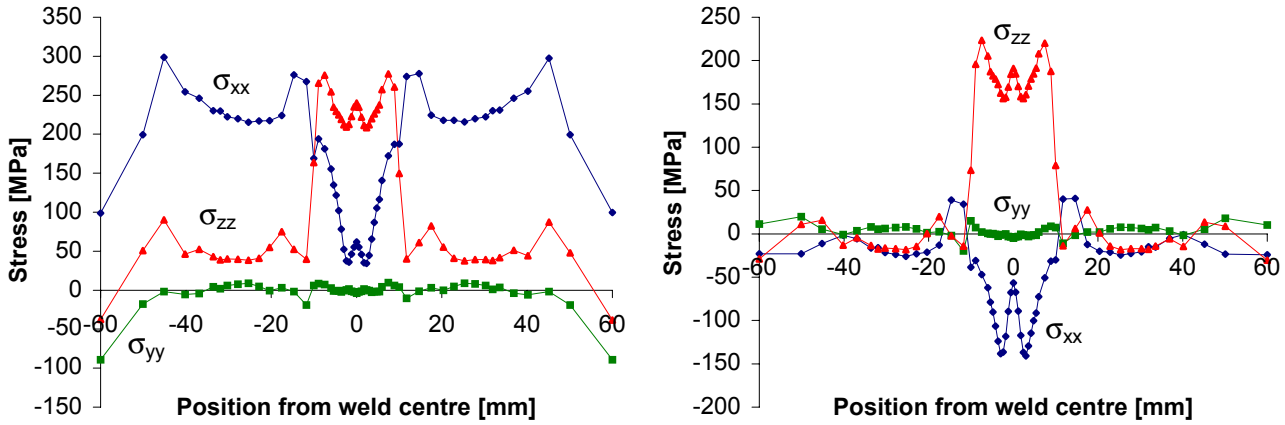

Figure 7: Stresses along the backside of the plate before (a.) and after (b.) release from the clamp.

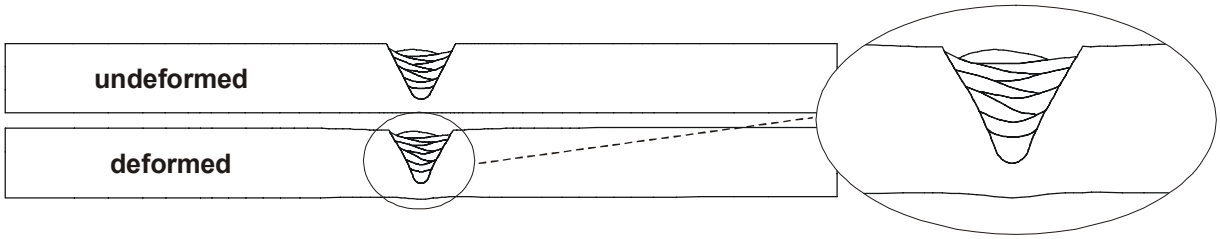

Figure 8: The undeformed plate and the deformed plate after release from the clamp.

Another result from the mechanical analysis is the distortion of the temperature field and temperature jumps of up to 200 °C were present in the deformation of the plate. These temperature jumps are caused by the displacements of the bodies that were not taken into account in the thermal analysis.

CONCLUSION

From the results of the thermal analyses it can be concluded that the distribution function is increasing to fast and the heat transfer coefficient for convection is too high.
A part of the material of the plate and the previous weld are (re)melted upon subsequent weld passes. The results from the mechanical analysis indicate that the deformation of the plate from the experiment is bigger than the computed deformations. This may be due to fact that the temperature at which strains are relieved is too low and that the clamping of the plate is not modelled correctly.
Due to body movement discrepancies occur in the temperature distribution. The use of contact bodies eliminates the need for mesh rezoning during the analyses of a multi-pass welding process. The method of using different bodies to model the filler material during multi-pass welding is promising. Using a coupled model, in which temperatures and deformations are computed at the same time, can solve the problem with the mismatch in temperature that occurs in the mechanical analysis.

REFERENCES

1. J.H. Argyris (1982), *Computer methods in applied mechanics and engineering* 33, 635.
2. MSC.Marc2000 Manuals, (2000) MSC.Software Corp.
3. S.B. Brown et al. (1981), *Welding Journal* 103, 66.
4. ASM Handbook, *Vol. 18 - Friction, Lubrication and Wear Technology*, 72.
5. ITER Materials Properties Handbook.

ICF100873OR

NANO-INDENTATION FRACTURE OF FUSED SILICA AND GLASSY CARBON WITH A CORNER CUBE AND 45° APICAL ANGLE INDENTERS.

J.S. Field[1], R. Dukino[2], N. Iwashita[1,3] and M.V. Swain[1].

[1]Biomaterials Science Research Unit, University of Sydney, Sydney Australia,
[2]BHP Research, Shortland, NSW Australia.
[3]Osaka National Research Institute, AIST, Japan

ABSTRACT:

Nano-indentation with sharp pyramidal indenters provides the ability to measure the elastic, plastic and fracture toughness properties of small volumes of material. In this study we investigate the ability to determine the fracture toughness of fused silica and a glassy carbon material, two isotropic amorphous materials. The behaviour of these materials subjected to 45º and 35.3º apical angle triangular pyramidal indenters is compared. Of particular importance is the difference in the force-displacement behaviour of these two indenters with a definitive discontinuity with the corner cube indenter. This behaviour is examined in an attempt to better understand the fracture response about the indenters. Two approaches are compared to analyse the toughness of the materials. A previous relationship with apical angle dependence is found to fir the data.

KEYWORDS

Indentation fracture, Nano-indentation, Fracture toughness, Silica, Glassy carbon,

INTRODUCTION

The use of pointed indenters to quantify the fracture toughness of brittle materials has a relatively recent history. Prior to which cracking about impressions was seen as an impediment to reliable hardness measurement. Most of the pioneering work in this field used Vickers indenters to generate the median/radial crack system about the impression from which the fracture toughness, K_c, was estimated from an expression of the form;

$$K_c = \Psi P/c^{3/2}, \qquad (1)$$

where P is the indentation load, c is the radial crack size and Ψ a constant related to the modulus to hardness ratio and an empirical constant [1]. There has been considerable discussion on the precise form of the constant Ψ as the remaining terms are precisely as expected for a center loaded penny shaped crack.

The initial work by Lawn and Swain [2] of direct optical observation of the cracking during loading and unloading of glass with Vickers indenters showed that initially a median crack formed beneath the indenter and that upon unloading radial cracks developed because of the residual stresses about the plastic impression. A critical review by Cook and Pharr [3], who also observed cracking about indentations in a wide range of

transparent glasses and single crystals, suggested that in most instances the radial cracks formed upon loading. Dukino and Swain [4] compared the influence of indenter geometry, namely Vickers and Berkovich, on the extent of cracking for a number of materials. They found that the cracks were somewhat longer with the Berkovich indenter and this was expected on the basis of fracture mechanics for a center loaded star crack. More recently Harding et al [5] have pioneered the use of nano-indentation with sharper corner cube indenters to generate cracks at much lower loads typically less than 20 mN. This development enables in principle the determination of the complete elastic-plastic-fracture properties of very small volumes of materials. The aim of this current study is to compare the deformation and fracture behaviour of two sharp indenters (corner cube and 45 apical angle) on two isotropic materials namely fused silica and a glassy carbon.

EXPERIMENTAL PROCEDURE

The materials used in this study were fused silica and a glassy carbon. The properties of these materials are listed below and were highly polished with a surface finish of < 2nm.

Indentation tests were conducted with an UMIS (Ultra micro-indentation system, CSIRO Australia). The indenter tips were of diamond and apical angles of 65.3˚ (Berkovich), 45˚ and 35.3˚ (corner cube). Indentation tests were made from 50-1000mN.

Table 1. Properties of Materials

Material	Fused Silica	Glassy Carbon
Elastic modulus	70 GPa	30 GPa
Fracture toughness, K_{1c}	0.8 MPa.m$^{1/2}$	1.15 MPa.m$^{1/2}$

RESULTS AND DISCUSSION

Typical force-displacement data generated with the indenters on the two materials of interest are shown in Figures 1 and 2. A noticeable feature of the results for the corner cube indenter was the discontinuity in the loading portion of the force-displacement curve for both materials. In both instances there were differences in the critical load to initiate this “pop-in” event but upon initiation the curves superimposed for the remainder of the loading and unloading portions. It was also observed that the extent of the “pop-in” was greater the higher the load for the initiation of this event. The load for the onset of this discontinuity was also found to vary with the sharpness of the indenter tip. Another significant feature is the difference in the extent of the residual impression with the sharper indenters for both materials. It is also apparent that the recovery was significantly greater for the glassy carbon materials than the fused silica and decreased with sharpness of the indenter tip.

Observations of the residual impressions following indentation revealed that radial cracks always formed about the indentations in the fused silica over the load range investigated for both indenters. Whereas for the glassy carbon cracks only formed about the corner

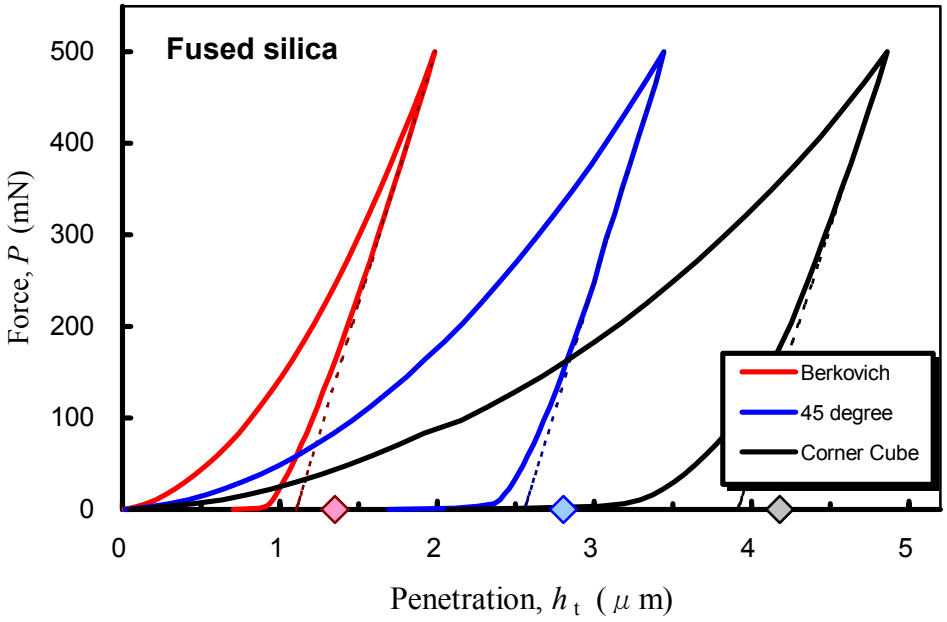

Figure 1. Force-displacement data with, Berkovich, 45˚ and corner cube indenters with fused silica, note the "pop-in" discontinuity with the latter.

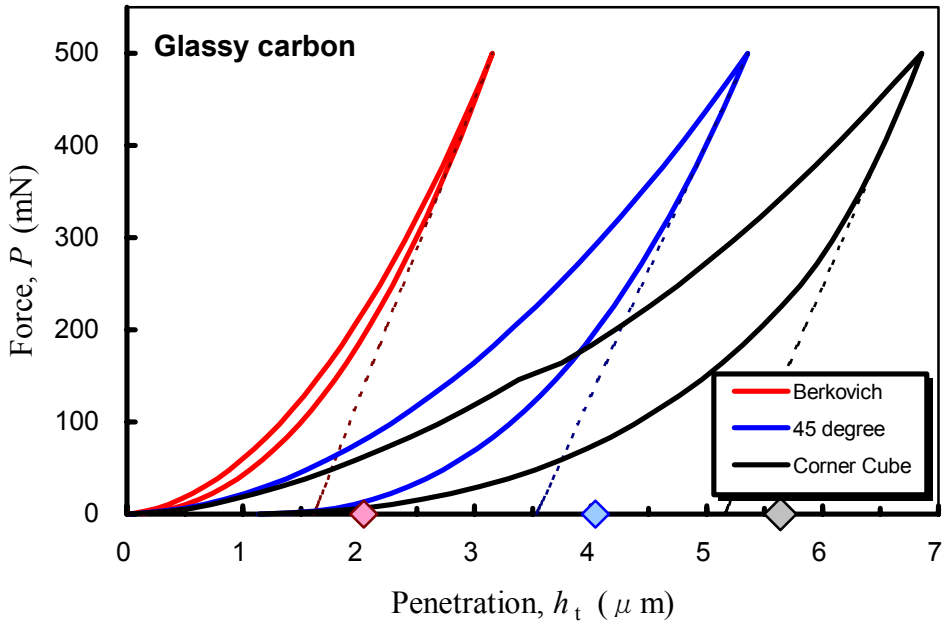

Figure 2. Force-displacement data for a glassy carbon material; comparing, Berkovich, 45 and corner cube indenters.

cube indenter and they were much more defined at loads in excess of the "pop-in" load. The radial cracks lengths were measured and the results plotted in the form expected from equation (1), that is, P versus $c^{3/2}$ and are shown in Figure 3. There is no significant difference in the case of the fused silica for radial crack lengths measured with and

without the "pop-in" discontinuity. In the case of the glassy carbon the crack lengths were far more difficult to measure irrespective of whether optical or scanning electron microscopic facilities were used.

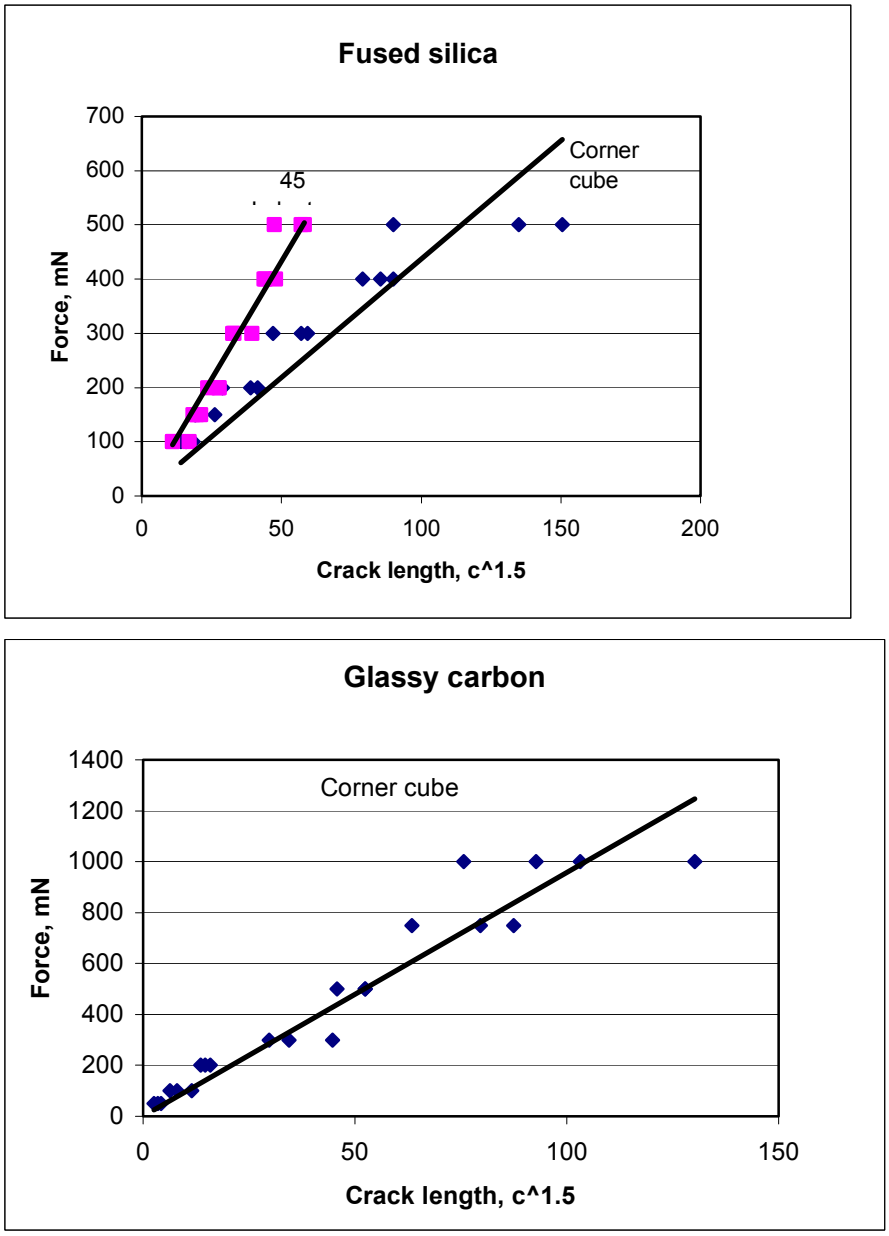

Figure 3. Crack length versus indenter load for the corner cube and 45º indenters.

The observations in Figure 3 show the equation (1) is appropriate but that the slope is dependent upon the indenter angle in the case of the fused silica. Lawn et al [2] in their initial derivation of the above relationship did include an angular dependence of the constant Ψ, namely, $\Psi = \gamma\ (E/H)^{1/2}\ (\tan\theta)^{2/3}$, where θ is the apical angle and γ is a constant. The present observations with the fused silica strongly support this relationship. Using the K_c for fused silica of 0.8 MPa$\sqrt{m}$ leads to a value of γ of 0.023. Using this relationship the toughness of the glassy carbon is 1.1 MPa$\sqrt{m}$, in agreement with conventional single edge notch bend test (SENB) measurements in Table 1

A major motivation of this work was to understand the behaviour of the materials and also to relate this to the fracture about the indentation. It is well established [6] that the loading curve of a pointed indenter may be described by an expression of the form $P = kh^2$. However for all of the present data a polynomial of the form, $P = kh^2 + bh + c$, was consistently found to be a better fit for all indenters and both materials, provided the load was below the pop-in value for the corner cube indenter. A detailed consideration of why this is a better approach is given elsewhere [7], but relates to the non-perfect form of the indenter tip. The unloading response could be modeled on the basis of an elastic unloading from a residual plastic impression, or elastic reloading of a preformed (pyramidal) conical impression and leads to an expression of the form, $P = (2/\pi)E'h_e^2 \tan\beta$, where E' is the biaxial modulus, h_e the elastic displacement and β is the effective apical angle of the difference between the residual impression and the indenter (conical equivalent) angle. Below the "pop-in" load for the corner cube indenter the fit of such expressions are excellent and the recovered values of hardness and elastic modulus are in good agreement with literature values although we do find that the hardness does increase with sharper indenters. The situation is slightly more complex with the glassy carbon as this material exhibits reversible or hysteretic deformation. For loads above the "pop-in" the above approach is still found to be an excellent fit to the unload portion of the force-displacement data provided the additional depth due to the "pop-in" event is removed. The alternative approach to interpret the data for the fused silica and glassy carbon is to use the classical Oliver and Pharr [8] analysis of a pointed indenter whereby the elastic modulus and hardness can be estimated from the slope of the initial unloading curve, as shown in Figs. 1 and 2. A comparison of the estimates of the hardness and modulus from the two approaches indicated that at loads prior to "pop-in" the values were very similar but decreased slightly at loads above "pop-in".

Comparison of the fused silica and glassy carbon show that for the 45º indenter radial cracks only form with the fused silica which does exhibit a classical "plastic" residual impression and would be expected to also generate residual stresses which would drive the radial cracks to an equilibrium size. In the case of the glassy carbon the near complete recovery of the impression upon unloading would minimize the magnitude of any residual stresses and hence the likelihood for radial crack development. For the corner cube indenter the sharper indenter angle does generate a greater residual impression for both materials and hence a greater residual stress thereby assisting with the extension of the radial cracks. It is unclear whether radial cracks are present during loading with the 45º indenter in fused silica. At "pop-in" we suggest that a radial-median crack or three, quarter penny, cracks are initiated and thereafter with increasing load are wedged further open. The consequence of such a situation is that crack mouth opening displacement develops along the indenter diagonal and hence the "effective" contact bearing area is reduced and also the indenter tip is able to penetrate within the opening median cracks.

The extent of "pop-in" displacement, that is extra displacement from the simple quadratic expression for the initial loading curve, with the corner cube indenter for both the glassy carbon and fused silica scales directly with the radial crack size and indentation load above the "pop-in" threshold, Figure 4. Another noticeable feature is the energetics of the indentation. There are two components; the irreversible work expended with permanent deformation and the reversible elastic strain energy. A comparison of the energy increment per unit volume of displaced material (Δv) ($W_p = p\Delta v$, with p the contact pressure) is shown for a corner cube indentation of fused silica in Figure 5. The results are compared with a model corner cube indentation without "pop-in". Both show

that initially the curves asymptote to a value of ~9 GPa and only at the onset of "pop-in" does the value jump to ~10 GPa. Other results for the 45º indenter asymptote to 9 GPa.

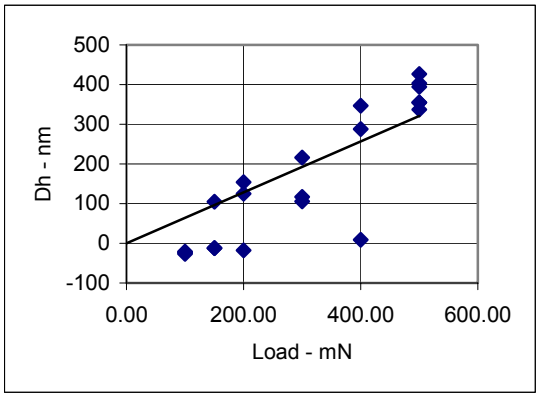

Figure 4. "Pop-in" depth versus indenter load for fused silica with corner cube indenter.

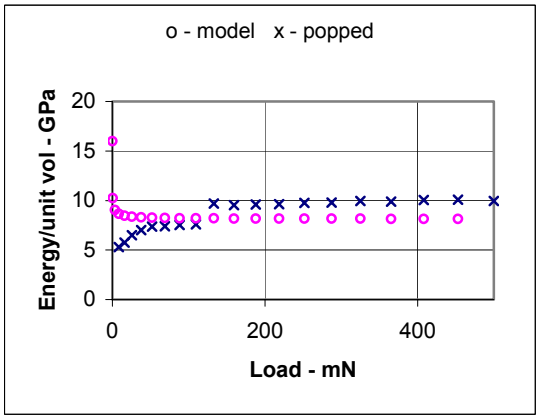

Figure 5. Change in energy per unit volume of fused silica with corner cube indenter and compared with model.

CONCLUSIONS

The present observations support the approach developed by Harding et al [5] to determine the fracture toughness of brittle materials using a corner cube indenter. There are a number of specific conclusions we can make:

1. Comparison of the determined fracture toughness using both the corner cube and 45º apical angle indenters suggests that there is an indenter angular dependence which is of the form predicted by Lawn et al [1], namely
   $K_c = \gamma (\tan \theta)^{2/3}(E/H)^{1/2}P/c^{3/2}$ with $\gamma = 0.023$.
2. The force displacement curves with the corner cube indenter suggest "pop-in" occurs during loading and appears to be associated with the development of a median crack (three quarter penny cracks) beneath the indenter. For the glassy carbon only with "pop-in" do radial cracks form about the impression, whereas for fused silica cracks are formed with both indenters. The hysteretic recovery of the glassy carbon and absence of residual stress associated with permanent set are considered responsible for the non-occurrence of cracking in this brittle material.
3. Although clear associations were established between 'pop-in" displacement, radial crack length and the change of the energetics, no non-optical measure of crack length from analysis of the force-displacement curves has been found.
4. It is possible to determine the intrinsic elastic and plastic properties of the materials using corner cube indenters by analysis of the force-displacement curves by removal of the additional displacement associated with "pop-in".

REFERENCES

1. Lawn, B.R., Evans, A.G., Marshall, D.B., J. Amer. Ceram. Soc. 63, 574 (1980).
2. Lawn, B.R., and Swain, M.V., J. Mater Sci., 10, 113 (1975)
3. Cook, R.F. and Pharr, G.M., J. Amer. Ceram. Soc. 73, 787 (1990)
4. Dukino, R. and Swain, M.V., J. Amer. Ceram. Soc. 75, 3299 (1992)
5. Harding, D.S., Oliver, W.C., Pharr, G.M., Mat. Res. Soc Symp. 356, 663 (1995)
6. Sakai, M. Acta metal et materialia 42, 2879 (1994)
7. Field, J.S and Swain, M.V. to be published
8. Oliver, W.C, and Pharr, G.M., J. Mater. Res. 7, 1564 (1992)

NANOINDENTATION AND FRACTURE ANALYSIS OF THIN SOLID FILMS

K.Sriram, R.Narasimhan and S.K.Biswas

Department of Mechanical Engineering,
Indian Institute of Science,
Bangalore 560012, India

ABSTRACT

In this paper, finite element simulations of spherical nanoindentation of a thin hard film deposited on a soft substrate are carried out. The energy release rate J associated with circumferential cracks extending inwards from the film surface is computed. The mechanics of fracture of the film during nanoindentation is studied by examining the variation of J with crack length and also the stress distributions in the uncracked film. Finally, methods for combining experimental load versus indentation depth data with simulation results in order to obtain the fracture energy of the film are proposed.

KEYWORDS

Thin solid films, nanoindentation, finite elements, energy release rate.

1. INTRODUCTION

In recent years, material components with protective surface coatings of micrometric thickness are being used quite extensively in various technological applications. The mechanical performance of these components is critically dependent on the strength and toughness of these films as well as on those of the film-substrate interface. Submicrometer indentation is a popular technique for investigating the mechanical properties such as hardness and elastic modulus of a coated specimen [1]. However, techniques for determining the fracture toughness of the film from nanoindentation test results are not well developed. Experimental studies [2-4] have shown that radial and circumferential cracks (through the film), as well as interfacial failure, may occur during nanoindentation tests. In situations where cracks form through the film, some steps in the load versus displacement response are observed [3,4]. The interpretation of such experimental data to obtain the fracture toughness of the film is generally based on approximate relationships [2], and also requires *a posteriori* measurement of crack lengths from the coated sample which is not a trivial task.

The first step towards providing a sound fracture mechanics methodology for analysing nanoindentation test results was taken by Weppelmann and Swain [4]. They conducted a detailed study of the stress fields that develop during spherical nanoindentation of thin hard films deposited on soft substrates. The focus of this study was to investigate the effects of indenter radius to film thickness ratio and plastic yielding in the substrate on the above fields. The weight function method was employed to compute the stress intensity factors associated with circumferential or cylindrical cracks in the film. However, a systematic investigation of the mechanics of fracture in the film during nanoindentation was not performed in their work. Further, the use of the weight function method entails the assumptions of plane strain (whereas, in reality, the domain is axisymmetric), and small geometry changes in the indented zone.

Hence, the primary objective of this paper is to investigate the mechanics of fracture in thin hard films due to occurrence of cylindrical cracks during spherical nanoindentation. The stress fields in the film, as well as the energy release rate associated with cylindrical cracks at different indentation depths are studied using finite element analyses. The film is assumed to be elastic, whereas plastic yielding in the substrate is considered. The energy release rate is computed directly from finite element analyses of cracked samples using the numerically accurate domain integral formulation [5]. Also, methods are proposed by which finite element simulations can be employed to interpret nanoindentation test results and yield information related to fracture behaviour of the film.

2. MODELLING ASPECTS

In this work, axisymmetric finite element analyses of spherical nanoindentation of the film-substrate system is carried out. An updated Lagrangian finite element formulation is employed. The contact between the (rigid) indenter and the film is assumed as frictionless and is modelled using a penalty approach [6]. The radius R_i of the indenter and the thickness t of the film are chosen as 0.67 μm and 1 μm, respectively. The radial dimension R_s of the film-substrate system and the substrate thickness t_s are taken as 0.2 mm and 0.1 mm respectively, so that boundary effects do not influence the stress distribution near the zone of indentation. The film is assumed to be linear elastic with Young's modulus E and Poisson's ratio ν taken as 480 GPa and 0.2, respectively, which correspond to TiN. A finite deformation, J_2 flow theory of plasticity model is employed for the substrate, with E, ν, initial yield strength σ_{ys} and tangent modulus E_t chosen as 210 GPa, 0.3, 600 MPa and 7.25 GPa, respectively, which pertain to an intermediate strength steel.

3. STRESS ANALYSIS

It is important to understand the stress variations in the film during indentation before investigating the mechanics of indentation fracture. To this end, indentation analysis of an uncracked film-substrate system is undertaken in this section. The variations of load P versus indentation depth h are shown in Figs.1(a) and (b). These figures pertain to maximum indentation depth h_m = 50 and 200 nm, respectively. The corresponding contact radii a are 170 and 295 nm, respectively. Both the loading and unloading segments (starting from the maximum indentation depth) are displayed in Figs.1(a) and (b).

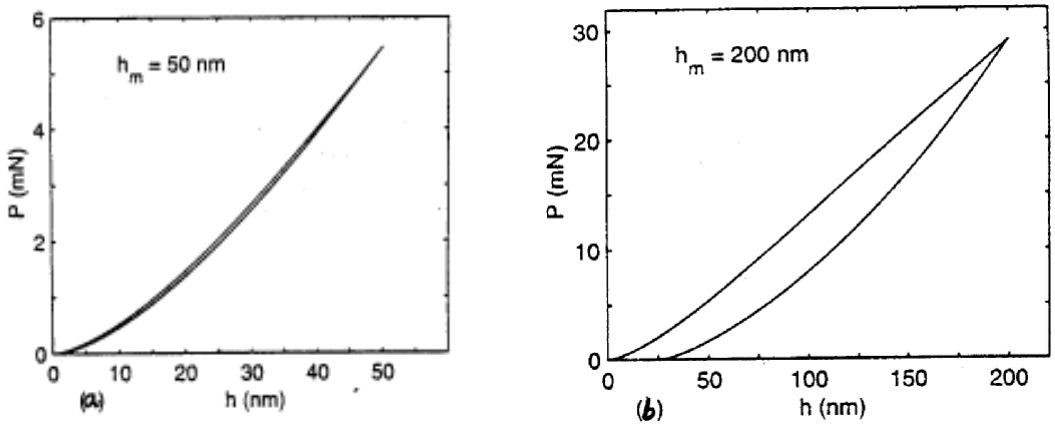

Figure 1: Load versus indentation depth for the uncracked film corresponding to maximum indentation depth of **(a)** h_m = 50 nm and **(b)** h_m = 200 nm.

It is observed from Fig.1a that the unloading curve almost coincides with the loading curve at low indentation depth, whereas it deviates substantially from the loading curve at large indentation depth (see Fig.1b). This is attributed to a significantly large plastic zone size in the substrate at large indentation depth. Thus, it was found from contours of plastic strain that the maximum plastic zone size in the substrate at h = 50 and 200 nm are 760 and 3100 nm, respectively.

The radial stress σ_{rr} at the film surface (z = 0) is compressive within the contact zone (r < a) [4]. However, the magnitude of σ_{rr} decreases as r increases within the contact zone and it becomes tensile as $r \rightarrow a$. It attains a peak tensile value just outside the contact zone (at r/a between 1 to 1.1). This implies that fracture in the form of cylindrical cracks just around the contact zone may occur during indentation [4]. Hence, in the fracture analyses conducted later, cylindrical cracks located just outside the contact zone, at different indentation depths are studied.

The variations of σ_{rr} with normalized distance z/t through the film thickness corresponding to h = 50 and 200 nm are shown in Figs.2(a) and (b), respectively. In these figures, the through thickness variations of σ_{rr} at different radial distances r/a are presented.

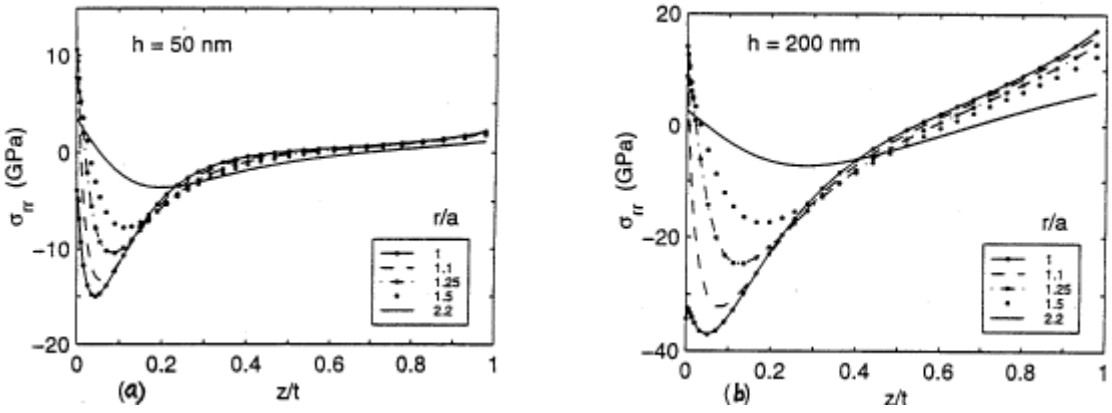

Figure 2: Variations of radial stress with normalized distance z/t through the film thickness at different radial locations r/a : **(a)** h = 50 nm and **(b)** h = 200 nm.

In all cases, σ_{rr} decreases rapidly from the tensile value at the surface and becomes compressive at a small distance z below the surface. It reaches a peak compressive value between z = 0.1t to 0.2t, and thereafter, increases. It may be seen from Fig.2(a) that at low indentation depths σ_{rr} has a very small magnitude for z > 0.4t. On the other hand, at large indentation depth, σ_{rr} becomes strongly tensile for z > 0.4t (see Fig.2(b)). Thus, for h = 200 nm, σ_{rr} = 17GPa at r/a close to 1 and z/t = 1 (i.e., at the film-substrate interface).

The variations of shear stress τ_{rz} with normalized distance z/t through the film thickness at different radial locations r/a corresponding to h = 50 and 200 nm are shown in Figs.3(a) and (b), respectively.

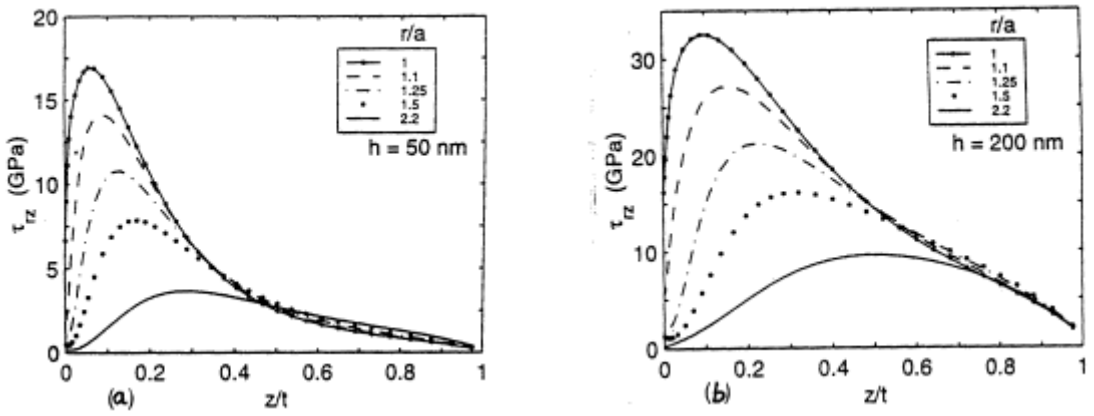

Figure 3: Variations of shear stress with normalized distance z/t through the film thickness at different radial locations r/a : **(a)** h = 50 nm and **(b)** h = 200 nm.

It may be observed from these figures that for all radial distances $r/a > 1$, τ_{rz} increases as z increases, reaches a peak value between 0.05t and 0.4t depending upon the radial location, and then decreases. As $z/t \rightarrow 1$, τ_{rz} is close to zero at all values of r/a. This implies that failure of the film-substrate interface cannot take place under shear. Finally, it may be seen from Figs.3(a) and (b) that at small distances z/t below the film surface, the maximum magnitude of τ_{rz} occurs at r/a close to 1 and decreases rapidly as r/a increases. By contrast, all curves shown in Figs.3(a) and (b) almost merge with each other in the range $z/t > 0.4$.

4. FRACTURE ANALYSIS

In this section, cylindrical cracks extending inwards from the film surface are introduced at different radial distances R. The indentation analysis is conducted till the contact zone approaches the crack surface. The normalized crack length, c/t , is varied from 0.1 to 0.9. The dimensions of the film-substrate system, radius of the indenter, other modelling aspects, and material properties are the same as mentioned in Section 2. The compressive radial stress prevailing below the film surface (see Fig. 2) leads to crack closure for shallow cracks and at small indentation depths. In these cases, the contact between the crack faces is also assumed to be frictionless and the associated constraints are imposed by the penalty approach [6]. On the other hand, there is opening of the crack faces due to tensile radial stress for deep cracks at large indentation depths and, hence, a mixed mode state prevails near the tip under these conditions. The energy release rate J is computed from the finite element results continuously throughout the indentation analysis using the domain integral method [5]. To this end, several rectangular domains of dimensions varying from 10 nm × 10 nm to 125 nm × 125 nm about the crack tip are considered. It is found that J computed from various domains differ by less than three percent.

The variation of J with normalized crack length c/t for cracks located at radial distances R = 180 and 200 nm, respectively, are shown in Figs. 4(a) and (b). These figures pertain to indentation depths of h = 50 and 200 nm, respectively.

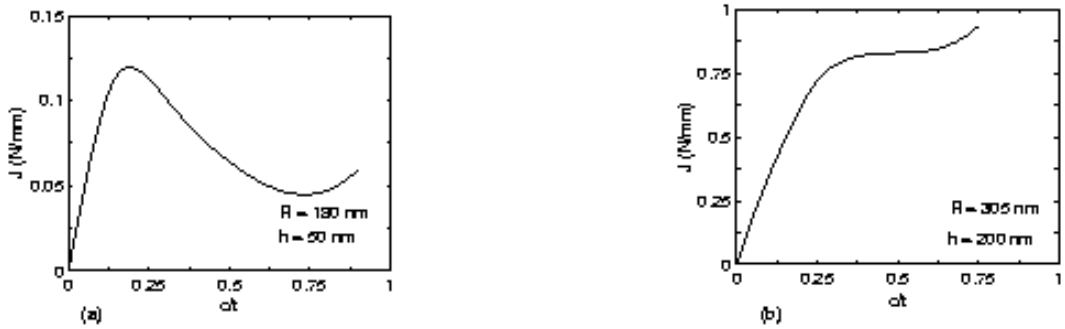

Figure 4: Variation of energy release rate J with normalized crack length c/t for cracks located **(a)** at R=180 nm corresponding to h=50 nm and **(b)** at R=305 nm corresponding to h=200 nm.

On examining Fig.4(a) which pertains to small indentation depth, it may be seen that J increases initially with crack length and reaches a peak at around $c = 0.2t$. It then decreases between $c = 0.2t$ and $0.75t$, and then shows a marginal increase for $c > 0.75t$. It can be seen from Fig.4(b) that at $h = 200$ nm, the decreasing branch of the J versus c/t curve has completely vanished, although J remains almost constant over the range of c/t from 0.3 to 0.6. The above trends can be understood by examining the stress distributions shown in Figs. 2 and 3. As already mentioned, shallow cracks are subjected essentially to Mode II loading since σ_{rr} is compressive leading to crack closure. Now, it may be recalled from Fig.3 that τ_{rz} at $r/a = 1.1$ reaches a peak value at z between 0.1 and 0.2t and, thereafter, decreases with increase in z. This leads to the drastic reduction in J with c/t, for $c/t > 0.2$ in Fig. 4(a). However, since σ_{rr} is strongly tensile as the film-substrate interface is approached at large indentation depth (see Fig.2(b)), it offsets any reduction in J caused by decrease in τ_{rz} with z/t. Hence, J increases monotonically with c/t in Fig.4(b).

The decreasing branch of the J versus c/t curve (between $c/t = 0.2$ and 0.75) in Fig.4(a) implies that crack growth over this range of crack lengths will be stable. In other words, the indentation depth will have to increase gradually in order to sustain further crack growth. In the case of Fig.4(b), crack growth will be unstable over the entire range of c/t from 0 to 1 since $\partial J/\partial c > 0$.

5. INTERPRETATION OF EXPERIMENTAL DATA

In Fig.5, a schematic illustration of an experimental P versus h curve with a step AB, which presumably corresponds to the growth of a cylindrical crack located at a radius R from the axis of symmetry, (similar to that observed in [4]), is presented. In order to estimate the fracture energy, J_f, of the film from this experimental curve, the extent of crack growth Δc must be first determined. To this end, a family of P versus h curves corresponding to different crack lengths c_1, c_2, etc., at the observed radial location R, generated by finite element analyses, are superimposed on the experimental data as shown in Fig.5. From this diagram, the extent of crack growth associated with the step AB may be deduced to be around $\Delta c = c_3 - c_2$.

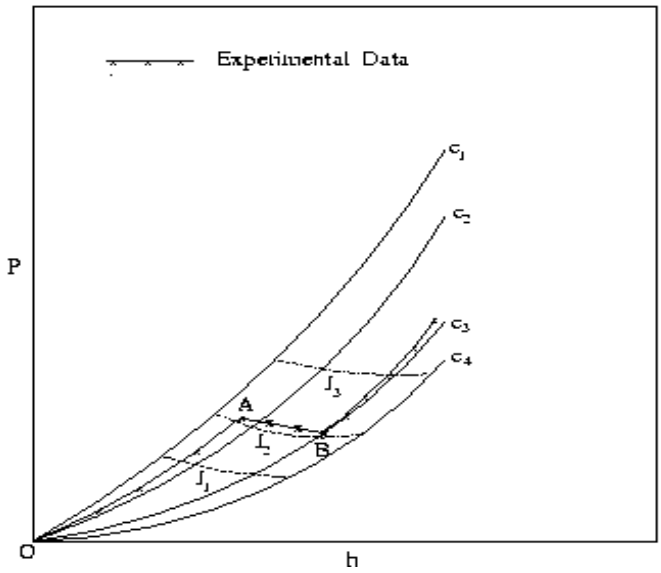

Figure 5: Schematic illustration showing experimental P versus h data superimposed on a nomogram consisting of numerically generated P - h curves corresponding to different crack lengths c_i and constant J trajectories.

The fracture energy J_f of the film may now be estimated in two ways. In the first method, J_f may be calculated as $A_f/(2\pi R\Delta c)$, where A_f is the area of the curved wedge OAB in Fig.5. Alternatively, J_f may be deduced by conducting further analysis of the results and plotting constant J trajectories corresponding to levels J_1, J_2 etc., along with the P versus h curves, as shown by the dash-dot lines in Fig.5. It may be seen from Fig.5 that the step AB in the experimental data lies close to the constant J line pertaining to the level J_2. Hence, J_f may estimated to be equal to J_2.

6. CONCLUSIONS

The radial stress is compressive below the film surface which leads to crack closure for shallow cracks and at low indentation depths. Thus, under these conditions, cylindrical cracks in the film are loaded under mode II and the energy release rate shows a decreasing branch for range of crack lengths between 0.2t and 0.75t. This implies that crack growth will be stable in this range and will occur under gradually increasing h. However, at large h, since σ_{rr} becomes tensile adjacent to the interface, J does not display any decrease with c and crack growth is expected to be completely unstable. Two methods for interpreting experimental P-h data and obtaining the fracture energy J_f of the film have been proposed.

REFERENCES

1. Phar, G.M. and Oliver, W.C. (1992) *MRS Bulletin* 28.
2. Haanappel, V.A.C., Vendel, D.V.D., Metselaar H.S.C., Van Corbach H.D., Fransen T. and Gellings, P.J. (1995) *Thin Solid Films* 254, 153.
3. Whitehead, A.J. and Page, T.F. (1992) *Thin Solid Films* 220, 277.
4. Weppelmann, E. and Swain, M.V. (1996) *Thin Solid Films* 286, 111.
5. Nakamura, T., Shih, C.F. and Freund, L.B. (1986) *Engng. Fract. Mech*. 25, 333.
6. Wriggers, P., Vu Wan, T. and Stein, E. (1990) *Comput. Struct*. 37, 319.

ICF100830OR

NEAR THE FATIGUE LIMIT IN GLASS

S.M. Wiederhorn[1], A. Dretzke[2] and J. Rödel[2]

[1] National Institute of Standards and Technology
Gaithersburg, MD 20814-8500
[2] Technische Universität Darmstadt
Darmstadt, Germany

10th International Congress of Fracture
Honolulu, Hawaii

3-7 December 2001

ORAL REFERENCE: ICF100830OR

NEAR THE FATIGUE LIMIT IN GLASS

S.M. Wiederhorn[1], A. Dretzke[2] and J. Rödel[2]

[1] National Institute of Standards and Technology
Gaithersburg, MD 20814-8500
[2] Technische Universität, Darmstadt
Darmstadt, Germany

ABSTRACT

The atomic force microscope is used to explore the nature of fracture surfaces in soda lime silicate glass formed near or below the apparent crack growth threshold. Conventional theory suggests that cracks in glass will blunt when subjected to stresses below the threshold. We see no evidence for blunting in this study. Cracks that are held below the apparent crack growth threshold for 16 h alter their mode of growth. The fracture plane changes from a flat surface to a surface that exhibits substantial out of plane growth. The crack changes its growth direction to an angle that lies between 3E and 5E to the original growth plane, leaving behind a wavy fracture surface. This change in crack morphology may be the cause of a time delay to restart crack motion when the applied stress intensity factor is again raised above the apparent crack growth threshold.

KEYWORDS

Glass, crack growth, static fatigue limit, ceramics, stress corrosion, atomic force microscopy

INTRODUCTION

Studies of crack growth in glass suggest that some glass compositions exhibit thresholds below which crack growth will not occur. In a study of this phenomenon, Wiederhorn and Bolz [1] showed that soda lime silicate glass and a chemically resistant borosilicate glass immersed in water gave evidence of a threshold stress intensity factor below which crack growth would not occur. Crack velocities greater than about 10^{-7} m/s could be expressed as an exponential function of the applied stress intensity factor, K_I. Below about 10^{-7} m/s, the crack velocity decreased at a rate that is faster than that suggested by

the exponential behavior. As the crack growth curve had a negative curvature, crack growth appeared to approach a threshold below which crack growth would stop as the applied stress intensity factor was reduced. These experiments on soda lime silicate glass have been confirmed by Kocer and Collins [2] to crack velocities as low as 10^{-14} m/s. In the light of the stress-corrosion theory by Charles and Hillig [3], Wiederhorn and Bolz interpreted this behavior as evidence for crack tip blunting. The radius of curvature of the crack tip was assumed to increase with time below the threshold. Hence, the crack became more difficult to propagate.

In a later study, Michalske [4] reinforced the idea that the downward curvature of the crack growth curve was due to crack tip blunting. Michalske applied a value of K_I that lay below the apparent crack growth threshold and held it for a 16 h period. He felt that if crack blunting occurred, then a time delay would be needed to restart a crack when the stress was raised to a value of K_I that lay above the apparent threshold for crack growth. Michalske found that a time delay did occur and that it depended on the level of K_I used to restart crack motion. If K_I were just slightly above the threshold limit, several thousand seconds were required to restart crack motion. However, if K_I were substantially above the threshold, then the crack would restart its motion without delay.

In addition to the time delay to restart the crack, Michalske observed a pattern of marks on the fracture surface that were clearly associated with the "arrested crack." These were a series of light and dark bands that lie along the crack front at the point of crack arrest. The nature of these bands was not obvious, but Michalske attributed them to the process of re-sharpening a blunted crack. To him it seemed that the crack became "segmented as it extends from its position during aging." These segments were believed to result from the "nucleation and growth of sharp cracks from the rounded crack tip." His conclusions on what was happening during the experiment were very reasonable. However, at the time there was no instrument available that would clearly define the nature of the markings at the arrested crack tip.

The atomic force microscope is an instrument that has both the lateral and normal resolution needed to fully characterize the marks first observed by Michalske. We use this instrument to show that these markings represent a non-planar propagation of the crack near the apparent crack growth threshold, such that some portions of the crack front propagate out of the projected crack plane and other portions propagate into the projected crack plane. The time delay for re-propagating the crack may be the time needed for the crack to again propagate on a single plane.

EXPERIMENTAL PROCEDURE

The experimental procedure was identical to that used by Wiederhorn and Bolz [1] and very similar to the one used by Michalske [4]. Double cantilever beam specimens 75 mm by 25 mm by 1.5 mm were dead weight loaded using a small laboratory pan balance to transmit the force. The glass was from the same batch as used by Wiederhorn and Bolz. Narrow side-grooves in the specimen maintained the advancing crack along the midline

of the specimen. We monitored the crack position with a 40x microscope having a filar eyepiece and determined the position of crack to an accuracy of 5 μm, using light reflected from the crack surface. Michalske did not use side-grooves and monitored the crack motion with transmitted light. Other that that, the same equipment was used in both experiments.

We adopted Michalske's experimental procedure to carry out our experiment. A crack was first propagated at a relatively high value of K_I. The value of K_I was then reduced to a value less than the apparent crack growth threshold. The crack was finally repropagated at the higher value of K_I. Studies reported in this paper were all carried out in water. The high K_I values for crack growth measurements ranged from about 0.35 MPa·m$^{1/2}$ to about 0.55 MPa·m$^{1/2}$. The lower K_I values used to induce Ablunting≅ ranged from 0.22 MPa·m$^{1/2}$ to 0.30 MPa·m$^{1/2}$. The measurement carried out at 0.30 MPa·m$^{1/2}$ was only held for eight hours; all others were held for 16 h. Once a crack started propagating, it was permitted to propagate approximately 1 mm and then again held at a lower stress intensity factor for 8 or 16 h. All measurements were carried out on a single specimen. Upon completing the crack growth experiments, we broke our specimen in half along the crack plane to expose both fracture surfaces and then examined and compared both surfaces with an optical and a Digital III atomic force microscope[1], using the contact mode to image the fracture surface.

EXPERIMENTAL RESULTS

We reproduced Michalske's earlier work in these studies. A time delay to restart the crack was observed when it was held at stress intensity factors in the range 0.22 MPa-m$^{1/2}$ to 0.30 MPa-m$^{1/2}$. We also observed the same microscopic arrest features

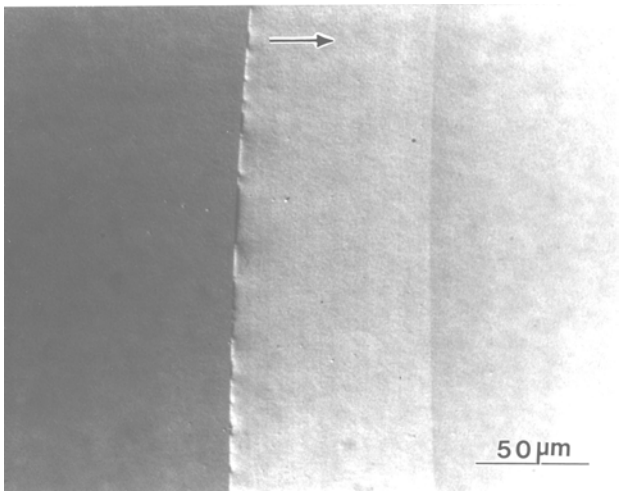

Figure 1: Crack tip that had been arrested and then restarted: K_I=0.23 MPa-m$^{1/2}$; hold time 16 h. The arrow indicates the direction of crack growth.

[1] The use of commercial names is for identification purposes only and does not imply endorsement by the National Institute of Standards and Technology

reported earlier by Michalske. When the crack was held at stress intensity factors in the range 0.22 MPa-$m^{1/2}$ to 0.30 MPa-$m^{1/2}$ for 16 h, light and dark bands decorated the crack front, Figure 1. By contrast, unloading and restarting the crack immediately left only a single faint mark where the crack had changed direction slightly, Figure 1. We observed some variability in the appearance of the marks that decorated the crack front of the arrested crack. Sometimes only a few dark and light bands were observed; in other cases there was only one light or dark band on the crack front.

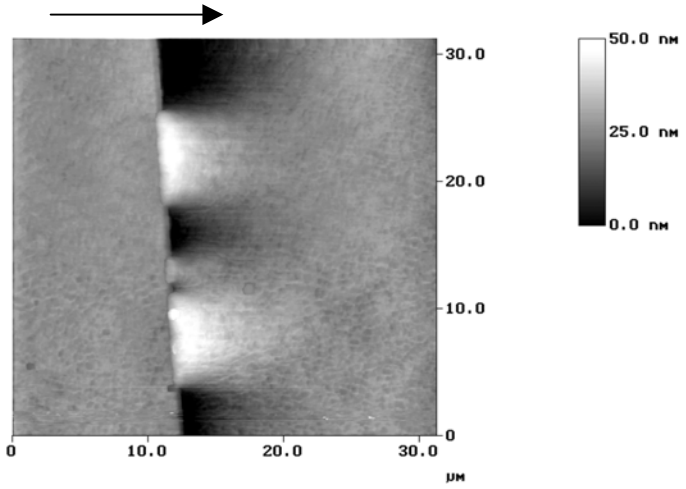

Figure 2: Direction of crack growth from left to right, see arrow. The lighter shades indicate an increase in the height of the fracture plane above the original fracture surface. This is not the same crack front as shown in Figure 1.

An AFM image of the fracture feature reveals what the optical microscope could not reveal, Figure 2. At the point of crack arrest, variations in the height of the fracture surface developed as a consequence of the hold time. As the crack advanced to the position where K_I was decreased, the crack was a smooth almost flat surface. The repropagated crack lay either above or below the original crack plane. As all parts of the repropagated crack were connected, these features suggest waviness to the crack front near the point of "arrest." As the crack grew, the waviness gradually disappeared, and the crack again propagated on a single plane.

Sectioning of the features in Figure 2 provides more details on the crack growth, Figure 3. Sectioning lines parallel to the direction of crack advance show that the crack propagated on a smooth plane prior to unloading. After reducing K_I, holding it for a period and then increasing it again, the direction of crack growth is found to have changed; some portions of the crack propagated into the projected crack plane, others propagated out of the crack plane. The new angle of propagation was ±3° to ±5° to the original crack surface. With continued crack growth, the direction of crack propagation gradually changed back to a single plane.

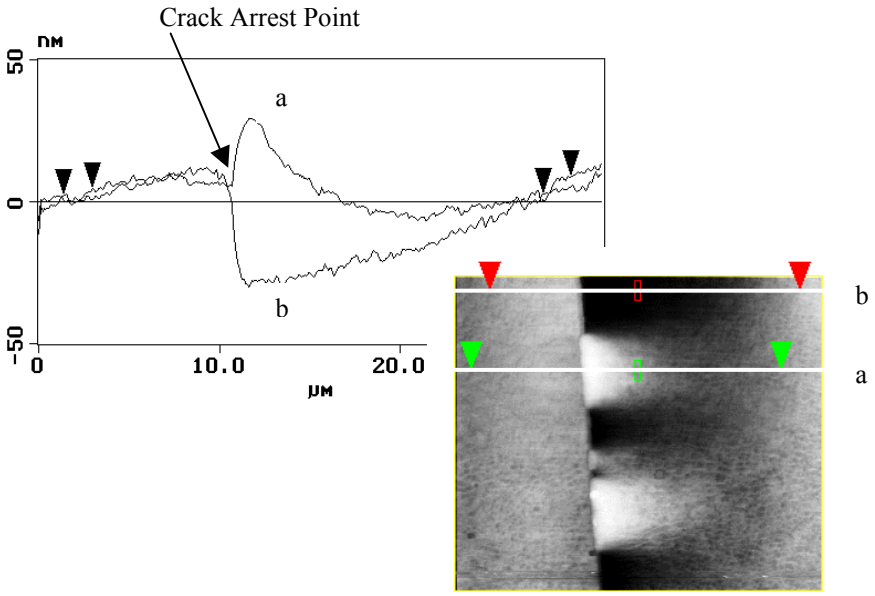

Figure 3: Sectioning of the features in Figure 2 shows a bifurcation in the crack propagation plane; part of the crack moves into the plane, the other part moves out.

In order to interpret the growth process, it is important to know how closely the opposing faces of the crack replicated one another. Presumably, if crack blunting occurred, the shape of the upper and lower fracture surfaces would be different. Hence, AFM pictures were taken from each surface of the crack, and the same feature on each surface was sectioned and compared. Overlaying the two sections, Figure 4, shows that the two sections replicate one another to an estimated accuracy of ±2 nm.

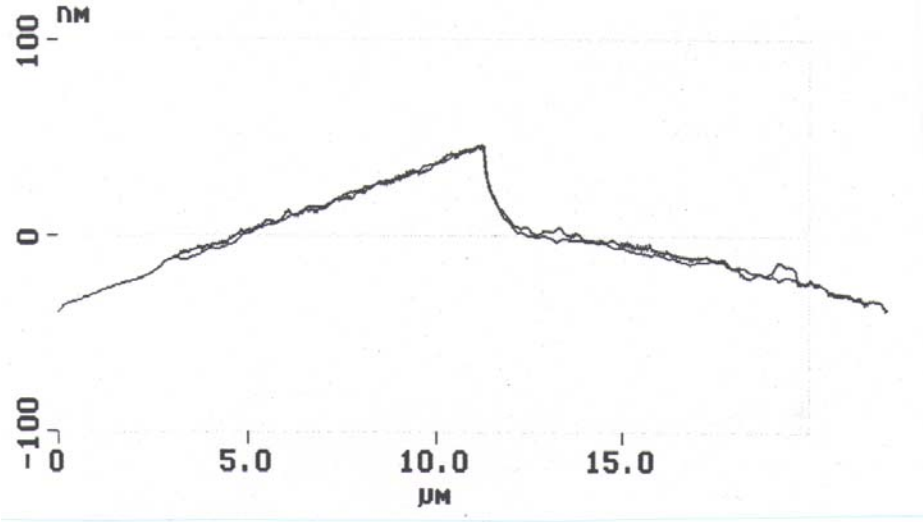

Figure 4: Section of the identical feature on opposite sides of the same crack. Within experimental scatter, the two images duplicate one another.

DISCUSSION

Within the accuracy of our AFM measurement, the crack propagates as a "sharp" crack in soda lime silicate glass, and does not appear to blunt during the hold period. If the crack is in fact sharp, the time delay for restarting crack growth cannot be attributed to a resharpening of the crack tip. Instead, the time delay to restart the crack may be the time needed for the crack to again propagate on a single plane.

Altering the far field applied stress will cause a change in the direction of crack growth. The changes along the crack front that we observe are clearly of the type that could be caused by Mode II loading, which cause the crack to propagate out of plane. However, if the features were due to a remotely applied stress, the entire crack front would be expected to propagate out of the original crack plane, and that does not happen. One could argue that the features are due to a stress applied to the crack surface near the crack tip. Accounting for the features in Figure 1 would require stresses to be active over a range of distances from 1 μm to 10 μm. As it is difficult to imagine the source of such surface stresses, we turn elsewhere for an explanation of our observations.

A possible source of the out of plane growth may be found in a modification of the Charles Hillig theory suggested recently by Chuang and Fuller [5]. In the Charles-Hillig theory, crack growth occurs because of a stress enhanced chemical attack of water on the glass surface of the crack. Charles and Hillig concentrated their theory on the curvature of the tip of the crack and the effect of the chemical reaction on that curvature. Their model suggested that below the threshold, cracks should blunt, whereas above the threshold, they should sharpen. The threshold was the stress at which the crack propagated in a self-similar manner. Chuang and Fuller expanded on this theory by exploring the change in surface corrosion rate over the entire crack surface, not just at the tip. Their model predicted that below the crack growth threshold, as defined by Charles and Hillig, the surface corrosion rate was no longer fastest at the crack tip, but at an angle to the original crack plane, which depended on the stress. Therefore, there is a tendency for out of plane crack growth. Whether this tendency can actually result in the kind of features we see has yet to be determined.

REFERENCES

1. Wiederhorn, S.M. and Bolz, L.H. (1970) *J. Am. Ceram. Soc.* 53, 543.
2. Kocer, J.and Collins, R.E. *J. Am. Ceram. Soc.* to be published.
3. Charles, R.J. and Hillig, W.B. (1962) in *Symposium on Mechanical Strength of Glass and Ways of Improving It*, pp. 25-29 Union Scientific Continentale du Verre, Charleroi, Belgium.
4. Michalske, T.A. (1977) in *Fracture Mechanics of Ceramics, Vol. 5, Surface Flaws, Statistics, and Microcracking*, pp. 277 to 289, Bradt, R.C., Evans, A.G., Hasselman, D.P.H. and Lange, F.F. (Eds.) Plenum Press, New York.
5. Chuang, T.-J. and Fuller, E.R., Jr. (1992) *J. Am. Ceram. Soc.* 75, 540.

NEAR TIP BEHAVIOR IN A PARTICULATE COMPOSITE MATERIAL UNDER CONSTANT STRAIN RATE INCLUDING TEMPERATURE AND THICKNESS EFFECTS

C. T. Liu
Air Force Research Laboratory
AFRRL/PRSM
10 E. Saturn Blvd.
Edwards AFB CA 93524-7680

C. W. Smith
ESM Department
Virginia Polytechnic Institute and State University
Blacksburg VA 24061

ABSTRACT

A series of tensile tests were conducted at a constant cross head speed (2.54 mm/min) and three temperatures (-53.9°C, 22.2°C, and 73.9°C) on edge cracked sheet specimens of two thicknesses (2.54 mm and 12.7 mm). The specimens were made from polybutadiene rubber embedded with hard particles. The effects of temperature and specimen thickness on local behavior and strain fields near the crack tip were investigated and the results are discussed.

INTRODUCTION

In recent years, a considerable amount of work has been done in studying crack growth behavior in highly filled polymeric materials [1-4]. The importance of these studies stems from the fact that the crack growth behavior in the material may significantly affect the integrity of the structure made of that material. The basic approach used in characterizing the particulate composite material is based on linear elastic or linear viscoelastic fracture mechanics. According to the theories, crack growth behavior is controlled by the local stress/strain near the crack tip. Therefore, the values of local stress/strain near the crack tip must be determined. Since the highly filled polymeric materials behave like viscoelastic materials, the fracture behavior near the crack tip can be strongly influenced by the testing temperature and the loading rate. Therefore, to obtain a fundamental understanding of crack growth and fracture behavior in a highly filled polymeric material, the effect of the aforementioned parameters on local strain fields and fracture behavior near the crack tip needs to be determined.

In the present study, the effect of testing temperature and specimen thickness on the local behavior near the crack tip and the crack growth behavior in the material were investigated and the results are discussed.

THE EXPERIMENTS

In this study, the local fracture behavior, the local strain fields near the crack tip, and the crack growth behavior in a particulate composite material, containing hard particles in a rubbery matrix, subjected to a constant strain rate of 0.1 min^{-1} at different temperatures were investigated. The specimens were 20.32 cm long and 5.08 cm wide (Fig. 1). Two different specimen thicknesses (2.54 mm and 12.7 mm) and three different temperatures (-53.9°C, 22.2°C, and 73.9°C) were considered. Prior to the test, a 23 mm crack was cut at the edge of the specimen. Since the specimens were quite soft, a special grating had to be developed from which displacements near the crack tip could be measured without affecting the stiffness of the specimen. A coarse grating consisting of squares of 0.2 mm on each side (approximately 1/2 of the largest size of the hard

particle) and which had a thickness of less than 2.5 x 10^{-2} mm was deposited in the neighborhood of the crack tip.

Prior to testing, the specimens were conditioned at the test temperature for 1 hour and were then tested at a constant strain rate until the specimen fractured. During the tests, photographs of the grid region were taken at various time intervals and they were used to determine the displacement fields near the crack tip. In addition, a strip chart recorder was used to record the load and time during the test. These data were used to determine the strain fields. In addition, a strip chart was used to record the load and time during the test. These data were used to determine the crack growth rate and the Mode I stress intensity factor.

DATA REDUCTION

The raw data obtained from the constant strain rate tests were the crack length, a, the time, t, and the load, p, corresponding to the measured crack length. The recorded experimental data, a, t, and p, were used to calculate the Mode I stress intensity factor, K_I, and the crack growth rate, da/dt. In calculating the stress intensity factor, K_I, for a given set of values of a and p, a nonlinear regression equation, which relates the normalized stress intensity factor, K_I/p, to the crack length, a, was used. The values of K_I/p for different crack lengths were determined from the ABAQUS computer program. In calculating the crack growth rate, da/dt, the secant method was used. In the secant method, the crack growth rate was computed by calculating the slope of a straight line connecting two adjacent a versus t data points. To avoid the time-consuming process of data reduction, a computer program was written to calculate K_I and da/dt.In addition, the displacements and the strain fields were determined by digitizing the data from the photographs. In calculating the strains, small strain definitions were used. Therefore, strain contours for strain level greater than 20% should be ignored.

RESULTS AND DISCUSSION

All curves in this section were constructed from averaging data of two tests. Figures 2 and 3 show the load per unit thickness as a function of global strain for thin and thick specimens tested at 73.9^{o}C and –53.9°C (results at 22.2^{o}C were similar to 73.9^{o}C). Figure 2 shows that at 73.9^{o}C, the load carrying ability for the thin specimen is consistently higher than the thick specimen. However, at –65^{o}F, the trend is reversed which suggests that some change in material properties had occurred before reaching this temperature. The increase in maximum load per unit thickness of the thin specimen above the thick ones at 73.9^{o}C may be attributed to the size effect and the damage initiation and evolution processes near the crack tip. At 73.9^{o}C The binder material softened to the point where it would support only small stress before the ligaments between the voids in the failure process zone ruptured. Also, the thermal energy facilitates interchain sliding, allowing the ligaments to thin more rapidly and rupture under lower tensile stress. Additionally, at elevated temperature, the bond strength at the particle/binder interface is decreased. This leads to a larger failure process zone and crack opening distance at the crack tip. However, at –53.9^{o}C, the bond strength and the binder strength increase significantly. Also, it was noted that at –53.9^{o}C blunting was significantly reduced and classical brittle fractures occurred in these tests with the crack propagating unstably across the specimens. The reduction of crack tip blunting suggests that voiding is suppressed due to the stiffening effect of the low temperature on the matrix material. This is believed to have allowed the development of transverse constraint in the thick specimens at –53.9°C and causes the material to behave almost as a single phase material. Also, the development of transverse constraint at –53.9° will decrease the material's ability to redistribute stresses and result in a greater load per unit thickness in the thick specimen than in the thin specimen.

Typical near tip displacement contours are shown in Fig. 4. From Fig. 4, the regularity of the displacement field suggests that this material may be described by continuum theory. In addition, the order of singularity at the crack tip when the crack intersects the free surface of the specimen was also investigated. According to fracture mechanics, the stresses and displacements in the neighborhood of the crack tip can be expressed as

$$\sigma_{i,j} = \gamma^{\lambda,5} f_{i,j}(\lambda, \theta, \phi), \qquad u_{i,j} = \gamma^{\lambda,u} (\lambda, \theta, \phi).$$

By confining displacement measurements to a region outside the highly voided failure process zone ahead of the crack tip, it was possible to measure the value of the dominant eigenvalue λ_u at the free surface using a continuum approach. Results of analyses show that the average value of $\lambda_u = 0.72$ agrees within 7.5% with the theoretical value predicted by Benthem for incompressible materials, $\lambda_u = 0.67$. The small differences between the measured and the calculated λ_u indicates that, even though the particulate composite material is anisotropic and heterogeneous on the micro scale, it may behave as an isotropic, homogeneous continuum when analyzed macroscopically.

Typical plots of normal strain fields, ε_y, for different specimen thicknesses and temperatures are shown in Fig.5. In general, these figures show that the contour lines are not smooth but irregular. It is believed that a portion of the irregularities may stem from the method of data collection and reduction, but they are mainly due to the nonhomogeneity of the material. The experimental data indicate that for a given temperature, specimen thickness has no significant effect on the strain distributions near the crack tip. Experimental data also indicates that large normal strains occur in small zones, or the intense strain zones, which are immediately ahead of the crack tip. It seems that the intense strain zone size is relatively insensitive to the change in specimen thickness and it decreases with decreasing testing temperature. Since the intense strain zone is very small as compared with the crack length and the dimensions of the specimen, linear fracture mechanics theories can be used to characterize crack growth behavior in the material.

The crack growth rate da/dt versus the Mode I stress intensity factor K_I are shown in Figs. 6 and 7. From these figures, it can be seen that a power law relationship exists between K_I and da/dt. Mathematically, it can be written as

$$da/dt = c\, K_I^{\,B}$$

in which C and B are constants, and they are shown in Table I. Figures 6 and 7 also reveal that the crack growth is much faster at -53.9°C.

CONCLUSIONS

The principal conclusions which can be derived from the results of this study are: (1) the local behavior near the crack tip and the crack growth behavior at –53.9°C are significantly different from that at 22.2°C and 73.9°C.; (2) the crack growth data reveal that a ductile-brittle transition occurs somewhere between –53.9°C and 22.2°C.; (3) except the thicker specimen tested at –53.9°C, the near tip mechanisms (blunting, voiding, coalescing, and growing) differ only in a quantitative sense; (4) a classical brittle fracture takes place when the thicker specimen tested at –53.9°C; (5) on a macro scale, the particulate composite material can be considered as a homogeneous continuum; and (6) a power relationship exists between the crack growth rate and the Mode I stress intensity factor.

REFERENCES

1. Liu, C.T., 1990. "Crack Growth Behavior in a Composite Propellant with Strain Gradients - Part II," Journal of Spacecraft and Rockets, 27: 647-659.
2. Smith, C.W. and Liu, C. T., 1991. "Effects of Near-Tip Behavior of Particulate Composites on Classical Concepts," Journal of Composites Engineering, 1, 4: 249-256.
3. Liu, C. T., 1993." Investigating the Near Tip Behavior and Damage Characteristics in a Particulate Composite Material," ASTM-STP-1189: 668-679.
4. Smith, C. W., Wang, L., Mouille, H., and Liu, C. T., 1993." Near Tip Behavior of Particulate Composite Material Containing Cracks at Ambient and Elevated Temperatures," ASTM-STP-1189: 775-787.

Table I-Summary of Regression analysis

Testing Temperature C^o	Specimen Thickness mm	Log C	B
-53.9	2.54	-13.37	2.91
22.2	2.54	-10.28	2.45
73.9	2.54	-9.33	2.27
-53.9	12.7	-46.23	10.32
22.2	12.7	-20.82	5.72
73.9	12.7	-12.37	3.38

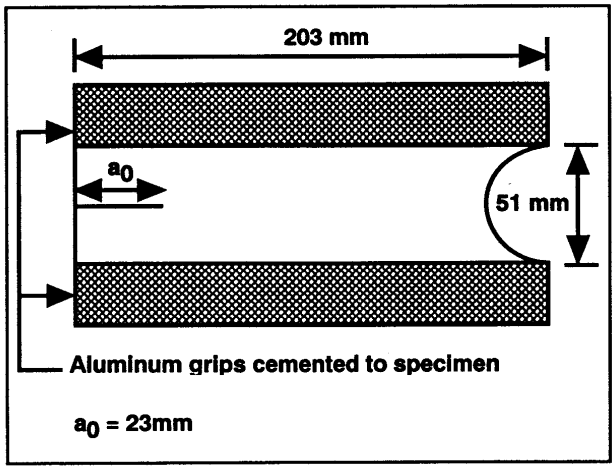

Fig.1 Specimen geometry

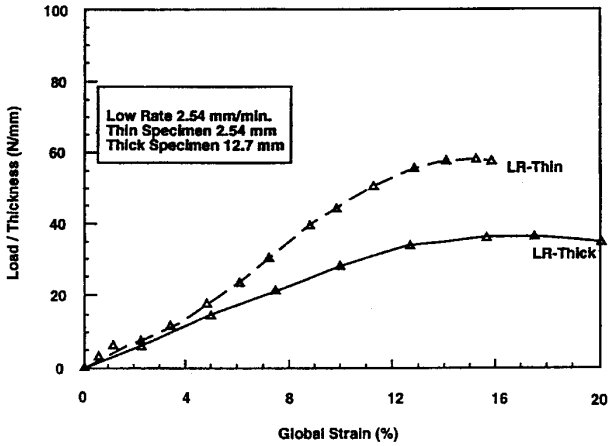

Fig. 2 Load-strain relations (T=73.9°C)

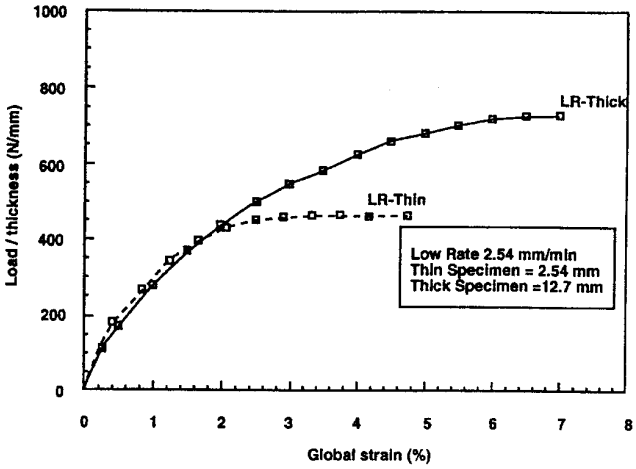

Fig. 3 Load-strain relations (T=-53.9 °C)

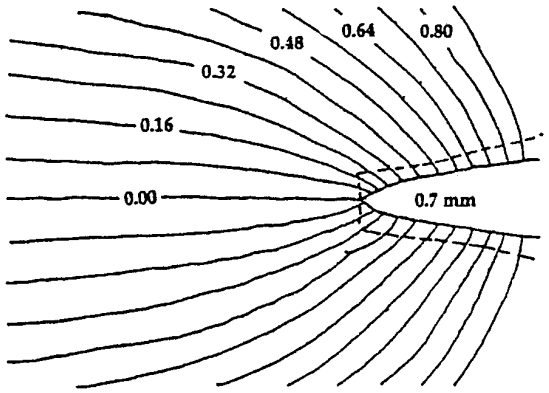

Fig. 4 Typical contour plots of normal displacement (T=-53.9 °C, t=2.54mm)

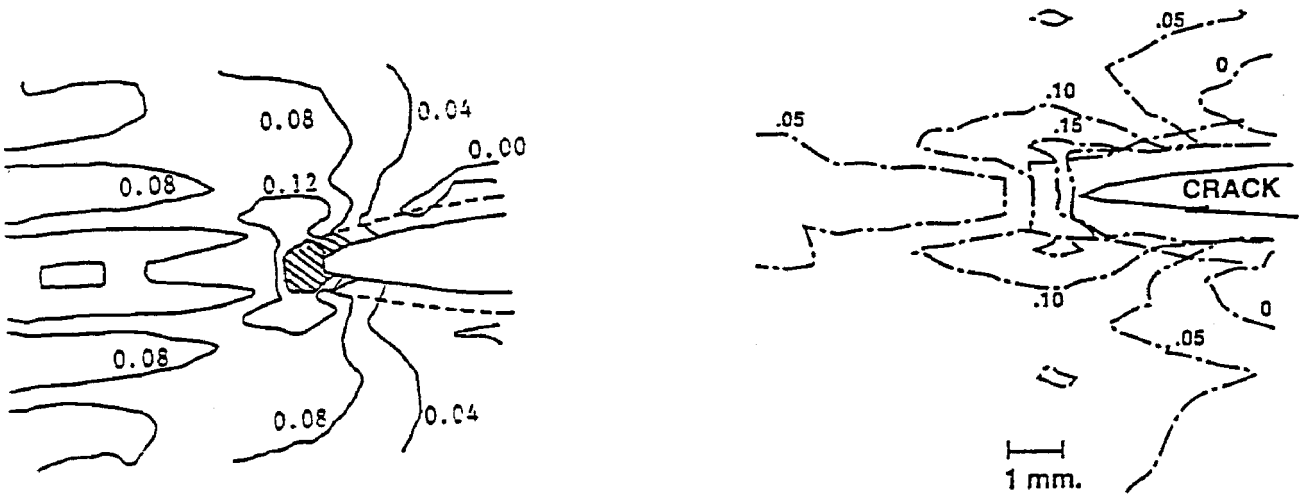

(a) Thickness = 2.54 mm

(b) Thickness = 12.7 mm

Fig. 5 Typical contour plots of normal strain (T=-53.9 °C)

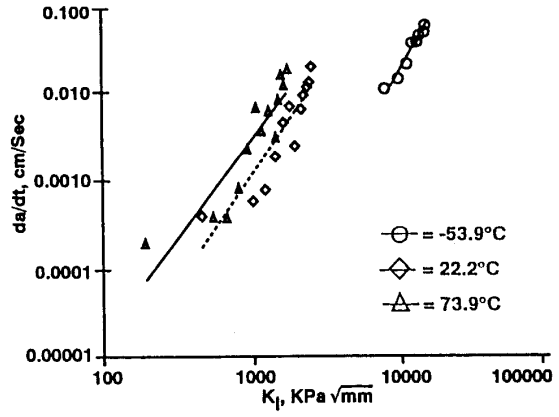

Fig. 6 Crack growth rate versus Mode I stress intensity factor (t=2.54mm).

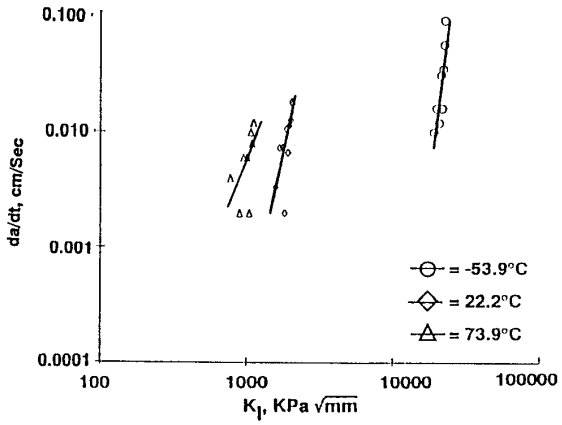

Fig. 7 Crack growth rate versus Mode I stress intensity Factor (t=12.7mm).

NEW CONSIDERATIONS AND RESULTS ON CRACK SEPARATION ENERGY RATES IN ELASTIC-PLASTIC FRACTURE MECHANICS

Y. Wadier and E. Lorentz

EDF, Division of Research and Development,
1, av. du Gal de Gaulle, 92141 Clamart, France

ABSTRACT

The definition of an energy release rate in elastic-plastic fracture mechanics, denoted by G_P, is proposed, and can be related to the parameter G^{Δ} proposed by Kfouri & Miller in 1976. New results obtained with this parameter and new considerations related to the well known « Paradox of Rice » are presented. In particular we find that this parameter is not zero if we consider the case of an elastoplastic material with a linear isotropic hardening. But it is necessary to consider a very fine mesh and very small crack propagations. Some applications are briefly presented in two cases where the J-approach is not valid.

KEYWORDS

Crack separation rate, Energy release rate, J-approach, Energy approach, Rice's paradox

INTRODUCTION

The J-approach is very limited and cannot be applied as soon as the loading become non proportional. It is necessary to develop other approaches as the two parameters approach or the local approach. Our choice is to reconsider the energetic approach where many parameters called « path independent integrals » have been proposed, without any consensus. We recall the definition of an energy rate in an elastoplastic media and we show that in the case of a stationary crack in an elastoplastic material with linear isotropic hardening, this parameter is not zero, in contradiction with the Paradox of Rice. Then it is possible to use it as a fracture parameter, and we will present two applications where the J- approach is not valid : 1/ the first one concerns the problem of unloading, 2/ the second one concerns the problem of the shallow crack effect.

DEFINITION OF AN ENERGY RELEASE RATE IN AN ELASTOPLASTIC MEDIUM

Brittle fracture in an elastic medium

The Griffith's criterion is widely used to predict whether a crack propagates or not in an elastic medium, considering only progressive and continuous crack propagation. But this approach cannot be used to predict crack initiation in a non-cracked medium, or the discontinuous propagation of a crack. This is the reason why Francfort and Marigo [1] have proposed a new theory where these two phenomena can be predicted. In this theory, we consider a discretisation of the load history where the true evolution of the structure during a

load increment is taken into account only through the state of the structure (displacement field *U* and cracks positions *S*) at the beginning and at the end of the load increment. Let's call E the energy defined by :

$$E(U, \Delta S) = E_D(U) + G_c \text{ area}(\Delta S)$$

where E_D is the strain energy, G_c the toughness and ΔS the newly created surface during the load increment, and Francfort and Marigo postulate that *U* and ΔS realise the minimum of E.

At this stage two remarks can be made :

- in case of progressive crack propagation, Griffith criterion can be retrieved by restricting ΔS (Δl in 2D) to a sufficiently small propagation *dS* (*dl* in 2D) and, if W_e is the potential energy of the structure, we can define an energy release rate G_{el} as :

$$G_{el}(dS) = -\frac{W_e(dS) - W_e(\varnothing)}{\text{Aire}(dS)} < G_c$$

- the minimisation principle can be linked to incremental formulations with global internal variables as soon as the first term (elastic energy) along with the kinematic admissibility conditions are identified as the free Helmhotz' energy F and the second term (the energy dissipated when the crack propagates) is identified as the dissipation potential D, see [2].

Brittle fracture in an elastoplastic medium

Exploiting this link, we extend Francfort and Marigo theory in the case of an elastoplastic material by introducing the energetic contribution due to plasticity into the free Helmhotz' energy and the dissipation potential, assuming that fracture mechanisms and plasticity are independent, see [3]. The energy available for propagation is called W, and an energy rate G_P can be defined for a sufficiently small propagation *dS*, as :

$$G_p(dS) = -\frac{W(dS) - W(\varnothing)}{\text{Aire}(dS)} < G_c$$

The G^{Δ} parameter proposed by Kfouri-Miller

The G_P parameter represents the energy available in the structure to obtain a *dS* propagation, divided by *dS*. In 1966, Rice considered a continuously growing crack in an elastoplastic material where the flow strength saturates to a finite value at large strain, and demonstrated that this value must be zero, see [4]. This is the « Paradox of Rice ». This result cannot be applied to a stationary crack or to a non bounded flow strength material, but in 1976, Kfouri and Miller, see [5], considered this case and they found a result in agreement with the Paradox of Rice. They proposed a parameter called G^{Δ} defined as $\Delta W/\Delta a$, ΔW being the work released during a small amount Δa of the crack, and found : G^{Δ} equal 0 when Δa goes to zero. Although the G_P definition is more general, it can be proved that in the case of a 2D elastoplastic media and for a sufficiently small propagation Δa, G_P is equal to G^{Δ}. In 1977, Rice used this result to generalise his paradox, see [6], and now it seems that it is a general and well accepted result. Nevertheless, if we reconsider it 25 years after, the numerical aspects of the modelisation used by Kfouri and Miller seem to be insufficient.

ANALYSIS OF THE G_P DEPENDANCE WITH RESPECT TO Δl

Definition of the problem

Let us consider a Centered Cracked Plate submitted to an increasing loading in mode I. The data related to geometry and material are presented on **Fig. 1**, and the mesh and a zoom of the mesh on the crack tip area are presented on **Fig. 2** and **3**. Due to symmetries only a quarter of the structure is represented, and the plane strain hypothesis is assumed. Different values of the size « Δl » of the element located at the crack tip and corresponding to different meshes are investigated as follows :

- M1 : mesh for $\Delta l = 0.0500$ mm, M2 : mesh for $\Delta l = 0.0125$ mm,
- M3 : mesh for $\Delta l = 0.0062$ mm, M4 : mesh for $\Delta l = 0.0025$ mm,
- M5 : mesh for $\Delta l = 0.0012$ mm

We consider 2 values (one low value, one high value) for the maximum loading :

- $U_{max} = 0.016$ mm and : $U_{max} = 0.100$ mm

For each loading and for each mesh we make the computation in 10 steps. After that and for each step, one element is released to obtain the propagation of the crack.

$E = 200\,000$ MPa $\quad \nu = 0,3$

$\sigma^y = 480$ MPa $\quad h = 5\,000$ MPa

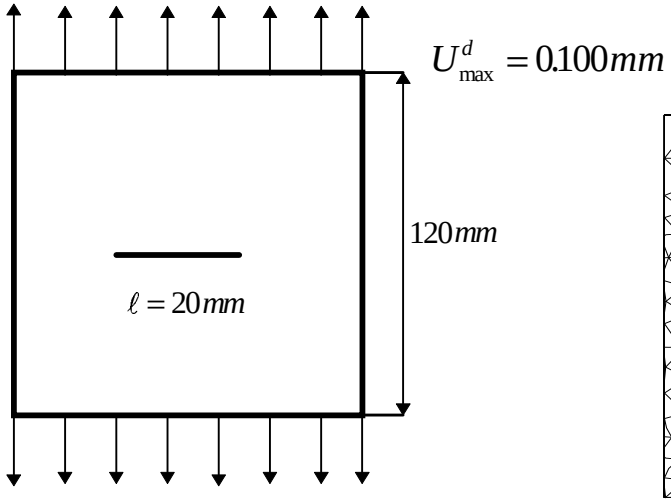

FIG. 1 - Geometry, material

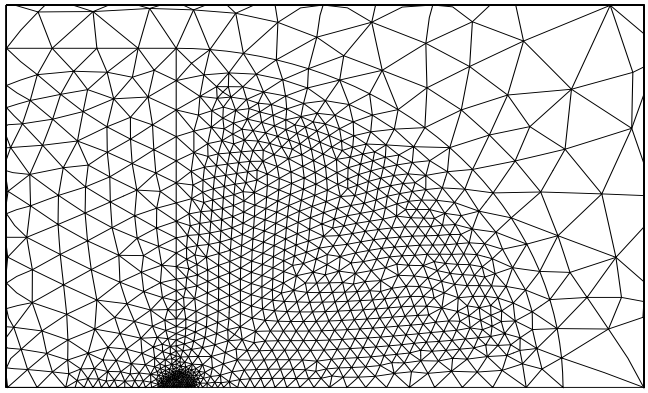

FIG. 2 - Zoom of the mesh in the crack tip area

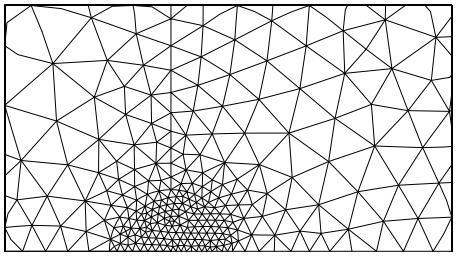

FIG. 3 - Zoom of the mesh near the crack tip

Results obtained

On **Fig. 4** the variation of G_P as a function of the loading is presented for the 4 meshes M2, M3, M4 and M5 and for the applied loading corresponding to the largest maximum value : Ud = 0.100 mm. We can see that the G_P value steadily increases while the loading is increasing, and that the values obtained for the 4 meshes seem to converge to a non zero value. In fact the curve obtained with the mesh M5 is very close to the curve extrapolated with all the results in order to obtain the result corresponding to Δl equal 0.

On **Fig. 5** the variation of G_P as a function of the loading is presented for the 4 meshes M2, M3, M4 and M5 and for the applied loading corresponding to the smallest maximum value : Ud = 0.016 mm. We can see that the G_P value steadily increases while the loading is increasing, but that the values obtained for the 4 meshes are mesh dependent (or Δl dependent) and seem to converge to a zero value.

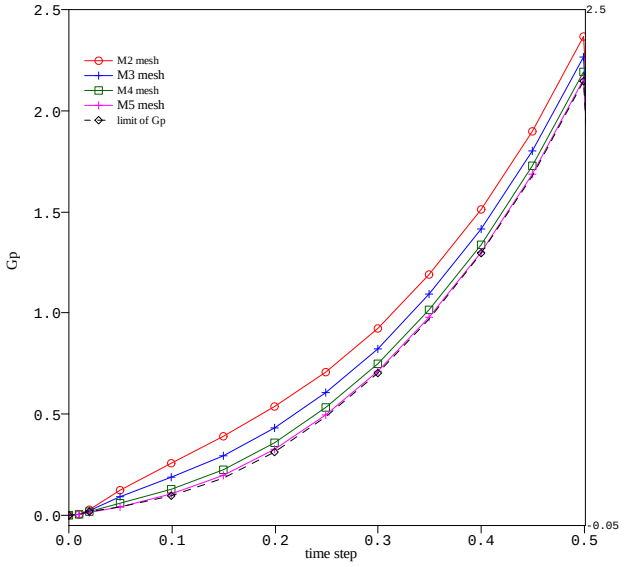

FIG. 4 - Results for different meshes : U = 0.100 mm

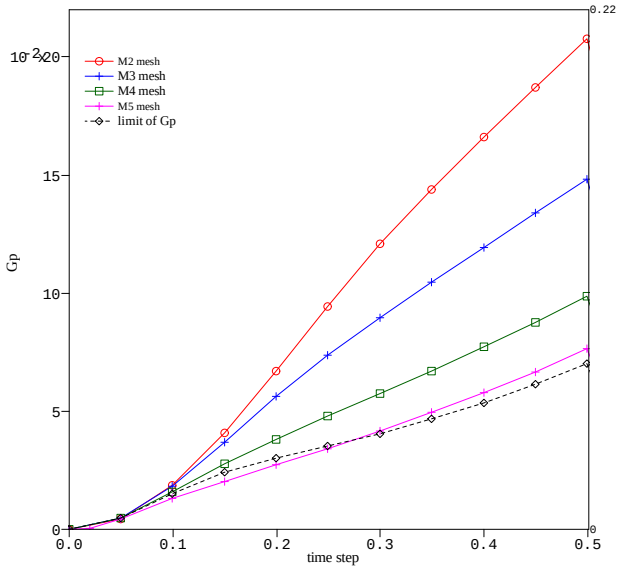

FIG. 5 - Results for different meshes : U = 0.016 mm

Explanation : a very important parameter has to be defined in order to understand these results : Np = Rp/Δl (Rp being the radius of the plastic zone). Obviously, the value of this parameter must be sufficiently high, and because the radius Rp is increasing from zero with the loading, it will be impossible to obtain a precise result on G_P if the loading is very low. That means that the value of Δl (even very low but fixed), will always be too high compared to the loading or to the radius Rp. We can verify this point on **Fig. 6** (zoom of **Fig. 5** for very low loading) where the different curves « Numerical G_P » are distributed, with respect to Δl, between the low curve « Theoretical G_P » (low, but not zero) and the high curve « G-elastic (or J) ». These curves are located in a very large area and we can conclude that the result obtained for a very low loading cannot be precise. We will always have an apparent dependence of the result with respect to Δl. Of course if the loading is higher, this phenomenon disappears and a precise result can be obtained. But for that it is necessary to consider a very fine mesh with very low values of Δl.

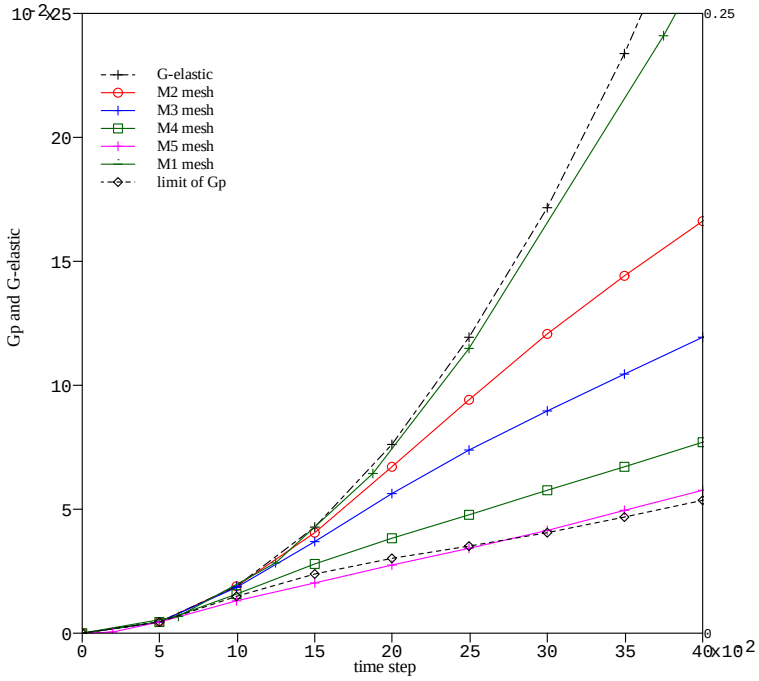

FIG. 6 - Zoom of figure 5

TWO APPLICATIONS WHERE THE J-APPROACH IS NOT VALID

The case of a structure submitted to loading and unloading

Let us consider again the case of the Centred Cracked Plate. Now it is submitted to a loading that is first increasing and then decreasing to zero. As soon as the loading decreases, it becomes non proportional, and the J-approach cannot be applied. On **Fig. 7** the variation of G_P, as a function of the loading, is presented for the applied loading corresponding to different maximum values of the loading. We can see that the G_P value steadily increases while the loading is increasing, and afterwards this value falls down suddenly to zero while the loading is decreasing. Then the G_P value stabilises at this zero value corresponding to the « closure » of the crack tip, when unilateral conditions are taken into account.

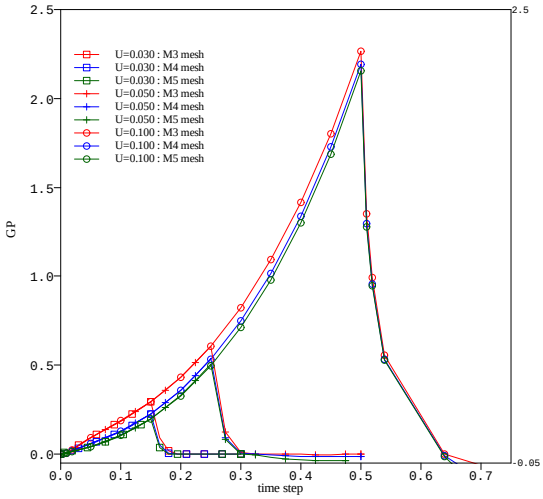

FIG. 7 - Increasing and decreasing of Gp as function of the loading

The variation of the G_P parameter during unloading is very interesting and it is possible to take advantage of that. Indeed, $G_P = 0$ means that there is no energy available in the structure to make the crack propagate. So the conclusion is that in such a case the initiation of the crack is impossible.

The case of the shallow crack effect

The toughness of a material is determined from a test on a CT specimen with a large crack. If we carry out another test on the same material but on a different specimen with a small crack, we find that the toughness is much higher. This is called « the shallow crack effect », and we would like to apply the G_P parameter to the interpretation of this effect. For that, let us consider two SENB specimens with different crack lengths.

Definition of the problem : 1/ Geometries of the SENB : Width : W = 50.mm, Height : H = 420.mm, Length of the crack A : A/W = 0.5 for the large crack, A/W = 0.05 for the small crack. 2/ Material of the SENB : the specimens are made in an A508 forging steel, Young modulus : E = 173528 MPa, Poisson's ratio : $\nu = 0.3$, Yield limit : $\sigma y = 617.8$ MPa, Hardening modulus : H = 1922.6 MPa. The toughness corresponds to a critical value of J, Jc = 42.kN/m in the case of A/W = 0.5 and to Jc = 88.kN/m in the case of A/W = 0.05. Plane strain hypothesis is assumed, and, due to symmetries, only one half of the structure is represented. The different meshes are equivalent to those presented for the CCP specimen.

Results obtained : On **Fig. 8** the variation of J as a function of G_P is presented for the two specimens. We can see that the two curves are very close. So, we can conclude that the G_P parameter seems to be equivalent to J, that is to say it is not able to predict the shallow crack effect. But, as we observe a sudden crack propagation (cleavage fracture), we are now looking at the G^{Δ} value, for finite values of Δl. On **Fig. 9** the variation of J as a function of G^{Δ} is presented for the two specimens, only in the case $\Delta l = 0.200$ mm, representative of the effect obtained for large values of Δl. We can see that the curve corresponding to A/W = 0.05 is higher than the curve corresponding to A/W = 0.5. The value : Jc(A/W=0.5) = 42.kN/m, corresponds to the value G^{Δ} = 10.5 kN/m, and to the value Jc(A/W=0.05) = 75. kN/m (to be compared to 88. kN/m). Therefore we can conclude that the G^{Δ} parameter seems to be able to predict the shallow crack effect.

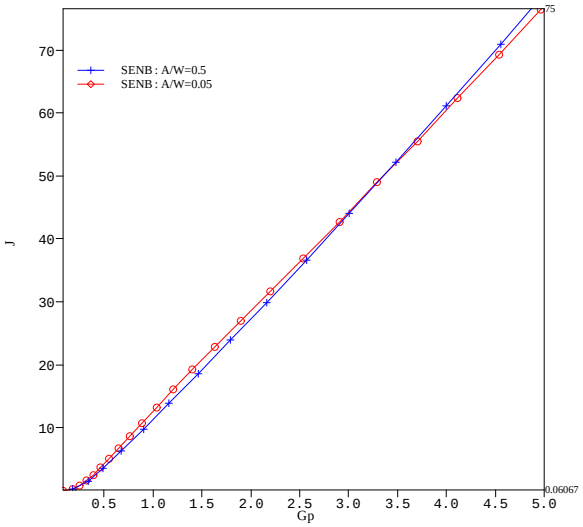

FIG. 8 - J as function of the Gp parameter

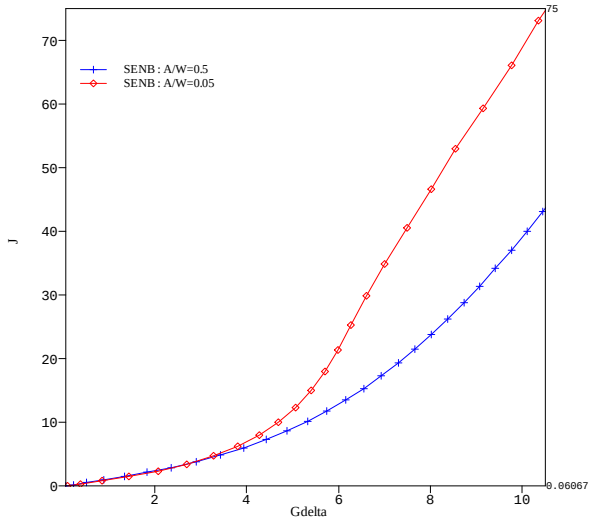

FIG. 9 - J as function of G^{Δ} ($\Delta l = 0.2$ mm)

CONCLUSION

An energy release rate G_P has been defined for an elastoplastic material, starting from the elastic fracture theory of Francfort and Marigo. This parameter can be related to the parameter proposed by Kfouri and Miller in 1976. Considering a stationary crack in an elastoplastic material with linear and isotropic hardening, we have obtained the following new results :

- the G_P values are increasing with the loading and if we consider the results obtained for high values of the applied loading, the G_P values tend clearly to a finite value when Δl goes to zero,
- if we consider the results obtained for very low values of the applied loading, these results are necessary mesh dependent, or Δl dependent, and it seems that these values tend to zero when Δl goes to zero,
- this apparent dependence could be explained if we consider the parameter Rp/ Δl corresponding to the mesh refinement in the plastic zone area, which must be sufficiently high,
- the G_P parameter can be used to analyse the case of a structure submitted to a loading that is first increasing and then decreasing ; in particular when $G_P = 0$, the initiation of the crack is impossible,
- an analysis of the shallow crack effect reveals that the G_P parameter is equivalent to J, and cannot explain this effect, but the G^{Δ} parameter corresponding to large crack propagation ($\Delta l > 0.2$ mm) gives a result in agreement with the experimental one.

References

[1] Francfort G. and Marigo. J.J. (1998), Revisiting brittle fracture as an energy minimisation problem. J. Mech. Phys. Sol., 46, no 8, pp. 1319-1342.

[2] Lorentz E. and Andrieux S. (1999), A variational formulation for nonlocal damage models. Int. J. Plast., 15 , pp. 119-138.

[3] Lorentz E., Wadier Y., Debruyne G. (2000), Mécanique de la rupture en présence de plasticité : définition d'un taux de restitution d'énergie. C.R.A.S. t. 328, série IIb.

[4] Rice J. R. (1966), An examination of the fracture mechanics energy balance from the point of view of continuum mechanics. Proc. 1st Int. Conf. Fracture, vol. 1, Sendai, Japan, ed. Yokobori et al., Japanese society for strength and fracture of materials, pp. 309-340.

[5] A.P. Kfouri and K.J. Miller (1976), Crack separation energy rate for crack advance in elastic-plastic fracture mechanics, Proc. Inst. Mech. Engrs. 190.

[6] A.P. Kfouri and J.R. Rice (1977), Elastic/plastic separation energy rate for crack advance in finite growth steps. in Fracture 1977, D.M.R. Taplin, Vol. 1, Univ. Waterloo Press.

ORAL REFERENCE: 822

NEW TYPE STEEL HAVING SUPERIOR BRITTLE CRACK ARRESTABILITY AND ITS APPLICATION TO IMPROVE STRUCTURAL INTEGRITY

T. Ishikawa[1], T. Inoue[1], Y. Hagiwara[1] and H. Yajima[2]

[1] Steel Research Laboratories, Nippon Steel Corporation,
Shintomo, Futtsu, Chiba, 293-8511 JAPAN
[2] Nagasaki Institute of Applied Science, Amiba, Nagasaki, 851-0193, JAPAN

ABSTRACT

Studies on the crack arrestability of steel have revealed that the shear lips formed at the surface of steel when brittle cracks propagate offer great resistance to the further propagation of these cracks. This knowledge led to the development of steel (SUF steel) having ultra fine grains at the surface and in the subsurface region (surface layers) that promote the formation of shear lips. Plates of SUF steel have extremely high crack arrestability and do not require any special alloy additions. It is expected that the use of such plates for ship structures will remarkably increase the structural integrity.
In this paper, new type steel plate having extremely high crack arrestability is introduced. Large-scale fracture model tests were conducted to determine the effect of the use of SUF steel plates in a ship structure as a crack arrestor. Furthermore, required value of crack arrestability to prevent long brittle crack propagation is discussed.

KEYWORDS

Brittle fracture, Crack propagation, Steel, Ship, Structure integrity, Crack arrest, Cleavage fracture

INTRODUCTION

Brittle fracture is one of the major causes of serious damage to structures, such as ships, when they have an accident. Damage increases vastly if brittle fracture occurs and propagates as a result of such disasters as collisions and groundings of ships, although the number of ship accidents due to brittle fracture has recently been reduced greatly. Such catastrophic expansion can be averted by preventing the propagation of brittle cracks. Therefore, the structural integrity of ships will be increased by the use of steel having a property to prevent the propagation and expansion of brittle fracture that might result from disasters (i.e., crack arrestability) for important members of structures.
In this paper, new type steel plate having extremely high crack arrestability is introduced and required crack arrestability to prevent large scale fracture is discussed.

CONCEPT OF IMPROVING CRACK ARRESTABILITY

Figure 1 shows the controlling factors for crack arrestability. Nickel-containing steel plates are used for applications requiring high crack arrestability. Grain refining technique has also been investigated to improve crack arrestability without adding special alloy elements. TMCP process has provied steel plates with fine grain microstructures. Further effective technologies to improve crack arrestability were derived from the mechanisms of unstable brittle crack propagating behavior. The effect of shear-lips on crack propagation behavior is one of the major factors to improve crack arrestability [1]. Shear lips are formed in the surface regions of steel plate when brittle cracks propagate. They can offer great resistance to the further propagation of these cracks. This knowledge led to the development of the new type steel plate, SUF steel (steel having Surface layers with Ultra-Fine grain microstructures) [2]. Shear lips are developed in the ultra-fine-grained layer region when brittle cracks propagate. Because the plastic deformation and ductile fracture, which accompany with shear-lips, prevent the propagation of brittle cracks, SUF steel plates have excellent crack arrestability.

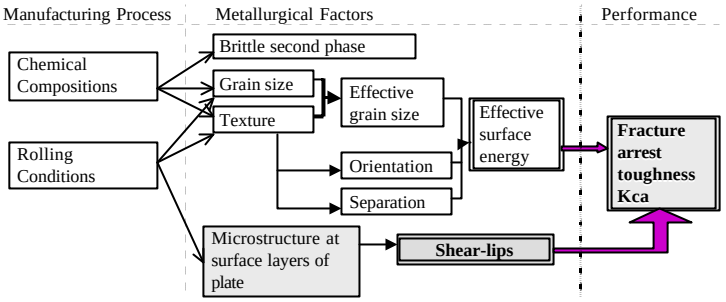

Figure.1: Controlling factors of brittle unstable crack arrest toughness

SUF STEEL PLATE

Figure 2 shows the macrostructure of the SUF steel plate together with the microstructures of the surface layers and midsection regions. The ultra-fine-grained region is the black layer observed at the surface of the steel plate, as shown in Fig.2. The average value of grain sizes in the surface layers is less than two micrometers. The distribution of the average grain size in the thickness-direction is also shown in Fig. 2. In the surface layer, the grain sizes are relatively homogeneous. The grain size changes significantly at the border of the surface layers and the mid-thickness of the plate. Charpy impact test results for SUF region suggested that remarkably lower brittle-ductile transition temperature is obtained in 'SUF' than in mid-thickness', although the chemical composition of the SUF steel plate is the same as that of ordinary steel plates without any special alloy elements. The tensile strength of the SUF steel plate is comparable to that of the 490 N/mm^2 class steel. Mechanical properties and welding performance of SUF steel satisfy the requirements of KE36 (EH36) class steel according to the NK (IACS) standard [3].

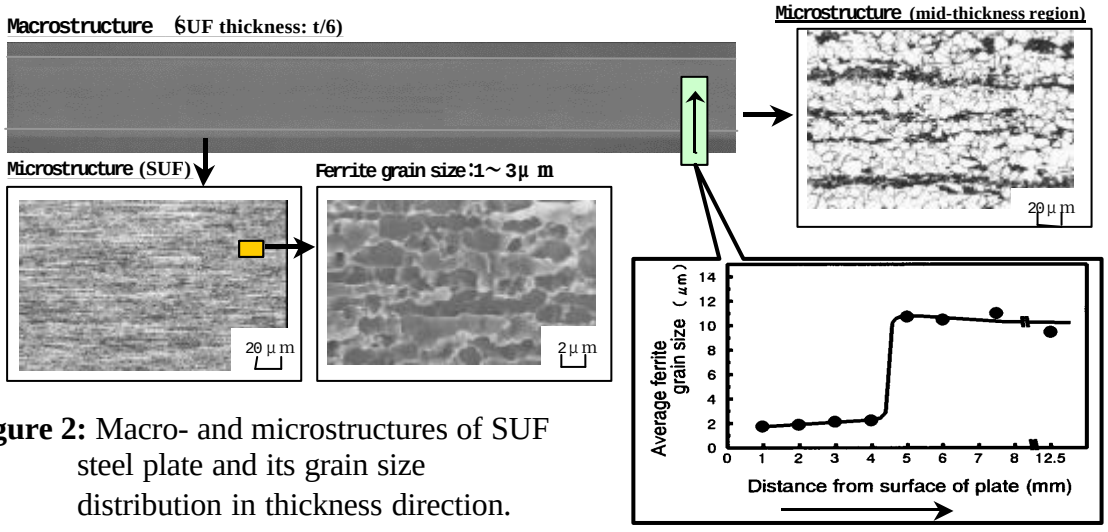

Figure 2: Macro- and microstructures of SUF steel plate and its grain size distribution in thickness direction.

CRACK ARREST TESTING AND RESULTS

Standard ESSO test

The standard temperature-gradient ESSO test was conducted to evaluate the crack-arrest toughness, the critical stress intensity factor for stopping the crack: Kca, of SUF steel and conventional EH36 steel. Figure 3 shows the fracture surface of the SUF steel plate used for the temperature gradient type ESSO test which evaluates crack arrestabilty. The inside of the plate was fractured brittlely, while the surface regions of the plate were not fractured brittlely but ductilely. The surface regions fractured ductilely with plastic deformation are called shear-lips, and these have a braking effect on unstable brittle crack propagation and further enhance the crack arrestability of the steel plate.

The results of standard ESSO test for SUF steel plate and of conventional steel plate (EH36 steel plate) are shown in Fig. 4. Both plates have equivalent chemical composition and the same 25mm thickness. Furthermore, the crack arrestability of the steel plates subjected to a plastic tensile strain of approximately 10% [4] was evaluated. It is clear from Fig. 4 that plastic pre-straining deteriorates crack arrestability. For the EH36 steel plate, the temperature indicating Kca=4000 N/mm$^{1.5}$ is about -40°C when plastic pre-straining is not given, however, the temperature rises to above 0°C when a 10% plastic tensile strain is given. On the other hand, although crack arrestability of SUF steel plate is also impaired by plastic pre-straining, SUF steel plate with 10% plastic tensile strain has higher crack arrest toughness (Kca) than that of EH36 steel plate without plastic pre-straining.

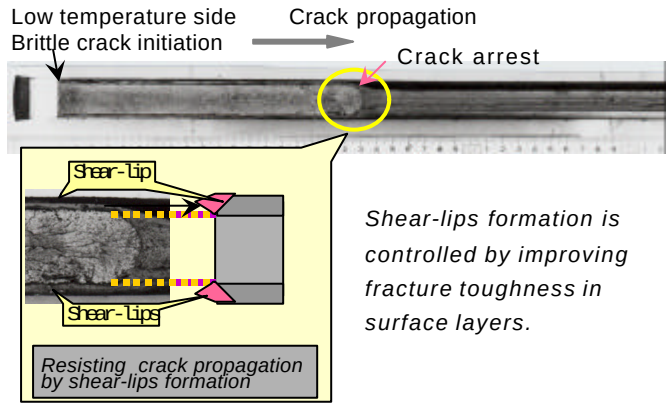

Figure 3: Fracture surface of standard ESSO test specimen for SUF steel plate

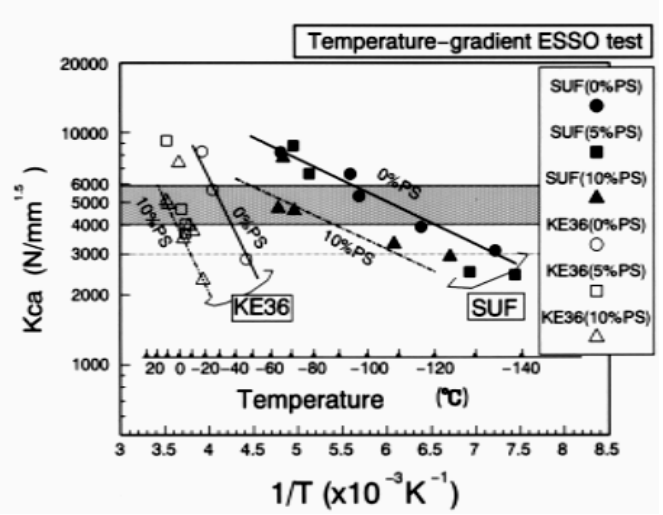

Figure 4: Results of temperature gradient type ESSO tests s

Effect of shear lips in improving crack arrest toughness

To confirm experimentally the effect of shear lips developed in the SUF region in improving the crack arresting performane of SUF steel plate, specimens of SUF steel plate were removed of the SUF portion by griding, and the Kca was evaluated by standard temperature-gradient type ESSO test. The ESSO test results of SUF steel plate specimens with the SUF retained on both sides (with SUF), with the SUF removed from one side (with 0ne-side UF), and with the SUF removed from both sides (without SUF) are plotted in Fig. 5. The chain linen in Fig. 5 shows the presumed Kca values of SUF steel plate calculated by adding the effect of shear lips in improving the Kca value as estimated by the Kraft model [5] to the Kca value of the specimens without SUF. The presumed Kca values of the specimens with one-side SUF are indicated by the dotted line in Fig. 5. The effect of shear lips in the SUF region can be explained fairly well by these rough approximations.

Ultra-wide plate duplex ESSO test

Crack arrestability against a large scale unstable brittle crack propagating at great speed was verified with the ultrawide plate duplex type ESSO test specimen shown in Fig. 6(a),. A conventional EH36 steel plate was used as an approach-plate through which the unstable brittle crack propagated, the SUF steel plate was used as the test plate. Figure 6(b) shows the appearance of the test specimen immediately after the test and the fracture surface. It was observed in this test that when the unstable brittle crack which had propagated through the EH36 steel plate reached the SUF steel plate, the unstable brittle crack was immediately arrested by the formation of shear-lips.

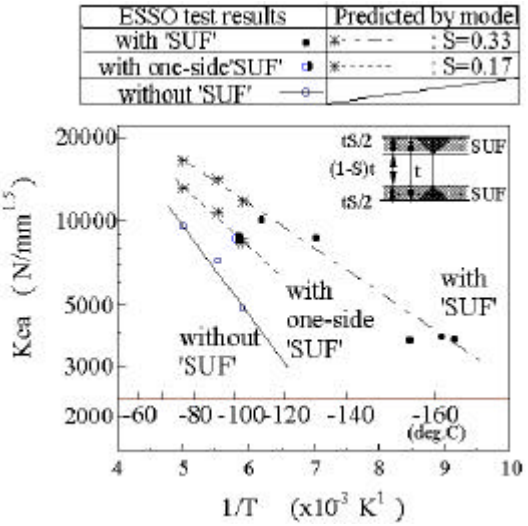

Figure 5: Effect of SUF on Kca

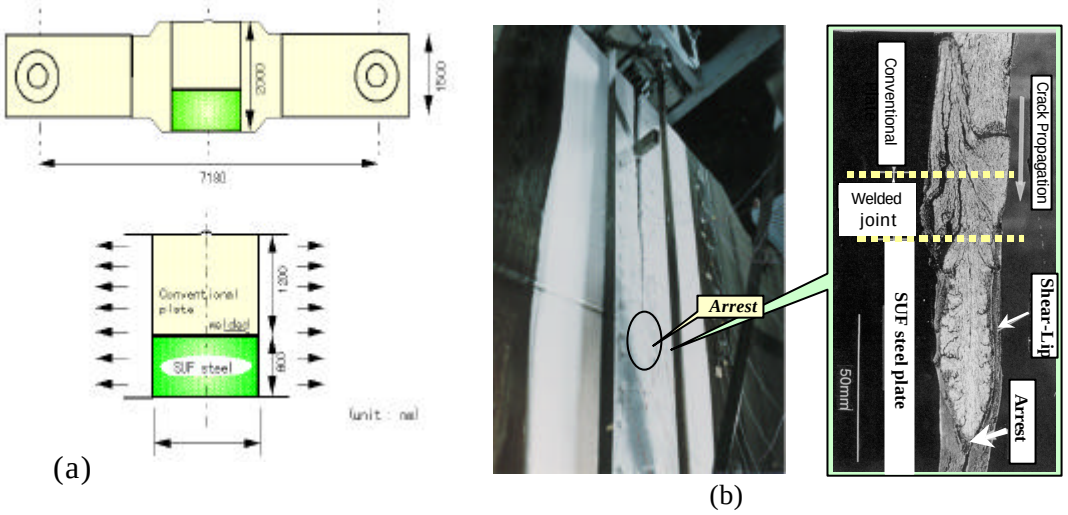

Figure 6: Ultra wide plate duplex ESSO test of SUF steel plate and its fracture surface.

REQUIRED Kca VALUE TO ARREST LARGE SCALE FRACTURE

When the crack length increases, the crack tip stress intensity factor (K) is reported to tend to saturate at a certain value of Keff (effective K) and not to reach the value of $K=\sigma\sqrt{(\pi a)}$ (which is calculated by linear fracture mechanics) [6]. One of the reasons is that the size of the plastic region formed at the crack tip is limited under its propagation. Then, a running brittle crack can be arrested if the following equation is satisfied: $Keff \leqq Kca$. However, it is not easy to calculate the Keff value since many factors like the dynamic effect of crack are involved. Therefore, the brittle crack arrest toughness required for the arrest of long cracks has been experimentally studied using large-scale crack arrest test.

Figure 7 shows the results of large-scale crack arrest test (ultra wide-plate duplex ESSO test) conducted with higher-strength hull structural steel plates (Grade EH36) generally used as materials of crack arrestor for ships [7]. In this figure, the brittle crack arrest toughness (Kca value) was obtained from standard test (temperature-gradient type standard ESSO test or double-tension test with a specimen width of 400 to 500 mm and a crack propagation region width of 150 to 250 mm) with relatively small effects on crack size and dynamic phenomenon.

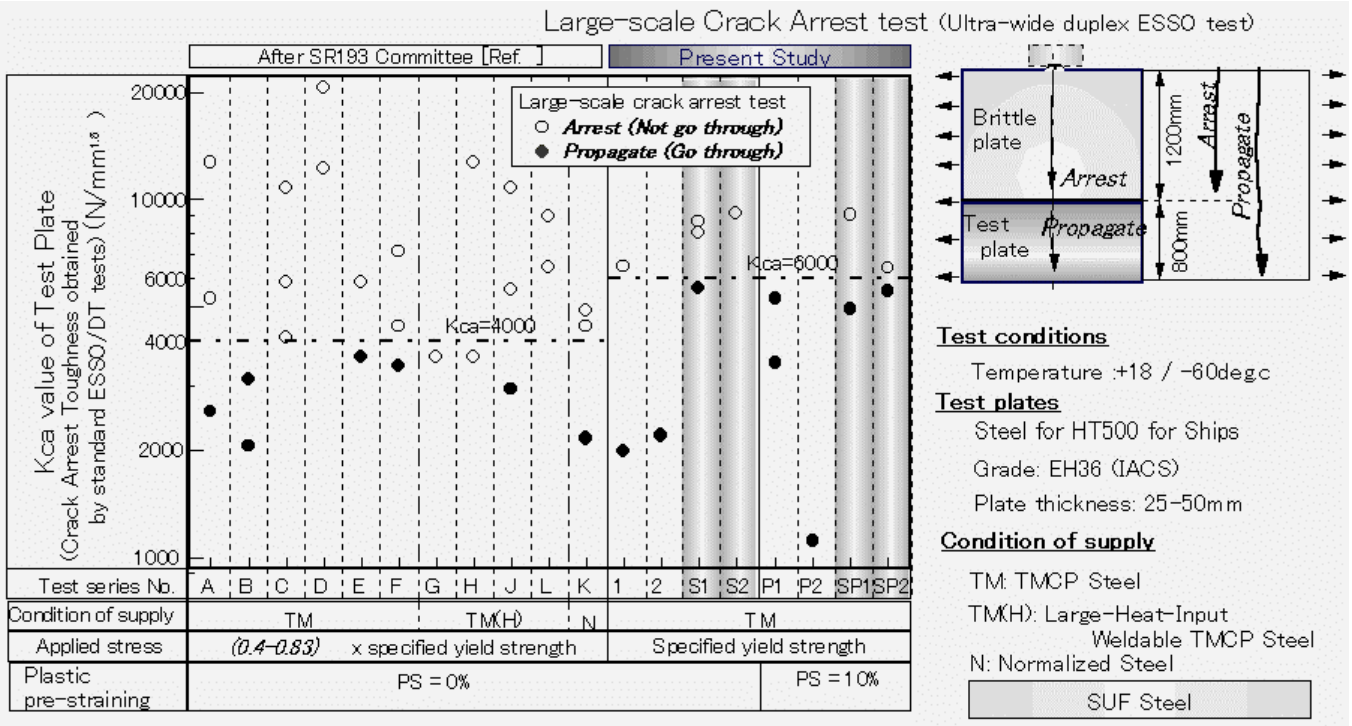

Figure 7: Results on large-scale fracture test, together with the results obtained by SR193 committee [7]

The study on crack arrestor by Dr. Kanazawa et al. [6], and the analysis reports on brittle fractures in actual ships [8] confirm that the propagation of long cracks can be arrested if the Kca value of the above standard test is 4000 to 6000 N/mm$^{1.5}$ or more. It is suggested that these research results approximately agree with the test results shown in Fig. 7.

In case of accidental conditions such as collision or grounding, where large plastic deformation is accompanied, the structure members seem to be subjected to the amount of plastic strain of 5 to 10 %, and to be loaded up to yield strength. Even in such situation, if Kca at design temperature is larger than 6000 N/mm$^{1.5}$, it is expected that crack propagation can be arrested.

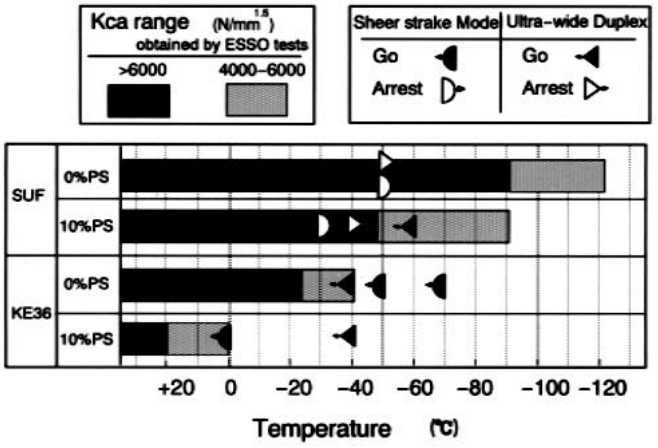

Figure 8: Summary of crack arrest arrestability for SUF steel plate and EH36 for reference.

The temperature regions where the SUF steel plate can maintain its crack arresting performance are shown in Fig. 8. The temperature region where the Kca value of the specimens obtained by the temperature-gradient ESSO test is not less than 6000 N/mm$^{1.5}$ is shaded dark. The temperature region where the Kca is 4000 to 6000 N/mm$^{1.5}$ is shaded light. The ultra-wide duplex ESSO test results and the large scale sheerstrake model fracture test results [3] are denoted by marks indicating "go (crack propagated)" and "arrest (crack arrested)" for specific temperatures. The lower limit temperature at which Kca = 6,000 N/mm$^{1.5}$ can be achieved is about 70 deg.C lower for the SUF steel than for the conventional EH36 steel. A plastic strain of 10% shifts the crack arrest performance of

both SUF and conventional EH36 steels by about 40 deg.C toward the high end of the test temperature range. The lower limit temperature at which Kca is about 6,000 $N/mm^{1.5}$ is -50 deg.C for the SUF steel and about +15 deg.C for the EH36 steel. Therefore, SUF steel plate can be expected to be fully able to arrest long cracks when applied to ships operating in seas at the lowest temperature of 0 deg.C even under accidental conditions.

APPLICATION

SUF steel plates or equivalents, which have sufficient crack arrestability ($Kca \geqq 6000$ $N/mm^{1.5}$) at the lowest service temperature even when 10% plastic strain is imposed, are authorized as high crack arrestability steel plates, and it has been decided to give the optional class-notation 'Higher crack arrestor' to ships in which these steel plates are used for important members [9]. SUF steel plates were applied for an LPG carrier for the first time in 1995, and for a bulk carrier in 1996, a tip carrier, a coal carrier and so on . The application of the SUF steel plate in large-scale steel structures requiring safety against brittle fracture, such as earthquake-resistant high-rise buildings and offshore structures, will contribute to higher structural integrity and the prevention of environmental problems such as tanker oil spills.

CONCLUSIONS

Focusing on that the shear lips formed at the surface of steel when brittle cracks propagate offer great resistance to the further propagation of these cracks, SUF steel plate having ultra fine grains in the surface layers has been developed. Large-scale fracture model tests were conducted to determine the effect of the use of SUF steel plates in a ship structure as a crack arrestor. It is expected that crack propagation can be arrested if Kca at design temperature is larger than 6000 $N/mm^{1.5}$, even in case of accidental conditions, where the structure members seem to be subjected to the amount of plastic strain of 10 %.

REFEERENCES

1. Machida,S., Yoshinari, H., Miyahara, T., and Nishiyama, G., Journal of The Society of Naval Architects of Japan, Vol.156, (1989).
2. Ishikawa, T., Nomiyama, Y., Hagiwara,Y., Yoshikawa, H, Oshita, S., and Mabuchi, H., Proceedings of the 14th International Conference on Offshore Mechanics and Arctic Engineering, Vol.3, 1995, p.357.
3. Ishikawa, T., Imai, S., Inoe, T., Watanabe, K., Tada, M., and Hashimoto, K., Proceedings of the 16th International Conference on Offshore Mechanics and Arctic Engineering, Paper No. 97-713.
4. Ishikawa, T., Hagiwara, Y., Oshita, S., Inoue, T., Hashimoto, K., Kuroiwa, T., Tada, M., and Yajima, H., Proceedings of the 15th International Conference on Offshore Mechanics and Arctic Engineering, Vol.3, 1996, p.183.
5. Kraft, J.M., Sullivan, A.M., and Boyle, R.W., Proc. Symp. Crack Propagation, Cranfield, 8 (1961).
6. Kanazawa, T., Machida, S., Yajima, H., Aoki, M., Journal of The Society of Naval Architects of Japan, Vol.11 Selected paper, 1973.
7. The 193rd Research Committee of The Shipbuilding Research Association of Japan, No.100, Vol.152 (in Japanese).
8. Yajima, H., and Kawano, H., Welding Research Committee, The Society of Naval Architects of Japan, May 1982.
9. Nishimura, M., Matsumoto, T., Kitada, H., Akiyama, H.,and Nomura, D., Proceedings of the 16th International Conference on Offshore Mechanics and Arctic Engineering, Paper No.97-712 (1997).

ORAL REFERENCE: ICF1001012

Non-contact Detection of Delamination in Impacted Cross-ply CFRP Using Laser Generated Lamb Waves

Y. Mizutani[1], H. Nishino[1], M. Takemoto[1] and K. Ono[2]

[1]Faculty of Science and Engineering, Aoyama Gakuin Univ. Tokyo, 157-8572, JAPAN
[2]Department of Materials Science and Engineering, UCLA, Los Angeles, CA 90095-1595, USA.

ABSTRACT

Structures of Carbon Fiber Reinforced Plastics (CFRPs) tend to suffer serious internal damage when they are impacted by flying objects. The damage significantly reduces the residual strength of CFRP plates and an advanced nondestructive inspection system is needed for maintenance. The aim of this study is to develop such a system for damaged CFRPs by using laser surface acoustic waves (SAWs). SAWs are generated by a Q-switched pulse YAG laser and detected by a heterodyne-type laser interferometer without contact. Both lasers scanned on the surface of damaged CFRPs. Distance between the incident and probe laser was 10 to 100 mm. Delamination shapes were revealed by comparing the similarity of SAWs and wavelet coefficients calculated from detected waves over sound and damaged zone. Internal damage was clearly detected by taking a cross-correlation factor of a wavelet images for a small specimen. Amplitudes of 250kHz wavelet coefficients are used for inspecting a large specimen.

KEYWORDS

CFRP, impact, internal damage, non-contact inspection, laser ultrasonic, surface acoustic wave, cross-correlation, wavelet analysis

INTRODUCTION

Carbon-fiber reinforced plastics (CFRPs) are widely used in transportation equipment due to their high specific strength and stiffness. Upon impact of even moderate energy, CFRPs are likely to suffer internal damages, and the damages significantly reduce the residual compressive strength. The thorough inspection of damage shape is important for aviation equipment.

In this study, we develop a non-contact damage inspection system by utilizing a laser ultrasonic system. Usefulness of laser-based ultrasonics for monitoring internal damage in thick composite members was demonstrated by Anastasi et al. [1]. In their report, ultrasonic waves generated by Q-switched YAG laser were detected by a Fabry-Perot laser interferometer, and used for evaluating impact damage and skin/stiffener interlaminar failure by using the time-of-flight scheme of bulk wave. This is basically a pulse-echo method, and requires a long inspection time. In our inspection system, SAWs can cover over a large distance. We utilized directional SAWs generated by a line-focused pulse YAG laser. Delamination in impacted cross-ply CFRP plates was detected using the similarity coefficients of monitored waveforms over damaged and non-damaged areas.

SPECIMENS AND EXPERIMENTAL SETUP

Two types of $[0^o_6/90^o_6]_{sym.}$ cross-ply CFRP plates were prepared, i.e., 90 mm square (called as a small specimen) and 185 mm square (a large specimen) plates. Small specimens were firmly held by steel flanges of 61-mm diameters, and impacted by a 30-m/s steel ball (7mm) at the front center . The large specimen was firmly clamped between flanges of 160-mm diameter and the center was quasi-statically loaded via steel ball (7mm). Load of 440 N was applied (with the deflection of 1.62 mm).

We first examined local damages by using a ultrasonic C-scan flaw-detection system (Hitachi AT-5000) from the back (layer 3) of the specimens. It was operated in the pulse-echo mode at 25 MHz using a focusing transducer of 8-mm diameter with a 10-mm focal distance. Ultrasonic C-scan method revealed double-tree-shaped delamination (50-mm-long for the small and 19-mm-long for the large specimen) between layers 2 and 3.

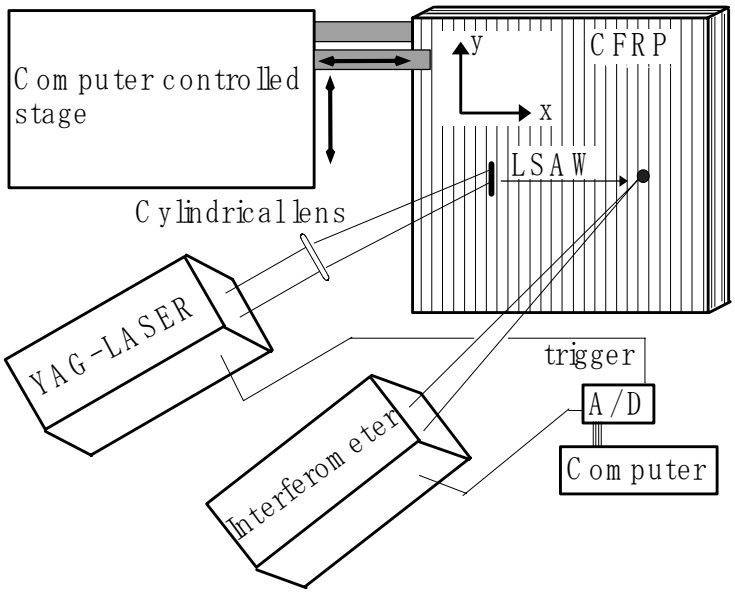

Figure 1: Non-contact impact damage inspection system by using LSAWs.

Figure 1 schematically illustrates the Laser SAW inspection system. The line-focused (0.04mm width and 4mm length) pulse YAG laser beam (half-value duration of 5ns) was irradiated on a surface of the impacted CFRPs. The SAWs are excited by an adiabatic thermal expansion of the surface at the focusing point. SAWs are monitored by a point-focused heterodyne laser interferometer at the distances of 10 mm (for the small specimen) and 100 mm (the large specimen).

The specimen was moved in both X- and Y-direction using a computer-controlled stage. Output of the interferometer was digitized by an A/D converter and fed to a computer for analysis.

RESULTS FOR THE SMALL SPECIMEN

Figure 2 shows the overlay of incident SAW positions (shown in vertical white line) and detection positions (black circle) on the C-scan image of the small specimen. The specimen was moved at 10 mm step in both X- and Y-direction. Typical SAWs detected are shown in the upper row of Fig. 3. SAWs propagate as dispersive Lamb waves. Detected SAWs on the damage area at (x, y) = (10, 20) and (20, 20) are quite different from the wave on the non-damage area at (0, 50). Waveforms themselves clearly indicate the presence of delamination. The middle row of Fig. 3 represents wavelet contour maps calculated from the detected SAWs (upper row). The images of wavelet contour maps show the characteristics of detected SAWs. High frequency components of SAWs are less-affected by the damage between layers 2 and 3. We next calculated low frequency components (250 kHz) of the wavelet coefficient (bottom row of Fig. 3).

Peak amplitudes and peak arrival times at damage areas ((10,20) and (20,20)) changed from those at non-damage area (0,50). We calculated cross-correlation of SAWs by taking the SAW at (x, y)=(0, 50) as the reference pattern. We defined a similarity coefficient (s.c.) as the maximum value of the cross correlation. The similarity coefficients show the waveform similarity from -1 to 1. The s.c. value of 1 represents the best matching. We next compared images of wavelet contour map by taking the image at (x, y) = (0, 50) as the reference pattern. Similarity coefficients for images are defined in our previous paper [2]. Calculated similarity coefficients are given in Fig. 3.

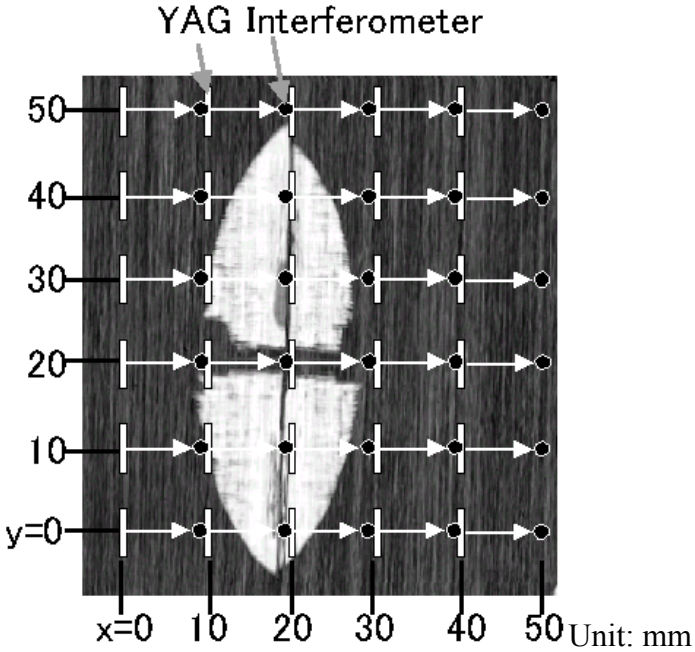

FIGURE 2: Over lapping of C-scan image and laser generated and detected points

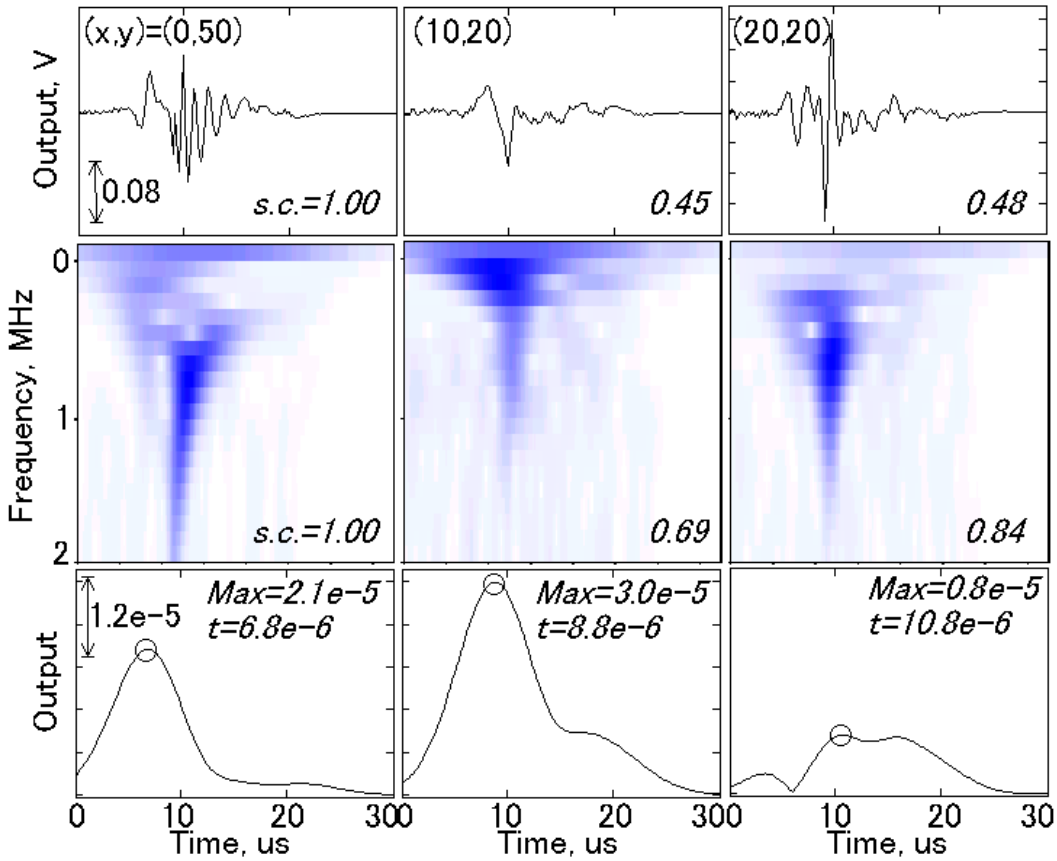

FIGURE 3: Detected waves (upper), wavelet contour map (middle) and 250-kHz wavelet coefficients over non-damaged and damaged area.

Contour maps of correlation factors of waveforms Fig. 4(a) and wavelet contour map Fig. 4(b) are shown. Here the black part corresponds with the correlation factor of 1.0. We next calculated peak-amplitude Fig. 4(d) and peak- time difference Fig. 4(c) of 250kHz wavelet coefficients by taking the coefficient at (0,50) as the reference data. White part indicates a large difference of peak amplitude or peak arrival time. The difference between damage and non-damage areas was small in both Fig. 4(c) and (d). This unsatisfactory result is primarily due to the short propagation length of SAWs (10mm) compared to the wave length of the frequency (250kHz). On the other hand, Fig. 4(a) and (b) clearly revealed the delamination zone. Difference of similarity coefficients is much smaller in (b) method than (a), but (b) method better detected the delamination zone.

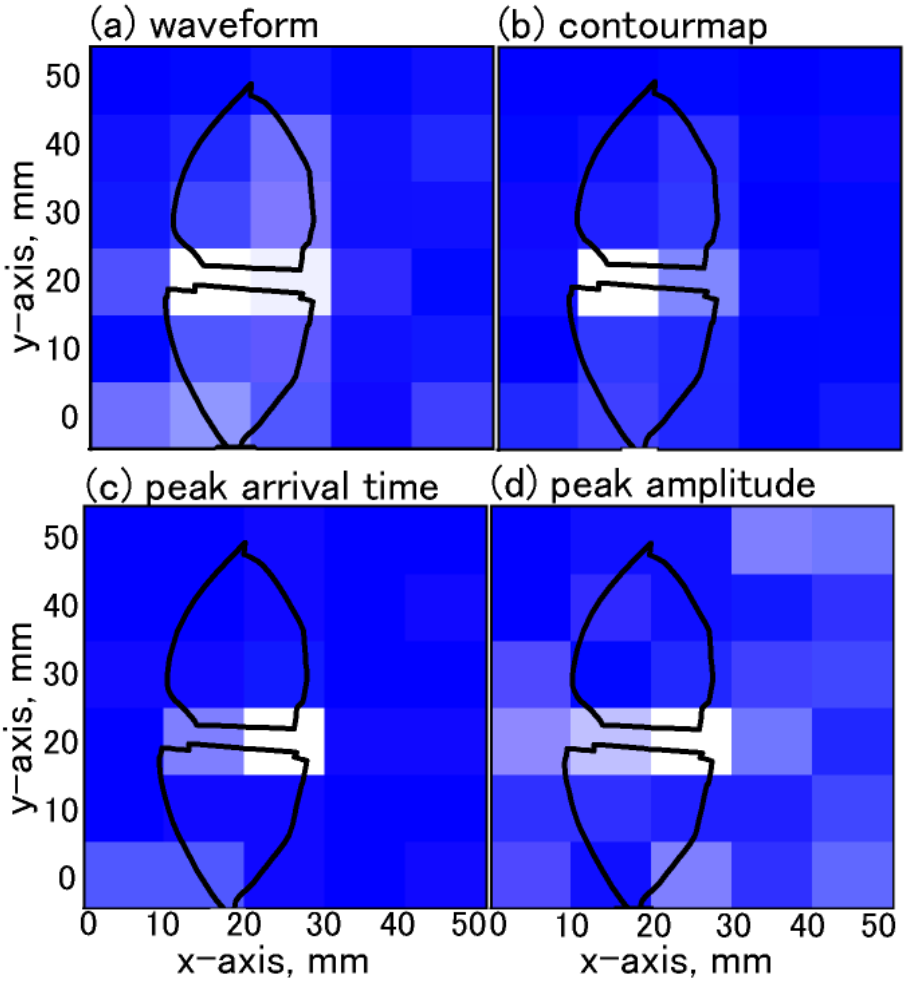

FIGURE 4: Contour map of similarity coefficients (waveform (a) and contour map (b)) and peak arrival time (c) and peak amplitude (d) of wavelet coefficients at 250kHz over an impacted CFRP with internal damage.

RESULTS FOR LARGE SPECIMEN

For efficient inspection of damage areas in large structural members, a laser SAW method is appropriate, but we have to scan the laser SAW at a large step over a long distance. We evaluated this method for a large specimen with delamination. Laser SAW scanning method and waveforms detected are shown in Fig. 5. SAWs were scanned in Y-direction at 10 mm step and monitored by an interferometer at 100 mm from the incident laser. Ultrasonic C-scan revealed delamination at the center as shown. Waveforms of SAWs resemble each other, but the arrival times of the second negative peaks at around 85 μs changed slightly, i.e, later arrival over the delamination area or at y=20 and 30 mm. Values in the figure represent similarity coefficients of these waves using SAW at 60 mm as the reference. Observed changes were too small to be useful. The contour map of similarity coefficients of waveforms is shown in Fig. 7(a). Damage was detected at y=20mm and 30mm axis; however, damage at y=40mm was not clearly detected.

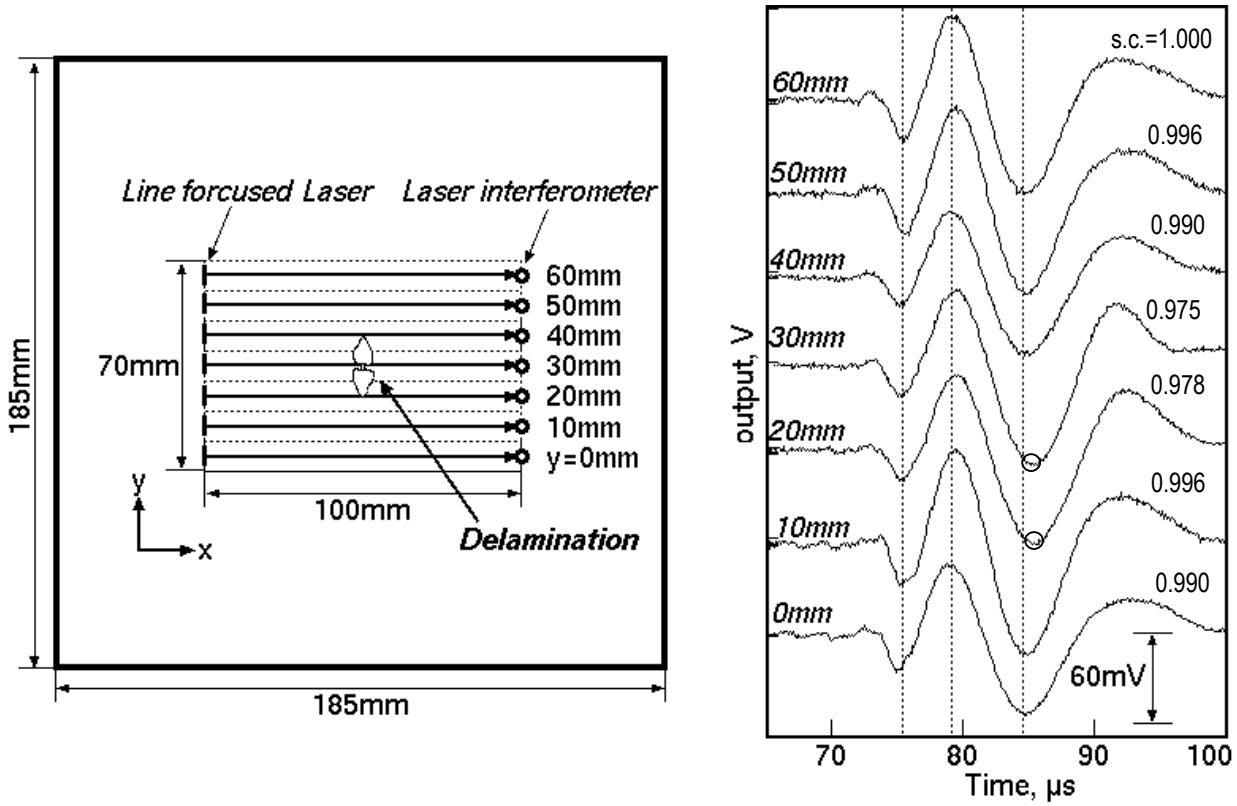

FIGURE 5: Laser SAW inspection method (the left) and Lamb waveforms detected for CFRP plate (right).

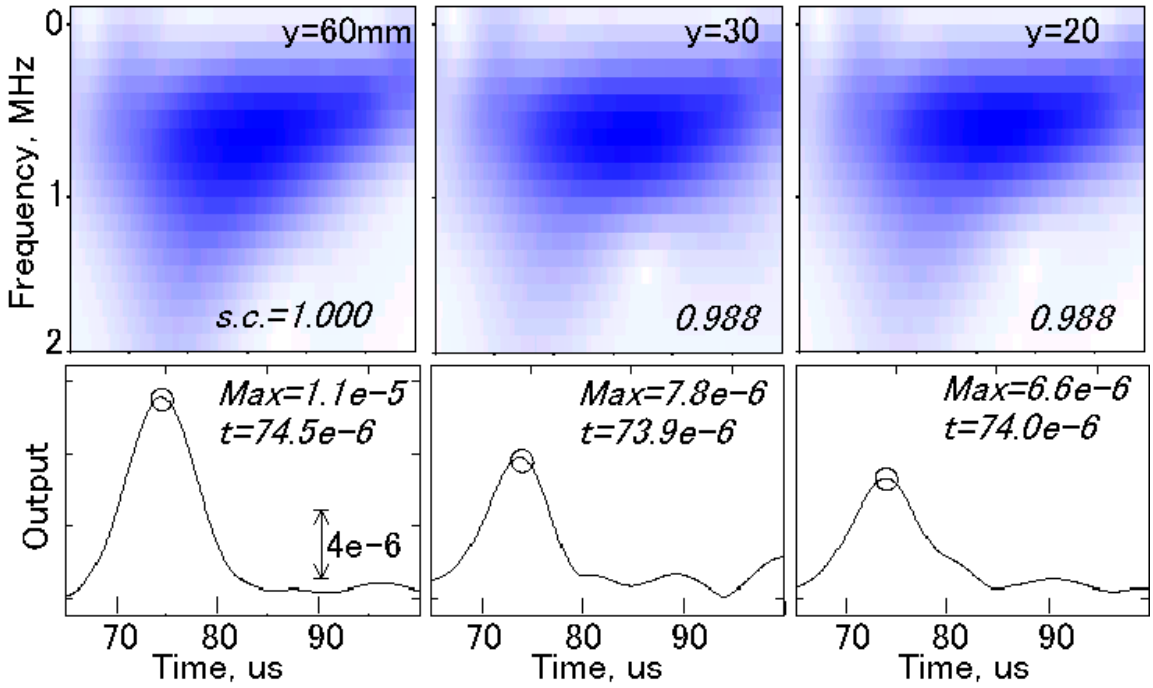

FIGURE 6: Wavelet contour map (top) and 250-kHz wavelet coefficients of detected waves over non-damaged and damaged areas.

We next constructed wavelet contour map (the top of Fig. 6) and calculated 250kHz wavelet coefficients (the bottom of Fig. 6). Wavelet contour maps over damaged (y=20, 30mm) and non-damaged (y=60mm) areas resemble each other, but the peak amplitude and peak arrival times of 250kHz wavelet coefficients show large differences. Similarity coefficients and peak value and peak arrival time are written in the figure.

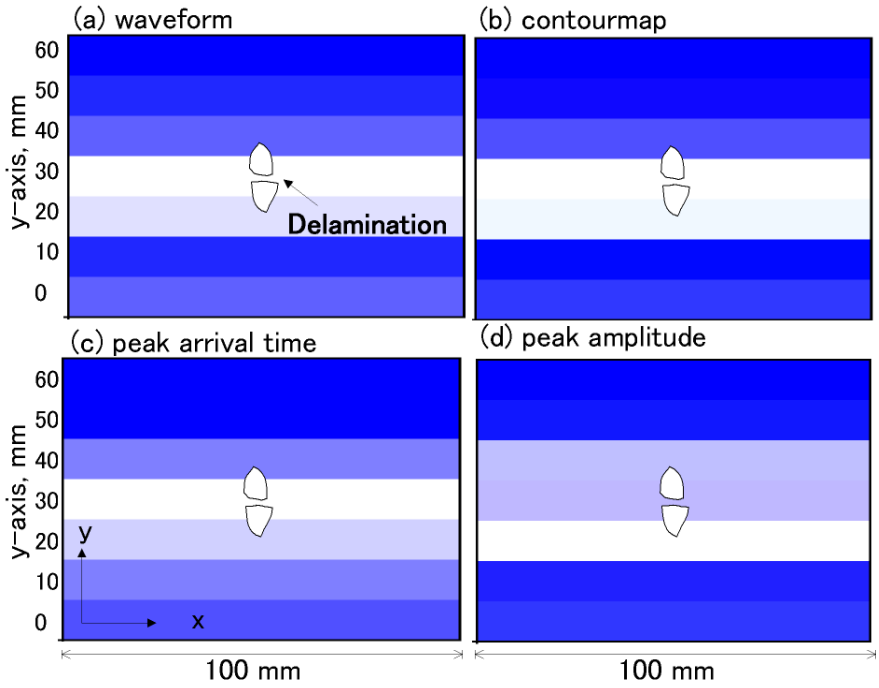

FIGURE 7: Contour map of similarity coefficients (waveform (a) and contour map (b)) and peak arrival time (c) and peak amplitude (d) of wavelet coefficients at 250kHz over an impacted CFRP with internal damage.

Contour maps are constructed by using similarity coefficients and peak value and peak arrival time of 250 kHz wavelet coefficients. The color definition is the same as in the previous section. The damages at y=20mm and 30mm are clearly detected by all the methods; however, only the method (c) detected damage at y=40 mm. This indicates that 100-mm propagation length can be used for 250 kHz SAW inspection. Extracted low frequency components is found to be effective in detecting impact damage.

CONCLUSION

A non-destructive and no-contact impact damage inspection system using laser-induced SAW is developed. SAWs were generated by a line-focus pulse YAG laser and monitored by a heterodyne type laser interferometer. Interlayer delaminations were revealed by similarity coefficients of wavelet contour map of detected waves for a small specimen. 250kHz-wavelet coefficients did not clearly represented the damage due to a short propagation length (10mm). The laser SAW inspection system is also used for a large specimen with the propagation length of 100 mm. For an impacted CFRP with the delamination area of 19-mm-long double-tree-shape, four different methods were utilized to detect the damage. The method using 250 kHz-wavelet coefficients was the most effective.

ACKNOWLEDGEMENT

A part of this research was supported by the fellowship to Y. Mizutani from the Japan Soc. for Promotion of Science and the Circle for the Promotion of Science and Engineering.

Reference

[1] R.F. Anastasi, A.D.Friedman, M.K.Hinders and E.I.Madaras (1997) 46th Defense Working Group on Nondestructive Testing, pp. 1-13.
[2] N. Saito, M. Takemoto, H. Suzuki and K. Ono (1998) Progress in Acoustic Emission IX, AEWG/AEG, Los Angeles, pp. V1-V10.

NONLINEAR DYNAMICS OF CRACK PROPAGATION (EXPERIMENTAL AND THEORETICAL STUDY)

O.B. Naimark, V.V.Barannikov, S.V. Uvarov

Institute of Continuous Media Mechanics, Russian Academy of Sciences,
1 Acad.Korolev street, 614013, Perm, Russia

ABSTRACT

Nonlinear dynamics of crack propagation is investigated experimentally and theoretically with a goal to clarify the nature of limiting crack velocity, the transition from steady-state to branching regimes of crack dynamics, the dynamics of crack arrest. Theoretical explanation of limiting steady-state crack velocity and the transition to branching regime was proposed due to the study of collective behavior of microcrack ensemble at the crack tip area. Experimental study of crack dynamics was carried out in the preloaded plate PMMA specimen using the high speed camera coupled with the photo-elasticity method, the point stress recording with a laser system, the failure surface roughness measurement.

Keywords: crack velocity limits, branching, crack arrest.

INTRODUCTION

The rebirth of interest in the issue of dynamic fracture is observed during last decade due to the variety of new experimental results which are not explainable within the prediction of classical fracture mechanics where it was shown [1] that the crack in infinite plane specimen has two steady-state velocities: zero and the Rayleigh speed. The recent experimental study revealed the limiting steady state crack velocity, a dynamical instability to microbranching [2,3], the formation of non-smooth fracture surface [4], and the sudden variation of fracture energy (dissipative losses) with a crack velocity [5]. This renewed interest was the motivation to study the interaction of defects at the crack tip area (process zone) with a moving crack. The still open problem in the crack evolution is the condition of crack arrest that is related to the question whether a crack velocity smoothly approaches to zero as the loads is decreased from large values to the Griffith point [6]. There is also problem at the low end of crack velocity. How a crack that is initially at rest might achieve its steady-state.

STATISTICAL PROPERTIES OF DEFECT ENSEMBLE

Microscopic and macroscopic variables for defect ensemble

Structural parameters associated with typical mesoscopic defects (microcracks, microshears) were introduced [7] as the derivative of the dislocation density tensor. These defects are described by symmetric

tensors of the form $s_{ik} = sv_i v_k$ in the case of microcracks and $s_{ik} = 1/2s(v_i l_k + l_i v_k)$ for microshears. Here $\vec{v}$ is unit vector normal to the base of a microcrack or slip plane of a microscopic shear; $\vec{l}$ is a unit vector in the direction of shear ; s is the volume of a microcrack or the shear intensity for a microscopic shear.The average of the "microscopic" tensor s_{ik} gives the macroscopic tensor of the microcrack or microshear density $p_{ik} = n\langle s_{ik} \rangle$ that coincides with the deformation caused by the defects, n is number of defects.

Statistical Model of Elastic Solid with Defects

Statistics of the microcrack (microshear) ensemble was developed in terms of the solution of the Fokker-Planck equation [7,8] in the phase space of the possible states of the microscopic variable s_{ik} concerning the size s and the orientation $\vec{v}, \vec{l}$ modes. This solution allowed the determination of the part of the free energy caused by defects.

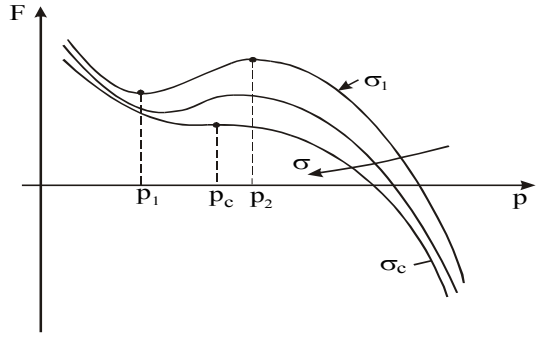

Figure 1: Free energy dependence on stress and defect density.

The free energy F for the nonlinear system "elastic solids with defects" corresponds to the form predicted by Fraenkel [9] (Fig.1). The metastability for the stress $\sigma < \sigma_c$ is the consequence of the orientation interaction in the defect ensemble. The free energy form, that was predicted by the statistical model, approaches to the Griffith form with the growth of the applied stress $\sigma \to \sigma_c$ (Fig.1). It is the consequence of the nucleation and growth of the defects with more pronounced orientation mode induced by the applied stress.

PHENOMENOLOGY OF QUASI - BRITTLE FAILURE

Free Energy

The simple phenomenological form of the part of the free energy caused by defects (for the uni-axial case $p = p_{zz}, \sigma = \sigma_{zz}, \varepsilon = \varepsilon_{zz}$) is given by sixth order expansion which is similar to the well-known Ginzburg-Landau expansion in the phase transition theory [7].

$$F = \tfrac{1}{2} Ap^2 - \tfrac{1}{4} Bp^4 - \tfrac{1}{6} Cp^6 - D\sigma\ p\ + \chi\left(\nabla_l p\ \right)^2 . \qquad (1)$$

The gradient term in (1) describes the non-local interaction in the defect ensemble in the so-called long wave approximation; A, B, C, D are positive phenomenological material parameters, χ is the non-locality coefficient.

Damage Kinetics in Quasi-Brittle Failure

The damage kinetics in quasi-brittle materials is determined by the evolution inequality [7] that leads to the kinetic equation for the defect density parameter

$$\frac{dp}{dt} = -\Gamma\left(Ap - Bp^3 - Cp^5 - D\sigma - \frac{\partial}{\partial x_l}(\chi \frac{\partial p}{\partial x_l}) \right), \qquad (2)$$

where Γ is the kinetic coefficient. Kinetic equation (2) and the equation for the total deformation $\varepsilon = \hat{C}\sigma + p$ ($\hat{C}$ is the component of the elastic compliance tensor) represent the system of constitutive equations of quasi-brittle materials with considered types of the defects.

COLLECTIVE PROPERTIES OF DEFECT ENSEMBLE

Equation (2) describes the characteristic stages of damage evolution. In the ranges of stress $\sigma < \sigma_c$ and the defect density $p < p_c$ the damage kinetics is subject to the "thermodynamic branch" corresponding to the local minimum of the free energy (Fig.1). At the approaching of stress to the critical value σ_c ($p \to p_c$) the damage kinetics is subject to specific spatial-temporal structures, which appear in the defect ensemble in the course of the interaction between defects [10,11]. These structures describe the damage localization. The subjection of damage kinetics to these structures reflects the qualitative change of the system symmetry due to the reduction of the number of independent coordinates in the damage field. The spatial-temporal structures are given by the self-similar solution of the kinetic equation (2) under the pass of the critical point p_c and reads

$$p(x,t) = \phi(t) f(\zeta), \quad \zeta = x/L_c, \quad \phi(t) = \Phi_0 (1 - \frac{t}{t_c})^{-m}, \qquad (3)$$

where $m > 0, \Phi_0 > 0$ are the parameters related to the nonlinear form of Eq.(2); L_c and t_c are the scaling parameters which can be found under the solution of the corresponding nonlinear eigen-function problem [12]. The self-similar solution (3) describes the blow-up damage kinetics for $t \to t_c$ on the set of the spatial scales $L_H = kL_c, \quad k = 1,2,...K$ [10]. The loss of metastability of the free energy under $\sigma \to \sigma_c$ (Fig.2) leads to the qualitative change of the general property of the system including the symmetry properties. In the area $\sigma > \sigma_c$ the stress field doesn't control the system behavior and the failure scenario is determined by the generation of the blow-up damage localization structures in the process zone.

ORIGIN OF CRACK TIP INSTABILITY

The kinetics of damage localization is determined by two parameters, which are given by the self-similar solution (3). These parameters are the spatial scales L_C of the blow-up damage localization and the so-called "peak time" t_c which is the time of damage localization in the self-similar blow-up regime. The velocity limit V_C of the transition from the steady-state to the irregular crack propagation is given by the ratio: $V_C \approx L_C / t_c$. The steady-state crack propagation is realized in the case when the stress rise in the process zone provides the failure time $t_f > t_c = L_C / V_C$ for the creation of the daughter crack only in the

straight crack path. The failure time t_f follows from the kinetic equation (2) and represents the sum of the induction time t_i (the time of the approaching of the defect distribution to the self-similar profile on the L_H scale) and the peak time t_c: $t_f = t_i + t_c$. For the velocity $V < V_C$ the induction time $t_i >> t_c$ and the daughter crack appears only along the initial main crack orientation. For the crack velocity $V \approx V_C$ there is a transient regime ($t_i \approx t_c$) of the creation of number of the localization scales (daughter cracks) in the main crack path. The crack velocity growth in the area $V > V_C$ leads to the sharp decrease of the induction time $t_i \to 0, t_f \to t_c$ that is accompanied by the extension of the process zone in both (tangent and longitudinal) directions where the multiple blow-up structures (daughter cracks) and, as the consequence, the main crack branching appears.

EXPERIMENTAL STUDY OF NONLINEAR CRACK DYNAMICS

Experimental setup

Direct experimental study of crack dynamics in the preloaded PMMA plane specimen was carried out with the usage of a high speed digital camera Remix REM 100-8 (time lag between pictures $10\,\mu s$) coupled with photo-elasticity method [13]. The experiment revealed that the pass of the critical velocity V_C is accompanied by the appearance of a stress wave pattern produced by the daughter crack growth in the process zone. Independent estimation of critical velocity from the direct measurement of crack tip coordinates and from pronounced stress wave Doppler pattern gives a correspondence with the Fineberg data ($V_C \approx 0.4 V_R$) [2].

Characteristic crack velocity

The dependence of crack velocity on the initial stress is represented in Fig.2. Three portions with different slopes can be shown. The existence of these portions determines three characteristic velocities: the velocity of the transition from the steady-state to the non-monotonic straight regime $V_S \approx 220\,m/s$, the transient velocity to the branching regime $V_C \approx 330\,m/s$ and the velocity $V_B \approx 600\,m/s$ when the branches behave autonomous. The characteristic velocity $V_C \approx 330\,m/s$ allowed us to estimate the peak time t_c to measure the size of the mirror zone $L_C \approx 0.3\,mm$: $t_c = L_C / V_C \approx 1 \cdot 10^{-6}\,s$.

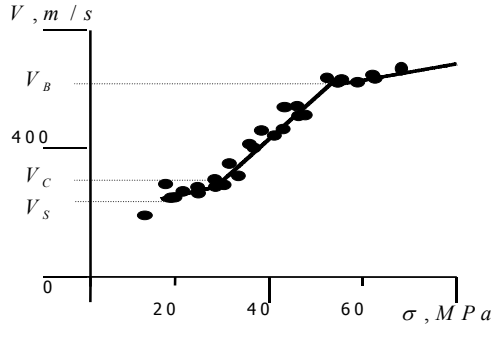

Figure 2.

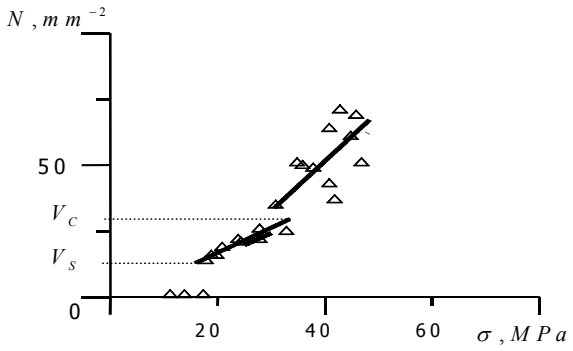

Figure 3.

In our experiments the dependence of the density of the mirror zones N on the stress also were studied (Fig.3). Actually, since the failure time for $V > V_C$ is approximately constant ($t_f \approx t_c \approx 1\mu s$), there is a unique way to increase the crack velocity to extend the size of the process zone. The crack velocity V is

linked with the size of the process zone $L_{PZ} \sim L_H$ by the ratio $V = {L_{PZ}}/{t_c}$. Since the branch length is limited by the size of the process zone, we obtain the linear dependence of branch length on the crack velocity. This fact explains the sharp dependence (quadratic law) of the energy dissipation on the crack velocity established in [5].

Scaling properties of failure

The scaling properties of failure were studied also under the recording of the stress dynamics using the polarization scheme coupled with the laser system. The stress temporal history was measured in the marked point deviated from the main crack path on the fixed (4 mm) distance. This allowed us to investigate the correlation property of the system using the stress phase portrait $\dot{\sigma} \sim \sigma$ (Poincare cross section) for slow and fast cracks, Fig.4.

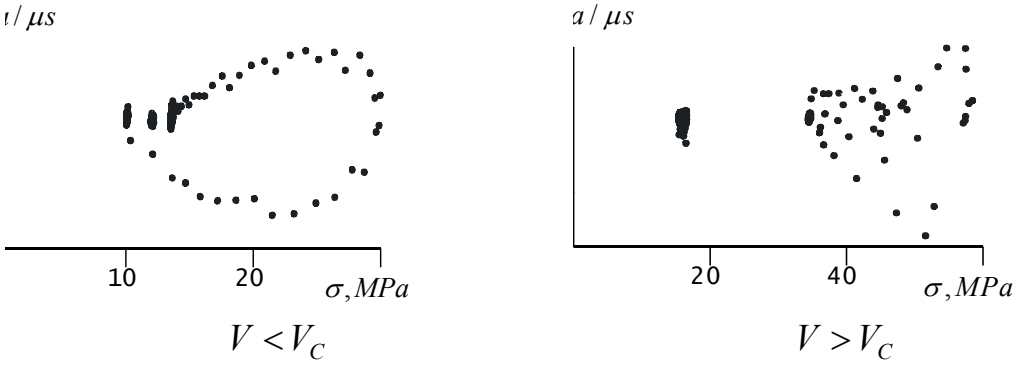

Figure 4: Poincare cross-section

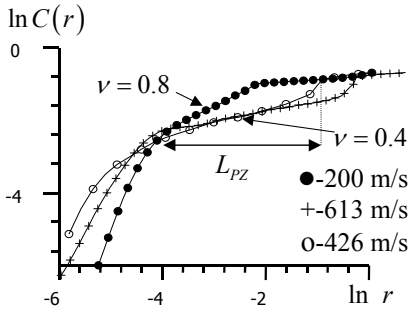

Figure 5: Correlation integral

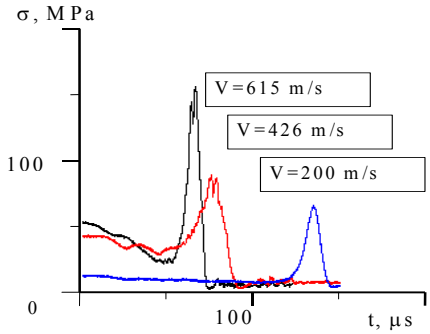

Figure 6: The stress history

These portraits display the periodic stress dynamics (Fig.4) that in the correspondence with the local ellipticity of Eq.(2) for $\sigma < \sigma_c$ ($V < V_C$) and the stochastic dynamics for $V > V_C$ corresponding to the second type of the attractor (Fig.4). The recording of the temporal stress history in the marked point for $V > V_C$ revealed the appearance of finite amplitude stress fluctuations which reflect the qualitative new changes in the process zone for the fast crack (Fig.5). The scaling properties were studied in the term of the correlation integral calculated from the stress phase pattern in the $\dot{\sigma} \sim \sigma$ space. The existence of the scales with the stable correlation index was established for the regimes $V < V_C$ and $V_B > V > V_C$. The values of the correlation indexes in these regimes show the existence of two scaling regimes with the deterministic ($V = 200 m/s$, $\nu \approx 0.8$, Fig.6) and stochastic ($V = 426, 613 m/s$, $\nu \approx 0.4$) dynamics. The extension of the portions with a constant indexes determines the scale of the process zone L_{PZ}. The length of the process zone increases with the growth of the crack velocity in the range $V_B > V > V_C$ with the maintain of the

scaling property of the dynamic system. Numerical simulation of the damage kinetics in the process zone allowed us to conclude that this scaling is the consequence of the subjection of the failure kinetics to the blow-up self-similar solution which determines the collective behavior of the defect ensemble in the process zone [14].

LOW VELOCITY LIMIT. CRACK ARREST.

In this part we have addressed the question of how a dynamic crack will approach zero velocity. This fact was discussed in [6] and it was shown considering a simplified version of the strip specimen with the radiation at the boundaries that steady-state velocity law with a square-rot behavior is expected as a function of the excess load over the Griffith load. This means that the steady-state velocity increases with an infinite slope near zero overload, but in a smooth fashion with a load. It was shown also that if the crack has no field inertia, the pass of the "trapping limit" will lead to the crack move. But if the crack has a field inertia the crack velocity will exhibit a transient oscillation. The similar conclusion can be made to compare the estimation of the crack velocity, given in [6] $V = w\sqrt{(E_e - 2\gamma)/(C(w))}$, where w is the Barenblatt cohesive zone of the crack, $(E_e - 2\gamma)$ is the Griffith static terms, $C(w)$ is material parameter, and the results predicted above statistical model. Taking in view that w is similar $L_{PZ} \sim L_H$, the root term is the inverse characteristic time t_C given by the self-similar solution. This fact allowed us to determine the range of the application of this generalized Griffith relation, where the crack can approach to the rest smoothly: $V < V_C$. For $V > V_C$, when the "wave part" of energy will increase with crack velocity, the crack arrest will appear non-smoothly for the energy metastability providing the "crack trapping". The similar view can be developed to analyze the crack overload above the Griffith value before any state motion.

This work was carried out in part during the author's stay at the LAMEFIP-ENSAM. The author is grateful to Professor J.-L.Lataillade for this opportunity and fruitful discussions.

References

1. Freund, L.B (1990) Dynamic Fracture Mechanics, Cambridge University Press, Cambridge, England.
2. Fineberg, J., Gross, S., Marder, M. and Swinney, H. (1991). *Phys.Rev.Lett*. **67**, 141
3. Sharon, E., Gross, S.P. and Fineberg, J. (1995). *Phys.Rev.Lett*., **74**, 5097.
4. Boudet, J.F., Ciliberto, S. and Steinberg, V. (1996). *J. de Physique,* **6**, 1993.
5. Sharon, E., Gross, S.P., Fineberg, F. (1996). *Phys.Rev.Lett* , **76**, 2117.
6. Holian, B.L. and Thomson, R.(1997). Phys. Rev. E, 56, 1, 1071.
7. Naimark, O.B. (1997). In: *Proceedings of the IUTAM Symposium on Nonlinear Analysis of Fracture*, Willis, J.R. (Ed). Kluwer Academic Publishers, Dordrecht, pp. 285-298.
8. Naimark, O.B. (1997). In: *Proceedings of IX Int.Conf.Fracture, B.Karihalloo* (Ed.). Sydney, Pergamon, 6, pp.2795-2806.
9. Fraenkel, Ya.I. (1952). *Journal of Technical Physics*, **22**, 11, 1857 (in Russian).
10. Naimark, O.B. (1998) . *JETP Letters*, **67**, 9, 751.
11. Naimark, O.B., Davydova, M.M. and Plekhov, O.A. (1998). In*: Proceedings of NATO Workshop "Probamat – 21 Century"*, G.Frantziskonis (Ed.). Kluwer, pp.127-142.
12. Kurdyumov, S.P. (1988). In: *Dissipative Structures and Chaos in Non-Linear Space*, Utopia, Singapure, **1**, pp.431-459.
13. Naimark, O.B. (2000). In: *Advanced in Mechanical Behavior, Plasticity and Damage*, v.1, pp.15-28, Miannay, D., Costa, P., Francois, D. and Pineau, A. (Eds). Elsevier.
14. Naimark, O.B., Davydova, M.M. and Plekhov, O.A. (2000). *Computers and Structures*, **76**, 67.

ICF100566OR

NONLINEAR FRACTURE MECHANICS OF DELAMINATION FAILURE IN A COMPOSITE STRENGTHENED CONCRETE BEAM

Christopher K.Y. Leung, Marcus Klenke, W.K. Tung and Herman C.Y. Luk

Department of Civil Engineering, The Hong Kong University of Science and Technology
Clear Water Bay, Kowloon, Hong Kong

ABSTRACT

The bonding of composite plates to the tensile side of concrete beams or slabs has recently been accepted as an effective retrofitting method. A concrete member retrofitted in this manner often fails through the delamination of the composite. Most existing models for the analysis of delamination assume linear elastic material behaviour until ultimate failure of the component. This is contradictory to experimental observations that clearly indicate the occurrence of non-linear damage processes at load levels far below the ultimate load. In this paper, a novel nonlinear fracture mechanics approach for the analysis of delamination failure is introduced. The delamination is modelled as an interfacial crack, with progressive interfacial damage represented by material softening at the crack wake. The focus of the paper is on the determination of the interfacial shear stress vs slip ($\tau_s - s$) relation. A new testing method to study progressive delamination is first described. A finite element model for the specimen is then set up, with softening elements at the plate/beam interface. By comparing experimental measurements to finite element results using different softening behaviour at the interface, the constitutive relation of the interface elements, in terms of shear stress vs sliding displacement, can be obtained. From our results, the softening behaviour exhibits a sharp drop followed by more progressive weakening, indicating sudden loss of cohesion/bond at a critical stress level, and a more gradual reduction in friction with increased sliding and damage.

KEYWORDS
Non-linear fracture, delamination, composite, interfacial softening, retrofitting, concrete

INTRODUCTION

After years in service, many concrete structures have deteriorated and are in need of repair. In some cases, due to change of use, members need to be retrofitted to provide a load carrying capacity higher than the original design value. For concrete beams or slabs, the bonding of fiber reinforced plastic (FRP) plates to the lower surface is found to be an effective and efficient strengthening technique. Depending on the design, a beam with a bonded plate can exhibit various failure modes (Meier [1], Arduini et al [2], Buyukozturk et al [3]). Delamination is the most commonly observed failure mechanism (Saadatmanesh et al [4], Meier et al [5]) that occurs with little warning (compared to conventional flexural failure). The investigation of delamination failure is hence an important research topic for plate-strengthened beams.

From a theoretical point of view, delamination may occur either at the end of the composite plate (cut-off point), or under a flexural (or flexural/shear) crack in the concrete member. Elastic stress fields at the plate end have been derived independently by Taljsten [6] and Malik et al [7], while that under the flexural crack has been obtained by Leung [8]. From these analyses, an important observation can be made. The stresses decrease rapidly with distance from the point of maximum stress, so high stresses exist over a relatively

small part of the interface. Similar to the stress singularity at a crack tip, this kind of stress field is expected to induce yielding or damage processes in a region around the point of maximum stress before ultimate failure occurs. For a quasi-brittle material such as concrete, the size of such a process zone can be quite large. This theoretical argument is supported by recent experimental results. In the experiments of Wu et al [9] on plain concrete beams strengthened with composite plates, stable growth of the delamination can be visually observed, indicating the gradual propagation of a damage process along a large part of the beam/plate interface. Buyukozturk et al [3] and Taljsten [10] tested strengthened beams with strain gauges placed along the composite plate. As loading increased, the measured strain values near the free end of the plate were found to increase initially but decrease after a certain load was exceeded. This decrease is an indication of the reduction in strain transfer capacity from the concrete to the plate, due to damage in the concrete adjacent to the interface. Based on experimental observations, the size of the damage process zone is large relative to the region of high stress indicated by the elastic analysis. As a result, purely elastic approaches, such as the models of Taljsten [6], Malik et al [7] and Leung [8] as well as LEFM-based interfacial fracture analysis (e.g., Hutchinson and Suo [11]), are not expected to provide accurate predictions of the ultimate failure load.

To model progressive failure within the concrete after delamination was initiated, Buyukozturk et al [3] and David et al [12] have carried out finite element analysis with non-linear material constitutive relations to describe concrete, steel, as well as the concrete/steel bond. A non-linear analysis was carried out until the loading can no longer be increased. With this approach, four different retrofitted specimens were analyzed in Buyukozturk et al [3] and the agreement with experimental result was not satisfactory. In David et al [12], numerical analysis for only one experiment was presented and good agreement was achieved. However, the authors pointed out that the determination of various parameters in the non-linear material models is a difficult task. From the paper, it was not clear if the material parameters were obtained from separate experiments, or simply selected to fit the experimental data.

For the delamination problem, the appropriate material parameters for concrete are indeed very difficult to obtain. Non-linear constitutive models for concrete are often determined from tests on standard cylinders or cubes, where the loading on the specimen generates a fairly uniform strain field over a representative volume of materials. However, delamination is governed by concrete failure near the interface where high strain gradients exist. It is questionable if material parameters determined from standard specimens are representative of those in the critical region where delamination failure occurs.

In the authors' opinion, the best way to analyze the delamination problem is to adopt a non-linear fracture mechanics approach that explicitly models the softening behaviour within the process zone around the concrete/composite interface. Experimental methods should be developed for the 'in-situ' determination of material properties within the critical region. The non-linear fracture approach, which is essentially an extension of Hillerborg's fictitious crack model [13] was first proposed by Taljsten [14]. To illustrate the concept, Taljsten [14] assumed a very simple shear stress vs slip relationship and derived analytical expressions to relate the direct force required for a bonded plate to delaminate. However, the critical issue of determining the constitutive behaviour in the process zone for real material systems, was not addressed.

The focus of this paper is on the determination of softening behaviour at the concrete/composite interface with a combined experimental/numerical approach. In the following, the modelling concept is first discussed in detail. An experimental set-up for the study of progressive delamination is then described. Using a representative set of experimental results, the derivation of interfacial softening behaviour (in terms of stress vs sliding) will be demonstrated.

A new modeling approach using nonlinear interface elements

To model progressive damage at the interface, a new non-linear interface element is introduced. The effect of damage is lumped into the softening of the interface element instead of allowing damage in the concrete elements. The justification is that the thickness of material over which damage occurs is small compared to the dimensions of the beam, therefore the damage can be modelled using a discrete rather than smeared approach.

The representation of concrete damage with non-linear interface elements is illustrated in Fig.1. As shown in Fig.1(b), after the non-linear effects are lumped into the interface elements, the concrete elements can be considered linear elastic at all times and the analysis is greatly simplified. Only the constitutive relation of the interface element is needed. As in Fig.1(c), the interface element consists of two springs. Movement of the horizontal spring represents sliding displacement between the concrete and the adhesive, while the vertical link models separation.

In the interface element, the horizontal spring carried a shear force equal to the shear stress (τ_s) times the area the element represents. The vertical link carries a normal force equal to the normal stress (σ_n) times the area. Both the spring and link are considered perfectly rigid before a critical shear stress τ_{cr} is reached. After τ_{cr} is reached, the vertical link will be free to open. That is, $\sigma_n = 0$ for any positive opening displacement (u). When the gap closes (i.e. u returns to 0), the link will be able to transmit compressive stress again. After reaching τ_{cr}, the shear stress in the horizontal spring becomes a function of both the relative shear displacement (s) and u. The reduction of τ_s with increasing shear displacement is illustrated in Fig.1(d) for a given u. The curve in Fig.1(d) is dependent on the opening displacement. In the model, the τ_s vs s relation is approximated by a multi-linear relation.

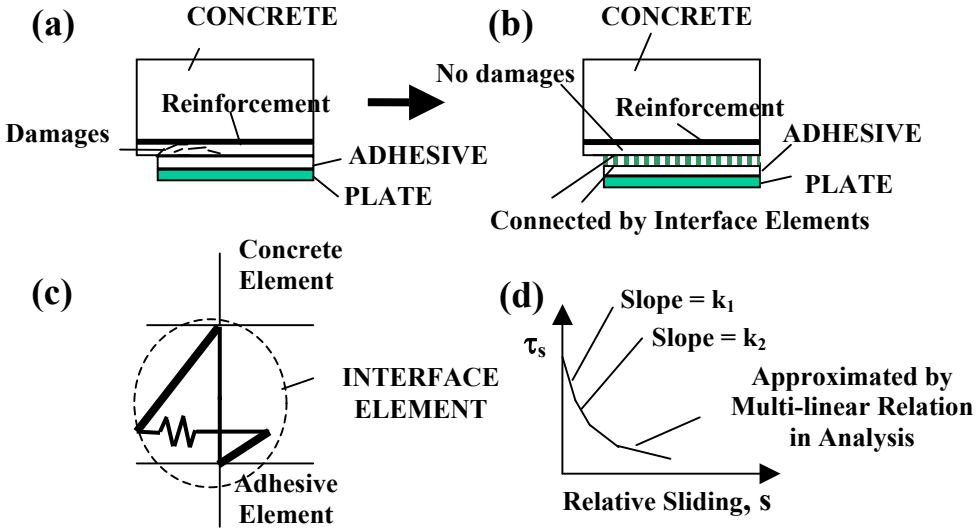

Fig.1 (a) and (b) Representation of concrete damage with non-linear interface elements
(c) the interface element, (d) Variation of element shear stress with sliding

Determining the constitutive relation of interface element

To obtain the constitutive relation of the interface element, a novel experimental procedure is developed (Fig.2). It consists of a concrete half-beam and a metal member connected together by a rod that acts as a hinge. A composite plate is to be glued to the bottom part.

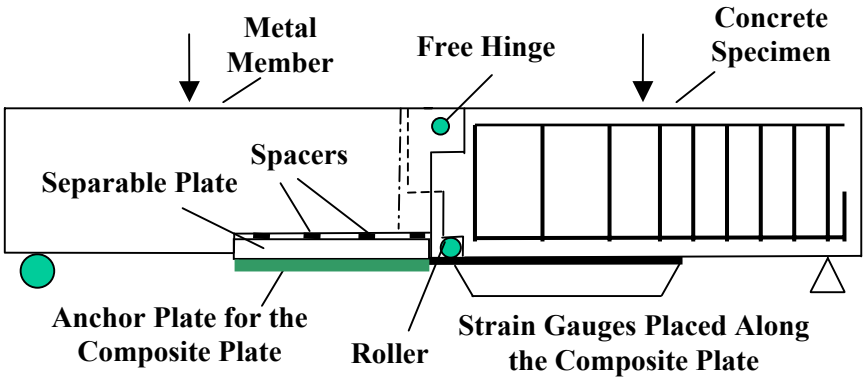

Fig. 2 Experimental set-up to determine constitutive relation of the interface element

As shown in Fig.2, strain gauges are glued along the composite surface and longitudinal strain is measured together with the applied load. A finite element model for the concrete member is set up. Interface elements such as those shown in Fig.1 are placed along the plate/concrete interface. The strain distribution along the plate can hence be theoretically predicted. Before the initiation of delamination, the strain field is elastic. The strain at any distance increases proportionately with the load. Based on the applied load when proportionality no longer holds, the critical shear stress can be obtained. After delamination starts, the strain variation is a function of the shear softening behaviour. For a load that is just above the delamination load, the composite strain is only dependent on the first branch of the shear-softening curve. Based on the fitting of experimental data, the slope of the first branch is determined. This branch is used for increasing loading until it no longer produces a good fit. The maximum shear displacement (s_1) on the last run is recorded, and the slope of next branch, which starts at $s = s_1$, is determined. Similar analysis can be continued to find the slopes of all subsequent branches. The slope of each branch is also a function of u. As a first attempt to determine the shear-softening relation at the interface, u is kept at zero.

Experimental Result and Analysis

The size of the metal member and concrete half-beams are around 1.1m x 0.2m x 0.22m (LxWxH). The composite employed is Sika Carbodur S-512. The total length of the composite is 950mm, half is bonded on the concrete. Starting from the internal bottom edge of the concrete member, 11 strain gauges are placed 21mm center to center on the composite. The testing was carried out in 4-point bending, with 1.8m support span and 0.6m between the loading points. The hinge of the specimen was placed at the middle of the two loading points. The concrete strength was 33 MPa. According to the supplier, the Young's modulus of the adhesive is 4.4 GPa. In each test, stable propagation of the delamination can be observed. The ability to induce progressive delamination is a major advantage of the present set-up for the investigation of the softening behaviour at the interface.

Here one set of results is presented. Fig.3 shows the variation of longitudinal strain with distance along the plate. From the figure, the five lowest curves are similar in shape, indicating elastic behaviour. From the sixth curve onwards, the shape of the curve starts to change, and the slope is found to decrease as the middle of the member (distance = 475mm) is approached. Since the slope represents the rate of strain change along the plate, which is proportional to the interfacial shear stress, a drop in the slope indicates shear softening at the interface. As loading increases, the slope change starts to occur at a larger distance from the middle, indicating progressive delamination along the interface. To obtain theoretical values of strain along the plate, a finite element model (Fig.4) was developed for the concrete member, using the program ADINA. Interface elements, in the form of springs, are placed between the adhesive and the concrete. In this case, with u = 0, spring elements are placed in the horizontal direction alone. Nodes on the two sides of the spring are constrained to move together in the vertical direction. The spring is set to be very rigid before critical shear stress is reached. Once the shear stress reaches the critical, the behaviour will follow a softening curve.

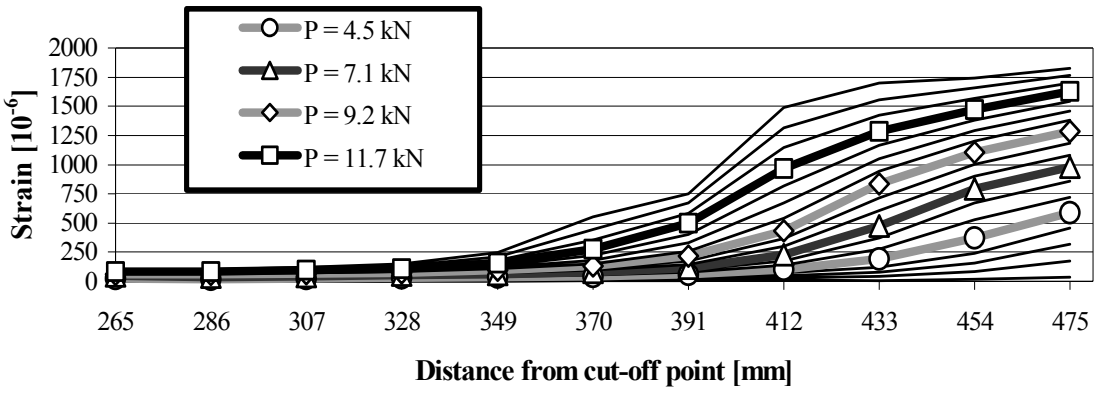

Fig.3 Variation of Measured Strain at Various Load Levels

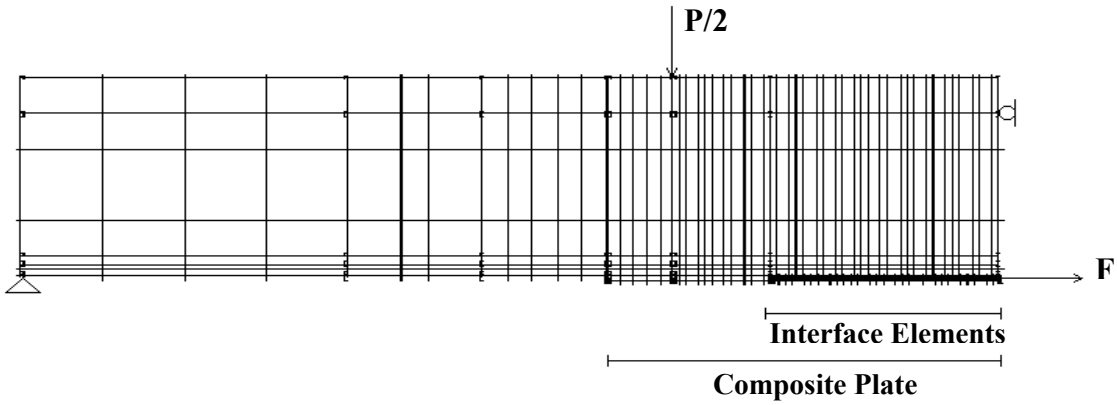

Fig.4 The Finite Element Mesh used in our Analysis

Figs. 5 to 6 show the comparison between experimental strain and finite element strain values. Fig.5 shows all the elastic cases, and results are normalized to that for 4.5kN. From the figures, the overall agreement can be considered quite satisfactory. The softening behaviour of the interface element is shown in Fig.7. Note that the curve exhibits a vertical drop followed by more gradual decrease. We believe the sudden drop is due to bond/cohesion failure, while the continual change indicates the reduction in friction with increasing sliding and damage.

An additional note regarding data fitting needs to be made. For the spring element used in our analysis, the softening slope cannot be too steep. Once a certain critical slope is exceeded, the analysis can no longer continue. To get around this problem, instead of representing interfacial behaviour with a single softening spring element, two spring elements are placed between the same two nodes. One of these elements is a softening spring element, while the other is a spring element that will rupture when a critical stress is reached. By making the second element ruptures at the same instance when the first element starts to soften, the two elements will combine to give a softening behavior with a sudden vertical drop (due to rupturing of one of the elements) followed by gradual decrease.

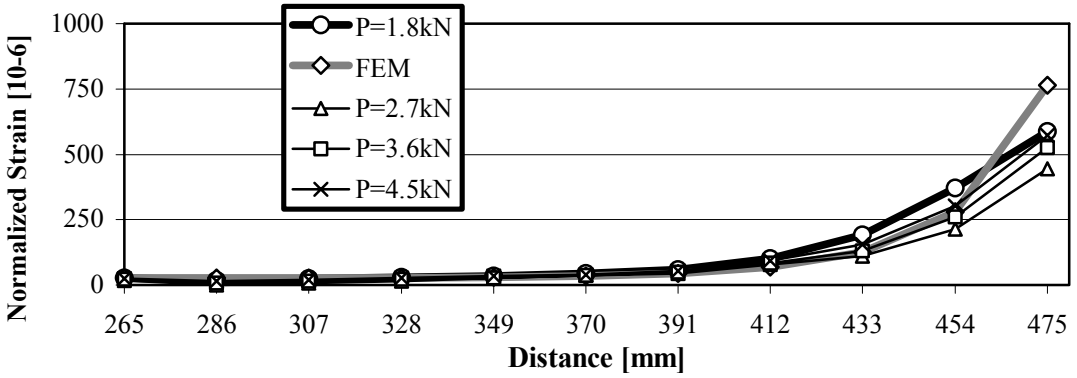

Fig.5 Comparison between normalized experimental and FEM results for P up to 4.5kN

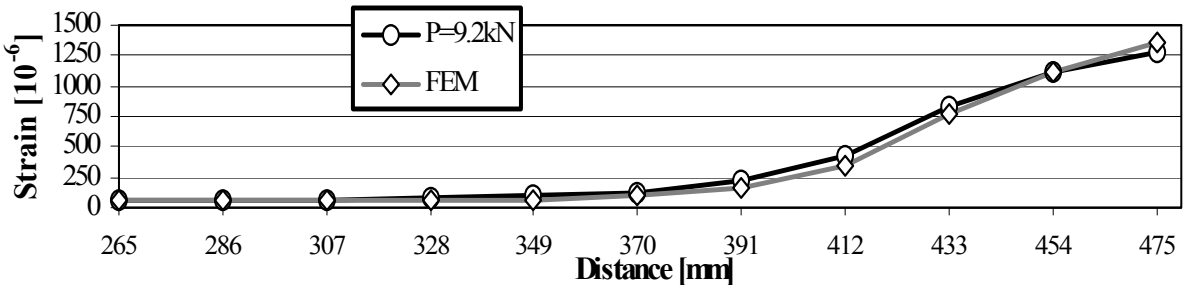

Fig.6 Comparison between Experimental and FEM results for P = 9.2 kN

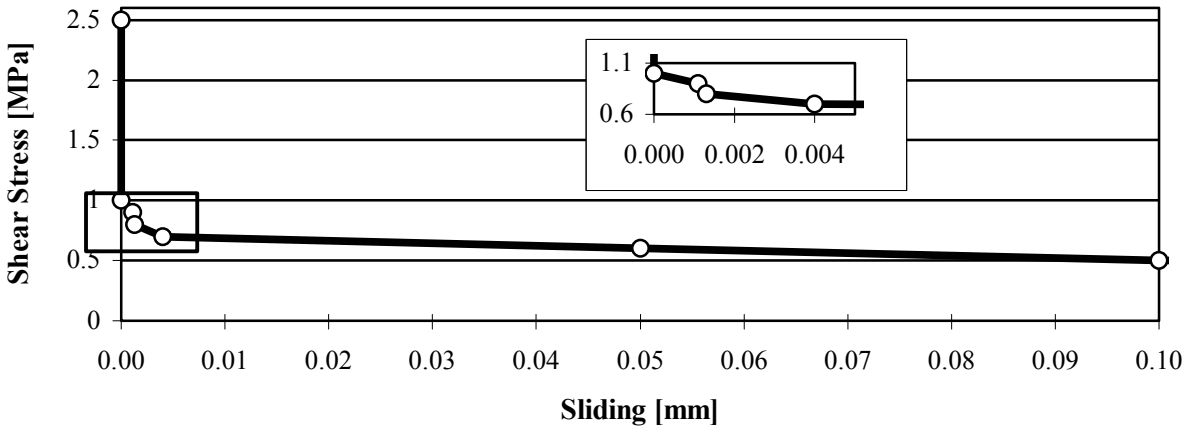

Fig.7 The Experimental Determined Interfacial Softening Relation

CONCLUSION

For the delamination of bonded plate from a concrete member, non-linear behaviour has been reported by many investigators. In this study, a combined experimental/ computational approach was developed for the quantitative determination of shear softening relation during delamination at the plate/bond interface. The feasibility of the approach has been verified with experimental results obtained from concrete specimens with bonded carbon fibre composite plates. The result indicates that delamination leads to rapid initial interfacial softening followed by more gradual reduction in shear stress. In this work, we have only studied the case with zero opening displacement at the interface. In the future, the effect of opening displacement should also be considered to develop a general interface element for the analysis of concrete members retrofitted in different manners.

References

1. Meier, U. (1995) *Construction & Building Materials*, 9, 341-353.
2. Arduini, M., Di Tommaso, A. and Nanni, A. (1997) *ACI Structures Journal*, 94, 363-370.
3. Buyukozturk, O., Leung, C., Hearing, B. and Gunes, O. (1998). In:*Fracture Mechanics of Concrete Structures*, pp. 1771-1782, Mihashi H. and Rokugo K. (Eds). AEDIFICATIO
4. Saadatmanesh, H. and Ehsani, M.R. (1991) *ASCE J. of Structural Engineering*, 117, 3417-3433.
5. Meier, U., Deuring, M., Meier, H. and Schwegler, G. (1992) In: *Advanced Composite Materials in Bridges and Structures*, *Canadian Society for Civil Engineering*, pp. 243-251.
6. Taljsten, B. (1997) *ASCE J. of Materials in Civil Engineering*, 9, 206-212.
7. Malik, A.M., Saadatmanesh, H. and Ehsani, M.R. (1998) *ACI Structures Journal*, 95, 142-152.
8. Leung, C.K.Y. (2001) *ASCE J. of Materials in Civil Engineering*, in press
9. Wu, Z., Matsuzaki, T. and Tanabe, K. (1997). In: Non-Metallic (FRP) Reinforcement for Concrete Structures, Vol.1, Proc. intern. symp. Sapporo, 319-326.
10. Taljsten, B. (1999). In: *Structural Faults & Repair – 99,* CD ROM, M. Forde (Ed).
11. Hutchinson, J.W. and Suo, Z. (1992). In: *Advances in Applied Mechanics*, pp. 63-191. Hutchinson J.W. and Wu T.Y. (Eds.), Academic Press.
12. David, E., Djelal, C., Ragneau, E. and Buyle-Bodin, F. (1999). In: *Structural Faults & Repair – 99,* CD ROM, M. Forde (Ed).
13. Hillerborg, A., Modeer, M. and Petersson, P.E. (1976) *Cement & Concrete Research*, 6, 773-782.
14. Taljsten, B. (1996) *Int. J. of Fract*., 82, 253-266.

ORAL/POSTER REFERENCE: ICF100440OR

NOTCH EFFECT OF MICRO POLYCRYSTALLINE SILICON CANTILEVER

S. Hamada, S. Tani, M. Horikawa, H. Otani, M. Tsugai and E. Yosikawa

Mitsubishi Electric Co., 8-1-1, Tsukaguchi-honmachi, Amagasaki city, 661-8661, Japan

ABSTRACT

A micro polycrystalline silicon cantilever is employed widely as a common structural member for microelectromechanical systems (MEMS). It is necessary to build up the reliability design criterion of the micro polycrystalline silicon explaining the strength of cantilever root area that is regarded as a fracture origin due to stress concentration in general. In this study, the bending tests using the micro scale cantilever beams of polycrystalline silicon with notch of several sizes are carried out in order to obtain the strength database of a micro polycrystalline silicon structures. The bending test results are analyzed by means of maximum peak stress σ_{max} at the notch root calculated by FEM models, and it is found that this approach does not describe the data. Therefore, a reforming approach are taken into account by use of the two parameters that are the peak stress σ_{max} and an area of 0.5 σ_{max}, S which indicates the stress extension around the position of peak stress representatively. By this two parameters approach, the test results are explained quantitatively and the limit state describing the fracture of micro cantilever is obtained as $\sigma_{max} = 4.19S^{-0.212}$.

KEY WORDS

MEMS, Polycrystalline Silicon, Notch effect, Stress Concentration

INTRODUCTION

Recently, micron meter order microstructure called microelectromechanical systems (MEMS) [1,2] attracts attentions. The MEMS technologies are applied to an ultra-micro motor, DMD [3], micro sensor [4] and so on. It is well known that a micro polycrystalline silicon cantilever is employed widely as a MEMS structural member in general. From an engineering viewpoint, it is important to establish the reliability design rule of the micro polycrystalline silicon [5-8] involving the explanation of the fracture phenomena of stress concentrated cantilever root area that is regarded as an origin of fracture. In present studies, the bending tests using the micro scale cantilever beams of polycrystalline silicon with notch of several sizes are carried out in order to obtain the strength design criterion of a micro polycrystalline silicon structures considering the notch effect.

TEST METHOD AND RESULTS

Specimen and test method

The bending tests of microcantilever are carried out at room temperature under the atmospheric environment. The specimen is illustrated in Figure 1 and the photographs of specimens are shown in Figure 2. The dimensions of the specimens are shown in Table 1. The specimens are made of 3.5 μm polycrystalline silicon film by a surface micromachining process. The substrate is single crystal silicon and the gap between cantilever and substrate is 2 μm. For the tests, two type specimens are prepared (Type-A and B). In the Type-A specimen, the notch of several sizes (1~5 μm) is introduced in the root area of cantilever on purpose. In the Type-B, although the notch is not introduced on purpose, by the microscopic observation, the notch of 1 μm radius is recognized indeed in the root area of cantilever beam as a result of surface micromachining process.

A dynamic ultra micro hardness tester (Shimadzu Co. DUH-W201) is used for the bending tests of microcantilever beams. Table 2 shows the properties of the test machine. The road conditions in the tests are shown in Table 3. The load conditions are changed corresponding to the length of specimen.

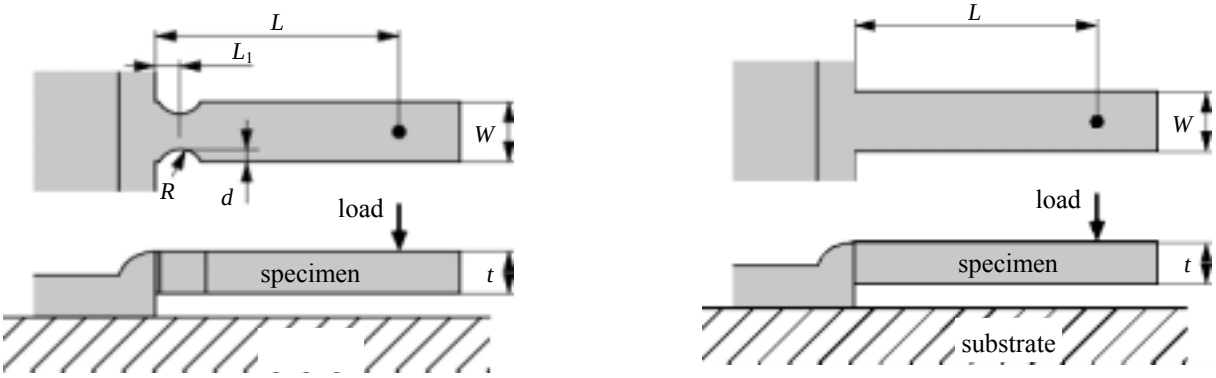

(a) notched specimen (Type-A) (b)no-notched specimen (Type-B)

Figure 1: Schematic diagram of the specimen

(a) notched specimen (Type-A of No. 3) (b) no-notched specimen (Type-B of No. 2)

Figure 2: Top view of examples of the specimen

TABLE 1

DIMENSIONS OF THE SPECIMEN (UNIT: μm) ALL SPECIMEN'S THICKNESS IS 3.5 μm

Type	No.	Width, W	Length, L	Notch root, R	Notch depth, d	Notch distance, L_1
A	1	5	15	1	1	1
	2			2	1	2
	3			3	1	3
	4			4	1	4
	5			5	1	5
B	1	5	10	no	no	no
	2		15	no	no	no

TABLE 2.
PROPERTIES OF THE TEST MACHINE

Load range	0.1 to 1961 [mN]
Minimum measurable load	0.2 [μN]
Indentation depth range	0 to 10 [μm]
Minimum measurable displacement	0.001 [μm]
Indenter	Tetrahedral
Notch root radius of indenter	Under 0.1 [μm]
Displacement measure method	Operation transformer
Loading method	Electromagnetic coil

TABLE 3
TEST CONDITIONS

Specimen	Maximum load	Load speed
Type-A No. 1 to 5, Type-B No. 2	1.96 [mN]	1.421 [mN/sec.]
Type-B No. 1	9.8 [mN]	14.21 [mN/sec.]

Test Results

Figure 3 shows examples of the relationship between the load and displacement of the bending tests. In this figure, it is known that the polycrystalline silicon deformed elastically until final catastrophic failure in room temperature, showing a brittle nature. In this figure, the behavior of specimen Type-A of No. 3 differs from other specimens in the part of A. This is because the free edge of microcantilever beam contacts to the substrate surface.

Figure 4 shows the fracture surface of the specimen (Type-A of No. 1) for example. The origin of the fracture surface is clearly shown in this picture. The fracture origin is located in a tensile side and notch root of the specimen. River pattern [9] can be seen on the fracture surface like other brittle materials.

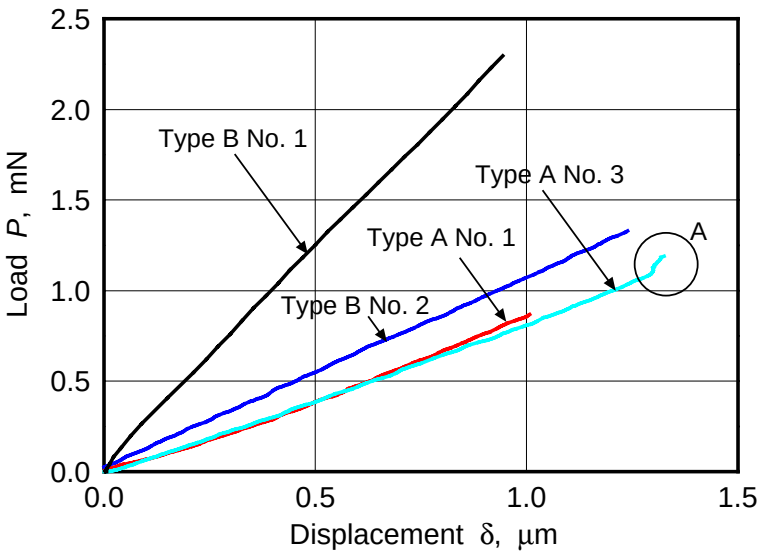

Figure 3: Examples of the relationship between load and displacement of the tests

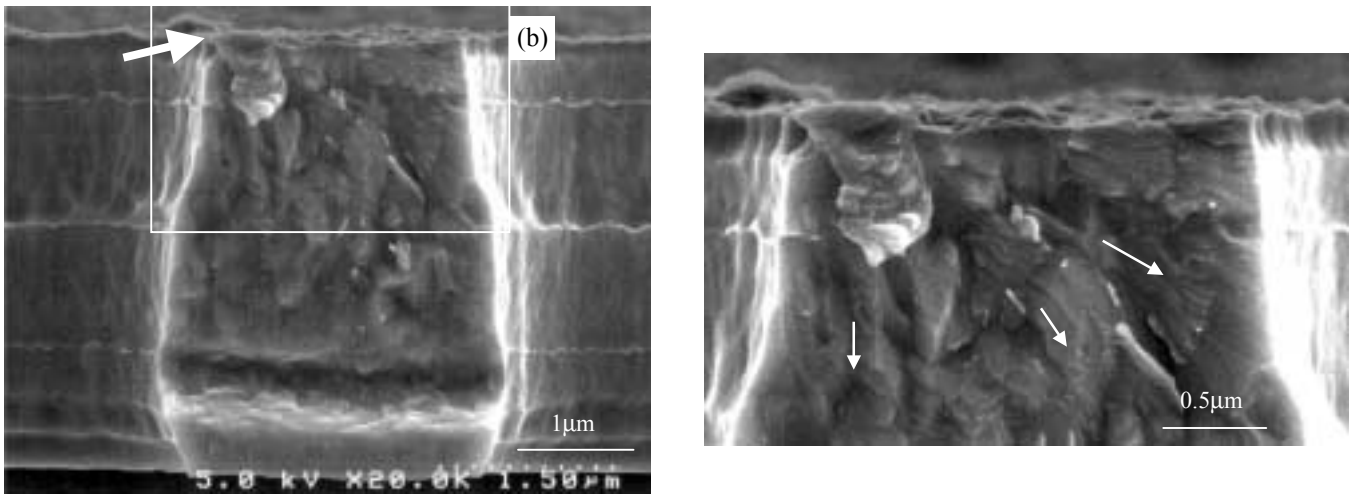

(a) Macroscopic view of fracture surface (arrow shows the fracture origin)

(b) Magnification of fracture origin (arrow shows the fracture direction)

Figure 4: Fracture surface of the specimen

FEM ANALYSIS OF MICROCANTILEVER BEAM

FEM model and analytical procedure

In order to quantify the fracture of specimens by the applied stresses in the tests, the three-dimensional finite element elastic analyses are performed. Table 4 shows the analyses conditions. Figure 5 indicates the examples of FEM models of the specimens (Type-A of No.1 and Type-B of No.1). For the Type-B specimen, the notch of 1 μm radius is taken into the model based on the microscopic observations mentioned above. The element sizes of the models are about 1 μm in the overall region and are about 0.1 μm in the stress concentration area near the notch root. Table 5 shows the material properties used in the analyses. The analyses are carried out under the load condition such as the deformation of loading point is equal to 1 μm.

TABLE 4
FEM CONDITIONS

Elements	3-dimensional 10-node Tetrahedral
Solver	I-DEAS Master Series 7
Load condition	1 μm displacement on the load point
Number of elements	About 6,400
Number of nodes	About 11,000

TABLE 5
MATERIAL PROPERTIES FOR FEM ANALYSES

Young's modulus	148 [GPa]
Poisson's ratio	0.2 [-]

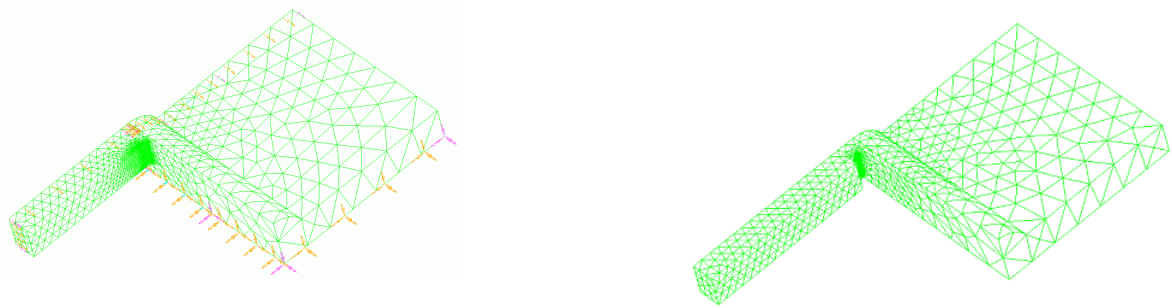

(a) notched model (Type-A of No. 1) (b) no-notched model (Type-B of No.1)

Figure 5: Examples of the FEM model

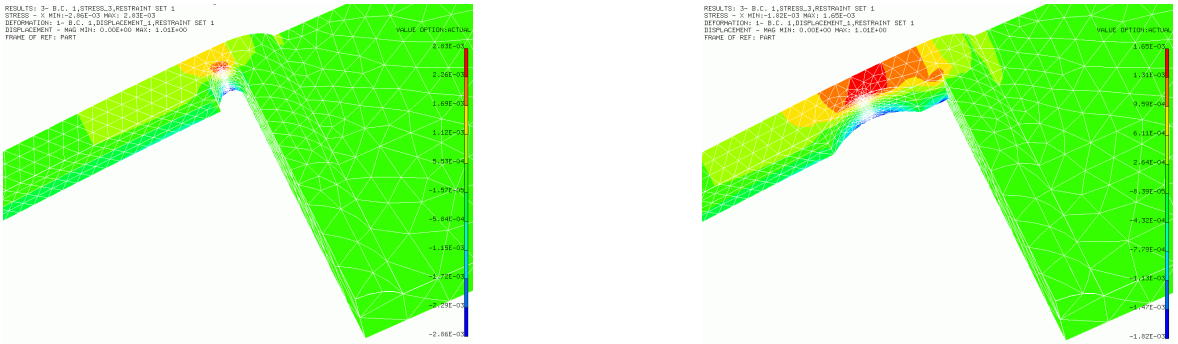

(a) Notched model (Type-A of No. 1) (b) Notched model (Type-A of No. 5)

Figure 6: Examples of the stress distribution around the notch roots

Analytical results

Table 6 shows the maximum stress of the longitudinal direction of beam obtained by FEM analyses, and Figure 6 indicates the stress distributions for example (Type-A of No. 1 and Type-A of No. 5). As the location of fracture origin shown in Figure 4 almost corresponds to the maximum stress area of notch root, the validity of analyses is confirmed qualitatively. Moreover, it is found that the area of stress intensity zone near the notch root is different with the each model corresponding to the difference of stress concentration.

TABLE 6
FEM ANALYSIS RESULTS (1μm DISPLACEMENT OF LOAD POINT)

Type	No.	Reaction Force, P [mN]	Maximum Stress, σ_{max} [GPa]
A	1	1.17	4.43
	2	1.19	3.47
	3	1.21	3.00
	4	1.23	2.67
	5	1.24	2.41
B	1	3.90	5.54
	2	1.42	3.08

DISCUSSIONS

Figure 7 shows an expression of the test results by use of maximum peak stress σ_{max} in the notch root. In this figure, the plots of solid mark means the data of fracture specimens and the open mark means the data of non-fracture specimens due to the contact of free edge to the substrate surface. In Figure 7, a tendency

can be seen that the plots by the σ_{max} move down with the increase in notch radius because of the effect of the difference on the stress distribution pattern. So, this approach using only maximum stress is not recognized as the criterion for the practical use. Therefore, the another approach are taken into account by use of the two parameters that are the peak stress σ_{max} and an area of 0.5 σ_{max}, S which indicates the stress extension around the position of peak stress representatively. Figure 8 shows the results of reforming approach mentioned above. In Figure 8, the mean values of maximum stresses are plotted in consideration of the non-fracture data statistically [10]. The relationship between the maximum stress σ_{max} and the area of $0.5\sigma_{max}$ is expressed by the following equation.

$$\sigma_{max} = 4.19S^{-0.212} \tag{1}$$

In above equation, the unit of S is μm^2 and σ_{max} is GPa respectively. Eqn. 1 represents the limit state of the fracture of microcantilever with satisfaction moderately as the design rule of micro scale structure of the polycrystalline silicon.

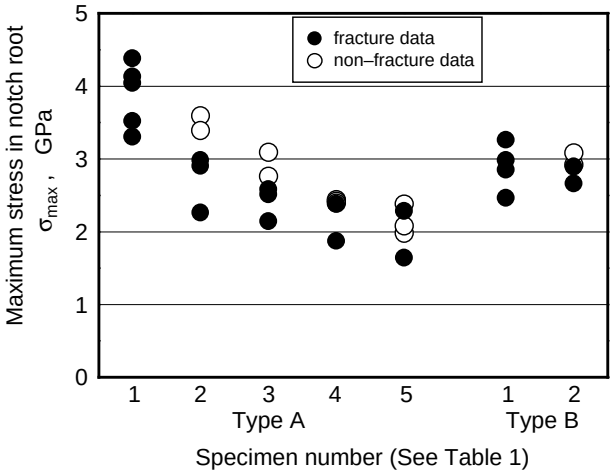

Figure 7: Relationship between maximum stress in notch root and specimen number

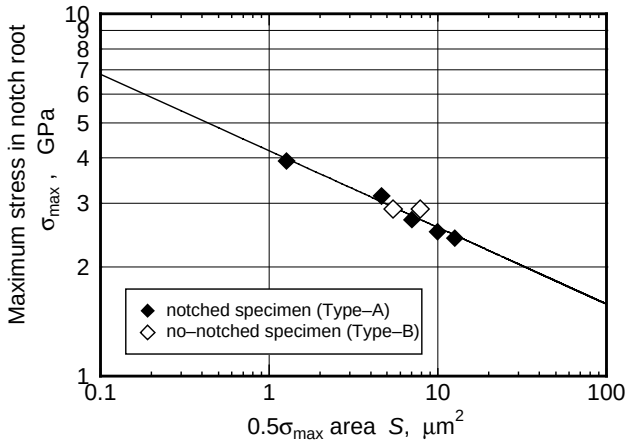

Figure 8: Relationship between maximum stress in notch root and $0.5\sigma_{max}$ area

CONCLUSIONS

The bending tests using the micro scale cantilever beams of polycrystalline silicon with notch are carried out in order to obtain the strength design rule. The original approaches are taken into account using the two parameters that are the peak stress σ_{max} and an area of 0.5 σ_{max}. By this approach, the test results are explained quantitatively and the validity of presented method is confirmed.

REFERENCES

1. Senturia, S. D. (2000). *Microsystem Design*. Kluwer Academic Publishers, Dordrecht.
2. Najafi, K. (2000). *Proc. 2000 Symposium on VLSI Circuits Digest of Technical Papers*. 6.
3. Douglass, M. and Sontheimer, A. (1998). *Texas Instruments Technical Journal*. 15-3, 128.
4. Lűder, E. (1986). *Sensors and Actuators.* 10, 9.
5. Greek, S., Ericson, F., Johansson, S. and Schweitz, J.- Å. (1997). *Thin Solid Films*. 292, 247.
6. Tsuchiya, T., Tabata O., Sakata J. and Taga Y. (1998). *J. microelectromechanical systems*. 7-1, 106.
7. Namazu, T., Isono Y. and Tanaka T. (2000). *Proc. 13th IEEE Int. Conf. Micro Electro Mechanical Systems*. 205.
8. Kapels, H., Aigner R. and Binder J. (2000). *IEEE Trans. Electron Devices.* 47-7, 1522.
9. Hull, D. (1999). *Fractography.* Cambridge University Press, Cambridge.
10. Johnson, L. G. (1964). *The Statistical Treatment of Fatigue Experiments*. Elsevier, New York.

ICF 100728 PR

NOTCH FRACTURE MECHANIC
A REVIEW OF FRACTURE CRITERIA USED IN ELASTIC AND ELASTOPLASTIC CASES

G PLUVINAGE

University of Metz, France

ABSTRACT

Notch fracture criteria are described in terms of stress, energy or strain parameters.

KEYWORDS

NOTCH, FRACTURE MECHANIC.

INTRODUCTION

The notch effect on fracture is characterised by the fact that the critical net stress acting on the ligament area below the notch is less than the ultimate strength of the material. This effect is very sensitive to the notch geometry which can be described by 3 parameters : the notch angle, notch radius and notch length. It is maximum for a crack (which is a particular case of notch with a notch radius and notch angle equal to zero) in a structure made with an elastic material.
The stress distribution at notch root in elastoplastic case can be divided into for zones (1) :
* Zone I : very close to the notch tip, the stress distribution increases to the maximum stress.
* Zone II : a transition between zone I et III.
* Zone III : in this zone the stress distribution decreases as a power function of the distance.
By analogy to purely elastic crack tip stress distribution, this part can be considered as a pseudo stress singularity. The stress distribution can be represented by the following relationship :

$$\sigma_{yy} = \frac{K_\rho}{(2\pi r)^\alpha} \qquad (1)$$

where K_ρ is the so-called notch stress intensity factor and α a power exponent. The limit between zone II and zone III is called the effective distance X_{ef} and it has been shown that it correspond to the limit of the fracture process zone (2).

* Zone IV far from notch tip, the stress value trends to reach the net stress value.

The mechanism of fracture emanating from notch or crack is fundamentally different from the traditional “hot spot“ approach (i.e. fracture occurs at the point of maximum stress). It is well known that it needs a fracture process volume. In this volume, the effective stress or fracture

stress can be considered as an average stress which takes into account the stress distribution and the stress gradient. This approach is called ” fracture volumetric approach” and can be used with, stress energetic or strain parameters.

LOCAL FRACTURE CRITERION FOR FRACTURE EMANATING FROM NOTCHES

In order to get the fracture effective stress, we have to take into account stress value and the stress gradient in the neighbouring of any point in the fracture process volume. This volume is assumed to be quasi-cylindrical by analogy with notch plastic zone which has a similar shape. The diameter of this cylinder is called the effective distance. The stress value in any point inside the process zone is weighted in order to take into account the distance from notch tip and the relative stress gradient. Fracture stress can be estimated by some average value of the weighted stresses.

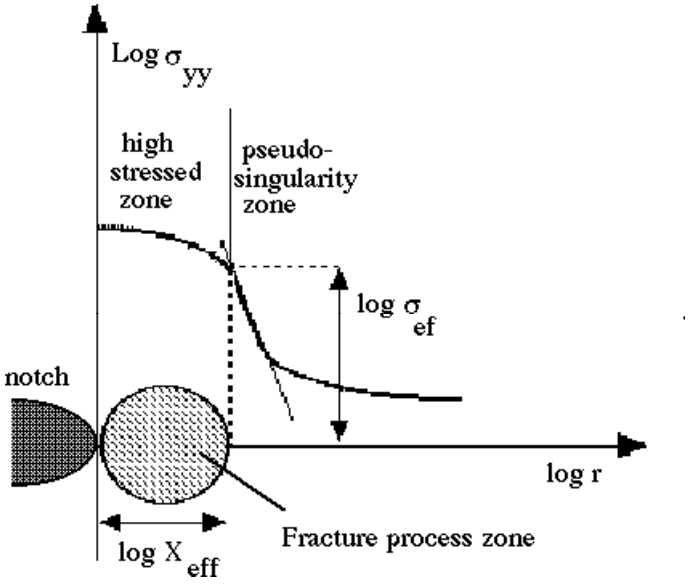

Figure 1 : Schematic presentation of a local stress criterion for fracture emanating from notches.

This leads to a local stress fracture criterion with two parameters : the effective distance X_{ef} and the effective stress σ_{ef} .A graphical representation of this local stress fracture criterion is provided in Figure 2 where the logarithm of the stress normal to the notch plane is plotted versus the logarithm of distance, effective stress and distance are presented. A graphical procedure for determination of X_{ef} has been proposed by [2]. It has been seen that the effective distance is connecting to the minimum of relative stress gradient χ defined by :

$$\chi = \frac{1}{\sigma_{yy}} \cdot \frac{d\sigma_{yy}}{dr} \qquad (2)$$

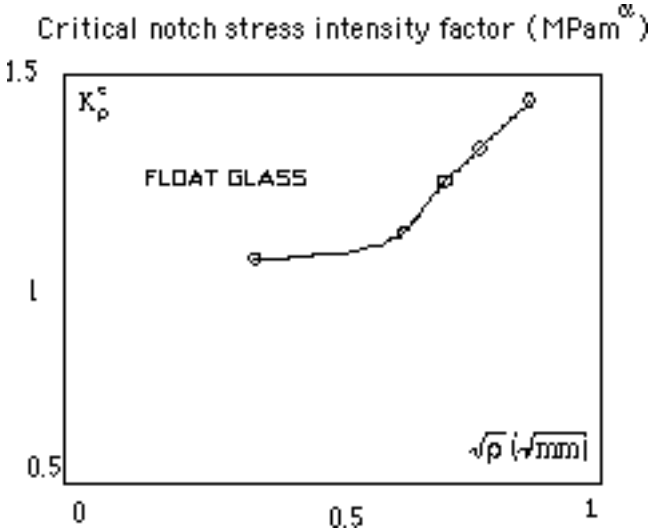

Figure 2 : Evolution of critical notch stress intensity factor versus the square root of notch radius for Float Glass.

The effective stress is defined as the average of the weighted stress inside the fracture process zone

$$\sigma_{ef} = \frac{1}{X_{ef}} \cdot \int_0^{X_{ef}} \widehat{\sigma_{ij}}\, dx \tag{3}$$

where the weighted stress is given by :

$$\widehat{\sigma_{ij}} = \sigma_{ij} \cdot (1 - \chi x) \tag{4}$$

The fracture criterion is a two parameter criterion. For a CrMoV steel with fine carbides (FC) microstructure (Yield stress 771 MPa), the mean value of the effective stress is 1223 MPa which can be compare to the average maximum local stress at fracture σ_{max} of 1310 MPa. Critical notch stress intensity factor can be used as a maesure of fracture toughness as it can be seen for Float Glass in figure 2.

ENERGETIC FRACTURE CRITERIA FOR NOTCHED COMPONENTS

Influence of notch radius on critical value of energetic parameter J

For a non-linear behaviour, two energy based fracture criteria can be used: the critical non-linear energy release rate of Liebowitz [3] (equ 5), and the energy parameter J of Turner [4] (equ 6).

$$\widetilde{G_{Ic}} = -\frac{1}{B} \cdot \frac{\partial U_{nl}}{\partial a} \tag{5}$$

$$J_{Ic} = \frac{\eta . U_{nl}^{c}}{B.b} \tag{6}$$

with b = W-a and U_{nl}^{c} the non-linear work done for fracture. Assuming that $J_{Ic} = \widetilde{G_{Ic}}$ we have :

$$\eta = -\frac{\partial \mathrm{Ln} U_{nl}}{\partial a} \tag{7}$$

From this formula we get the evolution of η, as a function of depth and notch root radius :

$$\eta = \eta(a, \rho) \tag{8}$$

The evolution of the η factor as a function of notch root radius shows an absolute minimum with the abscissa ρ_c (figure 3). Similarly, we notice that for radius values below ρ_c, the η factor decreases linearly with ρ. Beyond this critical abscissa, the η factor increases with ρ and becomes approximately constant for a radius ranging between 1.54 and 2 mm. The

difference between the η factor for cracks and notches with the same length can reach 36% of the latter one, which is important and justifies the present approach.

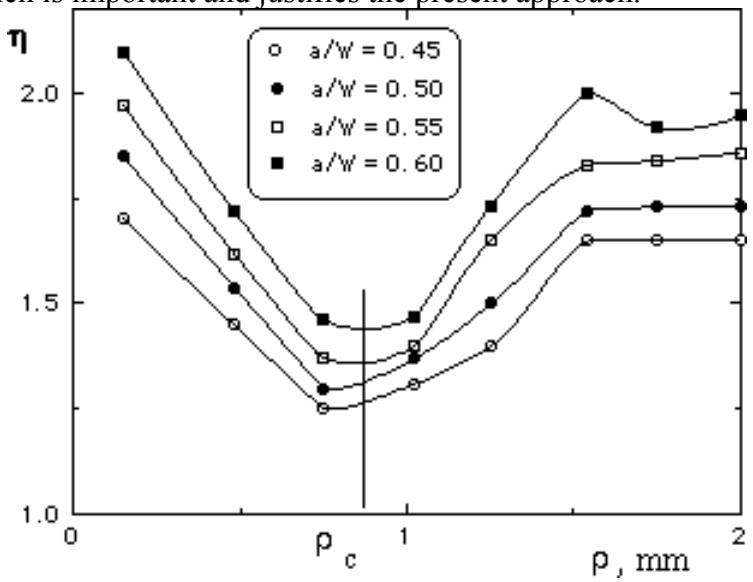

Figure 3 : Evolution of η with notch radius for constant relative depth Charpy U notch specimen.

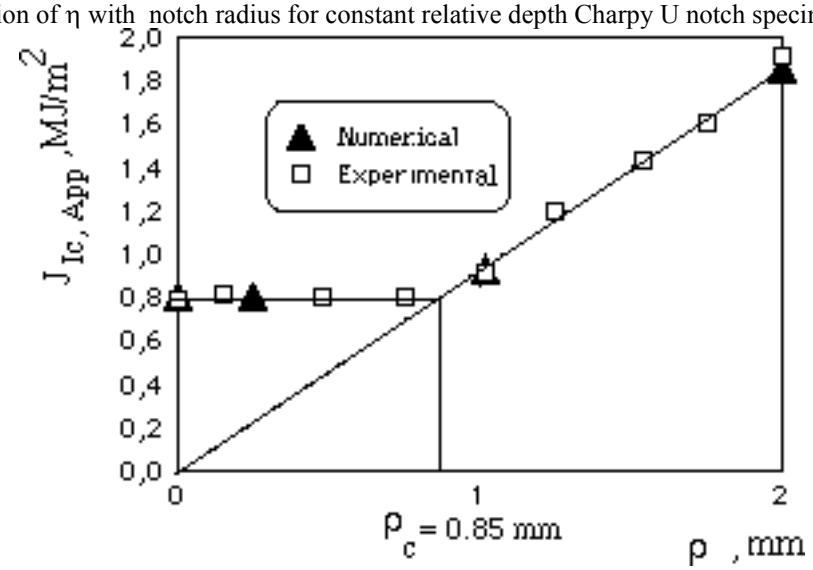

Figure 4 : $J_{Ic,App}$ versus notch radius for Charpy U notch specimen in steel .

In the following, we will call the fracture toughness given from notched specimen " apparent fracture toughness " written $J_{Ic,App}$, J_{Ic} is defined only for cracked specimens.

$$J_{Ic,App} = \frac{\eta(a,\rho).U_{nl}^{c}(a,\rho)}{B.b} \qquad (9)$$

An exemple of evolution of the apparent fracture toughness vesus notch radius is given in figure 4. We can notice that for radii less than a critical value, ρ has no influence on fracture toughness, but for radii beyond this critical value $J_{Ic,App}$ increases linearly.

Strain energy density at notch tip

If we plot the strain energy density versus the notch tip distance in a bilogarithmic graph, we get the following distribution presented in figure 5.

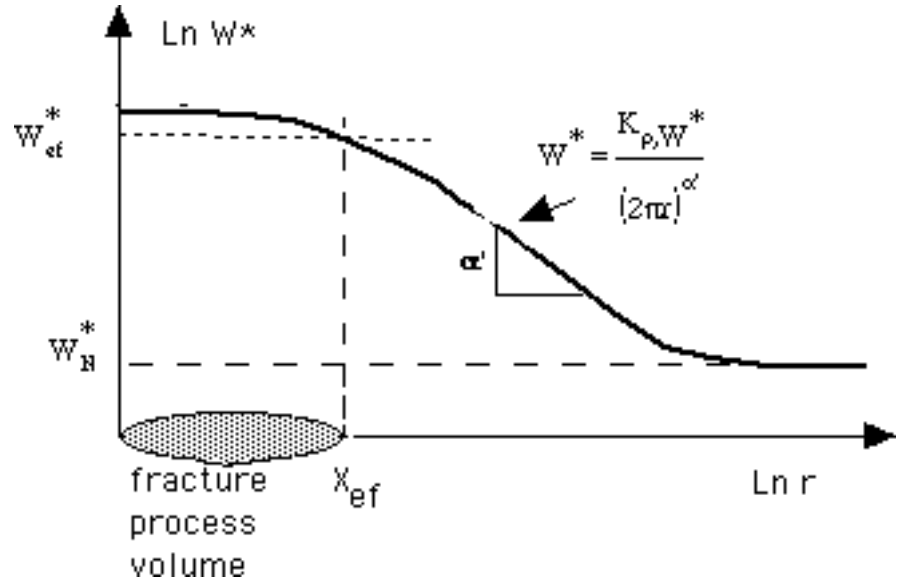

Figure 5 : Distribution of the strain energy density at notch tip

This distribution can be characterised by four parameters:

- W^*_{ef} : the effective strain energy density at notch tip,
- X_{ef} : the effective distance,
- α' : the slope of the linear part of the strain energy density distribution,
- W^*_N : the net strain energy density.

The strain energy density notch intensity factor has been defined in the area of the "pseudo strain energy density singularities" of the notch in figure 5. This distribution can be considered only for a distance greater than X'_m defined on this figure with the following form :

$$W^* = \frac{K_{\rho,W^*}}{(2\pi r)^{\alpha'}} \quad \text{for } r \square X'_{ef} \tag{10}$$

The strain energy density W^* at notch tip is a mechanical parameter which can be used as fracture criterion. For fracture, the average critical strain energy density W^*_{ef} in the fracture process volume can be used as a local energetic criteria. Fracture occurs when :

$$W^*_{ef} = W^*_c \tag{11}$$

LOCAL STRAIN FRACTURE CRITERION

Strain distribution can be presented similarly that stress distribution in a bilogarithmic graph (figure 6).

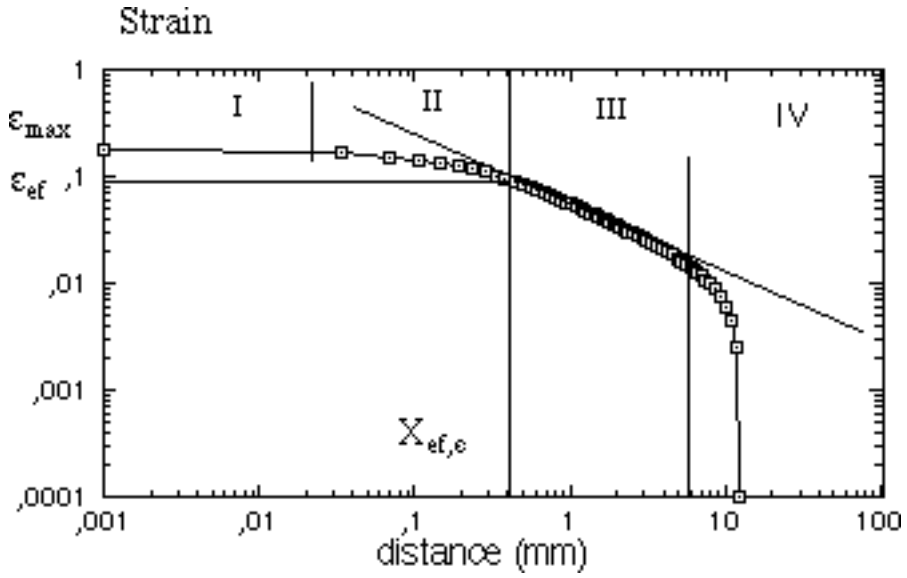

Figure 6 : Exempla of the elastoplastic strain distribution at the notch tip presented in a bilogaritmic graph.

Zone III which can be assimilated to a zone of train pseudo-singularity. In this area the strain-distance relationship has the following form

$$\varepsilon_{yy} = \frac{k_{\rho,\varepsilon}}{(2\pi r)^{\alpha''}} \tag{12}$$

A local strain fracture criterion is based also on the concept of fracture volume process which has been described in the case of local stress fracture criterion . The limit of this fracture process is also the beginning of the strain pseudo singularity which has for abscissa $X_{ef,\varepsilon}$. For the critical event the strain for this abscissa is the critical effective stress $\varepsilon_{ef,c}$.

The product $\varepsilon^{c}_{ef,\varepsilon}.\left(2\pi.X^{c}_{ef,\varepsilon}\right)^{\alpha''}$ "is precisely the critical notch strain intensity factor which can be taken as a measure of the fracture toughness.

$$K^{c}_{\rho,\varepsilon} = \varepsilon^{c}_{ef,\varepsilon}.\left(2\pi.X^{c}_{ef,\varepsilon}\right)^{\alpha''} \tag{13}$$

In other words fracture occurs when the notch strain intensity factor reaches a critical value :

$$K_{\rho,\varepsilon} = K^{c}_{\rho,\varepsilon} \tag{14}$$

the Notch Ductility Factor (NDF) differs from the critical strain intensity factor by a constant

$$NDF = \varepsilon^{c}_{ef}\left(X^{c}_{ef,\varepsilon}\right)^{\alpha''} = \frac{k^{c}_{\rho,\varepsilon}}{(2\pi)^{\alpha''}} \tag{15}$$

:

An exempla of evolution of notch ductility factor measured on SENT specimen made in steel is presented in figure 7.

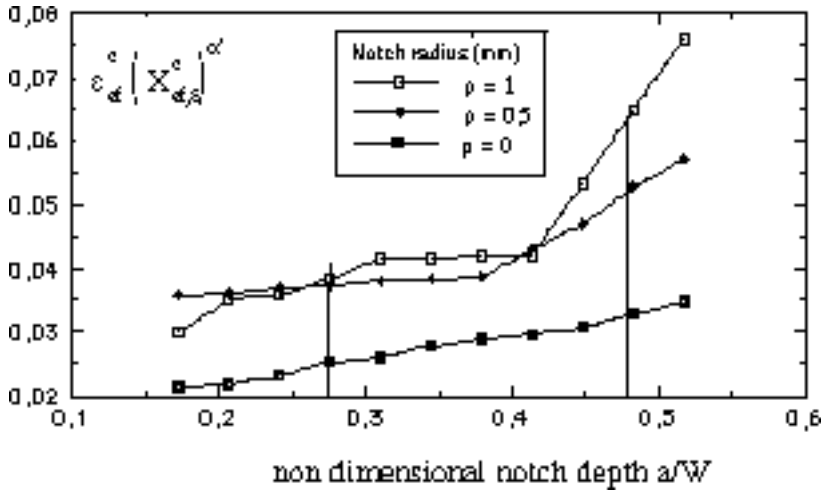

Figure 7. : Evolution of the Notch Ductility Factor with notch radius and non dimensional notch depth.

REFERENCES

1. Niu, L.S. Chehimi, C. Pluvinage, G. (1994).*Engineering Fracture Mechanics*, Vol. 49, N°3, p 325 – 335.
2. Pluvinage, G. (1998*). Physico Chemical Mechanics of Materials* No 6,Tome 34, pp7-20,
3. Liebowitz, H. and Eftis, J. (1971).*Engineering fracture mechanics*, pp. 267-281.
4. Turner,C.E. (1979) , *Post-yield fracture mechanics* pp. 23-210.

ICF100282OR

NOTCH FRACTURE OF MEMS SENSORS MADE OF SINGLE CRYSTAL SILICON

Z. L. Zhang[1], N. Vitorovich[2], E. Westby[3], D. T. Wang[4]

[1] SINTEF Materials Technology, Trondheim, Norway,
[2]NTNU, Trondheim, Norway, [3] SensoNor, Horten, Norway,
[4] SINTEF Electronics and Cybernetics, Oslo, Norway.

A paper to be presented by Z. L. Zhang at the ICF10.

Address before 1st August 2001:

Division of Engineering and Applied Science
Harvard University
Pierce 312, 29 Oxford Street
Cambridge 02138, USA
Tel: 1-617-495-2891
Fax: 1-617-496-0601
E-mail: zzhang@esag.harvard.edu

Address after 1st August 2001:

SINTEF Materials Technology
N-7456 Trondheim, Norway

NOTCH FRACTURE OF MEMS SENSORS MADE OF SINGLE CRYSTAL SILICON

Z. L. Zhang[1], N. Vitorovich[2], E. Westby[3], D. T. Wang[4]

[1] SINTEF Materials Technology, Trondheim, Norway, [2]NTNU, Trondheim, Norway, [3] SensoNor, Horten, Norway, [4] SINTEF Electronics and Cybernetics, Oslo, Norway.

ABSTRACT

Designers of silicon microstructures are often facing a so-called notch fracture problem. Anisotropic etching results in corners which are sharp on an atomistic length scale. Neither the stress-based design approach nor the well-established linear elastic fracture mechanics (LEFM) apply for such cases. In analogy to the LEFM for cracks, a notch fracture mechanics can be developed. In the present paper, a simple sensor-type plane-strain bending specimen with 23 μm thick membrane has been manufactured and tested to determine the critical notch stress intensity factor for silicon microstructures with notch opening angle 125.26^{o}. The resulting critical stress intensity factor has been used to predict the burst pressure test results of the same type sensor structures. Excellent agreement between the prediction and burst tests was observed. It indicates that the critical notch stress intensity factor can be taken as failure criterion for sensor structures with a thin membrane. The critical notch stress intensity factor is, however, about 20% lower than the value from bulk material. For design purpose of pressure sensors, an equation for calculating the notch stress intensity factor as a function of membrane thickness is given. The factors influencing the notch stress intensity factor and the possibility of a unified failure criterion for silicon microstructures with different notch angles are discussed.

KEYWORDS

Notch fracture, MEMS, Single Crystal Silicon, Failure Criterion.

INTRODUCTION

The development of the fast growing micro-electro-mechanical-systems (MEMS) has presented many new technological challenges. One of them is called notch fracture of silicon microstructures. Silicon is an ideal elastic brittle material. For failure analyses of structures made of brittle materials, the stress based strength approach and the LEFM approach can be applied. In the former, a maximum stress in the structure must be found while in the later a crack pre-exists and a stress intensity factor should be calculated. For silicon microstructures used in MEMS, the anisotropic etching process that etches different crystallographic planes with dramatically different speed, results in atomistically sharp reentrant notches. Early analysis by Williams [1] has shown that a stress singularity exists close to the notch tip.

The degree of the stress singularity depends on the notch opening angle. Thus, for silicon microstructures with sharp notches, neither the strength approach nor the LEFM may be applied. Hence, a notch fracture mechanics must be developed. By an asymptotic analysis, the stress field near the notch tip can be expressed by three terms, – a radial single term, an angular term and a stress intensity factor. Intuitively, we may think that the fracture mechanics for crack problems can be directly extended to the notch fracture problem. Because of the special singularity at crack tips, $(r)^{-0.5}$, where r is the distance to the crack tip, there is a mathematically beautiful one-to-one relation between the crack tip stress intensity factor and the surface energy. Irrespective of the local fracture process, the critical stress intensity factor links directly to the surface energy and can be formulated as the fracture criterion. For notch problems, this simple relation does not exist and the notch tip stress intensity factor loses the link to the energy argument. There is no strong theoretical basis and it needs to be proved experimentally that the notch stress intensity factor can be taken as a fracture (initiation) controlling parameter. Even if the critical notch stress intensity factor is a fracture parameter, it should work only for crack initiation and its value is dependent on the notch angle. How to develop a general failure criterion for silicon microstructure - how to link the critical notch stress intensity factors with the critical stress intensity factor is still an open question.

A considerable work has been done in the literature to determine the critical stress intensity factors [2-5], in particular by Suwito [3]. For a fixed angle, Suwito has shown that the critical notch stress intensity factor is a constant. The critical notch stress intensity factor is increasing with the increase of notch angle. The experiments carried out in the literature were mostly for bulk materials. In this paper, a sensor type specimen with thin membrane has been manufactured and tested to determine the critical stress intensity factor. The resulting critical stress intensity factor was then applied to predict the burst pressure of the same type structures. By finite element analysis, a stress intensity factor equation as a function of the membrane thickness is presented for pressure sensor design. The transferability of the critical stress intensity factor for bulk materials to thin membranes and various factors influencing the stress intensity factor are discussed.

NOTCH TIP STRESS FIELDS

Single crystal silicon is an an-isotropic elastic material. The stress fields in anisotropic elastic solids can be conveniently described by the Stroh's formalism [6-7]. For the coordinates system shown in Fig. 1, the general solution for displacements and stress functions can be written as

$$u_i = \sum_{\omega=\pm 1}^{\pm 3} a_{i\omega} f_\omega(z_\omega)$$
$$\phi_i = \sum_{\omega=\pm 1}^{\pm 3} b_{i\omega} f_\omega(z_\omega) \qquad (1)$$

where $z_\omega = x + \rho_\omega y$, ρ_ω are Stroh's 3-pair eigenvalues, f_ω are twice-differentiable one-variable functions, a_ω and b_ω are constants. Stroh has shown that eigenvalues can be solved from a standard six-dimensional linear eigenvalue problem. Detailed formulation of the eigenvalue problem can be found in [7]. By conducting an asymptotic analysis of the near tip stress fields , using the traction free conditions and neglecting the higher terms, we can finally write the near tip stress and displacement fields as

$$\sigma_{ij} = K_I^N f_{ij}^I(\theta) r^{\lambda_I - 1} + K_{II}^N f_{ij}^{II}(\theta) r^{\lambda_{II} - 1}$$
$$u_i = K_I^N g_{ij}^I(\theta) r^{\lambda_I} + K_{II}^N g_{ij}^{II}(\theta) r^{\lambda_{II}} \qquad (2)$$

where λ^I and λ^{II} are mode I and II degrees of singularity, K_I^N and K_{II}^N are notch stress intensity factors, and f_{ij} and g_{ij} are angular functions. For the notch considered in this paper with notch opening angle

between the (001) and (111) planes, 2β=125.26°, the mode I degree singularity, λ_I, is 0.6257 and mode II, λ_{II}, is 1, (not singular) [3,4]. Thus the near tip field can be written more explicitly

$$\sigma_{ij} = K^N f_{ij}^I(\theta) r^{-0.3743} + F_{ij}(\theta)$$
$$u_i = K^N g_{ij}^I(\theta) r^{0.6257} + G_{ij}(\theta) r \quad (3)$$

where the K^N is the notch stress intensity factor and *F* and *G* are angular constants. Here K^N is defined by normalizing the angular function such that $f_{ij}^I(\theta=0)=1.0$. By carrying out a finite element analysis for a given geometry and load, the K^N can be determined from either the opening stress along the x axis (θ=0) or from the opening displacement along the notch edge ($\theta=\pm\alpha$) by a least square fitting. In the present paper, the average opening displacement along the notch edge was applied. In finite element calculations, displacements are supposed to be more accurate than stress and strain. It should be noted that for silicon structures considered here, there is a rigid rotation around the notch tip and this rigid rotation has been subtracted prior to the curve fitting.

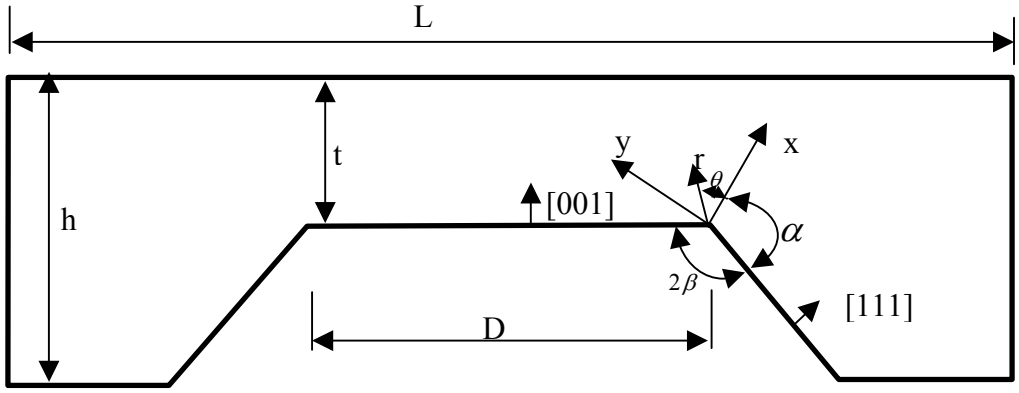

Fig. 1 Sketch of a sensor-type microstructure. The notch angles (2β=125.26°) are determined by crystallographic planes. The coordinates are used for material representation and asymptotic analysis.

SENSOR-TYPE SPECIMENS

MEMS structures are indeed composite. Fig. 2b shows a typical sensor-type microstructure (glass-silicon-glass sealed by anodic bonding). It is not easy to test the silicon microstructure itself. For bending tests, there are basically two possibilities to apply load to the microstructure shown in Fig.1 such that positive singular stress fields are generated at the notches. One way is to apply the load at the non-etched side. In this case the two supporting ends should be simple ends – fixed in vertical direction but free to move horizontally. Another way is to apply the load at the etched side. In this situation the two supporting ends on the top can be fixed in both horizontal and vertical directions. Specially prepared specimens with very thick membranes and loading at the non-etched side have been used in the literature [3-4]. The smallest *t/h* tested by Wuwito [3] was 0.8. For a typical silicon sensor structure, the membrane is very thin and the typical *t/h* value is about 0.02. It is questionable whether the critical notch stress intensity factor from bulk material can be applied to structures with such thin membranes. Furthermore, the fracture strength may be sensitive to the micromachining process and specially prepared specimens may not be representative of sensor structures from mass production. In this paper, bending specimens cut from a generic type sensor have been tested [8]. The dimensions of the generic sensor tested in this paper are *L*=1.95 mm, *D*=0.45 mm, *t*=0.023 mm, *h*=0.4 mm and width W=0.85 mm. Fig 2a shows the 3-point bending specimen.

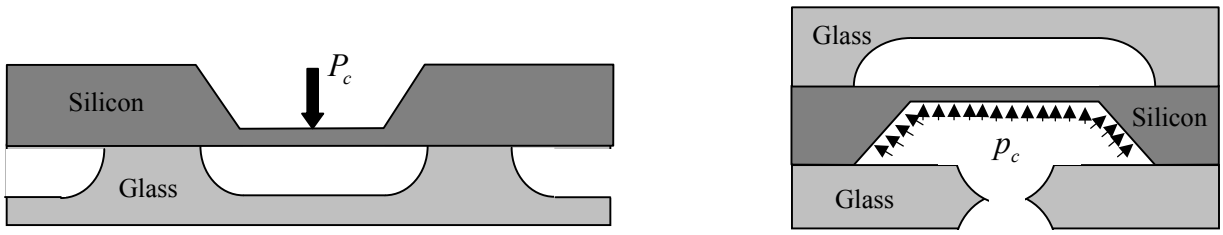

Figure 2: Sketches of a) the three point bending sensor-type specimen and b) the burst pressure specimen.

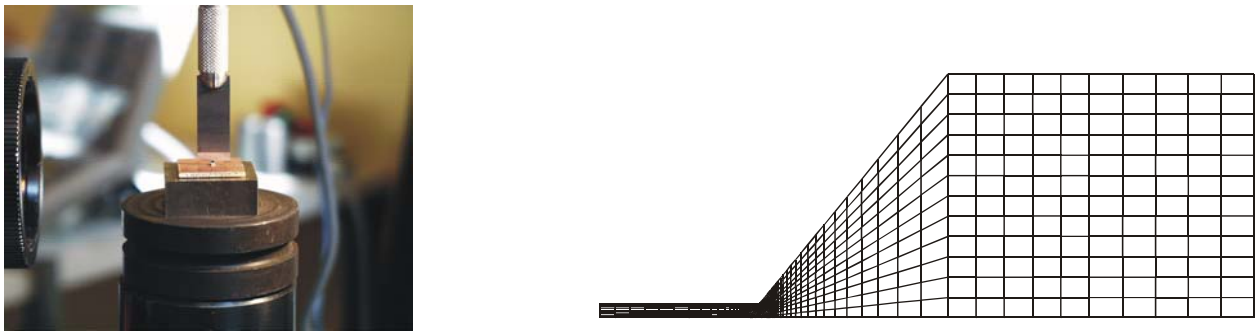

Figure 3 a) Lateral view of the loading blade and bending specimens, b) the finite element mesh used for the analyses.

The tests were conducted on a Darmtec tensile machine with a specially mounted micro load cell of sufficient accuracy. The load was applied through a super sharp flat blade made of quenched high alloy steel, see Fig. 3. The specimen was fixed with silicone glue on a copper layer of a thin resin plate of area 1.5 cm by 1.5 cm. The plate with the specimen was placed on a mobile micro table with four degrees of freedom. The test setup was equipped with an optical microscope for positioning. After accurate positioning of the blade parallel to the desired axis by manipulating the table translation and rotation degrees of freedom, the specimen was loaded with a cross-head speed 0.5 μm/s until its breakup. The details of the experimental technique are reported in [8].

The glass-silicon-glass specimens used for the burst pressure tests are shown in Fig. 2b. The composite structure is attached on top of a holed plate. A controlled increase in time of pressure was applied through the hole in the silicon cavity until the failure. Only the final burst pressure was registered for each specimen. It should be noted that the bending specimens were designed and loaded as 2D specimen while the burst testing specimen is 3D and the membrane has a dimension 1.0mm by 0.45 mm.

TEST RESULTS AND CRITICAL NOTCH STRESS FACTOR

For the bending tests, 9 specimens in total have been tested. Load-cross head displacement was monitored for each test. All showed linear relation up to final failure. Post-test examination shows that all the specimens fractured at the midpoints of the notch tip edges. For the specimens with width 0.85 mm, the averaged critical load of the 9 specimens is 1.04 N with a standard deviation 0.11 N, minimum 0.934 N and maximum 1.23 N. Finite element analyses were carried out to determine the critical notch stress intensity factor. Fig. 3b shows half of the finite element model used. A specially designed, very fine mesh was used at the notch tip. There are in total 3045 4-node plane strain ABAQUS elements in the model. The near tip elements are about 0.11 nm long. The elastic anisotropic constants with regard to the material coordinates shown in Fig. 1 were taken from [2]. As seen in the Fig 3b, the supporting glass was not

modeled. Instead, the interface between the silicon and glass was assumed to be rigid. Preliminary analyses have shown that the length of the rigid boundary has little influence on the notch tip stress field, because the membrane considered in this paper is very thin. The average opening displacement along the notch edges under the applied critical load were fitted by a non-linear curve fitting program with the following equation

$$u_{\theta(\theta=\pm\alpha)} = 0.000578^{0.6257} + 0.00056r \qquad (4)$$

The fitting range for the above equation is 3.5 μm which is 15% of the membrane thickness. Please note that in the above equation the unit for displacement and radius is [mm]. By comparing Eq. (4) with Eq. (3) and using $g_{\theta\theta(\theta=\pm\alpha)}=7.91\times10^{-6} MPa^{-1}$, we obtain the critical notch intensity factor K_C^N=73.0 MPa $mm^{0.3743}$ (5.5 MPa $m^{0.3743}$).

The same finite element mesh shown in Fig. 3b was slightly modified for analyses of the pressure sensor to take into account the boundary conditions. Analyses have revealed the following relation between the pressure and the notch tip stress intensity factor for the given structure: $p = 0.575K^N$, where the p is the applied pressure [bar]. By applying the critical stress intensity factor from the bending test, we finally predict the burst pressure would be 42 bar.

The burst pressure tests carried out included 8 specimens in total. Three of them failed at 40 bar, three failed below 40 bar with a minimum 38 bar, and two over 40 bar which is beyond the measurement limit. All specimens were reported to fail at the notch tip in the proximity of the one half of the long side of the rectangular membrane (1mm by 0.45 mm). The averaged burst pressure is about 39.7 bar which is very close to the predicted one. It should be noted that the calculations carried out in the paper were based on a 2D stress field, which is well justified for the bending specimens. For the burst pressure specimens, the stress field is clearly 3 dimensional. However, the experimental observation has indicated that the failure occurred in the middle of the long edge of the membrane and the long side is two times as long as the short side. The 2D plane strain calculations may therefore be justified.

For design purpose pressure specimens with different membrane thickness but otherwise identical dimensions have been analyzed. Six cases with membrane thickness, 18, 23, 30, 35, 40 and 50 μm were considered. Following relation between the applied pressure p [bar] and the notch stress intensity factor [MPa $mm^{0.3743}$]: $K^N = ph^{0.3743} f_N(t/h)$, where the unit of h is [mm] has been obtained:

$$f_N(\frac{t}{h}) = 6.37 - 0.08502(\frac{t}{h}) + 0.0003281(\frac{t}{h})^2 . \qquad (5)$$

DISCUSSIONS AND CONCLUDING REMARKS

A sensor-type specimen made of silicon and glass cut from real sensor has been mechanically tested. The sensors were produced using commercial production technique. The silicon microstructure in the specimens therefore should represent the typical surface conditions of commercial sensor products. The test results show that silicon microstructure fails when the notch has reached a critical notch stress intensity factor 5.5 MPa $m^{0.3743}$. This value has been used to predict the burst pressure of the same type of structure, and an excellent agreement was obtained. This finding indicates that this critical value can be used for the design of pressure sensors with thin membrane. It must be noted that this critical notch stress intensity factor is about 20% lower than the value reported in the literature for bulk materials [3]. How the membrane thickness influences the critical notch stress intensity is not quite know to us. There are two other possibilities that might have caused the discrepancy. Firstly, the surface conditions may be different

in our specimens and in others. It is known that the notch tip radius has a great effect on the fracture strength of silicon structures. Fig. 4 shows the notch tip geometry of our specimens at high magnification. We can observe that at 10000 magnifications there is no observable notch radius. An additional observation from Fig. 4 is that there are local "steps" close to the notch tip. The influence of the "steps" on the notch tip stress field is not clear to us yet. The notch tip radius in [3] was not reported, therefore it is not possible to compare. Secondly, the presence of residual stress in our specimens certainly contribute to the decrease of the critical notch stress intensity factor, while in [3] the specimens are basically residual stress free. The average thermal expansion of glass in the process temperature range is larger than that of silicon. When the cooling takes place from the bonding temperature of 400 C° to room temperature, a positive stress intensity factor might already have been built up at the notch tip.

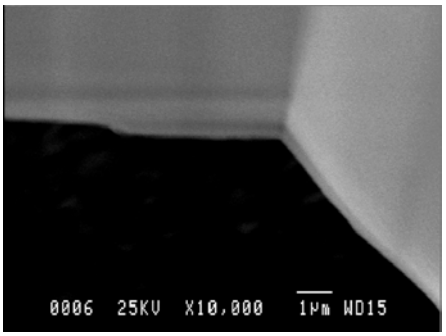

Figure 4: Notch tip geometry at high magnification.

An important question may be raised regarding the validity of the notch stress field for structures with a thin membrane. For our specimens with 0.023 mm thick membrane, the valid area of the K_C^N field at least has a radius of 3.5 μm which is far larger than the physically non-linear range at the notch tip of single crystal silicon. This can justify that the notch tip stress fields at failure are still controlled by the K_C^N.

So far, we have focused on the notch fracture of a fixed notch angle. It has been stated early that for cases with different notch angle, not only the value of the critical notch stress intensity factor will be different, but also the units. It is therefore not possible to transfer the critical notch intensity factor from one case to another. Currently a unified failure criterion for notch fracture based on cohesive model is being developed. In the unified criterion, the critical notch stress factor is linked to the cohesive energy (surface energy) via the material's cohesive strength. Details on this work will be reported elsewhere.

Acknowledgements - Part of the work was carried out by the first author during his sabbatical leave at Harvard University. The computational support from Harvard is greatly appreciated. Help from Hans Lange and Kjell Muller for carrying out the experiments are greatly appreciated.

References

1. Williams , M.L. (1952) *J. Applied Mech.* **74**, 526.
2. Suwito, W., Dunn, M.L. and Gunningham S. J. (1999) *J. Applied Physics* **85,**3519.
3. Suwito W. Ph.D thesis, University of Colorado, 1998.
4. Busch M., Kuna M. and Heizelmann M. (1994) in Proceedings of European Conference on Fracture, V 1.1.
5. Mazza E. and Dual J., (1999) *J. Mech. Phys. Solids* **47**, 1795.
6. Stroh A. N. (1962) *J. Math. Phys*. **41**, 77.
7. Ting T.C.T. (1986) *Int. J. Solids Structures* **22,** 965.
8. N. Vitorovic (2000), MSc thesis, Polytechnical University of Milan, Italy/NTNU, Norway.

NOTCH FRACTURE OF MEMS SENSORS MADE OF SINGLE CRYSTAL SILICON

Z. L. Zhang[1], N. Vitorovich[2], E. Westby[3], D. T. Wang[4]

[1] SINTEF Materials Technology, Trondheim, Norway, [2]NTNU, Trondheim, Norway, [3] SensoNor, Horten, Norway, [4] SINTEF Electronics and Cybernetics, Oslo, Norway.

ABSTRACT

Designers of silicon microstructures are often facing a so-called notch fracture problem. Anisotropic etching results in corners which are sharp on an atomistic length scale. Neither the stress-based design approach nor the well-established linear elastic fracture mechanics (LEFM) apply for such cases. In analogy to the LEFM for cracks, a notch fracture mechanics can be developed. In the present paper, a simple sensor-type plane-strain bending specimen with 23 μm thick membrane has been manufactured and tested to determine the critical notch stress intensity factor for silicon microstructures with notch opening angle 125.26^{o}. The resulting critical stress intensity factor has been used to predict the burst pressure test results of the same type sensor structures. Excellent agreement between the prediction and burst tests was observed. It indicates that the critical notch stress intensity factor can be taken as failure criterion for sensor structures with a thin membrane. The critical notch stress intensity factor is, however, about 20% lower than the value from bulk material. For design purpose of pressure sensors, an equation for calculating the notch stress intensity factor as a function of membrane thickness is given. The factors influencing the notch stress intensity factor and the possibility of a unified failure criterion for silicon microstructures with different notch angles are discussed.

ICF100109OR

NOTCH STRENGTH AND NOTCH SENSITIVITY OF POLYMETHYL METHACTYLATE

WANG Hong, YAN Junhui and ZHENG Xiulin

Department of Material Science and Engineering, Northwestern Polytechnical University, Xi'an 710072, P.R.China

Abstract: A formula to predict notch strength (σ_N) of polymethyl methacrylate (PMMA) under different stress concentration factors (K_t) from tensile properties of smooth specimens is given by analyzing the characteristics of stress and strain at notch and crack tip. The predicted values are in good agreement with test results. The curves derived from the formula mentioned above include three parts in different range of K_t. The upper level line controlled by ultimate tensile strength (σ_b) beginning at K_t=1 and ending at the notch sensitivity factor (K_N). The slope part of notch strength decreasing from the K_N to the sharp notch insensitivity factor (K_ρ) and the lower level line controlled by the fracture toughness beginning at the K_ρ. When $K_t > K_N$, the PMMA with the ratio $\sigma_N / \sigma_b <$ 1 is sensitive to notch. It is shown that the oriented PMMA has less notch sensitivity than the non-oriented PMMA because of the higher ductility of the former.

Key words: polymethyl methacrylate, notch strength, notch sensitivity, fracture toughness, tensile properties

1. Introduction

PMMA is an important material used in airplane. The scratch induced in its service and the discontinuity of profile due to the need of joining and structure design always exists in elements of PMMA and may be regarded as notch where the stress concentration occurs. The smooth element can be considered as the special notch specimen with notch radius $\rho \to \infty$ and the element with crack can be considered as another special notch specimen with notch radius $\rho \to 0$. Therefore, the notch strength theory not only offers the base for the reliability design of engineering structural elements, but also points out the inner relation between the strength theory of materials and the theory of fracture mechanic. The variation pattern of notch strength of different metals and ceramics under tension, bending and torsion loading have been investigated respectively [1,2]. PMMA is low ductility material, so, it is necessary and important to investigate the fracture of notched PMMA in order to meet the structural design and reliability assessment of PMMA elements. Nevertheless, there is a scant amount of study in the open literature on the notch strength and notch-sensitivity of PMMA [3~5].

In the study, attempt is made to estimate the notch strength and notch sensitivity of notched PMMA from the tensile properties of smooth specimens and the estimated results are checked by the test results of two types of PMMA used in airplane.

2. Expression for notch strength

The following equation between tension notch strength σ_{bN} and stress concentration factor K_t in plane strain state was given in ref [6]. Based on the strain analysis at notch root and the normal strain fracture criterion,

$$\sigma_{bN} = 0.64\sqrt{E\sigma_f\varepsilon_f} \Big/ K_t \tag{1}$$

where E is the Young's elastic modulus, $\varepsilon_f = -\ln(1-\Psi)$, $\sigma_f = \sigma_b(1+\Psi)$ are respectively the fracture strength and fracture ductility, where Ψ is the reduce ratio of the fracture section. PMMA is of low ductility material, when the thickness of the sheet specimen $B>2.5(K_{IC}/\sigma_{0.2})^2 \approx 3$mm, the notch root of the specimen is at the plane strain state, therefore, the notch can be estimated from the tensile properties of smooth specimen according to eqn(1).

Eqn(1) represents a straight line with a minus slope on a logarithmic scale, i.e., $\log K_t$ vs. $\log\sigma_N$ scale. In other words, σ_N decreases with the increasing K_t. However, for some engineering materials including PMMA [6~9], it is found that there is a critical stress concentration factor K_N called notch sensitivity factor, when $Kt<K_N$, σ_N is no less than the σ_b, when $Kt>K_N$, σ_N decreases with increasing Kt according to eqn(1). When Kt further increases with the decreasing radius of notch root ρ and reaches another critical value K_ρ, the notch strength does not further decreases with the increasing Kt and keeps at a value determined by the fracture toughness K_{IC}. The K_ρ is called the sharp notch non-sensitivity factor. Therefore, the complete expression for estimating notch strength can be rewritten in the form of eqn(2)

$$\sigma_N = \begin{cases} \sigma_b & K_t < K_N \\ \dfrac{0.64\sqrt{E\sigma_f\varepsilon_f}}{K_t} & K_N < K_t < K_\rho \\ \dfrac{K_{IC}}{Y\sqrt{\pi a}} & K_t > K_\rho \end{cases} \tag{2}$$

Where Y is the geometry function for calculating stress intensity factor K_I , 2a is the crack length of Griffith crack, for circumferentially notched round-bar specimen under tension [10]:

$$Y\sqrt{\pi a} = \sqrt{\pi d/2}\, f(d,D) \tag{2a}$$

$$f(d,D) = 0.5\sqrt{[1-(d/D)]}[1+0.5(d/D)+0.375(d/D)^2-0.363(d/D)^3+0.731(d/D)^4] \tag{2b}$$

Where D is the diameter of the smooth part of the notch specimen and d is the diameter of the notched section.

3. On the notch sensitivity factor K_N of PMMA

In early studies, the tension notch strength was measured by using notch specimen with a certain notch geometry and stress concentration factor. A parameter called the notch strength ratio ($NSR=\sigma_{bN}/\sigma_b$) was defined as the ratio of notch strength to ultimate strength to assess the notch sensitivity of materials. When $NSR\geq 1.0$, the material would be notch-ductile, when $NSR<1.0$, the material would be notch-brittle. In engineering applications, NSR could be used to qualitatively assess the safety of the structure details without crack-like defect. Nevertheless, NSR is obviously not a material constant. It's hard to predict the variation of notch strength and NSR values when the geometry and stress concentration factor changes. Consequently, let $K_N=NSR\times K_t$, the so-called notch sensitivity factor K_N, a new material constant is deduced for low-ductility materials like PMMA,

$$K_N = 0.64\sqrt{E\sigma_f\varepsilon_f} \Big/ \sigma_b \tag{3}$$

When the stress concentration factor of element is greater than K_N, i.e. $K_b > K_N$, notch strength

is lower than ultimate strength σ_b , so NSR<1.0, i.e., PMMA investigated is relatively sensitivity to notch.； when $K_b < K_N$ ， NSR≥1.0 and $\sigma_{bN} \geq \sigma_b$, PMMA is not sensitivity to notch.

4. On the sharp notch non-sensitivity factor K_ρ

According to fracture mechanic theory, the ideal radius at crack tip $\rho = 0$, but the crack tip in engineering materials can be blunted, and there is a critical blunted radius when the material element at crack tip fracture. As for the notch specimen, when the radius of notch root is smaller than a critical value ρ_c , the distribution characteristics of stress and strain near notch root is similar to that near the blunted area of crack tip. Thereby, the material element at notch root is under the approximately similar stress and strain state to that of material element at crack tip before fracture, therefore, the problem of notch becomes the problem of crack and there exist the following equation:

$$K_{IC} = \sigma_N \sqrt{\pi a} Y \tag{4}$$

For V-shape circumferentially notched cylindrical specimen,

$$K_{IC} = \sigma_N \sqrt{\pi d/2} f(d, D) \tag{4a}$$

Combining eqn.(1), (5) and (5a), we can obtain the expression for K_ρ,

$$K_{IC} = \sigma_N \sqrt{\pi d/2} f(d, D) \tag{5}$$

$$K_\rho = \frac{0.64\sqrt{\pi d E \sigma_f \varepsilon_f / 2}}{K_{IC}} f(d, D) \tag{5a}$$

As it may be seen, K_ρ is related with the geometry dimension of specimen and is not a material constant. However, the physical meaning for K_ρ is clear: if the notch depth and the dimension of the specimen keep constant, when $K_t \geq K_\rho$, the notch strength of the material keeps constant at the control of K_{IC}. The existence of K_ρ offers the theory base for investigating the problem of crack from the tensile properties of sharp notch specimen at certain condition.

5. Substantiate

For V shape circumferentially notched cylindrical specimen, the deformation at notch root is constricted and the plane strain state can be guaranteed, in this case, the following expression for stress concentration factor exists [11]:

$$K_t = (1.0 - 1.5183\lambda + 0.2530\lambda^2 + 2.2356\lambda^3 - 2.411\lambda^4) K_{tv} \tag{6}$$

$$K_{tv} = (1.035 + 0.0261\eta - 0.1451\eta^2 + 0.0842\eta^3) K_{te} \tag{6a}$$

$$K_{te} = (1.121 - 0.2846\eta + 0.3397\eta^2 - 0.5144\eta^3)(2 + \eta)/\eta \tag{6b}$$

$$\eta = \sqrt{\rho / t} < 1 \text{ , and } \lambda = 2t / D \tag{6c}$$

In order to obtain the high stress concentration factor, let $\lambda = 0.25$， then the notch depth $t = (D - d)/2 = 0.125D$.

The directed (type No: DP3) and non-directed (type No: NP3) PMMA sheet of 10mm depth used for airplane are taken as test material. The PMMA is first cut into the sheet of size of 10×10×100mm, and then accurately machined the sheet into round bar specimen with diameter of 8mm and scale length of 50mm in the middle part of the specimen. Finally, round V-shape notched specimens with constant depth of 1mm and variate notch radius are then made to obtain different stress concentration factor. The smooth round specimens are made with the scale size of 10×6×50mm.

The tensile tests are conducted on universal Electro-hydro-servo test machine at room temperature of 23℃. Take the tensile properties of smooth specimens listed in Table 1 into eqn.(3), then K_N are obtained and listed in Table 1 also. K_{IC} for NP3 and DP3 are respectively 1.3 and 2.3,

which are obtained by testing the CT standard specimens under the same testing condition. K_ρ is then obtained by taking K_{IC} into eqn.(5a). So the two predicted horizontal lines for each type of PMMA are obtained and drawn in Fig 1 according to eqn.(2).

Tab. 1 Test results of tensile properties of smooth specimens

NO.	NP3					DP3				
	E /GPa	σ_b /MPa	σ_f /MPa	ε_f /%	K_N	E /GPa	σ_b /MPa	σ_f /MPa	ε_f /%	K_N
1	3.1	76.4	82.8	8.6	1.3	2.9	84.3	108	32.1	2.4
2	3.1	78.1	84.3	8.3	1.2	2.9	84.9	109	32.9	2.4
3	3.1	76.9	83.0	8.3	1.2	2.9	85.3	111	36.1	2. 6
4	3.1	77.3	82.7	7.2	1.1	2.9	87.0	114	37.7	2.6
5	3.1	77.8	84.1	8.4	1.2	2.9	87.3	114	36.5	2.6
average	3.1	77.3	83.3	8.2	1.2	2.9	85.7	111	35.1	2.52

Tab. 2 Test results of notch strength in tensile experiment

NO	NP3		（DP3） σ_N /MPa			
	K_t	σ_N /MPa	(K_t=2.2)	(K_t=2.9)	(K_t=2.7)	(K_t=5)
1	1.6	60.1	90.7	64.8	72.5	68.6
2	1.6	62.9	87.0	66.9	70.4	62.0
3	1.9	50.3	83.5	70.1	80.2	67.6
4	1.9	50.6	87.4	60.5	76.4	66.9
5	2.5	38.8	85.2	58.9	72.7	64.5
6	2.5	39.5	82.6	59.6	67.0	67.6
7	3.1	33.6	83.0	63.4		67.9
8	3.1	35.1	87.4	58.4		63.8
9	6.0	36.1	84.0	58.9		
10	6.0	34.0				

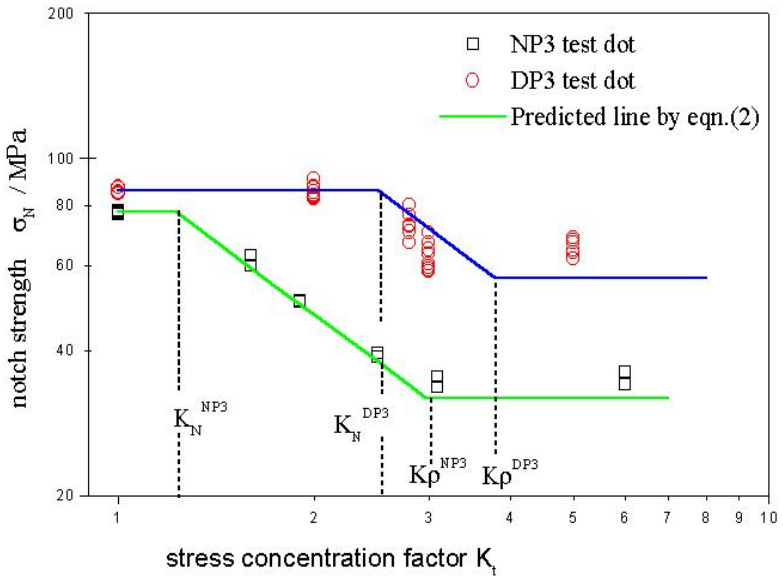

Fig.1 The predicted curve of notch strength and test results of Two kinds of PMMA

Fig 1 shows that the test data are in good agreement with the predicted values. The value of σ_b of the directed PMMA (DP3) is a little higher than that of non-directed PMMA (NP3), but the ductility of DP3 is much higher than that of NP3, therefore, the notch sensitivity factor for DP3 is

much greater, K_N=2.5 for DP3 and K_N=1.2 for NP3. When Kt> K_ρ, the notch strength for sharp notch of DP3 is approximately two times of that of NP3 because K_{IC} of DP3 is nearly twice of that of NP3. The above estimated results suggest that DP3 is much safer than NP3 under the same stress concentration.

6. Conclusions

1. The notch strength curves ($\sigma_N \sim K_t$) of PMMA are consisted of three parts, i.e., the upper horizontal lines are controlled by the value of material strength, the lower horizontal lines are controlled by the value of fracture toughness of materials and the middle part of the curves are estimated by the formula of notch strength (eqn.2).
2. The value of K_N estimated by tensile properties was that 1.2 for NP3 and 2.5 for DP3. This values shown that the directed PMMA has less notch sensitivity than that of non-directed PMMA.
3. The sharp notch strength of the directed PMMA is held at higher value because of the action of fracture toughness with higher value.
4. With the same Kt, the notch strength of directed PMMA is much higher than that of non-directed PMMA.

References

1. Kattus J R. Aerospace structural metal handbook. New York: Belfour stulen Inc, 1973. 37~43.
2. Wang Fenghui. Notch strength of ceramics and statistical analysis, Eng. Fract. Mech.1995,52(5):417~421.
3. Davenport James C W, Smith David J. Influence of plasticity and geometry on the mixed mode fracture of PMMA, ASTM Special Technical Publication,1995,1244(11): 344~360.
4. Dunn M L, Suwito W, Cunningham Sh. Fracture initiation at sharp notches: correlation using critical stress intensities. International Journal of Solids and Structures, 1997,34(29):3873~3883.
5. Cho Kilwon, Ahn Sunghee, Park Jinbae, et al. Evaluation of the weld-line strength of thermoplastics by compact tension test. Polymer Engineering and Science,1997,37(7):1217~1225.
6. Zheng X L. On an unified model for predicting notch strength and fracture toughness. Eng. Fract. Mech., 1989, 33(5): 685~695.
7. Zheng X L. Mechanics properties of materials. Xi'an, P. R. China: Press House of Northwestern Polytechanical University, 1991.57~61.
8. Zheng X L., Meng Liang, Wang Fenghui. Notch strength and notch insensitivity of materials. China mechanical engineering, 1998,9(1):81~83.
9. Meng L. Notch strength and stress concentration sensitivity of alloy 2090 with various cerium contents. Journal of materials science, 2000, 35:1481~1486.
10. Shabara M A N, El-Domiaty A A, Al-Ansary M D. Estimation of plane strain fracture toughness from circumferentially bluntly notched round-bar specimens. Eng. Fract. Mech., 1996, 54(4):533~541.
11. Noda N A, Sera M, Takase Y. Stress concentration factors for round and flat test specimens with notches. Int. J. Fatigue, 1995, 17(3):163~178.

ORAL REFERENCE: 111

NOTCH STRENGTH OF SPHEROIDAL GRAPHITE CAST IRON UNDER TENSION LOADING

Zhao Kang[1] Sun Jun[1] Wei Jianfeng[1] Yan Junhui[2] Zheng Xiulin[2]

[1]College of Materials Science & Engineering, Xi'an Jiaotong University
Xi'an 710049, P.R.China
[2]College of materials Science & Engineering, Northwestern Polytechnical University
Xi'an 710072, P.R.China

ABSTRACT

Experiments are carried out in this study to determine the notch strength of spheroidal graphite cast (SGC) iron by using notched specimens with various stress concentration factors. Test results show that only the uniform elongation but no necking occurs when the smooth test specimens of SGC iron fracture. Thus, the SGC iron belongs to the kind of low-ductility materials. Test results also show that the notch strength of SGC iron decreases with increasing stress concentration factor investigated. Analysis shows that the notch strength σ_{tN} of SGC iron can be expressed by following equation: $\sigma_{bN} = 0.64(E \sigma_f \varepsilon_f)^{1/2}/K_t$ The notch sensitivity of SGC iron is quantitatively assessed by the notch sensitivity factor, which value is also given.

KEYWORDS

Spheroidal graphite cast iron, Low-ductility materials, Notch strength, Notch sensitivity.

1. INTRODUCTION

Spheroidal graphite cast (SGC) iron has been widely applied in machine-building industry due to its high strength and certain ductility, excellent casting ability and low price [1-3]. The SGC iron bars with

various profiles and dimensions have been produced by using continuous-casting technique, which was developed in China in 1980s. The continuous-casting SGC iron bars have higher strength because of the fine and well-distributed graphite spheroids and less defects. As a result, the SGC iron bars can be used to produce the machine elements subjected to heavy loads. In addition, the cost of SGC iron elements can be reduced when the continuous-casting SGC iron bars are used. The reason is that the utilizing efficiency of continuous-casting SGC iron bars is higher and the price is lower than that of steels with the same level of strength. Thus, SGC iron bars have better prospect in engineering applications. Usually, the fetter holes, stages and ditches always exist in machine elements. These geometry discontinuity, which may be referred to as the notch, will induce the stress concentration and change the stress state at the notch tip[4]. Consequently, the strength and the ductility may be decreased. Therefore, it is necessary and important to investigate the effect of stress concentration of notch on the strength, i.e., the notch strength and notch sensitivity of SGC iron. However, the report on the notch strength of SGC iron has not been found in open literature, to authors' best knowledge. In the present study, experiments are carried out to determine the notch strength and the notch sensitivity of SGC iron produced by continuous-casting technology, and the test results are analyzed by using the formula for notch strength developed by one of the authors[5].

2. EXPERIMENTAL PROCEDURE

The continuous-casting SGC iron bars of 38 mm diameter produced by Xi'an Huayu Cast Iron Factory are taken as the test materials. The composition of bars tested is as follows (wt%): 3.22% C, 2.88% Si, 1.31% Mn, 0.04% P, 0.02% S, and balance Fe. The SGC iron bars were normalized in stairway, firstly heated to 960℃ and holding for 4 hours, then cooled in furnace to 800℃ and holding for 1.5 hours, and finally cooled to room temperature. After normalizing, the bars were longitudinally cut into two pieces, and then turned into smooth cylindrical tension specimens. The circuferntial notch were made in the middle of the specimen on the optical grinder, as shown in Fig. 1. The notch depth is 1.0 mm, and the notch radii are 0.22mm, 0.375mm, 0.75mm and 1.02mm, respectively. Correspondingly, the tensile stress concentration factors of the notched specimens, K_t are 4.3, 3.3, 2.8 and 2.1, respectively [6].Tension tests were carried out on a universal testing machine of type WE-30.

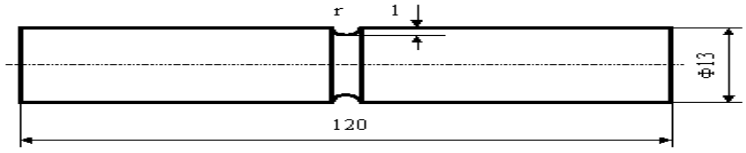

Figure.1: Geometry of the tensile notched specimen

3. TEST RESULTS

3.1 Fractograph

Fig. 2 shows the macrograph of the fracture of the notched and smooth specimen of SGC iron under tension loading. As it may been seen, the fractured surface of both the smooth and the notched specimens are nearly the planes perpendicular to the axis of specimens without any shear tip. The fracture surfaces of the notched specimens are located within the notch. However, the fracture surfaces are rough as shown in Fig. 3. On the other hand, only the uniform elongation but no necking was observed after final fracture of the smooth specimens of SGC iron. Therefore, the SGC iron displays the brittle fracture characteristics but has small ductility. Consequently, it may be thought that the SGC iron is one of the low-ductility materials [4].

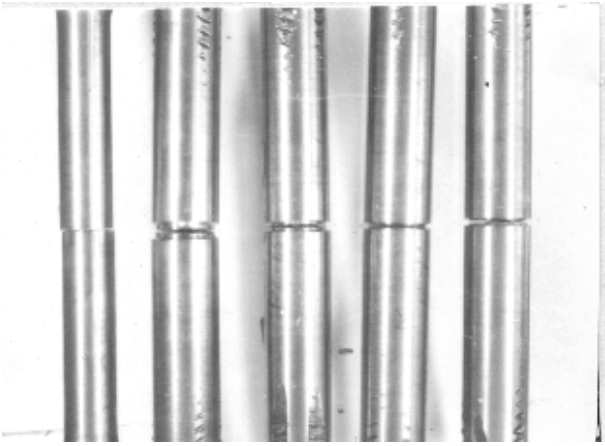

Fig. 2 Topography of notched and smooth specimens

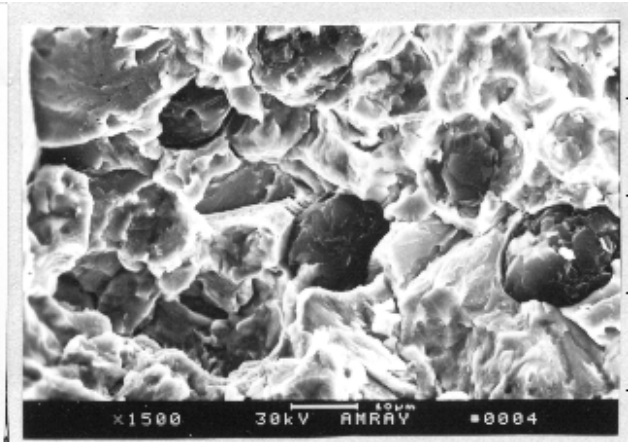

Fig. 3. Fractography of fracture surface of notched specimen under SEM

3.2 Test results of tensile notch strength

According to fracture characteristics of notched and smooth specimens, the notch strength (σ_{bN}) can be calculated by following expression:

$$\sigma_{bN}=P_f/0.25\ \pi\ d^2 \qquad (1)$$

where, P_f is the load of fracture, d is respectively, the minimum diameter of notch root for notched specimens, and the diameter of smooth specimen in gauge length. Test results of notch strength were listed in Table 1. It can be seen from Table 1 that the tensile notch strength of SGC iron decreases with increasing stress concentration factor (K_t).

4. BRIEF DISCUSSIONS

4.1 On the expression for notch strength

Based on the strain analysis of notch root and normal stain fracture criterion, an expression between the

tensile notch strength (σ_{bN}) and stress concentrate factor (K_t), was developed as follows[5]:

$$\sigma_{bN}=\alpha(E\sigma_f\varepsilon_f)^{1/2}/K_t \quad (2)$$

where, α is a constant related to the stress state at notch root, α=1 for the stress state and α=0.64 for the plane strain state; E is Young's modules; σ_f and ε_f are, respectively, the fracture strength and fracture ductility of smooth specimens, and may be estimated by ultimate tensile strength (UTS) and percentage elongation (EL) for low-ductility materials such as SGC iron as follows:

$$\sigma_f = \sigma_b(1+EL) \quad (3)$$

$$\varepsilon_f = \ln(1+EL) \quad (4)$$

TABLE 1

TEST RESULTS OF TENSILE NOTCH STRENGTH OF SGC IRON

Radius /mm	K_t	d /mm	σ_{bN} /MPa		
0.22	4.3	13.12	547.3	510.4	569.3
0.375	3.3	13.15	799.2	621.6	732.7
0.75	2.8	13.02	712.5	784.8	799.0
1.02	2.1	13.03	821.6	776.4	870.6
∞(smooth)	1.0	11.90	910.4	931.1	926.7

It was pointed out in Ref.[7] that for low-ductile materials, α can be taken to be 0.64 even for thin sheet tested. Since SGC irons are low-ductile materials. α can be taken 0.64. Thus, the tensile notch strength can be expressed as:

$$\sigma_{bN}=0.64(E\sigma_f\varepsilon_f)^{1/2}/K_t \quad (5)$$

For SGC iron, E = 180 GPa[8]. the value of σ_f for K_t=1.0 in table 1 can be taken as the fracture strength σ_f in equ(3). The value of the elongation was approximately taken to be is 4~6% because it is very difficult to accurately measure the value of elongation of the test specimen with brittle fracture characteristic. Substituting the value EL into equ (4) yields the value of σ_f of SGC iron. Put the above data into equ(5), the expression of tensile notch strength SGC iron can be obtained as follows:

$$\sigma_{bN} = (1666\sim2050)/K_t \quad (6)$$

The predicted lines of notch strength of SGC iron are drawn according to equ(6) and shown in Fig. 4. As it may be seen, the predicted notch strength of SGC iron are in agreement with test results within the range of K_t investigated.

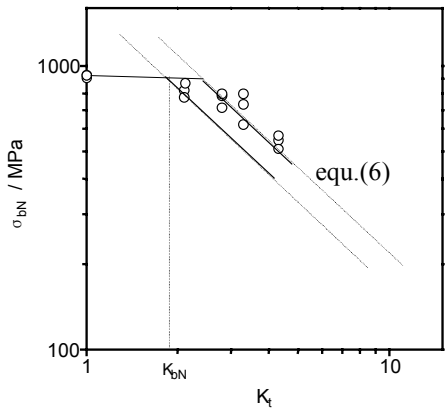

Figure. 4: Predicted line according to equ(6) and test results of notch strength of SGC iron

4.2 On the notch sensitivity of SGC iron

In the early research, the notch strength ratio, NSR, was adopted to evaluate the notch sensitivity of materials. NSR was defined as the value of the ratio of the notch strength to the ultimate strength, i.e., σ_{bN}/σ_b, where the notch strength was determined by using notch specimen with K_t less than 4 [4]. The materials would be notch-brittle, i.e., notch sensitive when NSR< 1.0, while materials would be notch ductile, i.e. notch insensitive when NSR $\geqslant$ 1.0, Obviously, NSR is not a material constant, and can not thus be applied to quantitatively assess the notch sensitivity. This is because it is difficult, even impossible to predict the notch strength and the value of NSR when the profile and thus the value of K_t of notched elements are changed. In ref.[5] a new material constant, i.e., the so-called notch sensitivity factor K_{bN} was defined as follows:

$$K_{bN}=0.64(E\sigma_f\varepsilon_f)^{1/2}/\sigma_b \tag{7}$$

For SGC iron tested,

$$K_{bN}=0.64(E\sigma_f\varepsilon_f)^{1/2}/\sigma_b =(1666\sim2050)/923\approx1.8\sim2.22 \tag{8}$$

In Fig 4 the location and its practical significance of K_{bN} are shown. When K_t of elements is greater than K_{bN}, i.e. $K_t>K_{bN}$, the notch strength is lower than σ_b, and varies according to equ(6), i.e., NSR $<$ 1.0, while the notch strength is equal to or higher than σ_b, i.e. $\sigma_{bN}\geqslant\sigma_b$, NSR$\geqslant$1.0 and equ(6) can not be used to predict the notch strength. Therefore, in the design of mechanical elements, the K_t of the elements should be controlled lower than K_{bN}, i.e. $K_t\leqslant K_{bN}$, and the elements will be safe when the allowable stress of the elements is controlled lower than σ_b. For the SGC iron tested in this study the K_t should be controlled lower than 1.8 theoretically.

4.3 On the dispersion of experimental results

For brittle materials there are high dispersion of the test results of strength and notch strength. So experiments containing big sample size and statistical analyze of the test data are required[9,10]. Test results of the notch strength of low-ductility AL-Li alloy sheets also displayed some dispersion [7]. For SGC iron, the size, the shape and distribution of graphite are varied. It is obvious that strength of SGC iron should have some dispersion. It can be seen from Table 1 and Fig. 6. The test results of strength distributed in a wider scatter band. Therefore, big sample size and statistical analysis of the test results of notch strength should be adopted in further work to provide reasonable basis for the design and reliability assessment of elements of SGC iron.

5. CONCLUSIONS

(1) SGC iron displays the brittle fracture characteristics but has some ductility. It may be thought that SGC iron is low-ductility material.

(2) In the range of K_t investigated the notch strength can be predicted from the tensile properties according to the following equation: $\sigma_{bN}=0.64(E\sigma_f\varepsilon_f)^{1/2}/K_t$ .The theoretically predicted lines agree well with test results.

(3) The theoretically predicted value of notch sensitivity factor (K_{bN}) of SGC iron is about 1.8~2.2, i.e. K_{bN}=1.8~2.2. Therefore K_t should be kept lower than 1.8, i.e. $K_t<1.8$ in the design of mechanical elements made of SGC iron produced by continuous casting technology.

6. REFERENCES

1. Yano, M. (1992)*35th Japan congress on Materials Research*. publisher Society of Materials Science, 9, 7
2. Cheng, H. (1996) *J.Mat. Sci.* 31, 765.
3. John, A. V. (1985) *American machinist*. 8, 79.
4. Huan, Z.(1991).*Mechanical Properties of Materials.* Publishing House of Xi'an Jiaotong University, Xi'an. pp: 94-96, (in Chinese).
5. Zheng, X.L. (1991).*Mechanical Properties of Materials*. Publishing House of Northwestern Polytechnical University, Xi'an. pp.3-13, (in Chinese).
6. Zhan S.M. (1984). *Stress concentration factors handbook.* Publishing Shaanxi science and technology, Xi'an. pp:198-199.
7. Meng, L. and Zheng, X.L. (1996) *Metal. Mater. Trans.* 27A, 3089.
8. *Cast Handbook*(1979) Publishing mechanical industry of China, Beijing, 1663
9. Yan, J.H. and Zheng X.L .(1997) *Int. J. Fracture*. 86,119.
10. Wang, F.H and Zheng X.L.(1995) *Eng. Fract. Mech*. 52,917.

ORAL/POSTER REFERENCE: ICF1001970R

NUMERICAL INVESTIGATION OF FATIGUED COMPOSITES UNDER CYCLIC COMPRESSION SPECTRA

Assimina A. Pelegri[1] and Diwakar N. Kedlaya[2]

[1] Assistant Professor [2] Graduate Student
Mechanical and Aerospace Engineering
Rutgers, The State University of New Jersey
98 Brett Road, Piscataway, NJ 08854-8058, USA

ABSTRACT

The effects of overloads on internal delaminations of IM7/G8552 graphite/epoxy composite laminates subjected to cyclic compressive load are investigated. An extensive numerical study has been performed on composites' fracture due to reduction in the intralayer and interlayer resistance resulting from randomly subjected overloads. The composite structure is already undergoing repeated buckling as a result of compressive loading. The energy release rate, G, is modeled considering the state of stress to be mixed mode, I and II. Fracture mechanics model and delamination buckling analysis deliver the required equations to build a model that incorporating the non-linearity caused by the overloads. The model predicts a relatively rapid accumulation of micro-damage due to overloads at the delamination front. Results are obtained with no restrictive assumptions on the plate thickness T and over varying mode mixity and delamination positions.

KEYWORDS

material, delamination, energy, fatigue, mode, numerical, overload, spectrum

INTRODUCTION

The damage tolerance of laminated composite components used in aerospace applications is dramatically altered once these structures are subjected to overloads. The overloads might be in the form of bird strikes, landings, wind gusts, shear winds and other mechanical and thermal

types of loading. The present study investigates the prediction of variable amplitude fatigue loading with randomly applied overloads.

Broutman and Sahu [1] were among the first to do significant work on prediction of multi-stress level fatigue in composite materials. Overloads were integrated until Yang and Liu [3] introduced a single overload of different intensities at regular intervals throughout a fatigue test. Previous work done on similar grounds is limited and typically involves FALSTAFF (Fighter Aircraft Loading Standard For Fatigue), which is one of the popular spectra used by researchers especially in compressive loading [4, 5].

In the presented study simulations of IM7/G8552 graphite/epoxy composite specimens subjected to cyclic compressive loading were performed. By varying the ratio between the magnitude of the strain overload and the magnitude of the normal fatigue strain the severity of the overloads was measured. Continuous tracking of the energy release rate, G, and prediction of the energy release rate reduction during in service loading was achieved using the proposed model.

NUMERICAL MODEL

The energy release rate of fatigued composites under compressive loading, with infliction of overloads at regular intervals, exhibits a behavior similar to the one supported by previously performed experiments on cyclic loading. A perturbation procedure, which is based on an asymptotic expansion of the load and deformation quantities in terms of a distortion parameter, i.e., the deformation of the delaminated layer, is used [9]. The model accounts for post-buckling and growth behavior of delaminations and it is based on Kardomateas' [9] model. For the interested reader, the complete model for isotropic and orthotropic materials is illustrated in the Refs [6,7,9]. In the current analysis only the parts of the model pertinent to the overload effect on the energy release energy are presented. In particular, the energy release rate, G, of a plane strain interface crack for a homogeneous system and homogeneous material [8], is

$$G = \frac{1-n}{4m}\left(\frac{P^{*2}}{Ah} + \frac{M^{*2}}{Ih^3} + \frac{P^* M^*}{\sqrt{AIh^2}}\sin g\right) \tag{1}$$

where $P^* = P - C_1 P + C_2 \frac{M_d}{h}$, and $M^* = M_d - C_3 M$ (2)

P^* and M^* are linear combinations of the loads from the post-buckling solution [9], and is the shear modulus. A and I are a positive dimensionless number and the angle which is restricted such that 2. More specifically:

$$A = \frac{1}{1+4h+6h^2+3h^3}\ ; I = \frac{1}{12(1+h^3)}\ ; \sin \quad = 6 \quad ^2\left(1 + \quad\right) \tag{3}$$

Asymptotic expressions for the forces and moments with respect to the perturbation parameter, , from the post-buckling solution, gives:

$$P^* = P^{*(1)} + \varepsilon^2 P^{*(2)} + \ldots \tag{4}$$

$$M^* = M^{*(1)} + \varepsilon^2 M^{*(2)} + \ldots \tag{5}$$

Therefore, the energy release rate and mode I and II intensity factors can be written in the form:

$$G^* = \varepsilon^2 G^{*(2)} + \varepsilon^3 G^{*(3)} + \ldots \tag{6}$$

$$K_{I\,II} = K_{I\,II}^{(1)} + \varepsilon^2 K_{I\,II}^{(2)} + \ldots \tag{7}$$

where $\Psi = \tan^{-1}\left(K_{II} / K_I \right)$ is the mode mixity.

The energy release rate of a delamination in an infinitely thick base plate, unlike the thin film model of Chai et al. [11], is predicted to be larger for higher levels of applied strain [12]. In this model the fatigue damage due to delamination is expressed as a function of the energy release rate, G, the load ratio, , and the mode mixity, Ψ, thus forming the following cyclic growth law:

$$\frac{da}{dN} = f(\overline{G}_{\max,}\, a, \Psi); \qquad \frac{da}{dN} = C(\Psi)\frac{\Delta \overline{G}^{m(\Psi)}}{1-\overline{G}_{\max}} \tag{8}$$

where $\overline{G}$ is the ratio of energy release rate over toughness. $C(\Psi)$ and $m(\Psi)$ values are determined independently using the following semi-empirical formulations:

$$m(\Psi) = m_1\left[1+(m-1)\sin^2\Psi\right] \qquad \text{where } m = \frac{m_{II}}{m_I} \tag{9}$$

$$C(\Psi) = C_1\left[1+(k-1)\sin^2\Psi\right] \qquad \text{where } k = \frac{C_{II}}{C_I} \tag{10}$$

The overloads are introduced in the system by increasing the applied strain at regular intervals as a close simulation of the performed experiments. More specifically, every 30-step change in delamination length an overload of 5% change of the applied strain, for a period of five steps, is imposed to each specimen. That is

$$\varepsilon_{appl} = \begin{cases} \varepsilon_0 & for \;\; \mathrm{mod}(n*I,30) \neq 1 \\ \\ \varepsilon_0 + \varepsilon_{overload} & for \;\; \mathrm{mod}(n*I,30) = 1 \;\; to \;\; n*I+5 \end{cases} \tag{11}$$

where n is the number of step increment in delamination, and
I is the unit step increment in delamination.

Considering five steps of overloading state of which the strain is increased by less than 5% of its initial strain, each overload cycle is described by:

$$e_0 = \frac{P}{E}; \qquad e_{overload\leq} 1.05 * e_0 \tag{12}$$

Therefore, the energy release rate expression will be modified as follows:

$$G(e_{appl}, \ell) = \frac{1}{2} Eh(1-\nu^2)(e_{appl} - e_{cr})(e_{appl} + 3e_{cr}) \tag{13}$$

where $e_{cr} = \frac{p^2 h^2}{12(1-\nu^2)}$ and the applied strain, $_{appl}$, as described in Eq. 11.

Numerical simulations of delamination buckling and growth in graphite/epoxy composites under cyclic compressive loading were developed based on the aforementioned model. The three specimen configurations that yielded interesting data during the experimental approach were used to simulate the system. The compressive loading in this case is simulated by an increase in the delamination length. Simulation results are presented in Figures [1, 2]. In each graph, the energy release rate of composites against the delamination ratio is plotted. Figures 1 and 2 demonstrate the reduced growth resistance of laminates through the reduction of *G* during delamination growth for three different delamination positions though the thickness of the specimens, i.e. h/T ratio. In particular, the graphs describe the behavior of composites with increased h/T ratio, i.e., 4/15, 5/29 and 4/24. As illustrated in these plots, the energy release rate reduces as the delamination length increases indicating that delamination growth requires smaller amounts of energy in order to progress. As seen in Figure 1, higher values of h/T ratio result in higher values of the energy release rate.

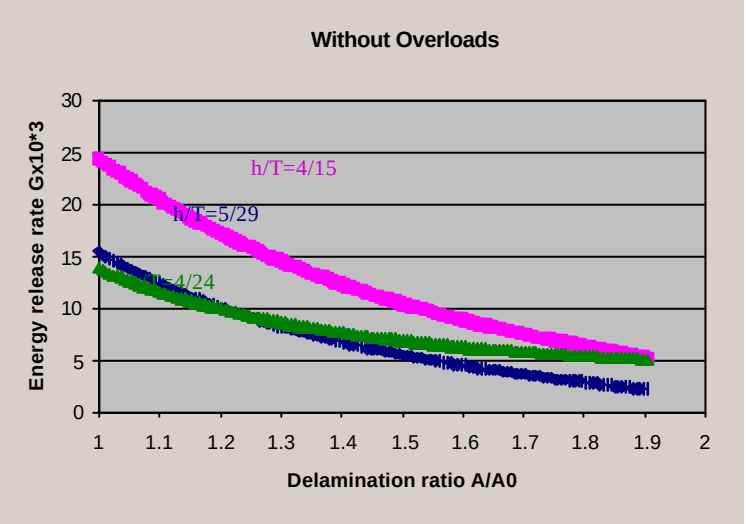

Figure 1: Growth behavior of IM7/G8552graphite/ specimens subjected to cyclic compressive loading

The graph in Figure 2, illustrates the energy release rate of the structure when subjected to an overload causing 5% change in applied strain at regular intervals as indicated above against the delamination ratio.

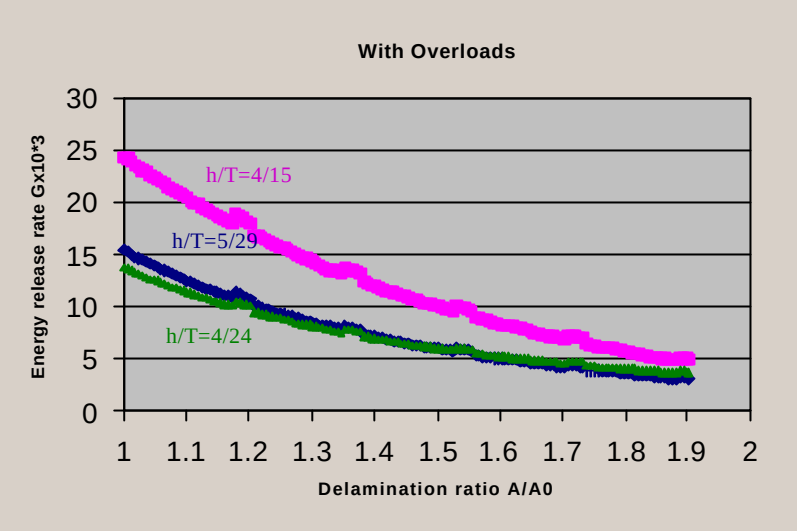

Figure 2: Growth behavior of IM7/G8552 graphite/epoxy specimens subjected to cyclic compressive overloads for varying h/T ratio.

The behavior observed in Figure 2 is similar, with the exception of the overloads, to the structural integrity degradation behavior observed in Figure 1. As the delamination length increases and the energy release levels decrease the effect of the overloads diminishes (compare the *G* peak values of the first and fourth overloads in Figure 2). Furthermore, the effect of the overloads is more severe when the delamination length is small and its energy release levels are high. This observation complements the findings of Refs [4, 6] in which small delamination length indicated large mode I (opening) component of the mode mixity. Here, as the delamination grows, the shear component increases and the effect of the overload diminishes. The increase in energy release rate due to overloads supports the inference from the experimental results, i.e., faster crack growth at the beginning of the experiments when the delamination length is relative small. Moreover, the formation of intralayer cracks during, or after, the overloads may be associated to the high levels of energy release rate during the overload application. Simulations indicate that as the delamination progresses the effect of the overloads on the system diminishes, see overload peaks in Figure 2.

CONCLUSIONS

In this paper, a numerical approach to variable amplitude cyclic compressive testing was performed on graphite/epoxy composite laminates. These simulations revealed that the energy release rate reduces as the delamination length increases indicating that delamination growth requires smaller amounts of energy in order to advance. Furthermore, higher values of applied strain result in higher levels of energy release rate independently of the overload application. Finally, as the delamination grows the number of intralayer cracks decreases implying that the energy release rate available for intralayer "jumps" reduces. This model can estimate the energy release rate of a certain composites under service loading and thus in turn predicting the life of the composite. Future work will involve matching the numerical prediction using experimental results by imposing random overloads [13] onto the cyclic compressive loading spectra. .

ACKNOWLEDGMENTS

The authors would like to gratefully acknowledge the financial support of the National Science Foundation, Civil and Mechanical Systems Division, NSF Career Grant 99-82023. The authors are thankful to the grant monitor Dr. Jorn Larsen-Basse for his interest and encouragement.

REFERENCES

1. Broutman, L. J., and Sahu, S, (1972), "A New Theory to Predict Cumulative Fatigue Damage in Fiberglass Reinforced Plastics," *Second Composite Materials Testing and Design Conference*, ASTM *STP 497*, pp. 170-188.
2. Hwang, W., and Han, K. S., (1989), "Fatigue of Composite Materials - Damage Model and Life Prediction," *Composite Materials Fatigue and Fracture*, ASTM *STP 1012*, 2, pp. 87-102.
3. Yang, J. N., and Liu, M. D., (1977), "Residual Strength Degradation Model and Theory of Periodic Proof Tests for Graphite/Epoxy laminates," *Journal of Composite Materials*, 11, pp. 176-203
4. Badaliance, R., Dill, H. D., and Potter, J. M., (1982), "Effects of Spectrum Variations on Fatigue Life of Composites," *Sixth Composite Materials: Testing and Design Conference*, ASTM *STP 787*, pp. 274-286.
5. Lee, L. J., Fu, K. E., and Yang, J.N., (1996), "Prediction of Fatigue Damage and Life for Composite Laminates Under Service Loading Spectra," *Composites Science and Technology*, 56, pp. 635-648.
6. O'Brien, T. K., (1982), "The Effect of Delamination on the Tensile Strength of Unnotched, Quasi-isotropic, Graphite/Epoxy Laminates," *Proceedings of the 1982 Joint Conference on Experimental Mechanics (SESA/JSME) Part I*, Oahu-Maui, Hawaii, pp. 236-243.
7. Pelegri, A. A., Kardomateas, G. A., and Malik, B. U., (1997), "The Fatigue Growth of Internal Delaminations Under Compressive Loading of Crossply Composite Plates," *Composite Materials: Fatigue and Fracture*, ASTM *STP 1285*, 6, pp. 143-161.
8. Kardomateas, G. A., and Pelegri, A. A., (1996), "Growth Behavior of Internal Delaminations in Composite Beam/Plates Under Compression: Effect of the End Conditions," *International Journal of Fracture*, 75, pp. 49-67.
9. Pelegri, A. A., (1996), "Test and Analysis on the Delamination Fatigue Growth in Glass/Epoxy Composite Plates," *37th AIAA/ASME/ASCE/AHS/ASC Structures, Structural Dynamics, and Materials Conference Part IV*, Salt Lake City, Utah, pp. 2567-2577.
10. Kardomateas, G. A., (1993), "The Initial Postbuckling and Growth Behavior of Internal Delaminations in Composite Plates," *Journal of Applied Mechanics*, ASME, 60, pp. 903-910.
11. Suo, Z. and Hutchinson, J. W., (1990), "Interface Crack Between Two Elastic Layers," *International Journal of Fracture*, 43, pp. 1-18.
12. Pelegri, A. A. and Kedlaya, D. N., (2000), "On the Energy Release Rate of Fatigued Composites Subjected to Compressive Overloads," *Journal of Engineering Materials and Technology*, ASME, 122, pp. 443-449.
13. Jan S. L. V. S., Clapworthy G. J. and Rooze M., (2000), "Morphology-based Data Elimination from Medicak Image Data," *Computer Graphics and Applications*, IEEE, pp. 46-51.

ORAL/POSTR REFERENCE: ICF 100 479 PR

RESIDUAL STRESS CONCENTRATIONS ASSESSMENT IN CERAMICS USING FEM

T.Niezgoda[1], W.Szymczyk[1], J.Małachowski[1] and M.Woropay[2]

[1] Military University of Technology,
2 Kaliskiego Street, 00-908 Warsaw, Poland
[2] University of Technology and Agriculture,
7 Kaliskiego Street, 85-796 Bydgoszcz, Poland

ABSTRACT
The paper discusses the determination of residual stress state in a cooled down orthotropic alumina ceramics with the use of FEM (finite elements method) numerical modelling. The discrete model takes into consideration the ceramics consisting of two dominating grain size fractions. The current model allows changing the proportion between grain sizes in the fractions. The results of computations are presented as distributions of the residual stress components. The stress concentration areas are responsible for cracks origination and path determination of their subcritical growth. The average value of the stress component σ_c is identified as the peak position of the proper distribution and it is quantity characteristic for a given ceramics. The presented model may be used for investigation of ceramics and ceramic composites as well.

KEYWORDS
Orthotropic microstructures, alumina ceramics, numerical modelling

INTRODUCTION

In cooling down polycrystalline alumina from sintering to room temperature the random variation in crystallographic orientation of orthotropy from one grain to another induces a very complex state of constraint. This leads to appearing and remaining of the complex three-dimensional residual stress state in the ceramic material at the room temperature. Stress concentration areas have fundamental significance for strength property, especially for the cracking resistance.

The complicated spatial variation of the residual stress field depends on the elastic properties of grains, the grain size and the shape distribution. The residual stress across the grain boundary can be sufficiently large to initialise boundary microcracking. In elastic solids the stress σ_T is given by Blendel and Coble (1982):

$$\sigma_T = \beta\, E\, \Delta\alpha\, \Delta T \tag{1}$$

where β is a coefficient dependent on the shape and the grain orientation ($\beta \in < 0.5, +0.5 >$)[1], E is Young's modulus, $\Delta\alpha$ is a difference in the single-crystal thermal expansion coefficients along the direction

considered, ΔT is a difference between the temperature T_c (at which the sample was stress-free) and the room temperature T_0. Value of $\Delta\alpha$ for alumina was found in the paper [2] and equals 0.9 E-6 K^{-1}.

Solution of the elastic body equilibrium problem, which is caused by thermal expansion orthotropy by finite elements method (FEM) leads to the solution of the body equilibrium equations with special materials model [7]. For the elastic materials the main matrix equation can be written as follows:

$$KU = P \tag{2}$$

where K is the stiffness matrix which depends on geometry and materials properties, U is the unknown nodal displacements vector and P is force loading vector. For the heating and cooling process the vector P is a function of thermal strains too. The strains depend on the temperature increment ΔT and thermal expansion coefficients, which show the phenomenon of orthotropy. Solution Eqn. 2 and calculation U vector allows us to calculate strains and then, using Hook's law, the body stress. The advantage of the FEM calculations presents the possibility of using the same finite elements mesh for any vector P (loading force which aggregates nodal forces, pressure and forces caused by temperature, etc.) and any boundary conditions. Finite elements method allows analysing of any real element of structure while taking into consideration real loads.

FEM MODELS OF POLYCRYSTALLINE ORTHOTROPIC CERAMICS

The calculations were made for a prism that was assumed to be an internal part of an „infinite" ceramic body, filling very small volume of the body. The body is an element of analysed ceramics structure and the prism is the volume containing a number of ceramic grains. The body can be a real element of any ceramic structure (macroscopic scale). The prism presents a finite volume of ceramic body in microscopic scale. The model contains cubic and polyhedral grains (Figure 1). It allows changing of the proportion between sizes of cubic and polyhedral grains in the model (Figure 2).

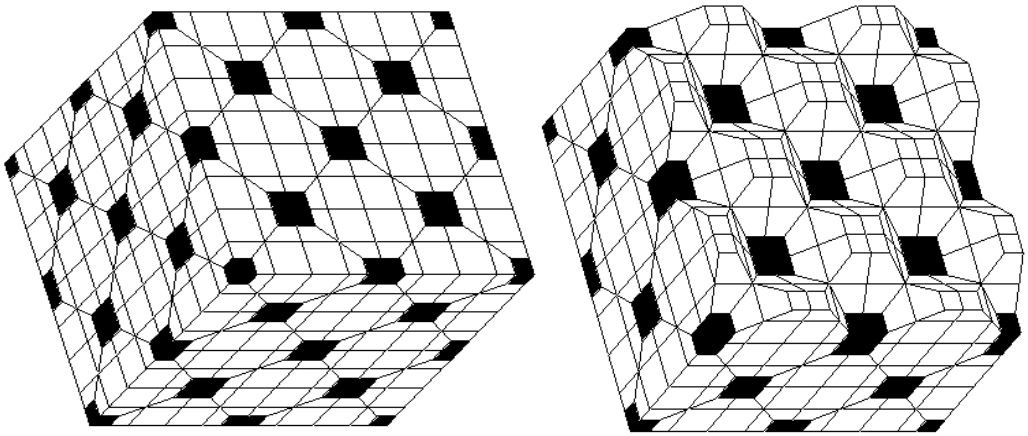

Figure 1: The model of cubes and polyhedrons

The grain size coefficient S was defined as a relation between current cubic grain size x and characteristic dimension of the finite element mesh X. The X value is constant for all of the models. For S=1 model contains only cubic grains. The other acceptable values of coefficient S vary from 0.3 to 0.7, to avoid computational errors resulting from excessive finite elements deformations. The set of grains labelled „A" begins in the corner of the model (Figures 1,2,3).

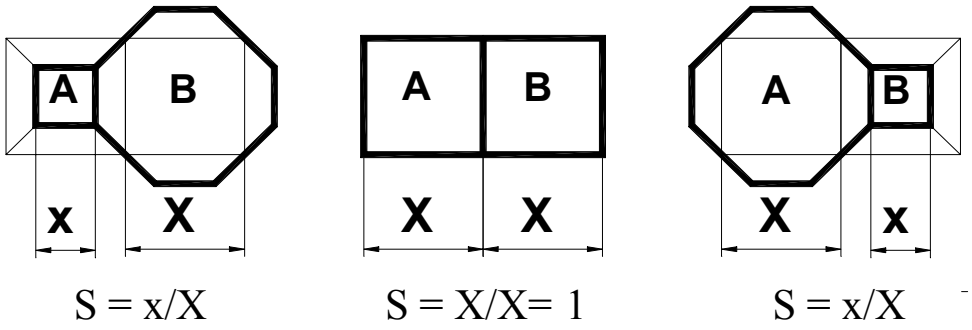

Figure 2: Definition of the grain size coefficient S=x/X

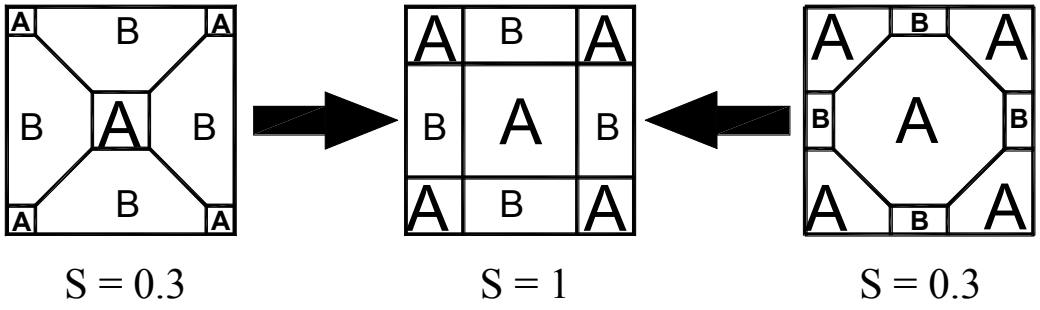

Figure 3: The unit of models may be obtained by changing size and shape of grains

For each grain the orthotropy direction c is chosen at random [6] from a set of possible axes. An exceptional requirement is verified during the randomising process. The directions of orthotropy must be different in the neighbouring grains. This requirement may be completed during the grain generation process by checking grains that had been defined earlier than the current grain (Figure 5a,b).

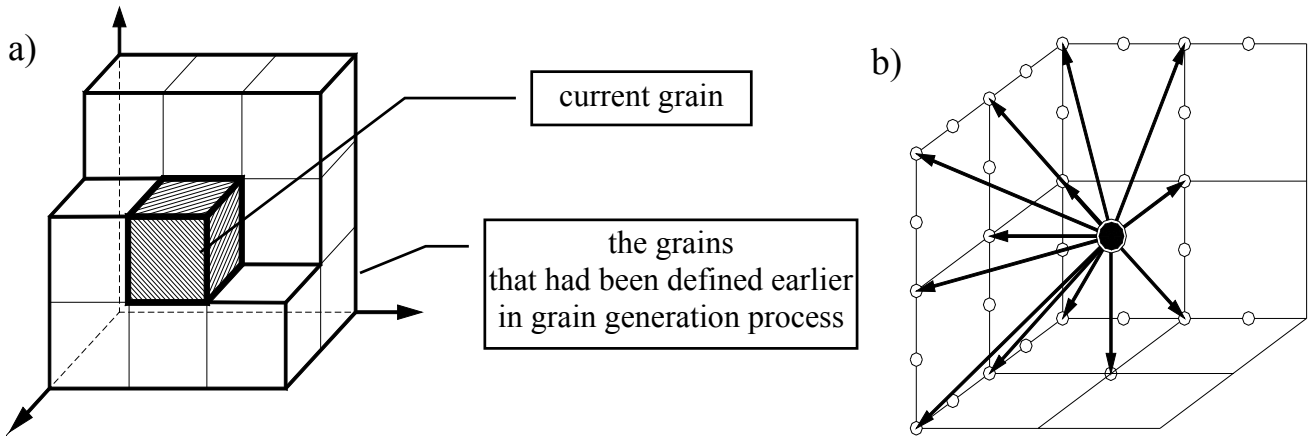

Figure 4: Scheme of grains generation and the set of possible directions

METHOD OF CALCULATIONS

A „two-steps" method was used for all the models. Firstly, it was assumed that the displacements of the prism boundaries were obtained from calculation for thermally loaded an isotropic element of ceramics structure. Secondly, it was assumed that the prism consists of ceramic grains. The grains were assumed to be thermally orthotropic. The calculations were made for the prism's boundary displacement from the first step and for the same thermal load. The calculations were made for the following values of parameters: Young's modulus E=380 GPa, Poisson's ratio ν=0.25, ΔT=1150 K, thermal expansion coefficients $\alpha_a=\alpha_b$=8.6E-6 K^{-1}, α_c=9.5E-6 K^{-1} (a, b, c – grain orthotropic axies), isotropic thermal expansion coefficient α = 8.9E-6 K^{-1}.

STATISTICAL POSTPROCESSING OF RESULTS

The distribution of each component of stress may be counted by summing the appropriate values calculated in integration points in the finite elements. The distribution may be obtained for the entire model, as well as for the cubic and polyhedral grains separately (Figures 5,6).

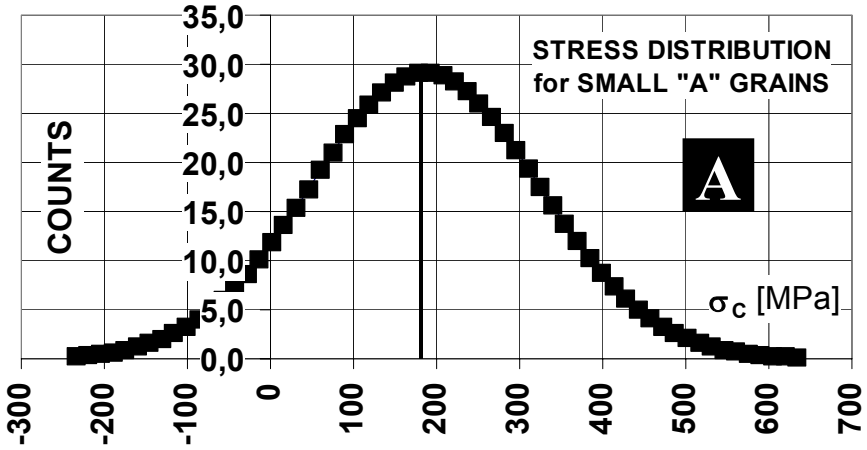

Figure 5: The σ_c distribution for small, cubic „A" grains, for the size coefficient S=0.3

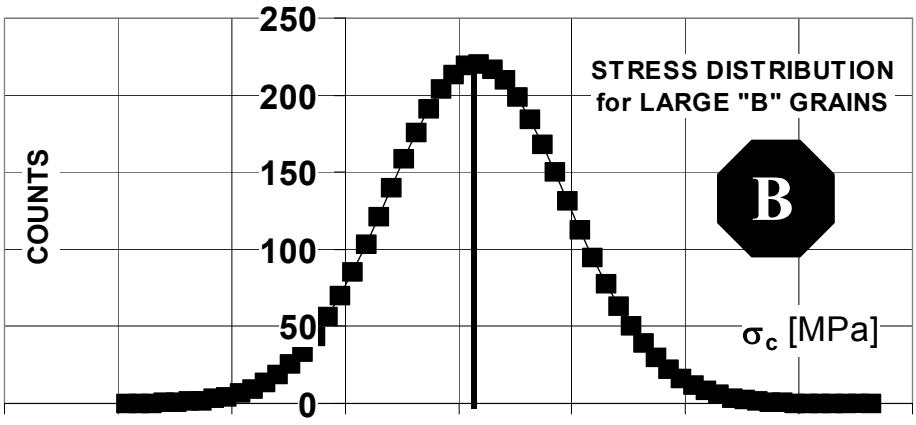

Figure 6: The σ_c distribution for large, polyhedral „B" grains, for the size coefficient S=0.3

Figure 7 shows the composition of σ_c average values (peak positions of stress distribution) obtained separately for „A" and „B" grains. They produce two separate curves. Each of them consists of two parts. Part A1 belongs to „A" grains of cubic shape and part A2 belongs to „A" grains of polyhedral shape. Adversely, part B1 belongs to polyhedral „B" grains and part B2 belongs to cubic „B" grains.
For example, part A1 shows that the σ_c value decreases from 186 MPa to 139 MPa when the grain size coefficient S enlarges from value of 0.3 to 0.7. For S=1 there are only cubic "A" and cubic „B" grains in the model with σ_c stress value of 133 MPa. Then, beyond this point, cubic „A" grains turns into polyhedral „A" grains and produce the curve A2.

An example of contour plot for σ_c stresses is presented below.

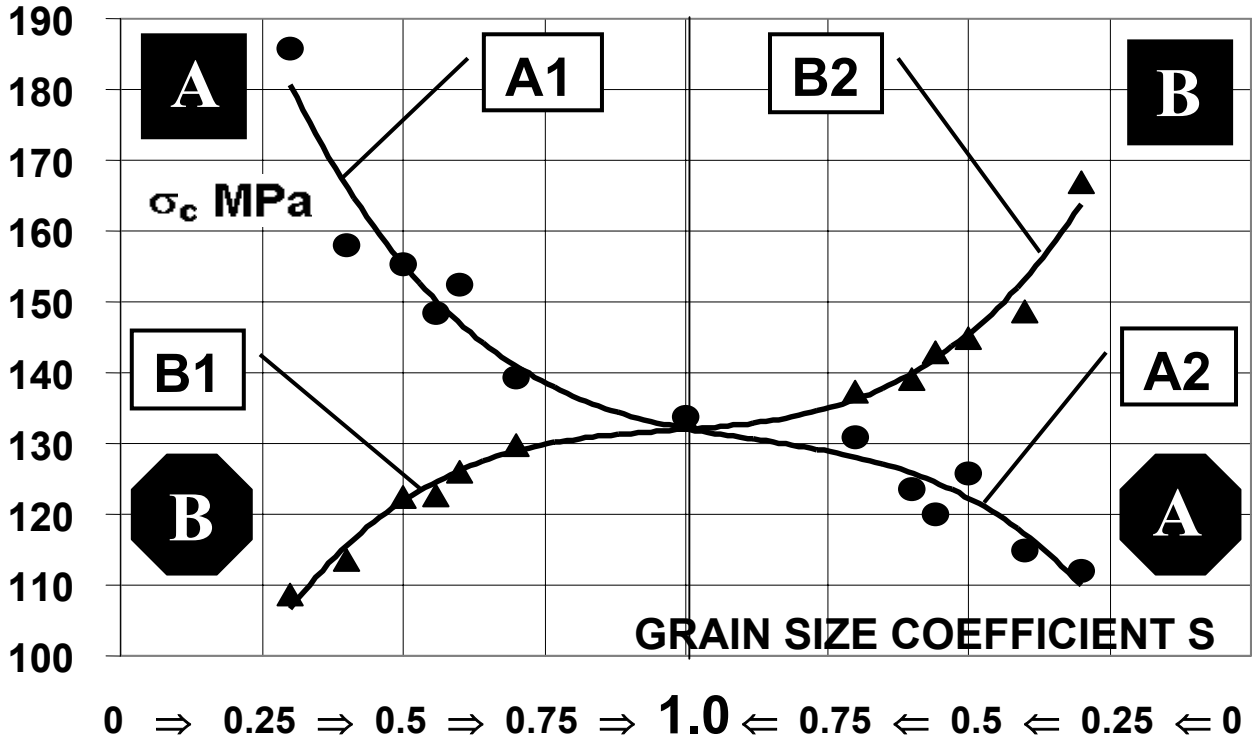

Figure 7: Composition of the σ_c average values that were obtained separately for ,,A" and ,,B" grains, for the unit of models with the same arrangement of ***c*** axes orientation, for various values of the grain size coefficient S

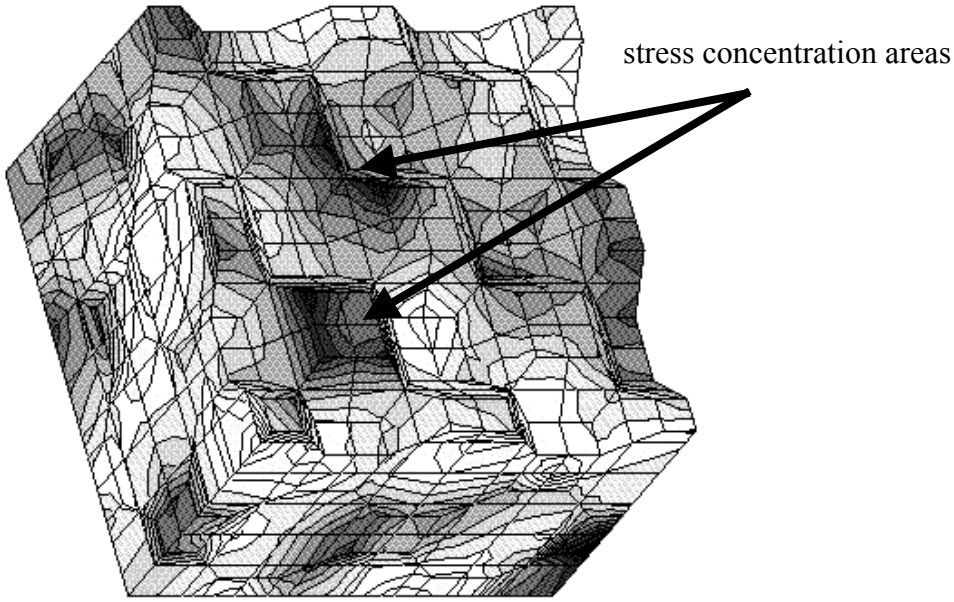

Figure 8: Example of contour plot for the values of σ_c , that is useful only for qualitative assessment of calculated stresses - it shows out the stress concentrations on external surfaces of grains

CONCLUSIONS

The proposed type of modelling of ceramic microstructure improved recently enables investigations of relative grain size influence on stress distribution, for neighbouring grains of different sizes grouped together in the same volume. The greater difference in size between neighbouring grains the higher stresses in small grains are observed. The model presented here may be used for investigations of ceramics (Al_2O_3) and ceramic composites (Al_2O_3 and ZrO_2) as well.

Using the statistic postprocessing of numerical results, the quantitative assessment of stresses in the modelled microstructure is possible [8]. The stress values calculated in integration points of finite elements are counted, to obtain stress distribution in the modelled volume of material. Then the peak position of the distribution is interpreted as the average stress value. This makes the numerical investigations similar to an experimental technique used for average residual stress measuring (the piezospectroscopic technique was enabled to verify numerical results).

The values of calculated average stresses are comparable with the results of our experiment [4] (the piezospectroscopic technique was enabled) and remain in a good agreement with those described in the works of other authors [1,3,5].

The results of calculations presented in the form of contour plots are useful for qualitative assessment of calculated stresses. They show that the significant part of internal energy in the modelled volume of microstructure is concentrated in the area close to the grain boundaries.

The advantage of numerical simulations is that the stress distribution may be counted separately for apportioned grains (e.g. of different size: small or large).

References

1. Blendel, J.E. and Coble, R.L. (1982). *J. Am. Ceram. Soc.* 65, 3, 174.
2. Rice, R.W. and Freiman, S.W. (1981). *J. Am. Ceram. Soc.* 64, 6, 350.
3. Ma, Q. and Clarke, D.R. (1994). *J. Am. Ceram. Soc.* 77, 2, 298.
4. Boniecki, M., Niezgoda, T. and Szymczyk, W. (1995). *Fourth Euro-Ceramics*, 3, 583.
5. Krell, A., Teresiak, A. and Schlafer, D. (1996). *J. Eur. Ceram. Soc.* 16, 803.
6. Niezgoda, T., Małachowski, J. and Szymczyk, W. (2000) In: *Proceeding of International Conference on Monte Carlo Simulation*, Monte Carlo.
7. Borkowski, W., Dacko, M., Niezgoda, T. and Wieczorek, M. (1994) *Finite elements method in mechanics of constructions*, Arkady, Warsaw, Poland.
8. Niezgoda T., Szymczyk W. and Małachowski J. (1999) In: *British Ceramic Proceedings*, No 60, pp. 483-484.

POSTER REFERENCE: ICF100528PR

NUMERICAL REPRESENTATION OF PLASTIC *J*-INTEGRAL VARIATION ALONG THE CRACK FRONT OF SEMI-ELLIPTICAL SURFACE CRACK UNDER UNIFORM TENSION.

Monir H. Sharobeam

Richard Stockton College of New Jersey,
Pomona, NJ 08240 USA

ABSTRACT

A mathematical form that represents the average plastic *J*-integral over the crack front of a semi-elliptical surface crack under uniform tension has been recently developed by the author. The form provides an estimate for the average plastic *J-Integral* at any stage of loading for wide array of surface crack geometries and material's hardening exponent. The purpose of this study is to introduce a numerical representation of the variation of the local plastic *J*-integral along the crack front. This is developed by studying the relationship between the average plastic *J*-integral and the local plastic *J*-integral at any point of the crack front. This relationship depends on the parametric angle, crack depth, crack width, and probably also geometry thickness to width ratio and the material hardening exponent. A wide array of crack geometries are used in this study. The crack depth to geometry thickness ratio varied from a shallow crack with a ratio of 0.1 to a deep crack with a ratio of 0.82. The crack depth to crack width ratio ranged from a narrow crack with a ratio of 2.0 to a wide crack with a ratio of 0.5. The finite element method has been used to develop the different models. About 35 different cases are included in the study to encompass the wide variation in the studied parameters.

KEYWORDS

elastic-plastic fracture; J-integral; surface cracks; load separation.

INTRODUCTION

The energy rate interpretation of *J*-integral, which was introduced by Rice [1] for two-dimensionsl geometries, can be applied for both: elastic *J*-integral, J_{el}, and plastic *J*-integral, J_{pl}. Hence, J_{pl} for two-dimensional geometries can be written as [1,2]:

$$J_{pl} = -\frac{1}{B}\left[\frac{\partial U_{pl}}{\partial a}\right]_{v_{pl}} \tag{1}$$

where U_{pl} is the plastic potential energy, B is specimen width, a is crack length and v_{pl} is the plastic load line displacement. It was also domenstrated that the relation between the load per unit thickness, P, and v_{pl} in two-dimensional geometries can be represented by a separable form [2,3,4] as:

$$P = G(a)H(v_{pl}) \tag{2}$$

where $G(a)$ and $H(v_{pl})$ are the geometry and deformation functions. The energy rate interpretation of J_{pl}, as represented by Eq. (1), and the load separation as represented by Eq. (2) led to the development of the single specimen J_{pl} expression for these geometries which can be written as:

$$J_{pl} = \frac{\eta_{pl}}{b} A_{pl} \tag{3}$$

where b is the uncracked ligament, A_{pl} is the area under the P versus v_{pl} record and η_{pl} is a factor that depends on the geometry and crack length [5,6,7].

The energy rate interpretation form given in Eq. (1) can be also written as:

$$-\left[\Delta U_{pl}\right]_{v_{pl}} = B\, J_{pl}\, \Delta a \tag{4}$$

This expression indicates that the infinitesmal difference in the plastic potential energy between two identical specimens with an arbitrary infinitesmal crack length difference of Δa at the same v_{pl} is equal to the crack driving force, $[BJ_{pl}]$, times the crack length difference. In three-dimensional geometries, such as surface cracks, this expression can be written as [8]:

$$-\left[\Delta U_{pl}\right]_{v_{pl}} = \int_S J_{pl}\, (\Delta a)\, dS \tag{5}$$

where S represents the crack front of the surface crack. J_{pl} varies along the crack front while Δa is arbitrary according to equation (4) and can be assigned a position function or a specific effective value along the crack front [8]. This can lead to an energy rate interpretation form for J_{pl} for surface cracks as:

$$J_{pl,av} = -\frac{1}{S}\left[\frac{dU_{pl}}{da}\right]_{v_{pl}} \tag{6}$$

where $J_{pl,av}$ is the average plastic J-integral across the crack front and can be written as:

$$J_{pl,av} = \frac{1}{S}\int_S J_{pl}\, dS \tag{7}$$

Sharobeam and Landes demonstrated load separation in the test records of surface crack geometry under uniform tension [8,9,10] for plastic load line displacement and also plastic crack mouth opening displacement. A separable load expression for this geometry can be written as:

$$\frac{\sigma_t}{\sigma_o} = G\left(\frac{a}{t}, \frac{a}{c}, \frac{t}{W}\right) H\left(\frac{v_{pl}}{t}\right) \tag{8}$$

where σ_t is the remote tensile stress, σ_o is yield stress, a is crack depth and c is crack width as shown in Fig. 1. t and W are specimen thickness and width, respectively. Load separation and the energy rate interpretation of $J_{pl,av}$ lead to a single specimen form for $J_{pl,av}$ for this geometry that can be written as:

$$J_{pl,av} = \zeta_{pl} \int \sigma_t\, dv_{pl} \tag{9}$$

The factor ζ_{pl} here is equivalent to (η_{pl}/b) in the single specimen J_{pl} form for two-dimensional geometries, as represented by Eq. (3), and it is a function of the crack depth to width ratio, a/c, crack depth to thickness ratio, a/t, and specimen thickness to width ratio, t/W. Sharobeam and Landes [8] demonstrated also that the ratio between plastic load line displacement and plastic crack mouth opening displacement is independent of the amount of deformation which allows using either in Eqs. (8) and (9) as v_{pl}. They also developed a mathematical representation for the single specimen $J_{pl,av}$ form using the plastic crack mouth opening displacement as:

$$J_{pl,ave} = \frac{n}{n+1}(\sigma_o t)\zeta_{pl}\ (G)\left(\frac{v_{pl}}{t}\right)^{\frac{n}{n+1}} \tag{10}$$

where n is the material hardening exponent and G is the geometry function. This expression is developed for Ramberg-Osgood materials, which follow the stress-strain relationship given as:

$$\frac{\varepsilon}{\varepsilon_o} = \frac{\sigma}{\sigma_o} + \alpha\left(\frac{\sigma}{\sigma_o}\right)^n \tag{11}$$

where ε is strain, ε_o is yield strain and α is a constant. Detailed expressions for the ζ_{pl} factor and the geometry function G are given in references [8] and [11], respectively, for surface cracks with wide range of *a/t*, *a/c*, *t/W* and *n* values.

The purpose of this study is to examine the variation of local J_{pl} along the crack front of semi-elliptical surface cracks and develop a relationship between the ratio of local J_{pl} to $J_{pl,av}$ and the location at the crack front represented by the parametric angle θ as shown in Fig. 2. Using this relationship together with Eq. (10), local J_{pl} at any point of the crack front of a surface crack can be obtained. To study J_{pl} variation along the crack front of a surface crack and develop the required relationship, numerical records of J-integral versus θ for wide array of semi-elliptical surface cracks were generated using the finite element method. Material was selected to be a Ramberg-Osgood material with a hardening exponent, n, equal to 5. The specimen width and half height were selected to be eight times the specimen thickness. Crack depth to thickness ratio varied from 0.1 to 0.82 while crack depth to crack width ratio varied from 0.5 to 2.0.

THE FINITE ELEMENT MODEL

The symmetry of the geometry allowed the consideration of only a single quarter of the geometry in the model. The model contains 3042 nodes and 402 20-node hybrid brick elements. The crack vicinity is represented by six rings of focused elements as shown in Fig. 3. Each ring contains 36 elements; six elements along the crack front times six along half the circumference of the ring. The structure of this model is close to those used by Kirk and Dodds [12] and Kim and Hwang [13]. To capture the plastic and elastic singularities at the crack tip, the crack tip side of the elements in the first ring are collapsed, the mid-side nodes of these elements are moved to the quarter point and the size of the elements in the first few rings are increased proportionally to the square root of their distance from the crack tip. A FORTRAN program was developed to generate the mesh for the model according to the selected *a/t*, *a/c* and *t/W* values. The program also generated the input file for the finite element code used in this study, ABAQUS. In an early study [8], results of this model have been found to be in a good agreement with the experimental elastic-plastic test records of specimens with identical crack geometries [11] and also Newman-Raju numerical solutions for elastic J-integral. The results of this model were also found in good agreement with the results of a more refined model with similar structure but additional 2555 nodes and 396 element just in the crack vicinity [11].

FINITE ELEMENT RESULTS

To study the effect of *a/t* on the distribution of $J_{pl}/J_{pl,av}$ along the crack front for different *a/c* values, models with *a/c*=0.5, 0.75, 1.0, 1.5 and 2.0 and *a/t* that varies from 0.1 to 0.82 were developed. For each crack geometry, the model was run twice; one with a linearly elastic material and another with a Ramberg-Osgood elastic-plastic material. The plastic component of J was obtained by subtracting J_{el} obtained using the elastic run from the total J obtained using the elastic-plastic run for the same load. $J_{pl,av}$ was, then, evaluated by integrating J_{pl} over the crack front as indicated by Eq. (7). The $J_{pl}/J_{pl,av}$ distribution along the crack front for the different crack geometries are shown in Figs. 4-8. It is clear from these figures that there are two trends for $J_{pl}/J_{pl,av}$ distribution along the crack front. For shallow, wide cracks ($a/t \le 0.4$ and $a/c \le 0.75$), the distribution begins with a low value at the surface ($\theta = 0$), then increases until it reaches maximum at the deepest point of the crack

($\theta = 90°$). For deep, wide cracks ($a/t \geq 0.6$ and $a/c \leq 0.75$) and all circular ($a/c = 1.0$) and narrow cracks ($a/c > 1.0$), the $J_{pl}/J_{pl,av}$ distribution begins also with a low value at the surface, reaches a maximum value mostly between $\theta = 15°$ and 30° then decreases gradually as θ increases. The maximum $J_{pl}/J_{pl,av}$ values for surface cracks that represent a transition between the two trends such as the two surface cracks: (a/t = 0.6 , a/c = 0.5) and (a/t = 0.5, a/c = 0.75) occurred between $\theta = 45°$ and 60°. For the cases where $J_{pl}/J_{pl,av}$ reaches a maximum before decreasing, it can be noticed that the rate at which $J_{pl}/J_{pl,av}$ decreases as θ increases depends on a/t such that the deeper the crack the higher the rate. Similar trends for normalized J distribution were obtained by Yagawa, Ueda and Takahashi [15] for four different surface cracks with $a/t = 0.4$ and 0.8 and $a/c = 0.2$ and 0.6. Kirk and Dodds [12] results also for a surface crack with $a/t = 0.13$ and $a/c = 0.38$ showed similar trend to that of the shallow, wide surface cracks in this study. The low value for $J_{pl}/J_{pl,av}$ at the surface is contributed to the low constraint condition which results in a reduced order of singularity in the surface boundary layer[12]. From the figures, it is also clear that, for each of the studied a/c values, the $J_{pl}/J_{pl,av}$ values for shallow cracks ($a/t =$ 0.1 to 0.4) are very close for the whole crack front. The difference is less than 6% at any point on the crack front. On the other hand, there is a wide scatter for the $J_{pl}/J_{pl,av}$ values for medium to deep cracks ($a/t > 0.4$ to 0.8) with $a/c = 0.5$, 0.75 and 1.0. This scatter, however, becomes narrow as a/c reaches 1.5 and collapses into almost a single line for the different surface cracks with $a/c = 2.0$.

To make sure that these distributions are uniquely related to the crack geometry (a/t and a/c) and not dependent on the amount of loading, $J_{pl}/J_{pl,av}$ was evaluated for four different surface cracks at different levels of loading. The results of these evaluations are given in Table 1 which shows that the $J_{pl}/J_{pl,av}$ values are almost identical for the different loading levels over the whole crack front except for the point at the surface ($\theta = 0$). This indicates that $J_{pl}/J_{pl,av}$ distribution along the crack front of a surface crack is independent of the loading level at least for the loading range included in this study which is from a little below the yield value up to almost twice the yield value.

NUMERICAL REPRESENTATION OF THE RESULTS

Several functions have been tried to provide a general fit for $J_{pl}/J_{pl,av}$ distribution along the crack front. It was difficult to find a function that can capture the two different trends and provide a perfect fit for all the data points along the crack front. The following function simulated the two different trends of distribution with a reasonably close fit.

$$f_1(\theta) = A_1 \sin\theta \quad + B_1\sqrt{\sin\theta} \quad + C_1\sqrt[3]{\sin\theta} \quad + D_1 \tag{12}$$

where $f_1(\theta)$ represents $J_{pl}/J_{pl,av}$ and A_1, B_1,C_1 and D_1 are the fit function coefficients. Figs. 9-12 show how this function fits the finite element data for $J_{pl}/J_{pl,av}$ versus θ distribution for four different cracks. This fit function is labelled as the first fit function in these figures. It provides an excellent fit for all data points except for a narrow range around the maximum point for the cases where the maximum occurs at low θ values ($\theta < 45°$). At these maximum points, the fit is off the finite element data by less than 4%.

When the surface point ($\theta = 0$), where $J_{pl}/J_{pl,av}$ value showed a little dependence on the load level, is not include in the fit, a simple polynomial function of the third order provided also a reasonable fit for both trends. It was off by less than 2% for most of the data points except again where there is a maximum at θ below 45°. The difference between the fit and the finite element value at the maximum point is typically less than 4%. This fit function is shown in Figs. 9-12 and is labelled as the second fit function. It can be written as:

$$f(\theta) = A\sin^3\theta \quad + B\sin^2\theta \quad + C\sin\theta \quad + D \tag{13}$$

where $f(\theta)$ represents $J_{pl}/J_{pl,av}$ and A, B, C and D are the fit function coefficients. This function is applicable for the range $\theta = 7.5°$ to 90° where $J_{pl}/J_{pl,av}$ values are found to be independent of the loading level. Because of the simplicity of this function and it is reasonable representation of the $J_{pl}/J_{pl,av}$ distribution along the crack front, it is adopted in this study. Table 2 lists the coefficients A, B, C and D for wide array of surface cracks.

TABLE 1: $J_{PL}/J_{PL,AV}$ VERSUS θ FOR DIFFERENT SURFACE CRACKS AT DIFFERENT LOADING LEVELS.

Crack	*a/t=0.6, a/c=1.63*			*a/t=0.3, a/c=0.75*			*a/t=0.4, a/c=2.0*			*a/t=0.82, a/c=1.0*		
	σ_t/σ_o =			σ_t/σ_o =			σ_t/σ_o =			σ_t/σ_o =		
θ	0.9	1.1	1.3	1.2	1.5	1.8	1.1	1.3	1.5	0.9	1.0	1.1
0.0	0.69	0.78	0.83	0.43	0.47	0.48	0.86	0.91	0.93	0.65	0.70	0.73
7.5	1.17	1.17	1.16	0.79	0.78	0.77	1.24	1.24	1.24	1.30	1.29	1.28
15.0	1.32	1.31	1.30	0.89	0.88	0.87	1.35	1.35	1.35	1.44	1.42	1.41
30.0	1.18	1.18	1.18	0.99	0.98	0.98	1.17	1.17	1.17	1.22	1.22	1.22
45.0	0.99	0.99	1.00	1.04	1.04	1.04	0.96	0.96	0.96	0.98	0.98	0.98
60.0	0.85	0.84	0.84	1.07	1.08	1.08	0.78	0.78	0.78	0.86	0.86	0.87
75.0	0.74	0.73	0.73	1.10	1.10	1.10	0.66	0.65	0.65	0.75	0.75	0.75
90.0	0.71	0.70	0.69	1.11	1.11	1.12	0.62	0.61	0.60	0.70	0.70	0.70

Using this fit function, $J_{pl}/J_{pl,av}$ distribution along the crack front of surface cracks with a/t=0.1, 0.2,…or 0.8 and a/c=0.5, 0.75, 1.0, 1.5 or 2.0 can be reconstructed. For surface cracks with different a/t and a/c values but within the studied ranges, $J_{pl}/J_{pl,av}$ distribution can be obtained using one or two-dimensional fitting functions between the $J_{pl}/J_{pl,av}$ distributions of neighboring surface cracks. Because of the small increments in a/t, a linear or quadratic fit function can be used to construct $J_{pl}/J_{pl,av}$ distribution for a surface crack geometry with a/t that is not included in the given array of surface cracks. For surface cracks with a/c values that are not included in the array, a second or a third order polynomial fit is recommended. There are many commercial math packages that provide one and two-dimensional fitting functions. Using $J_{pl}/J_{pl,av}$ distributions constructed by the fit functions given in Table 1 for surface cracks with same a/t but different a/c values in a third order polynomial surface fit, $J_{pl}/J_{pl,av}$ distributions a surface crack geometry with a new a/c value that is within the range of the included a/c values can be obtained. Figs. 13 and 14 show a comparison between $J_{pl}/J_{pl,av}$ distributions obtained by the finite element model and Mathcad 2000 two-dimensional fit for two surface cracks geometries with new a/c values. The two-dimensional fit provided $J_{pl}/J_{pl,av}$ distribution that is very close to the finite element data.

TABLE 2: THE FIT FUNCTION COEFFICIENTS FOR A WIDE ARRAY OF SURFACE CRACKS.

		a/t=							
		0.1	0.2	0.3	0.4	0.5	0.6	0.7	0.8
a/c=0.5	*A*=	-0.030	0.152	0.165	0.099	0.096	0.310	0.427	0.535
	B=	0.118	-0.193	-0.322	-0.365	-0.695	-1.381	-1.926	-2.462
	C=	0.592	0.826	0.943	1.003	1.185	1.602	1.845	2.059
	D=	0.546	0.458	0.438	0.453	0.526	0.519	0.605	0.711
a/c=0.75	*A*=	0.226	0.482	0.597	0.611	0.530	0.930	1.491	0.997
	B=	-0.569	-1.036	-1.309	-1.471	-1.517	-2.454	-3.606	-2.690
	C=	0.799	1.043	1.187	1.285	1.341	1.809	2.258	1.472
	D=	0.677	0.644	0.641	0.657	0.682	0.686	0.746	1.014
a/c=1.0	*A*=	0.628	0.827	0.912	0.664	0.839	1.295	1.748	1.909
	B=	-1.483	-1.822	-2.025	-1.639	-2.114	-3.096	-3.953	-4.040
	C=	1.022	1.203	1.323	1.123	1.397	1.879	2.149	1.781
	D=	0.834	0.804	0.793	0.834	0.822	0.811	0.875	1.092
a/c=1.5	*A*=	1.159	1.243	1.328	1.407	1.463	1.397	1.590	1.871
	B=	-2.740	-2.894	-3.050	-3.238	-3.381	-3.360	-3.610	-3.958
	C=	1.304	1.411	1.520	1.635	1.706	1.713	1.671	1.623
	D=	1.036	1.009	0.983	0.969	0.972	0.984	1.053	1.137
a/c=2.0	*A*=	0.985	1.103	1.181	1.311	1.323	1.452	1.502	1.314
	B=	-2.478	-2.720	-2.882	-3.150	-3.222	-3.491	-3.597	-2.994
	C=	1.043	1.142	1.204	1.311	1.372	1.523	1.550	1.019
	D=	1.129	1.131	1.136	1.140	1.132	1.115	1.129	1.253

CONCLUSION

$J_{pl}/J_{pl,av}$ distribution along the front of surface crack geometries with wide ranges of a/t and a/c values were developed using the finite element method. Width and height of each geometry were selected to be eight times the thickness and the material is considered as a Ramberg-Osgood material with a hardening exponent of 5. Two trends for $J_{pl}/J_{pl,av}$ distributions along the crack front have been observed. For shallow, wide cracks, the $J_{pl}/J_{pl,av}$ ratio begins with a low value at the surface then increases until it reaches its maximum at the deepest point. For most of other studied crack geometries, the $J_{pl}/J_{pl,av}$ ratio begins with a low value at the surface but reaches a maximum at θ below 45°, then decreases as θ increases. It was also observed that $J_{pl}/J_{pl,av}$ distribution for narrow surface cracks (a/c = 1.5 and 2) is less dependent on a/t than that for circular (a/c = 1.0) and wide (a/c = 0.5 and 0.75) cracks. A general fit function that encompasses both trends was developed. Such a function can be used to construct $J_{pl}/J_{pl,av}$ distribution for any surface crack with a/t and a/c within the studied ranges. Using the constructed $J_{pl}/J_{pl,av}$ distribution and the mathematical representation of $J_{pl,av}$ given in Eq. (10), a full representation of J_{pl} along the crack front at any stage of loading can be predicted. Other parameters that may influence $J_{pl}/J_{pl,av}$ distribution such as thickness to width ratio and material hardening exponent are now under consideration by the author.

REFERENCES

1. Rice, J. R. (1968) *Journal of Applied Mechanics,* 35, 379-386.
2. Paris, P. C., Ernst, H. and Turner, C. E. (1980) *Fracture Mechanics - Twelfth Conference,* ASTM STP 700, 338-351.
3. Sharobeam, M. H., and Landes, J. D. (1991) *International Journal of Fracture Mechanics*, 47, 81-104.
4. Sharobeam, M. H., and Landes, J. D. (1993) *International Journal of Fracture Mechanics*, 59, 213-226.
5. Rice, J. R., Paris, P. C., and Merkle, J. G. (1973) *Progress in Flaw Growth and Fracture Toughness Testing, ASTM STP 536*, 231-245.
6. Merkle, J. G. and Corten, H. T. (1974) *PVP-33, ASME*, 286-292.
7. Clarke, G. A. and Landes, J. D. (1979) *Journal of Testing and Evaluation, JTEV*, A7, 5,264-265.
8. Sharobeam, M. H., and Landes, J. D. (1994) *Fracture Mechanics: 25th Symposium, ASTM STP 1220*, 397-414.
9. Sharobeam, M. H. (1994) *FAA/NASA International Symposium on Advanced Structural Integrity Methods for Airframe Durability and Damage Tolerance, NASA CP-3274*, 2, 703-724.
10. Sharobeam, M. H., and Landes, J. D. (1993) *International Journal of Fracture*, 61, 379-395.
11. Sharobeam, M. H. and Landes, J. D. (1993) *Engineering Fracture Mechanics,* 63, 131-145.
12. Kirk, M. T. and Dodds, R. H., Jr. (1991) *Engineering Fracture Mechanics*, 39, 3, 535-551.
13. Kim, J. H. and Hwang, I. S. (1998) *PVP-365, ASME,* 325-331.
14. Newman, J. C. and Raju, I. S. (1983) *Fracture Mechanics: 14th Symposium, ASTM STP 791*, 283-265.
15. Yagawa, G., Ueda, H. and Takhashi, Y. (1986) *PVP-103, ASME,* 43-48.

NUMERICAL SIMULATION OF CONCRETE FAILURE IN PULL-OUT EXPERIMENTS

P. Pivonka, R. Lackner, and H. A. Mang

Institute for Strength of Materials
Vienna University of Technology, Vienna, Austria

ABSTRACT

This paper deals with the application of a 3D-constitutive model for concrete to simulations of pull-out experiments [1]. This material model is formulated within the framework of multi-surface plasticity. It consists of three Rankine yield surfaces for the simulation of cracking and a Drucker-Prager yield surface for the description of compressive failure of concrete. The Drucker-Prager surface is reformulated in order to account for the influence of confinement on the compressive strength and the ductility of concrete.
The predictive capability of the model is demonstrated by means of a finite element (FE) analysis of a pull-out test [1]. The influence of confinement on the peak load and the failure mode is investigated.

KEYWORDS

multi-surface plasticity, concrete, confinement, pull-out, ultimate load, failure mode

INTRODUCTION

The use of numerical tools such as the FEM allows simulation of real-life structures characterized by complex geometric properties and loading conditions. As regards the simulation of concrete structures, sophisticated material models are required in order to provide an appropriate description of the mechanical behavior of concrete. Such material models should account for crack opening in the case of tensile loading, crushing in the case of compressive loading, and compaction of concrete when subjected to hydrostatic pressure.

In the context of plasticity theory, failure may be described either by one failure criterion (single-surface plasticity) or by a combination of several failure criteria (multi-surface plasticity). As regards multi-surface plasticity, each failure criterion is used to describe a certain mode of material failure. For the simulation of cracking, the Rankine criterion gives the best results. In the compressive loading regime, the Drucker-Prager surface is commonly employed (see, e.g., [5][9]). The compaction of concrete may be considered by means of an additional cap (see, e.g., [7]).

In this paper a multi-surface plasticity model consisting of the Drucker-Prager criterion and the Rankine criterion is considered. As regards the Drucker-Prager criterion, a reformulation is proposed in order to extend its range of applicability. The influence of this reformulation on the numerical results is demonstrated by means of a FE analysis of a pull-out test.

In the following section, the material model is briefly presented and the proposed modification of the Drucker-Prager criterion is described. However, the main part of the paper is devoted to the numerical analysis of a pull-out test.

3D PLASTICITY MODEL FOR PLAIN CONCRETE

Concrete is a composite material, made of cement, aggregates, and water. In continuum mechanics, however, concrete is treated as homogeneous material. The respective scale of observation is referred to as macro-level. Stress-strain relations formulated at the macro-level relate macro-stresses to macro-strains. However, the mechanical behavior observed at the macro-level is associated with phenomena occurring at the micro-level of the material. E.g., inelastic macro-strains arise from micro-cracking of hydrates. For the description of phenomena at the micro-level, so-called internal variables $\boldsymbol{\alpha}$ are introduced in the material model. They are used to describe the microstructural change of the material. The energetically conjugated thermodynamic quantities are the hardening/softening forces $\mathbf{q}$. They are related to the internal variables via the state equation $\mathbf{q} = \mathbf{q}(\boldsymbol{\alpha})$. The hardening forces represent the actual strength of the material, defining the space of admissible stress states, $\mathbf{C}_E$:

$$\boldsymbol{\sigma} \in \mathbf{C}_E \quad \Leftrightarrow \quad f_k = f_k(\boldsymbol{\sigma}, \mathbf{q}(\boldsymbol{\alpha})) \leq 0 \quad \forall \quad k \in [1,2,...,N] \tag{1}$$

where f_k denotes the k-th yield function. In definition (1), the general case of multi-surface plasticity is considered. N denotes the number of employed yield functions.

The internal variables and the respective deformations related to plastic material response are obtained by means of evolution equations, reading

$$\dot{\boldsymbol{\alpha}} = \sum_{k \in J_{act}} \dot{\gamma}_k \frac{\partial H_k}{\partial \mathbf{q}}, \qquad \dot{\boldsymbol{\varepsilon}}^p = \sum_{k \in J_{act}} \dot{\gamma}_k \frac{\partial Q_k}{\partial \boldsymbol{\sigma}}, \tag{2}$$

where γ_k denotes the plastic multiplier of the k-th yield function. H_k and Q_k are potentials which, in general, depend on $\boldsymbol{\sigma}$ and $\mathbf{q}$.

The material model considered in this paper is formulated within the framework of multi-surface plasticity theory. It consists of four yield surfaces ($N = 4$): a Drucker-Prager (DP) yield surface for the description of concrete when subjected to compressive loading and three Rankine (RK) surfaces for the description of tensile failure. In the principal stress space, the failure criteria read

$$f_{DP}(\boldsymbol{\sigma}, q_{DP}) = \sqrt{J_2} - \kappa_{DP} I_1 - \frac{\bar{q}_{DP}}{\beta_{DP}}, \text{ with } \quad \bar{q}_{DP} = f_{cy} - q_{DP}, \tag{3}$$

and

$$f_{RK,A}(\sigma_A, q_{RK}) = \sigma_A - \bar{q}_{RK}, \text{ with } \quad \bar{q}_{RK} = f_{tu} - q_{RK}, \tag{4}$$

where the subscript A ($A = 1,2,3$) refers to one of the three principal axes. f_{tu} is the tensile strength and f_{cy} represents the elastic limit of concrete under uniaxial compressive loading. κ_{DP} and β_{DP} are constant material parameters.

For the description of microstructural changes of concrete, two internal variables are employed: α_{RK} and α_{DP}. They are computed by means of associated hardening/softening laws, i.e., $H_{RK,A} = f_{RK,A}$ and $H_{DP} = f_{DP}$, reading

$$\dot{\alpha}_{RK} = \sum_{A=1}^{3} \gamma_{RK,A} \frac{\partial f_{RK,A}}{\partial q_{RK}}, \quad \dot{\alpha}_{DP} = \sum_{A=1}^{3} \gamma_{DP} \frac{\partial f_{DP}}{\partial q_{DP}}. \tag{5}$$

Cracking of concrete is characterized by a continuous decrease of the tensile strength $\bar{q}_{RK}$. Accordingly, an exponential softening law is chosen, reading

$$\bar{q}_{RK} = f_{tu} \exp[-\alpha_{RK} / \alpha_{RK,u}], \tag{6}$$

where $\alpha_{RK,u}$ is a calibration parameter. Under compressive loading, however, the behavior of concrete is characterized by hardening as well as softening behavior. The chosen hardening/softening curve for the compressive strength $\bar{q}_{DP}$ is depicted in Figure 1(a).

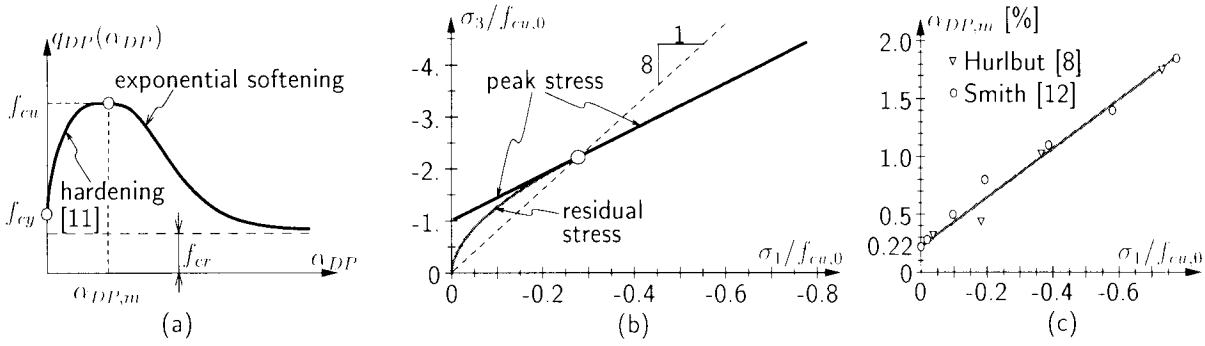

Figure 1: (a) employed hardening/softening curve for the Drucker-Prager criterion; influence of confinement on (b) the peak and residual stress (related to f_{cu} and f_{cr}) and (c) the ductility ($\alpha_{DP,m}$). The level of confinement is represented by the maximum principal stress σ_1 ($f_{cu,0}$: uniaxial compressive strength of concrete)

Commonly, the Drucker-Prager criterion is calibrated by means of uniaxial and biaxial compression tests, giving κ_{DP} and β_{DP} (see, e.g., [10]). For the application of the Drucker-Prager criterion to structures mainly experiencing biaxial stress states, this mode of calibration is appropriate. For confined stress states, however, large deviations between experimental data and numerical results were reported in [11]. Experimental data indicate an influence of confinement on both the compressive strength, described by the ultimate and the residual strengths, f_{cu} and f_{cr}, and the ductility [12]. The proposed modification of the Drucker-Prager criterion accounts for this influence by relating f_{cu}, f_{cr}, and $\alpha_{DP,m}$ to the actual level of confinement. Confinement is represented by the major principal stress σ_1, with $\sigma_1 \geq \sigma_2 \geq \sigma_3$, yielding $f_{cu} = f_{cu}(\sigma_3(\sigma_1))$, $f_{cr} = f_{cr}(\sigma_3(\sigma_1))$, and $\alpha_{DP,m} = \alpha_{DP,m}(\sigma_1)$ (see Figure 1(b) and (c)). f_{cu} and

f_{cr} are computed by means of the Drucker-Prager criterion, $f_{DP}=0$, using the stress state $\boldsymbol{\sigma}^T=[\sigma_1,\sigma_1,\sigma_3(\sigma_1)]$ (for details, see [11]).

FAILURE ANALYSIS OF PULL-OUT TEST

The focus of the present paper is on the influence of the underlying model formulation on numerical results obtained from failure analyses of anchor bolts in concrete, referred to as pull-out test. For this purpose, analyses on the basis of the material model described in the previous section were performed. The influence of confinement on the peak load and on the failure mode is investigated.

Geometric dimensions and material properties

Figure 2 contains the experimental setup of the considered pull-out test (Round-robin test [1]). It shows the geometric dimensions as well as the support conditions of the specimen. Further, the material properties of concrete and steel are given.

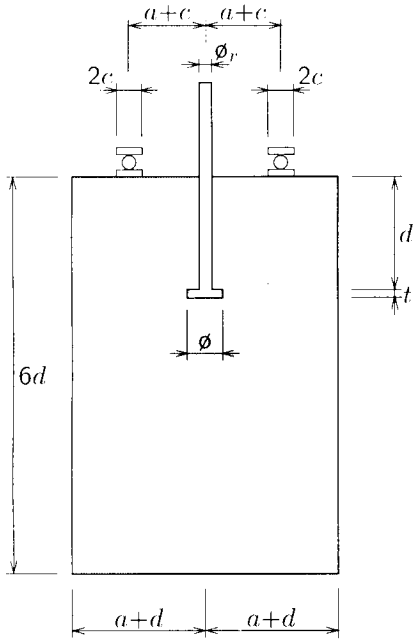

dimensions:

d=150 mm a=150 mm

t=15 mm c=22.5 mm

ø=45 mm $ø_r$=24 mm

concrete:

Young's modulus: E_c=30000 N/mm^2

Poisson's ratio: ν_c=0.2

uniaxial compressive strength: f_{cu}=40 N/mm^2

uniaxial tensile strength: f_{tu}=3 N/mm^2

fracture energy: G_f^I=0.1 Nmm/mm^2

fracture energy: G_f^{II}=50G_f^I

steel:

Young's modulus: E_s=210000 N/mm^2

Poisson's ratio: ν_s=0.3

Figure 2: Pull-out analysis: geometric dimensions and material properties

Numerical analysis

In the numerical analysis, the material behavior of the steel bolt is assumed to be linear elastic. For the description of concrete, the previously described material model is used.

Because of symmetry of the geometric properties and the loading conditions, the problem is solved by means of axisymmetric analyses. Figure 4 shows the employed FE mesh consisting of 677 four-node finite elements. As regards the mechanical model of the anchor bolt, only the anchor head is discretized. At the contact line between the anchor head and the concrete, no slip is considered. The analyses is performed displacement-driven. The displacement at the nodes of the anchor head located at the axis of symmetry is prescribed (see Figure 3).

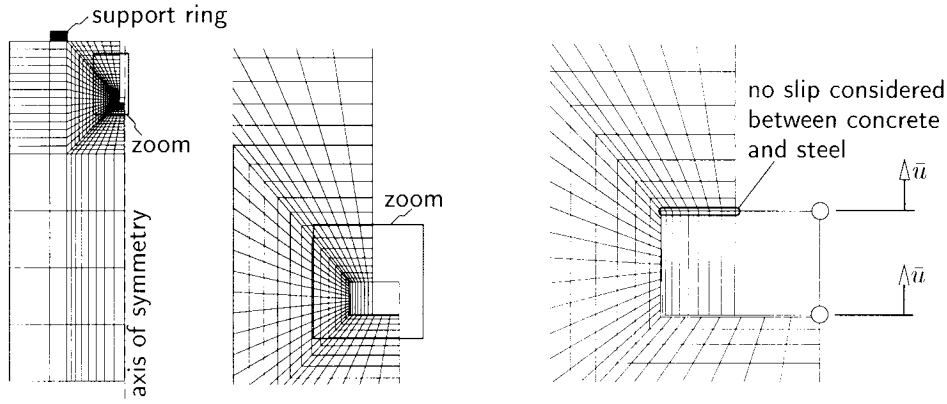

Figure 3: Pull-out analysis: FE discretization

Softening functions appearing in the formulations of the model were calibrated according to the fictitious crack concept [6]. The application of the fictitious crack concept to the simulation of radial cracks in axisymmetric analyses requires the input of the expected number of radial cracks. In the present analyses, four radial cracks are assumed to develop.

Figure 4 contains the obtained load-displacement curves. The peak load obtained from the Drucker-Prager criterion characterized by consideration of confinement (*modified* model) was found to be 340 kN. Neglection of the influence of confinement within the Drucker-Prager criterion (*original* model), i.e., setting $f_{cu} = const.$, $f_{cr} = const.$, and $\alpha_{DP,m} = 0.0022$, led to a reduction of the peak load by 47% (see Figure 4(a)).

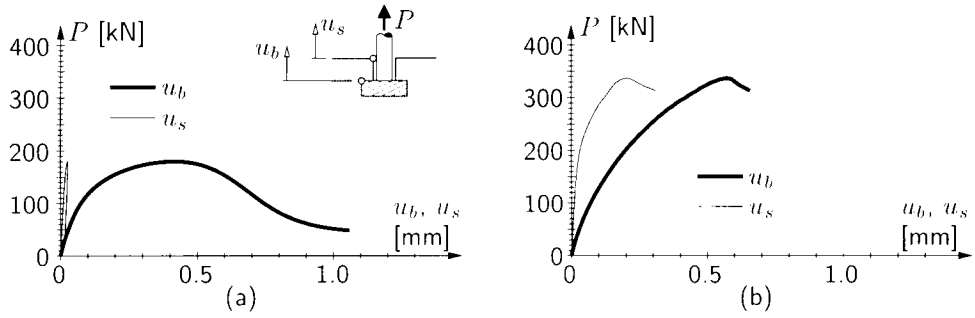

Figure 4: Pull-out analysis: load-displacement curves obtained from multi-surface model with (a) *original* and (b) *modified* Drucker-Prager criterion

The difference between the displacement at the anchor head and the concrete surface, $u_b - u_s$, is an indicator for compressive failure of concrete over the anchor head. An almost constant evolution of $u_b - u_s$ indicates a rigid body motion in consequence of formation of a cone-like failure mode (see, e.g., Figure 7(a)). Small values of u_s together with continuously increasing values of $u_b - u_s$ indicate local failure of concrete over the anchor head. This failure mode was obtained from the analysis based on the *original* model (see Figure 4(a)). The underestimation of compressive strength and ductility by neglecting the influence of confinement resulted in compressive failure of concrete over the anchor head. The respective $P - u_b$ curve shows similar characteristics as the underlying hardening/softening curve used for the Drucker-Prager model (see Figure 1(a)). Moreover, failure of concrete over the anchor head resulted in an unloading of the remaining part of the structure. This is reflected by the decrease of u_s in the post-peak regime. Consideration of confinement by the *modified* model led to an increase of the compressive strength over the anchor head. The almost constant evolution of $u_b - u_s$ in the post-peak regime (Figure 4(b)) indicates the development of a cone-like failure mode (see Figure 7(a)).

The distribution of α_{DP} is given in Figure 5 for both analyses at the respective peak loads. The compressive failure over the anchor head obtained from the *original* model is reflected by softening material behavior (see Figure 5(a)). Softening is characterized by $\alpha_{DP} > \alpha_{DP,m} = 0.0022$. On the other hand, confinement considered in the analysis based on the *modified* model resulted in an increase of $\alpha_{DP,m}$ over the anchor head (see Figure 5(c)). The distribution of α_{DP} is shown in Figure 5(b). The values of α_{DP} are lower than the respective values of $\alpha_{DP,m}$ indicating that the compressive strength in this area has not reached the ultimate strength f_{cu} (hardening regime).

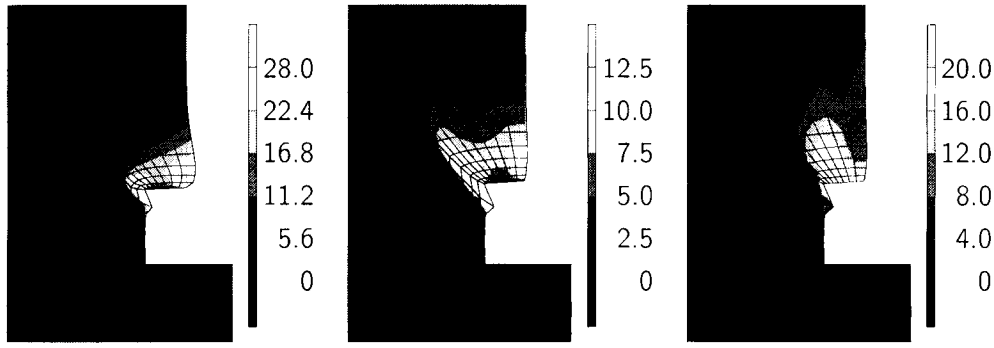

Figure 5: Pull-out analysis: distribution of, α_{DP} at peak load obtained from multi-surface model with (a) *original* and (b) *modified* Drucker-Prager criterion; (c) distribution of $\alpha_{DP,m}$ at peak load obtained from multi-surface model with *modified* Drucker-Prager criterion (10-fold magnification of displacements)

The strong influence of confinement on the obtained numerical results is a consequence of large compressive stresses over the anchor head. Recall, the major principal stress is used as a measure for confinement. If the major principal stress is positive, no confinement is considered. Figure 6 shows the distribution of the two principal stresses in the $r-z$ plane, denoted as $\sigma_{\min}$ and $\sigma_{\max}$, and the circumferential stress σ_{circ} at peak load obtained from the analysis based on the *modified* model. Over the anchor head, negative stresses are observed for all three principal stresses. Hence, $\sigma_1 < 0$, resulting in an increase of the compressive strength and the ductility (see Figure 1(b) and (c)).

The distribution of the minimum in-plane principal stress $\sigma_{\min}$ (see Figure 6(a)) provides insights into the load-carrying behavior of the concrete specimen. The applied load at the anchor head is transferred by a compressive strut from the confined area over the anchor head to the support ring (see [2][3] for similar results). The respective maximum principal stress in this strut resulted in the development of a circumferential crack. This crack started to open at the anchor head propagating towards the support ring finally causing cone-shaped failure of the specimen. The crack pattern obtained at peak load on the basis of the *modified* model is shown in Figure 7(a) by means of the distribution of the maximum plastic strain in the $r-z$ plane, $\varepsilon^p_{\max}$. In addition to the circumferential crack, radial cracks developed, starting from the corner at the concrete surface and propagating in the interior of the concrete block. Recall, four radial cracks were assumed to open in the context of the employed fictitious crack concept. In Figure 7(b), the location of these radial cracks is shown by means of the respective circumferential plastic strain, ε^p_{circ}.

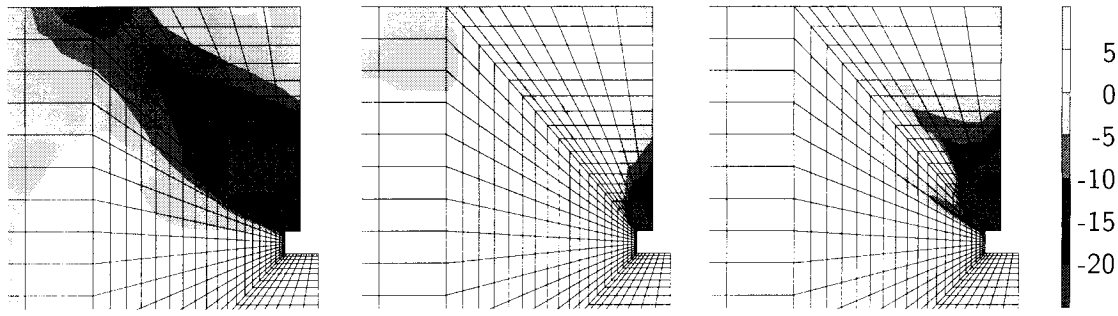

(a) σ_{min} (b) σ_{max} (c) σ_{circ}

Figure 6: Pull-out analysis: distribution of principal stresses in the $r-z$ plane, $\sigma_{\min}$ and $\sigma_{\max}$, and the stress component in the circumferential direction, σ_{circ}, at peak load obtained from multi-surface model with *modified* Drucker-Prager criterion (in [N/mm^2])

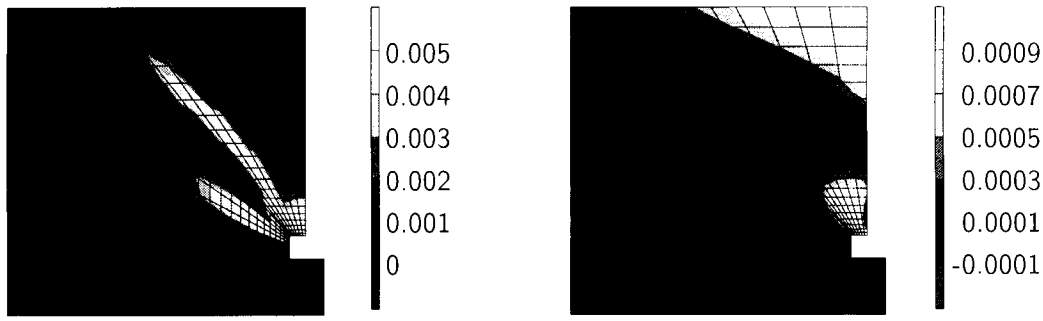

(a) ε^p_{max} (b) ε^p_{circ}

Figure 7: Pull-out analysis: distribution of the maximum plastic strain in the $r-z$ plane, $\varepsilon^p_{\max}$ and of the circumferential plastic strain ε^p_{circ} at peak load obtained from multi-surface model with *modified* Drucker-Prager criterion

CONCLUSIONS

In this paper, structural failure of anchor bolts placed in concrete was investigated. For this purpose a multi-surface plasticity model for plain concrete was used. This model was originally proposed by Meschke [9] (it is referred to as *original* model). The Drucker-Prager model was reformulated in order to account for the influence of confinement. The reformulated model is referred to as *modified* model. From the numerical simulations, the following conclusions concerning the structural response of the concrete specimen can be drawn:

- the concrete located between the anchor head and the support ring is subjected to strong non-uniform triaxal stress states, characterized by
  - hydrostatic pressure over the anchor head,
  - a compressive strut from the anchor head to the support ring, and
  - circumferential cracking caused by tensile loading perpendicular to this strut;
- the underlying model formulation has a crucial influence on the predicted failure mode characterized either
  - by local compressive failure over the anchor head, or

- by a cone-shaped failure surface in consequence of the development of circumferential cracks.

The cone-shaped failure surface, which presumably represents the correct failure mode, was obtained by the *modified* multi-surface model. Disregard of the influence of confinement on the material strength and ductility in the context of the *original* multi-surface model resulted in local compressive failure of concrete over the anchor head. The peak load related to this presumably incorrect failure mode was found to be significantly lower than the peak load obtained from the analyses characterized by cone-shaped failure.

REFERENCES

1. L. Elfgren. Fracture mechanics of concrete structures. Technical report, RILEM, Technical Committee 90, 1990.
2. G. Etse. *T*heoretische und numerische Untersuchung zum diffusen und lokalisierten Versagen in Beton. PhD thesis, Universität Karlsruhe, Karlsruhe, Germany, 1992. In German.
3. G. Etse. Finite element analysis of failure response behavior of anchor bolts in concrete. *Int. Journal of Nuclear Engineering and Design*, 179:245–252, 1998.
4. G. Etse and K. Willam. Fracture energy formulation for inelastic behavior of plain concrete. *Journal of Engineering Mechanics (ASCE)*, 120:1983–2011, 1994.
5. Ch. Hellmich, F.-J. Ulm, and H. A. Mang. Multisurface chemoplasticity I: Material model for shotcrete. *Journal of Engineering Mechanics (ASCE)*, 125(6):692–701, 1999.
6. A. Hillerborg, M. Modeer, and P. E. Petersson. Analysis of crack formation and crack growth in concrete by means of fracture mechanics and finite elements. *Cement and Concrete Research*, 6:773–782, 1976.
7. G. Hofstetter, J. C. Simo, and R. L. Taylor. A modified cap model: closest point solution algorithms. *Computers & Structures*, 46(2):203–214, 1993.
8. B. Hurlbut. Experimental and computational investigation of strain-softening in concrete. Master's thesis, University of Colorado, Boulder, USA, 1985.
9. G. Meschke. Consideration of aging of shotcrete in the context of a 3D viscoplastic material model. *International Journal for Numerical Methods in Engineering*, 39:3123–3143, 1996.
10. G. Meschke, R. Lackner, and H. A. Mang. An anisotropic elastoplastic-damage model for plain concrete. *International Journal for Numerical Methods in Engineering*, 42(4):703–727, 1998.
11. P. Pivonka, R. Lackner, and H. Mang. Numerical analyses of concrete subjected to triaxial compressive loading. In *CD-ROM Proceedings of the European Congress on Computational Methods in Applied Sciences and Engineering*, Barcelona, Spain, 2000.
12. S. Smith. On fundamental aspects of concrete behavior. Master's thesis, University of Colorado, Boulder, USA, 1987.

ORAL REFERENCE: ICF100362OR

NUMERICAL SIMULATION OF CRACK TIP FIELDS AND TOUGHENING MECHANISMS IN TERNARY POLYMER BLENDS

Th. Seelig[1], E. van der Giessen[2] and D. Gross[1]

[1]Institute of Mechanics, TU Darmstadt, D-64289 Darmstadt, Germany
[2]Micromechanics of Materials Group, University of Groningen, 9747 AG Groningen, The Netherlands

ABSTRACT

Crack tip fields in ternary polymer blends of PC/ABS are investigated numerically to address the effect of various microstructural features on the fracture initiation toughness. Under global small-scale yielding conditions, two-dimensional (2D) plane strain finite element analyses are carried out for the crack tip region featuring a process zone in which the blend microstructure is explicitly represented. The constitutive model accounts for large visco-plastic strains, the intrinsic softening-rehardening behavior of glassy polymers as well as plastic dilatation in the ABS phase due to rubber particle cavitation. Attention is focused on the influence of the blend composition and morphology on the competition between crazing and shear yielding in the PC matrix. A set of indicators is used to classify various blends with respect to their tendency to enhance toughness.

KEYWORDS

Polymer blends, toughening mechanisms, crack tip plasticity, craze initiation, rubber cavitation, morphology

INTRODUCTION

Although amorphous thermoplastics, such as polycarbonate (PC), are able to undergo large inelastic deformations under, for example, compression, they show a strong notch sensitivity. The reason is the concentration of hydrostatic stress ahead of crack tips or notches which may initiate brittle failure by ‘crazing’. Blending these materials with small rubber particles is a well-established route to increase their fracture toughness. The key mechanism for toughening is understood to be rubber particle cavitation, which delays crazing due to the relief in hydrostatic stress and promotes plastic flow (‘shear yielding’) in the matrix, hence increases energy absorbtion [1].

The class of ‘ternary’ blends like PC/ABS is much less well understood. In these materials, ABS (acrytonitril-butadiene-styrene) is itself a blend of SAN (styrene-acrytonitril, another thermoplastic) and rubber (butadiene) particles. A toughening effect is again attributed to rubber particle cavitation in the ABS phase and enhancement of shear yielding in the PC matrix [2,3]. However, the situation is complicated by several additional parameters (ABS composition, blend morphology) and additional mechanisms (multiple crazing in ABS, interface debonding). For example, there seems to be no clear consensus yet how the frequently reported ‘syn-

ergistic effect' of a maximum toughness of the blend at an ABS content of around 20 - 30 % depends on the ABS microstructure (e.g. rubber content), and experimental findings sometimes are contradictory [3]. Equally unclear is the influence of the blend morphology (particulate vs oriented ABS layers). The purpose of the present numerical investigation is to gain some basic insight into the role these parameters play in the process of toughening.

Earlier theoretical work has mainly focused either on crack tip fields (e.g. evolution of plastic zone) in homogeneous material [4,5] or on cell studies of blends (with rubber particles treated as voids) under uniform macroscopic load [6,7]. The latter type of modeling clearly revealed the enhanced plastic flow in blends by shear banding between the modifier particles as well as a reduction of hydrostatic stress. Chen and Mai [8] investigated a 3D model of a rubber particle interacting with a crack tip in PC described as a standard von Mises material. The present work is a first step to study the characteristic behavior of (ternary) polymer blends under loading conditions prevailing at crack tips. Since no failure mechanism is accounted for, we are concerned only with the situation prior to crack advance and implications on the fracture initiation toughness. We do so in a 2D plane strain model of a crack tip in PC surrounded by several ABS particles and study the spreading of the plastic zone (e.g. by shear banding between interacting particles), the stress distribution and the dissipated work. These characteristics are discussed in relation to the toughening effect of the blend composition and morphology.

PROBLEM FORMULATION

Since the inelastic processes to be investigated are localized at the tip of a pre-crack or notch small-scale yielding is assumed and only the K-field dominated region is modeled (Fig. 1a). Mode I loading is imposed in terms of the respective displacements as far-field boundary conditions (cf. [4,5]). A closer look at the crack tip (which then appears blunted) reveals the microstructure of the blend as a two-phase material with a PC matrix and ABS particles (Fig. 1a). At this level, i.e. in the so-called 'process zone', both phases are described as homogeneous materials by constitutive equations given in the next section. The even finer ABS microstructure of small rubber particles in a SAN matrix is only considered in a homogenized sense.

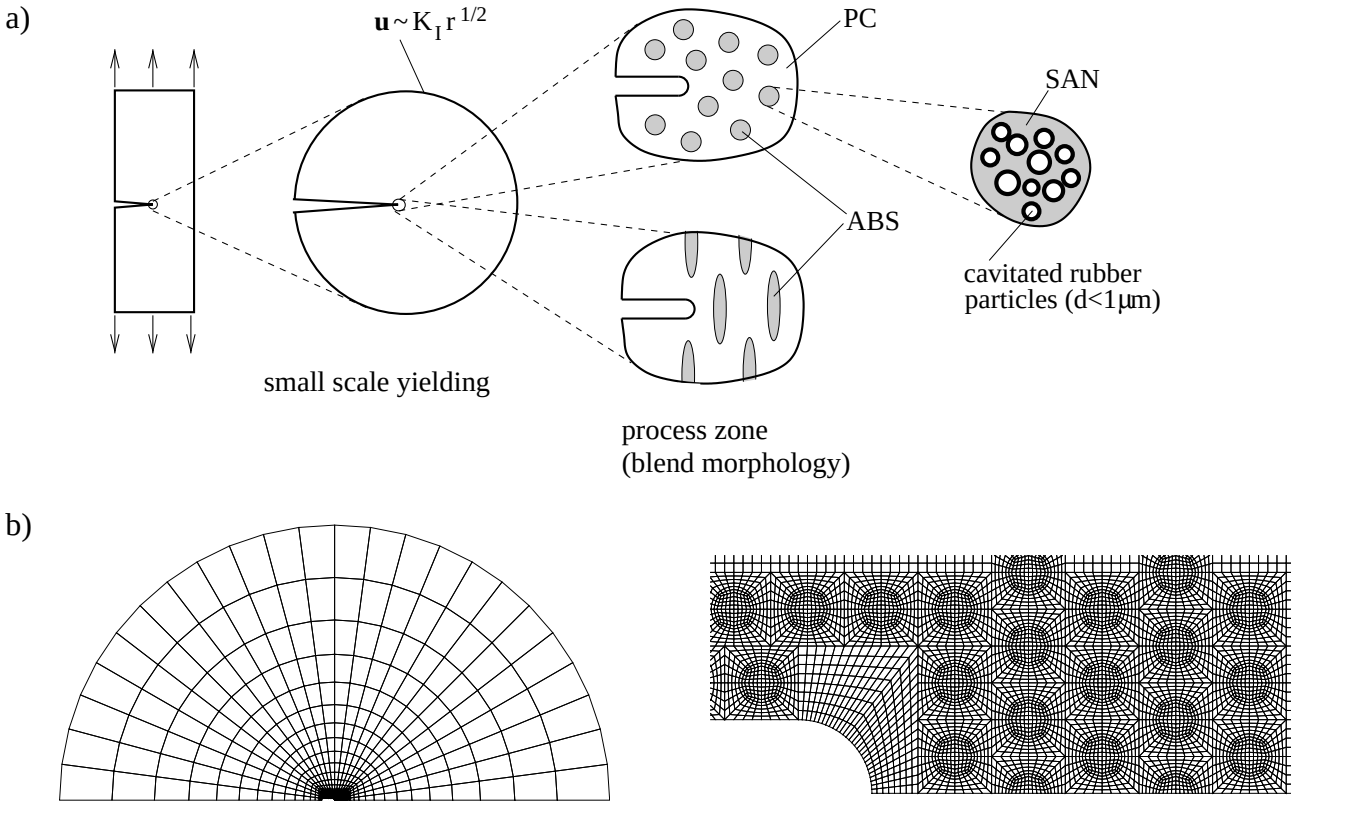

Figure 1: a) Crack tip modeling in ternary polymer blend. b) Finite element discretization of crack tip region and example of process zone (inner mesh).

Quasistatic loading of the crack tip region takes place at a prescribed constant rate $\dot{K}_I$. Details on the incremental solution procedure may be found in [4]. The finite element meshes used in a number of analyses to be presented are depicted in Fig. 1b, where the process region mesh (Fig. 1b, right) shows one of several investigated cases. Exploiting the symmetry of the model, only half of the problem has to be discretized.

CONSTITUTIVE EQUATIONS

The deformation behaviour of glassy polymers like PC or SAN is described by the same elastic visco-plastic constitutive model used in [4]. It employs a standard additive decomposition of the rate of deformation tensor into its elastic and plastic parts: $\boldsymbol{D} = \boldsymbol{D}^{\mathrm{e}} + \boldsymbol{D}^{\mathrm{p}}$. Since the elastic strains remain small they are governed by Hooke's law which in rate form can be written as $\boldsymbol{D}^{\mathrm{e}} = \boldsymbol{\mathcal{L}}^{-1} \overset{\triangledown}{\boldsymbol{\sigma}}$ where $\overset{\triangledown}{\boldsymbol{\sigma}}$ is the Jaumann rate of the Cauchy stress $\boldsymbol{\sigma}$, and $\boldsymbol{\mathcal{L}}$ is the standard fourth order isotropic elasticity tensor.

Matrix behavior
Rate-dependent yielding of the matrix material is specified through the visco-plastic constitutive equations

$$\boldsymbol{D}^{\mathrm{p}} = \frac{\dot{\gamma}^{\mathrm{p}}}{\sqrt{2}\tau}\bar{\boldsymbol{\sigma}}', \quad \dot{\gamma}^{\mathrm{p}} = \sqrt{\boldsymbol{D}^{\mathrm{p}} \cdot \boldsymbol{D}^{\mathrm{p}}}\,, \quad \tau = \sqrt{\frac{\bar{\boldsymbol{\sigma}}' \cdot \bar{\boldsymbol{\sigma}}'}{2}}\,, \quad \dot{\gamma}^{\mathrm{p}} = \dot{\gamma}_0 \exp\left[-\frac{As}{T}\left(1 - \left(\frac{\tau}{s}\right)^{5/6}\right)\right], \tag{1}$$

based on the equivalent plastic shear strain rate $\dot{\gamma}^{\mathrm{p}}$ being determined by the equivalent driving shear stress τ, with $\dot{\gamma}_0$ and A material parameters, and T the absolute temperature. Softening of the material upon yield is accounted for by the yield resistance s evolving with plastic strain, while rehardening due to stretching of the molecular network is described by the back stress tensor $\boldsymbol{b}$ incorporated in the purely deviatoric driving stress tensor $\bar{\boldsymbol{\sigma}}' = \boldsymbol{\sigma}' - \boldsymbol{b}$ (see [4] for details).

Homogenized ABS behavior
Once the rubber particles in the ABS phase have cavitated they are mechanically equivalent to voids because of the low modulus of the rubber. The overall behavior of ABS can then be approximated by that of porous SAN. The elasticity tensor now is expressed in terms of effective (e.g. Mori-Tanaka) elastic constants $\boldsymbol{\mathcal{L}}(f)$ where f is the porosity [9]. To allow for yielding of the porous material under deviatoric and hydrostatic stress states the equivalent driving stress τ in (1) is taken to be related to the deviatoric driving stress $\bar{\boldsymbol{\sigma}}'$ and the mean stress σ_m via the phenomenological macroscopic yield function

$$\Phi \equiv \frac{1}{2}\bar{\boldsymbol{\sigma}}' \cdot \bar{\boldsymbol{\sigma}}' + a f_0^b \sigma_m^2 - [(1-f)\tau c(f_0)]^2 = 0\,. \tag{2}$$

Here, a and b are 'pressure sensitivity' parameters to be fitted from cell calculations for porous SAN and f_0 is the initial porosity (rubber content in ABS). With $1-f$ being the volume fraction of the matrix material, $(1-f)\tau c(f_0)$ can be regarded as the equivalent driving stress of the porous material where the factor $c(f_0)$ accounts for initially localized yielding in the intervoid ligament discussed in [9]. For example, the equivalent driving stress initially, i.e. for $f = f_0$, is $(1-\sqrt{f_0})\tau$, if $c(f_0) = (1+\sqrt{f_0})^{-1}$ is chosen for the 2D case of cylindrical voids. In this case, the factor $1-\sqrt{f_0}$ is approximately the relative width of the ligament between voids where plastic flow is localized at the onset of macroscopic yield.
The function Φ serves to determine the driving stress τ (from $\Phi = 0$) as well as the plastic strain rate via the normality rule $\boldsymbol{D}^{\mathrm{p}} = \Lambda \partial\Phi/\partial\bar{\boldsymbol{\sigma}}$. The multiplier Λ is computed from the condition that the plastic work rate per unit volume in the porous material equals the dissipation in the matrix: $\bar{\boldsymbol{\sigma}} \cdot \boldsymbol{D}^{\mathrm{p}} = (1-f)\sqrt{2}\tau\dot{\gamma}^{\mathrm{p}}$.

CRAZE INITIATION

Crazing in the PC matrix can be regarded as a precursor of brittle failure of the blend material. Beside craze growth and final breakdown, the initiation phase is probably the least well understood part of this process

[10]. Since craze formation starts with microvoiding, the hydrostatic stress certainly plays a crucial role, and attainment of a critical value of σ_m can serve as a simplest initiation criterion [7]. Other criteria, as discussed by Estevez et al. [5], also incorporate shear stress due to the need for some plastic deformation. For example, the criterion of Sternstein (see [5]) can, under plane strain conditions, be cast into the form $F_c \equiv 2\tau - B_0/3\sigma_m + A_0 = 0$ where A_0 and B_0 are material parameters. No reliable data for craze initiation in PC are available yet. So, to compare various blends with regard to their tendency to matrix crazing we simply trace the peak values of σ_m and F_c attained in the PC phase in the course of a loading process. The experimental observation that highly stretched material is less prone to craze [10] is accounted for by recording $\sigma_m^{\max}$ and $F_c^{\max}$ only in material undergone a maximum stretch of less than 2.

RESULTS

All results to be presented have been obtained at a constant loading rate of $\dot{K}_I = 1\text{MPa}\sqrt{\text{m}}\text{sec}^{-1}$. Typical values for the material parameters of PC and SAN are taken from [6]. From cell studies for porous SAN (not reported here for brevity) the pressure sensitivity parameters in the yield function (2) have been determined to be $a = 1.0$ and $b = 0.7$. Based on the case study in [5] the values for the parameters entering the craze initiation criterion are chosen to be $A_0 = 0.7s_0$ and $B_0 = 3s_0^2$ where $s_0 \approx 100$MPa is the initial yield strength of PC. A dimensionless applied stress intensity factor $\bar{K}_{\text{app}}$ is defined by dividing K_I by $s_0\sqrt{r_{\text{tip}}}$ where r_{tip} is the crack tip radius, and $\bar{W}_{\text{diss}}$ denotes the dissipated work normalized by $s_0 r_{\text{tip}}^2/25$.

Effect of Morphology

The effect of the morphology of the ABS phase (in either case 30% ABS with 10% rubber) is illustrated in Fig. 2 showing the spreading of the plastic zone in terms of the equivalent plastic strain rate $\dot{\gamma}^{\text{p}}$. While plastic flow in homogeneous PC is highly localized in form of narrow shear bands intersecting ahead of the blunt crack tip [4], the presence of ABS causes far more distributed yielding. In the case of the blend with spherical ABS particles, one observes shear banding in the PC matrix between these particles. In the microstructure with ABS layers (highly elongated particles) perpendicular to the crack the plastic zone extends ahead of the crack tip and successively spreads along the layers.

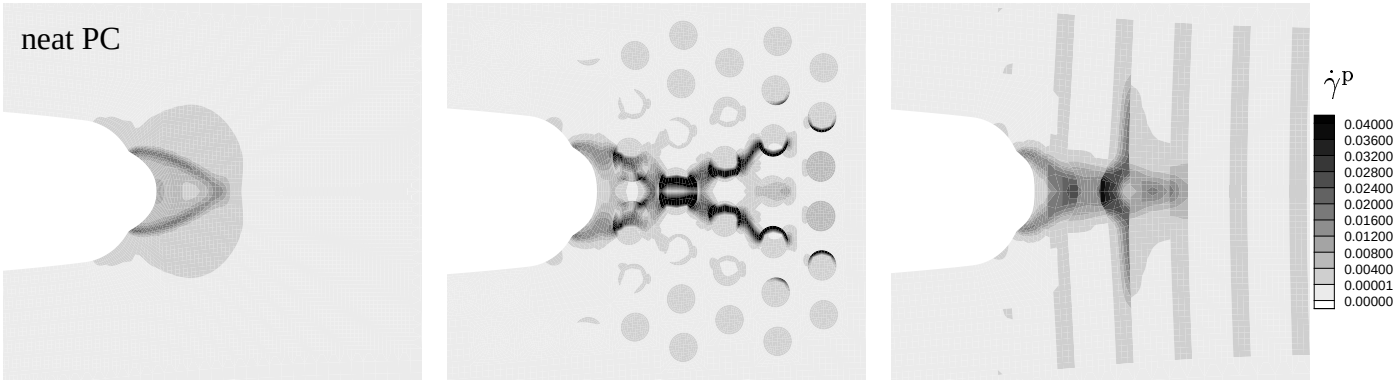

Figure 2: Equivalent plastic strain rate $\dot{\gamma}^{\text{p}}$ [sec^{-1}] at $\bar{K}_{\text{app}} = 2.25$; 30% ABS containing 10% rubber

The distribution of hydrostatic stress shown in Fig. 3 is seen to be less localized in case of the blends, possibly leading to a more distributed matrix failure and hence higher toughness. For both morphologies, σ_m in the ABS phase at locations further away from the crack tip is higher than in the surrounding PC matrix because of the higher elastic stiffness of ABS at low rubber content. The opposite can be seen inside the plastic zone where the capacity of ABS to carry hydrostatic stress has strongly decreased due to volumetric yielding. Hydrostatic stress is then concentrated in the PC matrix. Close to the crack tip volumetric expansion of the ABS material is quite pronounced and accompanied by necking of the PC ligament.

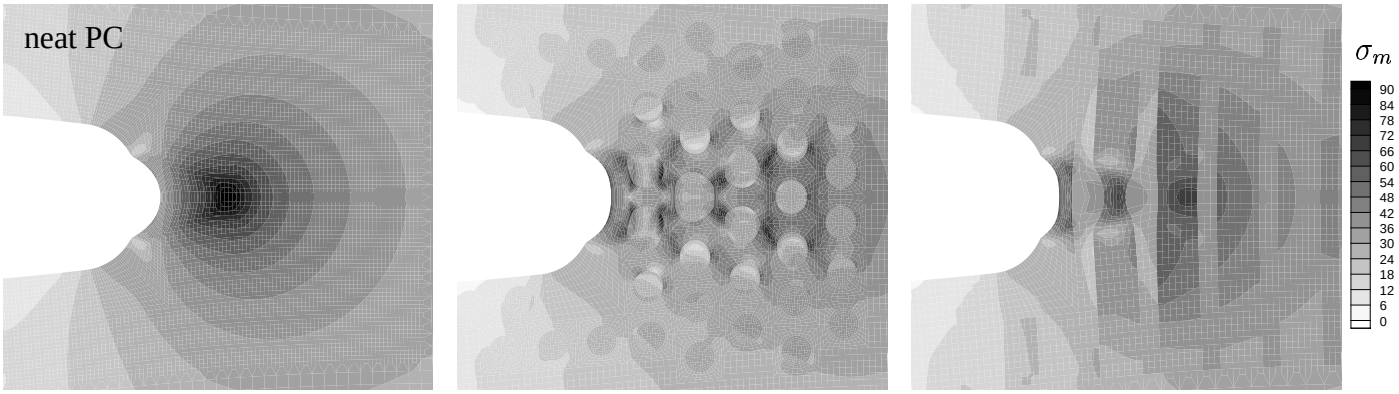

Figure 3: Hydrostatic stress σ_m [MPa] at $\bar{K}_{\text{app}} = 2.25$; 30% ABS containing 10% rubber

The influence of the microstructure is analyzed and compared to the situation in neat PC in terms of the dissipated work $\bar{W}_{\text{diss}}$ and the peak values (attained somewhere in the process zone) of hydrostatic stress $\sigma_m^{\max}$ and of the craze initiation indicator $F_c^{\max}$ as functions of the applied stress intensity factor. To smooth out local effects resulting only from a particular arrangement of the ABS particles around the crack tip, an 'ensemble averaging' over three different arrangements (realizations of statistically the same microstructure) is performed.

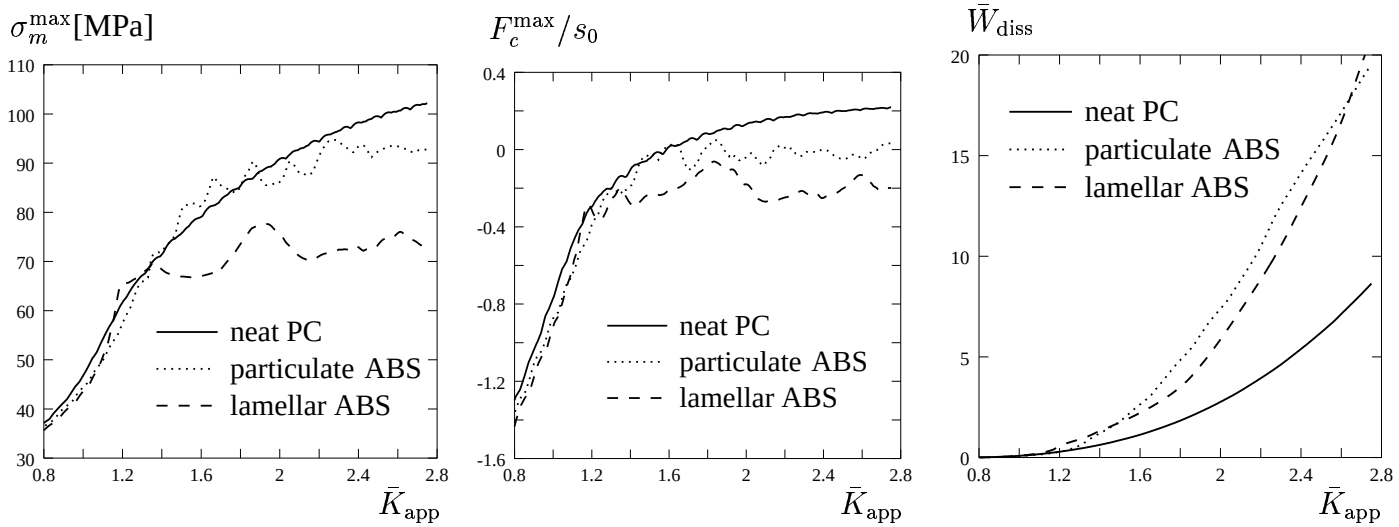

Figure 4: Effect of morphology; 30% ABS containing 10% rubber

From Fig. 4 we see that in both blends the peak values of hydrostatic stress and the craze initiation indicator are lower than in neat PC while the absorbed energy is significantly higher. This suggests that both blends should be expected to be significantly tougher than neat PC. However, which one of the two morphologies is more efficient is less clear; the lamellar microstructure yields lower values for the stress-based criteria whereas the particulate microstructure absorbs slightly more energy. It should be mentioned that the morphologies investigated here may prevail in real materials at different ABS content, with a higher volume fraction leading to a lamellar microstructure, at least for injection moulding [3].

Effect of Rubber Content in ABS

Another important parameter in the fracture behavior of PC/ABS blends is the rubber content in the ABS phase [2,3]. For a blend containing a volume fraction of 30% spherical ABS particles, the effect of the rubber content is shown in Fig. 5. Again, results are compared to those for neat PC. The extreme case of 0% rubber is in fact a blend of PC and SAN which – from the indicators inspected here – seems to yield no toughening effect. The addition of some rubber leads to a much higher energy dissipation and lower values of hydrostatic stress and the craze initiation indicator. Doubling the amount of rubber in ABS results only in a small improvement.

A similar ‘saturation’ effect has been observed when varying the ABS volume fraction in the blend at fixed rubber content.

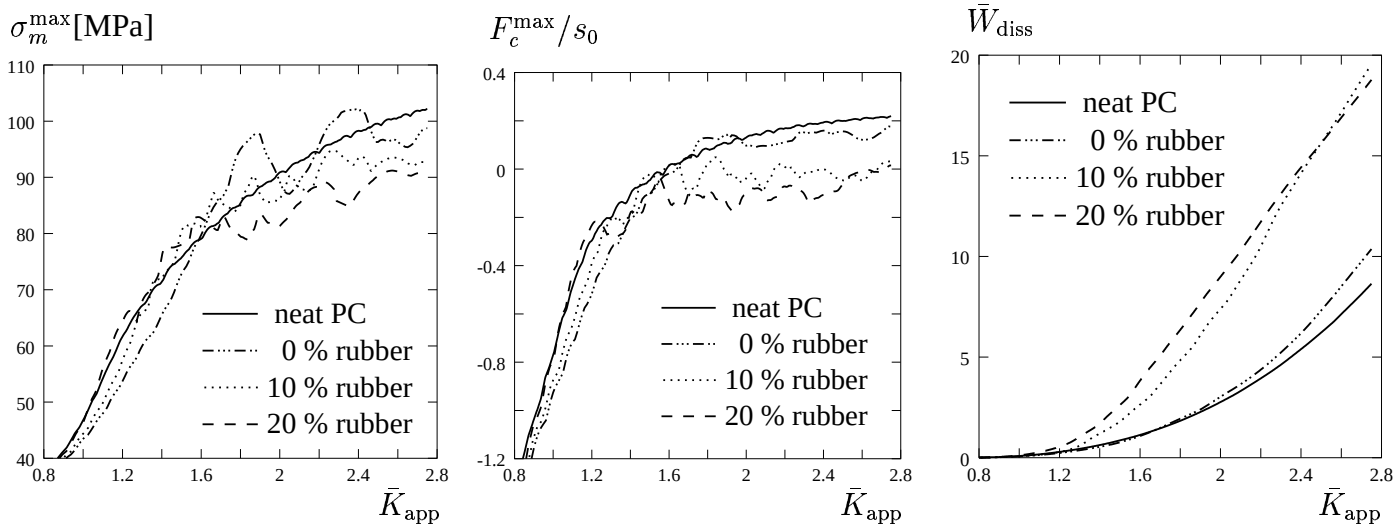

Figure 5: Effect of rubber content in ABS; 30% spherical particles

CONCLUSIONS

Crack tip fields in PC/ABS blends prior to crack growth have been simulated and analyzed with respect to their dependence on characteristic features of the microstructure, such as morphology and composition. Enhanced plastic flow and dissipation as well as the redistribution of stress with reduced peak values in case of blends could be interpreted as contributing to toughening compared to homogeneous PC. However, comparison with experimental observation has to be taken with caution since the occurrence of failure mechanisms, such as crazing, have been ignored here. It is possible that toughening mechanisms fully develop only during crack advance and are active mainly in the wake region of the crack as discussed in [6,11].

REFERENCES

1. Bucknall, C.B. (1997). In: *The Physics of Glassy Polymers*, pp. 363-412, Haward, R.N. and Young, R.J. (Eds.). Chapman & Hall, London.
2. Ishikawa, M. (1995) *Polymer* 36, 2203.
3. Greco, R. (1996). In: *Advanced Routes for Polymer Toughening*, pp. 469-526, Martuscelli, E., Musto, P. and Ragosta, G. (Eds.). Elsevier.
4. Lai, J. and van der Giessen, E. (1997) *Mech. Mater.* 25, 183.
5. Estevez, R., Tijssens, M.G.A. and van der Giessen, E. (2000) *J. Mech. Phys. Solids* 48, 2585.
6. Pijnenburg, K.G.W., Steenbrink, A.C. and van der Giessen, E. (1999) *Polymer* 40, 5761.
7. Socrate, S. and Boyce, M.C. (2000) *J. Mech. Phys. Solids* 48, 233.
8. Chen, X.-H. and Mai, Y.-W. (1999) *J. Mat. Sci.* 34, 2139.
9. Pijnenburg, K.G.W. and van der Giessen, E. (2001) *Int. J. Solids Struct.* 38, 3575-3598.
10. Donald, A.M. (1997). In: *The Physics of Glassy Polymers*, pp. 295-341, Haward, R.N. and Young, R.J. (Eds.). Chapman & Hall, London.
11. Thouless, M.D., Du, J. and Yee, A.F. (2000). In: *Toughening of Plastics*, pp. 71-85, Pearson, R.A., Sue, H.-J. and Yee, A.F. (Eds.). American Chemical Society, Washington DC.

Numerical Simulation of Micro and Nano Scale Fracture

M. Zhou

The George W. Woodruff School of Mechanical Engineering
Georgia Institute of Technology
Atlanta, GA 30332-0405, U.S.A.
(404) 894-3294, (404) 894-0186 (Fax)
min.zhou@me.gatech.edu

ABSTRACT

Damage and fracture in a titanium diboride/alumina (TiB_2/Al_2O_3) ceramic composite system is analyzed numerically. The materials have two-phase microstructures with various phase distributions. The simulations concern the effects of interfacial bonding strength and phase morphologies on damage and fracture development. A micromechanical model that provides explicit account for arbitrary microstructures and arbitrary damage and fracture patterns is developed and used. The approach uses both a constitutive law for the bulk solid constituents and a constitutive law for fracture surfaces. The interfacial relation allows the energy dissipation during fracture processes to be tracked. When assessed as a fraction of the cohesive energy for the undamaged interfaces, this irreversible energy loss can be used as a measure for damage associated with crack and microcrack development. The cohesive finite element model also allows fracture to evolve as an outcome of bulk material response, interfacial behavior and applied loading. Calculations show that the failure mode is significantly influenced by the interfacial bonding strength between the phases. When weak interfacial bonding exists, microcrack initiation and growth are the principal mode of failure. Whereas when strong interfacial bonding is derived from material processing, the extension of a dominant crack is observed.

KEY WORDS

Ceramic composites, fracture, cohesive finite element modeling

INTRODUCTION

An important issue for ceramic materials in applications is their failure resistance, including strength and fracture toughness, Komanduri (1989) [1] and Messer (1995) [2]. The fracture toughness of these materials is at least an order of magnitude lower than those of metals and polymers. Progress has been made in developing advanced ceramic materials using the fact that the materials derive significantly higher toughness from microscopic or nanosized reinforcements. For example, Niihara et al. (1993) [3] reported that a 5% population of SiC nanoparticles increases the tensile strength of Si_3N_4 from 350 MPa to 1 GPa and improves its fracture toughness from 3.25 to 4.7 $\mathrm{MPa}\sqrt{\mathrm{m}}$. Alumina/titanium diboride (Al_2O_3/TiB_2) composites with a wide range of microstructural phase sizes and morphologies have been developed, Logan (1992, 1996) [4-5]. The different microstructures are derived from a range of processing conditions through self-propagating high temperature synthesis or mixing of constituent powders followed by hot pressing. These materials have shown fracture toughness values between 3.5 and 4.9 $\mathrm{MPa}\sqrt{\mathrm{m}}$. These results suggest it is possible to further enhance

properties through microstructural engineering. Potential applications of these materials include cutting tool inserts, electrodes and ceramic armor. Although microstructure-induced, size-dependent toughening mechanisms at the micro and nano levels are demonstrated approaches for property enhancement, the physics for such effects has not been well quantified. In order to develop more advanced materials, it is necessary to characterize the influences of phase morphology, phase length scale, and interfacial bonding on fracture toughness.

Despite the success of continuum damage mechanics and fracture mechanics on the macroscopic level, damage and failure on microscopic levels are far from being well-characterized due to microstructural complexities and size-dependent deformation mechanisms. Most available models for the failure are, for the most part, continuum damage theories in which the net effect of fracture is idealized as a degradation of the elasticity modulus, see e.g. Curran et al. (1993) [6], Rajendran (1994) [7], Johnson and Holmquist (1992) [8], Espinosa et al. (1995) [9]. While capturing the macroscopic or effective response, these models do not explicitly consider the discrete nature of fracture through crack growth and coalescence. Thus, they lack the ability to account for the interaction among cracks. In addition, the effect of microstructural entities such as inclusions, fibers and grains on crack path and fracture toughness can not be explicitly analyzed. The lack of models that provide *explicit* account for arbitrary microstructural morphologies *and* microscopic fracture patterns makes it difficult to identify and design microstructural configurations which enhance fracture toughness. The nonexistence of analytical tools also poses a challenge to explicating size-induced toughening mechanisms which significantly influence the behavior of micro and nanostructured materials.

Explicit micromechanical modeling and simulation represent a unique means for analyzing nano and micro toughening mechanisms and for elucidating scaling laws. Through the consideration of actual microstructures, the effects of various fracture mechanisms can be delineated. A micromechanical cohesive finite element method (CFEM) for *explicit* fracture analysis has been developed recently, Zhai and Zhou (1999) [10]. Based on a cohesive surface formulation of Xu and Needleman (1994) [11], this approach allows explicit modeling and simulation of fracture over a range of length scales, providing a much-needed tool for studying microstructure-induced toughening in heterogeneous materials. The unique advantages of the CFEM include (1) it allows explicit account of real, arbitrary material microstructures, (2) it permits explicit modeling of fracture in a non-constrained manner therefore arbitrary crack paths or microcrack patterns are admitted, and (3) it is capable of resolving fracture explicitly over multiple length scales and is free of the limitations of any *ad hoc* fracture criteria applicable over only a certain range of sizes (e.g. continuum criteria which assume the existence of K-fields). The obviation of fracture criteria assigns a predictive power to models using this approach. Consequently, crack initiation, crack growth, crack path, crack or microcrack patterns, and crack speed evolve as natural outcomes of material response, applied loading, and boundary constraint.

The effects of microstructural morphologies on fracture resistance and the effect of interphase bonding strength on fracture mode have been analyzed by Zhai and Zhou (1998, 1999) [12, 10]. The analysis reported here concerns primarily the characterization of damage and the effect of interfacial bonding strength on damage distribution.

PROBLEM FORMULATION

To account for the finite strains involved in crack tip regions, a finite deformation formulation is used. The independent variables are the position of a material point in the reference configuration $\mathbf{x}$, and time t. Relative to a fixed Cartesian frame $\{\xi^i\}$, a material point initially at x occupies position $\bar{\mathbf{x}}$ in the current configuration. The displacement vector and the deformation gradient are defined as $\mathbf{u} = \bar{\mathbf{x}} - \mathbf{x}$ and $\mathbf{F} = \partial\bar{\mathbf{x}}/\partial\mathbf{x}$, respectively. The principle of virtual work includes a contribution from the cohesive surfaces and is written as

$$\int_V \mathbf{s} : \delta\mathbf{F} dV - \int_{S_{\text{int}}} \mathbf{T} \cdot \delta\boldsymbol{\Delta} dS = \int_{S_{ext}} \mathbf{T} \cdot \delta\mathbf{u} dS - \int_V \rho \frac{\partial^2 \mathbf{u}}{\partial t^2} \cdot \delta\mathbf{u} dV, \tag{1}$$

where $\mathbf{s}:\delta\mathbf{F} = s^{ij}\delta F_{ji}$, s is the nonsymmetric first Piola-Kirchhoff stress; $\boldsymbol{\Delta}$ is the displacement jump across a pair of cohesive surfaces; V, S_{ext} and S_{int} are the volume, external surface area and internal cohesive surface area, respectively, of the body in the reference configuration. The density of the material in the reference configuration is ρ. Also, $\delta\mathbf{F}, \delta\boldsymbol{\Delta}$, and $\delta\mathbf{u}$ denote admissible variations in F, $\boldsymbol{\Delta}$ and u respectively. The traction vector $\mathbf{T}$ and the surface normal in the reference configuration $\mathbf{n}$ are related through $\mathbf{T} = \mathbf{n}\cdot\mathbf{s}$. The volumetric constitutive law is hyperelastic, Xu and Needleman (1994) [11].

The constitutive law for cohesive surfaces relates the traction and displacement jumps across crack surfaces. In this formulation, an equivalent separation $\Delta = \sqrt{\Delta_n^2 + \alpha^2\Delta_t^2}$ and an equivalent traction $\overline{T} = \sqrt{T_n^{\,2} + T_t^{\,2}}$ are defined, where Δ_n and Δ_t denote the normal and tangential components of the relative displacement across a cohesive surface pair, T_n and T_t are normal and shear traction components, and $\alpha = \Delta_{nc}/\Delta_{tc}$ with Δ_{nc} and Δ_{tc} the corresponding critical normal and tangential separations at which cohesive stresses T_n and T_t vanish under pure mode I and mode II conditions, respectively. The cohesive relation is specified between $\overline{T}$ and Δ. A bilinear cohesive law is used, as illustrated in Fig. 1. The normal and tangential traction components are, respectively

$$\left.\begin{aligned} T_n &= \frac{\overline{T}(\Delta)}{\Delta}\Delta_n \\ T_t &= \frac{\overline{T}(\Delta)}{\Delta}\Delta_t \end{aligned}\right\}, \tag{2}$$

where

$$\overline{T}(\Delta) = \begin{cases} T_{max}\dfrac{\Delta}{\eta\Delta_c}, & \text{for } \Delta \le \eta\Delta_c; \\ \overline{T}(\Delta) = T_{max} - \dfrac{\Delta}{\Delta_c}, & \text{for } \Delta \ge \eta\Delta_c. \end{cases} \tag{3}$$

In the above expressions, Δ_c is the critical separation at which cohesive traction $\overline{T}$ vanishes and $0 < \eta < 1$ is a parameter specifying the separation ($\eta\Delta_c$) at which maximum traction T_{max} occurs. Loading and unloading follow the arrows in Fig. 1. During the stage of rising traction (A-B), the separation process is elastic and cohesive energy accumulated is recoverable. During the descending part of the traction-separation relation (B-C), damage is assumed to occur and unloading follows path P-A. The cohesive energy ϕ_0 is the amount of energy required to generate a unit crack surface area. It is a measure of the energy consumption during fracture. The above bilinear relation implies the partition of ϕ_0 into a recoverable part ϕ_r and an irreversible part ϕ_d. The irreversible part ϕ_d is partly converted into surface energy of crack surfaces and partly spent on causing damage in the material adjacent to crack surfaces through microcrack formation not explicitly modeled. Apparently, $\phi_d(\Delta)$ increases with Δ and when full separation is achieved, $\phi_d(\Delta_c) = \phi_0$. Consequently,

$$D = \frac{\phi_d}{\phi_0} \tag{4}$$

can be used a relatively measure for damage. Note that $0 \le D \le 1$, with $D = 0$ indicating fully recoverable interfacial separation and $D = 1$ signifying complete separation or total fracture. In the following analysis, D will be used as an internal state variable quantifying the degree of the damage, providing a phenomenological measure for failure analysis. The spatial and time variation of $D = D(\mathbf{x}, t)$ allows the distribution and evolution of damage in various microstructures to be analyzed.

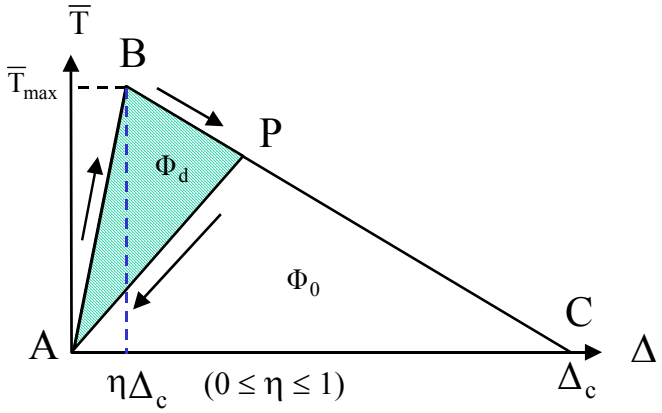

Fig. 1 Cohesive Separation Law

Computations are carried out for a center-cracked specimen. The specimen has an initial height of $2H = 1.6\,\text{mm}$ and an initial width of $2L = 1.6\,\text{mm}$. An initial crack of length $2a_i = 0.4\,\text{mm}$ exists along the ξ^1 axis. Only one half of the specimen $(\xi^1 > 0)$ is discretized and modeled in the simulations because of the symmetry with respect to the ξ^2 axis. Conditions of plain strain are assumed to prevail. The small region in front of the crack tip contains microstructures digitized from micrographs of actual composite materials. Inside this region, the material inhomogeneities and material phase distribution are explicitly modeled. In the microstructure analyzed here, TiB_2 particles are embedded in the alumna matrix. The average particle size is approximately 10-20 μm. The bulk properties of each finite element are those for either the particles or those for the matrix. The properties of each segment of potential fracture surface are specified according to its location as those belonging to the matrix, the reinforcements or the matrix/reinforcement interfaces. The choice of the cohesive law parameters assumes that $\sigma_{max} = E/200$ for each constituent with E being the Young's modulus and $\phi_0 = (1-\nu^2)K_{IC}^2/E$ with K_{IC} being the mode-I fracture toughness of the materials in question.

Two different sets of parameters for the Al_2O_3/TiB_2 interfaces are chosen. The first set of cohesive parameters characterizes the ideally bonded interfaces between the two phases (strong interface). This set of parameters assumes the interfaces have the same bonding strength and cohesive energy as the Al_2O_3 matrix ($\overline{T}_{max}^{interface} = \overline{T}_{max}^{matrix}, \phi_0^{interface} = \phi_0^{matrix}$). The second set of parameters represents significantly weakened interfaces along the phase boundaries. Specifically, the maximum traction $\overline{T}_{max}$ and ϕ_0 are 1/10 of those of the alumina matrix ($\overline{T}_{max}^{interface} = 0.1\overline{T}_{max}^{matrix}$, $\phi_0^{interface} = 0.1\phi_0^{matrix}$). Materials outside the crack-tip region are assumed to be homogeneous and are assigned a set of effective parameters representative of those for the Al_2O_3/TiB_2 ceramic composite. Both regions are discretized in the same manner, using both the bulk and the cohesive surface constitutive descriptions. The specimen is stress free and at rest initially. Tensile loading is applied by imposing symmetric velocity boundary conditions along the upper and lower edges of the specimen. For the results discussed here, the imposed boundary velocity is V_0=2 m/s for each edge with a linear ramp from zero to this maximum velocity in the first 0.01 μs of loading. All other specimen surfaces have traction-free boundary conditions.

The cohesive finite element method (CFEM) allows explicit resolution of fracture events as well as permitting the account of arbitrary microstructures. Through the use of the damage parameter D defined in (3), the spatial distribution and time evolution of damage and failure in different microstructures can be compared. This approach not only demonstrates the final outcome of fracture or the fully formed fracture surfaces but also reveals the partially formed fracture patterns or attempted fracture paths.

RESULTS

Two microstructures are considered here. One has the strong bonding and the other has the weak bonding between the phases. Both microstructures have the same TiB_2/Al_2O_3 phase morphologies. Figure 2 shows the distributions of the damage parameter D in these two microstructures. The microstructure in Fig. 2(a) has the strong bonding and the microstructure in Fig. 2(b) has the weak bonding. The plots are for t = 0.13 μs after the beginning of loading. The phase boundaries are outlined by solid lines for visualization of the phase morphologies. The pre-crack is on the left and crack propagation is toward the right. The result in Fig. 2(a) shows the propagation of a main crack from the tip of the pre-crack. The crack primarily goes though the matrix and the phase boundaries, although fracture of TiB_2 is also seen. In contrast, the mode of failure in Fig. 2(b) is the simultaneous formation of microcracks throughout the microstructure. There is not a primary crack path. Due to weakening by the distributed microcracks, the stress levels in the microstructure are lower compared with those in Fig. 2(a). In Fig. 2(a), damage is concentrated along crack surfaces. In addition, lower levels of damage are also seen in regions away from the fully formed crack paths. Severe damage occurs at the tip of the main crack tip. In Fig. 2(b), damage is distributed. The contours clearly indicate that separation occurs primarily along the interphase interfaces. This process can occur independently of the main pre-crack. Coalesced microcracks eventually link up with the pre-crack, resulting in the failure of the material.

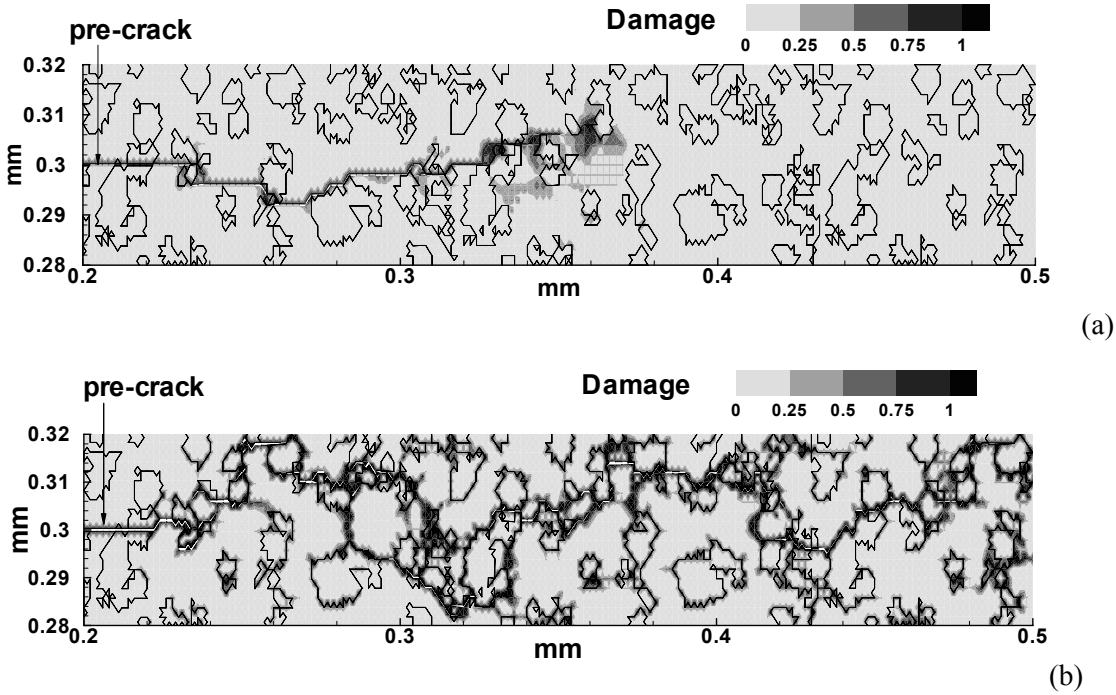

Fig. 2 A comparison of damage distributions for microstructures with (a) strong interphase bonding and (b) weak interphase bonding

CONCLUSIONS

A micromechanical framework of analysis has been developed and used to provide explicit incorporation of arbitrary material microstructures into numerical modeling and to resolve arbitrary, unconstrained fracture patterns in heterogeneous, brittle solids. The approach combines descriptions of bulk constituent response and fracture surface cohesion. This approach is especially appropriate for analyzing microscopic damage and failure over a range of length scales because material separation is a natural outcome of constitutive behavior, microstructure and loading in this model. The formulation is free from failure criteria valid over only certain length scales, for example, continuum mechanics criteria based on the existence of K-fields.

The interfacial relation allows the energy dissipation during fracture processes to be tracked. When assessed as a fraction of the cohesive energy for the undamaged interfaces, the irreversible energy loss can be used as a measure for damage associated with crack and microcrack development. The damage evolution in an Al_2O_3/TiB_2 composite system is analyzed under the context of a centered-cracked specimen and the

conditions of plane strain. The results demonstrated the effects of interphase bonding on damage and failure development. Calculations show that the failure mode is significantly influenced by the interfacial bonding strength between the phases. When weak interfacial strength exists, microcrack initiation and growth are the principal mode of failure. Whereas when strong interfacial strength is derived from material processing, the advancement of a dominant crack and crack branching are observed. Under the conditions of this analysis, the simultaneous formation of microcrack and their coalescence allow more energy to be dissipated in a material with weak interphase bonding than in a material with strong interphase bonding.

ACKNOWLEDGEMENT

Support from the U.S. Army Research Office through grant DAAG55-98-1-0454 and through NSF CAREER award CMS9984298 is gratefully acknowledged. Calculations are carried out on the Cray Computers at the San Diego Supercomputer Center, Jet Propulsion Laboratory and the Naval Oceanographic Office. We would like to thank Drs. K. V. Logan and N. Thadhani for helpful discussions on ceramic materials.

REFERENCES

Komanduri, R., (1989), Advanced ceramic tool materials for machining, *Int. J. Refract. Hard. Met.*, 8, pp. 125-132.

Messer, P.F., (1991), The Strength of Dental Ceramics, *J. Dent.*, 18, pp.227-235.

Niihara, K., Nakahira, A., and Sekino, T., (1993), New Nanocomposite Structural Ceramics, *Mat. Res. Soc. Sym. Proc.*, 286, pp.405-412.

Logan, K.V., (1992), Shapes Refractory Products and Method of Making the Same, U.S. Patent # 5141900.

Logan, K.V., (1996), Composite ceramics, final technical report, USSTACOM DAAEO7-95-C-R040.

Curran, D.R., Seaman, L., Cooper, T. and Shockey, D.A., (1993), Micromechanical Model for Continuum and Granular Flow of Brittle Materials under High Strain Rate Application to Penetration of Ceramic Targets, *Int. J. Impact Eng.*, 13, pp.53-58.

Rajendran, A.M., (1994), Modeling the Impact Behavior of AD85, Ceramic under Multiaxial Loading, *Int. J. Impact Eng.*, 15, 749-768.

Johnson, G.R. and Holmquist, T.J., (1992), A Computational Constitutive Model for Brittle Materials Subjected to Large Strains, High Rates, and High Pressure, Meyers, M.A., Murr, L.E., and Staudhammer, K.P., editors, Shcock Wave and High Strain Rate Phenomena in Materials, pp.1075-1081.

Espinosa, H. D., Brar, N. S., (1995), Dynamic Failure Mechanisms of Ceramic Bars: Experiments and Numerical Simulations, *J. Mech. Phys. Solids*, 43, pp. 1615-1638.

Zhai, J. and Zhou, M., (1999) Finite Element Analysis of Micromechanical Failure Modes in Heterogeneous Brittle Solids, to appear in *International Journal of Fracture*, special issue on *Failure Mode Transition in Solids*;

Xu, X. -P. and Needleman, A., (1994), Numerical simulations of fast crack growth in brittle solids, *J. Mech. Phys. Solids*, 42, pp.1397-1434.

Zhai, J. and Zhou, M., (1998) Micromechanical Modeling of Dynamic Crack Growth in Ceramic Composites, *Mixed Mode Crack Behavior*, ASTM STP 1359, K. Miller and D. L. McDowell, eds., 1998;

ORAL/POSTER REFERENCE: ICF100561OR

NUMERICAL SIMULATIONS OF DYNAMIC INTERFACIAL FRACTURE PHENOMENA

T. Nishioka [1], Q. Hu [1] and T. Fujimoto [1]

[1] Department of Ocean Mechanical Engineering,
Kobe University of Mercantile Marine,
5-1-1 Fukae Minamimachi, Higashinada-ku, Kobe 658-0022, JAPAN

ABSTRACT

In this paper, first, to extract mixed-mode stress intensity factors for interfacial cracks subject to impact loading as well as for dynamically propagating interfacial cracks, the component separation method of the dynamic J integral is developed. This method is more advantageous than the M integral method often used for interfacial crack problems, since the present method requires no auxiliary solution field that is sometimes not possible to construct in the M integral method. Next, dynamic interfacial crack propagation is simulated by using a moving finite element method. The dynamic J integral, and the separated dynamic J integrals which have the physical significance of the energy flow rate from individual material side, and the stress intensity factors are evaluated.

KEYWORDS

Bimaterial, Interface Crack, Dynamic Crack Propagation, Dynamic J Integral, Separated Dynamic J Integrals, Moving Finite Element Method, Component Separation Method, Mixed-Mode Stress Intensity Factors

INTRODUCTION

In recent years, dynamic fracture mechanics for nonhomogeneous materials has been a focus of much attention because of the broad applications of composite materials and jointed materials to important structures. For dynamic fracture mechanics, Nishioka and Atluri [1] derived the path-independent dynamic J integral, which has the physical significance of energy release rate. Furthermore, for dynamic interfacial fracture mechanics, Nishioka and Yasin [2] have recently developed the separated dynamic J integrals, which are equivalent with the separated energy release rates from individual material sides.

Also, some fundamental features of dynamic interfacial cracks have been discussed by Yang et al. [3] and more recently by Shen and Nishioka [4]. These two aspects set up the important basis of current component separation method. In early works on extracting mixed-mode stress intensity factors for interfacial cracks, Yau and Wang's M integral method [5] is commonly used. However, it is sometimes difficult to set up the auxiliary solution field that is necessary in the application of their method. For some complicate conditions such as crack kinking and branching, it is hard to get the auxiliary solution. Recently, the component separation method [6] has been extended to static interfacial crack problems [7]. This method has great

advantages over the M integral method, since no auxiliary solution field is needed.

In this paper, first, for dynamic interfacial fracture mechanics, the component separation method of the dynamic J integral is developed based on the theoretical studies of the interfacial crack tip field [3][4]. By choosing appropriate characteristic length and applying J-K relationship, explicit formulas for extracting the stress intensity factors from the dynamic J integral are derived. Next, numerical solutions of stress intensity factors are presented for dynamically propagating interfacial cracks. To cope with the propagating crack, a moving finite element method is used to comply with the dynamically moving property of crack tip.

DYNAMIC J INTEGRAL AND SEPARATED DYNAMIC J INTEGRALS

The well-known Eshelby-Rice static J integral has been widely used in static fracture mechanics. For dynamic fracture mechanics, Nishioka and Atluri [1] derived the path-independent dynamic J integral for a homogenous material as

$$J'_k = \lim_{\Gamma_\varepsilon \to 0} \int_{\Gamma_\varepsilon} [(W+K)n_k - t_i u_{i,k}]dS = \lim_{\Gamma_\varepsilon \to 0} \left\{ \int_{\Gamma+\Gamma_c} [(W+K)n_k - t_i u_{i,k}]dS + \int_{V_\Gamma - V_\varepsilon} [\rho \ddot{u}_i u_{i,k} - \rho \dot{u}_i \dot{u}_{i,k}]dV \right\}, \quad (1)$$

where W and K are the strain and kinetic energy densities. Γ_ε denotes the near field integral path, while Γ and Γ_c are the far field path and the crack face integral path, respectively (see Fig. 1(a)). The crack axis components of the dynamic J-integral J'^0_k can be obtained by the coordinate transformation: $J'^0_k = \alpha_{kl} J'_l$, where α_{kl} is the coordinate transformation tensor. The tangential component of the dynamic J integral J'^0_1 has the physical significance of the dynamic energy release rate G. Thus we have

$$J'^0_1 = J' = G. \quad (2)$$

Considering a nonhomogeneous plate with a dynamically propagating interfacial crack as shown in Fig. 1(b), recently Nishioka and Yasin [2] have derived the separated dynamic J integrals as

$$J'^{(m)}_k = \lim_{\Gamma^{(m)}_\varepsilon \to 0} \int_{\Gamma_\varepsilon} [(W+K)n_k - t_i u_{i,k}]dS = \lim_{\Gamma^{(m)}_\varepsilon \to 0} \left\{ \int_{\Gamma^{(m)}+\Gamma^{(m)}_c+\Gamma^{(m)}_I} [(W+K)n_k - t_i u_{i,k}]dS + \int_{v^{(m)}_\Gamma - v^{(m)}_\varepsilon} [\rho \ddot{u}_i u_{i,k} - \rho \dot{u}_i \dot{u}_{i,k}]dV \right\} \quad (m=1,2), \quad (3)$$

where $\Gamma_I^{(m)}$ (m=1,2) are the integral paths along the interface in the sides of the material 1 and 2. Also the crack axis components can be obtained by applying the coordinate transformation: $J'^{0(m)}_k = \alpha_{kl} J'^{(m)}_l$.

The separated dynamic J integrals also have the physical significance of the separated energy release rates $G^{(m)}$ (m=1,2) which are the energy flow rates from material m (m=1,2) into the propagating interfacial crack tip per unit crack extension. Thus, we have the following relations:

$$J'^{0(m)}_1 = G^{(m)} = J'^{(m)}_1 \cos\theta_0 + J'^{(m)}_2 \sin\theta_0, \qquad (m=1,2). \quad (4)$$

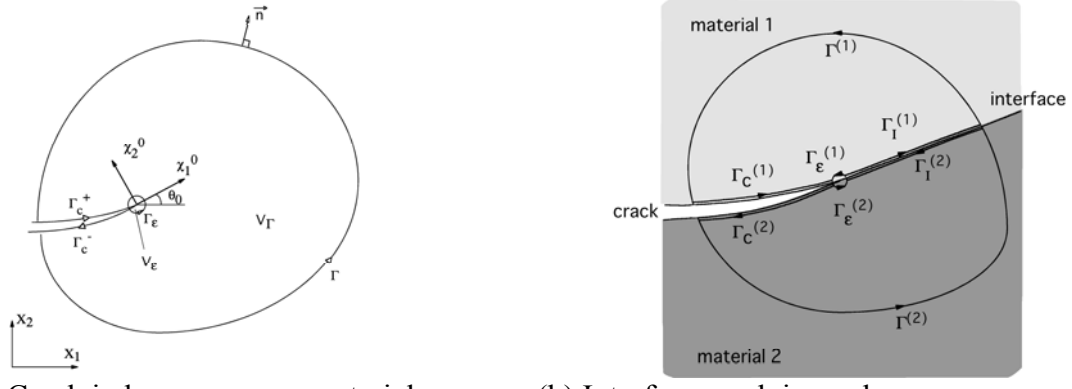

(a) Crack in homogeneous material (b) Interface crack in nonhomogeneous material

Figure 1: Definition of integral paths

Furthermore, the dynamic J integral and the energy release rate can be obtained by the sum of the separated dynamic J integrals:

$$J'^{0}_{1} = J'^{0(1)}_{1} + J'^{0(2)}_{1} = G = G^{(1)} + G^{(2)}. \tag{5}$$

COMPONENT SEPARATION METHOD OF DYNAMIC J INTEGRAL

Recently the component separation method [6] was extended to static interfacial fracture mechanics [7]. Furthermore, in this paper, using the dynamic J integral and the separated dynamic J integrals, the component separation method is extended to evaluate dynamic stress intensity factors.

The dynamic J integral and the dynamic energy release rate can be related to the stress intensity factors [3][4] as follows:

$$J'^{0}_{1} = J'^{0(1)}_{1} + J'^{0(2)}_{1} = G = \Lambda\,(K_1^2+K_2^2)=\Lambda\left(1+\alpha^2\right)K_1^2, \tag{6}$$

and

$$\Lambda = \overline{\mathbf{w}}^{T}(\mathbf{H}+\overline{\mathbf{H}})\,\mathbf{w}\,(K_1^2+K_2^2)/(4\cosh^2\pi\varepsilon). \tag{7}$$

The eigenvector **w** is determined by the traction resolution factor η as

$$\mathbf{w}^{T}=\frac{1}{2}\{\,-i\eta \;\; 1 \;\; 0\,\},\ \text{and}\ \eta=\left(H_{22}/H_{11}\right)^{1/2}. \tag{8.a,b}$$

where H_{ij} (i,j=1,2) are the components of the in-plane matrix **H**. The matrix **H** consists of three independent real components ($H_{12}=H_{21}$)

$$\mathbf{H}=\begin{bmatrix} H_{11} & iH_{12} \\ -iH_{12} & H_{22} \end{bmatrix}, \tag{9}$$

and this matrix can be determined by the Stroh's matrix **B** as follows:

$$\mathbf{H} = \mathbf{B}^{(1)}+\mathbf{B}^{(2)}\ ,\ \text{and}\ \ \mathbf{B} = \frac{1}{\mu D}\begin{bmatrix} \beta_2\left(1-\beta_2^2\right) & i\left(1+\beta_2^2-2\beta_1\beta_2\right) \\ -i\left(1+\beta_2^2-2\beta_1\beta_2\right) & \beta_1\left(1-\beta_2^2\right) \end{bmatrix}. \tag{10.a,b}$$

The wave reduction factors β_i (i=1,2) and the Rayleigh wave function D have the form

$$\beta_1 = \sqrt{1 - \rho C^2/C_{11}}\,,\ \ \beta_2 = \sqrt{1 - \rho C^2/C_{66}}\,,\ \ D = 4\beta_1\beta_2 - \left(1+\beta_2^2\right)^2, \tag{11.a,b,c}$$

where C is the crack velocity while C_{11} and C_{66} are the elastic constants. The oscillation index ε is determined by the Dunders parameter β

$$\varepsilon = (1/2\pi)\left[\ln\left\{(1-\beta)/(1+\beta)\right\}\right],\ \text{and}\ \ \beta=-H_{12}(H_{11}H_{22})^{1/2}. \tag{12.a,b}$$

The crack opening displacements in the x and y directions behind the crack tip, δ_x and δ_y, are obtained in [3] [4] as

$$\sqrt{\frac{H_{11}}{H_{22}}}\,\delta_y+i\delta_x = \frac{2H_{11}(K_1+iK_2)}{(1+2i\varepsilon)\cosh(\pi\varepsilon)}\sqrt{\frac{r}{2\pi}}\left(\frac{r}{l}\right)^{i\varepsilon}, \tag{13}$$

where *l* is a characteristic length used to define the stress intensity factors. Usually *l* = 2a (2a is the entire crack length) is used.

From Eqn. 13, the ratio of the stress intensity factors can be related to the ratio of crack opening displacements, as follows:

$$\alpha = K_2 / K_1 = \lim_{r \to 0} (\eta - S\delta_y/\delta_x)/(\delta_y/\delta_x + \eta S),\ S = (\tan Q - 2\varepsilon)/(1 + 2\varepsilon \tan Q), \text{ and } Q = \varepsilon \ln(r/l). \quad (14.a,b,c)$$

Taking limit is required to calculate the stress intensity factors. However, it is hard to get accurate results by using numerical results due to the quantity S that has the logarithmic and oscillatory singular terms. For this reason, and to derive explicit formulas for the component separation method, we eliminate the logarithmic and oscillatory singular terms S (S=0), taking tanQ=2ε. This can be achieve, choosing the following special character length:

$$l = \bar{r}/e^{\varepsilon^{-1}\tan^{-1}(2\varepsilon)}, \quad (15)$$

where $\bar{r}$ is the location of the nodal point at which the crack opening displacemets are evaluated. Then the ratio of the stress intensity factors can accurately be evaluated by

$$\alpha = \eta\delta_x/\delta_y. \quad (16)$$

Using Eqn. 16 in Eqn. 6, the explicit formulas for the component separation method can be derived as

$$K_k = \delta_k\sqrt{J_1^0 / \left\{\Lambda\left(\delta_1^2+\delta_2^2\right)\right\}} = \delta_k\sqrt{\left(J_1'^{0(1)}+J_1'^{0(2)}\right) / \left\{\Lambda\left(\delta_1^2+\delta_2^2\right)\right\}} = \delta_k\sqrt{G / \left\{\Lambda\left(\delta_1^2+\delta_2^2\right)\right\}},\ (k=1, 2) \quad (17)$$

where $\delta_1=\delta_y$ and $\delta_2=\eta\delta_x$ are defined as shown in Fig. 2.

The transformation to the stress intensity factors with the characteristic length $l'=2a$ or to those with a desired characteristic length l' can simply be conducted by the following equation:

$$\begin{Bmatrix} K'_1 \\ K'_2 \end{Bmatrix} = \begin{bmatrix} \cos\theta & -\sin\theta \\ \sin\theta & \cos\theta \end{bmatrix} \begin{Bmatrix} K_1 \\ K_2 \end{Bmatrix},\ \theta = \varepsilon \ln(l'/l). \quad (18.a,b)$$

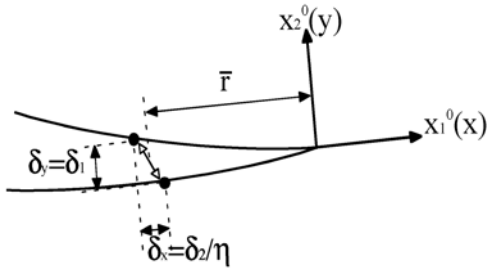

Figure 2: Crack open displacements

NUMERICAL SIMULATION RESULTS

Numerical simulations are carried out for dynamically propagating cracks. Figure 3 shows the computational model. The dimensions of the plate are W=2L=40mm. The initial mesh pattern for the moving finite element method and the dynamic J integral paths are also shown in Fig. 3. We assume that the upper material (material 1) is more compliant than the material 2. The mismatch ratio of Young's moduli is assumed as $\lambda=E^{(2)}/E^{(1)}=3.0$ with $E^{(1)}=29.4$GPa in this paper. The superscripts denote the material number. The mass densities and the Poisson's ratios of two materials are assumed as the same as $\rho^{(2)}=\rho^{(1)}=2.45\times10^3$kg/m^3, $\nu^{(2)}=\nu^{(1)}=0.286$.

The moving finite element method [2] is used for calculating the separated dynamic J integral. Along with the crack propagating, the mesh pattern for the elements around the crack tip translates in each time step in

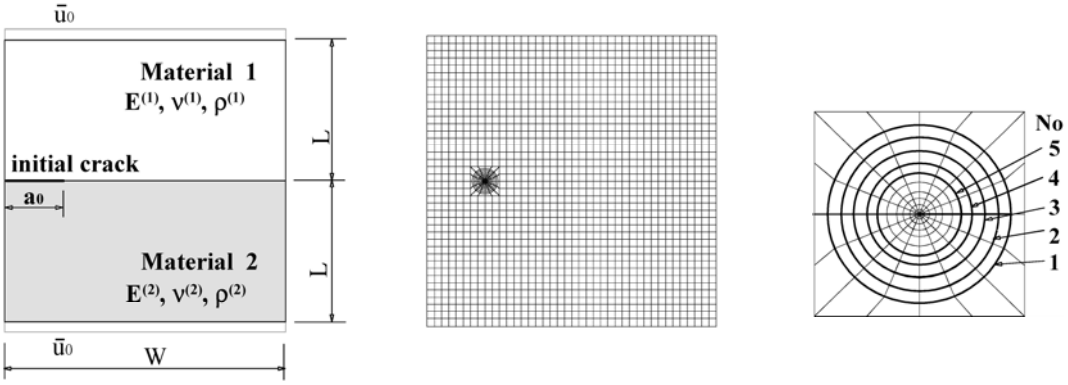

(a) Specimen geometry (b) Initial mesh pattern (c) Integral paths

Figure 3: Bimaterial plate with an interfacial edge crack

order to assure enough precision. The moving element method completely satisfies the boundary conditions near the propagating crack tip, while a fixed element method usually violates them. We assume that the crack always propagates along the interface and keeps a constant velocity C. The initial crack length is set as a_0=0.2W.

First, the dynamic finite element analysis of a propagating crack in the homogeneous plate (λ=1.0) subject to constrained displacements is carried out. The velocity is assumed as 40% of the shear wave velocity, C=0.4Cs. Using a fictitious interface along the symmetrical line, the separated dynamic J integrals and the dynamic J integral are evaluated. Both types of integrals show excellent path independence through out the simulation. Then, the dynamic J integral values are converted to the stress intensity factors using the component separation method (see Eqn. 17 with ε=0).

Figure 4 shows the variations of stress intensity factors. The K_1 values are normalized by the static stress intensity factor for a semi-infinite crack in an infinite-width strip [8]: $K_s = \bar{u}_0 E^{(1)}/\sqrt{L}\{1-(\nu^{(1)})^2\}$. The present results agree with the results obtained by moving singular element method [9,10] after certain amount of dynamic crack propagating, and agree with the Nilsson's steady-state solution [8]. Thus, this confirms the validity of the component separation method of the dynamic J integral when the problem reduces to the homogeneous condition (ε=0).

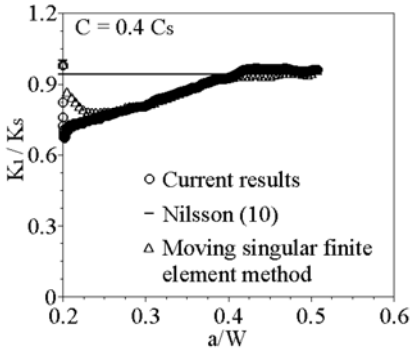

Figure 4: Normalized dynamic stress intensity factors in homogeneous plate

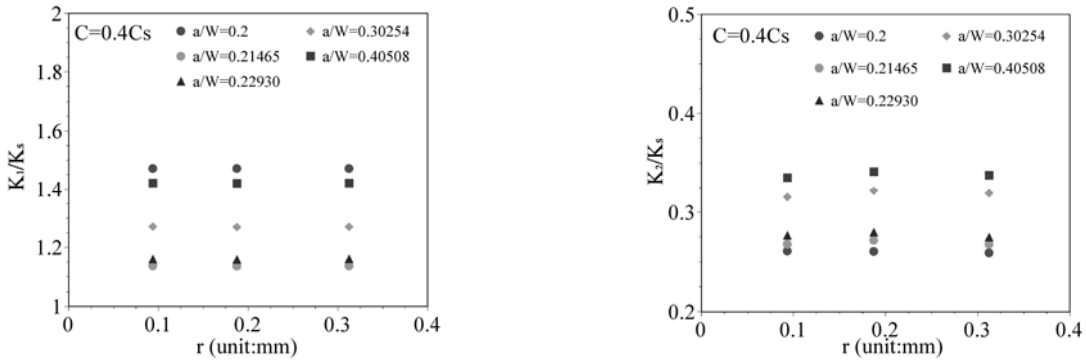

(a) Normalized K_1 (b) Normalized K_2

Figure 5: Stress intensity factors calculated for different crack face node pairs

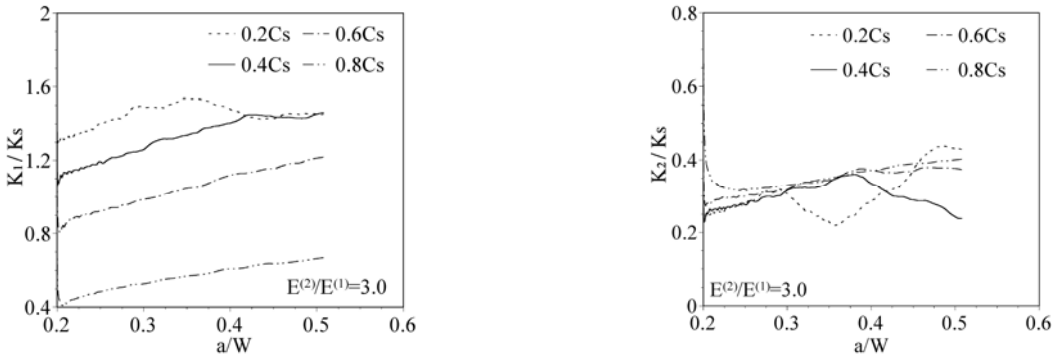

(a) Variation of normalized K_1 (b) Variation of normalized K_2

Figure 6: Stress intensity factors for dynamically propagating interfacial cracks

Next, in order to check the accuracy of the component separation method, the crack opening displacements at three pairs of the corner-nodes nearest to the propagating crack tip are tested. Figure 5 shows the variations of the stress intensity factors for different node pairs. In all cases, the stress intensity factors for three node pairs are almost constant. This indicates that the component separation method gives very accurate stress intensity factors. Also, the crack opening displacements at the nearest corner node pair give accurate results.

The stress intensity factors for the dynamically propagating interfacial cracks are shown in Fig. 6. We can see that K_2 has a nonzero value in all cases due to the existence of material mismatch. It is interesting to see that, in the early stage of dynamic crack propagation, for increasing crack velocity, the normalized K_1 decreases while the normalized K_2 increases.

CONCLUSIONS

In this paper, first, in order to evaluate accurate mixed-mode stress intensity factors for dynamic interfacial cracks, explicit formulas for the component separation method of the dynamic J integral were derived. This method has more advantages than the M integral method that commonly used for interfacial fracture mechanics problems. The features of the component separation method can be summarized as follows: (1) It can be expressed by the explicit formulas. (2) It does not require any auxiliary solution field. (3) It is applicable using the path independent separated dynamic J integrals. (4) The signs of the stress intensity factors are automatically determined by the signs of the corresponding crack opening displacements. (5) Since its formulas do not include the oscillatory and logarithmic singular terms, the numerical results for the stress intensity factors are stable and accurate. In addition, the moving finite element method and the path-independent separated dynamic J integrals as well as the component separation method demonstrated their great potentials in dynamic interfacial fracture mechanics studies.

Acknowledgments: This study was supported by the Natural Science Grant from Mitsubishi Foundation, and by the Grant-in-Aid for Scientific Research from the Ministry of Education, Science and Culture in Japan.

References

1. Nishioka, T. and Atluri, S.N. (1983) *Eng. Fract. Mech.*, 18, 1.
2. Nishioka, T. and Yasin, A. (1999) *JSME International Journal*, 42(1)A, 25.
3. Yang, W., Suo Z. and Shih, C.F. (1991) *Proc. R. Soc. Lon.*, A433, 679.
4. Shen, S. and Nishioka, T. (2000) *J. Mech. Phys. Solids*, 48(11), 2257.
5. Yau, J. F. and Wang, S.S. (1984) *Eng. Fract. Mech.*, 20(3), 423.
6. Nishioka, T. Murakami, R. and Takemoto, Y. (1990) *Int. J. Pres. Ves. & Piping*, 44, 329.
7. Nishioka, T., Syano, S., and Fujimoto, T., (2000) *Proc. JSME MMD Meeting*, No.00-19, 227.
8. Nilsson, F., (1972) *Int. J. Fract.*, 8(4), 403.
9. Nishioka, T. and Atluri, S.N., (1980) *J. Appl. Mech.*, 47(3), 570.
10. Nishioka, T. and Atluri, S.N., (1980) *J. Appl. Mech.*, 47(3), 577.

ORAL/POSTER REFERENCE : ICF0325

NUMERICAL STUDY OF THE TIME TO FAILURE OF GLASS UNDER STRESS CORROSION

H. AURADOU[1], D. VANDEMBROUCQ[2], C. GUILLOT[1] AND E. BOUCHAUD[1]

[1] Commisariat à l'Energie Atomique, Service de Physique et Chimie des Surfaces et Interfaces, Bât. 462, F-91191, Gif-sur-Yvette cedex, FRANCE
[2] Unité Mixte de recherche CNRS/Saint-Gobain "Surface du Verre et Interfaces", 39 quai Lucien Lefranc, F-93303 Aubervilliers cedex, FRANCE

ABSTRACT

The purpose of this paper is to examine the effect of a population of surface flaws on the time to failure of glass under static loading and subject to stress corrosion. The roughness of the glass surface is mapped onto a set of parallel elliptical cracks. The presence of the cracks modifies the stress field within the material and induces a shielding of the stress at the cracks tips which increases the lifetime of the material. We show that this effect becomes important when the length of the cracks is comparable to the distance separating them.

KEYWORDS

stress corrosion, surface flaws, glass, time to failure, shielding.

INTRODUCTION

An important practical problem is to predict the lifetime of a piece of glass under stress. The failure time depends upon the surface state, the loading and also on the environment. This delayed failure of glass is associated with *the stress-corrosion* growth of pre-existing tiny surface defects in the presence of humidity. The corrosion process has the important consequence that any (sufficient) stress tends to lengthen the flaw and that finally the object breaks after the flaw has reached a critical length. While the fundamental nature of these flaws remains unclear since it is difficult to observe them directly, the presence of surface defects has been clearly highlighted in various experimental conditions [1, 2, 3]. Mechanical contacts or thermal shocks can for example be responsible for surface cracks. However it is well known that freshly drawn fibers can be broken in a stress-corrosion regime while AFM studies could not reveal any flaw on their surface [4]. Later studies [5] showed that the nanometer scale roughness of the fiber surface presented long range correlations (up to 100nm); the surface is in fact self-affine

[6], meaning that it is statistically invariant under the transformation $x \to \lambda x$ and $z \to \lambda^H z$, where x is a distance in the mean plane of the surface and z a height difference. Here H is the Hurst exponent where $0 < H < 1$. Note that this very gentle roughness is responsible for fluctuations of the tangential stress at the surface, (see Ref.[7] for direct calculations of the stress field from the knowledge of the roughness *v*ia conformal mapping). In other words even if there is no evidence for flaws on the glass surface, there can be stress concentration effects due to the roughness. We, actually, propose in this work to map a rough surface onto a set of elliptical cracks distributed over a plane surface so that they are responsible for the same local stress concentrations. Then, we investigate the variations of the time to fracture due to the distribution of cracks. Moreover, we will consider that flaws are microcracks with atomically sharp tips which emerge normally at the external surface of the glass. Thus, we will not consider possible crack blunting [8, 9]. The glass is supposed to be perfectly elastic and submitted to constant remote tension. Due to the presence of neighboring cracks, the stress at the tip of each crack is altered and the cracks do not longer behave as isolated cracks. The following section describes the model used to take into account the cracks interactions in the growing process of the surface flaws.

DESCRIPTION OF THE MODEL

Initial configurations of the crack : We first start by considering a one dimensional self-affine profile with $H = 0.8$ consisting of M facets of size l when projected onto the horizontal plane. The lengths l and $L = Ml$ correspond respectively to the lower and the upper scales of the self-affine description. Furthermore, the average slope, s, of the facets are small enough to allow for the computation by conformal mapping [7] of the local stresses when the profile is considered under uniaxial tension σ_0. Since our interest focuses on the subpart of the profile where the stress is concentrated, parts of the profile where the stress is lower than σ_0 are removed from the computation. We then select from the remaining set of stress the local stress maxima i.e. parts of the profile where the stress is higher than the two closest remaining stresses. To each of the remaining stresses σ is associated an equivalent elliptical crack a long by l wide which is under a uniaxial stress σ_0. The length of the hole is chosen so that the stress at the tip of the major axis is the one obtained by the conformal mapping method *i.e.* $\sigma = \sigma_0(1 - 2a/l)$. The roughness of the profile is thus mapped onto a set of parallel elliptical cracks that emerge normally to the external surface. The average distance, b, between the cracks is of the order of few l and the cracks spread over a horizontal distance L. The self-affine profile generated is made of 20 to 200 facets and the final set of cracks typically contains from 5 to 50 cracks. The set of cracks is then reproduced by translation of constant steps L (periodic boundary conditions); the final crack configurations is thus a succession of identical sub-cracks set that contains cracks of various lengths.

Determination of the stress intensity factors : It is well known that the problem of a linear elastic solid with N cracks can be represented as a superposition of N problems involving one crack but loaded by unknown tractions induced by the other cracks and the remote loading; the so called *"pseudo tensions"* method [10, 11]. These tractions can be interrelated through a system of integral equations [12]. Recently, a simple and efficient technique to solve this problem based on the superposition technique and the idea of self-consistency applied to the average tractions on individual cracks has been proposed [13, 14]. The key assumption of the method is to decompose the stress on a crack into a mean part and a fluctuating part and to neglect the effect of the fluctuating stresses in the interactions. Thus the traction shed on a given crack by a second crack results from the uniform average traction on the second crack. This results in a major simplification of the problem, self-consistency imposing then to the averaged stresses to be the solution of a simple linear system. Other techniques using a

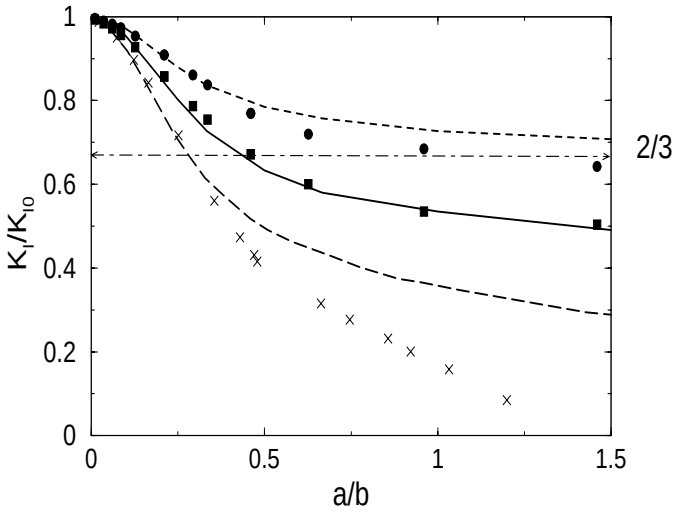

FIGURE 1. Curves of K_I/K_{I0} vs a/b for a semi infinite elastic plane containing a periodic array of N parallel cracks of same lengths a separated by a constant distance b and subjected to a uniform uniaxial stress σ_0 acting in a direction perpendicular to the cracks. $K_{I0} = 1.12\sigma_0\sqrt{\pi a}$ is the stress intensity factor for an isolated crack $N = 1$. Filled squares and filled circles represent the results obtained in our model for$N = 3$ cracks and correspond respectively to the inner and the outer cracks. The dashed and the solid lines show results from Isida [16]using a body force method for $N = 3$. The crosses show results obtained with our model for an infinite sequence of parallel cracks, these results are compared to the data of Bowie (long dashed line) [17].

polynomial approximation of the stress non-uniformities were also proposed [15], the method presented here is more efficient in terms of calculation time and was found sufficiently accurate.

Figure 1 compares results obtained by this method to other works[16, 17]. We see that while the ratio between the crack size and the distance between them is small enough, the results are in good agreement with previous works. Yet, discrepancy appears when the cracks length becomes of the order of the distance between them. This discrepancy comes from the fact that the non-uniformities of the tractions are not taken into account in our model. Moreover, it can be shown that the approach used is only valid for $K_I/K_0 > 2/3$; this lead to a major restriction on the ratio between the crack length a and the distance between them b which has to be less than unity.

Crack propagation law : From the experimental studies [8, 18, 19, 20], it is clear that crack velocity is strongly affected by the stress assisted corrosion reaction between the glass and the corrosive species in the atmosphere. Moreover, it appears that the velocity is uniquely related to the stress intensity factor. Depending on the stress intensity factor, three different regions are observed. In our work we mainly focus on the so called Region I which corresponds to the low speed regime. In this domain, the speed of the crack typically lies between $10^{-10}$and $10^{-5} m.s^{-1}$. In the other regions, crack propagation is fairly rapid and the range of stress intensity factors involved is narrow. Thus for long enough test times the contribution to the time before rupture in these regions is negligible.

Wiederhorn *et al* [19] carefully studied the low speed domain of the crack growth for various glasses and various environmental conditions. The data were found to fit the equation :

$$v(K_I) = v_0 exp(\frac{-E^* + cK_I}{RT}), \quad (1)$$

where $v(K_I)$ is the crack velocity, T the temperature. $E^*$is the apparent activation energy at zero load and c is the stress intensity factor coefficient. In this work we set the activation energy to zero. This has the consequence that under any applied stress, all the cracks are allowed to grow independently of their length. By normalizing the speed by the speed v_0 of the cracks at small stress intensity factor, equation 1 becomes :

$$v(K_I) = exp(c^* K_I) \quad (2)$$

with $c^* = c/RT$. The different steps of the simulation can be summarized as follows. We first compute the initial crack configuration. Using the method described in **??**, the stress intensity factor at the tip of each crack is calculated. The speed of each of the cracks is obtained using the crack growth law chosen (Eq. 1). The length of each crack is then incremented by $\Delta a = v(K_I)\Delta t$ where Δt is a fixed time step. The computation of the stress intensity factors and the crack growth are iterated until one of the cracks reaches the critical stress intensity factor K_{Ic} above which failure of the sample occurs. The lifetime of the material is defined as the time needed by the crack that reaches K_{Ic} the first to grow from its initial size to its final length.

In the following, we will study the effect of the cracks interactions on the life time of the material. We will first consider a single crack configuration.

QUALITATIVE DESCRIPTION OF THE CRACK GROWTH

Figure 2 shows, for a single crack configuration, the evolution of the ratio between the stress intensity factor for each of the cracks and the stress intensity factor of the cracks when considered as isolated. For small cracks size, which corresponds to the beginning of the simulation, the ratio of the stress intensity factors is close to one, meaning that each crack can be seen has isolated. But while the crack length increases, this ratio decreases until one of the cracks is long enough so that K_{Ic} is reached and that fracture occurs. We see from this example that the presence of a neighbourhood of cracks results in a decrease of the stress intensity factors. Due to this shielding effect, the speed of each crack is lower than what it would have been in the absence of shielding. The progression of the cracks is thus slowed down and as a consequence the lifetime of the material increases. Here the increase of the lifetime is of the order of 35%. When the shielding effect is absent and since the longest crack has the highest velocity, it is always this crack that reaches K_{Ic} the first. But it has to be pointed out that for some crack configurations, the shielding on the longest crack can be strong enough so that another crack which was not intially the longest one reaches K_{Ic} the frist. The shielding effect, thus, strongly depends on the initial cracks configuration. In the next section, we investigate the effect of the statistical distribution of the crack lengths on the lifetime of the material.

QUANTITATIVE RESULTS

Depending on the self-affine profile generated, different crack configurations can be obtained. These configurations differ in the the crack lengths and also in the arrangement of these cracks and, thus, each configuration will lead to a different lifetime.

Figure 3 shows the distribution of the ratio between the lifetime and the lifetime of the material when the longest crack is considered as isolated. We see that the times ratios are always larger than 1, meaning, as discussed previously, that the interactions between the cracks increase the life time of the material. Configurations obtained using $s = 0.1$ give rise to a broad distribution of lifetimes which gets sharpes when s decreases.

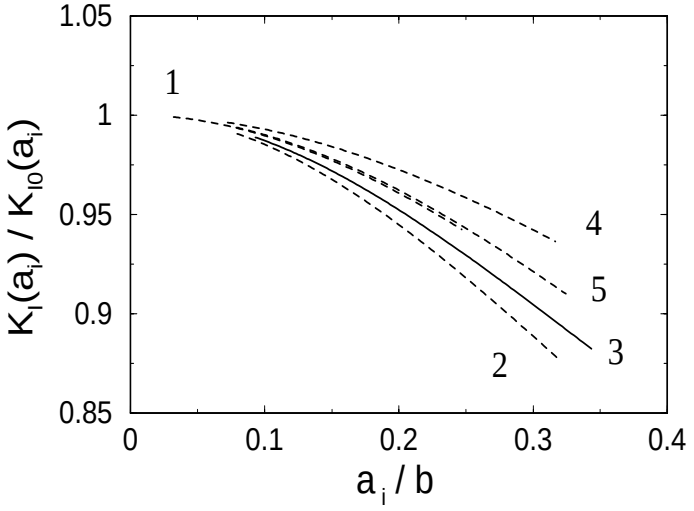

FIGURE 2. Evolution of the stress intensity factor for a single crack configuration as a function of the length a_i of crack i. A self-affine profile with roughness exponent $H = 0.8$ made of $M = 15$ facets of average slope $s = 0.1$ under uniaxial tension $\sigma_0 = 1$ is used to generate the configuration made of 5 cracks. Here, the relationship between the speed of the crack and the stress intensity factor is : $v(K_I) = exp(K_I)$ and $K_{Ic} = 1$. b is the distance between the cracks. $K_I(a_i)$ is the stress intensity factor of the crack i when cracks interact. $K_{I0}(a_i) = 1.12\sigma_0\sqrt{\pi a_i}$ corresponds to the stress intensity factor of an isolated crack of length a_i .

This effect is mainly due to the change in cracks lengths when the self-affine profile generated gets smoother. In fact, a decrease of the facets slope changes the length of the cracks that shrinks and as a consequence the ratio between the crack length and the distance separating them is decreased. For the configurations studied, the average crack length referred to the distance separating them is $< a > /b = 8.10^{-2}$ when the facets slope s is 0.1, while for $s = 0.01$ this ratio is 8.10^{-3} and drops to 8.10^{-4} when $s = 0.001$. As shown in the previous section, this will deeply influence the shielding effect, that has less influence on the growing process when the ratio $a/b << 1$.

For small $< a > /b$, the cracks grow as if they were isolated, and as a consequence the lifetime of the material is close to the time to failure without shielding. When $< a > /b$ becomes large enough, the shielding effect becomes important and this has a strong effect on the life time which can be quite larger than the life time without interaction.

CONCLUSION

We have developed a model of crack growth where the modification of the stress field due to the presence of neighboring cracks is taken into account. Our model allows for the computation of the stress intensity factors of a set of parallel sharp surface cracks submitted to tensile stresses. This model has been applied to stress corrosion growth of pre-existing surface flaws. The initial flaw configuration is obtained by mapping the self-affine roughness of the external surface of the glass considered under tension onto a set of parallel elliptical cracks. The growing rate of each crack is uniquely related to its stress intensity factors by a relation that fits previous experimental works. We have shown that the presence of neighboring cracks lead to a shielding of the stresses at the tip of the cracks and to an increase of the time to failure. Moreover this increase of the lifetime becomes non negligible when the shielding effect is important. This is

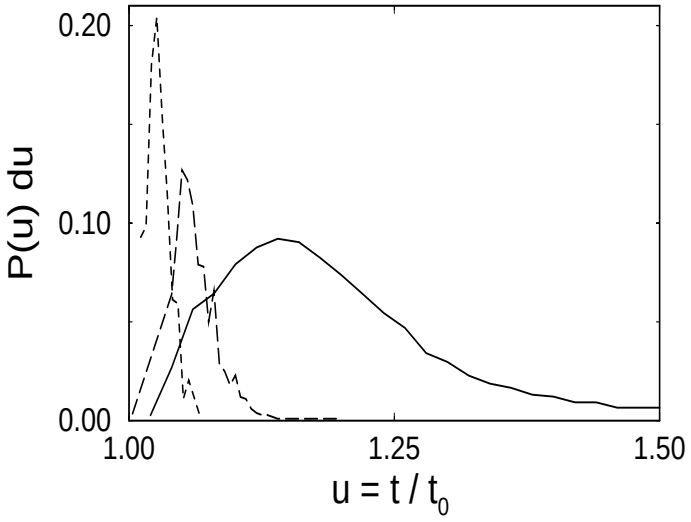

FIGURE 3. Distribution of the ratio of lifetime, t, when interaction are taking into account to the lifetime, t_0, in the absence of interactions. The data were obtained using 600 initial crack configurations generated using self-affine profiles made of facets of different slopes s. Solid, dotted and long dashed lines correspond respectively to $s = 0.1$, 0.01 and 0.001. The crack velocity law used is $v(K_I) = exp(K_I)$ and $K_{Ic} = 1$.

achieved when the crack lengths become of the order of the distance separating them. We have, also, pointed out that, due to shielding and depending on the crack configuration, others cracks than the longest can lead to the failiure of the sample. The effect of the remote tension an the lifetime has been studied also and it appears that the shielding effect has a strong influence on the lifetime when the remote tension is decreased. Further work is presently carried on to characterize the distribution of lifetime in terms of a Weibulh distribution.

REFERENCES

[1] da C. Andrade, E.N. and Tsien, L.C. (1937) *Proc. Roy. Soc.* A. 159, 346.
[2] Poloniecki, J.D. and Wilshaw, T.R. (1971) *Nature Physical Science* **229**, 226.
[3] Adams, R. and McMillan, P.W. (1977) *J. Mat. Sci.* **12**, 2544.
[4] Guilloteau, E. (1997), PhD Thesis, University Paris XI, France.
[5] Nghiêm, B. (1998). PhD Thesis, University Paris VI, France.
[6] J. Feder, Fractals, Plenum press, (1988).
[7] Vandembroucq, D. and Roux, S. (1997) *Phys. Rev. E.* **55** [5] 6186.
[8] Crichton, S.N. and Tomozawa, M. (1999) *J. Am. Ceram. Soc* **82** [11] 3097.
[9] Bando, Y., Ito, S. and Tomozawa, M. (1984) *J. Am. Ceram. Soc.* **67** [3] C36.
[10] Gong S.X. and Horii, H. (1989) *J. Mech. Phys. Solids* **37** (1), 27.
[11] Hori, M. and Hemat-Nasser, S. (1987) *J. Mech. Phys. Solids* **35** (5), 601.
[12] Datsyshin, A.P. and Savruk, M.P. (1973) *J. Appl. Math. Mech.* **37**, 306.
[13] Kachanov, M. (1985) *Int. J. Fracture* **27**, 113.
[14] Kachanov, M. and Montagut, E. (1986) *Eng. Frac. Mech.* 25, 625.
[15] Chudnovsky, A. and Kachanov, M. (1983) *Int. J. Engng. Sci* **21**, 1009.
[16] Isida, M. (1979) *Trans. Japan Soc. Mech. Engrs.*,**45** [392], 306.
[17] Bowie, O.L. (1972). In:*Method of analysis and solutions of crack problems*, ed. by G.C. Sih, Noordhof Int. Pub. Vol. I.
[18] Wiederhorn, S.M. (1967) *J. Am. Ceram. Soc* **50** [8], 407.
[19] Wiederhorn, S.M. and Bolz, L.H. (1970) *J. Am. Ceram. Soc* **53** [10], 543.
[20] Lawn, B.R., Jakus, K. and Gonzalez, A.C. (1985) *J. Am. Ceram. Soc.* **68** [1], 25.

ICF10063OR

MICROSTRUCTURE-PROPERTY DAMAGE ANALYSIS OF NOTCH TENSILE TESTS

M. F. Horstemeyer[1] , Ken Gall[2], K.W. Dolan[3], A. Waters[3], J.J. Haskins[3], D.E. Perkins[3], A. M. Gokhale[4], and M.D. Dighe[4]

[1]Center for Materials and Engineering Sciences, Solid & Material Mechanics Dept, Sandia National Laboratories, Livermore, CA 94550,
[2]Mechanical Engineering Dept., University of Colorado, Boulder, Co 80309,
[3]Lawrence Livermore National Laboratory, Livermore, CA 94550
[4]Materials Science and Engineering Department, Georgia Institute of Technology, Atlanta, GA 30332

ABSTRACT

Microstructure-property relations related to void nucleation, growth, and coalescence in A356 aluminum notch specimens were determined from a combination of experiments, finite element analysis, nondestructive analysis, and image analysis. Notch Bridgman tension experiments were performed on specimens to failure and then other specimens were tested to 90%, 95%, and 98% of the failure load. The specimens were evaluated with nondestructive x-ray tomography and optical image analysis. Finite element simulations of the notch tests were performed with an elastic-plastic internal state variable material model that incorporated the pertinent microstructures (silicon particle volume fraction and size distribution and porosity volume fraction and size distribution). The various methods all corroborated the same damage progression.

KEYWORDS

notch, finite element analysis, image analysis, x-ray tomography, A356 aluminum, damage, failure, porosity

RESULTS AND DISCUSSION

Computed tomography and optical microscopy results were used with finite element modeling in order to link microstructural features to the mechanical response of a cast A356 aluminum alloy. In particular, we focused on the damage progression by analyzing different notch test specimens which were loaded to different strain levels. Each of these specimens were analyzed nondestructively by computed tomography and

then sectioned for optical microscopy. The data were then compared to finite element simulations. In the finite element simulations, an internal state variable plasticity model was used [1] with rate equations for void nucleation, growth, and coalescence [2]). The rate equations were initialized with the volume fraction of voids, volume fraction of second phase particles, and the size of second phase particles.

Several issues related to size should be raised. The computed tomography results had a minimum resolution of 28 microns, and the optical microscopy had a minimum resolution of 0.5 microns. The average silicon particle size was 4 microns; the average initial pore size was 50 microns; and the average dendrite cell size was 25 microns.

Because variability in porosity levels and silicon particle distributions are evidenced in cast A356 aluminum structural components, we exercised the material model in the finite element analyses with homogeneous and random distributions based on size. Moreover, we included different initial void volume fractions that could arise from different casting processes. The notch test simulation results showed that the initially randomized porosity gives lower failure displacements than the homogeneous case. This difference lessened as the initial porosity level increased. The failure displacements ranged from approximately 0.05 mm to 0.11 mm (the gage radius was 4.7625 mm). The experimental failure displacement was approximately 0.11 mm indicating that our initial porosity assumptions were comparable to the experimental specimens.

The progression of damage in notch tensile specimens for this cast A356 aluminum alloy gives an understanding of the role of the nonhomogeneous distribution of initial porosity and second phase silicon on the final failure state. With this understanding, we now focus on comparisons of the finite element simulations and experimental results, which include image analysis and x-ray tomography of the physical specimens.

At a higher initial porosity level, pore growth and coalescence mechanism is more dominant than the void nucleation from the second phase material, albeit both interact together in the damage process. We summarize different initial porosity levels and distributions in Table 1 with data from the x-ray tomography. The finite element results show that porosity levels comparable to the experimental results can be achieved by the right combination of initial porosity and distribution level. It appears that three of the cases could match the experimental data, but clearly the homogeneous distribution with with an initial porosity of 0.0001 does not correlate well. Because three different specimens were used in the tests and the same simulation was used for the FEM data results, distinguishing whether the initial distributions were homogeneous or random is difficult. Clearly, the trends are similar, which suggests that the damage progression was driven more by the notch geometry and not the initial microstructure in this particular case.

Table 1. Peak void volume fractions within notch specimen at different strain levels.

Failure load %	x-ray tom.	FEM (ϕ_i = 0.0001 homog.)	FEM (ϕ_i = 0.0001 random)	FEM (ϕ_i = 0.001 homog.)	FEM (ϕ_i = 0.001 random)
90	0.028	0.003	0.056	0.069	0.071
95	0.186	0.017	0.124	0.155	0.168
98	0.451	0.123	0.445	0.483	0.520

Finite element and x-ray tomography results were not only determined over the highest spatial resolution, but comparisons to the image analysis results were considered by averaging over a larger region (three different sections). Comparisons were performed on specimens that were 90%, 95%, and 98% of failure.

Figure 2 shows a comparison of the image analysis montage, x-ray tomography picture, and a contour plot of total void volume fraction from the finite element simulation in which an initially random porosity level of 0.001 was assumed for the 98% of fracture load case. Note that small and large region averages are included for comparison. Figure 2a shows the x-ray tomography result; Figure 2b is a high resolution area montage that comprises 100 microstructural fields at 100X magnification of the microstructure and illustrates the porosity distribution in the entire notch region. The differences in the montage and x-ray tomography picture arise because the image analysis only shows one plane cutting axially through the specimen. The x-ray tomography results average 360 planes rotated at one degree throughout the specimen. As one would expect, the x-ray tomography results slightly differ than the image analysis results but closer the finite element analysis, since the same axisymmetric assumptions are included in the simulations. Although the peak values are different between the x-ray tomography and finite element simuations, the maximum void volume fraction is largest at z=0 in the axial direction for both and decreases as the direction z increases or decreases.

Figure 1 is the quantitative data retrieved from Figure 2. When comparing the x-ray tomography and FEM results, one can see that the FEM peak void volume fraction (total damage) is slightly higher (52% to 45%). This may arise due to the initial porosity level assumption. Since we did not quantify the initial porosity states, we would expect some void volume fraction differences. See Table 1 for other initial configurations. Other simulation comparisons at 90% and 95% of failure showed similar qualitative trends as Figures 1 and 2.

Differences in the x-ray tomography and optical image results arose because each of the measurements were from different specimens which had different initial porosity levels, while the finite element simulations were from a single calculation using an initial starting porosity level of 0.001 that provided qualitative damage progression agreement with both the x-ray tomography and optical metallography..

SUMMARY

Microstructure-property relations for damage have been quantified and confirmed by independent methods of evaluation for a cast A356 aluminum alloy notch tensile testing. The methods include experiments; x-ray computed tomography; optical microscopy/stereology metallography image analysis; and finite element simulations that include a history dependent elastic-plastic internal state variable plasticity model involving evolution equations for void nucleation, growth, and coalescence.

ACKNOWLEDGEMENTS

The work by M.F. Horstemeyer and Ken Gall was performed at the U.S. Dep. of Energy Sandia National Laboratories under contract DE-AC04-94AL85000. The work of K.W.

Dolan, J.J. Haskins, and D.E. Perkins was performed under the U.S. Department of Energy Lawrence Livermore National Laboratory under contract W-7405-Eng-48.

REFERENCES

1. Bammann, D.J., Chiesa, M.L., Horstemeyer, M.F. and Weingarten, L.I. (1993) Failure in Ductile Materials Using Finite Element Methods. *Structural Chrashworthness and Failure*, eds. N. Jones and T. Weirzbicki, Elsevier Applied Science.

2. Horstemeyer, M. F., Lathrop, J., Gokhale, A. M., and Dighe, M (2000) Modeling Stress State Dependent Damage Evolution in a Cast Al-Si-Mg Aluminum Alloy, *Theoretical and Applied Mechanics,* **33**, 31-47.

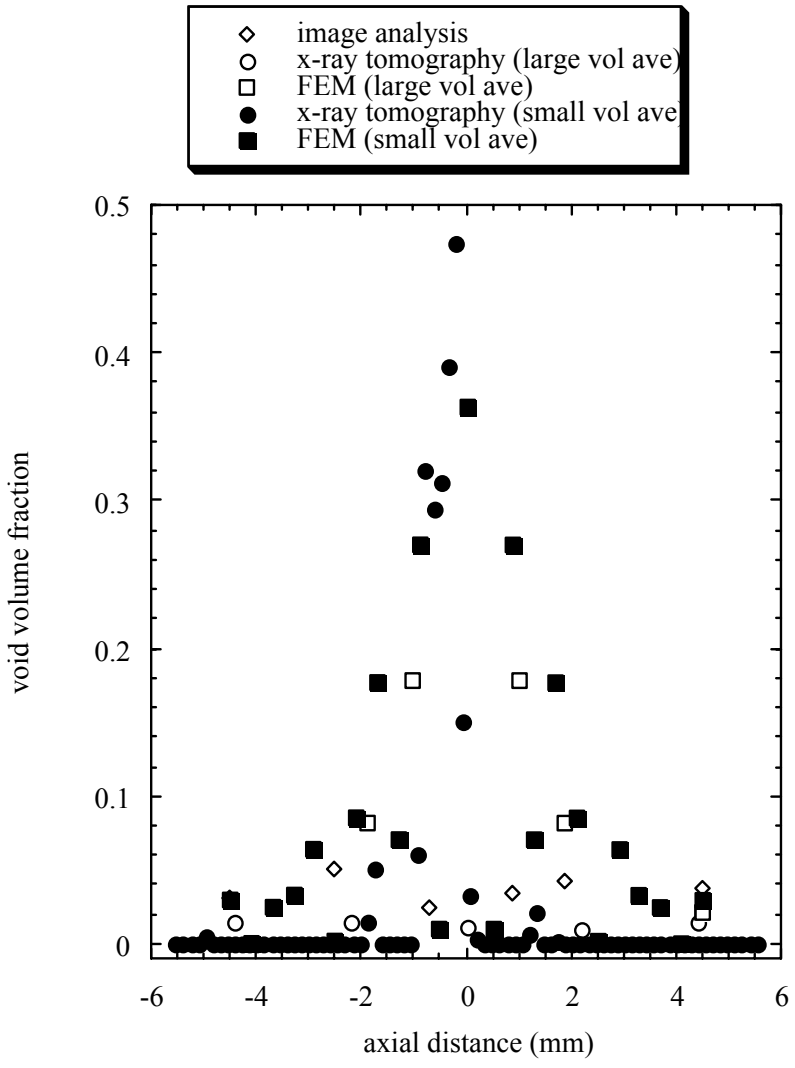

Figure 1. Total void volume fraction along axial distance determined from 98% of failure load specimen from x-ray tomography, image analysis, and finite element analysis with averaged regions similar to those taken for the tomography and image analysis measurements.

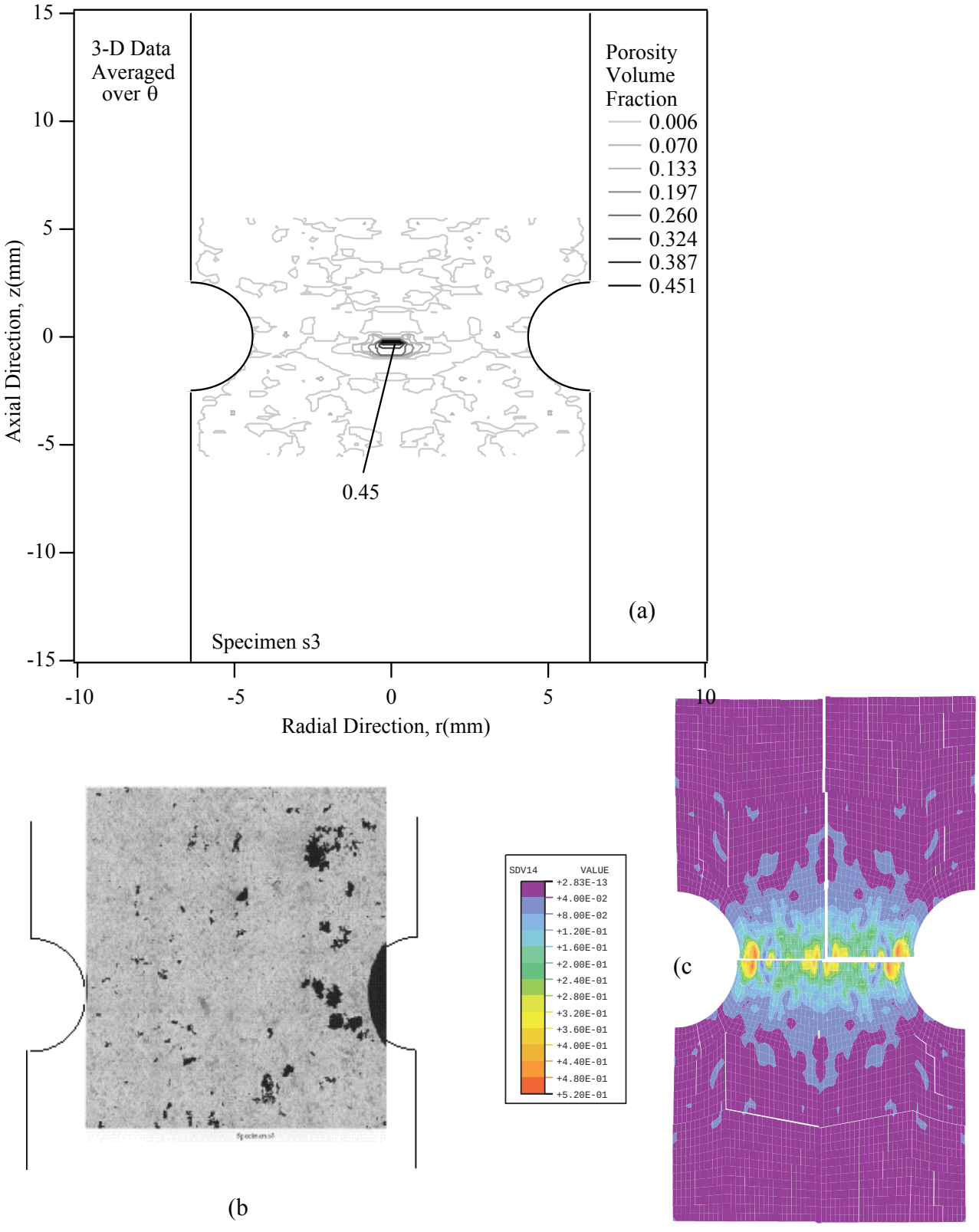

Figure 2. Pictorial illustration of porosity distribution for the 98% of failure load specimen from (a) x-ray tomography, (b) image analysis, and (c) finite element simulation with an initially random distribution of porosity at a level of 0.001.

ORAL REFERENCE: ICF100877OR

OBSERVATION OF FATIGUE CRACK INITIATION AND EARLY PROPAGATION IN ULTRAFINE-GRAINED STEEL BY ATOMIC FORCE MICROSCOPY

H. Kimura [1], Y. Akiniwa [2], K. Tanaka [2], J. Kondo [1] and T. Ishikawa [3]

[1] Graduate School, Nagoya University,
Furo-cho, Chikusa-ku, Nagoya 464-8603, Japan
[2] Department of Mechanical Engineering, Nagoya University,
Furo-cho, Chikusa-ku, Nagoya 464-8603, Japan
[3] Steel Research Laboratories, Technical Development Bureau, Nippon Steel Corporation,
20-1 Shintomi, Futtsu-city, Chiba 293-8511, Japan

ABSTRACT

Steel plates produced by an advanced thermo-mechanical control process have two regions: the ultrafine-grained surface layer with the average grain size of less than 2 μm and the intermediate region with medium-sized grains. Smooth specimens of the ultrafine and medium-sized grains were prepared to conduct fatigue tests under cyclic axial tension compression at room temperature. The effect of the microstructure on the fatigue crack initiation as well as the early propagation behavior was investigated by observing images of specimen surfaces replicated on plastic sheets by atomic force microscopy. In the specimens of the medium-sized grains, the fatigue cracks initiated from the simple straight slip lines. In the ultrafine-grained specimens, complex slip deformation in the shape of irregularities of the specimen surface was observed prior to the initiation of fatigue cracks. The initiation of fatigue cracks was observed at the grain boundary between the grains containing the complex slip deformation at an early stage of fatigue cycles. The crack propagation rate in the ultrafine-grained specimens decreases because of the crack deflection, bifurcation and the grain-boundary blocking at an early stage of the propagation.

KEYWORDS

ultrafine-grained steel, fatigue, crack initiation, crack propagation, microstructure, atomic force microscopy

INTRODUCTION

Steel plates with ultrafine-grained surface layers, called SUF plates, exhibit excellent crack arrestability against brittle fracture. They have already been put into practical use as the structural components of ships to prevent them from unexpected catastrophic fracture [1]. SUF plates are produced by an advanced thermo-mechanical control process to yield ultrafine-grained surface layers with the average grain size of less than 2 μm and relatively coarse microstructure in the intermediate region. Though the fatigue properties of SUF plates are also expected to be excellent [2,3], the mechanism of the improvement especially in the ultrafine-grained surface layer has not yet been clarified. Atomic force microscopy (AFM) will be a powerful tool to investigate the crack initiation process because the size of ultrafine grains is so small that it is difficult to observe the plastic sheets replicated from the specimen surface by scanning electron microscopy (SEM). AFM observations make it possible to study the fatigue crack initiation process based on the three-dimensional measurement of the specimen surface [4-6].
In this study, fatigue tests were conducted on the specimens prepared from the ultrafine-grained surface layer and the medium-grained intermediate region. The effect of the microstructure on the fatigue crack initiation as well as the early propagation behavior was investigated by AFM.

EXPERIMENTAL PROCEDURE

The advanced thermo-mechanical control process where accelerated cooling during the rolling of steel plates was followed by controlled rolling in the reheating process was employed to yield ultrafine grains on the surface layers with the thickness of 7 mm on the both sides of a 50-mm-thick plate. Chemical compositions of the basic components are 0.11wt%C, 0.20wt%Si, 1.44wt%Mn, 0.007wt%P and 0.005wt%S. The SEM images of the electrolytically polished specimen surfaces of the ultrafine-grained surface layer and the medium-grained intermediate region are shown in Fig. 1. The surface layer consists of ferrites and cementites dispersed at grain boundaries [7], whereas the intermediate region is composed of ferrites and pearlites. The mechanical properties and grain size are presented in Table 1. Grain sizes d_S, d_T and d_L correspond to the average grain length parallel to the axes S, T and L shown in Fig. 2 respectively. Specimens were prepared from the surface layer and intermediate region with the rolling direction parallel to the loading axis by electrical discharge machining followed by electrolytic polishing.

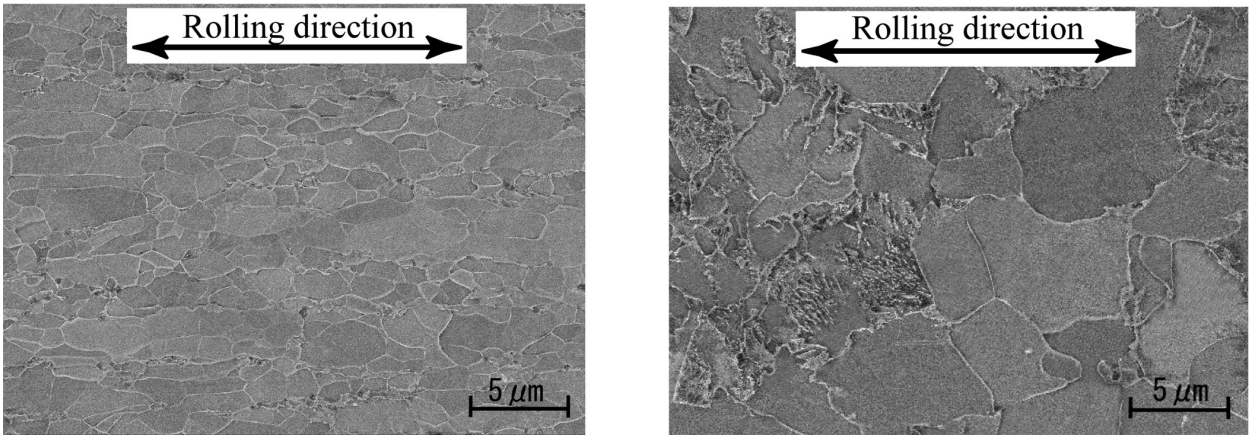

(a) Ultrafine-grained surface layer (b) Medium-grained intermediate region

Fig. 1. Specimen surfaces finished by electrolytic polishing.

Table 1 Mechanical properties and grain size.

Material	Mechanical properties (MPa)			Grain sizes (μm)		
	σ_Y	σ_B	σ_{W0}	d_S	d_T	d_L
Ultrafine-grained	463	537	285	1.8	3.1	4.5
Medium-grained	386	488	245	6.7	9.6	8.6

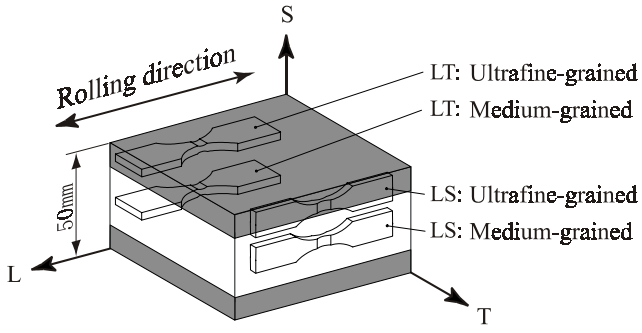

Fig. 2. Specimen orientation.

Smooth specimens were fatigued under cyclic axial loading with the stress ratio R=-1 in air at room temperature. The both sides of the specimen surface were replicated with cellulose acetate sheets under the maximum and minimum applied stresses. The observations were made on the cellulose acetate sheets by AFM and SEM. The AFM images presented in this paper are the images scanned on the cellulose acetate sheets where the grain boundaries are intrusions as opposed to the extrusions on the actual specimen surfaces.

EXPERIMENTAL RESULTS

Crack initiation in the medium-grained specimens

Figure 3 shows the AFM images of the replicated surface of the medium-grained L-S specimen under the maximum applied stress of σ_{max}= 250 MPa. The number of cycles at fracture N_f was 9.2×10^5. The uppercase letter "A" in the figure indicates a grain, whereas the lowercase letter "a" denotes the location of slip lines in the grain. The image in (a) is the one before the fatigue test. In the image at $N/N_f = 2.2\times10^{-2}$ in (b), slip lines at the location of M1a had initiated in the grain M1A and other slip lines were also clearly observed on the left of M1A. Those slip lines with the angle of approximately 45 degrees from the loading axis finally merged to form the main crack.

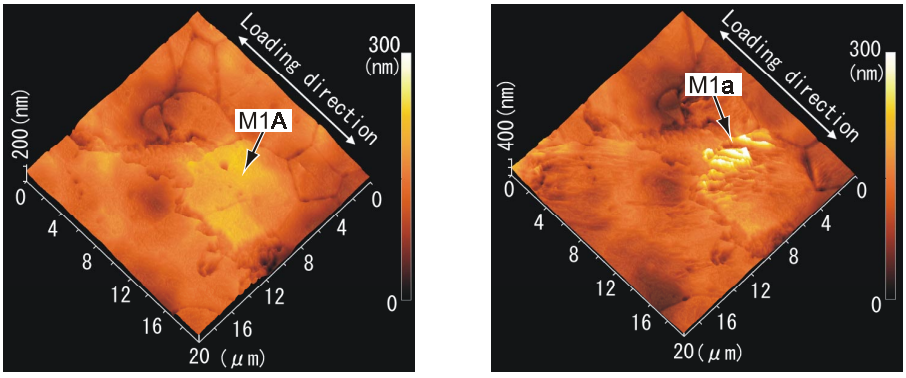

(a) $N/N_f = 0$ (b) $N/N_f = 2.2\times10^{-2}$

Fig. 3. AFM images of crack initiation (Medium-grained, σ_{max} = 250 MPa, $N_f = 9.2\times10^5$).

Crack initiation in the ultrafine-grained specimens

Figure 4 shows the scanning electron micrographs of the surface of the ultrafine-grained specimen fatigued under σ_{max} = 290 MPa up to N =2.6×10^5 with N_f =3.8×10^5. The image in (a) shows simple slip lines. The image in (b) shows the complex slip deformation in the shape of irregularities of the surface in contrast with the simple straight slip lines. This complex slip deformation was rarely observed on the medium-grained specimen surface.

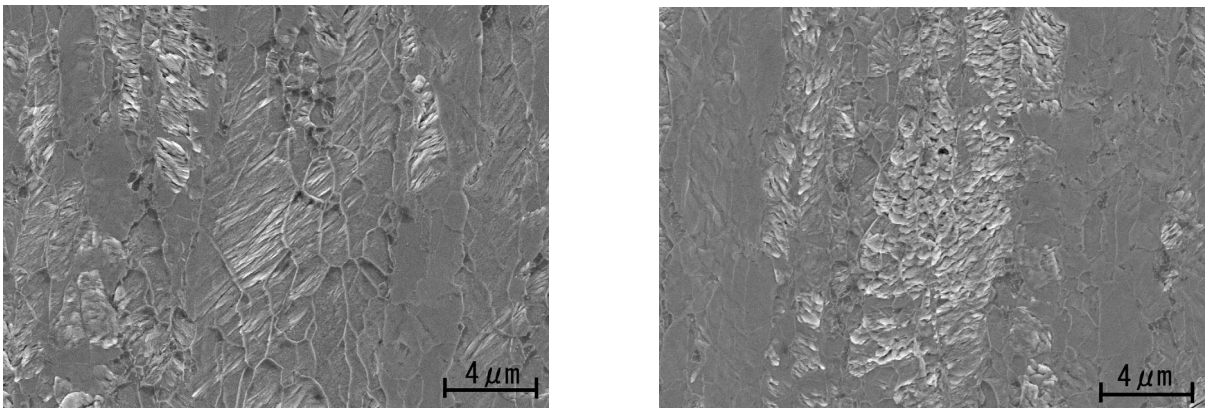

(a) Simple slip lines. (b) Complex slip deformation.

Fig. 4. SEM images of slip deformation (Ultrafine-grained, σ_{max} = 290 MPa, $N = 2.6\times10^5$).

Figure 5 is the AFM images of a crack initiation site. The image in (a) is before the fatigue test. A slip line initiated at U1a in the grain U1A at $N/N_f = 4.0\times10^{-3}$. At $N/N_f = 8.0\times10^{-3}$ in (b), U1b in the grain U1B and U1c in the grain U1A became protrusive due to complex slip deformation. At $N/N_f = 2.1\times10^{-2}$ in (c), the slip line initiated at U1a had propagated through the grain U1A to the opposite grain boundary. Another slip line U1d was formed in U1A. The complex slip deformation U1b in U1B had become more protrusive. The main crack initiated from the grain boundary between U1b and U1c after $N/N_f = 4.2\times10^{-2}$ as shown in (d).

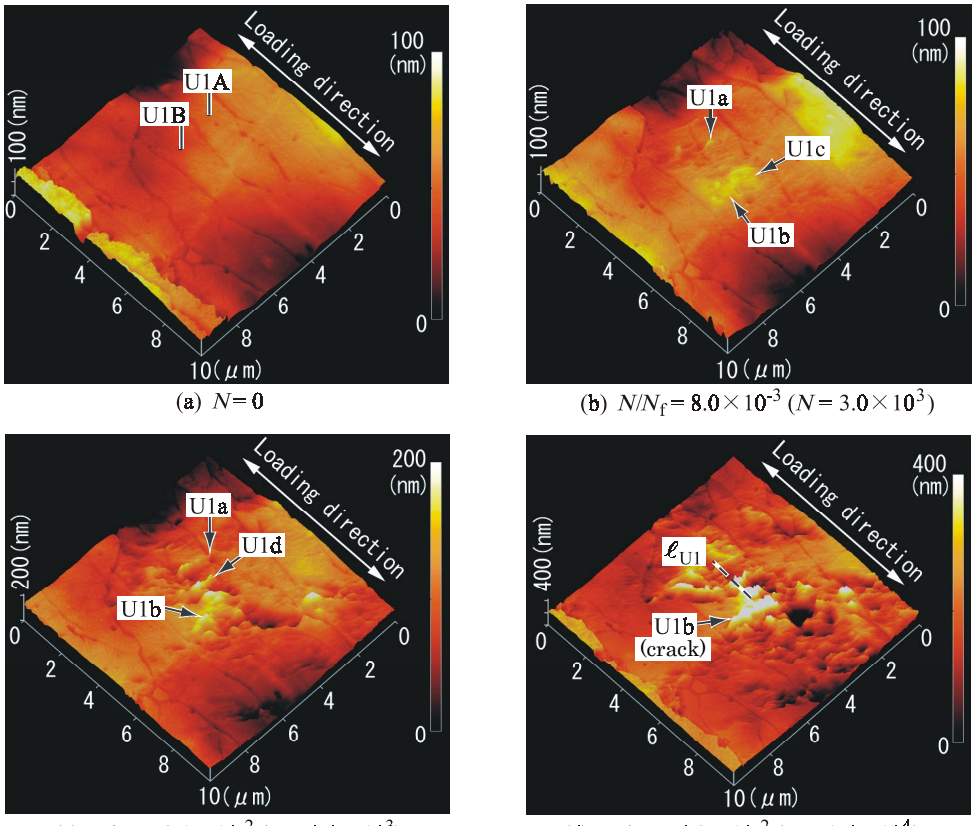

Fig. 5. AFM images of crack initiation (Ultrafine-grained, σ_{max} = 290 MPa, $N_f = 3.8\times10^5$).

Figure 6 (a) shows the change of the sectional profile along the line ℓ_{U1} shown in Fig. 5 (d). The line ℓ_{U1} is perpendicular to slip lines in the grain U1A, where the initiation of the first slip deformation was observed. Figure 6 (b) shows the change of the depth of intrusions, which is the height of extrusions on the replicated plastic sheets, at U1a and U1c. As the number of cycles increased, the depth of intrusion at U1a reached the plateau of 145 nm because it propagated through the grain U1A and came to a standstill at the opposite grain

boundary at $N/N_f = 2.1\times10^{-2}$ as shown in Fig. 5 (c). The depth of intrusion at U1c, however, had a tendency to increase as the number of cycles increased.

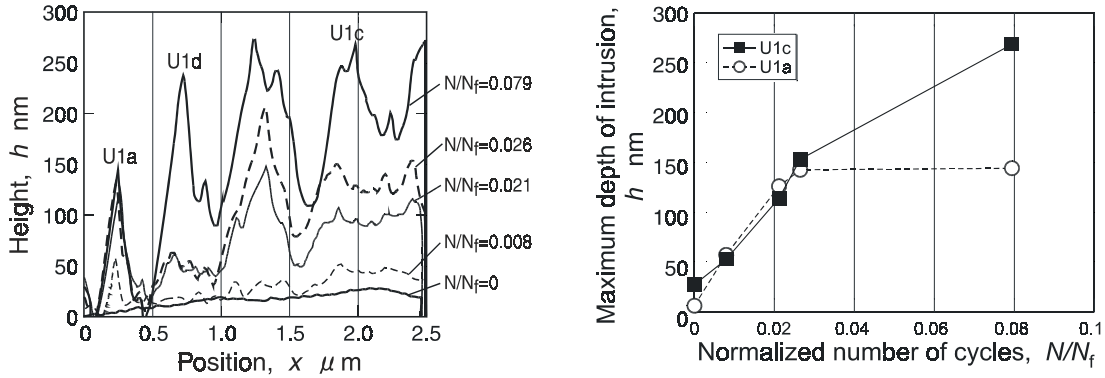

(a) Sectional profiles along the line ℓ_{U1} in Fig. 5(d). (b) Maximum depth of intrusion vs. N/N_f.

Fig. 6. Change of the surface morphology in the fatigue crack initiation process.

Figure 7 shows the AFM images under σ_{max} = 310 MPa with $N_f = 1.9\times10^5$. The image in (a) is before the fatigue test. Slip lines were observed at U3a in the grain U3A and U3b in the grain U3B at $N/N_f = 5.3\times10^{-3}$. The image in (b) was taken at $N/N_f = 1.6\times10^{-2}$. The surfaces of the both grains became irregular due to slip deformation. At $N/N_f = 5.3\times10^{-2}$, one of the slip lines in the grain U3A reached the grain boundary as shown in (c). At $N/N_f = 2.1\times10^{-1}$, a crack initiated from the grain boundary into the grains U3A and U3B as shown in (d). The directions of the crack propagation in those grains were not parallel to the directions of slip lines observed prior to the crack initiation.

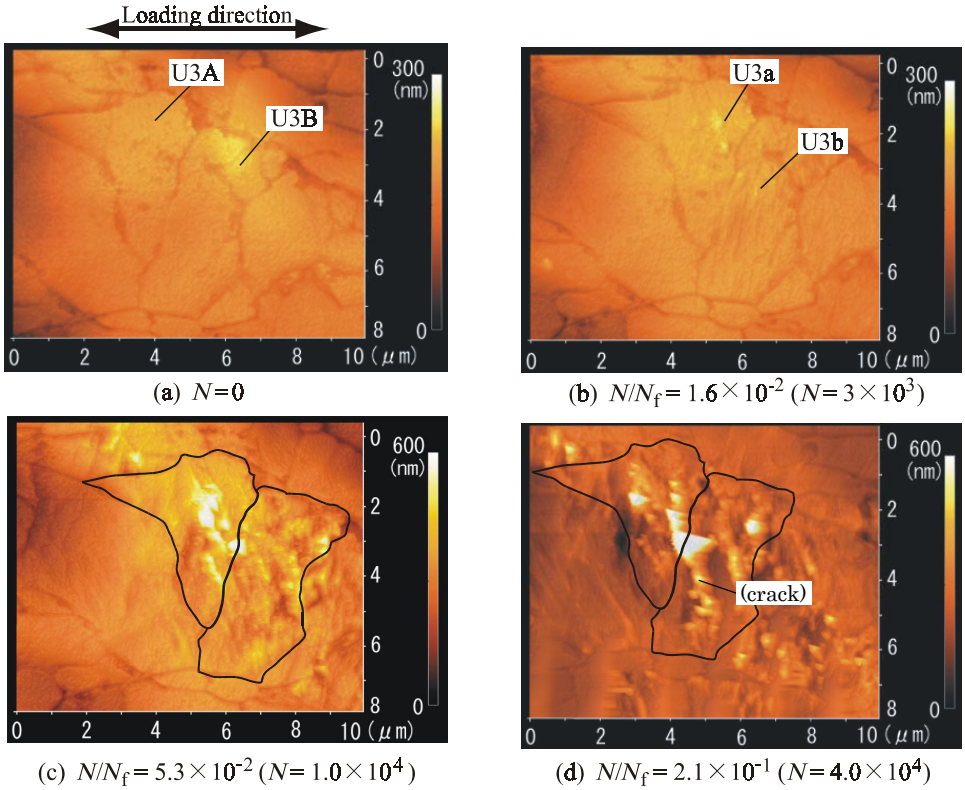

(a) $N=0$ (b) $N/N_f = 1.6\times10^{-2}$ ($N = 3\times10^3$)

(c) $N/N_f = 5.3\times10^{-2}$ ($N = 1.0\times10^4$) (d) $N/N_f = 2.1\times10^{-1}$ ($N = 4.0\times10^4$)

Fig.7. AFM images of crack initiation (Ultrafine-grained, σ_{max} = 310 MPa, $N_f = 1.9\times10^5$).

Fatigue crack propagation at an early stage

Figure 8 shows the relation between crack propagation rate da/dN and the crack-tip position a of the crack shown in Fig. 7 with the corresponding SEM image of the crack superimposed on the AFM image of the surface. The decreases in da/dN at A1 and A2 can be attributed to the deflection of the main crack

perpendicular to the loading axis by colliding into slip lines having initiated before the formation of the main crack with the angel of 60 degrees from the loading axis. The decreases in d*a*/d*N* at the points B1 and B2 are attributed to the blocking of the grain boundaries. In comparison with the case of the surface layer, d*a*/d*N* in the medium-sized grains was relatively larger in spite of the smaller applied stress.

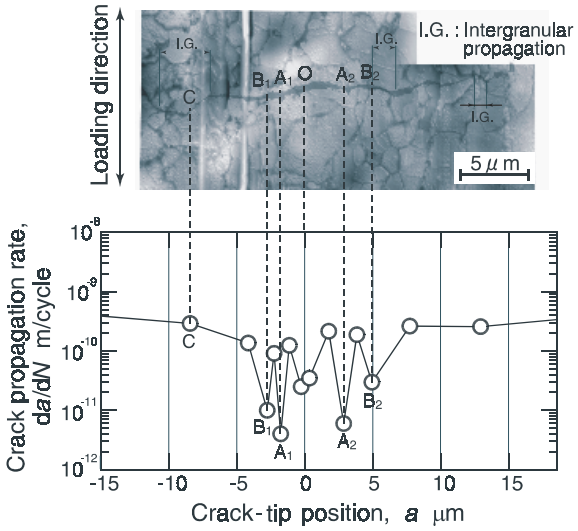

Fig. 8. Relation between crack propagation rate and crack-tip position *a* in ultrafine-grained specimen.

CONCLUSION

Fatigue tests were conducted in the ultrafine-grained and medium-grained specimens. The effect of the microstructure on fatigue crack initiation was investigated. The results are as follows:

(1) Fatigue crack initiation in the ultrafine-grained surface layer is characterized by the formation of complex slip deformation as well as simple slip lines in the grains at an early stage of fatigue cycles. The fatigue cracks initiate at the boundary between the grains with the complex slip deformation. Though simple slip lines were observed in places, none of them led to the formation of the main cracks.

(2) Fatigue crack initiation in the medium-grained specimens is from slip lines. The complex slip deformation formed on the ultrafine-grained specimens was rarely observed.

(3) The comparison of intrusions and extrusions of slip deformation showed no difference under maximum and minimum applied stresses in both ultrafine-grained and medium-grained specimens.

REFERENCES

1. Ishikawa, T., Nomiyama, Y., Hagiwara, Y. et al. (1995) *Materials Engineering*, ASME, New York.
2. Ishikawa, T. (1998) Proc. 24th Symp. Fatigue, The Soci.Mater. Sci., Jpn, 28
3. Kimura, H., Akiniwa, Y., Tanaka, K., Kondo, J. and Ishikawa, T. (2000) Proc. 10th Iketani Conf., 75
4. Nakai, Y., Ohnishi, K. and Kusukawa, T. (1999) Trans. Jpn. Soc. Mech. Eng. , 65-631, 483
5. Yoon, W.K., Inoue, T., Noguchi, H. and Higashide, K. (1998) Trans. Jpn Soc. Mech. Eng. , 64-622, 1435
6. Gerberich, W.W., Harvey S.E., Kramer, D.E. and Hoehn J.W. (1998) Acta Mater., 46-14, 5007
7. Mabuchi, H. and Ishikawa, T. (1997) Proc. Mat. Sol. '97 Accel. Cooling/Direct Quen. Steels, 43

Offset method for determination of lower-bound fracture toughness in the transition temperature region

T.Iwadate[1)] and H.Takemata[2)]

1) Research & Development Headquarters
The Japan Steel Works, Ltd.
2-2-1, Fukuura, Kanazawa-ku, Yokohama, 236-0004, Japan
2) Hokkaido Polytechnic Center
1-7-1,4-jyou, 24-ken, Nisi-ku, Sapporo, 063-0804, Japan

ABSTRACT

The fracture toughness K_{JC} values of small specimen in the transition temperature region were analyzed to confirm the offset method standardized by JSPS 129 Committee. The offset method is a very useful method for the determination of lower-bound fracture toughness K_{JCi} of material especially in the lower shelf temperature region where the stable crack growth is smaller than about 0.2 mm. The K_{JCi} values obtained from the offset method showed a good agreement with the K_{IC} value of large specimens per ASTM E399 and the K_{JCi} values from the fractography method standarized by JSPS 129 Committee.

KEY WORDS

Elastic plastic fracture, Fracture toughness, Transition region, J-integral,Testing Technique

INTRODUCTION

The J_{IC} testing method of JSME S001 and ASTM E813 using small specimens can measure the fracture toughness of materials in the upper shelf temperature region. However, in the transition temperature region, the J_{IC} testing method has a problem, that is, the large scatter of the measured fracture toughness(1-3). In the other hand, the K_{IC} testing method of ASTM E399 is useful in the transition temperature region, but the measure of K_{IC} values requires large specimens which leads to the large amount of testing cost and manufacturing cost of the specimen.

Recently, Japan Society for the Promotion Science (JSPS) 129 Committee (chairman, Takeo Yokobori)proposed the standaraized testing methods to obtain the lower-bound fracture toughness in the transition temperature region using small specimens which consists of the

fractrography method based on the observation of fracture surface of the specimens and the simplified offset method(4-5). This study is the background study of the offset method recommended by JSPS 129 Committee.

TEST METHOD

The materials used in this study are A508 Cl.3 and A533B nuclear pressure vessel steels of which the mechanical properties are shown in Table 1. Both steels were used for the international cooperative round robin tests by JSPS 129 Committee and MPC(Material Properties Council). The A533B steel is the material that the impurities elements were

Table 1 Mechanical properties of the steels used.

Steels	σ_{YS}(MPa)	σ_{TS}(MPa)	El.%	R.A.(%)	FATT(K)	NDTT(K)	CVN-us(J)
A508C1.3	456	599	24.8	75.9	258	243	245
A533B	504	692	20.2	52.0	323	-	70
A470	644	766	23.8	63.0	271	-	165

controlled by which the toughness was reduced(4-5). For the comparison of the fracture toughness between the offset method and K_{IC} tests method, the A470 Ni-Cr-Mo-V steel (Table 1) for turbine rotors was used.

The specimens used are 0.5T-CT, 1T-CT, 2T-CT, 4T-CT and 6T-CT specimens with 20% side grooves. Fatigue precracks of $a_o/W=0.50 \sim 0.65$ (a_o : precrack length,W : specimen width) were ntroduced under JSME S001 and ASTM E813. The specimens were fractured by strain controlled loading. The number of specimens used were more than five at the same test temperatures.

J-integral were culculated from the load-strain curve at the loading point, and converted to the fracture toughness using the equation.

$$K_{JC}=[J_C/(1-\gamma^2)]^{1/2} \qquad (1)$$

where E is the Young's modulus and γ is Poisson's ratio.

FRACTURE TOUGHNESS IN THE TRANSITION TEMPERATURE REGION

Figure 1 shows the test results of the fracture toughness of A508 Cl.3 steel obtained by the Japanese laboratories (4-5), and Figure 2 shows the test results of fracture toughness of A533B steel obtained by authors . The large scatter of fracture toughness K_{JC} values are observed in both steels, especially in the higher temperature region. And also, the scatter becomes larger as the specimens size is smaller. Figure 3 shows the fracture process of specimens. When the specimen with fatigue crack is loaded, with increasing the load, the

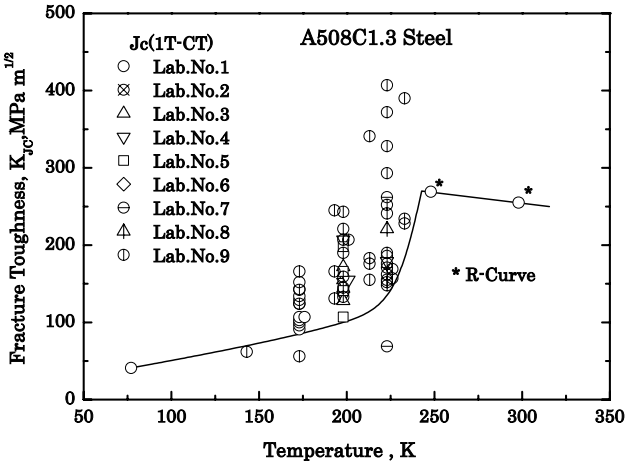

Fig.1 Fracture toughness K_{JC} values as a function of temperature for A508Cl.3 steel.

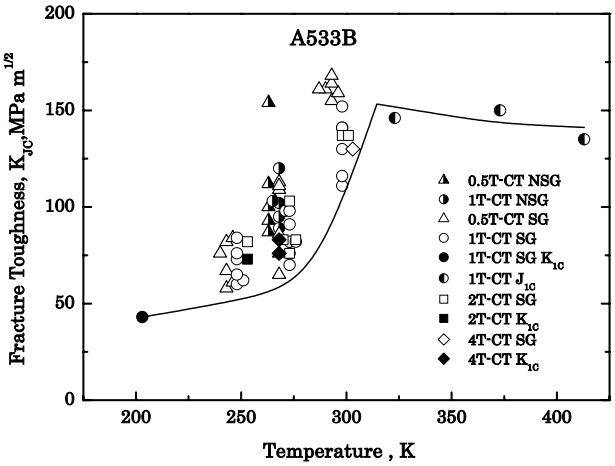

Fig.2 Fracture toughness K_{JC} values as a function of temperature for A533B steel.

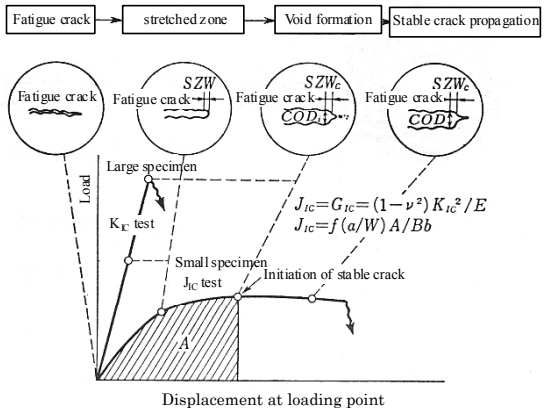

Fig.3 Fracture process around a crack tip.

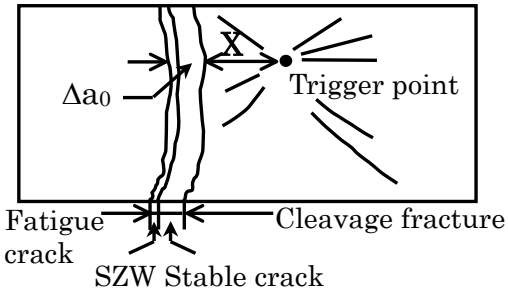

Fig.4 Schematic representation of Δa_o,X and Δa_o+X.

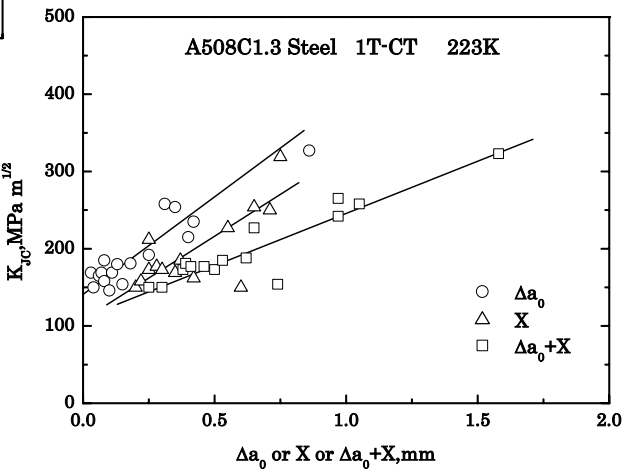

Fig.5 K_{JC} vs.Δa_0, K_{JC} vs.X and K_{JC} vs.Δa_0+X relationships.

crack tip is stretched and becomes blunt. And then, the boids initiates ahead of the stretched zone. During the following loading, the boids are combined, by which the stable crack initiates. After the initiation of stable crack, it grows larger when the load increases. The premature fracture occurs at the weakest point, that is, the trigger point which may be caused by the ununiformity of the material. Therefore, the scatter of the fracture toughness is controlled by the stable crack length, Δa_o, and the distances to the trigger point, X, and /or Δa_o+X (6-7).

The fracture surfaces of the broken specimens were observed using Scanning Electron Microscope (SEM). The stable crack length Δa_o , the distance from the tip of the stable crack front to trigger point X, and Δa_o+X in Fig.4 were measured. Figure 5 shows the relationship

between the fracture toughness K_{JC} and Δa_o or X or Δa_o+X. The K_{JC} values show the good relationship with Δa_o, X, Δa_o+X. The scatter of fracture toughness K_{JC} is controlled by the mount of Δa_o, X, and Δa_o+X. This is the background of the fractography method recommended by JSPS 129 Committee.

THE PROPOSAL OF OFFSET METHOD

The offset method proposed in this study is the simplified method to obtain the lowest value of fracture toughness J_{Ci} or K_{JCi}, which is based on the assumption that the slope dJ/da of the elationship between J_C and Δa_o, and /or the slope dK/da of the relationship between K_{JC} and Δa_o, are constant. The test procedure is as follows.

(1) At first, to obtain the J-R curve of the material, the fracture toughness test is conducted in the upper shelf temperature region using unloading compliance method. And the J-R curve shown by the relationship between J-integral and stable crack growth Δa_0 is obtained

(2) The offset line is drawn at the distance of Δa_o=0.2mm in the parallel to the trangent line of R curve from the original point as shown in Fig.6(a). Here, the K-R curve shown by the relationship between K_J and Δa_o can be used instead of J-R curve.

(3) The slope n is detetrmined by drawing the tangent line to R curve at the cross point between the offset line and J-R curve or K-R curve.

(4) And then, at the test temperature in the transition temperature region, the fracture toughness tests are conducted using 6 specimens. The relationship between J_C value at fracture and stable crack growth Δa_o,
or K_C value and Δa_o is obtained.

(5) The obtained six J_C and/ or K_C and Δa_o relationships are plotted as shown in Fig.6(b). And the parallel lines to the slope n are drawn to pass the each data. The smallest value at the cross point between the slope n and the longitudinal lines is defined as the lowest fracture toughness Jci and K_{JCi}.

(6) In the case that the measure of R-curve at the upper shelf temperature can not be conducted, the six test specimens are fractured at the test temperature using unloading compliance method with measuring J-R curve or K-R curve.

(7) The lines of the constant n=400J/m^3 to J-R curve or the lines of the constant n=300 MPa·m$^{1/2}$/mm to K-R curve are drawn to pass the J_C or K_{JC} points of each fractured specimen as shown in Fig.7.

(8) The smallest J_{Ci} or K_{JC} value determined by the cross points between thse line and longitudinal line is defined as the lowest fracture toughnesse J_{Ci} or K_{Ji}.

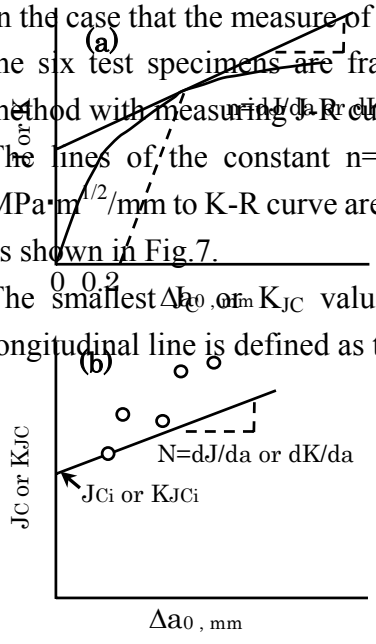

Fig.6 Representation of the offset method using slope n of R-curve.

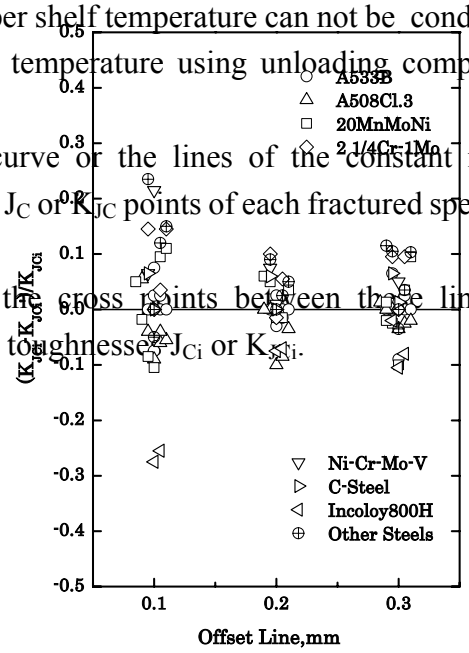

Fig.8 $(K_{JCi}-K_{JCi}')/K_{JCi}$ value at each offset tangent line.

DISCUSSIONS

In the case of the offset method, the slope n must be obtained by drawing the offset line of 0.2 mm in the upper shelf temperature region. Figure 8 shows the accuracy of the obtained fracture toughness, that is, the difference between K_{JCi}' and K_{JCi}, where K_{JCi}' was determined using the mean value of the slope n obtained at the cross point of 0.1, 0.2, 0.3 mm offset lines on K-R curves of 38 materials, and K_{JCi} was obtained from the slope n of each material. The difference between the fracture toughness K_{JCi}' and the fracture toughnesses K_{JCi} of each material is larger than ±10% in the use of the 0.1 mm offset line, and is within ±10% in the use of 0.2 mm and 0.3mm offset lines. In the other hand, according to the observation of the premature fractured specimens, the lengths of stable crack growth Δa_o were less than 0.2 mm. Therefore, the 0.2mm offset line was selected.

In the case that the fracture toughness test in the upper shelf temperature region can not be conducted, the more simplified method using the constant slope n was proposed. This proposal is very useful and very simple because anybody can measure the same fracture toughness K_{JCi} value. Figure 9 shows the slope n decided using 0.2 mm offset lines of 38 materials. To measure the lowest fracture toughness of material,the slopes n should be larger. From Fig.9, n=300 MPa·$m^{1/2}$/mm was selected as the slope which gives larger values more than 90% for K-R curves. And for J-R curves, the corresponding slope n=400J/m^3 was also selected.

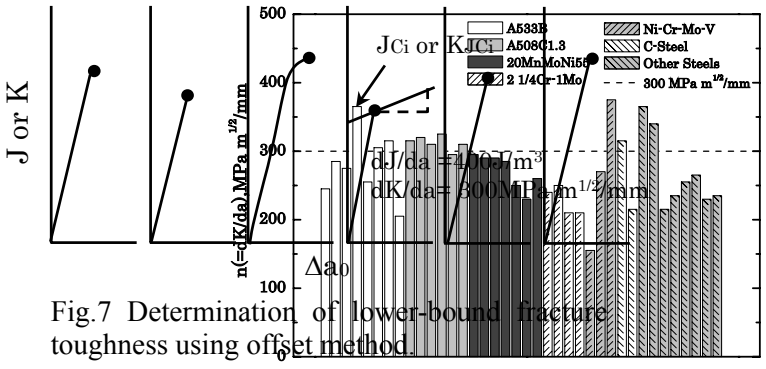

Fig.7 Determination of lower-bound fracture toughness using offset method.

Fig.9 Slope n determined from 0.2mm stable crack growth offset tangent line.

COMPARISON BETWEEN K_{JCi} FROM THE OFFSET METHOD AND K_{IC} OF LARGE SPECIMENS

Fig.10 and Fig.11 show the comparison among K_{JCi} values obtained using the offset method, K_{JCi} values obtained by the fractgraphy method[5] and the valid K_{IC} values of large specimens per ASTM E399 for A533B steel and A470Ni-Cr-Mo-V steel, respectively.

The K_{JCi} values obtained by the offset method showed a good agreement with K_{JCi} values from

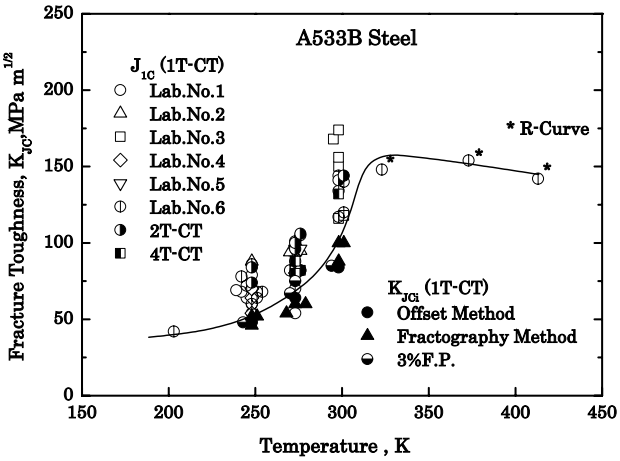

Fig.10 Comparison of K_{JCi} values obtained from the offset method and fractgraphy method and and fractgraphy method and valid K_{JC} values for A533B steel.

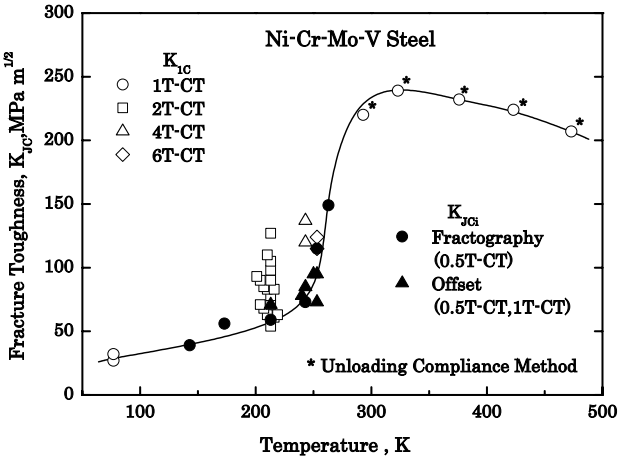

Fig.11 Comparison of K_{JCi} values obtained from the offset method and fractography method and valid KIC values for A470 Ni-Cr- Mo-V steel.

the fractgraphy method and the lowest value of K_{IC} of large specimens. This suggests that the offset method is valid for measuring the lower-bound fracture toughnesses K_{JCi} of materials in the transition temperature region.

CONCLUSION

In this study, the offset method is recommended as one of the standard test methods by JSPS 129 Committee to measure the lower-bound fracture toughnesses K_{JCi} in the transition temperature region using small specimens. The obtained K_{JCi} values using offset method showed a good agreement with the K_{IC} values of large specimens.

This study was conducted as one of the cooperative studies under the Toughness Testing Task Group of JSPS 129 Committee (chairman, Takeo Yokobori).

REFERENCES

[1]. J.D.Landes and D.H.Shaffer, Fracture Mechanics : Twelfth Conference, ASTM STP700, 368(1980).

[2]. D.E.McCabe and J.D.Landes, Scientific Paper 83-ID7-METEN-P3, Westinghouse Electric Corp.(1983).

[3]. T.Iwadate, Y.Tanaka, S.Ono and J.Watanabe, Elastic-Plastic Fracture : Second Synposium, Vol.3, ASTM STP803, 2-531(1983).

[4]. T.Iwadate and T.Yokobori, Fracture Mechanics : Twenty-Fourth Volume, ASTM STP1207, 233(1994).

[5]. Standard by JSPS 129 Committee “The standard test method of the brittle fracture

toughness in the ductile-brittle transition region", JSPS 129 Committee(1995).
[6].J.Watanabe, T.Iwadate, Y.Tanaka, T.Yokobori and K.Ando, Engineering Fracture Mechanics, 28, No.5/6, 589(1987).
[7]. Y.Tanaka, J.Watanabe and T.Iwadate, The Japan Society of Mechanical Engineers, Series A, 499,557(1988).

ON ANISOTROPY EFFECTS IN DUCTILE FRACTURE: THEORY AND APPLICATIONS

A. A. Benzerga[1], J. Besson[1] and A. Pineau[1]
[1] Ecole des Mines de Paris, Centre des Matériaux,
UMR CNRS 7633, BP 87, F91003 Evry Cedex

ABSTRACT

This paper proposes a general framework for post-coalescence modelling. Constitutive relations include an ad-hoc yield surface depending on the first and second invariants of the stress tensor along with evolution laws for the microstructural variables, namely ligament size, void shape and void spacing ratio. The loss of stress carrying capacity is then a natural outcome of the formulation. Anisotropic failure in a pipe steel is modelled using a finite element implementation of the model.

KEYWORDS

Anisotropic sheets, porous plastic solids, plastic anisotropy, void shape, post–coalescence

INTRODUCTION

Micromechanical modelling of coalescence is key to understanding the role of microstructure on the fracture properties of ductile solids. In a previous work [1], microstructural effects on the onset of coalescence were investigated; instead of being fitted on experiments, critical porosities were predicted and used to simulate failure in notched bars. Incorporating void shape effects is crucial at low stress triaxiality even with no initial anisotropy [2, 3]. At high stress triaxiality, the influence of void shape is less an issue, but the material undergoes as much deformation after the onset of coalescence as prior to it [4]. This raises the issue of modelling post–coalescence. To do so, void shape effects have to be accounted for [1]. In this paper, a new approach is used, which is based on a recent micromechanical model for post–coalescence [5]. A series of finite element calculations are carried out and compared with experiments conducted on a C–Mn pipe steel containing elongated inclusions.

MODELLING

Pre–coalescence Behaviour

The constitutive framework is that of anisotropic porous plastic solids. Anisotropy here refers to the plastic anisotropy of the matrix material [6] and to void shape effects [2]. For a solid containing spheroidal cavities and respecting transverse isotropy, the plastic potential reads in a frame $(\underline{\mathbf{e}}_x, \underline{\mathbf{e}}_y, \underline{\mathbf{e}}_z)$ related to cavities

$$\Phi = C\frac{||\underset{\sim}{\Sigma}' + \eta\Sigma_h\underset{\sim}{\mathbf{X}}||^2}{\sigma_\star^2} + 2q_w(g+1)(g+f)\cosh\left(\frac{\kappa\Sigma_h}{\sigma_\star}\right) - (g+1)^2 - {q_w}^2(g+f)^2 = 0 \tag{1}$$

where $(\,)'$ denotes deviatoric quantities, $\sigma_\star$ is the matrix flow strength, f is the void volume fraction and

$$\Sigma_h = \alpha_2(\Sigma_{xx} + \Sigma_{yy}) + (1 - 2\alpha_2)\Sigma_{zz} \tag{2}$$

$$\underset{\sim}{\mathbf{X}} = \frac{1}{3}(-\underline{\mathbf{e}}_x \otimes \underline{\mathbf{e}}_x - \underline{\mathbf{e}}_y \otimes \underline{\mathbf{e}}_y + 2\,\underline{\mathbf{e}}_z \otimes \underline{\mathbf{e}}_z) \tag{3}$$

$$q_w = 1 + (q-1)\cosh^{-1} S \tag{4}$$

where $\underline{\mathbf{e}}_z$ is the common axis of the voids and g, κ, α_2, η and C are scalar functions of the porosity, f, and the shape parameter, S, defined as the logarithm of the void aspect ratio. Analytical expressions of these functions can be found in [2, 5]. The evolution of porosity is the consequence of mass conservation and is derived from the potential Φ assuming normal flow [7]. The evolution of S is given by (see [2])

$$\dot{S} = \frac{3}{2}\left[1 + \frac{9}{2}h_{\mathcal{T}}(\mathcal{T})(1-\sqrt{f})^2\frac{\alpha_1 - \alpha_1^G}{1-3\alpha_1}\right]D'_{zz} + 3\left(\frac{1-3\alpha_1}{f} + 3\alpha_2 - 1\right)D_m \tag{5}$$

$$h_{\mathcal{T}} = 1 - \frac{\mathcal{T}^2 + \mathcal{T}^4}{9} \tag{6}$$

where D_m^{p} and D'^{p}_{zz} are the mean part of the plastic strain rate, $\underset{\sim}{\mathbf{D}}^{\mathrm{p}}$, and the axial component of $\underset{\sim}{\mathbf{D}}'^{\mathrm{p}}$ respectively. α_1 and ${\alpha_1}^G$ depend on S only and $\mathcal{T}$ is the stress triaxiality ratio.

Plastic anisotropy is introduced through the first term which appears in the development of the norm $||\ ||$ in (1). Based on an equivalent extension in the case of spherical or cylindrical cavities [6], it is suggested to replace the Mises stress by the Hill quadratic stress [8] using a frame $(\underline{\mathbf{E}}_X, \underline{\mathbf{E}}_Y, \underline{\mathbf{E}}_Z)$ pointing onto the principal directions. Correlatively, $\sigma_\star$ is replaced by the flow strength along X. Principal axes of orthotropy are taken to be the void axes and only loadings parallel to these axes are considered such that cavities do not rotate relative to the frame of orthotropy, Fig. 1. In this case, it is reasonable to assume that the voids rotate at the same velocity as the material. The voids, however, are allowed to be perpendicular to the loading; see Figure 1(b). In this case initial axisymmetry is broken and an approximated spheroidal shape is still assumed in average [5]. The first finite–element simulations using this constitutive model were discussed by Benzerga *et al.* [9].

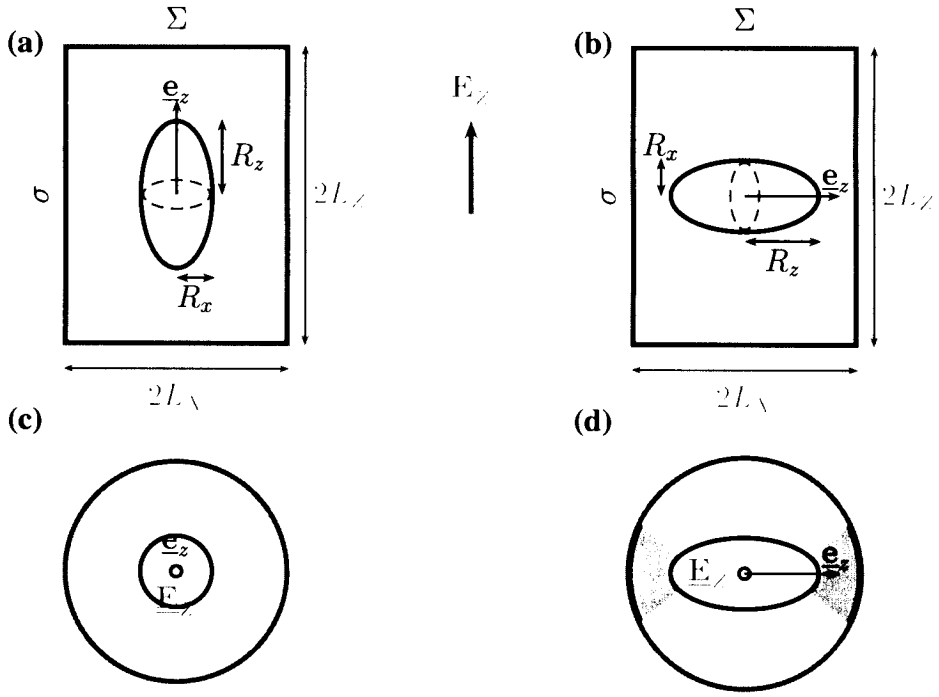

Figure 1: Schematic view for the treatment of initial anisotropy. *(a) case of* $\underline{\mathbf{e}}_z \parallel \underline{\mathbf{E}}_Z$ *with* $\chi \equiv R_x/L_X$ *given by (9), (b) case of* $\underline{\mathbf{e}}_z \perp \underline{\mathbf{E}}_Z$ *with* $\chi \equiv R_z/L_X$ *if* $S > 0$ *and* $\chi \equiv R_x/L_X$ *if* $S < 0$. *(c) and (d) views in the plane of coalescence corresponding to (a) and (b) respectively.*

Onset of Coalescence

Coalescence is taken to occur when the smallest ligament between neighbouring voids attains its limit–load [10]. A three–dimensional criterion for void coalescence is written as

$$(1-\chi^2)\,C_f(\chi, S) = \left(\frac{2}{3} + \mathcal{T}\right)\frac{3\,\underset{\sim}{\Sigma}' : \underset{\sim}{\mathbf{H}} : \underset{\sim}{\Sigma}'}{2\,\sigma_\star^2} \tag{7}$$

where χ is the ligament size defined as the ratio of current void diameter along X to current spacing along X, L_X; see Figure 1. $\underset{\approx}{\mathbf{H}}$ is Hill's tensor previously defined and C_f is the limit–load factor given by

$$C_f = 0.1\left(\frac{\chi^{-1}-1}{e^{-S}+\alpha\chi^{-1}}\right)^2 + 1.2\sqrt{\chi^{-1}} \tag{8}$$

where modification from an original form [11] has been included following [5]. In [11] C_f diverges for penny–shaped cracks. Here $\alpha = 0.14$. The expression of χ depends on the loading configuration [5]

$$\chi^3 = \begin{cases} \dfrac{3}{2} f\lambda\, \mathrm{e}^{-S} & S < 0 \\ \dfrac{3}{2} f\lambda & S > 0 \quad \text{and} \quad \underline{\mathbf{e}}_z \perp \underline{\mathbf{E}}_Z \end{cases} \tag{9}$$

where $\lambda \equiv L_Z/L_X$ is the spacing ratio. Refer to [1] for an evaluation of criterion (7) in the case $\underline{\mathbf{e}}_z \parallel \underline{\mathbf{E}}_Z$

Post–coalescence Behaviour

The model used here is based on [5] and defined by a set of constitutive relations including an expression of the yield surface along with appropriate evolution laws for the shape parameter and the ligament size ratio, χ.

Yield function

When criterion (7) is fulfilled, the behaviour is no longer given by (1–5). Indeed, localization, which pertains to post–coalescence, unambiguously sets the normal to the yield surface. The latter is then defined by

$$\Phi^{(c+)}(\underset{\approx}{\Sigma}, \chi, S) = \frac{\Sigma_{\mathrm{eq}}}{\sigma_\star} + \frac{1}{2}\frac{\underset{\approx}{\mathbf{I}} : \underset{\approx}{\Sigma}}{\sigma_\star} - \frac{3}{2}(1-\chi^2)\, C_f(\chi, S) \tag{10}$$

(10) is rigorously stated for isotropic plasticity. Using Σ_{eq} according to Hill, as previously defined, is the simplest heuristic extension to plastic anisotropy.

Evolution laws

These are appropriately formulated in terms of the shape parameter, S, and the ligament size ratio, χ. For an arbitrary convex shape, the ligament size ratio is given by (provided that $\underline{\mathbf{e}}_z \parallel \underline{\mathbf{E}}_Z$)

$$\chi = \left[3\gamma f \lambda \mathrm{e}^{-S}\right]^{1/3} \tag{11}$$

γ is a shape factor: $\gamma = 1/2$ for a spheroid and $\gamma = 1$ for a cone. The rates of χ and S are given by (see [5])

$$\dot{\chi} = \frac{3\gamma}{2}\frac{\lambda}{W}\left[\frac{3}{2\chi^2} - 1\right] D_{\mathrm{eq}} \tag{12}$$

$$\dot{S} = \frac{9}{4}\frac{\lambda e^{-S}}{\chi}\left[\frac{2(1+\gamma)}{3} - \frac{\gamma}{\chi^2}\right] D_{\mathrm{eq}} \tag{13}$$

The full model is implemented in the finite element code ZeBuLoN [12].

MATERIAL IDEALIZATION

The material modelled is a pipe steel cut from a rolled sheet of grade X52. The frame related to the sheet is (L,T,S) with L being the rolling axis, T the transverse axis and S the through–thickness axis. Material characterisation and tensile tests on round notched bars are presented elsewhere [1]. Due to the working process, the material exhibits a marked anisotropy of plastic flow, which can be represented using a quadratic yield criterion with the following Hill coefficients: $h_{\mathrm{L}} = 0.96$, $h_{\mathrm{T}} = 0.88$, $h_{\mathrm{S}} = 1.28$, $h_{\mathrm{TS}} = 1.30$, $h_{\mathrm{SL}} = 1.15$ and $h_{\mathrm{LT}} = 1.09$. The main inclusions involved in the damage process are equiaxed particles (mainly oxides),

with a volume fraction of 0.00035, and manganese sulfides (MnS stringers) with a volume fraction of 0.0004 [5]. Inclusion shape and spacing were characterised using metallography and Dirichlet tessellation techniques. For MnS particles, the average representative element is made of a stringer parallel to L and 1.5μm thick, embedded in a box with the dimensions: $\overline{S}_{\rm S} \approx 353\,\mu$m, $\overline{S}_{\rm L} \approx 420\,\mu$m and $\overline{S}_{\rm T} \approx 223\,\mu$m. The equiaxed particles were found to be isotropically distributed [5]. The hardening law used in the computations is

$$\sigma_\star(p) = R_0 + a\,p + Q\,\left(1 - e^{-b\,p}\right) \tag{14}$$

where p is the cumulated plastic strain, $R_0 = 426$MPa, $a = 239.8$MPa, $Q = 162.3$MPa and $b = 16.1$.

Nucleation is supposed to be homogeneous and the material is assigned an initial porosity, f_0, which is equal to the volume fraction of both sulfides and oxides or to that of sulfides only, depending on the fracture mechanism. To handle the 3D shape of sulfides, one needs to define an equivalent spheroidal shape based on the formula: $W_0 \equiv \sqrt{\overline{W}^{\rm T}\,\overline{W}^{\rm S}}$, where $\overline{W}^{\rm T} = 32$ and $\overline{W}^{\rm S} = 7.5$ are respectively the length–to–thickness and length–to–width ratios of the particle. The average initial shape parameter is then $S_0 = \ln(W_0) = 2.74$. Similarly, the average spacing ratio is calculated as $\lambda_0^{\rm L} \equiv \sqrt{\overline{\lambda}^{\rm T}\,\overline{\lambda}^{\rm S}}$, for loadings parallel to L, with $\overline{\lambda}^{\rm T} = 1.20$ and $\overline{\lambda}^{\rm S} = 1.90$ which gives $\lambda_0^{\rm L} = 1.5$. Using $\overline{\lambda}^{\rm L} = 0.63$ one also gets $\lambda_0^{\rm T} = 0.6$ for loadings parallel to T.

RESULTS

Notched bars are denoted $\rm AN_\zeta$ where ζ is ten times the ratio of notch radius to the minimal section diameter. Results are shown for two of the tested geometries: $\rm AN_{10}$ and $\rm AN_2$. 3D meshes are used for 1/8 of the specimen. For computational efficiency, the elements close to the minimal section are initially flat in order to have them roughly square at incipient fracture. The element size in the plane of coalescence is 325μm. Boundary conditions are imposed in terms of a prescribed displacement on the top of the specimen. Other symmetry conditions are used to eliminate any rigid–body motion as in [1]. Quadratic quadrilateral sub–integrated elements with updated Lagrangian formulation are used. In line with experimental observations, the values of the shape factor γ are 0.8 and 0.5 for L–loading and T–loading respectively.

Figure 2 shows selected curves of force versus diameter reduction, normalised by the initial diameter, $\Phi_0 = 1.95$mm. Experimental results are represented by points. These have been inferred from interrupted tests in order to follow the development of plastic anisotropy. For a major stress oriented along L (i.e. L–loading), the initial microstructure was $f_0 = 0.075\%$, $S_0 = 1.95$ and $\lambda_0^{\rm L} = 1.5$. It is assumed that the two populations of particles, MnS and oxides, nucleate voids. Comparison of Figs 2(a) and (b) clearly shows that the previous assumption is quite good for the $\rm AN_2$ specimen but that ductility of the $\rm AN_{10}$ specimen is overestimated. It is likely that the onset of coalescence at low triaxiality be due to voids nucleated at equiaxed particles, as supported by experimental observations [5].

For T–loading, we relax the assumption upon the initial equivalent microstructure. Hence, for the $\rm AN_{10}$ specimen, only MnS particles were taken into account and the values $f_0 = 0.04\%$, $S_0 = 2.35$ and $\lambda_0^{\rm T} = 0.6$ were used. On the other hand, the values $f_0 = 0.075\%$, $S_0 = 2.35$ and $\lambda_0^{\rm T} = 1$ were used in the case of the $\rm AN_2$ specimen, which means that the equiaxed particles are incorporated as for their contribution to the volume fraction and the distribution of initial voids. Comparison of Figs 2(c) and (d) suggests that the latter assumption provides better correspondence with experiments.

These results show that it is possible to predict the fracture anisotropy in the modelled steel provided that one has knowledge about the initial microstructure and fracture mechanisms. It is worth noting that two types of damage anisotropy emerge in these calculations. The first one is related to the shape and distribution of the MnS particles. At a given constraint, i.e. at fixed ζ, the material is much more resistant when the major stress is oriented along the longitudinal direction and the model accounts for this initial anisotropy. Second, there is an induced anisotropy due to plastic orthotropy of the matrix material as discussed in [6]. Contours of constant void volume fraction in any specimen loaded along L show that the development of damage is much more rapid in the transverse direction, although diameter reduction is lower.

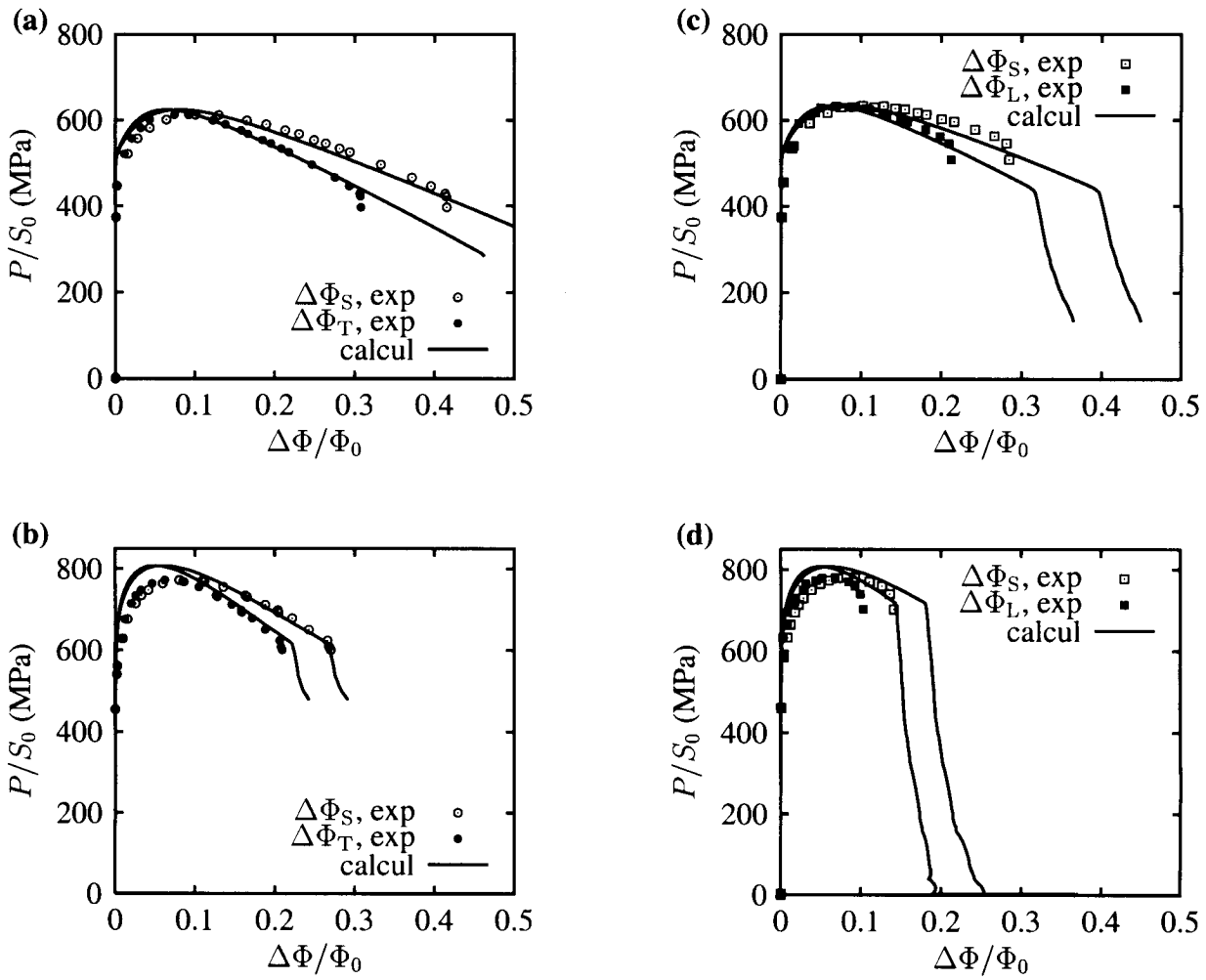

Figure 2: Load *vs* diameter reduction curves for round notched bars. *(a) L–loading and* $\zeta = 10$*; (b) T–loading and* $\zeta = 10$*; (c) L–loading and* $\zeta = 2$*; (d) T–loading and* $\zeta = 2$*. Points are for experimental results.*

Anisotropy of the fracture process is illustrated in Figure 3 in the case of the $AN_{10}T$ specimen. When criterion (7) is attained at the center of the specimen, Fig. 3(a), the macroscopic force drops for the first time (see Fig 2(c)) although there is no macroscopic crack yet. This is indicated by the activation of the post–coalescence index `pc` in Fig. 3(a) while the fracture index `broken` is still deactivated. The fact that `pc` $\neq 0$ means that the ligament size has attained its limit load. As a consequence, the behaviour of corresponding elements is given by (10-13). Upon continued deformation, the region which undergoes post–coalescence enlarges anisotropically as a result of plastic anisotropy. At stage (b), a macroscopic crack initiates. Crack propagation then occurs along the elements which have undergone post–coalescence until the force is reduced to zero. It is worth emphasizing that the material loses all stress carrying capacity as a natural outcome of ligament reduction as described by the post–coalescence model.

CONCLUSIONS

Microstructure effects were investigated in an anisotropic sheet using a micromechanical model which accounts for post–coalescence. No adjustable factor was used. Microstructural parameters needed as an input of the simulations were inferred from quantitative metallography. Hence, the calculations are by no means biased towards the experimental results. This in turn allowed for a full discussion of pertinent mechanisms that cause fracture. In a $AN_{10}L$ specimen, the average triaxiality is 0.8 and the elongated cavities nucleated on MnS particles hardly lead to coalescence; coalescence is rather due to equiaxed particles. This is the reason why ductility was overestimated in this case. In the sharply notched specimen AN_2L, however, the triaxiality is

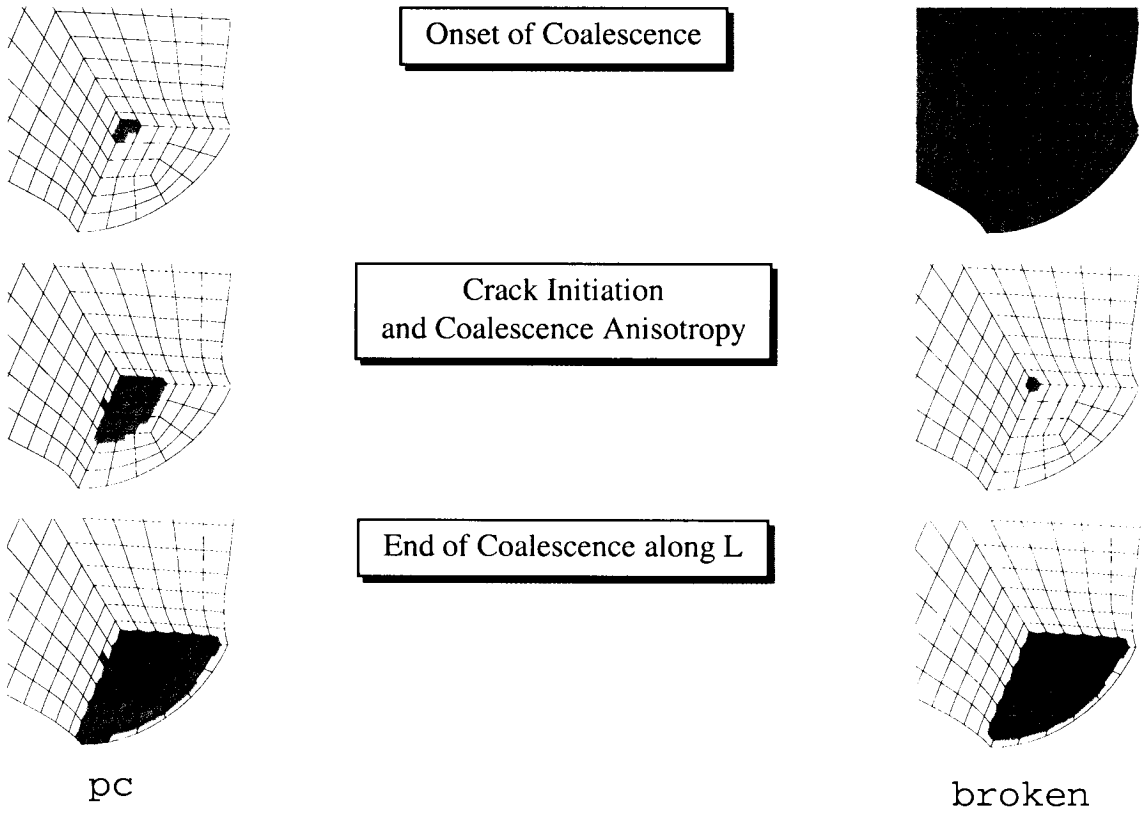

Figure 3: Coalescence anisotropy and crack growth in the notch region of AN_{10} specimen loaded along T–direction. *(a) post–coalescence index* `pc`*; elements undergoing coalescence are painted black. (b) Broken elements (i.e.* $\chi \equiv 1$*) are painted black.*

high enough to activate both populations of cavities and the results are then more consistent with experimental ones. Similar conclusions can be drawn for T–loading provided that the equiaxed particles are incorporated in the spatial arrangement.

Acknowledgements
Support from Gaz de France (Direction de la Recherche) is gratefully acknowledged. AAB thanks F. Curie for helpful contribution to the quantitative metallography.

References

[1] A. A. Benzerga, J. Besson, and A. Pineau. *J. Eng. Mat. Tech.*, 121(2):221–229, 1999.
[2] M. Gologanu, J.-B. Leblond, G. Perrin, and J. Devaux. In P. Suquet, editor, *Continuum Micromechanics*, pp 61–130. Springer–Verlag, 1995.
[3] P. Ponte Castañeda and M. Zaidman. *J. Mech. Phys. Solids*, 42:1459–1495, 1994.
[4] J. Koplik and A. Needleman. *Int. J. Solids Structures*, 24(8):835–853, 1988.
[5] A. A. Benzerga. PhD thesis, Ecole des Mines de Paris, March 2000. parts in english.
[6] A. A. Benzerga and J. Besson. *Eur. J. Mech.*, 2001. accepted.
[7] A. L. Gurson. *J. Eng. Mat. Tech.*, 99:2–15, 1977.
[8] R. Hill. *Proc. Roy. Soc. London A*, 193:281–297, 1948.
[9] A. A. Benzerga, J. Besson, R. Batisse, and A. Pineau. In M. W. Brown, E. R. de los Rios, and K. J. Miller, editors, 12^{th} *Eur. Conf. on Fracture*, pp 715–720. ESIS, Eur. Group on Fracture Publication, 1998.
[10] A. H. Cottrell. In B. L. Averbach, editor, *Fracture*, pp 20–53. Chapman and Hall, London, 1959.
[11] P. F. Thomason. *Acta Metallurgica*, 33(6):1079–1085, 1985.
[12] J. Besson and R. Foerch. *Comput. Methods Appl. Mech. Engrg*, 142:165–187, 1997.

Submitted to 10 International Conference of Fracture, which will be held December 3 – 7, 2001 at Honolulu, USA

ON BRITTLE FRACTURE IN F.C.C.-METAL

Peter Panfilov and Alexander Yermakov
Laboratory of Strength, Urals State University, 620083 Ekaterinburg, Russia

ABSTRACT

Fracture behavior of inherently brittle and environmentally induced brittle f.c.c.-metals, including evolution of cracks in bulk crystals and thin foils for transmission electron microscope, is considered in this paper. Refractory iridium and gallium covered aluminum are chosen as model substances. In spite of brittle fracture, these materials show good plasticity, which is considerably limited in polycrystalline aggregates because of low grain boundary strength. In both cases, inclination to brittle fracture takes place in bulk crystals only, while thin foils fail by ductile manner. The causes of brittle crack appearance in f.c.c.-metals and physical model of crack evolution in plastic metal are discussed.

KEY WORDS: brittle fracture, plastic deformation, cracks, f.c.c.-metal, iridium

INTRODUCTION

According to long term experience, ductility of crystalline solid does not allow it to fail by brittle manner, and impossibility of dislocation motion is usually considered as the main physical cause for brittleness [1]. The border situation, when ability of crystal to plastic deformation is substantially limited, has being the subject for many researches aimed on micro mechanisms of brittle fracture [2-5]. Conception of dislocation emission from crack tip turned out to be helpful instrument for study of brittle to ductile transition in materials, where dislocation motion is bothered. The model shows good agreement with mechanical behavior of high strength alloys and intermetallics having face centered cubic (f.c.c.) lattice, but it could not be applied to the pure metals, since no any dislocation barriers, particles of the second phase or strong directed interatomic bonds exist here. Despite this platinum group metal iridium fails by brittle manner under mechanical load and, in addition, meets few empirical criteria for brittle fracture [6]. Also, intercrystalline and transcrystalline brittleness of pure f.c.c.-metals could be induced by liquid metals [7]. Phenomenon of brittle fracture in f.c.c.-metal and its physical model, including crack growth, are discussed in this paper.

Iridium is unique f.c.c.-metal due to highest melting point (2443oC) and chemical inertia [6]. Strong interatomic bonds cause an anomaly in elastic modules, which are similar to ones for refractory body centered cubic (b.c.c.) metals [8,9]. Besides its workability is very poor and fracture modes are determined as brittle intercrystalline fracture (BIF) and brittle transcrystalline fracture (BTF) for poly- and monocrystalline states, respectively [10,11]. The problem of processing iridium was successfully solved, when refining technology, allowed to remove all dangerous impurities from the metal, has been elaborated [12]. However, impurities–free iridium crystals continues to cleave under tension in spite of huge elongation prior the failure (100% at 100oC!) [13], while an inclination to BTF mysteriously vanishes under compression tests [14]. In contrast with single crystals, ever high pure polycrystalline

iridium fails practically without preliminary deformation demonstrating 100% BIF on fracture surface [15]. Therefore, iridium was called inherently brittle f.c.c.-metal the more so it unexpectedly meets empirical criteria for brittle fracture [7,16]. The last means that fracture mechanics could be formally applied to this f.c.c.–metal without any limits, although physical reasons did not allow to do that [17]. Observations of V–shaped cracks on bulk crystals [7] seems like confirmation of inclination to brittleness, however both considerable plasticity of material and big angle of crack opening point to specific character of "iridium brittleness". In any case findings on fracture behavior of iridium are extremely important for understanding the mechanisms of brittle fracture in metallic materials, since it gives an fortunate opportunity to watch simultaneously evolution of cracks and deformation process around them by direct means.

The main cause of liquid metal induced brittleness in polycrystalline f.c.c.–metals is catastrophic decrease of grain boundary strength because of influence of liquid metal atoms [18]. BTF induced by liquid metals is very rare phenomenon, which is only observed in aluminum crystals covered by gallium or mercury, and, therefore, there are not generally accepted physical models of brittle crack growth in literature [7].

THE CAUSE OF BRITTLE BRACTURE IN IRIDIUM

Simplest arguments have been laid in the basis of presented physical model. Brittle fracture becomes possible when a crystal cannot be plastically deformed under mechanical load, inasmuch as either it is undeformable material or its resource of plasticity has been exhausted during preliminary deformation. Without a doubt, the second way should be chosen for high plastic f.c.c. –metal, whose fracture surface looks like BTF or mixture of BTF and BIF. Strong interatomic bonds are only one inherent distinction between refractory iridium and other f.c.c.–metals, but namely this circumstance causes low mobility of dislocations and as aftermath the highest value of yield stress at room temperature. Octahedral slip of <110> dislocations is the dominant deformation mechanism in iridium, therefore its strong hardening under load could not be connected with alternative ones like mechanical twinning or non-octahedral slip [19]. Consequently, mobile <110> dislocations should create the obstacles for octahedral slip, what, however, it is impossible in normal f.c.c.-metal ever at low temperatures [20,21]. Experiments have shown, that all huge plasticity of single crystalline iridium is realized on the easy slip stage when the sole permitted dislocation configuration is dislocation nets, whose dense seems like concentration of dislocations in irradiated metals [22]. In this case, the obstacles are <110> dislocations themselves, which have been situated in the net. Stress rising allows to hammer <110> dislocations in the net practically without any limit, until the time when tensile stress becomes enough for crack creation. Evidently, this condition never meets under compression, and, as a results, grain boundary (GB) free iridium behaves like normal f.c.c. –metal [23].

BIF is the cause of poor plasticity of polycrystalline iridium, but no differences between crystallographic characteristics of GBs in iridium and normal f.c.c. –metal have been revealed [24]. This is an experimental fact that at room temperature polycrystalline samples fail after easy slip stage, when <110> dislocations gain a tend to move through GBs. Neck region begins to form in polycrystalline aggregates at 400oC, since transition of dislocation structure from the net to small angle boundaries

become possible because of the rising of dislocation mobility [25]. However, necking to a point and flowing neck are observed in severe deformed (GBs free) iridium and its alloy at 1000oC, where GBs do not bother this transformation [26]. Anomalously wide diffusion zone, contained high concentration of vacancies, is the reason why GBs in iridium are opaque for <110> dislocations [27]. Workability of iridium could be improved by means of doping GBs by heavy metallic impurities, despite this never suppress BIF in material [28].

CRACK GROWTH IN BULK IRIDIUM CRYSTALS

Detail experimental data on transcrystalline cracks in iridium single crystals under tension and bending were published in [29,30]. It was shown that tiny cracks, whose length has been measured as 0.01?0.03 mm, appear on the edges of preliminary deformed crystal near notch like defects. They had V–shape with 10?15o angle of opening and advanced along a normal to tensile axis. No any deformation tracks were revealed near crack edges. More long cracks became sensitive to crystallographic orientation of sample, however this did not influence on their shape. So, cracks in crystals stretching along <110> changed their growth direction from 90o to 60o?70o, while cracks in samples with tensile axis of <100> continued to grow in the same direction. Simultaneously, thin deformation tracks appeared near crack edges, but this did not lead to crack tip blunting. Their orientation and shape were similar to geometry of octahedral slip bands advancing around notches in single crystals of normal f.c.c.–metal under tension along <110> and <100> directions, respectively. Deformation tracks ceased to leave from the edges of upper part of cracks, when crack length became over 0.1 mm. It important to note that such cracks, whose motion causes the failure, appeared before the moment of separation. Sometimes, long cracks could branch on two or more parts, each of them laid either primary or secondary cleavage planes ({100} and {210}, {110}). Under bending, cracks also possessed V–shape, but deformation tracks were observed near the longest cracks when tensile deformation became considerable.

EVOLUTION OF CRACKS IN THIN FOILS OF IRIDIUM FOR TRANSMISSION ELECTRON MICROSCOPE

Evolution of cracks in thin foils of iridium (and aluminum) was considered in [29–31]. Smallest objects in iridium foils, which could be determined as cracks, had the length approximately of 10-2 ?m . They and more longer cracks (up to 0.5 ?m in length) emitted perfect dislocation with <110> Burgers vectors from tips, which had a tend to move far away, but this never caused distinct blunting of cracks. In so doing, thin region of stacking fault leaved ahead the crack after passing of each dislocation. The growth of number of emitted dislocations led to rising the power of stacking fault and it transformed into twin lamella having clear visible “zebra” contrast. At that both stacking faults and twins extended from crack tip on the distance of 1 ?m . As a rule, in iridium foils emitted dislocations have been stopped on highly dense dislocation nets, situated on the distance of 3?7 ?m from the edge, and they began to look like dislocation pileups, while in aluminum emitted dislocations never met obstacles and flew in depth of foil without any trouble. Sometimes, transformation of emitted dislocation pileup in to a braid was observed in iridium. The crack length could reach the value of 1 ?m , if material around it did not contain highly dense nets. They always had “square” tips and began to emit perfect dislocations normally to initial growth direction. After that crack changed its growth direction on perpendicular one. As a re-

sult, crack obtained broken or zig–zag profiles. It is well known that motion of such crack causes the failure of thin foils of ductile metals [32–34], therefore in this case "brittle" iridium behaves like normal f.c.c.–metal.

FRACTURE BEHAVIOR OF GALLIUM COVERED ALUMINIUM CRYSTALS

Gallium (both in solid and liquid state) covered aluminum crystals (GCACs) failed under tension of 15–20%, while in air they shown elongation prior the failure of 35–50%, at that neck began to form at 15?20% [35]. Despite considerable elongation, no deformation relief and necking were observed in gallium covered aluminum crystals. According to metallographic study, gallium did not induce visible intensification of octahedral slip in the samples, although their yield stress was considerably lower than for pure aluminum crystal. Also, presence of gallium on the surface never led to activation of mechanical twinning and non-octahedral slip. V-shaped (iridium like) transcrystalline cracks (length is about 0.02?0.05 mm) were only revealed on the samples covered by gallium in solid state. Cracks appeared after preliminary deformation of 8?10 % on the power defects like notches or reper lines. Some of them could be grown up, but deformation tracks never lost their edges as it was reported in [7]. Appearance of slip band near the crack led to its transformation to pore–like defect, which grew in length and in width, simultaneously. Analysis has shown that the length of cracks transforming to pores is approximately in two times longer than for V–shape cracks. Pores were situated in narrow strip, where localization of plastic deformation took place. The dangerous crack formed as a result of junction of such pores along cross section of crystal covered by gallium in both solid and liquid state. Therefore, there are three stages of crack evolution in aluminum crystals covered by solid gallium. The first, growth of V–shape (iridium like) cracks; the second, transition from V–shape crack to pore and its growth; and, the third, junction of pores into dangerous crack.

DISCUSSION

It was shown that brittle fracture takes place in strengthened f.c.c.–metal only. Single crystals fail after considerable elongation, while poor plasticity of polycrystalline samples is synonymously connected with low cohesive strength of GBs. Any way, the cause of brittleness in plastic f.c.c.–metal is exhaust of resource of plasticity during preliminary deformation, if any dangerous defects, where cracks could appear, are absent in material. BTF in f.c.c.–metal becomes possible, when storage of plastic deformation occurs on the easy slip stage and sole permitted dislocation configuration is dislocation net. At that the crystal cannot lose ability to be deformable at the one moment because of heterogeneity of distribution of plastic deformation in the sample. It means that material is brittle in vicinity of cracks only, whereas it continues to be plastic in any other places. Therefore, neither crack appearance nor ever crack growth induce instantaneous separation of crystal. During deformation, volume of "brittle" substance is increasing until the motion of single crack causes failure of crystal. This is the reason why fracture behavior of iridium crystals is distinguished from fracture both non-metallic and b.c.c.–metallic crystals at temperatures lower than the point of brittle to ductile transition (BDT), although fracture surfaces of iridium, tungsten, molybdenum, iron, and silicon crystals in brittle state look similar.

Sharp V–shaped transcrystalline cracks in iridium crystals may be called the brittle cracks in f.c.c.–metal, since, the first, growth of one from them leads to BTF, and, the second, they have appropriate geometry. The cracks in GCACs on the first stage of evolution are also brittle ones, inasmuch as they look like that. An absence of deformation tracks near crack tips, at least, on initial and final stages of evolution, allows concluding that no plastic deformation occurs in crack tip or brittle crack in f.c.c.–metal does not emit dislocations from the tip. On the contrary, crack edges are "sources" of octahedral slip bands, if tensile stress has been applied to iridium crystal, however this should be considered exclusively as showings of residual plasticity of material far away from crack location. Indeed, brittle crack begins immediately transform to pore, as soon as octahedral slip appear near the tip, as it takes place in GCACs, where inclination to BTF shows in thin gallium reach layer near crystal surface1. Hereafter evolution of crack in GCACs includes elements of both brittle and ductile crack growth: sharp pores, laid on low index {100} and {111} planes, are jointing in dangerous crack. Such behavior is similar to ductile fracture in neck region of f.c.c.–metal [20]. Certainly, it does not mean that material ahead brittle crack has completely lost an ability to plastic deformation or dislocations cannot be generated at crack tip, however, it is absolutely clear that contribution of these processes to fracture behavior should be insufficient.

TEM observations give extremely important information about fracture process on micro scale. It seems to be that generation of perfect dislocations accompanies the breaking of interatomic bonds and form of crack surface is f.c.c.–metal. So, atomic scale crack, which does not look like atomically sharp crack, emits perfect dislocations. In contrast with physical model of crack considered in [3–5,33], dislocation emission does not lead to visible crack tip blunting and arrest of crack. Emitted dislocations are flowing into the foil, if the power obstacles are absent ahead. Highly dense net bother them to come through, and pileup of emitted dislocations begins to turn into a braid. As a result, new generated dislocations have not opportunity to leave crack tip what should cause the stoppage of crack in thin foil of f.c.c.–metal. This hypothesis sounds like physical model of BTF in bulk iridium crystal transferred on 2D media. Indeed, in both cases dislocation nets do not allow iridium behaves like plastic substance. Also, it is very interesting that twin lamella near crack is a track remained by moving <110> dislocations in the thin region of foil. Unfortunately, the findings cannot be used for explanation of brittleness in f.c.c.-metals, since iridium thin foils show typical ductile fracture behavior like aluminum, silver and gold [31–34,36]. Gallium does not change fracture mode of aluminum foils, too [7]. Another word, this chapter confirms conclusion that brittle crack in f.c.c.-metal does not emit perfect dislocations, although it conserves an ability to generate them, but new born dislocations cannot move from crack tip because of highly dense net or pileup.

The fact that high plastic iridium meets empirical criteria for brittle fracture [8,16] should be considered as casual coincidence, although some relations between strong interatomic bonds (it holds third position in melting points among the metals) and inclination to brittleness would exist. Despite this BTF happens in reality, and, therefore, fracture mechanics can be used for description of transcrystalline cracks in iridium crystals. Naturally, mechanical models should be applied to the area, where material has being in brittle or undeformable state, since the role of plasticity at crack

[1] It may be supposed that transition from brittle crack to pore happens when it comes through this layer

tip is insufficient in this case only. At that consideration of plasticity with a help of "coefficients in equations", which have not definite physical content, looks preferably than discussion on dislocation emission from brittle crack, inasmuch as this event never occurs in f.c.c.-metal. The more so, real mechanisms of plasticity ahead crack cannot be correctly described in the frames of fracture mechanics [37].

AKNOWLEDGEMENTS

This work was supported by the Ekaterinburg Non–Ferrous Metals Processing Plant, Russia.

REFERENCES

1. Yokobori, T. (1971). *An Interdisciplinary Approach to Fracture and Strength of Solids*. Wolters-Noordhoff Scientific Publications, Groningen (in Russian: Metallurgia, Moscow).
2. Bilby, B. A., Cottrell, A. H. and Swinden, K. H. (1963) *Proc. Roy. Soc*. A272, 304.
3. Rice, J. R. and Thomson, R. (1974) *Phil. Mag*. 29, 73.
4. Lin, I.-H. and Thomson, R. (1986) *Acta Metall*. 34, 187.
5. Argon, A. S. (1987) *Acta Metall*. 35, 185.
6. Richardson, F.D. (1958) *Platinum Metals Rev*. 2, 83.
7. Lynch, S. P. (1988) *Mater. Forum* 11, 268.
8. Hecker, S. S., Rohr, D. L. and Stein, D. F. (1978) *Metall. Trans*. 9A, 481.
9. MacFarlane, R.E., Rayne, J.A. and Jones, C.K. (1966) *Phys. Lett*. 20, 234.
10. Mordike, B. L. and Brookes, C. A. (1960) *Platinum Metals Rev*. 4, 94.
11. Douglass, R.W., Krier, A. and Jaffee, R.I. (1961) *Batelle Memorial Institute, Report NP-10939*.
12. Handley, J. R. (1986) *Platinum Metals Rev*. 30, 12.
13. Brookes, C.A., Greenwood, J.H. and Routbort, J.L. (1968) *J. Appl. Phys*. 39, 2391.
14. Reid, C. N. and Routbort, J. L. (1972) *Metall. Trans*. 3, 2257.
15. Brookes, C. A., Greenwood, J. H. and Routbort, J. L. (1970) *J. Inst. Metals* 98, 27.
16. Gandhi, C. and Ashby, M. F. (1979) *Acta Metall*. 27, 1565.
17. Garrett, G.G. and Knott, J.F. (1975) *Acta Metall*. 23, 841.
18. Kamdar, M.H., (1983). In: *Treatise on Materials Science and Technology. Vol. 25 Embittlement of Engineering Alloys,* Briant, C.L. and Banerji, S.K. (Eds) Academic Press, New York (in Russian: Metallurgia, Moscow, 1988).
19. Panfilov**,** P. (2000). In: *Iridium. Proceedings of the International symposium sponsored by the SMD division of the Minerals, Metals & Materials Society (TMS) held during the 2000 TMS Annual Meeting in Nashville, Tennessee, March 12-16, 2000,* pp.93 – 100, Ohriner, E. K., Lanam, R. D., Panfilov, P. and Harada, H. (Eds) TMS, USA.
20. Honeycombe, R. W. K. (1972). *The Plastic Deformation of Metals*. Edward Arnold, London. (in Russian: Metallurgia, Moscow).
21. Hirth, J. P. and Lothe, J. (1968). *Theory of Dislocations*. McGraw–Hill, London. (in Russian: Atomizdat, Moscow).
22. Timofeev, N., Yermakov, A., Dmitriev, V. and Panfilov, P. (1996). *Metallurgy and mechanical behavior of iridium*" Urals Branch of Russian Academy of Science, Ekaterinburg. (in Russian).

23. Yermakov, A., Panfilov, P. and Adamesku, R. (1990) *J. Mater. Sci. Lett*. 9, 696.
24. Rohr, D. L., Murr, L. E. and Hecker, S. S. (1979) *Metall. Trans*. 10A, 399.
25. Panfilov, P. and Yermakov, A. (2001) *Platinum Metals Rev*. 45, (in press).
26. Panfilov, P. and Yermakov, A. (2001) (to be published).
27. Klotsman, S.M. (2000). *Private communication*.
28. George, E.P. and Liu, C.T. (2000). In: *Iridium. Proceedings of the International symposium sponsored by the SMD division of the Minerals, Metals & Materials Society (TMS) held during the 2000 TMS Annual Meeting in Nashville, Tennessee, March 12-16, 2000*, pp.3–14, Ohriner, E. K., Lanam, R. D., Panfilov, P. and Harada, H. (Eds) TMS, USA.
29. Panfilov, P., Yermakov, A. and Baturin, G. (1990) *J. Mater. Sci*. Lett. 9, 1162.
30. Panfilov**,** P. (2000). In: *Iridium. Proceedings of the International symposium sponsored by the SMD division of the Minerals, Metals & Materials Society (TMS) held during the 2000 TMS Annual Meeting in Nashville, Tennessee, March 12-16, 2000*, pp. 27–40, Ohriner, E. K., Lanam, R. D., Panfilov, P. and Harada, H. (Eds) TMS, USA.
31. Panfilov, P., Novgorodov, V. and Baturin, G., (1992) *J. Mater. Sci. Lett.* 11, 229.
32. Lyles, R. L. and Wilsdorf, H. G. R., (1975) *Acta Metall.* 23, 269.
33. Ohr, S.M., (1985) *Mater. Sci*. Eng. 72, 1.
34. Robertson, I.M. and Birnbaum, H.K., (1986) *Acta Metall*. 34, 353.
35. Panfilov, P. and Gagarin, Yu. L., (1998) *J. Mater. Sci. Lett.*, 17, 1765.
36. Wilsdorf, H.G.R., (1982) *Acta Metall*. 30, 1247.
37. Knott, J. F. (1973). *Fundamentals of Fracture Mechanics*. , London. (in Russian: Metallurgia, Moscow).

ORAL REFERENCE: ICF10 061PR

ON FATIGUE LIMIT OF NOTCHED COMPONENTS

M.D. Chapetti[1], T. Tagawa[2] and T. Miyata[2]

[1]INTEMA, University of Mar del Plata
J.B. Justo 4302 (7600) Mar del Plata, Argentina

[2]Department of Material Science and Engineering, Nagoya University
Nagoya, 464-01, Japan

ABSTRACT

The most important parameters in defining the fatigue limit and the fatigue notch sensitivity of notched components are identified and analysed. On the basis of the experimental evidence that the fatigue limit (both plain and notched) represents the threshold stress for the propagation of the nucleated short cracks, a material resistance to crack growth as a function of the crack length is suggested, which can be estimated by using mechanical and microstructural parameters obtained through standardized mechanical tests and simple microstructural analysis.

KEYWORDS

Fatigue limit, Notch sensitivity, Microstructural threshold, Mechanical threshold.

INTRODUCTION

The fatigue limit of polycrystalline metals seems to be a function of a maximum non-propagating crack length associated with a particular stress level [1-10]. Up to a certain crack length the crack is non-damaging with respect to the fatigue limit, and for long cracks the fatigue limit decreases with increasing crack length. The effect of crack length on the fatigue limit can be described conveniently by means of Figure 1. It shows the threshold stress (defining the border between propagating and non-propagating cracks), as a function of a crack length. For a microstructurally short crack (MSC, crack length of the order of the microstructural dimensions) initiated from a plain surface, the plain fatigue limit $\Delta\sigma_{e0}$ defines the critical nominal stress range needed for continued crack growth. If the applied stress range $\Delta\sigma$ is smaller than $\Delta\sigma_{e0}$, cracks included in the microstructural short crack regime are arrested at microstructural barriers. On the other hand, the threshold for long cracks

(LC) is defined in terms of the threshold value of the stress intensity range, ΔK_{th}, thus long cracks can only grow by fatigue if the applied ΔK is greater than ΔK_{th}. In the physically short crack regime (PSC, crack length less than that (l) at which crack closure is fully developed), which corresponds to the transition between microstructurally short and long crack regimes (MSC and LC), the threshold is below $\Delta\sigma_{e0}$ and ΔK_{th}. The length d defines the plain fatigue limit and is given by the position of the strongest microstructural barriers.

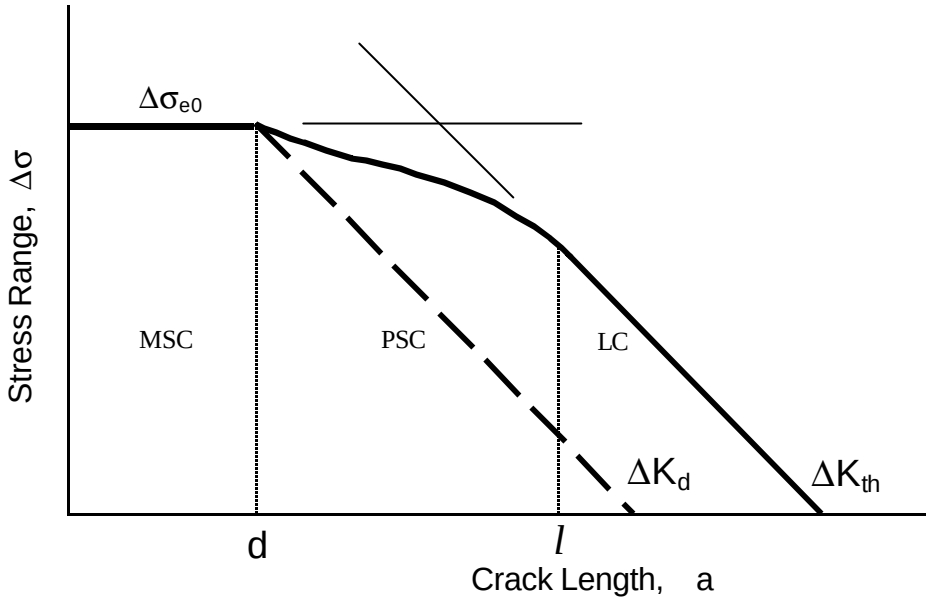

Figure 1. Threshold between propagating and non-propagating cracks.

It has been demonstrated that two patterns of notch fatigue behavior can occur [1-13]. In a smooth specimen once the crack initiate and overcomes the first predominant microstructural barrier at the position d (which defines the plain fatigue limit), the stress level is high enough to drive the crack to fracture [11-13]. As the stress gradient increases due to the presence of a blunt notch, deeper barriers define the fatigue limit, and the difference between the initiation limit and the fatigue limit increases. However, the position d of the first predominant microstructural barrier seems to estimate conservatively the fatigue limit of blunt notches [11-13].

Figure 2 shows the three most important parameters in defining the fatigue limit and the notch sensitivity of notched components [11]. Increasing $\Delta\sigma_{e0}$ (that is to say, increasing the resistance of the predominant microstructural barrier) causes the curve defining the fatigue limit of blunt notches to rise as a whole. If d is increased for a given $\Delta\sigma_{e0}$ and ΔK_{th} (that is to say the distance between two consecutive microstructural barriers is increased), that curve turns upward around the point given by $\Delta\sigma_{e0}$ and $k_t = 1$ (point A), decreasing the fatigue blunt notch sensitivity. For sharp notches the fatigue notch sensitivity is given by the mechanical threshold ΔK_{th} and the notch depth D.

From the above discussion is obvious that in order to develop a model to predict the fatigue limit of notched components, as well as fatigue crack propagation life, it is necessary to obtain an expression for the material resistance to crack propagation as a function of the crack length, including the short crack regime. In this work a material resistance to crack growth as a function of

the crack length is suggested, which can be estimated by using mechanical and microstructural parameters obtained through standardized mechanical tests and simple microstructural analysis.

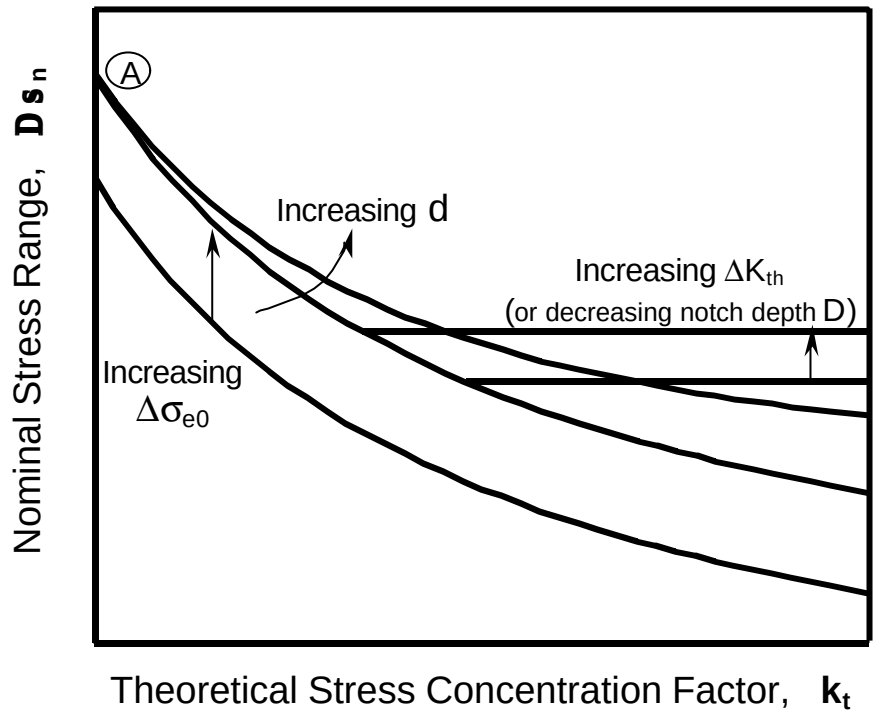

Figure 2. Mechanical, geometrical and microstructural parameters controlling the fatigue limit and fatigue notch sensitivity of notched components.

THRESHOLD STRESS VS. CRACK LENGTH

In the short crack regime, crack closure develops with an increase in crack length [1-10], and this crack closure reduces the effective range of the applied stress intensity factor. So it can be considered as an extrinsic material resistance. In this way a resistance curve to crack propagation can be defined adding the crack closure component of the stress intensity factor to the intrinsic crack grow resistance of the material. An intrinsic material resistance to microstructurally-short crack propagation ΔK_d, can be defined by the plain fatigue limit $\Delta\sigma_{e0}$ and the position of the strongest microstructural barrier *d*, as follows [14]:

$$\Delta K_d = \Delta s_{e0} \sqrt{p\ d} \tag{1}$$

where the plain fatigue limit $\Delta\sigma_{e0}$ represent the effective resistance to crack propagation of the strongest microstructural barrier, and its position *d* defines the notch sensitivity for very blunt notches. It seems reasonable to define the parameter ΔK_d as a microstructural threshold.

The material resistance to crack propagation as a function of the crack length, $\Delta\sigma_{th}(a)$, is then obtained as:

$$\Delta K_{th} = \Delta K_d + \left(\Delta K_{th} - \Delta K_d\right)\left[1 - e^{-k(a-d)}\right] = \Delta s_{th} \sqrt{p\ a} \qquad a \geq d$$

(2)

and then

$$\Delta s_{th} = \frac{\Delta K_d + (\Delta K_{th} - \Delta K_d)\,[1 - e^{-k(a-d)}]}{\sqrt{p\,a}} \qquad a \geq d \qquad (3.a)$$

$$\Delta s_{th} = \Delta s_{e0} \qquad a < d \qquad (3.b)$$

Where ΔK_{th} and $\Delta\sigma_{e0}$ (and so ΔK_d), are function of the stress ratio R.

Let find an expression for the factor k to take into account the development of the crack closure component of ΔK_{th}. It has been shown by Lankford [15] that short cracks may grow at the same rate as long cracks when the cyclic plastic zone size r_{pc} is approximately similar to the relevant microstructural dimension. So, we can suppose that the extrinsic resistance to crack propagation ($\Delta K_{th} - \Delta K_d$) has been developed when r_{pc} becomes equal to d.

The cyclic plastic zone size at the crack tip in plane strain condition can be estimated as [16]:

$$r_{pc} = \frac{1}{3p}\left(\frac{\Delta K}{2\,s_{ys}}\right)^2 \qquad (4)$$

where ΔK is the applied stress intensity factor range, and σ_{ys} is the yield stress of the material.

At the threshold stress (da/dn = 0):

$$\Delta K = \Delta K_{th} = \Delta s_{th}\sqrt{p\,a}$$

We assume that $\Delta\sigma_{th} = \Delta\sigma_{e0}$ and that $\Delta\sigma_{e0} = \sigma_u$ (the strength of the material)[16], so that the cyclic plastic zone size can be estimated with the following expression:

$$r_{pc} \approx \frac{a}{12}\left(\frac{s_u}{s_{ys}}\right)^2 \qquad (5)$$

In Eqn 2 the extrinsic crack growth resistance (second term in right hand) is equal to 87% of the total one when $k\,a = 2$ (with a >> d). We here suppose that at this state the extrinsic crack growth resistance is totally developed. Supposing that this also occur when $r_{pc} = d$, we get the following condition:

$$r_{pc} \approx d \approx \frac{a_{r_p = d}}{12}\left(\frac{s_u}{s_{ys}}\right)^2 \qquad (6)$$

From Eqn 6, and with the condition $k\, a_{rp=d} = 2$, we get the following expression to estimate the parameter *k*:

$$k \approx \frac{1}{6\, d}\left(\frac{s_u}{s_{ys}}\right)^2 \qquad (7)$$

Expressions (3) and (7) define a material resistance curve that can be estimated with the plain fatigue limit $\Delta\sigma_{eo}$, the position of the strongest microstructural barrier *d*, the mechanical threshold for long crack ΔK_{th}, the yield stress σ_{ys} and the strength σ_u of the material. These are mechanical and microstructural parameters, which can be obtained through standardized mechanical tests and simple microstructural analysis.

Figure 3 shows the crack growth resistance curve for a pressure vessel steel of the type 2.25 Cr 1 Mo (Yield Stress σ_{ys} = 400 MPa, Tensile Strength σ_u = 580 MPa, plain fatigue limit $\Delta\sigma_{e0}$ = 500 MPa, and threshold for long crack ΔK_{th} = 12 MPa $m^{1/2}$) [4]. Some experimental results obtained from the literature are also shown [4]. The distance between predominant microstructural barriers to crack propagation *d* can be supposed (see for instance ref. [11]) given by the mean packet size of bainite, 0.025 mm [4]. It can be seen that expression (3) predicts reasonably well the experimental results.

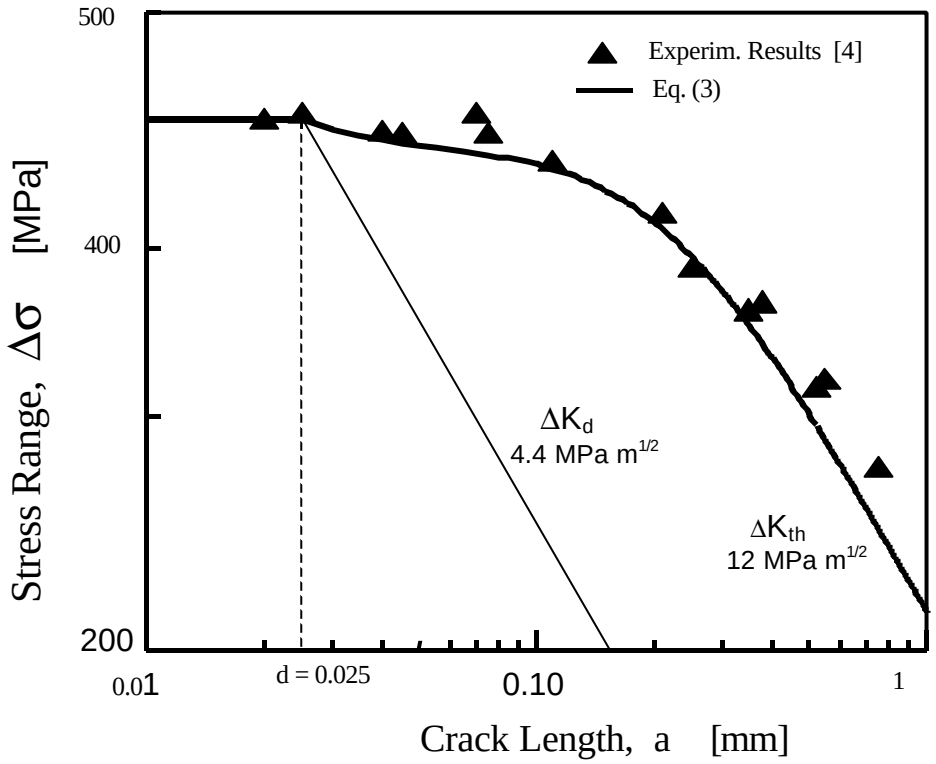

Figure 3. Estimated crack growth resistance for a pressure vessel steel of the type 2.25 Cr 1 Mo. Experimental results [4] are also included.

CONCLUSIONS

An expression for the material resistance to crack propagation as a function of the crack length is obtained from a depth given by the position *d* of the strongest microstructural barrier to crack propagation, which defines the plain fatigue limit. The plain fatigue limit $\Delta\sigma_{e0}$ and the position *d* define an intrinsic material resistance ΔK_d (microstructural threshold to crack propagation). An extrinsic threshold to crack propagation is defined by the difference between the mechanical threshold to crack propagation for long crack ΔK_{th} and the microstructural threshold ΔK_d, as a function of the crack length *a*.

A crack growth resistance curve is estimated for a pressure vessel steel, which seems to predict reasonably well experimental data.

ACKNOWLEDGEMENTS

One of the authors (M.D.Ch.) wishes to express his thanks for funding provided by CONICET (Consejo Nacional de Investigaciones Científicas y Técnicas), and by Agencia Nacional de Promoción Científica y Tecnológica (PICT'98 12-04585), Argentina.

REFERENCES

[1] K. Tanaka and Y. Nakai (1984) *Transactions of the ASME* Vol.106 pp.192.
[2] K.J.Miller (1993) *Fat Fract Engng Mater Struct* Vol.16 No9 pp.931.
[3] M.H.El Haddad, T.H.Topper and K.N.Smith (1979) *Engng Fract Mech* 11 pp.573.
[4] P.Lukás, L.Kunz, B.Weiss and R.Stickler (1989) *Fat Fract Engng Mater Struct* Vol.12 No3, pp.175.
[5] K.Tanaka, Y.Nakai and M.Yamashita (1981) *Int J Fract* Vol.17 No5 pp.519.
[6] N.E.Dowling (1979) *Fat Engng Mater Struct* Vol.2, pp129.
[7] A.J.McEvily and K.Minakawa (1987) *Engng Fract Mech* 28 No5/6 pp.519.
[8] K.Tanaka and Y.Akiniwa (1988) *Engng Fract Mech* Vol.30 No6 pp.863.
[9] J.C.Ting and F.V.Lawrence (1993) *Fat Fract Engng Mater Struct* 16 No1 pp.93.
Technical Note D-6376.
[10] P. Lukas and M. Klesnil (1978) *Materials Science and Engineering* 34, pp.61.
[11] M.D. Chapetti, T. Kitano, T. Tagawa and T. Miyata. (1998) *Fat Fract Engng Mat Struct*, Vol.21, pp.1525-1536.
[12] M.D. Chapetti, N. Katsura, T. Tagawa and T. Miyata. (2000) Accepted for publication *Int J Fatigue*.
[13] M.D. Chapetti, T. Tagawa and T. Miyata. (2000) Submitted to *Fat Fract Engng Mat Struct*.
[14] M.D. Chapetti. (2000) Submited to *Int Journal of Fatigue*.
[15] J. Lankford. (1985) *Fat Fract Engng Mat Struct* Vol.8 Nº2, pp.161.
[16] T.L. Anderson. (1995) *Fracture Mechanics*. CRC Press, Second Edition.

ABSTRACT REF NO: ICF100664OR

ON PREDICTIVE MODELING FOR THE ASSESSMENT OF FRACTURE BEHAVIOR IN FERRITIC ALLOYS

Amar N. Kumar

Applied Mechanics Department, Indian Institute of Technology,
Hauz Khas, New Delhi - 110016, India

ABSTRACT

A new simplistic model is proposed for structural alloys for assessing the macroscopic fracture behavior in the upper shelf region. A local approach integrating the stress and strain distribution in the vicinity of the crack tip has been followed. The model is based on uniaxial tensile ductility and fracture strength as these two are assumed to have greater significance and control on the fracture process. J-integral toughness values are assessed from the proposed model and also experimentally determined at various temperatures. Ferritic alloys with a wide variation in composition, treatment and microstructure are used to check the validity of the model. The experimental data for the upper shelf region are found to lie within the upper and lower boundaries as set by the limiting number of major dimple sizes. The proposed model also provides reasonable indication of the temperature for transition to upper shelf region.

KEYWORDS: J-integral toughness, strain, stress, ferritic alloys, dimple, upper shelf, temperature

INTRODUCTION

Considerable amount of research efforts have been directed over the past decades towards understanding of the micromechanisms of fracture process in structural parts and components operating under various service conditions [1-3]. In numerous applications (for instance, nuclear reactor plants) a classical fracture mode transition from low energy brittle fracture to high-energy ductile fracture occurs due to increase in operating temperature and/or decrease in strain rate [1]. A prediction of such transition in the behavior is highly significant for the assessment of the integrity of all critical components and structures. Two approaches have been commonly followed for assessing fracture behavior of structural steels, namely, global and local approaches. The fracture mechanics based parameters (like K_{IC}, COD, J_{IC} etc.) are determined at the critical condition in the global approach [2]. The local approach integrates micromechanistic criterion of failure with analytical or numerical crack tip stress-strain distribution to model the macroscopic fracture behavior. Void nucleation and coalescence mechanisms leading to localized failure are dubious issues as various criteria are proposed [4,5]. The present work is an attempt towards the development of a simplistic model using uniaxial tensile test data that can be used in the upper shelf regime for assessing the fracture toughness values as well as the prediction of transition temperature.

THEORETICAL CONSIDERATION

Stress Strain Gradient

A steep gradient in stress and strain ahead of sharp stationary crack exists in small scale yielding situation as demonstrated by HRR crack tip analysis. Rice and Johnson model accounts for the crack blunting effect and large crack tip geometry changes in the stress and strain fields in the close vicinity of crack tip [6,7]. Modeling of crack initiation process by local criterion requires both stress and strain factors and consideration of either of them is not likely to yield realistic assessment of ductile fracture behavior. The local approach defines the crack initiation event as the coalescence of blunting crack tip with at least one of the growing voids [8,9]. Both stress and strain fields control the crack initiation process and should be taken into consideration for dealing with local failure criterion.

Failure Criterion

A new parameter giving equal significance and weightage to both fracture stress and fracture strain terms is proposed as $\phi = \sigma_{fc}^{N} \times \varepsilon_c^{pl.}$. ϕ represents the local failure criterion where σ_{fc}^{N} is true fracture stress in normal and $\varepsilon_c^{pl.}$ is the equivalent plastic strain. ϕ may be defined as the plastic energy density having the dimension as Joule per cubic meter. The normalized (non-dimensional) form of ϕ may be given by $\phi_N = \sigma_{fc}^{N} \times \varepsilon_c^{pl.} / \sigma_y$ where σ_y is the uniaxial yield strength of the material in tension.

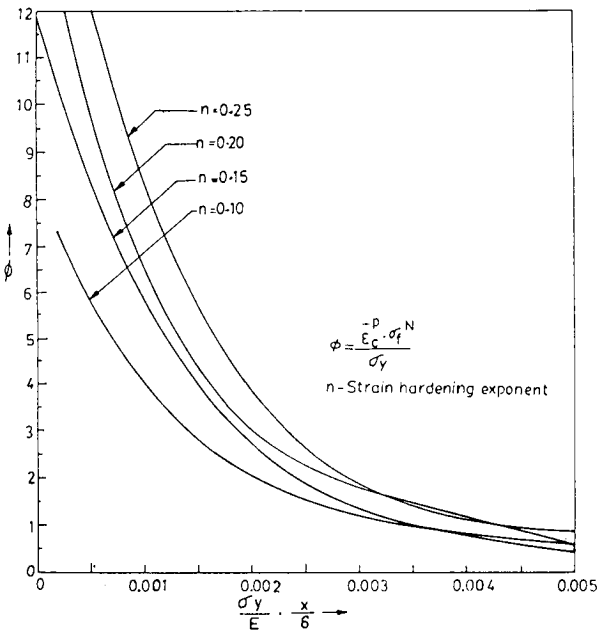

Figure.1 Normalized composite parameter, ϕ vs. normalized distance from crack tip

A limiting amount of energy per unit volume of material i.e. ϕ or ϕ_N is required for crack tip deformation leading to void formation and void coalescence mechanisms prior to crack initiation. A polynomial function of 4th order is established to represent ϕ or ϕ_N mathematically and the graphical variation of ϕ or ϕ_N vs. normalized distance is shown in Fig.1.

Assessment of J-Integral

The macroscopic fracture behavior of ferritic alloys in the upper shelf region is assessed by the critical J-integral value, J_{IC}. The critical plastic energy density is expected to prevail over the process zone at the onset of local failure. J_{IC} may now be obtained as

$$J_{IC} = \phi_c \times \text{process zone size in joules / m}^2$$

Mathematical description of the model is based on the stress distribution as represented by $\sigma_{yy} / \sigma_y = f(E, n, x/\delta...)$ where n is the strain hardening exponent, E is the elastic modulus, x is the distance from crack tip and δ is the crack opening displacement. The master curve can be used for the determination of J-integral toughness values corresponding to crack initiation. Bridgeman's analysis has been used to obtain equivalent

plastic strain as $\varepsilon_c^{pl.} = 2 \log_e d_0 / d_f$ where d_0 and d_f are the initial and final diameters of a cylindrical specimen [10]. Experimental ϕ_{NC} value is used to determine a constant, k which is a function of both σ_y and E. The minimum number of major dimples constituting the process zone is one. The critical δ i.e. δ_c value may be further used to obtain J-integral value as $J_{IC} = m.\sigma_y.\delta_c$, where constant 'm' defines the state of stress condition prevailing at the crack tip. An approximate and rapid estimation of J_{IC} may be obtained from the experimental value of plastic energy density, ϕ. ϕ_C when multiplied with x_c yields J_{IC}. The schematic representation of the J-integral measurement procedure is shown in Fig. 2. The size of x_c is assumed to be related with the critical length and depends on the major dimple size.

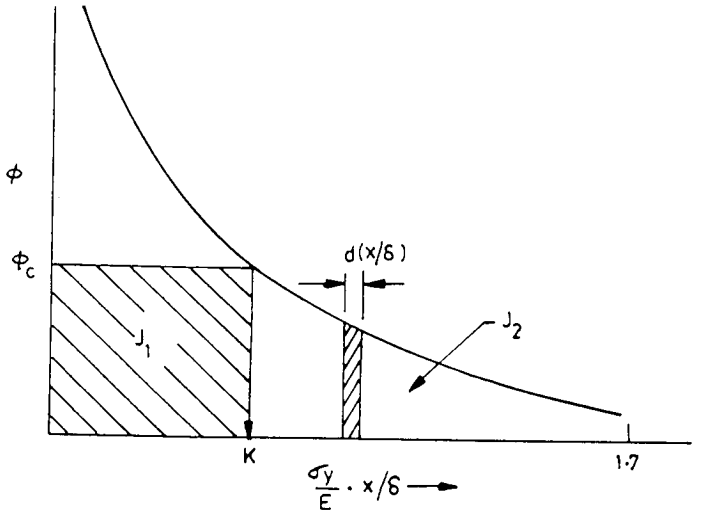

Figure. 2 Schematic illustration of J-integral computation from the proposed model

Sufficient Condition

It is argued that J_I is necessary to satisfy the requirement for local criterion for fracture. However, the global condition (region surrounding PZ) must also be set prior to local failure and accept any eventuality caused by local failure. In different words, J_I is a necessary criterion for localized failure, but not sufficient to meet the global requirement. If plastic energy density equivalent to J_I is supplied to cracked specimen. An estimate of J_2 may be made by considering the area under ϕ vs. x /δ plots (Fig. 2).

EXPERIMENTAL DETAILS

Fracture Toughness Test

Fracture toughness data were determined for a number of ferritic alloys at temperatures ranging from lower shelf region ($\approx$ 140K) to upper shelf region ($\approx$ 320K). Critical J- integral values were determined using 1T CT specimens following ASTM standards. Three J-values those are of primary interest to designers were determined, namely

(i) J_i at the onset of ductile crack initiation which is followed by stable crack growth,

(ii) J_c at the onset of cleavage fracture prior to initiation of ductile crack and

(iii) J_u at the onset of cleavage fracture following initiation of ductile crack.

A general variation of the fracture toughness with test temperature is displayed in Fig. 3 illustrating the region of temperatures where J_I, J_C and J_U were measured. Electrical potential technique was employed for monitoring crack initiation and growth in the CT specimens. At least four specimens were tested at each temperature to confirm the results. Uniaxial tensile tests were also conducted at each temperature using specimens of round cross-section (8 mm in diameter). The critical plastic energy density, ϕ was obtained from the tensile data at the corresponding temperature.

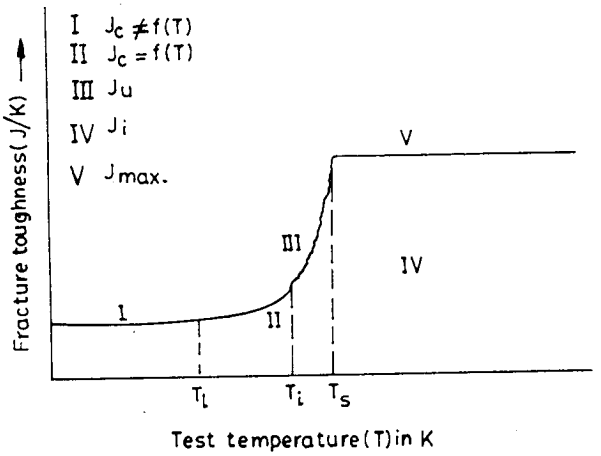

Figure. 3 Schematic representation of the fracture toughness with test temperature

Inclusion and Dimple Size Analysis

The small cut-out parts of the fracture surface from tested CT specimens were examined under SEM at different magnifications to facilitate measurement of the dimple size The fracture surfaces were gold coated for enhancement of contrast before examination. The average size of the primary voids (large) is given as 'D' while the average size for secondary voids (remaining) is represented as `d`. A typical fractograph displaying major dimples on the fracture surface is shown in Fig. 4. It was also found relevant to examine

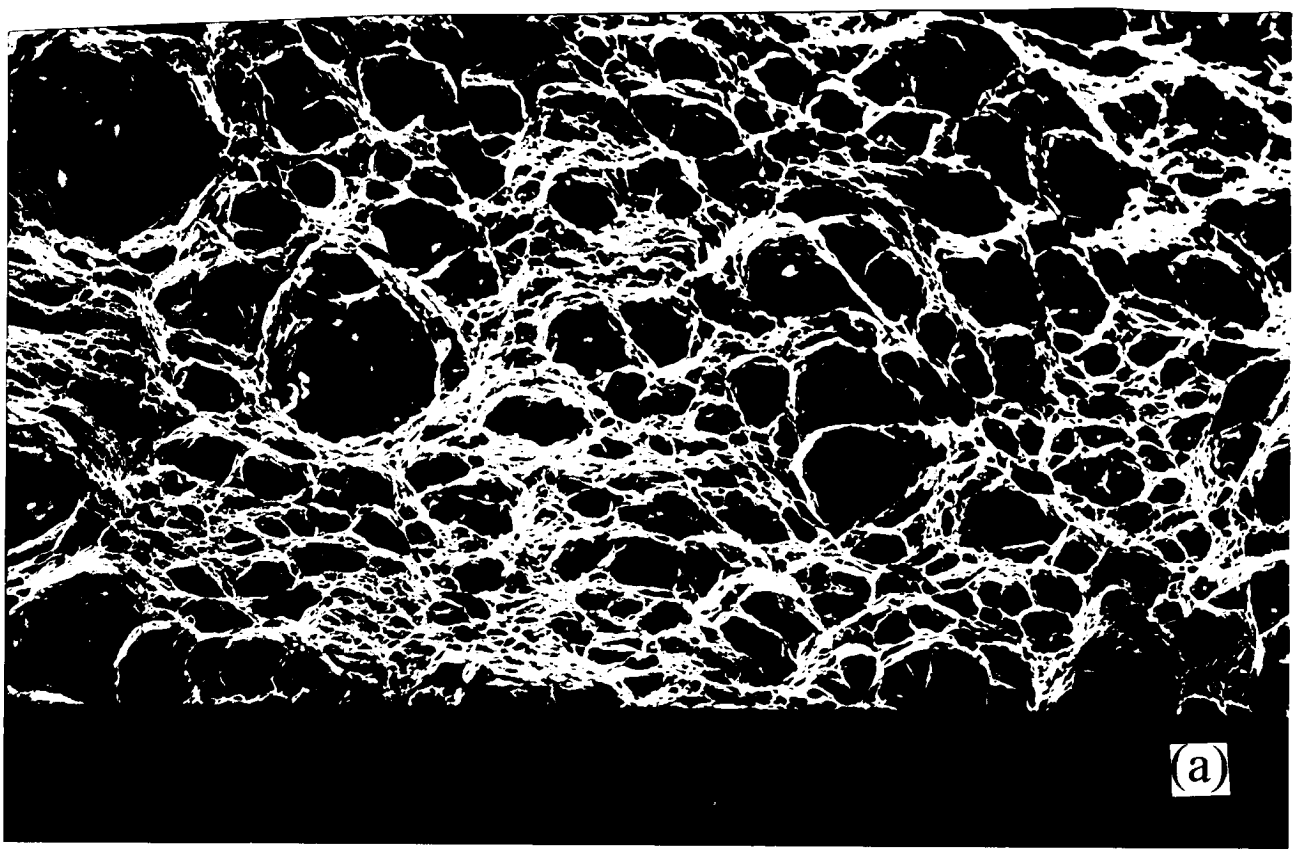

Figure 4. Typical fractograph showing major and minor dimples on the fracture plane in the thermomechanically treated sample.

the microstructures and the inclusion size distribution of the alloys. The inclusions and second phase particles are known to be the potential void initiators during the ductile fracture. The inclusions are occasionally observed inside the dimples irrespective of the microstructures. The inclusions are found to be dominantly of manganese sulphide type (MnS) and mostly in globular shapes. An attempt was made to establish a quantitative relation between the inclusion and dimple size to measure the extent of void growth up to the point of ductile failure initiation.

VERIFICATION OF MODEL

The validity of the proposed model is checked by comparison with the experimental data. The proposed model is essentially established for assessing the crack initiation fracture toughness, J_i in the upper shelf region. Fig. 5 displays the experimental J_i values for some of the alloys at different test temperatures. The J_C values corresponding to the cleavage fracture toughness in the lower shelf and transition temperature are also included in the figures. Considerable scatter of the observed data is evident. However, the J_i values are also found to be independent of temperature in the upper shelf region. The predicted values of J_i using the model are included for two conditions for each temperature of testing namely, assuming D =1 and D=2. Interestingly, in all most all cases, it is observed that the experimental data are falling within the two limits

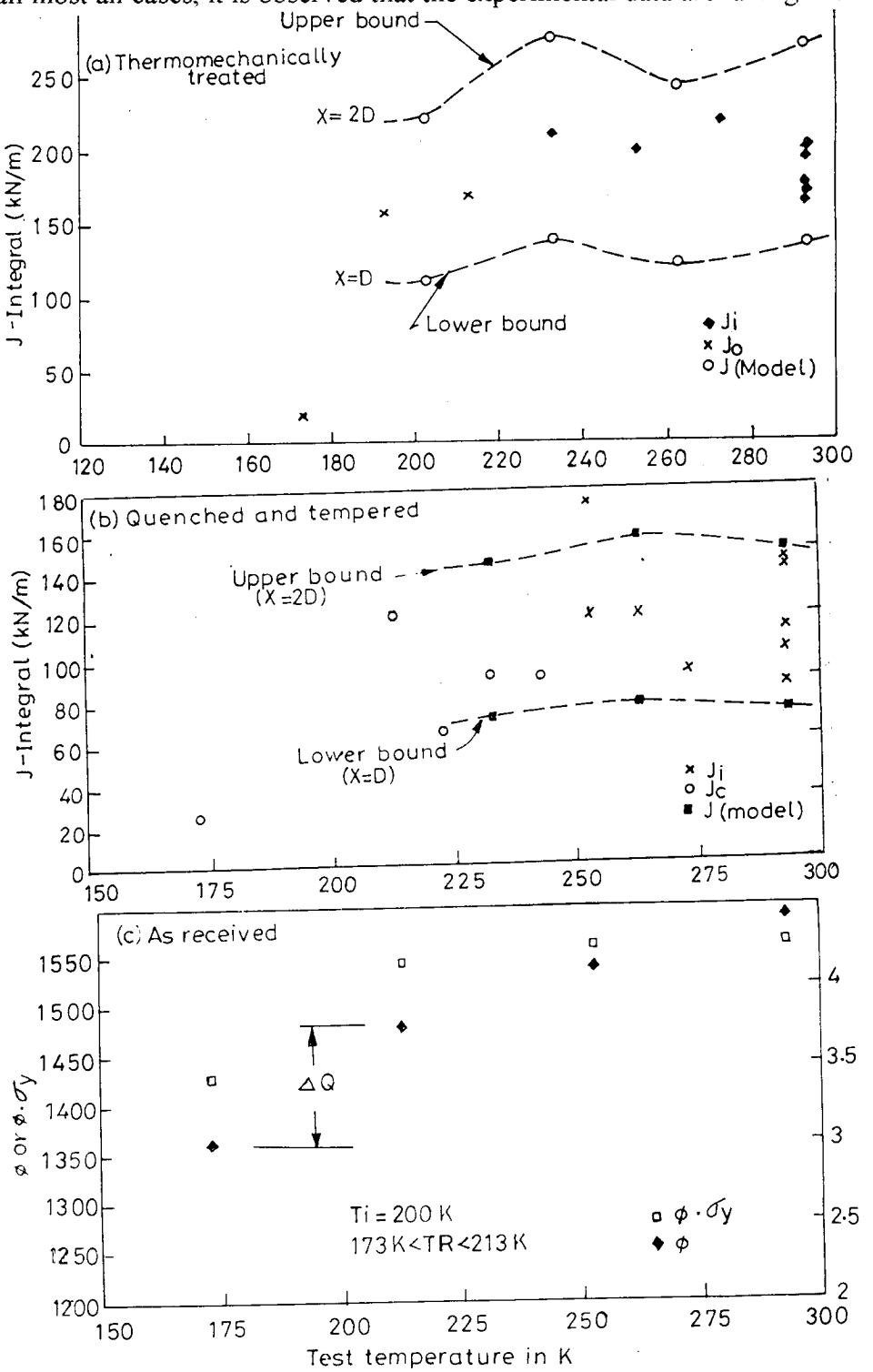

Figure 5. Comparison of the experimental and predicted fracture toughness data for ferritic alloys;

i.e. upper bound and lower bound values as shown in Fig. 5. The boundaries are shown by dotted lines. The lower line corresponds to D equals to 1 while D equals to 2 represents the upper boundary. The limits set by the two values of D represent the upper and lower bound for the scatter of the experimental data. Fig. 5c shows the quantum jump in the computed values of either ϕ or $\phi.\sigma_y$ around the transition temperature. The largest difference in the values of ϕ or $\phi.\sigma_y$ is proposed to give an indication for the transition to upper shelf region. In the particular case, the prediction for the transition is around 200K while the observation during the testing indicated the transition temperature to lie in the range of 173 K and 213K. This finding appears to be in contradiction to earlier claim that the process zone consist of a number of voids ahead of a sharp crack and linkage of all these voids are necessary for localized failure [1,11]. The present model clearly demonstrates that it is the formation, growth and coalescence of just one or two void(s) is sufficient for causing local failure. The blunted crack tip as gets deformed under increasing load links up with the major void formed over one or two inclusions. The number of voids taking part in the effective process of ductile crack initiation is thus found to be one at the least and two at the most. Consideration of the least number of dimple results in a conservative estimation of macroscopic fracture toughness values in the ferritic alloys.

CONCLUSIONS

1. A simplistic model based on the local fracture criteria is proposed, which integrates both the uniaxial fracture stress and fracture strain properties at the temperatures of interest. A composite dimensionless parameter, ϕ is found to be more logical and adequate to describe the fracture initiation behavior in the upper shelf region of the ferritic alloys. The proposed model based on the critical value of the parameter determines the fracture toughness data in structural alloys with fairly good matching with experimental data.
2. The macroscopic fracture toughness values have been assessed for a number of ferritic alloys with different microstructures and treatments using the proposed model. The lower and upper bound of the J-integral fracture roughness data are set by the limiting numbers (one to two) of the major dimples (voids) in all most all cases. The region between the two boundaries may be considered as the scatter band of the measured data. The critical J_{IC} values appear to be lowered by around 10 to 15 percent when the minor dimples are not taken into account. The quantum jump in the values of the critical energy density is observed and can be used to predict the transition temperature of the alloys.

ACKNOWLEDGEMENT

The author acknowledges the support received from Institute of Ferrous Metallurgy, Technical university, Aachen, Germany during his research stay in the Institute.

REFERENCES

1. Ritchie, R. O., Server, W. L. and Wullaert, R. A. (1979), *Metall. Trans.*, 10A, 1557.
1. Pineau, A. (1981), Procee. ICF5 (ed. Francois, D. et. al) 565-577.
2. Mackenzie, A. C., Hancock, J. W. and Brown, D. K.(1977), *Eng. Fract. Mech*, 9, 167.
3. Beremin, F. M. (1981), *Metall. Trans.*, 12A, 723
4. Chu, C. C. and Needleman, A. (1980*), J. of Engg. Mater. and Technol.*, 249.
5. Rice. J. R. and Rosengren, G. F.(1968), J. Mech. Physics of Solids, 16, 1.
6. Rice, J. R. and Johnson, M. A. (1970), Inelastic behavior of Soilds (Eds. Kannienen M. F. et. al.), Mc Graw Hill, NY, 641-672.
7. Hancock, J. W. and Mackenzie, A. C. (1976), *J. Mech. Phys. Solids*, 24, 147.
8. Ritchie, R. O., Knott, J. F. and Rice, J. R. (1973), *J. Mech. Phys. Solids*, 21, 395.
9. Bridgeman. P.W. (1952), Studies in large plastic flow and fracture, McGraw Hill, New York.
10. Kumar, A. N. and Pandey, R. K.(1984), *Eng. Fract. Mech.*, 19, 239

On size of quantum bag and cracking

Cheng Kaijia and Cheng Shuyu

Northwest Institute of Nuclear Technology, Xi'an 710024, China

Abstract

This paper deals with the size limit of material micro and nano-structure associated with its energy state of stability. From the viewpoint of mechanics, there exists the competition between the surface tension and coulomb factor in the electron layer on the surface of bulk. When the bulk size reduces to nm size, the surface effect is comparable to the bulk. The system could collapse into new many-body quantum state. Based on the revised Thomson-Fermi-Dirac(TFDC) theory, the limiting size of a stable material nano structure is obtained. The value of limiting size is of the order "nm" by a crude estimation for water.

1. Introduction

A modified Thompson-Fermi-Dirac (TFD) model [1] consists of a shell of electron cloud of tunneling electrons. It encloses the bulk material and shall be referred to as the "Quantum Bag". The shell of electrons prevails by two factors. One is the surface tension γ that exerts an inward pressure to the bulk material. The other gives an outward extension due to a double charge layer with opposite sign. For a large bulk, the surface tension is less effective than the coulomb factor. As the bulk decreases in size, the surface effect begins to dominate. Then, the crust of the shell will break and cracks would start. Hence, there exists a limit size for the bulk to be stable RL, below which the shell would not be tenable. It is then substituted by a collection of many bodies. There exists no sharp border. The value RL is of the order "nm" by a crude estimation for water.

2. Modified Themson-Fermi-Dirac theory of EOS

The total energy of a bulk material is given by [1]

$$E = K + \Phi + \Phi_s \tag{1}$$

where Φ_s is the energy of pseudpotential

$$\Phi_s = -\frac{Q^2}{\varepsilon_0 2R}, \qquad Q = 4\pi R^2 \sigma \tag{2}$$

where σ is the surface charge density. K and Φ are total inner kinetic and potential energy of the bulk, respectively.

On the surface of the bulk there exists a surface tension γ inside electron tunneling through the boundary which form a shell of electrons. It creates a pressure:

$$P_s = \frac{2\gamma}{R} \tag{3}$$

Note that R is radius of the bulk which can be taken as a sphere. Enclosing the bulk is a crust of tunneling electrons with surface charge density σ. A pressure due to extension is thus created:

$$P_\sigma = \frac{(4\pi\sigma)^2}{\varepsilon_0 8\pi} = 2\pi\sigma^2 / \varepsilon_o \tag{4}$$

It follows that eq. (2) can be written as

$$\Phi_s = -3PV = -\frac{Q^2}{\varepsilon_o 2R} \quad (Q = 4\pi R^2 \sigma) \tag{5}$$

in which ε_o is diaelectric constant.

The net pressure on the quantum bag is

$$P_i = P_s - P_\sigma = \frac{2\gamma}{R} - \frac{4\pi\sigma^2}{\varepsilon_o} \tag{6}$$

P_i must be negative, so that the shell of electrons should be stable. Hence,

$$\frac{2\gamma}{R} - \frac{2\pi\sigma^2}{\varepsilon_o} < 0 \ , \qquad R > \frac{\gamma\,\varepsilon_o}{\pi\sigma^2} = R_L \tag{7}$$

If $R < R_L$, the crust of electrons, being referred as "Quantum Bag", will be unstable and another state of electrons inside the bag will be build. This is a nm particle that would resist uniform aggregation. This explains the mechanism of the nm particle that would remain as an individual unit. That is nm water drops remaining in nm size and would not merge into a single bulk.

3. Pressure estimate

Application of the modified TDF theory could provide an estimate of the prevailing pressures by application of the zero pressure (free state) condition. Consider the pressure Pe of the electron on the surface:

$$P_e = \frac{h^2}{5m}\left(\frac{3}{8\pi}\right)^{2/3} n^{2/3} - \frac{1}{4}\left(\frac{3}{\pi}\right)^{1/3} e^2 n^{1/3} \tag{8}$$

where n is the density of electron at surface. The pseudopotential P_σ takes the form

$$P_\sigma = -\frac{2\pi\sigma^2}{\varepsilon_0} = -\frac{Q^2}{3V\varepsilon_0 2R} \tag{9}$$

In the free state, the two aforementioned pressures should balance such that Pe- P_σ =0. This leads to

$$P_\sigma = -P_e = -\left[\frac{h^2}{5m}\left(\frac{3}{8\pi}\right)^{2/3} n^{5/3} - \frac{1}{4}\left(\frac{3}{\pi}\right)^{1/3} e^2 n^{4/3}\right]. \tag{10}$$

4. Shell model of quantum bag: instability and cracking

Long range Coulomb interaction $-2\pi\sigma^2/\varepsilon_o$ gives a negative pressure in the shell while a short range interaction $2\gamma/R$ is related to the surface energy of tunneling electrons. The stability condition gives.

$$R > R_l = \frac{\gamma\varepsilon_o}{\pi\sigma^2} \tag{11}$$

For a system of molecules with molecule weight M and density ρ, the molecular radius r_o can be written as

$$\frac{4}{3}\pi r_0^3 \cdot \rho = \frac{M}{6.02\cdot 10^{23}} \quad , \quad r_0 = \left(\frac{M}{8\pi\cdot 10^{23}\rho}\right)^{\frac{1}{3}} \tag{12}$$

Let η be the number of tunneling electrons per molecule with radius r_o. The limit

$$R_L = \frac{\gamma \varepsilon_o}{\pi\left(\frac{e\eta}{\pi r_o^2}\right)^2} > 1.5\text{nm} \tag{13}$$

can be estimated by using the data for water as ρ=1, $\varepsilon_o = 88,\ \gamma = 75$ and $\eta < \frac{1}{3}$. Note that R is the limit of size for which the quantum bag is tenable; it is of the right order of magnitude in nm.

Stability is admissible when $\frac{2\gamma}{R}$ is negligible. Pseudopotential Φ_o would enhance the total energy of a solid block. When R<RL, surface and volume energy are comparable. The system attains a new state such that no distinction between boundary and volume energy would exist. A metastable state would result. It breaks down and cracking could prevail. Fracture occurs in the region of imhomogeneity with size R~RL.

With an external pressure is impressed, the condition of stability becomes

$$-P + \frac{2\gamma}{R} - \frac{(4\pi\sigma)^2}{\varepsilon_o 8\pi} < 0 \quad , \quad R_L < 2\gamma / \left(\frac{(4\pi\sigma)^2}{8\pi\varepsilon_0} + P\right) < R \tag{14}$$

For pressure acting on a bulk, the critical size of the bulk should be smaller than the limit size RL. On the contrary, it should be larger, if an external stress is applied. Hence cracking depends on size and pressure that give rise to a nonhomogeneous environment of micro size.

Cracking begins at a metastable state with dimension less than RL; it tends to exist in regions where impurities and disorders prevail.

5. Concluding

For a quantum bag, surface tension tends to expand the shell of tunneling electron cloud while Coulomb force pulls the electron cloud inward. The pulling force should be much larger than that of expansion, the former is responsible for the pseudopotential that gives a negative potential for all electrons inside. Note that $-\frac{(4\pi\sigma R^2)^2}{\varepsilon_o 2R}$ acts adiabatically, $-\frac{Q^2}{\varepsilon_o 2R}$. It is because the surface structure is quantized such that any small change can occur only adiabatically, leaving the quantization uneffected. That means that Q would be a fixed quantity when volume changes in a EOS.

When the bulk size decreases, the "quantum bag" becomes unstable and could collapes into a many-body system. There would not be a sharp boundary giving rise to a big molecule. Cracking is a transition when stress encounters such a small region where a stable solid serves as state decays into a big molecule of nm scale size.

Reference

[1] K.J. Cheng, S.Y. Cheng, Theoretical Foundation of Condensed Material, Progress in Nature Science, 6(1) (1996) 12-25.

ORAL REFERENCE: ICF100650OR

ON THE APPLICABILITY OF THE ESSENTIAL WORK OF FRACTURE METHOD TO THICK ABS SE(B)-SPECIMENS

P. Luna[1], P. Frontini[1]*, A. Cisilino[1], C. Bernal[1], B.Cotterell[2] and Y-W Mai[2]

[1] INTEMA, (UNMdP-CONICET), J. B. Justo 4302, 7600, Mar del Plata, Argentina.
[2] Mechanical and Mechatronic Engineering Department, The University of Sydney, NSW 2006, Australia.

ABSTRACT

This paper deals with the application of the EWF methodology to thick ABS SEN(B)-specimens in order to study its applicability to conditions other than plane stress. Different loading regimes were induced by varying the testing temperature. Post-mortem fracture surface appears to be completely stress whitened, indicating ductile fracture. Load-line displacement plots display geometric similarity over a well-defined range of ligament lengths for which the application of the EWF methodology was in principle possible. At the same time crack growth was observed to initiate before maximum load and the complete ligament yielding. Over a critical ligament length gross yielding occurred and the total specific work of fracture was found independent of ligament length. Below this critical ligament length, EWF methodology seemed to be still applicable and it was possible to extrapolate reliable w_e values. Besides, the EWF was simulated by elastic-plastic FEM analysis. Numerical results were consistent with experimental findings.

KEYWORDS: essential work of fracture (EWF) applicability; ABS; plane stress- plane strain regime; FEM modeling.

INTRODUCTION

The essential work of fracture (EWF) has developed as an efficient methodology to characterize the fracture toughness of ductile polymers films under the plane stress condition[1-4]. At the same time the simplicity of this methodology makes very attractive to extend its applicability to other loading conditions, such us the plane-stress plane-strain transition and pure plane-strain regimes [5-11]. In this sense the present work deals with the application of the EWF methodology to thick ABS SEN(B)-specimens, for which different loading conditions were induced by varying the testing temperature. Experimental results are complemented with numerical FEM simulations.

THE EWF METHODOLOGY

The EWF method is based on the assumption that the total work of fracture, w_f, consists of two work components: one referred to as the essential work of fracture, w_e, which is related to the failure mechanisms that occurs in an inner fracture process zone, and the other referred as the non-essential total work of fracture, w_p, which stands for the work dissipated in the outer plastic deformation zone and is geometry-dependent. To this extent application of the EWF must fulfil the following conditions [4]: (1) the ligament should yield prior to fracture initiation; (2) w_e should be proportional to the ligament length, l; and (3) w_p

should be proportional to the square of the ligament length, l^2. In terms of specific work theory and under a plane stress condition, this leads to the following relationship:

$$w_f = w_e + \beta w_p l \tag{1}$$

in which β is a geometrical shape factor for the outer plastic zone. Consequently, when plane stress conditions prevail for all ligament lengths, it is assumed that w_e is constant and can be obtained by linear extrapolation to zero ligament length. For conditions other than plane stress w_e is not only function of l, but of the specimen thickness B, *i.e.* $w_e=w_e(l,B)$, while βw_p does not depend on l. Under these conditions the essential work of fracture w_{Ie} can be also obtained by a non-linear extrapolation of data to zero ligament length [3].

EXPERIMENTAL PROCEDURE

Experimental set-up

Experiments were conducted on commercial acrylonitrile-butadiene-styrene terpolymer, Lustran ABS-740. Single-notched thick specimens were deformed in bending, SEN(B), as in [7]. Specimen dimensions were: span S=56 mm, width W=13 mm and thickness B as given in Figure 2. A V-notch 1 mm deep was machined at the compression side opposite the sharp notch to avoid hinging. Tests were performed at constant crosshead speed of 2 mm/min (quasi-static loading condition). Different loading regimes were induced by varying temperature (20 and 80°C). As reported in Table 1 yield stress is drastically reduced with the increment in temperature, promoting generalized plastic flow and inducing plane stress condition. The total work of fracture was calculated from the integration of the load vs. displacement data. Finally, and for the sake of simplicity, the EWF was computed by linear extrapolation of data to zero ligament length irrespectively of the stress state [6,8,10].

Experimental results

Fracture surfaces always appeared stress-whitened all over the full ligament. The whitened zones were elliptical, and hence their volumes scaled with the square of the ligament length (see Figure 1). Geometric similarity between specimens of different ligament length were assessed from load-line traces. Only short ligaments did not verify geometric similarity and consequently they were not used for w_e determination. EWF plots are shown in Figure 2, and the obtained w_e values in Table 1.

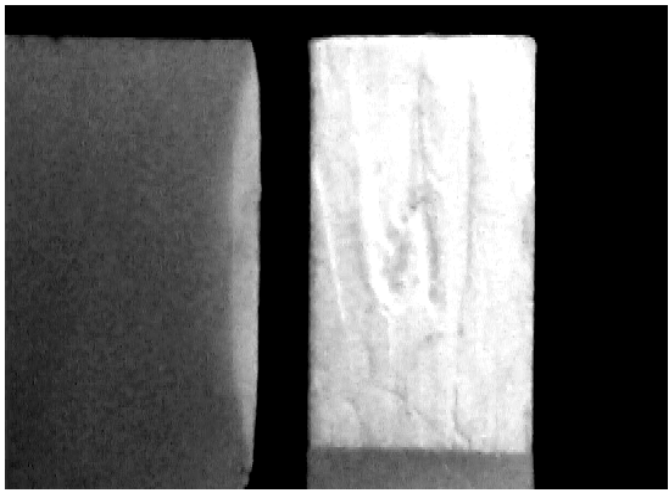

Figure 1: Fracture surface and side view of a broken sample of ABS.

The specific work of fracture was found to be independent of ligament size for long ligament lengths. The same effect was observed by other authors [3,8,12,13]. Among them Lesser and Jones [13] proposed that under this condition the failure mechanism is dominated by gross yielding of the material, and it is not significantly altered by the presence of the flaw. In Figure 2, additional experiments carried out on specimens with blunt starter notches are also shown. The obtained results suggested that the process is not only controlled by the presence of the sharp notch since edge effects are also significant.

TABLE 1

TENSILE YIELD STRENGTH AND SPECIFIC ESSENTIAL WORK OF FRACTURE

	w_{Ie} (N/mm)	σ_y (MPa)
T= 20 ºC, B= 7mm	4.4	42
T= 80 ºC, B= 4mm	6.1	22
T= 80 ºC, B= 7mm	6.3	22

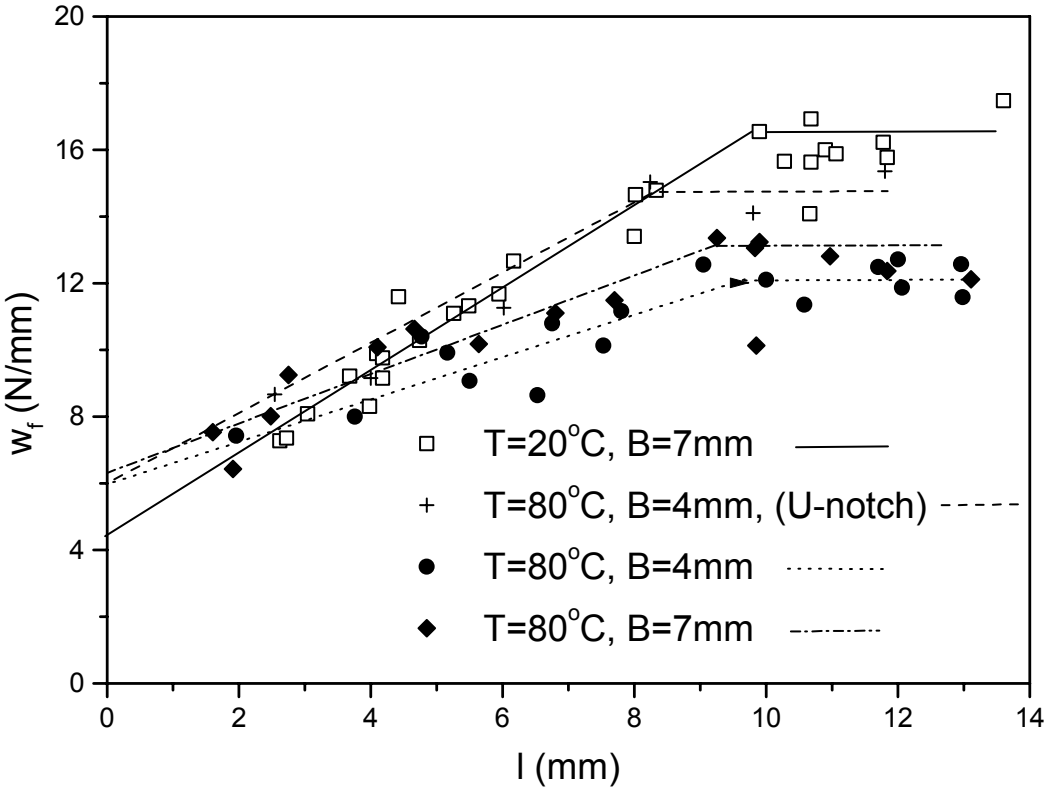

Figure 2: Specific fracture work versus ligament length.

For most of the specimens it was possible to optically check (See Figure 3) that cracks had clearly advanced before the full ligament yields and prior to the attainment of the maximum load. The stress-whitened zone advanced ahead of the crack as it propagated. To achieve the condition of yielding of the full ligament prior to crack propagation seems to be difficult in SEN(B) specimens due to the nature of the bending stress distribution. However, EWF seems to work properly providing that crack propagation occurs after a large plastic zone had developed (see Figure 3).

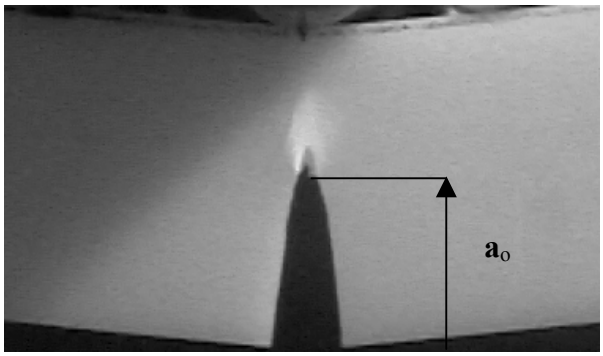

Figure 3: Side view of sample under loading showing that crack initiates before the full ligament yields.

NUMERICAL MODELING

Finite Element Modeling

The EWF was simulated by elastic-plastic FEM analysis by using the ABAQUS program. Crack-tip opening angle (CTOA) was selected as fracture criterion with the "DEBOND" and "FRACTURE CRITERION" options [14]. Two input parameters are needed for the CTOA, i.e. the normal critical displacement between the crack surfaces and the distance behind the current crack tip where the normal displacement is computed. Following the procedure detailed in [15] input parameters were set to 0.3 mm for the distance and 0.21 mm for the normal displacement. Eight-node quadrilateral plane-strain elements were used to discretize one half of the specimen.

Numerical results

Comparison of the numerical load-displacement curves with experimental data for a selection of ligament lengths are plotted in Figure 4 for the room temperature case. The specific work, w_f, is plotted against the initial ligament length in Figure 5.

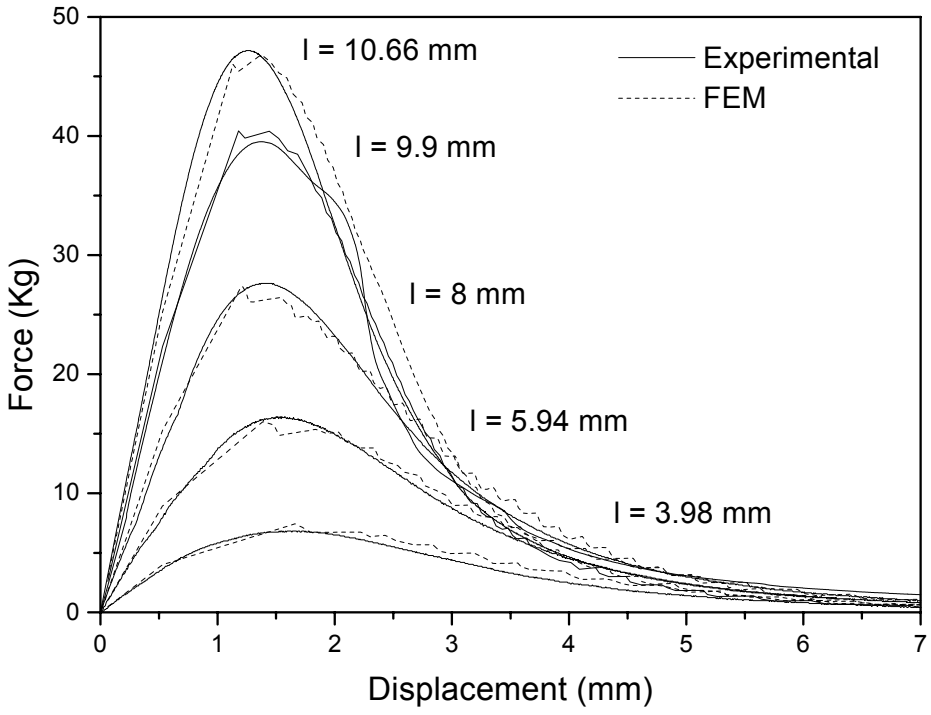

Figure 4: Experimental and numerical P-δ curves for a selection of ligaments

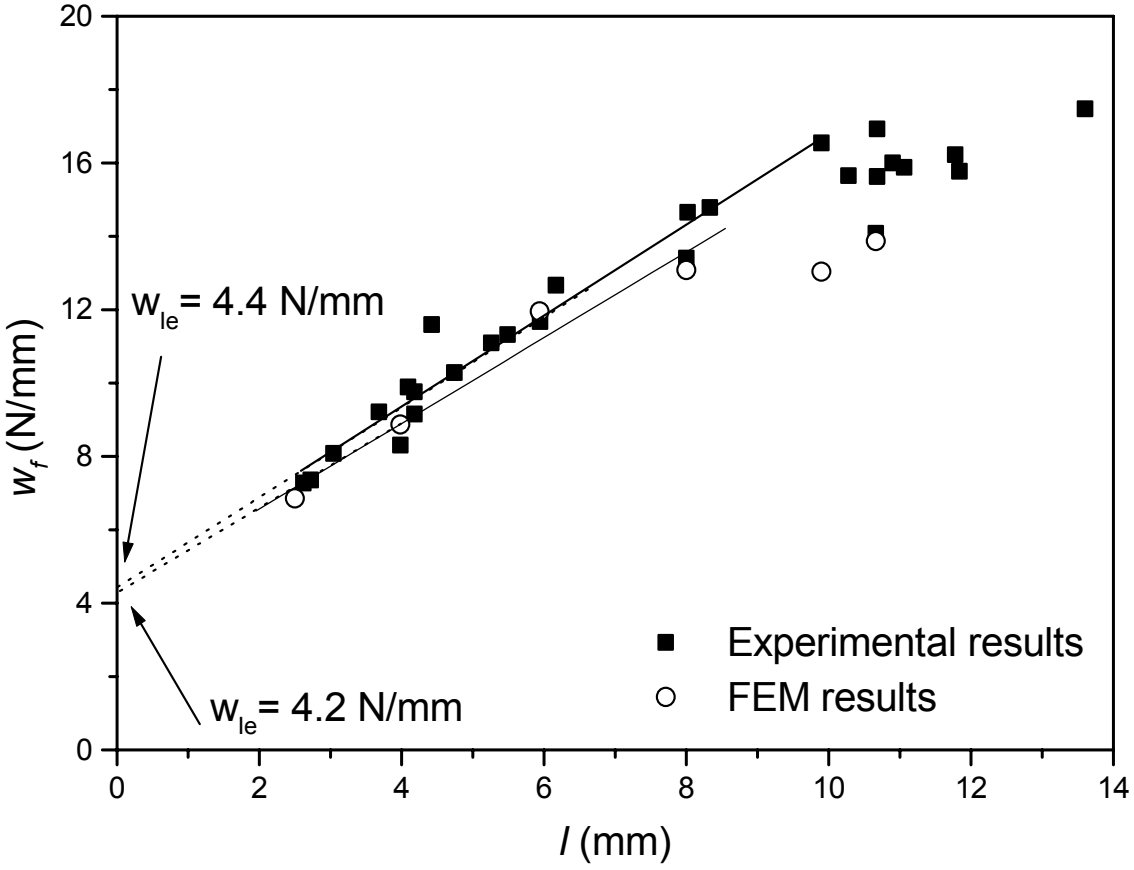

Figure 5: Specific total fracture work versus initial ligament length

Figure 6 shows the deformed configuration at crack initiation, together with the distribution of equivalent plastic strain. It is worth to note that as experimentally observed the numerical model predicts crack propagation before the full ligament yields.

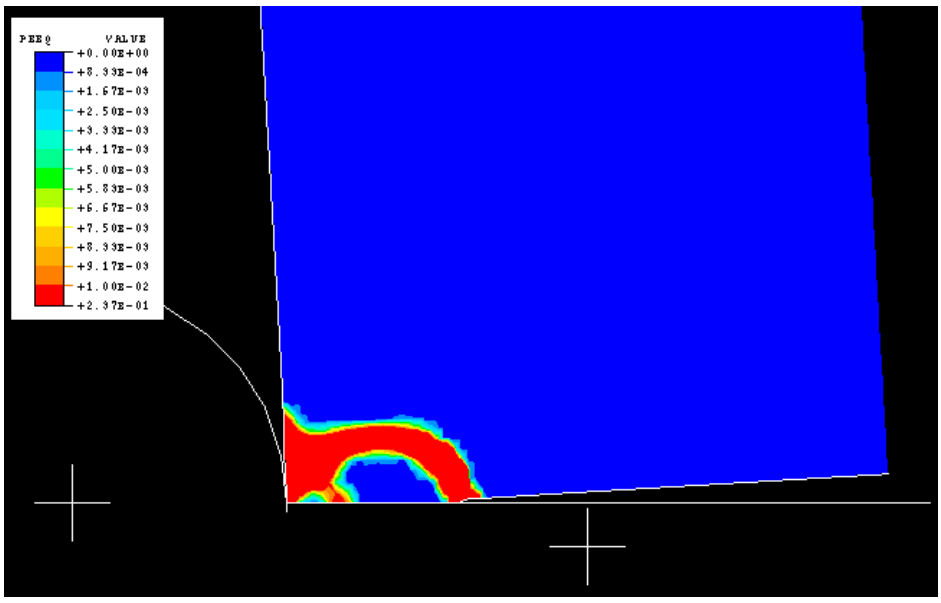

Figure 6: Equivalent plastic strain distribution at the onset of crack initiation

CONCLUSIONS

The EWF was applied to ABS thick specimens at different fracture regimes in bending under static loading conditions. Geometric similarity of the load-line displacement records was verified over a range of ligament lengths for which the extrapolated data led to apparent reliable w_e values. It was observed that in many samples crack growth took place prior the ligament was fully yielded. It seems that this fact does not compromise EWF application, provided a large zone of the ligament is anyway yielded and the stress-whitened zone continues advancing ahead the growing crack. Hence, the requirement for the specimen ligament to be fully yielded before crack propagation appears to be too restrictive for bending experiments.

The total work of fracture was found to be constant over a certain ligament length. These results provide evidence that an upper limit to the methodology validity could exist.

The EWF was successfully simulated numerically using FEM. Results were consistent with experimental findings.

ACKNOWLEDGMENTS

The authors would like to thank the Fundación Antorchas for the financial support of this project between Argentina and Australia.

REFERENCES

1. Broberg, K.V. (1968) *Int. J. Fract*, 4, 11.
2. Mai Y-W and Cotterell B. (1985) *Eng. Fract. Mech*., 21, 123.
3. Y-W Mai and Cotterell B. (1986). *Int. J. Fract.*,32, 105
4. ESIS *Test Protocol for Essential Work of Fracture (Version 5)*, European Structural Integrity Society, (1997).
5. Fasce L., Frontini P., Bernal C. and Mai Y-W.(2001), *Polym. Eng. Sci*, 41,1.
6. S. Hashemi and J.G. Williams, (2000) *Plast. Rubber and Composites*, 29, 294
7. Kudva R. A., Keskkula H. and Paul D. R. (2000) *Polymer*, 41, 335
8. Martinatti F. and Ricco T. (1995). In *Proceedings of Impact and Dynamic Fracture of Polymers and Composites*, ESIS 19, J.G. Williams and A. Pavan, eds. pp.83-91.
9. Vu-Khanh T. (1988) *Polymer*, 29**,** 1979.
10. Saleemi A.S. and Nairn J.A. (1991) *Polym. Engng. Sci*., 30, 211.
11. Mai Y-W. and Powel P. (1991). *J. Polym. Sci. Part B: Polym. Phys*., 29**,** 785.
12. Paton C.A., Hashemi S.. (1992). *J. Mat. Sci*., 27, 2279.
13. Lesser A. and Jones N. *J.* (2000) *Appl.Polym. Sci, 76, 763.*
14. ABAQUS/*Standard User's Manual*, Version 5.7, (1997)
15. Chen X-H., Mai Y-W., Tong P. and Zhang L-C. (2000).In *Proceedings of Fracture of Polymers, Composites and Adhesives*, ESIS 27, J.G. Williams and A. Pavan, eds.pp.175-186.

ON THE CRACK EXTENSION FORCE OF CURVED CRACKS

K. Eriksson

Department of Solid Mechanics, Luleå University of Technology
SE 97187 Luleå (Sweden)

ABSTRACT

A domain independent integral is obtained from the principle of virtual work. A suitable choice of the virtual displacement field allows variation of the position of a crack tip. For materials possessing a strain energy function Eshelby's [1] definition of the force on a point defect is used to obtain the crack extension force. The method is general and allows treatment of a crack whose surfaces and front are curved by using curvilinear coordinates. To illustrate the applicability of the method three examples of the point-wise crack extension force are given, with different combinations of crack surface and crack front curvature. A general expression of the crack extension force for curved cracks is suggested. In Cartesian coordinates the proposed expression is reduced to Rice's [2] *J*-integral.

KEYWORDS

Curved crack, Crack extension force, Domain independent integral, Elastic material.

INTRODUCTION

Eshelby's [1] definition of the force acting on a point defect in an elastic solid is briefly: minus the rate of increase of the total energy with respect to a variation of the position of the defect. The total energy is the sum of the strain energy of the part of the solid considered and of the potential energy of its external loads, if any. The force is expressed as an integral of a normal component of Eshelby's energy momentum tensor taken over a finite and closed surface containing the defect. Two essential features of this integral are that it is path independent and has a finite value as the integration area is shrunk towards zero around the defect. In crack problems the point defect is naturally associated with the tip of the crack and the force integral, which must be zero on stress-free crack surfaces, is called the 'crack extension force'.

In this work we start by constructing a domain independent integral by using the principle of virtual work. A suitable choice of the virtual displacement field allows variation of the position of the crack tip. For materials possessing a strain energy function a general expression of a domain independent integral is derived, which is not

associated with any geometry in particular. Application to a given crack geometry is most conveniently done by a suitable choice of coordinate system in which the description of the crack geometry is as simple as possible. The method is general and by choosing curvilinear coordinates, cracks with curved surfaces and front can be treated, the only restriction being that the curvilinear coordinate system must be orthogonal. This follows from the condition that crack extension is confined to the tangent plane of the crack and perpendicular to the crack front tangent and that the domain independent integral must vanish on stress free crack surfaces. The crack extension force is finally obtained by applying Eshelby's [1] definition.

Three examples of curved cracks are given, with different combinations of crack surface and crack front curvature. The first is the penny-shaped crack with radial crack extension (plane crack surface and curved crack front), the second the circular arc crack with crack extension circumferentially (curved crack surface and straight crack front) and the third the latter crack geometry but with crack extension axially (curved crack surface perpendicular to the direction of crack extension). In order to obtain the point-wise value of the crack extension force, loading and crack extension are assumed uniform along the crack front in all cases. The results imply the general form of the crack extension force for a crack with curved surfaces and a curved front. For a straight crack in Cartesian coordinates in two dimensions the general form of the crack extension force is reduced to Rice's [2] *J*-integral.

A DOMAIN INDEPENDENT INTEGRAL

Let q_i, $i = 1,2,3$ be orthogonal curvilinear coordinates and consider the integral

$$\delta I = \oint_S t_i \delta u^i \, dS - \int_V \delta W \, dV \tag{1}$$

where δ denotes variation and *S* and *V* are surface and volume of a body or any part thereof, respectively, t_i stress covector, u^i displacement and *W* strain energy. Superscripts denote contravariant and subscripts covariant tensor properties. Summation over indices appearing twice is implied.

Assume that there exists a strain energy function $W = W(u^i_{,j})$ such that $t_i^{\ j} = \partial W / \partial u^i_{,j}$, where t^i_j is stress and a comma (,) denotes covariant differentiation. Take the virtual displacement δu^i as minus the total differential of the "actual" u^i, (the solution to the problem studied), that is

$$\delta u^i = -u^i_{,k} \delta q^k, \tag{2}$$

where δq^k can be arbitrarily chosen. By the principle of virtual work the integral δI is zero for any regular region. Further, (2) allows modelling of crack extension in the direction of q_i through variation of the position of the crack tip.

Using the facts that i) variation and differentiation and ii) the second covariant derivative are commutative, the internal virtual work δW can now be written

$$\delta W = -\frac{\partial W}{\partial q^k} \delta q^k - t_i^{\ j} u^i_{,k} \delta q^k_j \tag{3}$$

Inserting in (1) yields

$$\delta I = \int_V \frac{\partial W}{\partial q^k} \delta q^k \, dV - \oint_S t_i u^i_{,k} \delta q^k \, dS + \int_V t_i^{\ j} u^i_{,k} \delta q^k_j \, dV \tag{4}$$

As *V* is arbitrary, the integral expression δI is domain independent if *V* is regular. Further, by using Cauchy's formula $t_i = t_i^{\ j} n_j$, where n_j is the outward positive unit normal vector on *S*, the divergence theorem, the equations of equilibrium, $t_{i,j}^{\ j} = 0$, then, as expected, (3) can be obtained from the integrand of the surface

integral in (1). Eqn. (4) is quite general and not associated with any geometry in particular. Application to a given crack geometry is most conveniently done through a suitable choice of coordinate system, as shown in the examples.

The penny-shaped crack

Let r, θ, z be cylinder coordinates. The non-zero Christoffel symbols are $\Gamma^r_{\theta\theta} = -r$ and $\Gamma^\theta_{r\theta} = \Gamma^\theta_{\theta r} = 1/r$. Let a and Ψ be suitable constants, $r \le a$, $z = 0$ the crack plane and δr an increment which is independent of θ. At $r = a$ in particular, the crack extension increment is δr. Also, let the loading be axisymmetric. In the last integral in (4) the only non-zero component of δq^k_j is $\delta q^\theta_{,\theta} = \delta r / r$. Writing the variation $\frac{\partial W}{\partial q^k}\delta q^k = \frac{\partial W}{\partial r}\delta r$ we obtain from (4)

$$\delta I = \int_V \frac{\partial W}{\partial r}\delta r \, dV - \oint_S t_i u^i_{,r}\delta r \, dS + \int_V t^q_i u^i_{,q}\frac{\delta r}{r} dV \qquad (5)$$

Adding and subtracting W/r to and from the first and second volume integral and writing the first volume integral as a surface integral, we get

$$\delta I = \oint_S \left(W n_r - t_i u^i_{,r}\right)\delta r \, dS - \int_V \frac{1}{r}\left(W - t^q_i u^i_{,q}\right)\delta r \, dV \qquad (6)$$

Let Γ_e and Γ_o be curves in the $r-z$-plane which enclose the crack tip, Γ_e infinitely close to and Γ_o remote from the crack tip and *V* a tubular volume generated by rotation of Γ_e and Γ_o in the sector $|\theta| \le \Psi/2$ around the z-axis. The surface *S* which surrounds a finite sector of the plane axisymmetric crack is divided into six parts; those generated by Γ_e and Γ_o, here denoted S_e and S_o, respectively, the crack surfaces and both ends of the tubular volume.

It is easily seen that the surface integral in (6) vanishes on the crack surfaces and the ends of the tubular volume. On the crack surfaces $n_r = 0$ and because they are stress free, $t_i = 0$. On the ends of the tubular region $n_r = 0$ and on account of axisymmetric loading and deformation $t_r = t_z = 0$ and $u_{\theta,r} = 0$ so that $t_i u^i_{,r} = 0$ there. Further, the only non-zero t^q_i-component in the volume integral is t^θ_θ.

The surface element on S_e and S_o can be written $dS = r\,\Psi\, d\Gamma$, where $d\Gamma$ is a curve element.
Take Γ_e and Γ_o positive counterclockwise on S_e and S_o, respectively. Then Eqn. (2), taking δr outside the integrals and writing the volume element $dV = \Psi\, r\, dA$, where dA is an area element and noting that all integrands are independent of θ, yield, as Γ_e is shrunk towards zero around the crack tip,

$$\delta I = -\Psi a \delta r \lim_{\Gamma_e \to 0} \oint_{\Gamma_e}\left(W n_r - t_i u^i_{,r}\right)d\Gamma + \Psi \delta r \oint_{\Gamma_o}\left(W n_r - t_i u^i_{,r}\right) r \, d\Gamma$$
$$- \Psi \delta r \int_{A_o}\left(W - t^q_\theta u^\theta_{,q}\right) dA \qquad (7)$$

where A_o is the area inside Γ_o.
Now $\delta I = 0$ implies a variation of the total energy of the domain considered in accordance with the definition of Eshelby [1]. As δr is the virtual displacement of the crack tip

$$F = \lim_{\Gamma_e \to 0} \oint_{\Gamma_e}\left(W n_r - t_i u^i_{,r}\right) d\Gamma \qquad (8)$$

must be the associated crack tip or crack extension force per unit length of the crack front. Cancelling common factors Eqs. (7) and (8) yield

$$F = \oint_{\Gamma_o}\left(W n_r - t_i u^i_{,r}\right) d\Gamma - \frac{1}{a}\int_{A_o}\left(W - t^q_\theta u^\theta_{,q}\right) dA \qquad (9)$$

Taking physical components (σ_{ij}, ε_{ij}, u_i, etc.) and using $\varepsilon_{qq} = u_{q,q}$ we get

$$F = \oint_{\Gamma_o} \left(W n_r - t_i u_{i,r} \right) d\Gamma - \frac{1}{a} \int_{A_o} \left(W - \sigma_{qq} \varepsilon_{qq} \right) dA \tag{10}$$

per unit crack front length circumferentially, which is also the point-wise value of the crack extension force.

The circular arc crack

Let r, θ, z be cylinder coordinates as above, b an additional constant and $r = a$, $|\theta| \le \Psi / 2$ and $|z| \le b/2$ the crack plane. We consider crack extension in two different directions; in the first, $d\theta = a d\theta_a / r$, where $d\theta_a$ is independent of θ_i, is an increment in general. At the crack tip $\theta = \Psi / 2$ the crack extension is $a d\theta_a$. The only non-zero component of $d\theta^k_{,j}$, which in this case is $d\theta^r_{,q} = -r d\theta$ and the variation $\frac{\partial W}{\partial \theta^k} d\theta^k = \frac{1}{r} \frac{\partial W}{\partial \theta} r d\theta$ yield with (4)

$$dI = \int_V \frac{1}{r} \frac{\partial W}{\partial \theta} r \, d\theta \, dV - \oint_S t_i u^i_{,q} \, d\theta \, dS - \int_V t^q_i u^i_{,r} \, r \, d\theta \, dV \tag{11}$$

Transforming the first volume integral into a surface integral, we get

$$dI = \oint_S \left(W n_q - t_i u^i_{,q} \right) d\theta \, dS - \int_V t^q_i u^i_{,r} \, r \, d\theta \, dV \tag{12}$$

Let V be a tubular volume along the crack tip considered and with plane ends in the z-direction. For simplicity we consider uniform loading along the crack front. In this case also, the surface integral in (12) is zero on both ends of the tube and in particular on the curved crack surfaces. The surface element can be written $dS = b \, d\Gamma$ and the volume element $dV = b \, dA$. With suitable redefinition of Γ_e etc., we arrive at the crack extension force, noting that $a d\theta_a$ is its physical displacement, with arguments similar to those for the penny-shaped crack

$$F = \oint_{\Gamma_o} \frac{1}{r} \left(W n_q - t_i u^i_{,q} \right) d\Gamma - \int_{A_o} (t^q_r u^r_{,r} + t^q_q u^q_{,r}) \, dA \tag{13}$$

In physical components (13) reads

$$F = \oint_{\Gamma_o} \left(W n_q - t_i u_{i,q} \right) d\Gamma - \int_{A_o} \frac{1}{r} (\sigma_{rq} u_{r,r} + \sigma_{qq} u_{q,r}) \, dA \tag{14}$$

per unit length of the crack front (in the z-direction).

Finally, we consider crack extension in the z-direction of the circular arc crack. Let dz be an increment that is independent of θ_i. The crack extension increment at $z = b/2$ is thus dz. Now, all $d\theta^k_{,j} = 0$ and the variation $\frac{\partial W}{\partial \theta^k} d\theta^k = \frac{\partial W}{\partial z} dz$ yield with (4)

$$dI = \int_V \frac{\partial W}{\partial z} dz \, dV - \oint_S t_i u^i_{,z} \, dz \, dS \tag{15}$$

Let V be a tubular volume around the crack tip considered and otherwise identical to that of the penny-shaped crack. The surface and volume element can in this case be written $dS = \Psi r \, d\Gamma$ and $dV = dr \, r \Psi \, dz$, respectively. Transforming the volume integral we get

$$dI = \Psi \oint_S \left(W n_z - t_i u^i_{,z} \right) r \, dz \, d\Gamma \tag{16}$$

The surface integral (16) is with arguments similar to the above cases zero on the curved crack surface. For uniform loading along the crack front the surface integral also vanishes on the ends of the tubular volume.

As $\Gamma_e \to 0$ implies that $r \to a$ it follows from Eqn. (8) that

$$\lim_{\Gamma_e \to 0} \oint_{\Gamma_e} \left(W n_z - t_i u^i_{,z} \right) r \, d\Gamma = aF \tag{17}$$

Taking $\delta I = 0$ and cancelling common factors Eqs. (16) and (17) yield

$$aF = \oint_{\Gamma_o} \left(W n_z - t_i u^i_{,z} \right) r \, d\Gamma \tag{18}$$

The integrand in (18) contains a singularity at the crack tip. This means that $r = a$ can be extracted from the integral (formal proof omitted here, compare however with the contour integral of the penny-shaped crack, Eqn. (10)) and cancelled. In physical components the crack extension force is

$$F = \oint_{\Gamma_o} \left(W \mathrm{n}_z - \mathrm{t}_i \mathrm{u}_{i,z} \right) d\Gamma \tag{19}$$

per unit length of the crack front circumferentially.

DISCUSSION

In the examples given we have considered uniform crack extension and loading only, in order to enhance the influence of curvature of the surface of the crack and of the crack front and determined a point-wise value of the crack extension force. In a general loading case the surface integrals on the plane ends of the tubular region around the crack tip (taken together) do not vanish. Because the surface integral contains a covariant derivative its value is dependent on curvature. However, the surface integrals in question are also different from zero for a plane crack with a straight crack front in a general loading case, expressed in Cartesian coordinates, as shown by Carpenter et al. [3]. This feature is thus not exclusive of curved cracks.

The increment δq^i in (2) can be arbitrarily chosen. In curvilinear coordinates the covariant derivative $\delta q^i_{,j}$ is however not necessarily always zero, even if δq^i is independent of q_j, although such cases can in fact be found. The last integral in (4) is thus in general not zero for curved cracks and this term is the source of the ”correction” terms to the well-known remaining part of the expression for the crack extension force, the contour integral. In Cartesian coordinates the covariant derivative reduces to its partial counterpart and all $\partial \delta q^i / \partial q^j$ are zero. The integral (4) is reduced to

$$\delta I = \int_V \delta W \, dV - \oint_S t_i u_{i,k} \delta q_k \, dS \tag{20}$$

and for crack extension e.g. in the x-direction in the x-y-plane results

$$F = \oint_{\Gamma_o} \left(W \mathrm{n}_x - \mathrm{t}_i \mathrm{u}_{i,x} \right) d\Gamma \tag{21}$$

The crack surface of the penny-shaped crack is plane. The surface integral in (10) is thus a correction term due to the curvature of the crack front. In this case the curvature is constant along the crack front. It is also seen in (7) that the correction term is constant per unit length circumferentially. The result (10) has been obtained previously by many, as recently reviewed by Eriksson [4].

For the circular arc crack and crack extension circumferentially the crack front is straight but the crack plane is curved. The area integral in (14) is in this case a correction term for the crack plane curvature in the direction of crack extension. An exact analytical solution of the stress intensity factors of the circular arc crack has been obtained by Cotterell and Rice [5]. Lorentzon and Eriksson [6] have found the effective stress intensity factor calculated from Eqn. (14) using results of a finite element analysis to be within 1 percent on the average from those of the analytical solution, for identical boundary conditions.

In the last example, the circular arc crack and crack extension axially, both the crack surface and the crack front are straight in the direction of crack propagation. In this case there is no correction term. We note however, that the crack plane is curved in a direction perpendicular to the direction of crack extension.

From the above results we conclude that the general expression for the point-wise crack extension force of a curved crack must be a sum of a contour integral and one or more area integrals. The contour integral corresponds to or can be reduced to (21). There are two types of area integrals, one that is due to the curvature of the crack front in the direction of crack extension and the other that is due to the curvature of the crack surface in the direction of crack extension. The contribution to the total crack extension force from both types of volume integral increases with curvature. The crack surface curvature in a direction perpendicular to the direction of crack extension does not affect the crack extension force.

If the crack front radius a in (10) tends to infinity the contribution from the correction term tends to zero and any finite segment of the crack front approaches a straight line. Similarly, if the radius r in (14) tends to infinity the contribution from the correction term tends to zero and the crack surface approaches a plane. All expressions for the crack extension force thus tend to (21) as curvature diminishes. We recognise of course this expression as identical to Rice's [2] J-integral in two dimensions.

References

1. Eshelby, J.D. (1975). *J. Elast.* 5, 321-335.
2. Rice, J.R. (1986). *J. Appl. Mech.* 35, 379-386.
3. Carpenter, W.C., Read, D.T. and Dodds, R.H. (1986). *Int. J. Frac.* 31, 303-323.
4. Eriksson, K. (1998). *Int. J. Fract.* 91, L31-L36.
5. Cotterell, B. and Rice, J.R. (1980). *Int. J. Frac.* 16, 155-169
6. Lorentzon, M. and Eriksson, K. (2000). *Engng. Frac. Mech.* 66, 423-439.

16 May 2001

Tracy Collier, ICF10 Conference Organiser
ICF10 Secretariat
Elsevier Science
The Boulevard
Langford Lane
Kidlington
Oxford OX5 1GB
U.K.

Re: Manuscript Number: ICF10079OR

According to Prof Karihaloo's instructions in his letter 9th May 2001, I enclose a) two hard copies of my manuscript "On the crack extension force of curved cracks", b) an electronic version on disk (Windows 95, World 7.0), c) a copyright form and d) a hard copy of the extended abstract.

The manuscript and the extended abstract are revised in that I have corrected some misprints, etc. There are no figures. The hard copies of the manuscript and the electronic version are all identical.

Kind regards

Kjell Eriksson

ORAL REFERENCE: ICF100121OR

ON THE CRACK STABILITY IN METAL PARTICULATE - REINFORCED BRITTLE MATRIX COMPOSITES

M. Kotoul[1] and R. Urbiš[1]

[1]Department of Solid Mechanics, Brno University of Technology, Technická 2, 616 69 Brno, Czech Republic

ABSTRACT

The model of reinforcing mechanism which improves the fracture toughness of brittle matrix composites reinforced by ductile particles is analyzed. The particles form a bridging zone and, thus, constrain the crack opening. The stress-crack opening displacement relationship relies upon the constant volume plastic flow of the particles according to the model suggested recently by Rubinstein and Wang [1]. This model incorporates in a certain way also the particle/matrix interface properties. The particles are allowed to deform using several different patterns which correspond to the particular strength of the particle/matrix interface. Contrary to Rubinstein and Wang's work the triaxiality of the stress state within particles is considered and its impact on the critical crack opening displacement is included. The fracture criteria are analyzed for several combinations of micromechanical parameters of composite system and the resistance curves are presented.

KEYWORDS

Fracture toughness, particulate composites, bridged cracks.

INTRODUCTION

In certain materials, the opening of a crack may be opposed by physical bridges between the crack faces. One example is a ceramic containing ductile metal particles (a particulate-reinforced ceramic). The restraining effect of the second-phase particles on an advancing crack front is the basis for a toughness increment. Stretched ductile particles (ligaments), e.g. Al particles in Al_2O_3/Al systems or Co enclaves in WC/Co composites, are detected at considerable distances l_p behind the crack tip. The basics of the mechanism of fracture toughness enhancement in brittle matrix composites with distributed ductile particles were analyzed in the literature, e.g. [3-6].

It is important to note that the particles's ductility alone is not sufficient for any significant improvement in toughness. It is observed that the quality of the particle/matrix interface also becomes of great importance because it strongly influences the particle deformation pattern. Specifically, some optimum interface debonding is needed to remove the geometric constraint and allow the particles to deform plastically in a significant part of their volume. An analytical approach, allowing detailed calculation of the development of the fracture toughness during loading, was presented by Rubinstein and Wang [1]. Particles were assumed to be elastic-ideally plastic and allowed to deform using several different patterns which correspond to the particular strength of the particle/matrix interface. The deformation patterns were simplified versions of those obtained by Tvergaard [2] using finite element computations. Namely, the initially spherical particles of the same radius R simultaneously

form during the plastic deformation a neck of a parabolic profile, as illustrated in Figure 1. The current radius of the bridging cross section of a particle r, the vertical coordinate of the intersection of the parabolic neck with the undisturbed spherical portion of a particle y_{pn} and the half of the crack opening displacement at the particle site $\Delta/2$ within the bridging zone are then related by

$$\frac{r}{R} = \sqrt{1 - \left(\frac{y_{pn}}{R} - \frac{\Delta}{2R}\right)^2} - A\left(\frac{y_{pn}}{R}\right)^2, \tag{1}$$

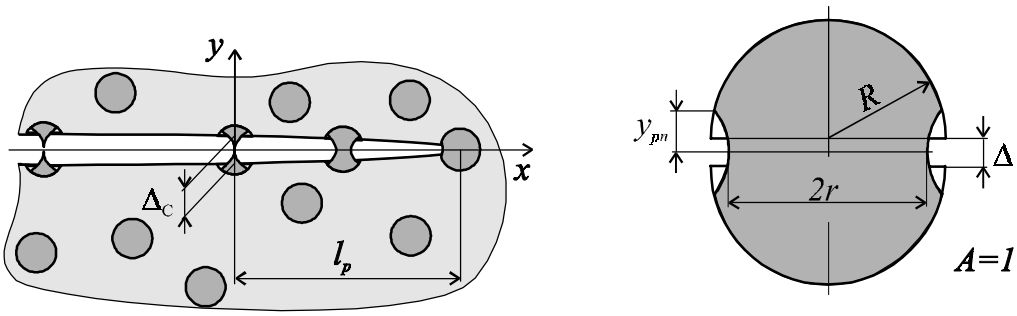

Figure 1: Scheme of bridged crack and particle deformation shape for $A = 1$

where parameter A specifies the curvature of the chosen parabolic profile, $x'/R = A\,(y/R)^2 + r/R$. The authors [1] suggest to associate this parameter with the strength of the particle/matrix interface and to use it as a parameter of the composite. The requirement of incompressibility of the particles provides then the additional condition for determination of r, y_{pn} and $\Delta/2$:

$$2 = \left(1 - \frac{y_{pn}}{R} + \frac{\Delta}{2R}\right)^2 \left(2 + \frac{y_{pn}}{R} - \frac{\Delta}{2R}\right) + 3\left[\frac{1}{5}A\left(\frac{y_{pn}}{R}\right)^2 + \frac{2}{3}A\frac{r}{R}\left(\frac{y_{pn}}{R}\right)^3 + \frac{y_{pn}}{R}\left(\frac{r}{R}\right)^2\right]. \tag{2}$$

A significant simplification was introduced in [1] by assuming a constant stress within the bridging section of each particle. In this paper we will make use of Eqns. 1. and 2. for analytical modelling of debonding of particle/matrix interface. The mean axial stress in the necked bridging section of particles is, however, assumed not to be constant but given by Bridgman's solution. The action of the system of discretely distributed ideally plastic particles is replaced by the action of smeared forces over the bridged zone length l_p. Small scale bridging is assumed, i.e. $l_p << a$, where a is the crack length. Thus, a semi-infinite crack, $x < 0$, $y = 0$, may be considered. The remote load is given through the boundary layer approach, so that the stress $\sigma_{yy} = K_I^N/\sqrt{2\pi x}$ for $x >> l_p$, $y = 0$, where K_I^N is the remote stress intensity factor which can be found by solving an appropriate boundary value problem on the macrolevel using e.g. FEM.

MATHEMATICAL MODELLING

The continuously distributed crack surface bridging load σ_0 can be determined as follows: if R is the average particle radius, l is the interparticle distance and f is the volume fraction of particles, then the restraining stress σ_0 is found to be $\sigma_0 = P/l^2 = P/R^2\,(3f/4\pi)^{2/3}$, where P is the bridging force of a single particle. The bridging force P relates to the mean axial stress σ_1 in the necked region of a particle and to the current radius of the bridging cross section of a particle r as $P = \pi r^2 \sigma_1$. The mean axial stress σ_1 is estimated from Bridgman's solution:

$$\sigma_1 = \sigma_y\left(1 + \frac{R}{Ar}\right)\ln\left(1 + \frac{Ar}{R}\right), \tag{3}$$

where $1/(2A)$ is the radius of curvature of the necked region profile in the normalized coordinates x'/R and y/R, see above, and σ_y is the uniaxial yielding stress of the ductile particle. Finally, the restraining stress σ_0 can be estimated as

$$\sigma_0 = \sigma_y\left(\frac{3f\sqrt{\pi}}{4}\right)^{2/3}\left(\frac{r}{R}\right)^2\left(1 + \frac{R}{Ar}\right)\ln\left(1 + \frac{Ar}{R}\right). \tag{4}$$

In order to obtain the restraining stress σ_0 as a function of the normalized crack opening displacement Δ/R within the bridging zone for the specified curvature of the chosen parabolic profile of the particle's neck, the normalized vertical coordinate y_{pn}/R of the intersection of the parabolic neck with the undisturbed spherical

portion of a particle is first eliminated between Eqns. 1. and 2. and the normalized current radius of the bridging cross section r/R is expressed as a function of Δ/R. Figure 2 shows the plots of the bridging cross

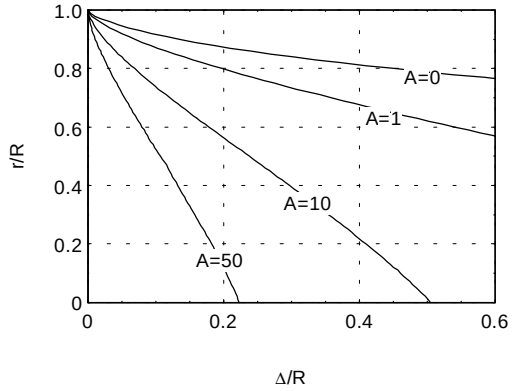

Figure 2: Plots of the bridging cross section r/R vs. Δ/R for several values of A

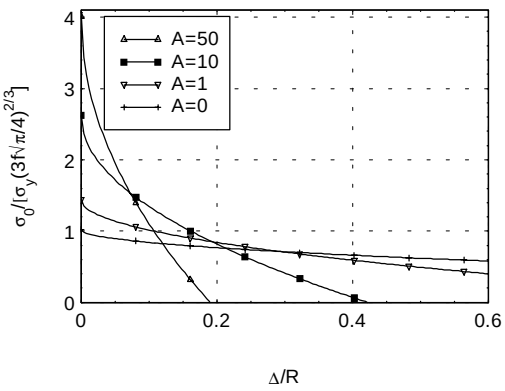

Figure 3: Plots of the normalized restraining stress vs. Δ/R for several values of A

section r/R against $\Delta/2R$ for several values of A. If the relation $r/R - \Delta/R$ is substituted into Eqn. 4. a desired function $\sigma_0(\Delta/R)$ is obtained. Figure 3 shows the course of the normalized restraining stress $\sigma_0/\left[\sigma_y\left(3f\sqrt{\pi}/4\right)^{2/3}\right]$ vs. the normalized half crack opening displacement $\Delta/2R$ for several values of the parameter A for ideally plastic material. Plots in Figure 3 indicate that the slope of $\sigma_0(\Delta/R)$ curve is negative in the stage of the plastic deformation of bridging particles and the bridging zone here exhibits softening behaviour. For the purpose of further analysis there is convenient to have a simple mathematical approximation of the curves in Figure 3. These curves were fitted to the function linear in $\sqrt{\Delta/R}$, i.e.

$$\frac{\sigma_0}{\sigma_y\left(\frac{3f\sqrt{\pi}}{4}\right)^{2/3}} \doteq -a\sqrt{\frac{\Delta}{R}} + b,\ (a>0,\ b>0). \tag{5}$$

Individual fits are not shown in Figure 3 because they are barely distinguishable from the exact numerical curves. The square root dependence of the normalized restraining stress upon the crack opening displacement in Eqn. 5. allows to use a simple perturbation method to the solution of the resulting integral equation.

The analytical formulation is based on the distribution dislocation technique and the boundary layer approach through which the remote load is introduced. The dislocation distribution is introduced only along the bridging zone, the traction-free crack faces are modelled via mirror stresses. The equilibrium condition across the bridging zone leads to a singular integral equation for the unknown Burgers vector density $b_y(x) = -\frac{d\Delta(x')}{dx'}$. Normalizing the integration interval to $\langle -1, 1\rangle$ and integrating by part we obtain after some algebra a strongly singular integral equation for the unknown normalized crack opening displacement $\Delta(\rho')/R$ as follows

$$\oint_{-1}^{1} \frac{d\rho'}{(\rho'-\rho)^2}\frac{\Delta(\rho')}{R} + \int_{-1}^{1} \frac{d\rho'}{(\rho'+\rho+2)^2}\frac{\Delta(\rho')}{R} = -\frac{2(1-\nu^2)}{ER}\left[\sqrt{2\pi}\sqrt{l_p}K_I^N - \pi(\rho+1)\,l_p\sigma_0\left(\frac{\Delta}{R}\right)\right], \tag{6}$$

where E is the Young modulus of and ν Poisson's ratio of composite, the symbol $\oint_{-1}^{1}$ denotes the finite part of the improper (strongly singular) integral in the sense of Hadamard.

NUMERICAL SOLUTION

Substitute the fit of the restraining stress σ_0 from Eqn. 5. in Eqn. 6. and rewrite it formally as

$$L_{-1}^{1}\left[\frac{\Delta}{R}\right](\rho) + \varepsilon\Lambda(\rho)\sqrt{\frac{\Delta(\rho)}{R}} = \Psi(\rho), \tag{7}$$

where L_{-1}^{1} is the integral operator defined by Eqn. 6, $\Lambda(\rho)$ and $\Psi(\rho)$ are linear functions $\Lambda(\rho) = a(\rho+1)$, $\Psi(\rho) = \varepsilon b(\rho+1) - \kappa$, where $\kappa = \frac{2(1-\nu^2)}{E}\sqrt{2\pi}\frac{\sqrt{l_p}}{R}K_I^N$ and ε is a parameter defined by

$$\varepsilon = \frac{2\pi(1-\nu^2)}{E}\sigma_y\left(\frac{3f\sqrt{\pi}}{4}\right)^{2/3}\frac{l_p}{R}, \tag{8}$$

which, in a wide range of typical values of materials properties, fulfills the inequality $\varepsilon < 1$. For $\varepsilon < 1$ an asymptotic expansion of $\Delta(\rho)/R$ in terms of ε can be considered

$$\frac{\Delta(\rho)}{R} \cong \sum_{p=0}^{N} \varepsilon^p \frac{\phi_p(\rho)}{R}, \ \phi_p(\rho) = 0 \text{ for } \rho = 1. \tag{9}$$

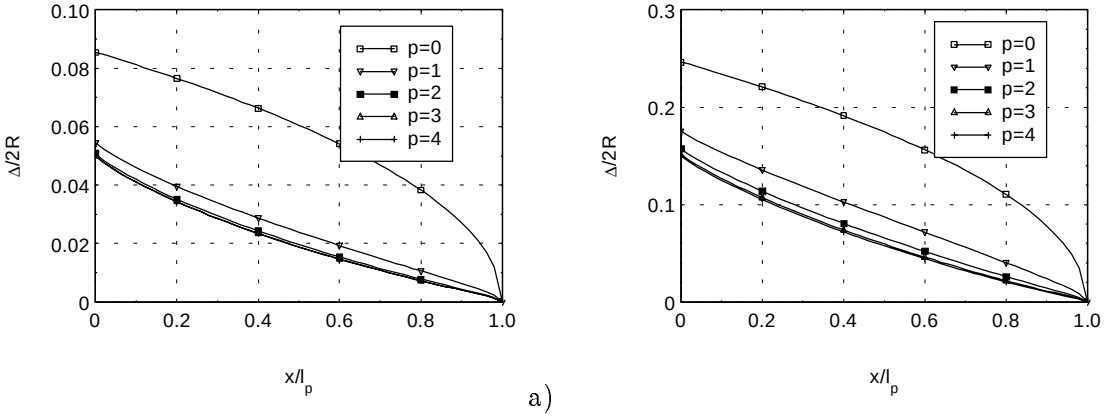

Figure 4: Change of the half of the normalized half crack opening displacement along the bridging zone as the number of terms in (9) increases for $k = 0.5$, $f = 0.25$, $\nu = 0.2$, $A = 1$ and a) $\Delta_c/R = 0.1$, b) $\Delta_c/R = 0.3$.

After substituting Eqn. 9 into Eqn. 7. a system of recursive linear singular equations for the coefficients of the corresponding powers of the parameter ε can be obtained. Solutions of these equations may be expressed in the form $\phi_p(\rho) = F_p(\rho)\, w(\rho)$, where F_p is unknown bounded function and $w(\rho) = \sqrt{1-\rho}$. The unknown function F_p is approximated by a truncated series as $F_p(\rho) \cong \sum_{j=0}^{s} a_{pj}\rho^j$ and the coefficients a_{pj} are determined by a simple collocation method. The influence of the number of terms in the asymptotic expansion of $\Delta(\rho)/R$ in Eqn. 9. is illustrated in Figure 4 which shows a change of the crack opening displacement along the bridging zone as the number of terms in Eqn. 9 increases for specified values of composite parameters and two values of Δ_c/R. The ratio of σ_y/E is not expected to vary significantly for different composite systems and is set to a reasonable value of 0.001. Once the solution is obtained, the local stress intensity K_I^{loc} is determined using the standard formula, see e.g. [7]:

$$K_I^{loc} = \frac{E}{2(1-\nu^2)}\lim_{\rho\longrightarrow 1-}\frac{\sqrt{\pi}\Delta(\rho)}{\sqrt{2l_p(1-\rho)(\rho+3)}} = \frac{K_{IC}}{8(1-\nu^2)}\frac{E}{\sigma_y}\frac{1}{k}\lim_{\rho\longrightarrow 1-}\frac{\pi\frac{\Delta(\rho)}{R}}{\sqrt{\frac{l_p}{R}(1-\rho)(\rho+3)}}, \tag{10}$$

where K_{IC} is the fracture toughness of the matrix and $k = \frac{K_{IC}}{2\sigma_y}\sqrt{\frac{\pi}{2R}}$ is another composite parameter which combines the fracture toughness of the matrix with the yield strength and the radius of the particles. Crack growth in the matrix is controlled by the value of the local stress intensity factor; it has to reach the critical value for the matrix K_{IC}. The bridged zone length l_p is controlled by the crack opening displacement which has to reach a critical value Δ_c. Thus, the fracture criteria are as follows

$$K_I^{loc} = K_{IC}, \ \Delta = \Delta_c. \tag{11}$$

NUMERICAL RESULTS AND DISCUSSION

Equations 11. have been solved for unknowns K_I^N/K_{IC} and l_p/R with various combinations of the parameters A, k, Δ_c/R, f, σ_y/E and ν. A solution for K_I^N/K_{IC} is denoted by $\left(K_I^N/K_{IC}\right)_{eff}$. This value, which is called the normalized effective fracture toughness of composite, describes the toughening effect of ductile particles.

The following computational strategy is adopted; for a given value of the parameter A the unknowns K_I^N/K_{IC} and l_p/R are calculated as functions of the normalized critical crack opening displacement Δ_c/R on a interval

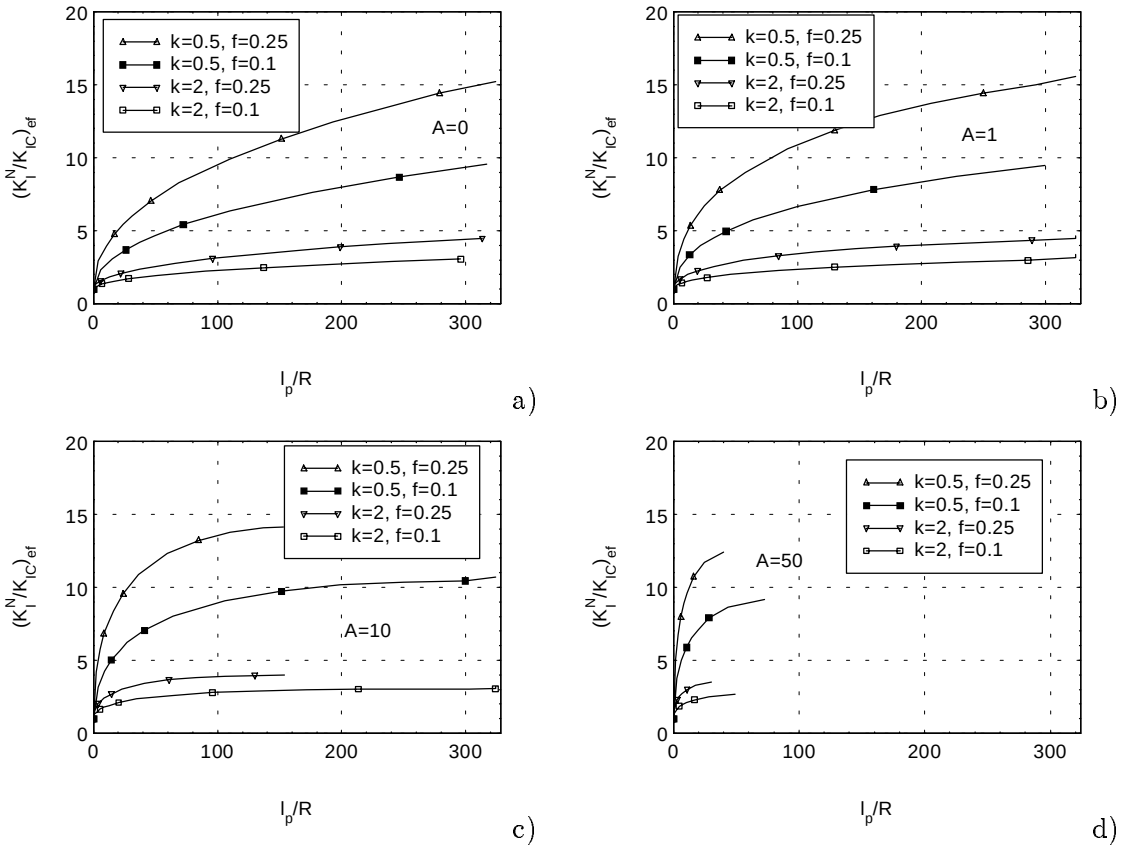

Figure 5: Plots of the normalized effective fracture toughness $\left(K_I^N/K_{IC}\right)_{eff}$ vs. the normalized length of the bridged zone l_p/R for two different values of the volume fraction f and the parameter k and a) $A = 0$, b) $A = 1$, c) $A = 10$, d) $A = 50$.

$0 < \Delta_c/R \leq \Delta_{\max}/R$, where $\Delta_{\max}/R$ is the intercept of the $\sigma_0 - \Delta/R$ relation with the Δ/R axis, see Figure 3. These calculations are performed for several values of the volume fraction of particles f and the composite parameter k. Thus, for each value of Δ_c/R (with f and k held constant) a pair of values of $\left(K_I^N/K_{IC}\right)_{eff}$ and l_p/R is obtained which allows to plot $\left(K_I^N/K_{IC}\right)_{eff}$ against l_p/R by changing Δ_c/R. The plots are shown in Figure 5. Note that with f held constant a higher value of the composite fracture resistance is predicted with decreasing value of the parameter k, i.e. with increasing the size of particles in a specified material system. The same trend was predicted in [1]. So far Δ_c/R has been treated as an independent model parameter and has changed arbitrarily within the interval $(0, \Delta_{\max}/R\rangle$. Note that Δ_c/R depends on the particle ductility and the stress triaxiality as well. The latter is governed by the parameter A which specifies the curvature of the chosen parabolic profile and associates with the strength of the particle/matrix interface. To compare an increase in the toughness $\left(K_I^N/K_{IC}\right)_{eff}$ for different A, the stress triaxiality factor should be included. To do this, a rupture criterion of bridging particles has to be formulated. Widely used in the local approach of ductile fracture is the criterion based on the Rice and Tracey [8] equation for the growth of an initially spherical void. On integrating this equation with the assumption that stress state remains constant and there is no void nucleation strain, the equivalent fracture strain $\overline{e}_{fr}$ is given by

$$\overline{e}_{fr} \equiv 2 \ln \left[(R/r)_A\right]_{fr} = \frac{\ln \frac{\overline{d}_p}{2\overline{p}}}{0.28 \exp\left(\frac{3}{2}\frac{\sigma_m}{\sigma_y}\right)}, \tag{12}$$

where σ_m is the hydrostatic stress, $\overline{d}_p$ and $\overline{p}$ stand for the mean spacing and the mean radius of inhomogeneities respectively. The absolute value of the fracture strain is not matter of interest because we intend only to compare the fracture strains of bridging particles with different curvature of the parabolic neck profile, i.e. with different stress triaxiality factor σ_m/σ_y. Thus, the knowledge of the microstructural parameter $\overline{d}_p/2\overline{p}$ is not essential.

Basing on Eqn. 12. and the relation $r/R = g(\Delta/R)$, see Figure 2, a relationship between $(\Delta_c/R)_{A>0}$ and $(\Delta_c/R)_{A=0}$ has been computed for several values of A. Figure 6 indicates that $(\Delta_c/R)_{A>0}$ is significantly reduced for higher values of A comparing to $(\Delta_c/R)_{A=0}$ due to the influence of the stress triaxiality factor.

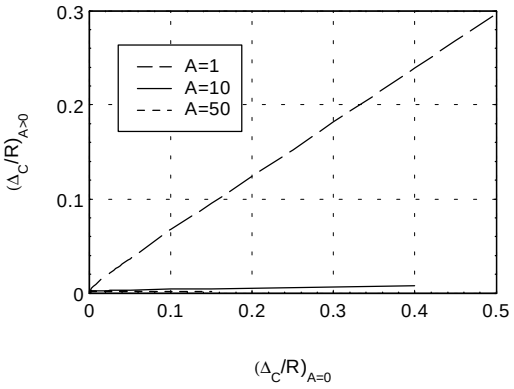

Figure 6: Relation between $(\Delta_c/R)_{A>0}$ and $(\Delta_c/R)_{A=0}$ for several values of A

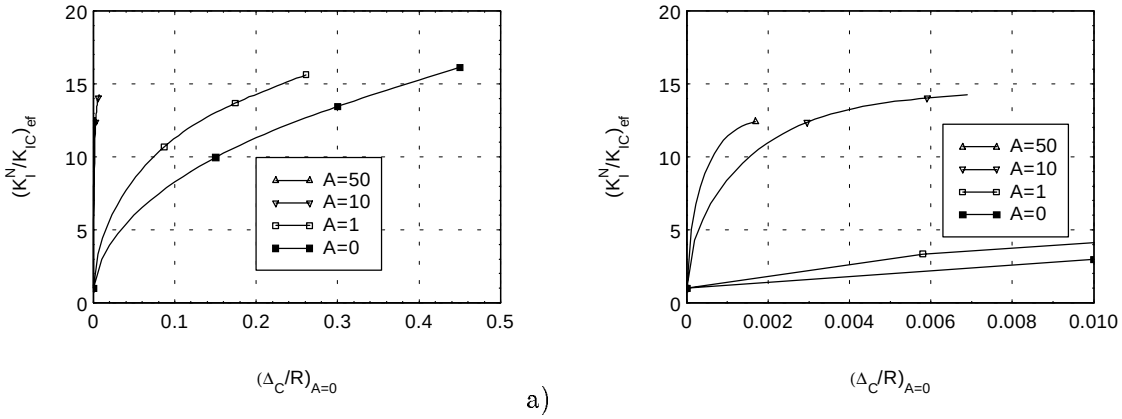

Figure 7: Relation $\left(K_I^N/K_{IC}\mid_{A\geq 0}\right)_{eff}$ vs. $(\Delta_c/R)_{A=0}$ including also the effect of the stress triaxiality factor upon the critical crack opening displacement, $k = 0.5$, $f = 0.25$. a) full scale diagram, b) zoomed detail of the left section of the diagram a).

The results in Figure 6 together with the previous computations of $\left(K_I^N/K_{IC}\right)_{eff}$ provide us with the relation $\left(K_I^N/K_{IC}\mid_{A\geq 0}\right)_{eff}$ vs. $(\Delta_c/R)_{A=0}$ as displayed in Figure 7. $(\Delta_c/R)_{A=0}$ serves as an independent variable which characterizes the ductility of bridging particles under the uniaxial stress state condition. Figure 7 reveals two counteracting influences of the particle/matrix interface strength. E.g., the cases of weak interface, i.e. low values of A, allow for higher value of the critical crack opening displacement which entails an increase in the fracture resistance of composite; however, due to the low stress triaxiality in this case, the restraining stress σ_0 is rather low, see Figure 3 and, consequently, the restraining stress intensity factor is also low which reduces the fracture resistance of composite. Summarizing, a certain optimal interfacial debonding is required to achieve an optimal fracture toughness of composite. At the same time, Figure 7 indicates that the optimal property for the interface is not necessary the case of $A = 0$ as stated elsewhere [1].

Acknowledgments-The support through grant GAČR No. 101/99/0829 and the Research Project No. MSM 262100001 is gratefully acknowledged.

1. Rubinstein, A.A. and Wang, P. (1998) *J. Mech. Phys. Solids* 46, 1139.
2. Tvergaard, V. (1992) *Int. J. Mech. Sci.* 34, 635.
3. Rose, L.R.F. (1987) *J. Mech. Phys. Solids* 35, 383.
4. Budiansky, B., Amazigo, J. and Evans, A.G. (1987) *J. Mech. Phys. Solids* 36, 167.
5. Erdogan, F. and Joseph, P.F. (1989) *J. Am. Ceram. Soc.* 72, 262.
6. Bao, G. and Hui, C-Y. (1990) *Int. J. Solids Structures* 26, 631.
7. Kotoul, M. and Urbiš, R. (2000) *Eng. Frac. Mechanics* 68, 89.
8. Rice, J.R. and Tracey, D.M. (1969) *J. Mech. Phys. Solids* 17, 201.

ON THE DEPENDENCE OF THE WEIBULL EXPONENT ON GEOMETRY AND LOADING CONDITIONS AND ITS IMPLICATIONS ON THE FRACTURE TOUGHNESS PROBABILITY CURVE USING A LOCAL APPROACH CRITERION

P.P. Milella [1] and N. Bonora [2]

[1] ANPA, via V. Brancati 48, 00144 Rome, Italy
[2] University of Cassino, Industrial Engineering Dept., 03043 Cassino, Italy

ABSTRACT

The present study addresses the issue of the dependence of the Weibull exponent *m* on geometry and loading conditions. It is shown that the amplitude and shape of the notch tip stress field and, in particular, the triaxiality characterising the stress state determines the value of the exponent *m*. Tests performed on RNB(T) specimens of carbon steel 22NiMoCr37, type A 508 Cl 3, at temperatures ranging from -18 ^{o}C to -196 ^{o}C actually indicate that *m* varies from ~ 6 to 40, depending on the notch depth and root radius while for specimens carrying sharp cracks its value drops down to ~ 4. This last result seems to be consistent with the Wallin hypothesis of a theoretical value equal to four, for fracture mechanics specimens with high constraint, such as C(T) or SE(B), with positive values of the Q-stress or T-stress and a triaxiality factor, TF, approaching 2.5. Temperature, in as long as it does not modify the stress state from plane strain to plane stress and the TF, has no effect on the value of *m* which is independent of the material as well.

Key words: *K* field, *HRR* field, *Q*-stress, triaxiality factor, process zone, fracture probability distribution.

INTRODUCTION

Local approach to fracture has been widely applied by many authors. Fontaine *et al.* [1] used local approach to predict brittle fracture in welded joints. Amar and Pineau [2] proposed a modified definition of the probability of failure to asses the behaviour of a structural steel in the brittle-ductile transition region. Saillard *et al*. [3] used this model to predict brittle fracture in a thick pressurised shell under thermal shock. In all these applications, the characteristic material parameters, *i.e.* the *m* exponent, the Weibull stress σ_w and the element volume V_o , have been inferred without a great accuracy. As to the Weibull exponent *m*, for instance, it was assumed equal to 22, as suggested by Mudry [4]. This value was also confirmed in a study by the authors [5] as part of an international round robin on local approach promoted by the European Structural Integrity Society (ESIS). Recently, the conclusion of the second round robin on local approach [6] has pointed out the difficulties in the determination of the material parameters and the large differences in their estimation

among the laboratories involved. In particular, the *m* exponent was found to range from 10 to 50 with a mean value of 16. This latter value is presently considered to be the most suitable for the steel considered, a low alloy carbon steel 22NiMoCr37, type A 508 Cl 3. The fact that needs to be pointed out is that in all the analyses the value of the Weibull exponent *m* was derived through a numerical-experimental procedure based on the use of round notch bars in traction, RNB(T), carrying notches of different root radii, generally from 0.2 to 20 mm. The question arises as to whether or not the value of the Weibull exponent assessed on RNB(T) specimens can be used in an analysis referring to a structure carrying a real crack rather than a notch. The difference between a sharp or natural crack and a notch is in the shape and amplitude of the stress field set up ahead of the tip: the blunter the notch the smother the stress field which, for larger root radii, can even lose the characteristic stress singularity $1/\sqrt{r}$ typical of the crack. We know that these differences in the stress field amplitude and profile have an impact on the attitude of the material towards brittle fracture, which is revealed by the well known fact that a sharp crack is much more dangerous than a blunted one or a notch and that a circular hole is used as a crack arrester. Then, the previous question becomes whether the stress field has an effect on the exponent *m*. If it does, a value of *m* derived from a particular specimen carrying a notch of given tip radius ρ cannot be used to asses the probability of failure of another specimen or geometry with a different ρ. This would actually imply that the Weibull exponent depends on the crack geometry. The present study is devoted to answering this question. At variance with the present assumption, it appears that, indeed, the value of the *m* exponent depends on the type of stress field set up ahead of the crack or notch tip and is not a characteristic of the material.

THE PRESENT STUDY

Wallin (7, 8) argued that in a specimen carrying a sharp crack, where the stress field is represented by K_I, the extension x_{eff} of the effective process zone ahead of the crack tip, where the existence of a brittle phase can trigger the fracture, must necessarily be proportional to $K_I{}^2$. Its volume ~ $(x_{eff})^2 \cdot t$, then, shall be proportional to the forth power of K_I. If we assume that the failure probability distribution P_f depends on that volume size and we write:

$$P_f = 1 - exp\left[-\left(\frac{K_I}{K_o} \right)^m \right] \tag{1}$$

then the *m* exponent in eq. (1) has to be equal to 4. If we move from a real sharp crack, to a blunted one, we can use the same arguments to derive a possible value of the *m* exponent. We can conveniently represent the stress field σ_{ij} ahead of a blunted crack using the HHR field with the introduction of a Q-stress:

$$\sigma_{ij} = \sigma_{ys} \left(\frac{EJ}{\alpha \sigma_{ys}^2 I_n x} \right)^{\frac{1}{n+1}} + Q \sigma_{ys} \delta_{ij} \tag{2}$$

where E is the Young's modulus, J the J-integral that determines the amplitude of the crack tip singularity, σ_{ys} the yield strength, x the distance from the tip, n the strain hardening coefficient, α and I_n are material constants. The Q stress in eq. (2) quantifies the constraint exerted over the crack tip plastic zone and is a measure of the degree of triaxiality existing ahead of a blunted crack. For a sharp crack under small scale yielding (SSY) conditions, Q is equal to zero. Therefore the extension of the process zone x_{eff} is proportional to J, as eq. (2) indicates, and its volume to J^2. Under these circumstances it is:

$$J = \left(1 - \nu^2\right) \frac{K_I^2}{E} \tag{3}$$

and, again, we find that the exponent m in eq. (1) is equal to 4. As the crack blunts, however, the system starts to lose constraint and triaxiality, resulting in growing negative Q values. A point is reached when SSY conditions are lost and the equivalence between J and K_I starts to vanish. This happens when the plastic enclave ahead of the blunted crack swells so much that K_I loses its physical meaning, since it is a linear elastic fracture mechanics parameter based on the assumption of a negligible plastic zone, typical of SSY. Now, even though the volume of the process zone still remains proportional to J^2, we cannot use eq. (1) any longer. In these conditions we should replace in eq. (1) K_I with J and the exponent 4 with 2. However, also a formulation of the probability of failure P_f in terms of J has a limit for at least two reasons. First, the J approach, even that of eq. (2) with the introduction of the *Q-stress*, is valid as long as the crack is stationary or undergoes a small stable growth. This may not be the case for a blunted crack when it experiences large stable growth before failure occurs. Secondly, as the blunting increases and the entire ligament becomes plastic, the J may no longer describe the stress field, even in the event of no-stable growth. Now, new tools are needed, such as the slip lines solution, except that the slip lines theory applies to rigid-plastic materials under plane strain conditions. In particular, round bars with notches having a tip radius greater than one millimeter, such as those used in the ESIS round robin, fail when the entire section is plastic. Even at –190 °C the specimens used in that program failed when the entire cross section was plastic. This is why a more general formulation of the probability of failure is required, using the true rupture stress σ_r rather than K or J as shown by eq. (4):

$$P_f = 1 - exp\left[-\left(\frac{\sigma_r}{\sigma_o} \right)^m \right] \tag{4}$$

In this case, however, the m exponent will no longer be necessarily equal to 4, as for the sharp crack in SSY, and this deviation can be seen already for a J controlled stress field when the Q stress assumes high negative values. This can be understood by observing that J is composed of a linear elastic component and a plastic one:

$$J = J_{el} + J_{pl} \tag{5}$$

The linear component J_{el} is precisely the energy release rate **G** and is proportional to the square of the applied σ, and therefore to K_I^2 as per eq. (3). The nonlinear one J_{pl} is not. J_{pl} is related to the applied stress σ through a power that depends on the compliance of the system, i.e., on the plastic load-deformation response, P-δ_{pl}, of the system containing the crack. This is because the area A under the P-δ_{pl} curve is proportional to J_{pl} and that area is also proportional to σ^{n+1} where n is also the exponent of the power low $\delta_{pl} = C \cdot P^n$ representing the P-δ_{pl} curve. Using the Rice definition of J [9], in fact:

$$\begin{aligned} J_{pl} &= \eta \cdot \frac{A}{t(w-a)}; \\ A &= \int_0^{\delta_{pl}} P d\delta \\ &= C \int P^n dP \rightarrow C \frac{n}{(n+1)} P^{n+1} \end{aligned} \tag{6}$$

where w is the specimen width and C its 'plastic' compliance. The plastic component J_{pl} will overwhelm J_{el} more and more as Q assumes larger and larger negative values and the SSY conditions are lost, i.e., as the blunting increases. Eventually, when the stress field will no longer be described by J, as in the case of a RNB(T), the value of m will depend on the compliance of the system, i.e., on the notch blunting. The fact that increasing negative values of Q can affect the value of the m exponent is

actually addressing the issue of triaxiality. The confinement of the plastic zone set-up at the notch tip and, therefore, of the process zone that determines the value of the Weibull exponent *m*, is, in fact, provided by the triaxial stress state existing ahead of the tip. The higher the triaxiality the smaller the plastic zone size. Let's consider the triaxiality factor, *TF*:

$$TF = \frac{\sqrt{2}}{3} \cdot \frac{\sigma_1 + \sigma_2 + \sigma_3}{\sqrt{(\sigma_1 - \sigma_2)^2 + (\sigma_1 - \sigma_3)^2 + (\sigma_2 - \sigma_3)^2}} \tag{7}$$

to asses the degree of triaxiality existing at the notch tip. The stresses σ_1, σ_2 and σ_3 in eq. (7) are the principal stresses on the notch plane. The maximum theoretical value of *TF* is infinity for $\sigma_1=\sigma_2=\sigma_3$, but in practice a full plane strain condition with $\sigma_1=\sigma_2$ and $\sigma_3=2\nu\sigma_1$, where ν is the Poisson's coefficient, results in a *TF* equal to about 2.8, that will be considered as the limiting value. FE calculations made by the authors, indicate that the *TF* for a CT specimen is equal to ~2.3 at the plastic-elastic border, with 2.5 at the crack tip, in the plastic zone. FE calculations, made by Milella, Bonora and Gentile [10] yielded a TF = 0.5 for ρ = 20 mm and 1.7 for ρ = 1.2 mm. Similar calculations presented in the paper by Milella e Bonora [11] indicate that for geometries like those used in Round Robin 1, the *TF* is 1.5 for a root radius ρ=2 mm, 1.2 for ρ=4 mm, 1 for ρ=6 mm and 0.9 for ρ=10 mm. This latter value is approaching the lowest one: TF = 0.33 pertaining to a smooth round bar in traction, RB(T), where $\sigma_2=\sigma_3=0$. In all cases the *TF* was computed at the center of the specimen section where triaxiality reaches its maximum. Finally, for a RNB(T) with a sharp notch of 0.2 mm, the TF is equal to 2.18 for an ideally elastic-plastic material. This is a rather high value very close to the one obtained for the CT specimen carrying a sharp crack. It must be pointed out that the round bar with the root radius equal to 0.2 mm was, in fact, the only one to fracture in a brittle fashion. If the same notch were present in a flat thin plate under uniaxial traction, where triaxility is much lower than in the RNB(T), the corresponding TF would drop sharply making the system behave in a completely different way to which it is associated a higher value of the *m* exponent. The same notch in a Charpy-VN specimen would yield a different TF. Since triaxiality introduces, as we have shown, a more general way to define a complex stress state, the original question of whether or not the root radius has an effect on the Weibull exponent *m*, now becomes whether the TF has an influence on *m*. Theoretical arguments presented so far have been checked against experimental results obtained on CT specimens, Charpy-VN, RNB(T) of different root radii and on smooth traction specimens, as well. As to the CT and in general to any specimen carrying a sharp or real crack, indeed there is not much to add to the results obtained by Wallin [7, 8] which clearly indicate that the Weibull exponent *m* is equal to 4. An experimental assessment of the *m* exponent for a notch having a tip radius ρ equal to 0.2 mm can be done using both Charpy-VN (ρ = 0.25 mm and *a* = 2 mm) or RNB(T) specimens. The results obtained by Milella on Charpy-VN specimens of A 508 Cl3 steel at –30 ^{o}C lead to a Weibull exponent *m* = 7.65. As to RNB(T) of root radius equal to 0.2 mm, the results obtained by the authors reanalyzing the tests performed by Beremin [12] on 22NiMoCr37 steel at –196 ^{o}C. The bar diameter was 14 mm and 7.5 mm in the reduced section. In their analysis of the experimental data, the authors have used eq. (4) in the evaluation of the failure probability distribution where the stress σ_r, as already explained, is the true failure stress on the reduced section of the specimen. The value of the exponent *m*, therefore, is inferred from the slope of the experimental data in a plot $ln\{ln[1/(1-P_f)]\}$,where P_f is frequency of failure, versus $ln\sigma_r$. A detailed description of the methodology can be found in ref. [10]. Using the same procedure, the authors have reanalyzed the experimental data available in the open literature relative to RNB(T) having notches of root radius equal to 1.2, 2, 2.4, 4, 6, 10, 20 mm and ∞, i.e. RB(T), [12, 13, 14]. The results are presented in table 1. Let's now plot *m* as versus the corresponding triaxiality factor TF. This is shown in figure 1 that clearly indicates the existence of a linear relationship between *m* and TF that can be expressed by the equation:

$$m = 55.4 - 22.4 \cdot TF \tag{9}$$

TABLE 1

m	ρ (mm)	Specimen	m	ρ (mm)	Specimen
4.69	crack	CT	44.66	2	RNB(T)
5.6	crack	CT	24.26	4	RNB(T)
5.44	0.2	RNB(T)	31.26	4	RNB(T)
7	0.2	RNB(T)	56.03	4	RNB(T)
7.6	0.25	CVN	30.22	6	RNB(T)
22	1.2	RNB(T)	38.37	10	RNB(T)
18.6	2	RNB(T)	40.99	10	RNB(T)
20.75	2	RNB(T)	44.73	20	RNB(T)
26.28	2	RNB(T)	46.29	∞	RB(T)

We have shown that the *m* exponent depends on the notch root radius ρ that determines the amplitude and shape of the stress fields generated at the notch tip and, more precisely, on the triaxiality existing in the cross section of the specimen. Therefore, we shall say that as long as temperature does not affect the stress field and triaxiality, it will not have any impact on the value of the Weibull exponent *m*. A detailed discussion of this conclusion can be found in reference [11]. Indeed, the analysis made by the authors on Charpy-VN specimens of A 533 B steel tested at temperatures equal to –75, –25, 0, 150 and 300 °C has shown that the *m* exponent was equal to 5.2 at –75 °C, 6 at –25 °C, 8 at 0 °C, jumping to 18 at 150 °C and even 23 at 300 °C, as expected. In general, we can say that, as long as temperature does not affect the triaxiality factor of a particular geometry, the Weibull exponent *m* will not be affected by temperature and this statement can be transferred to materials: as long as the change of material does not affect TF, *m* will be independent of the material used. The general statement therefore remains: equal *m* values will correspond to equal *TF*.

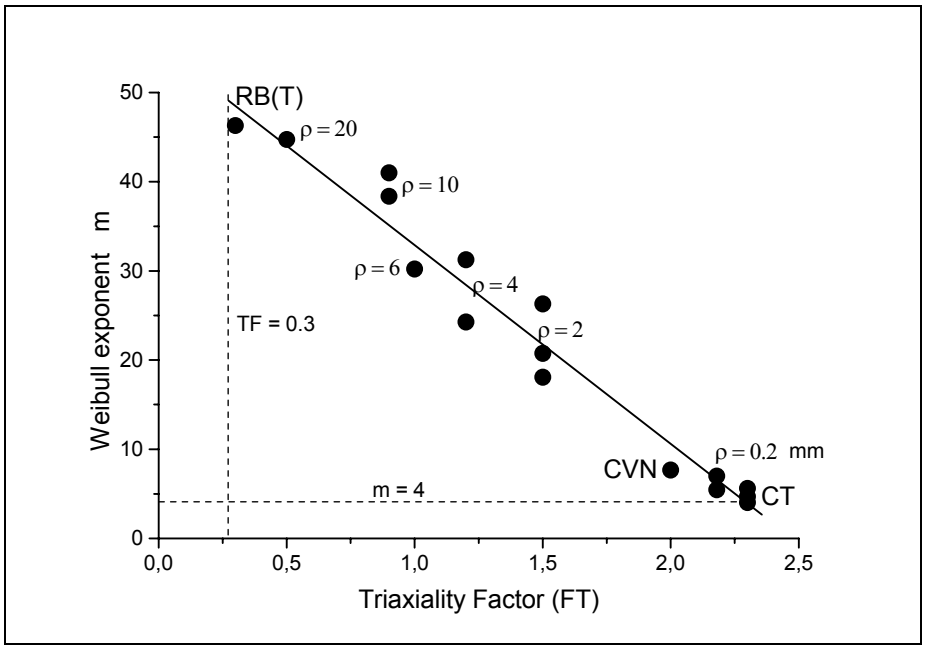

Figure 1 - Trend of the Weibull exponent *m* versus the triaxiality factor TF for the geometries considered. The vertical dashed line indicates the TF pertaining to a smooth round bar in traction RB(T). The horizontal one marks the value of *m* found by Wallin for specimens containing a sharp crack.

REFERENCES

1. Fontaine, A., Maas, E. and Tulou, J., Prevision of Cleavage Fracture Properties Using a Local Approach: Application to Welded Joint of a Structural C-Mn Steel, *Nuclear Engineering and Design*, **105**, (1987), pp. 77-81.
2. Amar, E. and Pineau, A., Application of a Local Approach to Ductile-Brittle Transition in a Low-Alloy Steel, *Nuclear Engineering and Design*, **105**, (1987), pp. 89-96.
3. Saillard, P., Devaux, J.C. and Pellissier-Tanon, A., Numerical Prediction of the Fracture of a Thick Pressurized Shell Subjected to a Liquid Nitrogen Shock, *Nuclear Engineering and Design*, **105**, (1987), pp. 83-88.
4. Mudry, F., A Local Approach to Cleavage Fracture, *Nuclear Engineering and Design*, **105**, (1987), pp. 65-76.
5. Milella, P.P., Maricchiolo, C., Pini, A., Bonora, N. and Marchetti, M., Cleavage Fracture Prediction and K_{Ic} Assessment of a Nuclear Pressure Vessel Carbon Steel Using Local Approach Criteria, *Nuclear Engineering and Design*, **144**, (1993), pp. 1-7.
6. Brocks, W., Numerical Round Robin on Micromechanical Models, *Proceedings of the 11th European Conference on Fracture*, ECF 11, Poitier (France), (1996), pp. 1-4.
7. Wallin, K., The Scatter in K_{Ic} Results, *Engineering Fracture Mechanics*, **19**, N. 6, (1984), pp. 1085-1093.
8. Wallin, K., The Size Effect in K_{Ic} Results, *Engineering Fracture Mechanics*, **22**, N. 1, (1985), pp. 149-163.
9. Rice, J.R., Paris, P.C. and Merkle, J.G., "Some Further on J-Integral Analysis and Estimates", *ASTM STP-536*, (1973) pp. 231-245.
10. Bonora, N., Gentile, D. and Iacoviello, F., Triaxiality and Ductile Failure in Round Notch Tensile Bar Specimens, *Proceedings of the XII Italian Group of Fracture Annual Meeting IGF12*, in Italian, Parma, Giugno 1996, pp. 93-102.
11. Milella, P.P. and Bonora, N., On the Dependence of the Weibull Exponent on Geometry and Loading Conditions and its implications on the Fracture Toughness Probability Curve Using a Local Approach Criterion, *Int. Jou. of Frac.*, (2000), **104**, pp. 71-87.
12. Beremin, F.M., A local Criterion for Cleavage Fracture of a Nuclear Pressure Vessel Steel, *Metallurgical Transactions Series A*, **14A**, (1983), pp. 2277-2287.
13. Kanditis, E., Marini, B., Allais, L. and Pineau, A., Validation of a Statistical Criterion for Intergranular Brittle Fracture of a Low Alloy Steel Through Uniaxial and Biaxial (Tension-Torsion) Tests, *International Journal of Fracture*, **66**, (1994), pp. 273-294.
14. Brocks, W., Numerical Round Robin on Micromechanical Models, Fraunhofer Institut fur Werkstoffmekanik, IWM-Bericht T 8/95, (1995).

ON THE DETECTION OF FATIGUE DAMAGE PRIOR TO SURFACE INDICATION

G. Wheatley*, D. Barton and K. Davey.

Structural Monitoring Systems Ltd., Perth, Western Australia (www.smsystems.com.au)
*Currently at: National Institute for Materials Science
1-2-1, Sengen, Tsukuba-shi, Ibaraki 305-0047, Japan

ABSTRACT

The aim of this study was to investigate the failure mechanism of riveted aluminium lap joints when exposed to constant load amplitude fatigue. Tests were conducted on lightweight aircraft grade aluminium sheet (2024-T4). Visual observations of the failure behaviour and lifetime records were supplemented by real-time, in-situ structural integrity (SI) measurements. Structural Monitoring Systems Ltd. (SMS) equipment, which owns the patent rights to the Comparative Vacuum Monitoring (CVM™) method, provided the SI measurements of the specimens during their fatigue life. SMS sensors were installed either on the surface or within the lap joint specimens. Observation of fatigue loading from the perspectives of the two differently installed SMS sensors has provided insight into the failure mechanism. Failure of the riveted lap joint is found to occur initially by a process of rivet shank/rivet hole fretting damage and damage accumulation within the anti-chaffing material prior to crack initiation within the aluminium plates and/or rivets. Major fatigue damage was detected at 50-70% of the fatigue life, despite visual indication being absent. The benefits of this technology to the aviation industry are large, as early detection of fatigue damage improves safety and allows increased flexibility in maintenance schedules.

CVM™ is applied to galleries containing a low vacuum and atmospheric pressure. The atmospheric pressure is often contained with a second set of galleries that alternate with the low vacuum galleries. If a flaw is not present, the low vacuum remains stable at the base value. If a flaw develops, air will flow from the atmospheric galleries through the flaw to the vacuum galleries. A transducer measures the rate of flow between the galleries and therefore gives an indication of flaw size. CVM™ is rapidly gaining acceptance as a technique for crack initiation detection, automated crack propagation measurement, localised yield stress determination and composite disbonding indication. The aviation industry has shown the greatest interest, with fatigue laboratories also including SMS technology in their testing equipment.

KEYWORDS

Condition monitoring, crack initiation detection, automated crack propagation measurement, yield stress detection, riveted lap joint

INTRODUCTION

The traditional method of laboratory tests that model industrial experience, followed by modelling is deficient in the study of riveted lap joints. Firstly, the detection of fatigue cracks in the laboratory, and indeed in practice, is complicated by cracks often initiating at the faying surface [1] and tunnelling prior to emerging [2] on the surface. The result is a delayed detection of crack initiation. Secondly, modelling is available in the literature, but it does not accurately model multi-site damage [2]. A simple tensile overload during fatigue can dramatically alter component life [3] and importantly, the in-service situation is not accurately reproduced in the laboratory due to the lack of

biaxial stress and the variation of hoop stress [2]. A pessimistic opinion was offered by Schijve, 'accurate predictions can not be expected' [4]. To assist in both these problem areas, an in-situ, real-time method of detecting fatigue cracks within a riveted structure would be beneficial.

The aim of this study was to investigate the failure behaviour of riveted lap joints when exposed to fatigue with constant load amplitude. Preliminary data has been presented in a previous paper [5]. Fatigue tests were conducted on aircraft grade aluminium sheet, and further supplemented with real-time, in-situ structural integrity (SI) measurements. Structural Monitoring Systems Ltd. (SMS) technology facilitated SI measurements of the specimens. The specimens were composed of two groups. One group had surface mounted SMS SI measuring sensors while the second group had SMS internally mounted SI sensors installed.

Structural Monitoring Systems Ltd. (SMS) offers equipment for real-time, in-situ detection of fatigue cracks. Structural Integrity (SI) measurements are determined by CVM™ of a steady-state, low vacuum maintained within the galleries of a sensor that is installed either on or within the component to be tested. When a fatigue crack grows to a certain length (cf. Fig. 1), the crack intersects the alternating galleries maintained at vacuum and atmospheric pressure. A variety of sensors and, if required, specialist consulting services to address specific testing issues are available.

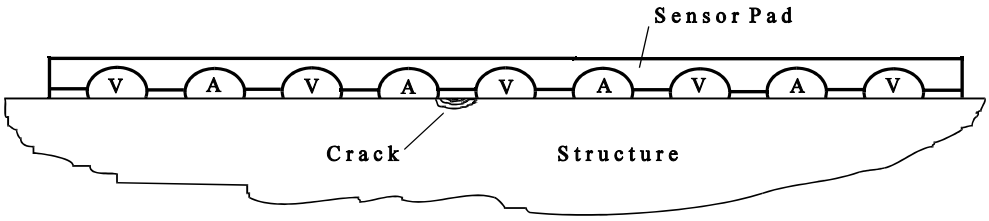

Figure 1: SMS surface sensor mounted on specimen (schematic). An increase in ΔP results when a crack intersects adjacent channels maintained at vacuum and atmospheric pressure.

The sensors are produced in a range of materials and have a sensitivity down to 250μm with an accuracy of 10μm (4%). An automated crack propagation measurement system for laboratory or industrial application is also available. SMS sensors are in use as localised yield stress indicators for self-piercing rivets and for the detection of disbonding within composite repairs/structures.

EXPERIMENT

The fatigue tests were performed under laboratory conditions at the University of Western Australia (Department of Mechanical and Materials Engineering). Testing was conducted upon an Instron 8501 servo-hydraulic testing machine with the SI measurements recorded on a lap top computer, via the SI monitor (SIM). No mathematical processing of data was carried out.

Two types of specimens were fabricated from 2024-T4 aluminium sheet. The first group of specimens was formed from two plates each measuring 60X115 mm and 1.8 mm thick. A chaffing protection layer of polysulphide material (PR-1440) was applied to the area of the plates that were to be riveted. Masking tape was applied to the edges of the plate and PR-1440 was spread with a spatula using the tape to control the thickness. After full cure of the PR-1440, the plates were fastened together with 6 countersunk rivets by using a squeeze rivet gun. No sealant was applied to the rivets during construction. Surface mounted SMS sensors were installed over approximately 2/3 of the rivet heads, cf. Fig. 2.

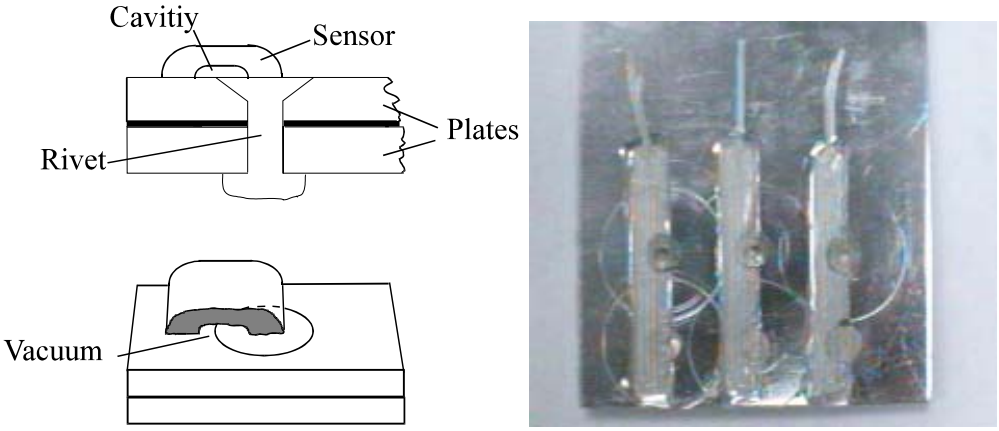

Figure 2: Placement of the surface sensor over the rivet (schematic - left).
Tested specimen with SMS surface sensors (right).

The sensors were connected in parallel and then to the SIM. In this manner, the SIM would detect failure from any sensor. A tensile test was carried out initially to determine a suitable fatigue testing waveform. A sinusoidal load profile with a maximum fatigue load of 7.0 kN, a load ratio of R = 0.1 and a frequency of 20 Hz was used in all tests. Testing was continued until failure and the cycle number recorded.

The second group of lap joint specimens were fabricated from 2mm thick 2024-T4 aluminium plate. Each plate was 60X140 mm. The plates were joined in an identical manner to group 1 specimens. Masking tape (width = 6 mm) was used as a stencil to mark out a cavity in the sealant. A photograph of a cavity is presented in Fig. 3. An exit from the cavity was provided and a SMS surface sensor attached to facilitate connection to the SIM.

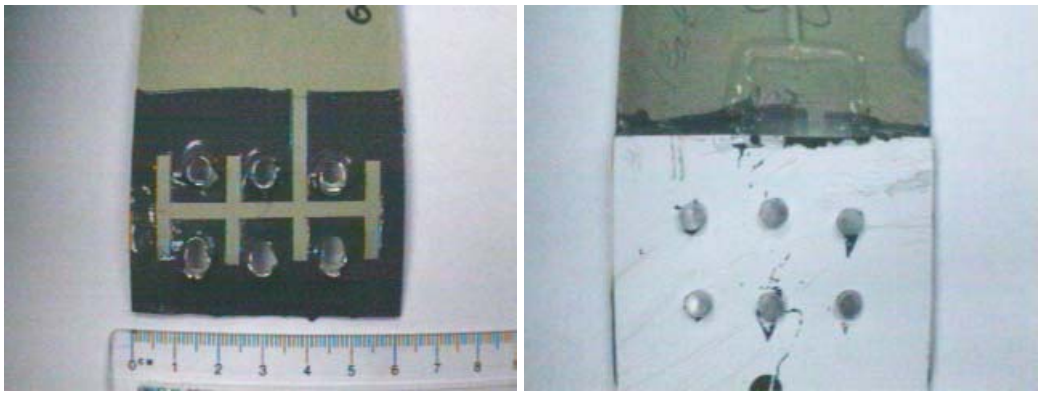

Figure 3: Single plate of lap joint illustrating PR-1440 sealant and cavity - note exit of cavity (left).

The masking tape was removed after the PR-1440 was applied. The plates were riveted together following full cure. No sealant was applied to the rivets during construction. The edge of the lap joint was sealed with a polyurethane based sealant (Sikaflex 221 T). In this manner, a gallery was created within the lap joint, cf. Fig. 4.

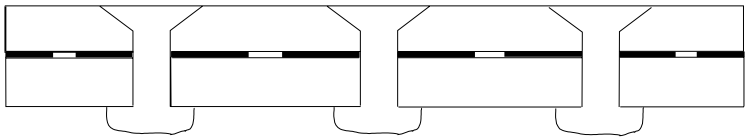

Figure 4: Cross-section of the SMS Integral Sensor within the lap joint (schematic).

Tensile tests were initially carried out to identify the critical load, P_C. Fatigue was then initiated at approximately 50% of this value. A maximum load of 7.0 kN, a load ratio of R = 0.1 and a frequency of 20 Hz was used in all tests. Crack initiation was observed optically. Fatigue loading was continued until failure and the cycle number recorded.

RESULTS

A representative plot of one specimen with surface mounted SMS sensors is presented in Fig. 5. The plots of Fig. 5 have the differential pressure (ΔP) as a function of the cycle number (left) and the percentage of fatigue life (right). The data to the left of the vertical axis indicates the differential pressure as a function of static loading. Fatigue loading begins from cycle number zero. The plateau at approximately 2 kPa was the ΔP reading when no load was applied. When the static load was increased to the mean load for fatigue cycling, ΔP increased to approximately 13 kPa. Initiation of fatigue saw a further increase in ΔP. A steady, but gradual increase in ΔP is observed with continued cycling. A full-scale reading of ΔP is observed at approximately 50% of the fatigue life. No visible fatigue damage was observed prior to catastrophic failure, which occurred at the rivets.

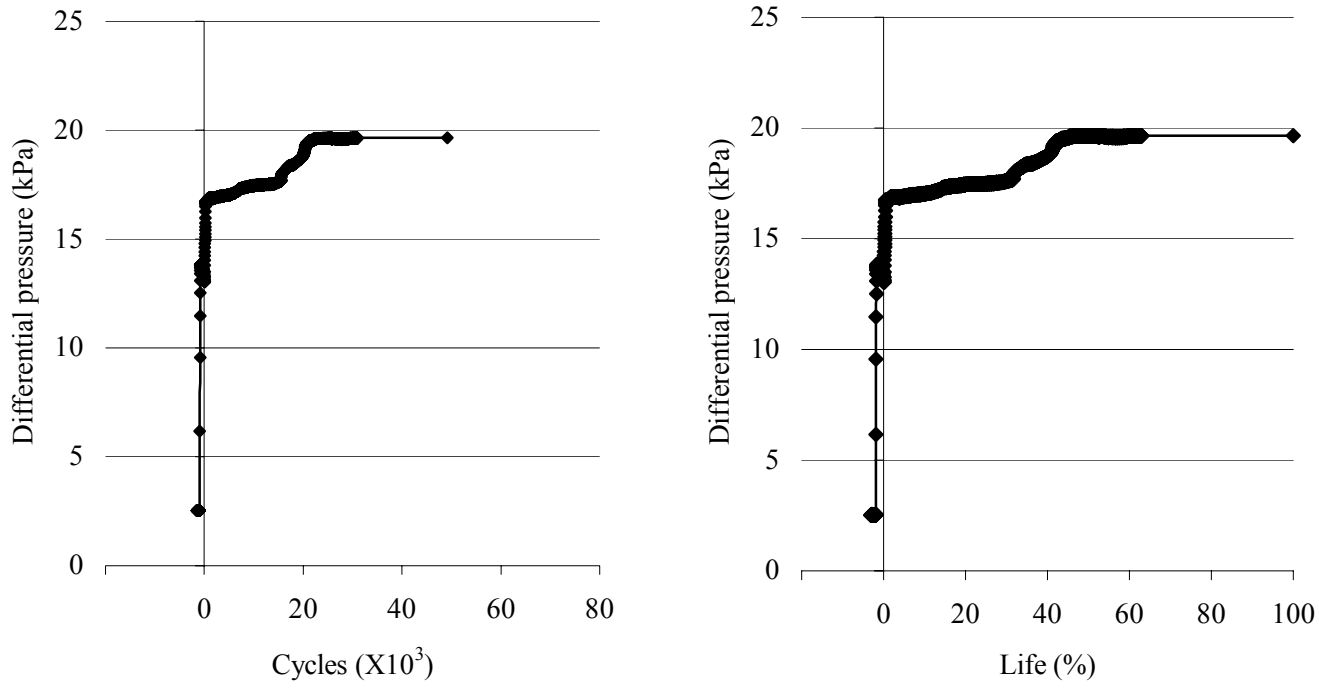

Figure 5: Differential pressure (ΔP) as a function of fatigue cycles (left)
and as a function of percentage of fatigue life (right) – One specimen with surface sensors.

Representative plots of two specimens with internally mounted sensors are presented in Fig. 6. As with Fig. 5, ΔP is plotted as a function of fatigue cycles (left) and percentage of fatigue life (right).

The fatigue life of this group of specimens is slightly higher than group 1 as these specimens were slightly thicker. As the sensors are mounted within the specimen and do not detect relative motion between the rivet and plate, there is no increase in ΔP as a result of static loading. A reading close to zero remains until failure begins to initiate. In contrast to the surface sensors, the internal sensors are remote to the rivets and therefore only the initiation of damage will cause an increase in ΔP. The early stage of failure is detected by the sensors at 50-70% of the fatigue life. Damage was detected prior to any surface indication. After the full-scale SI reading, fatigue cracks were observed at 90-95% of the fatigue life and grew to 3 and 5 mm prior to specimen failure for the specimens shown in Fig. 6. The sudden drop in ΔP observed at 50% of the fatigue life for one of the specimens was due to finger pressure on the loosening rivet. This pressure sealed the rivet and caused the drop in ΔP. Fatigue cracks were observed to initiate from the rivet that was identified to be loosening.

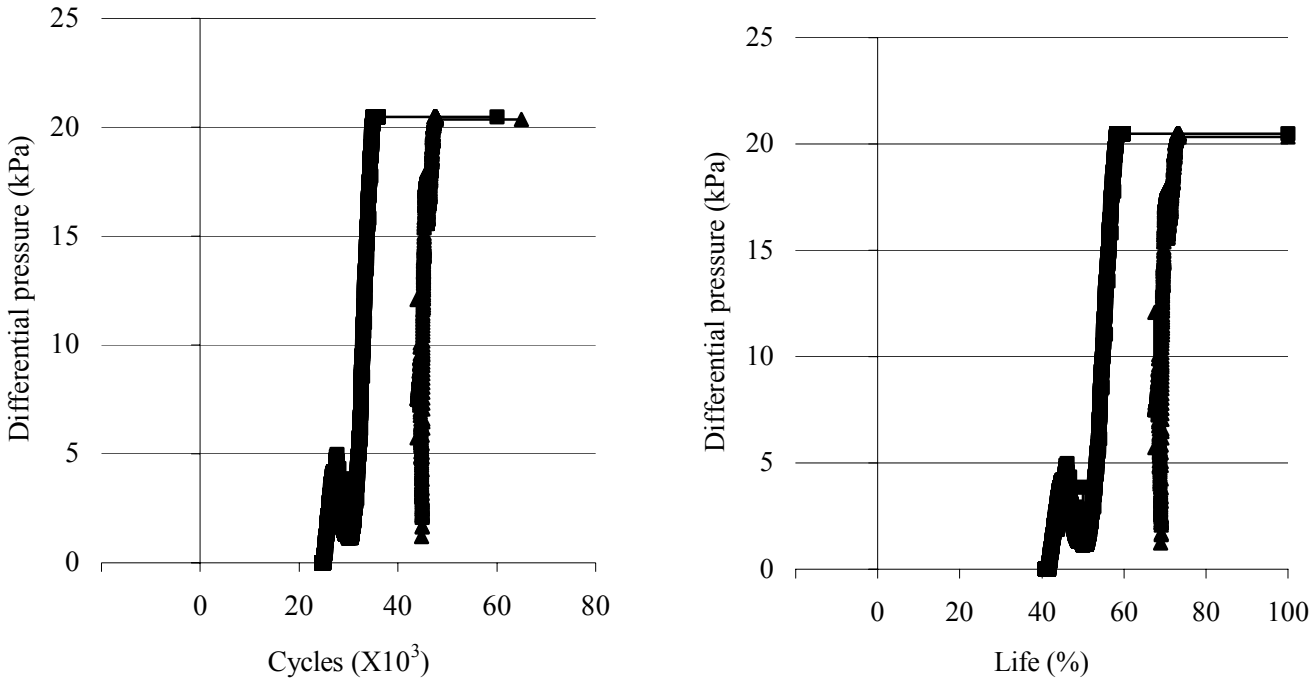

Figure 6: Differential pressure (ΔP) as a function of fatigue cycles (left)
and as a function of percentage of fatigue life (right) – Two specimens with Integral sensors.

DISCUSSION

As the rivet tail is mainly deformed during rivet installation, mechanical contact is higher between the rivet tail and the plate than between the rivet head and the plate. Figure 5 shows that static load on the specimen results in a reduction in the seal between the rivet head and the plate. The drop in sealing between the rivet head and plate is illustrated in Fig. 7.

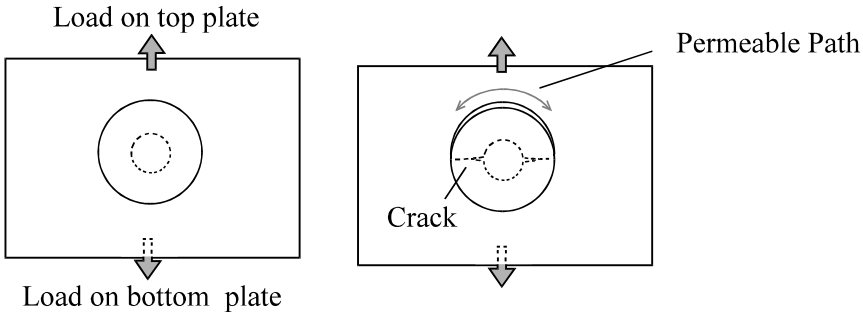

Figure 7: Behaviour of plate and rivet during fatigue loading (schematic).

The SI sensors are laid over 2/3 of the head of the rivet and therefore allow an ingress of atmosphere from the other portion of the rivet. This behaviour is currently being exploited by an SMS customer for the purpose of detecting the local yield point of the parent material around self-piercing rivets. Fatigue loading would repeat this relative motion between rivet and plate and cause fretting between the plate and the rivet head. The fretting initiates damage in the aluminium plate, the rivet shank and the anti-chaffing material.

Failure of the tested specimens occurred on the rivet head side. A consequence of Fig. 5 is that fatigue loading causes elastic deformation of the material around the rivet hole and therefore relative motion between the rivet hole and rivet shank. The fretting between the rivet hole and shank then results in damage that causes fatigue crack initiation. In Fig. 6, the SIM reading is seen to increase to full-scale over 4-5,000 cycles. Fatigue loading was such that a fatigue crack was grown over about two thousand cycles.

The SMS system indicated a reduction in structural integrity prior to any external visible indications of fatigue damage. The externally mounted sensors indicated the effect of static loading and the more gradual increase in ΔP as fretting damage increased in the rivet head or shank. The internally mounted sensors indicated the breakdown of the anti-chaffing material between the riveted plates and then fatigue crack initiation.

CONCLUSIONS

This investigation has revealed a number of observations. Firstly, surface mounted SMS sensors reveal the degree of mechanical contact between the plate and the rivet while the internally mounted sensors give only an indication of the early stages of crack initiation. Secondly, the loss of structural integrity of the lap joint is detected at 50-70% of the overall fatigue life. The mode of failure is concluded to be that of crack initiation as a result of fretting damage. The fretting results from relative motion between the plate and rivet.

Industry need for early detection of fatigue damage is recognised. The benefits of CVM™ are many. In terms of safety, the ability to detect a fatigue crack prior to external evidence of such is important. CVM™ is able to detect damage as a result of fatigue loading before it can be detected on the surface. In terms of scheduling, this system also offers the ability for operators to repair loosening rivets, monitor detected damage by other means and to monitor the damage as it accumulates.

CVM™ has gained a reputation with leading technical and scientific organisations for reliably detecting minute fatigue cracking in the specialised area of testing airframe structures. In fatigue testing the SMS technology has the advantage of detecting crack initiation and measuring crack propagation without stopping the test to carry out an NDT inspection. The monitoring system has been developed for installation on civil and military aircraft fuselage bulkheads and frames, wing stringers, spars and landing gear. SMS sensors have the capability of covering large areas and lengths and detecting minute flaws under painted surfaces to the extent of current tests. The SMS sensor can be used on peened surfaces. The SMS sensor is lightweight, will not corrode and is electrically inert, it will not interfere with on-board electrical systems, initiate corrosion or ignition. The sensor once installed can remain in-situ to record measurements continuously or periodically from locations that are either very difficult or impossible to inspect, by other than major disassembly of the structure.

An automated crack propagation measurement system for laboratory or industrial application is also available. SMS sensors are in use as localised yield stress indicators for self-piercing rivets and for the detection of disbonding within composite repairs/structures.

REFERENCES

1. Hartman, A. (1968). Internal Report, NLR TR 68072 U.
2. Fawaz, S.A., Schijve, J. and de Koning, A.U. (1997). In: *Fatigue in New and Ageing Aircraft*, pp. 553-574, Cook, R. and Poole, P. (Eds). Engineering Materials Advisory Services Ltd., Edinburgh.
3. Wheatley, G., Hu, X.Z. and Estrin, Y. (1999) *Fatigue Fract. Engng Mater. Struct*. 22, 1041.
4. Schijve, J. (1992). In: *Proceedings of the International Workshop on Structural Integrity of Aging Airplanes*, pp. 2-27. Atlanta Technical Publications, Atlanta.

5 Wheatley, G. and Davey, K. (submitted) *Fatigue Fract. Engng Mater. Struct*.

ICF10 01052PR

DUCTILE FRACTURE IN CYLINDRICAL TUBE BULGING UNDER IMPULSIVE LOADING

Y. SATO*, Y. KONO* and H. OGAWA**

*Faculty of Engineering, Tohoku Gakuin University,
1-13-1 Chuo, Tagajo, Miyagi, 985-8537 Japan
**Kitamoto Plant, Mitsubishi Materials Corp.,1975-2 Shimoishidokami,
Kitamoto, Saitama, 364-0022 Japan

ABSTRACT

The critical hoop strain, $\varepsilon_{\theta c}$, to cause the localized necking is determined experimentally for cylindrical tubes subjected to impulsive, electromagnetic pressure. As the tube is thin-walled and long, it behaves approximately under conditions of plane stress and conditions of plane strain. An approximate formulation of dynamic instability in high-speed expansion of such a tube was developed before in order to predict the forming limit. The analysis indicated that the hoop strain at the occurrence of dynamic instability was in range of n/2 to n for a material with the strain-hardening exponent n in the power law. It is revealed that the critical hoop strain determined experimentally satisfies the following conditions: $n/2 \leqq \varepsilon_{\theta c} \leqq n$.

KEYWORDS

ductile fracture, tube bulging, electromagnetic forming, dynamic instability, aluminum

INTRODUCTION

It is important to clarify the fracture strain at which the workpiece fractures during the plastic forming of materials. As for the ductile fracture of a thin-walled tube subjected to internal pressure, the localization of the deformation – namely, localized necking is ahead of the fracture. Therefore, the condition of the necking formation is a safety standard for the fracture criterion. The necking is generated axially at one spot in the thin-walled and long tube under quasistatic bulging by internal pressure. However, the localized necking prior to the fracture emerged also axially but at eight spots when a tube was subjected to the impulsive, electromagnetic pressure (Tobe et al.,1984). The bulging height of the tube expanded

impulsively was higher than that of the tube expanded quasistatically. Dynamic tube expansion is considerably different from quasistatic tube expansion in some aspects.

In this paper the critical hoop strain, $\varepsilon_{\theta c}$, to cause the necking is determined experimentally for the cylindrical tube subjected to impulsive, electromagnetic pressure. As the tube is thin-walled and long, it behaves approximately under conditions of plane stress and conditions of plane strain. The approximate formulation of dynamic instability in high-speed expansion of such a tube was developed before in order to predict the forming limit (Tobe et al.,1984). Karman's criterion for the dynamic tensile critical strain was employed. The analysis indicated that the hoop strain at the occurrence of dynamic instability was in range of n/2 to n for a material with the strain-hardening exponent n in the power law. It is shown that the critical hoop strain $\varepsilon_{\theta c}$ determined experimentally satisfies the following conditions: $n/2 \leqq \varepsilon_{\theta c} \leqq n$.

TESTING MATERIALS

Cylindrical tube specimens of 50 mm in outer diameter, 1mm in thickness and 200 mm long are drawn from commercially pure aluminum (JIS:A1050) and aluminum alloy (JIS:A6063). Tensile test specimen in dumbbell type and compressive test specimen in circular disk type are machined from plates. These plates are 0.75 mm in thickness from the thin-walled tube cut open and followed by flat-rolling. Then all the specimens are annealed at temperature 623 K for 3600 s in an electric furnace. At true strain beyond 0.1 the stress-strain curve determined from tensile test at quasistatic strain-rate was expressed by the power curve relation

$$\sigma = F \varepsilon^{n}, \qquad (1)$$

where σ is the true stress, ε the true strain, n the strain-hardening exponent and F the strength coefficient. The material constant n and F are shown in Table 1.

Table 1 Material constant F and n in the expression $\sigma = F \varepsilon^{n}$

	Static tension		Impulsive bulging	
	F [MPa]	n	F [MPa]	n
Aluminum (A1050-o)	124.	0.245	212.	0.23
Aluminum alloy (A6063-o)	150.	0.23	204.	0.20

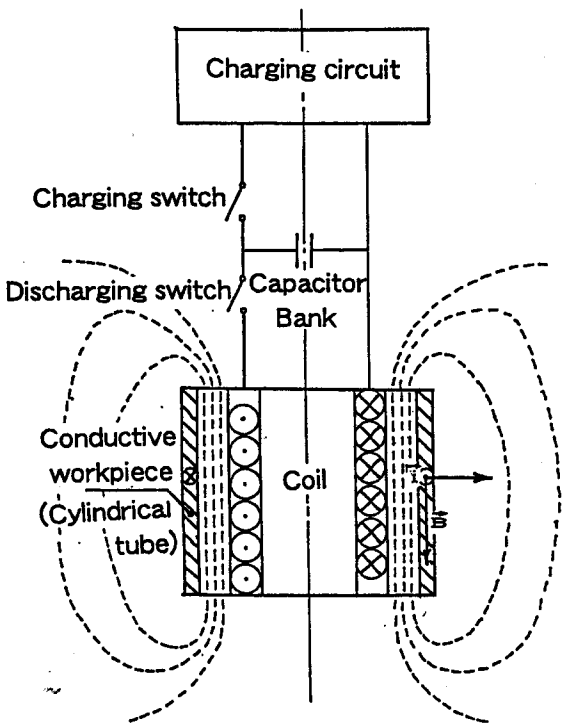

Fig.1 Basic circuit for electromagnetic forming

EXPANSION PROCESS OF TUBE

The dynamic bulging of thin-walled tubes are made use of the electromagnetic metal forming process (Baines et al., 1965-66; Jansen, 1968; Bruno, 1968; Lal, 1972). The basic circuit for electromagnetic forming is shown in Fig.1, in which the energy source is a bank of capacitors, charged to a predetermined voltage. The thin-walled tube of conducting material to be formed is placed over a solenoidal coil which is connected in series with the charged capacitor by means of a discharging switch. On closing the switch, the time-varying primary current in the coil sets up a transient axial magnetic field in the radial air gap and the tube wall, together with a secondary solenoidal current in the workpiece. The interaction of current and magnetic field induces radial body forces in the tube wall, which can be made sufficiently large to deform the workpiece.

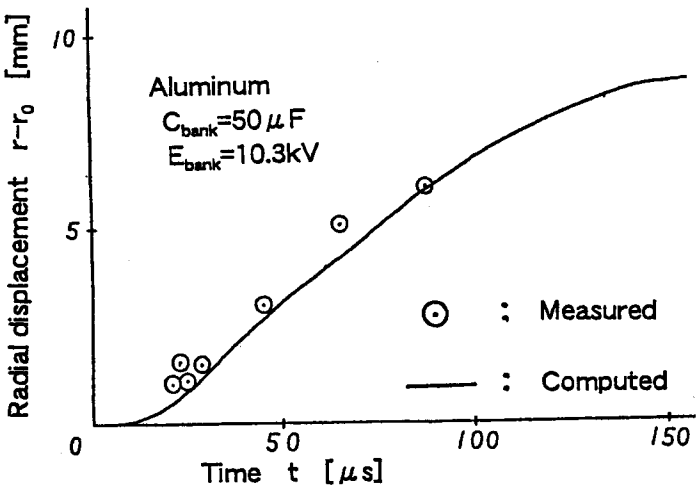

Fig.2 Radial displacement of aluminum tube subjected to electromagnetic pressure.

The radial movement of the tube wall, $r-r_0$, during the electromagnetic pressure pulse is expressed by the following equation:

$$\frac{d^2r}{dt^2} = \frac{\mu r_i^4}{2\rho r_0 h_0 p^2}\frac{i_1^2}{r^3} - \frac{F}{\rho}\left(\frac{2}{\sqrt{3}}\right)^{n+1}\left(\ln\frac{r}{r_0}\right)^n\frac{1}{r}, \quad (2)$$

where r and r_0 are the current and initial mean radius of the tube, respectively. h_0 and ρ are the initial thickness and density, respectively. t, μ, r_i, i_1 and p denote time, the permeability, the effective radius of coil, the coil current and the axial coil pitch, respectively. Here the hoop stress in the thin-walled tube (the thickness stress $\sigma_r \fallingdotseq 0$) under conditions of plane strain (the axial strain $\varepsilon_z \fallingdotseq 0$) is expressed as the equation: $\sigma_\theta = F(2/\sqrt{3})^{n+1}[\ln(r/r_0)]^n$, since the strain hardening characteristic is assumed to obey the equation, $\sigma_g = F\varepsilon_g^n$, where σ_g and ε_g are the generalized stress and strain, respectively.

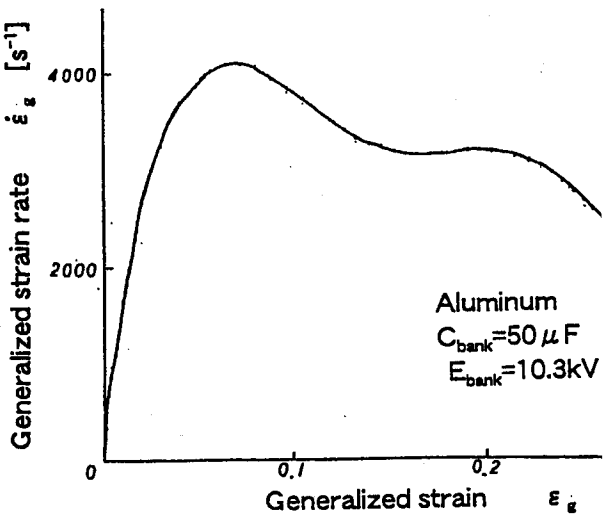

Fig.3 Relation between generalized strain rate and generalized strain for aluminum tube subjected to electromagnetic pressure.

The necking deformation occurred axially in the aluminum tube by applying a bank voltage of 10.3 kV for the capacitor bank of 50 μF. For the aluminum alloy tube such necking occurred by applying 12.7 kV for the capacitor bank of 50 μF. Hereafter the experiments were

conducted with these capacitor bank conditions.

The coil current i_1 was measured by integrating the output voltage of Rogowski coil. The radial velocity and the radial displacement of the tube at every moment were determined numerically by integrating equation (2). In Fig. 2 the computed, radial displacement for the aluminum tube is compared with the radial displacement which is measured on the basis of a Hopkinson bar method. This figure shows a similar tendency between the computed curve and the experimental points. The largest cause for the difference between analysis and experiment may be due to the neglecting of strain-rate effects of the tube materials. Therefore the history of hoop strain-rate was computed during the electromagnetic forming. Under conditions of plane strain the generalized strain-rate $\dot{\varepsilon}_g$ is expressed by the following equation : $\dot{\varepsilon}_g = 2\dot{\varepsilon}_\theta/\sqrt{3}$. Figure 3 shows the computed relation between generalized strain-rate $\dot{\varepsilon}_g$ and generalized strain ε_g for the aluminum tube during the forming. The maximum strain-rate in this figure reaches 4000 [s^{-1}] during the electromagnetic forming.

MATERIAL PROPERTIES DURING IMPULSIVE FORMING

Since the tube material shows sensitivity to strain-rate, those material properties have to be obtained during electromagnetic forming. Laminated, circular plates which were prepared are compressed within the strain rate range of 10^{-3} to 10^3 s^{-1}. A split Hopkinson pressure bar apparatus (Sato et al., 1988), an oil hydraulic press and a universal testing machine were used for the high strain rate (10^2 to 10^3 s^{-1}), medium strain rate (1 s^{-1}) and low strain rates (10^{-3} s^{-1}) tests, respectively. The flow stress is determined by applying an extrapolation method (Sato et al., 1988) to the above test results in order to eliminate the effect of friction.

For the aluminum tube, the flow stress-strain curves can be evaluated as follows:

$$\sigma = 137.9\varepsilon^{0.24}\left\{\dot{\varepsilon}/8\times10^{-4}\right\}^{0.03}[MPa]. \qquad (3)$$

Then a stress-strain curve along an arbitrary strain rate – strain path can be obtained on the basis of equation (3). Therefore, the stress-strain curve for the aluminum tube is determined along the strain rate – strain path, which is shown in Fig.3. Both the stress-strain curves for two kinds of tube during the electromagnetic forming under each condition could be expressed by the power curve equation (1). These material constants n and F are also shown in the column of "impulsive bulging" in Table 1.

CRITICAL HOOP STRAIN

To investigate the distribution of the thickness strain of a tube along the circumferential direction at the middle during the pulse forming, the tube is stopped to deform in its bulging stage by the stopping ring which is shown in Fig. 4. The thickness of the deformed tube is

measured at 48 points along its circumference at the middle. The ratio of current thickness h to mean thickness h_m is given against the angle at the circumference for the aluminum tube in Fig. 5, which shows the non-uniform thickness and that the tube has the thinner thickness at eight spots. In Fig. 6 the standard deviation of thickness measured for the aluminum alloy tube is plotted against the hoop strain which is determined by the inner diameter of stopping ring. This figure shows that according as the hoop strain increases the standard deviation increases and necking is generated.

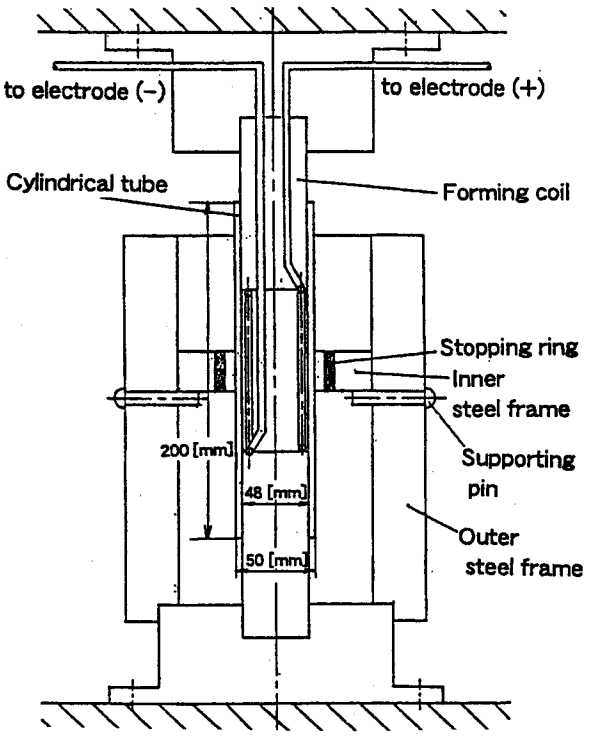

Fig.4 View of forming coil, cylindrical tube and stopping ring with steel frames.

According to close observation of the tubes with various deformations given by the stopping tests, it seemed that the tube surface at the thickness ratio h/h_m under 0.93 became depressed against the surrounding surface. When we made a decision concerning the formation of necking according to this basis, the hoop strain, ε_θ, with necking was the following: $\varepsilon_\theta \geqq 0.13$ for the aluminum tube, and $\varepsilon_\theta \geqq 0.17$ for the aluminum alloy tube, respectively. Therefore, the critical hoop strain, $\varepsilon_{\theta c}$, to cause the necking is 0.13 and 0.17 for the aluminum tube and the aluminum alloy tube, respectively.

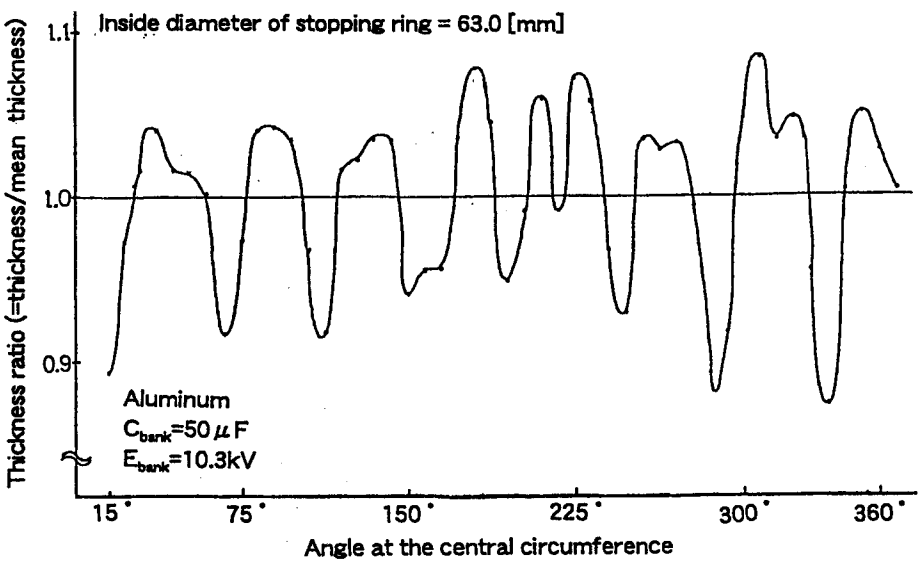

Fig.5 Distribution of thickness ratio along the central circumference. Inside diameter of stopping ring = 63 [mm].

The approximate formulation of dynamic instability in dynamic expansion of a cylindrical tube was developed in order to predict the forming limit (Tobe et al., 1984). The hoop strain, $\varepsilon_{\theta b}$, at the occurrence of dynamic instability was the following:

$$n/2 \leqq \varepsilon_{\theta b} \leqq n. \quad (4)$$

The lower bound of $\varepsilon_{\theta b}$ is the instability strain for the tube subjected to quasi-static internal pressure. It follows that n/2=0.12 for the aluminum tube. On the other hand the upper bound of instability hoop strain is expressed as n=0.23. Then the critical hoop strain $\varepsilon_{\theta c}$ determined experimentally satisfies inequality (4): $0.12 \leqq \varepsilon_{\theta c}=0.13 \leqq 0.23$ for the aluminum tube. In the same way for the aluminum alloy tube, $\varepsilon_{\theta c}$ also satisfies inequality (4): $0.1 \leqq \varepsilon_{\theta c}=0.17 \leqq 0.20$.

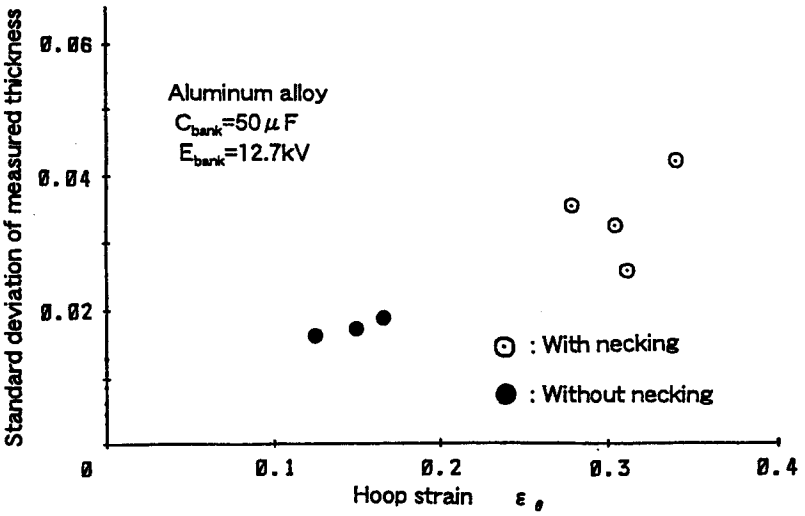

Fig.6 Standard deviation of thickness measured at 48 points along the central circumference against hoop strain for aluminum alloy tube with various deformations.

CONCLUDING REMARKS

In this paper the critical hoop strain, $\varepsilon_{\theta c}$, to cause the necking was determined experimentally for the aluminum and aluminum alloy tubes subjected to electromagnetic pressure. On the other hand the analytical formulation, which was developed before, indicated that the hoop strain at the occurrence of dynamic instability was in range of n/2 to n for a material with the strain-hardening exponent n. It was shown that the critical hoop strain $\varepsilon_{\theta c}$ determined experimentally satisfied inequality (4): $n/2 \leqq \varepsilon_{\theta c} \leqq n$. More accurate estimate of the instability strain is needed, since the instability strain $\varepsilon_{\theta b}$ is in a wide range as shown in inequality (4).

REFERENCES

Baines, K., J.L. Duncan and W. Johnson (1965-66), Electromagnetic metal forming, Inst. Mech. Engrs., **180**-Pt.1-4, 93-110.

Bruno, E.J. (1968), Magnetic pulse forming, In: High-Velocity Forming of Metals (E.J. Bruno, ed.), pp.155-184, ASTME, Michigan.

Jansen, H. (1968), Some measurements of the expansion of a metallic cylinder with electromagnetic pulses : IEEE Trans. I.G.A., **4**-4, 428-440.

Lal, G.K. (1972), Electromagnetic metal forming, IEEE Trans. Inds. Appl, July/August, 425-429.

Sato, Y., S. Matsui, M. Kobayashi and H. Takahashi (1988), A compression testing technique at high rates of strain for sheet metals, Journal de Physique, **C3**-9, 721-726.

Tobe, T., Y. Sato and N. Takatsu (1984), An analytical study on high-speed expansion of metal cylinders, J. Japan Soc. Technol. Plast., **25**-283, 716-722.

ON THE ESSENTIAL WORK OF FRACTURE : APPLICATION TO CHARACTERISE THIN POLYMER FILMS FRACTURE

L.Cousin-Cornet[1], M.Naït-Abdelaziz[2], C.Cazeneuve[3], G.Mesmacque[2]

[1] U.C.L, Unité P.C.I.M,1348 Louvain-la-Neuve, Belgium

[2] Laboratoire de Mécanique de Lille, Cité Scientifique, 59650 Villeneuve d'Ascq, France

[3] Centre Charles Zviak, Département de Physique Appliquée, Laboratoire Matériau et Surface, 92 580 Clichy, France

ABSTRACT

In this work, the Essential Work of Fracture (EWF) approach was used to characterise fracture of thin thermoplastic polymer films. The domain of validity in which the specific total work of fracture values, w_f, can be chosen to determine the specific essential work of fracture value, w_e, was first investigated. Then, the essential work of fracture is determined.
Our results show that it is possible to assess the terms w_e and βw_{pl} via two distinct intrinsic equations. These relations have been established using a different way from the one used by Cotterell and Reddel.

KEYWORDS

Essential Work of Fracture, Polymer, Thin films, Stress state transition, Intrinsic relations.

INTRODUCTION

The essential work of fracture theory was first developed by Broberg [1] to characterise fracture of elastic-plastic materials. Considering a cracked thin sheet submitted to uniaxial loading, he proposed to divide the plastic zone at the crack tip in two distinct regions (Figure 1(a)) by means:

- An inner region (end region) where the fracture process takes place (essentially by necking) and also called the fracture process zone (FPZ),
- An outer region where the material is fully plastified.

Following this idea, several authors [2,3,4] have therefore suggested to use such an approach to characterise thin polymer films fracture on DENT specimens (double edge notch in tension).

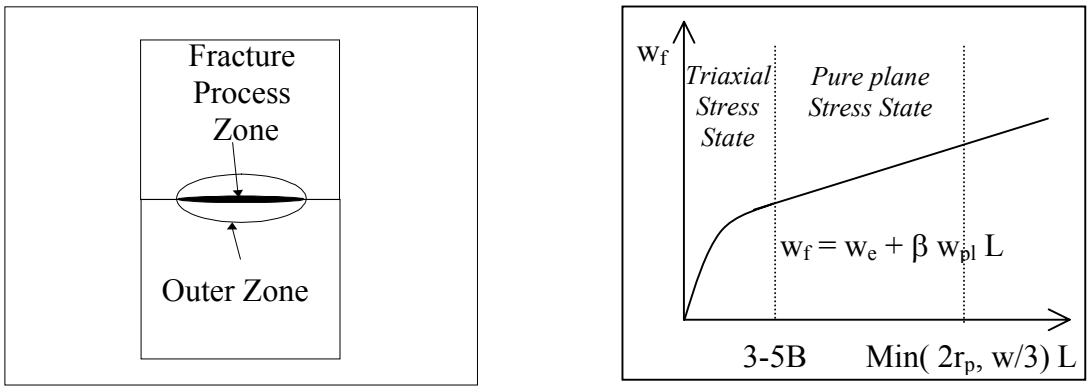

Figure 1: (a) Schematic representation of crack tip separation in two distinct zones; **(b)** Linear relationship between the total specific work of fracture and the ligament

The total work to fracture W_f (i.e the total area under the load-displacement curve of a cracked specimen) is written as:

$$W_f = W_e + W_{pl} \tag{1}$$

The essential work, W_e, is proportional to the ligament area B.L., while W_{pl} is function of the outer plastic zone volume. Thus, dividing eqn.1. by the ligament area leads to the following relationship:

$$w_f = w_e + \beta\, w_{pl}\, L \tag{2}$$

which predicts a linear relation between w_f and L. The linear fit is restricted to ligament lengths verifying some conditions we will further discuss and the specific essential work value, w_e, is obtained for L = 0 (Figure 1(b)).

EXPERIMENTAL INVESTIGATION

The material is a plasticised silicon acrylic belonging to the thermoplastic family. The fracture tests were performed on a universal tensile test device under a cross-head speed of 50 mm/mn at room temperature and 55% relative humidity. Note that a whole study of the mechanical behaviour of this material had shown that its properties are very sensitive to these parameters, revealing an elastic-viscoplastic behaviour [6]. The experiments are therefore carried out in an air-controlled room.

SENT specimens of about 0.4 mm thickness have been used with three different widths (18 mm, 24 mm, 30 mm), the length being constant and equal to 100 mm. The specimens were notched using a razor blade and several normalised crack length a/w have been tested ($0.3<a/w<0.9$). The fracture experiments were filmed allowing crack initiation time to be accurately located. Figure 2 shows as an example a set of load-displacement records obtained in such conditions for this material, dots locating crack initiation.

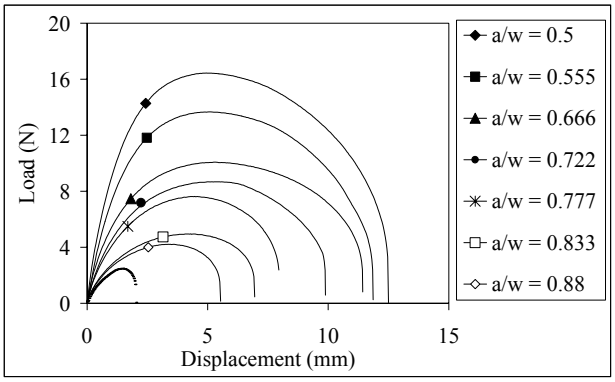

Figure 2: Load-displacement curves (w =18 mm)

RESULTS AND DISCUSSION

Conditions on ligament length

According to the literature [7,8], ligament lengths which can be used to determine w_e must satisfy the following conditions:

$$3 - 5.B < L < \min (2\, r_p, w/3) \quad (3)$$

The lower bound is to ensure pure plane stress state. More over, L must be smaller than the minimum of $2.r_p$, because the ligament must be entirely yielded before the crack initiation occurs, and w/3, to prevent that results are not influenced by edge effects.

Considering a rigid perfectly plastic material, Hill [9] showed that, for a double edge cracked sheet, a linear relationship exists between the reached maximum load , P_{max}, and L:

$$P_{max} = p \,.\, \sigma_y \,.\, L \,.\, B \quad (4)$$

The author noted the existence of necking since the corresponding net-stress, σ_n, is:

$$\sigma_n = P_{max} / (B.L) = p.\sigma_y = 2/\sqrt{3} \;.\; \sigma_y \quad (5)$$

So, if $\sigma_n > p.\sigma_y$, the stress state is triaxial and, if $\sigma_n = p.\sigma_y$, the pure plane stress state exists. The plastic-constraint factor p has then been found equal to $2/\sqrt{3}$ for DENT specimens. This result can be found using the limit load analysis assuming, as a first approximation, that the limit load is equal to the maximum recorded load, P_{max}. Using this kind of analysis and the previous approximation in the case of SENT specimens, p is found equal to 1.

The evolution of the net-stress deduced from our experimental results as a function of the ligament length is shown in Figure 3. Two distinct zones are clearly pointed out: the first one where σ_n is decreasing with respect to ligament length while it remains approximately constant in the second part. The ligament length corresponding to the stress state transition is here about 4 mm which is higher than the recommended value expressed by eqn.3. Such a difference has been already noted [10], suggesting that this lower bound depends on the material nature.

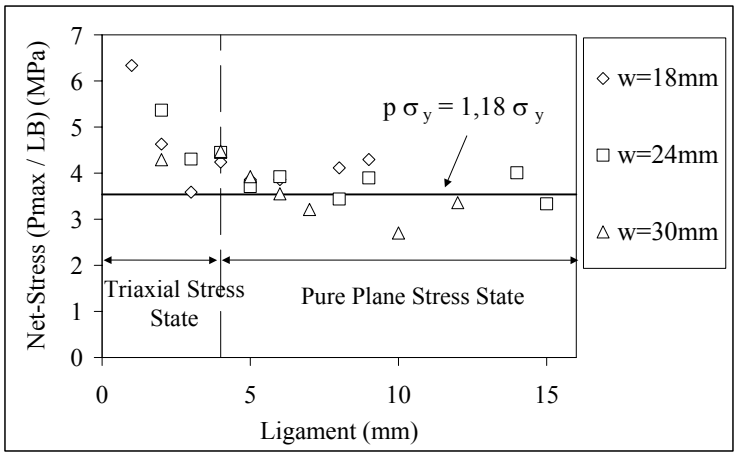

Figure 3: Net-stress evolution versus the ligament length

The yield stress value of this material was measured under the same conditions of temperature and strain rate. σ_y was found equal to about 3 MPa allowing the plastic-constraint factor estimation when using eqn.4. The p value we have calculated is 1.18 which is higher than 1. Nevertheless, it must be noted that the theoretical value is issued from the limit load analysis which assumes a rigid perfectly plastic material. Since our material reveals a strain-hardening behaviour, even if the ligament is entirely yielded when the crack

initiation occurs, the stress is increasing yet because of strain-hardening. This may explain that the constraint factor is overestimated and therefore suggest that the limit load is lower than P_{max} . Nevertheless, provided that a sufficient number of fracture tests on specimens containing varying crack lengths are available, the methodology to determine the lower bound by analysing the evolution of the net-stress in the ligament seems an interesting approach since it only requires to get the yield stress of the studied material.

Specific essential work of fracture determination

The total specific work, w_f, is plotted versus the ligament length in Figure 4 for the three specimens widths we have tested.

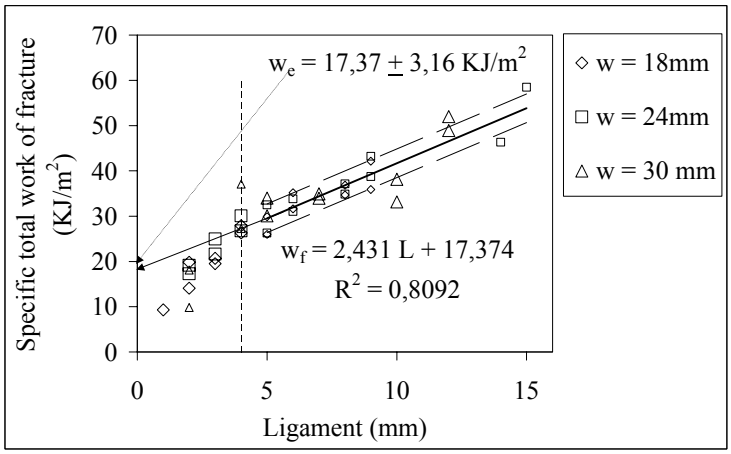

Figure 4: Specific total work of fracture evolution versus the ligament length

A linear evolution of w_f is highlighted when only retaining ligament lengths higher than 4 mm, i.e the above-mentioned lower bound . The linear fit leads to the essential specific work of fracture value which is here equal to 17,37 ± 3,16 kJ/m². Note that the upper limit has not been taken into account in this estimation since experimental values of w_f do not clearly reveal any transition when increasing the ligament length. Elsewhere, neither w_e nor the slope of the linear fit are significantly dependent on the specimen width [6].

Analytical expressions of w_e and βw_{pl}

For a given specimen geometry the total work to fracture, W_f, can be written as follows:

$$W_f(L) = \gamma(L).\ P_{max}(L).\ u_f(L) \tag{6}$$

Our experimental data are in a good agreement with eqn.6. The shape factor is found constant, equal to 0,78 [6].

Differentiation of eqn.6.leads to :

$$dW_f = \gamma \left[\frac{\partial P_{max}(L)}{\partial L} u_f\ dL \quad + P_{max} \frac{\partial u_f(L)}{\partial L}\ dL \right] \tag{7}$$

According to Mai and Cotterell [11], u_f can be expressed in the following form:

$$u_f = \delta_c + k\ L \tag{8}$$

Our results are in quite good agreement with such an expression as shown in Figure 5.

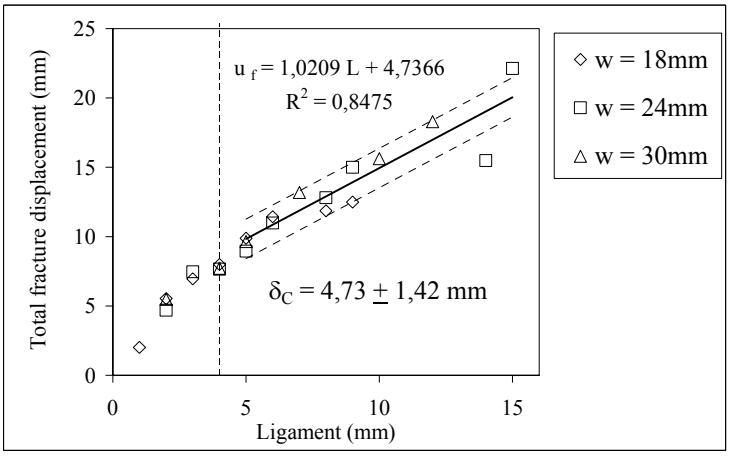

Figure 5: Total fracture displacement vs ligament length

Replacing P_{max} and u_f according to eqn.4. and eqn.8. respectively, we obtain:

$$\frac{dW_f}{dL} = \gamma.p.\sigma_y.B\left[\delta_c + 2kL\right] \tag{9}$$

In an other hand eqn.1. and eqn.2. give:

$$\frac{dW_f}{dL} = B\left[w_e + 2\beta w_{pl}L\right] \tag{10}$$

Identifying eqn.9. and eqn.10. allows to analytically express w_e and βw_{pl}. Indeed, these terms can be written as:

$$w_e = \gamma.p.\sigma_y.\delta_c \tag{11}$$

and

$$\beta w_{pl} = \gamma.p.\sigma_y.k \tag{12}$$

Eqn.11. is identical to that introduced by Cotterell and Reddel [5] but they established it using a different way.

Finally, replacing the different parameters by their own numerical values, we obtain $w_e = 13.2 \pm 4.2 kJ/m^2$ and βw_{pl} =2.8 $\pm$ 0.1 kJ/m^3. These values are in a quite good agreement with those above estimated indicating that the intrinsic relations give a reasonable estimation of these parameters.

CONCLUSION

In this study, The EWF approach has been successfully applied to investigate fracture properties of plasticized silicon acrylic polymer films. The following main results can be reminded:

- A systematic analysis of the maximal net-stress in the ligament is necessary to point out the stress state transition and therefore to validate the lower bound in terms of ligament lengths required to establish the w_e value. Indeed, this lower bound seems to be material nature dependent.
- The analytical expressions of w_e and βw_{pl} we have proposed lead to values which are in good agreement with those obtained when using a linear fit of w_f data. Nevertheless, the parameters values which are required to compute these two terms, have to be connected to other mechanical and/or physical properties.

NOMENCLATURE

W_f	:	Total work of fracture
w_f	:	Specific total work of fracture
W_e	:	Essential work of fracture, expended in the FPZ
w_e	:	Specific essential work of fracture
W_{pl}	:	Non-essential work of fracture, dissipated by plastic deformation in the outer region
w_{pl}	:	Specific non-essential work of fracture
B	:	Thickness specimen
P	:	Applied load
P_{max}	:	Maximun recorded load
u	:	Total displacement
u_f	:	Total displacement corresponding to the complete failure
β	:	Shape factor concerning the outer plastic zone
L	:	Ligament length
a	:	Crack length
w	:	Specimen width
r_p	:	Yielded zone radius
P	:	Plastic-constraint factor
σ_y	:	Yield stress
σ_n	:	Net-stress
$\gamma(L)$	:	Shape factor concerning the load-displacement curves
δ_C	:	Critical Crack tip opening displacement at initiation
k	:	Opening angle of the elaboration zone such as defined by Mai and Cotterell [11]

REFERENCES

1. Broberg, K.B.(1968) Inter. Jour.of Fract. Mech.,11.
2. Mai, Y.W. and Cotterell, B. (1986) Int Jour of Frac., 32, 105.
3. Chan, W.Y.F and Williams, J.G (1994) Polymer, 35, 1666.
4. Mai, Y.W. and Powell, P. (1991) Jour. of Poly. Sc., Part B, 29, 785.
5. Cotterell, B. and Reddel, J-K. (1977) Int. Jour. Of Frac.13, 267.
6. Cousin, L. (2000) PhD Thesis, Université de Lille, France
7. Paton, C.A and Hashemi, S. (1992) Jour. of Mat. Sc, 27, 2279.
8. Levita, G., Parisi, L. and McLoughlin, S. (1996) Jour. of Mat. Sc, 31, 1545.
9. Hill, H. (1952) Jour. of Mech. and Phy. of Sol., 1, 19.
10. Hashemi, S.(1997) Jour. of Mat. Sc, 32, 1563.
11. Wu, J.and Mai, Y.W. (1996) Polym. Eng. and Sc., 36, 2275.

Oral Reference: ICF0387

ON THE FATIGUE CRACK TIP DRIVING FORCE: ROLE OF CRACK TIP PLASTICITY

K. Sadananda[1], R. L. Holtz[1] and A. K. Vasudevan[2]

[1] Code 6323, Materials Science and Technology Division,
Naval Research Laboratory, Washington D.C. 20375
[2] Office of Naval Research, Washington D.C. 22217

ABSTRACT

The role of crack tip plasticity on fatigue crack growth is examined using dislocation concepts. Plastic flow originating from a crack will only open the crack. This is also reflected in the crack tip driving force due to plasticity. The dislocations in the plasticity induce a shielding effect when the zone is ahead of the crack and a very small antishielding effect when the zone moves into the wake. The interaction of the monotonic plastic zone provides a source for K_{max} threshold, retardation due to overloads and acceleration due to underloads. No crack closure however results from plasticity, that is in the crack wake.

Keywords

Fatigue crack growth, plasticity, K_{max} threshold, dislocation model, crack closure, overload effects, residual stresses, unified approach

INTRODUCTION

Elber [1] proposed that plasticity in the wake of the crack could cause premature closure of the crack. Hence the actual or effective stress intensity amplitude, ΔK_{eff}, is only a fraction of the applied amplitude, ΔK. Crack growth dependence on load ratio, R, has been attributed to crack closure. Rice [2] had analyzed earlier the crack tip plasticity under cyclic load and showed that crack closure can occur, but only under compression when the reverse plastic strain is equal to that of forward plastic strain. This requirement ensures that the crack tip opening displacement (blunting component) during tensile loading is canceled causing the two mating surfaces to come in contact. Elber [1] dismissed Rice's argument of non-closure with a statement that it "applies only to an idealized crack which is not propagating", indicating that crack closure can occur from plasticity for a propagating crack i.e. from the plasticity in the wake of the crack. Weertman [3] subsequently has shown using elegant dislocation analysis that plasticity cannot contribute to crack closure in a plane strain

incompressible solid. Elber established closure based on the load-displacement curves, since it is difficult to prove or predict analytically. But unfortunately, the changes in the macroscopic load-displacement curves arise from several sources and cannot be attributed solely to crack closure due to plasticity. Observations of premature contact of mating surfaces in SEM or TEM are common. These surface observations on somewhat thin samples neither prove nor disprove the plasticity induced crack closure. Any wake-interference could be result of asperities or overlapping hills resulting from faceted mode of crack growth. Such mode of crack growth arises mostly in planar slip materials and is not a general phenomenon. In addition such a wake-interference cannot be attributed to any compressive forces resulting from plasticity in the wake.

PLASTICITY INDUCED CRACK CLOSURE

Budianski and Hutchinson [4] have shown that plasticity in the wake can contribute to crack closure only under plane stress but not under plane strain. Intrinsic in their analysis are the assumptions that (a) a residual stretch of previously yielded material is attached to the crack surfaces and (b) upon unloading, this residual stretch leads to contact over the entire length of the fatigue crack. This residual stretch should have an equivalent crack opening displacement (ledge displacement) that should be greater than their closing displacements. The residual stretch can cause closure if the tensile stretch is replaced by reverse plastic flow that removes the ledges that are left in the crack wake that would otherwise keep the crack open [2].

Under plane stress, there is a lateral flow of matter from the sides contributing to pinching effect. Presumption is that the matter that flows inwards causing a dimple at the surface flows into the crack causing closure. It was, however, shown [5] that this flow of matter into the crack is energetically unfavorable. Polishing of the dimpled surface, the shear lips and the crack tip curvature at the surface accentuates the crack growth rates temporarily. These experiments neither prove nor disprove that the retardation at the surface is due to premature contact of the crack surfaces.

Furthermore at low ΔK values close to threshold, the stress state is predominantly under plane strain than plane stress. Hence load ratio dependence of threshold cannot be due to plasticity induced closure. Hence, other forms of closure such as oxide induced closure[6-14] roughness induced closure[15-20] etc, have been proposed. These can contribute in the reduction of the stress intensity amplitude as they prevent crack tip unloading by keeping it open rather than closed. Freezing of the crack tip from unloading provides the mechanism for the reduction in the effective amplitude at the crack tip.

PLASTICITY VERSUS ROUGHNESS INDUCED CLOSURE

Fig. 1 shows schematically comparison of the load-displacement curves and crack surface profiles for asperity induced closure and plasticity induced closure. The reduction in the effective stress amplitude from the applied ΔK that the crack tip region experiences during loading and unloading can be justified if displacement at the crack tip is frozen at the point of deviation from linearity in the load-displacement curve, K_c. Then the load-displacement curve will have an infinite slope for a rigid asperity since the crack face displacements are frozen. Then the effective amplitude will be equal to $(K_{max} - K_c)$. For the plasticity induced crack closure, such is not the case. Even if one argues that due to compressive residual

stresses in the wake the crack tip is closed prematurely, it is not a frozen-displacement condition at K_c as is the case for the asperities. The crack tip region experiences full unloading, albeit prematurely. This is true even if the closing of the mating surfaces occurs

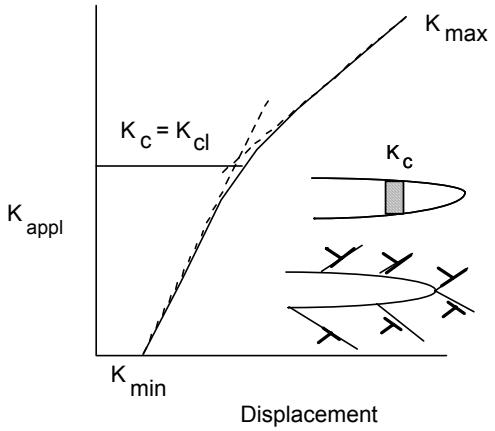

Fig. 1 Load-dislpacement curves - local asperity contact. No closure for stationary plastic crack. .

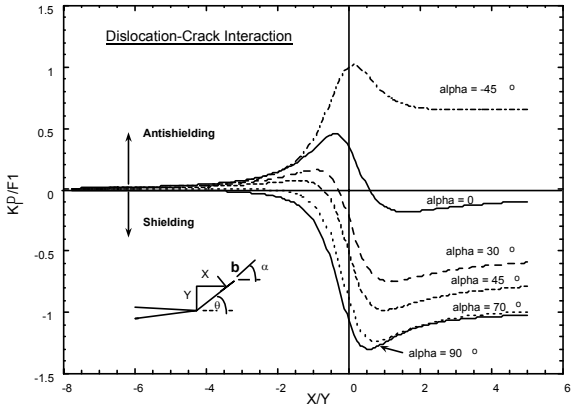

Fig. 2 Dislocation-crack interaction. X and Y are position coordinates and alpha defines dislocation orientation

gradually starting from the crack tip because of, say, some bending moments. Question essentially reduces to whether the material ahead of the crack tip is subjected to stress amplitude from K_{min} to K_{max} or not. If during unloading crack tip material goes from K_{max} to compression and not just K_{max} to K_{cl}, then it implies that full and not a fraction of the amplitude is encountered at the crack tip. Thus the loading and unloading conditions under the so-called plasticity induced closure are clearly distinct from that under asperity induced crack-wake interference as shown schematically in the insert in Fig. 1. It is therefore only a presumption rather than a fact that crack tip experiences reduction in amplitude by premature contact of the mating surfaces by plasticity, even if such contact occurs.

There have been several FEM analyses [21-27] of the problem and these conclude that plasticity induced closure can occur for propagating crack but not for a stationary crack. In addition, measurements of crack closure are mostly based on load-displacement curves presuming that changes in their slope correspond to crack closure. Besides the inaccuracies of these measurements [28], there is an inherent assumption that changes in the slope in the load-displacement curves are reflection of only crack closure. We have done extensive analysis of the crack behavior with and without asperities and the role of plasticity [29-30]. The asperity contributions depend on the position, size and width of the asperities but generally small of the order of 20% of K_c value, where K_c is point where the first contact occurs.

DISLOCATION ANALYSIS OF PLASTICITY

We outline here the essence of our arguments why the plasticity that originated from the crack tip does not contribute to crack closure. In particular: (a) every dislocation that originates at the crack tip or due to crack tip stress field, has to be a loop that forms a ledge at the crack while the rest forms part of plastic zone. (b) The plastic opening displacement at the ledge will always be greater than the elastic closing displacement from its counterpart in the plastic zone. (c) Even if the dislocations sources are ahead of the crack tip, the part of the loop that

opens the crack is attracted to the crack and the other part is repelled to form the plastic zone. (d) That the net displacement is positive is true for plasticity at the crack tip or behind the crack tip. In fracture mechanics terminology it is valid for both propagating and non-propagating cracks as well as loading and unloading conditions. (e) Dislocations that are not originated from the crack tip (pre-exiting ones due to notch tip stress fields etc. driven from sources other than the crack tip stress fields) can contribute to closure depending on their position and orientation with respect to the crack tip. In these cases their corresponding ledges are not at the crack tip to prevent the crack from closing. These arguments are in tune with the Rice continuum analysis [2]. This can also be ascertained by dislocation-crack interaction as deduced by Lin and Thomson [31]. Using their equation one can determine the stress intensity factor, K_D, due to dislocations stress field for various orientations and dislocation positions. As the dislocation glides towards the crack tip, the retarding force or shielding effect increases and reaches a maximum at $X/Y \approx 1$, where X and Y are coordinates of the dislocations in relation to the crack tip. As the dislocation bypasses the crack to form a crack-wake plasticity, the K_D term changes to predominantly antishielding type but rapidly goes to zero as the dislocation moves behind the crack. That the effect dies down rapidly can be understood from the fact that spacing between dislocation and the free surface of the crack becomes increasingly smaller in comparison to dislocation distance to the crack tip. In the single dislocation case depicted in Fig. 2 the maximum effect is narrow region at $X \approx Y$. But in real plastic zone such as in the case of distributed dislocations of pile-up the maximum effect smears to larger range of X values that the crack must overcome to bypass the deformed region. As the fatigue crack moves continuously in a plasticity field, a continuous retarding force must be felt by the crack tip and the driving force must exceed this maximum retarding force for the crack to move forward.

The behavior is the same if one replaces a single dislocation by a dislocation array representing a pile up or plastic zone. The only difference is that the distributed dislocations in the pile up, in contrast to a superdislocation of equivalent Burgers Vector, will have the same maximum retardation effect (within 10%) when the plastic zone is ahead of the crack tip, but the antishielding effect reduces to zero much more rapidly as the dislocations move behind the crack tip [32]. These dislocation-crack crack tip driving force reemphasizes the fact that plasticity has a major role to play when the plastic zone is ahead of the crack tip. Its effect on the crack tip driving force rapidly reduces to zero as it moves behind the crack tip. The implication is that plasticity in the wake does not contribute to any crack closure since there is no shielding effect for the dislocations in the wake. In addition any closing contributions for dislocations which are closely behind the crack tip are compensated by the crack tip blunting formed during the crack tip plasticity. Secondly, the maximum retarding effect of plastic zone on crack tip driving force will be felt when the crack tip moves into the plastic zone. However for the crack to move forward it has to overcome this resistance force. This contributes to a K_{max} threshold for crack growth. Note that this is not the ΔK threshold but K_{max} threshold since it is required to overcome the force of retardation due to shielding effect of the monotonic plastic zone ahead of the crack tip. Experimentally this can be determined using the technique developed by Lang and Marci [33]. Further implication of this is that the retardation effect of overloads or the acceleration effects due to underloads also arises from the residual stresses from dislocations in the overload-underload plastic zones ahead of the crack tip and not due to plasticity induced crack closure. This also explains the fact that the FEM analysis found closure effects only for a propagating crack and not for stationary crack. The propagating crack has to encounter the retarding effect from

dislocations as the crack moves forward into the monotonic plastic zone. Furthermore the delayed retardation effect encountered during the overload effects can also be accounted for since the maximum shielding occurs as the crack moves forward to X/Y ≈ 1 as shown in Fig. 2.

A more detailed analysis of a moving crack with continuously forming plastic zone has been analyzed using the Lin-Thomson equations. The analysis only reinforces the conclusions drawn above since most of effects arise from the plasticity ahead of the crack tip than that behind the crack tip. Nevertheless it points out the fact that the plastic zone ahead of the crack tip is the primary factor for the source of K_{max} threshold, while environment provides an additional factor influencing this driving force.

CONCLUSIONS

The role of crack tip plasticity is examined using dislocation-crack interactions deduced by Lin and Thomson. It is shown that dislocations stress field induces maximum shielding effect when it is ahead of the crack tip. As the dislocation moves behind the crack tip, the effect changes to antishielding type. The shielding effect causes crack tip retardation and to induce crack growth one has to overcome this retarding force. The existence of K_{max} threshold in the Unified Approach proposed by the authors is accounted for by this shielding effect of plasticity ahead of the crack tip. The analysis is in agreement with the experimental approach for the determination of K_{max} threshold by Lang and Marci[33].

REFERENCES

(1) Elber, W. Eng. (1970) Frac Mech. 2, 37.
(2) Rice, R. (1967) in Fatigue Crack Propagation, ASTM-STP 415, 247.
(3) Weertman, J. (1992) Phys. Stat. Sol., 172, 27.
(4) Budianski, B. and Hutchinson, J.W. (1978) J. Appl. Mech. 45, 267.
(5) Sadananda, K. Vasudevan, A.K. and N. Louat, N. (1997) "Dislocation Behavior Under Fatigue", in Recent Advances in Fracture, eds: Mahidhara et al., TMS, Warrendale, 395.
(6) Paris, P.C. Bucci, R.J. Wessel, E.T. Clark, W.G. and Mager, T.R. (1972) In Stress Analysis and Growth of Cracks, ASTM-STP, 513, 141.
(7) Ryder D.A. and Lynch, S.P.(1977) in The Influence of Environments on Fatigue, Institute of Mechanical Engineers, London, 21.
(8) Skelton R.P. and Haigh, J.R. (1978) Mater. Sci. Engrg., 36, 17.
(9) Tu, L.K.L. and Seth, B.B.(1978) J. of Testing and Evaluation, 6, 66.
(10) Ritchie, R.O. Suresh, S. and Moss, C.M. (1980) J. Eng. Mater. Tech., 102, 293.
(11). Stewart, A.T., (1980) Engrg. Frac. Mech., 13, 463.
(12) Suresh, S. Zamiski G.F. and Ritchie, R.O. (1981) Met. Trans. 12A, 1435.
(13). Vasudevan, A.K. and Suresh, S. (1982) Met. Trans., 13A, 2271.
(14). Liaw, P.K. Leax T.R. and Logsdon, W.A.(1983) Acta Metallurgica 31, 1581.
(15). Purushotthaman, S. and Tien, J.K. (1975) Scripta Met., 9, 923.
(16).Walker N. and Beevers, C.J.(1979) Fat. Engrg. Mat. Struc., 1, 135.
(17). Halliday M. D. and Beevers, C.J. (1981) J. of Testing and Evaluation, 9, 195.
(18). Ritchie, R.O. and S. Suresh, S. (1982) Met. Trans. 13A, 1627.

(19). Gray, G.T. Williams, J.C. and Thompson, A.W., (1983) Met. Trans. 14A, 421.
(20). Suresh, S.(1983) Met. Trans. A, 14A, 2375.
(21) Ohji, K. Ogura, K. and Yoshiji, O. (1975) Eng. Frac. Mech. 7, 457.
(22). Newman, J.C. (1976) in Mechanics of Fatigue Crack Growth, ASTM-STP, 590, 281.
(23). Newman, J.C. (1981) Methods and Models for Predicting Fatigue Fatigue Crack Growth Under Random Loading, STP 748, 53.
(24). Bloom A.F. and Holm, D.K. (1985) Engineering Fracture Mech. 22, 997.
(25). Fleck, N.A. (1986) Engrg. Frac. Mech., 25, 441.
(26). Fleck, N.A. and Newman, J.C., (1988) Mechanics of Fatigue Crack Closure, ASTM-STP, 982, 319.
(27). McClung, R.C. and Sehitoglu, H., (1989) Engrg. Frac. Mech., 33, 237.
(28) Donald, J.K. (1997) Int. J. Frac. 19, S191.
(29). Louat, N. Sadananda, K. Vasudevan, A.K. and Duesbery, M. (1993) Met. Trans., 24A, 2225.
(30) Vasudevan, A.K. Sadananda, K. Louat, N. (1994) Mat. Sci. Engrg., A188, 1.
(31) Lin I.H. and Thomson, R. (1986) Acta Met. 34, 187.
(32) Sadananda K. and Ramaswami, D. N. (2001) Phil. Mag., In Press.
(33) Lang, M. and Marci, G., (1997) Advances in Crack Closure, ASTM-STP, 1347. .

ON THE SIZE SCALING OF CLEAVAGE TOUGHNESS IN THE TRANSITION: A SINGLE VARIABLE EXPERIMENT AND MODEL BASED ANALYSIS

H. J. Rathbun, G. R. Odette and M. Y. He

Department of Mechanical and Environmental Engineering University of California, Santa Barbara
Santa Barbara, CA 93106, USA

ABSTRACT

A systematic investigation of the effects of specimen size on cleavage fracture toughness of a typical pressure vessel steel in the transition is reported. Size dependence of toughness may arise from two basic mechanisms. The first is related to the total volume of material acted on by high stress fields near a blunting crack tip, which is a function of the crack front length (B) in small scale yielding (SSY). We call this the statistical stressed volume (SSV) effect. The second is due to SSY constraint loss (CL), which depends on the ligament length (b) as well as B. Until now, it has not been possible to quantify the individual and combined effects of SSV and CL (or B versus b) size scaling laws, or even to verify fully the existence of the underlying mechanisms. In order to develop a single variable database on size effects, a complete B-b matrix of fracture specimens, fabricated from a single plate of steel from the Shoreham pressure vessel, was tested at a common set of conditions. The B ranged from 8 to 254 mm and b from 3.2 to 25.4 mm. The database was analyzed using 3-dimensional finite element simulations of the crack tip fields, calibrated to the local fracture properties of the Shoreham steel. The finite element based analysis shows that both SSV, giving rise to a $B^{-1/4}$-type scaling, as well as CL, evaluated in terms of in-plane areas within critical stress contours, can sometimes play a significant role in the size scaling of transition toughness. The significance of these results to the recently approved Master Curve standard (ASTM E 1921-97) is discussed briefly.

KEY WORDS: Cleavage toughness, statistical and constraint loss effects, fracture models, Master Curve

INTRODUCTION

There has been significant progress in understanding the mechanisms and mechanics mediating the fracture toughness (K_{Jc}) of steels in the cleavage transition regime that qualitatively rationalizes observations of both large scatter and explicit effects of specimen size and geometry. This understanding is based on: a) the concept of critically stressed regions containing a statistical distribution of cleavage trigger particles local to a blunting crack tip; and b) realistic finite element (FE) simulations of the corresponding stress fields, including 3-D computations, for conditions that deviate substantially from SSY [1,2,3]. Statistical considerations dictate that fracture toughness increases with decreasing volume of material under high stress, giving rise to an inverse power dependence on the crack front length, or thickness, B, in standard edge cracked specimens. We will refer to this as the statistically stressed volume (SSV) effect. Reductions in the crack tip stress amplitude associated with tri-axial constraint loss (CL) can also result in increasing toughness with decreasing specimen dimensions [3] outside the SSY regime. The challenge is to define the limits of SSY, which is complicated by the fact that both SSV and CL effects can appear to have quite similar dimensional scaling in some regimes [4].

Unfortunately, the body of data to quantify the individual and combined contributions of SSV and CL to size effects is rather sparse. A recent review found that the available fracture toughness database is generally inconclusive, since it is dominated by specimens with simultaneous variations in all dimensions, and most

often has ambiguous levels of constraint [5]. Further, the magnitude of CL depends on the detailed micromechanics of cleavage, hence, on the material and microstructure.

These fundamental issues have significant practical implications to the recent ASTM standard master curve (MC) method for measuring K_{Jc} in the transition (ASTM E 1921-97) [6]. The MC method uses an explicit SSV adjustment of $K_{Jc}(B)$ to a common reference B_r = 25.4 mm to account for size effects as $K_{Jcr} = K_{min} + [K_{Jc}(B) - K_{min}][B_r/B]^{1/4}$, where K_{min} = 20 MPa$\sqrt{m}$ is an assumed minimum toughness [1]. A relatively favorable constraint limit is used to 'censor' data affected by CL, and a statistical procedure is used to include the censored data in determining a reference temperature (T_o) at K_{Jc} of 100 MPa$\sqrt{m}$. The maximum toughness limit for uncensored data is determined from a non-dimensional CL factor $M = Eb\sigma_{ys}/K_J^2$ at M = 30, where σ_{ys} is the yield stress, E is the elastic modulus and b is the ligament length[2].

The overall objective of this work is to develop and analyze a single variable database on size effects on K_{Jc} in a typical pressure vessel steel. Specifically, we seek to assess, and physically model, the individual and combined contributions of SSV (B) and CL (b and B) mechanisms.

EXPERIMENTAL: A SINGLE VARIABLE SIZE SCALING STUDY

A full test specimen matrix included variations in B for a set of constant b, and variations in b for a set of constant B. The nominal values of B and b were 8, 16, 32, 64, 127 and 254 mm (B), and 25.4, 12.7, 6.3 and 3.2 mm (b), respectively[3]. A section of ASTM A533 Grade B Class 1 plate from the decommissioned Shoreham vessel was machined into single edge notched three point bend specimens (SENB) in the L-S orientation with span (S) to width ratio S/W=4 and a/W 0.5 . Individual specimen types were taken from randomized locations within the original steel plate. Pre-cracking procedures were developed to ensure straight crack fronts at a constant 1/4 plate thickness depth. Based on preliminary measurements of T_o using 1T C(T) specimens, all quasi-static loading rate tests were carried out at -91°C. With minor or necessary exceptions, including atypical specimen geometry (e.g., large and small B/W ratios), the fracture tests followed the basic ASTM E 1921-97 procedures. For b= 25.4 mm, M is greater than 100 up to 175 MPa$\sqrt{m}$, reasonably assuring negligible to modest CL effects in all but the thinnest specimens. The large range of B from 8 to 254 mm produces a maximum variation of a factor of about 2 in the mean toughness for SSV scaling. The variations in b were used to explore a wide range of constraint conditions, down to M values of less than ten[4]. Eight tests were carried out at each matrix point. Other characterization studies include: a) fracture tests on the 1T C(T), pre-cracked Charpy (PCC) bend bars with a/W of about 0.1 and 0.5, and 1/2 and 1/3-sized PCC bend bars; b) tensile properties at a wide range of temperature; c) metallograpy, micro-hardness and quantitative fractography[5]. Further details on the experimental procedures will be given in future publications.

EXPERIMENTAL RESULTS AND DATABASE

In all cases, fracture was by cleavage initiation with little or no stable crack growth[6]. Figure 1a shows a composite plot of the unadjusted toughness data for various specimens (K_{sp}) plotted against log B (in mm). For clarity, only the maximum and minimum K_{sp}, connected by lines, along with the K_{sp} average for a given B, are shown. The heavy dashed line is a least square fit to the average K_{Jc} data for the largest b = 25.4 mm specimens using the MC form as $K_{min} + [K_{Jc} - K_{min}] [B_r/B]^p$. In this case p = 0.26± 0.09, in almost exact agreement with the nominal SSV prediction. While they are somewhat difficult to see in this very busy plot, three other trends can be observed: a) the minimum K_{sp} is relatively independent of B and b; b) both the average and maximum K_{Jc} generally increase with decreasing B; and c) both the average and maximum K_{Jc} tend to be higher for smaller b. Figure 1b shows the SSV adjusted K_{ssv} averaged for the six B plotted on an

[1] The $B^{-1/4}$ size scaling fundamentally derives from the fact that for SSY, the in-plane area within a specified stress contour varies as the applied K_J^4. Thus, the corresponding volume within a specified stress contour scales with BK_J^4. Assuming a critically stressed volume cleavage criteria gives rise to the $B^{-1/4}$-type scaling.

[2] Other important specimen dimensions are the crack depth (a), width (W) and ligament length (b = W-a).

[3] Due to problems in reliable pre-cracking, the specimens at the matrix point b = 3 mm, B = 64 mm were not tested.

[4] Note, while we have characterized constraint in terms of the in-plane ligament dimension b, loss of out-of-plane (transverse) plane strain constraint also occurs in thin (small B) specimens

[5] The fractography-fracture reconstruction efforts include optical, scanning electron and confocal microscopy. These techniques are being combined to identify fracture initiation sites and process zone damage development sequences.

[6] The maximum stable crack growth in the smallest specimens with the highest toughness was less than 5% of the ligament.

expanded scale against b. Clearly, significant CL effects may occur at nominal values of M_{nom} (also shown, assuming K_{Jc} = 100 MPa m) greater than 30. However, given the large range of specimen geometry in this database, additional analysis of the SSV and CL effects requires application of more detailed size scaling models.

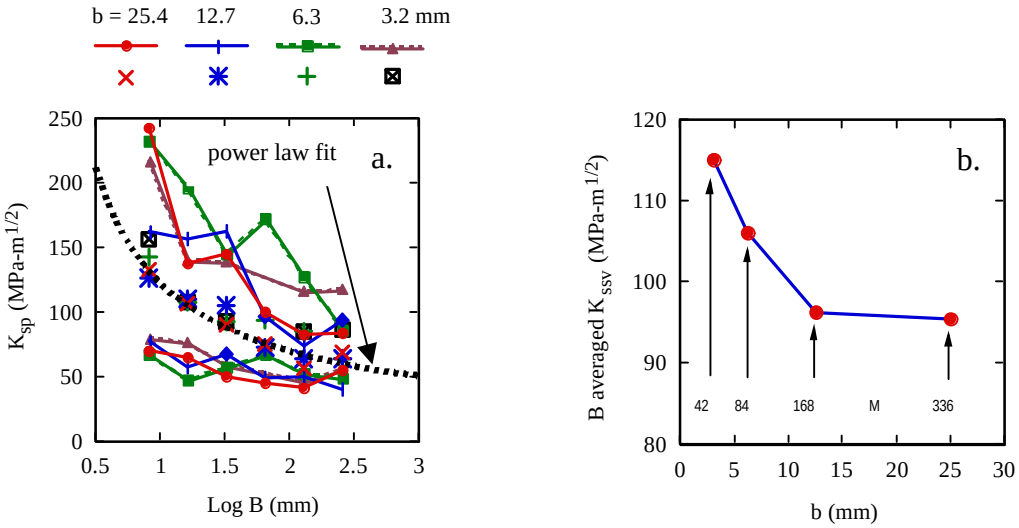

Figure 1 a) Maximum, minimum and average K_{sp} data vs. B; b) K_{ssv} data averaged over B vs. b.

FINITE ELEMENT MODELING OF TOUGHNESS AND SIZE SCALING

Three-dimensional (3-D) finite element (FE) simulations of crack tip stress and strain fields were used to analyze the database described in the previous section, following the general approach of Nevalainen and Dodds [3]. This method assumes that cleavage occurs when a specified principle stress ($\sigma_1 = \sigma^*$) contour encompasses a critical volume (V*) of material in front of the blunting crack tip[7]. Assuming B is fixed, the constraint adjustment is given by the ratio of the applied K_J for a finite specimen (K_{sp}) producing a particular stressed volume (V_{sp}), to the corresponding SSY K_{ssy} that produces the same stressed volume (i.e., $V_{ssy} = V_{sp}$), or K_{sp}/K_{ssy}. However, we also wish to consider variations in B relative to a reference thickness, B_r. Thus, it is most convenient to evaluate V_{sp} as $<A_{sp}>B$, where $<A_{sp}>$ is the stressed area averaged over the entire crack front. The corresponding reference V_{ssy} is $A_{ssy}B_r$, where A_{ssy} is the stressed area for plane strain conditions at a minimal level of global plastic deformation with no T-stress field. The measured toughness can be adjusted to SSY conditions at $B = B_r$, K_{Jcr}, by dividing by the corresponding FE based K_{sp}/K_{Jcr} factor at $<A_{sp}>B = A_{ssy}B_r$. Following Nevalainen and Dodds, the SSY $A_{ssy}(K_J, \sigma_1/\sigma_{ys})$[8] were computed based on an elastic boundary layer analysis using the general purpose FE code ABAQUS [7]. The mesh, consisting of 1200 two dimensional, eight-noded continuum plane strain elements, was very refined near the crack tip, and increased in size out to a large boundary radius. This ensured that the plastic zone was deeply embedded in an elastic zone bounded by imposed elastic displacements with a T-stress equal to 0.

A quarter-symmetry mesh composed of 2480 20-noded quadratic brick elements was used in the 3-D FE simulations for all the non self-similar specimen geometries. Wedge-shaped elements, with overlapping nodes at an initially sharp crack tip, were used to efficiently model blunting up to high levels of gross specimen plastic deformation, corresponding to a minimum M of less than 10. The K_{sp}/K_{Jcr} adjustment accounts for both SSV and CL mediated size-scaling effects[9]. In the SSY regime, $K_{sp}/K_{Jcr} = [B/B_r]^{1/4}$, while the effects of constraint loss can be isolated by assuming $K_{sp}/K_{Jcr} = [A_{ssy}(K_J)/<A_{sp}(K_J)>]^{1/4}$. For a given constitutive law, the CL adjustment depends only on $\sigma_1/\sigma_{ys} = \sigma^*/\sigma_{ys}$.

The A_{ssy} can be represented in a compact non-dimensional form as $A_o = \log[A_{ssy}(\sigma_1/\sigma_{ys})\sigma_{ys}^4/K_J^4]$, and fitted to a polynomial $f(\sigma_1/\sigma_{ys})$ [3]. This relation can be used to evaluate K_{Jc} at specified values of $\sigma_1 = \sigma^*$, $A_{ssy} = A^*$ and σ_{ys}. Further, it has been shown that the predicted $K_{Jc}(T)$ curve shape for unirradiated steels

[7] Statistical variations in trigger particle microstructures result in a corresponding distribution of σ*–V* leading to the inherent scatter of K_{Jc} data in the transition.

[8] The compact nomenclature in this paper uses K_J rather than J, as $K_J = JE'$, where E' is the plane strain modulus.

[9] Note that since the details of the FE computations and analysis procedure were somewhat different for the SSY boundary element and 3-D specimen cases, the A_{ssy}/A_{sp} approaches unity at $M \approx 200$. Thus, no constraint correction is applied for specimens in which the measured $M \geq 200$.

with T_o below 0°C is consistent with the MC shape assuming that σ* and A* are constant (independent of T) using a generic empirical $\sigma_{ys}(T)$ relation [8]. Thus, the model can be used to fit SSY $K_{Jc}(T)$ data to estimate the σ*-A*. The results of fitting are shown in Figure 2a, where the filled circles are data from 1T C(T) specimens and the open diamonds are for PCC specimens SSV adjusted to B_r = 25.4 mm (a/W 0.5 in both cases). Note that this data has not been CL adjusted, which would generally be small. The solid line is the MC shape with T_o = -91°C. The heavy dashed curve is the predicted $K_{Jc}(T)$ curve for A* = 3.7x10^{-8}m^2 and σ* = 1790 MPa - σ^*/σ_{ys}(= 591 MPa) 3. The light dashed lines show the results for fits with a σ^*/σ_{ys} ratios of 2.75 and 3.25. An additional fitting criterion for σ*-A* was that the predicted $K_{Jc}(T)$ match the MC shape in the lower shelf-knee regime (in this case down to –196°C). Thus, the nominal estimate of σ^*/σ_{ys} = 3 is certainly reasonable, but not completely unique. Figure 2b shows a 3-D plot of the effect of B/W and M on CL in terms of the K_{sp}/K_{ssy} for σ^*/σ_{ys} = 3. Additional details regarding the FE simulations and use of alternative statistical models, as well as the insight gained from the other characterization studies, will be presented in future publications.

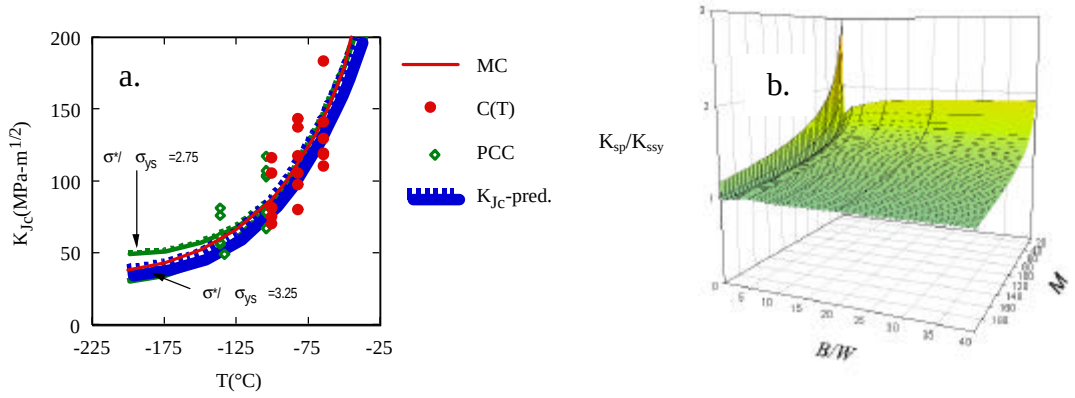

Figure 2 a) The fitted σ*-A* $K_{Jc}(T)$ model; b) FE K_{sp}/K_{ssy} adjustment factor vs. B and M.

ANALYSIS AND EVALUATION OF THE DATABASE

The SSV and CL adjusted K_{Jcr} are shown in Figure 3a plotting the average K_{Jcr} versus B at the 4 ligament (b) lengths. In all cases, the toughness averaged over all B at each b is slightly less than the preliminary estimate of 100 MPa m. The overall average at all B and b is 91.1±4 (at 1 SD) MPa m. The K_{Jcr} average over B for the three largest b are nearly identical at 93±0.2 MPa m, while the corresponding average is only 85.4 MPa m for the smallest b = 3.2 mm. The overall dependence of the average K_{Jcr} on B at various b, as well as on b at various B, is weak and statistically insignificant.

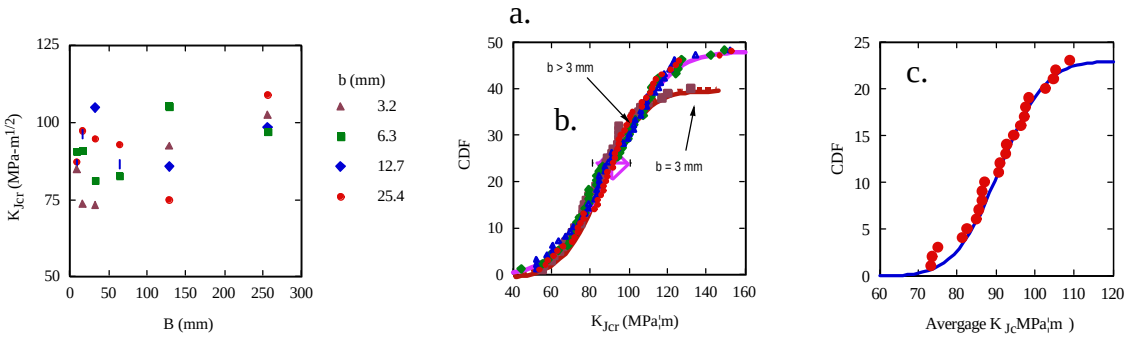

Figure 3 a) Average K_{JCr} for all b-B; b) CDF for the average K_{JCr}; c) CDF for all K_{Jcr}

Figure 3b plots the cumulative distribution of all 180 of the individual adjusted K_{Jcr} data points. The distributions are nearly identical for the three largest b (48 data points each) with a standard deviation (SD) of 23.0±1 MPa m. The corresponding distribution for the 40 data points at the smallest b = 3.2 mm is somewhat narrower and shifted to slightly lower K_{Jcr}. However, in both cases, the data are well represented by a normal cumulative distribution function (CDF), shown by the solid and dashed line for the appropriate average K_{Jcr} and SD. Figure 3c plots a cumulative distribution of the averages at each of the 23 B-b combinations. The standard deviation of this adjusted data set is ±10 MPa m. These data are also

reasonably consistent with a normal CDF, shown by the solid line. The largest deviations are for two of the small b = 3.2 mm specimens with somewhat atypical B/W ratios of about 2.5 and 5. A Monte Carlo simulation, assuming a population of K_{Jcr} data with a SD of 23 MPa m, gave a corresponding SD for the averages for the B-b combinations of 8.1 MPa m, close to the observed value of 10. Figure 4 shows Weibull plots of all the K_{sp}, K_{ssv} and K_{Jcr}, along with corresponding least square (dashed lines). The unadjusted K_{sp} data are for different specimen sizes, hence, are not expected to follow a Weibull distribution. However, to the extent that the SSV and CL adjustments 'work', size-independent Weibull distributions, with a slope approaching m = 4, can be anticipated for K_{ssv} and K_{Jcr}. Thus the low Weibull slope for K_{ssv} of m = 3.17, and deviations at higher toughness, again suggest that the SSV adjustment alone is not sufficient to account for size effects in this dataset. However, the combination of a SSV and CL adjustment results in Weibull slope of m = 3.85 and smaller deviations at high K_{Jcr}. At intermediate K_{Jcr}, the slope is almost exactly equal to the theoretical value of 4.

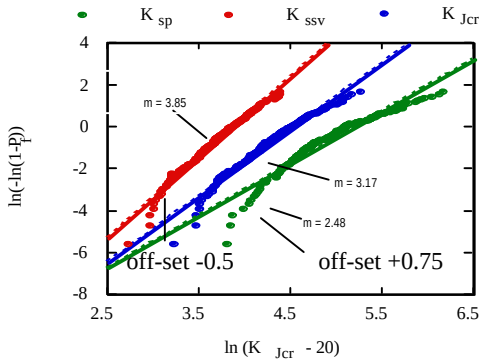

Figure 4 Weibull plots of the K_{sp} (far right), K_{ssv} (middle) and K_{Jcr} (far left) data (offset for clarity).

These results lead to two major conclusions. First, the Shoreham plate is relatively homogeneous at the sampling location with a mean reference toughness of about 92±8 MPa m at –91°C. Second, the combination of the CL and SSV adjustments produce a self-consistent K_{Jcr} data set. Thus, together with this database, the FE model-based adjustments provide a basis to distinguish the *separate and combined* effects of SSV and CL.

Figure 5a shows a decomposition of the adjustments for the various b and B. The unadjusted K_{sp} data point, furthest to the left, is connected to the adjoining K_{ssv} data point to its immediate right. Note, this *accepts* a primary $B^{-1/4}$ scaling adjustment, which reduces K_{ssv} relative to K_{sp} for B < 25.4 mm and has the opposite effect for B > 25.4 mm. The next point to the right reflects the additional CL adjustment that is needed, in some cases, to produce a fully size-independent to K_{Jcr} data set, based on the FE σ*-A* local fracture model. The solid and dashed lines are the average adjusted K_{Jcr} and the ±10 MPa m standard deviation respectively. As expected, the SSV adjustment increases with those B that deviate more from the reference B_r = 25.4 mm, and CL adjustments are most significant at small b and B.

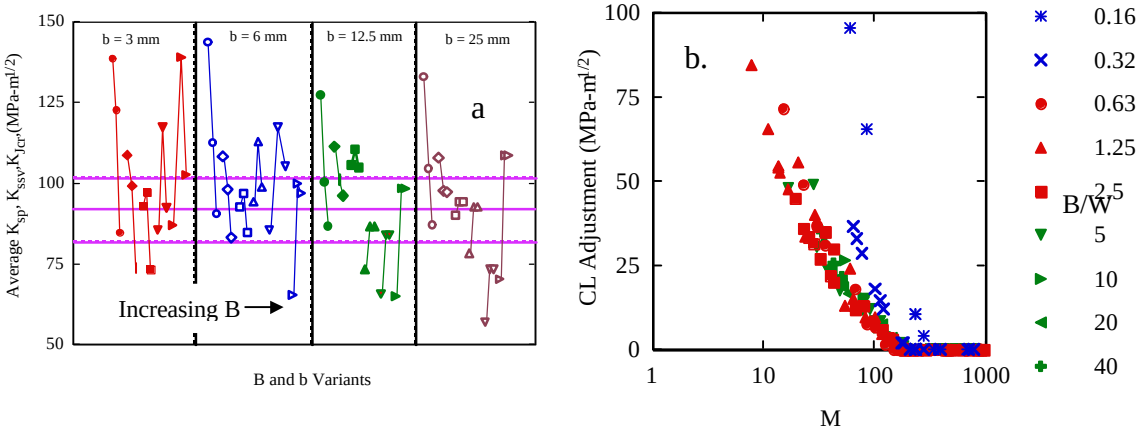

Figure 5 a) The K_{sp}, K_{ssv}, K_{Jcr} adjustment map, with increasing B in going from left to right;
b) the CL adjustment vs. M for various B/W.

Figure 5b plots the CL adjustments (= K_{ssv}-K_{Jcr}) versus M on a log scale (for clarity). The adjustments for the cases with atypically large and small B/W (< 0.5 and > 5) suffer somewhat (high B/W) to significantly (low B/W) larger CL at a given M. The mechanics leading to higher CL with very large B/W

will be discussed in future publications. The data points with B/W ratios from about 0.63 to 2.5, more typical of specimen configurations, are similar. These results suggest that CL begins at M 100 and becomes significant (CL adjustments 10 MPa m) for M from about 50 to 80. Note, a similar analysis using a σ^*/σ_{ys} = 3.25, rather than the nominal value of 3, suggests that CL begins at M slightly less than 100, and becomes significant for an M from about 30 to 50. Further, the M marking significant CL may be lower for compact tension specimens, with a smaller T-stress compared to bend bars.

The individual data sets can also be used to derive T_o, which average -84±9.3°C, and are also reasonably represented by a normal distribution. The highest T_o values are again for the b=3.2 specimen group with B/W = 2.5 and 5. Additional results on the effect of specimen size on the evaluation of T_o will be reported in the future.

SUMMARY AND FUTURE WORK

The results of this study present a remarkably clear picture of size scaling effects on K_{Jc} in the cleavage transition. They demonstrate that SSV *and* CL effects are both significant in some cases. Modeling the combined effects of SSV and CL, using FE simulations of crack tip stress fields, provides a basis for adjusting K_{Jc} data to a common reference size and SSY condition. The database and analysis supports the MC method approach to adjusting toughness data to account for the effect of B. However, the results also indicate that the use of M = 30 may not always fully account for CL.

The results and conclusions reported here should be considered preliminary. As well as additional modeling and statistical evaluations[10], information and physical insight emerging from both the broader characterization and toughness testing efforts will be incorporated in future data analysis. Further, additional testing may be warranted to fill in some gaps and resolve some uncertainties, such as the apparently low values of K_{Jcr} for two B at the smallest b.

ACKNOWLEDGEMENTS

This work was primarily supported by U.S. Nuclear Regulatory Commission Contract NRC-04-94-049. Support was also provided by the U.S. Department of Energy Grant #DE-FG03-87ER-52143 (for much of the FE modeling) and, most recently, the UCSB College of Engineering (for H. Rathbun). We also wish to acknowledge the collaboration of Dr. Robert L. Tregoning for assisting in testing of the largest fracture specimens at the Carderock Division Naval Surface Warfare Center, as well as Tom Huang, David Gragg and Kirk Fields for their help in the fracture testing carried out at UCSB. Finally, we thank Professors Gene Lucas, Robert Dodds and Kim Wallin for helpful discussions and suggestions.

REFERENCES

1. Ritchie, R.O., Knott, J.F., and Rice, J.R. (1973) *J. Mech. Phys. Solids*, 21, 395.
2. Wallin, K. (1991) In: *Defect Assessment in Components - Fundamentals and Applications*, ESIS/EGF9, pp. 415-445, Blauel, J.G. and Schwalbe, K.-H. (Eds.). Mechanical Engineering Publications, London.
3. Nevalainen, M. and Dodds, R.H., Jr. (1995) *Int. Journal of Fracture*, 74, 131.
4. Rathbun, H.J., Odette, G.R., He, M.Y., Lucas, G.E. and Sheckherd, J.W. (1999) In: *Fracture, Fatigue and Weld Residual Stress, PVP-Vol. 393*, pp. 17-22, Pan, J. (Ed.) ASME, New York.
5. Rathbun, H.J., Odette, G.R. and He, M.Y. (2000) In: *Applications of Fracture Mechanics in Failure Assessment, PVP-Vol. 412*, pp. 113-124, Lidbury, D. (Ed.) ASME, New York.
6. ASTM E 1921-97, "Standard Test Method for Determination of Reference Temperature, T_0, for Ferritic Steels in the Transition Range," ASTM 1998.
7. ABAQUS V5.8, ABAQUS Standard Users Manual, Hibbitt, Karlsson and Sorenson, Inc, Providence Rhode Island, 1998.
8. Odette, G.R. and He, M.Y. (2000) *Journal of Nuclear Materials*, 283-287, 120.

[10] Because of length limits in this paper, we have not discussed a number of important issues. These issues include interactions between SSV and CL effects and the trends observed in the lower tail of the K_{Jcr} distribution in relation to the proposal of a threshold toughness of 20 MPa m. These and other topics will be covered in future publications.

OPTIMAL SHAPE DESIGN OF STRESS RELEASING HOLES

Pauli Pedersen

Department of Mechanical Engineering, Solid Mechanics
Technical University of Denmark
Nils Koppels Allé, Building 404, DK−2800 Kgs. Lyngby, Denmark

Introduction and an illustrating example

The method of hole drilling near the crack tip is often used in fatigue damage repair. In the survey by Shin *et al.* (1996) comparisons with alternative methods are presented and it is concluded that hole drilling was most effective. A number of experimental results are presented. In a recent paper by Thomas *et al.* (2000) optimum location of the drilled holes are discussed. The specific problem of a centre cracked plate is studied with four relatively large holes (20−40 mm) placed symmetrically relative to the crack. Only circular holes are applied.

From shape optimization we know that the circular shape is by no means optimal, see e.g. Pedersen (2000, 2001). It is therefore important to find the shape of a hole, which in the most effective way, releases the stress concentration. A simple parametrization, used in earlier shape optimizations, is applied and it is shown that an almost uniform stress state can be obtained along the boundary of the hole. The shape of the hole is described by the superelliptic equation

$$(x/a)^\eta + (y/b)^\eta = 1 \tag{1}$$

where the x direction is the direction of the crack. If we use a square design domain $a = b$ (supercircle), then the only design parameter is η. We show in figure 1 three designs corresponding to $\eta = 2$ (circular), $\eta = 2.5$ (optimized) and $\eta = 6$. In the figure it is, by the red areas added to the boundary of the hole, illustrated how the strain energy density varies along the boundary of the hole (the same technique is applied in figures 3, 4 and 5). Values for relative maximum strain energy densities for the three designs are 1.00, 0.67 and 1.13 corresponding to relative maximum tangential stresses 1.00, 0.82 and 1.06. We note that considerably better distributions of stresses can be obtained. Even more uniform fields along the hole boundary can be obtained when more design parameters are included.

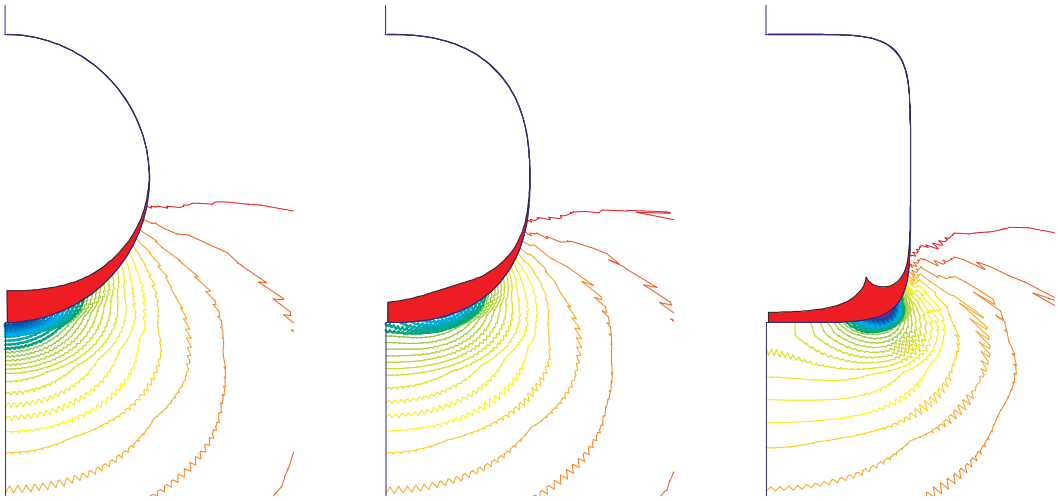

Figure 1: The energy distribution around half the holes, corresponding to $\eta = 2.0$, 2.5 and 6.0.

The objective of the optimal shape design in relation to cracks is not completely clear. At first we may argue that the objective should be to minimize the stress intensity factor. However, for non−sharp crack

tips the interpretation of the stress intensity factor is not clear. Thus we choose to minimize the maximum tangential stress at the boundary of the drilled hole. In the case of plane stress this also corresponds to minimizing the maximum von Mises stress or the energy density. For the cases of non−isotropic materials it seems most relevant to minimize the maximum energy density.

Stresses, stress intensity and energy release

We analyze the elementary case of Isida (1971), shown in figure 2 (the small hatched part corresponds to figure 1). With stress load $\bar{\sigma}$ in the $y-$direction the crack tip field expressed in principal stresses σ_1, σ_2 with direction ψ for the σ_1-direction is

$$\sigma_1 = \sigma\left(\cos\frac{\theta}{2} + \frac{1}{2}\sin\theta\right) \ , \ \sigma_2 = \sigma\left(\cos\frac{\theta}{2} - \frac{1}{2}\sin\theta\right) \ , \ \psi = \frac{\pi}{4} + \frac{3\theta}{4}$$

$$\sigma = K_I/\left(\sqrt{2\pi}\ \sqrt{r}\right) \ ; \ K_I = \bar{\sigma}\sqrt{\pi a}\ f_1\left(\frac{a}{w}\ , \frac{h}{w}\right) \tag{2}$$

with the geometry factor f_1 available in tables or graphs (for $a/w = 0.4$, $h/w = 0.5$ we find $f_1 = 1.63$). A finite element model (FEM) with a minimum element size of $6 \cdot 10^{-5} w$ and with 17300 degrees of freedom confirms this result. Two alternative methods (not described in the literature) for determining K_I confirm the value of f_1 with great accuracy. In the first method the fracture mechanics model and the FEM are only coupled through the matching of energy in a crack tip domain. In contrast to methods based on the $J-$integral we perform a domain integration (summation) that can be taken directly from a finite element model. In the second method the energy release $G = -d\Pi/da = K_I^2/E$ is found directly from a changed model, say with $\Delta a = a \cdot 10^{-2}$. ($\Pi$ is the total potential).

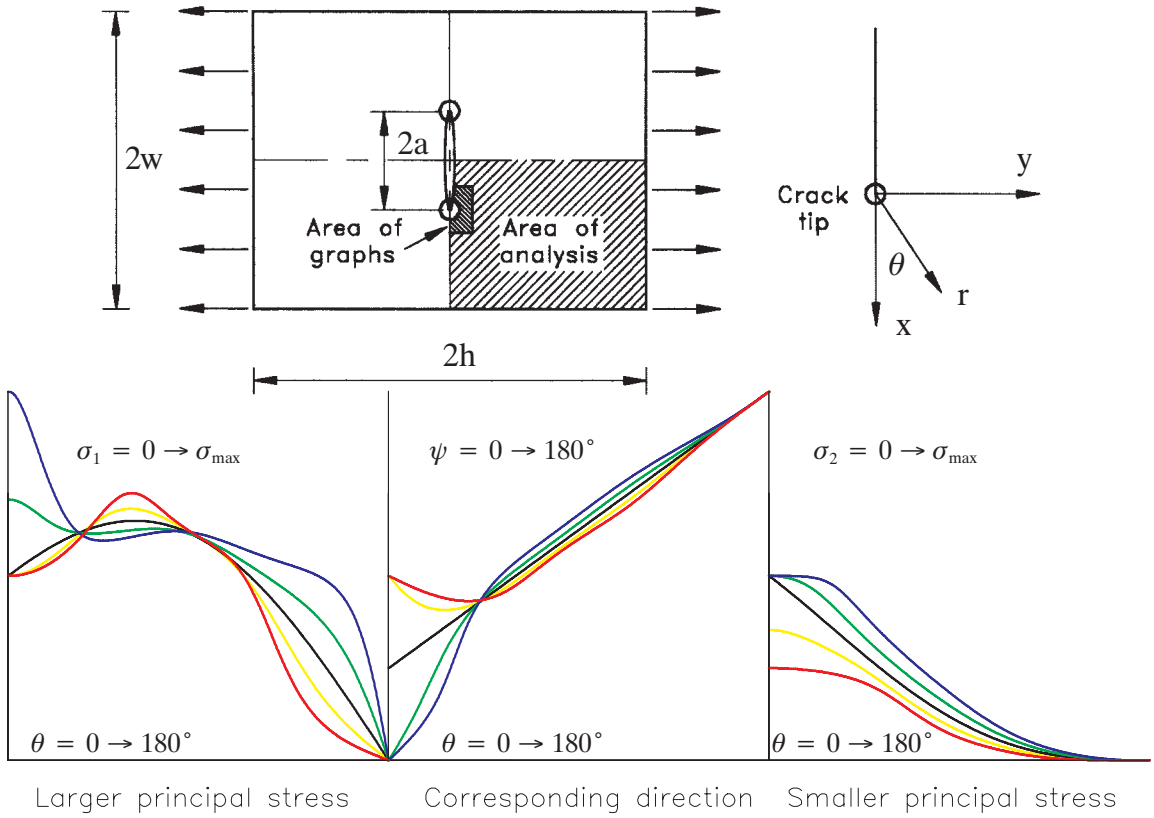

Figure 2: The analyzed elementary case with $w = 100$ mm, indicating also the area of the graphs (hole size $\approx$1 mm). Analytical stress fields at the crack tip (without hole) as a function of θ are shown for four cases of orthotropy and for isotropic material. The colour code is best shown in the σ_2 graph, where from below we have $E_C/E_T = 0.25, 0.5, 1.0, 1.5, 2.0$, respectively.

Because we shall also optimize shapes of holes in orthotropic materials, it may be informative to show a graph of the principal stresses (2) for the extended cases of $E_C/E_T = 0.25$, 0.50 , 1.0 (isotropic) , 2.0 and 4.0 where E_C is the modulus in the crack direction, and E_T is the modulus in the transverse direction. (In all cases we kept the major Poisson ratio $\nu_{CT} = 0.3$ and $E_T/G_{CT} = 2.6$) . By the method described above, the relative K_I values for these cases are determined to 1.35 , 1.13 , 1.0 , 0.90 , 0.82 , i.e. increasing with increasing flexibility in the crack direction. In figure 2 the actual model is shown together with the fracture mechanics analytical solutions. The blue curve is the isotropic case of eq. (2) and the red curve corresponds to $E_C/E_T = 0.25$, i.e. the case for which optimal shape will be shown.

Sensitivity of the optimal shape

The example shown in the introduction is based on a number of assumptions and a study of the sensitivity to these assumptions is needed.

Influence from the external load and size of the hole. Different external loads can be examined, either given stresses (forces) or given forced displacements. As expected only little influence is seen as long as the crack is loaded mostly in mode I. This follows from the fact that the near crack tip field will, as a function of the external load, only change with a common factor (the stress intensity factor). Optimization for cracks in mode II, mode III and combined modes needs further studies.

In table 1 we show the relative concentration of the energy density, for different size of the holes and for two alternative load cases. In all cases the best of the analyzed designs correspond to a superelliptic power of $\eta = 2.5$. Relative to the size of the hole $(0.5$, 1.0 , 1.5 and 2.0 mm) , with the 1 mm size as reference, we got 1.92 , 1.00 , 0.68 , 0.52 , and larger holes naturally gives a more efficient stress release. The size of the hole is assumed to be determined by alternative considerations.

Shape parameter		$\eta = 2.0$	$\eta = 2.25$	$\eta = 2.5$	$\eta = 3.0$	$\eta = 3.5$	$\eta = 4.0$	$\eta = 4.5$
size	stress load	1.0	0.857	**0.840**	0.876	0.934	0.994	1.05
0.5 mm	displ. load	1.0	0.854	**0.835**	0.863	0.916	0.973	1.03
size	stress load	1.0	0.857	**0.843**	0.894	0.970	1.05	1.13
1.0 mm	displ. load	1.0	0.852	**0.833**	0.875	0.944	1.02	1.09
size	stress load	1.0	0.856	**0.842**	0.895	0.974	1.06	1.14
1.5 mm	displ. load	1.0	0.850	**0.830**	0.872	0.943	1.02	1.10
size	stress load	1.0	0.854	**0.841**	0.894	0.973	1.06	1.15
2.0	displ. load	1.0	0.847	**0.826**	0.866	0.937	1.01	1.09

Table 1: Relative values of maximum energy density (for a circle, $\eta = 2$, the value is set to 1.0) . Corresponding values for stress are equal to the square−root of the shown values. Optimized values are shown in bold.

Influence from material power law non−linearity. In figure 3 is shown results based on analysis with material non−linearity. As expected from earlier results (Pedersen 2001) the optimal shape of the hole is rather insensitive to the power p $(p \leq 1)$ of the non−linearity. We still obtain almost uniform energy density (here von Mises stress) along the boundary of the hole. The isolines show equal levels of reduced stiffness, described by the factor $(\epsilon_e/\epsilon_0)^p$, where ϵ_e is effective strain and ϵ_0 is the corresponding value that gives the transition from linearity to non−linearity. The assumptions behind the calculations leading to the results in figure 3 correspond to deformation theory with a power law of $p = 0.1$. Relative values for these

results are for the squared maximum von Mises stress 1.0 , 0.98 , 1.11 and for the minimum stiffness reduction factors 0.305 , 0.336 , 0.280 .

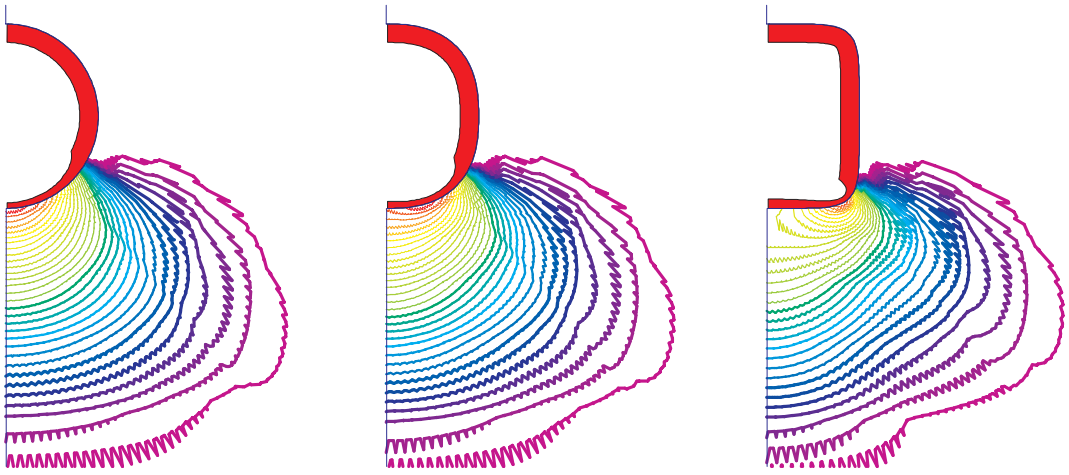

Figure 3: Isolines of stiffness reduction based on material non−linearity. The three designs correspond to $\eta = 2.0$, 2.5 and 6.0 as in figure 1.

Influence from material anisotropy. It is expected that anisotropic material behaviour will influence the optimal shape to a large extend, see Pedersen, Tobiesen and Jensen (1992). When the material is stiffer in the crack direction we see little influence on the optimal shape, but when it gets more flexible in the crack direction the influence is important. We have illustrated this in figure 4, where the ratio of the two moduli is set to $E_C/E_T = 0.25$.

The left most design is the optimized design of $\eta = 2.5$ from the isotropic case, which with only one design parameter (η) is improved to the middle design of $\eta = 4.0$. We note that an energy concentration will always appear for these pure superelliptic designs. With one modification function to the shape of the hole, as described in details in Pedersen *et al*. (1992), we obtain the right most design with almost uniform energy density along the hole boundary. Actual relative maximum values of energy density for the three cases are 1.0 , 0.98 , 0.78 and for maximum principal stresses the values are 1.0 , 0.91 , 0.89 . A study of the stress fields shown in figure 2 (see especially the red σ_1 curve), may give an understanding for the need of more advanced designs for these cases. From the results, the two parameter description seems sufficient.

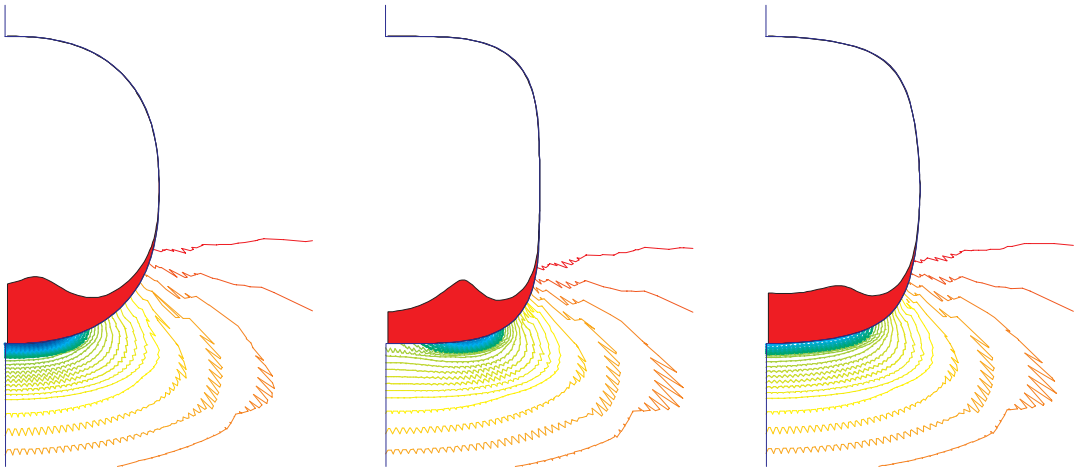

Figure 4: Levels of energy density for $E_C = 0.25E_T$ corresponding to superelliptic design with $\eta = 2.5$ to the left and $\eta = 4.0$ in the middle. The design to the right is a two parameter design with $\eta = 4.0$ and one modification function.

Influence from the domain of the hole. By including the elliptic halfaxes a , b as design parameters (the added condition of $a \cdot b$ = constant practically fixes the area of the hole), we may improve the optimal design results further. In figure 5 are shown the results corresponding to a/b = 1.0 , 0.9 , 0.8 , 0.7 , 0.6 , and 0.5 , illustrating the levels of squared von Mises stress. Note that in all cases we obtain almost uniform distribution along the highly stressed boundary. The resulting relative maximum values are 1.0 , 0.92 , 0.84 , 0.75 , 0.66 and 0.59 , and thus the superellipse has distinct advantages over the supercircle. The optimal superelliptic power η change with the ratio a/b and for the solutions shown, we got η = 2.5 , 2.4 , 2.3 , 2.15 , 2.10 , 1.95 , respectively.

The same six designs were analyzed based on a strong material non−linearity $(\sigma_e/\sigma_0)^{10}$ and again almost constant von Mises stress were obtained along the boundary, although now decreased with almost a factor of four. Relative to the results given for the linear solution, the values with the non−linear solution were 0.24 , 0.23 , 0.22 , 0.21 , 0.20 , 0.18 , respectively. The strong non−linearity levels out the difference, but still the possibility for smaller ratios a/b gives a better solution.

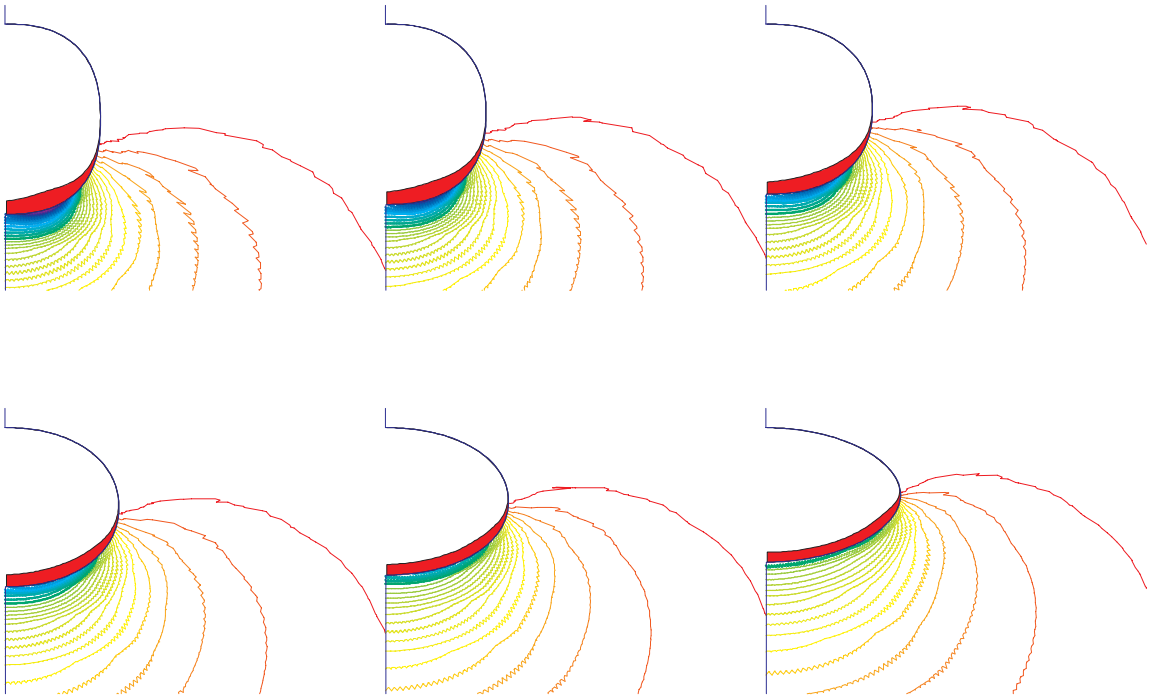

Figure 5: Levels of squared von Mises stress for optimized superelliptic power, when the ratio a/b of elliptic axes are prescribed to 1.0 , 0.9 , 0.8 / 0.7 , 0.6 , 0.5 , respectively.

Conclusion

With illustrative examples we have shown that the stress field, at the boundary of a drilled stress releasing hole, can be significantly improved. To a large extend the one parameter superelliptic shape is able to return a field of constant tangential stress along the boundary. This will diminish the possibility for further fatigue crack initiation.

References

Isida, M., Effect of width and length on stress intensity factors of internally cracked plates under various boundary conditions, *Int. J. of Fracture* **7**, 301–316, 1971.

Pedersen, P., On optimal shapes in materials and structures, *Struct. Multidisc. Optim.* **19**, 169–182, 2000.

Pedersen, P., On the influence of boundary conditions, Poisson's ratio and material non–linearity on the optimal shape, *Int. J. Solids Structures* **38**, 465–477, 2001.

Pedersen, P., Tobiesen, L. and Jensen, S.H., Shapes of orthotropic plates for minimum energy concentration, *Mech. Struct. Mach.* **20**(4), 499–514, 1992.

Shin, C.S., Wang, C.M. and Song, P.S., Fatigue damage repair: a comparison of some possible methods, *Int. J. Fatigue* **18**, 535–546, 1996.

Thomas, S.B., Mhaiskar, M.J. and Sethuraman, R., Stress intensity factors for circular hole and inclusion using finite element alternating method, *Theoretical and Applied Fracture Mechanics* **33**, 73–81, 2000.

ORAL/POSTER REFERENCE : ICF101017OR

OPTIMIZATION OF A DYNAMIC FRACTURE PROCESS WITH A 1D MODEL

H. Maigre and T. Carin

Laboratoire de Mécanique des Solides, UMR CNRS
Ecole Polytechnique, 91128 PALAISEAU CEDEX, FRANCE

ABSTRACT

This study presents a simplified model of a dynamic fracturation process. It is based on a 1-Dimensional mechanical model of a cracked structure under dynamic loading. Fracture parameters are the crack velocity and the energy release rate as in general but also the cohesion force which is the equivalent of the dynamic stress intensity factor in 2 dimensions. With these parameters we define two different criteria of propagation, the critical energy release rate and the critical cohesion force. Loading is generated by a striker of variable length, mechanical properties and initial velocity. Then optimization consists in finding the striker giving the maximum crack length for a given kinetic energy. The main results are that the striker should be of same mechanical impedance of the impacted bar and the optimal strike velocity depends on the criterion but should be high compared to the minimum required to initiate the propagation.

KEYWORDS

Crack Propagation, Dynamic Fracture

INTRODUCTION

Cracks in structures are always sources of failure and the aim of mechanics of fracture is to understand and generally prevent this kind of failure. In some particular case the objective is to make cracking easier. This will be the case in fracturing processes used in ballistic penetration, high speed machining or crushing of rocks. We can see that dynamic loading is preferred in these processes. In our present study we will try to find out the best loading condition to perform this fracturing. As dynamic fracture and dynamic crack propagation are very complicated subjects [1, 2] it is very difficult to perform a precise analysis of a dynamic fracturing process and it is even more difficult to perform its optimization. So we have decided to develop a 1-Dimensional model of dynamic fracture [3, 4] for which we can do exact optimization. With this model the relation between the applied loading and the mechanical state at the crack-tip is obtained analytically and the crack-tip location is a solution of a scalar differential equation depending only on the dynamic criteria of propagation. The optimization has been done using two kind of criteria.

1-DIMENSIONAL MODEL

Modelisation

We consider an elastic bar stuck on a rigid substratum with an initial debonding (the crack) of length a. The dynamic loading is generated by the impact of a second bar onto the first one as shown on Figure 1.

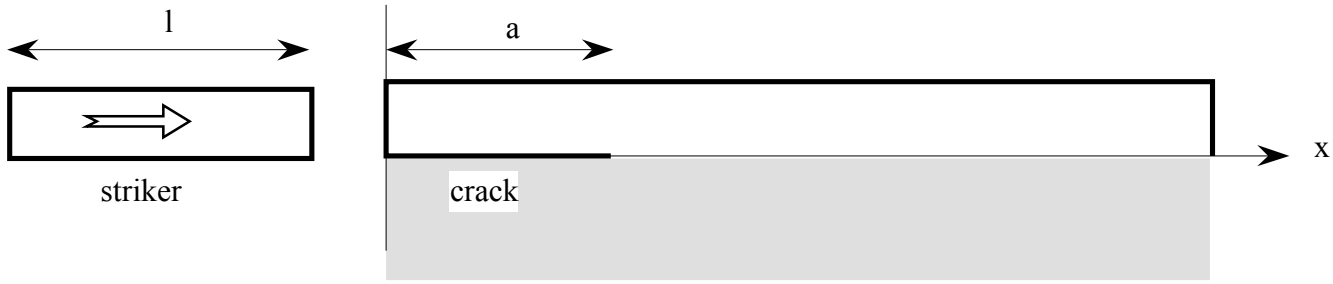

Figure 1: Dynamic fracture process model

We assume that the mechanical state is restricted to the longitudinal displacement u(x, t) and the normal force N(x, t) which are depending only on the abscissa x and time t. In this case the equations governing the problem are the elastic behaviour Eqn. 1. and the equation of motion Eqn. 2 :

$$N(x, t) = ES\, u_{,x}(x, t) \tag{1}$$
$$N_{,x}(x, t) = \rho S\, u_{,tt}(x, t) \tag{2}$$

where E, ρ, S are respectively the Young modulus, the density and the section of each bar.

Initial and boundary conditions

Before solving the problem we have to fix initial and boundary conditions. Initially we suppose the impacted bar at rest and time t = 0 the onset of the impact. So we have:

$$N(x, t) = 0 \quad ; \quad u(x, t) = 0 \quad \forall x > 0, \forall t < 0 \tag{3}$$

For the striker we assume a flying at uniform and constant velocity V :

$$N(x, t) = 0 \quad ; \quad v(x, t) = V \quad \forall x < 0, \forall t < 0 \tag{4}$$

where v(x, t) denotes the velocity field $u_{,t}(x, t)$.

For the boundary conditions, we prescribe a free boundary on the left side of the striker and a perfect unilateral contact between the striker and the bar:

$$N(-l, t) = 0 \quad ; \quad \begin{cases} N(0^-, t) = N(0^+, t) < 0 \quad ; \quad u_{,t}(0^-, t) = u_{,t}(0^+, t) \\ N(0^-, t) = N(0^+, t) = 0 \quad ; \quad u_{,t}(0^-, t) < u_{,t}(0^+, t) \end{cases} \tag{5}$$

Normally we should prescribe a boundary condition at the right end of the bar . In our case the impacted bar is free along the crack and totally fixed after the crack-tip:

$$u(x, t) = 0 \quad \forall x > a(t) \, , \forall t \tag{6}$$

This last boundary condition is then written like this:

$$u(a(t), t) = 0 \quad \forall t \tag{7}$$

A special attention have to be paid on this condition because this a moving condition with the crack propagation depending on the crack length which is also an unknown variable of the problem.

Criteria of propagation

The evolution of the crack length depends on the criterion of propagation chosen at the crack-tip. With this 1-D model there is no stress singularity and therefore no stress intensity factors to quantify the loading of the crack. To define this loading we calculate the energy release rate G(t) which is defined whatever the mechanical model of fracture is. In our case we finally obtained the following expression:

$$G(t) = \frac{1}{2ES} N^{-}(t)^2 \left(1 - \frac{\dot{a}^2}{c^2}\right) \tag{8}$$

Where $N^{-}(t) = N(a^{-}(t), t))$ is the normal force just before the crack-tip and $c = \sqrt{E/\rho}$ the celerity of the longitudinal elastic waves in the bar.

The normal force is not continuous at the moving crack-tip and the jump is obtained using the shock wave relation which leads to the definition of the normal force in front of the crack-tip:

$$N^{+}(t) = N(a^{+}(t), t) = N^{-}(t) \left(1 - \frac{\dot{a}^2}{c^2}\right) \tag{9}$$

Putting this result in the definition of G we obtain :

$$G(t) = \frac{1}{2ES} N^{-}(t)\, N^{+}(t) \tag{10}$$

This expression is very similar to the expression given in the 2-dimensional model with two stress intensity factors, the dynamic stress intensity factor and the kinematic intensity factor [5].

So in our model a criterion of propagation will appear as a function of these four quantities (G, N^{-}, N^{+}, $\dot{a}$) in which only two of them are actually independent.

OPTIMIZATION PROCEDURE

Equation of propagation

The general solution of Eqn. 1. and Eqn. 2. is a combination of two unknown scalar functions f and g for the striker and the impacted bar:

$$u(x, t) = f(t - x/c) + g(t + x/c) \tag{11}$$

Putting this expression in the initial and the boundary conditions we find a explicit relation between the loading and the criterion of propagation. This relation gives a non linear differential equation of the first order on a(t) [6]. To solve this equation we have to define the criterion of propagation. Generally one chooses the critical energy release rate criterion G_C:

$$\dot{a} \geq 0 \; ; \; G = G_C \quad \text{or} \quad \dot{a} = 0 \; ; \; G < G_C \tag{12}$$

Another choice is the critical normal force criterion N_C:

$$\dot{a} \geq 0 \; ; \; |N^+| = N_C \quad \text{or} \quad \dot{a} = 0 \; ; \; |N^+| < G_C \tag{13}$$

With this criterion we assume that the failure occurs when the cohesive force N^+ acting at the right side of the crack-tip reach the limit N_C. For identical toughness in quasi-static, fast crack propagation needs higher level of loading compared with the energy release rate criterion.
In the case of our impact and for both of the previous criteria the coefficients of the differential equation are stepwise functions of time and the crack propagates by step at constant velocity.

Case of striker and impacted bar made of identical material

We present here the results for a striker and a bar of same section S and made of the same material. To simplify we take E, S and ρ equal to unity.
Whatever the length of the striker the evolutions of the system are as follow:

1 - A compressive wave propagates backward in the striker and forward in the bar.
2 - The last wave reflects at the crack-tip making the crack propagates.
3 - The reflection of the first wave at the free end of the striker wave arrives to the crack-tip and stops the propagation.
4 - The striker goes back at uniform velocity and looses contact with the bar in which remain elastic waves with no more propagation.

The main results are reported in Table 1.

TABLE 1
RESULTS OF FRACTURATION BY IMPACT

Criterion	Energy release rate	Cohesion force
Loading parameter	$\beta = \frac{\sqrt{2\,G_C}}{V}$	$\gamma = \frac{N_C}{V}$
Condition for propagation	$\beta < 1$	$\gamma < 1$
Crack velocity $\dot{a}$	$\frac{1-\beta^2}{1+\beta^2}$	$1-\gamma$
Total length of propagation Δa	$\frac{1-\beta^2}{\beta^2} l$	$2\frac{1-\gamma}{\gamma} l$
Dissipated energy	$l\,V^2 \frac{1-\beta^2}{2}$	$l\,V^2 \frac{1-\gamma}{2-\gamma}$

In the optimization procedure we fix the initial kinetic energy W of the striker and we calculate the maximum length of fracture by changing the length and the velocity of the striker. The results are reported in Table 2.

As we can see the optimal solution depends strongly on the criterion. With the energy release rate criterion we can transform all the kinetic energy in fracture if the striker is short and thrown at a velocity must higher than the minimum required to initiate fracture. With the critical cohesion force criterion the impact velocity should be the double of the minimum required and at the most the half of the kinetic energy is used for fracturation.

TABLE 2
OPTIMAL FRACTURATION

Criterion	Energy release rate	Cohesion force
Initial impact energy W	$\frac{l V^2}{2} = \frac{l G_C}{\beta^2}$	$\frac{l V^2}{2} = \frac{l N_C^2}{2 \gamma^2}$
Total length of propagation Δa	$(1 - \beta^2) \frac{W}{G_C}$	$4 \gamma (1 - \gamma) \frac{W}{N_C^2}$
Optimal loading parameter	$\beta = 0$	$\gamma = 1/2$
Maximum length of propagation Δa	$\frac{W}{G_C}$	$\frac{W}{N_C^2}$
Maximum dissipated energy	W	W/2

Case of striker and impacted bar made of different material

Here the properties of the impacted bar are kept equal to unity and those of the striker will be defined by the two following parameters, the mechanical impedance z and the elastic celerity of wave c:

$$ES = z\,c \quad \text{and} \quad \rho S = z/c \tag{14}$$

If the striker is lighter than the bar ($z < 1$) there will be just one impact. At the opposite for heavier striker ($z > 1$) there be several impacts and several fracturation stages. Main results are shown in Table 3.

TABLE 3
OPTIMAL FRACTURATION ACCORDING TO IMPENDANCE OF THE STRIKER

Criterion	Energy release rate	Cohesion force
Impedance parameter	$k = \frac{z - 1}{z + 1}$	$k = \frac{z - 1}{z + 1}$
Loading parameter	$\beta = \frac{\sqrt{2\, G_C}}{V\,(1 + k)}$	$\gamma = \frac{N_C}{V\,(1 + k)}$
Total length of propagation Δa if one step advance	$(1 - \beta^2)(1 - k^2) \frac{W}{G_C}$	$4 \gamma (1 - \gamma)(1 - k^2) \frac{W}{N_C^2}$
Total length of propagation Δa if two steps advance	$(1 + k^2 - 2\beta^2)(1 - k^2) \frac{W}{G_C}$	$4 \gamma (1 + k - 2\gamma)(1 - k^2) \frac{W}{N_C^2}$
Optimal parameters	$\beta = 0$; $k = 0$	$\gamma = 1/2$; $k = 0$

Changing the constitutive material of the striker is not efficient to increase the fracturation and the best way to proceed is to take a striker of same impedance of the bar whatever the criterion.

CONCLUSIONS

We have presented a simplified model of dynamic fracturation. This 1-Dimensionnal model is rich enough to reproduce dynamic phenomena coupled with fracture mechanics but still simple to perform all calculation analytically. It has been used to find the optimal conditions of fracturation that is the maximum crack propagation for a fixed loading energy. In our study the loading was the kinetics energy of a striker and the optimization has been done for two criteria of propagation, the energy release rate criterion and the cohesion force criterion.
This model can not treat precisely real problems because it does not include three dimensional effects like stress singularities at the crack-tip. Moreover we have also simplified loading condition but the general conclusions about the nature of the striker and the influence of the criterion should apply to real problems. We can also do the optimization with more realistic criteria taking into account for example the thermo-mechanical coupling [7, 8], different crack criteria for initiation, propagation and arrest, ...

REFERENCES

1. Freund, L.B. (1990). *Dynamic Fracture Mechanics*. Cambridge University Press, Cambridge.
2. Rosakis A. J. and Ravichandran G. (2000)., *Int. J. Solids Structures* 37, 331.
3. Kanninen M. F. (1974). *Int. J. Fract.* 10, 415.
4 Mannion L. (1987). *Quat. Appl. Math.* XLV, 713.
5 Achenbach J. D. and Bazant Z. P. (1975). *J. Appl. Mech.* 42, 183.
6 Carin, T. (2000).Thèse de Doctorat, ENPC, France.
7. Bui H. D., Ehrlacher A. and Nguyen Q. S. (1980). *J. Méca.* 19, 697.
8 Rittel D. (1998) *Int. J. Solids Structures* 35, 2959.

ICF100196PR

ON ESTABLISHING FACTOR SIGNIFICANCE ON THE DELAMINATION FRACTURE TOUGHNESS OF A COMPOSITE LAMINATE

Assimina Pelegri[1] and Anand Tekkam[2]

[1,2] Department of Mechanical and Aerospace Engineering
Rutgers, The State University of New Jersey
Piscataway, NJ 08854-8058, USA

ABSTRACT

Interlaminar fracture is a dominant mode of failure in advanced composite materials. The resistance to delamination is quantified using Critical Delamination Fracture Toughness, G_c. Here, a methodology is developed using Designed Experiments and Taguchi concepts to analyze the contribution of various factors such as delamination length, stacking sequence, etc. and their first order interactions to the pure mode I delamination fracture toughness of a composite laminate. All the factors are considered at two levels and a Fractional Factorial experiment is conducted. F tests help in culling the appropriate factors. Both balanced and symmetric specimens are used with a [0/90] ply setup. A study of the effects of main factors and means of the interactions was done to establish the combination of factors that would yield the highest fracture toughness within a given set of constraints of the factors. An idea of significant factors and contributions is then used to obtain a response surface equation that is used to predict the interlaminar fracture toughness.

KEYWORDS

Laminates, Fracture Toughness, Optimization, Taguchi, Design of Experiments, Response Surface

INTRODUCTION

Composite laminates have high stiffness to weight and strength to weight ratios compared to conventional materials. Hence, they are a favorite choice for many applications ranging from sports to aerospace. As such, it has become essential to test the reliability of laminated composites under different conditions, and manufacture them for high strength and fracture toughness. Delamination is one major mode of failure of composites and it may be assumed that a variety of factors affect the delamination fracture toughness of composite structures. Though many papers [1,2] have been published to optimize G_c based on one single

factor, such as stacking angle using genetic algorithms, not one discusses the effect of the interactions of various factors, neither presents a technique to optimize G_{Ic} based on all factors.

In general, a delamination can occur in three modes, namely opening (mode I), shearing (mode II) and out-of-plane (mode III). The interlaminar fracture toughness is expressed in terms of strain energy release rate of mode I (G_I), mode II, and mode III (G_{III}). Of the three release rates, G_I is often the most critical, and hence a laminate fails by mode I delamination more often than the other two. Therefore, it becomes essential to optimize the mode I critical fracture toughness, G_{Ic}, for given set of constraints. This is achieved through use of statistical methods like Design of Experiments, Taguchi Arrays, and Response Surface Methodologies.

A variety of factors, all at two levels, will be assumed to be contributing to G_{Ic}. ASTM [3] standards for mode I interlaminar fracture toughness was followed. Since a factorial experiment would result in a huge number of runs, fractional factorial experimental concepts and Taguchi orthogonal arrays would be used in reducing the number of test runs. Highest order of interaction is used as the defining contrast. Two replications of the experiment will be conducted to gather more data and reduce error. Normality tests are performed on the data to assess the assumptions of normality. Yates [4] algorithm is then used to obtain the sum of squares. F tests on the sum of squares help in establishing the significant factors. Sum of squares will also be used to establish the percentage contribution of each factor and their first order interactions.

STATISTICAL METHODOLOGIES FOR OPTIMIZATION

The objective of the methodology developed here is to establish the factors that affect the delamination fracture toughness. In the simple beam theory analysis, the specimen can be assumed to consist of two identical cantilever beams with a built in end and split arm length equal to the length of the crack, that is the delamination length. According to beam theory, the energy release rate for a Double Cantilever Beam (DCB) test of a cross ply laminate is given by:

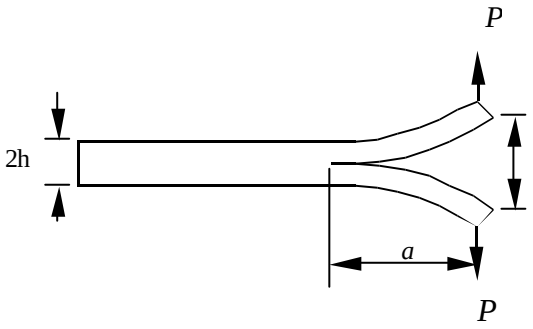

Figure 1: Double Cantilever Beam Analysis on Composite Laminate

$$G_I = \frac{12P^2}{b^2h^3E_{11}}\left[a^2 + \frac{2a}{l} + \frac{1}{l^2} + \frac{h^2E_{11}}{10G_{13}}\right] \text{ where } l = \frac{1}{h}\sqrt[4]{\frac{6E_{22}}{E_{11}}} \tag{1}$$

In the aforementioned mode I energy release rate, G_I, for quasi-static loading expression, the effect of shear deformation has been included.

Since composite laminates can be tailored to achieve required properties through different designs, one cannot take help of equation such as (1) to readily obtain the optimum combination of factors that can be used to tailor a high G_I composite laminate within the imposed constraints on all the factors.

To this extent, the following factors will be assumed to affect the fracture toughness: 1.Type of Loading, 2.Width of the specimen, 3.Length of the Specimen, 4.Thickness of the Specimen, 5.Lay up configuration, 6.Delamination length, 7.Material, 8.Ply thickness, 9.Thickness of Substrate, 10. Stacking Sequence.

Assuming each factor to be at two levels, one would need 2^{10} = 1024 experimental runs to study the effects of all the factors. Such huge number of runs is not practical and economical in laboratory conditions. Factors such as ply thickness, type of loading, material, thickness of substrate and lay up will be assumed to be constant while developing the model.

Model Equation

The model equation for the designed experiment would be assumed to be of the form,

$$Y_{ijklmn} = \text{Main Factors} + \text{Interactions} + \text{Error} (\ _n) \quad (2)$$

where subscripts i, j, k, l, m and n denote the subscript of the five factors and error. The levels of each of the five factors are given in the table below. ASTM [3] standards for testing were used.

TABLE 1
VALUES OF THE FACTORS AT TWO LEVELS

Factor	Low Level -1	High Level 1
Width (A)	0.5 inches	0.8 inches
Length (B)	6.0 inches	8.0 inches
Thickness of specimen (C)	0.14 inches	0.18 inches
Delamination length (D)	2.4 inches	2.6 inches
Stacking Sequence (E)	Balanced	Symmetric

Using Taguchi's [5] linear graph for orthogonal array L_{16}, a 2^{5-1} fractional factorial experiment will be run with 16 runs. Two replications will be used to increase accuracy. The treatment condition for the 16 runs is tabulated below in Table 2.

TABLE 2
TREATMENT CONDITIONS FOR THE EXPERIMENT USING L_{16}

		Specimen Number															
		1	2	3	4	5	6	7	8	9	10	11	12	13	14	15	16
Level of each factor	A	-1	-1	-1	-1	-1	-1	-1	-1	1	1	1	1	1	1	1	1
	B	-1	-1	-1	-1	1	1	1	1	-1	-1	-1	-1	1	1	1	1
	C	-1	-1	1	1	-1	-1	1	1	-1	-1	1	1	1	-1	1	1
	D	-1	1	-1	1	-1	1	-1	1	-1	-1	-1	1	-1	1	-1	1
	E	-1	1	1	-1	1	-1	-1	1	1	-1	-1	1	-1	1	1	-1

Data to test the Methodology

Random data was generated using the data obtained in previous experiments to test the methodology. Two replications would be done to increase the accuracy.

TABLE 2
TEST DATA FOR THE METHODOLOGY

Specimen Number	Replication I G_{Ic} in N/m	Replication II G_{Ic} in N/m
1	304.44	303.16
2	296.87	299.75
3	306.88	308.73
4	316.82	312.70
5	301.01	300.94
6	311.81	310.74
7	299.88	298.98
8	309.82	312.29
9	309.56	307.45
10	301.54	303.42
11	307.63	306.29
12	299.56	300.42
13	312.87	311.67
14	272.31	276.45
15	300.84	298.90
16	278.24	272.23

Normality Tests

The Analysis of variance technique that is used assumes the data to be from random samples, equal variances and normality. Therefore,it is essential to check the normality of the data. A Normal Probability plot, Figure 2, will be used to test the data for any outliers. A linear normal probability plot indicates that data is normal. The figure below shows a normal probability plot of the random data in table 2.

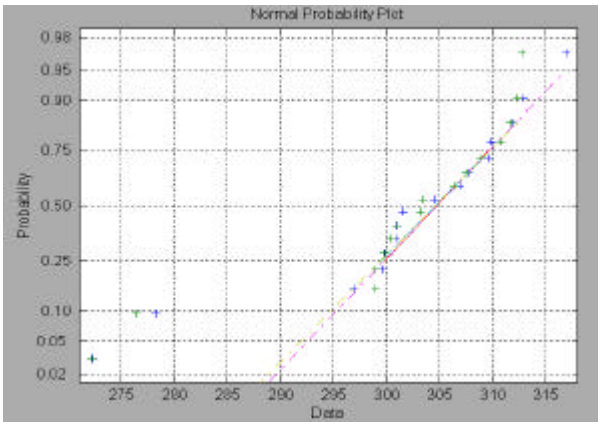

Figure 2: Normal probability of Test Data

Analysis of Variance

A two-way analysis of variance on the test data is shown in Table 3. The sum of squares of the treatment combinations were obtained using Yates [4] algorithm for fractional factorial experiments. Treatment combinations that has significantly smaller sum of squares compared to the other treatment combinations are pooled into the error sum of squares, thus increasing the degrees of freedom of error to approximately half of the total degrees of freedom. This increases the reliability of the results.

TABLE 3
ANALYSIS OF VARIANCE

Contrast	D.O.F	SS	MS	F	P
A	1	394.1028125	394.1028125	5.06	0.05104958
C	1	399.03125	399.03125	5.13	0.04977224
D	1	528.125	528.125	6.79	0.02846789
AD	1	1309.440313	1309.440313	16.84	0.00266212
CD	1	332.1753125	332.1753125	4.27	0.06876407
BE	1	535.4628125	535.4628125	6.88	0.02767558
Error	9	699.7838	77.75		

REPORT OF STATISTICAL ANALYSIS

It can be concluded based on the fictitious test data that factors A: Width, C: Thickness of Specimen, D: Delamination Length, and first order interactions AD: between width and delamination length, CD: between thickness of specimen and delamination length, and BE: between length and stacking sequence appear significantly contributing to the interlaminar fracture toughness. A study of two-way means on the interactions using reverse Yates [4] algorithm is done to further explore the interaction effects. The results of the two-way means are tabulated in Table 4 and 5.

TABLE 4
MEAN MODE I FRACTURE TOUGHNESS AT TWO LEVELS OF WIDTH, THICKNESS AND DELAMINATION LENGTHS.

Width	Delamination Length	
	Low	High
Low	302.43 N/m	307.72 N/m
High	308.83 N/m	287.91 N/m
Thickness of specimen	Low	High
Low	306.25 N/m	304.57 N/m
High	305.63 N/m	291.06 N/m

TABLE 5
MEAN MODE I FRACTURE TOUGHNESS AT TWO LEVELS OF LENGTH AND STACKING SEQUENCE

Length of specimen	Stacking Sequence	
	Balanced	Symmetric
Low	294.93 N/m	307.66 N/m
High	304.27 N/m	300.65 N/m

CONCLUSIONS

Based on the two-way means analysis on test data shown in tables 4 and 5, one can easily observe the combination of factors that can be used to tailor a composite laminate that would yield higher interlaminar fracture toughness G_{Ic} . Experiments can be performed to obtain real test data and the above methodology can be used to analyze the significant factors and interactions. A response surface equation (3) based on the significant factors and interactions can be obtained using techniques of Response Surface Methodologies. If the response equation has a discrete factor such as stacking sequence, two response equations can be derived for each level of the discrete factor as shown in equation (3). Here subscripts –1,1 indicate two levels of the discrete factor.

$$Y_{1,-1} = {}_0 + {}_1 A + {}_2 C + {}_{12} A C + \quad (3)$$

Equation (3) can also be used to predict the interlaminar fracture toughness G_{Ic} for a given set of values of the factors. Since each of the response equation consists only of continuous factors, optimization techniques based on gradient methods can be used to obtain the maximum fracture toughness within the constraints imposed. This reduces the amount of computational effort required tremendously, since discrete optimization techniques such as genetic algorithms need not be used.

ACKNOWLEDGMENTS

The authors would like to gratefully acknowledge the financial support of the National Science Foundation, Civil and Mechanical Systems Division, NSF Career Grant 99-82023. The authors are thankful to the grant monitor Dr. Jorn Larsen-Basse for his interest and encouragement.

REFERENCES

1. Todoroki, Akira and Haftka, Raphael T. (1998) *Composites Part B*, 29B, pp. 277-285.
2. Bruyneel, M., Vermaut, O., and Fleury, C., LTAS-Aerospace Laboratory, University of Liege, Belgium.
3. Standard Test Method for Mode I Interlaminar Fracture Toughness of Unidirectional Fiber-Reinforced Polymer Matrix Composites, (1994) *Annual Book of ASTM Standards*, D 5528, Vol. 14.02
4. Yates, F., (1937), Design and Analysis of Factorial Experiments, London: Imperial Bureau of Soil Sciences.
5. Ranjit Roy, (1990) A Primer on the Taguchi Concepts, Van Nostrand Reinhold Publications.

OPTIMIZING CEMENT-BASED COATINGS WITH RESPECT TO SHRINKAGE CRACK FORMATION

G. Martinola

Laboratory for Building Materials, Swiss Federal Institute of Technology Zürich, Switzerland,
ETHZ CH-8093 Zürich

ABSTRACT

Cement based layers are frequently used for the repair of reinforced concrete structures nowadays. They may restore the protection of the reinforcement, after contamination and removal, against the penetration of aggressive substances. In this way the service life of the repaired structure can be improved. To provide protection and to prevent the transport of harmful substances inside the reinforced concrete structure these layers have to be free from cracks during the planned service life. Under usual conditions such layers are submitted to different actions like thermal, hygral and autogenous shrinkage or swelling. These processes create a complex state of eigenstresses inside the system layer-substrate. The tensile stresses can lead to the formation of cracks and delamination of the protective layer after several years. This paper suggests an approach for the optimization of repair systems. For this purpose a modern tool i.e. numerical model is used in order to determine the time dependent stress distribution and the crack formation due to different loads and boundary conditions. On this basis the requirements for a layer can be formulated ad hoc as a function of the probabilistic properties of each damaged building and the risk of failure can be minimized.

KEYWORDS

cement-based layer, repair system, protective coating, shrinkage, crack formation, fracture mechanics, delamination, durability, numerical model, optimization

1. INTRODUCTION

In a traditional reinforced concrete element concrete has to take over two totally different assignments [1]. First, concrete has to provide a structural element with the required strength and stiffness and it has to anchor the steel reinforcement. At the same time, the concrete cover has to prevent corrosion of the steel reinforcement. Whether this second non-mechanical assignment is really fulfilled is rarely checked. As a consequence and because of bad execution, many concrete structures have to be repaired after a relatively short service life. This is the reason for the increased of expenditures for maintenance and repair of buildings and structures.
In many cases, carbonation depth reaches the reinforcement and/or the chloride content in the neighborhood of the steel reinforcement reaches critical values too rapidly. In order to restore the initial state the contaminated covercrete is removed. The reinforcement is freed from corrosion products and finally the concrete surface is restored with a new layer. In order to assure mechanical reliability and a long-term durability of the repaired concrete structure, both the mechanical and non-mechanical assignments must be fulfilled. It is also possible to apply cement based protective coatings in order to protect new reinforced concrete structures. In this case the structural concrete assures the load bearing capacity and the coating takes over the protection of the rein-

forcement. To offer protection and to prevent the transport of harmful substances into the reinforced concrete structure these layers have to be free from cracks during the planned service life and show low permeability and low capillary suction.
Mistakes in design, selection of materials and execution lead to crack formation with a drastic reduction of the durability of the repaired structures. One basic problem is that engineers so far have no quantitative tools to evaluate if a proposed repair design is appropriate for a given situation.
The use of durable repair materials does not ensure the durability of the system substrate (old concrete) / overlay (repair material), because the effectiveness of a repair measure is also related to the dimensional compatibility between overlay and substrate.
Overlay and substrate are subjected to different external and/or internal loads. Under usual conditions such systems are submitted to different actions like thermal and hygral gradients and autogenous shrinkage or swelling. If the resulting deformations of both components are different restraining action will give rise of stresses and eigenstresses inside the system layer-substrate. Failure of the repair system will occur when the stresses due to restraint or the imposed deformations can not be absorbed by the system. In this case crack formation will appear. The capacity of the materials of the system to absorb restraining actions is contained in its elastic deformation, creep deformation and strain softening. The complex competition between loads and the material is illustrated in Fig. 1.

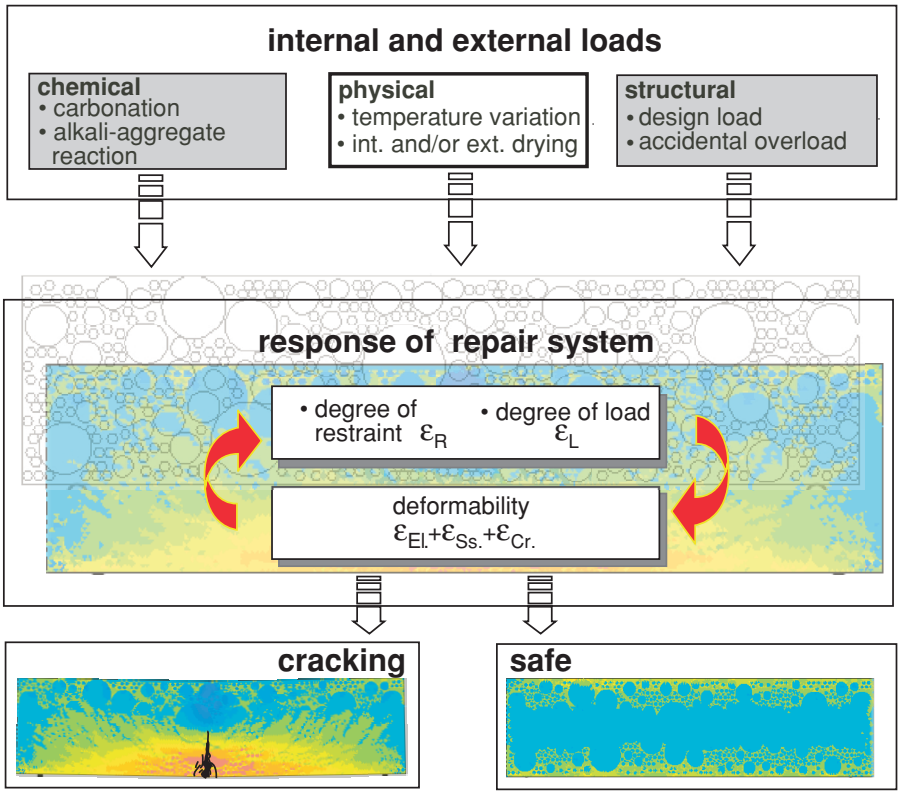

Figure 1: Analysis of the principal loads acting in a repair system and failure criteria. ε_{El}, $\varepsilon_{Ss.}$. and $\varepsilon_{Cr.}$ are the elastic, crack (strain softening) and creep strains respectively

A linear elastic stress analysis shows in Martinola [2] that, the most important factor influencing the state of restraint of the system is the hygral load and thermal load or a combination thereof. During drying or a rapid cooling tensile stresses until 20-25 MPa are induced in the system. Under these conditions practically every cement based material will be damaged. Usual structural loads can provoke failure of the system only in combination with physical loads. The chemical load can be avoided by the correct choice of the mix components of the overlay material and a detailed analysis of the environmental conditions.
A rigorous analysis based on the knowledge of material science (realistic constitutive laws) is an essential step in order to assess this problem. The effectiveness and the durability of concrete repair depend also of the environmental and mechanical boundary conditions. Such rigorous analysis can be carried out only with modern tools like FEM or BEM that are able to solve systems of non-linear differential equation.
The behavior of repair systems is investigated in this work with the Finite Element Method. A validated nu-

merical model [3] that allows us to calculate crack formation and crack propagation in such systems under different kind of solicitations (mechanical, thermal and hygral load) is applied for a parametric study. The results of the sensitivity analysis are used to formulate criteria for crack prevention in such layers. This criteria can be used for the optimization of the properties of the layer and in this way provide solutions for the design of repair of concrete structures.

2. EXAMPLE FOR A DAMAGE MECHANISM: RESTRAINED CEMENT BASED COATINGS

A typical concrete repair system consisting of a superposition of an old concrete element and a new concrete or mortar repair layer is shown in Fig. 2. Initially, the new material layer is in a quasi saturated state. Generally

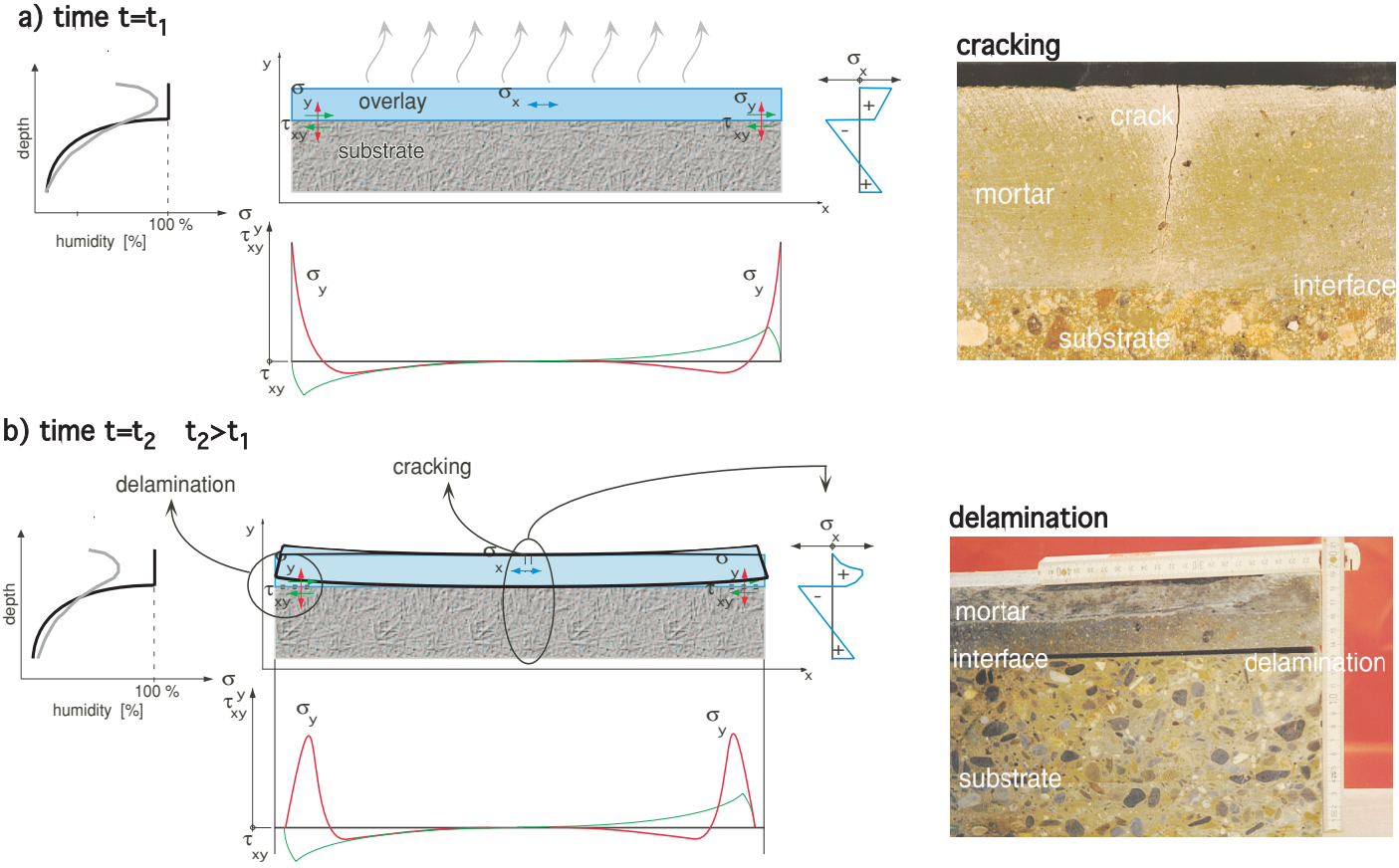

Figure 2: a) Schematic representation of a drying repair system and moisture distributions at different drying times b) Hygral-induced cracking and delamination and stress distributions

the upper surface of the composite system is in contact with the environment. If the surrounding relative humidity is low, compared with the pore humidity of the material of the new layer, the system begins immediately to dry. Cracks can occur in the upper layer due to the hygral gradients generated during the drying process. Simultaneously, the entire new layer is subjected to a global volume change. Depending on the composition of the cement-based material used for the repair layer, the volume variation can be much larger at an early stage if the material is subjected to endogeneous drying. This volume variation is generally restrained by the old concrete element. It must be underlined, that the degree of restraint depends not only on the compatibility of the hygro-mechanical parameters of both materials but also on the actual moisture gradient between the two materials and on the thickness of the new layer. As a consequence of the restraint, normal tensile stresses σ_y and bond shear stresses τ_{xy} will be induced in the interfacial zone. Fig. 2b shows schematically the state of the stresses and the possible damage, i.e. cracking of the overlay and decohesion of the interface. If the stresses are higher than the bond cohesion, then delamination will occur (see for example photo in Fig. 2b).

3. CRITERIA FOR MINIMIZING THE RISK OF SHRINKAGE CRACKING

Based on the reasonable agreement between the observed results obtained from different experiments performed on different materials and the numerical results, the proposed model has been used to carry out a parametric study [2]. The objective of this study is to identify the most relevant material parameters influencing shrinkage cracking and consequently to be able to decide which material parameter(s) must be optimized in order to reduce the risk of surface cracking as far as possible.
The results of this sensitivity analysis [2] showed that the shrinkage coefficient, the fracture energy and the Young‘s modulus are the most important parameters influencing cracking. It is of interest that tensile strength plays a minor role in the damage process.
By compiling the obtained numerical results, a diagram that shows the risk of crack formation as function of the above mentioned material parameters can be plotted as shown in Fig. 3a. In this figure, the z axis represents

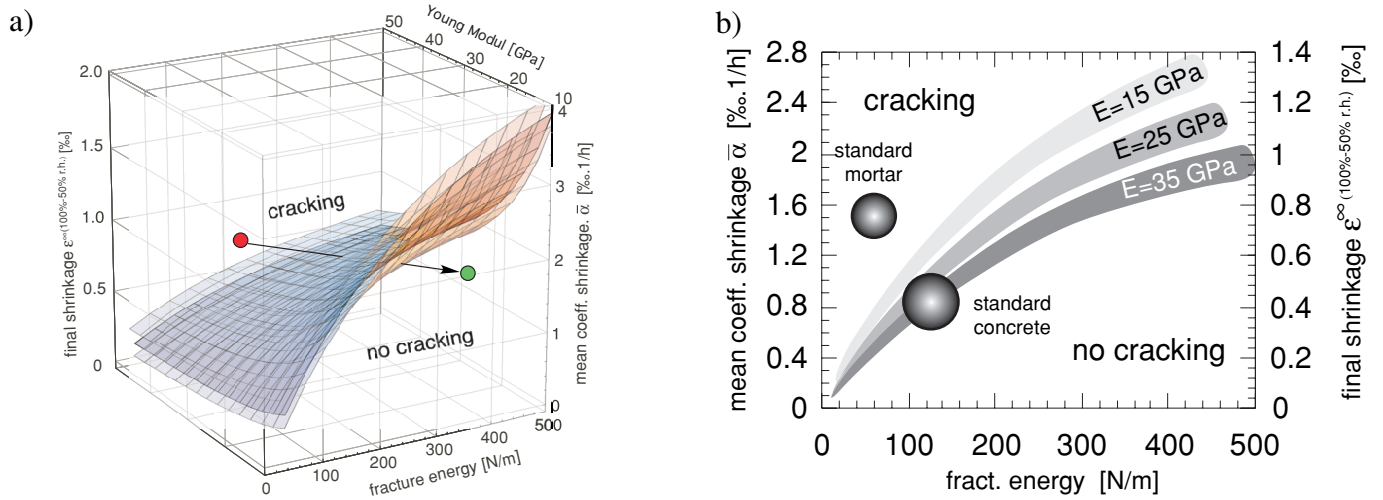

Figure 3: a) Surface separating conditions for cracking and no cracking of the repair layer as function of fracture energy, coeff. of shrinkage and Young´s modulus b) 2D representation of the risk of crack formation as function of fracture energy, coeff. of shrinkage and Young‘s modulus

the mean value of the coefficient of shrinkage $\bar{\alpha}$. In many standard codes the shrinkage is defined by the strain measured on a specimen during drying from 100% to 65% or 50% R.H. According to the presented theory a corresponding value can be approximated by the following expression:

$$\varepsilon_{meas}(100\%\text{–}65\%\ (50\%)) \cong \varepsilon(t \to \infty) = \bar{\alpha} \cdot (h_2 - h_1) \tag{1}$$

with $\varepsilon\ (t \to \infty)$ being the final shrinkage strain measured when the test specimen, initially at 100% RH, reaches a hygral equilibrium with 50% RH. If the combination of material parameters of a given mortar are localized above the surfaces shows on Fig 3a they will crack during the drying process. Fig. 3b) shows a 2D contour plot of the plane fracture energy versus shrinkage obtained from Fig. 3a). In order to introduce a safety factor for the interpretation and the utilization of the diagram which covers the variation of the results, a transitional area between the cracking and the crack free zone is defined.

4. USE OF THE PROPOSED CRITERIA FOR THE OPTIMIZATION OF A CEMENT BASED COATING

Using this 2D representation a minimization of the risk of shrinkage cracking of a particular cement-based material can be achieved. For instance a mortar A exposed to an external relative humidity of 65%, with a Young´s modulus of E=40 GPa, a fracture energy G_f=105 N/m and a final shrinkage strain of 1 ‰ (see point „mortar A“ in Fig. 4a) will crack during the drying period, in the case of restrained mechanical boundary conditions. In order to avoid crack formation the properties of this mortar have to be changed. The mortar A has to be modified and moved from the critical zone (cracking) to the safe zone (no cracking). All combinations of the ma-

terial parameters, that will lead to a shift of mortar A into the safe zone, are possible of course. For instance the mortar A may be modified by reducing the cement content and reducing the Young´s modulus to 14 GPa. In this way the shrinkage strain is reduced to 0.8 ‰ (see point „mortar B“ in Fig. 4a). A second possibility of optimization can be carried out by the addition of steel fibers. The mechanical behaviour of the mortar is completely changed. The fracture energy is increased to more then 500 N/m (see point „mortar C“ in Fig. 4a).

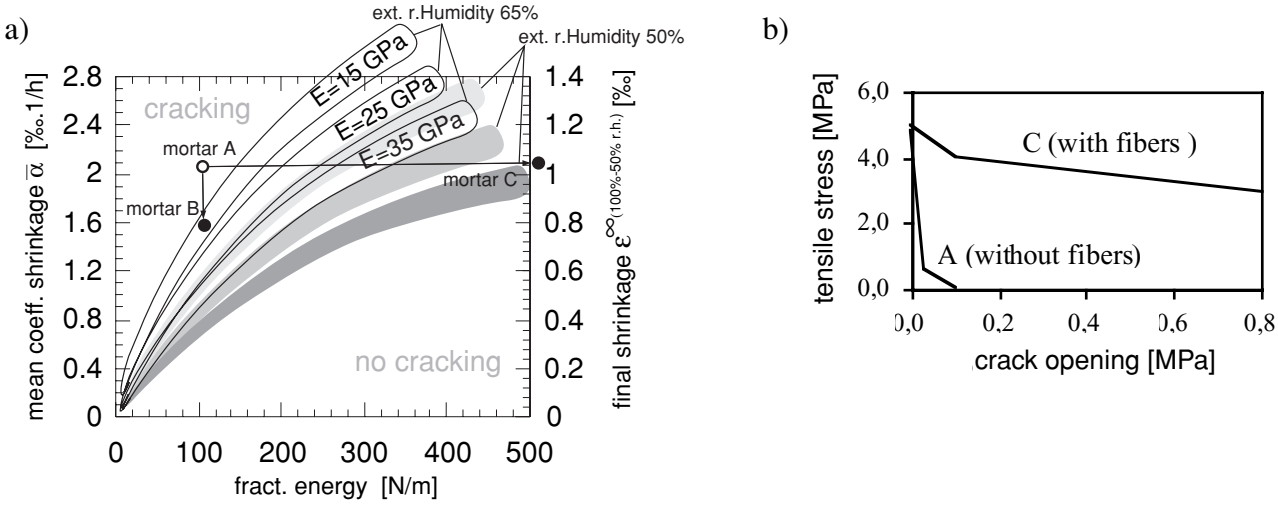

Figure 4: a)2D representation of the risk of crack formation for two different boundary conditions (ext. R.H of 50 and 65%) b) Mechanical behaviour of the mortar A and mortar C

In order to demonstrate the influence of the different combinations of material parameters with respect to crack formation under hygral variation, the numerical model is used to analyze these 3 different mortars when applied on the same substrate. The other relevant materials parameters of the repair mortars and of the old concrete which are needed in the numerical model have been held constant for the three analyses. In Fig. 5 results

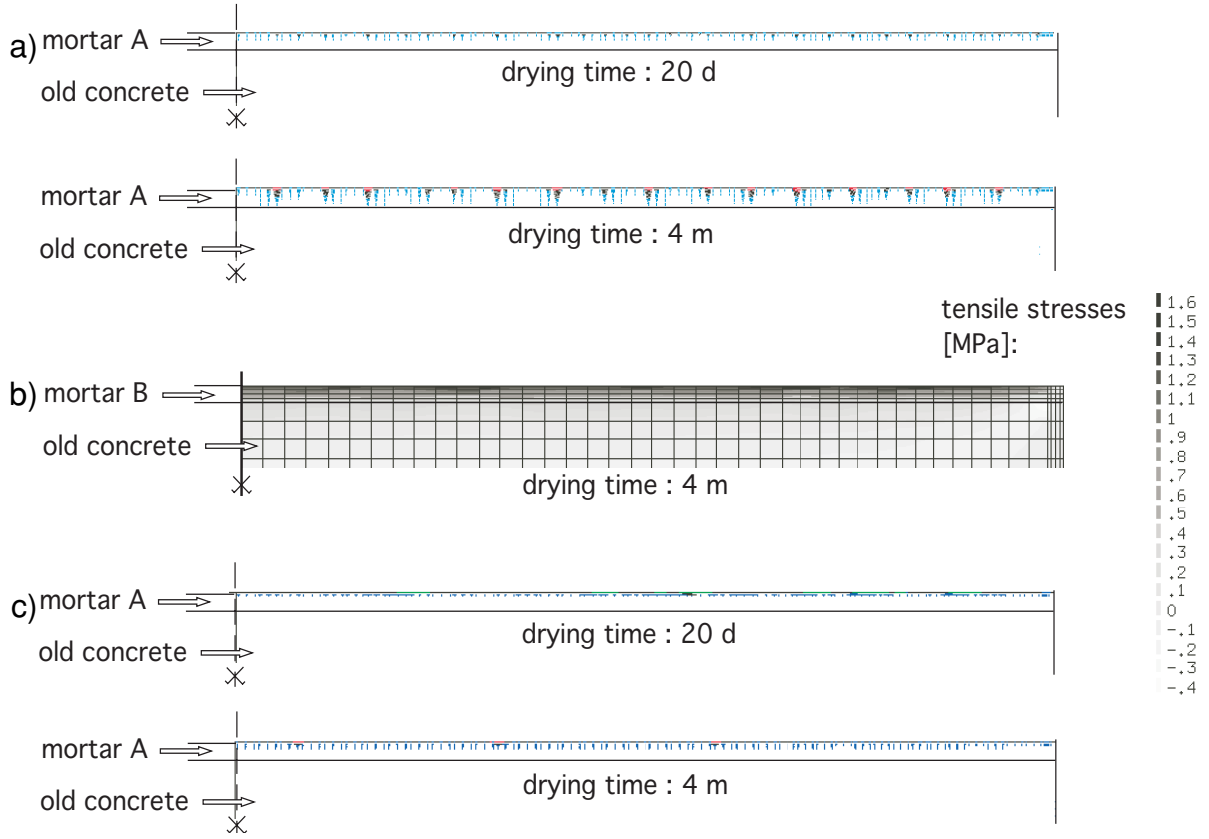

Figure 5: a) crack distribution for the repair system with the mortar A after 20 days and 4 months drying
b) stress distribution in the system with the mortar B after 4 months drying
c) crack distribution for the third repair system (mortar C) after 20 days and 4 months drying

are presented the of the hygro-mechanical analysis of the 3 repair systems are presented. As assumed the mortar A cracks under the imposed hygral load. After 20 days of drying many fracture process zones (FPZ) are activated near the surface of the mortar. As the drying proceeds, a limited number of FPZ becomes wider and wider and moves gradually towards the old concrete. Other process zones close due to stress redistribution. After an advanced drying time of 4 months, real cracks are developed in the outer layer of the overlay (see Fig 5a).
Fig. 5b shows the stress distributions in the global system (mortar B) after 4 months of drying. In this case, during the performed analysis, tensile stresses were always lower than the tensile strength. This means mortar B remains cracks free.
In the third analysis (mortar C) a lot of fracture process zones have been developed after a drying time of 20 days (see Fig. 5c) in the same way as in the case of mortar A, due to restrained shrinkage deformations. But after 4 months drying the situation is different as compared with mortar A. Due to the fact that steel fibers lead to a better distribution of the FPZ, most of those which have already been formed after 20 days of drying increased in depth and fictitious crack opening but none of them exceeded maximum fictitious crack opening. Therefore no real cracks have occurred in the mortar C. That means that the durability of the repair systems can be enhanced significantly by increasing fracture energy.

5. CONCLUSIONS

A numerical model based on realistic material laws has been developed. This model allows us to study damage evolution in new and repaired concrete structures subjected to different types of loading.
By applying the numerical model, a parametric study has been carried out. The results of this study allow us to define criteria for the risk of damage. The criteria can be use as a basis for optimizing cement-based materials in particular with respect to the prevention of shrinkage cracking and delamination.
The life-cycle of repaired structures can be considerably enhanced by an accurate design of the durability and a stringent quality control.

REFERENCES

1. Wittmann, F. H. (1998). In: *Fracture Mechanics of Concrete Structures*, Vol.3, pp. 1707-1714, Mihashi, H. and Rokugo, K. (Eds), Aedificatio Publishers, Freiburg, Germany
2. Martinola, G. (2000). *Rissbildung und Ablösung zementgebundener Beschichtungen auf Beton*, Building Materials Reports No. 12, Aedificatio Publishers, Freiburg, Germany, (in German)
3. Martinola, G., Sadouki, H. and Wittmann, F. H. (1997). In: 15th rencontres universitaires de Génie civil: Expérimentation et Calcul, EC. 97, Vol. 2, pp. 267-276, Strassbourg, France, (in French)

OPTIMIZING STRUCTURAL INTEGRITY THROUGH RELIABLE RESIDUAL STRESS MEASUREMENT

L. Edwards

Dept of Materials Engineering, Open University, Milton Keynes, MK7 6AA, UK

ABSTRACT

The determination of accurate reliable residual stresses is critical to many fields of structural integrity. Neutron stress measurement is a non-destructive technique that uniquely provides insights into stress fields deep within engineering components and structures. As such, it has become an increasingly important tool within engineering leading to improved manufacturing processes to reduce stress and distortion as well as to the definition of more precise lifing procedures. Furthermore, it is often the only means of measuring the stress state within engineering components and structures under conditions (temperature, stress, etc.) representative of those experienced in service. This paper describes recent advances in the utility of the technique through examples of residual stresses both beneficial and departmental to structural integrity.

KEYWORDS

Residual Stress, Structural Integrity, Neutron Diffraction, Stress Measurement

INTRODUCTION

Residual stresses exist in many manufactured components as a consequence of the thermal or mechanical processing. Local plastic deformation of a material will produce a residual stress variation; as will rapid cooling from elevated temperatures, where the materials yield strength is usually significantly lower than at room temperature. To many engineers, residual and applied stresses are separate entities. Applied loads and the stresses they cause are usually well understood, but the comparatively “unseen” residual stress state can often be extremely problematic. Whilst applied stresses can usually be easily estimated by a combinations of calculations and measurements, residual stresses are far more difficult to determine.

Historically, surface and near surface measurements could be made using semi-destructive techniques such as X-ray diffraction and hole drilling [1]. Full thickness measurements could also be made on simple geometries using various destructive sectioning methods [1]. The sparsity in reliable residual stress data has led to most design standards taking a conservative view of residual stress with upper bound yield values often being assumed. This is a reasonable approach if the structure can be assumed to be ‘defect-free’ at start of life. Under these conditions it may also be reasonable to derive a ‘safe life’ based on crack initiation procedures. However, damage tolerance based structural integrity remnant life assessments are now virtually mandatory in both the aerospace and nuclear power industries and such methodologies are increasingly used for any situation where safety is paramount. The principles of such an approach are shown in Figure 1. As the kinetics of defect growth can be strongly influenced by residual stresses a detailed knowledge of the variation in the residual stress tensor is required for such ‘fitness for purpose’ structural integrity assessments.

Neutron stress measurement is a non-destructive technique that has the unique ability to determine the full 3D stress tensor deep within engineering components and structures under conditions (temperature, stress, atmosphere, etc.) representative of those which might be experienced in service. As such, it has become an increasingly important tool within engineering leading to improved manufacturing processes to reduce stress and distortion as well as to the definition of more precise structural integrity lifing procedures. The technique was first developed 1970s [2] and started to gain popularity with the realisation of instrumentation specifically designed to measure residual stress [3]. This has engendered considerable industrial interest in the technique and has resulted in substantial further investment on both sides of the Atlantic. 20 million US$ is currently being invested by the UK/US alone to produce state of the art neutron stress measurement diffractometers at ISIS in the UK [4], ILL in Grenoble, France, and in the US at Los Alamos [5] and Oak Ridge. Complimentary developments are also underway both in Europe, Australia and Japan.

The purpose of this paper is to publicise the opportunities provided by recent advances in residual stress measurement by neutron diffraction using structural integrity based examples of both deleterious and beneficial residual stress fields.

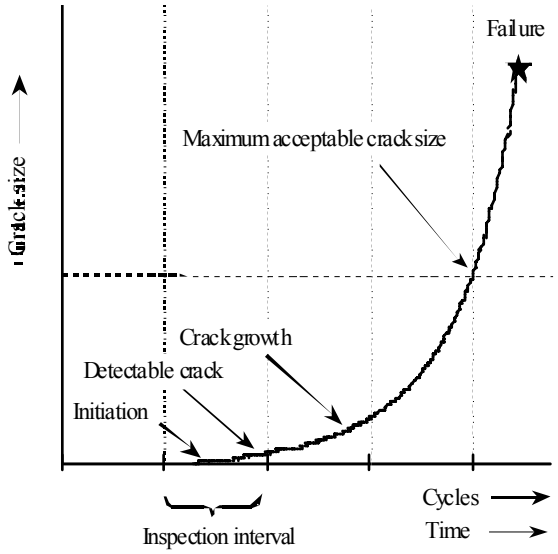

Figure 1 Damage Tolerence based life assessment

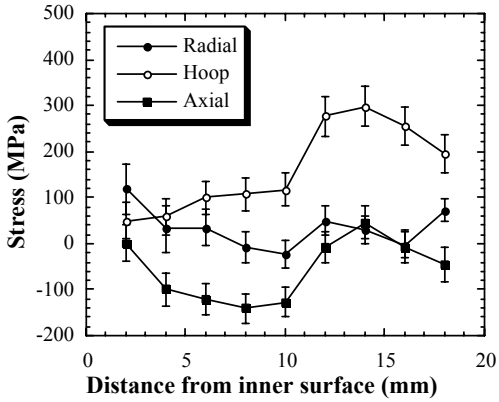

Figure 2 Residual stresses in weld HAZ

Structural assessment of Reheat cracking in Austenitic welds

Tensile weld residual stresses generally have an adverse effect on component life. When detailed structural integrity assessments are performed by industry, upper bound weld residual stress distributions from published compendia [5] are generally used. However, for safety-related plant it is sometimes vital to thoroughly understand the complete residual stress field and how it influences crack initiation, crack growth and fracture processes. For example, the principal stress magnitude and multi-axial stress-state are important factors affecting reheat crack initiation in stainless steel power plant operating at high temperatures. This cracking mechanism is caused predominately by the relaxation of welding residual stress, and therefore can initiate during service if creep temperatures prevail. To predict the kinetics of creep damage leading to reheat cracking, it is essential to know the full residual stress tensor, because tri-axial stresses can substantially affect creep relaxation, void growth and the creep ductility of the material [6].

FE methods are increasingly used to calculate residual stress distributions in multi-pass fusion welds by simulating both the thermal and mechanical response of the materials [7]. They have the advantage of providing a detailed map of the full residual stress tensor. But residual stress modelling is inherently more complex than conventional stress analysis and many approximations have to be made. So it is very important to independently validate predicted residual stress results and understand their limitations, before use in safety-critical structural integrity assessments. As an example, neutron diffraction measurements of residual stress and strain in the heat affected zone (HAZ) of a stainless steel pipe girth are described and compared to axi-symmetric FE weld residual stress simulations [8].

The welded test component studied was fabricated from two 316L austenitic stainless steel pipes. Following machining, the pipe was solution heat treated for one hour at 1050˚C with an air cool. The pipes were welded together using a Tungsten Inert Gas (TIG) root pass and a typical Manual Metal Arc (MMA) procedure. Neutron diffraction is now a well established technique for sub-surface strain measurements in metallic components. The change in the inter-planar distance in a crystalline material owing to any stress is determined in this technique by the observation of the change in position of diffraction peaks [2]. The present set of measurements was performed on the ENGIN spectrometer [3] which is based at the pulsed neutron source, ISIS, of the Rutherford Appleton Laboratory, UK

Through thickness measurements were performed across the tube. The hoop and radial measurements were performed with the pipe placed vertically whilst axial measurements were performed with the pipe placed horizontally on a support block. The measurement positions were determined by first aligning the specimen with the help of the telescopes and then confirming the precise location using the intensity of the diffracted beam as the gauge volume enters the specimen. The incident neutron beam was collimated to 3 x 3 mm. The focal width of the radial detection collimators used was 1.7 mm. The stress-free lattice parameter used in this work was obtained form the average of several measurements at different points through the thickness of a block (50 mm x 60 mm) cut from one end of the tube.

The ENGIN spectrometer uses the time of flight technique for the measurement of strain. Analysis of the resulting time of flight spectrum produces a lattice parameter a, which is obtained by fitting all the detectable peaks using the Rietveld refinement technique. The strain in the material is then given by: $\varepsilon=\Delta a/a_0$ where Δa is the lattice parameter shift, and a_0 is the stress-free lattice parameter. It has been shown that the strain calculated from a Rietveld refinement is a good approximation to the engineering strain in the component [9]. The stress is then calculated using Hookes Law thus :

$$\sigma_{ij} = \frac{E}{1+\nu}\ \varepsilon_{ij} + \frac{\nu E}{(1+\nu)(1-2\nu)}\ \delta_{ij}\,\varepsilon_{kk} \qquad (2)$$

where k is a dummy suffix summing over all k (*i.e.*, $\sigma_{kk} = \sigma_{11} + \sigma_{22} + \sigma_{33}$); E is Young's modulus; ν, Poisson's ratio; and δ, Kronecker's delta function.

Strain measurements were performed at the original girth weld heat affected zone (HAZ) 10.5 mm away from the weld centre-line. The full stress tensor was calculated for all the measured points, assuming that the hoop, axial and radial directions were the principal stress axes. The through-thickness variation of residual stress in the girth weld HAZ is given in figure 4 . The hoop stress profile peaks at 6 mm below the outer surface with a maximum value of 299 MPa (1% proof stress of base metal). The axial stresses in the HAZ exhibit a sine wave distribution (compressive towards the inner surface and tensile towards the outer), with a small compressive membrane stress equal to about –55 MPa. The radial stresses are generally low.

A numerical weld simulation was performed independently by British Energy (formerly Nuclear Electric) [8] using the ABAQUS finite element code to predict the residual stress field in the test component girth weld, that is prior to introduction of the repair. This involved a thermal calculation to predict the multi-pass weld temperature history at any point in the model, followed by a sequential non-linear mechanical analysis using thermal and mechanical properties for type 316 stainless steel up to its melting temperature. The axi-symmetric finite element model used provided a good representation of the test component geometry, weld preparation and weld bead lay-up.

The measured through-wall residual stresses at the 'original' girth weld are compared with finite element predictions in figure 3, both at the weld centre-line and in the HAZ. The predicted HAZ stresses at the –10.5 mm position are most relevant as these correspond to the last capping pass, where the neutron measurements were made. Predicted stresses from the +10.5 mm side are shown to illustrate the asymmetry arising from weld pass sequence effects. Overall, the correspondence between measured and predicted stress is impressive, particularly in the weld where a_0 errors arising from anisotropy and chemistry effects might be expected to distort the measured results.

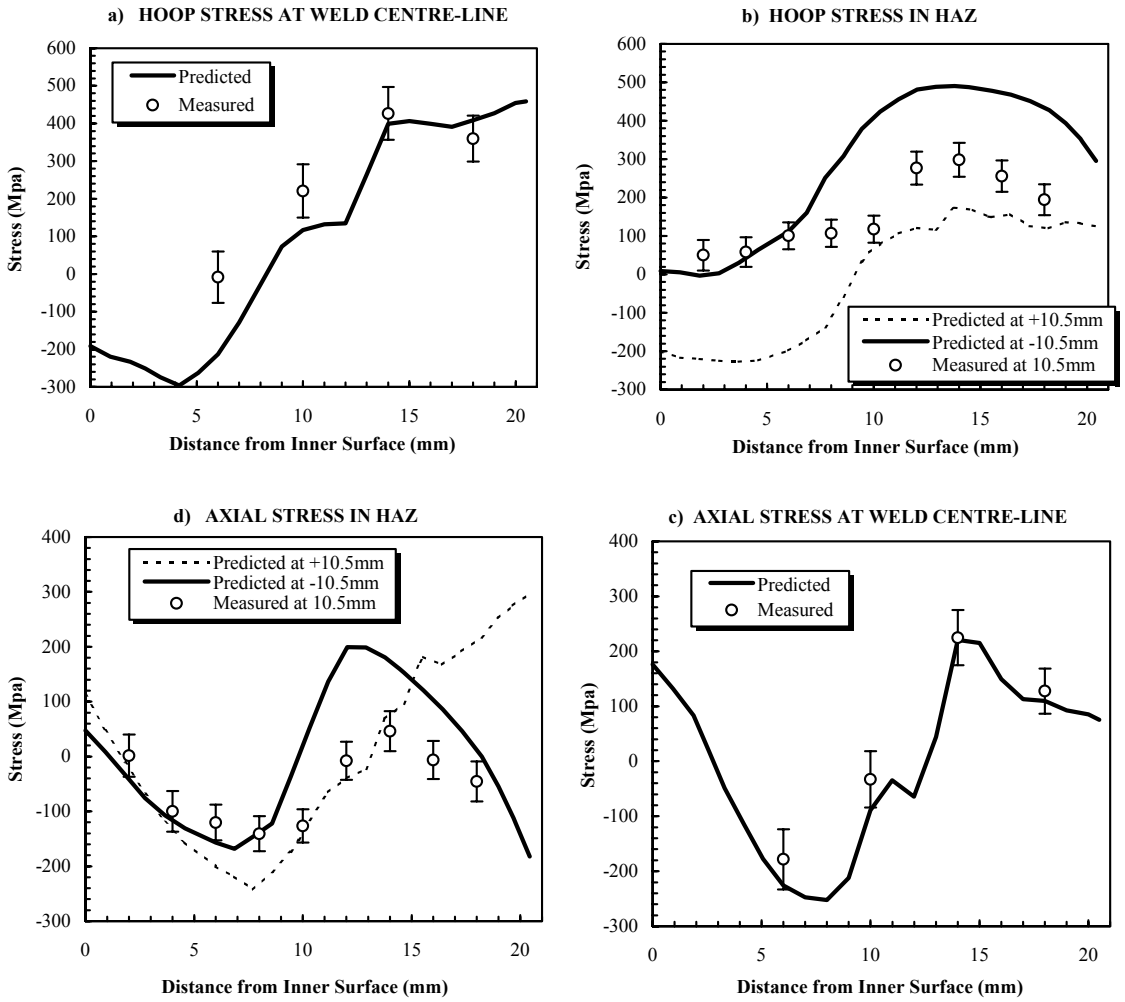

Figure 3: Comparison of measured and predicted residual stress in the HAZ of the 'original' girth weld

Both the measured and predicted hoop stresses demonstrate the same through-wall profile in both the weld fusion zone and HAZ; that is, exhibiting a peak at about 6 mm below the outer surface and a falling trend towards the inner surface. This characteristic profile is a global effect caused by the hoop contractions of outer weld passes applying a tourniquet compressive load on earlier passes. In the HAZ, it is evident that the predicted hoop stresses exceed those measured, particularly towards the outer surface. This conservative predictive feature has been observed in other weld analyses using similar modelling techniques and is the subject of on-going development work. The agreement between measured and predicted axial stress profiles is equally good (see figure 3). The measured profile in the HAZ shows the same sine wave characteristic predicted by the finite element model below the last capping pass.

In addition to validating the FE model, these results provide direct evidence of the residual stress profiles present in 19m thick Austenitic tube butt welds and have been used to aid assessment of the likelihood of reheat cracking occurring in specific in-service nuclear power plant welds [6].

Fatigue assessment of Cold Expanded Holes

The cold expansion of holes in metallic aircraft structures can considerably improve the fatigue life of fastener joints. Probably the most successful cold expansion process used is that developed by Fatigue Technology Inc., Seattle, USA (FTI). This process involves placing a longitudinally-split sleeve within the hole and then drawing an oversized tapered mandrel through the assembly so that the material undergoes permanent plastic deformation around the hole. Upon removal of the mandrel, owing to the spring-back of the surrounding elastic material, a self-equilibrating residual stress field is produced. In an annular region adjacent to the hole the residual stress field is compressive and results in improved fatigue behaviour.

At present, the benefits of cold expansion are not built in to the damage tolerant design of aircraft although their presence clearly impacts on the fatigue performance of the structure. In order for the crack growth life of cold expanded holes to be accurately determined adequate knowledge of both the original residual stress filed and how it is changed by the fatigue loading must be available. The usual way to account for the effect of residual stresses on crack propagation is invoke superposition so that an effective stress intensity factor can be defined as $K_{eff} = K_{appl} + K_{res}$. For a given residual stress distribution K_{res} can be found either using an integration method or using a weight function approach.

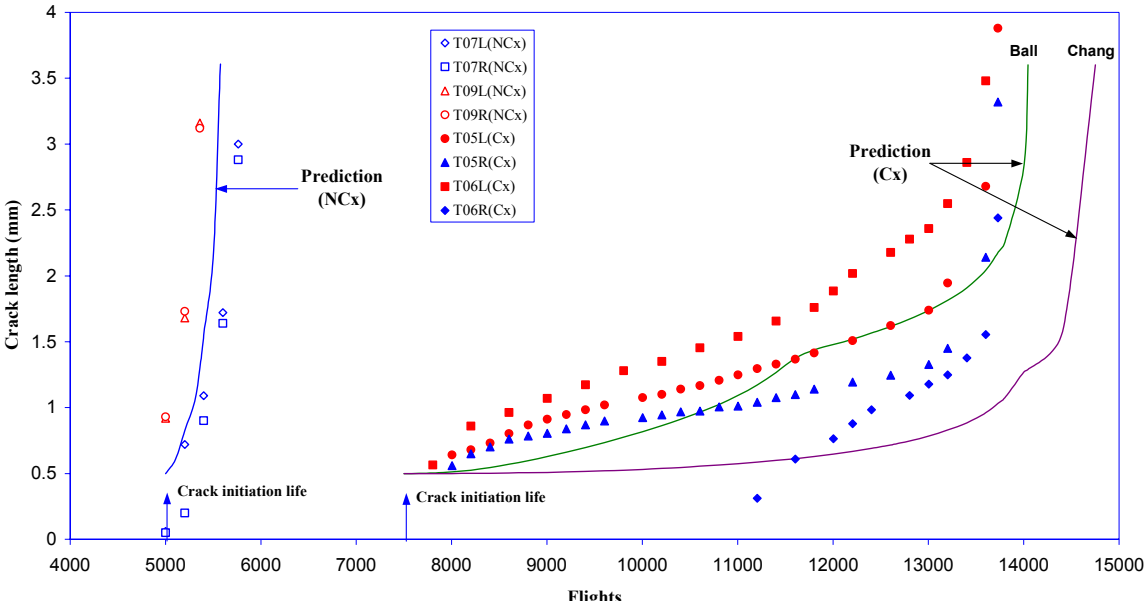

Figure 4. Measured and simulated fatigue crack growth using two different residual stress models.

One critical factor is whether the beneficial residual stress distribution imparted by the cold expansion process is changed by the applied loading. This can be particularly important for tactical aircraft which may be subjected to significant under and overloads in their flight load spectra. Under these conditions it can be difficult to predict both the local fatigue crack growth rate and the life of cold expanded holes subject to spectrum loading. This is illustrated by Figure 4 which shows attempts by Gaerke et al. [10] to predict crack growth from open (NCx) and cold expanded (Cx) 6mm holes in an 2024 aluminium alloy specimen subjected to the FALSTAFF load spectra [11]. This is a standard flight-by flight loading sequence meant to represent the stresses on the wing surface near the fuselage in a tactical aircraft. What is clear is that the two closed form solutions for the residual stresses around a cold expanded hole given by Ball and Lowry and Chang produce significantly different crack growth rate predictions. To investigate load interaction affects the effect of a 30KN under-load on the residual stresses surrounding a 6.25mm cold expanded hole in a 300 x 40 x 5 mm 7050 aluminium alloy plate have been determined using neutron diffraction [12,13].

Such an experiment is particularly suited to neutron diffraction as the technique is completely non-destructive. Thus the residual stresses were measured in the same specimen both after cold expansion and subsequent to the application of the compressive 30KN under-load. Measurements were performed on the ENGIN diffractometer as described earlier using a gauge volume of $2 \times 2 \times 1.5\ mm^3$. Hoop, transverse and radial strains were determined, from which the associated stresses were calculated. The stress-free value, a_0, was obtained by measuring a point 100 mm away from the hole. Stresses were then calculated using Hooke's Law (eqn. 2) assuming that the measured directions were the principal stress axes.

Figure 5 illustrates the effect of the 30 KN compressive underload on the hoop residual stress distribution at the mid-thickness of the plate. It can be seen that there are two distinct changes to the residual stress field. The magnitude of the maximum compressive residual stress has reduced in the area near to the hole from around –400 MPa to around –300 MPa, and the depth of this compressive zone has increased from 1 mm to 1.8 mm. Such a change is likely to have a substantial effect on the driving force for crack growth and illustrates the difficulties of producing damage tolerant fatigue life predictions in such circumstances.

These results show the potential benefits of neutron diffraction stress measurement for structural integrity determination through its unique ability to measure the stress tensor deep inside components and structures.

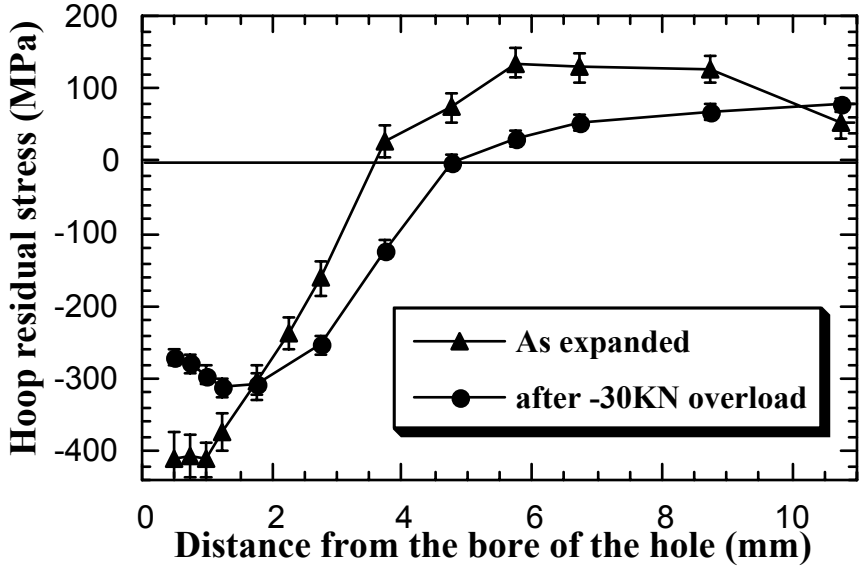

Figure 5. Hoop residual stresses at a 7050 cold expanded fastener hole before and after a –30 kN under-load.

The future

The future is bright for neutron diffraction stress measurement. There is significant investment in new instrumentation world-wide and the technique is constantly evolving to become more accessible for novice users. There will be a substantial growth in the user base and this growth provides a substantial opportunity for researchers and engineers involved in damage tolerance based structural integrity. One of the purposes of this paper is to publicise the power of the technique so that a vibrant engineering user community is waiting to use coming instrumentation when it comes on stream over the next few years.

Acknowledgements

The author would like to acknowledge the help of Monojit Dutta, David Wang and John Wright for their help performing the experiments and to John Bouchard and Robin Cooke for helpful discussions concerning their interpretation.

References s

1. Jian Lu, (ed.) (1996) *Handbook of Measurement of Residual Stresses*, SEM, US 1996
2. Allen, A, Andreani, C, Hutchings, M T, Windsor C. G, (1981) *NDT Int.,* 14 249
3. Johnson, M W, Edwards, L and Withers, P J, (1997) *Physica B* 234,1141
4. Nelson, R. O.; Bourke, M. A. M.; Bowling, P. S.; Cooper, G. M.; Kozlowski, T.; Lara, P. D.; Rose, C. R.; Ross, J. J.; Seal, J. R.; Williams, B. C. (2000) *IEEE Trans Nuc. Sci*., 7
5. BS7910 (1999) *British Standards Institution*, London.
6. Bradford R, (1998) *I Mech E Conf. Trans. Assuring It's Safe*, PEP Ltd., London, 287
7. Dong P, Zhang J, and Li MV, (1998) *ASME: Pressure Vessel Piping,* 373, 311-317.
8. Edwards L, Bouchard P J, Dutta M, Fitzpatrick, M E, (1998) *I Mech E Conf. Tran:s Integrity of High Temperature Welds*, , PEP Ltd., London, 181
9. Daymond MR, Bourke MAM, VonDreele RB, Clausen B, Lorentzen T, (1997) *J. Appl. Phys*, 82 1554
10. Gaerke,J., Zhang, X and Wang, Z. (2000) *Proc. Instn Mech. Engrs, Part G*, 214, 281
11. Dijk, V and de Jonge, J.B.(1975) NLR MP 75051 National Aerospace Laboratory, The Netherlands.
12. Wang, D.Q. and Edwards, L. (1998) *Proc. Fourth European Conference on Residual Stresses,* Ed. Denis, S et al, Société Française de Métallurgie et de Matériaux, Paris 2, pp.619-626
13. Stefanescu, D., Bouzina, A., Dutta. M, Wang, D.Q, Fitzpatrick, M.E. and Edwards, L. In Press J. Neutron Research

OXIDE FIBER-COATINGS FOR CONTROLLED FRACTURE IN ROBUST CERAMIC COMPOSITES

R. J. Kerans, T. A. Parthasarathy*, R. S. Hay, E. E. Boakye*,
K. A. Keller*, T. Mah* and M. K. Cinibulk

Air Force Research Laboratory, Materials and Manufacturing Directorate
AFRL/MLLN, Wright-Patterson AFB, OH 45433-7817
(*UES Inc., Dayton OH under AFRL contract)

ABSTRACT

There has been significant recent progress in the development of new fiber coatings to promote crack deflection and distributed damage mechanisms in ceramic composites. There is now definitive proof that oxide coatings can provide good composite behavior in real composites. Research to deduce viable approaches to the controlled-fracture-coating problem has uncovered other intriguing aspects of fracture behavior of constituents and composites. The evaluation of oxide based approaches required developing viable coating processes and solving pervasive problems with fiber degradation apparently due to previously unknown stress-corrosion effects. Microcomposite testing revealed interesting, potentially revealing and useful effects on fracture statistics. Finally, evidence of the desired crack deflection and beneficial effects on composite behavior are presented, and the surprising role of plasticity is briefly discussed.

KEYWORDS

coating, oxide, fiber, interface, interphase, pullout, fracture, composite

INTRODUCTION

The development of tough composites made of brittle constituents necessitates a higher degree of control of fracture processes than generally required. Fracture is most often an event to be avoided by all possible means, and once it happens the details are not so important. In other cases, while the fracture is to be avoided, it is desirable for a failure to occur in a relatively benign fashion, and design effort is devoted to that end. Examples include safety glass, containment of turbine engines, and shear connections on road signs. There are also examples of designed fracture behavior, such as perforated sheets, tamper resistant plastic and metal screw tops, pull tabs openers, snap-off knife blades, and a variety of forms of tamper-resistant medicinal packages. However, the design of structural materials such that the sequence of fracture events and crack paths are predetermined on a microstructural level pushes hard on the limits of our understanding of the details of crack initiation and propagation.

The basic requirement for a tough composite comprising brittle constituents is that cracks that initiate in the matrix not propagate into fibers but bypass them by deflecting into fiber-matrix debonding cracks. This requires that something in the fiber-matrix interfacial region -- an interface, a fiber coating, or the near-fiber-

surface region of the matrix -- be sufficiently weak to fail before the fiber fails. It is important to note the "sufficiently weak" means sufficiently weak relative to the fiber in the finished composite. This is important because virtually all processes have some effect on the strength of the fiber. The actual crack path is the result of a competition between fracture in the fiber, coating and matrix. C and BN have unusual combinations of properties that make them ideal choices for fiber coatings, except for oxidation resistance. The design of oxide substitutes is a significant challenge. See Refs. [1] and [2] for reviews.

The development of new fiber coatings has been greatly complicated by effects of processes on fiber properties, both in terms of direct process constraints and in terms of interpretation of composite behavior. Of the two coatings discussed here, monazite ($LaPO_4$) appears to be practically useful, while hibonite ($XAl_{12}O_{19}$) can not be processed at sufficiently low temperature to avoid damaging currently available, compatible polycrystalline fibers. Three interesting facets of fracture behavior in constituents and composites are briefly addressed. The first of these involves severe fiber degradation during coating, apparently by a stress-corrosion mechanism, and the eventual successfully modified process. The second involves fracture statistics of monofilament fibers with and without coatings and matrices applied. Finally, an example of successful use of oxide coatings in actual composites, with considerable improvement in high temperature life, is presented. The surprising discovery of low temperature plasticity in the oxide coatings is briefly discussed.

FIBER STRENGTH DEGRADATION

The strengths of monazite coated fibers were found to be highly dependant on the characteristics of the monazite precursor used for coating (Table 1). The sol eventually found to be benign to the fiber, Precursor 3, was purified by centrifugal separation of the sol particles from nitric acid solution and re-dispersed in deionized water. The pH of the purified sol was 3. A continuous vertical coater was used in all the coating experiments. [3]

Table 1
MONAZITE PRECURSORS USED FOR FIBER COATINGS

Precursor Number	Lanthanum Source	Phosphate Source
1. Aqueous solution	$La(NO_3)_3$	$(OCH_3)_3PO_4$
2. Aqueous sol	$La(NO_3)_3$	$(NH4)_4HPO_4$
3. Aqueous sol	$La(NO_3)_3$	H_3PO_4

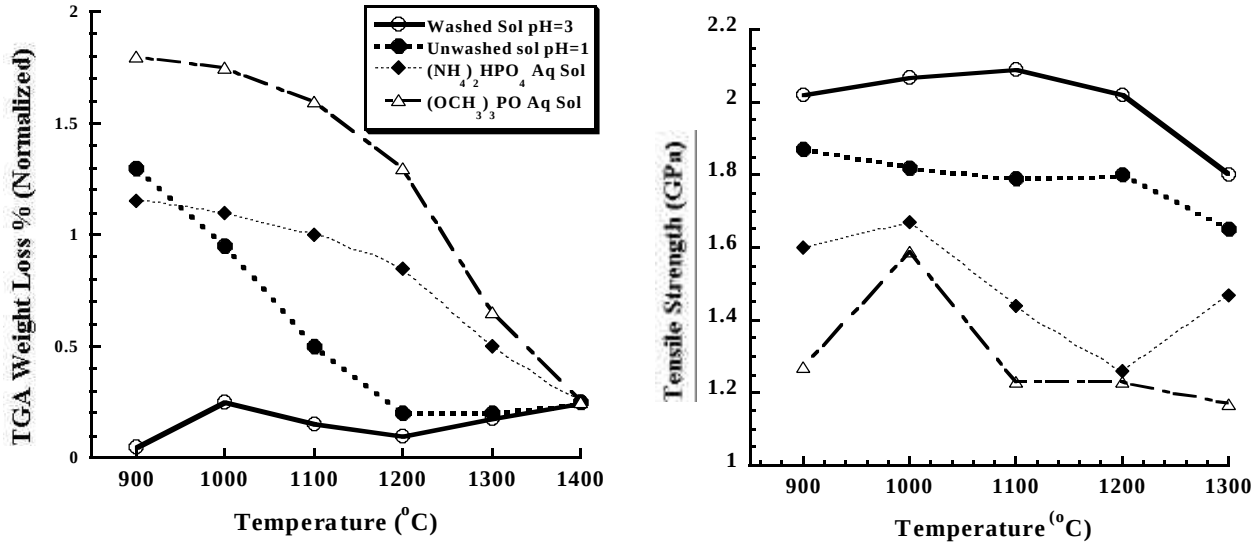

Fig. 1 a) TGA weight loss from different precursors. b) Effect of monazite precursors on fiber strength.

Evidence for stress corrosion comes from comparison of weight loss in different monazite precursors to the strengths of fibers coated with these precursors (Fig. 1). [4, 5] Fibers coated with precursors with high weight loss had low strength (Precursors #1 and #2). Fibers coated with precursors with low weight loss (Precursor #3) had the highest strengths. Filament strengths were also high after Nextel^{TM} 610, Tyranno-SA, Hi-Nicalon, Hi-Nicalon-S and Sylramic were coated with precursor #3.

Degradation at a particular temperature correlated with the amount of gas-phase decomposition products that remained in the coating at that particular temperature. [4] Partial pressures of precursor decomposition products in coating pores may be significantly higher than atmospheric pressure, and therefore enhance the activity of a corrosive species if the coating is hermetic. Coatings with high pore volume fraction will generally not be hermetic; the open porosity will provide escape pathways for the out-gassing species. Coatings made from precursor #3 were also the most porous; this may also account for higher coated fiber strength.

MICROCOMPOSITE FRACTURE TESTS

Axisymmetric cylinders of oxide/oxide microcomposites were fabricated and tested in tension to evaluate the effectiveness of monazite ($LaPO_4$) and hibonite ($CaAl_{12}O_{19}$) as interlayers (0.3 to 0.5 μm) in sapphire monofilament-reinforced alumina matrix composites. [6]

Fractography

The fractured surfaces of the control specimens (uncoated fiber in a matrix) showed that the fracture in the matrix and in the fiber are coplanar. Fracture surfaces of the hibonite-coating-microcomposites reveal short deflections in the coating resulting in steps to the fiber surfaces. The step is attributable to the easy-cleaving hibonite deflecting the crack, but there is no indication of a dominant debond crack; multiple deflections occur within the hibonite coating. The fracture surfaces of the monazite containing composites showed extensive evidence for crack deflection. The matrix cracks were periodic along the length of the fiber, with spacing in the neighborhood of a millimeter. When the exposed interface region was examined at higher magnifications, it was found that the debonding occurred at the matrix/monazite interface

Strengths and Weibull Moduli of Fibers, Coated Fibers and Microcomposites

All the specimens tested exhibited a linear load-displacement relationship until failure. The only quantitative parameter that can be used for evaluation is the reference stress and Weibull modulus of the ultimate failure load of the fibers and microcomposites. All loads were divided by the fiber cross-sectional area for comparison and the strengths thus calculated were plotted on a Weibull distribution. Figure 2a shows the strength of the control and monazite-coated microcomposites compared with each other and the respective fiber strengths. Figure 2b is the same plot for fibers and microcomposites with hibonite as the coating or interlayer. All of the fiber strength results are for fibers that were tested after they were given a heat treatment at 1450°C for 2 hrs to simulate the heat treatment used to sinter the matrix. Hibonite appears to degrade the fiber slightly while monazite has little effect; however in both coated fibers the Weibull modulus is much enhanced. From Fig. 2a, it is seen that the strengths of both composites are lowered after the matrix processing and the average strengths are not significantly different. However the monazite-coated composites have much-improved Weibull modulus. Essentially the same result was obtained for the hibonite coated composites, Fig. 2b. Since the monazite composites showed significant debonding, the lack of difference in strength between the control and monazite-coated composite is puzzling. To determine if this is due to having a poor matrix density, a second set of control and monazite-coated samples were sintered at 1500°C for 2 hrs to improve the matrix density. There was only a marginal improvement in the matrix density and essentially the same result was obtained (Fig. 2c) with some loss in strength, which can be easily rationalized as due to loss of fiber strength following the 1500°C heat treatment.

Discussion of Microcomposite Behavior

In the case of monazite, microstructures of fractured microcomposites show clear evidence for debonding at the coating/matrix interface confirming that the interface between monazite and the matrix alumina is

sufficiently weak to debond under axial loading of the composite in tension. Fractographs of hibonite-containing composites show evidence for crack deflection but the debond crack is not sustained beyond a few micrometers.

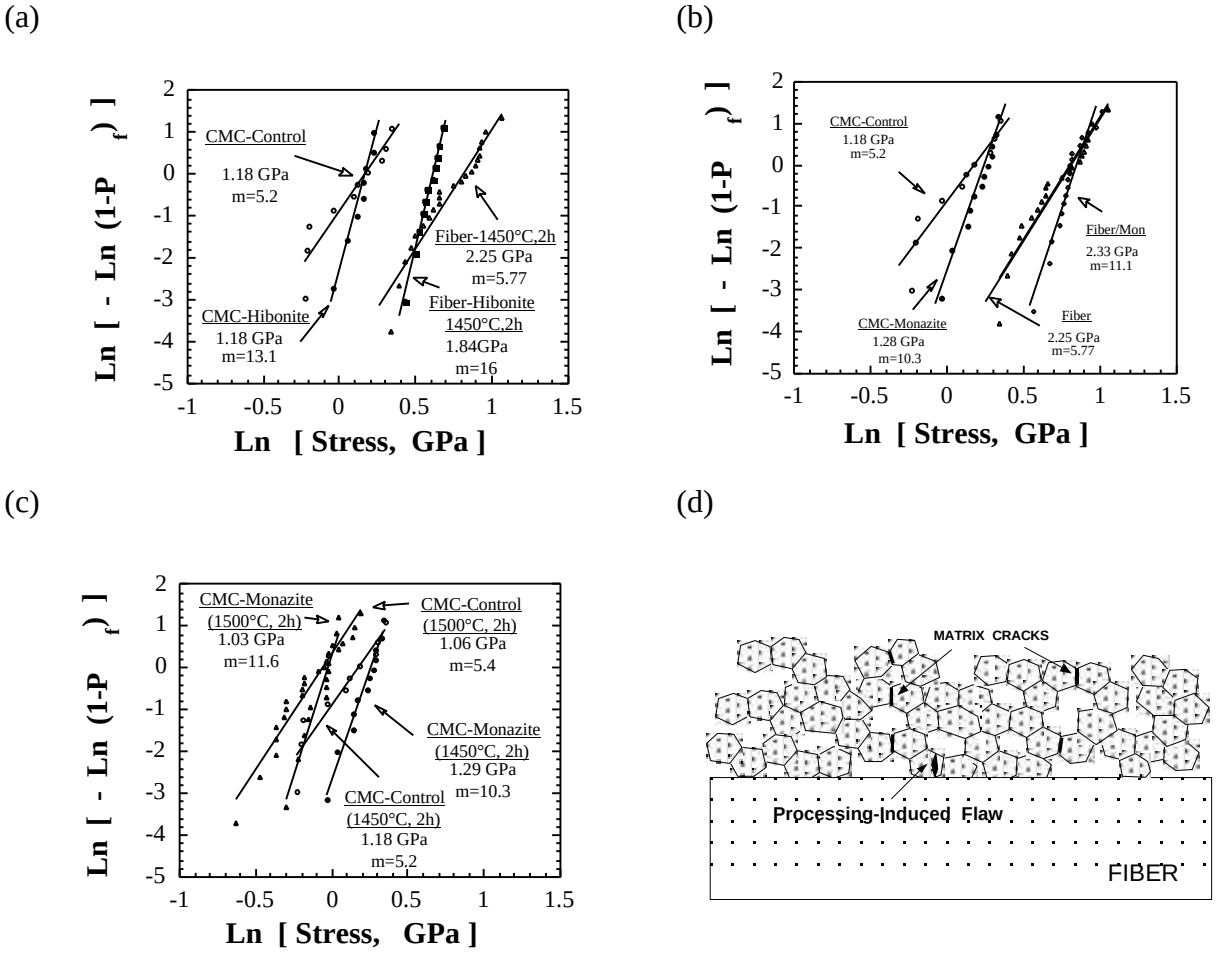

Figure 2: Weibull plot of the fracture stresses of monofilaments, and monofilaments with matrices around them (micro-CMCs) are shown for the cases of (a) hibonite and (b) monazite as interlayers. Uncoated filaments and control micro-CMCs are shown for comparison. (c) The same experiments as in (b) but with the matrix fired at higher temperature shows that the results are essentially the same. (d) A schematic of a plausible mechanism for the protection of a fiber from cracks in a porous matrix. [6]

The only positive indication in either case relative to the control specimens was a substantial increase in Weibull modulus and its retention in the final microcomposites. The effects on Weibull modulus and mean strength of both coating and matrix are not simply resolvable with a definitive model; an extensive discussion appears in Ref. [6]. Nevertheless, the beneficial effect of the coating on the strength statistics (in the monazite case) combined with the fractographic evidence is postulated to support earlier work [7] in indicating proper functioning of the coating. The scenario imagined is that mode I cracks deflect into debonding cracks in the desired fashion and that the coating serves to bridge the larger fiber flaws by way of the same mechanism in reverse, leading to the observed increase in Weibull modulus.

OXIDE COATINGS IN COMPOSITES

The effectiveness of monazite coatings in actual composites was evaluated using a Nextel™ 610 reinforced alumina system. [8] Composites containing either uncoated or monazite-coated fiber displayed satisfactory strengths after sintering at 1100°C/5 hours in air. At this degree of consolidation, the matrix is quite porous

(composite porosity ~30 – 35%) and the control composites behave as porous-matrix composites that do not require a fiber coating to deflect cracks; the debond occurs via matrix failure at the fiber surface. (See for example [9]) The control specimens (uncoated fiber) exhibited an average strength of 168 MPa, while specimens reinforced with monazite-coated fibers displayed a much higher average strength of 230 MPa. The fracture surfaces of both the uncoated and monazite-coated samples sintered at 1100°C showed "woody" type failures, with some bundle pullout.

After sintering for a short time (5 hours) at 1200°C, there was a distinct difference between the behavior of the uncoated and the monazite-coated composites (Table 2). The samples containing uncoated fibers displayed drastic strength losses of >70%, resulting in an average strength of 45 MPa, with approximately 0.03% strain. Such a decrease is typical of porous-matrix composites and is generally attributed to sintering of the matrix to a degree that suppresses debonding via matrix failure. [9] Conversely, the samples containing monazite-coated fiber showed a strength decrease of only ~14% to an average of 198 MPa. Stress-strain curves for the monazite-containing specimens revealed strain-to-failure values ranging from 0.25 – 0.4%. This indicates that there is a definite advantage to incorporating monazite coatings in the composite. The samples containing uncoated fiber exhibited brittle-type fracture surfaces, while the monazite-containing samples showed distinct fiber pullout, along with woody-type fracture.

Table 2

MEASURED COMPOSITE STRENGTHS AFTER NORMALIZING TO 20 VOL.% FIBER COMPOSITE

Sample Nextel™610//Alumina	**1100°C/5 h (initial process)**	**1200°C/5 h**	**1200°C/100h**
Control (no coating)	168 (±33)	45 (±20), 0.03%	-
Monazite	230 (±18)	198 (±12), 0.27%	143 (±7), 0.22%

The fracture surfaces of the monazite-coated samples indicated that debonding occurred in the region bounded by the matrix surface and the fiber surface. Preliminary indications suggest that the debonding crack tends to run in the coating near the fiber surface or at the coating/fiber interface, though this has not been thoroughly examined. Figure 3 shows a back-scattered image of the fracture surface of a specimen sintered at 1200°C/5 h. The bright areas visible in the fiber trough and on the fiber surface are the monazite coatings.

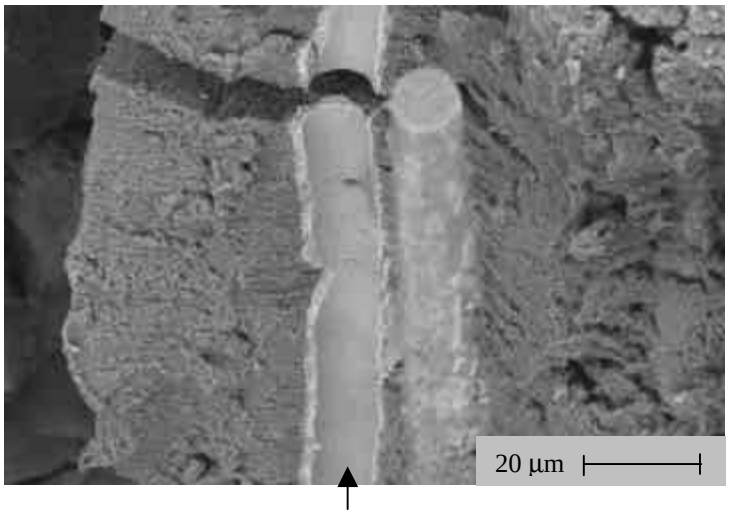

Figure 3: Back-scattered image of a fiber trough on the fracture surface of Nextel™ 610/monazite/alumina composite. Bright areas are monazite coatings. Coatings evident both in the trough and on the fiber surface in the foreground of the image.

Similar features were seen on the fracture surfaces of monazite-containing samples after heat treatment at 1200°C for 100 hours. There appeared to be a decrease in the amount and length of fiber pullout on the fracture surface. The strength decreased 38% from the as-processed value bringing the average strength to 143 MPa, with ~0.22% strain. This is markedly superior to control specimens exposed for only 5 hours at 1200°C. It is apparent that the monazite coating performs the crack deflection–debonding function and truly provides protection for the fibers in an actual composite. Manipulation of the monazite coating characteristics, such as thickness and uniformity, will allow for optimization of composite properties.

Grain growth in Nextel™ 610 fiber in composites has been observed to change with the presence of monazite coatings. The coatings serve to inhibit grain growth, or more likely to suppress accelerated grain growth, as compared to control composites. The loss in strength of the composites containing uncoated fiber can be attributed, in part, to grain growth in the Nextel™ 610 fiber. Neither the mechanisms involved nor the degree of contribution to composite strength retention have yet been determined.

It has become clear, though certainly surprising, that plasticity plays a substantial role in the crack-deflection and sliding behavior of monazite, even in room temperature composite tests. Early reports of apparent smearing of monazite in the wear tracks resulting from fiber sliding led to TEM confirmation of sufficient dislocation activity and deformation twinning, though in a very limited volume, to produce dynamic recrystallization. [10]

CONCLUSIONS

The search for oxide coatings to perform the crack deflection function in ceramic composites has not only led to an enhanced understanding of composite behavior, but has uncovered several surprising aspects of constituent and composite fracture behavior. Three interesting facets have been briefly addressed here. Each of these has implications broader than the immediate question of composite behavior. The vulnerability of high strength fibers to apparent stress-corrosion issues raises the question of the degree of ubiquity and importance of such processes. The interesting behavior of the failure statistics of microcomposites challenges our interpretation of fracture statistics and perhaps will provide a directly measurable parameter that answers the qualitative question “good composite or bad composite?” Finally, successful use of oxide coatings in actual composites, with considerable improvement in high temperature life, definitively confirms that the “long shot” substitution of oxides for C and BN is viable. It is thought provoking to consider that success of the first of these coating systems was predicated on their unanticipated low temperature plasticity.

References:

1. Kerans, R. J., Hay, R. S. & Parthasarathy, T. A. (1999) *Current Opinion in Solid State and Materials Science* 4**,** 445-451.
2. Faber, K. T. (1997) *Annu. Rev. Mater. Sci.* 27**,** 499-524.
3. Hay, R. S. & Hermes, E. E. (1993) Patent No. 5,217,533 USA
4. Boakye, E. E., Hay, R. S., Mogilevsky, P. & Douglas, L. M. (2000) *Submitted to J. Am. Cer. Soc* .
5. Hay, R. S. & Boakye, E. E. (2000) *Submitted to J. Am. Ceram. Soc* .
6. Parthasarathy, T. A., Boakye, E., Cinibulk, M. K. & Petry, M. D. (1999) *J. Am. Ceram. Soc.* 82**,** 3575-3583.
7. Morgan, P. E. D. & Marshall, D. B. (1995) *J. Am. Cer. Soc.* 78**,** 1553-63.
8. Keller, K. A., Mah, T., Parthasarathy, T. A., Boakye, E. E. & Cinibulk, M. K. (2001) *Ceram. Eng. Sci. Proc., in press* .
9. Levi, C. G., Yang, J. Y., Dalgleish, B. J., Zok, F. W. & Evans, A. G. (1998) *J. Am. Ceram. Soc.* 81**,** 2077-2086.
10. Hay, R. S. (2000) *Cer. Eng. Sci. Proc.* 21**,** 203-218.

OXYGEN ENHANCED CRACK GROWTH IN NICKEL-BASED SUPERALLOYS UNDER SUSTAINED AND FATIGUE LOADING

Robert P. Wei[1], Zhi-Fang Huang[1], Christopher Miller[2] and Gary W. Simmons[2]

[1]Department of Mechanical Engineering and Mechanics
[2]Department of Chemistry
Lehigh University
Bethlehem, PA 18015

ABSTRACT

To better understand the role of niobium and other strengthening elements in the enhancement of crack growth by oxygen in nickel-based superalloys at high temperatures, three powder metallurgy (P/M) alloys, with nominal composition similar to alloy IN-100, but with 0, 2.5 and 5 wt pct niobium, were investigated. This investigation complements a previous study of an ingot metallurgy (I/M) Inconel 718. These P/M alloys are γ′ strengthen (with comparable volume fractions of γ′ precipitates of about 53 pct), and were designed to suppress the formation of γ″ precipitates. The alloys were tested in high-purity oxygen and argon under sustained and fatigue loading, at 873, 923 and 973 K. Companion microstructural and surface chemistry studies, including the oxidation of Nb, Ni_3Nb and NbC, were conducted to identify the mechanisms for crack growth enhancement. In this paper, the results from these investigations are briefly summarized. The mechanisms for crack growth and the role of niobium and other elements (Al, Cr, Fe, Ni and Ti) are discussed, and the relationship between sustained-load and fatigue crack growth is considered.

KEYWORDS

Nickel-based superalloys, oxygen enhanced crack growth, mechanisms, oxidation, microstructure, fracture mechanics, surface chemistry

INTRODUCTION

The influence of oxygen and moisture on crack growth in nickel-based superalloys at high temperatures has long been recognized. The presence of oxygen can increase the rate of crack growth under sustained loading by 4 orders of magnitude over that in inert environments. Considerable efforts have been made to understand the mechanisms for this enhancement, for example (1-7). Floreen and Raj (1) have categorized the various mechanisms into two groups. The first group involves environmentally enhanced formation and growth of cavities, or micro-cracks, at grain boundaries ahead of the crack tip. One such mechanism attributed the enhanced crack growth to the reaction of oxygen with grain boundary carbides to produce CO/CO_2 at high pressures (2). The second type is associated with preferential formation of a grain boundary oxide layer at the crack tip, either through the formation of oxides of nickel and iron (NiO and FeO) (3) or through a two-step process of forming first NiO and FeO and subsequently Cr_2O_3 (6).

Recent studies (8-11) on an Inconel 718 alloy (under sustained loading) and a Ni-18Cr-18Fe ternary alloy (in fatigue) suggested that niobium (Nb) can play a significant role, and raised concerns regarding the viability of these proposed mechanisms for crack growth enhancement by oxygen. The results showed that sustained load crack growth rates in oxygen at 973 K were increased, for example, by more than 10^4X over those in high-purity argon for Inconel 718 (8). The enhancement in crack growth was attributed to the formation and rupture of a non-protective and brittle Nb_2O_5-type oxide film at the grain boundaries through the oxidation and decomposition of niobium-rich carbides and, perhaps, oxidation of γ″ precipitates at the grain boundaries. Crack growth rates in the ternary alloy, on the hand, were found to be essentially unaffected by

oxygen (11). A comparison of these results with those on a range of nickel-based superalloys in the literature showed the strong dependence of the environmental sensitivity factor (*i.e.*, the ratio of crack growth rates in the deleterious and inert environments) on Nb concentration (8). The sensitivity factor increased by up to 10^4X for Nb from 0 to 5 wt. pct, *albeit* the sensitivity varied widely among the alloys. These findings suggested that the role of Nb on enhancing crack growth in oxygen, heretofore not recognized, needs to be carefully examined. The "insensitivity" of the Ni-18Cr-18Fe ternary alloy, with copious amounts of $M_{23}C_6$ carbides at the grain boundaries, calls into question the viability of both groups of proposed mechanisms.

In this paper, the results from a series of coordinated crack growth, microstructure and surface chemistry studies to elucidate the role of niobium on crack growth in oxygen at high temperatures are summarized (12-16). These studies complement the earlier work on Inconel 718 at Lehigh University (8). Three γ′-strengthened powder metallurgy (P/M) alloys, with nominal composition similar to alloy IN-100, but with 0, 2.5 and 5 wt. pct. niobium, were investigated. The chemical compositions of these alloys (in wt pct) are as follows: Alloy 1 (Ni56.3 Cr12.7 Co18.9 Al4.8 Ti3.9 Mo3.3 Nb0); Alloy 2 (Ni56.4 Cr12.1 Co18.3 Al4.1 Ti3.3 Mo3.2 Nb2.5); and Alloy 3 (Ni54.5 Cr12.3 Co18.2 Al3.7 Ti3.3 Mo3.3 Nb4.9). These alloys were designed to suppress the formation of γ″ (and δ) precipitates. They have comparable volume fractions of γ′ precipitates of about 53 pct. The hardness and average grain size for alloys 1, 2 and 3 were about Rockwell C 45, 45 and 47, and 10, 45 and 45 μm, respectively. The average size of the γ′ precipitates within the γ matrix for all three alloys is approximately 150 nm, except for the presence of about 3 vol. pct of micrometer sized coarse γ′ precipitates in alloy 1. Surface chemistry studies were also carried out on Nb, Ni_3Nb and NbC to assess the reactivity of these phases to oxygen. Based on the findings and information in the literature, the mechanisms for crack growth and the role of niobium and of other elements are considered.

SUMMARY OF RESULTS

Crack Growth and Corollary Experiments

Sustained-load and fatigue crack growth experiments were conducted on the P/M alloys in the circumferential-radial (CR) orientation in high-purity oxygen at 873, 923 and 973 K (12,16). Because of the very slow rates of growth, testing in high-purity argon was limited to the intermediate K levels at 973 K for the alloys. The data, showing crack growth rates under sustained-load versus K, are presented in Fig. 1 as a function of temperature for alloys 1 and 3. The results show that the crack growth rates in oxygen at 135 kPa are strongly dependent on temperature, with apparent activation energy of about 250 kJ/mol. The rates and crack growth response in the Nb-containing alloy 3 parallel those of Inconel 718 and the growth rates were about 10^4X faster than those in argon ($p_{O_2} < 10^{-17}$ Pa) (see Fig. 1a). Results on the niobium-free alloy 1 were somewhat surprising in that the growth rates in oxygen were nearly 10^3X faster than those in argon at 973 K (see Fig. 1b); *i.e.*, with an environmental sensitivity that is well above the anticipated 1X to 10X. Data on alloy 2 were comparable to those of alloy 3 (12).

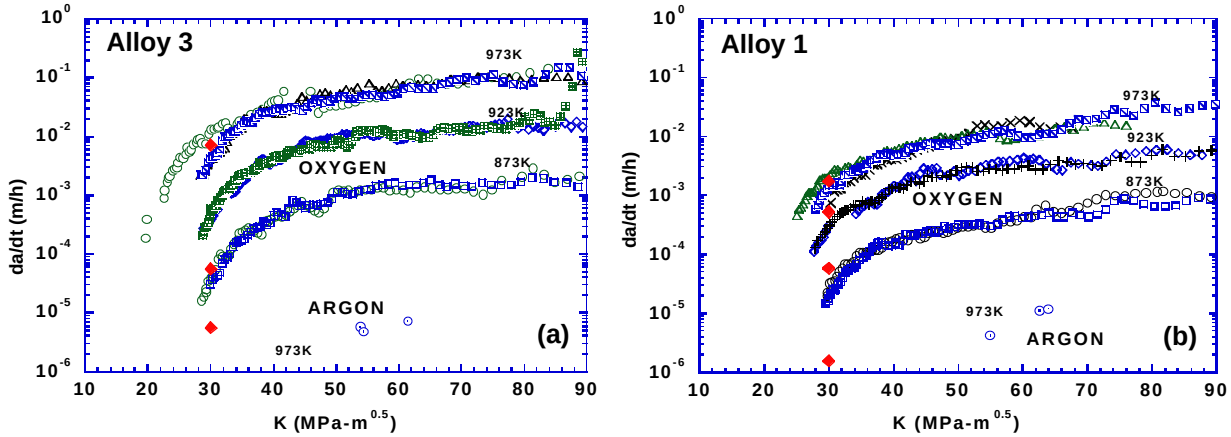

Figure 1: Kinetics of sustained-load crack growth (a) in the Nb-containing alloy 3 and (b) the Nb-free alloy 1 in high-purity oxygen and argon, and comparisons with crack growth rates inferred from the dwell-time fatigue tests (12,16).

Fatigue crack growth experiments were conducted as a function of dwell-time at peak load (from 0 to 30 s), using a trapezoidal waveform. The rise and fall time, at 0 s dwell-time, corresponds to a triangular-wave loading at 10 Hz. Representative data (for alloy 3 in oxygen) are shown in Fig. 2. Because of the strong sensitivity to oxygen enhanced growth, the fatigue crack growth rates were essentially dictated by the

growth during the dwell-time at load, and hence the sustained-load crack growth rate. This is reflected by the sustained-load crack growth rates that were back calculated from the fatigue data in Fig. 1 (12,16).

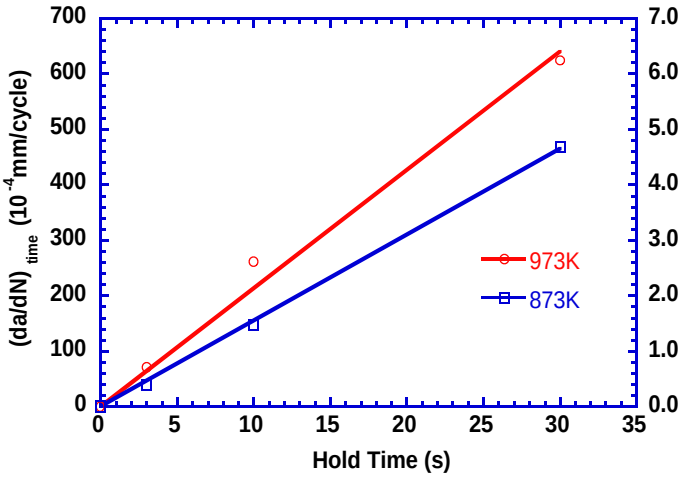

Figure 2: Effect of dwell-time on the time-dependent component of fatigue crack growth rate, $(da/dN)_{time}$, for alloy 3 in oxygen at DK = 27 MPa-m$^{1/2}$ (12,16).

Representative microfractographs of the niobium-free alloy 1 and niobium-containing alloy 3 tested in high-purity oxygen, under sustained load, at 973 K are shown in Fig. 3 (12,17). Cracking in alloy 1 was essentially intergranular and also followed along interfaces between the large (micrometer sized) γ′ precipitates and the matrix, some of which are indicated by the arrows in Fig. 3a. For alloy 3, cracking was predominately intergranular. Many small particles (appearing in white) are seen on the grain boundary surfaces, and were found through energy dispersive spectroscopic (EDS) analyses to be rich in Nb. These particles are consistent with the Nb-rich carbides found previously on the grain boundaries of Inconel 718 (18). The fracture surface morphology for the alloys tested in fatigue paralleled that of sustained loading, and indicated that the micromechanisms for oxygen enhanced crack growth were identical (12,16,17).

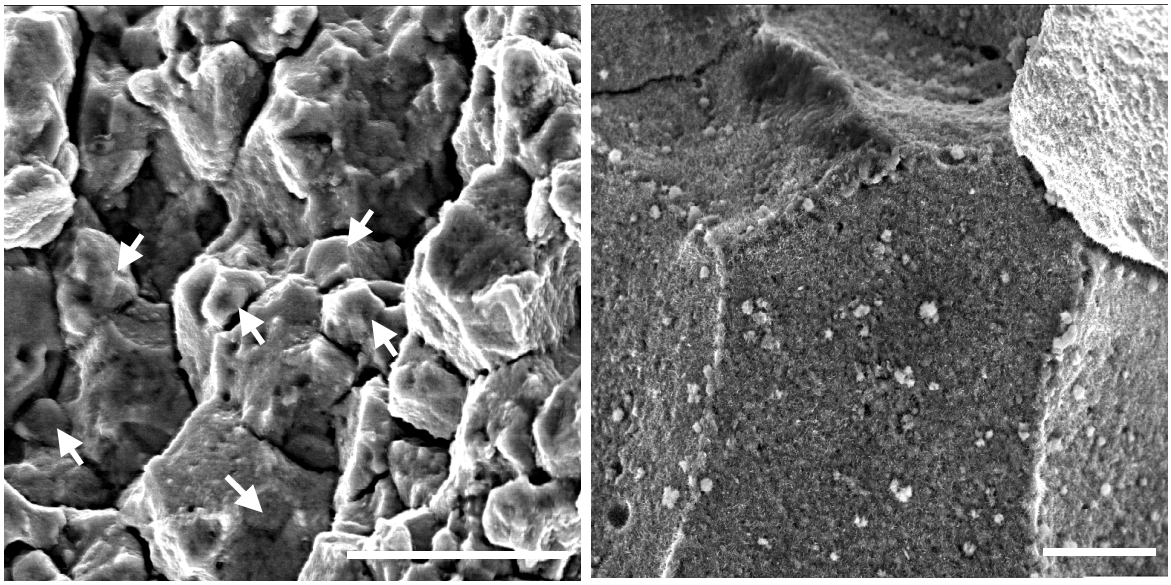

Figure 3: Microfractographs of (a) the Nb-free alloy 1 and (b) the Nb-containing alloy 3 tested in oxygen at 973 K (12,17).

Surface Chemistry Studies

To determine the reactivity of the alloys to oxygen, polished and ion-sputtered surfaces of alloys 1 and 3, as well as Inconel 718, were analyzed by X-ray photoelectron spectroscopy (XPS) in vacuum at 10^{-7} Pa, and following exposure to 5×10^{-4} Pa of oxygen at 873, 923 and 973 K for 2,700 s (14,15). The results suggest that preferential oxidization occurred, even at 10^{-7} Pa, for Al, Cr, Nb and Ti in alloy 3, and for Cr and Nb in Inconel 718.

To provide direct evidence for the reactions of Nb compounds with oxygen, specimens of Nb, Ni_3Nb (with γ″crystal structure) and a specially grown film of NbC were given the same exposure to oxygen at 873, 923

and 973 K and analyzed by XPS (13). Representative spectra for Ni_3Nb and the NbC film at 973 K are shown in Fig. 4 along with the component spectra for Ni_3Nb and NbC and the various oxides that were formed. The results confirm the fact that both Ni_3Nb and NbC react with oxygen at these temperatures to form niobium oxides of ranging stoichiometry, with a greater propensity for Ni_3Nb to oxidize to Nb_2O_5.

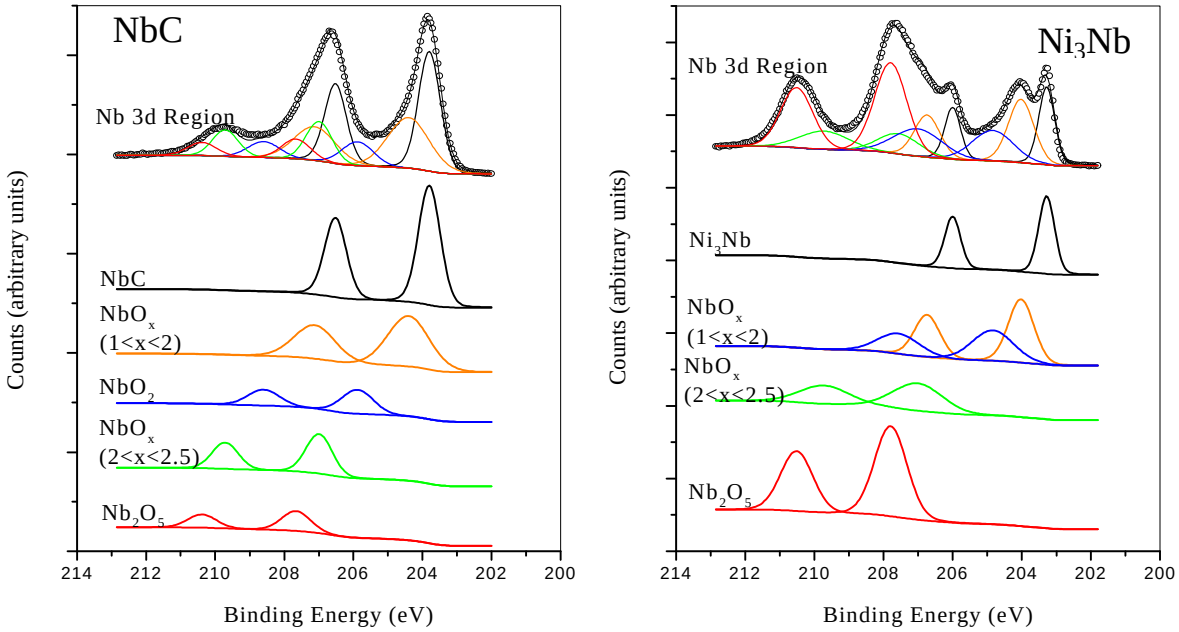

Figure 4: XPS spectra (Nb region: $3d_{3/2,5/2}$) of NbC and Ni_3Nb after oxidation at 973 K in 5 x 10^{-4} Pa of O_2 for 45 minutes (13).

Oxidation Ahead of the Crack Tip

To ascertain the existence of an "oxygen embrittled" zone ahead of the tip of a growing crack, interrupted experiments were carried out whereby sustained-load crack growth in oxygen was stopped. The specimen was partially unloaded and the test chamber was evacuated and back-filled with ultrahigh purity argon, and was then reloaded to the same test load. Representative crack growth response for a specimen of alloy 3 tested at K = 33 MPa-$m^{1/2}$ and 873 K is shown in Fig. 5 (12). The results showed the presence of an embrittled zone of about 80 μm over which the crack growth rate decreased from the pre-interruption rate in oxygen to that for argon. The profile is qualitatively consistent with that of the concentration profile associated with oxygen diffusion.

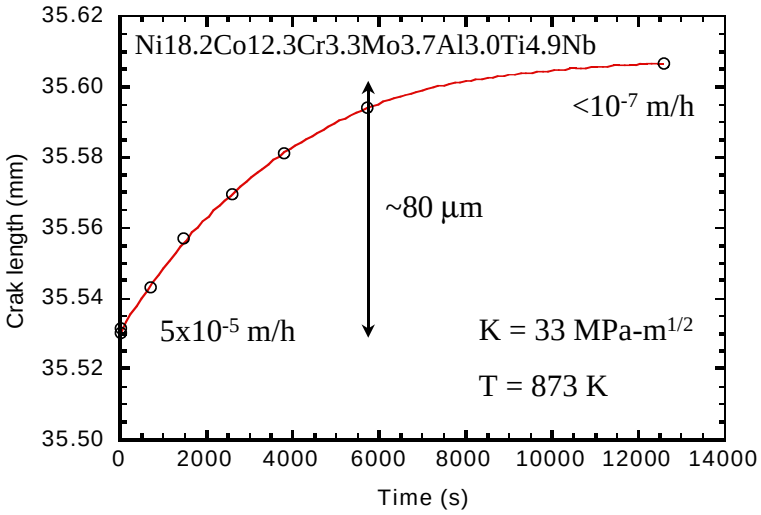

Figure 5: Representative crack growth response for a P/M alloy in ultrahigh purity argon following prior growth in oxygen (12).

To determine which elements might be oxidized ahead of the crack tip, samples containing the crack tip region (at K = 60 MPa-$m^{1/2}$) were cut from interrupted test specimens. They were electrolytically charged with hydrogen, and broken under ultrahigh vacuum and analyzed by XPS. Normalized oxidation profiles across the crack tip, for Inconel 718 and alloy 3, tested in oxygen at 973 K, are shown in Fig. 6. It is clear

that Nb and Cr oxidized ahead of the crack tip in Inconel 718 to an estimated distance of 150 μm, with Nb as the more active element. The finding was the same for alloy 3, except that the extent of reaction was less and the indicated depth of penetration was only about 100 μm. The difference between Inconel 718 and alloy 3 is attributed to the much higher concentration of Al and Ti in alloy 3, which would oxidize ahead of Nb and Cr. Because of instrumental limitations, information on Al and Ti could not be quantified; but oxidation ahead of the crack tip in alloy 3 is expected to extend out to 150 μm as well. Equally significant is the fact that there was no evidence for Fe and Ni oxidation ahead of the crack tip.

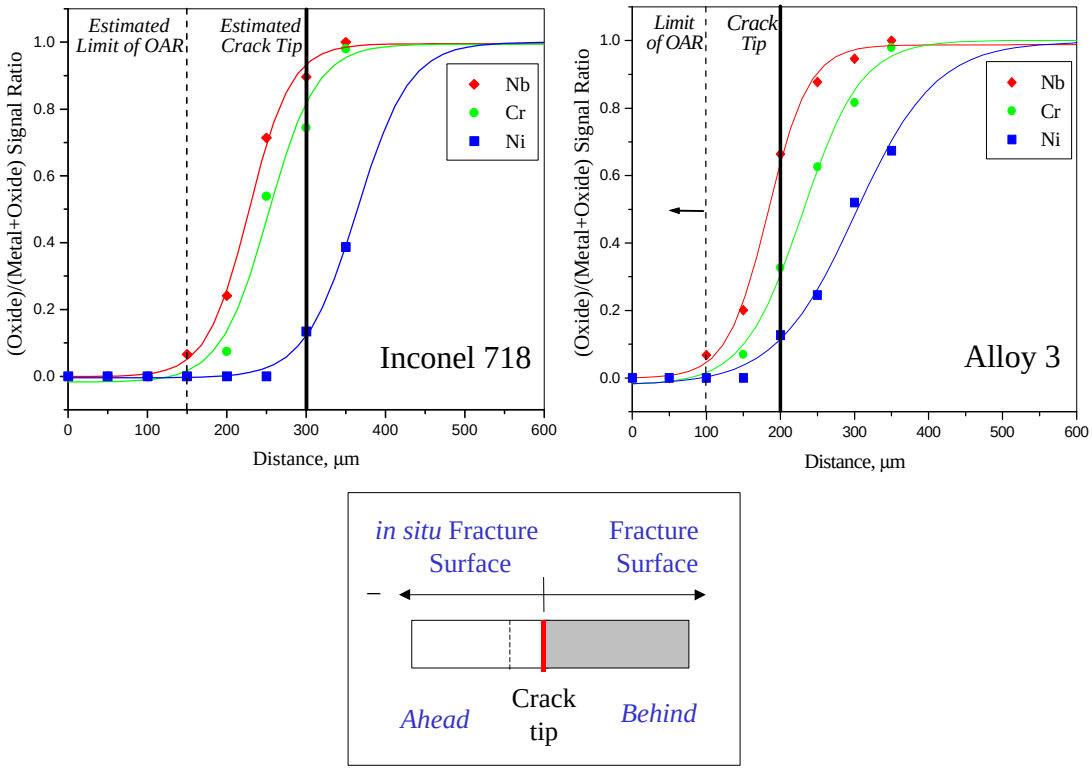

Figure 6. Normalized oxidation profile showing the oxide formation for Nb, Cr, and Ni on Inconel 718 fracture surfaces vs. distance (μm), and the estimated boundaries of the oxygen affected region (OAR).

MECHANISMS FOR OXYGEN ENHANCED CRACK GROWTH

These results confirmed the postulated role of niobium in enhancing the rate of crack growth in oxygen at high temperatures. The enhancement mechanism is the oxidation and decomposition of niobium rich carbides at the grain boundaries to form a brittle film of Nb_2O_5-type oxides on the boundary surfaces. The fact that these alloys were designed to suppress the formation of γ″-Ni_3Nb precipitates reinforces the role of niobium rich carbides as a source of Nb for embrittlement. The XPS results on the reactions of oxygen with Ni_3Nb, however, showed that Nb was preferentially oxidized over Ni, and that the reactions were more rapid than those with NbC. The Ni_3Nb precipitates, therefore, also play a significant role in the enhancement of crack growth in the γ″ strengthened alloys, such as Inconel 718. In the absence of Nb (*e.g.*, alloy 1), the oxidation of Al and Ti appears to be the cause for enhanced crack growth, and the site of "embrittlement has been identified with the γ-γ′ interfaces. The fact that results indicate that Ni and Fe do not oxidize ahead of the crack tip suggests that the mechanisms involving the oxidation of these elements may not be viable. Although Cr oxidizes, the absence of environmental sensitivity in the Ni-Cr-Fe ternary alloy suggests that it is also not a player. The observed environmental sensitivity, particularly to Nb, indicates that the embrittlement process involved oxidation, and suggests that oxygen adsorption *per se* is not a viable mechanism. The results were integrated and compared with available data on other superalloys. The role and contribution of the various phases were interpreted with the aid of a superposition model for crack growth (18); namely, between the niobium-rich carbides and the γ″ precipitates in Inconel 718, and between these carbides and γ′ precipitates in the P/M alloys (alloys 1, 2 and 3).

SUMMARY

As a part of a study to elucidate the role of niobium on crack growth in oxygen at high temperatures, crack growth experiments and microstructural analyses were carried out on three γ' strengthened powder metallurgy (P/M) alloys, with 0, 2.5 and 5 wt. pct. niobium. Companion surface chemistry studies of the oxidation of Nb, Ni_3Nb and NbC were also conducted. The results were integrated and compared with available data on other superalloys, and were interpreted with the aid of a superposition model for crack growth. The results indicate that niobium contributed significantly to the enhancement of crack growth by oxygen in both γ' and γ'' strengthened alloys. They support the previous suggested mechanism of oxidation and decomposition of Nb-rich carbides at the grain boundaries. For the Nb-free, γ' strengthened alloys, crack growth enhancement is attributed to the oxidation of Al and Ti (*versus* Cr, Fe and Ni) and is correlated with the volume fractions of fine and coarse γ' precipitates.

ACKNOWLEDGEMENT

The authors gratefully acknowledge the support of this research by the Division of Materials Research of the National Science Foundation, under Grant DMR-9632994, and the technical assistance and insightful discussions by Paul Reynolds of Pratt Whitney on the metallurgy of nickel-based superalloys, and by Alfred Miller of Lehigh University on x-ray photoelectron spectroscopy. CM also wishes to acknowledge the support of a NSF IGERT Traineeship during academic year 2000-01under Grant DGE-9987548.

REFERENCES

1. Floreen, S. and Raj, R. (1984). In: *Flow and Fracture at Elevated Temperatures*, pp. 383-405, Raj, R. (Ed.). Am. Soc. Metals, Metals Park, OH.
2. Woodford, D.A. and Bricknell, R.H. (1982) *Acta Met.* 30, 257.
3. Gabrielli, F. and Pelloux, R.M. (1982) *Met. Trans. A* 13A, 1083.
4. Bain, K.R. and Pelloux, R.M. (1984). In *Proc. of Conf. on Superalloys*, pp. 387-396. The Metall. Soc./AIME, Warrendale, PA.
5. Bain, K.R. and Pelloux, R.M (1984) *Met. Trans. A* 15A, 381.
6. Andrieu, E., Ghonem, H. and Pineau, A. (1991). *Elevated Temperature Crack Growth*, (Paper presented at the ASME Winter Annual Meeting, 25-30 November, 1990, Dallas, TX 1991), 25.
7. Lynch, S.P., et al. (1994) *Fatigue Fract. Engr. Mater. Struct.* 17, 297.
8. Gao, M. Dwyer, D.J. and Wei, R.P. (1995) In: *Superalloys 718, 625, 706 and Various Derivatives*, pp. 581-592 E.A. Loria, (Ed.). The Minerals, Metals & Materials Society, Warrendale, PA.
9. Gao, M., Dwyer, D.J. and Wei, R.P. (1995) *Scripta Met. et Mater*. 32, 1169.
10. Dwyer, D.J., Gao M.and Wei, R.P (1994), *Applied Surface Sci*. 81, 229.
11. Chen, S.F. and Wei, R.P. (1998) *Matls Sci. & Engr*. A256, 197.
12. Huang, Z.F., (2001) Ph.D. Dissertation, Lehigh University, Bethlehem, PA.
13. Miller, C.F., Simmons, G.W. and Wei, R.P. (2000) *Scripta Mater*. 42, 227.
14. Miller, C.F., Simmons, G.W. and Wei, R.P. (2001), *Scripta Mater*. 44, 2405.
15. Miller, C.F., (2001) Ph.D. Dissertation, Lehigh University Bethlehem, PA.
16. Wei, R.P. and Huang, Z.F. "Influence of Dwell-Time on Fatigue Crack Growth in Nickel-Base Superalloys", submitted to *Materials Sci. & Engr*.
17. Wei, R.P. (2000). In: *Advanced Technologies for Superalloy Affordability*, pp. 103-112 K.M. Chang, S.K. Srivastava, D.U. Furrer and K.R. Bain (Eds.). The Minerals, Metals & Materials Society, Warrendale, PA.
18. Gao, M. and Wei, R.P. (November 1997) *Scripta Mater.* 37(12), 1843.

PARTICULATE TOUGHENING OF UNSATURATED POLYESTER: EFFECT OF PARTICLE SIZE AND VOLUME FRACTION

Raman P. Singh

Department of Mechanical Engineering, State University of New York
Stony Brook, NY 11794.

ABSTRACT

Micron- and nanometer-sized aluminum particles were used as reinforcements to enhance the fracture toughness of a highly-crosslinked, nominally brittle, thermosetting unsaturated polyester resin. Both particle size and particle volume fraction were systematically varied to investigate their effects on the fracture behavior and the fracture toughness. It was observed that, in general, the overall fracture toughness increased monotonically with the volume fraction of aluminum particles, for a given particle size, provided particle dispersion and deagglomeration was maintained. The fracture toughness of the composite was also strongly influenced by the size of the reinforcement particles. Smaller particles led to a greater increase in fracture toughness for a given particle volume fraction. Scanning electron microscopy of the fracture surfaces was employed to establish crack front trapping as the primary extrinsic toughening mechanism.

KEYWORDS

Fracture, nanocomposite, particulate reinforcement, thermosetting polymer, crack trapping.

INTRODUCTION

Thermosetting polymers, such as epoxy resins and polyesters, are used extensively as adhesives, potting and encapsulating materials, tooling compounds, and as matrix materials for reinforced composites. These polymers exhibit a very high degree of cross-linking between the individual polymer chains, which results in many useful properties including high specific strength, high stiffness, dimensional stability at elevated temperature, and good solvent resistance. Unfortunately, this cross-linking also makes these materials inherently brittle with poor resistance to crack initiation and propagation, in comparison to other engineering plastics.

Improving the fracture toughness of thermosetting resins has been the subject of considerable research. However, the conventional approach of introducing micron-sized particles (elastomeric, thermoplastic or ceramic) into the polymer matrix has failed to yield significant improvements in the fracture toughness of highly cross-linked thermosetting polymers. Furthermore, other mechanical properties are often compromised, or there are processing problems.

Recent research indicates that the dispersion of *sub-micrometer* and *nanometer* sized inorganic particles

presents a viable alternative for improving the mechanical properties of polymers. Such materials, which include polymer nanocomposites, have the potential for significantly enhanced and unique properties as compared to polymers reinforced with conventional microscale fillers [1].

Nanoscale reinforcements in thermoplastic and thermosetting polymers are formed either as inorganic-organic hybrids [2, 3], or as intercalated/exfoliated polymer-silicate structures [4-6]. These materials can exhibit substantial enhancements in the modulus, yield strength and heat resistance of the polymer. While these studies have not focused on fracture toughness as the primary issue, there are clear indications that reducing the size of reinforcement particles could lead to significant improvements in fracture toughness and resistance to crack growth. Despite these observations there is limited fundamental information regarding the effects of reinforcement size on fracture processes, toughening mechanisms and the resulting overall fracture toughness.

This investigation addresses these issues and presents a systematic characterization of the fracture behavior of a highly cross-linked thermosetting polymer reinforced with high-modulus inorganic particles, as a function of particle size and particle volume fraction. Such an understanding is essential for identifying parameters that will lead to the design and fabrication of optimally toughened thermosetting polymers.

SPECIMEN FABRICATION

Composite materials were fabricated by incorporating aluminum particles in MR 10790 unsaturated polyester resin at different volume fractions. Reinforcement quantities of interest were 1%, 2%, 5% and 10% of the particles by weight, which resulted in volume fractions of 0.5%, 0.9%, 2.3% and 4.4%, respectively. Three distinct sizes of aluminum particles were used: 100 nm, 3.5μm and 20 μm. A direct mixing approach was used to provide flexibility in exercising independent control over reinforcement material and reinforcement geometry (size, morphology and size distribution) [7]. Tables 1 and 2 provide details for the polyester resin and aluminum particles.

TABLE 1
PROPERTIES OF THE MR 10790 POLYESTER RESIN

Polymer	MR 10790 Polyester Resin
Curing Agents	Methyl Ethyl Ketone Peroxide (0.85% pph) Cobalt Octoate (0.03% pph)
Curing Cycle	48 hrs at 25°C; 4 hrs at 52°C; 5 hrs at 63°C
Young's Modulus	3.25 GPa
Fracture Toughness	0.64 $MPa.m^{½}$
Density	1160 kg/m^3

TABLE 2
PROPERTIES OF ALUMINUM PARTICLES

Property	Aluminum A	Aluminum B	Aluminum C
Nominal Diameter	20 μm	3.5 μm	100 nm
Diameter Range	17-23 μm	3-4.5 μm	100 nm
Young's Modulus	70 GPa	70 GPa	70 GPa
Fracture Toughness	30 $MPa.m^{½}$	30 $MPa.m^{½}$	30 $MPa.m^{½}$
Density	2699 kg/m^3	2699 kg/m^3	2699 kg/m^3

FRACTURE TESTING

Three-point-bend single-edge-notched (3PB-SEN) fracture specimens were machined from the cast polyester sheets for testing. The specimens had a nominal length, *L*, of 55.9 mm, a height, *W*, of 12.7 mm and a thickness, *B*, of 6.35 mm, as shown in Figure 1. A 4.25 mm deep notch was first cut into the center of the specimen using a diamond saw. A fresh razor blade was then tapped into the cut with a hammer to create a naturally sharp crack. The actual length of the overall crack, *a*, was measured after the fracture experiment by observation in an optical microscope equipped with a micrometer stage. All the specimens used for valid fracture tests had a nominal crack length to specimen width ratio, *a/W*, of ~ 0.5, as per ASTM standard 5045 [8].

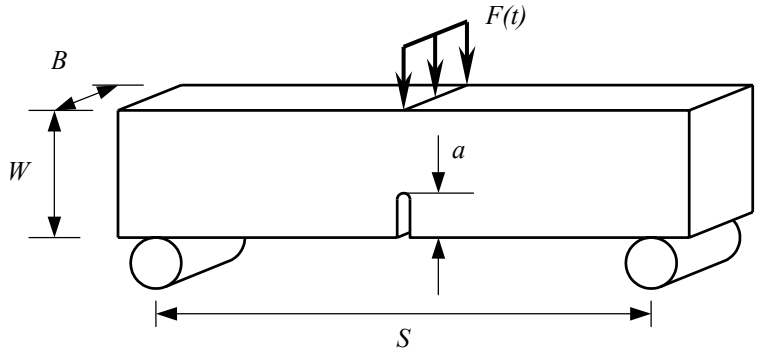

Figure 1: Three-point bend fracture specimen

The quasi-static fracture toughness of the polyester-aluminum composites was measured as a function of particle size and particle volume fraction. Single-edge-notched fracture specimens were loaded quasi-statically under three-point-bending until the initiation of fracture. The specimens were loaded in a displacement-controlled mode and the crosshead speed was fixed at 5 mm/minute to keep the loading rate constant. The maximum applied load at the point of failure was measured using a 500 N load-cell and then used to quantify the quasi-static fracture toughness of the composite being tested.

The mode-I stress intensity factor was determined from these measurements as per Eqn. 1 [9].

$$K_I(t) = \frac{3S\sqrt{a}}{2BW^2} Y\left(\frac{a}{W}\right) F_{\max} \tag{1}$$

Where, $F_{\max}$ is the force required for fracture, *B* is the specimen thickness, *W* is the specimen width, *S* is the span, *a* is the crack length and *Y* is a geometry factor [10].

Figure 2 shows the variation of composite fracture toughness as a function of the volume fraction of 20 μm, 3.5 μm, and 100 nm aluminum particles added to the polyester resin. For the case of 20 μm and 3.5 μm particles the fracture toughness of the polyester-aluminum composite increased monotonically with the volume fraction of aluminum particles. However, the relative increase in fracture toughness was significantly greater for reinforcement by 3.5 μm particles as compared to that observed for reinforcement by 20 μm particles. For reinforcement by 4.4% volume fraction of 3.5 μm aluminum particles the fracture toughness increased by 51%, which is more than twice the increase observed using 20 μm particles. When the size of the reinforcement aluminum particles was further decreased to 100 nm a different trend was observed, also shown in Figure 2. For this case the fracture toughness increased rapidly till a particle volume fraction of 2.3%. As the particle volume fraction was increased further the fracture toughness registered a sharp decrease. Thus, from Figure 2 it is evident that fracture toughness is strongly governed by the size of the reinforcement particles. Smaller particles lead to a greater increase in the overall fracture toughness for a given volume fraction. This trend is not observed only for the case of reinforcement by 100 nm aluminum particles in volume fractions greater than 2.3%.

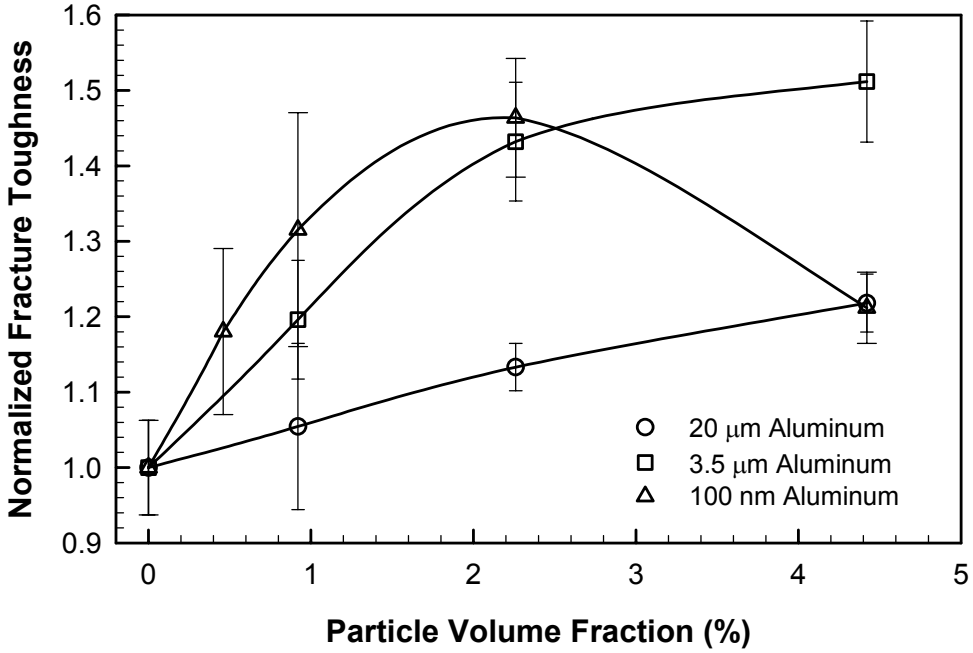

Figure 2: Effect of particle size and volume fraction of the fracture toughness of polyester resin reinforced with aluminum particles

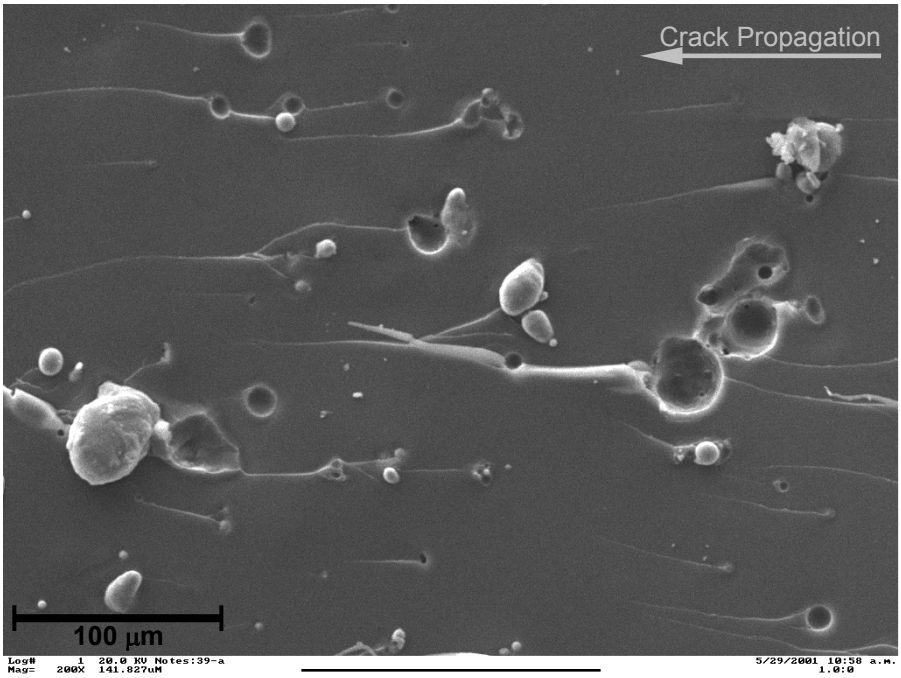

Figure 3: Fracture surface of polyester resin reinforced with 20 μm aluminum particles

Microscopic observations of the fracture surfaces were carried out using scanning electron microscopy (SEM) to characterize the interaction of the crack with the reinforcing particles and identify the extrinsic toughening mechanisms. Figure 3 shows an SEM micrograph of the fracture surface for polyester reinforced with 20 μm aluminum particles. The fracture surface showed evidence of crack front trapping [11] in the form of steps, or 'fracture tails', that emanated from the reinforcing particles along the direction of crack growth. Besides the formation of these steps, the fracture surface was fairly flat, which indicated that crack path deflection did not occur. Moreover, the aluminum particles appeared to be debonded from the polyester matrix and did not show any evidence of particle yielding and deformation. Thus, extensive crack face bridging did not occur either. Finally, microcracking of the polyester matrix was also not observed. In this manner, crack front trapping was established to be the primary extrinsic mechanism responsible for the increase in fracture toughness of polyester reinforced with 20 μm aluminum particles. These observations

were made for all particle volume fractions that were investigated. Similar observations were made using scanning electron microscopy of the fracture surface of polyester reinforced with 3.5 μm particles and crack front trapping was again identified as the primary toughening mechanism.

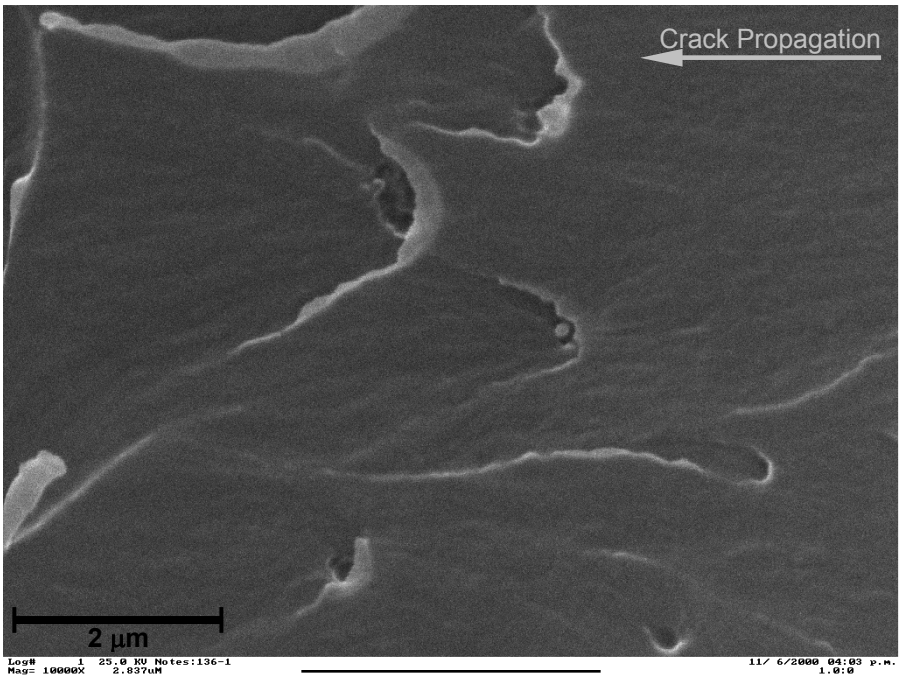

Figure 4: Fracture surface of polyester resin reinforced with 100 nm aluminum particles

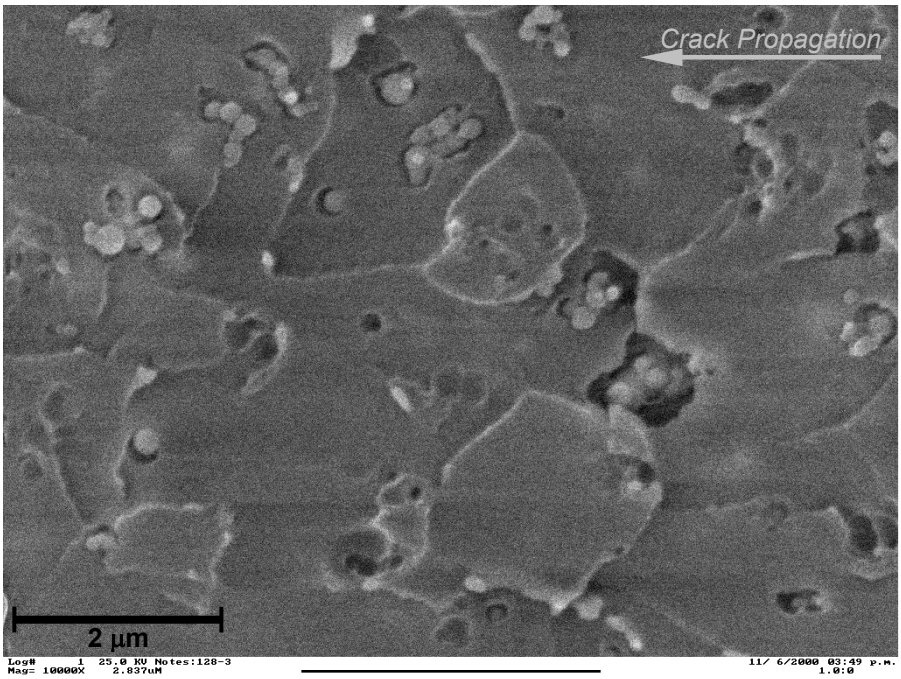

Figure 5: Fracture surface of polyester reinforced with 100 nm aluminum particles showing agglomeration

For the case of reinforcement by 100 nm aluminum particles fracture mechanisms were found to be dependent on particle volume fraction. For the case of low volume fractions (≤2.3%) the particles were uniformly distributed and contributed to crack front trapping, as shown in Figure 4. The fracture surface exhibited features similar to those observed for the case of 20 μm and 3.5 μm aluminum particles. In contrast, when the particle volume fraction was greater than 2.3%, the fracture surface exhibited marked differences, as shown in Figure 5. In this case, the aluminum particles tended to clump together and form agglomerates. These particle clusters inhibited proper wet-out, promoted the trapping of air and led to the

formation of voided spaces, which acted as damage initiation sites. As a result, the fracture surface appeared to be 'flaky' and no evidence of crack trapping was observed.

These observations of the fracture surfaces were consistent with the quantitative measurements of fracture toughness. Aluminum particles in the polyester matrix led to crack front trapping and hence an increase in the overall fracture toughness. This was observed for all the three sizes of aluminum particles except for greater volume fractions (≥2.3%) of 100 nm particles. In this case, the particles tended to agglomerate and were unable to promote crack trapping. The formation of these small agglomerates, at volume fractions greater than 2.3%, occurred despite the use of ultrasonic disruption. Thus, alternate chemical and/or mechanical treatments would be required to further disperse and deagglomerate 100 nm particles, which would probably lead to an enhancement in the overall fracture toughness.

SUMMARY

This investigation focused on the toughening of a highly cross-linked thermosetting unsaturated polyester by the incorporation of micron and nanometer sized aluminum particles. The effects of reinforcement particle size and particle volume fraction on the overall toughness and fracture behavior of polyester-aluminum composites was investigated by systematically varying the size (20 μm, 3.5 μm, 100 nm) and volume fraction (0.9%, 2.3%, 4.4%, 8.5%) of the aluminum particles. From experimental observations it was established that the enhancement of fracture toughness is strongly influenced by both these parameters. In general the fracture toughness increased monotonically with the volume fraction of aluminum particles, for a given particle size. Furthermore, it was observed that the increase in fracture toughness was significantly greater for smaller particles, for a given particle volume fraction.

Crack front trapping was established as the primary extrinsic toughening mechanism by conducting scanning electron microscopy of the fracture surfaces. It was observed that it is essential to maintain uniform particle dispersion and deagglomeration, and proper particle wet-out in order to ensure that the reinforcement particle promote crack trapping. While ultrasonic disruption has been found to be very effective in preventing the formation of large agglomerates [7], further chemical and/or mechanical treatments would be required to disperse and deagglomerate 100 nm aluminum particles at volume fractions greater than 2.3%.

ACKNOWLEDGEMENTS

The author gratefully acknowledges the Ashland Chemical Company for supplying the polyester resin.

REFERENCES

[1]. Gleiter, H. (2000) *Acta Mat.* 48, 1.
[2]. Novak, B.M. (1993) *Adv. Mater.*. 5, 422.
[3]. Mark, J.E. (1996) *Poly. Eng. Sci.* 36, 2905.
[4]. Okada, A., Kawasumi, M., Kurauchi, T. and Kamigaito, O. (1987) *Abstr. Pap. Am. Chem. Soc.* 194.
[5]. Giannelis, E.P. (1998) *Appl. Organometal. Chem.*12, 675.
[6]. LeBaron, P.C., Wang, Z. and Pinnavaia, T.J. (1999) *Appl. Clay Sci.* 15, 11.
[7]. Singh, R.P., Zhang, M. and Chan, D. (2001) *J. Mat. Sci.* In Press.
[8]. ASTM Designation D5045-99, (1999) *Annual Book of ASTM Standards*.
[9]. Anderson, T. L., Fracture Mechanics: Fundamentals and Applications. CRC Press. Inc. 1991.
[10]. Srawley, J. E., (1976) *Int. J. Fract.* 12, 475.
[11]. Lange, F. F., *Philos. Magazine*, Vol. 22, pp. 983, 1970.

POSTER REFERENCE : ICF100394PR

PLANE STRESS AND PLANE STRAIN IN SIDE-GROOVED CCT-SPECIMENS

Kees van Kranenburg[(1)(*)], Ton Riemslag[(1)], Saskia Benedictus-de Vries[(3)], Jan Zuidema[(1)] and Fred Veer[(2)]

[(1)] Laboratory of Materials Science, Delft University of Technology
[(2)] Faculty of Architecture, Delft University of Technology
[(3)] Netherlands Institute for Metals Research

ABSTRACT

To model the behavior of plasticity induced crack closure it is in the first place necessary to measure this behavior and then to manipulate and simulate this behavior.
The possibility of keeping a CCT specimen in plane strain during a CA experiment by implementing side-grooves has been investigated. If crack closure is caused by early contact of the crack flanks, a shift in the da/dN versus ΔK graph at different R-values in relation to tests without side grooves is expected. Putting side-grooves over the full width of the specimen did not result in an effect on the crack growth rate. However, side-grooves suppresses the development of shear lips. A series of experiments on specimens with varying length of side grooves shows that the development of shear lips is suppressed over the length of the side groove. After the side groove the shear lips develops quickly until full shear is achieved.

KEYWORDS

Crack closure, plane stress, plane strain, side-grooves

INTRODUCTION

Crack closure, caused by contact of the crack surfaces before zero load is reached is one of the causes of crack growth retardation. To model crack closure it is necessary to be able to measure it. A first step to measure crack closure is conducting tests on specimens where as much as possible closure is prevented. This can be achieved in a situation where plane strain dominates over plane stress. It is possible to create a dominant plain strain situation by:

- using thick specimens; in this case there is little plane stress related to plane strain.
- Introducing side-grooves that prevent deformation in the flanks and thus diminish the plane stress portion. This leads to a plane strain situation.

Schematically:

In the scheme in figure 1 a shift to the right of the Fatigue Crack Growth Rate Curves for decreasing R-values is observed. This shift is generally accepted as a result of crack closure. The closure effect is caused by plastic deformation and thus maximum in the plane stress flanks of the specimen. Except in very thin specimens both plane strain and plane stress are present.

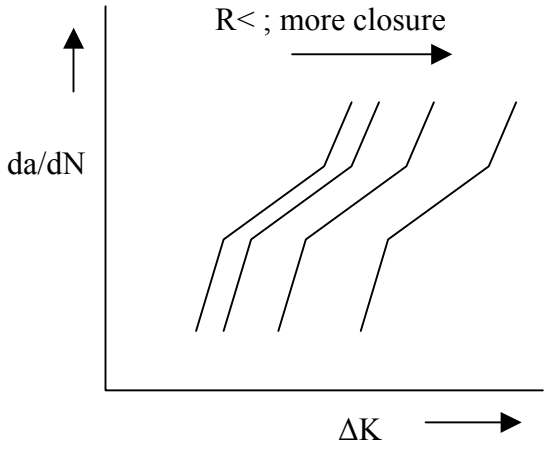

Figure 1: Different R's

Side-grooves:
By introducing side-grooves in CCT - specimens a predominantly plane strain situation is created because deformation in the flanks is prevented. This means that plasticity induced closure is avoided. In the da/dN-ΔK scheme a shift of the curves would be expected to the left, as shown in figure 2, in the direction of high R-values with a relatively low closure level.

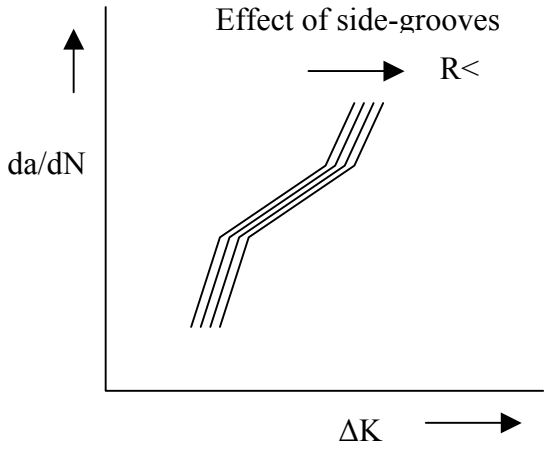

Figure 2: Scheme R's with side-grooves

EXPERIMENTAL DETAILS

Experiments have been conducted on AA5083. The material data is in table I

TABLE I
MATERIAL DATA (wt%) AA 5083 H-321

AA	Al	Fe	Si	Cr	Mg	Ti	Cu	Mn	Zn	other
5083	94.1	0.22	0.26	0.1	4.5	0.03	0.09	0.65	0.06	<0.05

Below an overview of the different geometry's that have been used :

Geometry's: (normal thickness 8 mm)

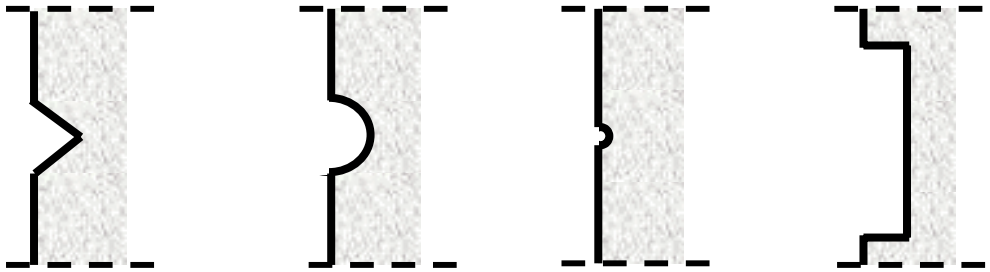

A B C D

A: Sharp groove, effective cross-section plate 6 mm
B: *Rounded groove* with a depth of 1 mm.
C: *Very small scratch*, 0.1 mm
D: *Reference*: milled back till 6 mm

The cracklength has been measured using the pulsed direct current potential drop technique. First, the different geometry's were calibrated using this technique. Subsequently the specimens are fatigued to failure by CA tests in laboratory air for different load ratios at a frequency of 10 Hz. For specific load data see Table II.
Initially the side grooves were created by milling on the full width of the specimens.
With geometry C more experiments are done with scratches along the full width, in the crack growth direction; scratches on one side and on the other side with a varying lengths of 0, 20 and 30 mm.
Data is analyzed using the procedures given in ASTM 647 [1]

TABLE II
LOADS

R	P-max	Freq (Hz)
0.7	83.5	10
0.5	35	10
0.1	35	10

RESULTS

First place the effect of the difference in geometry's A-D has to be analyzed. Figure 3 shows a da/dN-ΔK plot for different geometry's at a load ratio of 0.5. The two extremes: right in the graph is the result of geometry D; on the left the result of geometry B. The difference in geometry has only a marginal effect on the da/dN-ΔK results. For all the different geometry's tunneling occurs. In geometry B the crack front at the flanks lags behind to the rest resulting in a convex crack front. For a sharp groove this effect is opposite, a concave crack front is obtained. In none of the specimens with side grooves shear lips are formed.[2]

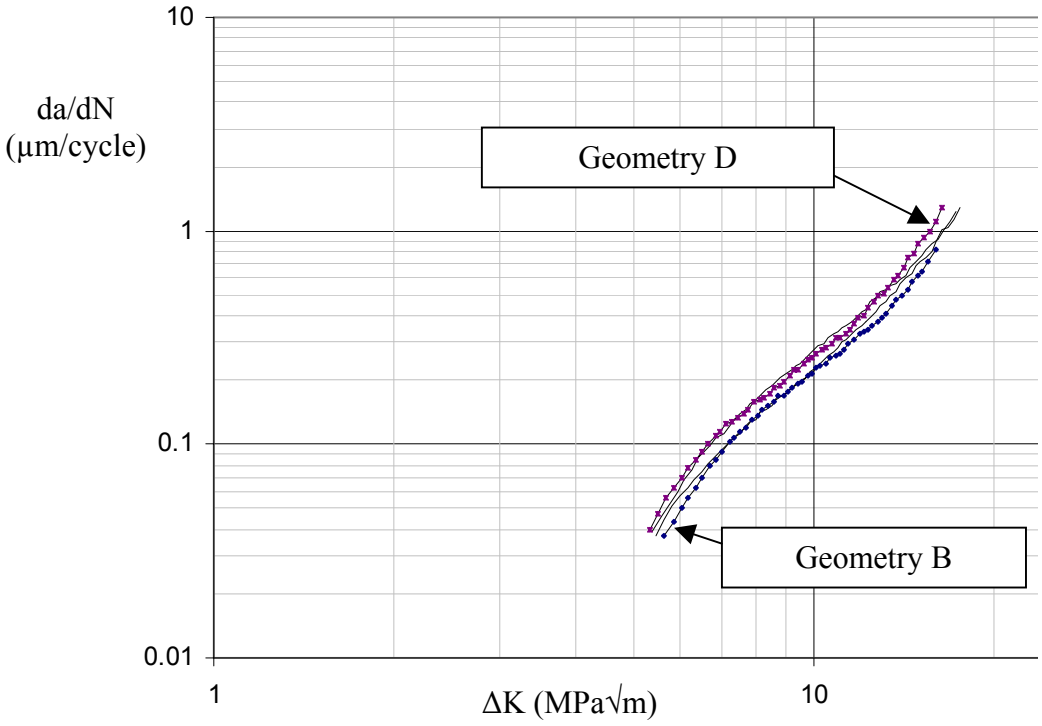

Figure 3: R=0.5 with different geometry's.

A. Hascariantono [3] found that in AA 5084 material the crack growth rates for R=0.5 and 0.7 are the same, suggesting the absence of crack closure. In figure 4 the results of tests at these load ratios *with* and *without* side-grooves are compared.

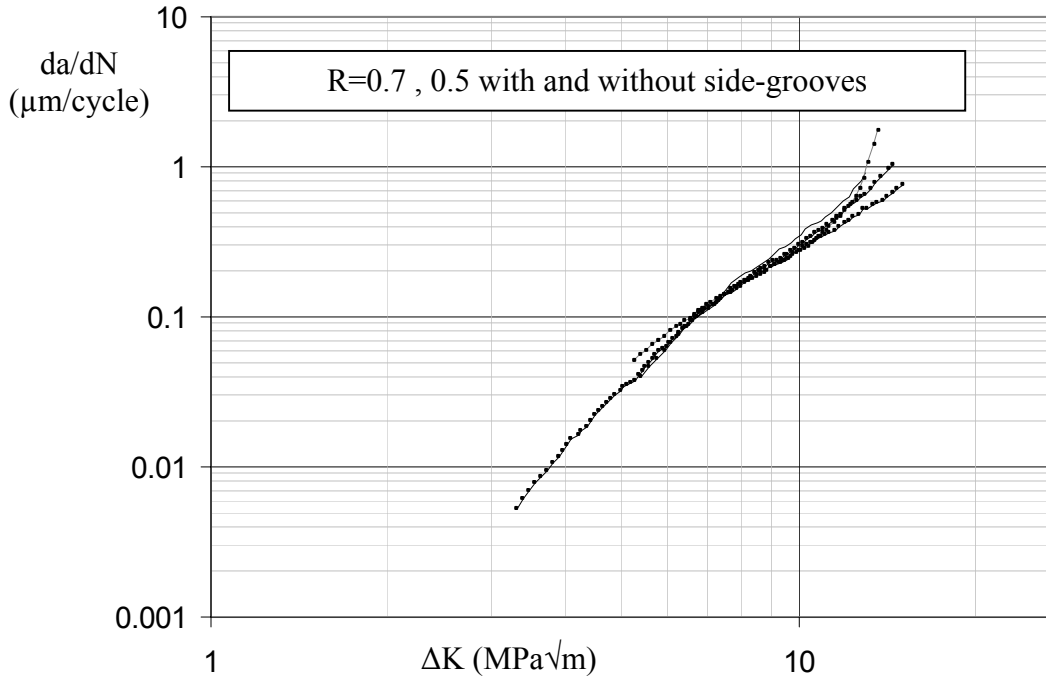

Figure 4 : R-values, no closure, without closure, with and without side-grooves

The results in figure 4 for different R-values and different geometry's show that there is no significant effect on the crack growth rate.
Finally the results at R=0.5, 0.7 (no closure) and R=0.1 (with closure) [1] are compared to R=0.1 *with* side grooves.

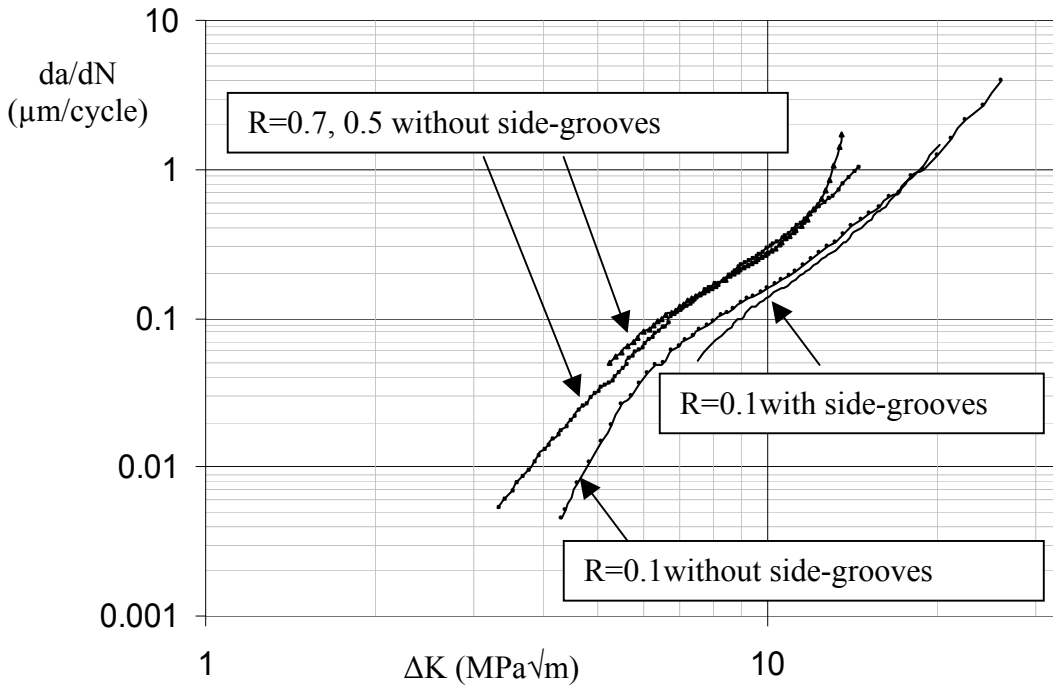

Figure 5: R's with and without side-grooves

The crack growth rates between specimens with and without side-grooves, even for R=0.1 show no significant differences. Thus introducing sidegrooves does not have the effect that we had in mind, namely changing the crack closure situation.

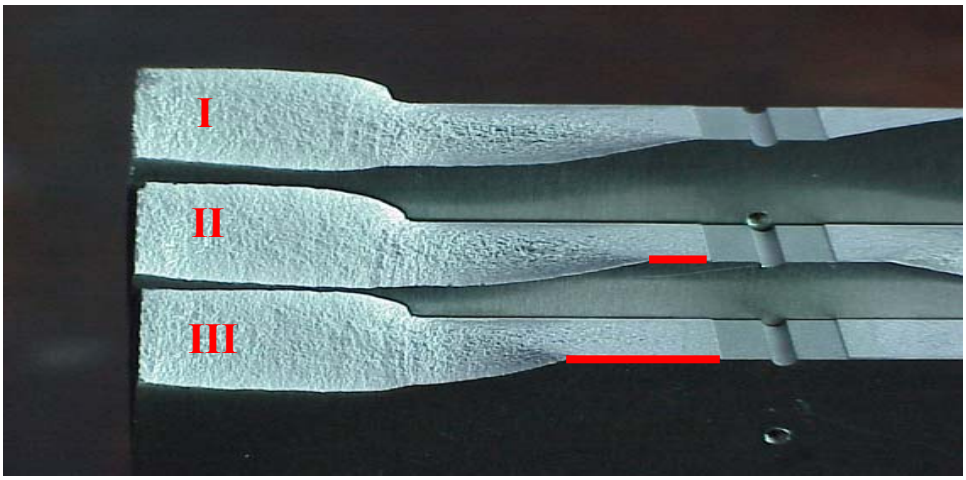

Figure 6: Geometry C with side grooves of varying length.

Figure 6 shows the results of three specimens of geometry C. They have been fatigued at a load ratio of 0.1 using a maximum load of P_{max}=95 kN. At one side the sidegroove is put on the full width, on the other side only partly.
At specimen I there is only one scratch on one side; on specimens II and III there are also scratches on the other side with a total length of 20 and 30 mm respectively. At specimen I shear lips develop immediately at one side. The other side remains smooth and follows the scratch, because sidegrooves prevent the development of shear lips. The *longer* the side groove gets (II and III), the faster the shear lip develops. At specimen III the shear lip grows in a relatively *very short* distance to full width. Despite the difference in the specimens, de crack growth rates are equal for all specimens.

CONCLUSIONS AND DISCUSSION

- For the results of the different side grooves no measurable difference in crack growth is observed in relation to the situations without sidegrooves. So the closure effect is not abolished.
- Different geometry's influence tunneling: a sharp side groove supports initiation of the crack in the flanks.
- Side grooves prevent the development of shear lips. Because there is only a marginal difference in crack growth rate with or without shear lips, the development of shear lips might not affect the crack growth rate.
- Side grooves force the crack in a certain direction. This is best seen with the rounded groove (geometry B). The crack tries repeatedly to grow *out* of the groove, but is redirected by the groove.

REFERENCES

1 ASTM E 647, (1999)Standard test method for measurement of fatigue crack growth rates, ASTM, Philidelphia, PA, USA

2 F.A. Veer, J. Zuidema, C. van Kranenburg et.al.(2000)
Onderzoek naar Crack-closure bij vermoeiing van aluminium 5083
Materiaalkunde TU Delft, in Dutch

3 J. Zuidema, S. de Vries, Adirakhmantyo P. Hascariantono (Sept 2000)
The accelerrated ΔK fatigue crack growth test on AA 5083-H321 and similitude validation.
The 13th European Conference on Fracture Fracture Mechanics, pag 94
San Sebastian, Spain

PLASTIC AND BUCKLING BEHAVIORS OF TUBULAR BEAMS UNDER COMBINED BENDING AND TORSION

G. H. Nie, R. Shi and R.J. Zhang

Key Laboratory of Solid Mechanics of MOE, Department of Engineering Mechanics,
Tongji University, Shanghai 200092, P.R. China

ABSTRACT

This paper presents theoretical, numerical and experimental analyses on plastic collapse and buckling behaviors of tubular cantilever beams under combined bending and torsion. A special set-up is designed and used to carry out experimental analysis for different ratios of bending and torsion (M/T=infinity, 2,4/3,1,0, respectively). All of tubular beam specimens are metal tubes of outer diameter 50mm and wall thickness 1.5mm. A concentrated force causes the combined load, and changing the torque arm thus induces various twisting moments. The two characteristic relations between the force and the transverse displacement at the free end (tip deflection), and between twisting moment and corresponding angle of twist have been measured. Local buckling occurring around the root of beam has been observed. On the other hand, based on the principle of complementary energy, a beam-model is proposed and applied to acquire the corresponding characteristic relations which are correlative to a load parameter (i.e. ratio of bending and torsion). Meanwhile, finite element method is used and a four-node shell-type element is chosen to predict buckling modes of the tubular beams. The computational results are compared with that of theoretical model and experimental data. Finally, some discussions on resulting errors are also given.

KEYWORDS

Tubular beams, bending and torsion, plasticity, buckling.

INTRODUCTION

Recently tubular beams or thin-walled circular tubes have been widely used in pipe networks, offshore and bridge structures. Compared with behaviors of solid cross-sectional beams, tubular beams show very different behaviors. For example, for tubular beams under bending [1,2], there will be cross-sectional flattening or ovalization, and local kinks occurring on the compression side. These phenomena can not be observed in the beams with solid cross-sections. For tubular beams under combined bending and twisting

[3,4], the elastic and plastic behaviors have been studied. It appears that there exists little work on plastic collapse and buckling behaviors of thin-walled circular tubes.

The present work presents plastic and buckling behaviors of tubular cantilever beams under combined bending and torsion. Experimental analysis for different ratios of bending and torsion has been performed. Observations on deformations and buckling are illustrated and experimental data are compared with the results by both finite element method and a simple beam model.

EXPERIMENTS

Material Properties

All tubular specimens are circular, metallic tubes of outer diameter 50mm and wall thickness 1.5mm. The stress-strain relation is obtained from tension test, as shown in Figure1.

A Designed Special Set-up

Figure 2 display a special set-up designed for combined bending and twisting. The length of tubular beam is 240mm, its one end is clamped in a supporting block mounted onto the base of the testing machine while the other end is connected to a rigid torque arm of length 360mm. A concentrated force causes the combined load, and changing the torque arm thus induces various twisting moments.

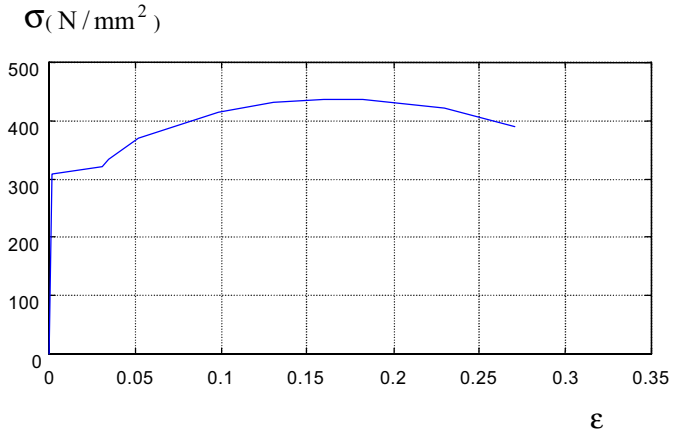

Figure 1: The stress-strain relation

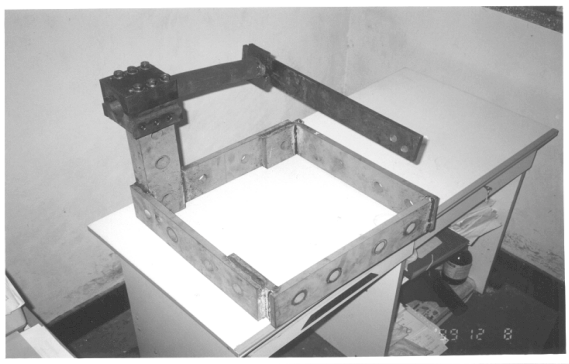

Figure 2: A designed set-up for experiment

Experimental Results

The curves for the concentrated force (P) and vertical displacement (δ), and twisting moment (T) and angle (φ) with the axis of the tube are illustrated in Figures 3 and 4 respectively. The values of half wave-lengths and angles of buckles are listed in Table 1. For two cases of pure bending or pure torsion, calculations of half wave-lengths of buckles are based on analyses by Yu *et al.* [1] and Yamaki [5] respectively. The computational results of angles of buckles are determined by using $\psi = \frac{1}{2}\arctan(T/M)$. It can be observed that a buckle is formed and developed in the region near the root when the value of force increases to a certain value. The cross-section of the tube will change eventually to be approximately oval. Figures 5 and 6 present deformations and buckling of tubular beams for various ratios of bending and torsion, i.e., $\infty, 2, 4/3, 1, 0$.

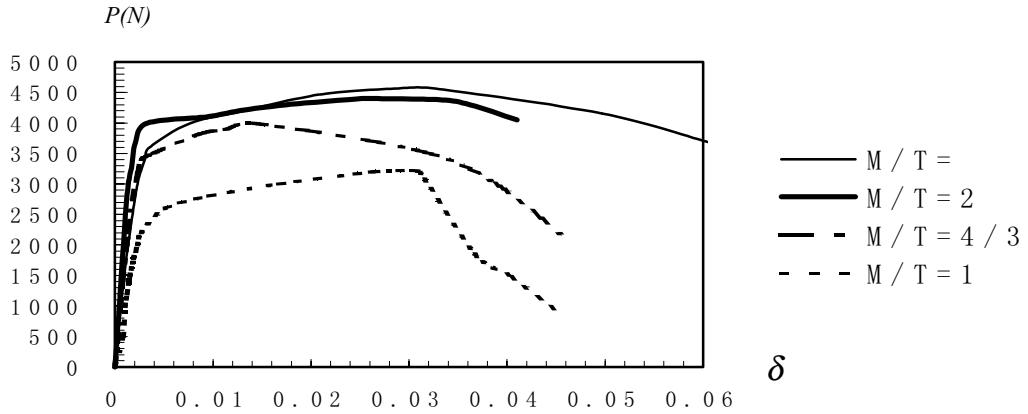

Figure 3: $P-\delta$ curves

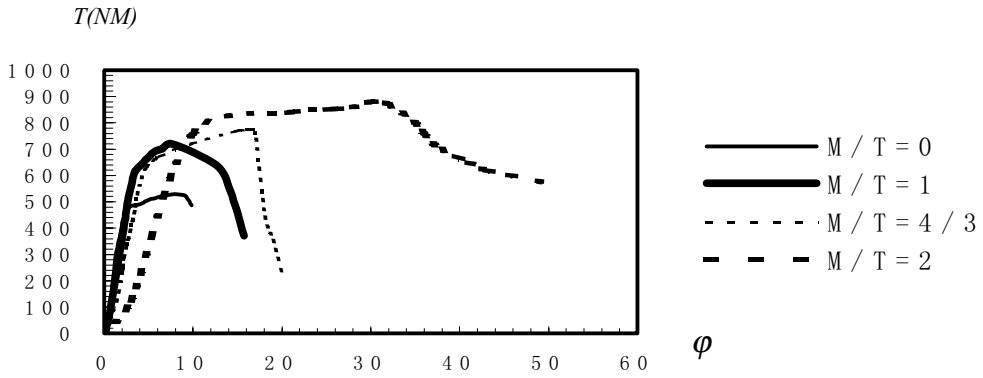

Figure 4: $T-\varphi$ **curves**

TABLE 1

HALF WAVE LENGTHS AND ANGLES OF BUCKLES

M/T		∞	2	4/3	1	0
λ (mm)	experiment	6.2	8	12	13	24
	theory	6				24
ψ (^{0})	experiment	0	11-13	16-18	20-22	40-45
	theory	0	13.3	18.4	22.5	45

A BEAM MODEL FOR ANALYSIS OF PLASTIC BEHAVIOR OF TUBULAR BEAMS

A commonly used plane hypothesis is applied for the tubular beam. According to stress-strain relations for pure tension or pure shear of the used specimen, the expression for complementary energy per unit volume of the tube can be obtained from the following formula

$$U^* = \int_0^\sigma \varepsilon \, d\sigma + \int_0^\tau 2\gamma \, d\tau \tag{1}$$

Figure 5: Front view for ratios $M/T = \infty, 2, 4/3, 1, 0$ (from left to right)

Figure 6: Side view for ratios $M/T = \infty, 2, 4/3, 1, 0$ (from left to right)

Applying the principle of complementary energy, the corresponding characteristic relations, $P-\delta$ and $T-\varphi$, can be derived from the following two equations respectively

$$\delta(z) = \frac{\partial U^*}{\partial P} \tag{2}$$

$$\varphi = \frac{\partial U^*}{\partial T} \tag{3}$$

which z is the distance indicating positions of the cross-section. The expressions for the relations are omitted due to limitation of space.

NUMERICAL RESULTS AND COMPARISONS

In this paper finite element method is used and a four-node shell-type element is chosen to predict buckling modes of the tubular beams. Buckling modes for the roots of tubes for different ratios are shown in Figure 7.

Numerical results for $P-\delta$ and $T-\varphi$ relations are compared with that of theoretical model and experiment in Figures 8 and 9 respectively. A good agreement can be observed, especially between numerical results and experimental data.

ANALYSIS AND DISCUSSION

The behaviors of tubular beams under combined bending and torsion are complex. It is very important to develop a simple and valid theoretical model to characterize the plastic and buckling of tubes. Actually, the cross-section of the tube will not keep a plane during deformation. So, use of a beam model based on plane hypothesis is not exact for analysis of plastic behaviors of such structures. A further consideration on local buckling and flattening should be made toward an improvement of beam model.

ACKNOWLEDGEMENTS

The work is partially supported first by the Key Speciality of the Shanghai Education Commission and later by the National Natural Science Foundation through grant number 10072042, Foundation for Science and Technology and for University Key Teacher through grant numbers 99164 and GG-130-10247-1197 respectively by the Ministry of Education of China.

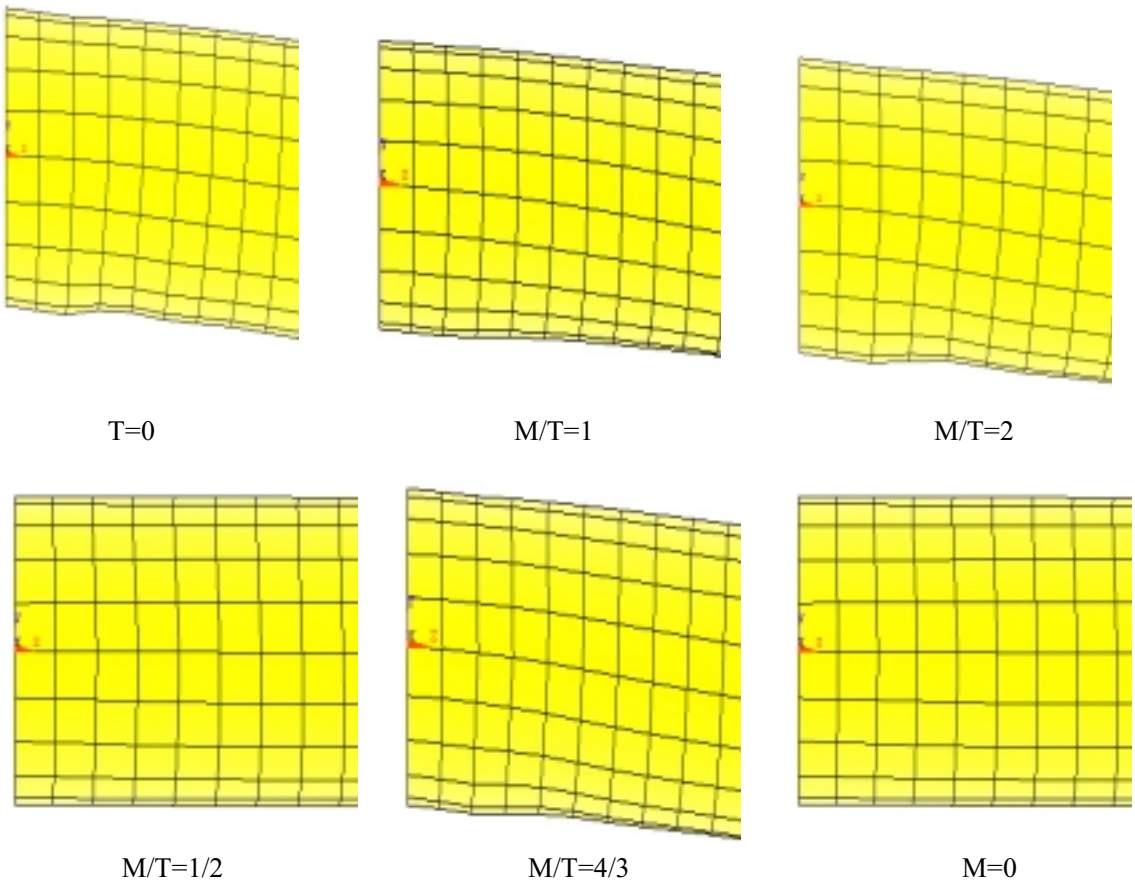

Figure 7: Buckling mode for the roots of tubular beams

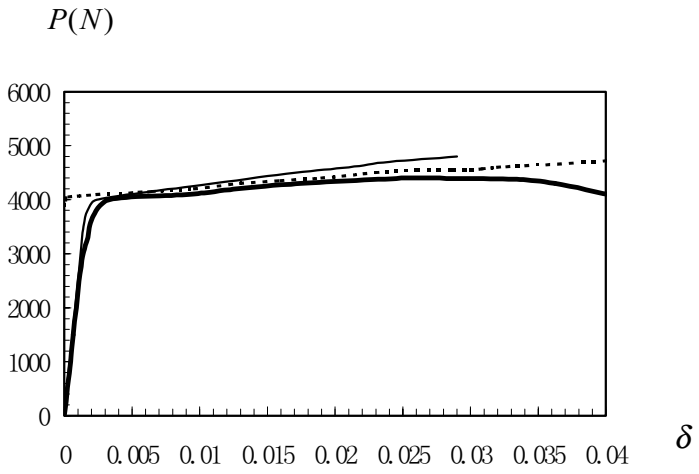

Figure 8: $P-\delta$ curves for M/T=2
(Bold solid line: experiment, thin solid line: FEM, broken line: theory)

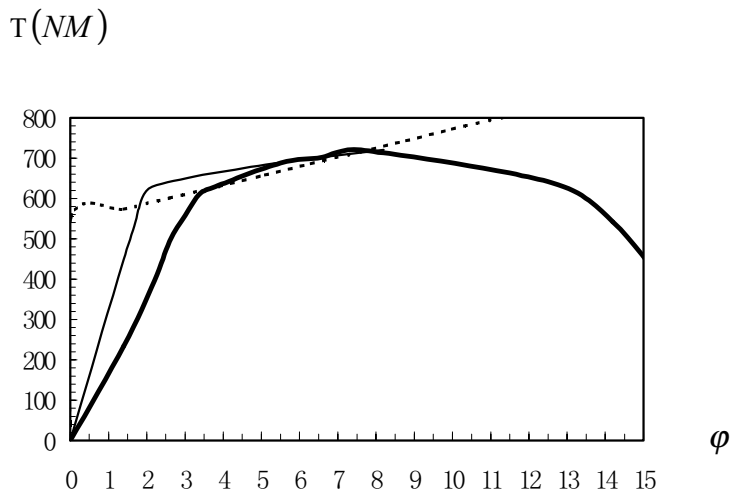

Figure 9: $T-\varphi$ curves for M/T=4/3

(Bold solid line: experiment, thin solid line: FEM, broken line: theory)

REFERENCES

1. Yu, T.X., Reid, S.R. and Wang, B. (1993). *Int. J. Mech. Sci.* 35, 1021.
2. Reid, S.R., Yu, T.X., and Yang, J.L. (1994). *Int. J. Mech. Sci.* 36, 1073.
3. Hodge, P.G. (1959). *Plastic Analysis of Structures*, McGraw Hill, New York.
4. Hill, R. and Siebel, M.P.L. (1951). *Phil. Mag.* 42, 722
5. Yamaki, N. (1984). *Elastic Stability of Circular Cylindrical Shells*, North-Holland, Amsterdam.

ORAL/POSTER REFERENCE: ICF100205OR

PLASTIC BEHAVIOR OF NANO-SCALE SILICON STRAUCTURE AT INTERMEDIATE TEMPERATURES

Yoshitada Isono[1], Takahiro Namazu[2] and Takeshi Tanaka[1]

[1] Department of Mechanical Engineering, Faculty of Science and Engineering,
Ritsumeikan University, 1-1-1 Nojihigashi, Kusatsu-si, Shiga 525-8577, JAPAN
[2] Graduate Student, Department of Mechanical Engineering, Faculty of Science and Engineering,
Ritsumeikan University, 1-1-1 Nojihigashi, Kusatsu-si, Shiga 525-8577, JAPAN

ABSTRACT

This paper focuses on revealing specimen size and temperature effects on plasticity of nano-scale self-supported single crystal silicon (Si) beams for the design of electronic and micro electro-mechanical system (MEMS) devices. Four kinds of Si beams with widths from 200 to 800 nm and a thickness of 255 nm were fabricated on an Si diaphragm by means of field-enhanced anodization using AFM and anisotropic wet etching. Mechanical properties of the Si beams were evaluated by AFM bending testing at intermediate temperatures ranging from 295 K to 573 K in high vacuum. Young's modulus of the nano-scale Si showed temperature dependency but had no size effect, which was similar trend in Si bulk. The bending strength of the 200 nm-wide beams ranged from 15.87 to 17.76 GPa, which were approximately 1.5 times larger than the strength of the 800 nm-wide beams. Critical resolved shear stress and plastic strain range also exhibited specimen size and temperature dependency. The plastic strain range obviously increased with a reduction of the specimen size and an increase of temperature. This research showed that the plastic flow was easily induced in smaller sized Si beams on a nano-scale even if test temperature was 373 K, which was close to room temperature. AFM observations suggested that the slip line density would have determined the plastic strain range of nano-scale Si at intermediate temperatures.

KEYWORDS

Single Crystal Silicon, AFM, Young's Modulus, Bending Strength, Plastic Strain Range, Slip Line

INTRODUCTION

The evaluation of mechanical properties of nano-scale Si beams at intermediate temperatures is very important for the design of high-density electronic and MEMS devices, since the devices are serviced at room and intermediate temperatures, which may induce thermal stress. This stress can produce plastic deformation based on a dislocation of the 1/2 <110> {111} slip system that prohibits the electric conduction in Si. So far, mechanical properties of Si have just been estimated on a micro and millimeter scale at room temperature because of difficulties in problems associated with measuring ultra-small physical phenomena in an experiment at elevated temperatures [1], [2]. Few mechanical characterizations of micro/nano-scaled Si specimens at high temperature have also been performed. Frühauf, J. et al [3] carried out a plastic deformation process of micro-scale Si elements at 700 K – 1000 K for reshaping of the elements, however they did not propose any design criteria for Si because their work was not aimed at mechanical characterization. For safe and reliable designs of high-density electronic components, nano-scale material testing of Si at elevated temperatures is essential.

The objective of this research is to reveal the specimen size and temperature effects on Young's modulus and bending strength of nano-scale Si beams at intermediate temperatures ranging from 295 K to 573 K. Bending tests for the Si beams were carried out using AFM and the fracture probability was discussed using Weibull plots. The specimen size and temperature dependency of the plastic deformation behavior were also discussed in the light of observations of the slip line using the AFM.

EXPERIMENTAL PROCEDURE

Fabrication of Nano-scale Si beam

The field-enhanced anodization with an AFM was carried out for making Si fixed beams on a nanometer scale. Field-enhanced anodization is a method to draw a silicon dioxide (SiO_2) film line with a width of less than 1 m on an Si surface [4], which is used as the high precision mask pattern for the anisotropic wet etching with a solution of 20 % tetra-methyl ammonium hydroxide (TMAH). It was then possible to fabricate a nanometer scale Si structure after the etching. Figure 1 shows the field-enhanced anodization process with AFM. In this research, the SiO_2 film was anodized on a SIMOX wafer at the bias voltage of 20 V and at the scanning speed of 0.4 m/s, whereat the thickness of SiO_2 reached about 5 nm that was a sufficient film thickness for the TMAH wet etching.

Four kinds of Si beams were prepared in AFM bending tests. The Si beams with widths of 200, 300, 550 and 800 nm were fabricated by the wet etching with TMAH after the field-enhanced anodization. Figure 2 depicts a SEM photograph of nano-scale Si beams. The beams are oriented along the [110] direction in the (001) plane. The cross-section of the beam is a trapezoid owing to the anisotropic wet etching process. The nominal dimensions of the beams are listed in Table 1. The width, length and thickness values for each of the beams were measured by the AFM prior to the bending test. Si beams within ±5 % error of the dimensions listed in Table 1 have been used in the bending tests.

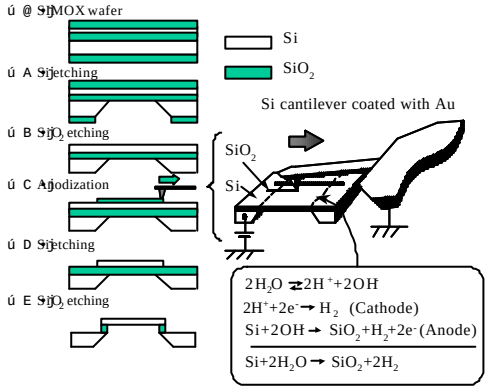

Figure 1: Fabrication process of nano-scale Si beam using field-enhanced anodization with AFM

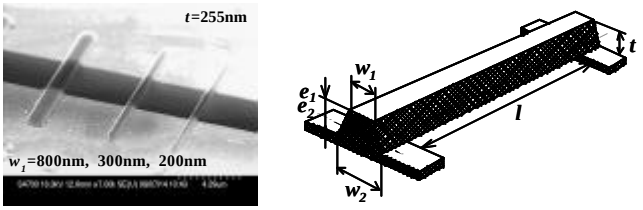

Figure 2: SEM photograph of Si beams along with a schematic of a beam

Table 1
Nominal dimensions of nano-scale Si beams

Upper width W_1 [nm]	Lower width W_2 [nm]	Thickness t [nm]	Length l [mm]
200	370	255	6
300	470	255	6
550	720	255	6
800	980	255	6

Test Procedure

Figure 3 illustrates a schematic diagram of the bending test using the AFM. A diamond tip with a tip radius of 100 nm mounted on a stainless steel rectangular cantilever was used for the bending test. The bending force, F_n, and the maximum displacement in the z-direction of the beam, D, were calculated from the following relations,

$$F_n = ((DIF_{init} + DIF_{ex}) / Sensitivity) \times k, \quad (1)$$

$$D = PZT(Z) - DIF_{ex} / Sensitivity, \quad (2)$$

where DIF_{init} [V] is the initial differential voltage produced by the deflection of the cantilever prior the bending test, DIF_{ex} [V] is the differential voltage during the test, k is the stiffness of the cantilever calculated from the Young's modulus of the stainless steel and dimensions of the cantilever, *PZT(Z)* [m] is the displacement in the z-direction of PZT actuator settled in AFM and *Sensitivity* [V/m] is the ratio of the cantilever's deflection to the displacement of the actuator.

Young's modulus and bending strength σ_B of Si beams were estimated by equations based on the assumption that the beams follow linear elastic theory of an isotropic material. This is due to high specimen length to width and length to thickness ratios and due to the length direction corresponding to the principal stress direction during the test. The Young's modulus and bending strength are expressed as

$$E = \frac{l^3}{192 I} m, \quad (3)$$

$$\sigma_B = \frac{(F_n)_{\max} \times l \times e_1}{8I}, \quad (4)$$

where l is the beam length, I is the moment of inertia for the beam cross-section, m is the gradient of the force - displacement curve, $(F_n)_{\max}$ is the maximum bending force, and e_1 is the vertical distance between the upper surface and the neutral plane.

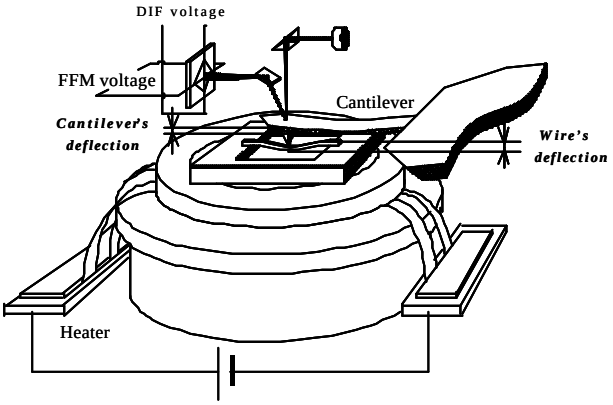

Figure 3: AFM bending testing of nano-scale Si beam at intermediate temperatures

RESULTS AND DISCUSSION

AFM Bending Test Results

Figures 4 (a) and 4(b) show maximum stress–strain curves of the beams with widths of 200 and 800 nm at each temperature. The stress at the zero strain before bending is due to a pre-load generated when the cantilever was set up on the top of the beam. The Si beam at room temperature fractures in a brittle manner, whereas plastic deformation of Si beams is obtained at intermediate temperatures. Especially, the plastic deformation of the 200 nm-wide beams is induced at even 373 K that is close to room temperature. The figures also show that the plastic strain range obviously increases with decreasing the specimen size and increasing temperature. Comparing the two sized beams above 373 K, the plastic strain range of 200 nm-wide beams is larger than that of 800 nm-wide beams. The specimen size on a nanometer scale has a great influence on the plastic deformation behavior of Si as well as temperature.

The variation of Young's modulus with an increase of temperature is shown in Fig. 5. The Young's modulus decreases with increasing temperature, but does not change with the specimen size. The Young's modulus at room temperature averages 170 GPa, which is comparable to that of micro- or millimeter scale beams [5]. The Young's modulus shows temperature dependency but has no size effect. The temperature dependency is attributed to an increase of the lattice constant of Si due to the thermal atomic vibration, which changes the shape of the interatomic energy curve between Si atoms.

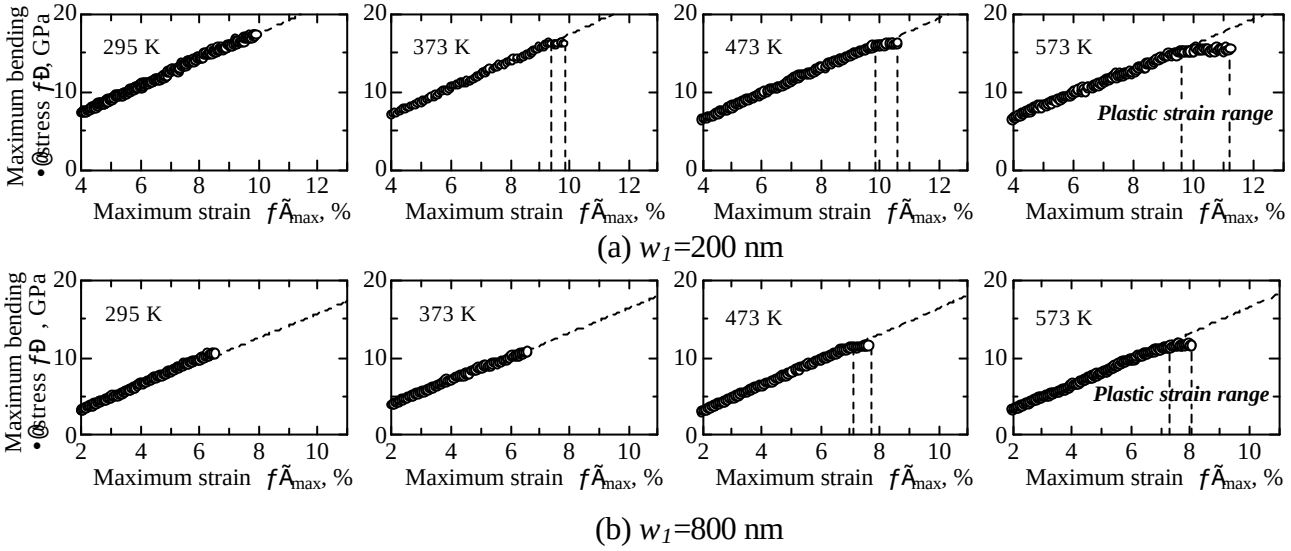

(a) w_1=200 nm

(b) w_1=800 nm

Figure 4: Maximum stress-strain curves in AFM bending testing

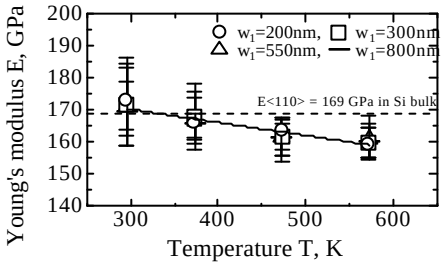

Figure 5: Variation of Young's modulus with increasing temperature

Weibull Plot

Figure 6 shows Weibull plots of the bending strength. The bending strength of the 200 nm-wide beams ranges from 17.76 to 15.87 GPa, which are approximately 1.5 times larger than that of the 800 nm-wide beams. The beam size therefore has large influence on the bending strength of Si beams. There is also the temperature effect on the bending strength, but it is smaller than the specimen size effect on the bending strength.

Figures 7 correlates the Weibull parameters with the effective volume V_E and effective surface area S_E in order to reveal the specimen size and temperature dependency of Weibull parameters [5]. The scale parameter b decreases with an increase of the effective volume and surface at each temperature. The parameter b also decreases with increasing the test temperature, which is caused by a reduction of the yield stress at higher temperature. The shape parameter m is larger in smaller sized beams, but the parameter m does not have temperature dependency at temperatures applied in the test. The scale parameter b therefore is affected by the beam size and temperature, but the shape parameter m is just influenced by the specimen size. In Fig. 8(a), Weibull parameters b of nano-scale Si beams can be predicted by a function as the following,

$$b = e^{(-3.07T \times 10^{-4} + 2.29)} \times S_E^{(5.03T \times 10^{-5} - 0.167)}. \quad (5)$$

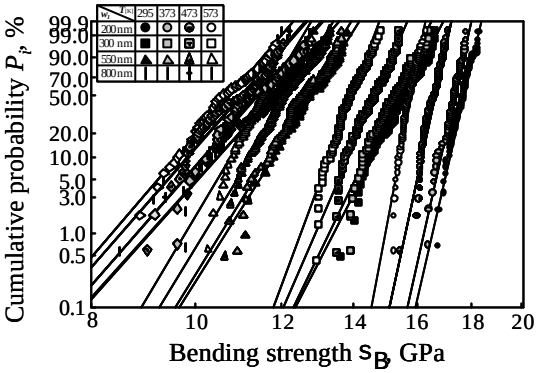

Figure 6: Weibull plots of bending strength

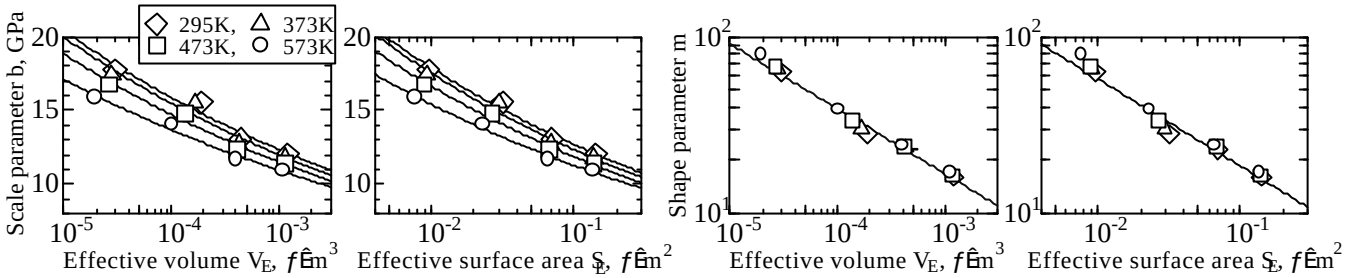

Figure 7: Specimen size dependency of Weibull parameters

Figure 8 shows the variation of the critical resolved shear stress $_c$ for 1/2 [0$1\bar{1}$] ($1\bar{1}\bar{1}$) slip with an increase of temperature, along with results of millimeter sized Si specimens (Casting *et al.* 1981. [6]). Closed plots indicate Si beams wherein the plastic deformation behavior is observed in the beams larger than 60 % of the total number of beams. Half closed and open plots mean Si beams deformed plastically in the beams from 30 to 60 % and less than 30 % of the total number of beams, respectively. The critical resolved shear stress does not only decreases with an increase of the specimen size, but also decreases with an increase of the temperature. So far, it has been reported that plastic deformation in Si on a millimeter scale was not induced below 548 K [6]. However, the plastic flow is obtained at temperatures ranging from 373 K to 573 K in a nanometer-scale specimen. The plastic deformation is then easily induced in smaller sized Si beams on a nano-scale even if test temperature is close to room temperature.

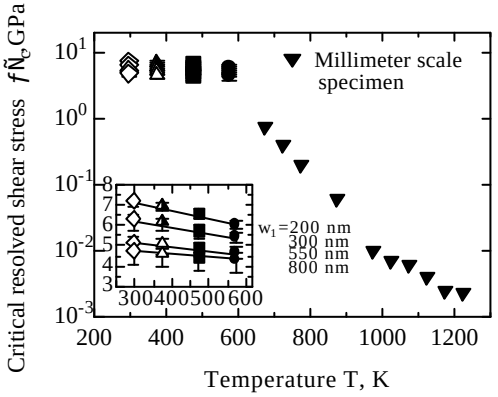

Figure 8: Relationship between critical resolved shear stress and temperature

AFM Observation of Slip Line

For better understanding the specimen size and temperature effects on the plastic deformation behavior, AFM images of the top surface were studied. To examine the slip line produced by dislocations during plastic deformation, the top surface at the end of beam was observed by the AFM as shown in Fig. 9. Several slip lines appear in a smaller sized beam at 373 K, but few slip lines are observed in the 800 nm-wide beams at the temperature. Each slip line is comprised of 1 to 5 nm-high steps as shown in the magnified images. Building up slip lines on an atomic scale, nano-scale Si beams can therefore deform plastically at intermediate temperature. By increasing the deformation temperature the number of slip lines is raised in all of beams. This is caused by an increase of the thermal activation of dislocation.

Figure 10 correlates the slip line density with the effective volume V_E and surface area S_E. The slip line density is higher in a smaller sized beam and at higher temperature, which was a similar trend to the beam size and temperature effects on the plastic strain range. The number of slip lines then would have determined the plastic strain range during the deformation. The slip line density in the beam ranges from 0.5×10^9 to 2.5×10^9 cm^{-2}, which is about 100 times larger than the slip line density in a micrometer scale specimen (Frühauf *et al*. 1999. [3]). Therefore, the dislocation can easily appear and travel in the nano-scale beam than the micrometer sized specimen. This could be attributed to the effect of an increase of the surface energy with a reduction of the specimen size on the activation energy of dislocation.

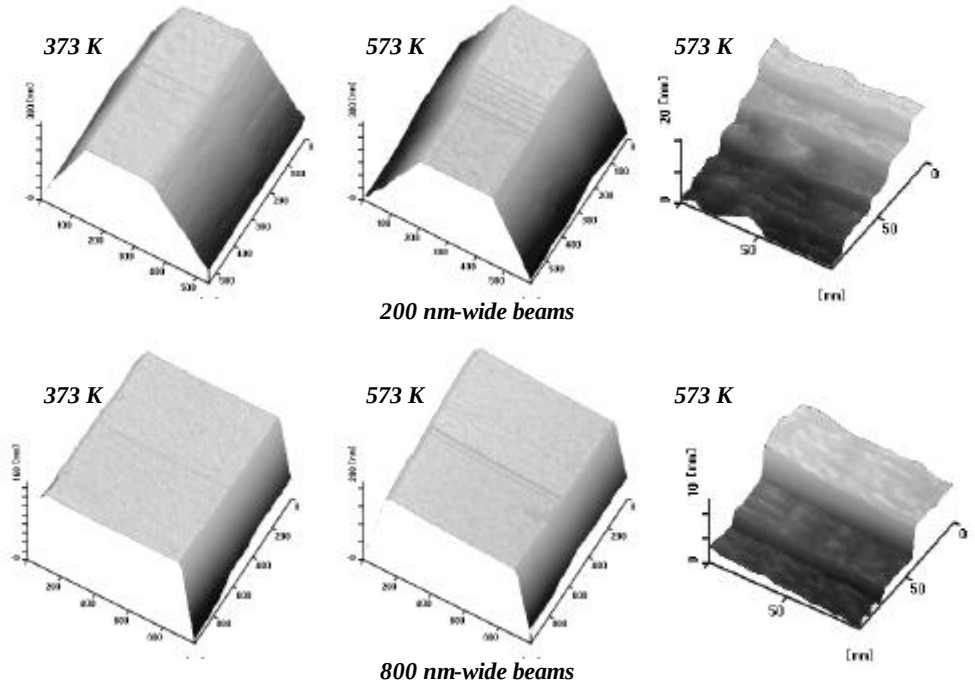

Figure 9: AFM images of slip lines at the top surface of Si beams

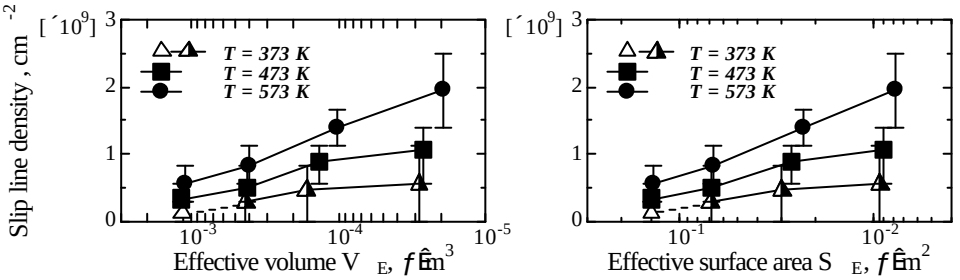

Figure 10: Variation of slip line density with a decrease of specimen size

References

1. Sharpe Jr., W. N., Yuan, Bin and Edwards, R. L. (1997). *Journal of MEMS*, **6**, 3, pp. 193
2. Yi, T. and Kim, C. J. (1999). *Meas. Sci. Technol.*, **10**, pp. 706
3. Frühauf, J., Gärtner, E. and Jänsch, E. (1999). *Appl. Phys. A*, **68**, 673, pp. 673
4. Hattori, T., Ejiri, Y. and Saito, K. (1994). *J. Vac. Sci. Technol. A*, **12**, 4, pp.2586
5. Namazu, T., Isono, Y. and Tanaka, T. (2000). *Journal of MEMS*, **9**, 4, pp. 450
6. Castaing J. (1981). *Phil. Mag. A*, **44**, 6, pp. 1407

Oral ICF10343

PLASTIC FLOW AND FRACTURE OF BULK NANOCRYSTALLINE CERAMICS AND INTERMETALLICS IN INDENTATION

Hiroshi Kimura
Department of Mechanical Engineering, School of Systems Engineering, National Defense Academy, Yokosuka, 239-8686, JPN

ABSTRACT
A study in model mechanics is performed to characterize the plastic flow and fracture in indentation of the full density nanocrystalline ceramics and intermetallics. An analysis of a load-depth curve in Berkovich indentation makes it possible to derive a relatively low level of 4.4 GPa for the value of the yield stress(σ_{yn}) of the nanocrystalline ZrO_2-20mol%Al_2O_3 sample, when assuming the non-strain hardening property. The dynamical indentation verifies that the yield stress for the fully dense nanocrystalline TiAl sample follows the formula of $\sigma_{yn}=\sigma_{ya}[1+V_f(E_c/E_a-1)]$ that is constructed on the basis of the rheological model for the nanocrystal with an amorphous network volume(V_f). The fracture toughness(K_{IC}), as estimated from the length of a crack occurred at the corners of pyramidal Vickers indent, exhibits an extremely high value of 34 MPa $m^{1/2}$ for the forged sample of nanocrystalline PSZ-20mol%Al_2O_3 consisting with the cubic and tetragonal phases.

KEYWORDS
amorphous ceramics, nanocrystallization, full density consolidation, yield stress, fracture toughness,

INTRODUCTION
The fully dense nanocrystalline material is becoming one of the most promising materials that have the outstanding mechanical characteristics necessary to realize a variety of the near-future technologies[1]. The author has proposed the non-equilibrium P/M processing that consists of the mechanical alloying and the electric discharge consolidation for the synthesis of the fully dense nano-amorphous materials[2][3], and then discovered an extremely high yield strength of 3.1 GPa in compression for the nanocrystalline TiAl intermetallic[4] and the high-speed superplasticity at a relatively low temperature in nanocrystalline ZrO_2-20mol%Al_2O_3[5]. A study in the model mechanics[6] has been carried out to give the formula of the super strength pertaining to the bulk nanocrystalline alloys and intermetallics using well-defined yielding[7]. Concomitantly, the Vickers hardness testing has been used to make clear the nature of the strength and the related phenomenon as a convenient method, namely in the bulk nanocrystalline materials that exhibit a brittle behavior in a uniaxial stress state at the present. Here, the author is going to provide a quantitative way of indentation to the derivation of the yield stress and the fracture toughness for the bulk nanocrystalline ceramics and intermetallics.

EXPERIMENTAL PROCEDURE
The amorphous powders of TiAl[8], ZrO_2-20mol%Al_2O_3[9] and PSZ-20mol%Al_2O_3[10] were produced by employing the rotating-arm reaction ball milling method[11]. The instrumented electric discharge consolidation method can be used to prepare the fully dense product of the nanocrystal synthesized via crystallization of the amorphous powder[3][12][13]. X-ray diffraction is used to characterize the ball milled powder and the consolidated product. The average grain size(d) is estimated from X-ray line broadening at the half of maximum using the conventional Scherrer formula. The Berkovich indentation method equipped with a depth-sensing system(Shimazu DUH-201S) is used to evaluate the yield stress in the bulk amorphous and nanocrystalline materials. The pyramidal Vickers hardness testing is employed to derive the fracture toughness for nanocrystalline ceramics on the basis of the indentation microfracture method.

RESULTS AND DISCUSSION

Plastic flow in dynamic indentation
Figure 1 shows the Berkovich indentation depth at various holding loads for the fully dense nanocrystalline ZrO_2-20mol%Al_2O_3 product, as prepared at the consolidation temperature of 1360 K[14]. The load-Bekovich

indent depth curve is smooth up to the applied load of 2 N at the maximum avoiding any cracking as shown in Figure 1. The indentation depth(d_1) at the applied load of 2 N nearly equals to the depth(d_2) after holding for 60 s in the case of the lowest loading rate of 1.4 mN s^{-1}, while the difference between d_1 and d_2 increases with increasing loading rate. Therefore, the Berkovich indentation depth(d_2) here is used as an accepted parameter. For nanocrystalline ZrO_2-20mol%Al_2O_3, the load-depth relations are almost identical at both loading rates of 1.4 and 71 mN s^{-1} as shown in Figure 1. Derive the yield stress in dynamical indentation. The formula for the load(P)-indentation depth relation has been constructed using the finite element method by Larsson et al.[15], and is applied to the quantitative evaluation of the yield stress(σ_y) at room temperature for the bulk amorphous and nanocrystalline materials as follows: $P=1.273(\tan 24.7^o)^{-2}\sigma_y(1+\sigma_r/\sigma_y)(1+\ln E\tan 24.7^o/3\sigma_y)d_2^2$ (1)where σ_r and E are the flow stress and Young s modulus. The analysis of the experimentally obtained load-depth relation on the basis of the equation (1) gives a relatively low level of 4.4 GPa for the value of the yield stress of the nanocrystalline ZrO_2-20mol%Al_2O_3 product with the average grain size of 11nm for a tetragonal phase, together with the proper value for Young s modulus. In this calculation, it is reasonably assumed that σ_r equals to the value of σ_y , when considering that the bulk nanocrystalline material is characterized as a nearly non-strain hardening solid as well as the amorphous alloy[7].The thus-derived yield stress can be coupled with the relatively low level of approximately 1000 DPN for Vickers hardness number(H_v) for the fully dense nanocrystalline ZrO_2-

Figure 1: The relationship between the holding load and depth in Berkovich indentation for fully dense nanocrystalline ZrO_2-20mol%Al_2O_3 sample, prepared by the electric discharge consolidation of the amorphous powder.

Figure 2: The load-depth relation in Berkovich indentation for the fully dense TiAl as consolidated below the glass temperature. The solid and broken lines are respectively the predictions for amorphous and nanocrystalline TiAl on the basis of the formula that is constructed on the basis of the rheological model. This figure includes the load-depth curve in the case of loading rate, 1.4 mN s^{-1}.

20mol%Al_2O_3 sample by a relation of $H_v/\sigma_y=\alpha$ where α is a constant ranging from 2 to 3 for amorphous and nanocrystalline alloys. Note that the fully dense nanocrystalline covalent and oxide ceramics, SiC[16] and PSZ-20mol%Al_2O_3[17] have two-third level of Vickers hardness numbers of ceramics as prepared by the conventional method. The yield stress at the room temperature is an important material parameter to discuss the mechanical characteristics such as softening, ductilization and enhanced fracture toughness in the bulk nanocrystalline ceramics as well as metals and alloys.
Figure 2 shows the load-depth relation in Berkovich indentation for the fully dense amorphous and nanocrystalline TiAl samples. So far, the compressive yielding in nanocrystalline TiAl has been fairly well expressed with a Hall-Petch type formula using the well-defined yield stress in the case of $d>d_c$ where d_c is the critical grain size. Here, consider the yielding in the case of $d<d_c$. The formula of the yield stress for nanocrystalline TiAl[7][19] is constructed on the basis of the rheological model as follows:

$$\sigma_{yn}=\sigma_{ya}[1+V_f(E_c/E_a-1)] \quad (2)$$

where V_f is the amorphous volume. For nanocrystalline TiAl, Young s modulus(E) obeys the mixture law of $E=E_cV_f+E_a(1-V_f)$ where E_c is Young s modulus for intermetallic TiAl, and a relation of $V_f=0.185d^{0.5}+0.77$ is experimentally obtained. The samples as in Figure 2 are synthesized by the consolidation of the mechanically alloyed amorphous powder and the isothermal annealing below the glass temperature at the applied pressure of 600 MPa[1][18], in order to obtain a single amorphous phase and an average grain size below the critical value(d_c). The load-depth relation for amorphous TiAl is fitted by the predicted curve of equation (1) with the yield stress(σ_{ya}) of 0.65 GPa and Young s modulus(E_a) of 40 GPa in the literature[7]. The prediction by equation (1) can give a good fit to the experimentally obtained load-depth relation in Berkovich indentation with the average grain size of 8 nm in a range of the observation by high-resolution electron microscopy[18]. In other words, a good agreement between the prediction and the experiment validates that equation (2) is applicable to the yielding in bulk intermetallic TiAl with $d<d_c$. While the equation (2) has been, so far, confirmed by a decrease in Vickers hardness number with decreasing average grain size[19].

Fracture in Vickers hardness testing

Figure 3 shows the relationship between the applied load and the length of a crack occurred at the corners of Vickers indent for the fully dense nanocrystalline PSZ-20mol%Al_2O_3 and ZrO_2-20mol%Al_2O_3 samples, and the forged sample. Evaluate the fracture toughness(K_{IC}). For a median/radial crack, the load-crack length relation is given by the following equation.

$$P/c_0^{3/2} = K_{IC}/A(E/H_v)^n \quad (3)$$

Figure 3: The relationship between the applied load and the length of a crack in indentation microfracture method using Vickers hardness testing for the fully dense nanocrystalline PSZ-20mol%Al_2O_3 and ZrO_2-20mol%Al_2O_3 samples. This figure also includes the result of the forged PSZ-20mol%Al_2O_3 sample. where c_0 is the length of a crack, A being the constant and n is the exponent. It can be seen that the applied load is proportional to $c_0^{3/2}$ for each of nanocrystalline oxide samples. Therefore, the fracture toughness can be derived by the slope by using the equation (3) with the customarily used values of A=0.016 and n=0.5, together with the proper values of E and H_v. For fully dense nanocrystalline PSZ-20mol%Al_2O_3 consisting of cubic and tetragonal phases, the fracture toughness is higher than that of submicron sized PSZ as prepared by conventional P/M methods, and shows a further increase from 11 to 12.4 MPa $m^{1/2}$ by decreasing average grain size. On the other hand, the fracture toughness for the fully dense nanocrystalline ZrO_2-20mol%Al_2O_3 samples is derived as 8.7 MPa $m^{1/2}$ although this sample has the lowest tetragonal grain size of 11 nm. This insufficient enhancement may results from the monoclinic phase involved as a second phase and an external Fe content incorporated during milling. Moreover, it is found that the nanocrystalline PSZ-20mol%Al_2O_3 sample, subjected to the high-speed superplastic forging with the compressibility of 64 %, has an extremely high fracture toughness of 34 MPa $m^{1/2}$ at the maximum within the experiment of this study. The low yield stress as stated before and the high microfracture stress give rise to the extraordinary fracture toughness in the fully dense nanocrystalline PSZ-20mol%Al_2O_3. Especially, the latter is resulting from the pore free consolidation, the synthesis of tetragonal and cubic phases, the high quality production of the amorphous powder avoiding external Fe contamination in non-equilibrium P/M processing. A further study on the indentation microfracture method is desired to evaluate an exact fracture toughness for bulk nanocrystalline ceramics, including the inspection of eqn. (3).

CONCLUSIONS

This article provides a study in model mechanics for the plastic flow and fracture in indentation of the bulk nanocrystalline ceramics and intermetallics. The Berkovich indentation is successfully used to derive a relatively low yield stress of 4.4 GPa that is coupled with the softening in Vickers hardness for the fully dense ZrO_2-20mol%Al_2O_3 sample with the grain size of 11 nm. Then, the dynamical indentation validates that the fully dense sample of nanocrystalline TiAl with $d<d_c$ follows the formula of $\sigma_{yn}=\sigma_{ya}[1+V_f(E_c/E_a-1)]$ that is constructed on the basis of the rheological model. On the other hand, the forged sample of nanocrystalline PSZ-20mol%Al_2O_3 with the cubic and tetragonal phases is found to exhibit an extremely high level of 34 MPa $m^{1/2}$ for the value of the fracture toughness, as estimated from the indentation microfracture method.

REFERENCES

1. Kimura, H. (1999). *Ceramics Japan*, **34**, 438.
2. Kimura, H. (1999). *Materials Integration*, **12**, 19.
3. Kimura, H. (1996). *Sci. Rep. RITU*, **A42**, 245.
4. Kimura, H. (1996). *Phil. Mag. A*, **73**, 723.
5. Kimura, H. and

Fujimoto, Y. (1999). *J. Japan Soc. Powder Powder Metallurgy*, **46**, 1274. 6. Kimura, H. and Masumoto, T. (1983). In: *Amorphous Metallic Alloys,* Butterworths, London, pp.187-230. 7. Kimura, H. and Hachinohe, A. (1997). *Advanced Particulate Mater. & Process,* West Palm Beach, 153. 8. Kimura, H., Kobayashi, S., Sugawara. S. and Fukazawa, E. (1993). *J. Japan Soc. Powder Powder Metallurgy*, **40**, 278. 9. Kimura, H. and Hongo, K. (1999). *Proc. Int. Conf. on Solid-State Phase Transformations 99(JIMIC-3)*, Japan Institute Metal, Kyoto, 1271. 10. Kimura, H. and Hanada, K. (1999). *J. Japan Soc. Powder Powder Metallurgy*, **46**, 1279. 11. Kimura, H., (1993). *Rapid Solidification Technology,* Technomic, Lancaster, pp.71-123. 12. Kimura, H., (1999). *Advances in Powder Metallurgy & Particulate Materials- 99(PM^{2}TEC 99)* , Vancouver, No.12, 55. 13. Kimura, H. and Hongo, K. (1999). *J. Japan Inst. Metals*, **63**, 649.

14. Kimura, H. and Hongo, K., to be submitted to *Materials Transaction, JIM.* 15. Larsson, P.-L, Giannakopoulos, A.E., Soderlund, E., Rowcliffe, D.J. and Vestergaard, R., (1996). *Int. J. Solids Structure*, **33**, 221. 16. Kimura, H. and Hanada, K. (2001). *to be published*. 17. Kimura, H., Catur Martowo Aji, Kikuchi, K. (2001). *Advances in Powder Metallurgy & Particulate Materials-2001(PM^{2}TEC 2001)* , New Orleans, in the press. 18. Kimura, H., Kumagai, T. and Shimoitaini, Y., *to be published*. 19. Kimura, H. and Kobayashi, S. (1994). *Materials Transaction, JIM*, **36**, 982.

ORAL REFERENCE: ICF100216OR

PLASTICALLY DOMINANT / ELASTICALLY DOMINANT FATIGUE INTERACTION

Y.K. Wong, X.Z. Hu and M.P. Norton

Department of Mechanical and Materials Engineering, University of Western Australia, 35 Stirling Highway, Crawley, WA 6009.

ABSTRACT

Interactions between High-Low (stress/strain) and Low-High (stress/strain) loadings have been studied extensively, yet the underlying fatigue mechanisms responsible for such interactions and thus the interaction between low cycle fatigue (LCF) and high cycle fatigue (HCF) are not clearly understood. Regimes under which High-Low and Low-High loading sequences are investigated should be specified clearly, (eg. High(LCF)-Low(HCF) where high stress/strain is in the LCF range and the subsequent low stress/strain is in the HCF range) as it can be appreciated that the mechanisms governing fatigue behaviour differ under varying regimes. Conventional classification of fatigue into LCF and HCF has been abandoned in favour of more precise terms being plastically dominant fatigue (PDF) and elastically dominant fatigue (EDF) respectively. This paper presents results on the interaction between PDF and EDF in 6061T6-aluminium alloy and highlights the significance of proper fatigue classification and specification particularly under strain controlled multilevel loading.

KEYWORDS

Plastically Dominant Fatigue (PDF), Elastically Dominant Fatigue (EDF), Low Cycle Fatigue (LCF), High Cycle Fatigue (HCF).

INTRODUCTION

Introduction of the Palmgren-Miner linear damage rule has motivated and inspired much research in multilevel loading for a vast array of materials as the problem of predicting service lives for engineering components subjected to non-uniform fatigue with any degree of accuracy has proved quite intractable. While extensive results on multilevel loading have been reported [1-7], the underlying fatigue mechanisms responsible for such interactions are not fully understood.

Historically, fatigue is classified into two main types, low cycle fatigue (LCF) and high cycle fatigue (HCF). The definition of LCF and HCF has been the subject of much ambiguity. LCF is commonly associated with fatigue lives ranging from 1 to 1000 cycles while HCF is concerned with failure corresponding to fatigue live cycles greater than 10^3. To date, the Coffin-Manson approach of determining transition life N_t, based on relative values of plastic and elastic strain, appears to be the most reliable method for defining the boundary between LCF and HCF. It is recognised that in order to avoid confusion and ambiguity with definitions involving LCF and HCF, the two regimes are more appropriately termed as plastically dominant fatigue

(PDF) and elastically dominant fatigue (EDF) respectively. Under two-level step loading, fatigue tests take the form of either High-Low or Low-High stress/strain type loading sequence. The regimes under which High-Low and Low-High (stress/strain) sequences are investigated should be specified clearly, (eg. High-Low stress/strain with both loadings in the EDF range, or a case where High stress/strain is in the PDF range and Low stress/strain is in the EDF range and vice versa) as it can be appreciated that the mechanisms governing fatigue behaviour differ under varying regimes. This paper aims to highlight the importance of specifying regimes under which multilevel loadings are conducted and present results on the interaction between PDF and EDF in 6061T6-aluminium alloy.

MATERIAL AND EXPERIMENTAL PROCEDURE

6061T6-aluminium alloy was used for fatigue testing. Hourglass shaped specimens were machined from cold rolled round bars in as-received condition having a nominal diameter of 6.35 mm and a gauge length of 31.75 mm. Mechanical polishing was carried out with No .400 and No. 1000 emery paper followed by finer grade EPA 1200 and EPA 2400 silicon carbide paper until visible machining marks were removed to give a smooth mirror-like surface finish. Tables 1 and 2 list the chemical composition and mechanical properties for 6061T6-aluminium alloy respectively.

TABLE 1
CHEMICAL COMPOSITION (% WT) OF 6061T6-ALUMINIUM ALLOY

Si 0.4-0.8	Fe 0.7 max	Cu 0.15-0.4	Mn 0.15 max	Mg 0.8-1.2
Cr 0.04-0.35	Zn 0.25 max	Ti 0.15	Others 0.05 max each, 0.15 max total	
Al remaining				

TABLE 2
MECHANICAL PROPERTIES OF 6061T6-ALUMINIUM ALLOY OBTAINED UNDER A TENSILE STRAIN RATE OF 0.001 S-1 OR 6%/MIN

Material	Yield Strength at 0.2% offset	Ultimate Tensile Strength	Young's Modulus	Elongation
6061T6 Al	295 MPa	324 MPa	68.3 GPa	19.0 %

Specimens were first exposed to various degrees of either PDF or EDF before cycling at PDF or EDF conditions to fracture. PDF was carried out at 1.0% and 0.6% strain amplitude, while EDF was conducted at 0.4% and 0.3% and strain amplitude. All tests were performed in push-pull mode uniaxial fatigue under strain controlled zero mean strain conditions.

EXPERIMENTAL RESULTS AND DISCUSSION

Classification of PDF and EDF

Traditionally, the most reliable method for defining the boundary between LCF and HCF was to determine transition life N_t, from the parameters obtained by fitting strain/life trends to the Coffin-Manson relationship. Fatigue lives less than N_t were classified as LCF while fatigue lives greater than N_t were considered as HCF. The terms LCF and HCF are abandoned by the present authors in favour of more precise terms namely PDF and EDF respectively, since for fatigue lives less than N_t (i.e. PDF), plastic strain contribution to total strain is larger than elastic strain while for fatigue lives greater than N_t (i.e. EDF), elastic strain contribution to total strain is larger than plastic strain. However, it was later found, that using the Coffin-Manson approach to define PDF and EDF is inadequate since EDF close to N_t still involves considerable plastic strain; enough to induce mean stress effects during multilevel loading, a characteristic which is only supposedly inherent in

PDF. Hence, an alternative method for classifying PDF and EDF is required. It is proposed that the boundary between PDF and EDF be represented by the cyclic yield strain determined by implementing a 0.05% offset to the cyclic stress-strain curve, similar to the 0.2% strain offset method used to determine the yield point for monotonic loading. A 0.2% strain offset was not used in this case as it was discovered that it too yielded too much plastic strain for elastic conditions to prevail. Cyclic yield strain was determined to be 0.46% meaning that fatigue strain amplitudes < 0.46% are classified as EDF while any amplitudes greater are considered as PDF.

PDF/EDF interaction

Results for both High(PDF)-Low(EDF) and Low(EDF)-High(PDF) loading sequences are summarised in Table 3 while the overall fatigue life trends are illustrated in Figures 1 and 2 respectively.

TABLE 3

AVERAGE TOTAL FATIGUE LIFE CYCLES AFTER PDF-EDF AND EDF-PDF INTERACTION

Sequence type*	% of initial PDF life exposure						
	0	17.0	34.0	51.1	68.1	100	-
PDF (1.0%) – EDF (0.3%)	39426	14653	13028	9930	7475	176	-
	% of initial EDF life exposure						
	0	5.1	12.9	25.6	40.9	63.4	100
EDF (0.3%) – PDF (1.0%)	176	2187	5234	10298	16398	25146	39426

*Numbers in brackets denote strain amplitudes at which fatigue was conducted

Figure 1 shows that a High(PDF)-Low(EDF) loading sequence will result in overall fatigue lives being less than Palmgren-Miner predictions. On the other hand, a Low(EDF)-High(PDF) sequence appears to conform rather well with Palmgren-Miner predictions and doesn't seem to show much interaction effect (Figure 2). However, when results for both load sequences are plotted in a cycle ratio plot (Figure 3), the interaction effects between PDF and EDF become increasingly evident. Cycle ratio accumulation trends seen in Figure 3 conforms to typical trends observed for High-Low (stress/strain) and Low-High (stress/strain) 2-step tests in that a High(PDF)-Low(EDF) sequence yields cycle ratio summations <1 while Low(EDF)-High(PDF) a sequence results in cycle ratio summations >1.

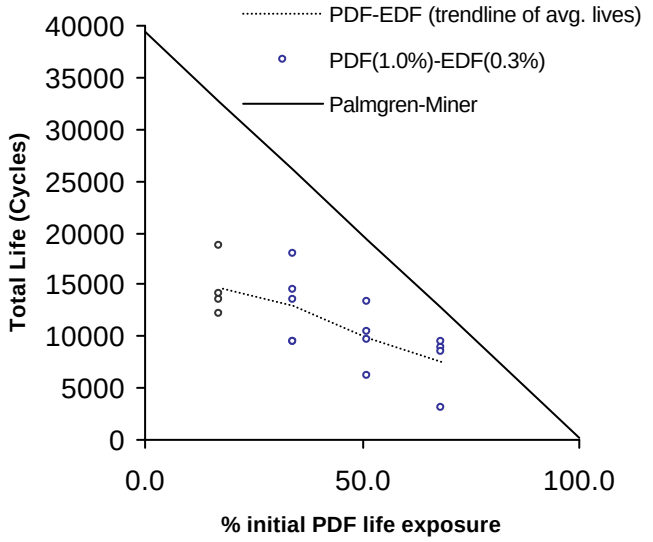

Figure 1: Fatigue life trend for High(PDF)-Low(EDF) interaction

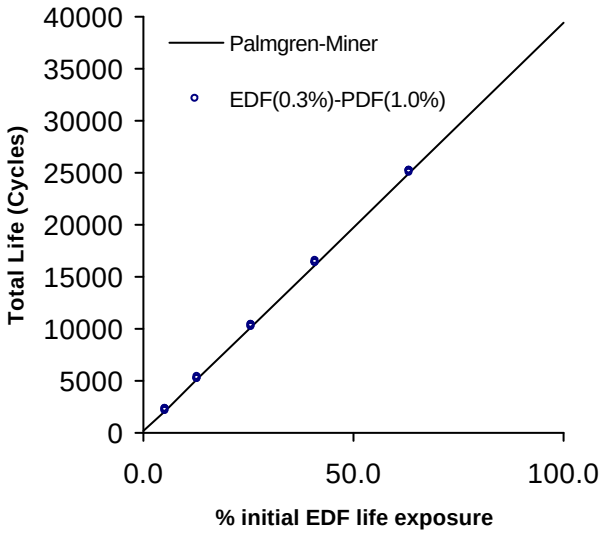

Figure 2: Fatigue life trend for Low(EDF)-High(PDF) interaction

Numerous "damage" theories have been proposed to take into account the sequence effects observed for multi-step load sequences, of which the crack growth approach first adopted by Zachariah and Miller [7] is favoured.

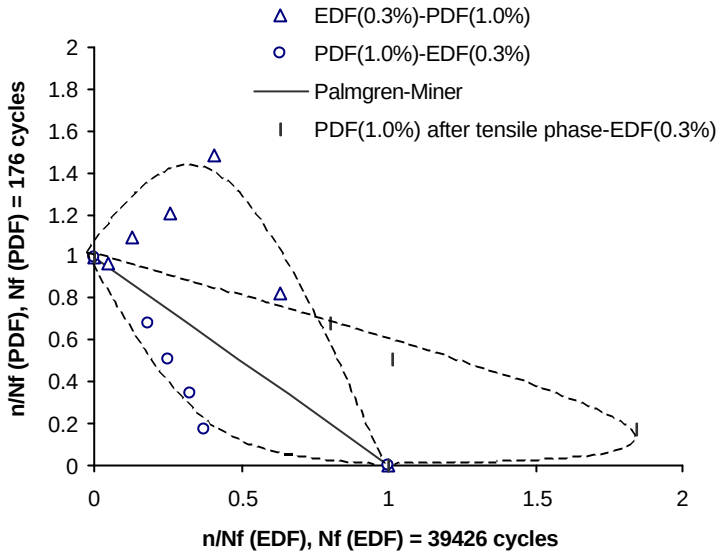

Figure 3: Cycle ratio accumulation for both PDF-EDF and EDF-PDF interaction.

Consider a fatigue crack growth behaviour for two different strain amplitudes, $_1$ and $_2$ presented in Figure 4 where a_o is the initial defect size, a_t is the transition crack size and a_f is the final crack length at complete fracture. It can be seen from Figure 4 that both a_t and the fraction of total fatigue life spent on stage II crack propagation increases with increasing strain amplitudes. As an example, in a High-Low sequence, assuming that a fraction (X_1) of fatigue life at $_1$ is initially applied before changing to $_2$, Palmgren-Miner rule predicts that the fraction of fatigue life remaining at $_2$ is $1-X_1$. According to the fatigue crack growth curve for $_1$, cyclic fatigue for X_1 fraction of life generates a fatigue crack of length, a_1. Assuming that the crack continues to grow from a_1 when stress amplitude is changed from $_1$ to $_2$, one finds that a crack length of a_1 corresponds to a fraction life X_2 at $_2$, which is $>X_1$, meaning that the actual fatigue life remaining is $1-X_2$ instead of $1-X_1$ and the summation of cycle ratios is <1. Conversely, in a Low-High loading sequence, if Y_2 fraction of fatigue life at $_2$ is applied, a crack corresponding to a length a_2 is generated. At $_1$, a_2 corresponds to life fraction Y_1 which is $< Y_2$, suggesting that the actual fatigue life remaining $1-Y_1$, is $> 1-Y_2$ and the summation of cycle ratios is >1.

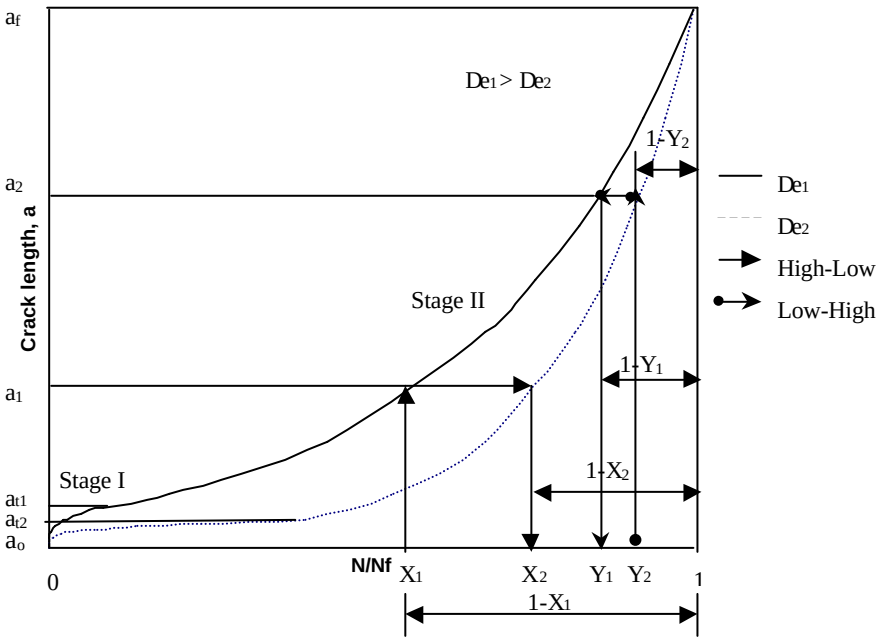

Figure 4: Fatigue crack growth behaviour at different strain amplitudes.

While the above model may help explain sequence effects and fatigue trends in most multilevel loading cases, certain limitations have to be highlighted to ensure that this model is used discriminately. Firstly, the model does not take into account important crack growth factors such as crack closure, residual stress and

mean stress effects. Hence, one would be expect discrepancies between fatigue accumulation trends rationalised using the above model and trends obtained experimentally to occur, especially in cases where mean stress, residual stress and closure effects are significant.

Significance of proper PDF and EDF classification

As mentioned in the introductory note, accurate definition of PDF and EDF is important when investigating any form of multilevel loading conducted under strain control. A great majority of results presented in past literature on multilevel loading failed to recognise this importance and regimes under which multi-level fatigue was conducted were not specified. Specification of the type of fatigue (PDF or EDF) loading for the various levels of loading involved, provides a great deal of information regarding the possible mechanisms which may be responsible for the interaction effects observed.

Mean stresses induced by prior high plastic strain levels can have a prominent role in affecting overall fatigue lives. Analysis of mean stress changes during PDF(1.0%)-EDF(0.3%) interaction (Figure 5) shows that a substantial tensile mean stress is induced by prior straining at 1.0% amplitude. Mean stress relaxation during EDF is marginal and tensile mean stress persists over the remaining life of the specimen. Figure 6 shows the changes in mean stress when transition from PDF to EDF occurs after the tensile phase of initial PDF. In this case, compressive mean stress is induced on transition and again minimal mean stress relaxation occurs over EDF. As evidenced in Figure 3, 2-step fatigue conducted with similar strain amplitudes show significantly different cycle ratio accumulation trends depending on the nature in which initial PDF ends. i.e. if transition from PDF-EDF occurs after PDF compressive phase, tensile mean stress is induced and cycle ratio summations tend to be < 1. Conversely, if transition from PDF-EDF occurs after PDF tensile phase, compressive mean stress is induced and cycle ratio summations take on values > 1.

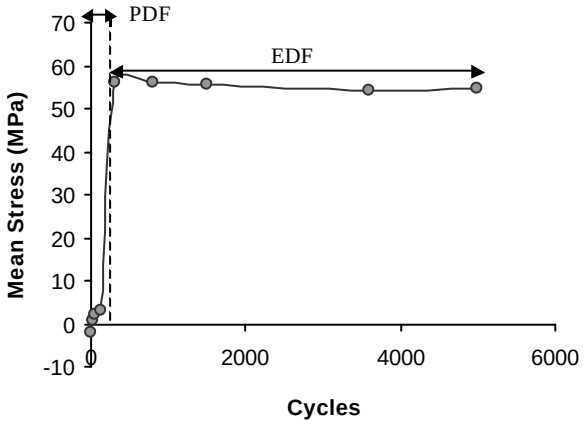

Figure 5: Mean stress changes for PDF(1.0%)-EDF(0.3%) interaction

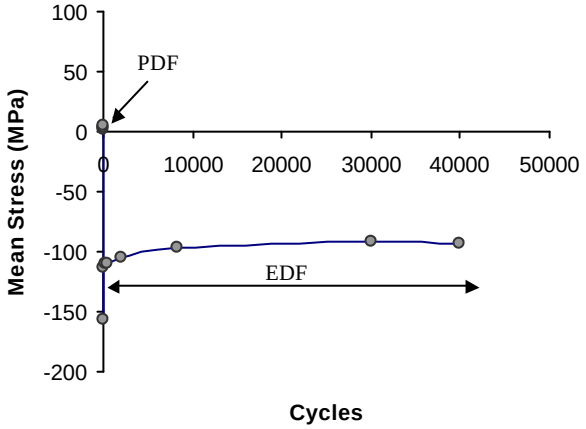

Figure 6: Mean stress changes for PDF(1.0%) after tensile phase-EDF(0.3%) interaction

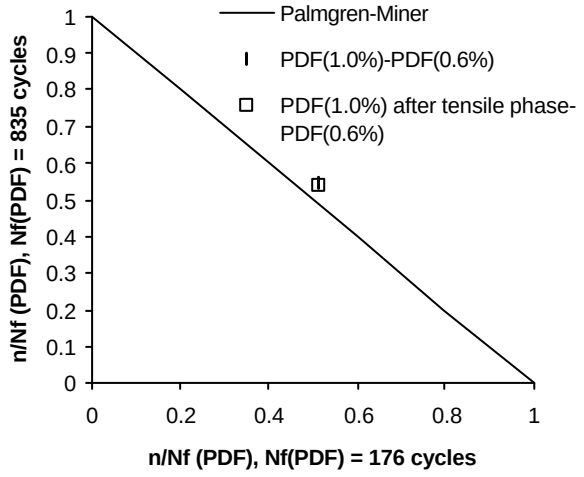

Figure 7: Cycle ratio accumulation for PDF(1.0%)-PDF(0.6%) interaction

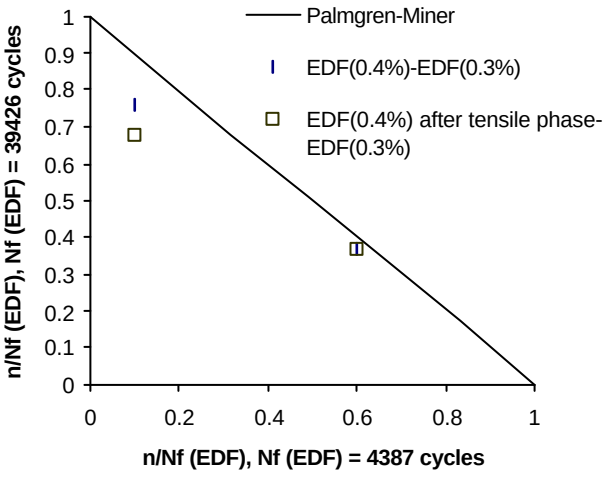

Figure 8: Cycle ratio accumulation for EDF(0.4%)-EDF(0.3%) interaction

Similar High-Low loading programs were implemented for PDF(1.0%)-PDF(0.6%) and EDF(0.4%)-EDF(0.3%) interactions. Figures 7 and 8 indicate that overall fatigue lives remain relatively unaffected regardless if initial strain level ended after a compressive or tensile phase. Zero mean stress is observed in the second stage of loading for all cases studied (Figures 9-12), further emphasising that mean stress plays no part in the interaction effects observed for PDF-PDF or EDF-EDF loading. Note that the negative mean stresses are observed in Figures 9-12 are the result of reduced crack opening tensile stress as rapid crack growth ensues on approach to fracture.

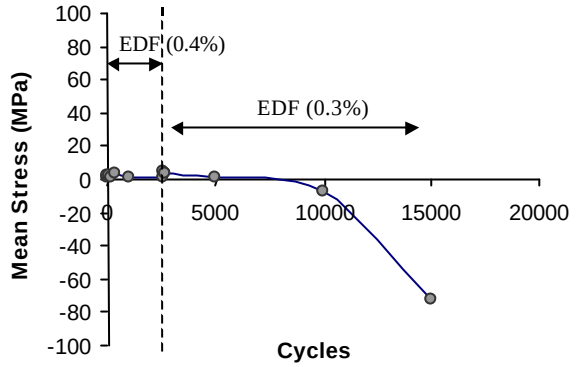

Figure 9: Mean stress changes for EDF(0.4%)-EDF(0.3%) interaction

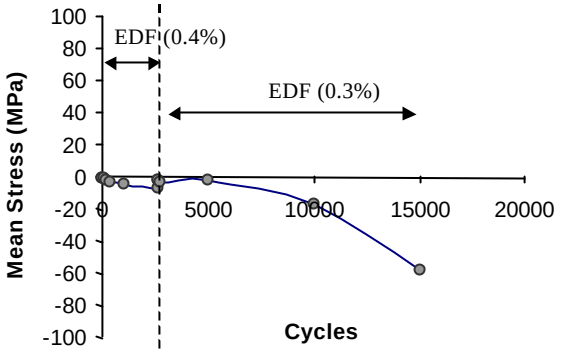

Figure 10: Mean stress changes for EDF(0.4%) after tensile phase-EDF(0.3%) interaction

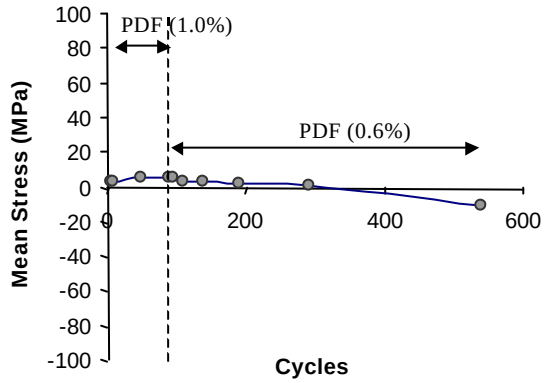

Figure 11: Mean stress changes for PDF(1.0%)-PDF(0.6%) interaction

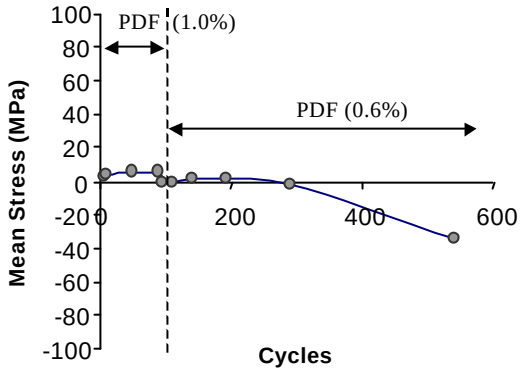

Figure 12: Mean stress changes for PDF(1.0%) after tensile phase-PDF(0.6%) interaction

CONCLUSION

1) High-Low sequences yield cycle ratio summations of <1 while Low-High sequences result in cycle ratio summations >1.
2) Mean stress effects are heavily involved in PDF-EDF interactions. Means stress induced (positive or negative) depends on the nature in which PDF ends (i.e. after compressive or tensile phase).
3) Mean stress plays no part in the interaction effects observed for PDF-PDF and EDF-EDF loading.
4) Proper definition and specification of the type of fatigue used in multilevel loading is important.

REFERENCES

1. Topper, T., Sandor, B., Morrow, J. (1969) *J. Mater*. 4, No.1, 189.
2. Thang, B., Dubuc, J., Bazergui, A., Biron, A. (1971) *J. Mater*. 6, 718.
3. Manson, S., Halford, G. (1986) *Eng. Fract. Mech*. 25, 539.
4. Bernard-Connolly, M., Thang, B., Biron, A. (1983) J. Eng. Mater. Tech.105, 188.
5. Skorupa, M. (1998) *Fatigue. Fract. Eng. Mater. Struc*. 21, 987.
6. Kujawski, D., Ellyin, F. (1988) *Int. J. Fract*.37, 263.
7. Miller, K., Zachariah, K. (1977) *J. Strain Analysis*, 12, No.4, 262.

ORAL REFERNCE: *0554*

PLASTIC-DAMAGE MODEL FOR STRESS-STRAIN BEHAVIOR OF SOILS

N. A. Al-Shayea[1], K. R. Mohib[1], and M. H. Baluch[1]

[1] Department of Civil Engineering, KFUPM, Dhahran 31261, Saudi Arabia

ABSTRACT

This paper presents a constitutive model for soil, which combines plasticity with damage mechanics to simulate the stress-strain behavior. This model is primarily suitable for soil types that exhibit a post-peak strain-softening behavior, like dense sand and stiff clay. The post-peak stress drop is captured by the elasto-damage formulation, while the plasticity is superimposed beyond the elastic range. The total strain increment is composed of elasto-damage strain increment and plastic strain increment. The elasto-damage strain increment is found using the elasto-damage formulation, while the plastic strain increment is found as a function of damage strain. To calibrate this model, Triaxial tests were conducted on cohesive and cohesionless soils, to obtain the model parameters. The model was coded in computer programs to simulate the stress-strain behavior of soils. The model was verified and found to predict the response of geomaterials well.

Key words: Damage mechanics, soil plasticity, strain softening, confining pressure.

INTRODUCTION

A plasto-damage model was developed for stress-strain behavior of cohesive and non-cohesive soils. The model was customized for the case of conventional triaxial compression (CTC), because of the abundant use of this test for determination of soil strength. Dense soils investigated in this work have damage effect, which is the degradation in material compliance, along with the plasticity effect, which is the irrecoverable permanent deformation. The elasto-damage component of the strain was obtained from the elasto-damage formulation derived for the CTC test. The post-peak stress-drop was also picked by the damage formulation. The plastic strain was taken as some factor times the damage strain. The total strain increment ($d\varepsilon$) is composed of elastic increment ($d\varepsilon^e$), damage increment ($d\varepsilon^d$), and plastic increment ($d\varepsilon^p$); i.e., $d\varepsilon = d\varepsilon^e + d\varepsilon^d + d\varepsilon^p$.

Analytical formulation was carried out to obtain the plasto-damage stress-strain behavior. Also, experimental program was conducted on two different types of soil to find model parameters. Furthermore, computer programs were developed based on the analytical formulation to simulate the soil behavior.

LITERATURE REVIEW

The theory of continuum damage mechanics (CDM) proposed by Kachanov [1], has been applied successfully to different materials, and is used to predict both strain-hardening and strain-softening type of behaviors. The damage phenomenon is explained in terms of damage variable (ω_n) associated with the normal $\vec{n}$, represents the area of the cracks and cavities per unit surface in a plane perpendicular to $\vec{n}$. Therefore, $\omega_n = 0$ corresponds to the undamaged state, $\omega_n = 1$ corresponds to the rupture of the element in two parts; and $0 < \omega_n < 1$ characterizes the occurrence of damage.

Chow [2] presented a modified damage effect tensor $\widetilde{M}(D)$ for the effective stress equations to take into account the effect of anisotropic material damage. Their model was applied on metals. Chow [3] developed a generalized damage characteristic tensor ($\widetilde{J}$), to characterize anisotropic damage evolution in combination with plasticity.

Sauris [4] presented a damage model for monotonic and cyclic loading of concrete. The compliance tensor presented for stress strain relationship was dependent on accumulated damage. Damage evolution was obtained by using a loading surface (f), a bounding surface (F), and a limit fracture surface (f_o); all defined in terms of the thermodynamic force conjugates of the damage variables. The model was applied for the case where the principal stresses and the strain axes coincided and did not rotate as the material deformed.

Abu-Labdeh [5] presented plasticity damage model for concrete under cyclic multi-axial loading. The model was based on bounding surface concept and combined plastic deformations with deformations due to damage. The total strain increment ($d\varepsilon$) was divided into elastic strain increment ($d\varepsilon^e$), damage strain increment ($d\varepsilon^d$) and plastic strain increment ($d\varepsilon^p$). Crouch [6] presented a constitutive model, which treated clays, silts, and sand in their loose and dense state under both monotonic and complex stress paths.

Karr [7] presented brittle damage model for rock. In their model, the effect of material degradation on failure mechanism of brittle damage materials was investigated. Gupta [8] presented a model for compressive failure of rocks via process of shear faulting. The model presented the progressive growth of damage. Khan [9] proposed a constitutive model for concrete based on CDM, using the damage-effect tensor ($\widetilde{M}$) with damage magnification factor α and β for tension and compression, respectively. The bounding surface concept, as introduced by Dafalias [10], was used for the constitutive relationship and evolution of damage.

DAMAGE FORMULATION FOR CTC

For the case of CTC test, $\sigma_2 = \sigma_3 = \sigma_{cell}$ = constant, and the deviator stress in the axial direction ($\Delta\sigma_1$) is changing. This case reduces to a uniaxial case. The deviator part of the of the stress vector, causing the shearing failure in the cylindrical soil specimen, is given as:

$$\sigma_{deviator} = \begin{bmatrix} \Delta\sigma_1 & 0 & 0 \end{bmatrix}^T \tag{1}$$

For CTC test, the compliance and stiffness terms for i = j = 1, with $\omega_1 = 0$ and $\omega_2 = \omega_3 = \omega$, are:

$$\widetilde{C}_{11} = \frac{1}{E_o(1-\beta\omega)^4}, \quad \text{or} \qquad \widetilde{D}_{11} = E_o(1-\beta\omega)^4 \tag{2}$$

where, E_o is the initial modulus of elasticity, and β is the peak strength factor or damage magnification factor. The strain energy density (ρW) for the deviator part of the CTC test is:

$$\rho W = \frac{1}{2}\{\sigma_i\}^T\left[\widetilde{C}_{ij}\right]\{\sigma_j\} = \frac{1}{2}\Delta\sigma_1^2\widetilde{C}_{11}^2 = \frac{1}{2}\frac{\Delta\sigma_1^2}{E_o}\left[\frac{(1-\beta\omega_1)^2}{(1-\beta\omega_2)^2(1-\beta\omega_3)^2}\right] \tag{3}$$

where, $\widetilde{C}_{ij}$ = effective compliance matrix, inverse of the effective stiffness matrix $\widetilde{D}_{ij}$, and

$\Delta\sigma_1$ = $\varepsilon_1 E_o \dfrac{(1-\beta\omega_2)^2(1-\beta\omega_3)^2}{(1-\beta\omega_2)^2}$

The thermodynamic force conjugates (R_i) can be obtained by taking the negative derivative of (ρW) with respect to (ω_n), which gives $R_1 = 0$ and $R_2 = R_3 = \varepsilon_1^2 E_o \beta(1-\beta\omega)^3$. R_1 is set to zero because a negative value of a thermodynamic force conjugate makes no physical sense and is not compatible with the thermodynamic conditions. This means that damage in this direction is also zero, i.e., $\omega_1 = 0$. For the CTC test, $\omega_2 = \omega_3 = \omega$, due to symmetry. The expression for strain energy release rate at onset of damage (R_o) is given as a function of $\Delta\sigma$, which is some percentage of the peak deviator strength ($\Delta\sigma_1$), according to:

$$R_o = \frac{\sqrt{2}\beta\Delta\sigma^2}{E_o} \tag{4}$$

The expression for critical value of strain energy release rate at failure (R_c) is given as:

$$R_c = \frac{\sqrt{2}\beta\Delta\sigma_1^2}{E_o(1-\beta\omega)^5} \tag{5}$$

For the deviatoric stress increment in axial direction is:

$$d\sigma_1 = \widetilde{D}_{11}d\varepsilon_1 - \varepsilon_1\frac{\partial\widetilde{D}_{11}}{\partial\omega_k}\frac{\partial f}{\partial R_k}d\lambda \tag{6}$$

where, $d\lambda$ = $\dfrac{2\sqrt{2}\beta\varepsilon_1 E_o(1-\beta\omega)^3 d\varepsilon_1}{\left(H + 3\beta^2\varepsilon_1^2 E_o(1-\beta\omega)^2\right)}$,

H = $D\delta/\langle\delta_{in}-\delta\rangle$ = damage modulus,

δ = normalized distance between f and F surfaces,

δ_{in} = maximum distance between F and f_o surfaces, and

D = parameter used to control the shape of the peak.

Substituting all the terms in Eqn. 6, the final form of the incremental stress for a strain-controlled formulation becomes:

$$d\sigma_1 = \left[E_o(1-\beta\omega)^4 - \frac{8\beta^2\varepsilon_1^2 E_o^2(1-\beta\omega)^6}{H + 3\beta^2\varepsilon_1^2 E_o(1-\beta\omega)^2}\right]d\varepsilon_1 \tag{7}$$

For the determination of the elasto-damage stress, Eqn. 7 was coded in a FORTRAN program, with inputs including the axial elasto-damage strain increment.

EXPERIMENTAL PROGRAM

In order to calibrate the model and to determine its parameters, an extensive experimental program was conducted. Two different types of soil materials were used, i.e., cohesive and non-cohesive soil (marl and sand). Both soils were prepared at high density to exhibit post-peak strain-softening behavior. Marl was tested at maximum value of dry density of 1.526 g/cm^3 and at optimum moisture content of 27.12% obtained form the compaction test. The minimum and maximum densities of sand were 1.86 g/cm^3 and 1.609 g/cm^3, respectively. Marl samples were prepared at the maximum density and optimum moisture content using in five layers under static compaction, to get uniform sample. Sand was tested at a density of 1.853 g/cm^3, which corresponds to a relative density of 98%. Pluviation technique was used for preparing sand samples. Unconsolidated drained triaxial compression tests were performed at cell pressures of 100, 200, 300, 400, and 500 KPa, for both soils. Testing apparatus were calibrated to ensure accurate measurements of stresses and strains.

RESULTS AND DISCUSSIONS

Elasto-damage parameters

Mechanical properties

The shear strength parameters, cohesion (c) and angle of internal friction (ϕ), were determined using the peak deviator stress value ($\Delta\sigma_1$) at different cell pressure values, by plotting Mohr stress circles and Mohr-Coulomb failure envelopes for both soils. For marl $\phi = 33.73°$ and c = 335 KPa. For sand $\phi = 42.96$ ° and $c = 0$. The initial modulus of elasticity (E_o) was obtained as the slope of the initial straight-line portion of the experimental stress-strain curve, for various values of cell pressure (σ_3). Expressions for E_o vs. σ_3 normalized to atmospheric pressure (P_a=101.325 KPa) are:

$$E_o = 682.5 P_a \left(\sigma_3 / P_a\right)^{0.238156} \quad \text{, for marl} \tag{8}$$

$$E_o = 1176.06 P_a \left(\sigma_3 / P_a\right)^{0.862364} \text{, for sand} \tag{9}$$

Strain Energy release rates

R_o was calculated using Eqn. 4 at 20% and 30% of the peak deviator stress value for marl and sand, respectively. This was decided on the basis of the experimental stress-strain data. The values of R_c were calculated using Eqn. 5, and found to be 0.1 and 0.2 KN.m/m^3 for marl and sand, respectively. These are the minimum values of R_c calculated at different cell pressures.

Peak factors (D) and (β)

The value of the peak shape factor (D) for marl and sand was found by trial and error, to be 0.0001 KN.m/m^3. The value of peak deviator stress factor (β) was calculated by matching the peak of the predicted stress-strain curve with the experimental curve. Figure 1-a shows the variation of β vs. peak deviator stress ($\Delta\sigma_1$) for marl and sand, which can be expressed as:

$$\beta = 0.5697 / \left(\Delta\sigma_1\right)^{0.916701} \quad \text{, for marl} \tag{10}$$

$$\beta = 0.87782 / \left(\Delta\sigma_1\right)^{0.785059} \quad \text{, for sand} \tag{11}$$

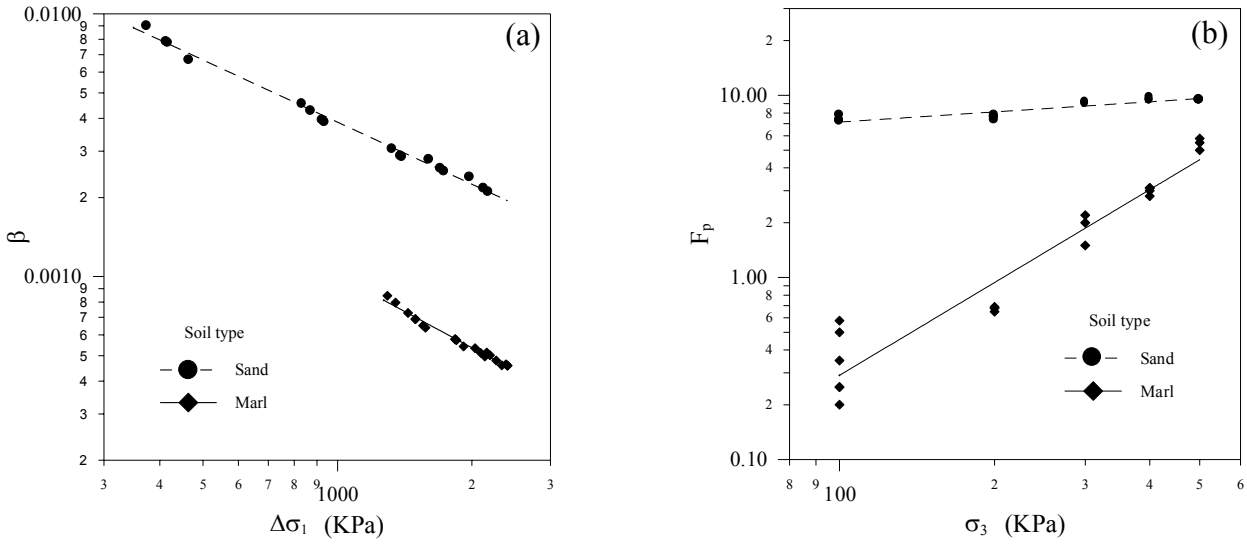

Figure 1: Model parameters: (a) β vs. $\Delta\sigma_1$, and (b) F_p vs. σ_3

Plastic strain

Plastic strain increment ($d\varepsilon^p$) was calculated as a factor (F_p) times the damage strain ($d\varepsilon^d$). Figure 1-b shows the variation of the plastic strain factor (F_p) with cell pressure (σ_3) for marl and sand, with the expressions:

$$F_p = 1.187 \times 10^{-4} (\sigma_3)^{1.694} \quad \text{, for marl} \tag{12}$$

$$F_p = 3.055 \times (\sigma_3)^{0.1845} \quad \text{, for sand} \tag{13}$$

The total strain was obtained by adding the plastic strain to the elasto-damage strain. Figure 2-a shows a comparison between the experimental and predicted stress-strain curve for sand at σ_3 = 200 KPa. It is clear that without the plastic strain component, the two curves are far apart from each other on the strain axis. After adding the plastic strain, the elasto-plasto-damage prediction, matches the experimental curve very closely. Figure 2-b shows a comparison between the experimental and the predicted stress-strain curves by this model at different cell pressures for sand. Similar curves were obtained for marl.

CONCLUSIONS

A new plasto-damage model is presented for the stress-strain behavior of dense soils. The model is suitable for post-peak strain-softening stress-strain behavior of soil. The model combines elasto- damage strain and plastic strain to determine the total strain. The predictions are excellent and able to pick all the features of the stress-strain behavior. It is observed that the model is good for both cohesive and non-cohesive types of soils. This model is very simple and needs few numbers of parameters to be calibrated. Only conventional triaxial test data is required, with no additional experimental data required for the calculation of plastic strain.

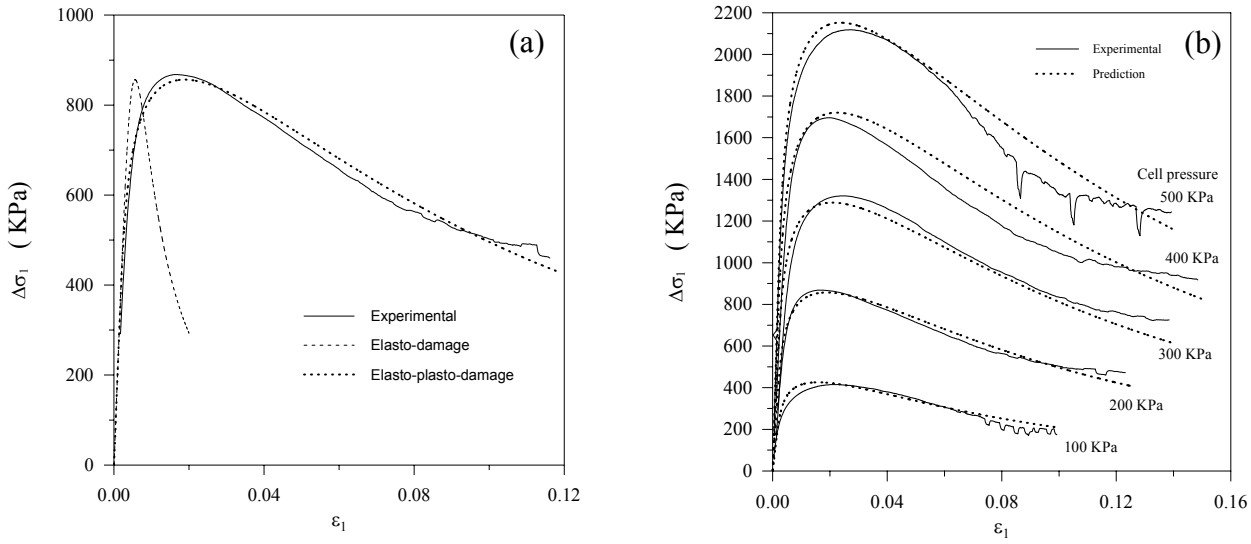

Figure 2: Comparison of stress-strain curves (a) Effect of Plastic strain, (b) curves for sand

ACKNOWLEDGEMENT

The authors acknowledge the support of King Fahd University of Petroleum and Minerals for providing computing and laboratory facilities. The help of Dr. Asad-ur-Rehman Khan is greatly appreciated.

REFERENCES

1. Kachanov, L. M. (1958). *Time of the Rupture Process under Creep condition*: Izv Akad Nauk, U.S.S.R, Otd. Tekh. Nauk,Vol. 8, pp. 26-31.
2. Chow, C.L. and Wang, J. (1987). *An Anisotropic Theory of Elasticity for Continuum Damage Mechanics: International Journal of Fracture*, pp. 3-16.
3. Chow, C. L. and Wang, J. (1988). *A finite Element Analysis of Continuum Damage Mechanics for Ductile Fracture: Engineering Fracture Mechanics*, pp. 83-102.
4. Sauris, W., Ouyang, C., and Ferdenando, V. M. (1990). *Damage Model for Cyclic Loading of Concrete: Journal of Engineering Mechanics and Physics*, pp. 1020-1035.
5. Abu-Lebdeh, T. M. and Voyiadjis, G. Z. (1993). *Plasticity Damage Model for Concrete under Cyclic Multi-axial Loading: Journal of Engineering Mechanics*, pp. 1465-1484.
6. Crouch, R. S. and Wolf J. P., (1995). *On a Three-Dimensional Anisotropic Plasticity Model for Soil: Geotechnique*, 45(2), pp. 301-305.
7. Karr, D. G., Wimmer, S. A., and Sun, X. (1996). *Shear Band Initiation of Brittle Damage Materials: International Journal of Damage Mechanics*, Vol. 5, pp. 403-421.
8. Gupta, V., and Bergstrom, J. S. (1997). *Compressive Failure of Rocks: International Journal of Rock mechanics and Mining Science*, Vol. 34, No.3-4.
9. Khan, A. R., Al-Gadhib, A. H. and Baluch, M. H. (1998). *An Elasto Damage Constitutive Model for High Strength Concrete: Proceedings of the Euro-C 1998 Conference on Computational Modeling of Concrete Structures*, Austria, pp. 133-142.
10. Dafalias, Y. F., and Popov, E. P. (1977). *Cyclic Loading for Material with a Vanishing Elastic Region: Nuclear Engineering Design*, Vol. 44, pp. 293-302.